A Wiley-Science Wise Co-Publication

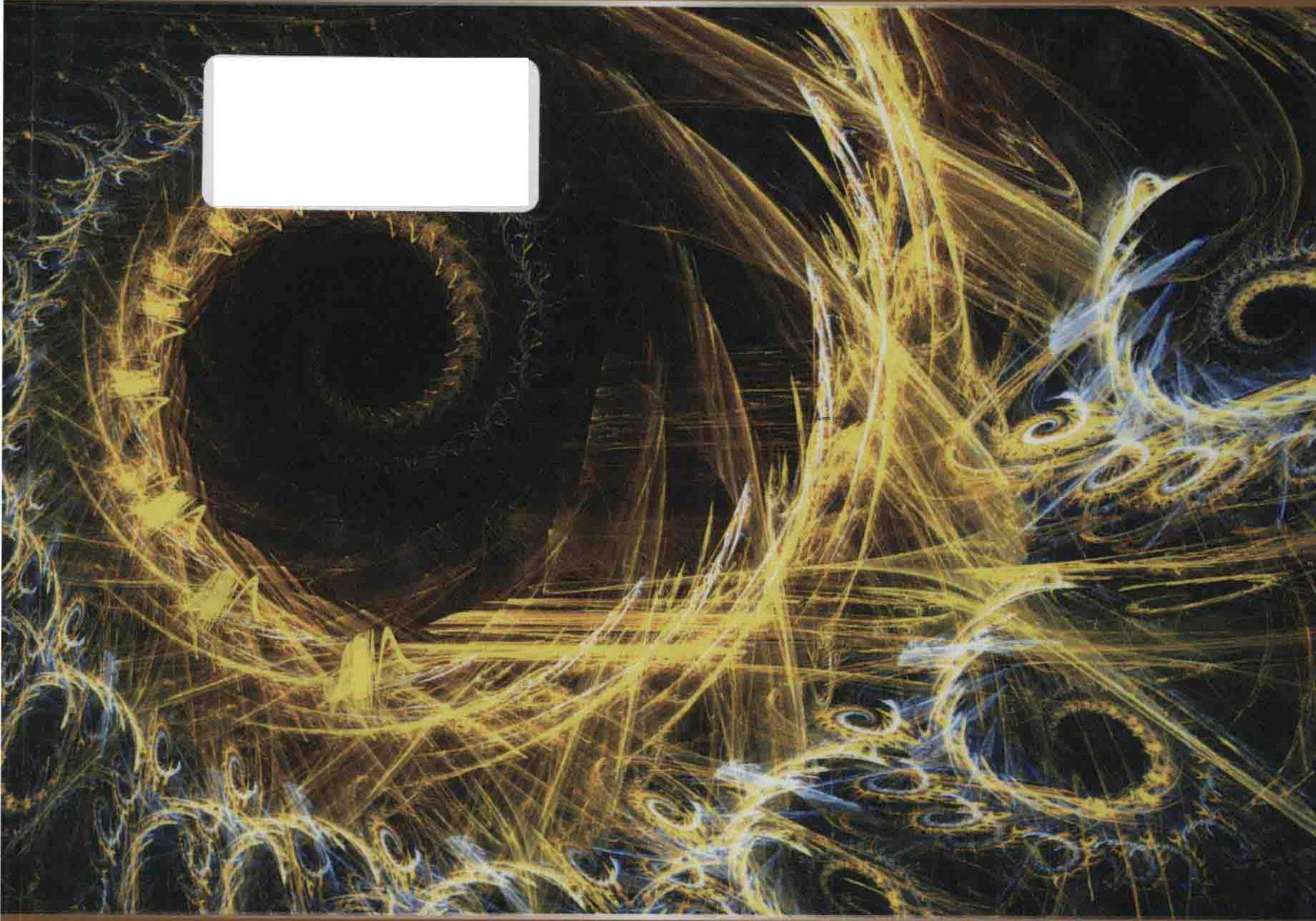

Photonics Volume 4

BIOMEDICAL PHOTONICS, SPECTROSCOPY, AND MICROSCOPY

David L. Andrews

SCIENCE WISE
PUBLISHING

WILEY

Discusses the basic physical principles underlying biomedical photonics, spectroscopy, and microscopy

This volume discusses biomedical photonics, spectroscopy, and microscopy, the basic physical principles underlying the technology and its applications. The topics discussed in this volume are: Fluorescence; Single Molecule Detection and Spectroscopy; Resonance Energy Transfer; Biophotonics of Photosynthesis; Optical Sectioning Microscopy and Biological Imaging; Cell Handling and Sorting; Tissue Polarimetry; Optical Waveguide Biosensors; Light Propagation in Highly Scattering Turbid Media; Photodynamic Therapy; Imaging and Probing Cells beyond the Diffraction Limit; and Ophthalmic Technology.

- Comprehensive and accessible coverage of the whole of modern photonics
- Emphasizes processes and applications that specifically exploit photon attributes of light
- Deals with the rapidly advancing area of modern optics
- Chapters are written by top scientists in their field

Written for the graduate-level student in physical sciences; industrial and academic researchers in photonics, graduate students in the area; college lecturers, educators, policymakers, consultants, scientific and technical libraries, government laboratories, NIH.

DAVID L. ANDREWS leads research on fundamental molecular photonics and energy transport, optomechanical forces, and nonlinear optical phenomena. He has over 300 research papers and a dozen of books to his name—including the widely adopted textbook, *Lasers in Chemistry*. The current focus of his research group is on optical vortices, novel mechanisms for optical nanomanipulation and switching, and light harvesting in nanostructured molecular systems. The group enjoys strong international links, particularly with groups in Canada, Lithuania, New Zealand, and the United States. Andrews is a Fellow of the Royal Society of Chemistry, a Fellow of the Institute of Physics, and a Fellow of SPIE, the international society for optics and photonics.

www.wiley.com

WILEY | SCIENCE WISE PUBLISHING

Also available as an e-book

ISBN 978-1-118-22555-4

9 781118 225554

Andrews

Photonics Volume 4

Biomedical Photonics, Spectroscopy, and Microscopy

WILEY

PHOTONICS

Scientific Foundations, Technology and Applications

Biomedical Photonics, Spectroscopy, and Microscopy

Volume IV

Edited by

DAVID L. ANDREWS
School of Chemical Sciences
University of East Anglia
Norwich, UK

WILEY

Copyright © 2015 by John Wiley & Sons, Inc. All rights reserved.

Published by John Wiley & Sons, Inc., Hoboken, New Jersey.
Published simultaneously in Canada.

No part of this publication may be reproduced, stored in a retrieval system, or transmitted in any form or by any means, electronic, mechanical, photocopying, recording, scanning, or otherwise, except as permitted under Section 107 or 108 of the 1976 United States Copyright Act, without either the prior written permission of the Publisher, or authorization through payment of the appropriate per-copy fee to the Copyright Clearance Center, Inc., 222 Rosewood Drive, Danvers, MA 01923, (978) 750-8400, fax (978) 750-4470, or on the web at www.copyright.com. Requests to the Publisher for permission should be addressed to the Permissions Department, John Wiley & Sons, Inc., 111 River Street, Hoboken, NJ 07030, (201) 748-6011, fax (201) 748-6008, or online at http://www.wiley.com/go/permissions.

Limit of Liability/Disclaimer of Warranty: While the publisher and author have used their best efforts in preparing this book, they make no representations or warranties with respect to the accuracy or completeness of the contents of this book and specifically disclaim any implied warranties of merchantability or fitness for a particular purpose. No warranty may be created or extended by sales representatives or written sales materials. The advice and strategies contained herein may not be suitable for your situation. You should consult with a professional where appropriate. Neither the publisher nor author shall be liable for any loss of profit or any other commercial damages, including but not limited to special, incidental, consequential, or other damages.

For general information on our other products and services or for technical support, please contact our Customer Care Department within the United States at (800) 762-2974, outside the United States at (317) 572-3993 or fax (317) 572-4002.

Wiley also publishes its books in a variety of electronic formats. Some content that appears in print may not be available in electronic formats. For more information about Wiley products, visit our web site at www.wiley.com.

Library of Congress Cataloging-in-Publication Data applied for.

Printed in the United States of America

10 9 8 7 6 5 4 3 2 1

PHOTONICS

LIST OF CONTRIBUTORS

Thomas Aabo DTU Fotonik, Department of Photonics Engineering, Technical University of Denmark, Kgs. Lyngby, Denmark

R. R. Alfano Institute for Ultrafast Spectroscopy and Lasers (IUSL), City College of New York, New York, NY, USA; and Physics Department, City College of New York, New York, NY, USA

David L. Andrews School of Chemistry, University of East Anglia, Norwich Research Park, Norwich, Norfolk, UK

Pinar Avci Wellman Center for Photomedicine, Massachusetts General Hospital, Boston, MA, USA; and Department of Dermatology, Harvard Medical School, Boston, MA, USA

Andrew Bañas DTU Fotonik, Department of Photonics Engineering, Technical University of Denmark, Kgs. Lyngby, Denmark

David J. S. Birch Photophysics Group, Department of Physics, Strathclyde University, Glasgow, UK

David S. Bradshaw School of Chemistry, University of East Anglia, Norwich Research Park, Norwich, Norfolk, UK

Yu Chen Photophysics Group, Department of Physics, Strathclyde University, Glasgow, UK

Christopher A. Clark School of Optometry, Indiana University, Bloomington, IN, USA

Antonello De Martino Ecole Polytechnique, Palaiseau, France

Rayomond Dinshaw Department of Chemistry, Institute for Optical Sciences and Centre for Quantum Information and Quantum Control, University of Toronto, Toronto, ON, Canada

Daphné Duval NanoBiosensors and Bioanalytical Applications Group, Centro Investigacion Biomedica en Red – Bioingenieria, Biomateriales y Nanomedicina, Consejo Superior de Investigaciones Cientificas, Institut Catala de Nanociencia i Nanotecnologia, Bellaterra, Barcelona, Spain

Ann E. Elsner School of Optometry, Indiana University, Bloomington, IN, USA

S. K. Gayen Physics Department, City College of New York, New York, NY, USA

Rakkiyappan Chandran Wellman Center for Photomedicine, Massachusetts General Hospital, Boston, MA, USA; and Department of Dermatology, Harvard Medical School, Boston, MA, USA; and Amity Institute of Nanotechnology, Amity University, Noida, India

Nirmalya Ghosh Department of Physical Sciences, Indian Institute of Science Education and Research, Kolkata, India

John Girkin Biophysical Sciences Institute, Department of Physics, Durham University, Durham, UK

Jesper Glückstad DTU Fotonik, Department of Photonics Engineering, Technical University of Denmark, Kgs. Lyngby, Denmark

Michael R. Hamblin Wellman Center for Photomedicine, Massachusetts General Hospital, Boston, MA, USA; and Department of Dermatology, Harvard Medical School, Boston, MA, USA; and Harvard-MIT Division of Health Sciences and Technology, Cambridge, MA, USA

Thomas Huser Biomolecular Photonics, Department of Physics, University of Bielefeld, Bielefeld, Germany

Ryszard Jankowiak Department of Chemistry, Kansas State University, Manhattan, KS, USA; and Department of Physics, Kansas State University, Manhattan, KS, USA

Laura M. Lechuga NanoBiosensors and Bioanalytical Applications Group, Centro Investigacion Biomedica en Red – Bioingenieria, Biomateriales y Nanomedicina, Consejo Superior de Investigaciones Cientificas, Institut Catala de Nanociencia i Nanotecnologia, Bellaterra, Barcelona, Spain

Michel Orrit Institute of Physics, Leiden University, Leiden, The Netherlands

Darwin Palima DTU Fotonik, Department of Photonics Engineering, Technical University of Denmark, Kgs. Lyngby, Denmark

Olaf J. Rolinski Photophysics Group, Department of Physics, Strathclyde University, Glasgow, UK

Magesh Sadasivam Wellman Center for Photomedicine, Massachusetts General Hospital, Boston, MA, USA; and Department of Dermatology, Harvard Medical School, Boston, MA, USA; and Amity Institute of Nanotechnology, Amity University, Noida, India

Gregory D. Scholes Department of Chemistry, Institute for Optical Sciences and Centre for Quantum Information and Quantum Control, University of Toronto, Toronto, ON, Canada

Mark Schüttpelz Biomolecular Photonics, Department of Physics, University of Bielefeld, Bielefeld, Germany

Tyler G. St. Denis Wellman Center for Photomedicine, Massachusetts General Hospital, Boston, MA, USA; and Department of Chemistry, Columbia University, New York, NY, USA

Daniela Vecchio Wellman Center for Photomedicine, Massachusetts General Hospital, Boston, MA, USA; and Department of Dermatology, Harvard Medical School, Boston, MA, USA

Alex Vitkin Medical Biophysics and Radiation Oncology, University of Toronto, Toronto, ON, Canada

L. Wang Institute for Ultrafast Spectroscopy and Lasers (IUSL), City College of New York, New York, NY, USA

W. B. Wang Institute for Ultrafast Spectroscopy and Lasers (IUSL), City College of New York, New York, NY, USA; and Physics Department, City College of New York, New York, NY, USA

Valter Zazubovich Department of Physics, Concordia University, Montreal, QC, Canada

PREFACE

Since its inception, the term "photonics" has been applied to increasingly wide realms of application, with connotations that distinguish it from the broader-brush terms "optics" or "the science of light." The briefest glance at the topics covered in these volumes shows that such applications now extend well beyond an obvious usage of the term to signify phenomena or mechanistic descriptions involving photons. Those who first coined the word partly intended it to convey an aspiration that new areas of science and technology, based on microscale optical elements, would one day develop into a comprehensive range of commercial applications as familiar and distinctive as electronics. The fulfilment of that hope is amply showcased in the four present volumes, whose purpose is to capture the range and extent of photonics science and technology.

It is interesting to reflect that in the early 1960s, the very first lasers were usually bench-top devices whose only function was to emit light. In the period of growth that followed, most technical effort was initially devoted to increasing laser stability and output levels, often with scant regard for possibilities that might be presented by truly photon-based processes at lower intensities. The first nonlinear optical processes were observed within a couple of years of the first laser development, while quantum optics at first grew slowly in the background, then began to flourish more spectacularly several years later. A case can be made that the term "photonics" itself first came into real prominence in 1982, when the trade publication that had previously been entitled *Optical Spectra* changed its name to *Photonics Spectra*. At that time the term still had an exotic and somewhat contrived ring to it, but it acquired a new respectability and wider acceptance with the publication of Bahaa Saleh and Malvin Teich's definitive treatise, *Fundamentals of Photonics*, in 1991. With the passage of time, the increasing pace of development has been characterized by the striking progress in miniaturization and integration of optical components, paving the way for fulfilment of the early promise. As the laser industry has evolved, parallel growth in the optical fiber industry has helped spur the continued push toward the long-sought goal of total integration in optical devices.

Throughout the commissioning, compiling, and editing that have led to the publication of these new volumes, it has been my delight and privilege to work with many of the world's top scientists. The quality of the product attests to their commitment and willingness to devote precious time to writing chapters that glow with authoritative expertise. I also owe personal thanks to the ever-professional and dependable staff of Wiley, without whose support this project would never have come to fruition. It seems fitting that the culmination of all this work is a sequence of books published at the very dawning of the UNESCO International Year of Light. Photonics is shaping the world in which we live, more day by day, and is now ready to take its place alongside electronics, reshaping modern society as never before.

DAVID L. ANDREWS

Norwich, U.K., July 2014

CONTENTS

List of Contributors ix

Preface xiii

1 Fluorescence 1

David J. S. Birch, Yu Chen, and Olaf J. Rolinski

1.1 Introduction, 1
1.2 Spectra, 2
1.3 Quantum Yield, 6
1.4 Lifetime, 12
1.5 Quenching, 23
1.6 Anisotropy, 30
1.7 Microscopy, 38
1.8 Conclusions, 48
Acknowledgments, 48
References, 49

2 Single-Molecule Detection and Spectroscopy 59

Michel Orrit

2.1 Introduction, 59
2.2 Experimental Setups, 62
2.3 Fluorescence Spectroscopy, 66
2.4 Fluorescence Correlation Spectroscopy, 72
2.5 Fluorescence Excitation Spectroscopy, 78

2.6 Other Detection Methods, 86
2.7 Conclusion, 93
Acknowledgments, 94
References, 94

3 **Resonance Energy Transfer** 101
David L. Andrews, David S. Bradshaw, Rayomond Dinshaw, and Gregory D. Scholes

3.1 Introduction, 101
3.2 History of RET, 102
3.3 The Photophysics of RET, 103
3.4 Investigative Applications of RET in Molecular Biology, 113
3.5 The Role of RET in Light-Harvesting Complexes, 118
Acknowledgments, 122
References, 122

4 **Biophotonics of Photosynthesis** 129
Valter Zazubovich and Ryszard Jankowiak

4.1 Introduction, 129
4.2 Structure of Pigment–Protein Complexes and Structure–Function Relationships, 130
4.3 Key Concepts in Physics of Pigment–Protein Complexes, 133
4.4 Experimental Techniques, 141
4.5 Examples, 145
4.6 Conclusions, 156
Acknowledgments, 157
References, 157

5 **Optical Sectioning Microscopy and Biological Imaging** 165
John Girkin

5.1 Introduction and Background, 165
5.2 Confocal Imaging, 168
5.3 Nonlinear Microscopy, 172
5.4 Practical Implementation of Nonlinear Microscopy, 181
5.5 Recent Advances in Nonlinear Microscopy, 184
5.6 Widefield Optical Sectioning by Specialized Illumination Methods, 186
5.7 Summary, 190
References, 191

6 **Cell Handling, Sorting, and Viability** 197
Darwin Palima, Thomas Aabo, Andrew Bañas, and Jesper Glückstad

6.1 Handling Cells with Light, 198
6.2 Optical Sorting, 215
6.3 Cell Viability, 220
References, 230

7 Tissue Polarimetry **239**

Alex Vitkin, Nirmalya Ghosh, and Antonello de Martino

7.1 Introduction, 239
7.2 Polarized Light Fundamentals, 240
7.3 Instrumentation, 266
7.4 Forward Modeling and Testing in Phantoms, 282
7.5 Applications, 297
7.6 Conclusions and Outlook, 313
References, 314

8 Optical Waveguide Biosensors **323**

Daphné Duval and Laura M. Lechuga

8.1 Introduction, 323
8.2 Fundamentals of Label-Free Optical Waveguide Biosensing, 324
8.3 Surface Biofunctionalization, 328
8.4 Evaluation of Optical Biosensors, 331
8.5 Integrated Optical Waveguide-Based Biosensors, 334
8.6 Optical Fiber-Based Biosensors, 349
8.7 Lab-On-A-Chip Integration, 354
8.8 Summary, 357
References, 358

9 Light Propagation in Highly Scattering Turbid Media: Concepts, Techniques, and Biomedical Applications **367**

R. R. Alfano, W. B. Wang, L. Wang, and S. K. Gayen

9.1 Introduction, 367
9.2 Physics Behind Optical Imaging Through a Highly Scattering Turbid Medium, 369
9.3 Study of Ballistic and Diffused Light Components, 378
9.4 Photon-Sorting Gates, 384
9.5 Transition From Ballistic to Diffuse Imaging in Turbid Media, 402
9.6 Conclusion, 404
Acknowledgments, 404
References, 404

10 Photodynamic Therapy **413**

Rakkiyappan Chandran, Tyler G. St. Denis, Daniela Vecchio, Pinar Avci, Magesh Sadasivam, and Michael R. Hamblin

10.1 Historical Overview of PDT, 413
10.2 Introduction to PDT, 415
10.3 Photosensitizer Structure and Photophysical Properties, 418
10.4 Light Dosimetry and Photodynamic Therapy Light Sources, 422
10.5 Light-Based Strategies to Enhance PDT, 423
10.6 PDT Targeting and Nanotechnology, 425

10.7 PDT for Dermatology, 428
10.8 PDT for Oncology, 433
10.9 PDT for Infectious Disease, 435
10.10 PDT in Ophthalmology, 445
10.11 PDT and The Immune System, 446
10.12 Conclusion, 449
Acknowledgment, 449
References, 449

11 Imaging and Probing Cells Beyond the Optical Diffraction Limit 469
Mark Schüttpelz and Thomas Huser

11.1 The Quest for Achieving Optical Resolution Beyond ABBE'S Limit, 469
11.2 Stimulated Emission Depletion Microscopy, 474
11.3 Photoactivated Localization Microscopy and Stochastic Optical Reconstruction Microscopy, 477
11.4 Structured Illumination Microscopy, 483
11.5 Super-Resolution Optical Fluctuation Imaging and Other Approaches, 491
11.6 Outlook, 495
Acknowledgments, 496
References, 497

12 Technology 503
Ann E. Elsner and Christopher A. Clark

12.1 Basic Ocular Anatomy and Physiology, 503
12.2 Measurement Techniques, 514
12.3 Anterior Segment Diagnostics, Refractive Measurements, and Treatment, 522
12.4 Diagnostic Applications and Treatment of Posterior Segment, 529
References, 534

Index 543

1

FLUORESCENCE

DAVID J. S. BIRCH, YU CHEN, AND OLAF J. ROLINSKI
Photophysics Group, Department of Physics, Strathclyde University, Glasgow, UK

1.1 INTRODUCTION

Within the wide range of spectroscopic techniques facilitated by photonics, fluorescence sits alongside the likes of spectrophotometry, Raman, FTIR, circular dichroism, and ultrafast in providing complementary and unique information. Although fluorescence can hardly be called a new phenomenon, there can be little doubt that it continues to facilitate many important new observations and techniques across a whole range of disciplines. Just as photonics has become an enabling technology so too fluorescence has become an enabling phenomenon. Fluorescence has made, and continues to make, particular impact in the biosciences and in healthcare. This has been dramatically demonstrated in recent years by the key role played by fluorescence in the complete sequencing of the human genome and in the displacement of radioactive markers by fluorescence probes in disease diagnostics. Underpinning the impact of fluorescence is a research base founded upon the fact that the nanosecond timescales and nanometer distances, in which the properties of fluorescence can be influenced, are ideally matched to many physiological processes and structures.

Originating from a spin-allowed singlet–singlet transition, fluorescence has a much higher quantum yield and is usually easier to study than its photophysical counterpart, phosphorescence, which involves a spin-forbidden triplet–singlet transition. Reflecting its more generic usage, and greater range of materials and conditions that facilitate fluorescence, here we concentrate on fluorescence rather than phosphorescence. Fluorescence is traditionally associated with aromatic molecules, of which there is a vast number, but recently there has been the emergence of a whole new

---

Photonics: Scientific Foundations, Technology and Applications, Volume IV, First Edition.
Edited by David L. Andrews.
© 2015 John Wiley & Sons, Inc. Published 2015 by John Wiley & Sons, Inc.

range of complementary luminescent nanoparticle emitters fabricated from semiconductors, gold and diamond.

When the readily accessible properties of fluorescence are combined with the high sensitivity afforded by photon counting photonics, fluorescence has enabled the ultimate limit of single molecule detection to be realized and this in turn is helping to open up new frontiers, such as molecular pathology, whereby metabolism, disease, and pharmacology can be studied at the most fundamental level. Taking the perspective of fluorescence as an enabling phenomenon, we have chosen in this chapter to survey the main techniques and measurements it "enables." We cover spectra, quantum yield, lifetime, quenching, anisotropy, and microscopy, in each case citing topical review articles, many of the original references, underlying theory and modern day applications. The applications are also supported by descriptions of the context, theory, instrumentation, and techniques. Throughout we focus on the methods which are in most widespread use, while highlighting many of the most recent developments. There are already plenty of excellent general texts that survey fluorescence in the wider context of photophysics, and its related techniques, and in more depth than we do here [1–4]. Nevertheless, we hope our approach will provide a useful introduction for readers seeking to learn the basics through to the current state of the field by means of examples of what fluorescence might be able to do for them.

1.2 SPECTRA

Measuring absorption and fluorescence spectra is usually the first place to start in any fluorescence study. The origins of many of the fundamentals of fluorescence lie within spectra and although at times they might lack specificity, the importance of spectra in providing supporting information should not be overlooked when more advanced implementations of fluorescence are being undertaken.

1.2.1 Background and Theory

Fluorescence can be viewed as a multidimensional contour of intensity, wavelength, quantum yield, decay time, polarization, and position that together characterize the emitting species. Fluorescence spectra are today quite simple to measure and reveal information on the energy levels of a fluorophore, in terms of electronic (~2–3 eV) and vibrational (~0.01 eV) properties, that are superimposed on what is effectively a rotational continuum. All of these are capable of being influenced by the local environment, and hence, fluorescence spectra are not only a fingerprint of a molecule, but also can be used as a probe of local interactions.

The fluorescence spectroscopy of aromatic molecules is predominantly in the near ultraviolet (UV) to near-infrared (IR) (~250–900 nm) as it is due to the excitation of weakly bound π-electrons rather than the more strongly bound σ-electrons. In general, where π-electron delocalization increases with the size of the molecule, the absorption and fluorescence spectra shift to longer wavelengths in the manner of a

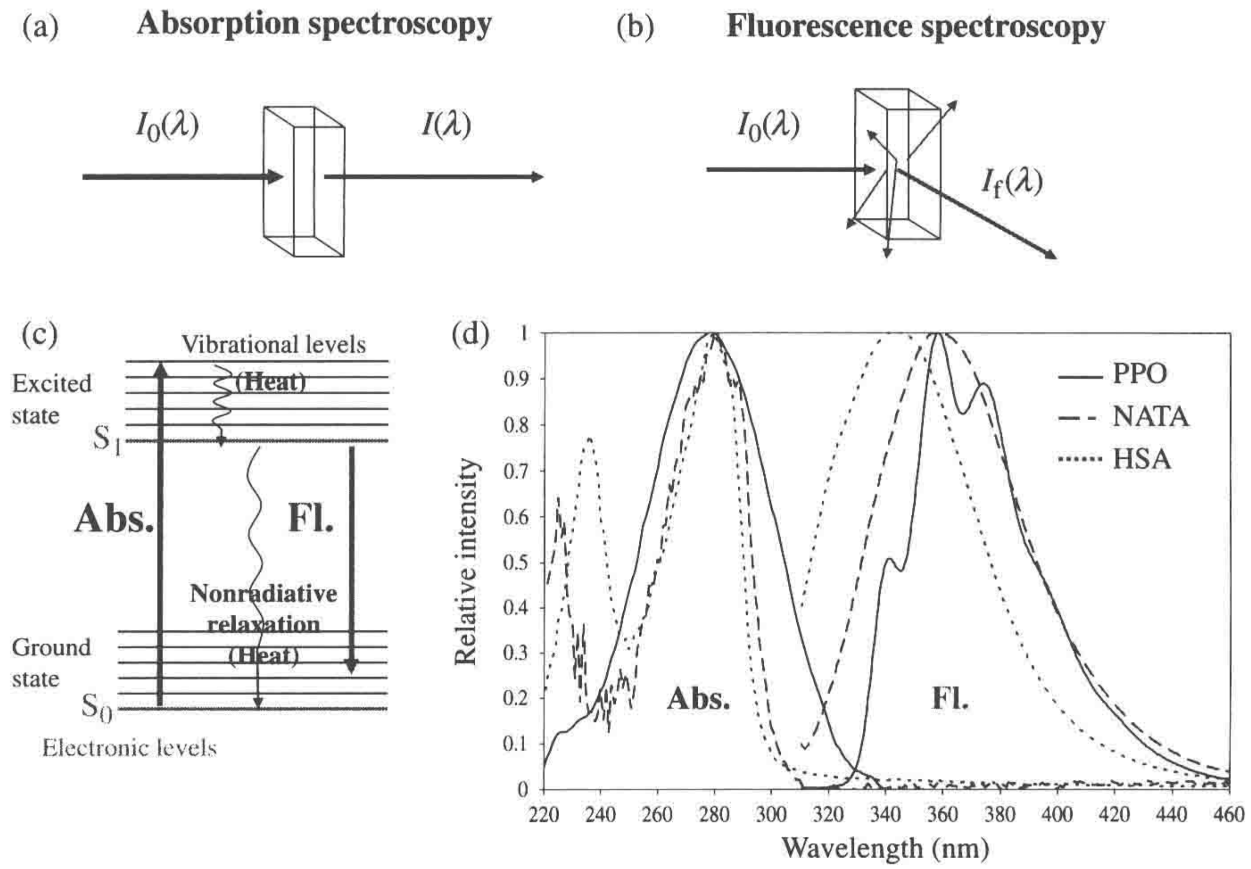
(a)
Absorption spectroscopy
$I_0(\lambda)$
$I(\lambda)$
(b)
Fluorescence spectroscopy
$I_0(\lambda)$
$I_f(\lambda)$
(c)
Vibrational levels
Excited state
(Heat)
S_1
Abs.
Fl.
Nonradiative relaxation
(Heat)
Ground state
S_0
Electronic levels
(d)
Relative intensity
Wavelength (nm)
Abs.
Fl.
— PPO
-- NATA
······ HSA
0
0.1
0.2
0.3
0.4
0.5
0.6
0.7
0.8
0.9
1
220
240
260
280
300
320
340
360
380
400
420
440
460

FIGURE 1.1 Geometries for the measurement of (a) absorption $(I_0 - I)$ and (b) fluorescence (I_f) spectra. (c) Simplified Jablonski energy level scheme for singlet states involved in fluorescence and (d) corresponding spectra measured in condensed media. PPO refers to the scintillator 2,5-diphenyloxazole, NATA is *N*-acetyl-L-tryptophanamide, a derivative of the fluorescent amino acid tryptophan, and HSA is the protein human serum albumin, which contains a single tryptophan.

particle in a box [2]. This can often lead to a useful intuitive expectation of where spectra occur for different molecules in respect to each other before any measurement is performed.

Figure 1.1 illustrates some of the basics of fluorescence spectroscopy. Unlike the measurement of absorption spectra, which by necessity requires the incident light and transmitted light to be detected in-line, fluorescence is usually detected off-axis in order to minimize the detection of the excitation light as this would otherwise swamp the much smaller fluorescence signal. In general, fluorescence is isotropic and is usually detected at 90° to the excitation as illustrated. The energy level scheme shown in Figure 1.1 just relates to the singlet manifold and is a simplified version of the Jablonski scheme [2]. The spectra shown illustrate the fact that in condensed media fluorescence occurs from the lowest vibrational level of the lowest electronic excited state S_1 to vibrational levels of the S_0 electronic ground state (Kasha's rule [2]). Therefore, whereas absorption spectra contain information on the vibrational spacing of the excited state, fluorescence spectra contain information on the vibrational spacing of ground state. The fact that vibrational levels, although quantized, are not well resolved is due to the spectral smearing generated by rotational modes of lower energy. Taken together these properties result in fluorescence being

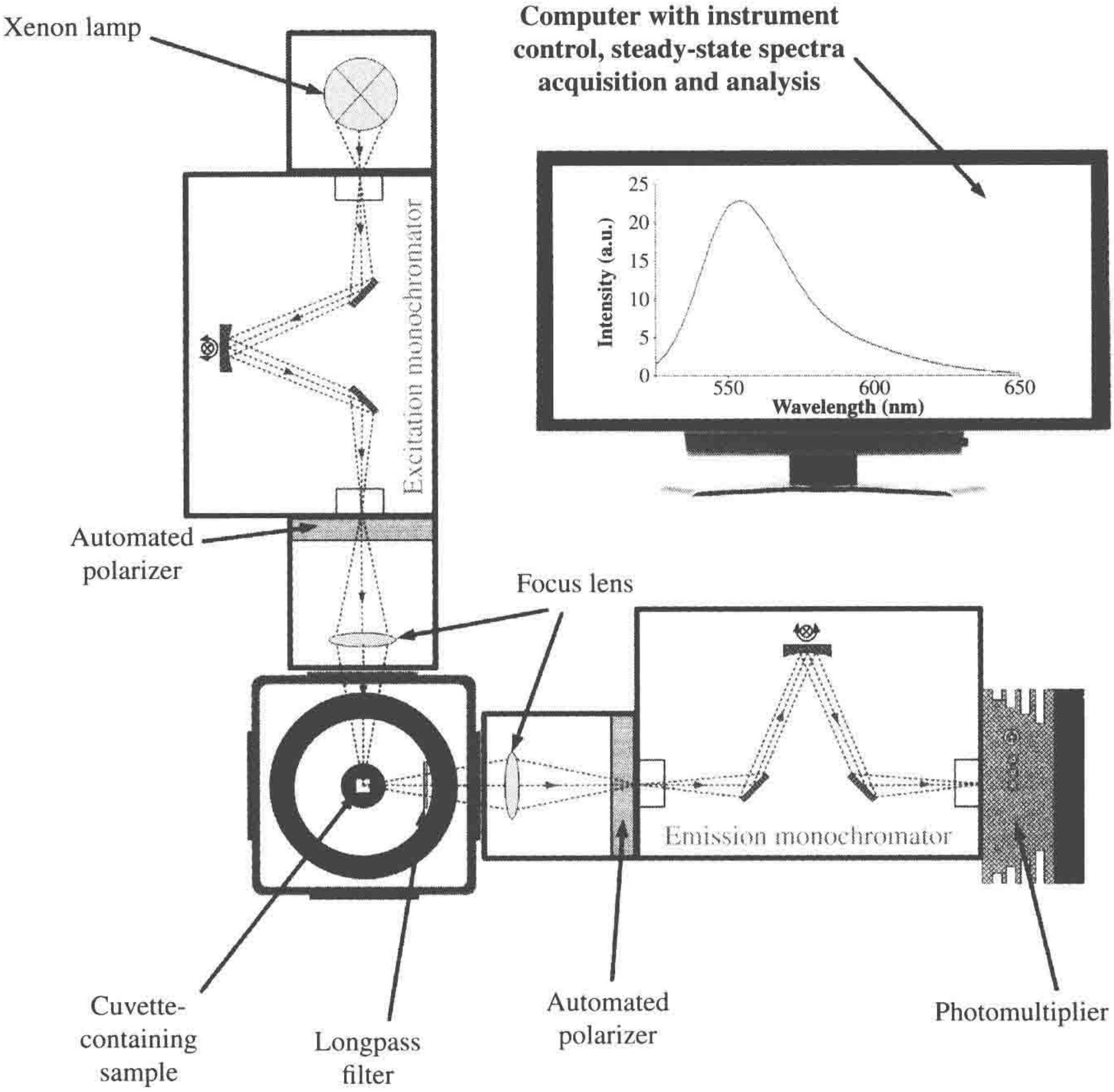
Xenon lamp
Computer with instrument control, steady-state spectra acquisition and analysis
Intensity (a.u.)
25
20
15
10
5
0
550
600
650
Wavelength (nm)
Excitation monochromator
Automated polarizer
Focus lens
Emission monochromator
Cuvette-containing sample
Longpass filter
Automated polarizer
Photomultiplier

FIGURE 1.2 Typical fluorimeter schematic for recording excitation and fluorescence spectra.

shifted to longer wavelengths as compared to absorption, the so-called Stokes shift, with both spectra often displaying mirror image symmetry across their overlap [1].

1.2.2 Experimental

Figure 1.2 shows the common L-format configuration of a fluorimeter for recording fluorescence spectra. It comprises a xenon source, excitation monochromator (e.g., Seya-Namioka geometry as shown here or Czerny-Turner), sample compartment, emission monochromator, and photomultiplier detector. Further optical components, either lenses or mirrors, for focusing are required in order to match the cone angles of the excitation and fluorescence to the monochromator *f* number. Polarizers, either dichroic for the visible or quartz prisms to extend down to the UV, are sometimes added (e.g., for use in anisotropy studies—see Section 1.6). Fluorescence spectra are usually corrected for the spectral response of the emission monochromator and detecting photomultiplier, by division of this combined instrumental function.

This configuration can also be used to record excitation spectra by keeping the monochromator tuned to an emission wavelength while scanning the excitation monochromator wavelength λ. For an optically dilute sample, the excitation spectrum is equivalent to the sample's absorption spectrum. From the Beer–Lambert law,

$$I(\lambda) = I_0(\lambda)\, 10^{-\varepsilon(\lambda)cd}, \tag{1.1}$$

where I is the transmitted intensity after sample absorption, I_0 the incident intensity, c the molar concentration in mol L^{-1} (M), d the sample path length in cm, and $\varepsilon(\lambda)$ the decadic molar extinction coefficient in mol^{-1} L cm^{-1}, the ordinate in an absorption spectrum and the molecular fingerprint which is described by the spectral shape. $\varepsilon(\lambda)cd$ is defined as the optical density or absorbance of the sample.

In the limit of dilute solution, defined as $\varepsilon(\lambda)cd \ll 1$, and defining the fluorescence quantum yield Φ_f as the ratio of the rate of total fluorescence emission I_f to the rate of absorption:

$$\Phi_\mathrm{f} = I_\mathrm{f}/(I_0 - I), \tag{1.2}$$

we obtain [5]

$$I_\mathrm{f} = 2.303\Phi_\mathrm{f}\varepsilon(\lambda)\, cd. \tag{1.3}$$

Because Φ_f is usually independent of excitation wavelength for aromatic molecules in condensed media, Eq. (1.3) shows how detecting fluorescence (even at only one emission wavelength), while scanning the excitation wavelength, leads to an excitation spectrum that is equivalent to the absorption spectrum for dilute solutions because $I_\mathrm{f} \propto \varepsilon(\lambda)$. In the case of absorption, the spectrophotometer used to measure spectra automatically corrects for the spectral distribution of the light source, the spectral response of the monochromator and detecting photomultiplier, by dividing the two signals generated in a dual beam arrangement of sample and reference channels. By similar means fluorescence excitation spectra need to be corrected for the light source spectral output and the excitation monochromator spectral response. In this regard, rhodamine B in ethylene glycol has long been used as a quantum counter [6] as its fluorescence yield is independent of excitation wavelength in the range 220–600 nm and this overcomes the wavelength response of the photomultiplier. The limit of detection for fluorescence is orders of magnitude lower than that of absorption (e.g., $\sim 10^{-12}$ M compared to 10^{-8} M) because the latter ultimately relies upon measuring a small difference between two large signals in the sample and reference channel. Fluorescence on the other hand compares a signal with zero signal or low background, which is a much easier measurement.

1.2.3 Application Example—Melanin Spectra

In order to illustrate how absorption and fluorescence spectra often interplay in tandem, we consider the example of the auto-oxidation of 3,4-dihydroxy-L-phenylalanine (L-DOPA) to produce melanin (Fig. 1.3). L-DOPA is a small molecule as aromatics go, but during its auto-oxidation a complex series of intermediaries are

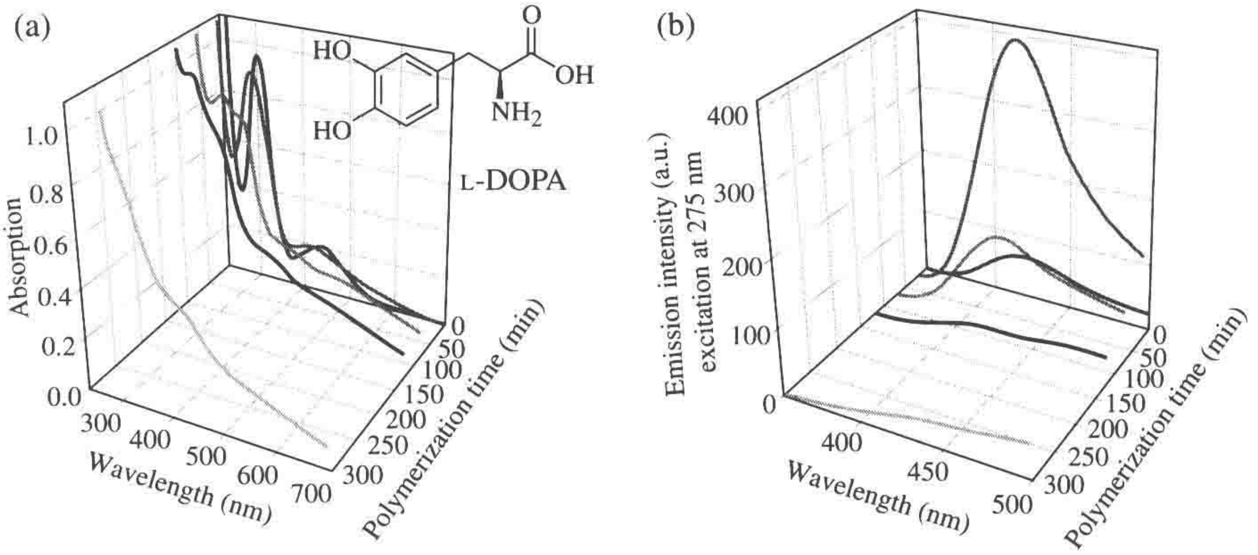

FIGURE 1.3 (a) Absorption and (b) fluorescence spectra as eumelanin is polymerized from the auto-oxidation of an aqueous solution of L-DOPA at pH 12. The fluorescence excitation wavelength is 275 nm. (*For a color version of this figure, see the color plate section.*)

formed before an extended structure, believed to bear a close similarity to natural eumelanin, is formed [7].

Initially the phenyl ring of L-DOPA is seen to dominate the absorption spectrum with a peak occurring below 300 nm, similar to that for benzene, toluene, and the three fluorescent amino acids phenylalanine, tyrosine, and tryptophan. At these times, the fluorescence is quite strong. However, as time progresses, more extended structures are formed to give the characteristically broad band attenuation spectrum of melanin describing the photoprotective action of melanin and the 275-nm excitation generates less fluorescence as the excitation energy is dissipated nonradiatively [8]. Ideally it is preferable to use intrinsic fluorescence to report on structure. This is because it does not distort native structure as extrinsic fluorescence probes can do. However, complex heterostructures such as melanin usually contain multiple fluorophores and give a complex intrinsic fluorescence signature that is difficult to interpret. The same is true of the many types of protein that contain multiple fluorescent amino acids.

1.3 QUANTUM YIELD

Measuring absolute fluorescence quantum yield is not so common an objective these days since most of the fundamental processes of aromatic are well-established and the focus of fluorescence has shifted more toward biological molecules, where their natural environment is usually saturated with the quencher oxygen. However, recording relative changes is still very important in many studies.

1.3.1 Theory

Because the time-averaged rate of absorption must equal the total decay rate (otherwise energy would be piling up in a molecule), we can also express

Eq. (1.2) describing the fluorescence quantum yield Φ_f in terms of intramolecular processes as

$$\Phi_f = k_r/(k_r + k_{nr}), \tag{1.4}$$

where k_r is the radiative decay rate (units s^{-1}), k_{nr} the nonradiative decay rate (composed of internal conversion to the ground state or intersystem crossing to the lowest triplet state), and their sum is the total decay rate. For this reason floppy molecules generally have a lower Φ_f than more rigid molecules. External interactions, for example, collisional quenching by oxygen, bring additional terms to the denominator and further reduce Φ_f. For this reason, oxygen needs to be removed, usually by freeze-pump-thaw cycles or by nitrogen bubbling, for the unquenched Φ_f to be determined correctly. It will be seen that Φ_f can have a maximum value of 1. Unfortunately the simplicity of the definition of Φ_f belies the difficulty of determining it.

1.3.2 Experimental

It can be appreciated from Eq. (1.2) that, in principle, measuring the fluorescence quantum yield requires the determination of the number of photons absorbed and emitted due to fluorescence in a given time. This is a difficult requirement for which integrating spheres can be used. The sample is placed inside a reflective sphere with excitation and emission ports in an attempt to collect all the isotropic fluorescence over a 4π solid angle. Multiple reflections relay the fluorescence to the exit port. Both solids and solutions can be measured. Figure 1.4 shows one such configuration for an integrating sphere. Excitation and fluorescence rays are depicted and re-excitation by one of the fluorescence pathways shown illustrates a common source of error.

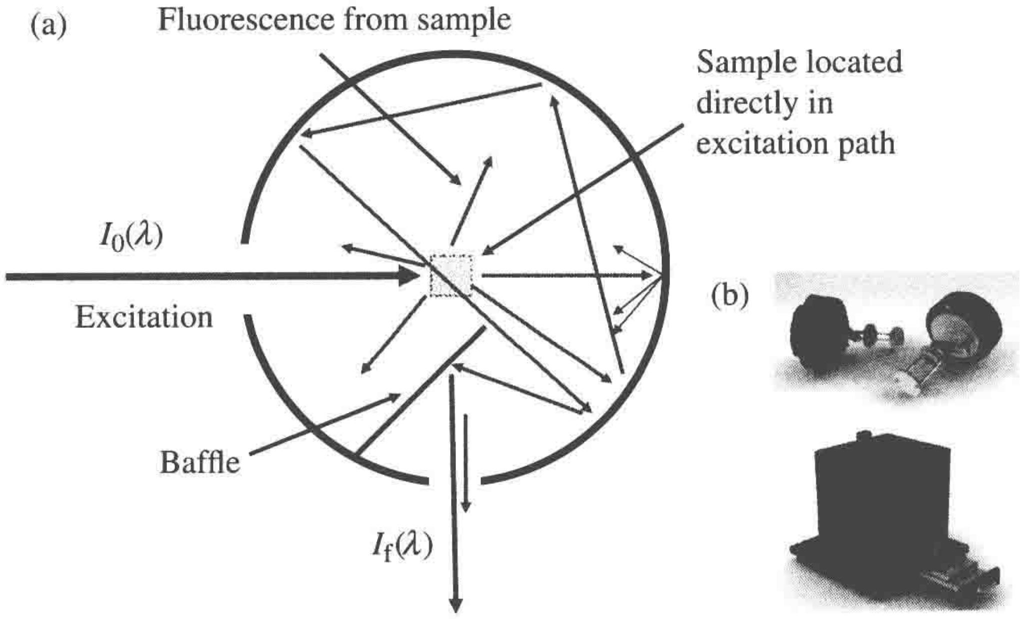

FIGURE 1.4 (a) Typical integrating sphere light paths and (b) construction with sample loading mechanism displayed for cuvettes (top) and solid samples and powders (bottom). Photos courtesy of Horiba Scientific.

A baffle is usually incorporated to minimize reflections from the entrance to exit ports. Excitation light still needs to be spectrally filtered out after the exit port.

Integrating spheres have a long-established [9] and ongoing role to play in the quantification of standards, though they tend to be somewhat impractical and hence not in widespread use. Other absolute methods include calorimetry, photoacoustic spectroscopy actinometry, and thermal lensing. However, the usual recourse is to ratio the spectrally corrected fluorescence spectra of the unknown sample and a suitable reference standard of known quantum yield, that is, to determine a relative rather than an absolute quantum yield. A literature survey soon reveals that fluorescence quantum yields have often courted controversy over the years due to inconsistent measurements between different laboratories. Procedures for absolute and relative quantum yield measurements in solution are discussed in a recent article along with a comprehensive list of references on previous work and recommendations for standards (Table 1.1) [10].

The process by which relative quantum yields are determined involves first correcting the fluorescence spectrum for the spectral responses of the emission monochromator and detecting photomultiplier in order to obtain a true and undistorted fluorescence spectrum. For the sample S and reference standard R, of absorbance A_S and A_R, and respective solvent refractive indices n_S and n_R, we obtain

$$\Phi_{fS} = \frac{\Phi_{fR} I_{fS}(\lambda) A_R n_S^2}{I_{fR}(\lambda) A_S n_R^2}, \tag{1.5}$$

where $I_{fS}(\lambda)$ and $I_{fR}(\lambda)$ refer to the integrated and spectrally corrected fluorescence spectra over wavelength for the sample and reference, respectively. Ideally the same solvent is used for both the sample and reference, but the n^2 ratio corrects for the effect of any solvent difference on the optical geometry over which fluorescence is collected [11]. Solvent refractive index also influences the fluorescence lifetime and the higher precision of lifetime measurement has proved useful in resolving seemingly conflicting results for quantum yield standards [12].

The accuracy in Φ_f is typically no better than 5–10% and such a spread in values is clearly evident in the literature [10]. This seems incongruous with modern day instrumentation, but in fact relative changes of either peak or integrated fluorescence, without measurement of the actual Φ_f, or even spectral correction, are often adequate. The accurate determination of fluorescence quantum yield, like removing the quencher oxygen from solutions before measurement, is no longer of importance in many applications. This is illustrated by the following example.

1.3.3 Application Example—ThT Detection of Sheet Structure

Sheet structures occur in nature, for example, as stacks of graphite and β-sheets of protein or peptide that sometimes form fibrils [13]. Currently sheet structures are of considerable interest when synthesized as isolated monosheets in carbon nanotubes and graphene [14]. Thioflavin T (ThT) is a fluorescent dye (see Fig. 1.5) that has been

TABLE 1.1 Some fluorescence quantum yields (Φ_f) with errors ($\Delta\Phi_f$) at 25°C that can be useful as standards for comparison and determining relative quantum yields

Dye	Quinine sulfate	Coumarin 153	Fluorescein	Rhodamine 6G	Rhodamine 101	Oxazine 1	HITCI	IR125
Solvent	0.105 M $HClO_4$	Ethanol	0.1 M NaOH	Ethanol	Ethanol	Ethanol	Ethanol	DMSO
Absorbance (nm)	270–400	350–500	400–550	425–575	475–620	500–710	535–825	550–875
Emission (nm)	385–700	465–750	490–690	505–750	540–750	615–950	700–950	750–1000
Φ_f	0.59	0.53	0.89	0.91	0.915	0.15	0.30	0.23
$\Delta\Phi_f$	0.04	0.04	0.04	0.04	0.028	0.01	0.01	0.01

Source: Reprinted from Reference 10 with permission of Macmillan Publishers Ltd.

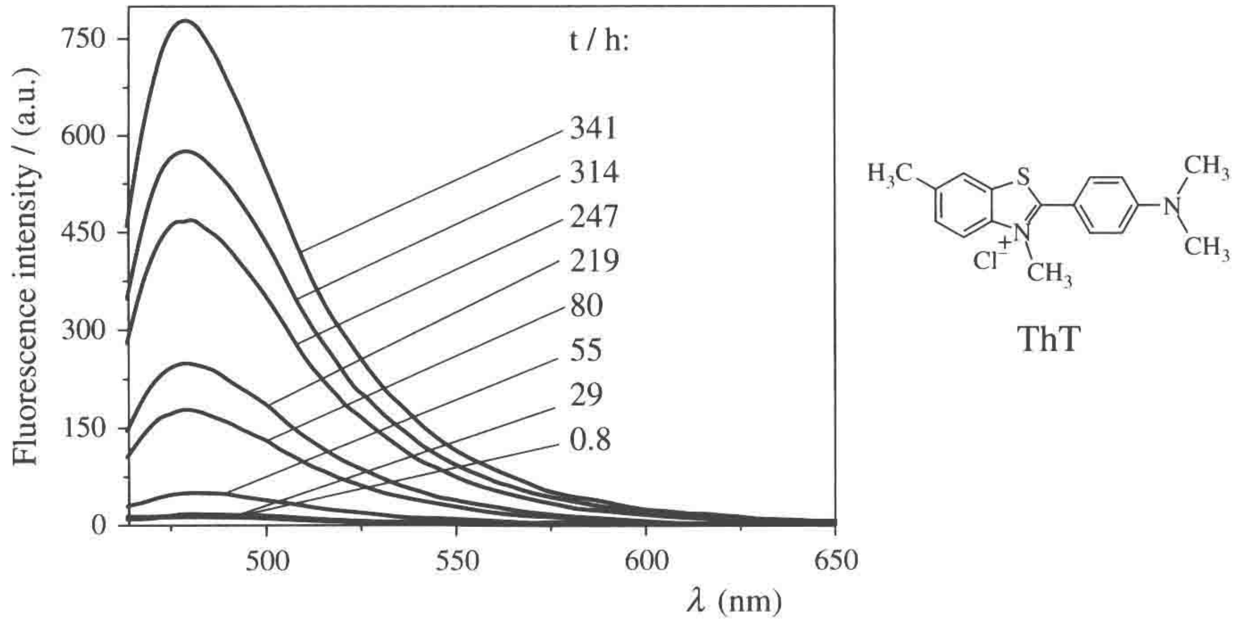

FIGURE 1.5 Increase in ThT fluorescence as beta sheets of Aβ are formed. The excitation wavelength is 450 nm and the fluorescence peak is at 480 nm. Reprinted from Reference 17 with permission from Elsevier.

widely used for revealing the formation of sheet structures [15], most notably when studying the aggregation of the peptide beta-amyloid (Aβ); the early oligomers of which are thought to be the precursor to Alzheimer's disease. As already mentioned, floppy molecules generally have a low fluorescence yield due to having more favorable dissipative pathways other than fluorescence. Conversely rigidity imparts a higher fluorescence yield. ThT behaves as a molecular rotor and upon excitation undergoes intramolecular rotation to a low-fluorescent twisted intramolecular charge transfer (TICT) state [16]. This rotation is restricted between sheet structures, increasing the fluorescence quantum yield, which can thus be used as a probe of sheet formation. Figure 1.5 shows the peak wavelength and shape of the fluorescence spectrum of ThT in Aβ are constant as β-sheets are formed [17]. Hence it is perfectly workable to use the relative change in fluorescence quantum yield to monitor structural changes without actually having to put a number to Φ_f.

One of the limitations of using ThT to detect Aβ aggregation is that the early-stage oligomers, that are thought to disrupt neuronal cellular membranes and initiate Alzheimer's disease, are not detected since only the β-sheets formed later lead to an increase in fluorescence. Changes in fluorescence lifetimes (to be discussed in the next section) have recently been shown to address this short-coming by using the intrinsic tyrosine fluorescence lifetime in the case of Aβ [17] and ThT fluorescence lifetime in the case of insulin fibrils [18].

In cases like eumelanin, where the intrinsic fluorescence is complex (see Fig. 1.3) due to the presence of multiple fluorophores, extrinsic probes with bespoke structural sensing characteristics like ThT come to the fore. Surprisingly, although the composition of melanin is well known to be largely dihydroxyindoles, its secondary structure, the minimum functional unit, and the very existence of a protomolecule

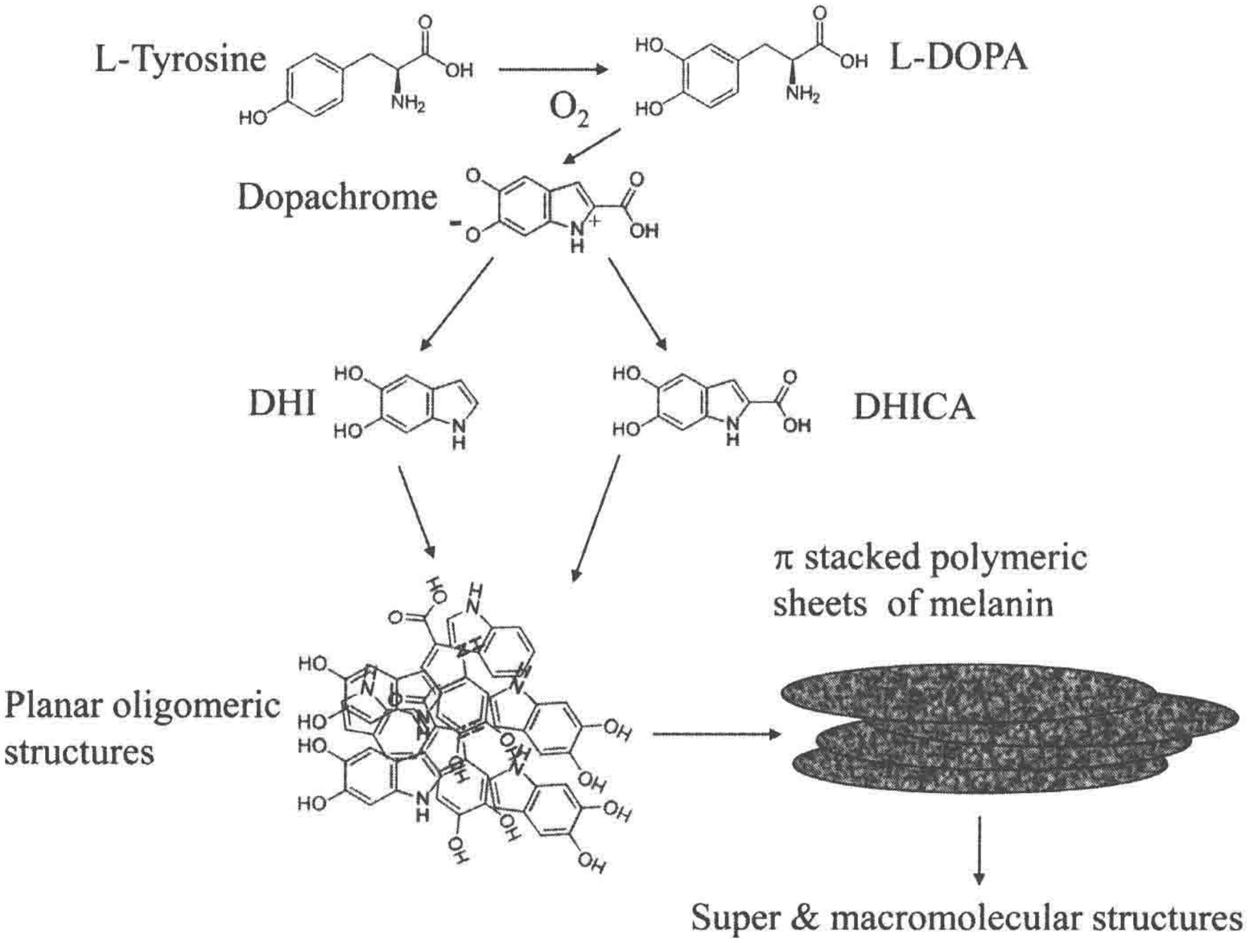
L-Tyrosine
O
OH
HO
NH2
O2
HO
O
OH
L-DOPA
HO
NH2
Dopachrome
O
-O
N+
H
O
OH
DHI
HO
HO
N
H
HO
HO
N
H
O
OH
DHICA
π stacked polymeric
sheets of melanin
Planar oligomeric
structures
OH
Super & macromolecular structures

FIGURE 1.6 Probable structural steps in eumelanin synthesis.

that can be replicated to form a secondary structure remains unclear despite decades of research with a whole gamut of techniques [7,8]. The significance of not knowing the structure of eumelanin has bearing on a whole range of topics from bioelectronics (melanin is an efficient conductor and readily binds metal ions) to melanoma, the most virulent form of skin cancer. The likely structural steps in melanin synthesis are depicted in Figure 1.6.

Planar oligomeric structures of dihydroxyindoles are thought to form sheets that are bound together by π–π interactions. The oxidation of primary structures, either spontaneously or catalyzed, is generally thought to give rise to protomolecules (oligomers) composed of four or five monomers. These combine into planar sheets that stack due to π bonding, albeit less strongly bound than σ covalent bonds, thus accounting for eumelanin's softness in the manner of graphite. The close packing, including π–π^* interactions (~0.3–0.4 nm apart [8]), being consistent with eumelanin's photo-protection via ultrafast nonradiative relaxation. The larger sheet structures have been proposed to form onion-like layers [19]. Recent fluorescence studies, based on the increase in ThT fluorescence quantum yield as eumelanin is formed by auto-oxidation of L-DOPA, support the notion of assembly via a protomolecule that subsequently forms sheets rather than assembly by monomer addition [20]. This is illustrated in Figure 1.7.

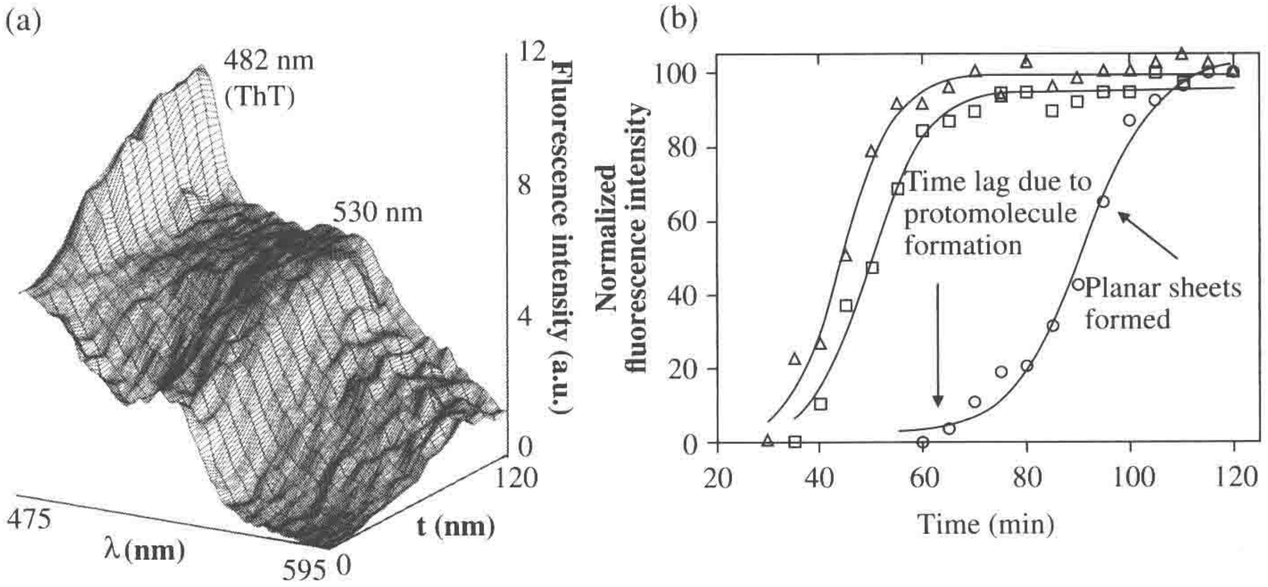

FIGURE 1.7 (a) Fluorescence spectrum of ThT, excited at 450 nm and peaking at 482 nm, superimposed on the intrinsic fluorescence background, as eumelanin is synthesized at pH 10 by the auto-oxidation of L-DOPA. (b) ThT fluorescence at 482 nm as the eumelanin synthesis progresses at pH 10 (○), pH 10.8 (□) and pH 11.4 (Δ). Reproduced from Reference 20 with permission from AIP Publishing LLC.

The melanin growth, as reflected by the increase in ThT fluorescence can be described using a classic sigmoidal function analogous to that encountered in amyloid fibrillation such as that of Aβ [21]:

$$I_f(t) \sim I_{f0} + I_{max}/\{1 + \exp[-k_m(t - t_{1/2})]\}, \tag{1.6}$$

where $I_f(t)$ is the fluorescence intensity and I_{f0} is the initial or background fluorescence intensity. The parameter I_{max} is the fluorescence maximum above the background, k_m is the rate of melanin formation, and $t_{1/2}$ is the time when the fluorescence intensity has reached the half maximum value.

The very existence of the time-lag suggests that eumelanin is not formed by monomer addition, but rather it requires a protomolecule (or protomolecules) in a "binding ready" conformation to be preformed first. Moreover, the increase in ThT fluorescence in itself further supports the presence of sheet-like structures in eumelanin with the fluorescence no longer increasing when the eumelanin-forming reaction is complete.

1.4 LIFETIME

The fluorescence lifetime of a molecule is the average time it spends in the excited state before emitting a fluorescence photon. Typically in the nanosecond region, the fact that the fluorescence lifetime has a finite value is due to local perturbations and therein rests its usefulness as a probe on the angstrom scale.

Lifetime measurement has emerged in recent years as the most powerful and versatile technique in fluorescence spectroscopy. It can be performed in either the time or frequency domain. In comparison to spectra, quantum yield, and intensity, lifetime provides more kinetic information, a visual image that is easier to interpret, is analogous to a movie compared to a photo, resolves dynamics more closely, provides a more stringent test of kinetics models, and is easier to calibrate. Fluorescence lifetime is also making a mark beyond spectroscopy. For example, in sensing and fluorescence lifetime imaging microscopy (FLIM), to be discussed in Section 1.7.

1.4.1 Theory

The fluorescence lifetime τ_{f} for aromatic fluorophores can be defined in terms of rate parameters, consistent with the definition for the fluorescence quantum yield Φ_{f} (Eq. 1.4), as [2]

$$\tau_{\mathrm{f}} = \frac{1}{k_{\mathrm{r}} + k_{\mathrm{nr}}}. \qquad (1.7)$$

In the time domain, τ_{f} can be conveniently visualized as it describes the fluorescence impulse response to δ-function excitation at $t = 0$ given by

$$i(t) = i(0)\exp - (t/\tau_{\mathrm{f}}), \qquad (1.8)$$

and $i(t)$ is the solution to the rate equation defining the decay of the concentration (population) of the S_1 singlet excited state M^*, due to fluorescence emission:

$$\frac{d\,[M^*]}{dt} = -(k_{\mathrm{r}} + k_{\mathrm{nr}})[M^*] = -\frac{[M^*]}{\tau_{\mathrm{f}}} \qquad (1.9)$$

if multiple and noninteractive fluorescent emitters are present, the same treatment can be extended linearly by simply adding further exponential terms describing different lifetimes. The application of fluorescence lifetimes has benefitted greatly from the fact that most aromatic fluorophores possess a single exponential decay.

Combining Eqs. (1.4) and (1.7) we obtain

$$\tau_{\mathrm{f}} = \frac{\Phi_{\mathrm{f}}}{k_{\mathrm{r}}}. \qquad (1.10)$$

Equation (1.10) illustrates why the fluorescence lifetime can be used to monitor changes that influence fluorescence, as providing the radiative rate k_{r} remains constant, τ_{f} offers equivalent information to Φ_{f}, is easier to measure, more precise and less prone to systematic error. Conversely if Φ_{f} and τ_{f} are measured, k_{r} and k_{nr} can be determined.

k_r can be described by the Einstein coefficient A and the transition dipole moment operator M as [2]

$$k_r = \sum_m Au0 \rightarrow \mathrm{lm} \propto / < \psi_l^* / M / \psi_u > /^2 \tag{1.11}$$

where, unlike for spectral lines in the simpler atomic case, A has to be summed over the whole fluorescence spectrum attributed to the lowest vibrational level u of the excited S_1 singlet state to the different vibrational levels m of the singlet S_0 ground state.

The Strickler–Berg expression [22] and its variants [2] enable k_r to be determined more easily by introducing the Einstein B coefficient relating to the absorption spectrum:

$$k_r = 2.88 \times 10^{-9} n^2 < \upsilon_F^{-3} > A_v^{-1} \int \frac{\varepsilon(\upsilon) d\upsilon}{\upsilon}, \tag{1.12}$$

where $< \upsilon_F^{-3} > A_v^{-1}$ is the reciprocal of the mean value of υ_F^{-3} over the fluorescence spectrum ($\upsilon = 1/\lambda$) and $\int \frac{\varepsilon(\upsilon)d\upsilon}{\upsilon}$ relates to the area under the absorption frequency spectrum.

The fluorescence lifetime dependence on n^2 via the Strickler–Berg equation has been shown to probe refractive index in cells using protein labeled with the green fluorescent protein [23].

Equation (1.12) can be approximated to

$$k_r \sim 10^{-4} / \varepsilon_{\max}. \tag{1.13}$$

Given $\varepsilon_{\max} \sim 10^5$ mol^{-1} cm^{-1} for a strong absorber, Eq. (1.13) predicts that, in the absence of intramolecular nonradiative processes or intermolecular quenching, τ_f is ~1 ns. It should be cautioned that agreement between Eqs. (1.10) and (1.12) can be quite variable [24] due to potential sources of experimental error (see Section 1.3) and the presence of more complex photophysics, for example, quinine sulfate having a bi- not mono-exponential fluorescence lifetime decay [25]. Significant discrepancies between k_r determined from Eq. (1.10) (which monitors the emitting state) and Eq. (1.12) (which monitors the absorbing state) have often been used to determine the presence of "hidden states," such as those present in polyenes that are facilitated by intra-molecular twisting [26,27].

In the frequency domain, the equivalent expressions to Eq. (1.8) are

$$\tan \phi = -\omega \tau_f \text{ and} \tag{1.14}$$

$$m = 1 / \left(1 + \omega^2 \tau_f^2\right)^{1/2}, \tag{1.15}$$

where ω is the modulation frequency (in rad s^{-1}) and m a modulation factor that describes the relative amplitude of the fluorescence and excitation wave forms. The negative sign in Eq. (1.14) simply denotes the fluorescence lags the excitation by a phase angle ϕ.

Equations (1.14) and (1.15) lead to an alternative method for measuring fluorescence lifetime as discussed below.

1.4.2 Experimental

There are two main approaches to measuring fluorescence lifetime. Pulse fluorometry in the time domain and phase-modulation fluorometry in the frequency domain [2–4]. The two different approaches are in theory equivalent and complementary, as they are linked by Fourier transforms. For example, δ-function excitation in the time domain is equivalent to exciting with a white frequency spectrum. However, in experimental implementation and data analysis, there are some significant differences that have bearing on the relative merits of the two methods. With phase modulation, the excitation light is modulated or chopped and the fluorescence lifetime determined from either the phase shift or modulation depth of fluorescence with respect to excitation. With pulse fluorometry, a temporally sharp excitation pulse is used and the fluorescence decay recorded with as close a representation of Eq. (1.8) as possible.

Equation (1.14) in particular can be very useful, in so far as it underpins a simple and quick method of determining a single exponential lifetime by measuring ϕ and knowing ω. However, if we think in terms of the equivalence of time and frequency domain measurements the difference is that Eq. (1.14) is a single point (frequency) measurement, whereas Eq. (1.8) offers the prospect of measuring over a wide time range and thus providing a more rigorous test of any kinetic model. This limitation has been ameliorated to some extent by the introduction of various multifrequency methods [3, 28, 29], but at the expense of the simplicity and speed afforded by Eq. (1.14). Despite the advantage of a quick measurement using Eq. (1.14), it would seem pulse fluorometry has found more widespread favor for fluorescence lifetime measurement. The most popular implementation of pulse fluorometry is time-correlated single-photon counting (TCSPC) [30, 31]. Based on delayed coincidence techniques developed for nuclear physics, and then adapted for recording scintillation decay [32], TCSPC and its variants have some critical advantages over other methods, particularly when researching unknown kinetics. The main advantages are

1. Single-photon counting sensitivity down to the single molecule limit such that data precision can be simply enhanced by increasing the measurement time.
2. Temporal display of the kinetics aiding interpretation of data.
3. Known statistical basis (Poisson) and therefore meaningful and objective assessment of the kinetics.
4. As a digital technique it minimizes the effect of signal amplitude variations that can distort analog methods.

Figure 1.8 shows a schematic and photograph of a typical TCSPC fluorometer. The arrangement is very similar to the fluorimeter shown in Figure 1.2, illustrating

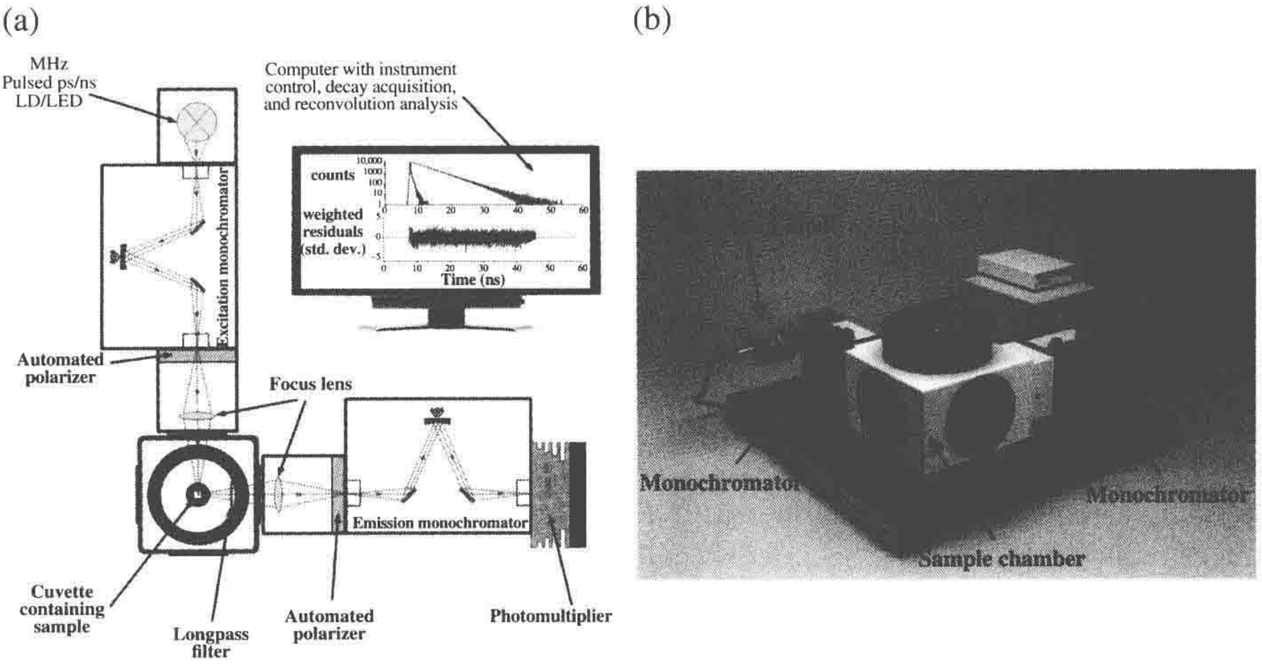
(a)
(b)
MHz
Pulsed ps/ns
LD/LED
Computer with instrument control, decay acquisition, and reconvolution analysis
counts
10,000
1000
100
10
1
weighted residuals (std. dev.)
5
0
-5
0
10
20
30
40
50
60
Time (ns)
Excitation monochromator
Automated polarizer
Focus lens
Emission monochromator
Cuvette containing sample
Longpass filter
Automated polarizer
Photomultiplier
Monochromator
Monochromator
Sample chamber

FIGURE 1.8 (a) Schematic of a typical pulse fluorometer and (b) a modular implementation incorporating ps diode laser excitation and microchannel photomultiplier detection. Photo courtesy of Horiba Scientific.

how hybrid instruments can be easily engineered and measurements interchanged simply by swapping components or routing light paths. Polarizers are used primarily for anisotropy decay studies and are not generally needed for lifetime measurements with low viscosity solvents such as water, ethanol, and cyclohexane. However, in viscous solvents, where the fluorophore rotational correlation time is comparable to τ_f, polarizers are used in order to correct for any intrinsic polarization of the fluorometer, such as that caused by diffraction gratings, laser excitation, and so on (see Section 1.6).

These days a semiconductor laser diode (LD) or light-emitting diode (LED) is typically used for excitation. Perhaps surprisingly, a conventional photon counting and timing photomultiplier based on a vacuum tube is still the most widely used detector [33, 34]. Photomultipliers incorporate electron amplification using either discrete or continuous dynodes, the latter incorporated in the microchannel plate photomultiplier, which offers the fastest response. Today semiconductor sources can provide the wavelengths needed to excite most fluorophores. Previously, most pulse fluorometers used the broad spectral continuum of pulsed spark sources [35]. Even though these nanosecond sources were of low repetition rate (~30 kHz) and low energy (~10 pJ overall wavelengths), it was still possible to achieve a full spectroscopic capability by using a monochromator rather than a filter on the emission as well as the excitation channel [36]. Semiconductor excitation sources first appeared in TCSPC as red/near-IR AlGaAs diode lasers [37]. The subsequent development of GaN technology [38] provided visible LDs and brought LEDs into the measurement frame [39]. The switch from flashlamps to semiconductor sources was made complete when the critically important area of protein fluorescence was demonstrated using AlGaN LED excitation [40–42]. LED pulse energies are only ~1 pJ and comparable to spark sources, but their MHz repetition rates and temporal stability give them clear advantages. TCSPC at repetition rates as high as 100 MHz have been achieved with laser diodes [43]. However, to avoid re-excitation and a "saw tooth" fluorescence decay that is difficult to analyze, this is only practicable for fast lifetimes that fully decay within the 10 ns measurement time window.

Pulse fluorometry measures the photon-time distribution describing the fluorescence decay by using a timing device to measure a "start"–"stop" time interval between excitation of fluorescence and its detection. There are a number of ways to achieve this. These include fast oscilloscopes, sampling oscilloscopes (boxcar integrators), multichannel scaling, stroboscopic detector gating, and a time-to-amplitude converter (TAC), as traditionally used in TCSPC. The TAC converts the time difference t to a voltage v, which is then digitized in an analog to digital convertor and stored as a detected photon count event in a multichannel analyzer (MCA) such that $v \propto t$. Repeating the cycle in accordance with the excitation pulse frequency allows a histogram of counts to be accumulated that is representative of the fluorescence decay, such that D_t is the number of decay counts registered at a time t. Some further refinements and precautions are necessary though.

The pulse height of photomultiplier output for single photon detection is variable due to photoelectrons having different paths and their statistical fluctuation in number. For this reason, and to discriminate against the lower pulse height distribution derived from noise, the timing of photomultiplier signals is derived at a constant fraction of the pulse height (constant fraction discrimination, CFD) [31]. Temporal delays due to optical paths, the photomultiplier, cables, and electronics are inherent, but have no bearing on the quality of measurement, provided they remain constant. A time delay (cable or electronic) that can be varied between measurements to ensure the decay profile is observable and can be moved within the TAC range is essential though. Traditionally nuclear instrument modules (NIMs) were used for the timing electronics, but these have by and large been superseded by customized PC cards or stand-alone modules.

One limitation of the original (simplex) form of TCSPC as described so far is its inefficiency. For the histogram of photon arrival times to reproduce the fluorescence decay curve, the fluorescence detection rate has to be reduced to ~1% of the source repetition rate in order to avoid data pileup [30, 31]. Otherwise photons arriving early at the peak of the distribution are preferentially recorded and the decay time appears anomalously shortened. This needs a little thought when encountered for the first time, although the 1% ratio also has a statistical basis in that it ensures the probability of detecting two photons per excitation pulse is negligible. Ways of correcting for this inefficiency have long been the focus of attention. Early approaches included statistical analysis [44] and discrimination between one- and multiphoton pulse signals using either photon pulse height or timing [45]. These methods were generally unsatisfactory. In reality, as the repetition rate of sources increased into the MHz range with the advent of mode-locked lasers and semiconductor sources, the 1% count rate was no longer a limitation for cuvette studies and this is still the case today.

However, as the repetition rate of sources increases to the MHz region a second inefficiency of TCSPC emerges; the dead time of the timing electronics when processing a "stop" signal. This was typically ~10 μs with traditional TCSPC using a TAC and MCA, thus limiting count rate to ~100 kHz. This is adequate for many purposes, but much more restrictive than the 1% pile-up limitation when the source repetition rate exceeds 10 MHz. The first step to minimizing the effect of dead time is to simply reverse the "start–stop" roles of the source rate and fluorescence rate, thus reducing the duty cycle of the timing electronics. For the study of transient samples, such as in single-molecule microscopy studies, this is still not good enough. Consequently, faster timing electronics have been developed with such applications in mind that have also become of more general benefit to cuvette-based spectroscopy. At least two orders of magnitude reduction in TCSPC dead time is now common [46], with <10 ns recently reported [43]. Hence measurement times in the millisecond region, with adequate statistics for recording single exponential decay times, are now available.

Another more general limitation of the original simplex form of TCSPC is its inadequacy for accessing much of the multidimensional contour of fluorescence (i.e., intensity, time, polarization, spectra, position) other than through sequential measurements, which can be onerous. For example, time-resolved fluorescence spectra are traditionally measured by sequentially recording the fluorescence decay at different emission wavelengths and then assembling intensity slices at different time delays or recording the whole emission spectrum sequentially at different time delays during the fluorescence decay [3]. The introduction of multiplexed TCSPC [47–49], whereby multiple decay curves are acquired simultaneously, started to address this and continues to be developed using multiple detection channels and timing. Multiplexing techniques are of particular benefit to single-molecule fluorescence microscopy and lifetime imaging [50, 51]. The trend toward miniaturization through lab-on-a-chip developments [52, 53] has facilitated an increase in the number of measurement channels and out-of-the-lab applications [54].

The requirements for data analysis in TCSPC are complicated by the finite duration of the temporal response of the fluorometer. Even if the excitation pulse is effectively a δ-function (i.e., $\ll\tau_f$), the measured fluorescence response will not be identical to the sample's impulse response (e.g., that given by Eq. 1.8). This is largely because of the intrinsic jitter in photoelectron mean transit time in the photomultiplier, to a lesser extent contributed to by the differences in wavelength and optical paths between measuring the excitation and fluorescence. Jitter in the timing electronics, such as the CFD, also contributes, with all these time spreads contributing to the overall instrumental response half-width, approximately as the sum of their squares [31].

The solution is to use convolution analysis, whereby the excitation pulse is considered to be composed of a series of δ-functions and the fluorescence decay a linear superposition of the corresponding fluorescence impulse responses [31] i.e.

$$F(t) = \int_0^t P(t')i(t-t')dt' = P(t) \otimes i(t), \tag{1.16}$$

where $F(t)$ is the expected fluorescence decay, which is broader than the fluorescence impulse response $i(t-t')$ because of the effect of the finite instrumental response or prompt $P(t')$. The variable t' is a moving time delay that defines the instant at which each δ-function component of the instrumental pulse generates the start of a fluorescence response, the whole procedure often denoted as $\otimes$ to denote the convolution. $P(t')$ is usually measured by tuning the fluorescence monochromator to the excitation wavelength and replacing the fluorescent sample with a colloid (LUDOX silica [55] is often used) that simulates the isotropic nature of fluorescence by diffuse scattering of the excitation pulse.

Using Eq. (1.16) to analyze fluorescence decay requires numerical analysis using reconvolution rather than deconvolution. That is to say $i(t-t')$ in Eq. (1.16) is iterated to give τ_f from Eq. (1.8) when $F(t)$ best describes the measured decay data D_t, as recorded at channels corresponding to t. Usually nonlinear least squares (NLLS) is the fitting procedure used with a $\chi 2$ goodness-of-fit criterion conveniently providing a single figure of merit for ease of comparison [56]:

$$\chi^2 = \sum_{\substack{\text{Data}\\ \text{channels}}} \left[\frac{D_t - F(t)}{\sqrt{D_t}}\right]^2, \tag{1.17}$$

where $D_t - F(t)$ is the actual deviation (residual) at each datum (squared to allow for the deviations being both positive and negative), $\sqrt{D_t}$ the expected standard deviation, since the statistics are Poisson and for a good fit $\chi^2/(n-\nu) \simeq 1$ for n data channels, and ν the number of parameters to be fitted (decay constants, amplitudes, etc.). In order to interpolate between the temporal widths of the data channels and to provide a first-order correction to the wavelength dependence of the photomultiplier, an additional parameter that shifts $F(t)$ with respect to D_t is usually included.

Other statistical methods are available to further assess the goodness of fit [56]. The weighted residuals, Wt (Eq. 1.18), are also often presented as their distribution underpins χ^2; random rather than systematic deviations being taken to indicate a good fit to the data:

$$W_t = \frac{D_t - F(t)}{\sqrt{D_t}}. \tag{1.18}$$

Figure 1.9 illustrates the foregoing discussion by showing a typical fluorescence decay that is of comparable duration to the excitation pulse and successfully analyzed using reconvolution. Depending on their relative decay times and amplitudes up to three exponential decay components is usually quite straight forward to extract using reconvolution.

While NLLS reconvolution is still the workhorse for decay analysis in TCSPC, other approaches are useful in special cases, for example, the maximum entropy method [57], describing lifetime distributions, and maximum likelihood for handling poor data statistics [58].

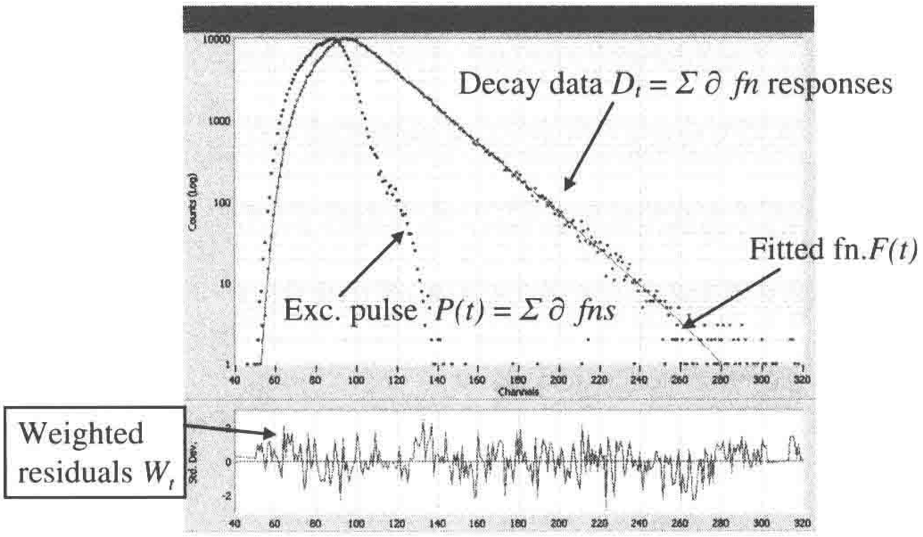

FIGURE 1.9 Reconvolution analysis of a fluorescence decay.

Standards for fluorescence lifetimes have been suggested from a Round-Robin study by nine laboratories that compared results using both pulsed and phase fluorometry for dilute and degassed solutions [59]. Although the idea of chemical standards of time is perhaps in some ways peculiar, they can be quite useful when initially testing fluorometers or in providing confidence in new measurements. Table 1.2 shows some of the average values of up to eight measurements using both TCSPC and phase-modulation measurements taken from this Round-Robin study. Agreement with the TCSPC and phase-modulation results was within a few percent.

1.4.3 Application Example—In Vivo Glucose Sensing

One of the ongoing challenges in biosensing is metabolic monitoring through, and in, the complex barrier of skin and tissue. Monitoring blood glucose for diabetes control is the archetypical measurement problem [60], with the concentration range of physiological interest ~5–30 mM. At present diabetics rely largely on finger-prick blood sampling applied to a reagent strip for glucose analysis, but this has poor patient compliance and is intermittent. Continuous glucose monitors are available that are

TABLE 1.2 Some suggested fluorescence lifetime (τ_f) standards

Dye and solvent	Excitation (nm)	Fluorescence (nm)	τ_f (ns)
Rubrene in methanol	300–514	550–610	9.90 ± 0.30
9,10-Diphenyl anthracene in methanol	295–360	400–475	8.70 ± 0.50
Anthacene in methanol	295–360	375–442	5.10 ± 0.30
2,5-Diphenyloxazole in methanol	295–330	340–400	1.65 ± 0.05
Erythrosin B in methanol	488–568	550–580	0.47 ± 0.02

Source: Adapted from Reference 59 with permission from the American Chemical Society.
Measurements were performed on deoxygenated solutions at 20°C and represent the average of up to eight measurements across different laboratories using both pulsed and phase fluorometry.

based on subcutaneously implanted amperometric enzyme electrodes or microdialysis sensing platforms. Although undoubtedly of benefit and improving, they still have drawbacks that include suboptimal accuracy, drift, and frequent calibration [61]. So far the search for a minimally invasive sensor that can reliably operate continuously has defied advances in modern technology. Many alternative technologies are being investigated, including near-IR, Raman, impedance and photoacoustic spectroscopy, as well as optical coherence tomography, and polarimetry, but none has yet reached routine clinical application [62].

Fluorescence also shows significant promise in this area. It would be ideal if the intrinsic fluorescence of tissue could be used, for example, glucose-induced cellular metabolism of NAD(P)H [63], but the photo-protective action of endogenous absorbers such as melanin makes this impractical. Extrinsic fluorescence platforms include those based on boronic acid [64], concanavalin A [65], carbon nanotubes [66] and enzymes, such as hexokinase [67], and glucose/galactose binding protein [68]. Each of these assays has strength and weakness, but ultimately a workable assay will need to operate in the red/near-IR therapeutic spectral window in order to minimize absorption and scattering by endogenous species. However, some such sensing schemes have been reported [66,69,70].

The advantages of fluorescence lifetime over intensity measurements come to the fore in applications like glucose sensing. Fluorescence lifetimes are essentially independent of fluorophore concentration, photobleaching, and ground-state quenching, they can discriminate against scattered excitation light and auto-fluorescence, and are easy to calibrate absolutely. Moreover, recent developments in semiconductor photonics and on-chip integration, some are already mentioned, combined with fiber optics, mean that ergonomic and miniaturized instrument systems, using either pulse or phase fluorometry, are well within reach for glucose sensing.

By way of an example, here we describe a reversible fluorescence lifetime platform based on glucose/galactose-binding protein (GBP) from *Escherichia coli.* GBP has a single polypeptide chain that folds into two lobular domains, separated by a hinge region where glucose binds (Fig. 1.10). Binding is accompanied by a marked conformational change in the protein, with the two lobules closing round the glucose molecule to form a “closed-form” of GBP. When appropriately labeled, the glucose-induced conformational change in GBP can produce a significant change in fluorescence [71]. In Figure 1.10 the environmentally sensitive probe badan (6-bromoacetyl-2-dimethylaminonaphthalene) is attached to position H152C (i.e., a mutant where histidine is substituted by cysteine at position 152 of the polypeptide chain near the glucose-binding site). The addition of glucose results in a 300% increase in fluorescence intensity [71]. In the presence of glucose the fluorescence decay can be described well by an impulse response comprising two time constants of $\tau_{f1} \sim 1$ ns and $\tau_{f2} \sim 3$ ns. These components are associated with an equilibrium that depends on the glucose concentration between the open (and quenched) glucose-free and closed (and enhanced) glucose-bound forms of GBP, respectively. The fluorescence impulse response, with reference to Eq. (1.8), is

$$i(t) = i_1 \exp - (t/\tau_{f1}) + i_2 \exp - (t/\tau_{f2}). \tag{1.19}$$

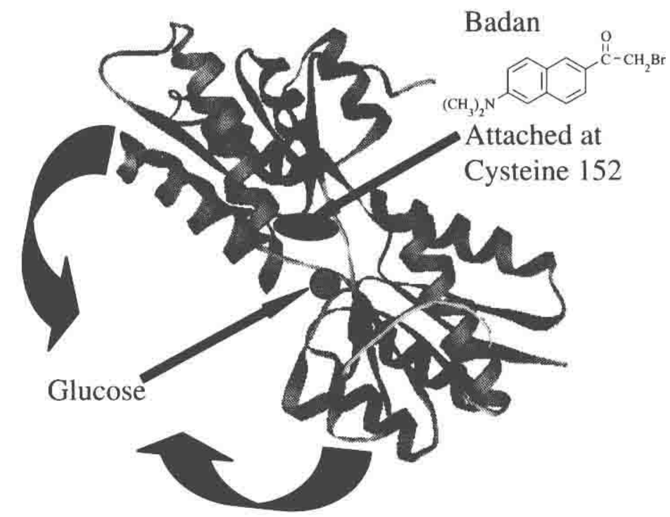

FIGURE 1.10 Glucose/galactose-binding protein (GBP), genetically modified and labeled with badan [71]. When glucose enters the cleft, the hinged lobes fold together, increasing the fluorescence of the badan label.

Figure 1.11a shows the relative change in fluorescence fractions F_1 and F_2 as the glucose concentration is varied in neutral buffer to include the 5–30 mM physiological range. This is in terms of the weighted average $<\tau_f>$ for the two decay components:

$$< \tau_f >= \frac{i_1\tau_{f1}}{i_1\tau_{f1} + i_2\tau_{f2}}\tau_{f1} + \frac{i_2\tau_{f2}}{i_1\tau_{f1} + i_2\tau_{f2}}\tau_{f2} = F_1\tau_{f1} + F_2\tau_{f2}. \quad (1.20)$$

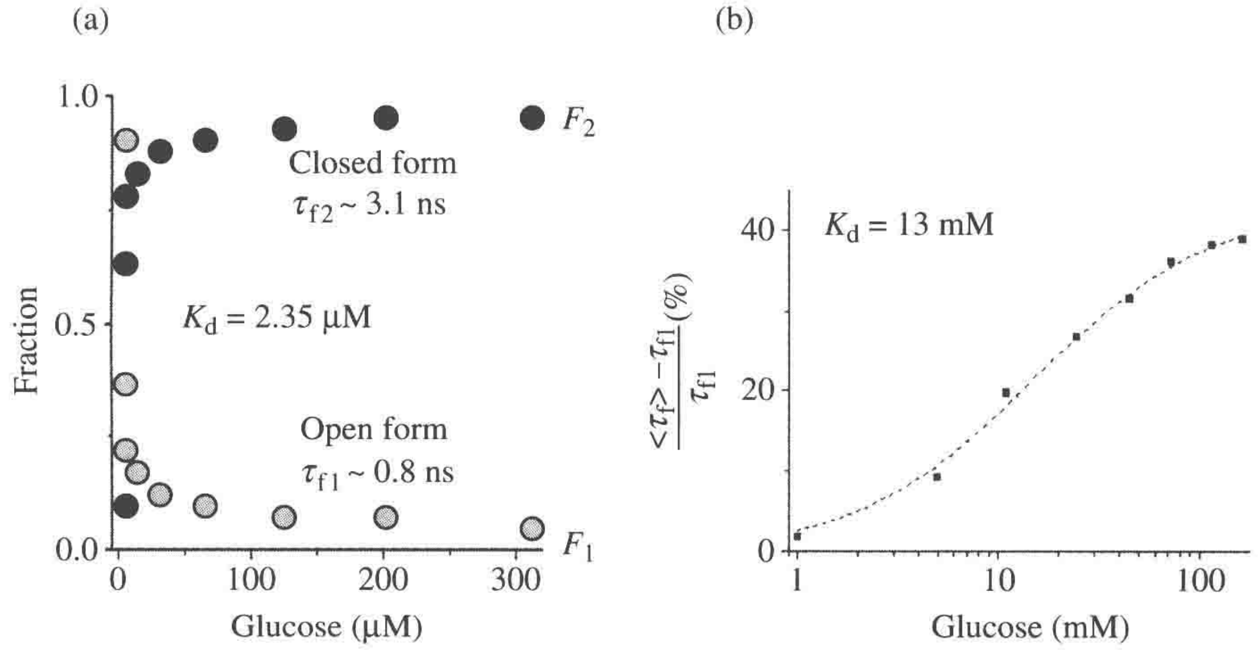

FIGURE 1.11 (a) Fractions of fluorescence due to open, F_1, and closed, F_2, forms of GBP-badan with $K_d = 2.35$ μM in PBS buffer at pH 7.4. (b) Percentage change in average lifetime $\frac{<\tau_f>-\tau_{f1}}{\tau_{f1}}$ (cf. Eq. 1.20) as a function of glucose concentration for a GBP mutant, immobilized on agarose beads coupled to an optical fiber in PBS buffer at pH 7.4, with K_d of 13 mM designed for the physiological range [72].

Figure 1.11b was obtained for badan-GBP immobilized on agarose beads coupled to an optical fiber in neutral buffer, an approach which could also be suitable for implanting in subcutaneous tissue [72]. The dissociation constant K_d is 13 mM and ideal for monitoring over the physiological range of glucose. The measurand is the fractional increase in $<\tau_f>$ on addition of glucose as compared to the fluorescence lifetime at zero glucose τ_{f1}.

GBP labeled with acrylodan (a similar dye to badan) has recently been successfully demonstrated in preclinical trials on swine using a fiber optic insert in the subcutaneous tissue and found to be free from significant effects of common interferents [73]. Badan-GBP has also been encapsulated on a micron scale in layer-by-layer assemblies of poly-lysine and poly-glutamic acid and demonstrated in plasma, paving the way to a minimally invasive implementation as a smart tattoo [74].

The underlying mechanism behind the large increase in badan-GBP fluorescence when glucose binds, and GBP folds, is likely to be complex. Badan is well known to be environmentally sensitive with a fluorescence spectrum that shifts with solvent polarity; however, in this case the fluorescence spectrum shows little change. Some of the more commonly encountered fluorescence quenching mechanisms are discussed in the next section.

1.5 QUENCHING

A fluorescence quencher can be simply defined as any species, which, by interacting with the fluorophore, reduces its quantum yield. There are many molecular mechanisms of quenching, each lowering the proportion of the number of radiative transitions in respect to the number of photons absorbed (Eq. 1.4).

Quenching studies are useful in gaining information on accessibility to the quencher, determining location of fluorophores, diffusion parameters, and permeability and structure of media and macromolecules. They have also led to a whole range of sensors for detecting different analytes. The primary experimental techniques for studying quenching have already been described, namely spectra (both absorption and fluorescence), quantum yield, and lifetime. Again the latter is better placed to reveal most about the quenching kinetics and bring to bear advantages in sensing already mentioned for the case of glucose monitoring. In all fluorescence quenching studies it needs to be kept in mind that a single quenching mechanism is not always present and often more complicated hybrid kinetics are observed. Here we summarize the most commonly encountered forms of fluorescence quenching.

1.5.1 Theory

1.5.1.1 Static Quenching Perhaps the most trivial form of quenching is so-called static quenching where the quencher molecules Q form ground-state complexes with the fluorophore M (Fig. 1.12a). The MQ complexes can still be excited, but either do not fluoresce or have a reduced fluorescence quantum yield.

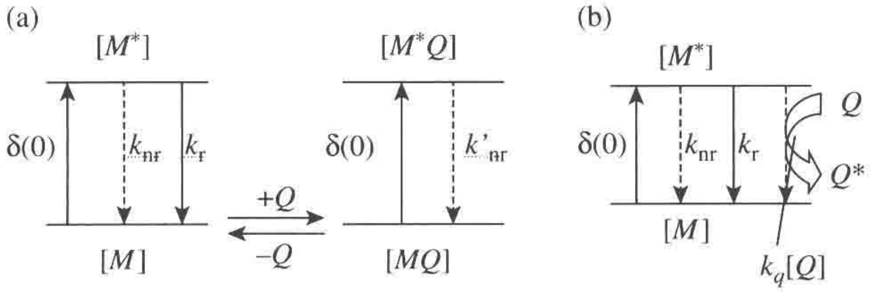

FIGURE 1.12 (a) Schematics of the mechanism of static quenching. The *MQ* complex can be excited, but is not fluorescent. As *Q* does not affect the *M* excited state, there is no change in its fluorescence lifetime. (b) Dynamic quenching.

The association constant, K_s, controls the equilibrium between free and fluorophore–quencher complexes:

$$K_s = \frac{[MQ]}{[M]_q[Q]} = \frac{[M]_0 - [M]_q}{[M]_q[Q]}, \tag{1.21}$$

where $[M]_q$, $[Q]$, and $[MQ]$ are the concentrations of the ground state molecular fluorophore, quencher, and fluorophore–quencher complex, respectively, in the presence of the quencher. $[M]_0$ is the initial concentration of the fluorophore in the absence of the quencher and $[M]_q$ the concentration of the fluorophore in the presence of the quencher. Equation (1.21) can be easily converted into the well-known Stern–Volmer equation [3]:

$$\frac{I_f}{I_{fq}} = \frac{[M]_0}{[M]_q} = 1 + K_s[Q], \tag{1.22}$$

where I_f and I_{fq} are the fluorescence intensities measured in the absence and presence of the quencher, respectively. The absorption spectrum can reveal evidence for the presence of static quenching as *MQ* will be likely to have a different spectrum to *M*. However, because static quenching does not interfere with the excited-state kinetics, but only reduces the concentration of the fluorescent dye, no change in fluorescence lifetime is observed. In addition to well-known static quenchers, for example, mercury ions, some newly developed materials, such as graphene [75] and carbon nanotubes [76], have also been recently found to act as static quenchers for certain dyes.

1.5.1.2 Dynamic Quenching

Dynamic quenching occurs during the collision of the electronically excited molecule *M** and the quenching molecule *Q* (see Fig. 1.12b). During the collision, the excitation energy is transferred to the quencher and dissipated as heat. Because the excited state kinetics is affected, the fluorescence lifetime in addition to the yield is reduced.

The kinetic equations for the concentration of the excited dye $[M^*]$, following δ-function excitation at $t = 0$, in the absence and in the presence of a quencher Q, are given by Eq. (1.9) and Eq. (1.23), respectively.

$$[Q] > 0 \Rightarrow \frac{d[M^*]}{dt} = -(\tau_{\mathrm{f}}^{-1} + k_{\mathrm{q}}[Q])[M^*], \tag{1.23}$$

where τ_{f} is the fluorescence lifetime in the absence of quencher and k_{q} is the diffusion-controlled quenching rate constant. In the steady state $d[M^*]/dt = 0$. These equations yield the Stern–Volmer equation for dynamic quenching and fluorescence intensities analogous to static quenching, but this time including the lifetime:

$$\frac{I_{\mathrm{f}}}{I_{\mathrm{fq}}} = \frac{\tau_{\mathrm{f}}^{-1} + k_{\mathrm{q}}\,[Q]}{\tau_{\mathrm{f}}^{-1}} = 1 + \tau_{\mathrm{f}} k_{\mathrm{q}}\,[Q]\,. \tag{1.24}$$

The solution of Eq. (1.23) (equivalent to Eq. (1.8), but including quenching) is $[M^*] = [M^*]_0 \exp(-t/\tau_{\mathrm{fq}})$, where

$$\frac{1}{\tau_{\mathrm{fq}}} = \frac{1}{\tau_{\mathrm{f}}} + k_{\mathrm{q}}\,[Q]\,. \tag{1.25}$$

This indicates that the fluorescence decay of the dynamically quenched dye remains exponential, but with a reduced lifetime $\tau_{\mathrm{fq}} < \tau_{\mathrm{f}}$. After simple rearrangement of Eq. (1.25), we obtain the Stern–Volmer dependence for lifetimes:

$$\frac{\tau_{\mathrm{f}}}{\tau_{\mathrm{fq}}} = 1 + \tau_{\mathrm{f}} k_{\mathrm{q}}\,[Q]\,. \tag{1.26}$$

The right-hand side of this equation is the same as in Eq. (1.24) with both steady-state and time-resolved fluorescence yielding the Stern–Volmer constant $K_{\mathrm{SV}} = \tau_{\mathrm{f}} k_{\mathrm{q}}$ of dimension M^{-1}.

Several compounds, often containing heavy atoms to facilitate intersystem crossing to the triplet state, are well known as dynamic quenching agents when present at sufficiently high concentration. This has led to a wide range of structural probes and analyte sensors based on the Stern–Volmer equation. For example, oxygen, with a triplet ground state and occurring at $\sim 10^{-3}$ M in aliphatic solvents, is a highly efficient dynamic quencher of fluorescence (diffusion constant in water $\sim 10^{-5}\ \mathrm{cm}^2\ \mathrm{s}^{-1}$). Oxygen sensors based on the long-lived excited states of transition metal complexes have been extensively developed [77,78]. Other quenchers include chloride, bromide, and iodide ions [79,80]; transition, noble, and heavy metals [81,82]; amines; carbon tetrachloride; and acrylamide [83,84].

In some cases, collisional interactions can result in the formation of an excimer or exciplex [2] which have their own fluorescence characteristics and add complexity to the kinetics. Indeed carbon tetrahalides have been shown to exhibit hybrid quenching composed of static, dynamic, and exciplex components [2].

In addition, k_q is not always a constant, but has a $\sqrt{t}$ time dependence that in the simplest case can be derived from Smoluchowski's solution [85] of the diffusion equation

$$k_q = 4\pi RD \left[1 + \frac{R}{\sqrt{\pi Dt}} \right], \tag{1.27}$$

where D is the sum of the diffusion coefficients of the fluorophore and quencher and R is the sum of their interaction radii.

This leads to a nonexponential impulse response given by [3]

$$i(t) = i_0 \exp\left[-t/\tau_{fq} - 2b\left(t/\tau_{fq}\right)^{1/2} \right], \tag{1.28}$$

where $b = 4R^2 N_A (\pi D)^{\frac{1}{2}} [Q]/1000$ and N_A = Avogadro's number.

Such transient effects are exaggerated in higher viscosity solvents such as glycerol, which reduces collisional quenching, but can be observed even in low viscosity solvents such as ethanol at higher time resolution. It can be observed as a departure from an exponential decay at short times in both TCSPC and phase fluorometry, with and without excimer/exciplex formation [86–88].

1.5.1.3 Förster Resonance Energy Transfer Direct collisional contact between the dye and the quencher is not required in the third common mechanism of quenching that we will consider. Förster resonance energy transfer (FRET) has become popular in recent years as a "spectroscopic ruler" for measuring distances and studying the structure and dynamics of macromolecular and microheterogeneous molecular systems [89]. Named after Theodor Förster, who discovered and described the quantum-mechanical nature of this phenomenon in the late 1940s, the mathematical description of FRET is obtained by applying perturbation methods to an excited dye–quencher pair, which are denoted donor D and acceptor A (see Fig. 1.13). The interaction is usually dipole–dipole in origin, and the spectral overlap (the "resonance") between the donor fluorescence and acceptor absorption is a prerequisite for FRET and this gives it higher intrinsic specificity than collisional quenching.

Förster's treatment gives the rate of D–A energy transfer k_{DA} to be

$$k_{DA} = \frac{1}{\tau_D} \left(\frac{R_0}{r} \right)^6, \tag{1.29}$$

where r is the D–A distance (both D and A are regarded as point dipoles and thus assumed to have no spatial dimension) and τ_D is the fluorescence lifetime of the donor in the absence of acceptor (τ_f as defined previously). Since the k_{DA} is proportional to the inverse sixth power of the distance r, FRET can be used as an extremely sensitive mechanism for determining D–A separations and thus measuring molecular distances. The actual scale of this "molecular ruler" is determined by the parameter

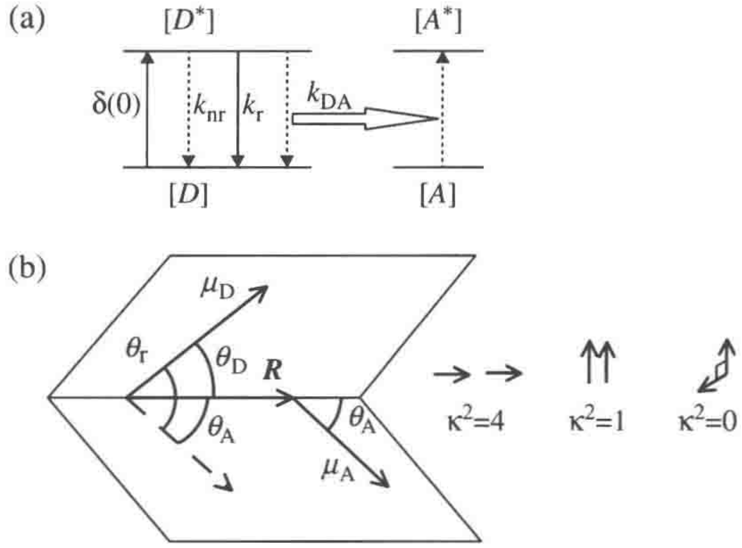

FIGURE 1.13 (a) The mechanism of Förster resonance energy transfer. (b) The orientation factor in FRET. μ_D and μ_A are the transition dipole moments of donor and acceptor molecules and R is the separation vector.

R_0, the Förster or critical transfer distance. According to Förster's theory, R_0 can be calculated using the relevant spectroscopic properties of the donor and acceptor:

$$R_0^6 = \frac{9000 \ln(10) \kappa^2 \Phi_f}{128 \pi^5 N_A n^4} \int_0^\infty I_D(\lambda) \varepsilon_A(\lambda) \lambda^4 d\lambda, \tag{1.30}$$

where κ^2 is the orientational factor, Φ_f the quantum yield of donor fluorescence (without acceptor), N_A the Avogadro's number, and n the refractive index of the intervening medium. The integral in Eq. (1.30) represents the degree of spectral overlap between the donor fluorescence spectrum $I_D(\lambda)$ and the acceptor absorption spectrum $\varepsilon_A(\lambda)$. Significant spectral overlap ensures a high critical transfer distance R_0 (typical values vary from ~10 to 100 Å) and thus a high rate of FRET. Equation (1.29) allows the determination of D–A separations; this simple equation finds numerous applications in the materials and life sciences. The other critical factor affecting R_0 is the orientational factor κ^2, defined as

$$\kappa^2 = [\cos\theta_T - 3\cos\theta_D \cos\theta_A]^2. \tag{1.31}$$

The angles are defined in Figure 1.13b, where some limiting situations have also been depicted for $0 < \kappa^2 < 4$.

For fast and freely rotating donor and acceptor molecules, κ^2 can be averaged over time and equals 0.67 and this assumption often has to be made even when not strictly correct. If the mutual orientation of D and A is not fully random, the orientational effects may significantly affect FRET, which can be explored to extract extra structural information. The orientational dependence of FRET has been discussed in numerous studies [90] and recently conclusively demonstrated using labeled nucleic acids [91].

The presence of FRET is manifest in the fluorescence spectrum of the sample by a decrease in the intensity of the donor spectrum and increase in the acceptor spectrum (if the acceptor is fluorescent). FRET not only reduces the intensity of donor fluorescence but also affects its fluorescence decay. In the simplest case, if the original donor decay is a single exponential with the lifetime τ_D and D and A are separated at the fixed distance r_{DA}, then the fluorescence impulse response is

$$i(t) = i_0 \exp\left[-\left(1+\left(\frac{R_0}{r_{DA}}\right)^6\right)\frac{t}{\tau_D}\right]. \tag{1.32}$$

Equation (1.32) shows that the decay remains a single exponential, but with a reduced lifetime that allows determination of the D–A distance.

In the presence of acceptors distributed around the donors according to the D–A distribution function $\rho(r)$, the fluorescence impulse response is modified to

$$i(t) = i_0 \exp[-t/\tau_D - \int_0^\infty \left(1 - tk_{DA}(r)\right)\rho(r)\,dr]. \tag{1.33}$$

Equation (1.33) shows the potential of FRET for not only determining distances but also studying the morphology of a medium on the sub-nanometer scale. Unfortunately, although initially promising, without making *a priori* assumptions, interpretation of FRET in amorphous materials such as silica was found to be limited to fractals and simple model geometries [92, 93] and not give the detailed morphology sought. The underlying problem is the ill-posed nature of Eq. (1.33), such that a unique solution for the distribution function $\rho(r)$ does not usually exist. The usual approach is to assume a hypothetical formula for $\rho(r)$ and then try to determine the "best-fit" parameters.

Fortunately Eq. (1.33) can be solved for the most commonly encountered special case, namely that of a random distribution of acceptors $\rho(r) \sim r^2$, leading to the well-known Förster decay function

$$i(t) = i_0 \exp[-t/\tau_D - \gamma\left(t/\tau_D\right)^{1/2}], \tag{1.34}$$

where $\gamma = [A]/C_A$, and

$$C_A = \frac{3}{4\pi^{3/2}R_0^3 N_A}, \tag{1.35}$$

where $[A]$ is the actual acceptor concentration and C_A the critical molar acceptor concentration.

Equation (1.34) can be implemented in different ways. For example R_0 can be determined from Eq. (1.30) to give C_A using Eq. (1.35). Then by reconvoluting Eq. (1.34) in order to fit to the experimental fluorescence decay, the local concentration of the acceptor in the donor environment can be found. In microheterogeneous systems, this may well not be the same as the bulk concentration, thus indicating structure, accessibility, or other information from the donor–acceptor proximity. The measurement is effectively the same when FRET is used as a sensor platform for determining the presence and concentration of analytes of interest and we illustrate this in the next section.

1.5.2 Application—Metal Ion Quenching

Metal ion detection has widespread relevance to many important areas that include human metabolism, neurology, and the environment. By way of an example of fluorescence-based sensing, we consider here the quenching by copper ions in different media of the red/near-IR fluorescent dye carbocyanine dye, 3,3-diethylthiadicarbocyanine iodide (DTDCI). Hydrated copper ions ($Cu^{2+}\cdot 5H_2O$) can quench both collisionally and by FRET via an overlapping broad band absorption that peaks around 800 nm.

Figure 1.14 presents the result of fitting Eq. (1.34) to the fluorescence decay for DTDCI quenched by hydrated copper ions in propylene glycol (a and b), and in water pools (c and d) of a hydrated perfluorosulfonate ion exchange membrane (Nafion, Dupont Corp.) [94]. Plots a and b show a "pure" FRET example that is described by Eq. (1.34), that is, a constant value of the donor lifetime τ_D and γ increasing linearly with copper ion concentration. Plots c and d show an example of a not infrequent case of hybrid kinetics where FRET is accompanied by collisional quenching, which leads to a decrease of the donor lifetime with increasing quencher concentration.

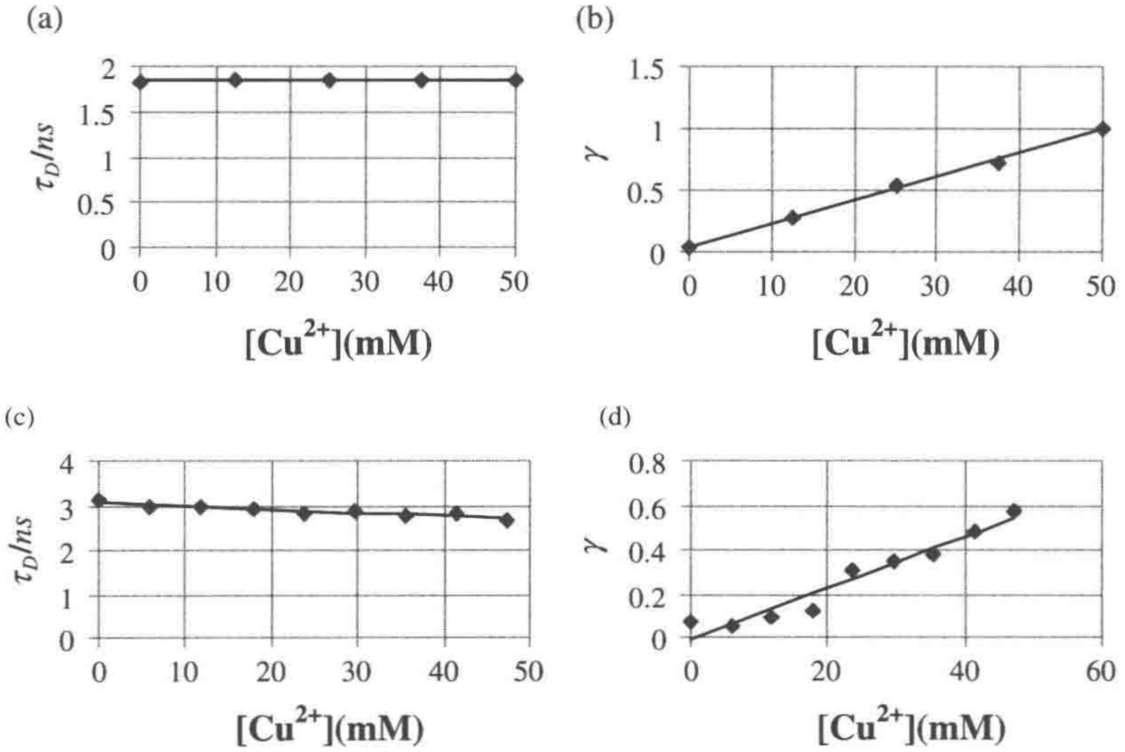

FIGURE 1.14 Donor lifetimes τ_D and γ values for the DTDCI→Cu^{2+} quenching in propylene glycol (a and b), and in Nafion (c and d) [94].

Notwithstanding the homogeneous and heterogeneous differences in the two media, the dominant difference between the two cases is the much lower diffusion coefficient ($\sim 10^{-7}$ cm^2 s^{-1}) in propylene glycol. Such behavior has been observed in numerous other combinations, for example, Cu^{2+} sensing down to 10 ppb in Nafion using rhodamine 800 as a donor [95]. Models of increasing complexity have been proposed for handling such hybrid kinetics, starting with essentially linear combinations of collisional and FRET terms [96].

Two of the advantages of using hydrated transition metal ions as acceptors are their good approximation to the point dipole demanded by Förster's theory and minimal disturbance of native structure. These have been recently put to good effect when measuring distances in model α-helical peptides [97, 98]. However, transition metal ion acceptors have the disadvantage of a relatively short R_0 value ($\sim$1–2 nm) caused by the weak d–d transitions as compared to the π–π^* transitions of aromatic acceptors. This problem can be overcome in sensing by using a chelating molecule, for example, bathocuproine used for Cu(I) [99]. For FRET sensing of the colorless metal ion zinc, a fluorescently labeled enzyme, carbonic anhydrase II, has been successfully used [100, 101]. Quantum dots are emerging as a more robust donor than aromatic dyes for sensing metal ions, although their decay time kinetics can also be complex [102]. Although comparatively large in size ($\sim$2–6 nm) [103], they are still a useful alternative to conventional dyes when bound to protein for FRET studies [104]. Similarly green fluorescent protein [105] and its subsequent other visible forms are finding increasing use with FRET [106].

1.6 ANISOTROPY

Fluorescence anisotropy describes the polarization of fluorescence and along with quenching, is one of the most important methods in fluorescence spectroscopy, particularly when time-resolved using similar techniques to those already described for the measurement of fluorescence lifetimes. Just as fluorescence quenching is influenced by translational diffusion or proximity for FRET to occur, fluorescence anisotropy is influenced by rotational diffusion and energy migration. The importance of FRET and anisotropy can be judged from their sub-nanometer spatial resolution, which is over an order of magnitude better than any techniques using an optical microscope. This has led to their application as a tool for molecular nanometrology.

1.6.1 Theory

The basis of fluorescence anisotropy techniques is to use polarized excitation to create a spatially selected, non-random, distribution of excited fluorescent molecules which then randomize, most commonly by Brownian rotation, but also at times by energy migration depending on the system. The extent by which the fluorescence emission is depolarized depends on the rotation of the fluorophore (or extent of energy migration or both), which in turn brings with it the measurement of parameters that influence molecular rotation. Figure 1.15 shows a typical geometrical arrangement with respect

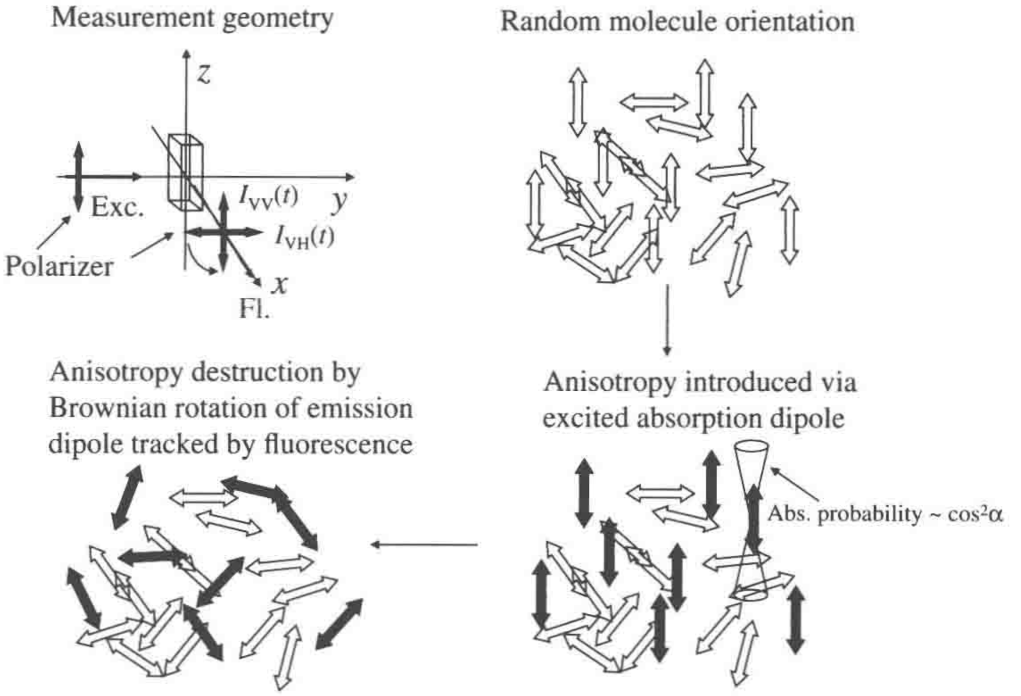
Measurement geometry
Random molecule orientation
z
Exc.
Polarizer
$I_{VV}(t)$
y
$I_{VH}(t)$
x
Fl.
Anisotropy destruction by Brownian rotation of emission dipole tracked by fluorescence
Anisotropy introduced via excited absorption dipole
Abs. probability ~ cos²α

FIGURE 1.15 Measurement geometry for anisotropy studies, selective excitation using polarized light and depolarized fluorescence emission due to Brownian rotation. The probability of excitation goes as $\cos^2\alpha$, where α is the angle between the plane of polarization and the absorption dipole.

to the spectrometers shown in Figures 1.2 and 1.8 and the photoselection in a random distribution of molecules that is designed to be produced. Both steady-state and time-resolved anisotropy can be performed using the configuration shown in Figure 1.15.

The theory of fluorescence anisotropy has developed over many years from the work of Perrin, Jablonski, Weber, Wahl, and others [3] and has been frequently reviewed [107, 108].

Both steady-state and time-resolved anisotropy can be measured using the configuration of Figure 1.15. By recording vertically (V) and horizontally (H) polarized fluorescence decay curves, $I_{VV}(t)$ and $I_{VH}(t)$, orthogonal to vertically (V) polarized excitation, a time-resolved anisotropy function $r(t)$ can be generated that is much more revealing (particularly if heterogeneous depolarization mechanisms are present) than the steady-state anisotropy, that provides just a time average, as it neglects the time dependence, that is,

$$r(t) = \frac{I_{VV}(t) - GI_{VH}(t)}{I_{VV}(t) + 2GI_{VH}(t)}, \tag{1.36}$$

where G is a factor ($G = I_{HV}(t)/I_{HH}(t)$) determined for horizontal orientation of the excitation polarizer in order to correct for differences in the polarization transmissions of the fluorescence detection channel at V and H, which are largely due to the emission monochromator. The factor of 2 in the denominator arises because there is a plane in the direction of the excitation in which depolarization of fluorescence is not detected, but which is identical to that detected in the emission channel. Because the denominator in Eq. (1.36) describes all three planes of polarization, it actually also describes the fluorescence decay undistorted by any polarization bias. This can be seen from inserting Eqs. (1.37) and (1.38) below into Eq. (1.36) for the simplest depolarization case where a fluorophore can be treated as a spherical rigid rotor undergoing Brownian isotropic rotation in a medium such as a solvent for

$$I_{\mathrm{VV}}(t) = \exp(-t/\tau_{\mathrm{f}})[1 + 2r_0 \exp(-t/\tau_{\mathrm{c}})], \tag{1.37}$$

$$I_{\mathrm{VH}}(t) = \exp(-t/\tau_{\mathrm{f}})[1 - r_0 \exp(-t/\tau_{\mathrm{c}})], \tag{1.38}$$

whereby we obtain

$$r(t) = r_0 \exp\left(-\frac{t}{\tau_{\mathrm{c}}}\right), \tag{1.39}$$

where r_0 is the initial anisotropy at $t = 0$, which has a maximum value of 0.4 for one photon excitation, and τ_{c} the rotational correlation time, which describes the rate of depolarization due to isotropic rotation.

In this case, τ_{c} can be described by the Stokes–Einstein equation:

$$\tau_{\mathrm{c}} = \frac{\eta V}{kT} = \frac{1}{6D}, \tag{1.40}$$

where η is the microviscosity, V the hydrodynamic volume $= 4\pi R^3/3$ prescribed by the rotor of hydrodynamic radius R, T the temperature, k the Boltzmann constant, and D the rotational diffusion coefficient.

The denominator in Eq. (1.36) can be useful in determining τ_{f} free from errors due to polarization effects when τ_{f} is comparable to the rotational correlation time τ_{c}, such as might occur for aromatic fluorophores in viscous solvents. An alternative adaptation of Figure 1.15 achieves the same by having vertical excitation polarization and the emission polarizer at the so-called magic angle of 54.8° to the vertical. The same aim can also be achieved at other specific polarizer orientations [30].

In the case where a fluorophore is partitioned between two different environments characterized by τ_{c1} and τ_{c2} or has a bimodal anisotropic rotation [109], then providing τ_{f} is the same for each rotational component:

$$r(t) = (1 - f)r_0 \exp\left(-\frac{t}{\tau_{\mathrm{c1}}}\right) + fr_0 \exp\left(-\frac{t}{\tau_{\mathrm{c2}}}\right), \tag{1.41}$$

where f defines the fraction of fluorescence associated with each decay component.

Equation (1.41) finds wide-ranging application, including that of nanoparticle metrology in the example given in Section 1.6.3 [110].

If the fluorophore undergoes restricted motion such as in a lipid bilayer [111], or wobbles when tethered to a slowly rotating macromolecule such as a protein [107], then Eq. (1.41) is modified for these special cases, since $\tau_{c2} \gg \tau_{c1}$, to give

$$r(t) = (1 - f)r_0 \exp\left(-\frac{t}{\tau_{c1}}\right) + fr_0, \tag{1.42}$$

fr_0 is sometimes referred to as the residual anisotropy r_∞ and in the case of lipid bilayer membranes leads to the determination of an order parameter S for the membrane from [111]

$$S = \sqrt{\frac{r_\infty}{r_0}}. \tag{1.43}$$

Although often an approximation sometimes Eqs. (1.41) and (1.42) can be combined to useful effect to give

$$r(t) = (1 - f - g)r_0 \exp\left(-\frac{t}{\tau_{c1}}\right) + fr_0 \exp\left(-\frac{t}{\tau_{c2}}\right) + gr_0 \tag{1.44}$$

For example, Eq. (1.44) is useful where unbound dye coexists alongside dye wobbling when bound to a slowly rotating nanoparticle.

1.6.2 Experimental

The experimental methodologies for steady-state and time-resolved anisotropy measurements are achieved by combining the techniques described in Sections 1.2 and 1.4, respectively, with the polarization orientations shown in Figure 1.15. One extra point of care is to ensure that in determining fluorescence anisotropy from Eq. (1.36) any fluctuations in the source intensity are corrected. This is usually achieved by averaging out any drift by alternating between the measurement of $I_{VV}(t)$ and $I_{VH}(t)$, and sometimes by the use of a T-format, which offers continuous correction [48].

Although there are different approaches to the analysis of anisotropy decay data, the usual method is to use NLLS in an analogous manner to that described in Section 1.4.2 for fluorescence lifetime analysis. Rearranging the anisotropy function given by Eq. (1.36), we obtain

$$d_t = r(t)[I_{VV}(t) + 2GI_{VH}(t)] = I_{VV}(t) - GI_{VH}(t). \tag{1.45}$$

The function within square brackets in Eq. (1.45) is the fluorescence decay, which we can fit to separately using as many decay parameters as required to give a good fit in order to obtain the fluorescence impulse response $i(t)$ and then keep it fixed, that is, with reference to Eq. (1.19) i_1, τ_{f1}, i_2, τ_{f2}, and so on. The function on the right-hand side of Eq. (1.45) contains the difference data d_t that carries the rotational information and which we can iteratively fit to using NLLS reconvolution of $P(t)$ with anisotropy impulse response functions $r(t)$ that are intuitively thought to be applicable (e.g., Eq. 1.39, 1.41, or 1.44). Then, we obtain r_0, τ_{c1}, and τ_{c2}, again using χ^2 as the goodness-of-fit criterion, that is,

$$\chi^2 = \sum_{\substack{\text{Data}\\ \text{channels}}} \left[\frac{d_t - P(t) \otimes r(t)i(t)}{\sqrt{d_t}} \right]^2 \tag{1.46}$$

Since the rotation is tracked by the fluorescence decay, ideally τ_c should be $\sim\tau_f$.

In comparison to fluorescence quantum yield and lifetime, there are not really any established standards for rotational correlation time. The rotation of rhodamine 6G has perhaps been studied the most and is probably the nearest to a standard. Some rotational measurements on rhodamine 6G are listed in Table 1.3. The effect of solvent in sticking to rotating fluorophores needs to be kept in mind when considering fluorescence anisotropy [108].

The advantages of using rhodamine 6G as a standard are that it is an isotropic rotor, has a monoexponential fluorescence decay ($\tau_f \sim 4$ ns [115, 116]) and a high fluorescence quantum yield (0.91 in ethanol [10]), is commercially available in high purity, and is photo- and chemically stable over a wide range of pH (<2 to >12). Other xanthene dyes, for example, rhodamine 101, have also been considered as rotational standards, and a useful IUPAC Technical Report [117] recently listed rotational data on a range of fluorophores, including rhodamine 6G and rhodamine 101, and made recommendations for checking the accuracy of measurements. It should be noted however that r_0 for rhodamine 6G decreases quite rapidly when excited below its 0-0 transition, which is ~515 nm [117].

TABLE 1.3 Some reported rotational parameters for rhodamine 6G using one-photon excitation and a range of techniques

Hydrodynamic radius R (Å)	Temperature (°C)	Excitation (nm)	τ_c (ps) in ethanol	τ_c (ps) in methanol	τ_c (ns) in propylene glycol
6.0 ± 0.03 [112]					
5.4 [113]	Not specified. Probably room temperature	530	175 ± 13	91 ± 8	
5.4 [114]	21	580	195 ± 5	95 ± 3	
5.6 ± 0.1 [115]					
5.3 ± 0.3 [116]					
	27	400			6.16 ± 1.10 [117]

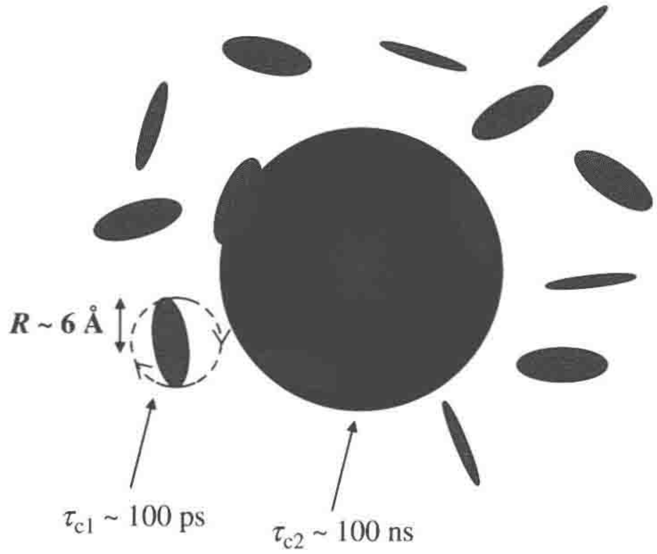

FIGURE 1.16 Depiction of the coexistence of dual anisotropy kinetics for the case of a fluorophore bound to a much larger nanoparticle and also unbound, both entities rotating freely under Brownian motion in solution. Since from Eq. (1.40) $\tau_c \propto R^3$, three orders of magnitude difference in rotational correlation time is observed for only one order of magnitude difference in radius. This helps reduce error propagation when measuring the radius. For the same reason, the dimensions of the fluorophore usually have negligible effect.

1.6.3 Application Example—Nanoparticle Metrology

Fluorescence anisotropy using fluorescence probes has undoubtedly been most widely used in biomolecular research for the study of structure and dynamics in protein [107] and membranes [118]. Here, we choose a different and in principle simpler example that concerns the measurement of nanoparticle size, and which uses the theory of multiple anisotropy decay components already described.

There has been a recent upsurge in interest in nanoparticles, concerning research not only into their new forms such as semiconductors and gold, but also into their older forms such as carbon and silica. Part of the interest lies in concern over the toxicology and environmental aspects of all types of nanoparticles, particularly those in the 1–10 nm range, which can easily traverse cellular membranes. Measuring such small sizes in in situ presents a significant challenge to metrology, though one in which fluorescence anisotropy decay is ideally suited.

The situation depicted by Figure 1.16 of a fluorophore bound to a much larger nanoparticle, and also unbound, can be realized using either electrostatic or covalent binding. Figure 1.17 illustrates a real example [119]. In Figure 1.17a, the non-binding of anionic fluorescein to the anionic nanoparticles (rotational correlation time ~200 ns) of LUDOX [55] silica AM30 is reflected with little change in the anisotropy decay when the dye is added to the colloid. Figure 1.17b shows how the cationic rhodamine 6G binds to the nanoparticles, but has too fast a fluorescence lifetime (~ 4 ns) to effectively track the much slower depolarization as the nanoparticles rotate and is therefore still unsuitable for metrology purposes. Figure 1.17c shows that the binding and longer fluorescence lifetime (~25 ns) of the cationic 6-methoxyquinolinium

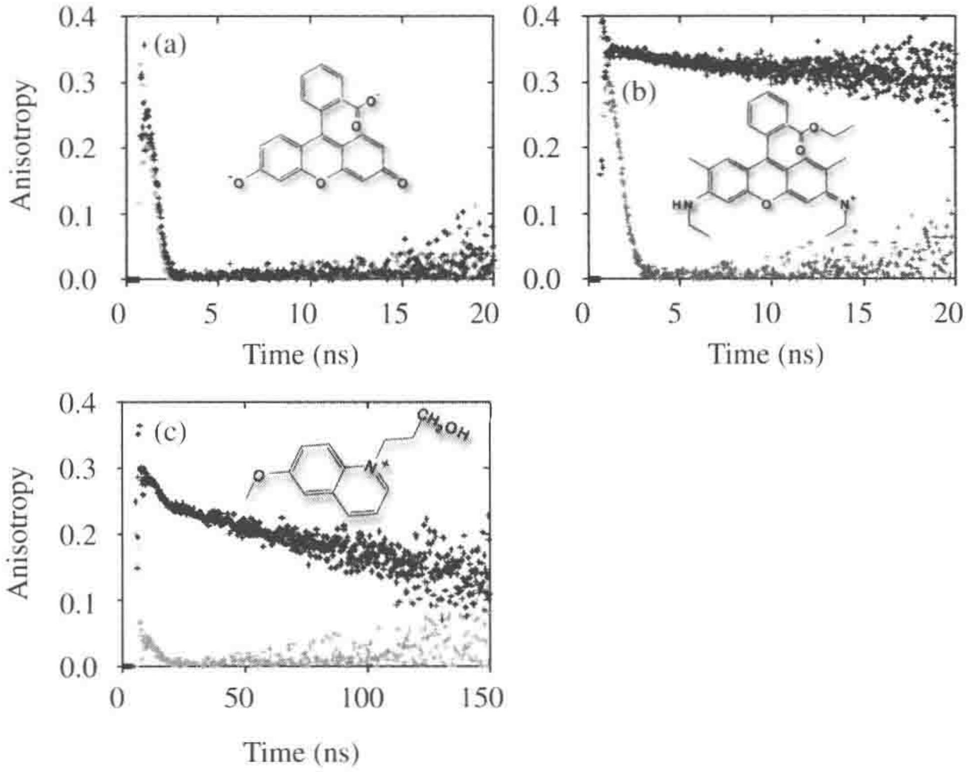

FIGURE 1.17 Effect on the fluorescence anisotropy decay (black data points) of adding different fluorophores to LUDOX [55] AM30 at pH 8.9: (a) Fluorescein, (b) rhodamine 6G, (c) 6-methoxyquinolinium (structures also shown). For comparison, the gray data points describe the dye rotation in methanol without LUDOX [119].

fluorophore are good enough to track the rotation, revealing the particle rotation and enabling the measurement of its radius.

The simplest case is when all the dye binds to the nanoparticle and then Eqs. (1.39) and (1.40) can be used. However, in this case, the microviscosity has to be already known or found from a separate anisotropy measurement or other means. If the anisotropy can be described by the presence of fluorophores that are both free and also bound to a nanoparticle, then a single anisotropy decay, analyzed using Eqs. (1.40) and (1.41), enables both the microviscosity of the medium and the nanoparticle radius to be conveniently determined in a single measurement [110,116]. However, things are not always so straight forward. Other effects, which may be present, and can influence the measured $r(t)$, include nanaoparticles aggregating and fluorophores wobbling on the nanoparticle, diffusing on the surface of the nanoparticle, aggregating on or off the nanoparticle, undergoing homo-FRET, and having a different fluorescence lifetime on and off the nanoparticle [119, 120]. Fortunately, some of these, though not all of these together, can usually be handled in the data analysis and, moreover, the sample can be designed at the outset to minimize such effects. Note also that having a complex multiexponential fluorescence decay tracking a nanoparticle rotation is not in itself any handicap whatsoever as long it is taken into account in the data analysis in Eq. (1.45).

One important difference between measuring anisotropy decay and fluorescence decay is the higher statistical precision (number of counts) needed in $I_{VV}(t)$ and

TABLE 1.4 Rotational parameters for LUDOX silica colloids labeled with a 6-methoxyquinolinium dye [120] and obtained by fitting the anisotropy decay to Eq. (1.44)

LUDOX	τ_{c1} (ns)	τ_{c2} (ns)	gr_0	r_0	χ^2	Peak in d_t	R_m (nm)	R_{fa} (nm)
SM30	24	65 ± 15	0.12	0.24	1.26	1×10^5	3.5	4.0 ± 0.4
AM30	17	273 ± 60	0.06	0.28	1.23	5×10^5	6.0	6.4 ± 0.5
AS40	10	1400 ± 590	0.07	0.28	1.27	1×10^6	12	11.0 ± 1.6

d_t is the peak count in the difference curve in Eq. (1.45). The data channel width was 28 ps. R_m is the manufacturers quoted value for the nanoparticle radius, most probably obtained using electron microscopy on the dry colloid. R_{fa} is the radius obtained from the τ_{c2} component of the fluorescence anisotropy decay. gr_0 is attributed to colloidal nanoparticle aggregates. τ_{c1} is too long to be free dye rotation, and may reflect dye wobbling and/or diffusing on the surface of the nanoparticle.

$I_{VH}(t)$ before a meaningful comparison of rotational models can be made. This is because it is not the absolute value, but the difference of $I_{VV}(t)$ and $I_{VH}(t)$ that is used in the anisotropy function (Eq. 1.36). The anisotropy measurements shown in Figure 1.17 were obtained using TCSPC with ~10,000 counts in the peak channel of the difference curve [119] and this is adequate for many purposes. However, if a more complex model, such as that of Eq. (1.44) is to be deployed then much higher statistical precision is required. This is illustrated in Table 1.4 for a range of LUDOX colloids [120].

The nanoparticle radii obtained using fluorescence anisotropy decay and those from the manufacturer's data sheet [55] are in good agreement. It is also worth noting that in the case of AS40 $\tau_{c2}/\tau_f \sim 56$, which is way outside usual practice and only possible because of the large number of counts obtained in d_t.

This need for increasingly high statistical precision in the face of correlations between the fitted parameters, when more than one rotational correlation time is present, is the reason why the determination of rotational correlation time distributions (which would lead to useful nanoparticle size distributions in this example) is extremely difficult using fluorescence anisotropy decay. The problem is analogous to the difficulty of determining distance distributions in FRET in so far as unique solutions do not in general exist.

One way of improving the measurement capability is to increase the dynamic range of r_0 above its maximum of 0.4 by the use of multiphoton excitation, though this is at the expense of the simplicity of measurement as it requires femtosecond laser excitation [116]. Multiphoton excitation enforces a higher angular alignment of the absorption dipole with the plane of polarization of excitation with a probability $\cos^{2j}\alpha$ (Fig. 1.15), where j is the number of photons absorbed. For two- and three-photon excitation, r_0 increases from 0.4 for one-photon excitation to a maximum of 0.57 and 0.67, respectively, where β, the angle between the absorption and emission dipoles, is taken to be zero [116] as given by

$$r_{0n} = \frac{2j}{2j+3}\left[\frac{3}{2}\cos^2\beta - \frac{1}{2}\right]. \tag{1.47}$$

Given the paucity of standards for rotational time measurements, Table 1.4 suggests that well-defined silica colloids also have something to offer in this capacity. Equally there is a recognized lack of international standards for nanoparticle metrology in general. When compared with traditional methods for nanoparticle metrology such as small-angle neutron, X-ray, or light scattering and electron microscopy, fluorescence anisotropy decay offers an inexpensive alternative that enables measurements in situ, with sub-nanometer resolution, in the important 1–10 nm range.

Fluorescence anisotropy decay can be used to measure the size of other types of nanoparticles apart from silica, provided they can be labeled extrinsically with a fluorophore. Nanoparticle intrinsic fluorescence is not necessarily helpful because internal depolarization mechanisms, as in the case of carbon soot nanoparticles [121], can distort the measurement.

So far we have considered only the situation where the fluorescence lifetime associated with each rotational correlation time is the same. This is not always the case and such a change can lead to some peculiar anisotropy decay curves. For example, where a fluorescence lifetime associated with a longer rotational correlation time is longer than that of a faster fluorescence decay time associated with a faster rotational correlation time, that is, $\tau_{f1} < \tau_{f2}$ and $\tau_{c1} < \tau_{c2}$. In this case, $r(t)$ initially falls with time, goes through a dip, and then rises again as the longer lived fluorescence and rotational components start to dominate. Such effects have been observed and analyzed in protein and lipid bilayer membranes [122], often reflecting structural heterogeneity, but also with silica nanoparticles for free and bound dye [123]. This behavior can be successfully modeled by reworking Eqs. (1.37) and (1.38) to take account of the different fluorescence lifetime and then reformulating $r(t)$.

Finally, in addition to the examples already mentioned, both steady-state and time-resolved fluorescence anisotropy continue to find multifarious applications. These include metal ion sensing [124], drug compliance monitoring [125], beta-amyloid aggregation [126], surface modification [127], and pH meter measurement of nanoparticle growth during silica hydrogel production [128].

1.7 MICROSCOPY

Fluorescence microscopy is a noninvasive, nondestructive technique, capable of imaging at levels from a single molecule, cell, tissue, to human. No other method can interrogate molecules in living cells with anything remotely approaching fluorescence microscopy's combination of spatial resolution, sensitivity, selectivity, and dynamical insight. The capability to visualize biomolecules, by virtue of either intrinsic or extrinsic fluorescence, enables the study of elementary biochemical reactions in cells and, not surprisingly, this has become a prominent technique in biological research. Moreover, it is fair to say that fluorescence microscopy has enjoyed somewhat of a renaissance in recent years with a growth paralleled across fluorescence only by lifetime measurements. Much of this growth has been fueled by the translation of spectroscopy, molecular photophysics, and laser photonics as we will illustrate here.

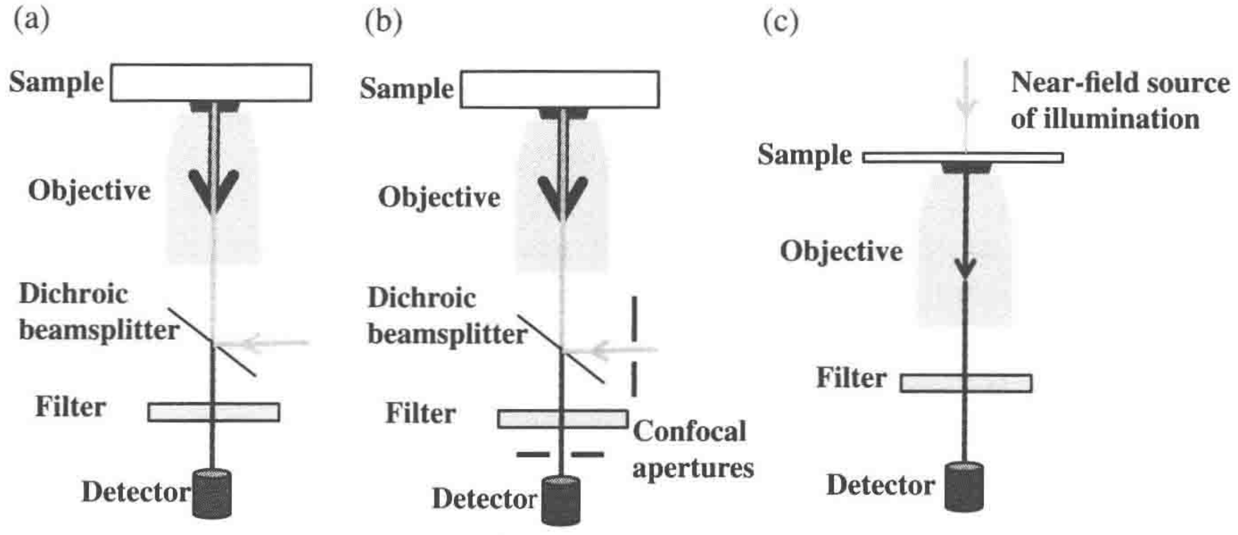

FIGURE 1.18 Schematics of some common fluorescence microscope configurations: (a) wide-field; (b) confocal; and (c) near-field.

1.7.1 Systems and Techniques

Figure 1.18 illustrates a schematic of some common fluorescence microscope configurations. Figure1.18a is representative of the most common configuration, a conventional epifluorescence (wide-field) microscope, which is traditionally operated with only incoherent optical excitation, such as from a high pressure mercury lamp fitted with a wavelength filter. The subsequent development of the confocal microscope and laser-based techniques greatly improved the spatial resolution and imaging capability of fluorescence microscopes. In a confocal microscope, as shown in Figure 1.18b, optical sections are illuminated through a pinhole aperture, and the fluorescence signal is channeled via another pinhole near the detector. The image is then compiled from laser scans of the surface. By means of the pinholes, the confocal microscope is able to discriminate against out-of-focus fluorescence and display-enhanced contrast in comparison with wide-field optical microscopes, allowing the reconstruction of three-dimensional (3D) structures from the images obtained. The development of 3D microscopy gained extra impetus with the introduction of Ti:sapphire ultrafast laser technology. This made multiphoton excitation much more routine than hitherto had been the case [129].

Multiphoton excitation microscopy generally uses long wavelength (near-IR) light and excites fluorescent dyes through an additive process, whereby the energy of two photons give the equivalent energy of one photon (cf. Fig. 1.1). While the advantages of multiphoton excitation in spectroscopy, for example, in increasing the dynamic range of anisotropy decay measurements, have already been mentioned (Eq. 1.47), further advantages accrue in microscopy. Using near-IR, multiphoton excitation minimizes the scattering in the sample, the background fluorescence, and photo-bleaching by virtue of the greater confinement of the excitation volume. The latter also facilitates the 3D imaging of sections over a greater optical penetration depth than is possible with one-photon confocal excitation [130].

The equivalent expression to one-photon absorption (Eq. 1.3) for j photons absorbed is nonlinear:

$$I_{\mathrm{f}} = \eta(\Phi_{\mathrm{f}}/j)Nd\sigma_j\rho^j, \tag{1.48}$$

where I_{f} is the rate of fluorescence, η the fluorescence detection efficiency, Φ_{f}/j the fluorescence quantum yield corrected for j-photon absorption, N the absorber number density (cm^{-3}), d the optical path length (cm), σ_j the absorption cross-section for j photons ($\mathrm{cm}^{2j}\ \mathrm{s}^{j-1}$) and ρ the excitation photon flux density (photons $\mathrm{cm}^{-2}\ \mathrm{s}^{-1}$, typically GW cm^{-2} over a 10-μm spot size).

From Eq. (1.48) it can be seen that the slope of $\log_e I_{\mathrm{f}}$ versus $\log_e \rho$ should give a straight line of slope j. This is a useful method of determining the number of photon absorbed (see Section 1.7.2). Multiphoton excitation can also be used to selectively excite fluorophores and quantum states according to their different selection rules. Several reviews are available on the application of multiphoton excitation to biological molecules in microscopy [131] and in spectroscopy [132].

If fluorescence spectroscopy has progressed through the development of temporal resolution, then much of the push in fluorescence microscopy in recent years has been dominated by improving spatial resolution. This has been both in terms of sectioning in depth and lateral resolution such that sample volumes ~10 fL can now be excited and this is sufficiently small for single molecules to be studied in isolation.

Conventional optical microscopes operate in the far field and have a diffraction-limited resolving power described by the Abbe criterion:

$$\Delta = \frac{\lambda}{2\mathrm{NA}}, \tag{1.49}$$

where Δ is the smallest possible resolvable distance between two point sources, given an emission wavelength, λ, and an imaging system with a numerical aperture (NA). NA is defined as $n\sin\theta$, where n is the refractive index of the imaging medium and θ is the half-angle of the maximum cone of light collected by the objective. This diffraction limit constrains the spatial resolution for visible wavelength to approximately 200–300 nm.

Progress in terms of depth resolution using multiphoton confocal microscopy has been complemented by other approaches. For example, total internal reflection fluorescence (TIRF) microscopy employs an evanescent wave generated when incident light is totally internally reflected at a glass–water/air interface to achieve selective illumination. Penetration depths of $\leq$100 nm in the low-refractive index medium have been achieved [133].

Improvements in lateral resolution have been obtained using a variety of techniques in recent years. This has created the exciting new area of single-molecule microscopy, which overcomes the ensemble smearing of information. This promises to provide heterogeneity and other fundamental information that might answer some of the big questions that underpin disease and therapeutics. For example, in protein does all protein of a given type fold by the same path? Can we monitor, and thereby

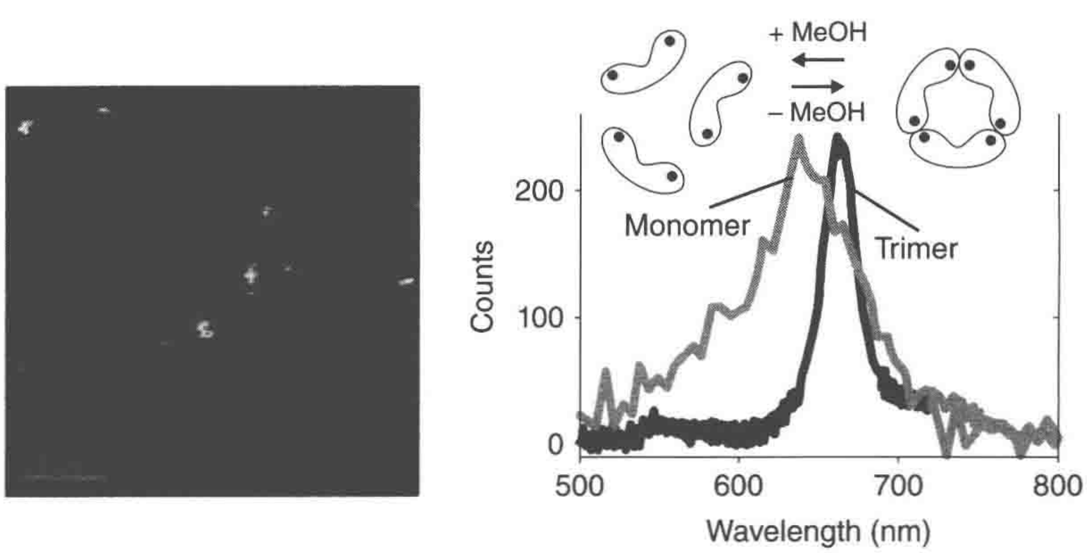

FIGURE 1.19 (a) Scanning confocal microscope images of single allophycocyanin (APC) molecules entrapped in hydrated pores of a thin silica film fabricated around the protein using the sol-gel process. The excitation wavelength is 532 nm. (b) The fluorescence spectra for the trimer (red) and monomer (blue) single molecule forms are shown. Dissociation of the trimer is induced by alcohol. Each APC unit contains two phycocyanobilin fluorophores, which are indicated by red dots. Reproduced from Reference 134 with permission from Springer Science + Business Media. (*For a color version of this figure, see the color plate section.*)

better understand, metabolism, disease, and therapeutics in cells at the level of binary molecular interactions? Figure 1.19 shows confocal microscope images and fluorescence spectra of a single protein aggregate and disaggregated monomer encapsulated for ease of observation in a hydrated silica nanopore [134].

Single-molecule microscopes come in different forms. Whatever their form, one of the underlying objectives is to enhance the fluorescence signal-to-noise ratio by reducing the lateral resolution and this can be adequately achieved using a confocal microscope. Such an arrangement is commonly used in fluorescence correlation spectroscopy (FCS), whereby a fluorescent entity (dye, protein, nanoparticle, etc.) is observed by a photon detector as it diffuses in solution in and out of the focal spot [135]. The autocorrelation function of the resultant fluorescence signal can be interpreted in terms of simple diffusion dynamics to provide information on size, aggregation, microviscosity, and diffusion constants that complement fluorescence quenching and anisotropy data. Two-photon excitation can also be used for excitation with confocal FCS in order to further confine the excitation volume [136].

Near-field scanning optical microscopy (NSOM) also enables single-molecule studies and breaks through the far-field resolution limit (Eq. 1.49), like TIRF, by exploiting the properties of evanescent waves (Fig. 1.18c). Here excitation is via a scanning single-mode optical fiber, which has a tapered tip with an internally reflective (aluminum-coated) sub-wavelength aperture that is held ~10 nm from the sample. The resolution depends on the aperture diameter rather than the wavelength of the light in this case and can reach ~50 nm [137], though the technique does not lend itself to depth profiling. Fluorescence lifetime measurements have been achieved using NSOM [138], but early promise was not realized due to a lack of reproducibility in lifetime measurements caused by the plasmonic effect of the aluminized tip.

The ability to probe metabolism, disease, and therapeutics inside cells is a challenging task, but one in which single-molecule fluorescence, combined with spectroscopic techniques, has considerable potential to advance our knowledge. Several excellent reviews of fluorescence techniques applied to the study of single molecule are available [139–141].

One difficulty encountered in single-molecule microscopy is bleaching of the fluorophore during a measurement, since multiple excitations (often using MHz lasers) mean the likelihood of even low-probability nonemissive transitions being populated is high. For example, a single fluorophore with Φ_f as high as 0.9 might be seen to have a negligible probability for photobleaching p (say $\sim 10^{-6}$), but it only has to be excited $1/p$ times to be likely to bleach. Blinking also occurs where a fluorophore goes from the singlet excited state into a long lived triplet ("dark") state, which may or may not then repopulate the singlet state and allow the continuation of fluorescence. Figure 1.20 illustrates both these phenomena.

As already mentioned, oxygen is a ubiquitous quencher of fluorescence, and it also facilitates the bleaching of dye molecules. Although purging with nitrogen or freeze-pump-thaw cycles might be adequate for enhancing the fluorescence yield and lifetime in ensemble spectroscopy, oxygen scavenging chemicals are frequently used

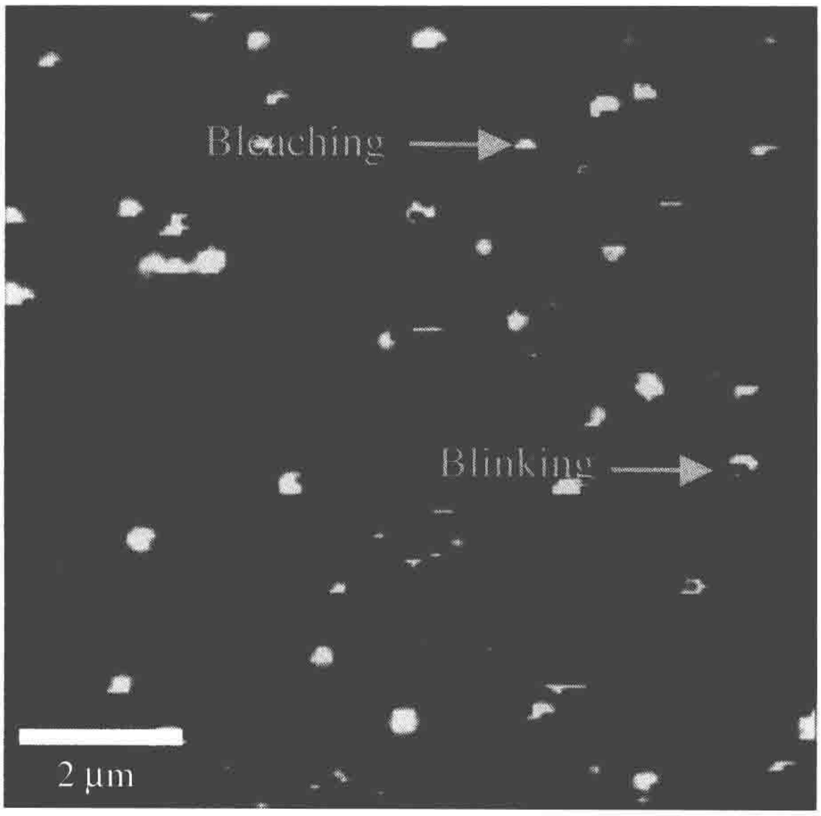

FIGURE 1.20 Laser scanning confocal microscope image of single rhodamine B molecules on a glass slide, illustrating the bleaching and blinking of dye molecules, these being a characteristic behavior of single molecules. The image acquisition time was 5.5 min using 40 nm × 40 nm pixels with an integration time of 5 ms. Reproduced from Reference 142.

in single-molecule microscopy in order to mitigate bleaching. Triplet quenchers can also be used to minimize blinking [143].

Perhaps somewhat ironically the quenching of fluorescence has been developed as means to enhance resolution in fluorescence microscopy. In the last two decades a whole new range of super-resolution light microscopy (nanoscopy) techniques have emerged for imaging in the far field and yet which break through the diffraction limit by means of active control of the fluorescence [144]. Stimulated emission depletion microscopy (STED) [145] was an early example overcoming the Abbe limitation (Eq. 1.49). Here the emission of fluorescence excited by an ultrafast laser pulse is confined to a region that is much smaller than that covered by the diffraction limit by following up the initial excitation with a further ultrafast excitation pulse that defines the resolution by depleting the fluorescence of dye within a doughnut around the central spot. Various other methods have been developed that are also based on the fundamental principle of active control of fluorescence, but using different mechanisms to achieve <20 nm resolution (i.e., superior to NSOM). These include photoactivated localization microscopy (PALM) [146], stochastic optical reconstruction microscopy (STORM) [147], and fluorescence PALM (FPALM) [148]. All these require a low concentration of well-separated fluorophores and then controlling their emission in order to avoid spatial overlap of emission that would otherwise blur the reconstruction of the image. Three-dimensional imaging is also possible and recently multicolor 3D super-resolution imaging has been demonstrated with a precision <10 nm by means of stochastically switching fluorophores [149]. Structured illumination microscopy [150] is an alternative approach and gives rapid 3D super-resolution imaging of cells by analyzing Moiré interference fringes.

Some quite spectacular and well-resolved images have been produced using these techniques and they are opening-up new possibilities for intracellular research in particular. Figure 1.21 illustrates this for images [151] obtained using direct photoactivation dSTORM [152], which uses direct excitation of a single fluorophore rather than a coupled pair of fluorophores. The super-resolution image typically generated is a computational reconstruction of the localized fluorophore density compiled from detecting fluorophores blinking.

The advantages of bringing more of the multidimensional nature of fluorescence to bear on microscopy became evident from quite early on. Traditionally, contrast in fluorescence microscopy is provided by fluorescence intensity. This is dependent on fluorophore extinction coefficient, quantum yield, the number of fluorophores present, and excitation intensity. The early fluorescence lifetime measurements with microscopes were only point-by-point single measurements [153] and the use of fluorescence lifetime as a means of contrast came later through the introduction of fluorescence lifetime imaging microscopy (FLIM). The advantages of fluorescence lifetimes mentioned in Section 1.4 also translate to microscopy. For example, the lifetime does not change with intensity; therefore, lifetime measurements are not dependent on the local concentration of fluorophore, bleaching, optical path of the microscope, excitation light intensity, or detection efficiency. Furthermore, the fluorescence lifetime usually depends on the intrinsic characteristics of the fluorophore and the local environment (e.g., microviscosity, pH, refractive index), as well as

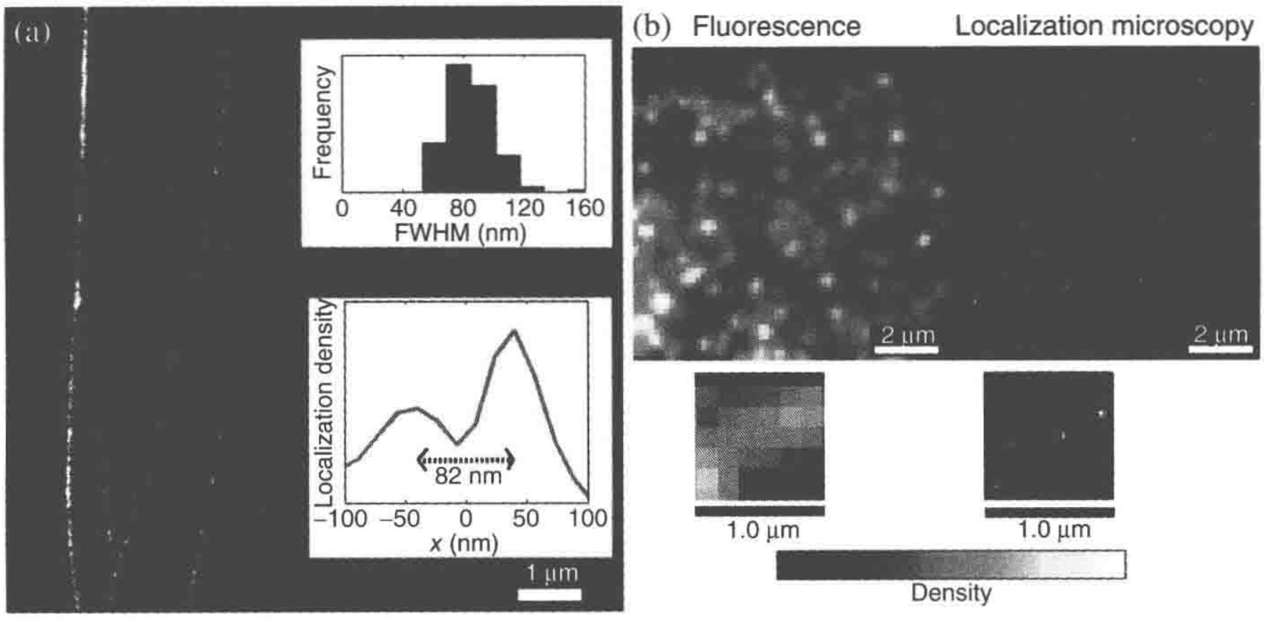

FIGURE 1.21 Super-resolution dSTORM images of (a) actin filaments stained with phalloidin-Alexa Fluor 647 on glass [151]. The spread in full width half maximum (FWHM) of the actin filament is shown in the upper boxed area. The localization density of a cross-section through two crossing filaments is shown in the lower boxed area. (b) Epidermal growth factor (EGF) is conjugated to Alexa Fluor 647 on HeLa cell surfaces, and bound to EGF receptors. Activation of EGF receptors results in dimerization of receptors and clustering into pits and vesicles with diameters ranging from 50 to 150 nm. Note how the localized microscopy image obtained by using a Gaussian intensity distribution at each point to find the center improves the resolution dramatically over the diffraction-limited fluorescence image that is actually recorded. Compare also with the improvement over the single-molecule confocal image without localization shown in Figure 1.20 on the same scale.

interactions with other molecules, such as through collisional or FRET quenching. Thus, as well as helping to distinguish spectrally overlapping fluorophores, imaging of the fluorescence lifetime can be used to probe the surroundings and dynamical processes of a fluorophore. FLIM can be integrated with wide-field, confocal, two-photon, and other microscopy systems and has been extensively reviewed [154, 155,156]. All the optical sources used for fluorescence lifetime spectroscopy can be used in FLIM. Similarly, for scanning FLIM systems, the same detectors as for spectroscopy can be used. Single-photon avalanche diodes (SPADs) are more widely used for detecting fluorescence in microscopy than in spectroscopy. SPADs have high detection efficiency and their small active area is more compatible with microscope than monochromator images and can also serve as a confocal aperture [157].

Both TCSPC and phase-modulation methods, as described in Section 1.4, can be used for FLIM. The relative merits of each in spectroscopy also translate to a large extent to microscopy, for example, speed of FLIM with wide-field phase-modulation and precision of TCSPC with confocal scanning. FRET [158] and anisotropy [159] (Sections 1.5 and 1.6, respectively) can be combined with FLIM, both as a further means of contrast and also for the molecular information they can provide, for example, intracellular microviscosity and refractive index using the Strickler-Berg expression (Eq. 1.12).

1.7.2 Application Example—Gold Nanorods in Cells

Nanoparticles have emerged in recent years as providing new approaches to imaging, sensing, drug delivery, and therapeutics [160]. Noble metals and quantum dots in particular have been shown to complement aromatic fluorophores, not only by generating their own distinctive emission but also by modifying aromatic fluorescence [161]. Just as Raman has benefitted from surface plasmon resonance (SPR) enhancement, so too can fluorescence be enhanced and plasmonics tuned to further good effect [162, 163].

In its bulk form, gold has an extremely low luminescence quantum yield ($\sim 10^{-10}$) but in nanoparticle form it not only has a workable quantum yield, but has advantages over conventional aromatic probes in so far as it is less cytotoxic and does not photobleach. In the context of fluorescence the interest in nanoparticles, already mentioned in Section 1.6.3, is primarily twofold. First, as more needs to be learned about the intra- and intercellular transport properties of nanoparticles with respect to toxicity [164], gold provides a useful paradigm. Second, the intracellular imaging properties of gold nanoparticles offer a new approach to this fundamental area of biology.

As compared to in the bulk, gold spheres of dimensions <5 nm have been found to have a much enhanced quantum yield of $\sim 10^{-5}$–10^{-4}, which is thought to be due to electron-hole recombination following absorption of a photon to promote an electron from the narrow d band to the sp band above the Fermi level [165]. Gold nanorods were subsequently found to have an even higher quantum yield of ($\sim 10^{-4}$ to 10^{-3}) when exciting the transverse surface plasmon mode [166]. One-photon excitation is convenient, but a higher quantum yield would be desirable for cellular imaging purposes. Multiphoton excitation of surface plasmon modes to obtain resonant coupling in gold nanorods has also been demonstrated and shown to offer comparable emission intensity to aromatic flurophores [167, 168]. This significant development brought the additional advantages of multiphoton excitation to bear on cellular microscopy studies with gold, as we illustrate below. More recently, quantum-confined fluorescent gold clusters (a few tens of atoms with a radius ≤ 1 nm) have been found to have "molecular-like" properties and relatively intense emission upon one-photon excitation. The clusters are synthesized and stabilized in protein and were recently reviewed [169].

The seeded growth method is typically used for synthesizing gold nanorods [170]. Typically, the steps are 2.5 mL $HAuCl_4 \times 3H_2O$ (0.001 M) and 0.6 mL ice-cold $NaBH_4$ (0.01 M) are added into 7.5 mL cetyltrimethylammonium bromide (CTAB) (0.1 M) to prepare the seed solution. The growth solution is then synthesized by adding 0.15 M BDAC, 50 mL $HAuCl_4 \times 3H_2O$ (0.001 M), 2 mL $AgNO_3$ (0.004 M), and 700 μL ascorbic acid (0.778 M) to 50 mL CTAB solution (0.1 M). The 80 μl seed solution is then injected into the growth solution to grow gold nanorods.

The absorption spectrum of gold nanorods is characterized by two SPR absorption bands that depend on the aspect ratio. Figure 1.22 shows a scanning electron microscope (SEM) image of gold nanorods, the emission power dependence confirming the two-photon nature of the fs Ti:sapphire laser excitation (Eq. 1.48) and typical absorption spectra featuring longitudinal and weaker transverse plasmon modes over a range of aspect ratios.

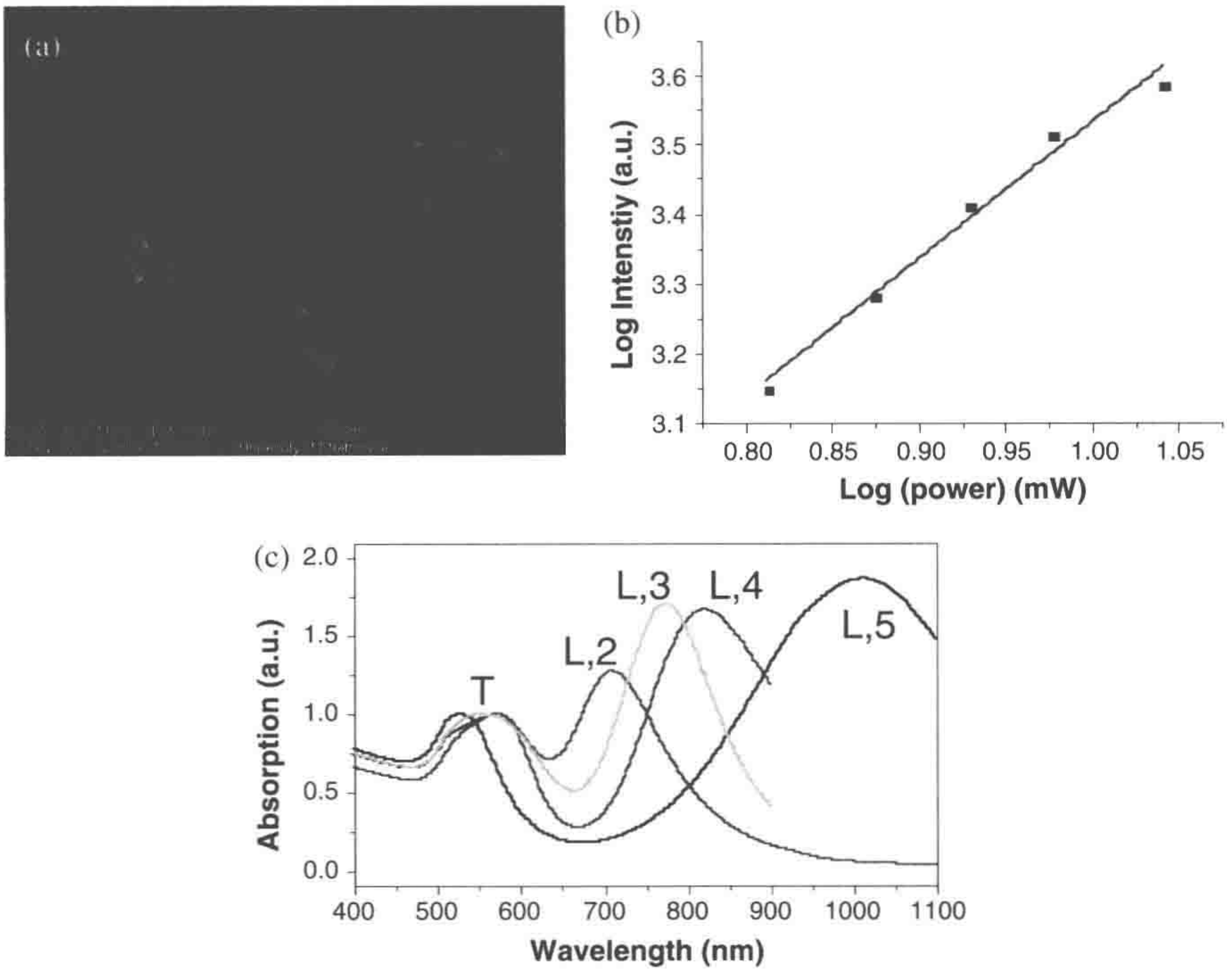

FIGURE 1.22 Gold nanorods: (a) SEM measurement. (b) Emission intensity dependence on laser excitation power giving a slope of 1.97, confirming two-photon excitation at 750 nm. (c) Plasmon absorption bands showing transverse (T) and longitudinal (L, AR) modes for aspect ratios (AR) of 2, 3, 4, and 5. (*For a color version of this figure, see the color plate section.*)

Gold nanorods are of great interest for biological imaging due to their remarkable absorption and emission in the visible and near-IR regions when enhanced by SPR. Especially, the absorption band between 700 and 900 nm corresponding to the longitudinal SPR when excited by two photons in order to generate luminescence of high intensity that is compatible with the spectral window in cells and tissue. Two-photon emission from gold nanorods has been found to be sensitive to the polarization of the incident excitation and has enabled single particle imaging. All these properties make gold nanorods attractive probes for in vitro and in vivo imaging and their properties, applications, and synthesis have been reviewed [171, 172].

To prepare cell culture samples, gold nanorods dispersions are centrifuged and redispersed in deionized water. In our example here Madin-Darby canine kidney (MDCK) cells are then treated with 100 μL of gold nanorod solution and incubated for 3 h under standard cell culture conditions at 37°C and 5% CO_2. The cells are washed and can then be stained with a fluorophore, in our case 4′,6-diamidino-2-phenylindole (DAPI). The sample is then dispersed on a glass slide with a cover slip for imaging.

Figure 1.23 compares the intensity image and lifetime image of gold nanorods in MDCK cells. The elliptical shapes in (a) and (b) correspond to nuclei stained

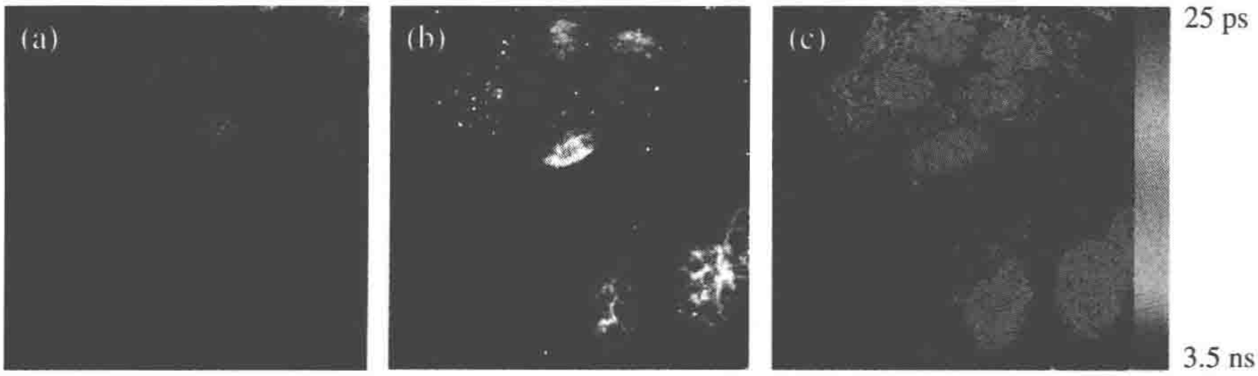

FIGURE 1.23 Two-photon excited MDCK cells stained with DAPI: Fluorescence intensity image (a) without gold nanorods and (b) with gold nanorods. (c) FLIM image. Images are obtained using two-photon 750 nm excitation in the longitudinal plasmon band with emission collected over 535–590 nm. The scanning areas are (a) 133 μm × 133 μm, for (b) and (c) 67 μm × 67 μm 173. (*For a color version of this figure, see the color plate section.*)

by DAPI, and the bright spots in (b) are due to two-photon excited emission from gold nanorods which are not present in (a). The fluorescence lifetime of DAPI in cells is found to be typically a few nanoseconds, while the two-photon excited decay time of gold nanorods is measured here to be <100 ps (limited by the instrumental resolution), as confirmed by a FLIM study of pure gold nanorods on a glass slide and time-resolved luminescence measurement of gold nanorods in a cuvette. The FLIM image, (c), taken from the same sample area as in (b), with different coded colors representing different lifetimes, clearly distinguishes the emissions from DAPI (blue) and gold nanorods (orange). Previous work has shown that in fact the decay constant associated with the gold nanorod emission is as low as a few ps [174, 175]. Figure 1.23 illustrates how fluorescence lifetime can provide a highly selective contrast parameter for gold nanorods with respect to dye stains and endogenous fluorophores.

Opportunities with energy transfer to fluorophores are also available with gold nanorods. This is illustrated in Figure 1.24a, again using a two-photon FLIM image of gold nanorods incubated in MDCK cells [176]. Concentrating on the detailed structures, lifetime decays from rectangular regions labeled A and B are displayed in Figure 1.24b. A decay curve of only DAPI in the cell culture is plotted as a reference, and is described well by a single-exponential decay with a lifetime of 2.5 ns. Both decay curves in the regions A and B can be described by a biexponential model, with a shorter component less than 100 ps ascribed to gold nanorods and a longer ns component to DAPI. For decay curve in region A, the longer component is 2.5 ns. A reduced lifetime component of 0.9 ns for DAPI is found for the decay curve derived from region B, indicating energy transfer between DAPI and gold nanorods in this region.

Clearly, as well as using the ultrafast decay time of gold nanorods for contrast, some of the other properties of gold nanorods such as dual plasmon modes, polarization dependence of excitation, FRET and ability to conjugate can all be brought to bear on intracellular studies. Finally, although previously mentioned here only briefly, gold

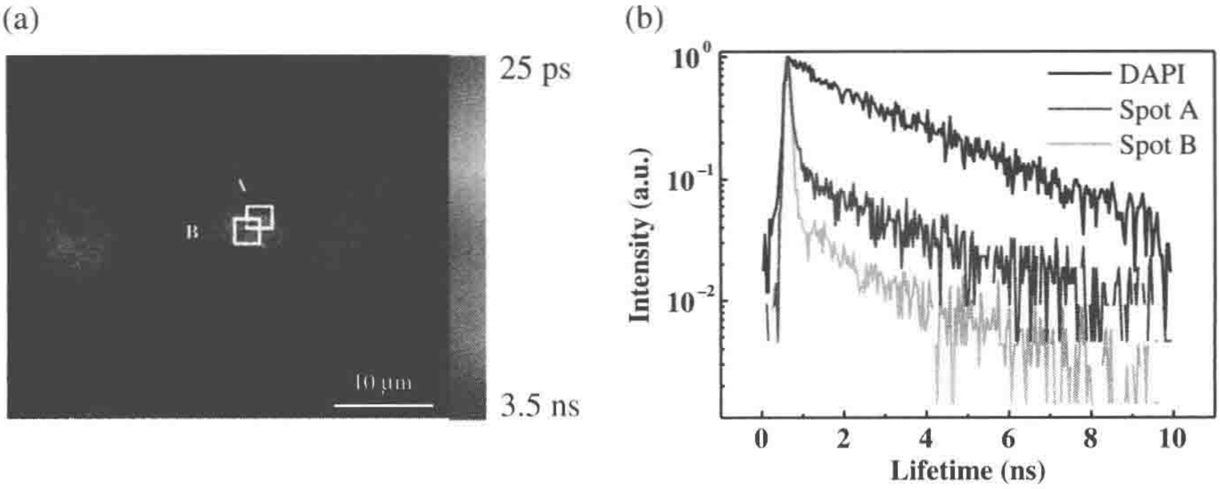

FIGURE 1.24 (a) Two-photon excited FLIM image of GNRs incubated in MDCK cells. Experimental conditions are as for Figure 1.23, but with a scanning area of 67 μm × 67 μm. (b) Normalized fluorescence decay curves derived from regions A and B, with the fluorescence decay curve of DAPI shown for reference. Reproduced from Reference 176 with permission from AIP Publishing LLC. (*For a color version of this figure, see the color plate section.*)

nanoclusters of a few atoms synthesized in protein [169] would also seem to have much to offer, for example in intracellular sensing of metal ions [177].

1.8 CONCLUSIONS

In this chapter, we have surveyed some of the main capabilities, techniques, and measurements that are enabled by fluorescence. This has been supported by references to both original articles and reviews of each topic. Space constraints dictate that we are unable to provide the rigor of complete and dedicated texts [1–4], but we hope that we have been able to go some way toward bridging the gap between the fundamental principles and the perspectives and opportunities generated by modern day applications of fluorescence [178].

Although there are important theoretical aspects still to be solved, the field of fluorescence is largely driven by its experimental applications. One important experimental aspect, that has so far received comparatively scant attention, is the methodology and tricks-of-the-trade that are so essential for good practice in fluorescence measurements. A recent text seeks to address such a requirement, including all the main areas covered here, and provides a useful complement to the present body of literature [179].

ACKNOWLEDGMENTS

The authors wish to acknowledge the research support of EPSRC, BBSRC, and SFC. They are also grateful to Dr. Ashok Ganesan for granting permission to include Figure 1.3.

REFERENCES

[1] I. B. Berlman, *Handbook of Fluorescence Spectra of Aromatic Molecules*, 2nd ed. (Academic Press, New York, 1971).

[2] J. B. Birks, *Photophysics of Aromatic Molecules* (Wiley-Interscience, London, 1970).

[3] J. R. Lakowicz, *Principles of Fluorescence Spectroscopy*, 3rd ed. (Springer, New York, 2006).

[4] B. Valeur, *Molecular Fluorescence Principles and Applications*, 2nd ed. (Wiley-VCH, Weinheim, 2012).

[5] C. A. Parker and W. T. Rees, "Correction of fluorescence spectra and measurement of fluorescence quantum efficiency," *Analyst* **85**, 587–600 (1960).

[6] W. H. Melhuish, "Calibration of spectrofluorimeters for measuring corrected emission spectra," *J. Opt. Sci. Am.* **52**(11), 1256–1258 (1962).

[7] T. B. Fitzpatrick, G. Szabo, M. M. Wick, and J. A. Parrish, "Biochemistry and physiology of melanin pigmentation," in *Biochemistry and Physiology of the Skin*, edited by L. A. Goldsmith (Oxford University Press, New York, 1983), pp. 687–712.

[8] P. Meredith and T. Sarna, "The physical and chemical properties of eumelanin,"*Pigm. Cell Res.* **19**, 572–594 (2006).

[9] W. R. Ware and W. Rothman, "Relative fluorescence quantum yields using an integrating sphere. The quantum yield of 9,10-diphenylanthracene in cyclohexane," *Chem. Phys. Lett.* **39**(3), 449–453 (1976).

[10] C. Würth, M. Grabolle, J. Pauli, M. Spieles, and U. Resch-Genger, "Relative and absolute determination of fluorescence quantum yields of transparent samples," *Nat. Prot.* **8**, 1535–1550 (2013).

[11] W. H. Melhuish, "Distribution of fluorescence from a disk-shaped cuvette," *J. Opt. Sci. Am.* **51**, 278–279 (1961).

[12] D. J. S. Birch and R. E. Imhof, "Fluorescence lifetimes and relative quantum yields of 9,10-diphenylanthracene in dilute solutions of cyclohexane and benzene," *Chem. Phys. Lett.* **32**, 56–58 (1975).

[13] I. W. Hamley, "Peptide fibrillization," *Angew. Chemie. Int. Ed.* **46**, 8128–8147 (2007).

[14] A. K. Geim, and K. S. Novoselov, "The rise of graphene," *Nat. Mater.* **6**, 183–191 (2007).

[15] H. LeVine III, "Thioflavine T interaction with synthetic Alzheimer's disease β-amyloid peptides: detection of amyloid aggregation in solution," *Protein Sci.* **2**, 404–410 (1993).

[16] V. I. Stsiapura, A. A. Maskevich, V. A. Kuzmitsky, V. N. Uversky, I. M. Kuznetsova, and K. K. Turoverov, "Thioflavin T as a molecular rotor: fluorescent properties of thioflavin T in solvents with different viscosity," *J. Phys. Chem. B* **112**(49), 15893–15902 (2008).

[17] O. J. Rolinski, M. Amaro, and D. J. S. Birch, "Early detection of amyloid aggregation using intrinsic fluorescence," *Biosens. Bioelectron.* **25**(10), 2249–2252 (2010).

[18] J. Mohanty, S. D. Choudhury, H. Pal, and A. C. Bhasikuttan, "Early detection of insulin fibrillation: a fluorescence lifetime assay to probe the pre-fibrillar regime," *Chem. Commun.* **48**, 2403–2405 (2012).

[19] A. A. R. Watt, J. P. Bothma, and P. Meredith, "The supramolecular structure of melanin," *Soft Matter.* **5**, 3754–3760 (2009).

[20] J. Sutter, T. Bidláková, J. Karolin, and D. J. S. Birch, "Eumelanin kinetics and sheet structure," *Appl. Phys. Lett.* **100**, 13701 (2012).

[21] N. Benseny-Cases, M. Cócera, and J. Cladera, "Conversion of non-fibrillar β-sheet oligomers into amyloid fibrils in Alzheimer's disease peptide aggregation," *Biochem. Biophys. Commun.* **361**, 916–921 (2007).

[22] S. J. Strickler and R. A. Berg, "Relationship between absorption intensity and fluorescence lifetime of molecules," *J. Chem. Phys.* **37**, 814–822 (1962).

[23] K. Suhling, J. Siegel, D. Phillips, P. M. W. French, S. Leveque-Fort, S. E. D. Webb, and D. M. Davis, "Imaging the environment of green fluorescent protein," *Biophys. J.* **83**(6), 3589–3595 (2002).

[24] W. R. Ware and B. A. Baldwin, "Absorption intensity and fluorescence lifetimes of molecules," *J. Chem. Phys.* **40**(6), 1703–1705 (1964).

[25] D. V. O'Connor, S. R. Meech, and D. Phillips, "Complex fluorescence decay of quinine bisulphate in aqueous sulphuric acid solution," *Chem. Phys. Lett.* **88**, 22–26 (1982).

[26] J. B. Birks, "Radiative lifetime anomalies," *Z. Phys. Chem.* **101**, 91–104 (1976).

[27] D. J. S. Birch and R. E. Imhof, "The origin of fluorescence from trans-trans diphenylbutadiene," *Chem. Phys. Lett.* **88**, 243–247 (1982).

[28] J. R. Lakowicz, G. Laczko, H. Cherek, E. Gratton, and M. Linkeman, "Analysis of fluorescence decay kinetics from variable-frequency phase shift and modulation data," *Biophys. J.* **46**, 463–477 (1984).

[29] D. W. Piston, G. Marriott, T. Radivoyevich, R. M. Clegg, T. M. Jovin, and E. Gratton, "Wide-band acousto-optic light modulator frequency domain fluorometry and phosphorimetry," *Rev. Sci. Instrum.* **60**(8), 2596–2600 (1989).

[30] D. V. O'Connor and D. Phillips. *Time-Correlated Single Photon Counting* (Academic Press, London, 1984).

[31] D. J. S. Birch and R. E. Imhof, "Time-domain fluorescence spectroscopy using time-correlated single-photon counting," in *Topics in Fluorescence Spectroscopy*, Vol. 1: Techniques, edited by J. R. Lakowicz (Plenum Press, New York, 1991), pp. 1–95.

[32] L. M. Bollinger and G. E. Thomas, "Measurement of the time-dependence of scintillation intensity by a delayed coincidence method," *Rev. Sci. Instrum.* **32**, 1044–1052 (1961).

[33] G. Hungerford and D. J. S. Birch, "Single-photon timing detectors for fluorescence lifetime spectroscopy," *Meas. Sci. Technol.* **7**, 121–135 (1996).

[34] M. D. Eisaman, J. Fan, A. Migdall, and S. V. Polyakov, "Single-photon sources and detectors," *Rev. Sci. Instrum.* **82**, 071101 (2011).

[35] D. J. S. Birch and R. E. Imhof, "Coaxial nanosecond flashlamp," *Rev. Sci. Instrum.* **52**, 1206–1212 (1981).

[36] D. J. S. Birch and R. E. Imhof, "A single-photon counting fluorescence decay-time spectrometer," *J. Phys. E. Sci. Instrum.* **10**, 1044–1049 (1977).

[37] T. Imasaka, A. Yoshitake, K. Hirata, Y. Kawabata, and N. Ishibashi, "Pulsed semiconductor laser fluorometry for lifetime measurements," *Anal. Chem.* **57**, 947–949 (1985).

[38] S. Nakamura, "InGaN-based violet laser diodes," *Semicon. Sci. Technol.* **14**, R27–R40 (1999).

[39] W. J. O'Hagan, M. McKenna, D. C. Sherrington, O. J. Rolinski, and D. J. S. Birch, "MHz LED source for nanosecond fluorescence sensing," *Meas. Sci. Technol.* **13**, 84–91 (2002).

[40] C. D. McGuinness, K. Sagoo, D. McLoskey, and D. J. S. Birch, "A new sub-nanosecond LED at 280 nm: application to protein fluorescence," *Meas. Sci. Technol.* **15**, L19–L22 (2004).

[41] C. D. McGuinness, K. Sagoo, D. McLoskey, and D. J. S. Birch, "Selective excitation of tryptophan fluorescence decay in proteins using a subnanosecond 295 nm light-emitting diode and time-correlated single-photon counting," *Appl. Phys. Lett.* **86**, 261911–261913 (2005).

[42] C. D. McGuinness, A. M. Macmillan, K. Sagoo, D. McLoskey, and D. J. S. Birch, "Excitation of fluorescence decay using a 265 nm pulsed light-emitting diode: evidence for aqueous phenylalanine rotamers," *Appl. Phys. Lett.* **89**, 063901–063903 (2006).

[43] D. McLoskey, D. Campbell, A. Allison, and G. Hungerford, "Fast-time-correlated single-photon counting fluorescence lifetime acquisition using a 100 MHz semiconductor excitation source," *Meas. Sci. Technol.* **22**, 067001 (2011).

[44] P. B. Coates, "The correction for photon "pile-up" in the measurement of radiative lifetimes," *J. Phys. E. Sci. Instrum.* **1**, 878–879 (1968).

[45] C. C. Davis and T. A. King, "Single photon counting pileup corrections for time-varying light sources," *Rev. Sci. Instrum.* **41**(3), 407–408 (1970).

[46] W. Becker, "*Advanced Time-Correlated Single Photon Counting Techniques* (Springer, Berlin, 2005).

[47] D. J. S. Birch, R. E. Imhof, and A. Dutch, "Pulse fluorometry using simultaneous acquisition of fluorescence and excitation," *Rev. Sci. Instrum.* **55**, 1255–1264 (1984).

[48] D. J. S. Birch, A. S. Holmes, J. R. Gilchrist, R. E. Imhof, S. M. Al-Alawi, and B. Nadolski, "A Multiplexed single photon instrument for routine measurement of time-resolved fluorescence anisotropy," *J. Phys. E. Sci. Instrum.* **20**, 471–473 (1987).

[49] D. J. S. Birch, A. S. Holmes, R. E. Imhof, B. Z. Nadolski, and K. Suhling, "Multiplexed array fluorometry," *J. Phys. E. Sci. Instrum.* **21**, 415–417 (1988).

[50] W. Becker, A. Bergmann, E. Haustein, Z. Petrasek, P. Schwille, C. Biskup, L. Kelbauskas, K. Benndorf, N. Klöcker, T. Anhut, et al., "Fluorescence lifetime images and correlation spectra obtained by multidimensional time-correlated single photon counting," *Micr. Res. Tech.* **69**, 186–195 (2006).

[51] W. Becker, A. Bergmann, and C. Biskup, "Multispectral fluorescence lifetime imaging by TCSPC," *Micr. Res. Tech.* **70**, 403–409 (2007).

[52] D. McLoskey, D. J. S. Birch, A. Sanderson, K. Suhling, E. Welch, and P. J. Hicks, "Multiplexed single-photon counting, I. A time-correlated fluorescence lifetime camera," *Rev. Sci. Instrum.* **67**, 2228–2237 (1996).

[53] B. R. Rae, C. Griffin, J. McKendry, J. M. Girkin, H. X. Zhang, E. Gu, D. Renshaw, E. Charlton, M. D. Dawson, and R. K. Henderson, "CMOS driven micro-pixel LEDs integrated with single photon avalanche diodes for time resolved fluorescence measurements," *J. Phys. D. Appl. Phys.* **41**, 094011 (2008).

[54] Y. Wang, B. R. Rae, R. K. Henderson, Z. Gong, J. McKendry, E. Gu, M. D. Dawson, G. A. Turnbull, and I. D. W. Samuel, "Ultra-portable explosives sensor based on a CMOS fluorescence lifetime analysis micro-system," *AIP Adv.* **1**, 032115 (2011).

[55] DuPont. *LUDOX Colloidal Silica: Properties, Uses, Storage and Handling: Data Sheets* (DuPont, 1987).

[56] P. R. Bevington. *Data Reduction and Error Analysis for the Physical Sciences* (McGraw-Hill, New York, 1969).

[57] A. K. Livesey and J. Skilling, "Maximum entropy method," *Acta Crystallogr.* **A41**, 113–122 (1985).

[58] C. Zander, M. Sauer, K. H. Drexhage, D.-S. Ko, A. Schulz, J. Wolfrum, L. Brand, C. Eggeling, and C. A. M. Seidel, "Detection and characterization of single molecules in aqueous solution," *Appl. Phys. B* **63**, 517–523 (1996).

[59] N. Boens, W. Qin, N. Basaric, J. Hofkens, M. Ameloot, J. Pouget, J.-P. Lefevre, B. Valeur, E. Gratton, M. VandeVen, et al., "Fluorescence lifetime standards for time and frequency domain fluorescence spectroscopy," *Anal. Chem.* **79**, 2137–2149 (2007).

[60] J. C. Pickup, "Diabetic control and its measurement," in *Textbook of Diabetes*, 3rd ed. edited by J. C. Pickup and G. Williams (Blackwell, Oxford, 2003), pp. 34.1–34.17.

[61] J. C. Pickup, F. Hussain, N. D. Evans, and N. Sachedina, "In vivo glucose monitoring: the clinical reality and the promise," *Biosens. Bioelectron.* **20**, 1897–1902 (2005).

[62] A. Ciudin, C. Hernandez, and R. Simo, "Non-invasive methods of glucose measurement: current status and future perspectives," *Curr. Diab. Rev.* **8**, 48–54 (2012).

[63] N. D. Evans, L. Gnudi, O. J. Rolinski, D. J. S. Birch, and J. C. Pickup, "Non-invasive glucose monitoring by NAD(P)H autofluorescence spectroscopy in fibroblasts and adipocytes: a model for skin glucose sensing," *Diabet. Technol. Ther.* **5**, 807–816 (2003).

[64] T. D. James, K. R. R. A. S. Sandanayake, and S. Shinkai, "A glucose-selective molecular fluorescence sensor," *Angew. Chem. Int. Ed.* **33**, 2207–2209 (1994).

[65] S. Mansouri and J. S. Schultz, "A miniature optical glucose sensor based on affinity binding," *Biotechnology* **2**, 885–890 (1984).

[66] P. W. Barons, R. S. Parker, and M. S. Strano, "In-vivo fluorescence detection of glucose using a single-walled carbon nanotube optical sensor: design, fluorophore properties, advantages, and disadvantages," *Anal. Chem.* **77**, 7556–7562 (2005).

[67] F. Hussain, D. J. S. Birch, and J. C. Pickup, "Glucose sensing based on the intrinsic fluorescence of sol-gel immobilized yeast hexokinase," *Anal. Biochem.* **339**, 137–143 (2005).

[68] T. Tolosa, I. Gryczynski, L. R. Eichhorn, J. D. Dattelbaum, F. N. Castellano, G. Rao, and J. R. Lakowicz, "Glucose sensor for low-cost lifetime-based sensing using a genetically engineered protein," *Anal. Biochem.* **267**, 114–120 (1999).

[69] O. J. Rolinski, D. J. S Birch, L. J. McCartney, and J. C. Pickup, "A time-resolved near-infra-red fluorescence assay for glucose: opportunities for trans-dermal sensing," *J. Photochem. Photobiol. B* **54**, 26–34 (2000).

[70] K. J. Thomas, D. B. Sherman, T. J. Amiss, S. A. Andaluz, and J. B. Pitner, "A long wavelength fluorescence glucose biosensor based on bioconjugates of galactose/glucose binding protein and Nile Red derivatives," *Diabet. Technol. Ther.* **8**, 261–268 (2006).

[71] F. Khan, L. Gnudi, and J. C. Pickup, "Fluorescence-based sensing of glucose using engineered glucose/galactose-binding protein: a comparison of fluorescence resonance energy transfer and environmentally sensitive dye labelling strategies," *Biochem. Biophys. Res. Commun.* **365**, 102–106 (2008).

[72] T. Saxl, F. Khan, M. Ferla, D. Birch, and J. Pickup. "A fluorescence lifetime-based fibre-optic glucose sensor using glucose/galactose-binding protein," *Analyst* **136**, 968–972 (2011).

[73] K. Weidemaier, A. Lastovich, S. Keith, J. B. Pitner, M. Sistare, R. Jacobson, and D. Kurisko, "Multi-day pre-clinical demonstration of glucose/galactose binding protein-based fiber optic sensor," *Biosens. Bioelectron.* **26**(10), 4117–4123 (2011).

[74] J. C. Pickup, Z.-L. Zhi, F. Khan, T. Saxl, and D. J. S. Birch, "Nanomedicine and its potential in diabetes research and practice. Diabetes/Metabolism," *Res. Rev.* **24**, 604–610 (2008).

[75] M. De Miguel, M. Alvaro, and H. Garcia, "Graphene as a quencher of electronic excited states of photochemical probes," *Langmuir* **28**, 2849–2857.

[76] D. K. Singh, P. K. Iyer, and P. K. Giri, "Role of molecular interactions and structural defects in the efficient fluorescence quenching by carbon nanotubes," *Carbon* **50**, 4495–4505 (2012).

[77] C. Preininger, I. Klimant, and O. S. Wolfbeis, "Optical fiber sensor for biological oxygen demand," *Anal. Chem.* **66**, 1841–1846 (1994).

[78] J. N. Demas and B. A. DeGraff, "Design and applications of highly luminescent transition metal complexes," in *Topics in Fluorescence Spectroscopy*, Vol. 4: Probe Design and Chemical Sensing, edited by J. R. Lakowicz (Plenum Press, New York, 1994), pp. 71–107.

[79] C. D. Geddes, K. Apperson, J. Karolin, and D. J. S. Birch, "Chloride sensitive fluorescent indicators," *Anal. Biochem.* **293**, 60–66 (2001).

[80] F. Kielar, C. P. Montgomery, E. J. New, D. Parker, R. A. Poole, S. L. Richardson, and P. A. Stenson, "A mechanistic study of the dynamic quenching of the excited state of europium(III) and terbium(III) microcyclic complexes by charge- or electron transfer," *Org. Biomol. Chem.* **5**, 2975–2982 (2007).

[81] O. S. Wolfbeis and W. Trettnak, "Fluorescence quenching of acridinium and 6-methoxyquinolinium ions by Pb^{2+}, Hg^{2+}, Cu^{2+}, Ag^{2+} and hydrogen sulphide," *Spectrochim. Acta A* **43**, 405–408 (1987).

[82] B. Juskowiak, "Efficient quenching of the fluorescence of binapthyl-based amphiphiles by mercury(II) complexes," *Anal. Chim. Acta* **320**, 115–124 (1996).

[83] S. P. Van and G. S. Hammond, "Amine quenching of aromatic fluorescence and fluorescent exciplexes," *J. Am. Chem. Soc.* **100**(12), 3895–3902 (1978).

[84] D. M. Davis, D. McLoskey, D. J. S. Birch, P. R. Gellert, R. S. Kittlety, and R. M. Swart, "The fluorescence and circular dichroism of proteins in reverse micelles: application to the photophysics of human serum albumin and *N*-acetyl-l-tryptophanamide," *Biophys. Chem.* **60**, 63–77 (1996).

[85] M. Smoluchowski, "Search for a mathematical theory of kinetic coagulation of colloid solutions," *Z. Phys. Chem.* **92**, 129–168 (1917).

[86] J. R. Lakowicz, M. L. Johnson, N. Joshi, I. Gryczynski, and G. Laczko, "Transient effects in quenching detected by harmonic-content frequency domain fluorometry," *Chem. Phys. Lett.* **131**, 343–348 (1986).

[87] D. J. S. Birch, A. Dutch, R. E. Imhof, B. Nadolski, and I. Soutar, "The effect of transient quenching on the excimer kinetics of 2,5-diphenyloxazole," *J. Photochem.* **38**, 239–254 (1987).

[88] N. Periasamy, S. Doraiswany, B. Venkataraman, and G. R. Fleming, "Diffusion controlled reactions: experimental verification of the time-dependent rate equation," *J. Chem. Phys.* **89**(8), 4799–4806 (1988).

[89] L. Stryer and R. P. Haugland, "Energy transfer: a spectroscopic ruler," *Proc. Natl. Acad. Sci. USA* **58**, 719–726 (1967).

[90] S. Saini, G. Srinivas, and B. Bagchi, "Distance and orientation dependence of excitation energy transfer: from molecular systems to metal nanoparticles," *J. Phys. Chem. B* **113**(7), 1817–1832 (2009).

[91] A. Iqbal, S. Arslan, B. Okumus, T. J. Wilson, G. Giraud, D. G. Norman, T. Ha, and D. M. J. Lilley, "Orientation dependence in fluorescent energy transfer between Cy3 and Cy5 terminally-attached to double-stranded nucleic acids," *Proc. Natl. Acad. Sci. USA* **105**, 11176–11181 (2008).

[92] J. Klafter and A. Blumen, "Direct energy transfer in restricted geometries," *J. Lumin.* **34**, 77–82 (1985).

[93] O. J. Rolinski and D. J. S. Birch, "Structural sensing using fluorescence nanotomography," *J. Chem. Phys.* **116**(23), 10411–10418 (2002).

[94] O. J. Rolinski, D. J. S. Birch, and A. S. Holmes, "Metal ion quenching kinetics of DTDCI in viscous solution and Nafion membranes: model system for near infrared fluorescence sensing," *J. Biomed. Opt.* **3**(3), 346–356 (1998).

[95] D. J. S. Birch, O. J. Rolinski, and D. Hatrick, "Fluorescence lifetime sensor of copper ions in water," *Rev. Sci. Instrum.* **67**(8), 2732–2737 (1996).

[96] U. Gösele, M. Hauser, U. K. A. Klein, and R. Frey, "Diffusion at long range energy transfer," *Chem. Phys. Lett.* **34**, 519–522 (1975).

[97] J. W. Taraska, M. C. Puljung, and W. N. Zagotta, "Short-distance probes for protein backbone structure based on energy transfer between bimane and transition metal ions," *Proc. Natl. Acad. Sci. USA* **106**(38), 16227–16232 (2009).

[98] J. W. Taraska, "Mapping membrane protein structure with fluorescence," *Curr. Opin. Struct. Biol.* **22**, 507–513 (2012).

[99] O. J. Rolinski and D. J. S. Birch, "A fluorescence lifetime sensor for Cu(I) ions," *Meas. Sci. Technol.* **10**, 127–136 (1999).

[100] R. B. Thompson and M. W. Patchan, "Lifetime-based fluorescence energy transfer biosensing of zinc," *Anal. Biochem.* **227**, 123–128 (1995).

[101] T. K. Hurst, D. Wang, R. B. Thompson, and C. A. Fierke, "Carbonic anhydrase II-based metal ion sensing: advances and new perspectives," *Biochim. Biophys. Acta (Proteins and Proteomics)* **1804**, 393–403 (2010).

[102] J. U. Sutter, D. J. S. Birch, and O. J. Rolinski, "CdSe/ZnS core/shell quantum dots as luminescence lifetime sensors for Cu^{2+}," *Meas. Sci. Technol.* **23**, 055103 (2012).

[103] M. Bruchez Jr, M. Moronne, P. Gin, S. Weiss, and A. P. Alivisatos, "Semiconductor nanocrystals as fluorescent biological labels," *Science* **281**, 2013–2015 (1998).

[104] A. R. Clapp, I. L. Medintz, J. M. Mauro, R. F. Brent, M. G. Bawendi, and H. Mattoussi, "Fluorescence resonance energy transfer between quantum dot donors and dye-labelled protein acceptors," *J. Am. Chem. Soc.* **126**, 301–310 (2004).

[105] R. Y. Tsien, "The green fluorescent protein," *Annu. Rev. Biochem.* **67**, 67509–67544 (1998).

[106] A. J. W. G Visser, S. P. Laptenok, N. V. Visser, A. van Hoek, D. J. S. Birch, J.-C. Brochon, and J. W. Borst, "Time-resolved FRET fluorescence spectroscopy of visible fluorescent protein pairs," *Eur. Biophys. J.* **39**, 241–253 (2010).

[107] R. F. Steiner, "Fluorescence anisotropy: theory and applications," in *Topics in Fluorescence Spectroscopy*, edited by J. R. Lakowicz (Plenum Press, New York, 1991), Vol. 2, pp. 1–52.

[108] A. Kawski, "Fluorescence anisotropy: theory and applications of rotational depolarization," *Crit. Rev. Anal. Chem.* **23**(6), 459–529 (1993).

[109] M. D. Barkley, A. A. Kowalczyk, and L. Brand, "Fluorescence decay studies of anisotropic rotations of small molecules," *J. Chem. Phys.* **75**(7), 3581–3593 (1981).

[110] D. J. S. Birch and C. D. Geddes, "Sol-gel particle growth studied using fluorescence anisotropy: an alternative to scattering techniques," *Phys. Rev. E* **62**, 2977–2980 (2000).

[111] M. P. Heyn, "Determination of lipid order parameters and rotational correlation times from fluorescence depolarization experiments," *FEBS Lett.* **108**(2), 359–364 (1979).

[112] G. Porter, P. J. Sadkowski, and C. J. Tredwell, "Picosecond rotational diffusion in kinetic and steady state fluorescence spectroscopy," *Chem. Phys. Lett.* **49**(3), 416–420 (1977).

[113] H. J. Eichler, U. Klein, and D. Langhans. Measurement of orientational relaxation times of rhodamine 6G with a streak camera," *Chem. Phys. Lett.* **67**(1), 21–23 (1979).

[114] R. Wijnaendts Van Resandt and L. De Maeyer, "Picosecond rotational diffusion by differential single-photon fluorescence spectroscopy," *Chem. Phys. Lett.* **78**(2), 219-223 (1981).

[115] U. Narang, R. Wang, P. N. Prasad, and F. V. Bright, "Effect of aging on the dynamics of rhodamine 6G in tetramethyl orthosilicate-derived sol-gels," *J. Phys. Chem.* **98**, 17–22 (1994).

[116] C. D. Geddes, J. Karolin, and D. J. S. Birch, "1 and 2-photon fluorescence anisotropy decay in silicon alkoxide sol-gels: interpretation in terms of self-assembled nanoparticles," *J. Phys. Chem.* **106**, 3835–3841 (2002).

[117] M. Ameloot, M. vandeVen, A. U. Acuña, and B. Valeur, "Fluorescence anisotropy measurements in solution: methods and reference materials," *Pure Appl. Chem.* **85**, 589–608 (2013).

[118] B. R. Lentz, "Membrane 'fluidity' as detected by diphenylhexatriene probes," *Chem. Phys. Lipids* **50**, 171–190 (1989).

[119] P. Yip, J. Karolin, and D. J. S. Birch, "Fluorescence anisotropy metrology of electrostatically and covalently labelled silica nanoparticles," *Meas. Sci. Technol.* **23**, 084003 (2012).

[120] K. Apperson, J. Karolin, R. W. Martin, and D. J. S. Birch, "Nanoparticle metrology standards based on the time resolved fluorescence anisotropy of silica colloids," *Meas. Sci. Technol.* **20** 025310 (2009).

[121] A. Bruno, C. de Lisio, P. Minutolo, and A. D'Alessio, "Characterization of ultrafast fluorescence from nanometric carbon particles," *J. Opt. A. Pure Appl. Opt.* **10**, S578–S584 (2008).

[122] L. Brand, J. R. Knutson, L. Davenport, J. M. Beecham, R. E. Dale, D. G. Walbridge, and A. A. Kowalczyk, "Time-resolved fluorescence spectroscopy: some applications of associative behavior to studies of proteins and membranes," in *Spectroscopy and the Dynamics of Biological Systems*, edited by P. Bayler and R. E. Dale (Academic Press, London, 1985), pp. 259–305.

[123] T. A. Smith, M. Irwanto, D. J. Haines, K. P. Ghiggino, and D. P. Millar, "Time-resolved fluorescence anisotropy measurements of the adsorption of rhodamine B and a labeled polyelectrolyte onto colloidal silica," *Colloid Polym. Sci.* **276**, 1032–1037 (1998).

[124] R. B. Thompson, B. P. Maliwal, and V. L. Feliccia, "Determination of picomolar concentrations of metal ions using fluorescence anisotropy: biosensing with a 'reagentless' enzyme transducer," *Anal. Chem.* **70**(22), 4717–4723 (1998).

[125] Z. Gryczynski, O. O. Abugo, and J. R. Lakowicz, "Polarization sensing of fluorophores in tissues for drug compliance monitoring," *Anal. Biochem.* **273**, 204–211 (1999).

[126] D. Allsop, L. Swanson, S. Moore, Y. Davies, A. York, O. M. A. El-Agnaf, and I. Soutar, "Fluorescence anisotropy: a method for early detection of Alzheimer beta-peptide (A beta) aggregation," *Biochem. Biophy. Res. Commun.* **285**, 58–62 (2001).

[127] D. Tleugabulova, A. M. Duft, M. A. Brook, and J. D. Brennan, "Monitoring solute interactions with poly(ethylene oxide)-modified colloidal silica nanoparticles via fluorescence anisotropy decay," *Langmuir* **20**, 101–108 (2004).

[128] A. Cleary, J. Karolin, and D. J. S. Birch, "pH tracking of silica hydrogel nanoparticle growth," *Appl. Phys. Lett.* **89**, 113125–113127 (2006).

[129] W. Denk, J. H. Strickler, and W. W. Webb, "Two-photon laser scanning fluorescence microscopy," *Science* **248**, 73–76 (1990).

[130] V. E. Centonze and J. G. White, "Multiphoton excitation provides optical sections from deeper within scattering specimens than confocal imaging," *Biophys. J.* **75**, 2015–2024 (1998).

[131] A. Diaspro, G. Chirico, and M. Collini, "Two-photon fluorescence excitation and related techniques in biological microscopy," *Quart. Rev. Biophys.* **38**, 97–166 (2005).

[132] D. J. S. Birch, "Multiphoton excited fluorescence spectroscopy of biomolecular systems," *Spectrochim. Acta.* **57**, 2313–2336 (2001).

[133] N. L. Thompson and J. K. Pero, "Total internal reflection microscopy: applications in biophysics," in *Fluorescence Spectroscopy in Biology*, edited by O.S. Wolfbeis, M. Hof, R. Hutterer and V. Fidler (Springer, Berlin, 2005), pp. 79–103.

[134] A. M. Macmillan, J. Karolin, D. Panek, C. D. McGuinness, J. C. Pickup, D. Graham, W. E. Smith, and D. J. S. Birch, "Improved biocompatibility of protein encapsulation in sol-gel materials," *J. Sol-Gel Sci. Technol.* **49**, 380–384 (2009).

[135] N. Thompson, "Fluorescence correlation spectroscopy," in *Topics in Fluorescence Spectroscopy*, edited by J. R. Lakowicz (Plenum Press, New York, 1991), Vol. 2, pp. 337–378.

[136] J. Mertz, C. Xu, and W. W. Webb, "Single-molecule detection by two-photon excited fluorescence," *Opt. Lett.* **20**(24), 2532–2534 (1995).

[137] J. K. Trautman, J. J. Macklin, L. E. Brus, and E. Betzig, "Near-field spectroscopy of single molecules at room temperature," *Nature* **369**, 40–42 (1994).

[138] X. Sunney Xie and R. C. Dunn, "Probing single molecule dynamics," *Science* **265**, 361–364 (1994).

[139] W. E. Moerner, and D. P. Fromm, "Methods of single-molecule fluorescence spectroscopy and microscopy," *Rev. Sci. Instrum.* **74**, 3597–3619 (2003).

[140] M. Kumbhhakar, S. Nath, T. Mukherjee, J. P. Mittal, and H. Pal, "Single-molecule detection in exploring nanoenvironments: an overview," *J. Photochem. Photobiol C. Photochem. Rev.* **5**, 113–137 (2004).

[141] J. Hohlbein, K. Gryte, M. Heilemann, and A. N. Kapanidis, "Surfing on a new wave of single molecule fluorescence methods," *Phys. Biol.* **7**, 031001-22 (2010).

[142] D. Pánek. "Developments for Single Molecule Studies," PhD thesis, University of Strathclyde, Glasgow, UK, 2011.

[143] T. Ha and P. Tinnefeld, "Photophysics of fluorescent probes for single-molecule biophysics and super-resolution imaging," *Annu. Rev. Phys. Chem.* **63**, 595–617 (2012).

[144] M. A. Thompson, M. D. Lew, and W. E. Moerner, "Extending microscopic resolution with single-molecule imaging and active control," *Annu. Rev. Biophys.* **41**, 321–342 (2012).

[145] S. W. Hell and J. Wichmann, "Breaking the diffraction resolution limit by stimulated emission: stimulated-emission-depletion fluorescence microscopy," *Opt. Lett.* **19**(11), 780–782 (1994).

[146] E. Betzig, G. H. Patterson, R. Sougrat, O. W. Lindwasser, S. Olenych, J. S. Bonifacino, M. W. Davidson, J. Lippincott-Schwartz, and H. F. Hess, "Imaging intracellular fluorescent proteins at nanometer resolution," *Science* **313**, 1642–1645 (2006).

[147] M. J. Rust, M. Bates, and X. Zhuang, "Stochastic optical reconstruction microscopy (STORM) provides sub-diffraction-limit image resolution," *Nat. Meth.* **3**, 793–795 (2006).

[148] S. T. Hess, T. P. K. Girirajan, and M. D. Mason, "Ultra-high resolution imaging by fluorescence photoactivation localization microscopy," *Biophys. J.* **91**, 4258–4272 (2006).

[149] D. Aquino, A. Schönle, C. Geisler. C. Middendorff, C. A. Wurm, Y. Okamura, T. Lang, S. W. Hell, and A. Egner, "Two-color nanoscopy of three-dimensional volumes by 4Pi detection of stochastically switched fluorophores," *Nat. Meth.* **8**(4), 353–359 (2011).

[150] M. G. Gustafsson, "Surpassing the lateral resolution limit by a factor of two using structured illumination microscopy," *J. Microsc.* **198**(Pt 2), 82–87 (2000).

[151] E. J. Rees, M. Erdelyi, D. Pinotsi, A. Knight, D. Metcalf, and C. F. Kaminski, "Blind assessment of localization microscope image resolution," *Opt. Nanosc.* **1**, 1–12 (2012).

[152] M. Heilemann, S. van de Linde, Schüttpelz, R. Kasper, B. Seefeldt, A. Mukherjee, P. Tinnefeld, and M. Sauer, "Subdiffraction-resolution fluorescence imaging with conventional fluorescent probes," *Angew Chem. Int. Ed.* **47**, 6172–6176 (2008).

[153] M. A. J. Rodgers, and P. A. Firey, "Instrumentation for fluorescence microscopy with picosecond time resolution," *Photochem. Photobiol.* **42**(5), 613–616 (1985).

[154] X. F. Wang, A. Periasamy, and B. Herman, "Fluorescence lifetime imaging microscopy (FLIM): instrumentation and applications," *Crit. Rev. Anal. Chem.* **23**(5), 369–395 (1992).

[155] T. French, P. T. C. So, C. Y. Dong, K. M. Berland, and E. Gratton, "Fluorescence lifetime imaging techniques for microscopy," *Meth. Cell. Biol.* **56**, 277–304 (1998).

[156] J. W. Borst, and A. J. W. G. Visser, "Fluorescence lifetime imaging microscopy in life sciences," *Meas. Sci. Technol.* **21**, 102002 (2010).

[157] G. S. Buller, and R. J. Collins, "Single-photon generation and detection," *Meas. Sci. Technol.* **21**, 012002 (2010).

[158] A. Periasamy, "Fluorescence energy transfer microscopy: a mini review," *J. Biomed. Opt.* **6**(3), 287–291 (2001).

[159] K. Suhling, P. M. W. French, and D. Phillips, "Time-resolved fluorescence microscopy," *Photochem. Photobiol.* **4**, 13–22 (2005).

[160] T. L. Doane, and C. Burda, "The unique role of nanoparticles in nanomedicine: imaging, drug delivery and therapy," *Chem. Soc. Rev.* **41**, 2885–2911 (2012).

[161] V. Biju, T. Itoh, A. Anas, A. Sujith, and M. Ishikawa, "Semiconductor quantum dots and metal nanoparticles: syntheses, optical properties, and biological applications," *Anal. Bioanal. Chem.* **391**, 2469–2495 (2008).

[162] J. R. Lakowicz, Y. B. Shen, S. D'Auria, J Malicka, J. Y. Fang, and Z. Gryczynski, "Effects of silver island films on fluorescence intensity, lifetimes, and resonance energy transfer," *Anal. Biochem.* **301**(2), 261–277 (2002).

[163] J. R. Lakowicz, "Radiative decay engineering: biophysical and biomedical applications," *Anal. Biochem.* **298**(1), 1–24 (2001).

[164] R. Tantra and A. Knight, "Cellular uptake and intracellular fate of engineered nanoparticles: a review on the application of imaging techniques," *Nanotoxicology* **5**(3), 381–392 (2011).

[165] J. P. Wilcoxon, J. E. Martin, F. Parsapour, B. Wiedenman, and D. F. Kelley, "Photoluminescence from nanosize gold clusters," *J. Chem. Phys.* **108**(21), 9137–9143 (1998).

[166] M. B. Mohamed, V. Volkov, S. Link, and M. A. El-Sayed. "The 'lightening' gold nanorods: fluorescence enhancement of over a million compared to gold metal," *Chem. Phys. Lett.* **317**, 517–523 (2000).

[167] R. A. Farrer, F. L. Butterfield, V. W. Chen, and J. T. Fourkas, "Highly efficient multiphoton-absorption-induced luminescence from gold nanoparticles," *Nano Lett.* **5**(6), 1139–1142 (2005).

[168] K. Imura, T. Nagahara, and H. Okamoto, "Near-field two-photon-induced photoluminescence from single gold nanorods and imaging of plasmon modes," *J. Phys. Chem. B* **109**(27), 13214–13220 (2005).

[169] D. M. Chevrier, A. Chatt, and P. Zhang, "Properties of protein-stabilized fluorescent gold nanoclusters: short review," *J. Nanophoton.* **6**, 064504-01–064504-16 (2012).

[170] J. Murphy, T. K. Sau, A. M. Gole, C. J. Orendorff, J. Gao, L. Gou, S. E. Hunyadi, and T. Li, "Anisotropic metal nanoparticles: synthesis, assembly, and optical applications," *J. Phys. Chem. B* **109**, 13857–13870 (2005).

[171] X. Huang, S. Neretina, and M. A. El-Sayed, "Gold nanorods: from synthesis and properties to biological and biomedical applications," *Adv. Mater.* **21**, 4880–4910 (2009).

[172] R. Sardar, A. M. Funston, P. Mulvaney, and R. W. Murray, "Gold nanoparticles: past, present, and future," *Langmuir* **25**(24), 13840–13851 (2009).

[173] Y. Zhang, J. Yu, D. J. S. Birch, and Y. Chen, "Gold nanorods for fluorescence lifetime imaging in biology," *J. Biomed. Opt.* **15**(2), 020504-3 (2010).

[174] O. P. Varnavski, M. B. Mohamed, M. A. El-Sayed, and T. Goodson III, "Relative enhancement of ultrafast emission in gold nanorods," *J. Phys. Chem. B.* **107**, 3101–3104 (2003).

[175] P. Biagioni, M. Celebrano, M. Savoini, G. Grancini, D. Brida, S. Mátéfi-Tempfli, M. Mátéfi-Tempfli, L. Duò, B. Hecht, G. Cerullo, et al., "Dependence of the two-photon photoluminescence yield of gold nanostructures on the laser pulse duration," *Phys. Rev. B* **80**, 045411-5 (2009).

[176] Y. Zhang, D. J. S. Birch, and Y. Chen, "Two-photon excited surface plasmon enhanced energy transfer between DAPI and gold nanoparticles: opportunities in intra-cellular imaging and sensing," *App. Phys. Lett.* **99**, 103701-3 (2011).

[177] C. V. Durgadas, C. P. Sharma, and K. Sreenivasan, "Fluorescent gold clusters as nanosensors for copper ions in live cells," *Analyst* **136**, 933–940 (2011).

[178] D. J. S. Birch, "Fluorescence detections and directions," *Meas. Sci. Technol.* **22**,052002 (2011).

[179] Y. Engelborough and A. J. W. G. Visser (eds.), *Fluorescence Spectroscopy and Microscopy Methods and Protocols* (Springer, New York, 2013).

2

SINGLE-MOLECULE DETECTION AND SPECTROSCOPY

MICHEL ORRIT
Institute of Physics, Leiden University, Leiden, The Netherlands

2.1 INTRODUCTION

At the end of the ninteenth century, evidence had accumulated for the existence of atoms and molecules. Final hard proofs appeared at the beginning of the twentieth century, with the quantization of charge, Brownian motion, and most importantly the diffraction of X-rays by crystals. Already at that time, Jean Perrin [1] proposed and attempted to observe single fluorescent molecules directly by eye in an optical microscope. To decrease background, he used black soap films, which scatter only minute amounts of light, mostly through Rayleigh scattering, with low concentrations of fluorescent molecules. Unfortunately, because of the limited responsivity of the human eye, of the low brightness of light sources and the poor quality of optical filters and of the fluorescent dyes of those days, Perrin could not detect single molecules by eye. Instead, he performed a very interesting study of fluorescent black films, where he found another evidence for molecular structures, the quantized thickness of soap multilayers. Thanks to spectacular progress in all above-mentioned components, including optical microscopes, light sources and detectors, filters, and dyes, Perrin's thought experiment can nowadays be done in a straightforward manner, and single molecules can even be seen in an optical microscope with the bare eye.

Even long after Perrin's first heroic attempt, it was thought that molecules were much too weak emitters to be detected optically. The progress of electron microscopy led to observe single rows of atoms in crystals already in the 1950s, but the resolution

---

Photonics: Scientific Foundations, Technology and Applications, Volume IV, First Edition.
Edited by David L. Andrews.
© 2015 John Wiley & Sons, Inc. Published 2015 by John Wiley & Sons, Inc.

was too low, and the irradiation damage too high, to observe individual molecules under the electron microscope. More recently, however, higher selectivity and better collection of secondary electrons have made it possible to observe individual isolated heavy atoms in a sample made of light atoms with an electron microscope. The detection of single atoms and single molecules on surfaces first became a reality in the early 1980s with the invention of the scanning tunneling microscope (STM) [2], and later of its variant for insulating substrates, the atomic force microscope (AFM) [3]. These two techniques have opened the way to microscopic investigations of matter at the single-atom and single-molecule levels and are widely used today in many laboratories.

Meanwhile, thanks to lasers and general progress in optical techniques, it had become possible in the 1970s to observe single atoms in the gas phase, in dilute atomic beams. The atoms were detected via the short bursts of fluorescence light they emitted when crossing the laser focus. Then, single trapped ions were also detected by their fluorescence. Yet, observing a single fluorescent atom in gas phase is a very different problem from observing a single molecule in condensed phase, for the main two reasons:

- First, condensed matter produces strong optical background via Rayleigh and Raman scattering. Moreover, other fluorescent impurities in the sample may easily dominate the fluorescence from a single molecule; therefore, the purity of the sample is crucial. This problem obviously does not arise in vacuum.
- Second, a single atom usually can fluoresce millions of photons per second, without any degradation. An atom in vacuum is a stable system, even in its excited state. It can thus perform indefinitely many excitation–emission cycles, which facilitates detection considerably. This convenient property of atoms is unfortunately not shared by most fluorescing systems in condensed matter. The immense majority of them are subject to irreversible transformations putting an end to their luminescence. Those processes are called photobleaching and will be discussed briefly later on.

In the late 1980s and early 1990s, progress in sources, optics, and detectors has opened the way to detect single molecules in condensed matter. These experiments have been extended to other single luminescent objects, including semiconductor nanocrystals or quantum dots, metal particles, color centers, and so on. They are nowadays performed in condensed matter environments as diverse and complex as facets of catalyst crystals or live biological cells. Part of the driving force behind this research domain is the broad current interest for nanoscience, that is, the structure and dynamics of matter at nanometer scales. By coupling lasers to optical microscopes, the powerful spectroscopic techniques developed in the 1970s and 1980s have been transported not only down to sub-micron scales, but even down to nanometer scales if a single object can be selected. Moreover, as we will see in this chapter, the selection of single objects opens new motivations, methods, and results. This relatively young field of investigation is called single-molecule optics or nano-optics.

In this chapter, we briefly review the principles of optical microscopy and of the fluorescence method, as these two techniques are the workhorses of single-molecule studies. Let us stress again how small a molecule really is. If a dew drop was magnified to the size of the Earth, a single water molecule would be about the size of a person. It may appear hopeless to look for optical signals from such a tiny source in the background of all other molecules in the drop. This is possible, however, due to the special properties of the fluorescence signal, and to two tricks:

- First, the size of the illuminated sample must be reduced as much as possible. For a given light intensity, that is, for a given signal from the molecule, the background will be proportional to the number of illuminated sample molecules, that is, proportional to the volume of the illuminated sample. Reducing background will require reducing the illuminated spot, usually by focusing the laser beam very tightly into the sample. This focusing step thus performs a *spatial selection*.
- Second, the *intrinsic* background of the detection method used must in principle be low enough for the single molecule's signal to dominate the background from all sample molecules in the illuminated volume. An illuminated volume of 1 μm [3] contains about 10^9 sample molecules. The detection method must therefore have a selectivity ratio, that is, the ratio of signals from the molecule of interest to that of a sample molecule, higher than 10^9. Only very few optical methods present such a high selectivity. Fluorescence does. The high selectivity of fluorescence arises from optical resonance. A fluorescent molecule must first absorb a laser photon, which a sample molecule cannot do. Therefore, the laser frequency performs a *spectral selection* on the molecules contained in the sample. Only molecules resonantly excited by the laser can emit fluorescence. It is interesting to compare fluorescence to infrared absorption, for example, which might open up studies of single chemical bonds. Unfortunately, the selectivity of IR absorption is 1000 at best, because of the width and shape of vibrational resonances. Therefore, such a method could only be applied to a single bond in combination with spatial selection of less than 1000 molecules. Selection of such a small excited sample cannot be achieved by diffraction-limited optics alone.

We then proceed to discuss particular implementations of the fluorescence technique and give examples of the results that can be obtained with them. Fluorescence of immobilized molecules (Section 2.3) is the easiest to discuss, as the signal arises from a single system with a fixed emission dipole. Such recent developments as superresolution microscopy are based on the fluorescence of immobilized single molecules. When molecules can move and tumble, fluorescence signals are subject to even more dynamical processes. Their evaluation requires statistical methods, in particular autocorrelation of fluorescence time traces. The associated technique, known as fluorescence correlation spectroscopy (FCS), is discussed in Section 2.4. In the special case of cryogenic experiments at low temperatures, much information can be obtained from fluorescence excitation spectroscopy, which will be discussed in Section 2.5. These conditions give rise to narrow resonance lines, which make it possible to perform highly accurate quantum optics experiments. Finally, single molecules and single nano-objects can be detected by other far-field optical techniques such as scattering or photothermal detection. Several experiments have been demonstrated in the last years. These new methods will be discussed in Section 2.6 with their applications to single metal nanoparticles and other small objects.

2.2 EXPERIMENTAL SETUPS

2.2.1 Principles

The basis of single-molecule optical detection is an optical microscope [4], which in principle is nothing else than a simple lens system for magnifying small objects. The first lens, called the objective, has a short focal length (a few millimeters) and creates an image of the object in the intermediate image plane. This image in turn can be looked at with another lens, the eye piece. Typical magnification ratios are in the range of 40–100. The resolution of the image provided by the microscope is limited by diffraction. The Abbe-Rayleigh criterion states that, for a wavelength λ, the smallest distance d resolvable between two point sources as deduced from diffraction theory is $d = 0.61\frac{\lambda}{\mathrm{NA}}$, where $\mathrm{NA} = n \sin \alpha$, called numerical aperture of the objective lens, is proportional to the index of refraction n in the object space, and α is half the maximal angle under which the objective lens collects light from the object (see Fig. 2.1b). In single-molecule experiments, the numerical aperture should be as large as possible for two different reasons:

- (i) The spatial resolution improves for larger NA, both laterally and axially (see below).
- (ii) The collection efficiency, that is, the brightness of the image, increases very quickly with NA, quadratically for small apertures. In addition to angle considerations, the index of refraction of the object medium is a very important factor in the numerical aperture. Indeed, because of total reflection at interfaces, a high index enables collection over a wider range of angles. This is the reason why most microscopes use immersion to enhance resolution and collection efficiency.

The main difficulty in manufacturing microscope objectives is to achieve a good correction of all aberrations (spherical, chromatic) also for off-axis rays with incidence angles which can be larger than 60°. This is achieved by assembling several lenses (sometimes more than 10) made out of different glasses, and which have to be anti-reflection-coated for a good luminosity. Good microscope objectives are therefore quite advanced and expensive pieces of technology. Immersion oil objectives reach an NA of 1.4, corresponding to collection angles close to 90°.

An ideal microscope lens will image a point source as an Airy pattern if a circular iris or diaphragm limits the aperture. This point-spread function (PSF) has therefore

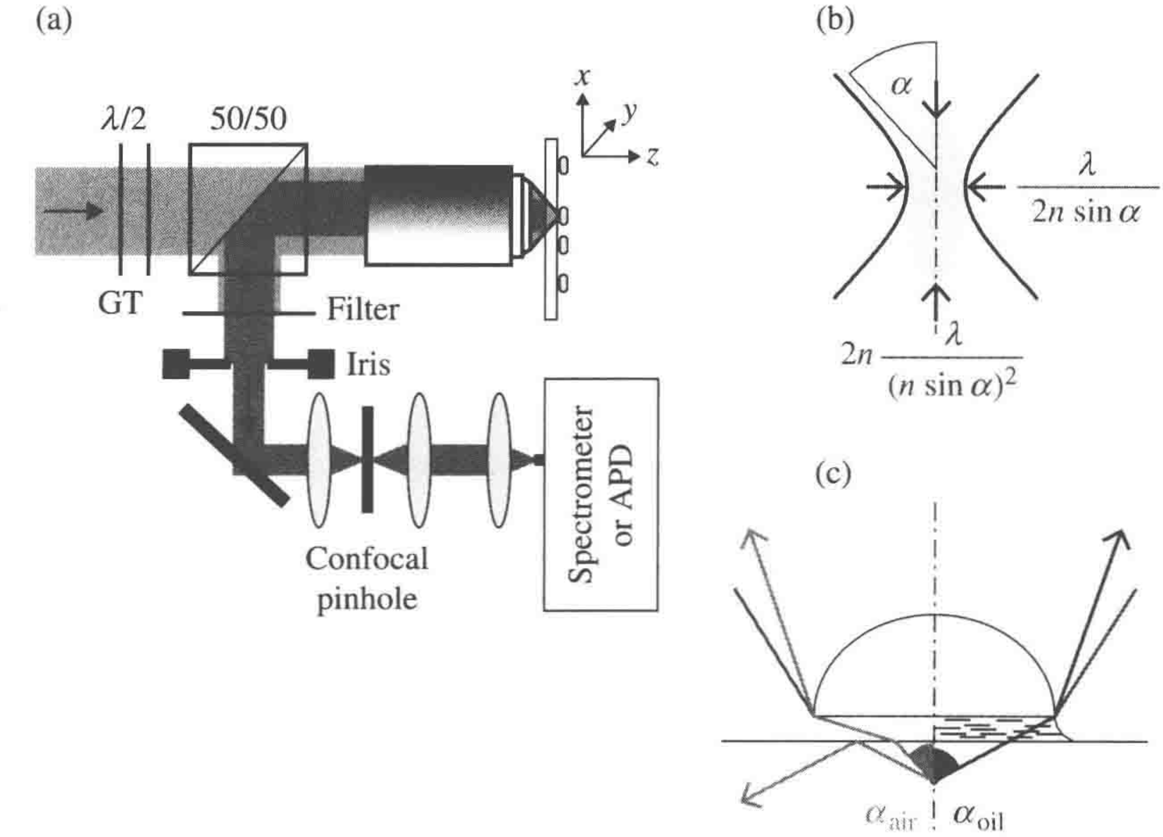

FIGURE 2.1 (a) Scheme of a confocal setup for single nano-object spectroscopy. The confocal spot can be scanned with mirrors and a telecentric lens system (not shown) or simply by scanning the sample with a translation stage (after Reference 90). (b) Definition of the numerical aperture $\mathrm{NA} = n \sin \alpha$ and its relation to the lateral and axial resolutions. (c) For sources placed in a refringent material, a wetting layer of a high-index liquid (immersion oil) considerably increases the numerical aperture. This has the double advantage of enhancing both the resolution and the collection efficiency.

the classical form of the diffraction spot from a round hole. If the light collected is a Gaussian beam instead, provided it is fully included in the acceptance pupil of the objective, the PSF will be a Gaussian spot. For many experiments in 3D samples, it is important to consider the depth of focus, that is, the length of the PSF in the axial direction. This size L (sometimes called Rayleigh length) is approximately

$$L = 2n\frac{\lambda}{\mathrm{NA}^2}.$$

The 3D appearance of the PSF is thus an elongated (prolate or cigar-shaped) ellipsoid (Fig. 2.1b). Decreasing this length is a third reason to make the numerical aperture as high as possible, as the volume of the PSF scales as NA^{-4}.

The numerical aperture is proportional to the refraction index. Therefore, it is of advantage to collect light through glass, or through high-index oil, when possible (Fig. 2.1c). Special water-immersion objectives are used for biological samples. To fully benefit from high index, the index must of course be matched between the sample and objective glass. This is achieved thanks to the immersion oil. A further advantage of immersion is the higher efficiency of fluorescence collection. An air gap leads to light losses by total internal reflection at the interface from high- to low-index media (see Fig. 2.1c). For emitters placed at an air–glass interface, the situation is even worse, as a large fraction of the emitted light (up to 90%) is radiated into the high-index material. Collecting emission on the air side therefore entails big losses of intensity, in addition to losses in resolution.

2.2.2 Correction of Aberrations

The ideal microscope objective would image a planar object onto a plane field, without distortion, and without change in image with wavelength (achromatism). To achieve this, the following aberrations must be corrected:

(i) Chromatic aberrations from the dispersion of glasses (their refractive index is larger for blue than for red light). Even with well-corrected objectives, the focus often moves by some microns when the wavelength varies over the visible spectrum.

(ii) Geometrical aberrations: spherical (change of focal point with distance from axis), coma, due to changes of the image point with ray direction, field curvature (image focus is not obtained on a plane but on a curved surface), field distortion (pincushion or barrel images), and so on.

Simple spherical lenses made out of ordinary dispersive glass suffer from all these aberrations and cannot fulfill the requirements of the ideal lens for large numerical apertures. For example, a planoconvex lens has spherical aberrations which are minimized by placing the convex surface on the side of the parallel beam. Aspheric singlets used in CD readers correct in principle perfectly for their focus, but are designed to work at one wavelength only and have strong chromatic aberrations. To approximate the ideal lens' requirements, one uses combinations of spherical lenses possessing various radii of curvature, thicknesses, and materials, and one varies their positions. To design objectives and other multilens systems, special codes calculate imaging with rays far from paraxial for arbitrary systems of lenses. A good objective may contain more than 10 lenses, which have to be positioned with specifications as narrow as microns for some of them. The air–glass interfaces have to be antireflection coated to reduce reflection losses, and small gaps between the lenses are often bridged with a high-index medium, usually UV-polymerizable glue, after the respective position of the lenses has been adjusted by hand. Therefore, objective lenses are expensive and sensitive optical components.

Nowadays, most objectives are infinity-corrected. This means that they are not calculated to form their image directly in the intermediate image plane, but to form an image at infinity. Another lens called tube lens then images the plane waves into the intermediate image. Some manufacturers use the tube lens to correct some aberrations. In that case, tube lens and objective must be used in combination for optimal correction. The advantages of infinity-corrected objectives are essential in confocal microscopy, polarization studies, and spectroscopy, because plane waves are easier to filter and manipulate than spherical waves (e.g., they are not distorted by flat windows).

2.2.3 Polarization Structure at the Focus

The electric field of a laser wave is a vector quantity, which complicates the polarization structure in the case of high numerical apertures. We will briefly discuss the polarization of the field at the focus of a linearly polarized laser wave [4]. For low NA, the polarization of the spot is the same as that of the incident beam. At the focal point itself, by symmetry, the polarization of the incident beam is conserved. At high NA, however, and for parts of the PSF away from the center, interference of the incoming rays leads to deviations from this polarization. For large incidence angle and a linearly polarized incident beam, simple consideration of the interference of different rays shows that the axial (i.e., polarized along the axis) component of the field has a node at the center and presents two (weak) lobes in the focal plane. The third transverse component (perpendicular to the axis and to the incoming polarization) is even weaker and presents four lobes. By using annular illumination, and/or by introducing phase masks in the incoming beam, the polarization of exciting laser light at the focus can be manipulated, and can even present a PSF with a single lobe for the longitudinal polarization. This is of great interest to determine the full 3D orientation of single absorbers, since their transverse polarization can be easily probed with linearly polarized light and normal illumination.

A similar, but distinct problem is to find the polarization structure of a wave radiated by a linear dipole at the focus, and collimated into a plane wave by an objective with large numerical aperture. In the case of a dipole lying in the focal plane, it can be shown [5] that the polarization is linear throughout the field, parallel to the dipole along the horizontal and vertical directions (N, S, E, W), and significantly tilted in the NW, NE, SW, SE positions. In the case of a dipole perpendicular to the focal plane, the polarization is radial.

2.2.4 Various Microscopy Methods

There are several ways to record images with a microscope. We briefly mention the most important ones for single-molecule studies.

2.2.4.1 Confocal Microscopy In this method, only one point of the sample is imaged onto a photodetector. If the sample is scanned in three dimensions, a 3D image is obtained by recording the optical signal as a function of sample position. To reduce background, that is, to ensure that the signal arises only from the focus, a diaphragm or pinhole is inserted in one of the image planes (see scheme in Fig. 2.1a). To scan the area to be imaged, one can move either the sample itself with piezoelectric transducers (sample scanning), or the focus by means of tilting mirrors (beam scanning). In the latter case, a telecentric system images the spot of the illumination beam on the scanning mirror onto the input lens of the objective. In this way, the two points remain conjugated when the mirror is tilted during scanning. Fluorescence is collected in the backward scattered geometry and is folded back exactly onto the incoming path by the mirror-telecentric system assembly.

2.2.4.2 ***Wide-Field Imaging*** In this method, a large part of the field is illuminated by an unfocused beam (epi-illumination), and the image is formed on a multichannel detector such as a CCD camera or an image intensifier. For a 3D sample, this design leads to background arising from emission by planes below and above the imaged plane of the sample.

2.2.4.3 Total Internal Reflection Illumination To reduce the background, the excitation light can be sent at a large incidence angle on the surface, achieving total internal reflection (TIR). Fluorescence and other emissions can be collected either across the interface, or on the same side as the illumination. In that case, collection has to be performed in a solid angle where no illumination light is present, which requires a large NA.

The confocal configuration schematically presented in Figure 2.1 is particularly useful to detect single molecules because of its simplicity and of its low background. This design has the advantage that only the focus is excited with high efficiency, thus limiting photobleaching in other sample planes. Moreover, fluorescence arising from other points does not reach the detector. The spatial selection of single molecules or single nano-objects is therefore performed in two steps, with equivalent selectivity:

- Excitation selection, by focusing the laser beam on a small spot.
- Detection selection, by detecting light arising from the same area only.

Several other optical designs have been developed in the last 20 years with various elements for excitation and collection: single-mode optical fiber, parabolic mirror, aspheric lenses, gradient index lenses, and so on. An overview can be found in Reference 6.

2.3 FLUORESCENCE SPECTROSCOPY

2.3.1 Introduction, Signal-to-Noise Ratio

If single molecules are immobilized in or on a solid or in a highly viscous sample, it becomes possible to study the same molecule for long periods of time. This situation is very different from experiments in liquid solutions, where statistics over a large number of molecules usually always give a signal, even in difficult conditions with strong background and noise. For molecules immobilized in solids or on surfaces, it is of crucial importance to be able to "recognize" the molecule, that is, to distinguish its signal from background and noise.

The following discussion of the signal/noise ratio applies not only to microscopic images, but also to other signals from immobilized single molecules, for example, their spectra. Let us consider the background B and the signal S of the molecule as functions of a scanning parameter (typically one position coordinate of the sample).

If t is the acquisition time per channel or pixel, the number of acquired background counts is Bt. Assuming shot noise to be dominant (which is usually the case for weak signals), the noise from the background is $\sqrt{Bt}$, which has to be compared to the signal St. The most favorable case to detect the molecule is when its signal occupies about one pixel or one channel width (a broad structure is more difficult to distinguish from noise than a sharp one). The molecule will be detectable if and only if the signal-to-noise ratio is significantly larger than unity, let us say, equal to 3:

$$St > 3\sqrt{Bt}, \text{or}\, t > 10\frac{B}{S^2}.$$

For a typical background of 100 counts per second arising from the dark counts of the avalanche detector, and for an acquisition time of 1 s, it follows that the signal has to be larger than 30 counts per second to be clearly distinguished from noise. This condition becomes only a lower bound if the molecule's image is spread over more than one pixel.

2.3.2 Sample Preparation

In fluorescence experiments, the main source of background is fluorescence from residual impurities or from optical elements. Raman scattering is often negligible. To observe single molecules, it is therefore crucial to reduce contamination by fluorescent impurities, and to work with very clean optical parts. The excited volume must be as small as possible, and the substrate should be nonfluorescent (fused silica, or very pure glass). Hereafter, we cite a few usual methods to prepare samples.

2.3.2.1 Spin Coating Quick spinning of a flat substrate with a thin layer of solution leads to a uniform film, draining slower and slower as time goes on. At the same time, evaporation decreases the thickness too, and increases the concentration and the viscosity. In a first phase, viscous draining is dominant in reducing the thickness, then evaporation takes over. The combination of viscous draining and evaporation leads to uniform films of tunable thickness, for example, to prepare photoresists in the semiconductor industry. Typical spin-coating parameters (1000 rpm, 1% weight of polymer in a solvent like water) lead to thicknesses between 10 nm and a few microns. Spin coating is very interesting to reduce the illuminated volume, and therefore the background, by reducing the thickness.

2.3.2.2 Langmuir–Blodgett Films Even thinner, monomolecular films are obtained by the Langmuir–Blodgett technique, that is, deposition onto a substrate from a monomolecular layer at the air–water interface. The fluorescent dye molecules are usually introduced at low concentration in the spreading solution of the amphiphilic molecules, but may also be adsorbed from an aqueous solution.

2.3.2.3 Bilayers, Membranes, and Black Lipid Films These thin layers are particular cases of a pair of monomolecular layers, which can be either deposited on a substrate or suspended to a hole. Cell and vesicle membranes are particularly important matrixes for single biomolecules.

2.3.2.4 Other Preparation Methods Molecules can be deposited directly from solution in a volatile solvent substrate (in that case they are more sensitive to oxygen and water), included in nanocrystals, etc., or simply selected or imaged within a 3D sample, such as a cell, for example. In the latter case, a thin sample should be preferred to limit background.

Much information can sometimes be obtained from images with diffraction-limited single-molecule spots. Counting them can provide concentrations, the stoichiometry of complexes [7], and so on. Another important application is colocalization [8], which makes it possible to test interactions between biomolecules labeled with two different fluorophores. However, much progress has been done recently in superresolution imaging, as will be discussed below.

2.3.3 Orientation

The orientation of the in-plane component of the molecular transition moment can be obtained easily by polarization measurements. Two different methods are used dominantly:

2.3.3.1 Polarization Analysis in Detection The fluorescence beam is sent to a polarizing beam splitter and the two beams are sent to different detectors. An example of polarization-dependent images is given in Figure 2.2, where the polarization

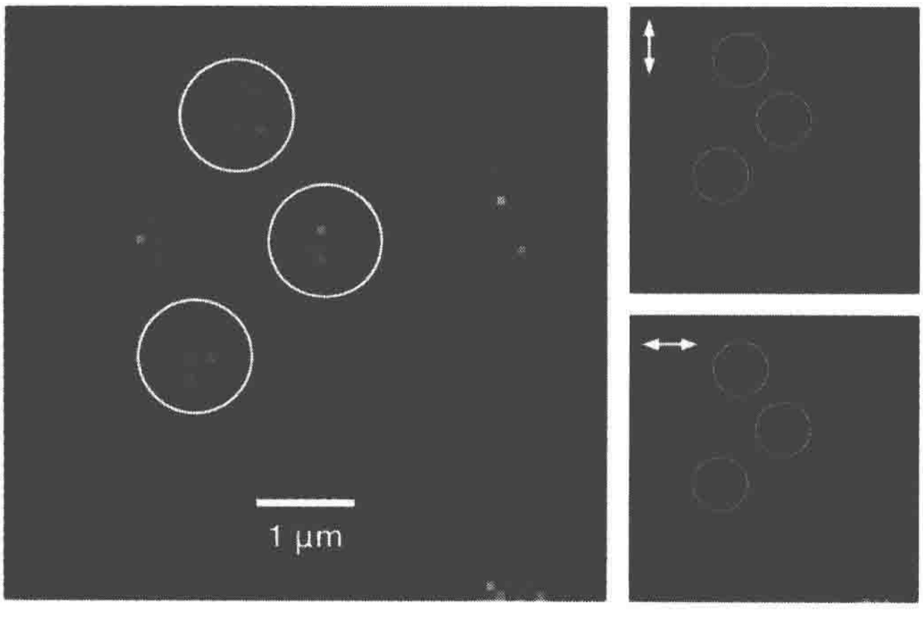

FIGURE 2.2 Example of rotational diffusion of single dye molecules in glycerol at low temperature (200 K), monitored via intensity fluctuations in two orthogonal fluorescence polarizations (left panels). On the right panel, the polarization is color-coded, red for vertical, green for horizontal. The diffusion times of molecules are comparable to the scan time, about 1 s per line. (*For a color version of this figure, see the color plate section.*)

direction of the fluorescence of single dye molecules is color-coded. The intensity ratio gives two possible solutions for the in-plane orientation. Discriminating between those requires a third measurement. In combination with polarized excitation, polarized analysis gives the fluorescence anisotropy, related to the angular mobility and rotational diffusion of the fluorophore during fluorescence. This method is very useful to monitor rotational relaxation of slowly moving objects, such as dyes in highly viscous glass formers [9, 10]. These experiments show that different single molecules diffuse as Brownian particles on short timescales, but that different molecules diffuse at different rates, and that this diffusion can change in time. This inhomogeneity gives rise to the complex (nonexponential) behavior of the glass just above the glass transition. Single-molecule experiments directly confirm the spatial heterogeneity of glass dynamics.

2.3.3.2 ***Polarization Modulation in Excitation*** The polarization of the exciting beam can be modulated in time, for example, with a rotating polarizer. The phase and amplitude of the sinusoidal variation of the detected intensity gives information about the orientation and diffusion of the fluorophore. For a fixed molecule, the modulation is sinusoidal with maximum contrast. For a fast diffusing molecule, however, the intensity modulation depths decrease, indicating diffusion or hampered diffusion [11].

As discussed in the section on optical microscopy, the full 3D orientation of the dipole moment can be obtained with a widely opened excitation beam, or by measuring the distribution of fluorescence photons as a function of the angles of emission and comparison to the emission pattern of a dipole. This latter method requires a matrix of detectors for fast determination.

2.3.4 Blinking

When the fluorescence intensity of a nano-object is recorded as a function of time (in a so-called fluorescence intensity trace), random variations of the average emission intensity are often observed [12]. The variations can sometimes be progressive, but often present sudden jumps between bright and dark states. We discuss only the latter behavior here, which is commonly known as blinking or intermittency. Blinking is a characteristic feature of the emission of single nano-objects, which has been observed for organic molecules, semiconductor nanocrystals, and color centers. Figure 2.3 presents typical blinking fluctuations in the luminescence signal of a single semiconductor nanocrystal. In large populations, blinking is almost always hidden because the fluctuations of individual objects are not synchronized. In some cases, an external parameter can synchronize the blinking of all objects (an obvious example is switching the exciting laser on). In those cases, blinking will appear as a transient variation of the average signal. It is one of the most powerful features of single-molecule methods that no synchronization is needed to observe such fluctuations directly, as the example of blinking shows.

Several possible mechanisms can lead to blinking. Most of them involve a "dark" state of the emitter, that is, a state which does not fluoresce, either because it does not

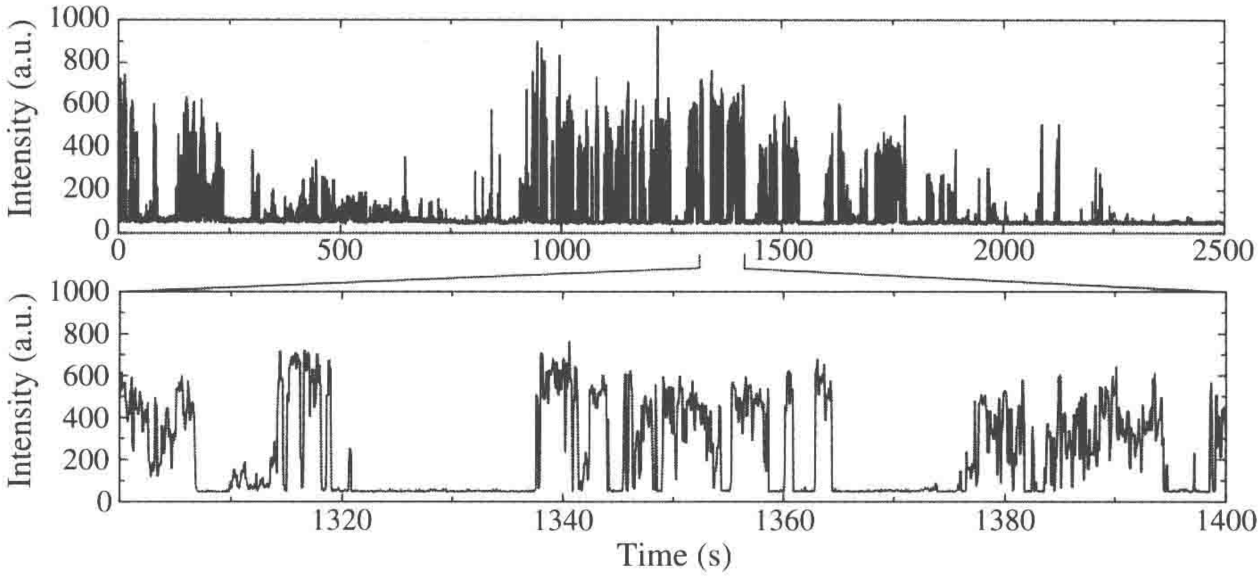

FIGURE 2.3 Example of blinking luminescence traces of a semiconductor nanocrystal (CdSe core with a ZnS shell), showing bright and dark periods with a wide distribution of durations. After Reference 12.

absorb efficiently, or because its fluorescence yield is too low. Hereafter, we examine a few possible sources of blinking.

2.3.4.1 ***Triplet State*** A molecule in its triplet state can in theory absorb and emit photons, but usually with very low fluorescence yield only. Moreover, the laser wavelength is normally not suited to excite triplet–triplet transitions. Therefore, the triplet state is dark. The molecule's fluorescence trace presents dark periods lasting for the triplet lifetime on average. Depending on the molecule, this time can be as short as microseconds and as long as tens of milliseconds for usual dyes. Atmospheric oxygen has a strong influence on triplet lifetime. Since O_2 has a triplet ground state, it can exchange electrons with a molecular triplet, yielding two singlet states, one the ground state of the dye, the other one singlet oxygen, a very reactive and phosphorescent species.

2.3.4.2 ***Electron Transfer*** The excited molecule may accept an electron from its environment, or give one electron to it [12]. The radical ion left often has very low fluorescence yield. The charge-transfer state lives as long as the electron is away, giving rise to dark states with lifetimes longer than seconds if the electron goes far away, as the example of rhodamine 6G in polyvinyl alcohol shows [13]. This process appears to be very general, as was recently demonstrated in the groups of Sauer and Tinnefeld. Charge transfer rates can be controlled by adding redox species to the solution. This scheme (known as ROXS) [14] profoundly modifies the lifetimes of the triplet state and of the charged dark states, which can have the added benefit that bleaching (see next paragraph) is also significantly reduced.

2.3.4.3 ***Other Reversible Photochemical Reactions*** Excited molecules may change conformation. If the change is reversible, and if the two forms have different optical properties, blinking will follow. An example of intramolecular reactions of this kind is cis-trans isomerization, which is common in cyanine dyes. The excited molecule may also react with its environment, for example, by abstracting a proton from a nearby molecule or from an acid matrix. Several dyes present protonated "leuco" forms, in which an additional proton shortens the conjugation path and shifts the absorption spectrum to the blue. The main feature of these photochemical reactions involving large rearrangements of atoms is that they often require large activation energies and are therefore frozen at low temperatures.

2.3.4.4 Other Sources of Blinking They may exist in principle. For example, the orientation of the molecule could switch between parallel and perpendicular to the excitation polarization. The absorption spectrum of the molecule could also shift between different spectral positions. This spectral diffusion is a prominent effect in low-temperature experiments (see below), and has also been observed at room temperature in polymers [15]. However, such "physical" processes do not seem to lead to significant blinking, entailing large intensity fluctuations.

2.3.5 Bleaching

Many photochemical reactions are irreversible. In that case, the molecule stays in the dark state the first time it goes there. Fluorescence is lost for good, and a new single molecule must be found. At room temperature, all fluorescent organic molecules photobleach sooner or later. Much effort has been spent to screen, adapt, and design dyes able to resist photobleaching as far as possible. This has been crucial for laser dyes, but also for fluorescent labeling in biology. In spite of several decades of efforts, little is known about photobleaching and how to control it. Atmospheric oxygen and small reactive molecules such as water obviously open efficient channels for photobleaching. Production of highly reactive singlet oxygen from the triplet state of the dye is a well-characterized degradation channel. That is the reason why red and infrared dyes with their triplet state below the energy of singlet oxygen are highly photoresistant, even in air. Because of the important role of oxygen, many single-molecule fluorescence studies are done in the presence of reducing agents (oxygen scavengers, mercaptoethanol, Trolox®, etc.). The ROXS scheme (see above), by shortening the lifetimes of metastable and reactive states, also improves the resistance of dyes to bleaching. However, even in inert and dry atmosphere, or under high vacuum, photobleaching still occurs, albeit at a lower rate. Because photobleaching involves barrier crossing in chemical reactions, it is likely that low temperatures considerably decrease the process. Temperature studies of rhodamine in PVA have shown that indeed, bleaching is reduced by several orders of magnitude at low temperatures for some molecules, but not for all of them [16]. Recent articles report dyes of the perylene or terrylene-diimide family, which present excellent resistance to bleaching, and still can be made water soluble by convenient substitution [17].

2.3.6 Superresolution

The size of the PSF, for example, the image spot of a single molecule, is limited by diffraction. However, as was realized from the very beginning of single-molecule observations, the center of the image of a single molecule can be found with accuracy much higher than the width of the PSF. If N photons are detected, we can exploit our knowledge that all of them arise from the same single molecule, a point-like region of space. Therefore, the position of their center of gravity is determined down to roughly $\Delta x/\sqrt{N}$, where Δx is the spatial width of the PSF. Indeed, the probability distribution of the average of N random variables, each of them distributed along the same normal Gaussian probability law, is itself a Gaussian with width reduced by $\sqrt{N}$.

In low-temperature experiments (see Section 2.5), single molecules can be discriminated by their resonance frequency. The selection of many different molecules at many different laser frequencies gives rise to a superresolved image [18], where each molecule provides one point with $\Delta x/\sqrt{N}$ accuracy. Because a large number of photons can be accumulated for each single molecule, the accuracy can reach a few nanometers only. This has been done recently on a sample of millions of molecules in a crystal at low temperature [19], providing a superresolved image of the crystal. In 2006, three important papers appeared almost simultaneously, demonstrating superresolution based on photochemical switching of single molecules [20–22]. These three papers proposed the same idea of using photochemical reactions to switch molecules on and off, and localizing the on-molecules with superresolution accuracy. The proposed photochemical reactions differed, however, ranging from transitions to dark states in autofluorescent proteins to blinking or bleaching reactions in dyes. In all cases, the central idea of superresolution imaging with photoswitches is to randomly select a small subpopulation of all fluorescent molecules present in the sample by switching them to a bright state, either with an auxiliary laser or by spontaneous blinking in the right conditions [23]. The concentration of these activated switches should be low enough that each one of them gives rise to a spot isolated from the others. Because these spots are well separated from each other, one can find their centers very accurately. For the brightest molecules, providing many photons, the spot center can be located to an accuracy of a few tens of nanometers, sometimes even better. Another related superresolution method uses the transient binding of fluorescent molecules to the surface or object to be imaged [24]. Only the immobile molecules give rise to a measurable spot, whose center determines with superresolution the source's location.

2.4 FLUORESCENCE CORRELATION SPECTROSCOPY

We now discuss the case of fluorescent molecules diffusing in a fluid environment, for example, a drop of solution, a thin liquid film or a Langmuir film, a membrane, a capillary channel, a cell, and so on. The most important feature of such experiments is that molecules come into the focal volume and leave it again, and that statistics over large numbers of molecules are both possible and necessary to extract useful information. Usually, there are not enough photons emitted during each crossing of the focal volume for a detailed study of each single molecule; therefore, one has to accumulate data collected over large numbers of molecules. Microscopy and spectroscopy methods in fluid solutions are therefore a special type of single-molecule methods, in which usually only one molecule is detected at a given time (although fluorescence correlation also works for small numbers of molecules simultaneously present in the detection volume), but in which it is in general impossible to focus on individuals or to compare different individuals. In this sense, these correlation methods are related to ensemble measurements, and give statistical histograms. In some applications, however, for example, in multiparameter analyses, statistical correlations between different quantities are obtained. This analysis method is really a single-molecule method.

2.4.1 Photon Counting Histograms, Burst Analysis

A first way to statistically analyze the fluorescence signal is to plot a histogram of the signal intensity, that is, the number of counts during a given time interval, for example, a few tens of microseconds for intense signals [25]. For a single emitter with constant emission rate, the distribution is Poissonian. In the case of diffusing molecules, the distribution of the number of molecules is also Poissonian, and the observed histogram is a convolution of these two distributions. Diffusion during the emission broadens the distributions even more. Note that this method does not give the time dependence of fluctuations, unless the time window is varied.

A variant of this method is the analysis of burst sizes. This is particularly useful in the case of a solution flowing in a capillary. Each fluorescent molecule crossing the laser focus gives a burst of light with the same maximal intensity, and with a duration determined mainly by the flow velocity (if the flow is faster than diffusion over the focus). Burst size analysis is used in fluorescence biomedical assays.

2.4.2 Fluorescence Correlation Spectroscopy

The principle of this method is to keep track of intensity fluctuations of a fluorescence time trace $I(t)$. The second-order correlation function $g^{(2)}(\tau)$ used to characterize the fluctuations is given by

$$g^{(2)}(\tau) = \frac{\langle I(t)I(t+\tau)\rangle}{\langle I(t)\rangle^2},$$

where the angular brackets indicate averaging over a very long integration time under assumption of a stationary fluorescence time trace. In practice, the integration time is finite and must be taken into account in the evaluation of the correlation function from real data.

The first application of this method was proposed by Hanbury Brown and Twiss to analyze the coherence from astronomical light sources. The correlation method was then applied in the 1970s to analyze thermodynamic fluctuations of fluids via light scattering. Quasielastic light scattering can be measured in the spectral domain (first-order correlation of the field), or in the intensity domain (second-order correlation). It was then realized that one of the fluctuating quantities could be the number of emitting molecules in the focal volume, giving rise to FCS [26]. FCS really took off in the early 1990s with the large increase in detection efficiency thanks to avalanche photodiodes (APDs), microscope optics, and better filters. The method is very powerful and now widely used for the following reasons:

- It gives access to a wide range of times, often more than eight orders of magnitude. This range is limited by the photon count rate and the detector dead time (but this limitation can be circumvented by cross-correlating the signals of two detectors) on the short-time side, and only by the experiment's duration on the long-time side.
- Because the correlation data are averaged over a long integration time which can reach minutes or hours, noise is considerably reduced, enabling weak and subtle effects to be detected.
- FCS is much less sensitive to concentration requirements than single-molecule measurements. It also works for small numbers of molecules in the focus, at the expense of a lower contrast, only partly offset by the higher signal. Because the number of molecules used is high, FCS is also less sensitive to photobleaching. The illumination doses received by each molecule are much lower than in other single-molecule observations.

All sources of fluctuations of the fluorescence will give rise to a signature in the correlation function. Hereafter, we examine the main sources of fluctuations [27].

2.4.2.1 Translational Diffusion A molecule crossing the laser focus can be seen as a concentration fluctuation, which will relax according to Brownian diffusion. From elementary diffusion theory, we know that the mean squared displacement of a diffusing molecule increases linearly with time, and therefore that the volume in which the molecule has the highest probability of being found increases as a power 1.5 of time. The correlation function thus decays as $\tau^{-1.5}$ for long times. Because the initial position cannot be known more accurately than the PSF, the fluctuation decay is cutoff for short times by the diffusion time within the focus, $\tau_{\mathrm{D}} = \Delta x^2/4D$, where Δx is the size of the focus and D is the diffusion coefficient. For a fluorescent dye in water, $D \approx 1\ \mu\mathrm{m}^2\ \mathrm{ms}^{-1} = 10^{-9}\ \mathrm{m}^2\ \mathrm{s}^{-1}$. One can give a more rigorous treatment based on a Fourier transform of the diffusion equation, assuming the fluorescence efficiency to vary spatially as a Gaussian, which is valid in the transverse plane for a Gaussian laser beam, but only approximately valid in the axial direction. This calculation gives for the correlation function

$$g^{(2)}(\tau) = 1 + \frac{1}{N}\left(1 + \frac{4D\tau}{\Delta x^2}\right)^{-1}\left(1 + \frac{4D\tau}{\Delta z^2}\right)^{-1/2},$$

where Δx and Δz are the transverse and axial beam waists, respectively, and N is the average number of molecules in the excitation volume. Einstein related the diffusion coefficient to the local viscosity η around the molecule and its diameter $2R$ (if the molecule is a sphere) by

$$D = \frac{k_B T}{6\pi\eta R}.$$

The diffusion coefficient therefore is inversely proportional to the viscosity of the medium and to particle radius. Big molecules such as proteins will diffuse slower than small dyes, but the times will scale only linearly with radius.

2.4.2.2 Rotational Diffusion A molecule absorbs and fluoresces as a dipole, although not necessarily with the same dipole direction and magnitude. Therefore, rotation of the molecule has an influence on the absorption of laser light, even when the exciting laser light is unpolarized, and on the detected fluorescence if there is an analyzer in the detection path. Rotational diffusion in three dimensions is a complex process, which obeys a second-order diffusion equation. Its solution involves spherical harmonics and Legendre polynomials, and in general displays multiexponential relaxation. In the case of a spherical rotor, however, the general solution is much simplified and the rotational relaxation is single-exponential [27]. It is interesting to note the difference from the translational case: because the space of available angles is finite, the equilibrium is reached more rapidly. A reasoning similar to the one for translational diffusion gives the rotational diffusion constant as a function of viscosity and of the hydrodynamic volume V_H of the diffusion object (close to the actual volume), by the Debye–Stokes–Einstein relation:

$$\tau_{\text{rot}} = \frac{\eta V_H}{k_B T}.$$

We see that this time now scales as the volume of the particle, instead of its radius for translational diffusion. For small dye molecules, rotational diffusion times in water are on the order of nanoseconds, comparable to fluorescence lifetimes. This means that the orientation of a molecule may vary considerably during fluorescence. This can be detected in steady state or in pulsed experiments by measuring fluorescence polarization, yielding an observable called fluorescence anisotropy. Rotational diffusion of small dyes is usually too fast to detect it by FCS in water. Rotational diffusion can be followed in highly viscous environments, or if the dyes are rigidly fixed to larger diffusing objects, such as big proteins.

2.4.2.3 Dark State (Triplet) We now consider variations of the fluorescence intensity due to molecular transitions to a different state, usually a dark one in which fluorescence is suppressed. Figure 2.4 shows as an example the correlation of fluctuations induced by transitions of a molecule in its triplet state. Chemical or physical changes in the molecule or its environment can lead to changes in the absorption, or more often to quenching of the fluorescence. The resulting fluorescence fluctuations are due to

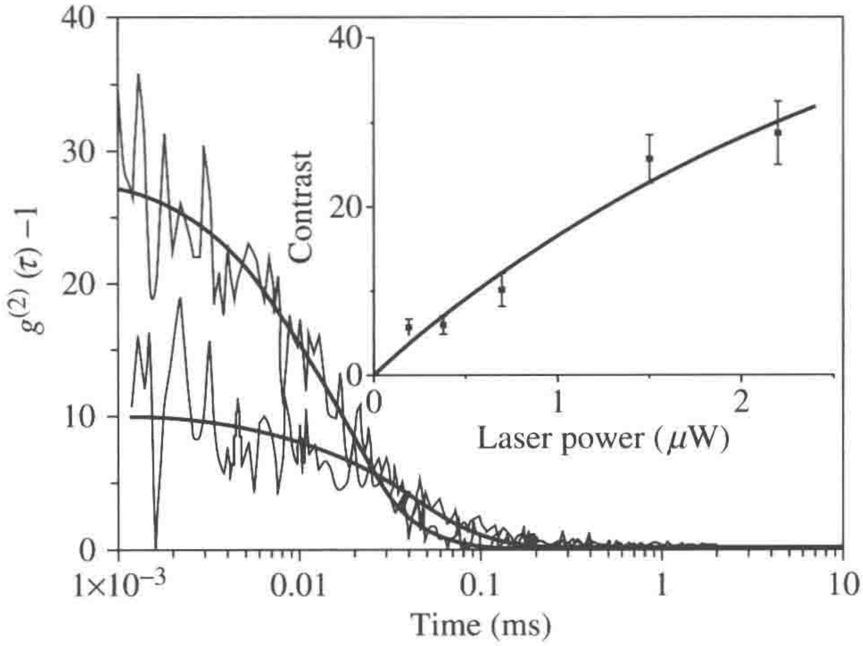

FIGURE 2.4 Autocorrelation functions of the fluorescence intensity of a terrylene molecule in an anthracene crystal for two excitation intensities. The intensity fluctuations are due to intersystem crossing (ISC) into and from the triplet state. The high contrast of the correlation indicates that the on-times are much shorter than the off-times. In the present case, intersystem crossing is induced by coupling to the anthracene matrix.

random passages in the dark state, so that the signal of each single molecule resembles a random telegraph. The correlation function of a random telegraph switching between two states with intensities I_1, I_2 at rates $k_1 (k_2)$ to leave state 1 (2) for state 2 (1) is given by [25]

$$g^{(2)}(\tau) - 1 = \frac{k_1 k_2 (I_1 - I_2)^2}{(k_2 I_1 + k_1 I_2)^2} \exp[-(k_1 + k_2)\tau].$$

In the special case $I_2 = 0$, the contrast of the correlation becomes k_1/k_2. This expression shows that short excursions to high intensities generate a higher contrast, and therefore will be more visible, than short excursions to low intensities. We also note that the decay rate of the correlation is always the sum of the two relaxation rates of the two states. The two individual rates can be recovered by combining knowledge of time and contrast.

In general, molecules in fluid solution are subject to the three effects mentioned above, and the correlation function can be rather complex. In many cases, the fluorescence intensity can be written approximately as a product of independently fluctuating quantities (e.g., translational diffusion, rotational diffusion, and chemical fluctuations). The correlation function then can be expressed as a product of averages, that is, as a product of the functions pertaining to each type of fluctuations alone,

$$I(t) = f(t) \times g(t) \text{ entails that } \langle I(t)I(t')\rangle = \langle f(t)f(t')\rangle\langle g(t)g(t')\rangle,$$

which means that, if the timescales are well separated, each type of fluctuations can be recognized on a logarithmic timescale, nearly independently of the other processes.

2.4.2.4 ***Variants of FCS*** The correlation function is a general method, which provides time-resolved information from a fluctuating signal. It can obviously be applied to other signals than fluorescence intensity, for example, fluorescence lifetimes, but also nonoptical signals such as currents in ion channels, for instance. Hereafter, we mention a few extensions of FCS.

Two different signals can be correlated with one another, for example, two intensities. This is cross-correlation [28]. For example, dual-color FCS is very important in molecular biology. The fluorescence signals of two different dyes are separated by a dichroic beam splitter and measured by two detectors. If the two dyes diffuse together (e.g., because they are attached to two interacting proteins), the translational diffusion of the complex will appear in the cross-correlation. If the molecules do not interact, the fluctuations will be independent of each other, and no cross-correlation will appear.

Fluorescence can be generated by two-photon or three-photon pulsed excitation. The advantages of this scheme are that there is less scattering of the longer excitation wavelengths, and that the focal volume is limited by the nonlinearity; therefore, no pinhole is needed in the detection to obtain a slice of the sample (this effect is called optical sectioning). Photobleaching is suppressed altogether for out-of-focus molecules, although it is often enhanced for the molecules in the focus.

Correlation can also be applied to any optical signal, linear or nonlinear. A good example is Coherent Anti-Stokes Raman Scattering (CARS). Being a coherent process, CARS would be very difficult to observe with a single molecule. However, it can be observed with small particles down to 100 nm in diameter, such as organelles in cells. Correlation techniques can also be applied to the strongly fluctuating fluorescence signals obtained upon enhancement by metal nanostructures.

2.4.3 Multiparameter Analysis

Fluorescence gives rise to several different observables such as intensity, lifetime, spectrum, polarization, and FRET. In order to fully exploit the fluorescence signal of a single molecule, one ideally would like to measure all of them with a time resolution as high as possible [29]. Because the number of fluorescence photons per unit time is limited, one has to choose the more relevant parameters and measure these with suitable time resolution. Determination of a fluorescence lifetime with an accuracy of a few percentages requires at least a thousand photons. A polarization measurement (or a crude measurement of the shift of a fluorescence spectrum) can be done with two detectors and a polarizing beam-splitter (or a dichroic beam splitter) and requires at least a few tens of photons. Once two (or more) quantities are measured for a population of molecules which have crossed the excitation volume, the quantities can be cross-correlated. The correlation may reveal different conformations of proteins, protein–protein or protein–DNA complexes.

2.5 FLUORESCENCE EXCITATION SPECTROSCOPY

2.5.1 Zero-Phonon Line and Phonon Wing

Fluorescence excitation is usually equivalent to absorption. It is mostly useful in low-temperature studies of single molecules, where certain lines become extremely narrow and intense. In that case, high resolution is more easily reached by excitation with a narrow single-frequency laser than by other spectroscopic devices such as spectrographs. Before discussing low-temperature spectroscopy, we need some basic knowledge of the optical spectroscopy of impurities in solids. We start with the simple case of only one molecule in a solid at zero temperature. If there was no coupling to vibrations, the absorption spectrum would consist of a single line, with a width given by the excited state lifetime. However, the electronic system of a molecule is in principle coupled to all possible vibration modes in the molecule and in the solid matrix around it. In the Born–Oppenheimer picture, this coupling arises from changes in vibrational potential between ground and excited electronic states: Because the nuclear wavefunctions in the excited state differ from those in the ground state, exciting the electron modifies the nuclear movement, that is, it can bring about vibrations in the molecule. Fortunately, one does not have to consider all possible vibration modes to understand the absorption and fluorescence spectra. Usually only a few of these modes are coupled strongly to the optical transition, which simplifies the analysis considerably. We first consider coupling of the electron to a single harmonic vibration mode. Often, a totally symmetric C–C stretching mode (breathing mode) is responsible for most of the coupling. We further assume that only the equilibrium position of the nuclei along the associated vibration coordinate is modified. This case is called linear vibronic coupling.

We first consider only one deformation mode R of a molecule, with a harmonic potential $E_g(R)$ in the ground state $|g\rangle$. The minimum of this potential is displaced by ΔR in the excited state $|e\rangle$ with potential $E_e(R)$, without a change in the curvature. In the crude Born–Oppenheimer approximation, we can write the wavevectors as products:

$$|g, m\rangle \simeq |g\rangle|m\rangle, \text{ and } |e, n\rangle \simeq |e\rangle|\tilde{n}\rangle,$$

where $\tilde{n}$ means n quanta in the excited well potential, and m means m quanta in the ground state potential. One usually calls Franck–Condon amplitude the overlap amplitude:

$$f_m^n = \langle \tilde{n} \mid m \rangle ,$$

and Franck–Condon factor the square modulus of this overlap:

$$F_m^n = |\langle \tilde{n} \mid m \rangle|^2 .$$

The Franck–Condon factors represent the intensities of the *m-n* transitions from the ground to excited states. The first ones are the 0–0 and 0–1 transitions. These factors can be expressed analytically from the overlap of harmonic oscillator wavefunctions. The special case where one of the wavefunctions is the ground vibrational state is most important. It can be shown easily that the Franck–Condon factors have the following form:

$$F_0^n = \frac{\xi^{2n}}{n!} e^{-\xi^2},$$

where $\xi = \Delta R \sqrt{\frac{M\Omega}{2\hbar}}$ is the displacement of the harmonic oscillator upon excitation in dimensionless units of the spatial spread of the ground state. M is the mass and Ω the angular frequency of the oscillator.

The absorption spectra of a molecule at low enough temperature are recorded starting from the ground vibrational state of the ground electronic state, and going to all vibrational states of the excited electronic state (these states are called vibronic [vibr-onic] states). The intensities of these absorptions are proportional to the Franck–Condon factors. A similar argument applies to the emission or fluorescence spectrum, starting from the ground vibrational state of the excited electronic state, and going to all vibrational states of the ground electronic state. For linear vibronic coupling, the intensity distributions of the absorption and emission spectra are symmetric with respect to the zero-phonon line (ZPL). Absorption and fluorescence spectra are mirror images of each other with respect to the 0–0 transition.

We now consider the coupling of a molecule to a large number of modes, for example, to a branch of phonons in a host crystal. Each mode is now weakly coupled (weak ξ) and contributes a weak 0–1 absorption sideband shifted to the blue of the main absorption line (which corresponds to the 0–0 transition). Neglecting the 0–2 transitions (although they are weak, their number is large, of order N^2, with N the number of modes), we find a broad band on the blue side of the 0–0 line. The 0–0 line, which is common to all modes, is called ZPL, and the blue-shifted broad band is the phonon wing (PW). The intensity of the ZPL is called the Debye–Waller factor and is analogous to the intensity of spots in X-ray diffraction, or to the intensity of the recoil-free structure in Mössbauer spectroscopy. This intensity decreases very rapidly with temperature. One often uses the following approximated formula for the oscillator strength of the ZPL:

$$I_{\mathrm{ZPL}} \approx \exp\left[-\xi^2 / \tanh\left(\frac{\hbar\Omega}{2k_{\mathrm{B}}T}\right)\right].$$

The intensity of the ZPL therefore decreases exponentially with temperature. In most organic materials, the intensity of the ZPL becomes negligible at temperatures higher than 30 K. In diamond, which is a much harder material with a high Debye temperature (about 1000 K), the ZPL of certain impurities can still be observed at room temperature.

In the preceding model, the ZPL is a narrow line, with a linewidth given by the excited state lifetime. However, several processes contribute to its broadening:

- Higher-order coupling to phonons, notably via the change in curvature of the potential. The associated process is called quadratic coupling.
- Anharmonicity of the vibrations.
- Slower processes, called spectral diffusion, which arise from drift and jumps of the resonance frequency due to dynamics in the molecule's environment.

If spectral diffusion is neglected, the homogeneous linewidth of a molecule is composed of two contributions, one from the lifetime T_1 of the excited state, the other one from "pure dephasing." This process, often called "decoherence" in quantum optics, arises from interactions with phonons and other dynamical modes activated at finite temperatures. One therefore writes the full width at half maximum of the optical line, measured in units of angular frequencies ω as

$$\gamma_{\text{hom}} = \frac{1}{T_1} + \frac{2}{T_2^*},$$

where T_2^* represents the "pure dephasing" time, that is, the lifetime of the coherence between the two electronic levels, determined by bath fluctuations at relatively low frequencies (phonons, etc.). At very low temperatures, the pure dephasing rate tends to zero, since no degrees of freedom are activated any more. In many molecular crystals, this limit is reached already at a few Kelvins, which means that the optical width is limited by the lifetime of the excited state only. For an allowed transition the lifetime is of the order of a few nanoseconds, corresponding to a width of 30 MHz, or one-thousandth of a cm^{-1}.

When coupling to both phonons and intramolecular vibrations is considered, the absorption spectrum of a single molecule consists of a single very sharp line at the lowest frequency, the ZPL of the 0–0 transition. At higher energies, we find the phonon wing (PW) of the 0–0 transition, the ZPL of 0–1, 0–2, ... transitions of various intramolecular vibrations, followed by their PWs. Note that the vibronic ZPLs are much broader than the pure electronic ZPL because of the width of the vibrational levels, determined by the lifetime of the molecular vibration, rarely longer than a few picoseconds. Each intramolecular vibration mode gives rise to its own vibronic progression, ZPLs and PWs, but only the pure electronic ZPL is common to all modes.

2.5.2 Inhomogeneous Broadening

In usual samples, billions of molecules are observed at the same time. Because of defects and disorder, the electronic transition of each individual molecule is shifted with respect to the average value. This phenomenon is called inhomogeneous broadening. It is nearly independent of temperature, because it is determined by structure, and structure is nearly frozen at low temperatures (at least as long as the matrix is solid). The size of this inhomogeneous broadening depends strongly on the quality of the sample and on the way the impurity molecules are embedded in the matrix. For optical transitions of molecules, the inhomogeneous width varies from about 300 cm^{-1} (10 THz) in a polymer or in a frozen solution, to less than 3×10^{-2} cm^{-1} (1 GHz) in unstressed sublimation-grown crystals, which are the best molecular crystals one can grow. A typical value of inhomogeneous broadening for substitutional impurities in a low-quality molecular crystal is about 10 cm^{-1}. Therefore, in all cases, the inhomogeneous width is several orders of magnitude broader than the lifetime-limited linewidth of a single molecule at low temperature. The broad absorption profiles observed in ensemble experiments result from the superposition of the many randomly shifted narrow lines of individual molecules.

Comparatively little is known about the inhomogeneous distributions and the associated lineshapes. They are determined by the local structure around the impurity. In many cases, the local structure is relatively well defined and can be considered as perturbed by many independent defects, such as vacancies, grain boundaries, or dislocations in crystals. Assuming the contributions of such defects to be approximately equal, and applying the central limit theorem, we then expect a Gaussian inhomogeneous lineshape. However, other models give different shapes. For example, a uniform distribution of defects interacting with an inverse cubic dependence on distance (dipole–dipole interaction) gives rise to a Lorentzian lineshape. In general, however, the inhomogeneous distribution is neither Gaussian nor Lorentzian, and often is asymmetrical.

In crystals, a guest molecule often may occupy several imbedding positions, called insertion sites. They give rise to multiplets of ZPLs in absorption spectra or in fluorescence spectra recorded with broad excitation, or excited at high energies (several thousands of wavenumbers) above the 0–0 transition. Each one of these sites corresponds to molecules with slightly different atom configurations, giving rise to slightly different vibrational spectra, lifetimes, and so on. A particularly important case is that of Shpol'skii matrices, which are crystals of linear *n*-alkanes. Their crystal structure is layered with the long axis of the molecules nearly perpendicular to the layer. Narrow Shpol'skii lines are often obtained when the guest molecule matches the holes left in the crystal when removing one or a few host molecules. Shpol'skii systems are very current and useful in molecular spectroscopy.

2.5.3 Hole-Burning [30]

Spectral hole-burning is a nonlinear optical technique applied to large ensembles of molecules, in which a spectral feature (the hole) results from a modification by light of the optical properties of a material. Let us consider an ideal hole-burning experiment at zero temperature. An ensemble of molecules absorbing with very narrow *homogeneous* lines (ZPLs) but a broad *inhomogeneous* distribution of optical resonance frequencies is irradiated with a monochromatic (or very narrow) laser. In first approximation, if the laser intensity is not too high, only the resonant molecules will absorb light. The other ones do not see the laser. Now, an excited molecule may undergo a number of possible photophysical and photochemical processes. For example, the molecule can be temporarily stored in the triplet state, with a different (usually lower or zero) absorption. During the lifetime of the triplet, the sample will absorb less at the frequency of the illuminating laser. If an absorption spectrum of the sample is measured, it will show a hole—a transient spectral hole—at the frequency of the laser. But a molecule can also enter a much longer-lived dark state. Some of these product states may have very long (for all practical purposes infinite) lifetimes, in particular if the molecule undergoes a (photo-)chemical reaction. If the spectral hole is permanent, one calls the process persistent spectral hole-burning (PSHB).

Molecules in solid matrices at low temperatures can undergo a number of different processes leading to photochemical and photophysical hole-burning. Photochemistry may involve electron, proton transfers, or large rearrangements of atoms. Photochemical hole-burning generally leads to very large shifts of the photoproducts, which means that products of the reaction do not absorb in the same spectral regions as the educts (in other words, no antiholes can be found in the spectrum). In photophysical processes, the conformation of neighboring atoms or groups of atoms is modified by illumination, leading to a shift of the absorption line, much larger than the homogeneous width, but usually smaller than the inhomogeneous bandwidth. The resulting antihole is much broader than the hole, and can only be measured after very deep and broad holes have been burned. Photophysical hole-burning is also called "light-induced spectral diffusion" in the context of single-molecule spectroscopy.

The experimental method to burn persistent holes is very simple, since the holes are long-lived. A single tunable narrow-band laser suffices. It is first used to irradiate the sample somewhere in the inhomogeneous bandwidth. Then, the laser is scanned to record an absorption spectrum, revealing the hole. Contrast enhancement methods can be used to detect narrow holes, for example by holography, polarization, or lock-in detection methods. The hole-burning method is very useful in molecular spectroscopy (determination of lifetimes, vibrational spectroscopy), in the spectroscopy of molecules or ions with spin-multiplet states (via the analysis of satellite holes), for the study of dynamical degrees of freedom in solids at low temperatures, notably glasses, for the effect of external perturbations such as electric and magnetic fields, pressure, and stress. A hole being very narrow, it enhances the sensitivity of these experiments by several orders of magnitude as compared to bulk experiments. In the past 20 years, hole-burning materials have also been proposed as optical memories. A hole-burning sample can be seen as a photographic plate sensitive to several millions of different colors. However, practical difficulties, such as the low temperature and the problem of burning while reading, have limited their applications so far. Current research aims at using such media as analyzers and processors of optical information, which could treat many different wavelengths in a massively parallel way, or as nonlinear media for photonics applications [31].

2.5.4 Single-Molecule Spectroscopy

We now consider a host–guest system in which molecules are very stable, that is, in which hole-burning is inefficient or unlikely. If we focus our laser on a very small

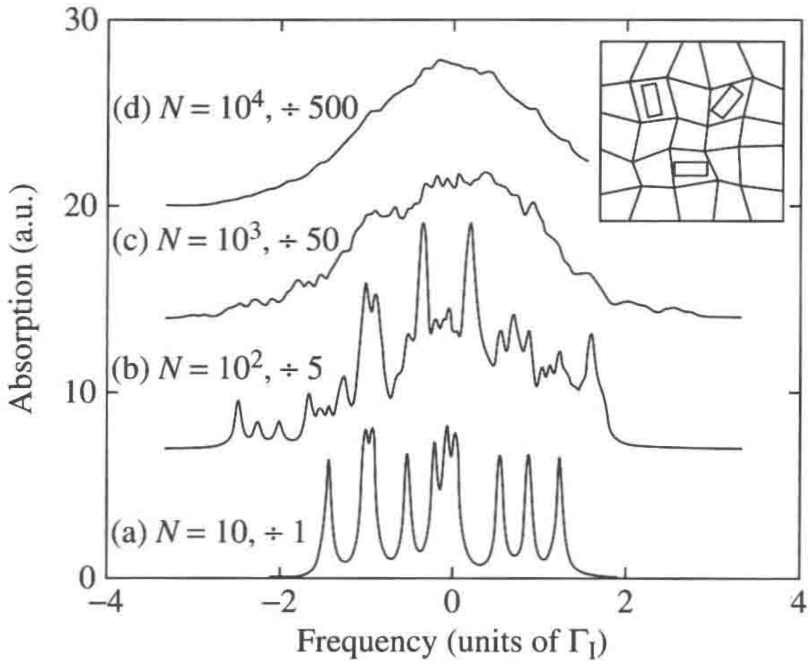

FIGURE 2.5 For a large number of molecules (*d*: 10,000 molecules), the absorption spectrum appears smooth and reproduces the inhomogeneous band profile. At lower and lower numbers of molecules, spectral fluctuations start to appear, until single-molecule zero-phonon lines are completely resolved (a, here for 10 molecules). Figure after Reference 36. The natural width of the zero-phonon lines has been greatly exaggerated for illustration purposes.

volume of sample and move it spatially, we will start to see statistical fluctuations of the number of molecules in resonance with the laser. If we scan the frequency of our laser at a fixed spot in the sample, we will see characteristic fluctuations of the optical absorption, or of the total fluorescence of the sample. These fluctuations have been first detected by Moerner in 1987 and are called statistical fine structure [32]. Analysis of this structure provides the homogeneous width of the molecules. In the same way that FCS reveals the average diffusion time in an ensemble of molecules, the autocorrelation of the statistical fine structure provides a peak whose width is related to the homogeneous linewidth. As illustrated in Figure 2.5, if we further reduce the focal volume and/or the concentration, the relative amplitude of the statistical fine structure increases, as it scales with the inverse square root of the average number of molecules in the focus. In the regime where the average number of molecules is less than unity, the spectrum ideally consists of a set of resolved sharp lines on a low background. Each single peak corresponds to the absorption line of a single molecule.

The first optical signal of a single molecule has been detected in 1989 by Moerner and Kador with a complex method, involving a double frequency modulation (laser frequency and molecular resonance frequency were modulated at different frequencies) of the absorption of a thin sample of pentacene in a para-terphenyl crystal. Although this method is very sensitive, its application to a single molecule is difficult because of photon noise and of optical saturation. The absorption signal is measured as a weak variation of the intensity of the transmitted beam. In order to reduce the relative photon noise on that beam, the intensity has to be large, and as a consequence, the molecular signal saturates (in other words, the absorption cross-section of the molecule decreases). Orrit and Bernard showed in 1990 that a fluorescence excitation method provides a much better signal/noise ratio. Since then, the fluorescence excitation method has been improved and generalized. It was first used for low-temperature spectroscopy, then for microscopy at room temperature.

2.5.5 Scope of Low-Temperature Single-Molecule Spectroscopy

We will not review the wealth of new results brought by single-molecule spectroscopy at low temperatures during the past 20 years, as such reviews have been published already [33–36]. We only give a brief summary of the different types of experiments that have been done with fluorescence excitation of single molecules.

2.5.5.1 ***External Field Effects*** Just as with spectral hole-burning, the narrow lines of single molecules provide a vastly enhanced sensitivity of optical signals to external perturbations such as electric or magnetic fields and mechanical pressure and stresses. The unique advantage of single molecules for such probing of external actions is that a molecule reports local conditions in its surroundings, free of ensemble averaging. This can be useful in many cases in nanoscience, for example, to probe trapped charges in organic conductors [37,38].

2.5.5.2 ***Optically Detected Magnetic Resonance and Quantum Optics*** Electron paramagnetic resonance (EPR) is a powerful technique to explore the electronic structure of materials. However, this technique requires billions of spins to provide measurable magnetic resonance signals. Optically detected magnetic resonance (ODMR) transfers the sensitivity of optical measurements to the magnetic domain and enhances to sensitivity of EPR by orders of magnitude. The optical detection of a single molecule has made it possible to detect a single electron spin with high signal-to-noise ratio [39,40]. This experiment has been recently extended to single color centers in diamond, which present paramagnetic ground and excited states. Using the electron spin as a probe for neighboring nuclear spins, several groups have proposed a broad range of quantum optical manipulations on nuclear spins, ultimately detected through changes of optical signals [41–43].

A single molecule is also a well-defined electronic system, in which the quantum state can be manipulated. Single quantum systems can be applied to deliver single photons on command [44] for a variety of experiments, from near-field imaging [45] to photon number interference [46].

2.5.5.3 ***Spectral Diffusion*** Spectral diffusion of a single-molecule line results from changes of the molecule's optical resonance frequency. These changes are themselves caused by slow motion or transitions in the molecule's neighborhood, with ranges varying from nanoseconds (comparable to the fluorescence lifetime) to minutes or even longer. Some examples of spectrally diffusing molecules with widely different dynamics in the same samples are presented in Figure 2.6. In such a wide-spread time window, many processes can contribute to spectral diffusion. Single molecules enable

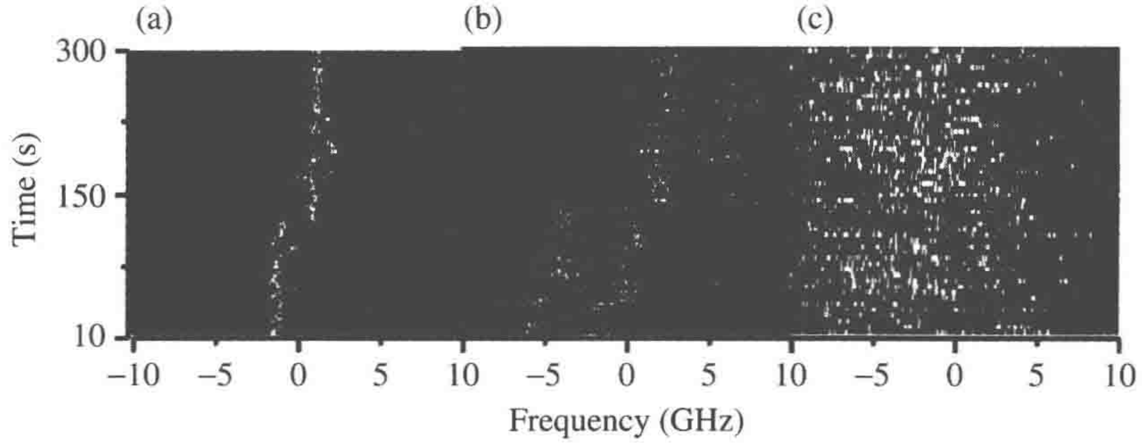

FIGURE 2.6 Example of spectral diffusion traces measured for single terrylene molecules in a 2,3-dimethylanthracene crystal [47]. The dynamics is attributed to methyl group conformational changes. Figure reproduced from Reference 47 with permission from © 2012 Wiley-VCH Verlag.

a study of these different processes on a truly local scale, without ensemble averaging. Among the most studied degrees of freedom have been the tunneling systems of glasses and polymers at cryogenic temperatures. Single molecules signals show random telegraph blinking assignable to switching of individual two-level systems [48], as well as more complex behavior [49,50]. Another well-studied example is the flipping of the central phenyl group of para-terphenyl in a crystal at low temperature, studied through the spectral diffusion of probe molecules such as pentacene [51] or terrylene [52]. These studies have proved that host molecules at crystal defects such as domain walls are particularly prone to conformational changes. Flipping phenyl groups lead to nearly independent two-level systems and to a specific pattern of spectral diffusion for the probe molecules [53, 54]. Many other slow degrees of freedom in low-temperature matrices can lead to spectral diffusion, such as subtle reorientations of methyl groups [55], or correlated molecular motions characteristic for incommensurate phases [56].

2.5.5.4 Interacting Single Molecules In regular single-molecule experiments, excited molecules are very far from each other, so as to achieve spatial and spectral selection. Sometimes, however, molecules can be close enough to significantly interact and give rise to new coupled states. One such example is given by the chromophores of individual antenna complexes studied by Van Oijen et al. [57]. These authors found in the same individual complex weakly coupled states from the B800 ring as well as strongly coupled states demonstrating delocalized exciton states in the B850 ring. These systems have been recently studied at room temperature by ultrafast single-molecule spectroscopy and found to exhibit quantum coherence even at room temperature [58]. Applying variable electric fields to single molecules gives access to a wider range of frequencies, and may help reaching the resonance condition for two neighboring molecules. This effect was used by Hettich et al. [59] to study the nonlinear optical response of two terrylene molecules in a crystal and demonstrate their excitonic coupling. Yet another possibility to enhance the probability to find coupled chromophores is to link them covalently. This technique has allowed Basché's group to study energy transfer between single donor and acceptor moieties [60].

This short overview shows the wide scope of single-molecule experiments at low temperature. Much remains to be done, in particular concerning the interaction of single molecules with plasmonic structures. For these experiments, the main advantage of low-temperature experiments is that a large number of distinguishable single molecules can be coupled to the same plasmonic structure.

2.6 OTHER DETECTION METHODS

In this section, we review the main techniques used to detect individual nano-objects, in particular metal nanoparticles, through their effect on a probing laser beam. The object or particle can be observed in dark field, that is, with a high contrast in a direction where no intensity is scattered in the absence of the particle. It can also be detected in bright field, by comparing scattered intensities with and without the particle in the beam. This latter scheme amounts to an interferometric detection of the particle. Finally, pump-probe methods exploit a change of the scattered probe wave which is conditional to pump excitation. Therefore, these methods have the power to selectively detect absorbing (e.g., metal) nanoparticles against any background of nonabsorbing (dielectric, nonmetallic) scatterers. These different optical techniques have become widespread in the past few years and given rise to a large body of work. Here, we only mention the main advances, stressing the underlying detection principles.

2.6.1 General Considerations on Signal, Background, and Noise

To detect a small object, usually less than 100 nm in size, in the optical far field, one should optimize its interaction with the light beam. This is achieved by placing the object at the focus of a spherical wave or of a Gaussian beam, or very close to this focus. Indeed, the sensitivity optimum is not always exactly at the wave focus. To a good approximation, a small object in an optical field behaves as an oscillating dipole, radiating a scattered wave. Superposition of this scattered wave with the incoming wave leads to measurable intensity changes in different spatial regions. Hereafter, we briefly discuss the three main ways to measure these changes and to detect and study individual particles.

2.6.1.1 Dark Field The relative change of intensity is the strongest in directions where the incident wave, in the absence of a particle, would not produce any intensity. The wave scattered by the particle will thus contribute a nonzero intensity appearing on a dark background. That principle is called dark-field scattering. For ideal conditions, it can in principle provide an arbitrarily large signal-to-background ratio. This property is very similar to that of fluorescence, because no fluorescence background exists where no fluorescent object is present. In practice, however, these ideal low-background conditions are very difficult to achieve for Rayleigh scattering, because small defects in the substrate, impurities, or small structures also scatter light in all directions. This problem is particularly serious in biological cells, because of scattering by organelles, vesicles, and other small cell structures.

2.6.1.2 Bright Field The wave scattered by a small object also presents an amplitude in the direction of the transmitted wave, and thereby interferes with it. In the forward direction, the interference always reduces the intensity of the incident wave, leading to extinction of the incident wave. The relation between extinction and the scattering amplitude is given by the optical theorem in scattering theory [61]. The optical theorem expresses the conservation of energy: the energy removed from the incident wave is either locally absorbed, or scattered away. There, it appears as new scattered waves and as a simultaneous weakening of the transmitted wave. Local absorption can give rise to heat release or to re-emitted radiation at different (usually lower) frequencies, that is, as fluorescence or photoluminescence. A similar interference effect occurs in other propagation directions of the incident wave, particularly when this wave is reflected by an interface, or scattered by a bigger object. The following reasoning thus applies to those cases as well.

Let us discuss the signal/noise ratio in such an extinction experiment. The detected intensity ΔI change results from a sum of a reference (incoming) field r and of a small scattered field s:

$$\Delta I = |r + se^{i\phi}|^2 - |r|^2 \approx 2\mathrm{Re}(r^* se^{i\phi}),$$

where ϕ is the phase difference between the incident field and the scattered field at a large distance, taking all phases into account (including propagation, Gouy shifts, and phase shift due to the polarizability of the particle). For example, a pure absorber placed at the focus of a plane wave has a dipole in quadrature with the incident field. The spherical wave it scatters introduces an additional Gouy phase of $\pi/2$. The combination of these shifts gives rise to destructive interference between transmitted and scattered waves, attenuating the incident wave.

In dark field scattering, there is no reference field, no background, and the signal-to-noise ratio can in principle be arbitrarily large. Note, however, that the intensity scattered by a small object is very weak and is easily drowned by background from experimental imperfections.

In a bright-field experiment, the scattered intensity $|s|^2$ is negligible for a small object. The signal arises mostly from the interference term $2rs\cos\phi$ (for real reference and scattered fields), which has to be detected against the background $|r|^2$ of the intensity transmitted or reflected by the substrate. This bright-field difference signal therefore scales as the *amplitude* of the scattered field, that is, as the volume of the scatterer. For measurements limited by photon noise, the noise on the background scales as the square root of the background, therefore as the *amplitude* of the reference field, just as the signal does. Therefore, the signal-to-noise ratio is independent of the intensity of reference field. This useful property allows one to adapt the experimental configuration to available sources and detectors. Choosing a weak reference field (e.g., a weak reflection from the interface between two nearly index-matched media [62]) is a convenient means to suppress laser noise (which scales as $|r|^2$) without losing signal/noise ratio. A similar reduction can be achieved by means of an interferometer [63], but at the cost of a more complex setup and of more difficult adjustments.

2.6.1.3 Absorption Detection The dissipation of light energy by the single object, due to absorption processes, may give rise to a number of secondary effects, including local heat production, luminescence, and other emissions. These effects can also be used to detect true absorption, as opposed to extinction, and provide a means to distinguish metal nanoparticles from dielectric scatterers. As we have seen above, fluorescence or photoluminescence is a highly selective and sensitive way to detect absorbers, but heat-induced, photothermal and pump-probe effects are also useful to detect metal particles with a high selectivity. The signal-to-noise ratio in such experiments will depend on the sources of background, which can be very low in luminescence or photothermal measurements.

In the next sections, we successively discuss these three big classes of methods with experiments from the past few years on small metal nanoparticles.

2.6.2 Dark-Field Scattering, Total Internal Reflection

Dark-field microscopy was first used by Zsigmondy around 1900 to study the scattering of suspensions of gold nanoparticles with his "ultramicroscope." His observations helped clarify the structure of colloidal suspensions and convince the last skeptics of the reality of atoms and molecules [64]. In 1998, Feldmann's group published first experiments in near-field [65], while Yguerabide et al. [66] studied individual nanoparticles in far-field in view of labeling in biological applications. Studying the dark-field scattering of silver nanoparticles, Schultz pointed out the high interest of nanoparticles of different sizes and shapes for multicolor labeling [67].

Light scattered by a small object can be detected against a dark background in a variety of ways, often also used in fluorescence microscopy. Microscope companies offer dark-field condensers with associated objectives to specifically observe scattering objects. Alternatively, high-numerical-aperture objectives can accommodate annular illumination with detection in the center of the pupil, or vice-versa. Total internal reflection offers a convenient way to illuminate particles when they are situated close to an interface on the low-index side. Scattered light can be observed on that same side with very low background. The main advantage of dark-field scattering is its ease of operation, because it only requires a standard microscope with a regular objective. Moreover, it also allows for wide-field imaging and makes it possible to follow hundreds of particles in parallel at the same time. Scattering spectra are observed directly, without any need for background subtraction or post-processing. Hereafter, we mention some recent results obtained by dark-field scattering of metal nanoparticles. Soennichsen et al. [68] used dark-field scattering images to obtain the spectra of nanorods and nanospheres of various shapes and sizes. These spectra are free from the large broadening resulting from inhomogeneity in ensemble experiments. They demonstrated a spectacular reduction in plasmon width for rods and attributed the main channel of plasmon damping to relaxation toward electron–hole pairs for small particles. They recognized the importance of radiative damping for large particles. The radiative channel broadens the plasmon resonance for large sizes, whereas surface-induced broadening becomes noticeable for small sizes, 10 nm and lower, so that a minimum in broadening occurs at about 30 nm.

Dark-field scattering in combination with scanning electron microscopy (SEM) reveals the plasmon bands of more complex assemblies of nanoparticles such as the pairs of nanorods studied by Funston et al. [69]. Various relative positions of the rods give rise to hybridized or coupled plasmon bands, in agreement with calculations. The polarization of scattered light can be obtained by a rotating polarizer. With this technique, a large number of silver and gold nanoparticles can be monitored in parallel during their growth. Dark-field scattering is a very versatile method allowing many correlated measurements in parallel thanks to its ease of operation. Its limitation, however, is that the scattered intensity scales as the squared volume of the nanoparticles. Therefore, for small particles, dark-field scattering is easily overcome by signals from dielectric impurities, substrate roughness, or even thermodynamic fluctuations of the medium. Its application to small objects requires very clean substrates, and often reaches its limits around 30 nm for gold nanospheres under standard conditions of optical quality and cleanliness.

2.6.3 Absorption, Extinction, Interference-Based Methods

The reduction in transmitted intensity due to a small object is called extinction. As compared to the dark-field scattering signal, the extinction signal scales as the amplitude of the field scattered by the object, instead of its intensity. However, this signal has to be detected against a strong background of transmitted light. Similarly, a change in reflection intensity scales with the field amplitude and therefore the volume of the particle, but has to be detected against the background of light reflected by the interface.

The first discussion of this interference effect for a single molecule in reflection was given by Plakhotnik and Palm [70] for a low-temperature spectroscopy experiment. The spectral shape of the interference line can change from absorptive to dispersive, depending on the phase difference between the two fields. This difference was varied by choosing molecules at different distances from the interface. The authors proposed to extend this technique to nonfluorescent objects. Lindfors et al. [62] studied the plasmon resonance of a single gold nanoparticle immobilized on a surface and surrounded by immersion oil with a similar reflection technique. For large particles, the scattered intensity dominated the weak reflection from the nearly index-matched glass–oil interface, but for small particles the reflection was stronger. Destructive interference of the scattered field led to reduced reflection, enabling detection of particles down to 10 nm in diameter against the weak reflected background. The reflection of a water–glass interface was used as the reference signal by Jacobsen et al. [71] to demonstrate fast and wide-field detection of gold nanoparticles immobilized on a glass surface but in contact with an aqueous phase, which is interesting for the detection of biomolecules. Metal nanoparticles were distinguished from dielectric scatterers such as particles or substrate defects by their plasmon resonance probed at two different wavelengths. This scattering method in transmission or reflection has recently been improved so as to reach the threshold of a single molecule's absorption [72].

The main limitation of the scattering method, however, is not its sensitivity. Different principles of subtraction have been used to extract the small extinction signal from the strong transmitted or reflected background. A more serious obstacle to this method of detection of small particles is the lack of specificity of their scattering signals against those from other scatterers. These can be dielectric particles in suspension, impurities, corrugations or refractive index inhomogeneities of the substrate, or organelles in biological cells. To distinguish those from metal nanoparticles, one needs specific signals arising from the absorption itself instead of the extinction. As explained in the next section, pump-probe methods do provide such specificity.

2.6.4 Pump-Probe and Photothermal Detections

Pump-probe detection techniques achieve selectivity by measuring only that part of the scattered probe signal which is conditional to the presence of the pump. Whereas this usually entails a significant loss in signal amplitude, it has the considerable benefit that only *resonantly* absorbing objects, such as metal nanoparticles, semiconductor nanocrystals, or dye molecules, have sufficient nonlinear susceptibilities to produce a sizable signal. Cross talk between pump and probe beams induced by the nonlinear $\chi^{(3)}$ susceptibility of transparent dielectrics is negligible at the intensities used in microscopy of absorbing objects. In pump-probe techniques, one measures the change of intensity of the transmitted or reflected probe beam caused by a pump beam. The wave measured is a superposition of the scattered probe field with the transmitted or reflected probe beam, as explained above (Section 2.6.1.2). Now, however, the subtracted intensity is not that of the probe beam without the particle, but rather the probe intensity without pump excitation. This subtraction is usually done by modulating the pump power at high frequency (often around 1 MHz) and by detecting the change in probe intensity with a lock-in amplifier. Any nonlinearity of the $\chi^{(3)}$ type will give rise to a change of scattered probe field due to the presence of the pump, by a signal proportional to the probe amplitude and to the pump intensity (or squared amplitude). The physical origin of the nonlinearity can be the heat dissipation due to pump absorption (photothermal effect), an electronic response (electronic pump-probe, ground-state depletion), or a vibrational response (vibrational pump-probe, stimulated Raman scattering).

2.6.4.1 Pump-Probe For excitations at the plasmon frequency of a metal particle, the pump mainly excites conduction electrons. The energy dumped into these electronic degrees of freedom launches transient responses of, in turn, the collective plasmon oscillations, then incoherent motions of conduction electrons, then phonons and vibrations of the nanoparticle as a whole. Finally, the energy is dissipated in the environment and diffuses away from the particle. The activation of these degrees of freedom takes place on different timescales, determined by their coupling strengths.

Plasmonic excitations are damped in less than 10 fs, the electron bath equilibrates with the lattice within a few picoseconds, the nanoparticle vibrations are damped in some hundreds of picoseconds, and heat dissipation into the environment proceeds between nanoseconds and microseconds, depending on the length scale considered. According to which optical technique is used and to the timescale, these different degrees of freedom can contribute to a pump-probe signal.

We first discuss pulsed experiments with 200 fs pulses. This pulse duration is too long to resolve the nonlinearity of plasmon oscillations, but it clearly shows a prompt optical response of hot electrons, which decays within a few ps. This response arises from the transient distribution of hot electrons and holes, which causes changes in real and imaginary parts of the optical permittivity. It is strong enough to allow for detection of gold nanospheres down to 10 nm in diameter. With a laser repetition rate of 80 MHz, however, the signal-to-noise ratio is much lower than that of photothermal detection. Indeed, because of the low duty cycle, much less photons are absorbed and used as probes in the pulsed experiments. The advantage of these pulsed experiments, however, is that they give access to the time-resolved response up to 12 ns, and thereby probe vibration frequencies and damping rates. Single-nanoparticle studies have the unique advantage of revealing full distributions of shape and size as well as rare cases of composed particles such as dumbbells, and of providing access to intrinsic damping mechanisms, which are often hidden by inhomogeneity in ensemble measurements. Optical probing of vibrations of single metal nanoparticles has been recently reviewed [74]. In metal nanospheres, because the isotropic heating process does not break the spherical symmetry, only radial vibration modes are efficiently excited. The fundamental normal mode and higher-order ones (overtones) can be observed [75]. A nonradial extensional mode appears in the pump-probe trace when the spherical symmetry is broken, either by the shape in slightly elongated particles, or by the contact with another spherical particle in pairs of touching nanospheres (dumbbells) [76]. In the dumbbell, optical excitation also leads to low-frequency oscillations of the centers of the two component particles around their equilibrium positions, resembling the stretching mode of a diatomic molecule. Transient vibrational traces of gold nanorods [77] mainly show the breathing mode and the extension mode at a much lower frequency, as the example of Figure 2.7 shows. The ratio of their frequencies depends on the rod's shape and gives information about the elastic moduli of the single-crystal rods. Silver nanocubes were recently studied by Staleva et al. [78]. Again, the fundamental breathing mode is the dominant one in the traces, with sometimes nonradial modes at lower frequency, possibly arising from a deviation from cubic symmetry. The origin of the damping of mechanical vibrations of gold nanoparticles was explored by experiments in optical traps [79], and confirmed the importance of intrinsic damping [80] pointed out in ensemble experiments on high quality samples [81].

2.6.4.2 Photothermal Contrast In photothermal microscopy, the pump beam is again absorbed by the particle to be detected, whereas the probe beam monitors the change of index of refraction in the environment of the absorber. As the probe wavelength is usually chosen out of the absorption range of the particle, it is

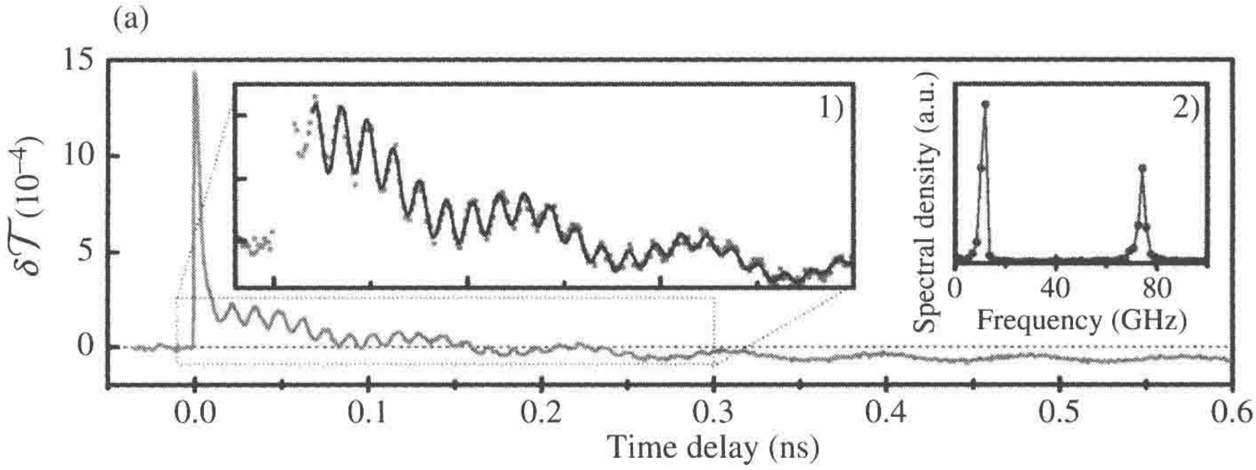

FIGURE 2.7 A pump-probe time trace of a single gold nanorod (25 nm × 60 nm) showing the fast electronic response in the first few picoseconds, followed by coherent oscillations of the diameter (high frequency) and of the length of the rod (low frequency). Reproduced from Reference 73 with permission from © 2012 American Chemical Society.

advantageous to increase the probe intensity as much as possible to reduce photon noise. The heating beam is modulated at a high frequency in the MHz range, and the ensuing variations of scattered intensity of the continuous-wave probe beam are detected with a lock-in amplifier. The photothermal signal thus makes use of a weak effect, the change of refractive index of the surrounding medium with temperature, but as it accumulates the contributions of many photons, both for pumping and for probing, it can still achieve excellent signal-to-noise ratios. The method has been implemented in microscopy in different ways, first on silver nanoparticles in free solution by Matawari et al. [82], then in a polarization-sensitive configuration by Boyer et al. [83] in a confocal microscope. Berciaud et al. improved on this method and pushed the sensitivity to gold nanoparticles 1.4 nm in diameter [84]. The photothermal method has been adapted to wide-field microscopy by Absil et al. [85] by exploiting image subtraction at video rate and recently pushed to single-molecule sensitivity by Gaiduk et al. [86] (see Fig. 2.8).

Photothermal detection of small gold nanoparticles requires the absorption of many photons and, by its very principle, an associated heating. The ensuing temperature rise at the particle may be a limitation for probing application in biology or soft matter studies. Moreover, even temperatures as low as 100°C can cause reshaping of gold nanorods and of complex nanoparticles. Therefore, a compromise must be found between particle size, integration time, and maximum allowed temperature rise. In glycerol, an absorbed power of 3 nW can be detected with a signal-to-noise ratio of 8 in an integration time of 10 ms, corresponding to a temperature increase of less than 0.1 K for a 20-nm gold particle [87]. Such high sensitivities enable the photothermal detection of single nonfluorescent molecules, as shown in Figure 2.8. In water, this signal is reduced by a factor of about 5.

2.6.4.3 Electronic Response and Ground-State Depletion This detection technique closely resembles photothermal contrast, but relies on an electronic nonlinearity instead of a thermal one. A pump beam is modulated at high frequency (MHz or

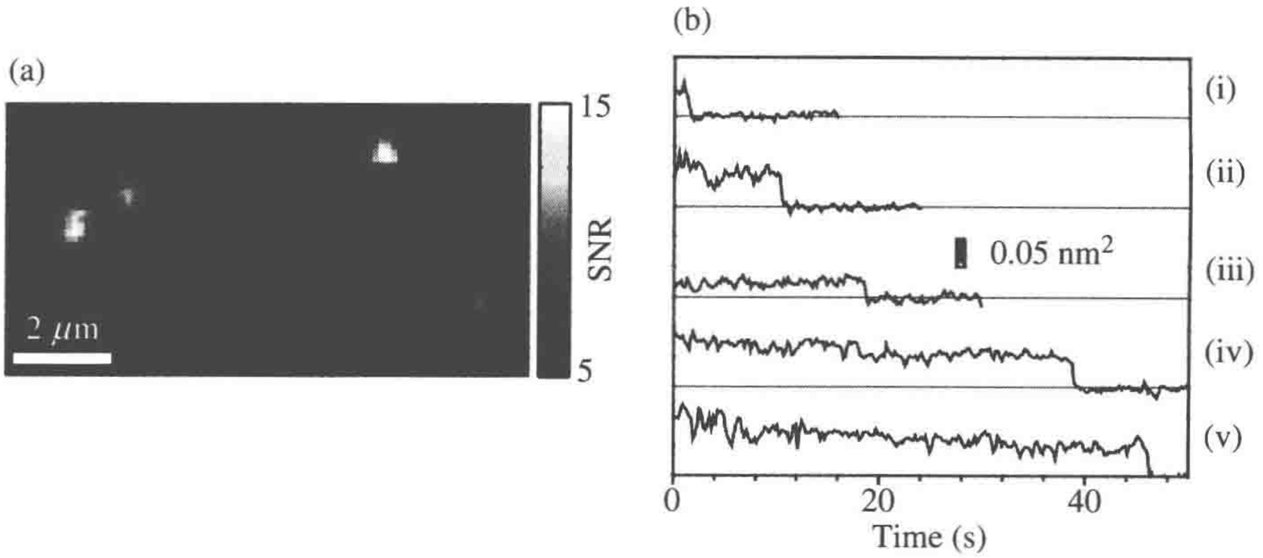

FIGURE 2.8 (a) Photothermal image showing signals originating from single absorbing molecules. The right panel (b) shows time traces recorded on some of the spots, showing one-step photobleaching after several seconds of illumination at high intensity [86]. Reproduced from Reference 86 with permission from © 2010 AAAS.

higher) and the modulation of a confocal probe beam is detected with a lock-in amplifier. However, the probe frequency is now chosen in an absorption band of the object to be detected, which may be the same as the one addressed by the pump. The pump and probe frequencies should be far enough apart to be efficiently separated before detection of the probe. For a molecule, the depletion of ground state population by the pump obviously leads to a decrease of probe absorption. For a metal particle, the hot electrons and holes created by the pump change the optical response to the probe in a manner similar to the time-resolved experiments described above. Chong et al. [88] used this method to image immobilized gold nanoparticles (diameter 20 nm). Moreover, the sensitivity of the technique was enough to detect single Atto647 dye molecules. This technique will be a useful alternative to photothermal microscopy in cases where heating is undesirable, or in media where temperature-induced refractive index changes are small.

2.7 CONCLUSION

In this review chapter, we have described the main optical methods used for detection and studies of single small objects, from molecules to metal nanoparticles. Fluorescence is still the workhorse method of single-molecule detection and has been recently augmented by fascinating applications in superresolution imaging. Fluorescence-related methods have been immediately extended to a broad range of emitting objects, including semiconductor nanocrystals [89] and metal nanoparticles [90]. Although the photoluminescence yield of gold nanoparticles is very low, of the order of 10^{-6}, their coupling to light is dramatically improved by their plasmonic properties, generating very large absorption cross sections. Therefore, the fluorescence (or photoluminescence) signals of plasmonic particles can be comparable or even stronger than that of fluorescent molecules. However, gold particles are much more stable and durable than molecules. Their main disadvantage is their rather large size.

In addition to fluorescence, a number of new optical signals have been proposed during the last few years, of which we reviewed some here. The most direct ones are based on scattering in dark or bright field in linear optics. They are very general and experimentally simple, but often lack sensitivity and selectivity for the objects of interest. By relying on nonlinear spectroscopy, more refined methods can enhance selectivity through one or several resonant steps. One example is photothermal detection, which provides contrast for absorbing objects only, or the closely related methods of ground state depletion and stimulated Raman scattering. Pump-probe spectroscopy gives time-resolved information, which can be exploited to obtain phase-sensitive information [91].

Among the new developments that were hardly mentioned in this review is the coupling of optically active nano-objects to plasmonic nanostructures [92]. Large field enhancement in the vicinity of metallic nanostructures can lead to spectacular enhancement of the coupling to light of molecules and other nano-objects, in absorption as well as in emission. These lead to surface-enhanced Raman scattering of single molecules [93], tip-enhanced Raman scattering [94, 95], enhanced fluorescence by bowtie antennas [96], nanorods [97], or antennas in boxes [98]. Enhanced electric fields in metallic nanostructures will certainly raise many fundamental questions and find a broadening range of applications in the coming years.

ACKNOWLEDGMENTS

We acknowledge financial support by ERC (Advanced Grant SiMoSoMa). The work presented in this chapter was done within the research program of the "Stichting voor Fundamenteel Onderzoek der Materie," which is financially supported by the Netherlands Organization for Scientific Research (NWO).

REFERENCES

[1] J. Perrin, "La Fluorescence," *Ann. Phys* **9**, 133 (1918).

[2] G. Binnig, H. Rohrer, and C. Gerber, "Surface studies by scanning tunneling microscopy," *Phys. Rev. Lett.* **49**, 57–61 (1982).

[3] G. Binnig and H. Rohrer, "Scanning tunneling microscopy—from birth to adolescence," *Rev. Mod. Phys.* **59**, 615–625 (1987).

[4] L. Novotny and B. Hecht, *Principles of Nano-Optics* (Cambridge University Press, 2006).

[5] J. T. Fourkas, "Rapid determination of the three-dimensional orientation of single molecules," *Opt. Lett.* **26**, 211–213 (2001).

[6] D. P. Fromm and W. E. Moerner, "Methods of single-molecule fluorescence spectroscopy and microscopy," *Rev. Sci. Instrum.* **74**, 3597–3619 (2003).

[7] T. Schmidt, G. J. Schütz, and H. J. Gruber, "Local stoichiometries determined by counting individual molecules," *Anal. Chem.* **68**, 4397–4401 (1996).

[8] G. J. Schütz, W. Trabesinger, and T. Schmidt, "Direct observation of ligand colocalization on individual receptor molecules," *Biophys. J.* **74**, 2223–2226 (1998).

[9] L. A. Deschenes and D. A. Vanden Bout, "Heterogeneous dynamics and domains in supercooled o-terphenyl: a single molecule study," *J. Phys. Chem. B* **106**, 11438–11445 (2002).

[10] R. Zondervan, F. Kulzer, G. C. G. Berkhout, and M. Orrit, "Local viscosity of supercooled glycerol near Tg probed by rotational diffusion of ensembles and single dye molecules," *Proc. Natl. Acad. Sci. USA* **194**, 12628–12633 (2007).

[11] T. Ha, T. Enderle, D. S. Chemla, P. R. Selvin, and S. Weiss, "Single molecule dynamics studied by polarization modulation," *Phys. Rev. Lett.* **77**, 3979–3982 (1996).

[12] F. Cichos, C. von Borczyskowski, and M. Orrit, "Power-law intermittency of single emitters," *Curr. Opin. Coll. Interf. Sci.* **12**, 272–284 (2007).

[13] R. Zondervan, F. Kulzer, S. B. Orlinskii, and M. Orrit, "Photoblinking of rhodamine 6G in poly(vinyl alcohol): radical dark state formed through the triplet," *J. Phys. Chem. A* **107**, 6770–6776 (2003).

[14] J. Vogelsang, R. Kasper, C. Steinhauer, B. Person, M. Heileman, M. Sauer, and P. Tinnefeld, "A reducing and oxidizing system minimizes photobleaching and blinking of fluorescent dyes," *Angew. Chem. Int. Ed.* **47**, 5465–5469 (2008).

[15] H. P. Lu and X. S. Xie, "Single-molecule spectral fluctuations at room temperature," *Nature* **385**, 143–146 (1997).

[16] R. Zondervan, F. Kulzer, M. A. Kol'chenko, and M. Orrit, "Photobleaching of rhodamine 6G in poly(vinyl alcohol) at the ensemble and single-molecule levels," *J. Phys. Chem. A* **108**, 1657–1665 (2004).

[17] M. Davies, C. Jung, P. Wallis, T. Schnitzler, C. Li, K. Müllen, and C. Bräuchle, "Photophysics of new photostable rylene derivatives: applications in single-molecule studies and membrane labelling," *Chem. Phys. Chem.* **12**, 1588–1595 (2011).

[18] A. M. van Oijen, J. Köhler, J. Schmidt, M. Muller, and G. J. Brakenhoff, "3-Dimensional super-resolution by spectrally selective imaging," *Chem. Phys. Lett.* **292**, 183–187.

[19] A. V. Naumov, A. A. Gorshelev, Y. G. Vainer, L. Kador, and J. Köhler, "Far-field nanodiagnostics of solids with visible light by spectrally selective imaging." *Angew. Chem. Int. Ed.* **48**, 9747–9750 (2009)

[20] E. Betzig, G. H. Patterson, R. Sougrat, O. W. Lindwasser, S. Olenych, J. S. Bonifacino, M. W. Davidson, J. Lippincott-Schwartz, and H. F. Hess, "Imaging intracellular fluorescent proteins at nanometer resolution," *Science* **313**, 1642–1645 (2006)

[21] M. J. Rust, M. Bates, and X. W. Zhuang, "Sub-diffraction-limit imaging by stochastic optical reconstruction microscopy (STORM)," *Nat. Methods* **3**, 793–795 (2006).

[22] S. T. Hess, T. P. K. Girirajan, and M. D. Mason, "Ultra-high resolution imaging by fluorescence photoactivation localization microscopy," *Biophys. J.* **91**, 4258–4272 (2006).

[23] M. Heilemann, S. van de Linde, A. Mukherjee, and M. Sauer, "Superresolution imaging with small organic fluorophores," *Angew. Chem. Int. Ed.* **48**, 6903–6908 (2009).

[24] A. Sharonov and R. M. Hochstrasser, "Wide-field subdiffraction imaging by accumulated binding of diffusing probes," *Proc. Natl. Acad. Sci. USA* **103**, 18911–18916 (2006).

[25] M. Lippitz, F. Kulzer, and M. Orrit, "Statistical evaluation of single nano-object fluorescence," *Chem. Phys. Chem.* **6,** 770–789 (2005).

[26] D. Magde, E. L. Elson, and W. W. Webb, "Fluorescence correlation spectroscopy. 2. An experimental realization," *Biopolymers* **13**, 29–61 (1974).

[27] J. Widengren and U. Mets, "Conceptual basis of fluorescence correlation spectroscopy and related techniques and tools in bioscience," in *Single Molecule Detection in Solution*, edited by C. Zander, J. Enderlein, and R. A. Keller (Wiley-VCH, Berlin, 2002), Chap. 3, pp. 69–120.

[28] J. Ries and P. Schwille, "Fluorescence correlation spectroscopy," *Bioessays* **34**, 361–368 (2012).

[29] P. J. Rothwell, S. Berger, O. Kensch, S. Felekyan, M. Antonik, B. M. Wohrl, T. Restle, R. S. Goody, and C. A. M. Seidel, " Multiparameter single-molecule fluorescence spectroscopy reveals heterogeneity of HIV-1 reverse transcriptase: primer/template complexes," *Proc. Natl. Acad. Sci. USA* **100**, 1655–1660 (2003).

[30] W. E. Moerner, *Persistent Spectral Hole-Burning: Science and Applications Topics in Current Physics* (Springer, Berlin, 1988), Vol. 44.

[31] G. Heinze, C. Hubrich, and T. Halfmann, "Stopped light and image storage by electromagnetically induced transparency up to the regime of one minute," *Phys. Rev. Lett.* **111**, 033601 (2013).

[32] W. E. Moerner and T. P. Carter, "Statistical fine structure of inhomogeneously broadened absorption lines," *Phys. Rev. Lett.* **50**, 2705–2708 (1987).

[33] W. E. Moerner and M. Orrit, "Illuminating single molecules in condensed matter," *Science* **283**, 1670–1676 (1999).

[34] Ph. Tamarat, A. Maali, B. Lounis, and M. Orrit, "Ten years of single molecule spectroscopy," *J. Phys. Chem. A* **104**, 1–16 (2000).

[35] T. Plakhotnik, E. A. Donley, and U. P. Wild, "Single-molecule spectroscopy," *Ann. Rev. Phys. Chem.* **48**, 181–212 (1997).

[36] M. Orrit and W. E. Moerner, "High-resolution single-molecule spectroscopy in condensed matter," in *Physics and Chemistry at Low Temperatures*, edited by L. Khriachtchev (Pan Stanford, Singapore, 2011), pp. 381–417.

[37] M. A. Kol'chenko, A. A. L. Nicolet, M. D. Galouzis, C. Hofmann, B. Kozankiewicz, and M. Orrit, "Single molecules detect ultra-slow oscillators in a molecular crystal excited by ac-voltages," *New J. Phys.* **11,** 023037 (2009).

[38] A. A. L. Nicolet, M. A. Kol'chenko, C. Hofmann, B. Kozankiewicz, and M. Orrit, "Nanoscale probing of charge transport in an organic field-effect transistor at cryogenic temperatures," *Phys. Chem. Chem. Phys.* **15,** 4415–4421 (2013).

[39] J. Köhler, J. A. J. M. Disselhorst, M. C. J. M. Donckers, E. J. J. Groenen, J. Schmidt, and W. E. Moerner, "Magnetic resonance of a single molecular spin," *Nature* **363**, 242–244 (1993).

[40] J. Wrachtrup, C. von Borczyskowski, J. Bernard, M. Orrit, and R. Brown, "Optical detection of magnetic resonance in a single molecule," *Nature* **363**, 244–245 (1993).

[41] L. Childress, M. V. G. Dutt, J. M. Taylor, A. S. Zibrov, F. Jelezko, J. Wrachtrup, P. R. Hemmer, and M. D. Lukin, "Coherent dynamics of coupled electron and nuclear spin qubits in diamond," *Science* **314**, 281–285 (2006).

[42] R. Hanson, V. V. Dobrovitski, A. E. Feiguin, O. Gywat, and D. D. Awschalom, "Coherent dynamics of a single spin interacting with an adjustable spin bath," *Science* **320**, 352–355 (2008).

[43] T. van der Sar, Z. H. Wang, M. S. Blok, H. Bernien, T. H. Taminiau, D. M. Toyli, D. A. Lidar, D. D. Awschalom, R. Hanson, and V. V. Dobrovitski, "Decoherence-protected quantum gates for a hybrid solid-state spin register," *Nature* **484**, 82–86 (2012).

[44] C. Brunel, B. Lounis, P. Tamarat, and M. Orrit, "Triggered source of single photons based on controlled single molecule fluorescence," *Phys. Rev. Lett.* **83** 2722–2725 (1999).

[45] J. Michaelis, C. Hettich, J. Mlynek, and V. Sandoghdar, "Optical microscopy using a single-molecule light source," *Nature* **405**, 325–328 (2000).

[46] R. Lettow, Y. L. A. Rezus, A. Renn, G. Zumofen, E. Ikonen, S. Götzinger, and V. Sandoghdar, "Quantum interference of tunably indistinguishable photons from remote organic molecules," *Phys. Rev. Lett.* **104**, 123605 (2010).

[47] Y. Tian, P. Navarro, B. Kozankiewicz, and M. Orrit, Spectral diffusion of single dibenzoterrylene molecules in 2,3-dimethylanthracene," *Chem. Phys. Chem.* **13**, 3510–3515 (2012).

[48] A. Zumbusch, L. Fleury, R. Brown, J. Bernard, and M. Orrit, "Probing individual 2-level systems in a polymer by correlation of single molecular fluorescence," *Phys. Rev. Lett.* **70**, 3584–3587 (1993).

[49] A. M. Boiron, P. Tamarat, B. Lounis, R. Brown, and M. Orrit, "Are the spectral trails of single molecules consistent with the standard two-level system model of glasses at low temperatures? *Chem. Phys.* **247**, 119–132 (1999).

[50] A. V. Naumov, Y. G. Vainer, and L. Kador, Does the standard model of low-temperature glass dynamics describe a real glass? *Phys. Rev. Lett.* **98**, 145501 (2007).

[51] W. P. Ambrose, T. Basché, and W. E. Moerner, "Detection and spectroscopy of single pentacene molecules in a para-terphenyl crystal by means of fluorescence excitation," *J. Chem. Phys.* **95**, 7150–7163 (1991).

[52] F. Kulzer, S. Kummer, R. Matzke, C. Bräuchle, and T. Basché, "Single-molecule optical switching of terrylene in p-terphenyl," *Nature* **387**, 688–691 (1997).

[53] P. D. Reilly and J. L. Skinner, "Spectral diffusion of individual pentacene molecles in p-terphenyl crystal—stochastic theoretical model and analysis of experimental data," *J. Chem. Phys.* **102**, 1540–1552 (1995).

[54] E. Geva, P. D. Reilly, and J. L. Skinner, "Spectral dynamics of individual molecules in glasses and crystals," *Acc. Chem. Res.* **29**, 579–584 (1996).

[55] Y. X. Tian, P. Navarro, B. Kozankiewicz, and M. Orrit, "Spectral diffusion of single dibenzoterrylene molecules in 2,3-dimethylanthracene," *Chem. Phys. Chem.* **13**, 3510–3515 (2012).

[56] M. Paers, V. Palm, and J. Kikas, "Single-molecule probing of incommensurate biphenyl," *Low Temp. Phys.* **36**, 448–450 (2010).

[57] A. M. van Oijen, M. Ketelaars, J. Köhler, T. J. Aartsma, and J. Schmidt, "Unraveling the electronic structure of individual photosynthetic pigment-protein complexes," *Science* **285**, 400–402 (1999).

[58] R. Hildner, D. Brinks, J. B. Nieder, R. J. Cogdell, and N. F. van Hulst, "Quantum coherent energy transfer over varying pathways in single light-harvesting complexes," *Science* **340**, 1448–1451 (2013).

[59] C. Hettich, C. Schmitt, J. Zitzmann, S. Kuhn, I. Gerhardt, and V. Sandoghdar, "Nanometer resolution and coherent optical dipole coupling of two individual molecules," *Science* **298**, 385–389 (2002).

[60] B. Fückel, G. Hinze, F. Nolde, K. Müllen, and T. Basché, "Control of the electronic energy transfer pathway between two single fluorophores by dual pulse excitation," *Phys. Rev. Lett.* **103**, 103003 (2009).

[61] H. van de Hulst, *Light Scattering by Small Particles* (Dover, New York, 1981).

[62] K. Lindfors, T. Kalkbrenner, P. Stoller, and V. Sandoghdar, "Detection and spectroscopy of gold nanoparticles using supercontinuum white light confocal microscopy," *Phys. Rev. Lett.* **93**, 037401 (2004).

[63] F. V. Ignatovich and L. Novotny, "Real-time and background-free detection of nanoscale particles," *Phys. Rev. Lett.* **96**, 013901 (2006)

[64] R. Zsigmondy, Colloids and the Ultramicroscope: A Manual of Colloid Chemistry and Ultramicroscopy, translated by J. Alexander (John Wiley & Sons, New York, 1909).

[65] T. Klar, M. Perner, S. Grosse, G. von Plessen, W. Spirkl, and J. Feldmann, "Surface-plasmon resonances in single metallic nanoparticles," *Phys. Rev. Lett.* **80**, 4249–4252 (1998).

[66] J. Yguerabide and E. E. Yguerabide, "Light scattering submicroscopic particles as highly fluorescent analogs and their use as tracer labels in clinical and biological applications," *Anal. Biochem.* **262**, 137–156 (1998).

[67] S. Schultz, D. R. Smith, J. J. Mock, and D. A. Schultz, "Single-target molecule detection with nonbleaching multicolor optical immunolabels," *Proc. Natl. Acad. Sci. USA* **97**, 996–1001 (2000).

[68] C. Sönnichsen, T. Franzl, T. Wilk, G. von Plessen, J. Feldmann, O. Wilson, and P. Mulvaney, "Drastic reduction of plasmon damping in gold nanorods," *Phys. Rev. Lett.* **88**, 077402 (2002).

[69] A. M. Funston, C. Novo, T. J. Davis, and P. Mulvaney, "Plasmon coupling of gold nanorods at short distances and in different geometries," *Nano Lett.* **9**, 1651–1658 (2009).

[70] T. Plakhotnik and V. Palm, "Interferometric signatures of single molecules," *Phys. Rev. Lett.* **87**, 183602 (2001).

[71] V. Jacobsen, P. Stoller, C. Brunner, V. Vogel, and V. Sandoghdar, "Interferometric optical detection and tracking of very small gold nanoparticles at a water-glass interface," *Opt. Express* **14**, 405–414 (2006).

[72] P. Kukura, M. Celebrano, A. Renn, and V. Sandoghdar, "Single-molecule sensitivity in optical absorption at room temperature," *J. Phys. Chem. Lett.* **1**, 3323–3327 (2010).

[73] P. V. Ruijgrok, P. Zijlstra, A. Tchebotareva, and M. Orrit, "Damping of acoustic vibrations of single gold nanoparticles," *Nano Lett.* **12**, 1063–1069 (2012).

[74] A. L. Tchebotareva, P. V. Ruijgrok, P. Zijlstra, and M. Orrit, "Probing the acoustic vibrations of single metal nanoparticles by ultrashort laser pulses," *Laser Photon. Rev.* **4**, 581–597 (2010).

[75] M. A. van Dijk, M. Lippitz, and M. Orrit, "Detection of acoustic oscillations of single gold nanoparticles by time-resolved interferometry," *Phys. Rev. Lett.* **95**, 267406 (2005).

[76] A. L. Tchebotareva, M. A. van Dijk, P. V. Ruijgrok, V. Fokkema, M. H. S. Hesselberth, M. Lippitz, and M. Orrit, "Acoustic and optical modes of single dumbbells of gold nanoparticles," *Chem. Phys. Chem.* **9,** 111–114 (2009).

[77] P. Zijlstra, A. L. Tchebotareva, J. M. W. Chon, M. Gu, and M. Orrit, "Acoustic oscillations and elastic moduli of single gold nanorods," *Nano Lett.* **8**, 3493–3497 (2008).

[78] H. Staleva and G. Hartland, "Transient absorption studies of single silver nanocubes," *J. Phys. Chem. C* **112**, 7535–7539 (2008).

[79] P. V. Ruijgrok, N. R. Verhart, P. Zijlstra, A. L. Tchebotareva, and M. Orrit, "Brownian fluctuations and heating of an optically aligned gold nanorod," *Phys. Rev. Lett.* **107**, 037401 (2011).

[80] P. V. Ruijgrok, P. Zijlstra, A. L. Tchebotareva, and M. Orrit, "Damping of acoustic vibrations of single gold nanoparticles optically trapped in water," *Nano Lett.* **12**, 1063–1069 (2012).

[81] M. Pelton, J. E. Sader, J. Burgin, M. Liu, P. Guyot-Sionnest, and D. Gosztola, "Damping of acoustic vibrations in gold nanoparticles," *Nat. Nanotechnol.* **4**, 492–495 (2009)

[82] K. Matawari, T. Kitamori, and T. Sawada, "Individual detection of single nanometer-sized particles in liquid by photothermal microscopy," *Anal. Chem.* **70**, 5037–5041 (1998).

[83] D. Boyer, P. Tamarat, A. Maali, B. Lounis, and M. Orrit, "Photothermal imaging of nanometer-sized metal particles among scatterers," *Science* **297** 1160–1163 (2002).

[84] S. Berciaud, L. Cognet, G. A. Blab, and B. Lounis, "Photothermal heterodyne imaging of individual nonfluorescent nanoclusters and nanocrystals," *Phys. Rev. Lett.* **93**, 257402 (2004).

[85] E. Absil, G. Teissier, M. Gross, M. Atlan, N. Warnasooriya, S. Suck, M. Coppey-Moisan, and D. Fournier, "Photothermal heterodyne holography of gold nanoparticles," *Opt. Express* **18**, 780–786 (2010).

[86] A. Gaiduk, M. Yorulmaz, P. V. Ruijgrok, and M. Orrit, "Room-temperature detection of a single molecule's absorption by photothermal contrast," *Science* **330,** 353–356 (2010).

[87] P. Gaiduk, P. V. Ruijgrok, M. Yorulmaz, and M. Orrit, "Detection limits in photothermal microscopy," *Chem. Sci.* **1,** 343–350 (2010).

[88] S. Chong, W. Min, and X. S. Xie, "Ground-state depletion microscopy: detection sensitivity of single-molecule optical absorption at room temperature," *J. Phys. Chem. Lett.* **1**, 3316–3322 (2010).

[89] O. Schwartz and D. Oron, "A present understanding of colloidal quantum dot blinking," *J. Chem.* **52**, 992–1001 (2012).

[90] P. Zijlstra and M. Orrit, "Single metal nanoparticles: optical detection, spectroscopy and applications," *Rep. Prog. Phys.* **74**, 106401, 55pp. (2011)

[91] D. Brinks, F. D. Stefani, F. Kulzer, R. Hildner, T. H. Taminiau, Y. Avlasevich, K. Müllen, and N. F. van Hulst, "Visualizing and controlling vibrational wave packets of single molecules," *Nature* **465**, 905-U5 (2010).

[92] E. Ringe, B. Sharma, A. I. Henry, L. D. Marks, and R. P. Van Duyne, "Single nanoparticle plasmonics," *Phys. Chem. Chem. Phys.* **15**, 4110–4129 (2013).

[93] P. G. Etchegoin and E. C. Le Ru, "A perspective on single molecule SERS: current status and future challenges," *Phys. Chem. Chem. Phys.* **10**, 6079–6089 (2008).

[94] E. M. V. Lantman, T. Deckert-Gaudig, A. J. G. Mank, V. Deckert, and B. M. Weckhuysen, "Catalytic processes monitored at the nanoscale with tip-enhanced Raman spectroscopy," *Nat. Nanotechnol.* **7**, 583–586 (2012).

[95] R. Zhang, Y. Zhang, Z. C. Dong, S. Jiang, C. Zhang, L. G. Chen, L. Zhang, Y. Liao, J. Aizpurua, Y. Luo, et al., "Chemical mapping of a single molecule by plasmon-enhanced Raman scattering," *Nature* **498**, 82–86 (2013).

[96] A. Kinkhabwala, Z. F. Yu, S. H. Fan, Y. Avlasevich, K. Mullen, and W. E. Moerner, "Large single-molecule fluorescence enhancements produced by a bowtie nanoantenna," *Nat. Photon.* **3**, 654–657 (2009).

[97] H. F. Yuan, S. Khatua, P. Zijlstra, M. Yorulmaz, and M. Orrit, "Thousand-fold enhancement of single-molecule fluorescence near a single gold nanorod," *Angew. Chem. Int. Ed.* **52**, 1217–1221 (2013).

[98] D. Punj, M. Mivelle, S. B. Moparthi, T. S. van Zanten, H. Rigneault, N. F. van Hulst, M. F. Garcia-Parajo, and J. Wenger, "A plasmonic 'antenna-in-box' platform for enhanced single-molecule analysis at micromolar concentrations," *Nat. Nanotechnol.* **8**, 512–516 (2013).

3

RESONANCE ENERGY TRANSFER

David L. Andrews,[1] David S. Bradshaw,[1]
Rayomond Dinshaw,[2] and Gregory D. Scholes[2]

[1] *School of Chemistry, University of East Anglia, Norwich Research Park, Norwich, Norfolk, UK*

[2] *Department of Chemistry, Institute for Optical Sciences and Centre for Quantum Information and Quantum Control, University of Toronto, Toronto, ON, Canada*

3.1 INTRODUCTION

The absorption of ultraviolet or visible light by an atom or molecule, resulting in its electronic excitation, is a familiar and staple photophysical process. Owing to the quantization of electronic states, the associated ultraviolet/visible absorption spectrum contains bands reflecting fixed energy gaps. It is of significant interest to ascertain the destination of the discrete energy held within an electronic excitation, and the mechanism by which the excitation arrives there. One such photodynamical process involves energy transfer from one molecule (or atom) to another. Remarkably, this "hopping" occurs over spatial dimensions that are typically much larger than the cross-section of a molecule and, in some cases, the effect is completed on a timescale in the sub-picosecond range. This chapter gives an introduction to the key aspects of this energy transfer, from its photophysics to its applications to molecular biology.

Formally, resonance energy transfer (RET) or electronic energy transfer (EET) is a photophysical process wherein excitation is transferred from an initially populated donor molecule (or chromophore) to an acceptor molecule through intermolecular interactions. It is a ubiquitous process found in numerous systems including conjugated polymers, light-harvesting proteins, and various other multichromophore systems. A common application of energy transfer—and, indeed, one deployed

---

Photonics: Scientific Foundations, Technology and Applications, Volume IV, First Edition.
Edited by David L. Andrews.
© 2015 John Wiley & Sons, Inc. Published 2015 by John Wiley & Sons, Inc.

in nature for solar energy conversion by plants—is the migration of incident light energy, captured at the periphery of a chromophore array, to a central chromophore, effectively concentrating the excitation. Traditionally, energy transfer within light-harvesting complexes is understood according to Förster RET theory, which will be introduced in the following sections. In recent years, researchers have also become interested in special circumstances where Förster theory fails to adequately describe energy transfer, since these cases are likely to inspire new applications and will certainly indicate new physical concepts.

3.2 HISTORY OF RET

3.2.1 The First Experiments

RET, the process in which the energy of an excited atom or molecule (usually called the donor, but known historically as the "sensitizer") is transferred nonradiatively to an acceptor molecule (activator), occurs through intermolecular dipole–dipole coupling. The origins of its discovery can be traced back to 1922, when the phenomenon of RET (sensitized fluorescence) was first experimentally observed by Cario and Franck [1–3] in the gas phase. Their spectroscopic experiment involved illuminating a mixture of mercury and thallium vapors at a wavelength absorbed solely by the mercury; the resulting fluorescence spectra proved to include frequencies that could only be emitted from thallium. Such energy transfer in vapors was at first assumed to be uniquely associated with interatomic collisions, but a discovery that transfer could occur at larger separations than the collision radius showed that this was not necessarily the case. Soon RET was also being observed in solutions [4], and over the following years in a rapidly increasing number of other physical systems.

3.2.2 Early Developments of Theory

The first theoretical explanation of the phenomenon was proposed by Jean Perrin [5], later a Nobel laureate. Recognizing that energy could be transferred from an excited molecule to its neighbors amongst closely spaced molecules through dipole interactions, he named this process *transfert d'activation*, and his paper on the subject became the earliest attempt to describe nonradiative (near-field) energy transfer. Despite its initial success, however, Perrin's model incorrectly predicted that nonradiative energy transfer should be possible between dye molecules up to an intermolecular distance of 1000 Å, an error deriving from an inaccurate assumption that the molecules would act as Hertzian oscillators with exactly defined resonance frequencies. Five years later [6], Perrin's son Francis developed a corresponding quantum mechanical theory of RET, based on Kallman and London's results [7]. In this work he recognized a "spreading of absorption and emission frequency" due to the interactions of the dye with the solvent, reducing the probability of energy transfer. As a result, efficient transfer was calculated to occur up to 150–250 Å, still approximately a factor of three more than had been experimentally observed. A detailed and highly readable survey of these early contributions of J. Perrin and F. Perrin can be found in a review by Berberan-Santos [8].

3.2.3 Förster Theory

Extending the ideas of J. Perrin and F. Perrin, Förster developed the first essentially correct theoretical treatment of RET [9–11]. Förster determined that energy transfer, through dipolar coupling between molecules, mostly depends on two important quantities: spectrum overlap and intermolecular distance. Following the observation that "the absorption and fluorescence spectra of similar molecules are far from completely overlapping," he found a means to quantify the spectral overlap integral. The static dipole–dipole interaction was known to have an inverse proportionality on the cube of the molecular separation. Since the rate of energy transfer is proportional to the square of such a coupling, it thus depends on the sixth power of the separation—that is, the now-famous R^{-6} distance-dependence law. Moreover, the acceptor distance at which this rate equates to that of spontaneous emission by the donor, later termed the Förster radius R_0, was calculated to lie between 10 and 100 Å, agreeing with experimental observations.

Much later, the distance dependence predicted by Förster was fully verified by fluorescence studies of donor-acceptor pairs at known separations [12, 13], leading to the suggested employment of RET as a "spectroscopic ruler" by Stryer and Haugland [13]; hence, a technique to measure the proximity relationships and conformational change in macromolecules was realized (see Section 3.4). With the introduction of the first lasers in the 1960s, the modern understanding of RET led to a raft of modern applications. An excellent in-depth review on the modern history of RET is given by Clegg [14].

3.3 THE PHOTOPHYSICS OF RET

RET is a process that is known to operate across a diverse and extensive range of physical systems, encompassing not only gases and dye solutions, but also protein complexes, doped crystals, and polymers, to name but a few. Nonetheless, at a fundamental level it is possible to identify numerous common features in the underlying photophysics.

3.3.1 Primary Excitation Processes

To approach the subject in detail, let us commence with the photoexcitation process that creates the conditions for RET to occur. When resonant ultraviolet or visible radiation impinges on any nonhomogeneous dielectric material, the primary result of photon absorption is the population of electronic excited states in individual atomic, molecular, or other nanoscale centers—henceforth, the latter are to be grouped together under the generic term "chromophore." Typically, such absorption is immediately followed by a rapid but partial degradation of the acquired energy, the associated losses (largely due to vibrational dissipation) ultimately to be manifest in the form of heat. This effect is reflected in the principle that the release of electronic energy by fluorescence generally occurs from the lowest vibrational level of

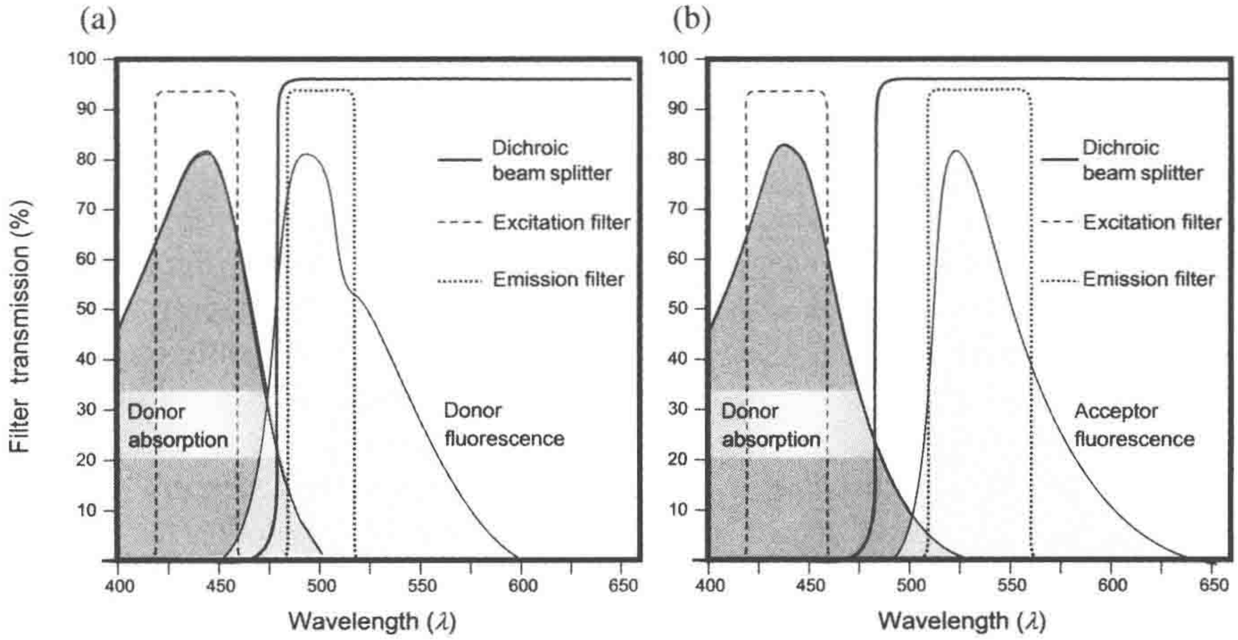

FIGURE 3.1 Typical spectral discrimination between the fluorescence from donor and acceptor species (here notionally based on a cyan fluorescent protein donor and a yellow fluorescent protein acceptor): (a) the transmission characteristics of a short-wavelength filter ensure initial excitation of only the donor; a dichroic beam splitter and another narrow emission filter ensuring that only the (Stokes-shifted) fluorescence from the donor reaches a detector; (b) in the same system a longer-wavelength emission filter ensures capture of only the acceptor fluorescence, following RET.

the excited state. However, if any nearby chromophore has a suitably disposed electronic state, of a similar or slightly lower energy, that neighbor may acquire the major part of the electronic excitation through RET—a process that takes place well before any further thermal degradation of the excited state energy occurs. The mechanism is most commonly studied through spectrometric differentiation of fluorescence emerging from the initially excited energy donor and from the energy acceptor species, as illustrated in Figure 3.1. As will be shown in the following, the propensity for energy to be transferred between any two chromophores is severely restricted by distance, and if no suitable acceptor is within reach, the donor will generally shed its energy by fluorescence or local dissipation.

3.3.2 Coupling of Electronic Transitions

In systems where RET occurs, the donors and acceptors are usually also fluorophores, that is, chromophores that have the capacity to decay by fluorescent emission. Moreover, in RET, the transitions of donor decay and acceptor excitation are generally electric dipole-allowed—although other possibilities do occasionally arise. Accordingly the theory of energy transfer, for donor–acceptor displacements beyond the region of significant wavefunction overlap, is traditionally conceived in terms of an electrodynamical coupling between transition dipoles.

Consider the pairwise transfer of excitation between two chromophores D and A. In the context of this elementary mechanism, D is designated the donor and A the acceptor. Specifically, let it be assumed that prior excitation of the donor generates an electronically excited species D*. Forward progress of the energy is then accompanied by donor decay to the ground electronic state. Acquiring the energy, A undergoes a transition from its ground to its excited state. The RET process may be expressed by the following photophysical equation:

$$\mathrm{D}^* + \mathrm{A} \rightarrow \mathrm{D} + \mathrm{A}^*. \tag{3.1}$$

The excited acceptor, A*, subsequently decays either in a further transfer event, or by another means such as fluorescence. As the D* and A* excited states are real, with measurable lifetimes, the core process of energy transfer itself is fundamentally separable from the initial electronic excitation of D and the eventual decay of A; the latter processes do not, therefore, enter into the theory of the pair transfer.

Since Förster theory explicitly relies on the electric dipole approximation, that is, energy transfer occurring through electric dipole couplings, the model breaks down in certain circumstances and becomes invalid. Consequently, problems of interpretation can arise when an electronic transition is electric dipole-forbidden, but allowed via magnetic dipole or higher-order multipoles; weak interactions may develop, to facilitate the energy transfer, that are unaccounted for by the Förster theory. This scenario often occurs for interactions between highly symmetric chromophores. In the Taylor series expansion of the Coulombic interaction between transition moments, the leading nonzero term involves electric dipole moments while the higher orders relate to magnetic dipoles, and to electric and magnetic multipoles. All of these additional terms are more strongly dependent on distance and, therefore, multipolar interactions are significant at very small donor–acceptor separations; an alternative mechanism described by Dexter theory [15] should be considered when there is donor–acceptor wavefunction overlap (*vide infra*).

3.3.3 Dissipation and Line Broadening

To delve more deeply into the nature of the RET process, it needs to be recognized that Eq. (3.1) tells only part of the story, dealing as it does with only electronic excitations. In general, other dissipative processes are also engaged. In a solid, the linewidth of optical transitions manifests the influence of local electronic environments that, in the case of strong coupling, may lead to the production of phonon side-bands. Similar effects in solutions or disordered solids represent inhomogeneous interactions with a solvent or host, while the broad bands exhibited by chromophores in complex molecular systems signify extensively overlapped vibrational levels, including those associated with skeletal modes of the superstructure. In each case, the designation of RET as a "resonance" process has not only the connotation of overall energy conservation, but also conveys the sense that energy can transfer from any level within the continuum of the donor-excited state to a corresponding level in the excited state continuum of the acceptor. The overall transfer efficiency thus involves a factor known as the spectral overlap [16], which denotes a frequency-weighted integral product of the donor emission and acceptor absorption profiles, as illustrated in Figure 3.2.

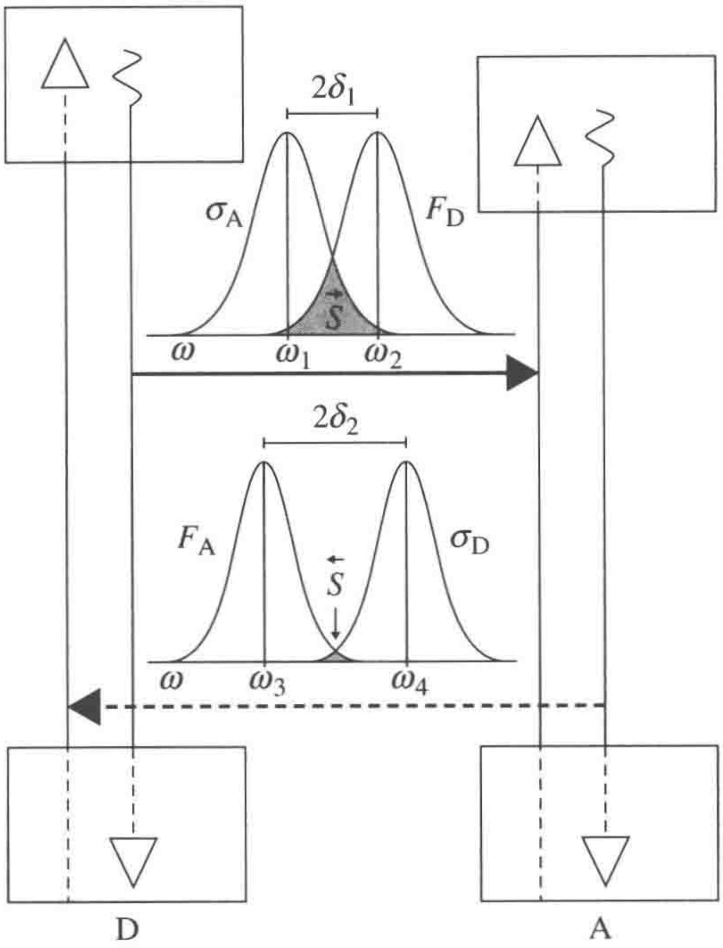

FIGURE 3.2 Energetics and spectral overlap features (top) for energy transfer from D to A (and below, potentially backward transfer from A to D). For each chromophore, F denotes the fluorescence spectrum and σ the absorption. Wavy downward lines denote vibrational dissipation.

Förster theory relies on a crucial assumption relating to the microscopic description of the dynamics, namely that the electronic coupling between donor and acceptor is very weak in comparison to line broadening. The electronic coupling acts as a small perturbation to promote energy transfer, but it is not sufficiently large to support delocalized excited states. In this weak coupling regime, vibrational equilibrium is achieved much faster than the rate at which RET occurs, and thus the electronic and vibrational states are essentially decoupled when RET takes place. When the excitation is localized on one molecule at any time and the transfer of excitation from the donor to the acceptor occurs incoherently, in an irreversible "hopping" fashion, the dynamics can be described according to conventional kinetic rate equations. Accordingly, a time-independent transfer rate can be determined from Fermi's golden rule—a quantum mechanical prescription that underpins most of molecular spectroscopy [17].

To formulate other energy transfer theories that relax this assumption is a great challenge, strongly depending on how the magnitude of the interchromophore interaction compares to the interaction of this system with the "bath"—the latter term being commonly used in this context to signify the surroundings of the donor–acceptor pair. The interchromophore interaction is characterized by direct electronic coupling, while the system-bath interaction can be characterized by a quantity called the "reorganization energy," which quantifies the extent to which the host or solvent and other environmental degrees of freedom accommodate the change of electron distribution on promotion of a molecule from its electronic ground to excited state. A fundamental breakdown of Förster theory occurs in the intermediate and strong coupling regimes. Here, the interchromophore coupling between donor and acceptor molecules can no longer be regarded as sufficiently small to promote incoherent energy transfer. In the strong coupling limit, when the coupling between the donor and acceptor molecules is large compared to the system-bath coupling, delocalized excitonic states are created; the excitation is coherently shared, being no longer localized on either the donor or acceptor [18]. The applicable description of the strong coupling regime is known as Redfield theory [19]. In Redfield theory, it is the bath that promotes energy transfer and relaxation through stochastic fluctuations.

In the intermediate coupling regime, widely applicable to multichromophore light-harvesting proteins, the electronic coupling is similar in magnitude to the system-bath coupling. Such cases, in which the understanding of energy transfer becomes far more difficult, are currently the subject of extensive studies [20].

3.3.4 Förster Equation

The Förster theory delivers an expression for the rate of pairwise energy transfer, w_{F}, for any donor–acceptor separation, R, that is substantially smaller than the wavelengths of visible radiation. For systems where the common host material for the donor and acceptor has refractive index n, at an optical frequency corresponding to the mean transferred energy, the Förster result is expressible as follows [21–23]:

$$w_{\mathrm{F}} = \frac{1}{\tau_{\mathrm{D}}^{0}} \left[\frac{R_0}{R}\right]^6, \tag{3.2}$$

where τ_{D}^{0} is the radiative decay lifetime of the donor molecule in the absence of transfer. The Förster radius R_0 (in Ångstroms)—that is, the distance at which the rates of donor deactivation by RET and by spontaneous fluorescence become equal—is defined by

$$R_0 = 0.2108\left[\kappa^2 \Phi_{\mathrm{D}}^{0} n^{-4} J\right]^{\frac{1}{6}}. \tag{3.3}$$

In this expression, Φ_{D}^{0} is the fluorescence quantum yield of the donor with transfer absent, κ is the orientation factor (*vide infra*), and J represents an integral of the product of the donor emission spectrum with the acceptor absorption spectrum (in units of $\mathrm{M}^{-1}\ \mathrm{cm}^{-1}\ \mathrm{nm}^4$); the latter denotes a spectral overlap which, as stated earlier, is a key determinant of energy transfer efficiency. It is evident from Figure 3.2, that the propensity for forward transfer is usually significantly greater than that for backward transfer, due to a sizeable difference in the spectral overlaps for the two processes. Similar to the rate, the transfer efficiency Φ_{T} is expressible as

$$\Phi_{\mathrm{T}} = \frac{1}{1+(R/R_0)^6} = 1 - \frac{\tau_{\mathrm{fl}}}{\tau_{\mathrm{D}*}} = 1 - \frac{I_{\mathrm{fl}}}{I_{\mathrm{D}*}}, \tag{3.4}$$

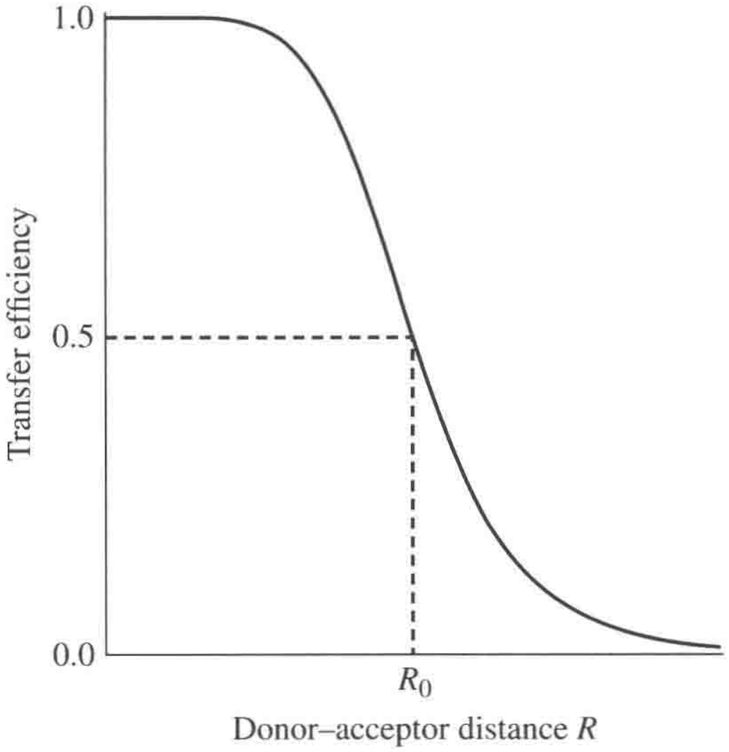

FIGURE 3.3 Distance dependence of the transfer efficiency between a pair of chromophores, calculated according to Eq. (3.4).

where I_{fl} and I_{D*} are the intensities of the donor fluorescence with the acceptor present and excluded, respectively, and τ_{fl} specifically denotes the fluorescence lifetime of the donor measured within its RET environment. As graphically depicted in Figure 3.3, a donor–acceptor displacement equal to R_0 corresponds to a transfer efficiency of 50%.

The third equality on the right of Eq. (3.4), which holds provided decay processes follow single-exponential decay kinetics, provides a formula that is cast in terms of easily measurable quantities. This is particularly useful since it allows energy transfer efficiencies to be calculated simply on the basis of intensity measurements (e.g., using a fluorimeter), obviating the separate time-resolved measurements that would otherwise be generally necessary for evaluation of the characteristic decay lifetimes τ_{fl} and τ_{D*}. When a given electronically excited chromophore is situated within a distance R_0 of a suitable acceptor, RET will generally be the dominant decay mechanism; conversely, for distances beyond R_0, spontaneous decay (usually fluorescence) will be the primary means of donor deactivation.

3.3.5 Orientation Dependence

The κ factor depends on the orientations of the donor and acceptor, both with respect to each other, and with respect to their mutual displacement unit vector $\hat{\boldsymbol{R}}$, as follows:

$$\kappa = (\hat{\boldsymbol{\mu}}_D \cdot \hat{\boldsymbol{\mu}}_A) - 3(\hat{\boldsymbol{R}} \cdot \hat{\boldsymbol{\mu}}_D)(\hat{\boldsymbol{R}} \cdot \hat{\boldsymbol{\mu}}_A). \tag{3.5}$$

For each chromophore, $\hat{\boldsymbol{\mu}}$ designates a unit vector in the direction of the appropriate transition dipole moment—a measure of charge displacement during the associated transition, which can be calculated using quantum theoretical methods [24]. The

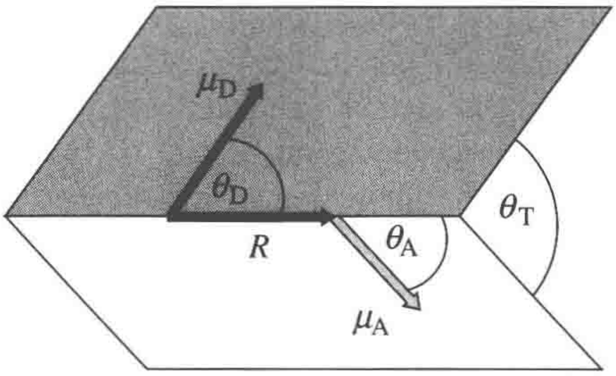

FIGURE 3.4 Relative orientations and positions of the donor and acceptor and their transition moments: angles θ_D and θ_A are subtended by donor and acceptor transition moments ($\boldsymbol{\mu}_D$ and $\boldsymbol{\mu}_A$, respectively) against the interchromophore displacement vector, **R**; the symbol θ_T is the angle between the transition moments.

possible values of κ^2, as featured in Eq. (3.3), lie in the range (0, 4). It is evident that in the case of fixed chromophore positions and orientations the result delivered by (3.5) is a function of three independent angles, as shown and defined in Figure 3.4:

$$\kappa = \cos\theta_T - 3\cos\theta_D\cos\theta_A. \tag{3.6}$$

Unfavorable orientations can thus reduce the rate of energy transfer to zero; other configurations, including many of those found in photobiological systems, optimize the transfer rate. The angular disposition of chromophores is therefore a very important facet of energy transfer. It is important to note that transfer is not *necessarily* precluded when the transition moments lie in perpendicular directions—provided that neither is also disposed orthogonally to $\boldsymbol{R}(= R\hat{\boldsymbol{R}})$.

In any at least partially fluid or disordered system, the relative orientation of all donor–acceptor pairs may not be identical, and it is then the distributional average of κ^2 that determines the overall measured response. In the isotropic case (completely uncorrelated orientations) the κ^2 factor averages to $^2/_3$; departures from this value provide a quantitative signature of the degree of orientational correlation. In molecules of sufficiently high symmetry it can also happen that either the donor or the acceptor transition moment is not unambiguously identifiable with a particular direction in the corresponding chromophore reference frame. Specifically, the electronic transition may then relate to a transition involving a degenerate state—as can occur with square planar complexes, for example [25]. Alternatively, the same observational features might indicate rapid but orientationally confined motions. The considerable complication which each of these effects brings into the trigonometric analysis of RET has been extensively researched and reported by van der Meer [26, 27].

3.3.6 Polarization Features

When linearly polarized laser light is used to excite any specific species within a complex disordered solid or liquid system, the probability for initial excitation of any particular molecule is proportional to $\cos^2\theta$, where θ is the angle between the appropriate excitation transition moment and the electric polarization vector of the input radiation. Consequently the population of excited molecules has a markedly anisotropic distribution, a phenomenon associated with the term *photoselection*. If radiative decay were to ensue instantaneously, that is, from precisely the initially populated excited level, then the fluorescence would carry the full imprint of that anisotropy and itself exhibit a degree of polarization—the highest value possible. Accounting for the necessary three-dimensional rotational average [28], it is readily shown that the fluorescence intensity components polarized parallel to and perpendicular to the polarization of the excitation beam, $I_{||}$ and $I_{\perp}$, respectively, would then lie in the ratio 3:1. Commonly observed departures from this result thus signify the extent to which the orientation of the emission dipole differs from that of the prior, initial excitation—which may be due to intervening decay, molecular motion, or intermolecular energy transfer.

The two most widely used quantitative expressions of polarization retention are the *fluorescence anisotropy*, r, or the *degree of polarization*, P. Both convey the same information; they are defined and related as follows:

$$r = \frac{I_{||} - I_{\perp}}{I_{||} + 2I_{\perp}}, \qquad P = \frac{I_{||} - I_{\perp}}{I_{||} + I_{\perp}} \qquad \Rightarrow \qquad r = \frac{2P}{3 - P}. \tag{3.7}$$

The denominator of the expression for r designates the net fluorescence intensity. In a specific situation where the donor and acceptor have transition dipole moments oriented in parallel, then $r = 0.4$ and $P = 0.5$.

A key molecular factor determining any loss in polarization is the angle θ between the directions of the absorption and emission transition dipole moments. In terms of this parameter and its influence on the measured fluorescence anisotropy, the case where internal decay intervenes between excitation and fluorescence decay within a single molecule is no different from that of a donor–acceptor pair in which the absorption and emission processes are spatially separated—provided the donor and acceptor in the latter case have a fixed mutual orientation (the orientation of the pair being random). The following result, derived by Levshin [29] and Perrin [30], can be applied in both situations:

$$P = \frac{3\cos^2\theta - 1}{3 + \cos^2\theta}. \tag{3.8}$$

In the case of a donor–acceptor pair, θ is to be interpreted as the angle θ_T shown in Figure 3.4. Equation (3.8) thus allows direct calculation of this microscopic parameter, through measurement of the macroscopic quantity P. Moreover when P proves to exhibit a time-dependent decay, a study of the kinetics provides information on the extent of rotational motion intervening between the absorption and emission events.

Very different behavior is observed for RET systems in which the donor and acceptor are orientationally uncorrelated, that is, where they are both, independently, randomly oriented. In such cases there is a very rapid loss of polarization "memory," and it transpires that the associated degree of anisotropy is precisely 1/25, that is, $r = 0.04$ [31]; two or more energy transfer jumps will therefore usually, to all intents and purposes, destroy any polarization in any ensuing fluorescence. However, it should be noted that there is a surprising recovery in the anisotropy at distances approaching the transfer wavelength. The effect is sufficiently strong to warrant attention in dilute solution studies [32].

3.3.7 Diffusion Effects

So far only RET between a donor–acceptor pair has been considered. The discussion is now extended to an ensemble of donors D and acceptors A, all units of which are distributed randomly within an m-dimensional volume. For systems in which translational diffusion is extremely slow compared to the rate of energy transfer, the time dependence of the donor intensity decay at time t, $I_{D^*}(t)$, as obtained by Förster [11], is given by the following expression:

$$I_{\mathrm{D}^*}(t) = I_{\mathrm{D}^*}(0)\exp\left[-\frac{t}{\tau_{\mathrm{D}^*}} - 2\gamma\left(\frac{t}{\tau_{\mathrm{D}^*}}\right)^{\frac{m}{6}}\right]. \tag{3.9}$$

The most commonly applied form of this expression is when the m equals 3, that is, RET in three dimensions. In Eq. (3.9), the parameter γ is explicitly written as

$$\gamma = \frac{2}{3}\pi^{\frac{3}{2}}C_{\mathrm{A}}R_0^3, \tag{3.10}$$

in which C_A is the concentration of acceptors (number per unit volume) and $(4/3)\pi R_0^3 C_{\mathrm{A}}$ represents the average number of acceptor chromophores in a sphere of radius R_0; the orientational factor is again set as $2/3$.

Cases where diffusion is comparable to the transfer rate become very complicated, and calculations by Butler and Pilling [33] have shown that large errors arise on using Förster theory for systems with diffusion coefficients in excess of 10^{-5} cm^2 s^{-1}. To address such systems, a successful approximation was developed by Gösele et al. [34]. This approach involves the insertion of a multiplier G within the second term in the exponential of Eq. (3.9). With $m = 3$, the parameter G is given by

$$G = \left(\frac{1 + 5.47x + 4.00x^2}{1 + 3.34x}\right)^{\frac{3}{4}}, \tag{3.11}$$

in which $x = D(R_0^6/\tau_{\mathrm{D}^*})^{-1/3}t^{2/3}$, where D is the mutual diffusion coefficient. In contrast to the Förster theory, the above method provides an excellent approximation—as was verified by the authors of Reference 33.

Förster theory also fails at donor–acceptor displacements similar in magnitude to chromophore dimensions for another reason. This is because transition dipole moments no longer appear point-sized, and the centers of the transition moments, from which charge displacement is measured, become difficult to define. Circumstances where this is especially apparent are extended chromophores such as carotenoid, chlorophyll, and other photosynthetic substances. An expedient solution to the problem is the transition density cube (TDC) method, which involves explicit calculations of the interactions between relevant transition densities on the donor and acceptor [35]. The key advance of transition densities over their approximation via the Taylor expansion is that exact Coulombic coupling is determined, that is, all the terms in the expansion are retained, and the wavefunction shapes of the interacting chromophores are captured. In fact the shapes of the transition densities (which are related to the wavefunctions) are vital in understanding the molecular interactions. In its original form, the TDC method uses quantum mechanical computations to obtain the transition densities between ground and excited states. These are discretized into infinitesimal volume elements, followed by a summation over all Coulombic interactions. Higher order energy transfer processes can occur via electric quadrupole–electric quadrupole interactions or second-order electric dipole–electric dipole couplings [36].

3.3.8 Long-Range Transfer

It was originally assumed that a "radiative" mechanism would correctly describe energy transfer for donor–acceptor separations over and beyond 100 Å, and some recent literature on the subject still perpetuates this over-statement. Certain sources wrongly treat Förster "radiationless" energy transfer as exact, distinct, and separable from "radiative" energy transfer—the latter signifying successive but independent processes of fluorescence emission by a donor, and capture of the ensuing photon by an acceptor.

Although that certainly is the observed character of RET over very long distances—as for example between donor and acceptor components in a dilute solution—it is now known that both "radiative" and Förster transfer are simply the long- and short-range limits of one powerful, all-pervasive mechanism. The latter, determined from quantum electrodynamical calculations, is the outcome of the unified theory of RET [37]. This not only embraces Förster and "radiative" energy transfer, but also addresses the intermediate range in which neither of these mechanisms is fully valid. An expression for the total pairwise energy transfer rate, ranging from molecular dimensions up to interstellar distances, is written as

$$w = w_{\mathrm{F}} + w_{\mathrm{I}} + w_{\mathrm{rad}}, \tag{3.12}$$

where w_{F} represents the Förster rate of Eq. (3.2), equally expressible in an alternative form as follows [38, 39]:

$$w_{\mathrm{F}} = \frac{9\kappa^2 c^4}{8\pi\tau_{\mathrm{D}}^0 n^4 R^6} \int F_{\mathrm{D}}(\omega)\sigma_{\mathrm{A}}(\omega)\frac{d\omega}{\omega^4}, \tag{3.13}$$

where $F_{\mathrm{D}}(\omega)$ denotes the normalized fluorescence spectrum of the donor, $\sigma_{\mathrm{A}}(\omega)$ represents the linear absorption cross-section of the acceptor, and ω is an optical frequency in radians per unit time. Returning to Eq. (3.12), w_{rad} is the rate of "radiative" energy transfer—explicitly given by

$$w_{\mathrm{rad}} = \frac{9\kappa'^2}{8\pi\tau_{\mathrm{D}}^0 R^2} \int F_{\mathrm{D}}(\omega)\sigma_{\mathrm{A}}(\omega)\,d\omega, \tag{3.14}$$

and w_{I} is the intermediate term that is cast as

$$w_{\mathrm{I}} = \frac{9c^2}{8\pi\tau_{\mathrm{D}}^0 n^2 R^4}(\kappa^2 - 2\kappa\kappa') \int F_{\mathrm{D}}(\omega)\sigma_{\mathrm{A}}(\omega)\frac{d\omega}{\omega^2}. \tag{3.15}$$

In both Eqs. (3.14) and (3.15), the symbol κ' denotes an orientation factor identical to (3.5) but with the factor of "3" omitted from the second term. In summary, the unified theory of RET contains not only the R^{-6} term of Förster theory and the R^{-2} term denoting the inverse-square law of "radiative" transfer, but also a previously unidentified R^{-4} intermediate term.

3.3.9 Dexter Transfer

Before concluding this section, it is worth observing that other forms of donor–acceptor coupling are also possible, although considerably less relevant to the systems of interest in the following account of applications. For example, the transfer of energy between atomic components with significantly overlapped wavefunctions is usually described in terms of Dexter theory [40]—where the coupling involves electron exchange and is associated with an exponential decay with distance, directly reflecting the radial form of overlapping wavefunctions and electron distributions. Unlike Förster transfer, singlet–triplet energy exchange ($^3\mathrm{D}^* + {}^1\mathrm{A} \rightarrow {}^1\mathrm{D} + {}^3\mathrm{A}^*$) may also be allowed by the Dexter mechanism. This is because Dexter transfer, which is not simply expressible in terms of transition moments, is not precluded by the dipole-forbidden character of the transitions $T_1 \rightarrow S_0$ and $S_0 \rightarrow T_1$ within chromophores D and A, respectively. The Dexter mechanism requires only the conservation of total spin. Compared to materials in which the donor and acceptor orbitals do not spatially overlap, such systems are of less use for either device or analytical applications. The Dexter mechanism is generally operational only at very short distances (<10 Å), and other terms dominate the electronic coupling in cases of orbital overlap. The reader is referred to References 15 and 41 for relevant discussions.

3.4 INVESTIGATIVE APPLICATIONS OF RET IN MOLECULAR BIOLOGY

Without doubt, the field in which measurements of RET have had the greatest impact is molecular biology. The importance of RET to this subject, especially in application to biological macromolecules, was first realized following the construction of spectroscopic equipment for routine fluorescence measurements [42–45]. Toward the turn of the twenty-first century, RET underwent a period of significant redevelopment as a spectroscopic technique [46]. This resurgence arose mainly due to the advent of new experimentation methods, for example, single-pair RET [47], and further advances in instrumentation. The key advantage of RET techniques over others is that fluorescence measurements are highly sensitive, being made against a zero background; moreover, the UV/visible signals are relatively easy to detect and are specific and the required instrumentation is noninvasive.

3.4.1 Spectroscopic Ruler

A major use of RET, based on its strong distance dependence, exploits its capacity to supply accurate spatial information about molecular structures. This derives from a quantitative assessment of the interchromophore separations, based on comparisons between the corresponding RET efficiencies [48–51]. Such a technique is popularly known as a "spectroscopic ruler." The elucidations of molecular structure by such means usually lack information on the relative *orientations* of the groups involved, and as an expedient the calculations usually ignore the kappa parameter (3.5). The apparent crudeness of this approach becomes more defensible on realizing that, even if it were to introduce a factor of two inaccuracy, the deduced group spacing would still be in error by only 12% (since $2^{1/6} = 1.12$). Refinements to the theory to accommodate the effect of fluctuations in position or orientation of the participant groups introduce considerable complexity, although progress is being made in several areas [52–56].

3.4.2 Conformational Change

Through identification of motions in macromolecules, that is, the variation in proximity of one chromophore with respect to another, a number of valuable RET applications arise, including the detection of conformational changes and folding in proteins [49, 57–59], and the inspection of intracellular protein–protein [24, 60–63] and protein–DNA [64, 65] interactions (see, e.g., Figure 3.5). These and other such processes can be registered by selectively exciting one chromophore using laser light and monitoring either the decrease in fluorescence from that chromophore, or the rise in the generally longer-wavelength fluorescence from the other chromophore as it adopts the role of acceptor. The judicious use of optical dichroic filters can make this RET technique perfectly straightforward—see Figure 3.1. In cases where the two material components of interest lack suitably overlapped absorption and fluorescence

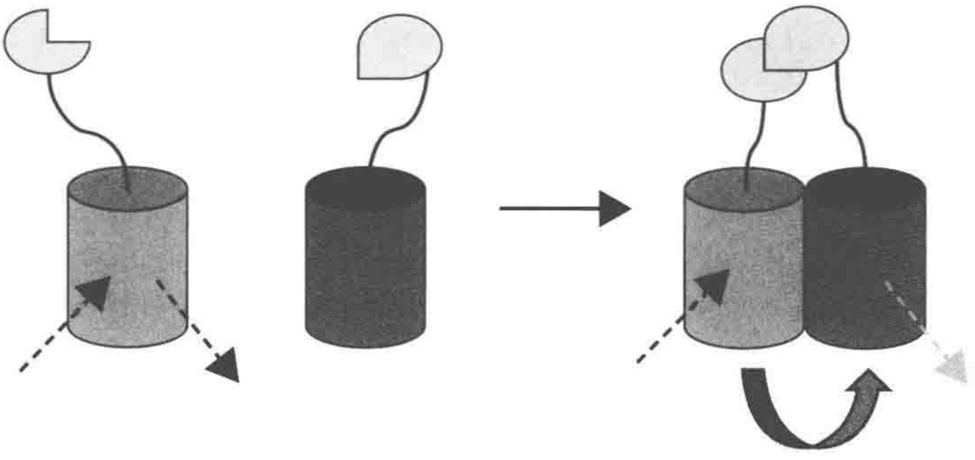

FIGURE 3.5 RET method for the detection of protein–protein interactions. Biochemical interactions between the proteins result in the attached chromophores becoming closer in proximity—thus allowing energy transfer to occur between them. As a consequence, the emission frequency will differ to those cases where energy transfer is absent.

features in an optically accessible wavelength range, molecular tagging with site-specific "extrinsic" (i.e., artificially attached) chromophores can solve the problem. Located at a molecular site of interest, and being selected on the basis of a significant spectral overlap with the counterpart component, such tags can act either in the capacity of donor or acceptor. Lanthanide ions, with their characteristically prominent and line-like absorption features, prove particularly valuable in this connection [66]. Also useful in this respect are the semiconductor nanocrystals known as quantum dots. These crystalline nanoparticles offer several unique traits, including size- and composition-tunable emission from visible to infrared wavelengths, the possibility of a single light source simultaneously exciting different-sized dots, large absorption coefficients across a wide spectral range, and very high level of photostability [67,68].

3.4.3 Intensity-Based Imaging

In the last two decades, there has been burgeoning interest in microscopy based on RET [69–75], typical instrumentation for which is illustrated in Figure 3.6. There are three specific types of RET method routinely used in the production of biological images. The principles of sensitized-emission RET have already been described (Fig. 3.1). For microscopy purposes this method is fairly inaccurate; no RET donor–acceptor pair is ideal, that is, there will almost always be some overlap between the donor and acceptor absorption bands, and also the donor and acceptor emission

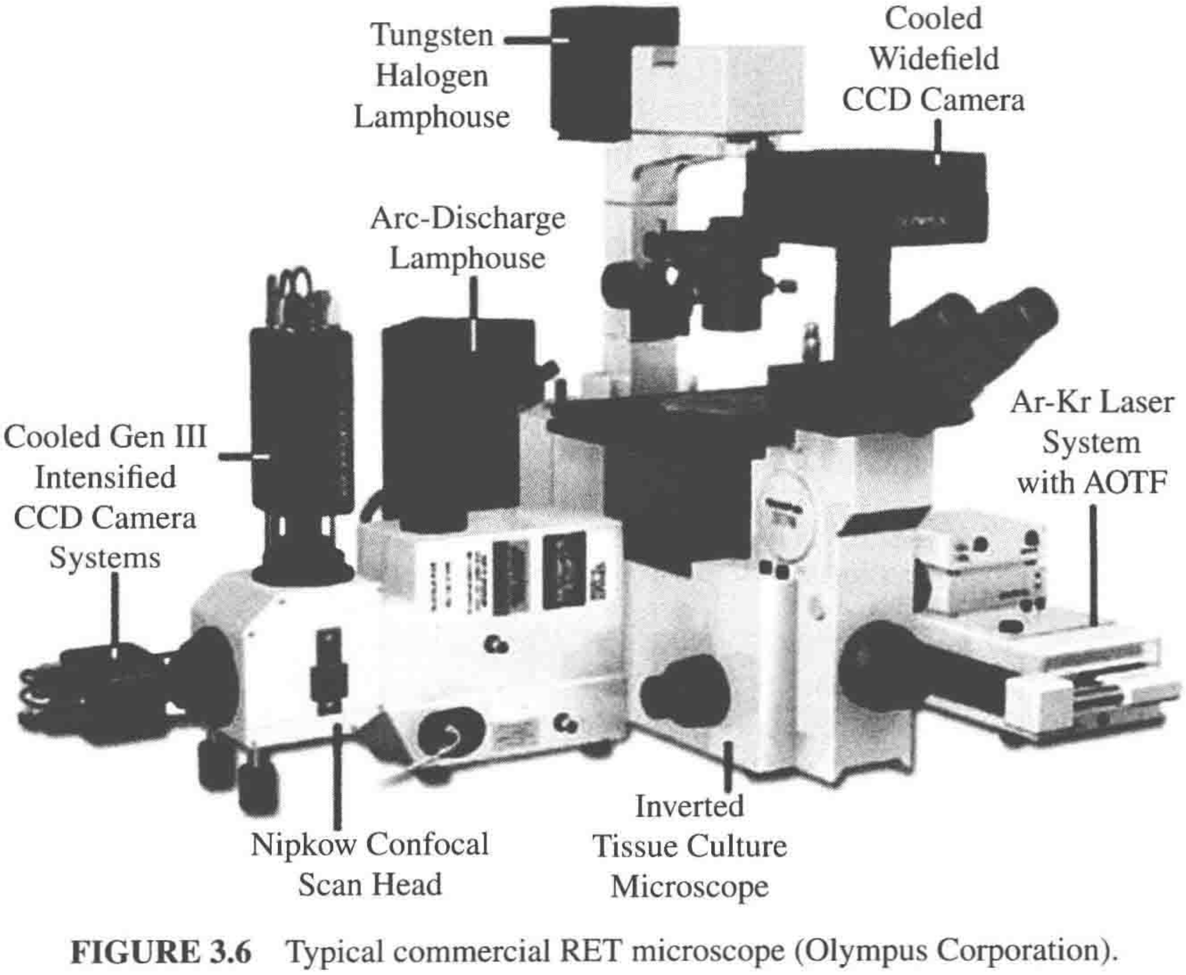
Tungsten Halogen Lamphouse
Cooled Widefield CCD Camera
Arc-Discharge Lamphouse
Ar-Kr Laser System with AOTF
Cooled Gen III Intensified CCD Camera Systems
Inverted Tissue Culture Microscope
Nipkow Confocal Scan Head

FIGURE 3.6 Typical commercial RET microscope (Olympus Corporation).

spectra. Therefore, filters that completely separate these kinds of spectrum are difficult to design. Various calculational algorithms [76–78] have been proposed to compensate for this problem, although the methods are complex and no single procedure has received universal acceptance.

A widely used alternative, experimental approach [79, 80] involves deliberately photobleaching the acceptor, the result of which is complete exclusion of RET. In this method, the donor emission is analyzed before and after the acceptor is bleached by the input of an intense laser beam (at a suitable wavelength). The difference between the donor intensities, with and without the laser input, enables a determination of the transfer efficiency by employing Eq. (3.4). Here, account is taken of spectral bleed-through between the two absorption bands, and equally between the two emission bands. Signal contamination is still not entirely eliminated, due to a small amount of back-transfer through donor excitation by acceptor emission. Often the main disadvantage in prolonged illumination of the acceptor is the possibility of damage to the sample. Therefore, in practice, photobleaching is seldom appropriate for *in vivo* studies.

3.4.4 Lifetime-Based Imaging

Fluorescence need not be characterized from excitation and emission spectra alone; highly significant information can also be secured from lifetime measurements. Thus, when suitable time-resolved instrumentation is available, the determination of decay kinetics (usually on the nanosecond timescale) enables analysis through RET-based fluorescence lifetime imaging microscopy (FRET-FLIM) [81–84]. In this method, spectral bleed-through is no longer an issue since measurements are made only for the determination of donor lifetimes; back-transfer is usually extremely low and within the noise level. The presence of the acceptor within the local environment of the donor influences the fluorescence lifetime of the donor. By measuring the donor lifetime in the presence and absence of the acceptor one can accurately calculate the transfer efficiency by the use of Eq. (3.4). Drawbacks to FRET-FLIM are the technical challenges the technique presents, and the expense of the equipment. Nonetheless, in optical systems that are equipped to provide both intensity and lifetime measurements, a comparison of the two types of image affords a particularly rich source of information, as illustrated by the cancerous cell images of Figure 3.7.

3.4.5 Other Applications

Beyond the realm of molecular biology, RET has value in a number of more specifically chemical applications. In connection with quantum dots of variable size, the viable operation of a biomimetic scheme known as a “nanofountain” (Fig. 3.8) has been proven experimentally by Ohtsu’s group [85]. Other prominent examples are found in the fields of synthetic macromolecules and chemical sensors. In polymer science, building on the pioneering principles of Morawetz [86], RET is now used to determine morphological information on polymer interfaces. Such studies have, for instance, enabled the quantitative characterization of interfacial thickness in polymers

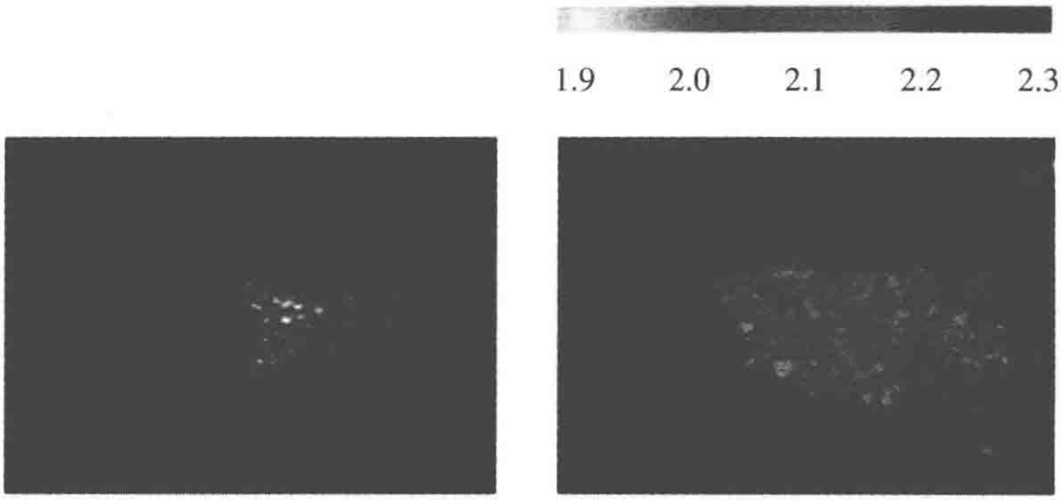

(a) (b)

FIGURE 3.7 MDA-MB-231 cancerous cell images recorded with argon laser two-photon excitation, RET microscope based on (a) intensity and (b) fluorescence lifetime (ns). In the latter, areas of locally reduced lifetime signify clustered intracellular vesicles. Adapted from Reference 84.

of various structures [87]. Moreover, RET has been utilized in the study of polymer conformational dynamics. One especially interesting application is the effective differentiation between various collapsed and/or ordered homopolymer chain conformations through the associated distribution of transfer efficiencies [88, 89].

The fabrication of RET-based, analyte-specific sensors has enabled detection of a variety of species, including dimers of functionalized calixarenes in organic solutions [90], copper(II) in aqueous solution [91], hydrogen peroxide [92], phosgene [93], and many others. These chemical sensors usually work on the principle of a donor–acceptor system designed such that the presence of the analyte causes the acceptor chromophore to move within closer proximity to a donor, enabling an RET process that is not observed in the absence of the analyte. Therefore, on irradiation of the system with the relevant chemical present, a strong emission from the acceptor signals the presence of the analyte.

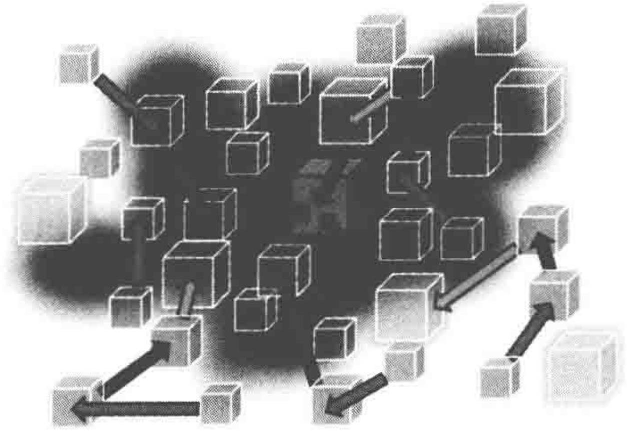

FIGURE 3.8 Scheme for an optical nanofountain composed of 2–10 nm CuCl quantum dots, distributed in an NaCl matrix. (*For a color version of this figure, see the color plate section.*)

3.5 THE ROLE OF RET IN LIGHT-HARVESTING COMPLEXES

3.5.1 Introduction

Light-harvesting proteins play the functional role of capturing solar radiation and transferring the resulting excitation to the reaction centers where they are used to carry out photosynthetic chemical reactions [94]. In high-order plants and many algae, the major light-harvesting protein is Light-Harvesting Complex II (LHC-II) which contains the green pigment chlorophyll. In addition to chlorophyll-containing complexes, some plants, algae, and bacteria utilize other light-harvesting antennae including phycobilisomes and phycobiliproteins to supplement the absorption of sunlight. These peripheral light-harvesting proteins transfer photoexcitation to chlorophyll-*a* molecules located in the membrane, which subsequently pass the excitation on to photosystem I (PSI) and photosystem II (PSII). At the center of the PSII complex resides the reaction center, the site of water oxidation catalyzed by a Mn_4O_xCa complex. The oxidation of water by PSII, along with processes carried out by other protein complexes including PSI, mobile electron carriers, and the cytochrome bf complex, complete the photosynthetic cycle. These other processes include the release of molecular oxygen, the reduction of nicotinamide–adenine dinucleotide phosphate (NADP+) and adenosine diphosphate (ADP), as well as the generation of a proton gradient across the membrane.

Photosynthesis starts with the absorption of light by a chromophore, such as chlorophyll, in a light-harvesting protein, resulting in an electronic transition from the ground state to an excited state. The excited state is short-lived, relaxing to the ground state after a mere nanosecond, so that the first events of photosynthesis involving the transport of this electronic excitation to reaction centers must be ultrafast [95]. The requirement of ultrafast energy migration beyond a nearest neighbor means that these systems are often highly optimized multi-chromophore complexes. The optimization lies in the structure of the light-harvesting complexes that bind the chromophores. Figure 3.9 shows absorption spectra recorded for several such complexes, illustrating their broad spectral cross-sections, often specialized in a particular wavelength range. Figure 3.10 shows structural models elucidated from X-ray crystallography for two light-harvesting complexes. The extraordinary density of chromophores is notable, particularly in LHC-II, the major light-harvesting complex of higher plants and green algae.

Photosynthetic organisms achieve numerous advantages by employing different complexes to harvest sunlight and to drive chemical reactions [95]: (a) Light-harvesting proteins are able to increase the spatial and spectral cross-section for the absorption of sunlight without being costly to the organism, in many photosynthetic species the reaction center may be serviced by tens of light-harvesting proteins; (b) the wide variety of these complexes allows individual species the ability to survive in varying light conditions; (c) light-harvesting antennae have evolved photoprotection responses, such as down-regulation, to avoid damage in the case of excessive exposure to sunlight.

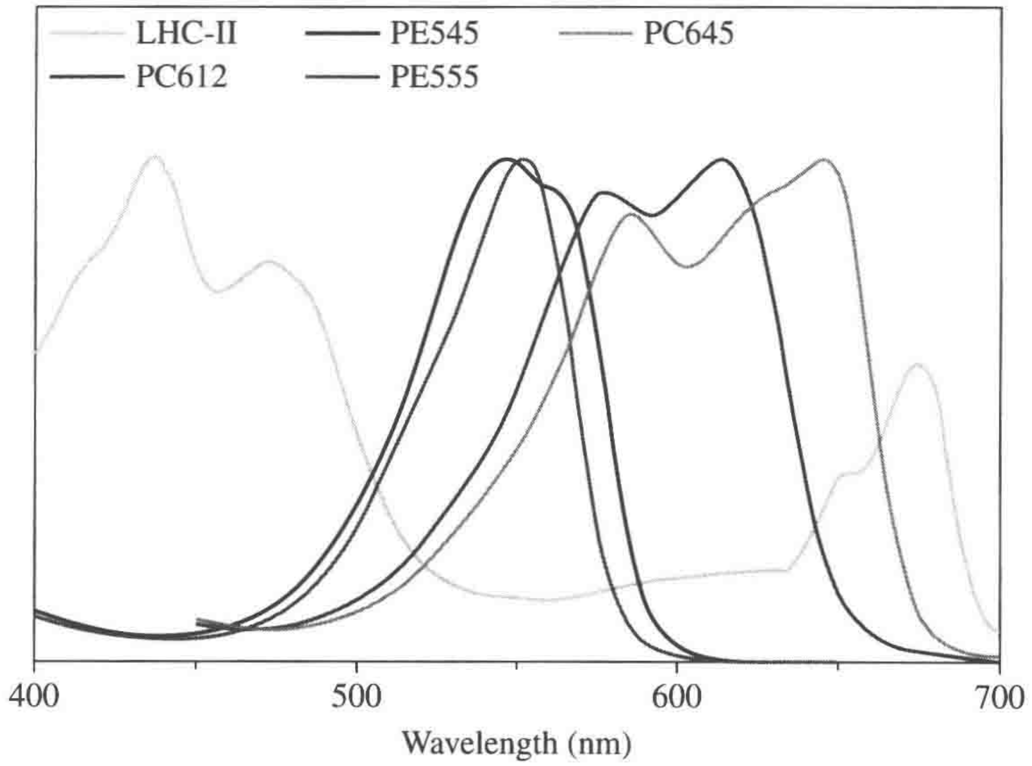

FIGURE 3.9 Normalized absorption spectrum of LHC-II (green); the main light-harvesting protein in high order plants along with the normalized absorption spectra of four cryptophyte light-harvesting proteins: PE545 (blue), PE555 (pink), PC612 (purple), and PC645 (red). The different region in which these complexes absorb is clearly evident. (*For a color version of this figure, see the color plate section.*)

3.5.2 Photosynthetic Excitons

Within a light-harvesting complex, strong electronic interactions between chromophores can result in new delocalized excited states. Although not always present, these delocalized excited states known as excitons can extend over multiple chromophores and can have a profound impact on the electronic structure and energy

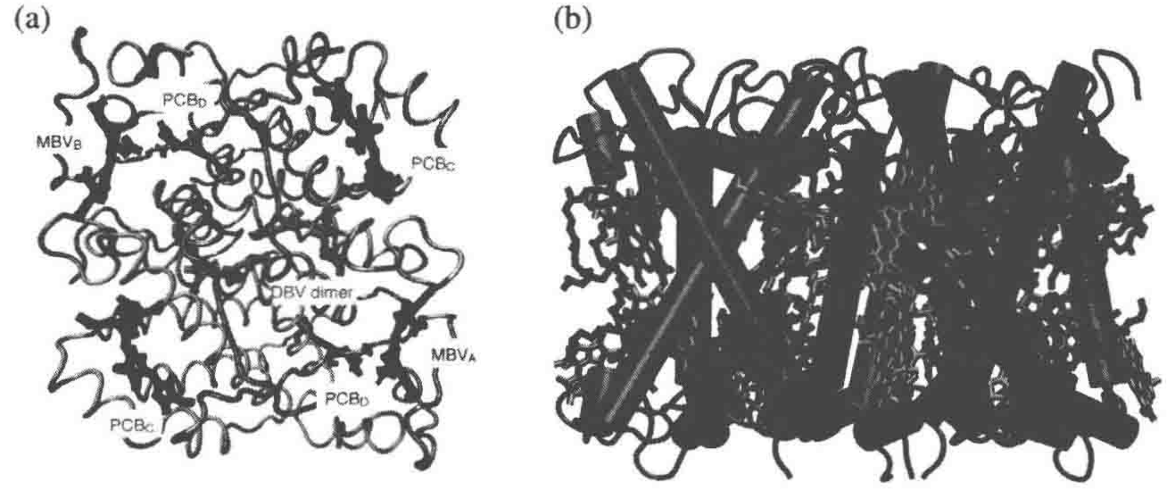

FIGURE 3.10 Structural models of two photosynthetic light harvesting complexes: (a) a cryptophyte PC645 antenna complex, and, (b) the major chlorophyll-*a/b* complex from higher plants and green algae, LHCII. (*For a color version of this figure, see the color plate section.*)

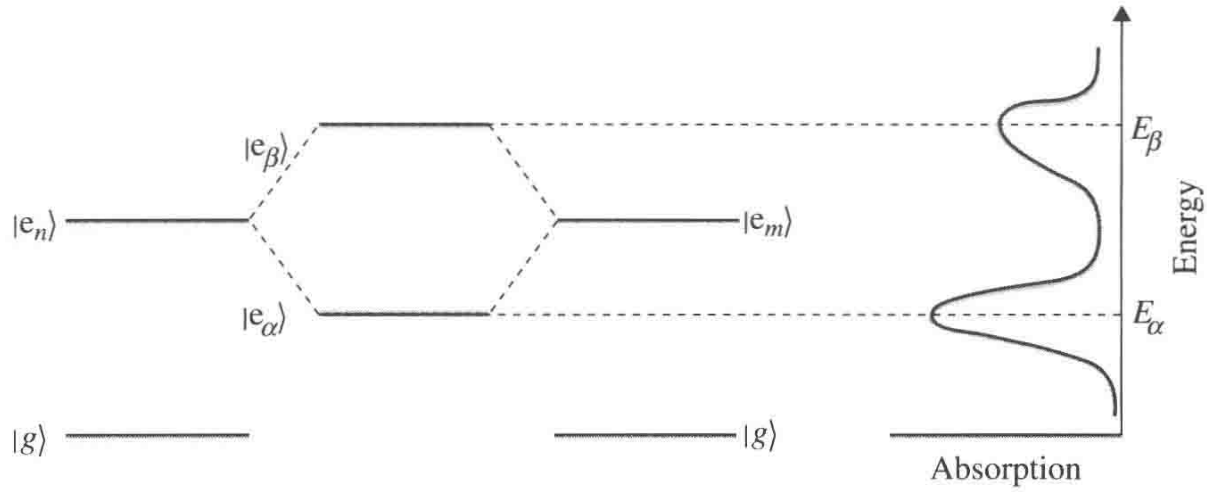

FIGURE 3.11 Illustration of the electronic energy spacing of a homodimer, which consists of two identical chromophores, each modeled as a two-level system. Molecular excited states e_n and e_m are coupled by an electronic potential, V_{nm}, resulting in delocalized excited states e_α and e_β. Absorption frequencies of the dimer occur at the corresponding energies E_α and E_β.

transfer dynamics within a light-harvesting protein. The Frenkel or molecular exciton model describes delocalized excited states in biological systems and molecular aggregates arising from the superposition of localized molecular excited states [18]. In other words, several molecules can cooperatively (in phase) absorb light and share the excitation quantum mechanically.

Delocalization of the excited state results in an increase in the spatial extent of the excited state, changing the nature of the chromophore (Fig. 3.11). The LH2 complex, isolated from purple bacteria, one of the most widely studied light-harvesting complexes, provides a clear example of how excitons can substantially change the electronic structure of a protein as well as the energy transfer dynamics [96-98]. The LH2 complex only contains one type of chromophore, bacteriochlorophyll-*a* molecules; 27 of these molecules are arranged into two rings. In one ring, there are 18 closely packed B850 bacteriochlorophyll-*a* molecules; due to their close proximity to each other along with their preferential orientations the coupling between these chromophores is strong, with nearest neighbor coupling being approximately 300 cm^{-1}. In the B800 ring, there are nine loosely packed bacteriochlorophyll-*a* molecules where adjacent molecules have a 30 cm^{-1} electronic coupling. Photon absorption in the B800 ring occurs at 800 nm, corresponding to electronically isolated chlorophyll-*a* molecules, while the B850 ring is red-shifted to 850 nm (Fig. 3.12). This shift is in part a response to interactions between the chromophores and the protein; however, a significant contribution is due to the strong excitonic coupling of molecules. In addition to changing the electronic landscape of the system, excitons in LH2 also change the energy transfer dynamics by setting up a gradient which allows excitation to flow "downhill" from the high energy B800 ring to the lower energy B850 ring.

Förster theory for molecules cannot capture the consequences of delocalized excitation, and therefore, the unexpectedly rapid timescale for energy transfer in several light harvesting complexes were a mystery for many years. Eventually it was realized

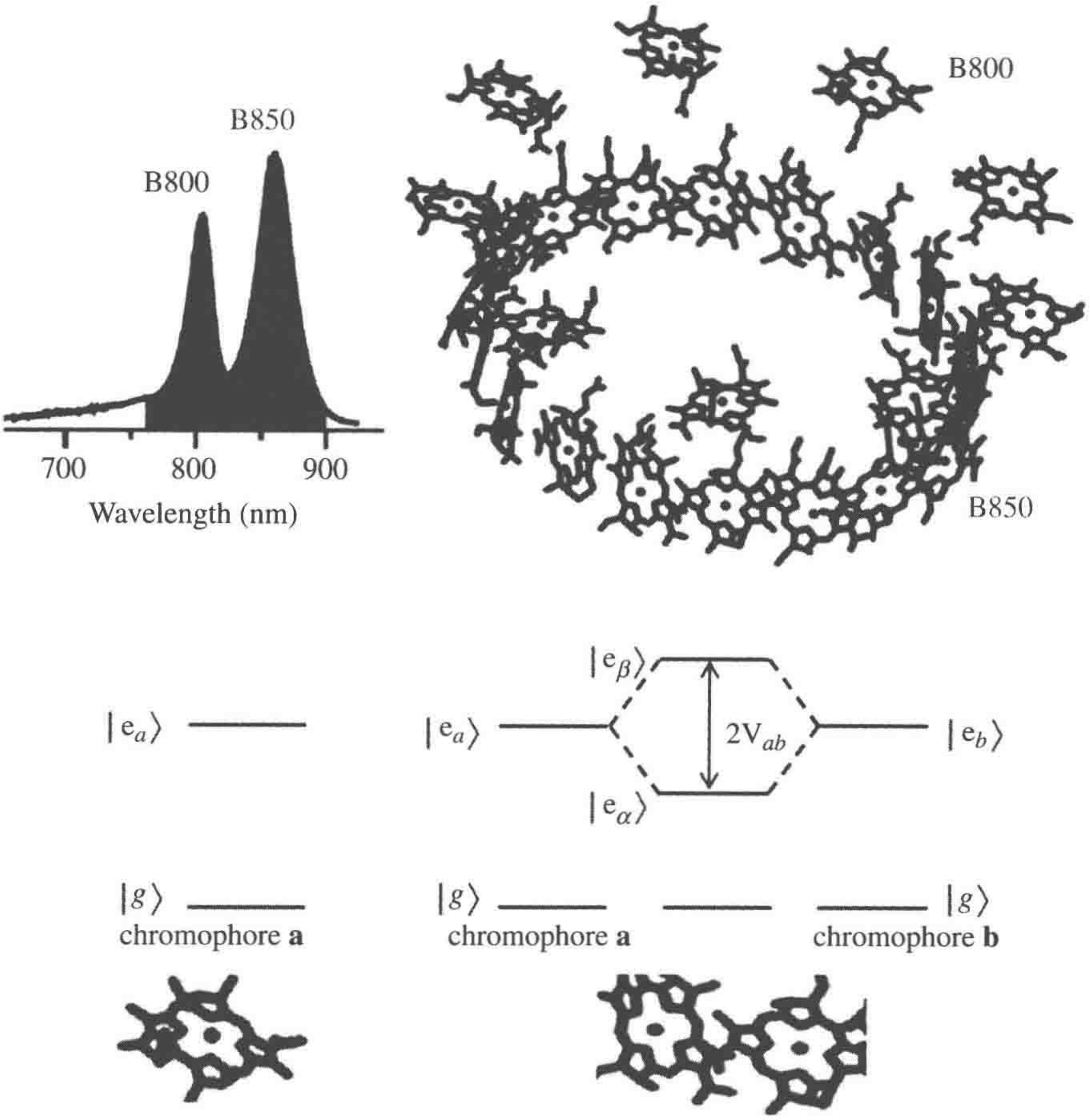
B850
B800
700
800
900
Wavelength (nm)
B800
B850
$|e_a\rangle$
$|g\rangle$
chromophore **a**
$|e_\beta\rangle$
$|e_a\rangle$
$2V_{ab}$
$|e_b\rangle$
$|e_\alpha\rangle$
$|g\rangle$
$|g\rangle$
chromophore **a**
chromophore **b**

FIGURE 3.12 (a) Absorption spectrum of LH2 extracted from a strain of the purple bacterium *Rhodopseudomonas acidophila*. The B800 ring absorbs at 800 nm and is due to the nine weakly coupled BChl chromophores, while the B850 ring absorbs at 850 nm and is due to the 18 tightly packed BChl molecules. (b) X-ray crystallography structure of LH2 from *Rps. acidophila* (strain 10050) illustrating 27 bacteriochlorophyll-*a* chromophores. Blue-colored chromophores indicate the B800 ring, while red-colored chromophores indicate the B850 ring. Energy-level diagrams for chromophores in the (c) B800 ring and (d) B850 ring. Adapted from References 101 and 102. (*For a color version of this figure, see the color plate section.*)

that donors and acceptors needed to be redefined in order to formulate an appropriate theory, called Generalized Förster Theory (GFT) [99, 100] that could quantitatively predict energy transfer in excitonic systems. The idea is to partition the system into both strongly coupled chromophores and weakly coupled chromophores, then choose effective donor and acceptor electronic states. GFT is applicable when multiple chromophores, which are strongly coupled, act together as a donor and are weakly coupled to another group of strongly coupled acceptors.

ACKNOWLEDGMENTS

Research at the University of East Anglia is supported by the Leverhulme Trust and EPSRC. The work at the University of Toronto is supported by the Natural Sciences and Engineering Research Council of Canada and the US Air Force Office of Scientific Research (FA9550-10-1-0260).

REFERENCES

[1] J. Franck, "Einige aus der Theorie von Klein und Rosseland zu ziehende Folgerungen über Fluorscence, photochemische Prozesse und die Electronenemission glühender Körper," *Z. Phys.* **9**, 259–266 (1922).

[2] G. Cario, "Über Entstehung wahrer Lichtabsorption un scheinbare Koppelung von Quantensprüngen," *Z. Phys.* **10**, 185–199 (1922).

[3] G. Cario and J. Franck, "Über Zerlegugen von Wasserstoffmolekülen durch angeregte Quecksilberatome," *Z. Phys.* **11**, 161–166 (1922).

[4] E. Gaviola and P. Pringsheim, "Über den einfluß der konzentration auf die polarisation der fluoreszenz von farbstofflösungen," *Z. Phys.* **24**, 24–36 (1924).

[5] J. Perrin, "Fluorescence et induction moléculaire par résonance," *C. R. Acad. Sci.* **184**, 1097–1100 (1927).

[6] F. Perrin, "Théorie quantique des transferts d'activation entre molecules de même espéce. Cas des solutions fluorescents," *Ann. Phys.* **17**, 283–314 (1932).

[7] H. Kallman and F. London, "Über quantenmechanische Energieübertragung zwischen atomaren Systemen" *Z. Phys. Chem. B* **2**, 207–243 (1928).

[8] M. N. Berberan-Santos, "Pioneering contributions of Jean and Francis Perrin to molecular luminescence," in *New Trends in Fluorescence Spectroscopy. Applications to Chemical and Life Sciences*, edited by B. Valeur and J.-C. Brochon (Springer, Berlin, 2001), Chap. 2.

[9] T. Förster, "Energiewanderung und fluoreszenz," *Naturwissenschaften* **33**, 166–175 (1946).

[10] T. Förster, "Zwischenmolekulare Energiewanderung und Fluoreszenz," *Ann. Phys.* **2**, 55–75 (1948).

[11] T. Förster, "10th Spiers Memorial Lecture. Transfer mechanisms of electronic excitation," *Discuss. Faraday Soc.* **27**, 7–17 (1959).

[12] S. A. Latt, H. T. Cheung, and E. R. Blout, "Energy transfer: a system with relatively fixed donor-acceptor separation," *J. Am. Chem. Soc.* **87**, 995–1003 (1965).

[13] L. Stryer and R. P. Haugland, "Energy transfer: a spectroscopic ruler," *Proc. Natl. Acad. Sci.* **58**, 719–726 (1967).

[14] R. M. Clegg, "The history of FRET: from conception through the labors of birth," in *Reviews in Fluorescence*, edited by C. D. Geddes and J. R. Lakowicz (Springer, New York, 2006), Vol. 3, Chap. 1.

[15] G. D. Scholes, "Long-range resonance energy transfer in molecular systems," *Annu. Rev. Phys. Chem.* **54**, 57–87 (2003).

[16] D. L. Andrews and J. Rodríguez, "Resonance energy transfer: spectral overlap, efficiency and direction," *J. Chem. Phys.* **127**, 084509 (2007).

[17] L. Mandel and E. Wolf, *Optical Coherence and Quantum Optics* (University Press, Cambridge, 1995), p. 871.

[18] G. D. Scholes and G. Rumbles, "Excitons in nanoscale systems," *Nat. Mater.* **5**, 683–696 (2006).

[19] V. May and O. Kühn, *Charge and Energy Transfer Dynamics in Molecular Systems* (Wiley-VCH, Weinheim, 2004).

[20] A. Ishizaki, T. R. Calhoun, G. S. Schlau-Cohen, and G. R. Fleming, "Quantum coherence and its interplay with protein environments in photosynthetic electronic energy transfer," *Phys. Chem. Chem. Phys.* **12**, 7319–7337 (2010).

[21] J. R. Lakowicz, *Principles of Fluorescence Spectroscopy*, 2nd ed. (Kluwer Academic, New York, 1999), Chap. 10.

[22] B. Valeur, *Molecular Fluorescence: Principles and Applications* (Wiley-VCH, Weinheim, 2002), Chap. 9.

[23] S. E. Braslavsky, E. Fron, H. B. Rodríguez, E. San Román, G. D. Scholes, G. Schweitzer, B. Valeur, and J. Wirz, "Pitfalls and limitations in the practical use of Förster's theory of resonance energy transfer," *Photochem. Photobiol. Sci.* **7**, 1444–1448 (2008).

[24] T. Ansbacher, H. K. Srivastava, T. Stein, R. Baer, M. Merkx, and A. Shurki, "Calculation of transition dipole moment in fluorescent proteins—towards efficient energy transfer," *Phys. Chem. Chem. Phys.* **14**, 4109–4117 (2012).

[25] C. Galli, K. Wynne, S. M. Lecours, M. J. Therien, and R. M. Hochstrasser, "Direct measurement of electronic dephasing using anisotropy," *Chem. Phys. Lett.* **206**, 493–499 (1993).

[26] B. W. van der Meer, G. Coker, and S.-Y. Chen, *Resonance Energy Transfer Theory and Data* (VCH, New York, 1994).

[27] B. W. van der Meer, *Resonance Energy Transfer*, edited by D. L. Andrews and A. A. Demidov (Wiley, New York 1999), pp. 151–172.

[28] D. L. Andrews and T. Thirunamachandran, "On three-dimensional rotational averages," *J. Chem. Phys.* **67**, 5026–5033 (1977).

[29] W. L. Levshin, "Polarisierte Fluoreszenz und Phosphoreszenz der Farbstofflosungen. IV," *Z. Phys.* **32**, 307–326 (1925).

[30] F. Perrin, "La fluorescence des solutions," *Ann. Phys.* **12**, 169–275 (1929).

[31] V. M. Agranovich and M. D. Galanin, *Electronic Excitation Energy Transfer in Condensed Matter* (Elsevier/North-Holland, Amsterdam, The Netherlands, 1982).

[32] D. L. Andrews and G. Juzeliunas, "The range dependence of fluorescence anisotropy in molecular energy transfer," *J. Chem. Phys.* **95**, 5513–5518 (1991).

[33] P. R. Butler and M. J. Pilling, "The breakdown of Förster kinetics in low viscosity liquids. An approximate analytical form for the time-dependent rate constant," *Chem. Phys.* **41**, 239–243 (1979).

[34] U. Gösele, M. Hauser, U. K. A. Klein, and R. Frey, "Diffusion and long-range energy transfer," *Chem. Phys. Lett.* **34**, 519–522 (1975).

[35] B. P. Krueger, G. D. Scholes, and G. R. Fleming, "Calculation of couplings and energy transfer pathways between the pigments of LH2 by the ab initio transition density cube method," *J. Phys. Chem. B* **102**, 5378–5386 (1998).

[36] D. L. Andrews and J. M. Leeder, "Resonance energy transfer: when a dipole fails," *J. Chem. Phys.* **130**, 184504 (2009).

[37] D. L. Andrews, "A unified theory of radiative and radiationless molecular-energy transfer," *Chem. Phys.* **135**, 195–201 (1989).

[38] A. A. Demidov and D. L. Andrews, in *Encyclopedia of Chemical Physics and Physical Chemistry*, edited by J. H. Moore and N. D. Spencer (Institute of Physics, Bristol, 2001), Vol. 3, pp. 2701—2715.

[39] D. L. Andrews, "Mechanistic principles and applications of resonance energy transfer," *Canad. J. Chem.* **86**, 855–870 (2008).

[40] D. L. Dexter, "A theory of sensitized luminescence in solids," *J. Chem. Phys.* **21**, 836–850 (1953).

[41] D. L. Andrews, C. Curutchet, and G. D. Scholes, "Resonance energy transfer: beyond the limits," *Laser Photon. Rev.* **5**, 114–123 (2011).

[42] I. Z. Steinberg, "Long-range nonradiative transfer of electronic excitation energy in proteins and polypeptides," *Annu. Rev. Biochem.* **40**, 83–114 (1971).

[43] L. Stryer, "Fluorescence energy transfer as a spectroscopic ruler," *Ann. Rev. Biochem.* **47**, 819–846 (1978).

[44] C. G. dos Remedios, M. Miki, and J. A. Barden, "Fluorescence resonance energy transfer measurements of distances in actin and myosin. A critical evaluation," *J. Muscle Res. Cell Motil.* **8**, 97–117 (1987).

[45] P. Wu and L. Brand, "Resonance energy transfer: methods and applications," *Anal. Biochem.* **218**, 1–13 (1994).

[46] P. R. Selvin, "The renaissance of fluorescence resonance energy transfer," *Nat. Struct. Biol.* **7**, 730–734 (2000).

[47] T. Ha, T. Enderle, D. F. Ogletree, D. S. Chemla, P. R. Selvin, and S. Weiss, "Probing the interaction between two single molecules: fluorescence resonance energy transfer between a single donor and a single acceptor," *Proc. Natl. Acad. Sci. USA* **93**, 6264–6268 (1996).

[48] S. Hohng, C. Joo, and T. Ha, "Single-molecule three-color FRET," *Biophys. J.* **87**, 1328–1337 (2004).

[49] B. Schuler, "Single-molecule fluorescence spectroscopy of protein folding," *Chem. Phys. Chem.* **6**, 1206–1220 (2005).

[50] S. V. Koushik, H, Chen, C. Thaler, H. L. Puhl III, and S. S. Vogel, "Cerulean, venus and venus$_{Y67C}$ FRET reference standards," *Biophys. J.* **91**, L99–L101 (2006).

[51] H. Sahoo, "Förster resonance energy transfer–a spectroscopic nanoruler: principle and applications," *J. Photochem. Photobiol. C* **12**, 20–30 (2011).

[52] C. G. dos Remedios and P. D. J. Moens, "Fluorescence resonance energy transfer spectroscopy is a reliable 'ruler' for measuring structural changes in proteins—dispelling the problem of the unknown orientation factor," *J. Struct. Biol.* **115**, 175–185 (1995).

[53] F. Tanaka, "Theory of time-resolved fluorescence under the interaction of energy transfer in a bichromophoric system: effect of internal rotations of energy donor and acceptor," *J. Chem. Phys.* **109**, 1084–1092 (1998).

[54] Z. G. Yu, "Fluorescent resonant energy transfer: correlated fluctuations of donor and acceptor," *J. Chem. Phys.* **127**, 221101 (2007).

[55] M. Isaksson, N. Norlin, P.-O. Westlund, and L. B.-Å. Johansson, "On the quantitative molecular analysis of electronic energy transfer within donor-acceptor pairs," *Phys. Chem. Chem. Phys.* **9**, 1941–1951 (2007).

[56] S. Jang, "Generalization of the Förster resonance energy transfer theory for quantum mechanical modulation of the donor-acceptor coupling," *J. Chem. Phys.* **127**, 174710 (2007).

[57] D. S. Talaga, W. L. Lau, H. Roder, J. Tang, Y. W. Jia, W. F. DeGrado, and R. M. Hochstrasser, "Dynamics and folding of single two-stranded coiled-coil peptides studied by fluorescent energy transfer confocal microscopy," *Proc. Natl. Acad. Sci. USA* **97**, 13021–13026 (2000).

[58] T. Heyduk, "Measuring protein conformational changes by FRET/LRET," *Curr. Opin. Biotechnol.* **13**, 292–296 (2002).

[59] B. Schuler and W. A. Eaton, "Protein folding studied by single-molecule FRET," *Curr. Opin. Struct. Biol.* **18**, 16–26 (2008).

[60] T. Zal and N. R. J. Gascoigne, "Using live FRET imaging to reveal early protein–protein interactions during T cell activation," *Curr. Opin. Immunol.* **16**, 418–427 (2004).

[61] M. Parsons, B. Vojnovic, and S. Ameer-Beg, "Imaging protein–protein interactions in cell motility using fluorescence resonance energy transfer (FRET)," *Biochem. Soc. Trans.* **32**, 431–433 (2004).

[62] W. B. Frommer, M. W. Davidson, and R. E. Campbell, "Genetically encoded biosensors based on engineered fluorescent proteins," *Chem. Soc. Rev.* **38**, 2833–2841 (2009).

[63] A. W. Nguyen, X. You, A. M. Jabaiah, and P. S. Daugherty, "Fluorescent protein FRET applications," in *Reviews in Fluorescence*, edited by C. D. Geddes (Springer, New York, 2010), Chap. 13.

[64] A. Hillisch, M. Lorenz, and S. Diekmann, "Recent advances in FRET: distance determination in protein–DNA complexes," *Curr. Opin. Struct. Biol.* **11**, 201–207 (2001).

[65] F. G. E. Cremazy, E. M. M. Manders, P. I. H. Bastiaens, G. Kramer, G. L. Hager, E. B. van Munster, P. J. Verschure, T. W. J. Gadella, and R. van Driel, "Imaging in situ protein–DNA interactions in the cell nucleus using FRET–FLIM," *Exp. Cell Res.* **309**, 390–396 (2005).

[66] P. R. Selvin, "Principles and biophysical applications of lanthanide-based probes," *Annu. Rev. Biophys. Biomol. Struct.* **31**, 275–302 (2002).

[67] W. C. W. Chan, D. J. Maxwell, X. Gao, R. E. Bailey, M. Han, and S. Nie, "Luminescent quantum dots for multiplexed biological detection and imaging," *Curr. Opin. Biotechnol.* **13**, 40–46 (2002).

[68] A. R. Clapp, I. L. Medintz, and H. Mattoussi, "Förster resonance energy transfer investigations using quantum-dot fluorophores," *Chem. Phys. Chem.* **7**, 47–57 (2006).

[69] R. M. Clegg, "Fluorescence resonance energy transfer," in *Fluorescence Imaging Spectroscopy and Microscopy*, edited by X. F. Wang and B. Herman (John Wiley & Sons, New York, 1996), Chap. 7.

[70] A. Periasamy, *Methods in Cellular Imaging* (Oxford University Press, New York, 2001).

[71] F. S. Wouters, P. J. Verveer, and P. I. H. Bastiaens, "Imaging biochemistry inside cells," *Trends Cell Biol.* **11**, 203–211 (2001).

[72] A. Hoppe, K. Christensen, and J. A. Swanson, "Fluorescence resonance energy transfer-based stoichiometry in living cells," *Biophys. J.* **83**, 3652–3664 (2002).

[73] E. A. Jares-Erijman and T. M. Jovin, "FRET imaging," *Nat. Biotechnol.* **21**, 1387–1395 (2003).

[74] A. Periasamy and R. N. Day, *Molecular Imaging: FRET Microscopy and Spectroscopy* (Oxford University Press, New York, 2005).

[75] R. N. Day and M. W. Davidson, "Fluorescent proteins for FRET microscopy: monitoring protein interactions in living cells," *Bioessays* **34**, 341–350 (2012).

[76] G. W. Gordon, G. Berry, X. H. Liang, B. Levine, and B. Herman, "Quantitative fluorescence resonance energy transfer measurements using fluorescence microscopy," *Biophys. J.* **74**, 2702–2713 (1998).

[77] Z. Xia and Y. Liu "Reliable and global measurement of fluorescence resonance energy transfer using fluorescence microscopes," *Biophys. J.* **81**, 2395–2402 (2001).

[78] J. van Rheenen, M. Langeslag, and K. Jalink, "Correcting confocal acquisition to optimize imaging of fluorescence resonance energy transfer by sensitized emission," *Biophys. J.* **86**, 2517–2529 (2004).

[79] T. S. Karpova, C. T. Baumann, L. He, X. Wu, A. Grammer, P. Lipsky, G. L. Hager, and J. G. McNally, "Fluorescence resonance energy transfer from cyan to yellow fluorescent protein detected by acceptor photobleaching using confocal microscopy and a single laser," *J. Microsc.* **209**, 56–70 (2003).

[80] E. B. van Munster, G. J. Kremers, M. J. W. Adjobo-Hermans, and T. W. J. Gadella, "Fluorescence resonance energy transfer (FRET) measurement by gradual acceptor photobleaching," *J. Microsc.* **218**, 253–262 (2005).

[81] P. I. H. Bastiaens and A. Squire, "Fluorescence lifetime imaging microscopy: spatial resolution of biochemical processes in the cell," *Trends Cell Biol.* **9**, 48–52 (1999).

[82] R. R. Duncan, A. Bergmann, M. A. Cousin, D. K. Apps, and M. J. Shipston, "Multi-dimensional time-correlated single photon counting (TCSPC) fluorescence lifetime imaging microscopy (FLIM) to detect FRET in cells," *J. Microsc.* **215**, 1–12 (2004).

[83] H. Wallrabe and A. Periasamy, "Imaging protein molecules using FRET and FLIM microscopy," *Curr. Opin. Biotechnol.* **16**, 19–27 (2005).

[84] M. Peter, S. M. Ameer-Beg, M. K. Y. Hughes, M. D. Keppler, S. Prag, M. Marsh, B. Vojnovic, and T. Ng, "Multiphoton-FLIM quantification of the EGFP-mRFP1 FRET pair for localization of membrane receptor-kinase interactions," *Biophys. J.* **88**, 1224–1237 (2005).

[85] T. Kawazoe, K. Kobayashi, and M. Ohtsu, "Optical nanofountain: a biomimetic device that concentrates optical energy in a nanometric area," *Appl. Phys. Lett.* **86**, 103102 (2005).

[86] H. Morawetz, "Studies of synthetic polymers by nonradiative energy transfer," *Science* **240**, 172–176 (1988).

[87] J. P. S. Farinha and J. M. G. Martinho, "Resonance energy transfer in polymer interfaces," *Springer Ser. Fluoresc.* **4**, 215–255 (2008).

[88] G. Srinivas and B. Bagchi, "Detection of collapsed and ordered polymer structures by fluorescence resonance energy transfer in stiff homopolymers: bimodality in the reaction efficiency distribution," *J. Chem. Phys.* **116**, 837–844 (2002).

[89] S. Saini, H. Singh, and B. Bagchi, "Fluorescence resonance energy transfer (FRET) in chemistry and biology: non-Förster distance dependence of the FRET rate," *J. Chem. Sci.* **118**, 23–35 (2006).

[90] R. K. Castellano, S. L. Craig, C. Nuckolls, and J. Rebek, "Detection and mechanistic studies of multicomponent assembly by fluorescence resonance energy transfer," *J. Am. Chem. Soc.* **122**, 7876–7882 (2000).

[91] C. Cano-Raya, M. D. Fernández-Ramos, and L. F. Capitán-Vallvey, "Fluorescence resonance energy transfer disposable sensor for copper(II)," *Anal. Chim. Acta* **555**, 299–307 (2006).

[92] A. E. Albers, V. S. Okreglak, and C. J. Chang, "A FRET-based approach to ratiometric fluorescence detection of hydrogen peroxide," *J. Am. Chem. Soc.* **128**, 9640–9641 (2006).

[93] H. Zhang and D. M. Rudkevich, "A FRET approach to phosgene detection," *Chem. Commun.* 1238–1239 (2007).

[94] R. E. Blankenship, *Molecular Mechanisms of Photosynthesis* (Blackwell Science, Oxford, 2002).

[95] G. D. Scholes, G. R. Fleming, A. Olaya-Castro, and R. van Grondelle, "Lessons from nature about solar light harvesting," *Nat. Chem.* **3**, 763–774 (2011).

[96] G. D. Scholes and G. R. Fleming, "On the mechanism of light-harvesting in photosynthetic purple bacteria: B800 to B850 energy transfer," *J. Phys. Chem. B* **104**, 1854–1868 (2000).

[97] R. J. Cogdell, A. Gall, and J. Köhler, "The architecture and function of the light-harvesting apparatus of purple bacteria: from single molecules to in vivo membranes," *Q. Rev. Biophys.* **39**, 227–324 (2006).

[98] J. Strümpfer, M. Sener, and K, Schulten, "How quantum coherence assists photosynthetic light harvesting," *J. Phys. Chem. Lett.* **4**, 536–542 (2012).

[99] G. D. Scholes, X. J. Jordanides, and G. R. Fleming, "Adapting the Förster theory of energy transfer for modeling dynamics in aggregated molecular assemblies," *J. Phys. Chem. B* **105**, 1640–1651 (2001).

[100] S. Jang and Y.-C. Cheng, "Resonance energy flow dynamics of coherently delocalized excitons in biological and macromolecular systems: recent theoretical advances and open issues," *WIREs Comput. Mol. Sci.* **3**, 84–104 (2013).

[101] J. L. Herek, W. Wohlleben, R. J. Cogdell, D. Zeidler, and M. Motzkus, "Quantum control of energy flow in light harvesting," *Nature* **417**, 533–535 (2002).

[102] F. Kulzer and M. Orrit, "Single molecule optics," *Annu. Rev. Phys. Chem.* **55**, 585–611 (2004).

4

BIOPHOTONICS OF PHOTOSYNTHESIS

VALTER ZAZUBOVICH[1] AND RYSZARD JANKOWIAK[2,3]
[1]Department of Physics, Concordia University, Montreal, QC, Canada
[2]Department of Chemistry, Kansas State University, Manhattan, KS, USA
[3]Department of Physics, Kansas State University, Manhattan, KS, USA

4.1 INTRODUCTION

Biophotonics (an extension of photonics), in a broad sense, refers to techniques and phenomena related to interaction between biological matter and light (i.e., photons). For example, Nature uses biophotonics to harvest photons to achieve photosynthesis and to create vision. Light-absorbing pigments in various biological systems start a highly complex series of photoinitiated processes. Photosynthesis is likely the best-known and most widespread process involving interaction between light and biological entities. In photosynthesis, light is harvested and its energy is used to drive chemical reactions that support nearly all life on Earth. Photosynthetic organisms possess a large variety of pigment–protein complexes (which perform as either light-harvesting antennae or as reaction centers (RCs) where primary photochemistry takes place), containing dense networks of chlorophylls (Chls) and other pigments. In plants, algae, and cyanobacteria, these proteins are grouped into Photosystem I (PS I) and Photosystem II (PS II) that work together as parts of the electron transfer chain [1, 2]. Other organisms, incapable of oxygenic photosynthesis, have various dissimilar antenna arrangements, but, interestingly, the RC design is similar for all known photosynthesizing species (see below). Detailed information on structures of various photosynthetic proteins was obtained by X-ray crystallography [3–10].

Photonics: Scientific Foundations, Technology and Applications, Volume IV, First Edition.
Edited by David L. Andrews.
© 2015 John Wiley & Sons, Inc. Published 2015 by John Wiley & Sons, Inc.

Photosynthesis research is a dynamic field, with most efforts currently directed toward detailed understanding of PS II functioning, hydrogen and biofuel production, as well as utilizing solutions tested by Nature in light-harvesting complexes to improve solar cells. Another field related to biophotonics of photosynthesis involves studies of pigment–protein interactions and protein dynamics, at both physiological and low temperatures. In this case, one is interested not only in protein influence on excitation energy transfer (EET) and/or charge separation (CS) rates, but also in the effect of the protein scaffolding on pigment-site energies.

Photosynthetic proteins serve as model systems for protein research in general. Natural photosynthetic complexes (PCs) are excellent working models for the development of better artificial PCs that will serve human needs. Optical spectroscopies (both in time and frequency domains) can directly probe interactions of pigment–protein complexes with light and are widely used in studies of the primary processes of photosynthesis.

This chapter is to some extent based on our recent review of hole burning (HB) and related spectroscopies [11], but also includes the most recent developments in the field of photosynthesis biophotonics. Due to space limitations, regrettably many interesting and important issues will not be addressed in any detail; in particular, not much attention will be devoted to time-domain methods used in the area of photosynthesis research. Readers interested in these methods are referred to an excellent book [12]. The recently developed two-dimensional electronic spectroscopy (2D-ES), which probes excitonic couplings and EET on the femtosecond time scale, and serves as a unified framework for most time- and frequency-domain techniques, is discussed in References 13–15. Brief description of the 2D-ES, following [13] and some recent photosynthesis-related results were reviewed also in Reference 11.

In this chapter, we will discuss relevant experimental techniques, key physical concepts, and some information gained from frequency-domain optical spectroscopic studies of PCs. Particular attention will be devoted to results of single photosynthetic complex spectroscopy (SPCS), as well as to those of complementary subensemble frequency-domain techniques such as (non-photochemical) spectral hole burning (NPHB). The chapter is concluded with comments on current efforts and future directions in frequency-domain spectroscopies in the area of photosynthesis.

4.2 STRUCTURE OF PIGMENT–PROTEIN COMPLEXES AND STRUCTURE–FUNCTION RELATIONSHIPS

4.2.1 Photosystem I (PS I) and Photosystem II (PS II)

These PCs, involved in oxygenic photosynthesis, use chlorophyll (Chl) molecules or their magnesium-free analogs, pheophytins (Pheo), as both donors and acceptors of energy and electrons; various other pigments (e.g., carotenoids) are employed to increase the range of useful absorbed wavelengths and to assist in photoprotection. The electrons are produced by PS II via the light-induced splitting of water; other members of the electron transport chain, for example, Cytochrome b_6f, further

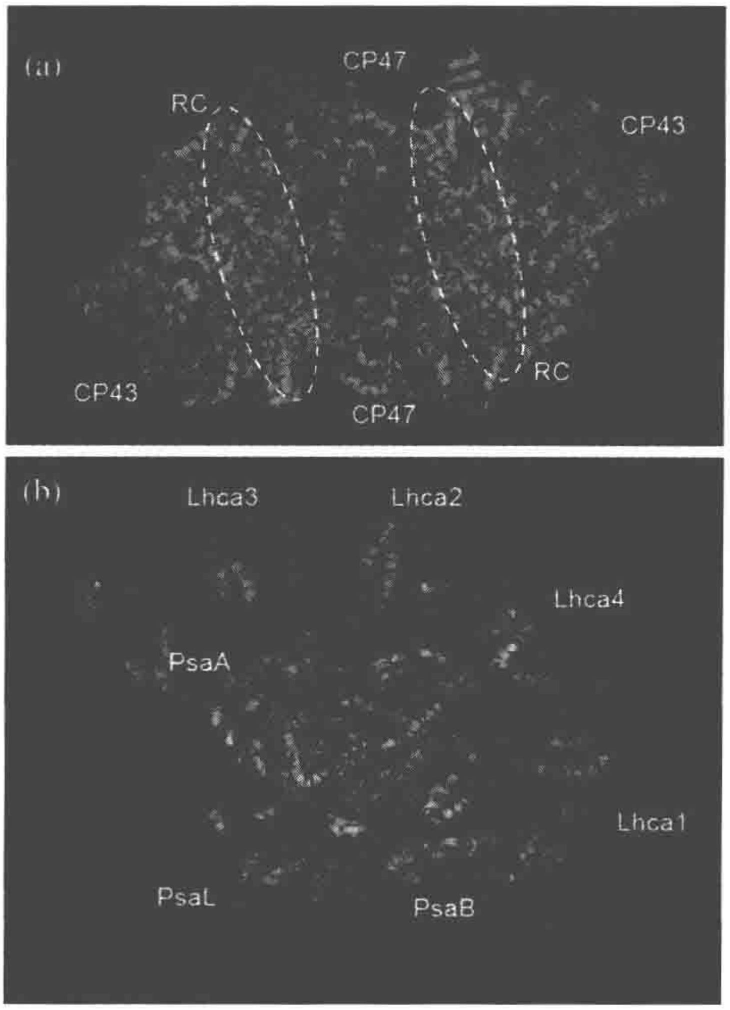

FIGURE 4.1 (a) Photosystem II dimeric core, 3ARC.pdb [3]; peripheral light-harvesting complexes not depicted. (b) Plant Photosystem I, 3LW5.pdb [4]. Gray/green: Chl *a*; dark blue: Pheo *a*; yellow: carotenoids; red: quinones; orange: non-heme iron (PS II); orange/yellow: FeS clusters (PS I). Both complexes are depicted with stromal side facing the viewer. This and subsequent structure figures were produced with RasMol software. (*For a color version of this figure, see the color plate section.*)

contribute to the transmembrane proton gradient [16]. The electrons are shuttled through a variety of electron carriers to the PS I complex where a second light-induced CS reaction takes place, and electrons are used to reduce $NADP^+$ to NADPH. The proton gradient is used by ATP-ase, and ATP and NADPH are then employed to power the Calvin cycle and create the carbohydrates.

Figure 4.1 shows structures of two PCs from higher plants, PS II (frame A [3]) and PS I (frame B [4]). The PS II core is dimeric, with each monomer consisting of the core antenna complexes CP43 and CP47, and the RC. Additionally, the PS II core is surrounded by peripheral antenna complexes LHC II [9], CP24, CP26, and CP29, not depicted in Figure 4.1a [16]. The plant PS I supercomplex pictured in Figure 4.1b consists of the core complex (most notably the PsaA and PsaB Chl-binding proteins) and the LHC I peripheral light-harvesting complexes (Lhca1-4) [4]. In cyanobacteria, the PS I core occurs in a trimeric form, and Lhca-type antenna complexes are not present [7]. In the trimer, the monomers are oriented with the PsaL subunit (see Fig. 4.1) toward the C_3 symmetry axis. Environmental conditions can cause significant

(a)
D1
D2
OEC
(b)
H
L
M

FIGURE 4.2 (a) Arrangement of pigments in active (D1) and inactive (D2) branches of the PS II RC; 3ARC.pdb [3]. Green: Chl *a*; dark blue: Pheo *a*; yellow: carotenoids; red: quinones; orange: non-heme iron; brown/purple: oxygen-evolving cluster, (b) Pigment arrangement in BRC, 1M3X.pdb [5]. Green: BChl *a*; dark blue: BPheo *a*; yellow: carotenoids; red: quinones; orange: non-heme iron. Gray wireframe represents protein and some lipids. (*For a color version of this figure, see the color plate section.*)

changes in supercomplex structures. For instance, cyanobacteria grown in iron-deficit conditions exhibit one or more rings of *IsiA* (CP43′) protein, homologous to CP43, surrounding the trimeric PS I core; a fraction of LHC II complexes is known to migrate between PS II and PS I, depending on the illumination levels. Structures shown here are meant only to give a flavor of the complex organization of photosynthetic proteins.

Figure 4.2a shows a schematic arrangement of the six chlorophylls (Chls) and two pheophytins (Pheos) in PS II RC based on the structure of *T. vulcanus* [3]. The P_{D1} and P_{D2} Chls are analogous to the P_A and P_B bacteriochlorophylls (BChls) of the bacterial reaction center (BRC) special pair (Fig. 4.2b), respectively, while the $Chl_{D1,D2}$ and $Pheo_{D1,D2}$ molecules correspond to the monomeric $BChl_{A,B}$ and the bacteriopheophytin ($BPheo_{A,B}$) molecules of the BRCs. By analogy with the BRCs, it is believed that the P_{D1}/P_{D2}, Chl_{D1}, and $Pheo_{D1}$ molecules participate in primary CS in the PS II RC, although the nature of the primary electron donor in isolated PS II RCs is still a matter of debate (see Section 4.5.5). An obvious difference between PS II RC and BRC is that the former contains two additional peripheral Chls (i.e., $Chlz_{D1}$ and $Chlz_{D2}$). However, both are weakly coupled to the remaining pigments and do not affect CS dynamics significantly.

4.2.2 PCs of Purple Bacteria

Unlike plants, algae, or cyanobacteria, purple bacteria are incapable of oxygenic photosynthesis. However, design features of bacterial reaction centers (BRCs) closely resemble those of higher plants (Fig. 4.2). BRC contains two main subunits, L and M, approximately related to each other by C_2 symmetry, as well as the H-subunit and the cytochrome [5]. L and M proteins provide the scaffold for two nearly symmetrical arrangements of BChl and BPheo molecules, see Figure 4.2b. Upon excitation of any RC pigments, the energy is quickly transferred to the pair of strongly coupled BChl *a* molecules (special pair), which serves as a primary electron donor. Despite the nearly symmetric two-branch arrangement, the electron transfer occurs along the L- (A in PS I, D1 in PS II) branch in wild-type organisms. The electrons are quickly

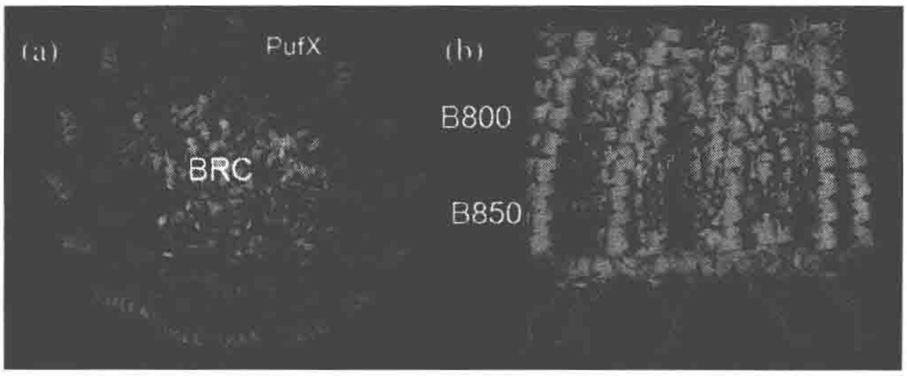

FIGURE 4.3 (a) The BRC-LH1 complex structure, 1PYH.pdb [10]. PufX subunit is not depicted, but its location is indicated. The complex is depicted with H subunit (see Fig. 4.2) toward the viewer. (b) LH2 structure, 2FKW.pdb [6], depicted with the cytoplasm side up. In both frames, gray/green: Bchl *a*; yellow: carotenoids. (*For a color version of this figure, see the color plate section.*)

transported to Q_A immobile quinone and then to Q_B mobile quinone acceptors. The lowest energy absorption of the BRC belongs to the special pair, and is located at a wavelength ranging from ~870 nm to ~960 nm, depending on the particular species.

The BRC is surrounded by the LH1 antenna protein (Fig. 4.3a). Although initially it was believed that LH1 exhibits nearly perfect C_n symmetry, recent AFM and cryo-microscopy studies indicated the perfect ring is broken by the PufX protein subunit [10]. Nevertheless, the LH1 complex is an assembly of n identical protein subunits holding in place an array of strongly coupled BChl *a* molecules. Each subunit contains two BChl *a* molecules in a slightly nonidentical local environment. The LH1-BRC assembly is surrounded by multiple copies of the LH2 antenna complex [6]. The latter is approximately of C_n symmetry (with $n = 8$ or 9, depending on the species), Figure 4.3b. Unlike LH1, LH2 contains two distinct rings of BChl *a* molecules. While in the B850 ring (labeling refers to the wavelengths of the strongest absorption band associated with respective ring, see also Section 4.5.1), center-to-center distances between neighboring BChl *a* molecules are of the order of 9 Å, electrostatic couplings are strong and respective excitations are highly delocalized, and molecules of the B800 ring are relatively weakly interacting. Overall, energy harvested by the B800 ring of the LH2 is transferred to the B850 ring in about 1.6 ps at low temperatures and in less than one picosecond at physiological temperatures. In several picoseconds the excitation energy is transferred to the LH1 complexes and then to the BRCs. Net effectiveness of this chain of processes approaches 100% in terms of the number of primary CS events per number of photons absorbed.

4.3 KEY CONCEPTS IN PHYSICS OF PIGMENT–PROTEIN COMPLEXES

The physical concepts behind light-harvesting and primary CS, and their optical spectroscopic manifestations, have been addressed in numerous books and reviews [2, 11, 12, 16–19]. Thus, here we will briefly discuss the most relevant concepts and phenomena, which are essential for understanding the examples in Section 4.5.

4.3.1 Excitons

As evident from the previous section, light-harvesting complexes are networks of interacting pigment molecules. The concept of an exciton, the excited electronic state delocalized over many molecules, proved extremely useful in describing the processes occurring in light-harvesting complexes and their spectroscopic properties. It originates from condensed-matter physics; namely, due to the electrostatic interactions between identical molecules in the crystal, the excitation becomes delocalized, and excitation energy can travel from molecule to molecule in a wave-like fashion [20]. In other words, the resulting excited state becomes a superposition of excited states of multiple molecules (in case of a perfect crystal—of all molecules in the crystal). Such excitons are called Frenkel excitons.

In order to offer a simple illustration, we consider the case of a pigment dimer. The logic of this example can be easily extended to PCs containing more than two pigment molecules. Consider an isolated molecule with eigenfunctions φ^i and eigenenergies E^i defined by the Hamiltonian

$$H\varphi^i = E^i\varphi^i, \tag{4.1}$$

where $i = g$ or e for ground and excited electronic states, respectively. If one now introduces one more identical molecule into the system, interacting with the first one with the (electrostatic) potential energy V, total wavefunctions become combinations of products of wavefunctions of individual molecules. The wavefunction for the dimer ground state becomes $\varphi_1^g\varphi_2^g$ and the single-excited states localized on molecules 1 and 2 become $\psi_1^e = \varphi_1^e\varphi_2^g$ and $\psi_2^e = \varphi_1^g\varphi_2^e$, respectively. Wavefunctions of the excitonically coupled dimer may be written as $\psi_\pm = \frac{1}{\sqrt{2}}(\psi_1^e \pm \psi_2^e)$, with

$$\begin{aligned}\langle\psi^g|H_1 + H_2 + V|\psi^g\rangle &= 2E^g + D^g \text{ and} \\ \langle\psi_\pm|H_1 + H_2 + V|\psi_\pm\rangle &= E^g + E^e + D^e \pm V_{1,2}\end{aligned}, \tag{4.2}$$

where $D^g = \langle\psi^g|V|\psi^g\rangle$ is van der Waals interaction or dispersion energy for the ground state, $D^e = \langle\psi_1^e|V|\psi_1^e\rangle = \langle\psi_2^e|V|\psi_2^e\rangle$ is the van der Waals interaction for the excited dimer, and $V_{1,2} = \langle\psi_1^e|V|\psi_2^e\rangle = \langle\psi_2^e|V|\psi_1^e\rangle$ is the resonance transfer integral determining the EET rate and dimer excitonic splitting. The sign and magnitude of $V_{1,2}$ are determined by the orientation of the transition dipole-moment vectors of the two molecules. For long enough interpigment distances (>1 nm), the interpigment coupling $V_{1,2}$ can be sufficiently reliably calculated in dipole–dipole approximation [12]:

$$V_{1,2} = \kappa\frac{\mu_1\mu_2}{4\pi\varepsilon R^3}, \tag{4.3}$$

where μ_1 and μ_2 are transition dipole moments of molecules 1 and 2, κ is orientation factor (−2...+2), and R is the distance between the molecules. Smaller distances require more elaborate approximations.

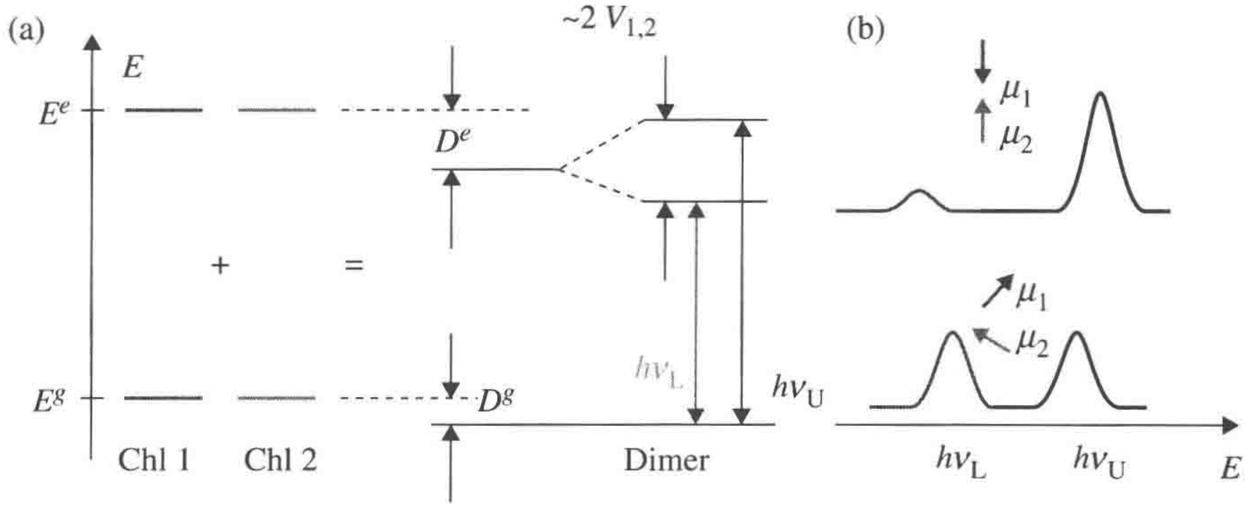

FIGURE 4.4 Effects of exciton interaction on the energy levels in a degenerate dimer of Chls. The splitting is equal to $2V_{1,2}$. Schematic spectra on the right are shown for two cases: (a) "head-to-tail" dimer (top spectra) and (b) a dimer with two perpendicular orientations of the dipole moments (lower spectra). $h\nu_L$ and $h\nu_U$ correspond to the energies of transitions to the lower and upper excitonic states, respectively. The same coupling was assumed for both configurations of the dipole moments. Adapted with permission from Reference 11. Copyright (2011) American Chemical Society.

Skipping the detailed treatment of D^g and D^e, one can depict excitonic splitting into upper ($h\nu_U$) and lower ($h\nu_L$) components in the case of the dimer shown in Figure 4.4. Distribution of the oscillator strength and the magnitude of splitting depend on the orientation of the transition dipole moments of the two pigments as shown in Figure 4.4b. In the upper part of Frame B, the higher-energy state possesses most of the oscillator strength. However, for different structural arrangements the higher-energy state can be weak or even forbidden. In the lower case in Frame B, the two bands have equal intensity. We stress that excitonic states are still delocalized in this case. The extent of delocalization is reduced if the pigments involved have different transition energies in the absence of interaction ("site energies," determined by the local environment) to begin with.

In general, in multipigment cases, new eigenstates of the system can be described as

$$\phi_k = \sum_{n=1}^{N} c_{nk}\psi_n, \tag{4.4}$$

where ψ_n are the locally excited states. Energies and oscillator strengths of the excitonic states are found by determining eigenvalues and eigenvectors of a matrix which has site energies as diagonal elements and interpigment couplings as off-diagonal ones. The c_{nk} in Eq. (4.4) can be found from the eigenvectors of that matrix. Determination of site energies is the major problem, despite several different approaches developed for this purpose (see [21, 22] for PS I, for example). In particular, interactions such as hydrogen bonding, coordination state of Chls, and environment-induced deviations of pigments from planarity are difficult to account for. Thus, site energies are usually left as free parameters while attempting a simultaneous fit to as many different optical spectra as possible; the search for realistic site energies is guided by experimental constraints and aided by fitting algorithms [23,24]. If the couplings $V_{n,m}$ within certain groups of pigments are large, and the couplings to other pigments in the complex are small (smaller than the differences in site energies and smaller than the reorganization energy), such groups could be treated as independent domains, and the optical spectra of the complex can be calculated as a sum of the excitonic spectra of such groups.

4.3.2 Excitation Energy Transfer

In PCs, due to electrostatic coupling between the pigments, (radiationless) EET can take place from one pigment to another. In general, EET occurs from a manifold of vibrational states, associated with the excited electronic state of the donor molecule, into a manifold of vibrational states associated with the ground state of the acceptor molecule. Thus, the nature of pigment–pigment and pigment–protein interactions is critical in understanding EET. If coupling between chromophores is weak (i.e., excitations are localized on single pigments), the energies of the chromophores are considered to be independent even if there is a finite probability of EET. Such EET can be described by the Förster theory [25]. When electronic coupling is weak enough that inter- and intramolecular relaxation processes occur on a time scale faster than EET, the rate of EET, $k_{1\to 2}$, can be described by Fermi's golden rule rate expression:

$$k_{1\to 2} = \frac{4\pi^2}{h}|V_{1,2}|^2 \rho(E), \tag{4.5}$$

where $\rho(E)$ is related to the energy "matching" of the energy levels of the donor and acceptor molecules (i.e., Franck–Condon (FC) weighted density of states), h is Planck's constant, and $V_{1,2}$ is the coupling between pigments 1 and 2 as indicated in Figure 4.4. Note all parameters related to the vibrational states are combined in

$$\rho(E) = \int_{E=0}^{\infty} dE G_{\mathrm{D}}(E) G_{\mathrm{A}}(E), \tag{4.6}$$

where $G_{\mathrm{D}}(E)$ and $G_{\mathrm{A}}(E)$ are Franck–Condon weighted and thermally averaged combined densities of states. Förster showed [25] that $G_{\mathrm{D}}(E)$ and $G_{\mathrm{A}}(E)$ can be related to absorption (molar extinction coefficient $\varepsilon_{\mathrm{A}}(\omega)$) and fluorescence ($f_{\mathrm{D}}(\omega)$) spectra of donor and acceptor pigments, which will be discussed in Section 4.3.3 and which can be experimentally determined using spectral hole-burning (SHB), fluorescence line narrowing (FLN), or ΔFLN (combination of SHB and FLN) [26–33].

For very short interpigment distances, both Coulomb and exchange interactions need to be taken into account. The exchange mechanism was described by

Dexter [34]. The mechanisms involving electrostatic and exchange interactions have different distance dependence and different spin selection rules. Since the exchange mechanism depends strongly on the overlap of the electronic wavefunctions, the mechanism is restricted to rather short distances. In contrast, Förster mechanism permits EET over several nanometers. On the other hand, the exchange mechanism does not have the spin restriction and permits EET from a triplet state to a singlet state. For instance, quenching chlorophyll triplets by carotenoids require an exchange mechanism [2, 35, 36]. The more recently developed Redfield EET framework has been discussed in References 17 and 18.

If couplings within certain group of pigments are large enough, this group should be treated as one supermolecule, and optical spectra and transition dipoles of relevant states of such system must be calculated as described in the previous section. Thus, one can consider EET with one or both donor and acceptor being strongly coupled groups of pigments. Excitation transfer between higher and lower states of the same excitonically coupled system has to be also taken into account. Relaxation to the lower state can occur by exchanging energy with the bath; the coupling with the bath is represented by the spectral density of states, $\rho(\omega)$. Detailed description of EET processes in strongly coupled systems is beyond the scope of this review. Qualitatively, in the case when $\tau_{\mathrm{EET}} \ll \tau_{\mathrm{vib}}$, where $\tau_{\mathrm{EET}} = k^{-1}_{1\rightarrow 2}$(see Eq. 4.5) is the transfer time and τ_{vib} corresponds to the vibrational relaxation time, the exciton can move freely from molecule to molecule. Since this type of motion requires fixed-phase relations between exciton wavefunctions of different molecules, it is called coherent transfer [37, 38]. If $\tau_{\mathrm{vib}} \ll \tau_{\mathrm{EET}}$, it is impossible to construct a meaningful wavefunction which involves large contributions from different molecules. The excitation can hop from pigment to pigment (i.e., there is no phase correlation between the excitation before and after the hop; incoherent regime). Different regimes of excitation motion can be described also by the density matrix approach. In summary, partially coherent energy relaxation is expected within the strongly coupled domains, while incoherent EET can occur between the low energy states of each domain.

4.3.3 Homogeneous and Inhomogeneous Broadening, Zero-Phonon Lines (ZPLs), and Phonon Sidebands (PSBs)

The information on primary processes within PC can be obtained using various time-domain methods including pump-probe, time-resolved fluorescence, and 2D-ES. However, information about the dynamics of the system, for instance about the EET or CS rates, is contained also in the widths of the so-called homogeneously broadened lines, Γ_{hom}. The Γ_{hom} is related to the T_2 relaxation time by

$$\frac{1}{T_2} = \pi c \Gamma_{\mathrm{hom}} = \frac{1}{2T_1} + \frac{1}{T_2^*}, \tag{4.7}$$

where T_1 is the excited-state lifetime and T_2^* is the pure dephasing time that strongly depends on temperature since dephasing is caused by phonon scattering. Thus, in order to obtain information on the EET or CS processes affecting T_1, one has to

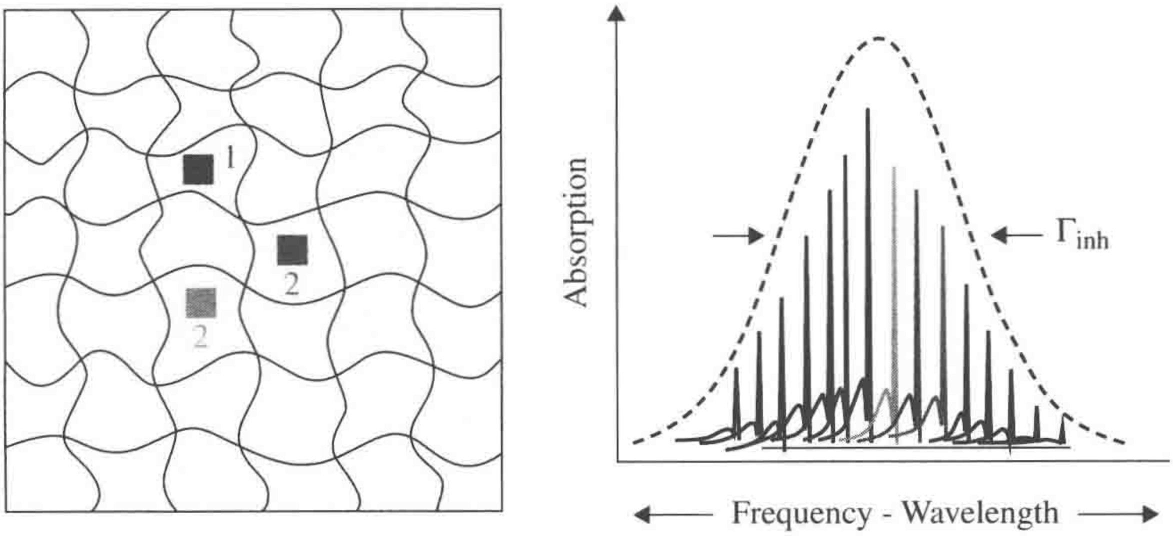

FIGURE 4.5 Pigments dispersed in an amorphous solid matrix and the SDF (of width Γ_{inh}) describing the probability to find a molecule with given zero-phonon transition frequency; see text. Adapted with permission from Reference 11. Copyright (2011) American Chemical Society. (*For a color version of this figure, see the color plate section.*)

perform frequency-domain experiments at low temperatures. At liquid helium temperatures, and in the presence of picosecond timescale or faster EET (typical for PCs), the homogeneous linewidths are strongly dominated by T_1, with T_2^* being just a minor contribution.

Proteins at low temperatures behave, to a significant extent, as amorphous solids. It is well known that electronic transitions in amorphous phases are subject to inhomogeneous broadening due to variations of the local environment. This broadening obscures the information on the dynamics of the individual complexes contained in the homogeneously broadened lines. The origin of inhomogeneous broadening is illustrated in Figure 4.5. Consider an ensemble of pigments in a rigid disordered matrix, as shown schematically in the left frame; the immediate environments of the identical pigment molecules (labeled as sites 1, 2, and 3) in the disordered matrix are different, and as a result, the molecules absorb at somewhat different energies, ω_1, ω_2, and ω_3, respectively. This is illustrated by the three narrow spectra (colored solid lines) shown in the right frame of Figure 4.5 (In a perfect crystal, all three transitions would have the same frequency, that is, $\omega_1 = \omega_2 = \omega_3$, and the resulting narrow absorption band would be only homogeneously broadened.)

The narrow lines, as depicted in Figure 4.5, are known as zero-phonon lines (ZPLs). A comprehensive theory of impurity spectra in solids, describing the ZPLs, can be found, for example, in an excellent book by Rebane [39]. For zero-phonon transition, there is no net change in the number of phonons. Building on each ZPL (of width Γ_{hom}) is a broad phonon (delocalized lattice vibration) wing, so-called phonon sideband (PSB). It is located at higher energies from ZPL in absorption (see Figure 4.5), and at lower energies from ZPL in emission spectra. Since the PSB contributes to the ensemble absorption and fluorescence origin bands, the width of the respective ensemble spectra is approximately given by $\Gamma_{inh} + S\omega_m$, where ω_m is the mean phonon frequency (for PC typically about 20 cm^{-1}) and S is a

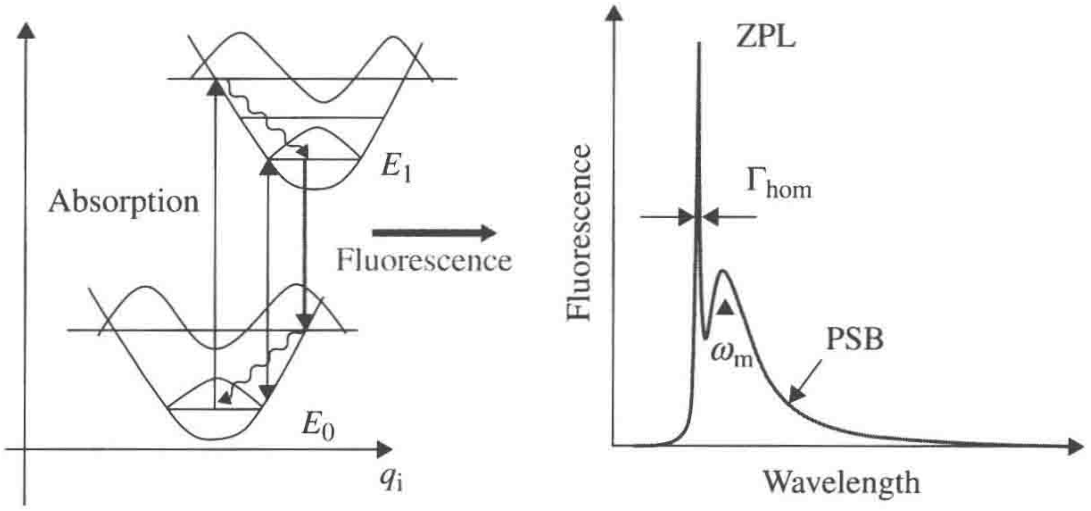

FIGURE 4.6 Left: Potential curves in the case of linear electron–phonon coupling, $\hbar\omega_g = \hbar\omega_e$ and single molecule fluorescence spectrum for a transition between two vibronic states of a guest molecule embedded in an amorphous host. Optical transitions are shown as vertical arrows in accordance with the Franck–Condon principle. The most likely transitions are those with the largest wavefunction overlap; the zero-phonon transition is relatively unlikely in the depicted strong electron–phonon coupling case. Right: Single molecule fluorescence spectrum. The PSB is displaced to lower energies by ω_m, which corresponds to the mean phonon frequency. Γ_{hom} is the homogeneous linewidth. Adapted with permission from Reference 11. Copyright (2011) American Chemical Society.

dimensionless parameter called the Huang-Rhys factor (S). S in the low temperature limit is defined as

$$S(T = 0) = \sum_i \frac{M_i\omega_i}{2\hbar}(\Delta q_i)^2, \tag{4.8}$$

where M_i and ω_i are the reduced mass and frequency of the phonon mode i, respectively. One can think of S as the average number of phonons excited in the course of electronic transition.

Weak interaction between the electronic transition and the delocalized phonon modes correspond to small equilibrium position changes Δq_i and a correspondingly small value of S. In the absorption/fluorescence spectrum, weak coupling ($S \ll 1$) is reflected in an intense ZPL and a weak PSB. Conversely, a large value of S ($S > 1$) corresponds to strong coupling, producing a weak ZPL and an intense PSB. For very strong coupling ($S \gtrsim 10$), the ZPL is so weak that it is masked by realistic experimental noise. In general, the (linear) electron–phonon (el–ph) coupling is strong and S is large for molecules which experience large geometry changes and/or large changes of the electronic charge distribution upon electronic excitation. Figure 4.6 illustrates the above points. Here the configurational coordinate diagram of the ground and excited states of a hypothetical molecule is shown for a single phonon mode. The two parabolas represent the potential energy; the electronic ground state and the first excited state are labeled as E_0 and E_1, respectively. Energy levels of a pigment molecule are depicted in the interaction with the local phonon with $\hbar\omega_g = \hbar\omega_e$.

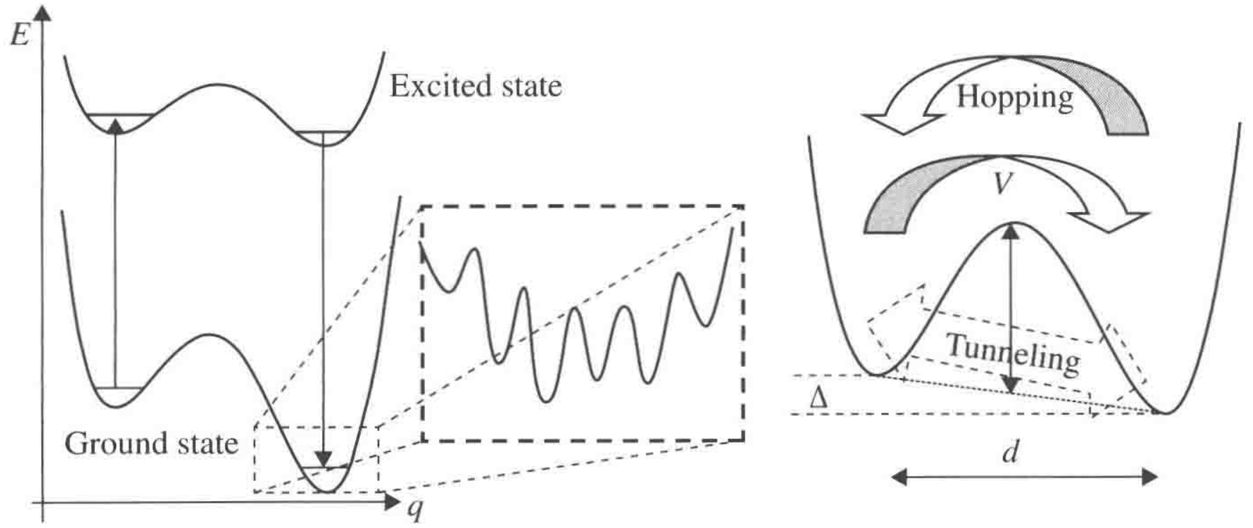

FIGURE 4.7 Schematic representation of the two tiers of the protein energy landscape, as well as the processes responsible for crossing the barriers. Both ground and excited states of the pigment molecule embedded in the protein are shown. Adapted with permission from Reference 43. Copyright (2012) American Chemical Society.

Within the linear el–ph coupling approximation, only the equilibrium position, but not the frequency ω_i of the phonon mode i (with $i = g, e$), is changed between the two electronic states. In this case, q_i represents the lattice normal coordinate belonging to phonon mode i, and Δq_i corresponds to the change of the equilibrium position.

In the low temperature limit, an intuitive formula describing the whole shape of the single-molecule spectrum, including both ZPL and PSB, but not intramolecular vibrations, was first given in Reference 40 (see [11] for more sophisticated treatments):

$$L_{A/F}(\omega - \Omega_0) = \underbrace{e^{-S} l_0(\omega - \Omega_0)}_{\text{ZPL}} + \underbrace{\sum_{R=1}^{\infty} S^R \frac{e^{-S}}{R!} l_R(\omega - \Omega_0 \mp R\omega_m)}_{\text{PSB}}, \tag{4.9}$$

where $-R\omega_m$ and $+R\omega_m$ correspond to absorption $L_A(\omega)$ and fluorescence $L_F(\omega)$, respectively. The first term represents the Lorentzian ZPL $l_0(\omega - \Omega_0)$, which peaks at Ω_0 and possesses a homogeneous width Γ_{hom}. The second term is the PSB, consisting of a sum over all R-phonon transitions; the function $l_1(\omega)$ is the *one-phonon profile* (i.e., the normalized spectral density function discussed above). Guided by experimental data, the one-phonon profile l_1 is often approximated by a Gaussian at its lower frequency wing and by a Lorentzian at its higher frequency wing. However, one can also directly employ the PSB profiles measured by ΔFLN spectroscopy [28–30]. Obviously, the profile described by Eq. (4.9) is directly related to $G_D(E)$ and $G_A(E)$ discussed above (see Eq. 4.6). However, Eq. (4.9) is valid only for a relatively narrow one-phonon profile when the mean-phonon approximation is reasonable (M. Reppert and R. Jankowiak, unpublished data).

4.3.4 Proteins at Low Temperatures

As follows from the discussion above, in order to use homogeneous linewidths for the determination of excited-state lifetimes (i.e., EET and CS times), one needs to minimize T_2^* and work at as low temperatures as possible. Low temperature experiments trap biomolecules in a physical state in which large-scale motions necessary for crossing the high barriers are frozen out, while the motions within the lower hierarchical tiers of the protein energy landscape potentially remain active. The idea of hierarchically structured protein energy landscapes was introduced by Frauenfelder et al. [41,42]. The whole protein energy landscape may be represented by the so-called "folding funnel."

From a somewhat different perspective, application of the energy landscape concept to pigment–protein complexes could also be considered as an extension of theories developed in condensed-matter physics to explain the anomalous low temperature properties of glasses. According to those theories, glasses owe their unusual low temperature properties, including heat capacity and heat conductivity, as well as optical/spectroscopic properties [44–46], to the presence of the so-called two-level systems (TLS). The exact atomic origins of the TLS are not known in most cases, but in general they are groups of atoms which can assume two different configurations, with (phonon-assisted) tunneling being possible between these configurations. The so-called standard TLS model [44–46] implied lack of interaction between individual TLS. However, the standard model failed to explain some experimental observations, and TLS–TLS interactions or multilevel systems (MLS) had to be introduced, even for glasses. While glasses exhibit just the broad barrier parameter distributions (the particular functional shape of which is a matter of debate, see Section 4.5.4), responsible for broad distributions of conformational change rates, in proteins these distributions additionally have hierarchal character [41,42]. Figure 4.7 presents the adaptation of the TLS model to proteins, and includes two hierarchal tiers of the energy landscape. The model includes both ground- and excited-electronic states of the pigment molecule surrounded by the amorphous host and being in interaction with TLS (or multi-well energy landscape), as the excited state processes are important in treatment of optical spectroscopy experiments (see Section 4.4). Barriers on the higher tier of the landscape, with pigment in the ground state, are high enough, and corresponding relaxation times may vary from hours to days and beyond at liquid helium temperatures. In terms of optical experiments, this corresponds to the (relatively infrequent) shifts of the spectral lines (slow spectral diffusion). Barriers on a lower tier can be crossed by thermally induced hopping or by tunneling at a much higher rate. If tiny conformational changes on that lower barrier tier are occurring much faster than the time scale of the experiment, this fast spectral diffusion would contribute to the observed width of the optical spectral line (or hole, see below) [47,48].

4.4 EXPERIMENTAL TECHNIQUES

4.4.1 Spectral Hole-Burning, Fluorescence Line-Narrowing, and ΔFLN

Several low temperature, laser-based techniques have been developed that can overcome the inhomogeneous broadening and access the homogeneous (natural) ZPL width, which can provide dynamical information. These techniques are SHB [46–52], fluorescence line-narrowing (FLN) [53], and, ultimately, single-molecule (or, in the context of this work—single PC) spectroscopy (SPCS) [54–56].

SHB involves selective excitation of the pigment molecules by narrow-band laser and phototransforming either those molecules themselves or their immediate environment. As a result of either process, the molecule ceases to absorb at its original wavelength. A particular variety of HB, known as nonphotochemical hole-burning (NPHB) [33, 46, 50, 57, 58] is dominant in amorphous solids, including PCs. In the case of NPHB, the pigment molecules in PC do not experience photochemical transformations and remain parts of the coupled pigment network. The shift of the pigment's transition frequency occurs as a result of small conformational changes in the protein surrounding the pigment molecule, a phenomenon that can be treated as tunneling through the barrier on the multi-well protein energy landscape (see above), at least at temperatures below 10 K (see Section 4.5.4). The "strength" of the barrier can be described with the tunneling parameter $\lambda = d\sqrt{2mV}/\hbar$, where d is the displacement along a generalized coordinate, m is the effective mass of the entity rearranging during conformational change, and V is the barrier height. It appears (otherwise persistent HB would be impossible) that in most amorphous solids, including proteins, barriers in the excited state are lower than in the ground state and can be crossed with sufficient probability within the lifetime of the excited state. The absorption spectrum, after burning at ω_B with photon flux P for time t, can be described with SHB master equation [33, 58]:

$$D(\Omega, t) = 1.5 \int d\omega L(\Omega - \omega) G(\omega) \int d\lambda f(\lambda) \times \int d\alpha \sin\alpha \cos^2\alpha e^{-P\sigma\varphi(\lambda, T_1) L(\omega_B - \omega) t \cos^2\alpha}. \tag{4.10}$$

Here σ and ϕ are the integral absorption cross-section of the pigment and the HB quantum yield, respectively. The latter depends on the tunneling parameter λ:

$$\varphi(\lambda, T_1) = \frac{\Omega_0 \exp(-2\lambda)}{\Omega_0 \exp(-2\lambda) + T_1^{-1}}. \tag{4.11}$$

$f(\lambda)$ is the distribution of λ and T_1 may include EET or CS times, as well as radiative lifetime, but not T_2^*. $L(\omega_B - \omega)$ is the single site-absorption profile (Eq. 4.9). $\Omega_0 \sim 10^{12}$ Hz can be interpreted as an attempt frequency. Alpha is the angle between the laser polarization and the transition dipole moment. $G(\omega)$ is the site-distribution function (SDF), which is Gaussian with the width Γ_{inh} before burning, and it describes the probability of finding a pigment with a ZPL at a given frequency. Since convolution of a Lorentzian with itself is a Lorentzian with twice the width, the width of the (shallow) resonant spectral hole is twice the Γ_{hom}. Since in NPHB pigment molecules do not experience photochemical changes, they continue contributing to the absorption spectrum, just at different wavelengths. These pigments with altered environments are redistributed around the spectral hole, giving rise to the broad anti-hole (or "photoproduct"). The true NPHB spectrum is conservative.

FLN spectroscopy [53] involves measurement of fluorescence spectra selectively excited with a narrow-band laser. The advantage of FLN over SHB is that no phototransformations are required, either in the pigment molecule or in its immediate environment. On the downside, in FLN experiments it is difficult to disentangle different contributions to the PSB part of the spectrum [26, 27], and the intensity of the ZPL part is difficult to determine due to scattering of excitation light. Recently, a combination of FLN with SHB, the ΔFLN spectroscopy, has been applied to a number of PCs [28–30], providing new insights into the el-ph coupling parameters. ΔFLN directly yields the correct PSB shape due to double selection [30]. Whether the ZPL contribution can also be measured with sufficient precision in the ΔFLN experiments is not completely clear, and likely depends on the design of a particular experimental setup. FLN and ΔFLN allow for the measurement of intramolecular vibrational frequencies, providing a selective tool for the identification of Chls with unique interactions with the surrounding protein.

Parameters provided by SHB yield information on (a) lifetimes (T_1) of the *zero-point level* of $S_1(Qy)$-states due to EET or ET, as determined by the widths of zero-phonon holes (ZPH); (b) Γ_{inh} values, typically ~50–200 cm^{-1} derived from the SHB action spectrum (see, e.g., [59]), the ZPH depth dependence on wavelength for constant irradiation dose; (c) the extent of correlation and excitonic interaction between the absorption bands of different Qy-states, using satellite hole-burning; and (d) Franck–Condon factors and frequencies of Chl molecular vibration modes active in electronic transitions as determined by vibronic satellite HB spectroscopy. Electron–(protein) phonon coupling parameters (Huang-Rhys factors, S, and PSB shape) can be also obtained. These vibration data can also be obtained by ΔFLN. Parameters (a)–(d) are essential for understanding EET since they determine spectral density ρ (see above). Other quantities are important for determining particular origins of relevant excitonic states, or the parameters of local protein environments. In terms of protein dynamics, SHB may be used to determine pure dephasing of Q_y-optical transitions due to coupling with MLS of proteins (smallest barrier tier of the protein energy landscape)—by measuring the temperature dependence of the Γ_{hom}, as well as the parameters of the higher tiers of the protein energy landscapes—from hole evolution upon burning and recovery, at fixed (burn) temperature and upon thermocycling [51, 60, 61]. Additionally, the linear pressure shift rates for Q_y-absorption bands and ZPH, as well as their broadening rates, provide information on the nature of excitonic coupling between neighboring Chl molecules; specifically, contributions from electrostatic and electron-exchange interactions. The latter lead to charge-transfer (CT) character for Q_y-states. In the absence of excitonic interactions, the pressure-shift rates reflect local compressibility of the protein. The large permanent dipole-moment changes ($\Delta\mu$) of the $S_0 \rightarrow S_1$ transitions can be used to identify states with significant CT character [31–33]. Aside from detecting CT states, the ability to resolve closely spaced states is also enhanced by high pressure and Stark HB spectroscopy [31–33].

4.4.2 Single Photosynthetic Complex Spectroscopy

The key advantage of SPCS is that this approach, by definition, eliminates the problem of automatic subensemble averaging inherent in other techniques for overcoming inhomogeneous broadening, such as SHB. The vast majority of SPCS experimental setups are based on confocal fluorescence microscopes, with the microscope objective located with the sample inside the cryostat in the case of low temperature experiments. The small amount of fairly diluted sample is spin-coated onto a proper substrate, ensuring that only one complex at a time is present in the diffraction-limited volume selected by the microscope objective. Then one can obtain its fluorescence or fluorescence excitation spectra. Large amounts of SPCS data are available for a number of PC (the following references represent just a fraction of available works), including LH2 antenna complexes of purple bacteria at low [56, 62–72] and room temperatures [73,74], and cyanobacterial PS I [75–83]. Some measurements on LHC II antenna complex of PS II had been performed at cryogenic temperatures a while ago [84]; recently a number of works have been published on room-temperature conformational switching in this complex [85, 86]. SPCS studies of conformational switching were extended to peripheral antenna proteins of plant PS I [86]. Some SPCS results were reported also for the LH1 complex of purple bacteria [87, 88]. SPCS experiments on minor antenna complexes of PS II—CP24, CP26, and CP29 have been mentioned in Reference 85 but not many details were presented, as this work focused mainly on the LHC II and Lhca complexes. SPCS on a number of other photosynthetic systems were reported in Reference 89. Figure 4.8 contains a schematic of a typical single molecule/SPCS experiment, as well as raster-scan results obtained in Reference 77 for *Synechocystis* PCC6803 PS I.

It is important to recognize with respect to comparisons between NPHB and SPCS, that (a) light intensities by necessity employed in SPCS experiments are orders of

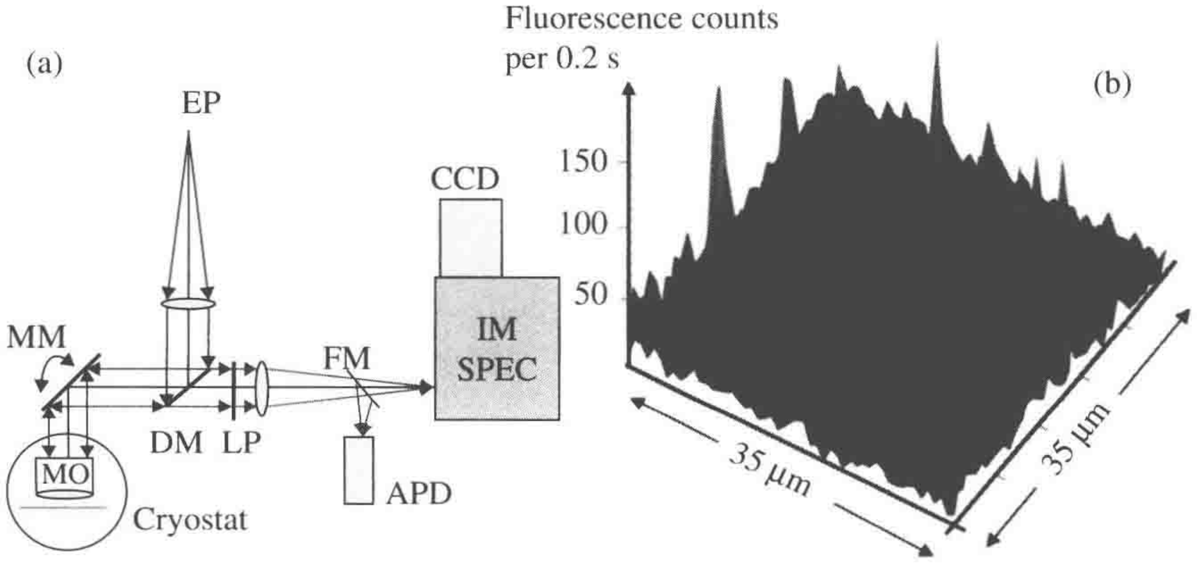

FIGURE 4.8 (a) Scheme of the confocal microscope used for individual complex spectroscopy. EP is excitation pinhole, DM is dichroic mirror, MM is motorized mirror, MO is microscope objective, LP is long-pass filter, and FM is flipping mirror. APD itself and the entrance slit of the imaging spectrograph (IM SPEC) effectively comprise the detection pinholes. (b) Raster-scan image of the thin film containing single PS I complexes from *Synechocystis* PCC 6803 (red peaks) [77]. Complexes were excited with 250 nW μm^{-2} (25 W cm^{-2}) at 680 nm and fluorescence was collected at > 700 nm. $T = 10$ K. Adapted with permission from Reference 77. Copyright (2007) American Chemical Society. (*For a color version of this figure, see the color plate section.*)

magnitude higher than in NPHB experiments; (b) if the system is capable of NPHB, as is the case for various PCs, a majority of line shifts observed in SPCS in that system will be light-induced (line shifts as NPHB on a single-molecule level) [90]; and (c) the average of the multiple SPCS experiments should be compatible with sub-ensemble averages delivered by NPHB. More extensive discussion on these issues is presented in Section 4.5.

4.5 EXAMPLES

4.5.1 LH2 Antenna Complex of Purple Bacteria

LH2 has been widely studied by SHB, SPCS, and time-domain methods. As mentioned in the introduction, LH2 is a cyclic structure possessing approximate C_n symmetry, see Figure 4.3b. It contains two rings of Bchl *a* molecules, B800 and B850. The absorption spectrum of the LH2 complex is shown in Figure 4.9. The circular symmetry of the LH2 complex and small interpigment distances in the B850 ring result in strong excitonic effects. According to excitonic calculations and in

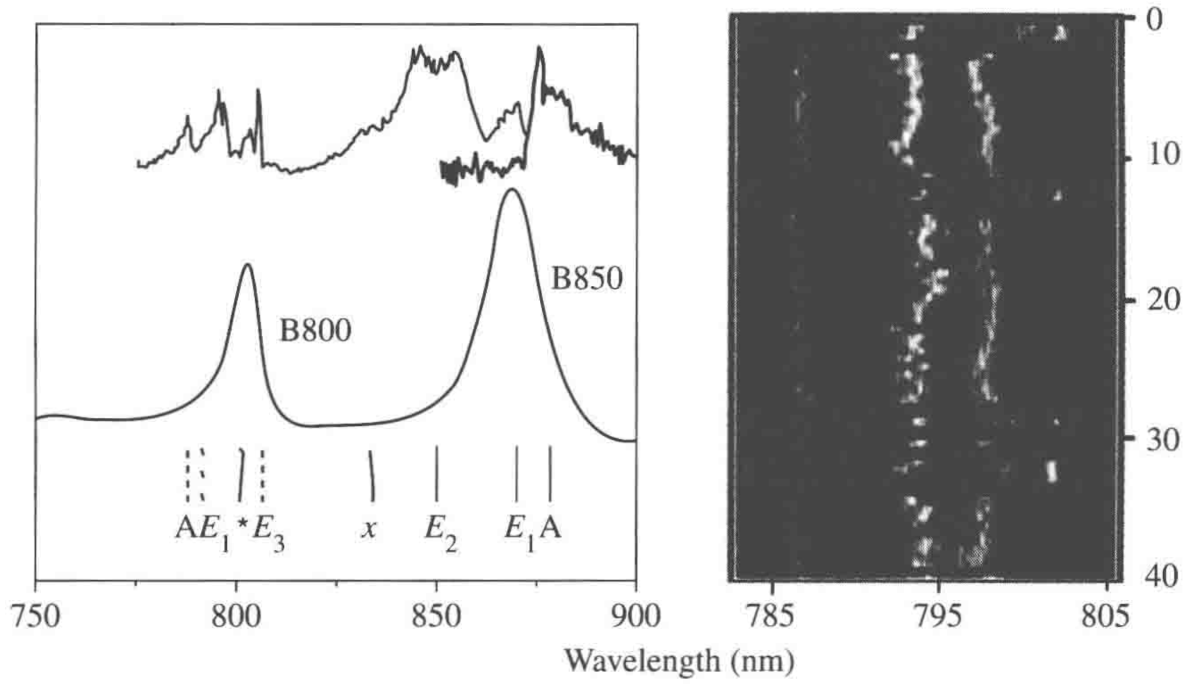

FIGURE 4.9 Left: Absorption spectrum of LH2 complex of *Rhodopseudomonas acidophila* and the scheme of excitonic levels from Reference 91. Asterisk indicates overlapping E_4 level of the lower manifold and E_2 of the upper manifold; x indicates overlapping E_3 of the lower manifold and E_4 of the upper manifold. The frame also contains a 1.5 K single-complex emission (blue) and fluorescence excitation spectra of LH2 from *Rb. acidophila.* Adapted with permission from Reference 71. Copyright (2012) American Chemical Society. Right: The B800 region of the single-complex spectra, exhibiting both small and large spectral shifts due to conformational changes involving different tiers of the protein energy landscape. Adapted with permission from Reference 66. Copyright (2004) IOP Publishing. (*For a color version of this figure, see the color plate section.*)

agreement with the experiment (see [91] and references therein), most of the oscillator strength of the B850 ring is concentrated in a doubly degenerate, second-lowest (exciton) energy level. The scheme of B850 excitonic levels from Reference 91 is presented below the absorption spectrum. In the ideal ring, the lowest energy level of the B850 (referred to as B870) is forbidden by symmetry considerations; however, due to diagonal and off-diagonal energy disorder, this level gains some oscillator strength and can be observed in spectroscopic experiments. The shape of the SDF of this state was uncovered using ZPH action spectroscopy [59, 92]. The B870 state is also visible in the satellite hole structure resulting from the excitation into the B800 band and subsequent downhill EET. Narrow line in the blue single complex emission spectrum shown in Figure 4.9 likely belongs to B870.

Another issue extensively explored for LH2 is energy transfer within the B800 ring and from B800 to B850 Chls. HB into the red edge of the B800 band, where B800→B800 EET is not present, allows one to estimate the B800→B850 EET time. The ~2 ps B800→B850 EET time has been determined by SHB [91] and early SPCS experiments [62]. Several times faster EET has been observed within the B800 band. However, the SHB-based 2 ps 5 K EET time is somewhat longer than those observed by time-domain techniques [93, 94]. One must remember that SHB is expected to preferentially probe the longer lifetime side of the EET time distribution if such a distribution is present (EET time as T_1 in Eq. 4.11 for the HB yield). Due to dispersion of donor–acceptor energy gaps in PCs in general, and in LH2 in particular, there should be a distribution of the EET times. It has been suggested that the whole B850 density of states, including the upper excitonic components (see Fig. 4.9), defines the B800-B850 EET rates [95, 96]. Very recently we have confirmed [90], using extensive HB modeling, that the evolution of the spectral holes burned into the B800 band is indeed in agreement with B800→B850 EET time distributions reported in References 95 and 96 (and not with the conventional Förster models). However, it is not clear how these results could be reconciled with results of pressure-tuning of spectral holes (and bands) [91], which suggest that B800→B850 EET time does not depend on the energy gap between the B800 and B850 bands (which is pressure-dependent), that is, it is not dependent on the positions of upper excitonic components of B850 manifold. Thus, the exact mechanism of B800→B850 EET remains elusive.

The LH2 is the pigment–protein complex which is by far the most thoroughly studied by means of SPCS (References 56, 62–74, are just a fraction of the papers devoted to SPCS in LH2). For instance, the direct observation of excitonic bands due to the strongly coupled BChls of the B850 manifold has been reported [63] (see black single-complex excitation spectrum in Figure 4.9; note the splitting of E_1 level and appreciable strength of the E_2 level due to energy disorder). This data, along with the analysis presented in Reference 64, indicates that the C_8 (or C_9) symmetry of the LH2 complex may be disturbed, that is, that these complexes could exhibit elliptical distortion. Whether this is the case in vivo, or it is an effect of a particular sample preparation procedure, is still a matter of debate, as no elliptical distortion has been observed for LH1 [88]. This issue has been revisited very recently [72], with the conclusion that SPCS, based on fluorescence detection, favors LH2 complexes with certain kinds of symmetry distortion. Polarization-sensitive measurements on the B800 band, as well as correlated shifts of several lines in the B800 spectrum, proved that even for relatively weak ($V_{1,2} \sim 25$ cm^{-1}) interactions between the B800 molecules, the respective electronic states can be significantly delocalized [66]. The fluorescence spectra of the single LH2 (as well as LH1) [87] complexes have been used to support invoking exciton self-trapping in B850 (B875 in LH1) [26, 27]. Single B800 molecule excitation spectra containing both ZPL and PSB were recently reported [67].

Spectral diffusion and underlying low temperature protein dynamics are the key subjects of the majority of recent LH2 SPCS publications [56, 65–70]. Spectral fluctuations resulting from protein dynamics at room temperature have been considered in References 73 and 74. It has been demonstrated that spectral diffusion behavior of the B800 spectral lines is in agreement with the models [41, 42], predicting the presence of several hierarchical tiers in the protein energy landscape [65, 66] (see right part of Figure 4.9). The likely distances between pigment molecules and entities experiencing conformational changes responsible for spectral shifts of various magnitudes have also been suggested [56, 69]. It remains to be seen if the reported SPCS data is statistically sufficient to serve as representative of the *typical* or *average* low temperature behavior of the LH2 protein, or if some fractions of these observations reflect the dynamics of the surrounding amorphous host or host–protein interface rather than that of the "pure/intact" LH2 proteins. Our comparison of SPCS and NPHB results (including evolution of ZPH width and NPHB anti-hole), indicates that while NPHB data is in qualitative agreement with SPCS results and the underlying multi-tier energy landscape models, quantitatively SPCS and SHB data are in disagreement [90]. The ~4.5 cm^{-1} B800 hole ($\Gamma_{\text{hom}} < 2.25$ cm^{-1}) is not broadening noticeably in several hours and definitely is not approaching the shape/width of the first cumulant distributions based on SPCS data [69] (see Figure 4.10), as would be expected if both SPCS and SHB observations reflected the same thermally induced protein dynamics. In other words, the fastest, smallest-barrier tier dynamics attributed in Reference 68 to the surface TLS [97] does not manifest in SHB data. This indicates that this smallest-barrier tier dynamics in SPCS experiments might either be sample-preparation- or amorphous host-dependent, or are characteristic for complexes favored by SPCS [72]. The important principal questions are (1) Would the line shifts observed in SPCS experiments occur anyway, whether they are observed or not; or are they, in fact, light-induced (i.e., are the NPHB on a single-molecule scale?) and (2) What is the mechanism responsible for the line shifts on a molecular level? Interestingly, temperature dependence of the shift rates observed in Reference 70 suggested both tunneling and barrier hopping were present in comparable proportions. On the other hand, our analysis of SHB results [90] indicated that for photon budgets typically used in SPCS experiments, most shifts should be light-induced, with the NPHB process obeying the model based on excited-state tunneling.

The above discussion illustrates that both SHB and SPCS provide valuable complementary information on EET and protein dynamics in LH2. In particular, SHB offers the average values serving as benchmarks in SPCS experiments, helping to determine if observed phenomena are statistically relevant features of the protein

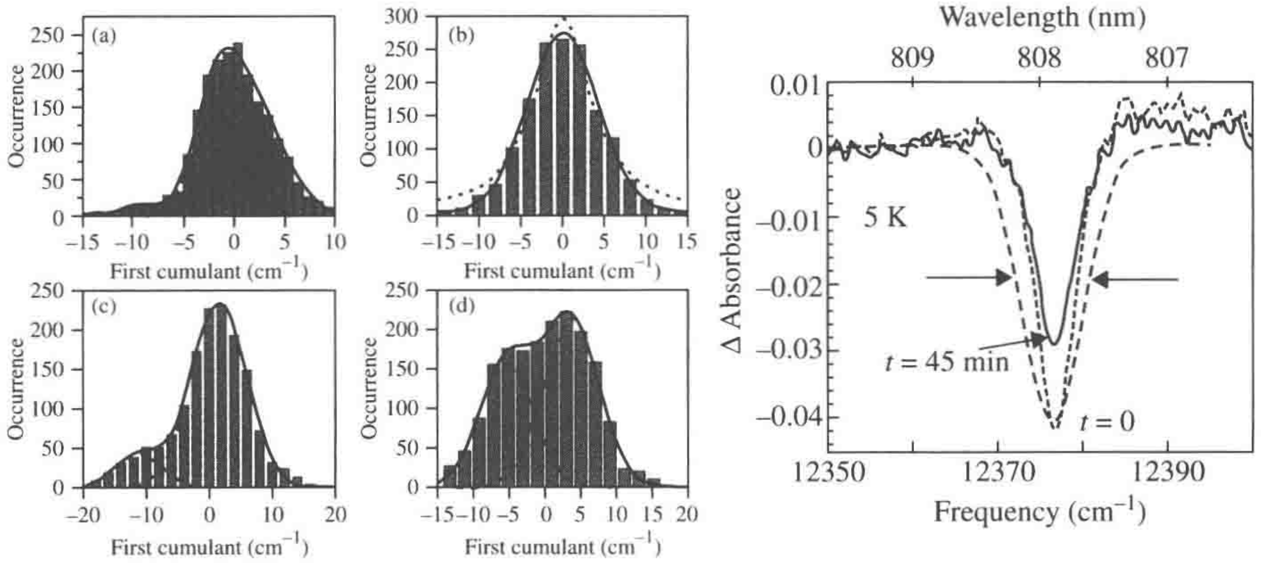

FIGURE 4.10 Left: The first cumulant distributions from [69]. Two tiers of the LH2 protein energy landscape correspond to two-tiered shift distribution. Each spectral line experiences frequent shifts about its equilibrium location, as well as infrequent shifts between different equilibrium locations. Adapted with permission from Reference 69. Copyright (2008) American Physical Society. Right: Spectral hole burnt at the red edge of the B800 band (dotted curve) does not exhibit broadening and its width (4.5 cm^{-1}) does not become comparable to the width of the first cumulant distribution (dashed line). Hole recovery is due to the white light of the FTIR spectrometer; recovery in the dark is negligible. Solid curve represents the same hole 45 minutes after burning. Adapted with permission from Reference 90. Copyright (2010) American Chemical Society.

dynamics of intact protein per se. More work is needed to resolve the questions raised above.

4.5.2 Cyanobacterial Photosystem I

As shown in Section 4.2, PS I is a quite complicated entity, with the core including almost 100 Chl *a* molecules per monomer (i.e., per P700 primary donor, see Figure 4.1B). The Q_y absorption of all these molecules is concentrated in a relatively narrow spectral region, resulting in a high degree of spectral congestion (see left frame of Fig. 4.11). Thus, most of the SHB and SPCS studies of PS I so far focused on the so-called “red antenna states,” or states absorbing lower in energy than the P700. At physiological temperatures, these low energy pigments are capable of the uphill EET to the P700, and the organism benefits from extending photosystem absorption to a broader wavelength range. While in cyanobacteria the respective pigments are part of the core antenna, in plant PS I they belong to the Lhca peripheral antenna complexes. (For recent review on structure and intersubunit EET in plant and cyanobacterial PS I, see Reference 98.) Understanding which particular chlorophylls known from structural data are responsible for the red states promises to offer insight into the functioning of the PS I antenna, to provide benchmarks for excitonic calculations, and to help determine which particular methods of theoretically calculating pigment-site energies are the most correct. The 5 K absorption spectra of PS I from *Thermosynechococcus elongatus* and *Synechocystis* PCC 6803 are presented in Figure 4.11a,

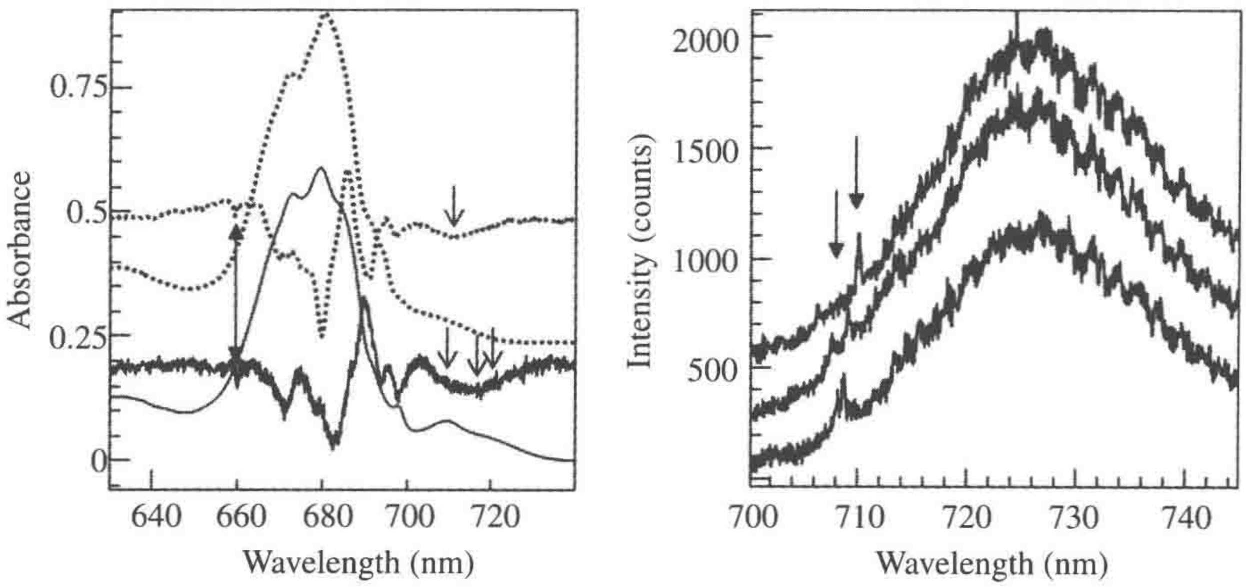

FIGURE 4.11 Left: 5 K absorption spectra of PS I from *T. elongatus* (solid line) and *Synechocystis* PCC 6803 (dotted line), along with respective satellite hole structures obtained with illumination at 660 nm (double arrow). The hole spectra were rescaled for clarity. Short arrows indicate satellite holes belonging to red states. Right: Single-complex spectra of PS I of *T. elongatus* [77]. Note shifts of the spectral lines likely belonging to the C710 state between sequentially measured spectra (arrows). The structure on the red edge of the spectrum is due to CCD etaloning. Adapted with permission from Reference 77. Copyright (2007) American Chemical Society.

along with the satellite hole structures resulting from high energy excitation (e.g., at 650 nm) [31–33, 99]. It was the careful analysis of such satellite hole structures, and their irradiation dose dependence, which first allowed the identification of two separate red states for *Synechocystis* [31, 99] and three for *T. elongatus* [32]. Existence of two (three) states has been confirmed by pressure- and Stark-SHB experiments [32, 99] as differences in pressure-induced shifts; dipole-moment change and electron-phonon coupling (S) can be utilized to distinguish between partially overlapping bands. It has been demonstrated that the lowest energy states of both cyanobacteria (C714 and C719, respectively) exhibit large values of all three of these parameters and therefore they most likely possess significant charge-transfer character.

The first PS I SPCS results were reported in Reference 75 for trimeric PS I from *T. elongatus*. The single-complex fluorescence spectra were dominated by broad structureless bands peaked at ~730 nm and resembling the bulk-emission spectra. At that time it was believed the latter emission originates from the lowest energy C719 state. This observation of broad bands in SPCS is in agreement with SHB data, demonstrating the C719 state possesses significant CT character and is characterized by very large el-ph coupling. In addition to this broad band, some narrow lines have been observed at around 710 nm, both in fluorescence and in fluorescence excitation spectra. Figure 4.11b depicts several fluorescence spectra of the single trimeric PS I from *T. elongatus* from Reference 77. For *Synechocystis* PCC 6803, the broad band peaked at ~722 nm has been observed in Reference 77 in the fluorescence spectra of single PS I complexes, in agreement with the similarity between the lowest energy states of *T. elongatus* (C719) and *Synechocystis* (C714) [30–32, 99]. Narrow lines were observed in *Synechocystis* PS I in later works [78, 81]. These narrow lines experience spectral shifts (see Figure 4.11) which are a manifestation of (likely light-induced, see previous section) spectral diffusion/protein dynamics. At about the same time, the data on PS I from *T. elongatus* with prereduced P700 were reported, including an additional emission band at 745 nm [76]. It was later demonstrated that the location of the lowest energy emission band is strongly dependent on the oxidation state of the P700 both in single-complex and bulk samples, and in several species, with oxidized P700 serving as a strong quencher of the lowest of the red states (see [83] and references therein). Thus, it currently appears likely that in *T. elongatus*, the 745 nm emission originates from the C719 state, while ~730 nm emission originates from the C715 state, with the latter state also exhibiting strong el-ph coupling, and likely being the main contributor to (shallow) ZPH observed so far by us [32] at ~720 nm. It was recognized early on that red states most likely belong to groups of strongly coupled Chls [21, 22]. However, in PS I, such groups are numerous and one cannot base such assignments on interpigment couplings alone. Assignment of the red states to various chlorophyll dimers and trimers known from the structure data is a topic of continuous lively discussions [32, 76, 79, 81, 83, 99], with suggestions based on energy transfer, protein dynamics, electron–phonon coupling, effects of monomerization, and other arguments. Currently there appears to be an agreement that the origin of the lowest energy red band is the B7-A32 dimer [32, 83]. If B31-B32-B33 trimer is the origin of either C715 or C710 state remains a matter of debate. In view of the above discussion, the narrow lines belonging to the C715 state may not be observed in SPCS experiments due to strong electron–phonon coupling rather than fast spectral diffusion, just as for the C719 state.

Very recently, low temperature SPCS studies have revealed strong anticorrelation between the fluorescence of different PSI emitters from *Synechocystis* PCC 6803 and *T. elongatus*, suggesting there may be no unique EET pathways within a given complex [82]. Rather, fluctuations of the protein environment may dynamically modify the site energies, producing multiple alternating EET pathways even at low temperatures. These results further support the idea that protein dynamics may play a critical role in the very efficient EET in light-harvesting complexes, in agreement with observations based on recent 2D-ES experiments [100].

In summary, more studies elucidating various properties of the red bands of PS I, as well as their similarities and differences between different species, are necessary. These may include, for example, studies of EET times and their distributions, spectral hole-growth kinetics, NPHB antihole shape, and hole-recovery experiments (see Section 4.5.4 for an example of application of these techniques to a simpler system, CP43), the latter accessing the distribution of the barriers in the protein energy landscape in the ground, rather than an excited, electronic state. In view of the discussion on LH2 above, one may also suggest the spectral diffusion behavior of different lowest energy states of PS I is affected not only by the supposed looseness of the respective protein pockets, but also by pigments' closeness to the protein/amorphous host interface and by the nature of that host. The final assignment should simultaneously explain the low-temperature, light-induced spectral dynamics [78–83] as well as other effects accessible by SPCS, SHB, and lower resolution techniques.

4.5.3 Plant LHC II—Single Complex Spectroscopy and Nonphotochemical Quenching

LHC II, the peripheral antenna complex of PS II, is the most abundant PC, containing about half of all Chl pigments in chloroplasts. LHC II naturally occurs in trimeric form [9]. Each monomer binds eight Chl *a* and six Chl *b* molecules, as well as four carotenoids. LHC II is responsible for both effective capturing of photons and EET toward the reaction center, and for protection against excess light and reactive oxygen species. In LHC II, these two tasks are accomplished by conformational switching between light-harvesting and dissipating states [101, 102], while in minor light-harvesting complexes of PS II (e.g., CP29), the carotenoid radical is likely formed [35, 36]. Chls in each monomeric subunit form several clusters of strongly coupled molecules, and intramonomer EET rates are fast. The rate of the intermonomeric EET is still a matter of debate. In early low temperature SPCS experiments [84], trimeric LHC II complexes usually exhibited three separate emission lines, while monomeric LHC II exhibited single emission line. This indicates that intermonomer coupling is weak. The same result was recently obtained by SHB [103]. On the other hand, in Reference 85, it has been suggested that intermonomer energy transfer is present.

Recent LHC II SPCS works were devoted to conformational switching [85, 86]. While the majority of observed single LHC II complexes exhibited a single-emission band at about 682 nm (at room temperature one is not expected to resolve three separate bands for the trimer even in the absence of intermonomer EET), a ~5% fraction of the complexes demonstrated additional longer wavelength band. The appearance, disappearance, or shifts of that additional band did not significantly affect the 682 nm band, except for intensities of the two bands being anticorrelated. Blue spectral shifts have also been observed occasionally. Figure 4.12 presents the structure of the LHC II trimer, as well as examples of SPCS results from Reference 85.

The analysis based on the Redfield theory and the disordered exciton model showed that shifts of fluorescence bands within ~670–705 nm range could be explained by changes in the realization of static disorder of the pigment site energies [17]. These changes, if light-induced, would represent higher temperature analogs of NPHB on a single-complex level. Spectral shifts beyond the above range represent the emergence of special protein conformations, with resulting excited states possessing strong CT character. Such a Chl–Chl CT state has been proposed as the key player in one of the models describing non-photochemical quenching, the high light protection mechanism (Other models are reviewed in Reference 104). However, in Reference 104 it has been proposed, based on Stark spectroscopy results, that two different emitting states are present in the dissipative state of LHC II. One of these was attributed to the CT state involving Chls 610-611-612, while the other supposedly is a Chl-carotenoid mixed-excitonic/CT state (similar to that in minor PS II antenna complexes [35, 36]).

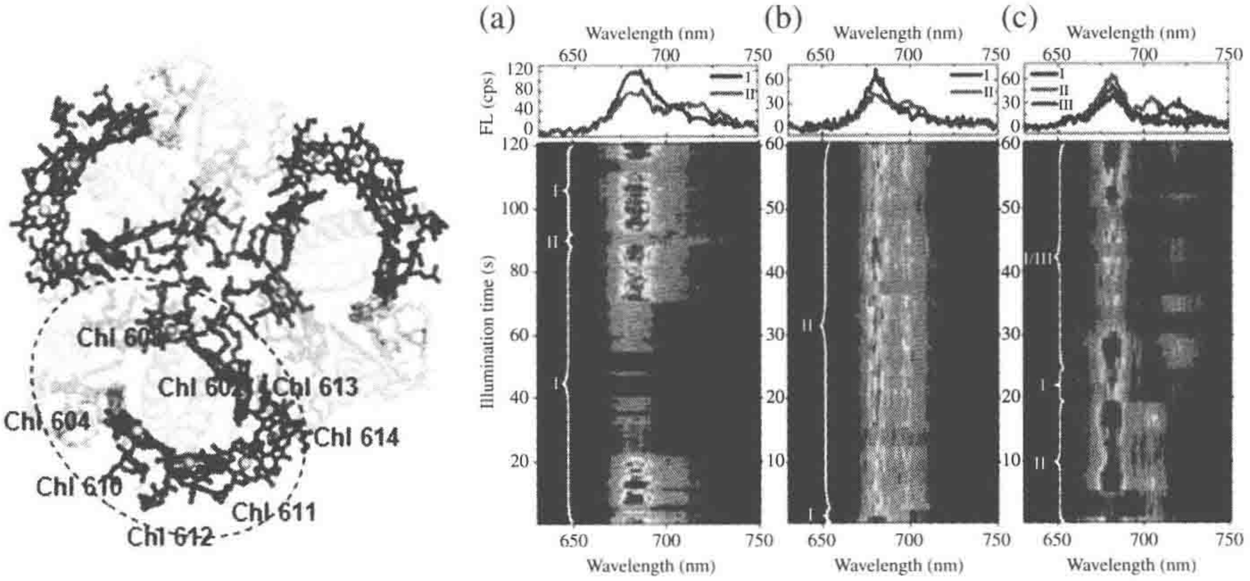

FIGURE 4.12 Left: The structure of the LHC II trimer based on Reference 9. Highlighted (groups of) pigments were considered as possible origin of the lowest energy band of LHC II. Adapted with permission from Reference 103. Copyright (2011) American Chemical Society. Right: Examples of single RT LHC II fluorescence spectra and their evolution. Adapted with permission from Reference 85. Copyright (2010) Elsevier. (*For a color version of this figure, see the color plate section.*)

4.5.4 CP43—The Protein Energy Landscape Parameters

Analysis of the results of both SHB and SPCS experiments often requires disentangling the effects due to spectral diffusion/protein dynamics from others, for example, those related to EET or CS rates (and distributions thereof, see Sections 4.5.1 and 4.5.5). Although LH2 and PS I proved to be ideal systems for low temperature SPCS research, due to the large spectral separation between absorption and emission, in some sense these complexes are too rich in various interesting physics. It is beneficial to explore protein dynamics/spectral diffusion in a simpler system, in order to gain better understanding of the protein energy landscapes alone. CP43 core antenna complex of PS II offers such an opportunity. CP43 contains just 13 Chl molecules [8]. It was extensively explored by means of optical spectroscopy and, for instance, the SDF of the lowest energy states and the electron–phonon coupling parameters are well known [103, 105–108]. It was also agreed that the lowest energy ("A") state of CP43 is likely localized on a single Chl molecule. The absorption spectrum, hole-growth kinetics (HGK), and hole-recovery (HR) data for holes burnt at 686 nm (no downhill EET), into A-band, are presented in Figure 4.13. The left frame contains the HGK data obtained for 5 K. The insert represents the absorption spectrum with the SDF of the two lowest energy states of CP43 [103, 105–108].

SHB yield ϕ (see Eq. 4.11) in CP43 does not depend on temperature up to ~12 K [43]. The HGK curves such as depicted in Figure 4.13, but for temperatures up to 12 K, result from the increase of Γ_{hom} (T) [105] alone, without change of ϕ, which proves that tunneling in the excited state of the pigment–protein system is indeed the origin of NPHB (or single-molecule line shifts, if SPCS experiments were performed

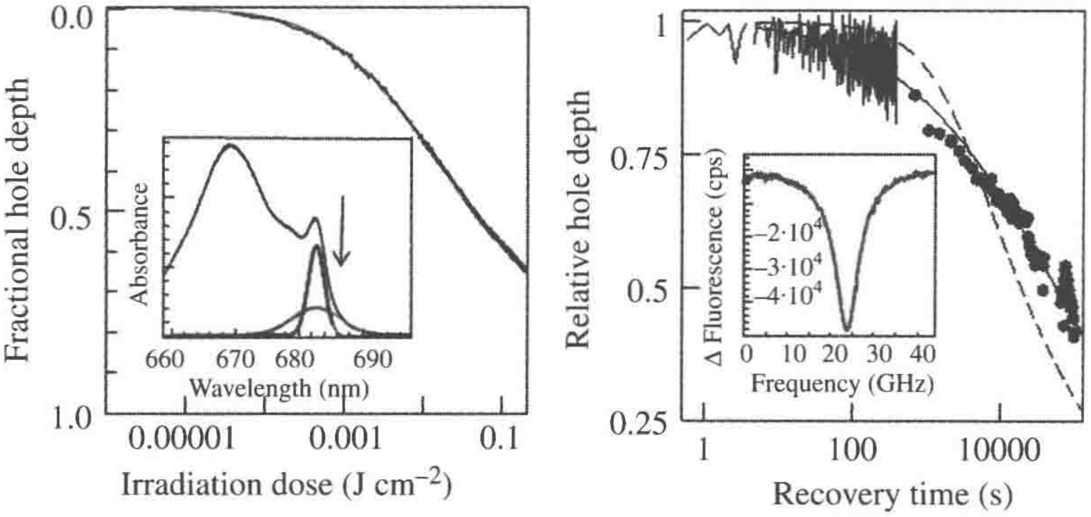

FIGURE 4.13 Left: The 5 K HGK curve and its fit, yielding the parameters of the excited-state barrier distribution; $\lambda_B = 686$ nm. The insert contains the absorption spectrum of CP43 with the SDF of the two lowest energy states, A (red) and B (blue) [105]. Right: Hole-recovery data for 20%-deep hole. Smooth solid curve (good fit to experimental data) results from modeling in Gaussian λ-distribution framework (see left frame of Fig. 4.14), while dashed curve results from modeling in uniform λ-distribution framework (see right frame of Fig. 4.14). The insert represents a sample hole spectrum. Adapted with permission from Reference 43, 103. Copyright (2011, 2012) American Chemical Society. (*For a color version of this figure, see the color plate section.*)

on CP43). The phonon-assisted tunneling rate is expected to be weakly temperature-dependent for realistic TLS asymmetry Δ (see Figure 4.7) values [109]. The latter can be estimated based on the shape of the NPHB anti-hole. From this, as well as from the hole thermocycling data, the upper limit of the md^2 parameter, characterizing the tunneling entities, was determined ($md^2 = 1\cdot10^{-46}$ kg·m^2). This indicates that the conformational changes triggered by excitation of the pigment most likely involve the lighter ones of the protein side-groups moving less than 1 Å. Proton tunneling also cannot be excluded at the moment.

Unfortunately, HGK data alone does not allow distinguishing between different λ or barrier distribution shapes, and this problem is addressed in HR experiments. The issue of the barrier distribution shape is an important one—widespread theories of low temperature amorphous solids predict and hole-recovery experiments indeed seem to indicate a $\sim1/\sqrt{V}$ ground-state barrier distribution in glasses [47,48, 51, 60, 61] (this would correspond to uniform λ-distribution), while Gaussian λ-distribution has routinely been used to model the hole-burning process [33, 57, 58, 109]. A superposition of $\sim1/\sqrt{V}$ and Gaussian terms has been deduced from hole recovery for a protein (phycobilisomes) in Reference [60]. Recently we noticed, however, that holes which are far from saturation are contributed to by sub-distributions of λ (or V), that are quantitatively, and sometimes qualitatively, different from true full λ (or V) distributions. Figure 4.14 depicts the partial λ distributions actually contributing to the holes of different depths burnt at 686 nm in CP43. Modeling shows that the shape of the sub-distributions encoded in the (non-saturated) holes is drastically different in

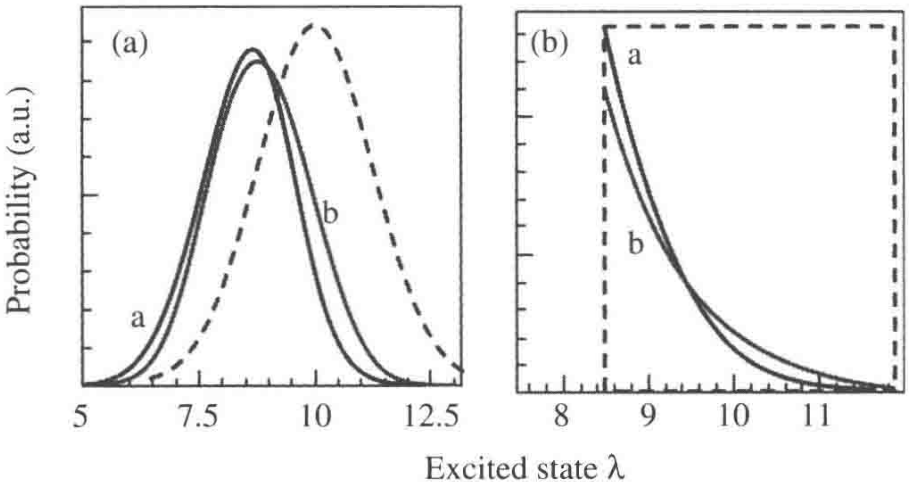

FIGURE 4.14 (a) Calculated excited-state partial λ-distributions for Gaussian true full λ-distributions [43] (black: 20%-deep hole, *a*; blue: 55%-deep hole, *b*). Areas under curves are normalized to same value. (b) Same for uniform λ-distribution. Dashed lines represent respective full true λ-distributions. Adapted with permission from Reference 43. Copyright (2012) American Chemical Society. (*For a color version of this figure, see the color plate section.*)

two cases, and Gaussian distributions lead to HR predictions more consistent with the experiment. In Figure 4.13, right frame, solid line providing better fit to experimental data originates from the Gaussian distribution model, while dashed line providing poorer fit originates from the uniform λ-distribution ($\sim 1/\sqrt{V}$) model. An important feature of this analysis is that it is actually not protein-specific, and would apply to any amorphous system, including glasses. The only condition we imposed on our modeling was that the ground-state partial barrier (or λ-) distributions have the same qualitative shape as the excited state ones, depicted in Figure 4.14. Thus, it might well be that fitting the HR data with $\sim 1/\sqrt{V}$ barrier distributions is not sufficiently justified in glasses as well, and the past success of respective fittings might be coincidental.

4.5.5 Probing Electron Transfer (ET) Times and Their Distributions in Photosynthetic RCs by SHB

In the final example of this chapter, we demonstrate how SHB can be employed to study the ET processes in photosynthetic RCs. A particular variety of SHB, called transient or triplet-bottleneck HB, is used to access fast, picosecond-timescale ET rates. Generation of transient HB spectra requires the presence of a third, relatively long-lived state. That is, the singlet excited state evolves into a triplet state or another long-lived (μs to ms range) product (e.g., a CS-state). In photosynthetic RCs, the formation of a triplet state is the result of a recombination of the original charge-separated state formed after the first couple of steps of the primary CS process. The pigment's ground state is depopulated for the lifetime of the long-lived state and the respective spectral hole can be observed, but only for the duration of this lifetime. The transient holes discussed below are acquired as the difference between the absorption spectra measured with the excitation on and off (after saturation of a persistent hole component, if any), that is, they are a result of a dynamic equilibrium.

A quite clear picture of CS processes and factors affecting rates of the primary CS steps has been achieved for BRC [110]. The primary electron donor in BRC is the strongly coupled Bchl *a* dimer (see Fig. 4.2b), and the primary CS times are of the order of ps. No significant distribution of CS times was observed; fast CS combined with extremely strong electron–phonon coupling [110] lead to negligible persistent HB in BRCs. However, the primary CS processes in the RC of PS II are not understood sufficiently. The coupling between P_{D1} and P_{D2} Chls in PS II RC (Fig. 4.2a) is weaker than the special pair coupling in BRC; in fact, couplings between most pigments in PS II RC are comparable. That led to multimer models for PS II RC [111], and to the proposal that the exact nature of the primary electron donor may vary from RC to RC due to particular realizations of disorder [112–115] in a given RC. Additionally, it is not clear if the structure and pigment–pigment and pigment–protein interactions in RC are preserved during the isolation, that is, if the isolated RC samples studied by different groups correctly represent the RCs inside the intact PS II core (Fig. 4.2a) [114–116].

An example of resonant transient HB spectra (0.5 cm^{-1} resolution) obtained for PS II RC of *Chlamydomonas reinhardtii* (from [114]) is shown in Figure 4.15a. These transient holes are obtained with λ_B = 682.0 (green curve a), 684.0 (red curve b), 686.0 (brown curve c), and 688.0 nm (blue spectrum d). Curves (a) and (b) possess prominent ZPH. Curve (c) reveals an extremely weak ZPH, as indicated by the brown arrow. The ZPH widths, which varied from 2.4 to 7.6 cm^{-1} at 682 nm, depending on illumination dose, are believed to reflect a distribution of CS time (τ_{CS}). The

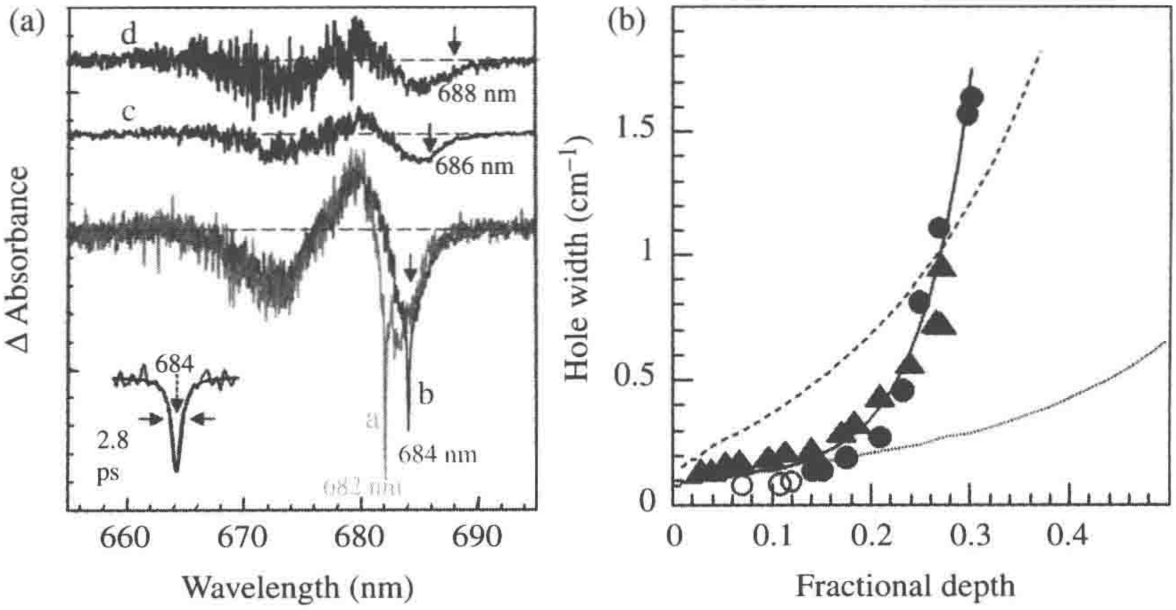

FIGURE 4.15 (a) Resonant transient HB spectra for *Chlamydomonas reinhardtii*; spectra a, b, c, and d were obtained with λ_B of 682.0, 684.0, 686.0, and 688.0 nm, respectively. Adapted with permission from Reference 114. Copyright (2012) American Chemical Society. The inset corresponds to the Lorentzian fit (black curve) of ZPH of curve b. (b) Persistent hole width versus depth data for λ_B = 686 nm (circles) and 680 nm (triangles) obtained for isolated PS II RC from spinach, and modeling results with the CS time distribution (dashed curve), without any distribution (dotted curve), and with best distribution (solid curve, see text for details). Adapted with permission from Reference 108. Copyright (2011) American Chemical Society. (*For a color version of this figure, see the color plate section.*)

ZPH widths shown in Figure 4.15a correspond to τ_{CS} in the range of 1.4–4.4 ps, in agreement with previous data obtained for primary CS in spinach RCs ([116, 117] and references therein). The presence of a distribution of τ_{CS} is consistent with data obtained by 2D ES for spinach RCs at 77 K [118], and with earlier photon echo and modeling data [117]. It has been suggested, based on time-domain data, that two CS pathways are active in PSII RCs, namely P_{D1} and/or Chl_{D1} CS path, according to the nature of the primary electron donor [112, 113]. It was suggested the P_{D1} path is dominant for longer wavelengths and is characterized by sub-picosecond CS times, while the Chl_{D1} CS path corresponds to longer CS times. The depicted HB results are in agreement with this picture. Note the ZPHs are nearly absent at $\lambda_B = 686$ nm and entirely absent at 688.0 nm and longer wavelengths, suggesting that excited states of cofactors are strongly coupled with the CT state(s) lying in the long-wavelength region [113]. This assignment is in agreement with [119] where it was shown that excitation at wavelengths as long as 695.0 nm ($T = 1.7$ K) can induce Q_A^- formation in PS II cores.

It was suggested long ago that the distribution of CS rates in PS II RC might be very broad, with the longest CS times reaching nanosecond range [117]. The 2D-ES [118] did not explore the latter range of CS times, as their analysis included only a single 2-ns exponent in this range, which could as well be assigned to fluorescence lifetime. In Reference 112 it was argued that for a fraction of RCs, the low temperature CS times are slow for both P_{D1} and Chl_{D1} CS paths. The slow CS is most effectively probed by persistent HB. In Reference 116, we suggested that persistent and transient HB probe slow and fast ends, respectively, of the CS time distribution. The transient holes in Reference 116 were in reasonable agreement with the fast end of the CS time distribution of Reference 117. Recently we explored the slow end of the CS time distribution for PS II RC from spinach [108]. Figure 4.15b depicts the dependences of persistent hole width on (fractional) hole depth for $\lambda_B = 686$ nm (circles) and $\lambda_B = 680$ nm (triangles), and results of modeling for no CS time distribution (dotted line), CS time distribution from Reference 117 (dashed line); and a distribution containing ~40% of slow (hundreds of ps) CS times and 60% of fast (sub-distribution centered on 1.5 ps) CS times, solid line, with the latter distribution obviously providing better fit to the experimental data. Interestingly, the SHB results are incompatible with significant contribution of the intermediate, tens of ps, times to the distribution [118].

4.6 CONCLUSIONS

Due to space limitation, this chapter did not touch many interesting issues/phenomena related to biophotonics of photosynthesis. However, our main objective was to make the reader aware and appreciative of the potential of SHB and SPCS, and the intricacies of protein structure(s) and complexity of EET and CS processes ultimately responsible for sustaining life on Earth. We anticipate application of information-rich techniques briefly discussed in the chapter, that is, SPCS, SHB, FLN, and ΔFLN, will continue to unravel the rich physics underlying the excitonic structure and various dynamic processes in these important biological systems. Resonant (persistent) holes burned into the lowest energy state of various RCs and antenna pigment complexes (and their modeling), as well as nonresonant hole-burning, should continue to provide information on spectral diffusion and interactions of pigments within the protein environment. That is, SHB and SPCS can offer complementary information on protein motion in conformational phase space and on the distributions of the barriers on protein energy landscapes. We have also illustrated how transient HB spectra can provide CS rates in photosynthetic RCs. Advanced descriptions of various optical spectra, more accurately reflecting the influences of el-ph coupling, lifetime broadening, and coupling to vibrational modes, as well as experimentally determined spectral density profiles, are desired to further advance application of frequency-domain techniques in the area of photosynthesis research.

ACKNOWLEDGMENTS

Authors would like to thank our long-time collaborators, as well as graduate students and postdoctoral fellows. V.Z. acknowledges support from NSERC and CFI. RJ acknowledges support from the Division of Chemical Sciences, Geosciences, and Biosciences, Office of Basic Energy Sciences of the U.S. Department of Energy; grant DE-FG02-11ER16281.

REFERENCES

[1] H. T. Witt, A. Müller, and B. Rumberg, "Electron-transport system in photosynthesis of green plants analysed by sensitive flash photometry," *Nature* **197**, 987–991 (1963).

[2] R. E. Blankenship, *Molecular Mechanisms of Photosynthesis* (Blackwell Science Ltd, London, 2008).

[3] Y. Umena, K. Kawakami, J.-R. Shen, and N. Kamiya, "Crystal structure of oxygen-evolving photosystem II at a resolution of 1.9 Å," *Nature* **473** 55–60 (2011).

[4] A. Amunts, H. Toporik, A. Borovikova, and N. Nelson, "Structure determination and improved model of plant photosystem I," *J. Biol. Chem.* **285**, 3478–3486 (2010).

[5] A. Camara-Artigas, D. Brune, and J. P. Allen, "Interactions between lipids and bacterial reaction centers determined by protein crystallography," *Proc. Natl. Acad. Sci. USA* **99**, 11055–11060 (2002).

[6] V. Cherezov, J. Clogston, M. Z. Papiz, and M. Caffrey, "Room to move: crystallizing membrane proteins in swollen lipidic mesophases," *J. Mol. Biol.* **357**, 1605–1618 (2006).

[7] P. Jordan, P. Fromme, H. T. Witt, O. Klukas, W. Saenger, and N. Krauβ, "Three-dimensional structure of cyanobacterial photosystem I at 2.5 Å resolution," *Nature* **411**, 909–917 (2001).

[8] B. Loll, J. Kern, W. Saenger, A. Zouni, and J. Biesiadka, "Towards complete cofactor arrangement in the 3.0 Å resolution structure of photosystem II," *Nature* **438**, 1040–1044 (2005).

[9] J. Standfuss, A. C. Terwisscha van Scheltinga, M. Lamborghini, and W. Kuehlbrandt, "Mechanisms of photoprotection and nonphotochemical quenching in pea light-harvesting complex at 2.5 Å resolution," *EMBO J.* **24**, 919–928 (2005).

[10] A. W. Roszak, T. D. Howard, J. Southall, A. T. Gardiner, C. J. Law, N. W. Isaacs, and R. J Cogdell, "Crystal structure of the RC-LH1 core complex from *Rhodopseudomonas palustris*," *Science* **302**, 1969–1972 (2003).

[11] R. Jankowiak, M. Reppert, V. Zazubovich, J. Pieper, and T. Reinot, "Site selective and single complex laser-based spectroscopies: a window on excited state electronic structure, excitation energy transfer, and electron-phonon coupling of selected photosynthetic complexes," *Chem. Rev.* **111**, 4546–4598 (2011).

[12] H. van Amerongen, L. Valkunas, and R. van Grondelle, *Photosynthetic Excitons* (World Scientific, Singapore, 2000).

[13] D. Abramavicius and S. Mukamel, "Energy-transfer and charge-separation pathways in the reaction center of photosystem II revealed by coherent two-dimensional optical spectroscopy," *J. Chem. Phys.* **113**, 184501 (2010).

[14] M. Cho, "Coherent two-dimensional optical spectroscopy," *Chem. Rev.* **108**, 1331–1418 (2008).

[15] T. Brixner, J. Stenger, H. M. Vaswani, M. Cho, R. E. Blankenship, and G. R. Fleming, "Two-dimensional spectroscopy of electronic couplings in photosynthesis," *Nature* **434**, 625–628 (2005).

[16] J. Barber, "Photosystem II: the engine of life," *Q. Rev. Biophys.* **36**, 71–89 (2003).

[17] V. I. Novoderezhkin and R. van Grondelle, "Physical origins and models of energy transfer in photosynthetic light-harvesting," *Phys. Chem. Chem. Phys.* **12**, 7352–7365 (2010).

[18] R. van Grondelle and V. I. Novoderezhkin, "Energy transfer in photosynthesis: experimental insights and quantitative models," *Phys. Chem. Chem. Phys.* **8**, 793–807 (2006).

[19] T. Renger and E. Schlodder, "Primary photophysical processes in photosystem II: bridging the gap between crystal structure and optical spectra," *Chem. Phys. Chem.* **11**, 1141–1153 (2010).

[20] A. S. Davydov, *Theory of Molecular Excitons* (Plenum, New York, 1971).

[21] A. Damjanovic, H. M. Vaswani, P. Fromme and G. R. Fleming, "Chlorophyll excitations in photosystem I of *Synechococcus elongatus*," *J. Phys. Chem. B* **106**, 10251–10262 (2002).

[22] M. Byrdin, P. Jordan, N. Krauβ, P. Fromme, D. Stehlik and E. Schlodder, "Light harvesting in photosystem I: modeling based on the 2.5-Å structure of photosystem I from synechococcus elongatus," *Biophys. J.* **83**, 433–457 (2002).

[23] M. Reppert, K. Acharya, B. Neupane, and R. Jankowiak, "On the unusual temperature-dependent emission of the CP47 antenna protein complex of photosystem II," *J. Phys. Chem. Lett.* **1**, 2310–2315 (2010).

[24] G. Raszewski and T. Renger, "Light harvesting in photosystem II core complexes is limited by the transfer to the trap: can the core complex turn into a photoprotective mode?", *J. Am. Chem. Soc.* **130**, 4431 (2008).

[25] T Förster, "Intermolecular energy migration and fluorescence," *Ann. Phys.* **2**, 55–75 (1984).

[26] A. Freiberg, M. Rätsep, K. Timpmann, G. Trinkunas and N. W. Woodbury, "Self-trapped excitons in LH2 antenna complexes between 5 K and ambient temperature," *J. Phys. Chem. B* **107**, 11510–11519 (2003).

[27] K. Timpmann, M. Rätsep, C. N. Hunter and A. Freiberg, "Emitting excitonic polaron states in core LH1 and peripheral LH2 bacterial light-harvesting complexes," *J. Phys. Chem. B* **108**, 10581–10588 (2004).

[28] J. Pieper, M. Rätsep, K.-D. Irrgang and A. Freiberg, "Chromophore-chromophore and chromophore-protein interactions in monomeric light-harvesting complex II of green plants studied by spectral hole burning and fluorescence line narrowing," *J. Phys. Chem. B* **113**, 10870–10880 (2009).

[29] M. Rätsep, J. Pieper, K.-D. Irrgang and A. Freiberg, "Excitation wavelength-dependent electron-phonon and electron-vibrational coupling in the CP29 antenna complex of green plants," *J. Phys. Chem. B* **112**, 110–118 (2008).

[30] M. Reppert, V. Naibo and R. Jankowiak, "Accurate modeling of fluorescence line narrowing difference spectra: direct measurement of the single-site fluorescence spectrum," *J. Chem. Phys.* **133**, 014506 (2010).

[31] J. M. Hayes, S. Matsuzaki, M. Rätsep and G. J. Small, "Red chlorophyll a antenna states of photosystem I of the cyanobacterium *Synechocystis* sp. PCC 6803," *J. Phys. Chem. B* **104**, 5625–5633 (2000).

[32] V. Zazubovich, S. Matsuzaki, T. W. Johnson, J. M. Hayes, P. R. Chitnis and G. J. Small, "Red antenna states of photosystem I from cyanobacterium *Synechococcus elongatus*: a spectral hole burning study," *Chem. Phys.* **275**, 47–59 (2002).

[33] T. Reinot, V. Zazubovich, J. M. Hayes, and G. J Small, "New insights on persistent nonphotochemical hole burning and its application to photosynthetic complexes," *J. Phys. Chem. B* **105**, 5083–5098 (2001).

[34] D. A. Dexter, "Theory of sensitized luminescence in solids," *J. Chem. Phys.* **21**, 836–851 (1953).

[35] N. E. Holt, D. Zigmantas, L. Valkunas, X. P. Li, K. K. Niyogi and G. R. Fleming, "Carotenoid cation formation and the regulation of photosynthetic light harvesting," *Science* **307**, 433–436 (2005).

[36] T. K. Ahn, T. J. Avenson, M. Ballottari, Y. C. Cheng, K. K. Niyogi, R. Bassi, and G. R. Fleming, "Architecture of a charge-transfer state regulating light harvesting in a plant antenna protein," *Science* **320**, 794–797 (2008).

[37] G. S. Engel, T. R. Calhoun, E. L. Read, T.-K. Ahn, T. Mančal, Y.-C. Cheng, R. E. Blankenship and G. R. Fleming, "Evidence for wavelike energy transfer through quantum coherence in photosynthetic systems," *Nature* **446**, 782–786 (2007).

[38] G. D. Scholes, "Quantum-coherent electronic energy transfer: did nature think of it first? *J. Phys. Chem. Lett.* **1**, 2–8 (2010).

[39] K. K. Rebane, *Impurity Spectra of Solids* (Plenum, New York, 1970).

[40] J. M. Hayes, J. K. Gillie, D. Tang, and G. J. Small, "Theory for spectral hole burning of the primary electron donor state of photosynthetic reaction centers," *Biochim. Biophys. Acta* **932**, 287–305 (1988).

[41] H. Frauenfelder, S. G. Sligar, and P. G. Wolynes, "The energy landscapes and motions of proteins," *Science* **254**, 1598–1603 (1991).

[42] P. W. Fenimore, H. Frauenfelder, B. H. McMahon, and R. D. Young, "Proteins are paradigms of stochastic complexity," *Physica A* **351**, 1–13 (2005).

[43] M. Najafi, N. Herascu, M. Seibert, R. Picorel, R. Jankowiak, and V. Zazubovich, "Spectral hole burning, recovery, and thermocycling in chlorophyll-protein complexes:

distributions of barriers on the protein energy landscape," *J. Phys. Chem. B* **116**, 11780–11790 (2012).

[44] P. W. Anderson, B. I. Halperin, and C. M. Varma, "Anomalous low-temperature thermal properties of glasses and spin glasses," *Phil. Mag.* **25**, 1–9 (1972).

[45] W. A. Phillips, "Tunneling states in amorphous solids," *J. Low. Temp. Phys.* **7**, 351–360 (1972).

[46] R. Jankowiak and G. J Small, "Hole-burning spectroscopy and relaxation dynamics of amorphous solids at low temperatures," *Science* **237**, 618–625 (1987).

[47] J. Zollfrank, J. Friedrich, J. M. Vanderkooi, and J. Fidy, "Conformational relaxation of a low-temperature protein as probed by photochemical hole burning: horseradish peroxidase," *Biophys. J.* **59**, 305–312 (1991).

[48] K. Fritsch, J. Friedrich, F. Parak, and J. L. Skinner, "Spectral diffusion and the energy landscape of a protein," *Proc. Natl. Acad. Sci. USA* **93**, 15141–15145 (1996).

[49] W. E. Moerner, *Topics in Current Physics, Persistent Spectral Hole Burning: Science and Applications* (Springer, New York, 1987), Vol. 44.

[50] R. Jankowiak, J. M. Hayes, and G. J Small, "Spectral hole-burning spectroscopy in amorphous molecular solids and proteins," *Chem. Rev.* **93**, 1471–1502 (1993).

[51] Y. Berlin, A. Burin, J. Friedrich, and J. Köhler, "Spectroscopy of proteins at low temperature. Part I: experiments with molecular ensembles," *Phys. Life Rev.* **3**, 262–292 (2006).

[52] R. Purchase and S. Völker, "Spectral hole burning: examples from photosynthesis," *Photosynth. Res.* **101**, 245–266 (2009).

[53] R. I. Personov, E. I. Al'shitz, and L. A. Bykovskaya, "The effect of fine structure appearance in laser-excited fluorescence spectra of organic compounds in solid solutions," *Opt. Commun.* **6**, 169–173, (1972).

[54] W. E. Moerner and D. P. Fromm, "Methods of single-molecule fluorescence spectroscopy and microscopy," *Rev. Sci. Inst.* **74**, 3597–3619 (2003).

[55] F. Kulzer and M. Orrit, "Single-molecule optics," *Ann. Rev. Phys. Chem.* **55**, 585–611 (2004).

[56] Y. Berlin, A. Burin, J. Friedrich, and J. Köhler, "Low temperature spectroscopy of proteins. Part II: experiments with single protein complexes," *Phys. Life Rev.* **4**, 64–89 (2007).

[57] L. Shu and G. J. Small, "Mechanism of nonphotochemical hole burning: cresyl violet in polyvinyl alcohol films," *J. Opt. Soc. Am. B* **9**, 724–731 (1992).

[58] T. Reinot, N. C. Dang, and G. J. Small, "A model for persistent hole burned spectra and hole growth kinetics that includes photoproduct absorption: application to free base phthalocyanine in hyperquenched glassy ortho-dichlorobenzene at 5 K," *J. Chem. Phys.* **119**, 10404–10414 (2003).

[59] H.-M. Wu, M. Rätsep, I.-J. Lee, R. J. Cogdell, and G. J. Small, "Exciton level structure and energy disorder of the B850 ring of the LH2 antenna complex," *J. Phys. Chem. B* **101**, 7654–7663 (1997).

[60] W. Köhler, W. Friedrich, and H. Scheer, "Conformational barriers in low-temperature proteins and glasses," *Phys. Rev. A* **37**, 660–662 (1988).

[61] W. Köhler, J. Zollfrank, and J. Friedrich, "Thermal Irreversibility of optically labeled low-temperature glasses," *Phys. Rev. B.* **39**, 5414–5424 (1989).

[62] A. M. van Oijen, M. Ketelaars, J. Köhler, T. J. Aartsma, and J. Schmidt, "Spectroscopy of individual light-harvesting 2 complexes of *Rhodopseudomonas acidophila*: diagonal disorder, intercomplex heterogeneity, spectral diffusion, and energy transfer in the B800 band," *Biophys. J.* **78**, 1570–1577 (2000).

[63] M. Ketelaars, A. M. van Oijen, M. Matsushita, J. Köhler, J. Schmidt, and T. J. Aartsma, "Spectroscopy on the B850 band of individual light-harvesting 2 complexes of *Rhodopseudomonas acidophila*. I. experiments and Monte Carlo simulations," *Biophys. J.* **80**, 1591–1603 (2001).

[64] M. Matsushita, M. Ketelaars, A. M. van Oijen, J. Köhler, T. J. Aartsma, and J. Schmidt, "Spectroscopy on the B850 band of individual light-harvesting 2 complexes of *Rhodopseudomonas acidophila*. II. Exciton states of an elliptically deformed ring aggregate.," *Biophys. J.* **80**, 1604–1614 (2001).

[65] C. Hofmann, T. J. Aartsma, H. Michel, and J. Köhler, "Direct observation of tiers in the energy landscape of a chromoprotein: A single-molecule study," *Proc. Natl. Acad. Sci. USA* **100**, 15534–15538 (2003).

[66] C. Hofmann, T. J. Aartsma, H. Michel, and J. Köhler, "Spectral dynamics in the B800 band of LH2 from *Rhodospirillum molischianum*: a single-molecule study," *New J. Phys.* **6**, 8–15 (2004).

[67] C. Hofmann, H. Michel, M. van Heel, and J. Köhler, "Multivariate analysis of single-molecule spectra: surpassing spectral diffusion," *Phys. Rev. Lett.* **94**, 195501 (2005).

[68] J. Baier, M. F. Richter, R. J. Cogdell, S. Oellerich, and J. Köhler, "Do proteins at low temperature behave as glasses? A single-molecule study," *J. Phys. Chem. B* **111**, 1135–1138 (2007).

[69] J. Baier, M. F. Richter, R. J. Cogdell, S. Oellerich, and J. Köhler, "Determination of the spectral diffusion kernel of a protein by single-molecule spectroscopy," *Phys. Rev. Lett.* **100**, 018108 (2008).

[70] H. Oikawa, S. Fujiyoshi, T. Dewa, M. Nango, and M. Matsushita, "How deep is the potential well confining a protein in a specific conformation? A single-molecule study on temperature dependence of conformational change between 5 and 18 K," *J. Am. Chem. Soc.* **130**, 4580–4581 (2008).

[71] R. Kunz, K. Timpmann, J. Southall, R. J. Cogdell, A. Freiberg, and J. Köhler, "Exciton self trapping in photosynthetic pigment−protein complexes studied by single-molecule spectroscopy, *J. Phys. Chem. B* **116**, 11017−11023 (2012).

[72] S. Jang, R. J. Silbey, R. Kunz, C. Hofmann, and J. Köhler, "Is there elliptic distortion in the light harvesting complex 2 of purple bacteria?" *J. Phys. Chem. B* **115**, 12947–12953 (2011).

[73] V. I. Novoderezhkin, D. Rutkauskas, and R. van Grondelle, "Dynamics of the emission spectrum of a single LH2 complex: interplay of slow and fast nuclear motions," *Biophys. J.* **90**, 2890–2902 (2006).

[74] J. Janusonis, L. Valkunas, D. Rutkauskas, and R. van Grondelle, "Spectral dynamics of individual bacterial light-harvesting complexes: alternative disorder model," *Biophys. J.* **94**, 1348–1358 (2008).

[75] F. Jelezko, C. Tietz, U. Gerken, J. Wrachtrup, and R. Bittl, "Single-molecule spectroscopy on photosystem I pigment−protein complexes, *J. Phys. Chem. B* **104**, 8093–8096 (2000).

[76] A. F. Elli, F. Jelezko, C. Tietz, H. Studier, M. Brecht, R. Bittl, and J. Wrachtrup, "Red pool chlorophylls of photosystem I of the cyanobacterium *Thermosynechococcus elongatus*: a single-molecule study," *Biochemistry* **45**, 1454–1458 (2006).

[77] K. J. Riley, T. Reinot, R. Jankowiak, P. Fromme, and V. Zazubovich, "Red antenna states of photosystem I from cyanobacteria *Synechocystis* PCC 6803 and *Thermosynechococcus elongatus*: single-complex spectroscopy and spectral hole burning study," *J. Phys. Chem. B* **111**, 286–292 (2007).

[78] M. Brecht, H. Studier, A. F. Elli, F. Jelezko, and R. Bittl, "Assignment of red antenna states in photosystem I from *Thermosynechoccocus elongatus* by single-molecule spectroscopy," *Biochemistry* **46**, 799–806 (2007).

[79] M. Brecht, J. B. Nieder, H. Studier, E. Schlodder, and R. Bittl, "Red antenna states of photosystem I from *Synechococcus* sp. PCC 7002," *Photosynth. Res.* **95**, 155–162 (2008).

[80] M. Brecht, H. Studier, V. Radics, J. B. Nieder, and R. Bittl, "Spectral diffusion induced by proton dynamics in pigment-protein complexes," *J. Am. Chem. Soc.* **130**, 17487–17493 (2008).

[81] M. Brecht, V. Radics, J. B. Nieder, H. Studier, and R. Bittl, "Red antenna states of photosystem I from *Synechocystis* PCC 6803," *Biochemistry* **47**, 5536–5543 (2008).

[82] M. Brecht, V. Radics, J. B. Nieder, and R. Bittl, "Protein dynamics-induced variation of excitation energy transfer pathways," *Proc. Natl. Acad. Sci. USA* **106**, 11857–11861 (2009).

[83] E. Schlodder, M. Hussels, M. Cetin, N. V. Karapetyan, and M. Brecht, "Fluorescence of the various red antenna states in photosystem I complexes from cyanobacteria is affected differently by the redox state of P700," *Biochim. Biophys. Acta* **1807**, 1423–1431 (2011).

[84] C. Tietz, F. Jelezko, U. Gerken, S. Schuler, A. Schubert, H. Rogl, and J. Wrachtrup, "Single molecule spectroscopy of the light-harvesting complex II of higher plants," *Biophys. J.* **81**, 556–562 (2001).

[85] T. P. J. Krüger, V. I. Novoderezhkin, C. Ilioaia, and R. van Grondelle, "Fluorescence spectral dynamics of single LHCII trimers," *Biophys. J.* **98**, 3093–3101 (2010).

[86] T. P. J. Krüger, E. Wientjes, R. Croce, and R. van Grondelle, "Conformational switching explains the intrinsic multifunctionality of plant light-harvesting complexes," *Proc. Natl. Acad. Sci. USA* **108**, 13516–13521 (2011).

[87] M. Ketelaars, C. Hofmann, J. Köhler, T. D. Howard, R. J. Cogdell, J. Schmidt, and T. J. Aartsma, "Spectroscopy on individual light-harvesting 1 complexes of *Rhodopseudomonas acidophila*," *Biophys. J.* **83**, 1701–1715 (2002).

[88] U. Gerken, F. Jelezko, B. Goltze, M. Branschädel, C. Tietz, R. Ghosh, and J. Wrachtrup, "Membrane environment reduces the accessible conformational space available to an integral membrane protein," *J. Phys. Chem. B* **107**, 338–343 (2003).

[89] Y. Saga and H. Tamiaki, "Fluorescence spectroscopy of single photosynthetic light-harvesting supramolecular systems," *Cell Biochem. Biophys.* **40**, 149–165 (2004).

[90] D. Grozdanov, N. Herascu, T. Reinot, R. Jankowiak, and V. Zazubovich, "Low-temperature protein dynamics of the B800 molecules in the LH2 light-harvesting complex: spectral hole burning study and comparison with single photosynthetic complex spectroscopy," *J. Phys. Chem. B* **114**, 3426–3438 (2010).

[91] V. Zazubovich, R. Jankowiak, and G. J. Small, "A high-pressure spectral hole burning study of correlation between energy disorder and excitonic couplings in the LH2

Complex from *Rhodopseudomonas acidophila*" *J. Phys. Chem. B* **106**, 6802–6814 (2002).

[92] H.-M. Wu, N. R. S. Reddy, and G. J. Small, "Direct observation and hole burning of the lowest exciton level (B870) of the LH2 antenna complex of *Rhodopseudomonas acidophila* (Strain 10050)," *J. Phys. Chem. B* **101**, 651–656 (1997).

[93] H.-M. Wu, S. Savikhin, N. R. S. Reddy, R. Jankowiak, R. J. Cogdell, W. S. Struve, and G. J. Small, "Femtosecond and hole-burning studies of B800's excitation energy relaxation dynamics in the LH2 antenna complex of *Rhodopseudomonas acidophila* (Strain 10050)," *J. Phys. Chem.* **100**, 12022–12033 (1996).

[94] T. Pullerits, S. Hess, J. L. Herek, and V. Sundström, "Temperature dependence of excitation transfer in LH2 of *Rhodobacter sphaeroides*," *J. Phys. Chem. B* **101**, 10560–10567 (1997).

[95] G. D. Scholes and G. R. Fleming, "On the mechanism of light harvesting in photosynthetic purple bacteria: B800 to B850 energy transfer," *J. Phys. Chem. B* **104**, 1854–1868 (2000).

[96] S. Jang, M. D. Newton, and R. J. Silbey, "Multichromophoric förster resonance energy transfer," *Phys. Rev. Lett.* **92**, 218301 (2004).

[97] A. Heuer and P. Neu, "Tunneling dynamics of side chains and defects in proteins, polymer glasses, and OH-doped network glasses," *J. Chem. Phys.* **107**, 8686–8696 (1997).

[98] M. K. Sener, C. Jolley, A. Ben-Shem, P. Fromme, N. Nelson, R. Croce, and K. Schulten, "Comparison of the light-harvesting networks of plant and cyanobacterial I photosystem," *Biophys. J.* **89**, 1630–1642 (2005).

[99] M. Rätsep, T. W. Johnson, P. R. Chitnis, and G. J. Small, "The red-absorbing chlorophyll a antenna states of photosystem I: a hole-burning study of *Synechocystis* sp. PCC 6803 and its mutants," *J. Phys. Chem. B* **104**, 836–847 (2000).

[100] H. Lee, Y.-C. Cheng, and G. R. Fleming, "Coherence dynamics in photosynthesis: protein protection of excitonic coherence," *Science* **316**, 1462–1465 (2007).

[101] A. A. Pascal, Z. Liu, K. Broess, B. van Oort, H. van Amerongen, C. Wang, P. Horton, B. Robert, W. Chang, and A. V. Ruban, "Molecular basis of photoprotection and control of photosynthetic light-harvesting," *Nature* **436**, 134–137 (2005).

[102] A. V. Ruban, R. Berera, C. Ilioaia, I. H. M. van Stokkum, J. T. M. Kennis, A. A. Pascal, H. van Amerongen, B. Robert, P. Horton, and R. van Grondelle, "Identification of a mechanism of photoprotective energy dissipation in higher plants," *Nature* **450**, 575–578 (2007).

[103] N. Herascu, M. Najafi, A. Amunts, J. Pieper, K.-D. Irrgang, R. Picorel, M. Seibert, and V. Zazubovich, "Parameters of the protein energy landscapes of several light-harvesting complexes probed via spectral hole growth kinetics measurements," *J. Phys. Chem. B* **115**, 2737–2747 (2011).

[104] M. Wahadoszamen, R. Berera, A. M. Ara, E. Romero, and R. van Grondelle, "Identification of two emitting sites in the dissipative state of the major light harvesting antenna," *Phys. Chem. Chem. Phys.* **14**, 759–766 (2012).

[105] R. Jankowiak, V. Zazubovich, M. Rätsep, S. Matsuzaki, M. Alfonso, R. Picorel, M. Seibert, and G. J. Small, "The CP43 core antenna complex of photosystem II possesses two quasi-degenerate and weakly coupled Q_y-trap states," *J. Phys. Chem. B* **104**, 11805–11815 (2000).

[106] N. C. Dang, V. Zazubovich, M. Reppert, B. Neupane, R. Picorel, M. Seibert, and R. Jankowiak, "The CP43 proximal antenna complex of higher plant photosystem II revisited: modeling and hole burning study. I," *J. Phys. Chem. B* **112**, 9921–9933 (2008).

[107] J.L. Hughes, R. Picorel, M. Seibert, and E. Krausz, "Photophysical behavior and assignment of the low-energy chlorophyll states in the CP43 proximal antenna protein of higher plant photosystem II," *Biochemistry* **45**, 12345–12357 (2006).

[108] N. Herascu, S. Ahmouda, R. Picorel, M. Seibert, R. Jankowiak, and V. Zazubovich, "Effects of the distributions of energy or charge transfer rates on spectral hole burning in pigment-protein complexes at low temperatures," *J. Phys. Chem. B* **115**, 15098–15109 (2011).

[109] N. C. Dang, T. Reinot, M. Reppert, and R. Jankowiak, "Temperature dependence of hole growth kinetics in aluminum–phthalocyanine–tetrasulfonate in hyperquenched glassy water," *J. Phys. Chem. B* **111**, 1582–1589 (2007).

[110] H. Wang, S. Lin, J. P. Allen, J. C. Williams, S. Blankert, C. Laser, and N. W. Woodbury, "Protein dynamics control the kinetics of initial electron transfer in photosynthesis," *Science* **316**, 747–750 (2008).

[111] J. R. Durrant, D. R. Klug, S. L. S. Kwa, R. van Grondelle, G. Porter, and J. P. Dekker, "A multimer model for P680, the primary electron donor of photosystem II," *Proc. Natl. Acad. Sci. USA* **92**, 4798–4802 (1995).

[112] V. I. Novoderezhkin, E. Romero, J. P. Dekker, and R. van Grondelle, "Multiple charge-separation pathways in photosystem II: modeling of transient absorption kinetics," *Chem. Phys. Chem.* **12**, 681–688 (2011).

[113] V. I. Novoderezhkin, J. P. Dekker, and R. van Grondelle, "Mixing of exciton and charge-transfer states in photosystem II reaction centers: modeling of stark spectra with modified redfield theory," *Biophys. J.* **93**, 1293–1311 (2007).

[114] R. Jankowiak, "Probing electron-transfer times in photosynthetic reaction centers by hole-burning spectroscopy," *J. Phys. Chem. Lett.* **3**, 1684–1694 (2012).

[115] K. Acharya, V. Zazubovich, M. Reppert, and R. Jankowiak, "Primary electron donor(s) in isolated reaction center of photosystem II from *Chlamydomonas reinhardtii*," *J. Phys. Chem. B* **116**, 4860–4870 (2012).

[116] K. Riley, R. Jankowiak, M. Rätsep, G. J. Small, and V. Zazubovich, "Evidence for highly dispersive primary charge separation kinetics and gross heterogeneity in the isolated PS II reaction center of green plants," *J. Phys. Chem. B* **108**, 10346–10356 (2004).

[117] V. I. Prokhorenko and A. R. Holzwarth, "Primary processes and structure of the photosystem II reaction center: a photon echo study," *J. Phys. Chem. B* **104**, 11563–11578 (2000).

[118] J. A. Myers, K. L. M. Lewis, F. D. Fuller, P. F. Tekavec, C. E. Yocum, and J. P. Ogilvie, "Two-dimensional electronic spectroscopy of the D1-D2-yt b559 photosystem II reaction center complex," *J. Phys. Chem. Lett.* **1**, 2774–2780 (2010).

[119] E. Krausz, J. L. Hughes, P. Smith, R. Pace, and S. Peterson Årsköld, "Oxygen-evolving photosystem II core complexes: a new paradigm based on the spectral identification of the charge-separating state, the primary acceptor and assignment of low-temperature fluorescence," *Photochem. Photobiol. Sci.* **4**, 744–753 (2005).

5

OPTICAL SECTIONING MICROSCOPY AND BIOLOGICAL IMAGING

JOHN GIRKIN
Biophysical Sciences Institute, Department of Physics, Durham University, Durham, UK

5.1 INTRODUCTION AND BACKGROUND

Optical imaging has played a key role in the development of biology and indeed until the discovery of DNA, and its role in life, was probably the core scientific technology forming the basis of all discoveries. Initially this imaging was just undertaken with the scientist using their eyes to observe and subsequently record what was going on. However, the invention of the lens over 2000 years ago meant that biological samples could be studied in finer detail, indeed Pliny the Elder described their use in surgery both for observing fine tissue damage and to use the sun to cauterize wounds [1]. The subsequent invention of the microscope around 400 years ago brought about a revolution in biological thinking as cells were visualized and appreciated for the first time and these results were first recorded by Robert Hooke [2]. The development of the optical microscope, to visualize ever finer structure, has also prompted advances in the understanding of optics such as the work on diffraction by Abbe and around 70 years ago by Zernike [3,4], thus the growth of optical microscopy and advanced physics has been synergistic. These significant improvements in optical imaging led to a real desire in biology to visualize, with as finer detail as possible, in real time, the motion of cells, and their subcellular structure, and in the past 30 years this has become possible, initially with the advent of practical confocal microscopy, and more recently with a range of nonlinear-based methods.

Photonics: Scientific Foundations, Technology and Applications, Volume IV, First Edition.
Edited by David L. Andrews.
© 2015 John Wiley & Sons, Inc. Published 2015 by John Wiley & Sons, Inc.

This chapter will explore the physical processes that lie behind the modern methods of obtaining optically sectioned images with an emphasis on the practical details that should be taken into consideration when selecting a specific method. Clearly in that decision it is important always to put the biological context first. Understanding the basic physics behind the different methods is important in helping to choose the best tool for a specific task. Frequent compromises have to be made trading off image quality, with speed, resolution, and minimal damage to the sample and all aspects should be considered before following a certain route. Understanding how an imaging method works is clearly crucial to obtaining and interpreting the most accurate data to reflect what is taking place within the sample. This chapter does not go into a rigorous mathematical derivation of optically sectioned imaging but core references are provided, where applicable, for the interested reader.

5.1.1 The Biological Context and Limitations

Before considering the physics and optics behind optical sectioning methods, it is important to place these into the correct biological context, as this frequently places limitations on the instrumentation. Ideally, the life scientist would like to observe all processes taking place inside as intact a system as possible, and clearly this would be in an intact, living organism. Although this may be possible in single-cell creatures (within the limits imposed for diffraction, etc.), for more complex organisms this clearly become much harder. Prior to the invention of optical sectioning microscopes, studying dynamic processes within biology was undertaken by fixing a range of physically sectioned samples taken at different points from different samples and trying to develop a model for the processes taking place. An analogy is that of trying to work out the rules of a sport, say football, or soccer, by going to one match and digging a hole in the pitch after one minute (one is perturbing the system radically), pointing a camera in a specific direction and taking a single image. One then goes to a second match, digs another hole, in what you believe is the same place on the pitch, after 2 mins and recording a second image and so on for a full 90 separate minutes at 90 different matches. One then takes all the single images and attempts to determine the rules. Clearly a much better route would be to watch a single match, from above the pitch, and monitor what is taking place. There is a risk that the ball, or perhaps players, might hit the camera but that is clearly less invasive than watching a number of matches in which you have dug holes.

With modern optically sectioning systems, one is thus trying to have a method that enables one to observe the biology with minimal perturbation, in real time. Clearly even using an optical sectioning technique one is perturbing the system, as the internal cells of biological systems are not used to being subject to light, but this is clearly less significant than physically sectioning the sample!

Crucial to any imaging method is the contrast mechanism that is being utilized to obtain the microscopic image. In most biological imaging at present this is based around fluorescence and the details of this process are covered in chapters elsewhere in this book though from an imaging perspective there are two important points. First, the labeled sample will be excited at one wavelength and then will emit light, a short time later, at a different wavelength. In conventional single-photon imaging, the light emitted is at a longer wavelength than the excitation light. The delay in the fluorescence is known as the fluorescence lifetime and can be used to enhance the detection and also to provide information on the exact conditions present near the fluorophore. A full detailed explanation of all aspects of fluorescence is well beyond the scope of this chapter, and indeed this volume, and the interested reader may try the currently accepted gold standard book by Lakowicz [5].

Biologically the development of fluorescent labels that go to a specific feature of a cell have been crucial in helping to understand all of the processes of life. This technique was revolutionized in the mid-1990s with the development of fluorescent proteins (initially green fluorescent protein or GFP) in which the cell produces its own fluorophores when specific genes are active [6, 7]. Again it must be remembered that this is not "noninvasive" as the cell does not normally produce this compound and these large molecules (238 amino acids) are consuming chemicals within the cell thus slightly altering its natural biochemistry. However, the fluorescence (protein) is produced only when a targeted gene is active and can thus be very specific. GFP, in line with many other fluorophores, is also not perfectly stable when subjected to repeated excitation and emission cycles, and when the compound eventually breaks down, the resulting chemicals can be toxic to the cells in which they are present in a process known as phototoxicity.

Other contrast mechanisms presently used do not, generally, require the presence of a fluorescent compound, either indigenous or introduced. These include harmonic generation (second and third are now routinely used) along with Raman-based imaging methods, most specifically Coherent Anti-Stokes Raman (CARS) and full details of these methods are presented later in this chapter. The crucial feature with all of the approaches to develop optically sectioned data is that within an image the most important parameter that sets the imaging limitation is the method of contrast. Without contrast no features can be seen and the remaining parts of this chapter can be viewed as methods of just improving the contrast in a specific volume or optical slice of tissue.

5.1.2 Definitions and Terms

In order to be self-consistent the next section explains the terms used throughout the rest of the chapter.

Numerical Aperture (NA). This is the light-collecting ability of any lens. It is defined as sine of the half angle of the light cone entering the lens. The higher the numerical aperture of a lens the greater its light-collecting ability and the finer detail that can be seen in the image. In all optical microscopy systems, this sets the ultimate resolution. By definition $\mathrm{NA} = n\mathrm{Sin}(\theta)$, where θ is the half angle of light cone produced by the lens and n is the refractive index [8].

Refractive Index (n). The ratio of the speed of light in a material to its speed in a vacuum is expressed by the refractive index, such that the higher the refractive index, the slower the light travels in the material. As light passes from one refractive index to another, unless it impacts the new surface at 90°, its path will be changed.

The size of this change is determined by the relative values of the refractive indices through which the light is traveling [8]. By manipulating the refractive index (e.g., using oil and water objectives) it is possible to develop microscope objective lenses with a numerical aperture greater than 1 leading to higher resolution as noted below. For reference $n \sim 1$ in air, ~ 1.33 in water, and ~ 1.5 in oil and glass.

Lateral Resolution. In a perfect imaging system, the resolution in the imaging plane (*XY* plane in this chapter) is set by the longest wavelength of light involved in the imaging process and the numerical aperture of the lens. A definition of the resolution of a system is the minimum separation between two points at which these two points can each be seen or resolved. In effect what takes place is that each point produces an Airy disc and as the points become closer together the finite peaks at the center of the discs start to overlap until you can no longer distinguish between the two points. Using the Rayleigh criteria [8], the lateral resolution is given as

$$d = \frac{(0.61 \times \lambda)}{\mathrm{NA}}, \tag{5.1}$$

where λ is the wavelength of the light used for the imaging and NA the numerical aperture of the lens.

Axial Resolution. In a system producing optical sectioning, the ultimate axial resolution (along the optical axis of *Z* direction in this chapter) is also given by the wavelength and numerical aperture though the resolution is now nonlinearly dependant on the numerical aperture

$$d_{\mathrm{axial}} = \frac{(1.78 \times \lambda)n}{(\mathrm{NA})^2}. \tag{5.2}$$

5.2 CONFOCAL IMAGING

After a brief introduction to confocal imaging, the basic physical principles will be explained and the most practical implementation of the confocal microscope will be described. The more advanced optical sectioning methods all build upon this core concept and optical configuration.

5.2.1 Introduction to Confocal Imaging

The most basic form of optical sectioned imaging is that of a confocal microscope. The concept was first developed by Marvin Minsky in 1957 and subsequently accepted as a granted patent in 1961 [9]. The basic principles of a confocal imaging system have changed very little since this original design, and in 1957, the concept was very much an instrument ahead of its time. High spectral brightness light sources were not available (the laser being the obvious source invented in 1960), and solid-state detectors and electronics were also in their infancy. The main concept that was introduced, and the basis of all confocal imaging systems, is that of a pinhole that is "confocal" with the focal plane of the objective as shown in Figure 5.1.

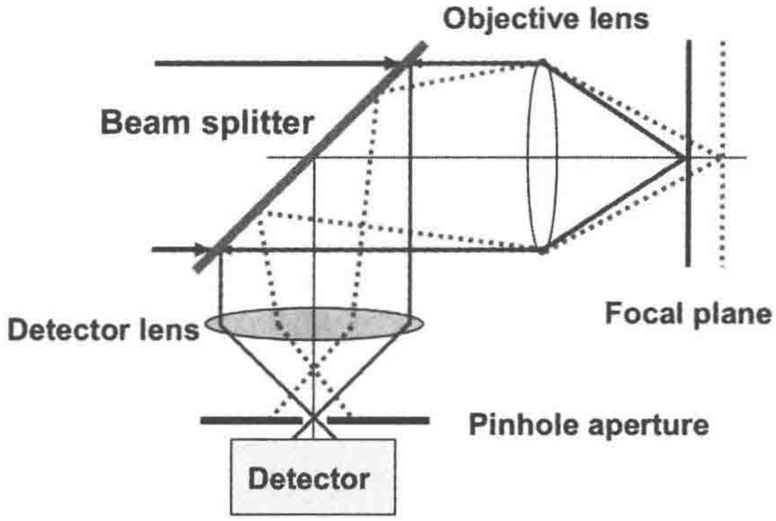

FIGURE 5.1 Basic optical configuration of a confocal imaging system. (*For a color version of this figure, see the color plate section.*)

In this simplified diagram, light enters from the left-hand side (in blue) and passes through the beam splitter (in a typical biological confocal system this is a dichroic beam splitter that transmits one wavelength and reflects another) and is subsequently focused by the objective lens. Fluorescent light (or backscattered light in many configurations) from the focal plane (shown as purple) then passes back through the objective and is subsequently reflected by the beam splitter and focused down through a pinhole onto the detector. Light from outside the objective's focal plane (shown in red dotted line) passes back through the objective and is also reflected by the beam splitter but, as this light is not from the focus, on passing through the lens it is rejected by the pinhole and the majority of this light thus fails to reach the detector. The system thus only permits light from the focal plane to reach the detector. Different depths can then be imaged by moving the focus through the sample.

Minsky's original system used long-life oscilloscope screens to display the image, but this was not practical and the first more biological friendly system was built by Egger and Petrăn [10] who used it to image ganglion cells and brain tissue in reflection mode. Several systems were subsequently built on this model and the theoretical aspects were then fully explained by Sheppard and Wilson [11]. All of these early systems suffered from one major drawback, namely the sample had to be scanned through the focused spot in both the X and Y axes to produce a single image plane. The paper by Sheppard and Wilson explained ways around this limitation and the first practical beam scanned system was built in 1987 [12, 13] using a laser illumination source and photomultipliers as detectors. The optical configuration of most confocal microscopes has not changed significantly from this date.

5.2.2 Point Scanned Microscopy

The most commonly used method of scanned confocal microscopy is one in which the excitation spot is raster scanned across the sample using a pair of scanning mirrors.

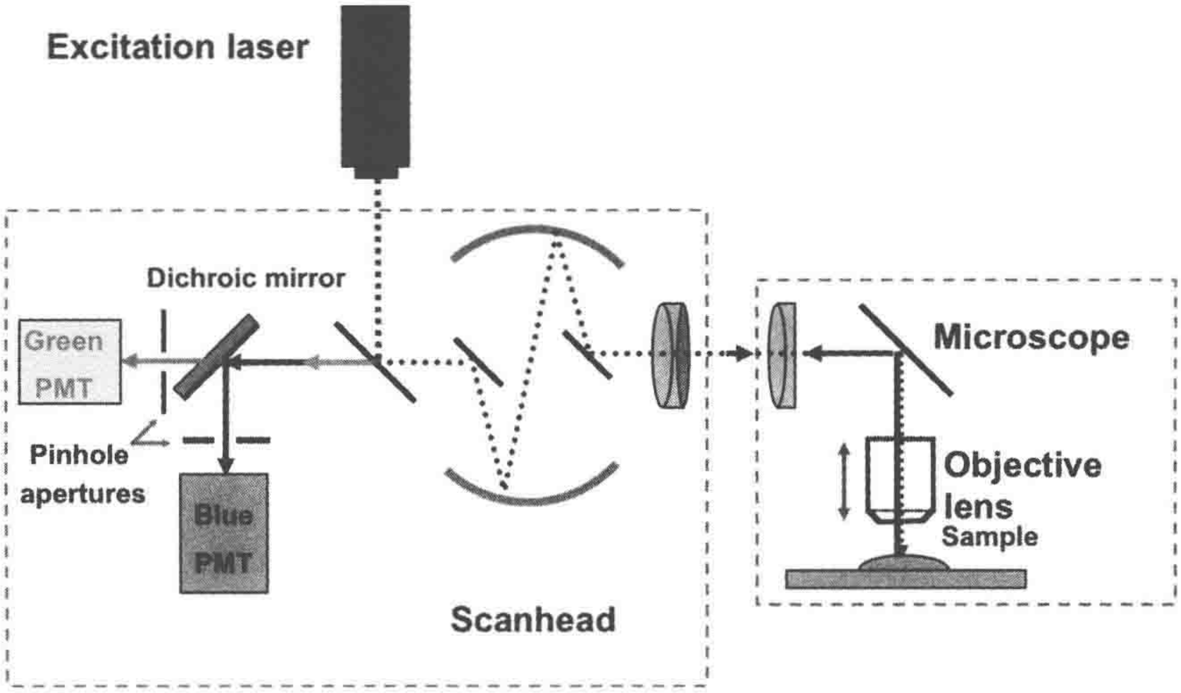

FIGURE 5.2 Beam scanning confocal microscope.

Each point in the plane is thus illuminated in sequence. Figure 5.2 illustrates the basic principles of the technique.

Light from the excitation source (almost universally a laser as a high brightness, good quality light beam is required) is directed onto the sample using a dichroic beam splitter (though a partially reflecting optic can be used for reflection imaging). The light then passes onto a pair of scanning galvanometer mirrors before being directed onto the back aperture of the microscope objective. Two configurations of scanners are possible, *close-coupled* (where the orthogonal scanners are mounted as close together as possible) and *reimaged* (where the scanners are reimaged onto each other using lenses or concave mirrors). The returned light is then reimaged by the objective onto the scanning mirrors in which the beam is descanned to pass through the dichroic mirror and the pinhole to reach the detector. Without the descanning on the returned path the beam would only pass through the pinhole in one position of the scan and the descanning thus means that only a single pinhole is required rather than one for each position of the scan. In many systems, a multiple series of dichroic mirrors is used with several detectors enabling the fluorescence for a number of fluorophores to be collected simultaneously (in figure 5.2 one would collect blue light, the other green). In the above figure, the optics will work both for fluorescence and reflection imaging and the latter is an underused method in complete biological samples as the reflection image can help place the fluorescence image in context. This is even more valid when an infrared light source is used with its greater penetration. The returned signal for each point on the scan is stored in a computer and the image thus built up pixel by pixel. After a scan has been obtained for one plane the objective can be moved toward or away from the sample to build a full three-dimensional image of the specimen. Typically, a single image plane can be recorded in around 1 second (for a 512 × 512 pixel image).

System variations are also possible in which the beam scanning is undertaken using acousto-optic modulators. These are optical devices in which a high frequency sound wave (typically around 40 MHz) is sent across a crystal to produce a Bragg diffraction grating. If the sound wave is a traveling wave the output beam is scanned as the diffraction angle changes at very high frequency permitting high speed scanning. The major complication, ignoring expense and drive challenges, is that the device is spectrally sensitive and different wavelengths are diffracted at different angles. This method of imaging will be returned to in Section 5.3 when the method is considered for nonlinear excitation.

With the use of the confocal pinhole in the imaging system, there is an additional improvement in the lateral resolution beyond that of wide-field imaging and full details of confocal imaging can be found in the excellent text edited by Pawley [14]. By adjusting the size of the pinhole the user can reject more or less of the light from outside the focal plane of the objective. Normally, the pinhole will be closed down to obtain the best possible resolution (the exact size being set by the optical configuration of instrument and beyond the scope of this chapter) but with feint samples, or ones in which the excitation level has to be kept low to reduce photobleaching, it may be opened. As mentioned above, typically a laser is used for excitation and until a few years ago this was almost universally an air-cooled argon ion laser with a lifetime of only a few thousand hours and a source of considerable heat in the laboratory. With the advent of laser diodes (in particular those which operate in the blue) in the late 1990s, compact and reliable sources are now available with high reliability [15]. Detection of the low light levels emitted is normally via a photomultiplier or avalanche photodiode and the selection of the correct detector is an important decision in the purchase and use of a scanning confocal system.

A variation on the beam scanned confocal microscope is through the use of a Nipkow spinning disc.

As illustrated in Figure 5.3, an expanded laser beam is incident on a rapidly rotating array of microlenses. These focus part of the beam down onto a matching array of holes and onto the sample. The returned light then passes back up through the same hole and is reflected back onto a CCD detector (or in fact, the eye can be used). By careful arrangement of the lenses in a spiral pattern it is possible to scan the entire sample at high speed. Typically, over 7000 lenses and holes will be used rotating at speeds of 1000 rpm.

These systems provide some optical sectioning capability, but are not as efficient as rejecting the out-of-focus light as the more conventional point scanned system [16]. In addition, they are wasteful of the laser light as only a small portion of the beam is used at any one time. The main advantage that such a system has is that very rapid imaging is possible with frame rates well in excess of 75fps, the limitation mainly being due to the sensitivity of the camera and fluorescence efficiency of the sample. They are well suited to imaging calcium transients, microtubule dynamics, and fluorescence from highly punctuate samples at high speed and are commercially available from several sources. Later in this chapter this method of high speed optical sectioning microscopy will be compared with single plane illumination.

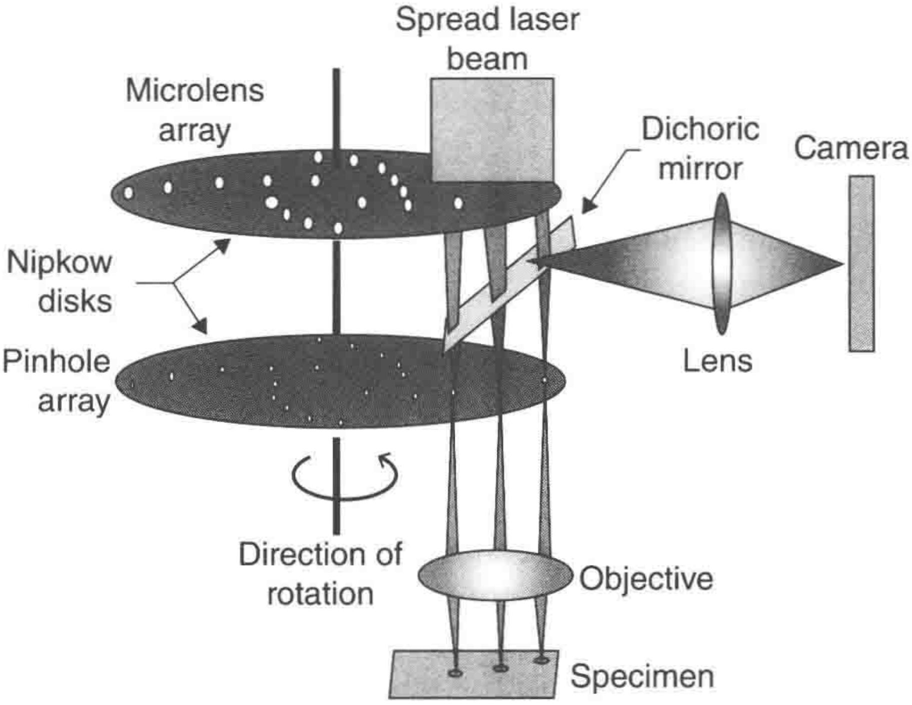

FIGURE 5.3 Nipkow spinning disk confocal.

5.2.3 Summary on Basic Confocal Microscopy

Confocal microscopy, using a pinhole to reject the out-of-focus light is thus clearly a powerful instrument to help develop three-dimensional images of complete biological structures. High resolution (diffraction limited) images can be captured in three dimensions and the method works very well on samples up to a depth of around 50 microns. Beyond this depth, the image contrast is lost for several reasons. These include light from outside the focal plane being scattered through the pinhole, and light from the focal plane being scattered away from the pinhole. The short wavelength excitation normally used in confocal microscopy, to match the excitation peak of most common fluorophores, is also scattered before reaching the focal plane thus reducing the number of excitation events at the focus of the objective. Thus for relatively thin (perhaps up to around 50 microns) samples, confocal microscopy provides an excellent method of capturing three-dimensional, optically sectioned images, but a more sophisticated method is required for imaging at greater depths.

5.3 NONLINEAR MICROSCOPY

In confocal microscopy, described earlier, the crucial feature that enables optical sectioning is the use of a pinhole to reject *emission* light returned from areas outside the focal plane; in all forms of nonlinear microscopy, the optical sectioning is achieved by localized *excitation*. In the last few years, the terms multiphoton and non-linear microscopy have been used interchangeably which is scientifically incorrect. In the following section, a convention has been adopted based upon the processes involved in generating the detected signals. All methods produce a nonlinear response in the material due to the interaction with light. In the case of fluorescence it is the

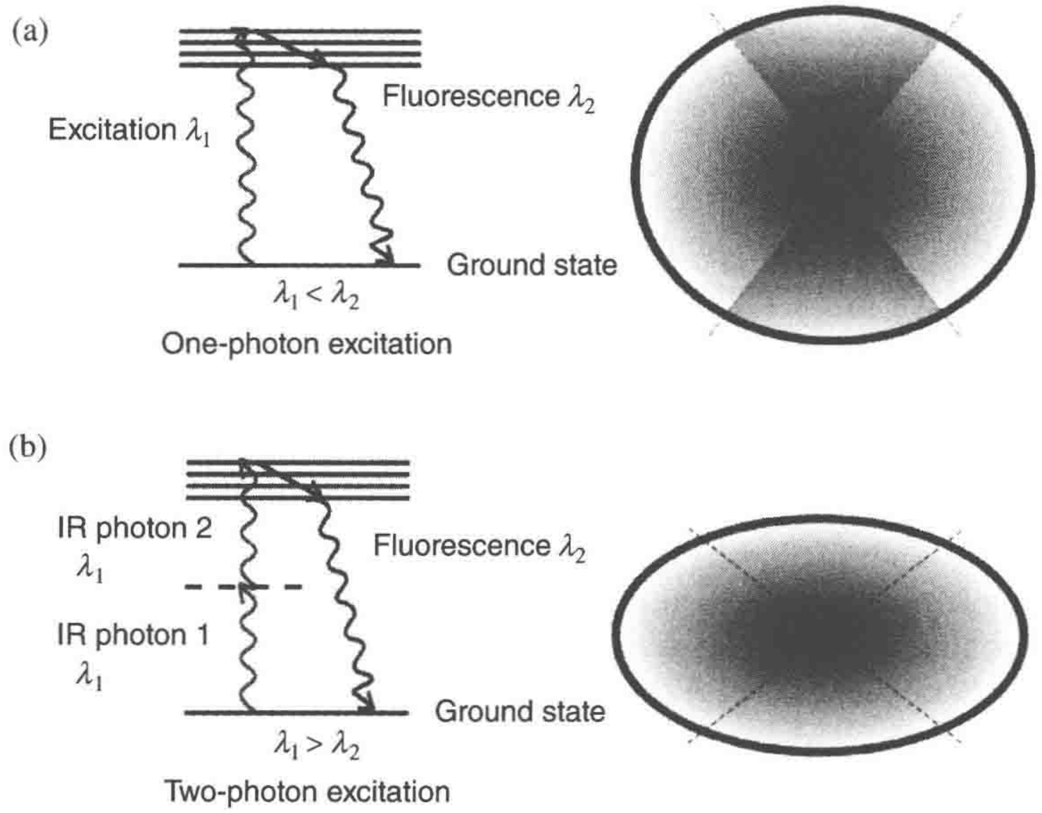
(a)
Excitation λ_1
Fluorescence λ_2
Ground state
$\lambda_1 < \lambda_2$
One-photon excitation
(b)
IR photon 2
λ_1
IR photon 1
λ_1
Fluorescence λ_2
Ground state
$\lambda_1 > \lambda_2$
Two-photon excitation

FIGURE 5.4 (a) Single-photon excitation and (b) two-photon excitation.

absorption of two or more photons with a resulting emission of a single longer wavelength photon; this will be termed multiphoton fluorescence microscopy or more normally multiphoton microscopy. The other methods are harmonic and Coherent Anti-Stokes Raman Scattering (CARS) and the physical basis behind these methods will be explained later which will also show how they are nonlinear, but should not technically be thought of as multiphoton.

The most important common feature in all of these methods is that the material being excited behaves in a nonlinear manner with the excitation intensity, leading to localized excitation due to the focusing of the excitation beam. Figure 5.4 illustrates the difference in the excitation through linear (5.4a) and nonlinear (5.4b) excitation, with the localized effect being clearly shown at the focus.

The resulting signal can then only have come from the focus of the light beam and by scanning this point of excitation around in the sample an image can be reconstructed, which is in 3D due to the inherent optical sectioning, as a consequence of the local excitation. The different methods will now be examined in detail.

5.3.1 Multiphoton Fluorescence Microscopy

The basic concept of multiphoton (two or three photon) fluorescence imaging is straightforward and the basic physical theory was first put forward by Goeppert-Mayer in 1931 [17], for which she was awarded the Nobel Prize in Physics in 1963. Using the then recently developed theory of quantum mechanics she postulated, and demonstrated mathematically, it was possible for electrons to move between different quantum mechanical levels through the absorption, or in fact emission, of two or more quanta of light (photons), the total energy of the photons being the equivalent of a single photon at a shorter wavelength. As the probability of such a multiple photon event happening is very low (compared to single-photon transitions), this effect was very much viewed as a mathematical, or quantum mechanical, curiosity. The theoretical details of these effects are covered elsewhere in this book. However, in practical terms with the invention of the laser in 1960 with its very high photon density, when focused, the first reported observation of this effect was made in 1961 using a ruby laser as the light source [18]. The first use of the effect was then in high resolution laser spectroscopy and the measurements of fundamental constants [19], and the first mention as an application for microscopy followed in 1978 [20,21], but it was a further 13 years before the method was first reported in the now seminal paper by Denk, Strickler, and Webb [22]. In this paper, the team undertook a heroic experiment using an optically complex colliding pulse dye laser, but they demonstrated that optically sectioned microscopy was practical. Indeed this paper then opened the way for the array of nonlinear-based microscopy methods that have emerged in the following 20 years. Although the concept of nonlinear microscopy had been discussed before, and indeed in nonbiological systems shown, Denk's paper showed that nonlinear imaging, with minimal damage to the sample, was possible and this paper stimulated thought in a number of innovative researchers around the world. As described below the number of different excitation routes rose rapidly with each method having its strengths and weaknesses but the core practical concept was now out and available.

A major reason for the previous slow adoption of nonlinear methods, into fields outside atomic laser spectroscopy, was due to the lack of suitable laser sources. In order to achieve suitable excitation rates, laser powers of around 1 kW are required, though continuous–wave, two-photon excitation was subsequently reported, but has never been used routinely [23]. Thus one requires a short, intense pulse of light, but not too intense, to cause either thermal (generally a slow continuous wave effect) or explosive (Q-switched or nanosecond pulse) damage to the sample. For imaging purposes even with the correct form of laser pulse sufficiently high intensities can only be found at the focus of high NA microscope objectives when the required flux is only present in a very small volume localized in three dimensions.

Typically, the excitation source will be at twice the single-photon excitation wavelength (half the photon energy). However, to be of practical use the excitation source should not be linearly absorbed within the sample, otherwise one will have heating and in the case of live biological samples cell death. In order to minimize such linear events, most multiphoton imaging is undertaken using ultra-short pulse laser sources typically with around 100 fs (100×10^{-15}) pulse durations. One thus has a high peak power (leading to high excitation rates) but a low average power minimizing heating effects. A number of factors therefore affect the size of the fluorescent signal but most notably the number of excitation events. For a pulsed laser, this is given by [24]

$$N = I_{\text{peak}}^2 \delta \left\{ \frac{\pi * \mathrm{NA}^2}{h * c * \lambda} \right\}^2, \qquad (5.3)$$

where $I_{\text{peak}} = \frac{P_{\text{avg}}}{\Delta\nu * \tau_{\text{p}}}$.

Here I_{peak} is the peak intensity, P_{avg} the average power on the sample, τ the pulse width, ν the repetition rate of the laser, NA the numerical aperture of the objective lens, λ the laser wavelength and h, c, and π have their normal physical meanings; δ is the two-photon absorption cross-section for the transition at the laser wavelength and is typically around 10^{-50} (cm^4s) per photon per molecule. For practical implementation of this equation in microscopy, the repetition rate is limited by considering the fluorescence lifetime of the fluorophore and also the speed with which one wishes to image. (A laser at 1 Hz may have a low repetition rate giving a high N, but scanning a 512 × 512 pixel image would not be practical.) These considerations will be revisited when recent advances in laser sources are discussed.

The main advantages to the researcher of the multiphoton fluorescence technique are that it enables imaging at significantly greater depths within samples and maintains the viability of live samples, provided the conditions are correct. The main reason for the ability to image more deeply arises from two physical principles. The excitation wavelength is typically in the near-infrared (~720–950 nm from a Ti:Sapphire laser) and this wavelength is not linearly absorbed by most of the biological tissues and scattering is reduced compared to visible wavelengths. Hence, as one moves deeper into the sample, he/she is therefore able to increase the laser power and maintain a high peak power despite the loss of a few photons due to scattering or aberration caused by the optical properties of the tissue being imaged.

The second, more important, principle is that as a result of the localization of the excitation one can collect all of the fluorescent light. In the other main optical sectioning microscope, the confocal microscope, the fluorescent light has to pass back through the instrument and then a pinhole in order to obtain the required sectioning ability [25]. In the case of the multiphoton system all the light can be utilized to build up the image, without the need to be descanned and pass through optical apertures, as all the signal photons can only have come from the focal volume. It is possible to image live samples with minimal damage as the number of phototoxic events within the sample is significantly reduced under the correct conditions [26]. The entire depth of the sample is not subjected to potentially damaging blue or ultraviolet light and any damage that is caused by multiphoton processes can be limited to the focal plan. By careful control of the imaging conditions, it is therefore possible to obtain images from deep within the sample.

5.3.2 Harmonic Microscopy (SHG and THG)

Harmonic microscopy is based upon another nonlinear effect that takes place within certain molecules, though this time more classical in nature rather than quantum mechanical. The effect was known of for many years but was again only seen with the invention of the laser. As an aside, the first paper in 1961 [27] contains a classic editorial error where the spectral line showing the light at a specific wavelength was removed by the editor as being dust on the photograph. However, before considering the effect within a microscopic, or imaging, context, the basis of the process should be considered.

Harmonic generation is best not considered as the direct addition of two photons to produce one-half of the wavelength (or twice the frequency) or further additions for high order harmonics (third, fourth, fifth, etc.). If one considers light as a wave hitting a molecule, the electric field will cause changes in the charge distribution within the molecule, inducing a dipole moment within the molecule. Under normal circumstances, this effect is very small and the size of the dipole is linear with the electric field. The dipole moment per unit volume of the material (intrinsic and induced by the electromagnetic wave) is known as the polarization. The total polarization (P_{total}) can then be considered as the intrinsic value with a subsequent series of additional changes that depend on the incoming electric field (E). Mathematically, this is expressed in a simplified form as

$$P_{\text{total}} = P_1^0 + x^{(1)}E^1 + x^{(2)}E^2 + x^{(3)}E^3, \tag{5.4}$$

where the term P_1^0 is the permanent polarization, $p^1 = x^{(1)}E^1$ has the change in polarization being linear with the applied electric field, $p^2 = x^{(2)}E^2$ (the second-order polarization) has the change varying with the square of the electric field and so on. Full details can be found in any textbook on nonlinear optics [28]. The light wave (electric field) is just propagated by the P^1 term but the second term causes both a linear continuation of the light field and crucially a wave in which the electric field has exactly twice the incoming frequency. At normal intensities of light this effect is very small but at high electric field (such as those seen in high power lasers) this harmonic wave can become large enough to be detected and seen. The simple effect is illustrated in Figure 5.5 with the $x^{(2)}$ coupling with the incoming wave of frequency ω to produce an output containing light at two frequencies ω and 2ω. The diagram also illustrates that the wave produced travels in the same direction as the incoming light, thus the emission is in the forward direction in an imaging system and this can be important in the detection method selected as discussed in Section 5.4.

This is the basis of, for example, green laser pointers, where the fundamental laser is based on Nd and lases around 1064 nm but with a crystal inside the laser cavity the light is doubled (wavelength halved) to 532 nm.

However, this process is coherent with the incoming waves of light and thus all light produced by this process is coherent. In most normal situations, this means that the waves produced by one molecule will destructively interfere with the waves from the molecule next door. In crystals with a noncentrosymmetric structure the light fields produced are such that they do not cancel out and the second harmonic is viewed. This effect continues for the third harmonic and further up the frequency chain but with decreasing amplitude.

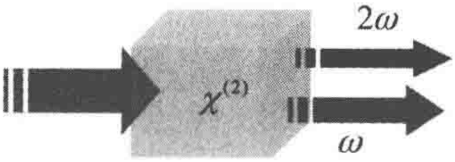

FIGURE 5.5 Illustration of second harmonic generation.

At a base level, one can think of the molecule as vibrating in response to a wave. If the amplitude of the wave becomes very large, then harmonics can be produced at twice, three times, and so on, up the series of the frequency of the fundamental wave. In many cases, the individual molecules will be arranged in such a way that these harmonics all cancel out, but with the correct pattern they will all be in phase and the harmonic will be seen.

In the case of microscopy, most materials are aligned such that they do not have any second harmonic terms. The potential of nonlinear imaging was first described by Sheppard et al. [29] in 1977, which was subsequently followed by a further paper by the same group [30] in which they described a scanning microscope with an optical enhancement cavity around the sample to increase the signal that would be suitable for biological samples. Roth and Freund [31] first reported biological samples in an international journal in 1981. Having demonstrated that collagen could be imaged by second harmonic generation (SHG), they then applied the method to help solve a real biological question, that of the structure and order of collagen within a rat's tail [32].

The method now has gained widespread acceptance and is of particular value in the imaging of in vivo tissue as the collagen structure can be visualized without the need for an exogenous fluorophore and thus its structure can be used to place other fluorescent markers in a physical context. As the light is emitted at exactly half the incoming wavelength, it is also easy to separate the SHG signal from other fluorescent markers using narrowband dichroic filters.

Over the next few years, little was done in biological imaging, and as with multiphoton fluorescence microscopy it was only really with the advent of biologist-friendly femtosecond laser sources that the method really established a role within biological microscopy. Various tissue samples were imaged over the next few years, but the most significant advance was made when a dye was placed inside the cell membrane; rather than exciting the molecule by tuning to a two-photon absorption band and detecting the subsequent fluorescence, the authors used the dye as a source of harmonic generation [33]. This was achieved as the dye was in the cell membrane, and thus in a very thin layer, such that the molecules were generally aligned in one direction. This means that there was no destructive interference of the light. Indeed this paper took the work one stage further as the dye was voltage sensitive; thus as the potential within the cell changed, fewer or an increasing number of the molecules aligned themselves within the membrane, and thus, the SHG signal provided a read-out of the membrane potential. Moreaux et al. [34] then took this further by tuning the laser close to the florescence wavelength and thus had an enhancement in the signal due to the inherent amplification of matching the wavelength to the dipole of the molecule.

Third harmonic imaging (THG), although used less commonly primarily due to the lower excitation rate, has also been shown to have real advantages for label-free imaging of lipids under the correct conditions [35]. This method has since been advanced through improved detection and was first applied to significant biological challenges in 2006 [36].

The method had also at that point been applied to in vivo imaging of the cornea but, potentially more interestingly, as a method of tumor detection [37]. This demonstrated

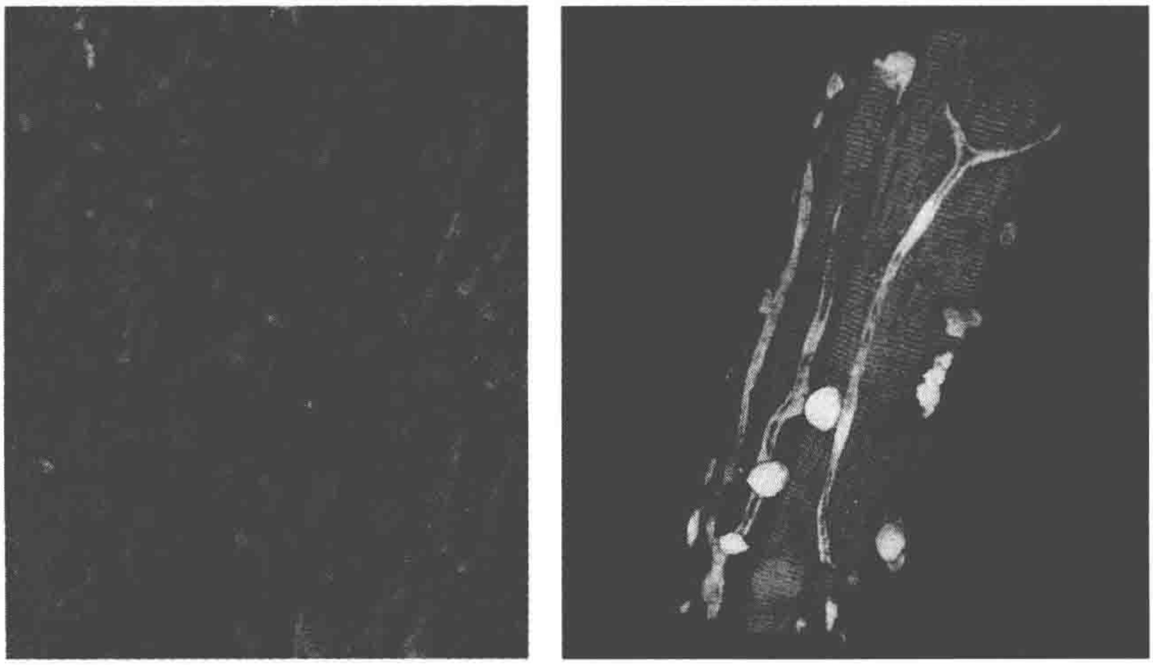

FIGURE 5.6 A combined SHG and multiphoton image of yellow fluorescent protein illustrating the advantage of a combination imaging method. The SHG provides the biological context for the structure and position of the YFP expressing pericytes. Image courtesy of Dr. Paul Thomas, Henry Wellcome Laboratory for Cell Imaging, University of East Anglia. *(For a color version of this figure, see the color plate section.)*

that SHG was a viable tool for in vivo use. The advance in the method can be seen in the work published in 2013 where human adipocytes have been imaged directly using third harmonic microscopy [38]. Both of these papers illustrate the major potential in harmonic imaging for in vivo human use as no exogenous compounds were introduced. The method can also be linked with more conventional two-photon fluorescence, where the SHG provides the information about the structure of the sample and the fluorophore (yellow fluorescent protein, YFP, as an example in Figure 5.6), a specific biological tissue type. In this case with the laser tuned to 950 nm (close to the two-photon peak for YFP), the collagen and muscle fibers emitted at the SHG of 475 nm (well away from the YFP emission peak around 560 nm).

5.3.3 Coherent Anti-Stokes Raman Scattering Microscopy

CARS (coherent anti-Stokes Raman scattering) is the third, and most recently developed, method of nonlinear microscopy. CARS is a four-wave mixing process in which a pump beam at frequency ω_{p} (with a wavelength λ_{p}) and a Stokes beam at frequency ω_{s} interact with a sample to generate an anti-Stokes signal at frequency $\omega_{\mathrm{as}} = 2\omega_{\mathrm{p}} - \omega_{\mathrm{s}}$. The CARS process was originally discovered in the Ford Motor Company [39], but the acronym does not relate to its place of invention. CARS can either be considered as a classical wave process, in a similar manner to that which harmonic imaging was explained, or as a quantum mechanical photon process.

If we consider the classical model, in Eq. (5.4), we need to examine the E^3 term. In the case of CARS, we have three laser beams and therefore the electric field is not a

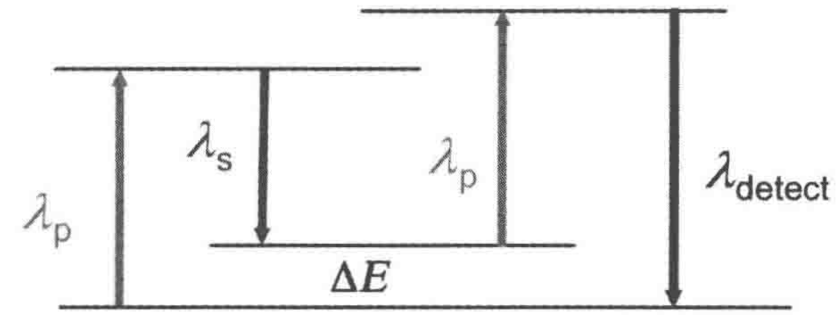

FIGURE 5.7 Energy diagram for basic CARS microscopy.

single cubic term. The three beams interact with each other through the $x^{(3)}$ term with the high peak powers of the electric fields driving the polarization of the molecules. By considering the molecular vibrations as a classical oscillator, with a frequency ω_v, this interaction effect can be enhanced by driving the system at a resonance (i.e., the difference in the energy levels within the molecule). In CARS, this oscillator is not driven by a single optical wave, but by the beat frequency ($\omega_p - \omega_s$) between the pump and the Stokes beams. When this beat frequency is close to ω_v (where ΔE is the energy difference corresponding to ω_v in Figure 5.7), the molecular oscillator is driven very efficiently. It is the movement of the electrons within the molecule that give rise to the $x^{(3)}$ polarization term, and in effect this periodic motion is probed by a third beam (actually ω_p) whose frequency is altered by the addition of the beat frequency to produce the ω_{CARS} emission at the so-called anti-Stokes wavelength.

In the quantum mechanical situation, a photon of wavelength λ_p (frequency ω_p) is absorbed (where the higher energy level may be a virtual) and then a second photon at wavelength λ_s drives the excited electron down to a real vibrational state. A third photon can now be absorbed sending the electron to another virtual state from which it is again instantaneously driven down, in this case to the ground state emitting light at the energy difference, which is then detected (λ_{detect}).

In both processes, the emitted light and driving of the various energy levels is undertaken coherently and thus all the individual molecules within the volume emit light at the same time and in phase giving an enhancement in the signal providing the *phase matching* condition is achieved. In order for constructive rather than destructive interference to take place, the three wavelengths involved in the process need to have the correct relative phase relationship. This is given by

$$\frac{n(\lambda_{det})}{\lambda_{det}} = \frac{n(\lambda_P)}{\lambda_P} + \frac{n(\lambda_s)}{\lambda_s}, \tag{5.5}$$

where n is the refractive index of the material (at the given suffix wavelength) and λ is the wavelength. In many optical techniques where CARS or other nonlinear parametric process are used, this places a significant constraint on the conditions (in frequency doubling for example the size and cut of crystals). However, in nonlinear microscopy, due to the high numerical aperture of the lenses involved, the excitation volume has a radius of around a micron, not much longer than the wavelength of the light, and thus this constraint can be largely ignored.

As noted above, the process is driven by the $x^{(3)}$ term and the light is strongly emitted in the forward direction. As the process is parametric and the electrons end up back in their original state, no energy is lost in the process and no heating of the sample takes place, thus there is no risk of the molecule being damaged. The downside of this is that in fact no resonant molecule needs to be present at all in the focal volume leading to a nonresonant background. The removal of this background is a considerable practical complication and the details can be found in Section 5.4.

We now need to consider how this method has been used in a microscopic imaging context. The first practical system was demonstrated in 1999 by Sunney Xie's team, based at the Pacific Northwest National Laboratory [40], where the optical performance of the instrument was assessed as well as its use in live cells was demonstrated. In the following 5 years, a number of papers were published, mainly by the same group who had subsequently moved to Harvard, all demonstrating variations on the basic method. Initially, improved epi detection [41], followed polarization sensitivity [42]. An excellent review of all the advances made in this period can be found in the work by Cheng and Xie [43]. Beyond the technical advances, the method has been increasingly applied to real biological challenges.

5.3.4 Stimulated Raman Scattering Microscopy

Although CARS is a very powerful non-inear imaging method, it has a few drawbacks. First, the signal includes a nonresonant background term that can be hard to avoid and affects the signal-to-noise ratio, and second, the spectra that are determined (by tuning the lasers) are not always those expected in conventional Raman spectroscopy and thus the results can be confusing. A variation of CARS in that it is a nonlinear process using Raman transitions is stimulated Raman scattering [44]. Here, the two laser wavelengths are tuned such that their beat frequency is close to a Raman vibration. When this beat frequency exactly matches the Raman frequency of a vibration, molecular mode amplification of the Raman signal is achieved by what can be viewed of as "stimulated emission." The pump beam can be thought of as exciting a mode up to a virtual state and it is then driven back down to a state close its original state by the Stokes beam. This state will have a slightly higher energy than the original ground state with the energy difference being the vibrational mode or Raman frequency.

As the virtual state is driven down by the Stokes beam one now has in effect two Stokes photons (the stimulating photon and the energy from the excited state decaying down), the loss of a pump photon and a molecule now in a slightly higher vibration level. The imaging signal can thus be detected by looking for either a loss in intensity of the pump beam (SRL) or an increase in intensity of the Stokes beam (SRG). If the frequency difference between the two incoming beams does not match a vibrational mode, the excited molecule is not driven down to the lower energy state and thus there is no background signal. This process relies on the intensity of two light sources and is thus again nonlinear. Although the nonresonant background seen in CARS is not present, one is now looking to detect a small change in intensity on a signal that comes directly from the laser leading to practical challenges.

5.4 PRACTICAL IMPLEMENTATION OF NONLINEAR MICROSCOPY

The core of all nonlinear microscope optical designs are common, but before considering each aspect of a multiphoton microscope in detail and how recent advances in the technology and physics has lead to improved imaging, we will consider what is needed for a multiphoton microscope. In a practical multiphoton system, the required components are shown in Figure 5.8.

Light from a mode-locked laser source is directed into an optical microscope using an *XY* scanning system in a very similar method to that used in the confocal system, but with one important practical difference, that is, it lacks optical fiber which is frequently used for beam coupling in confocal systems. When ultrashort laser pulses are sent down an optical fiber, two effects start to take place. First, due to the high peak power, nonlinear effects start to take place within the fiber. This can alter the spectrum of the light emerging, generally broadening the optical spectrum and crucially removing light from the wavelengths required for the imaging. Although this can be useful in certain methods of producing ultrashort pulses in general, this causes problems. Further details, and a summary of the laser types and complications for use of lasers in nonlinear microscopy, can be found in Reference 45. The second effect for femtosecond laser sources, those preferred for multiphoton fluorescence and harmonic imaging, is that the optical pulses lengthen in time due to group velocity dispersion (gvd). Femtosecond laser pulses have a significant optical bandwidth due to their ultrashort nature. As a typical example, a 100-fs laser pulse at 800 nm (typical

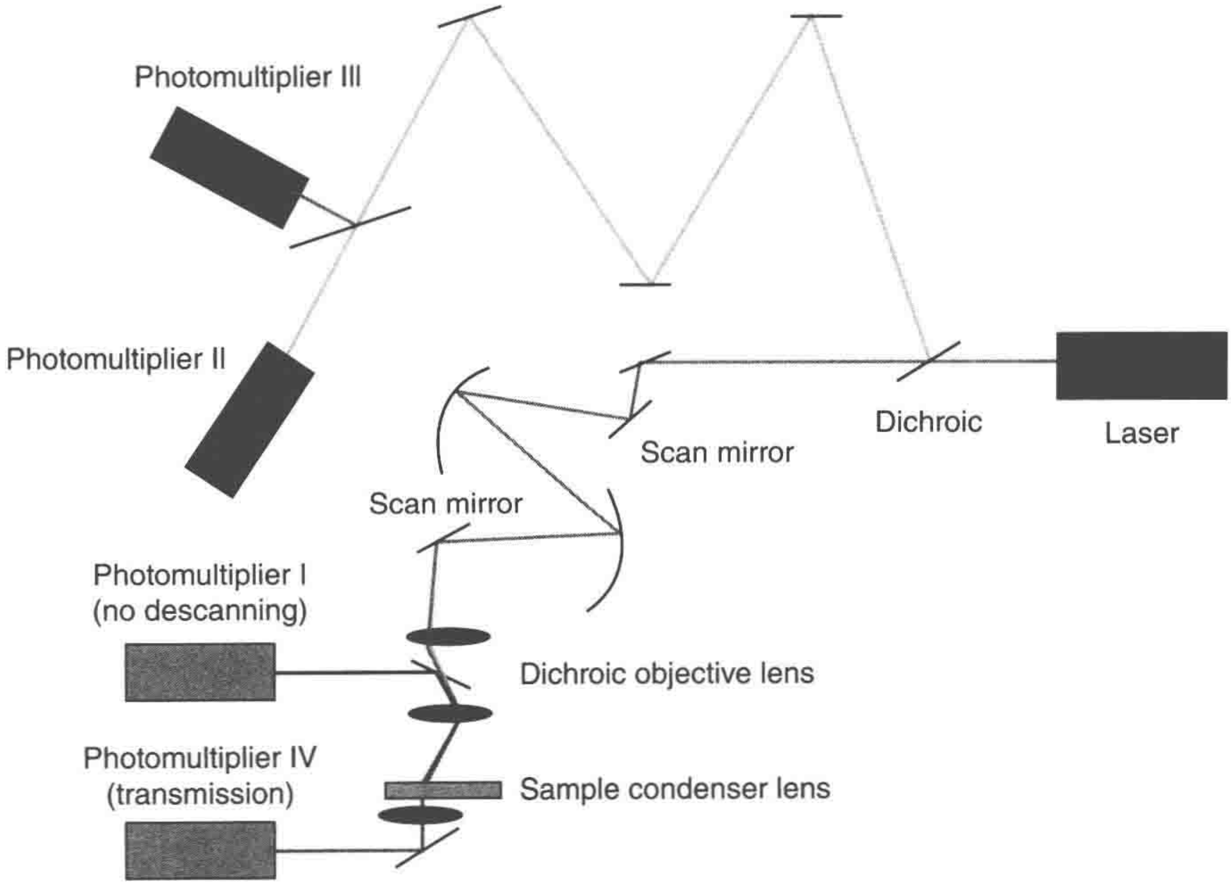

FIGURE 5.8 Basic optical configuration for nonlinear microscopy.

for multiphoton imaging) will have a spectral width of around 15 nm. As this light enters an optical fiber, the longer wavelengths travel more rapidly through the fiber due to the refractive index change with wavelength; thus at the end of the fiber the blue light will trail the red light that emerges at the front of the pulse. For the typical laser pulse quoted above, in around 1 m of optical fiber, the pulse may be lengthened to 2 ps, lowering the peak power and signal according to Eq. (5.3) with the concomitant loss of signal. Thus, the preferred route to beam delivery is using conventional optics rather than mirrors.

The light is then passed through a high numerical aperture microscope objective (in order to minimize the focal volume and to increase the excitation rate and resolution). It is important to note here that not all microscope objectives are equivalent when it comes to delivering infrared ultrashort pulses. As can be appreciated from the comments above relating to optical fibers, one effect is that the pulses can be lengthened [46]. A high numerical aperture objective may contain 16 lenses made of a range of glasses. These have the effect of lengthening the pulse due to their dispersion properties. Lengthening our typical pulse from its initial 100 fs to around 300–400 fs produces a loss of signal. Generally, the higher the magnification and NA of the lens the higher the dispersion due to the complexity of design. Thus, it is always worth arranging with the microscope manufacturer to try several lenses before settling on the preferred choice for the imaging you wish to undertake.

There are practical methods for removing this lengthening effect by making the light at the leading temporal edge of the pulse to travel a further distance than the trailing edge and hence the different wavelengths "bunch up." This can be achieved using a spectrally dispersive element to separate the wavelengths spatially and then letting the required wavelengths to travel further before the pulse is spectrally recombined. This dispersion compensation can be achieved in a number of configurations using gratings, prisms, or complex optical coatings. Weiner [47] provided an excellent review of the methods and this provides far more detail than is required in this chapter. Commercial femtosecond lasers now incorporate the option of dispersion compensation within the sample and imaging optics.

As well as the dispersion in the glass, there is also the complication of chromatic aberration. Many high performance lenses designed for fluorescence imaging are very well optimized for use across the visible spectrum (plan-fluor lenses being corrected from 405–647 nm), but with nonlinear imaging the input wavelength may be around 1200 nm or longer with the signal being emitted at less than 600 nm. This means that chromatic aberration can be a significant issue, with the lens concentrating the excitation light at one plane, but the light collection being higher at another. In addition, the optical coatings in typical lenses are optimized for visible use and may even become reflectors at the longer wavelengths. Again, the only solution to these practical issues is through experimentation, though in the last few years the major microscope companies have become aware of these problems and designed lenses suitable for nonlinear microscopy, and as the field grows, the desire for suitable optics is only likely to increase.

In the case of the CARS systems, one requires two laser wavelengths that are tuned to the vibration difference one wishes to probe. The most conventional method of undertaking this now is through the use of one fixed wavelength and a tunable source that is synchronized to the fixed wavelength. This synchronization, and tuning, can be achieved simultaneously by using one laser to pump an optical parametric oscillator and using the output from that source, along with the original pump source, as the light to excite the CARS signal. This is now the general configuration that is used, and as mentioned above, the pulse lengths are typically around a few picoseconds in order to have a high peak power but good spectral overlap with the specific vibrational modes being examined [48].

Having delivered the light sufficiently well to the target, the resulting emission light can then either be detected using a nondescanned detector (placed as close as possible to the back of the objective after a suitable dichroic mirror) or the signal can go back through the scanning optics and be collected on the detectors normally used for confocal imaging. The non-descanned detector uses the inherent optical sectioning of nonlinear microscopy to collect as much signal light as possible. Every signal photon can only have come from the focus of the beam and thus collecting the light as soon as possible makes sense. Even with the best mirrors in the configuration shown above, the light will pass off an additional 11 surfaces if the descanned detectors are used, leading to a loss of signal. In certain circumstances, some of the incoming light can be scattered to local focal maxima and this can lead to signal being generated outside the focal plane, one such tissue sample being the brain. There are methods to overcome this complication by altering the incoming beam and undertaking image subtraction, but the details [49] are beyond the scope of this chapter.

In all nonlinear imaging systems, however, it is also possible to collect the light in the forward direction. In the case of fluorescence, the light is emitted at all solid angles (4π steradians) and thus as much light goes forward as backwards (though frequently through more samples and thus a potential loss of signal). In the case of second and third harmonic imaging, the emitting dipole has a preference for the forward direction and thus collecting after the sample, as shown above, is a very sensible option [50].

For the CARS microscopy, the situation is more complex. As described above, the CARS signal is generated by a parametric process and this means that no energy is transferred to the sample. Thus, CARS can occur when no resonant molecules are present in the focal volume as the energy difference between the pump and Stokes wavelength is simply removed as a nonresonant background, though the CARS signal is much larger when there is a resonant molecule present. This nonresonant background signal can limit the sensitivity and the method of detection can be critical in achieving a high signal-to–noise ratio. In the Forward CARS configuration [51], the signal is detected in the forward direction using a high NA objective on the far side of the sample (transmission detector in the above diagram). This F-CARS signal is large (due to the process of scattering being forward-biased in this situation) and thus the nonresonant background (frequently caused due to the water in the sample) can be removed by simple image subtraction. However, in the epi configuration, the back-scattered light is detected, when the nonresonant light is not present [41]. This method is particularly suitable when objects being imaged are smaller than the excitation wavelength as more light is directed back through the system. It is also a preferred method in highly scattering samples (e.g., brain) when the normally forward propagating CARS signal is back-scattered.

There is one other consideration that is frequently overlooked in signal detection in nonlinear microscopy. All practical systems now use a pulse laser source running at a high repetition frequency and thus lock-in, or phase-sensitive detection is possible [52]. Using a radio-frequency lock-in detector (such as the chips present in every mobile phone) background light caused by room lights (typically around 100–120 Hz) is rejected very easily as the laser sources are typically running around 80 MHz. Indeed by adjusting the phase of the detector it is possible to make a measurement of fluorescent lifetimes, or separate the SHG and CARS signals (which are virtually instantaneous with the laser pulse) from fluorescent signals, which are typically delayed by several nanoseconds due to the inherent fluorescent lifetime in all fluorescent processes.

5.5 RECENT ADVANCES IN NONLINEAR MICROSCOPY

5.5.1 Miniature Instrumentation and Clinical applications

It is now clear that the basic methodologies in nonlinear microscopy are now well established, but it is worth considering the current directions that research projects are taking. One obvious line of activity is to reduce the size and complexity of the instrumentation. In terms of laser sources, as described above, this has already taken place and, from that perspective, it is now the cost rather than the complexity that is the limiting factor. For beam-scanned systems, again the technology currently available in commercial systems performs well in the standard biological imaging laboratory. However, the next moves are clearly toward miniaturization as the imaging methods move toward less-invasive and more in vivo applications, where the ultimate goal may well be for routine clinical use.

The first published work in the direction of miniaturization was undertaken in around 2001 in Bell Labs [53]. Here, the system delivered the ultrashort pulses to a miniature scanning device within a rat brain. The end of the fiber was driven in a figure-of-eight pattern so that a specific area of the brain was imaged. The animal was free to move though tethered through the optical fiber. The pulse lengthening effect of sending ultrashort pulses through a length of the optical fiber was compensated for using a prechirping technique. Here, for the standard optical fiber in which the longer wavelengths travel more quickly using a grating or prism, the shorter wavelengths of light can be sent into the optical fiber first such that by the time the light reaches the end of the fiber the different wavelengths are again back together temporally, and one has ultra-short pulses [54]. The emitted light was collected by the same scanning fiber and detected after the tethering system. Two years later the method was used to understand a biological questions that had not previously been possible to even ask as the imaging methodology was not available [55].

The resolution of this method was around 3–5 μm and an alternative method has been the development of a more rigid probe that is placed in an anesthetized animal. In order to make the probes as small as possible, a technology originally developed for the telecoms markets, that of graded index (GRIN) optics, has been used [56]. Again the light is delivered via an optical fiber with pulse compression, but the emerging light is reimaged from the end of the fiber into the sample using two GRIN lenses. This means that one has a relatively high numerical aperture imaging systems with a diameter of around 2 mm. Subsequently, though not used in a nonlinear manner, a single longer GRIN optic has been used [57], along with a combination of GRIN and conventional optics in a nonlinear system [58]. This technology has also been applied to CARS imaging [59] though the detection via the excitation fiber is not ideal as explained above due to the directionality of the CARS emission. An alternative route to optically sectioned imaging is via a coherent optical fiber bundle, this clearly increased the diameter of the probe but has the advantage of potentially higher resolution images [60].

Thus, the route to miniaturized probes has clearly made very rapid progress and some of these methods are now making their way into the clinic primarily as a potential cancer diagnostic instrument. Generally, here the full range of nonlinear imaging methods are thrown at the challenge with the different modalities highlighting different aspects of the tissue, most frequently skin [61]. For obvious reasons, the application of fluorescently labeled fluorophores is ethically much harder in the clinic, and thus endogenous compounds have to be excited by one of the nonlinear methods described above. In the reference quoted, multiphoton fluorescence, harmonic excitation, and CARS are all used to examine the skin in one of the first full-scale clinical trials of nonlinear imaging as a method of optical bioscopy.

5.5.2 Adaptive Optics for In-Depth Imaging

It should also be noted that as well as the development of miniature probes for minimally invasive in-depth imaging, conventional non-linear microscopes can have their depth and resolution increased through the use of active optical elements, or adaptive optics [62, 63]. Typically in microscopy the optical element is a mirror whose shape can be changed via the application of a control voltage. As one images deeply into the sample, the tissue through which the light has to pass has an optical effect on the excitation light increasing the focused spot size. This leads to a loss of resolution and also a loss of signal as the excitation light is spread over a larger volume. Figure 5.9 illustrates the way that the method works and has mostly been applied in beam scanned systems. Here the incoming laser beam is directed off an adaptive optical element before entering the back aperture of the lens. By placing the opposite wavefront distortion on the incoming light to that induced by the tissue optics the result at the focus of the imaging system is a plane wavefront, and the resolution and signal levels can be restored.

There are several methods to determine the actual shape of the mirror, but the vast majority currently use an image metric based method. Various mirror shapes are applied to the adaptive optic element and the effect on the quality of the image (using a factor such as contrast, brightness, edge definition) is used to determine if that mirror shape has improved the image. Using different optimization algorithms

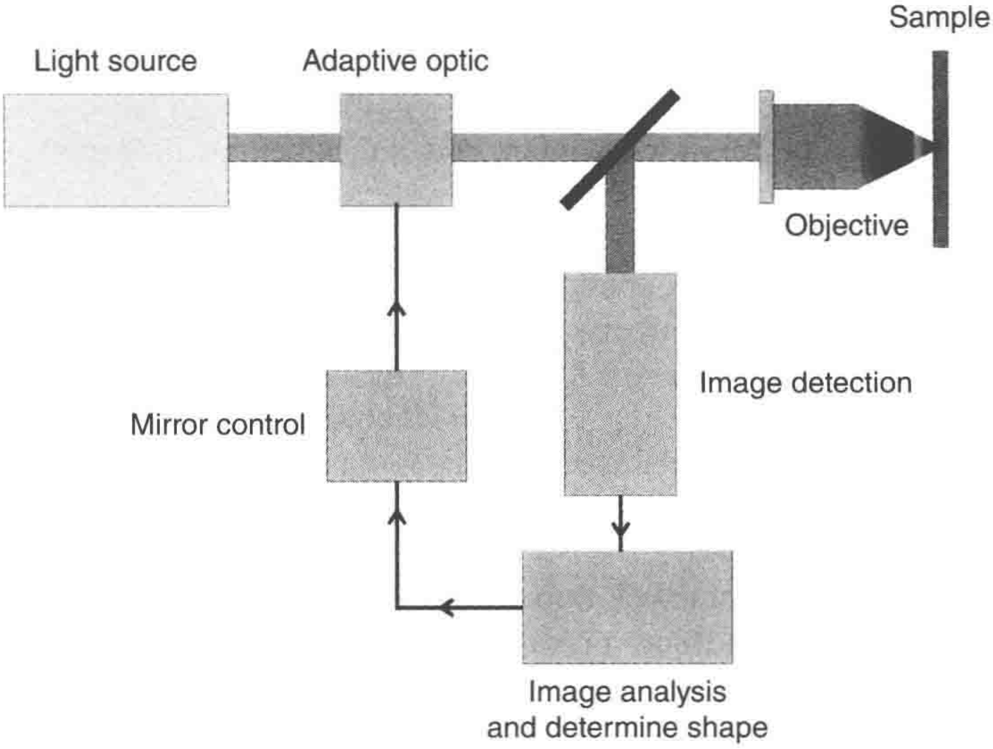

FIGURE 5.9 Basic implementation of adaptive optics to compensate for optical aberrations.

(as described in the two papers quoted) the best mirror shape can be approached very rapidly. In one practical implementation when the technique was applied to CARS microscopy for the first time [64] the signal at a depth of 750 microns (when the objective hit the sample) was larger than the original signal without adaptive optics at a depth of 20 microns. In addition to removing sample-induced aberrations, adaptive optics can also remove the residual aberrations present in an optical system even when it has been aligned.

5.6 WIDEFIELD OPTICAL SECTIONING BY SPECIALIZED ILLUMINATION METHODS

In all of the systems described above a point source of illumination has been used that has subsequently been scanned across the sample to build up an image pixel by pixel. While this without doubt provides the highest resolution images (without considering sub-diffraction imaging methods) the beam scanning is inherently slow compared to using a camera to record an entire image in one shot. However, in most situations this does not provide any level of optical sectioning but through the use of controlled light patterns optical sectioning can take place.

5.6.1 Single Plane Illumination Microscopy (SPIM)

In the first method, Single (or selective) Plane Illumination Microscopy, a sheet of light is used to illuminate the sample [65]. The basic configuration is illustrated in Figure 5.10. Here light is introduced to the sample (which needs to be transparent such

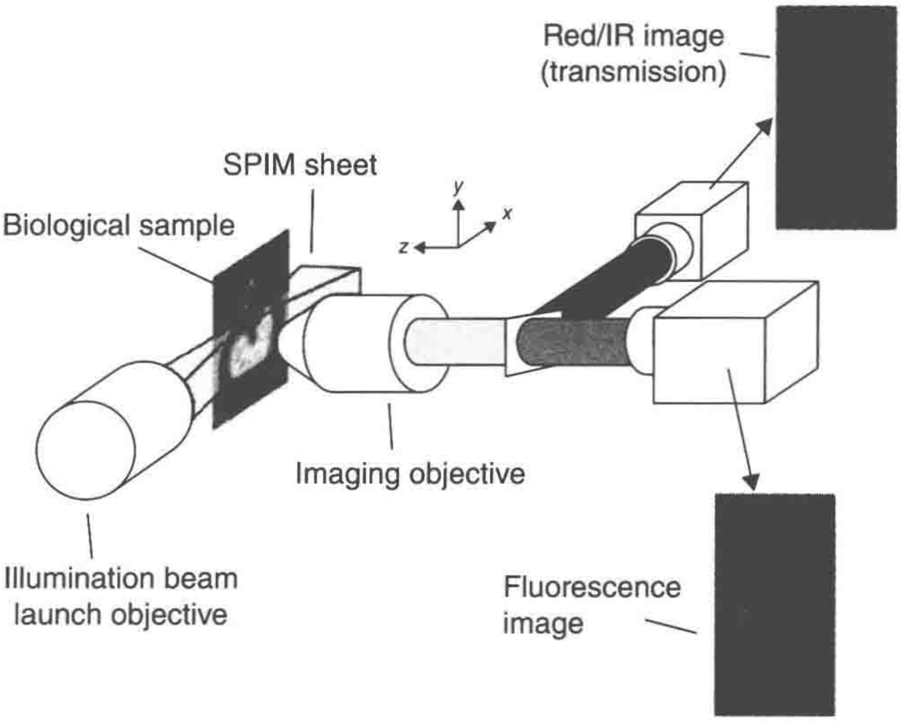

FIGURE 5.10 Basic single-plane illumination microscope configuration.

as an embryo) in a sheet produced using a cylindrical lens and microscope objective combination. This creates a sheet of light within the sample only illuminating a single plane. With a sample that is fluorescently labeled only the areas illuminated will produce fluorescence, which is then viewed perpendicular to the illumination source through a second microscope objective.

One has thus taken a single optical slice through the sample and captured an entire optical plane in a single camera exposure. By then moving the sample through this illumination system an entire three-dimensional image can be built up rapidly. In the illustration of Figure 5.10 an additional feature is present, that of an infrared transmission image, which can be used to synchronize any repeated movement in the sample, for example, from a beating heart, to effectively freeze the motion without needing to stop the heart beating [66, 67]. There are a large number of variations in the method, for example, using nonlinear excitation within the beam [68] and through the use of multiple angles of excitation [69, 70] but the basic principle of illuminating and observing perpendicular, or nearly so, applies.

5.6.2 Structured Illumination Microscopy

An alternative approach to obtaining optical sectioning is provided by the method of structured light [71] and a brief description is included here as a commercial "add-on" to a standard microscope is now available. The basic system is shown in Figure 5.11.

Light from a noncoherent source, and even a candle has been used as the method is highly efficient, is collimated and directed onto a grid with a regular pattern of lines, ideally high contrast sine waves of a single frequency. This grid pattern is then projected onto the sample through the objective and the returned light is detected on

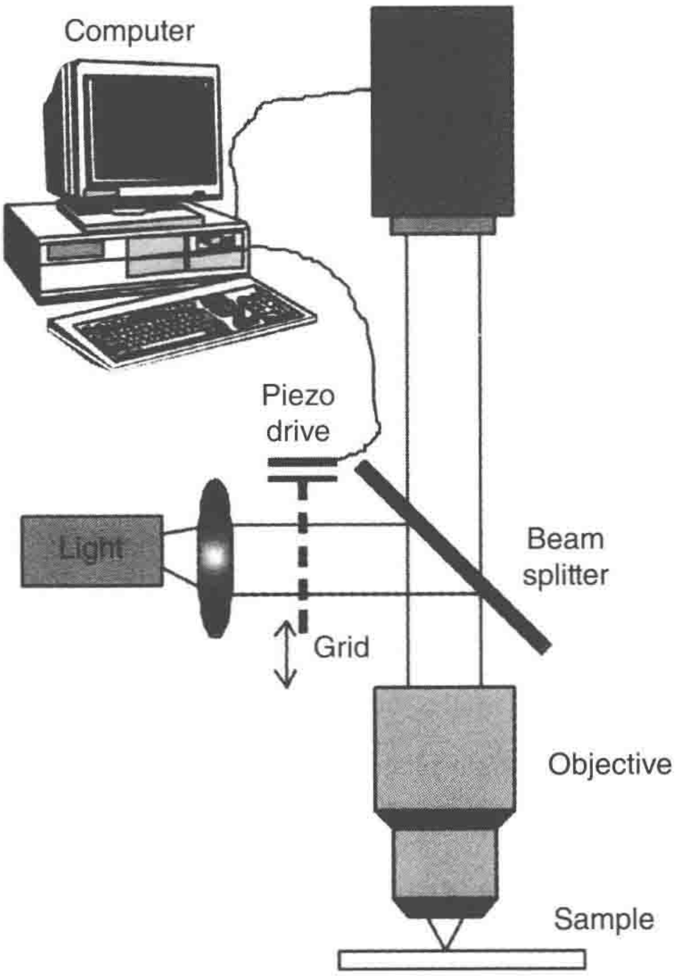

FIGURE 5.11 Basic structured illumination configuration.

a CCD camera in either fluorescence or a reflection mode and an image is captured. The grid is then translated laterally by a third of its spacing and second image taken before it is advance a further third and the final picture stored.

Each of the images has the grid pattern present and if all the three images are directly added together one just has the conventional wide field image. However, if the images are manipulated in another way,

$$I_{\text{section}} = [(I_1 - I_2)^2 + (I_1 - I_3)^2 + (I_2 - I_3)^2]^{1/2}, \tag{5.6}$$

where I_1, I_2, and I_3 are the three individual images, then in the focal plane the pattern adds in such a way as to remove the structured illumination to give a uniform illumination. However, the light from outside the focal plane combines to leave a uniformly dark image. This means that after combining the images one only has the image from the focal plane left, and hence an optical section has been obtained.

This method does not provide the high optical sectioning of the pinhole, in practical instruments, but is significantly simpler than any scanned system and hence has a role as a low cost optical sectioning system. The method has also been combined with both rigid and flexible endoscopes to produce miniature high speed optically sectioned images [72]. The advantage over other systems described above is the speed of imaging as the beam does not need to be scanned to every pixel. The method of placing a pattern onto the image has also been combined with an SPIM system to improve the resolution and contrast in the images [73].

5.6.3 Sub-diffraction-Limited Imaging

It is worth a brief final comment on methods that have been developed to beat Abbe's diffraction limit for imaging resolution [3]. If these methods truly beat Abbe's theory is a subject for conjecture far beyond the scope of this chapter, but several methods without doubt now produce images in which the resolution is around a tenth of that predicted by Abbe and frequently even higher resolution images are possible under ideal circumstances. The brief synopsis below does not attempt to cover all of the methods, but outlines three.

The first method to be mentioned is that pioneered by Stefan Hell and lateral resolutions of 28 nm have been reported through the use of stimulated emission to deplete the fluorescently excited volume with a second laser pulse [74, 75]. In Stimulated Emission Depletion (STED) microscopy two laser beams are aligned co-linearly through the objective, but with different beam profiles Figure 5.12.

A pulsed excitation beam is used to excite the fluorescence within the sample with pulses up to 100 ps. A second pulse between 100 fs and 300 ps, tuned to the emission wavelength, is timed to arrive at the end of the excitation pulse and with a spatial profile that overlaps the excitation pulse, but generally has a dark "hole" overlapping the central point of the original excitation beam. This second beam causes stimulated emission from the sample and hence a gated detector (activated after the end of the second pulse) only receives fluorescent light from the undepleted, central portion of the initial excitation volume. Increasing the intensity of the stimulating beam effectively reduces the "size" of the central dark regions meaning that the remaining fluorescence comes from a smaller area, which can be sub-wavelength. To build up images, either the sample or the beam needs to be scanned in a point-by-point manner, and clearly, this means that the imaging method is not rapid.

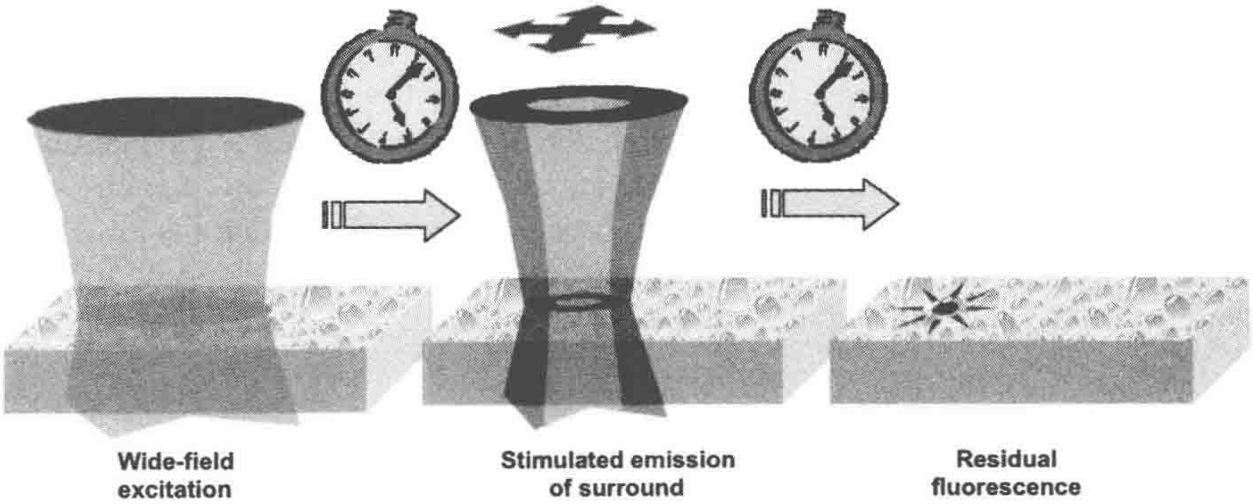

FIGURE 5.12 STED microscopy using the dark region at the center of an annular beam to get sub-wavelength resolution.

Structured illumination can also be used to build up sub-diffraction-limited imaging and this method has been pursued by many groups in a number of different formats and reviews of the early work can be found in two major articles written by Gustafsson [76] and Heintzmann [77]. In simple terms, the detail in any image is carried by the high spatial frequencies and the limiting element in transmitting these spatial frequencies is typically set by the numerical aperture of the objective lens. To overcome this limitation, a moiré fringe method is adopted. A spatial light pattern is placed onto the sample of known frequency and this pattern is rotated to several positions, typically nine or fifteen, with images being taken at every angle. The pattern of light interacts with the high frequency detail in the sample, producing a low "beat frequency" determined by the spatial frequency difference between the pattern and detail within the sample. This low frequency information is able to pass through the objective lens and all of the images are subsequently processed (via Fourier transforms in a computer) adding back the original pattern frequency to produce a high resolution image. Typical images are now possible at around 10 nm, and as the images are captured using a wide field camera, the method is faster than point scanning.

The most recent method of beating the diffraction limit involves the use of special fluorophores that can be switched from an active to inactive state (i.e., their fluorescence properties are controllable). These methods have developed two names for basically the same process, namely STORM [78] or PALM [79, 80]. Here a photoswitchable fluorophore is introduced into the substance. Initially all of the fluorophores are in the "off-state." A very low level of light (typically UV) is then directed onto the sample, which has the effect of altering some of the fluorescent molecules into the "on-state" through a photo-induced molecular shape change. A conventional wide field fluorescent image is then taken from the small number of fluorescent molecules. A third burst of light then "switches-off" all the fluorophores. This process is then repeated many times stochastically switching on the fluorophores in the sample. The images are subsequently analyzed as each fluorescent molecule will have illuminated a small array of pixels on the camera. The center of mass of each array of pixels is found (typically this can be done with an accuracy of around 2–10 nm) and this is then assumed to be the point of light emission. Thus by building up a large number of images one assumes that every potential fluorophore has been excited and where there are several then they will have been excited many times to build up the contrast in the image. In a variation of this, it has been found that many fluorescent molecules have a natural tendency to move from the "off" to "on" state when imaged rapidly enough and when the concentration of molecules is low. Thus by applying the correct mathematical formulae one can build up the same form as those with the photoswitchable fluorophores [81].

5.7 SUMMARY

This chapter has only touched upon the methods available for optical microscopy based upon fluorescence and can only provide an outline of the work undertaken in the field. There are many high quality textbooks on the subject, some of which have been referenced, and the reader is encouraged to study those for the specific details of methods mentioned here. The practical implementation of standard instruments has been covered with an outline of the physical processes behind the different excitation methods. With increasing complexity the chapter has ended with three-dimensional imaging techniques with optical resolutions down to 10 nm, approaching that of electron microscopes. Optical microscopes have developed a long way in 400 years and it is to be anticipated that with advances in new technologies new tools will soon be provided to users of optical microscopy.

REFERENCES

[1] Pliny the Elder. *The Natural History* (H.G Bohm, London, 1893; translated by John Bostock) Book XXXVII, Chap 10.

[2] R. Hooke, *Micrographia: or, Some Physiological Descriptions of Minute Bodies Made by Magnifying Glasses* (J. Martyn and J. Allestry, London, 1665).

[3] E. Abbe, "On the estimation of the aperture in the microscope," *J. R. Microsc. Soc.* **2**, 388–423 (1881).

[4] F. Zernike, "The concept of degree of coherence and its application to optical problems," *Physica* **5**, 785–795 (1938).

[5] J. R. Lakowicz, *Principles of Fluorescence Spectroscopy* (Springer, New York, 2010).

[6] R. Heim, A. Cubitt, and R. Tsein, "Improved green fluorescence," *Nature* **373**, 663–664 (1995).

[7] N. Shaner, P. Steinbach, and R. Tsien, "A guide to choosing fluorescent proteins," *Nat. Methods* **2**, 905–909 (2005).

[8] E. Hecht, *Optics*, 4th ed. (Pearson, 2003).

[9] M. Minsky, US Patent No. 3,013,467, 1961.

[10] M. D. Egger and M. Petrăn, "New reflected-light microscope for viewing unstained brain and ganglion cells," *Science* **157**, 305–307 (1967).

[11] C. J. Sheppard and T. Wilson, "The theory of the direct-view confocal microscope," *J. Microsc.* **124**, 107–117 (1981).

[12] J. G. White, W. B. Amos, and M. Fordham, "An evaluation of confocal versus conventional imaging of biological structures by fluorescence light microscopy," *J. Cell Biol.* **105**, 41–48 (1987).

[13] G. Van Meer, E. H. K. Stelzer, R. W. Wijnaendts-van Resandt, and K. Simons, "Sorting of sphingolipids in epithelial (Madin–Darby canine kidney) cells," *J. Cell Biol.* **105**, 1623–1635 (1987).

[14] J. Pawley, *Handbook of Biological Confocal Microscopy*, 3rd ed. (Kluwer Academic Publishers, 2006).

[15] J. M. Girkin, A. I. Ferguson, D. L. Wokosin, and A. M. Gurney, "Confocal microscopy using an InGaN violet laser diode at 406nm," *Opt. Exp.* **7**, 336–341 (2000).

[16] A. Egner, V. Andresen, and S. W. Hell, "Comparison of the axial resolution of practical Nipkow-disk confocal fluorescence microscopy with that of multifocal multiphoton microscopy: theory and experiment," *J. Microsc.* **206**, 24–32 (2002).

[17] M. Goeppert-Mayer, "Ueber Elementarake mit zwei Quantenspruengen," *Annu. Phys.* **9**, 273–283 (1931).

[18] W. Kaiser and C. G. B. Garrett, "Two photon excitation of CaF_2:Eu^{2+}," *Phys. Rev. Lett.* **7**, 229–231 (1961).

[19] S. A. Lee, R. Wallenstein, and T. W. Hansch, "Doppler free two photon spectroscopy," *Phys. Rev. Lett.* **35**, 1262–1265 (1975).

[20] C. J. R. Shepherd and R. Kompfiner, "Resonant scanning optical microscope," *Appl. Opt.* **17**, 2879–2891 (1978).

[21] T. Wilson and C. J. R. Shepherd, "Non-linear microscopy," in *Theory and Practice of Scanning Optical Microscopy* (Academic Press, Boston, MA, 1984), Chap. 10.

[22] W. Denk, J. H. Strickler, and W. W. Webb, "Two-photon excitation in laser-scanning fluorescence microscopy," *Science* **248**, 73–76 (1990).

[23] P. E. Hannienen, E. Soni, and S. W. Hell, "Continuous wave excitation two-photon fluorescence microscopy," *J. Microsc.* **176**, 222–225 (1994).

[24] W. Denk, D. W. Piston, and W. W. Webb, "Two-photon excitation in laser scanning microscopy," in *Handbook of biological confocal microscopy*, 2nd ed., edited by J. B. Pawley (Plenum Press, New York, 1995), pp. 445–458.

[25] J. M. Girkin and D. L. Wokosin, "Practical multiphoton microscopy," in *Confocal and Multiphoton Microscopy*, edited by A. Diaspro (John Wiley & Sons, New York, 2000), Chap. 31.

[26] K. Koenig, Y. Tadir, P. Patrizio, M. W. Berns, and B. J. Tromberg, "Effects of ultraviolet exposure and near infrared laser tweezers on human spermatozoa," *Hum. Reprod.* **11**, 2162–2164 (1996).

[27] P. Franken, A. Hill, C. Peters, and G. Weinreich, "Generation of optical harmonics," *Phys. Rev. Lett.* **7**, 118–120 (1961).

[28] R. Boyd, *Nonlinear Optics*, 3rd ed. (Elsevier, 2008).

[29] C. J. R. Sheppard, J. N. Gannaway, R. Kompfner, and D. Walsh, "The scanning harmonic optical microscope," *IEEE Trans. Quantum Electron.* **13**, 100D (1977).

[30] C. J. R. Sheppard and R. Kompfner, "Resonant scanning optical microscope," *Appl. Opt.* **17**, 2879–2882 (1978).

[31] S. Roth and I. Freund, "Optical second harmonic scattering in rat-tail tendon," *Biopolymers* **20**, 1271–1290 (1981).

[32] S. Roth and I. Freund, "Second harmonic generation and orientational order in connective tissue: a mosaic model for fibril orientational ordering in rat-tail tendon," *J. Appl. Crystallogr.* **15**, 72–78 (1982).

[33] P. J. Campagnola, M. D. Wei, A. Lewis, and L. M. Loew, "High-resolution nonlinear optical imaging of live cells by second harmonic generation," *Biophys. J.* **77**, 3341–3349 (1999).

[34] L. Moreaux, O. Sandre, M. Blanchard-Desce, and J. Mertz, "Membrane imaging by simultaneous second-harmonic generation and two-photon microscopy," *Opt. Lett.* **25**, 320–322 (2000).

[35] Y. Barad, H. Eisenberg, M. Horowitz, and Y. Silberg, "Nonlinear scanning laser microscopy by third harmonic generation," *Appl. Phys. Lett.* **70**, 922–924 (1997).

[36] D. Debarre, W. Supatto, A. Pena, A. Fabre, T. Tordjmann, L. Combettes, M.-C. Schanne-Klein, and E. Beaurepaire, "Imaging lipid bodies in cells and tissue using third-harmonic generation microscopy," *Nat. Methods* **3**, 47–53 (2006).

[37] Y. Guo, H. E. Savage, F. Liu, S. P. Schantz, P. P. Ho, and R. R. Alfano, "Subsurface tumor progression investigated by noninvasive optical second harmonic tomography," *Proc. Natl. Acad. Sci. USA* **96**, 10854–10856 (1999).

[38] C.-K. Tsai, T.-D. Wang, J.-W. Lin, R.-B. Hsu, L.-Z. Guo, S.-T. Chen, and T.-M. Liu, "Virtual optical biopsy of human adipocytes with third harmonic generation microscopy," *Biomed. Opt. Exp.* **4**, 178–186 (2013).

[39] P. D. Maker and R. W. Terhune, "Study of optical effects due to an induced polarization third order in the electric field," *Phys. Rev.* **137**, 7–10 (1965).

[40] A. Zumbusch, G. R. Holtom, and X. S. Xie, "Three-dimensional vibrational imaging by coherent anti-stokes Raman scattering," *Phys. Rev. Lett.* **82**, 4142–4145 (1999).

[41] A. Volkmer, J. Cheng, and X. S. Xie, "Vibrational imaging with high sensitivity via epidetected coherent anti-stokes Raman scattering microscopy," *Phys. Rev. Lett.* **87**, 023901 (2001).

[42] J. Cheng, L. D. Book, and X. S. Xie, "Polarization coherent anti-Stokes Raman scattering microscopy," *Opt. Lett.* **26**, 1341–1343 (2001).

[43] J. Cheng and X. S. Xie, "Coherent anti-Stokes Raman scattering microscopy: instrumentation, theory, and applications," *J. Phys. Chem. B* **108**, 827–840 (2004).

[44] C. W. Freudiger, W. Min, B. G. Saar, S. Lui, G. R. Holtom, C. He, J. C. Tsai, J. X. Kang, and X. S. Xie, "Label-free biomedical imaging with a high sensitivity by stimulated Raman scattering microscopy," *Science* **322**, 1857–1861 (2008).

[45] J. M. Girkin, "Laser sources for non-linear microscopy," in *Handbook of Biomedical Nonlinear Optical Microscopy*, edited by B. Masters and P. So (Oxford University Press, 2008), Chap. 8.

[46] M. Müller, J. Squier, R. Wolleschensky, U. Simon, and G. Brakenhoff, "Dispersion pre-compensation of 15 femtosecond optical pulses for high-numerical-aperture objectives," *J. Microsc.* **191**, 141–150 (1998).

[47] A. M. Weiner, "Femtosecond pulse shaping using spatial light modulators," *Rev. Sci. Instrum.* **71**, 1929–1951 (2000).

[48] F. Ganikhanov, S. Carrasco, X. S. Xie, M. Katz, W. Seitz, and D. Kopf, "Broadly tunable dual-wavelength light source for coherent anti-Stokes Raman scattering microscopy," *Opt. Lett.* **31**, 1292–1294 (2006).

[49] A. Leray and J. Mertz, "Rejection of two-photon fluorescence background in thick tissue by differential aberration imaging," *Opt. Exp.* **14**, 10565–10573 (2006).

[50] N. Moreno, J. A. Feijo, and G. Cox, "Implementation and evaluation of a detector for forward propagated second harmonic signals," *Micron* **35**, 721–724 (2004).

[51] A. Zumbusch, G. R. Holtom, and X. S. Xie, "Three-dimensional vibrational imaging by coherent anti-Stokes Raman scattering," *Phys. Rev. Lett.* **82**, 4142–4145 (1999).

[52] W. G. Fisher, D. W. Piston, and E. A. Wachter, "Phase sensitive demodulation in multiphoton microscopy," *Microsc. Microanal.* **8**, 191–202 (2002).

[53] F. Helmchen, M. S. Fee, D. W. Tank, and W. Denk, "A miniature head-mounted two-photon microscope. High-resolution brain imaging in freely moving animals," *Neuron* **31**, 903–912 (2001).

[54] R. L. Fork, O. E. Martinez, and J. P. Gordon, "Negative dispersion using pairs of prisms," *Opt. Lett.* **9**, 150–152 (1984).

[55] F. Helmchen, "Dynamic confocal imaging of living brain miniaturization of fluorescence microscopes using fibre optics," *Exp. Physiol.* **87**, 737–745 (2002).

[56] D. Bird and M. Gu, "Two-photon fluorescence endoscopy with a micro-optic scanning head," *Opt. Lett.* **17**, 1552–1554 (2003).

[57] C. D. Saunter, S. Semprini, C. Buckley, J. Mullins, and J. M. Girkin, "High spatial resolution fluorescent imaging," *Biomed. Opt. Exp.* **3**, 1274–1278 (2012).

[58] R. P. J. Barretto, B. Messerschmidt, and M. J. Schnitzer, "In vivo fluorescence imaging with high-resolution microlenses," *Nat. Methods* **6**, 511–512 (2009).

[59] B. G. Saar, R. S. Johnston, C. W. Freudiger, X. S. Xie, and E. J. Seibel, "Coherent Raman scanning fiber endoscopy," *Opt. Lett.* **36**, 2396–2398 (2011).

[60] S. Santos, K. K. Chu, D. Lim, N. Bozinovic, T. N. Ford, C. Hourtoule, A. C. Bartoo, S. K. Singh, and J. Mertz, "Optically sectioned fluorescence endomicroscopy with hybrid-illumination imaging through a flexible fiber bundle," *J. Biomed. Opt.* **14**, 030502 (2011).

[61] K. König, H. G. Breunig, R. Bückle, M. Kellner-Höfer, M. Weinigel, E. Büttner, W. Sterry, and J. Lademann, "Optical skin biopsies by clinical CARS and multiphoton fluorescence/SHG tomography," *Laser Phys. Lett.* **8**, 465–468 (2011).

[62] M. J. Booth, "Adaptive optics in microscopy," *Phil. Trans. A Math. Phys. Eng. Sci.* **365**, 2829–2843 (2007).

[63] J. M. Girkin, S. Poland, and A. J. Wright, "Adaptive optics for deeper imaging of biological samples," *Curr. Opin. Biotechnol.* **20**, 106–110 (2009).

[64] A. J. Wright, S. P. Poland, J. M. Girkin, C. W. Freudiger, C. L. Evans, and X. S. Xie, "Adaptive optics for enhanced signal in CARS microscopy," *Opt. Express* **15**, 18209–18219 (2007).

[65] J. Huisken, J. Swoger, F. Del Bene, J. Wittbrodt, and E. H. K. Stelzer, "Optical sectioning deep inside live embryos by selective plane illumination microscopy," *Science* **305**, 1007–1009 (2004).

[66] J. M. Taylor, C. D. Saunter, G. D. Love, J. M. Girkin, D. J. Henderson, and B. Chaudhry, "Real-time optical gating for three-dimensional beating heart imaging," *J. Biomed. Opt.* **16**, 116021 (2011).

[67] J. M. Taylor, J. M. Girkin, and G. D. Love, "High-resolution 3D optical microscopy inside the beating zebrafish heart using prospective optical gating," *Biomed. Opt. Express* **3**, 314–321 (2012).

[68] J. Palero, S. I. C. O. Santos, D. Artigas, and P. Loza-Alvarez, "A simple scanless two-photon fluorescence microscope using selective plane illumination," *Opt. Express* **18**, 8491–8498 (2010).

[69] J. Swoger, J. Huisken, and E. H. K. Stelzer, "Multiple imaging axis microscopy improves resolution for thick-sample applications," *Opt. Lett.* **28**, 1654–1656 (2003).

[70] J. Huisken and D. Y. R. Stainier, "Even fluorescence excitation by multidirectional selective plane illumination microscopy (mSPIM)," *Opt. Lett.* **32**, 2608–2610 (2007).

[71] M. A. A. Neil, R. Juskaitis, and T. Wilson, "Method of obtaining optical sectioning by using structured light in a conventional microscope," *Opt. Lett.* **22**, 1905–1907 (1997).

[72] N. Bozinovic, C. Ventalon, T. Ford, and J. Mertz, "Fluorescence endomicroscopy with structured illumination," *Opt. Express* **16**, 8016–8023 (2008).

[73] P. J. Keller, A. D. Schmidt, A. Santella, K. Khairy, Z. Bao, J. Wittbrodt, and E. H. K. Stelzer, "Fast, high-contrast imaging of animal development with scanned light sheet-based structured-illumination microscopy," *Nat. Methods* **7**, 637–642 (2010).

[74] S. W. Hell and J. Wichmann, "Breaking the diffraction resolution limit by stimulated emission': stimulated-emission-depletion fluorescence microscopy," *Opt. Lett.* **19**, 780–782 (1994).

[75] T. A. Klar, E. Engel, and S. W. Hell, "Breaking Abbe's diffraction resolution limit in fluorescence microscopy with stimulated emission depletion beams of various shapes," *Phys. Rev. E* **64**, 066613 (2001).

[76] M. G. L. Gustafsson, "Nonlinear structured-illumination microscopy': wide-field fluorescence imaging with theoretically unlimited resolution," *Proc. Natl. Acad. Sci.* **102**, 13081–13086 (2005).

[77] R. Heintzmann and M. G. L. Gustafsson, "Subdiffraction resolution in continuous samples," *Nat. Photon.* **3**, 362–364 (2009).

[78] M. J. Rust, M. Bates, and X. Zhuang, "Sub-diffraction-limit imaging by stochastic optical reconstruction microscopy (STORM)," *Nat. Methods* **3**, 793–796 (2006).

[79] E. Betzig, G. H. Patterson, R. Sougrat, O. W. Lindwasser, S. Olenych, J. S. Bonifacino, M. W. Davidson, J. Lippincott-Schwartz, and H. F. Hess, "Imaging intracellular fluorescent proteins at nanometer resolution," *Science* **313**, 1642–1645 (2006).

[80] S. T. Hess, T. P. K. Girirajan, and M. D. Mason, "Ultra-high resolution imaging by fluorescence photoactivation localization microscopy," *Biophys. J.* **91**, 4258–4272 (2006).

[81] S. Cox, E. Rosten, J. Monypenny, T. Jovanovic-Talisman, D. T. Burnette, J. Lippincott-schwartz, G. E. Jones, and R. Heintzmann, "Bayesian localization microscopy reveals nanoscale podosome dynamics," *Nat. Methods* **9**, 195–200 (2012).

6

CELL HANDLING, SORTING, AND VIABILITY

DARWIN PALIMA, THOMAS AABO, ANDREW BAÑAS,
AND JESPER GLÜCKSTAD

DTU Fotonik, Department of Photonics Engineering, Technical University of Denmark, Kgs. Lyngby, Denmark

The significance of optics in the study of biological cells is highlighted by the fact that the invention of the microscope in the 1700s enabled the discovery of the cell itself. Another highlight occurred two centuries later when improvements in microscope aberration-correction supported the development of cell theory, which established the cell as a fundamental unit of life [1]. The enabling role of optics in biology continues in contemporary biophotonics that no longer just uses light for basic imaging, but can exploit optical energy to enable new microscopic modalities, trigger biomolecular processes, or perform cellular microdissection and microsurgery. Moreover, the optical momentum has been effectively utilized for precision mechanical manipulation using noncontact optical forces that arise when light exchanges momentum with the material, for example, during light scattering, reflection, or refraction. These developments can help realize an all-optical "lab-on-a-microscope" concept [2], where spatially sculpted light is used to assemble structures, perform optical fractionation, and control the functionality of light-driven pumps, valves, and mixers inside microfluidic channels.

This chapter focuses on the applications of optical forces for creating optical traps and micromanipulation systems for biological cells. The optical force can be used to handle cells, for example, to measure their mechanical properties, keep them held away from substrates and other surfaces to avoid perturbations, or to move and deflect cellular populations having distinct characteristics for sorting in microfluidic

---

Photonics: Scientific Foundations, Technology and Applications, Volume IV, First Edition.
Edited by David L. Andrews.
© 2015 John Wiley & Sons, Inc. Published 2015 by John Wiley & Sons, Inc.

environments. As we will see, light energy can be a concern in this case and care must be exercised to avoid triggering unwanted parasitic effects that can potentially interfere with cellular functions and affect cell viability.

6.1 HANDLING CELLS WITH LIGHT

Ashkin's pioneering 1970 demonstration [3] on using light to exert mechanical forces on microscopic objects was motivated by atom trapping and, for over a decade, optical trapping studies used nonbiological objects. The report on the first optically trapped atoms [4] even came out shortly before the first demonstration of optical handling of cells where Ashkin et al. used visible light (Argon ion laser, $\lambda = 514.5$ nm) to trap and manipulate viruses and bacteria (tobacco mosaic virus and *Escherichia coli*) [5]. Although they claimed trapping with no apparent damage, nevertheless, they quickly followed up with a report using near-infrared (Nd:YAG laser, $\lambda = 1.06$ μm) for optical micromanipulation of yeast cells (*Saccharomyces cerevisiae*) and bacteria (*Escherichia coli*), motivated by having improved optical traps with less optical damage [6]. These reports used "optical tweezers"—at the time a newly developed tool, originally intended for atom trapping [7], which can trap cells using a single beam tightly focused by high numerical aperture microscope objectives. Optical tweezers has since become the *de facto* tool for optical manipulation of cells. However, traps using weakly focused counter-propagating beams can be preferable when the intensity hotspots from sharply focused optical tweezers are problematic for cell viability. We will return to the important issue of cell viability in more detail in Section 6.3 but, first, we start by taking a quick review of the basic principles that enable light to mechanically handle cells and proceed to survey various examples of optical cell handling and optical sorting applications.

6.1.1 Light–Cell Interaction: Momentum Exchange

Light can exert force and induce mechanical effects on cells and other objects by exchanging momentum with it. This momentum exchange depends both on the spatial distribution of the illuminating light as well as the spatial distribution of the cell's refractive index and absorption. Light–matter interaction can lead to the exchange of both linear and angular momentum, the latter leading to optical torque and rotational dynamics [8].

Dielectric microspheres have been used since Ashkin's pioneering experiments [3], and they remain as preferred structures for optical trapping research, partly owing to their practical accessibility when performing experiments as well as the tractability of a dielectric microsphere model for theoretical analyses. This model is relevant for cell handling, either as a simplified model of the cell itself or for the actual modeling of trapped dielectric microspheres that are often used as handles for indirectly manipulating cells with light.

A simplified ray optics model is shown in Figure 6.1, which illustrates the optical force that arises when light interacts with a dielectric sphere, here manifesting as

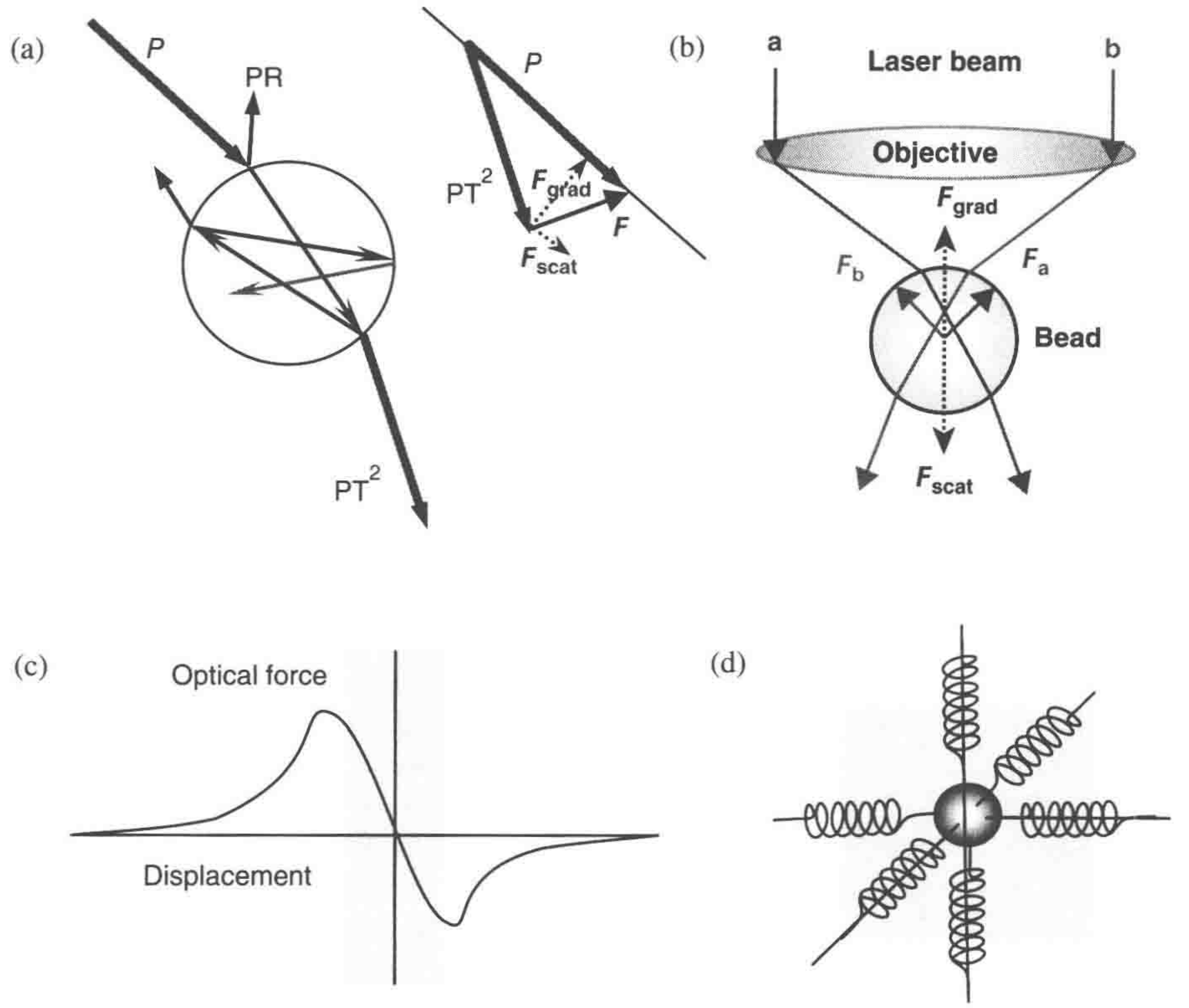

FIGURE 6.1 Ray optics model of optical force on a dielectric microsphere. (a) Illustration of a single incident ray—geometry, optical force, and force components F_{grad} and F_{scat}. (b) Illustration of a focused beam showing total F_{grad} and F_{scat}. (c) Typical plot of optical force versus displacement with a linear region for small displacements. (d) Elastic spring model for small displacements with stiffness k_x, k_y, k_z.

refraction at the interface. In this picture, the optical force balances the rate of optical momentum change due to light deflections in accordance with the momentum conservation principle. In the ray model (valid for larger objects, size $\gg \lambda$), the optical force may be decomposed into components parallel and orthogonal to the incident ray, which may be denoted as scattering force and gradient force, respectively [9]. Upon summing the respective force components from all incident rays, we can get some correspondence with the electromagnetic wave model that similarly decomposes the optical force into scattering and gradient force components [10,11] (valid for Rayleigh scattering regime [10] but can be extended in some cases [11] up to size $\leq \lambda$). In this decomposition, the scattering force describes the force from the scattering of wavevectors associated with the plane-wave components. The gradient force accounts for interference between these plane waves that can create spatially nonuniform fields that, in turn, exert nonzero force on induced dipoles in the trapped material directed along the intensity gradient.

When light having optical power, P, which is incident within a medium with refractive index, n_{m}, illuminates a cell, the optical force exerted by light on the cell due to the interaction may be written as [9]

$$F = Q\frac{n_{\mathrm{m}}P}{c}. \tag{6.1}$$

The quality factor, Q, is a measure of how well the system generates force, which depends on how much it alters the incident light momentum flux, $n_{\mathrm{m}}P/c$ (where c/n_{m} is the speed of light in the surrounding material)[1]. For example, perfect plane-wave reflection at normal incidence corresponds to $Q = 2$, while total absorption leads to $Q = 1$.

Achieving high quality factors is highly desirable, especially when handling cells, to get the most force, while keeping modest input powers, and to avoid parasitic effects from high intensities. For a beam incident in water ($n_{\mathrm{m}} = 1.33$), a quality factor of $Q = 1$ can exert 4.44 pN for every 1 mW of incident power. For the trapped microsphere illustrated in Figure 6.1, the optical force and quality factor depend on the bead position (typically similar to the simplified version shown in Figure 6.1c). For small displacements, the optical force can be modeled as an elastic spring obeying Hooke's law, $\boldsymbol{F} = -k_s$. The optical force decays with further displacements beyond a characteristic displacement comparable to the bead radius[2]. For comparison, we may take, as a point of reference, Ashkin's estimates, based on ray optics model, that found $-0.276 < Q_{\mathrm{axial}} < 0.490$ for a dielectric sphere that is axially translated along its equilibrium point (relative refractive index = $n_{\mathrm{sphere}}/n_{\mathrm{m}} = 1.2$, e.g., polystyrene in water, NA = 1.25, fully utilized, e.g., by overfilled objective illumination). The quality factor falls down to $-0.019 < Q < 0.147$ when the numerical aperture is lowered to NA ~ 0.64 (now based on Gaussian apodization, e.g., with underfilled objectives).

In contrast, Ganic et al. [12] used a more elaborate modeling based on a fully vectorial diffraction approach to model the focused beam and its interaction with the particle, with the possibility to account for the expected spherical aberration due to the index mismatch between the immersion oil and the aqueous trapping environment. The volume field information obtained allows the calculation of the Maxwell stress tensor, which forms the basis of the force calculation. A comparison of their simulation and experimental results for the maximum trapping efficiency is shown in Figure 6.2 with the size-independent ray-optics calculation indicated for comparison. It is interesting to note that, although the ray-optics result is strictly valid only for radius $r \gg \lambda$, the more sophisticated model gives a comparable result and exhibits a

---

[1] It may seem counterintuitive that light traveling n_{m} times slower in a medium increases its momentum by n_{m} times, compared to vacuum, instead of decreasing by the slowdown factor. Actually, this momentum dependence on the refractive index is the subject of the so-called Abraham–Minkowski controversy, with Minkowski for the proportional relation and Abraham for the inverse relation. Interested readers can refer to reviews on the subject (e.g., [126, 127]).

[2] Hence, the peak force may be determined, using an *escape force method*, by applying a monotonically increasing external force, for example, using precalibrated fluid drag, and then noting the escape point.

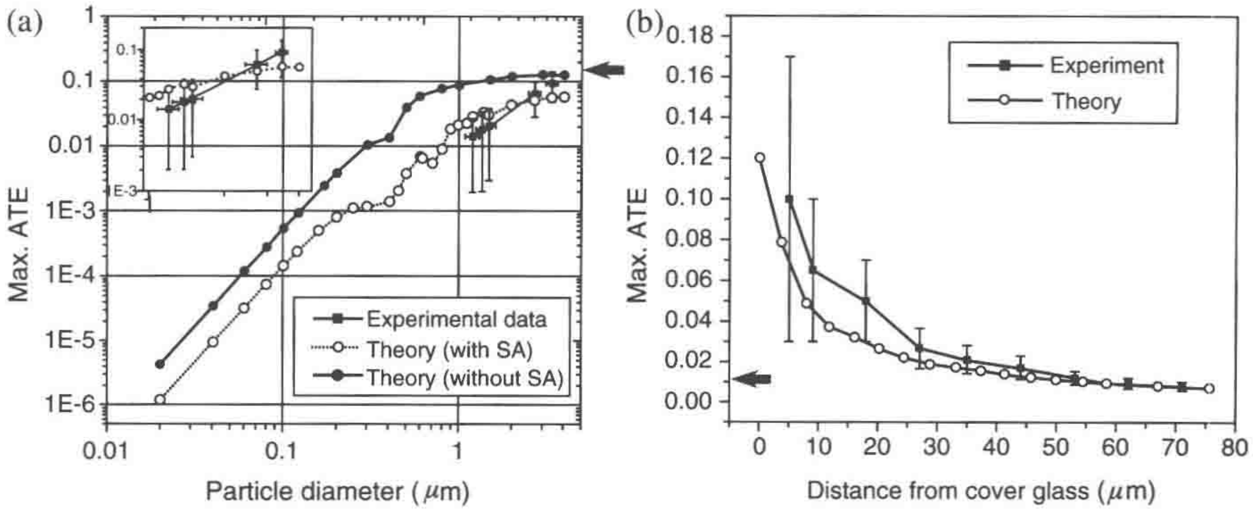

FIGURE 6.2 Peak axial trapping efficiency, ATE, of glass particles suspended in water, illuminated by a laser beam ($\lambda_0 = 1.064$ μm), focused by an oil immersion microscope objective (NA = 1.3): (a) as a function of particle size; the effect of SA is considered at a depth of 9 μm from the cover glass; the arrow indicates the ray-optics result; (b) as a function of the distance from the cover glass for particle diameter $D = 2.7$ μm; the arrow indicates the transverse trapping efficiency obtained for mammalian cells [16]. Plots adapted from Reference 12.

very weak size dependence already starting at $2r \sim \lambda$ (with the observed r^3 dependence for $r < \lambda$ is expected from Rayleigh scattering model). These experimentally determined values of trapping efficiencies are similar to those reported by others, who also typically get lower Q than the theoretical calculations (e.g., $Q = 0.026 \sim 0.18$ for microspheres with radius $r = 5$ μm illuminated at NA = 1.3) [13]. Trapping through a thick sample chamber can also degrade trapping efficiencies by an order of magnitude, due to aberrations, as illustrated in Figure 6.2b. A similar degradation based on spherical aberration is expected based on two-component analysis (scattering and gradient force) when trapping subwavelength particles [14]. However, the low power levels sufficient for trapping when using aberration correction [15] suggests that the higher Q values can be revived even when trapping through turbid medium.

A generic setup for these experimental force measurements is shown in Figure 6.3. Force calibrations require a sensitive position detector due to the position dependence of the optical force. Also, it is crucial to properly measure the power at the trapping region, for example, a dual-objective method [17] to account for the optics losses when direct *in situ* power measurement is not practical.

Overfilling the objective can utilize the full numerical aperture and give higher Q values. In practical terms, however, given the fixed available power in a laser beam, overfilling reduces the incident power on the sample and, hence, underfilling microscope objectives by an amount that depends on the size of the trapped particle optimizes the optical force [18]. This also avoids the laser heating of overfilled microscope objectives.

Single-beam optical tweezers use diffraction-limited trapping beams in the order of the wavelength. Consequently, the trapping stiffness and trapping efficiency start to exhibit only a weak dependence on particle sizes larger than the wavelength from the

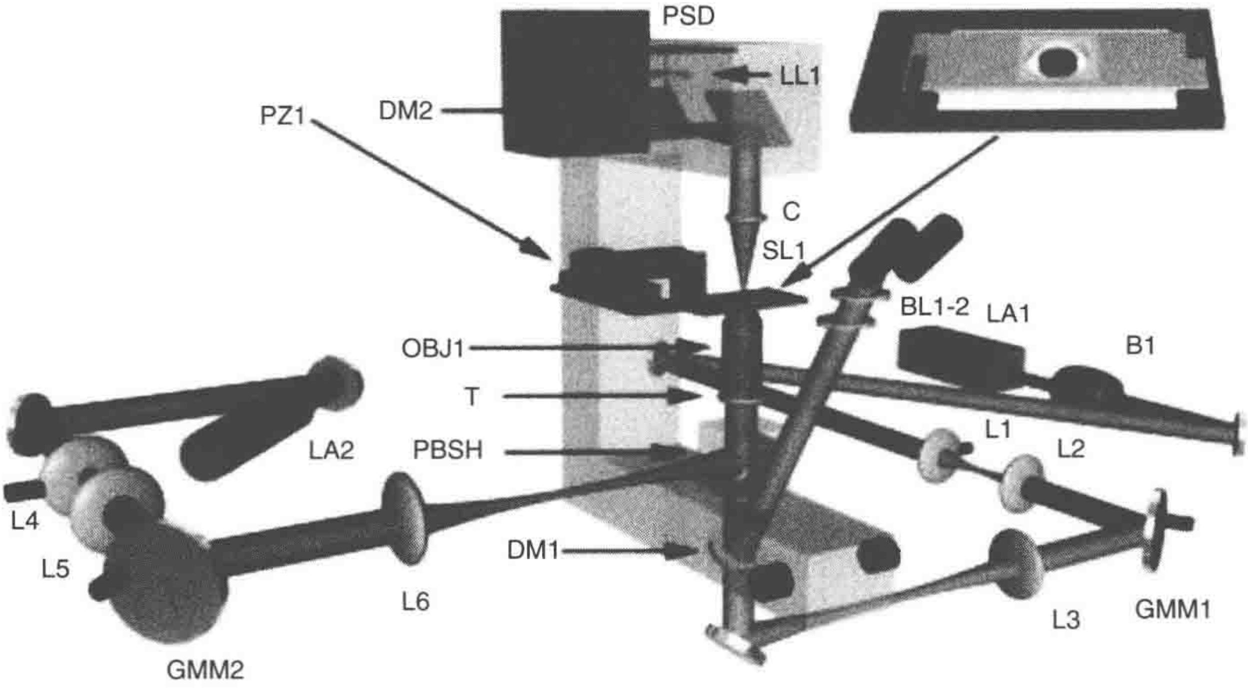

FIGURE 6.3 Schematic illustration of typical components in an optical force measurement system (adapted from Reference 19): LA1—Ar^+-pumped Ti:Sapphire trapping laser; LA2—HeNe position probe laser; B1—beam expander; L1–L6—assorted lenses; GMM1, GMM2—computer-controlled gimbal mounted mirrors; DM1, DM2—dichroic mirrors; PBSH—polarizing beam splitter; BL, BL2—block filters; OBJ1—high NA microscope objective; SL1—tailor-made sample slide; PZ1—piezo-controlled sample stage; C—oil immersion condenser to collect the probe laser light; PSD—position-sensitive detector; LL1—laser line filter. The system also includes a low noise preamplifier and a computer equipped for data acquisition (not shown).

initial r^3 dependence for subwavelength particles, as shown in Figure 6.2a. However, it is actually the trapping beam size, rather than the wavelength, that determines particle-size dependence. This is illustrated, for example, in Figure 6.4 which plots the trapping stiffness measurements based on results reported by Wei et al. [20] using dual-beam traps. In contrast to single-beam optical tweezers that require diffraction-limited tightly focused beams for stable axial trapping, dual-beam traps can use two counter-propagating trapping beams that are broader than the wavelength. Dual-beam traps may be generated, for example, using diverging beams exiting from two well-aligned fibers or as counter-propagating beams delivered using a pair of low NA microscope objectives [21]. Figure 6.4 shows that for these broad beams, the trapping stiffness still varies as $\sim r^{2.6}$ for particles already several times larger than the wavelength (but smaller than the trapping beams). The figure also plots the trapping stiffness for Chinese Hamster ovary (CHO) cells. Although it achieves trapping stiffness comparable to the polymer beads, the CHO cell result falls below the $r^{2.6}$ fit due to a lower trapping efficiency, which is the case for many biological cells.

6.1.2 Dielectric Tagging: Using Microspheres as Optical Handles

Dried cells can have refractive index comparable to polystyrene microspheres [22], but living biological cells have high water content and so typically have lower

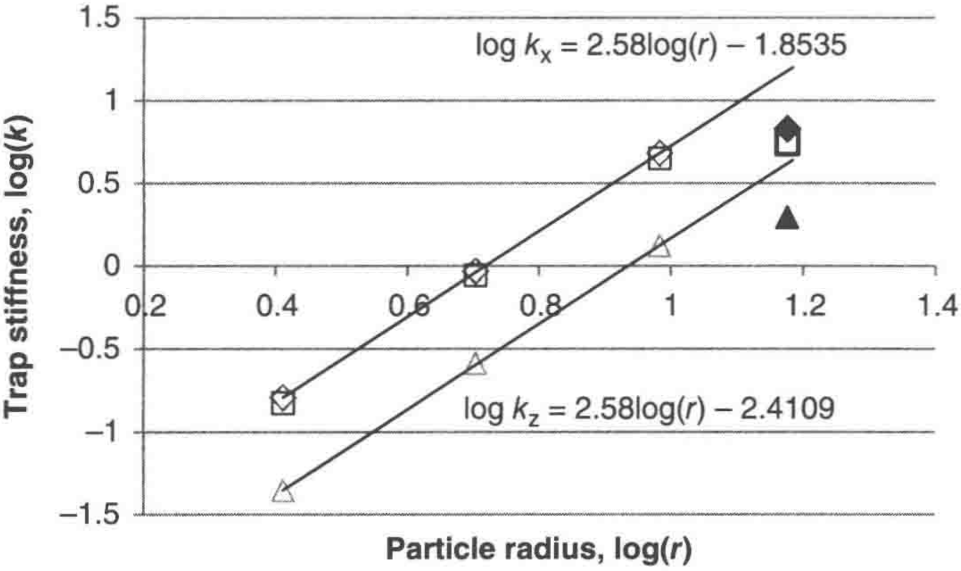

FIGURE 6.4 Optical force constants for different sizes of silica particles. The slope of this log(k) versus log(r) plot indicates that k varies as $r^{2.58}$. Stiffness measurements for CHO cells fall below the interpolated line. Plots are based on data from Reference 20. Optics express.

refractive indices closer to that of water (see some values in Table 6.1). Compared to polystyrene, which has 1.572 refractive index at 1064 nm, it is clear that these cells will generate less light deflections when trapped in aqueous media and, consequently, lowers the achievable Q-values.

Although it can be useful to describe the mean optical parameters of cells, such as refractive index, these cells are actually not homogeneous spheres; subcellular structures such as the cell membrane, nucleus, and organelles, together with other inhomogeneities, can add cell-dependent scattering effects [24] that can potentially enhance the optical force. However, recalling the r^3 dependence of Q in Figure 6.2, the smallest structures cannot be expected to substantially alter the optical force. Detailed analysis of the light scattering profile in light scattering spectroscopy, however, can reveal details on the subcellular, subwavelength structures [25], which can have some value for distinguishing between different cells subpopulations.

Experimental measurements on some mammalian cells yield lateral Q-values ~ 0.03, as shown by the leftmost bars in Figure 6.5a. This is comparable to the experimental values when trapping microspheres in the presence of aberrations (Fig. 6.2b).

TABLE 6.1 Refractive index of different cell types

Cell type	Refractive index
Escherichia coli	1.387
Hemoglobin cytoplasm	1.387
Blood plasma	1.351
Mammalian cells	1.38–1.41
Fibroblasts	1.358–1.374

Source: Adapted from Reference 23.

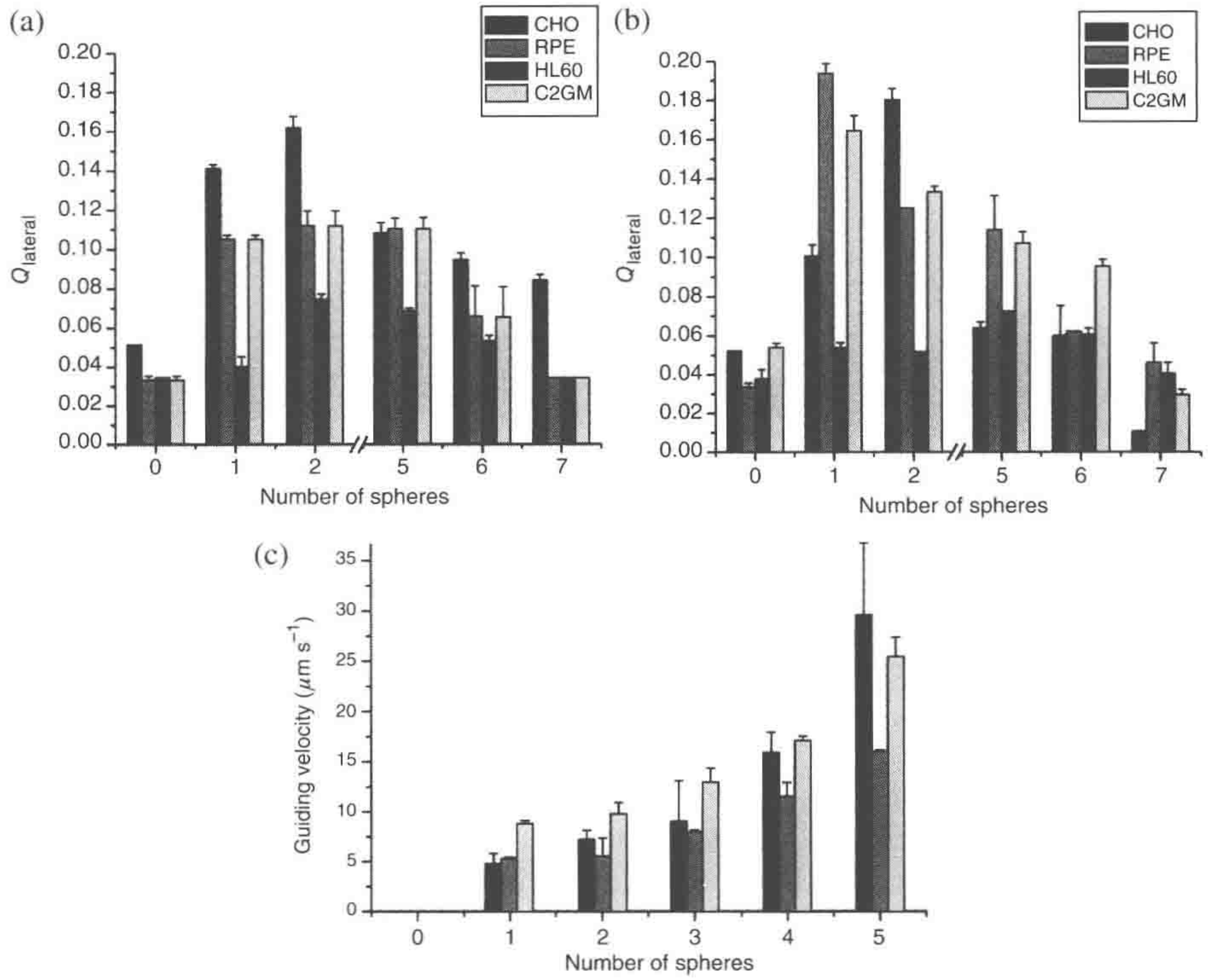

FIGURE 6.5 Effect of dielectric tagging. Lateral Q-values of different cell types containing different amounts of (a) 2-µm and (b) 3-µm polymer microspheres. (c) Axial cell guiding data, displaying maximum guiding velocities for cells containing different numbers of microspheres per cell. Cells with no spheres displayed no axial guiding. CHO, Chinese Hamster ovary cells; RPE, retinal pigment epithelial cells; human, promyelocytic leukemia cells; C2GM, hematopoietic stem-cell-like cells. Adapted from Reference 16. (*For a color version of this figure, see the color plate section.*)

The low Q-values achieved when optically handling cells can present an obstacle for generating sufficient force using only minimal, biologically safe power levels. There are many dyes available for staining cells to produce clearer microscope images of otherwise mostly transparent cells, but increasing cellular absorption defeats the purpose of using lower intensities in the first place (i.e., to minimize energy absorption within the cell). On the other hand, the Kramers–Kronig relations imply that the enhanced absorption in stained cells is accompanied by changes in the refractive index [22]. It would be interesting to find out whether illuminating at off-resonance wavelengths can achieve desired refractive index change at acceptable absorption levels that maintain cell viability (assuming we have available dyes that are suitable for live-cell staining).

Without staining, we can improve the handle we have on the cell by using suitable structures that can be strongly trapped to serve as handles for the cell. Inspired by intracellular tagging techniques, a so-called intracellular dielectric tagging was demonstrated to improve the optical handle on mammalian cells [16]. Using the cells' ability for phagocytosis—a cellular process for ingesting foreign solid matter (optimal uptake after 24 hours incubation [16])—it was shown that the ingested polymer microspheres can serve as intracellular handles, which leads to improved optical manipulation of the cell. The resulting improvement in the lateral Q-values, using different number of ingested microspheres, for different mammalian cells is shown in Figure 6.5a and b. The longitudinal effect, measured in terms of the velocity improvement when axially pushing the cell, is shown in Figure 6.5c.

Instead of trapping beads inside the cell, an alternative that does not require incubation is to trap dielectric microbeads outside the cell and use them as "optical grippers" to grab the cell, in analogy to robotic grippers in mechatronics systems. An example of this indirect manipulation is presented in Figure 6.6. Besides enhancing the optical force, the use of extracellular optical handles also shifts the high intensity of the sharply focused trapping beams away from the cell, which helps maintain its viability during manipulation (in contrast, the directly trapped cell died after 12 s of optical manipulation). Aside from cells, the indirect manipulation using dielectric microspheres has also been extensively applied for manipulating

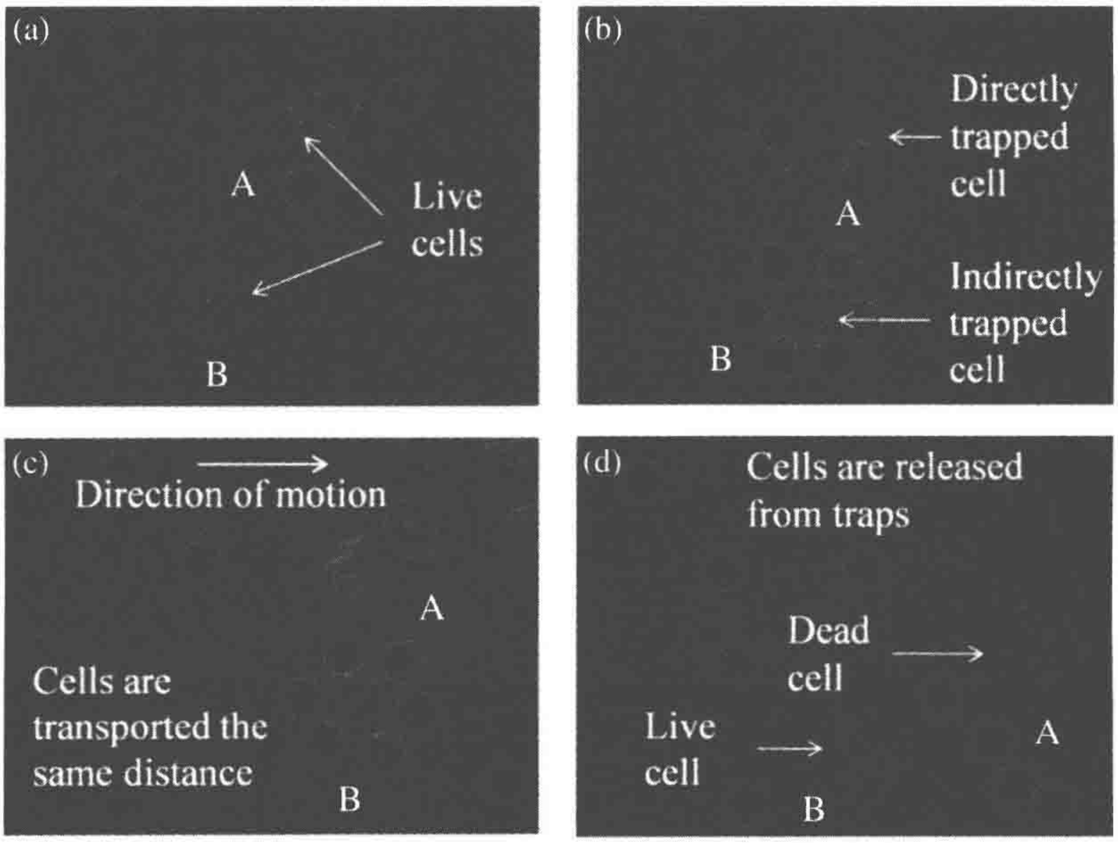

FIGURE 6.6 Indirect cell handling using trapped microspheres increases the optical force and minimizes harmful radiation on directly trapped cell. (a) Solution of *Dictyostelium discoideum* cell and inert silica microspheres; (b) $t = 0$ s: one cell, A, is trapped directly, while another cell, B, is trapped indirectly; (c) $t = 12$ s: the cells are being transported; (d) $t = 15$ s: the cells are released—the directly trapped cell, A, is dead; the indirectly manipulated cell, B, is still alive. Adapted from Reference 30. IEEE Conference.

tethered biomolecules like nucleic acids and proteins. This indirect approach is surveyed in a recent work by Banerjee et al. [26]. Using properly calibrated precision trapping systems—with Angstrom displacement resolutions and 0.1–100 pN force range—tethering biomolecules to trapped microspheres has been highly successful for investigating single-molecule biophysics to reveal the mechanical properties of individual biomolecules, as reviewed by Svoboda and Block [27] and recently by Perkins [28]. The force dynamic range has recently been extended to the nanonewton regime using antireflection-coated, high refractive index microspheres [29], which should open more possibilities previously available only using AFM-based manipulation. For the remainder of this chapter, we focus on cell-level applications of optical forces; readers interested on single-molecule biophysics applications are referred to the abovementioned reviews.

6.1.3 Cell Positioning

One of the more direct applications of optical forces is to hold cells fixed at a designated position. Cells can be moved using beam modulation techniques to shift the location of the trapping beam, provided the optical force is sufficient to move the cell against the drag force and follow the beam. Multiple cells can be simultaneously handled, for example, by scanning to create time-share a single beam, or creating multiple dynamic traps by holography or generalized phase contrast [31]. The noncontact nature of optical forces enables reaching into sterile microbiological environments, including sealed ones, and doing mechanical adjustments without risking contamination and without the space/overcrowding problems of contact-based approaches such as micropipettes and AFM. Indeed, optical traps can even manipulate intracellular components without puncturing the cell. Optical traps, created, repositioned, or removed on demand, offer a higher degree of specificity in terms of particle targeting and positioning and more versatile 3D control compared to other field-type approaches based on hydrodynamic, electric, and/or magnetic fields. It is also a practical advantage that the optical trapping systems are typically implemented in the same microscope that is already being used to study the cells. However, optical traps do have some weaknesses, and so hybrid approaches combining the strengths of the different techniques sounds appealing, subject to overcoming some technical implementation issues. We look at some applications of optical cell positioning below.

6.1.3.1 Single-Cell Analysis: Microscopy and Microspectroscopy One of the motivations for handling single cells is to perform fundamental tests that are capable of resolving variability between individual cell behaviors, as opposed to bulk testing whose population-averaged results is affected by the level of cellular heterogeneity and of little value when the interest is in rare subpopulations (e.g., circulating tumor cells). Performing these single-cell studies require tools for monitoring cells while they are held by optical traps for sufficient time intervals to complete testing. Various microscopic imaging modalities can reveal morphological information, which can indicate ongoing cellular processes or help determine the cell's mechanical properties using observed deformations. Optical trapping systems have been combined with different imaging modalities such as brightfield imaging, phase contrast, and digital holographic microscopy [32], which can also retrieve quantitative phase information [33, 34]. Optical trapping systems have also been combined with spectroscopic imaging, some of which will be discussed below.

The need for sensitive monitoring of trapped cells may be addressed by integrating various instrumentation for realizing environmental controls and sensors, where the specific instrumentation depends on the cells under study. One such *Biophotonics workstation* is schematically depicted in Figure 6.7. This system integrates the capacity for simultaneous optical manipulation, heat stress, fluorescence, and intracellular

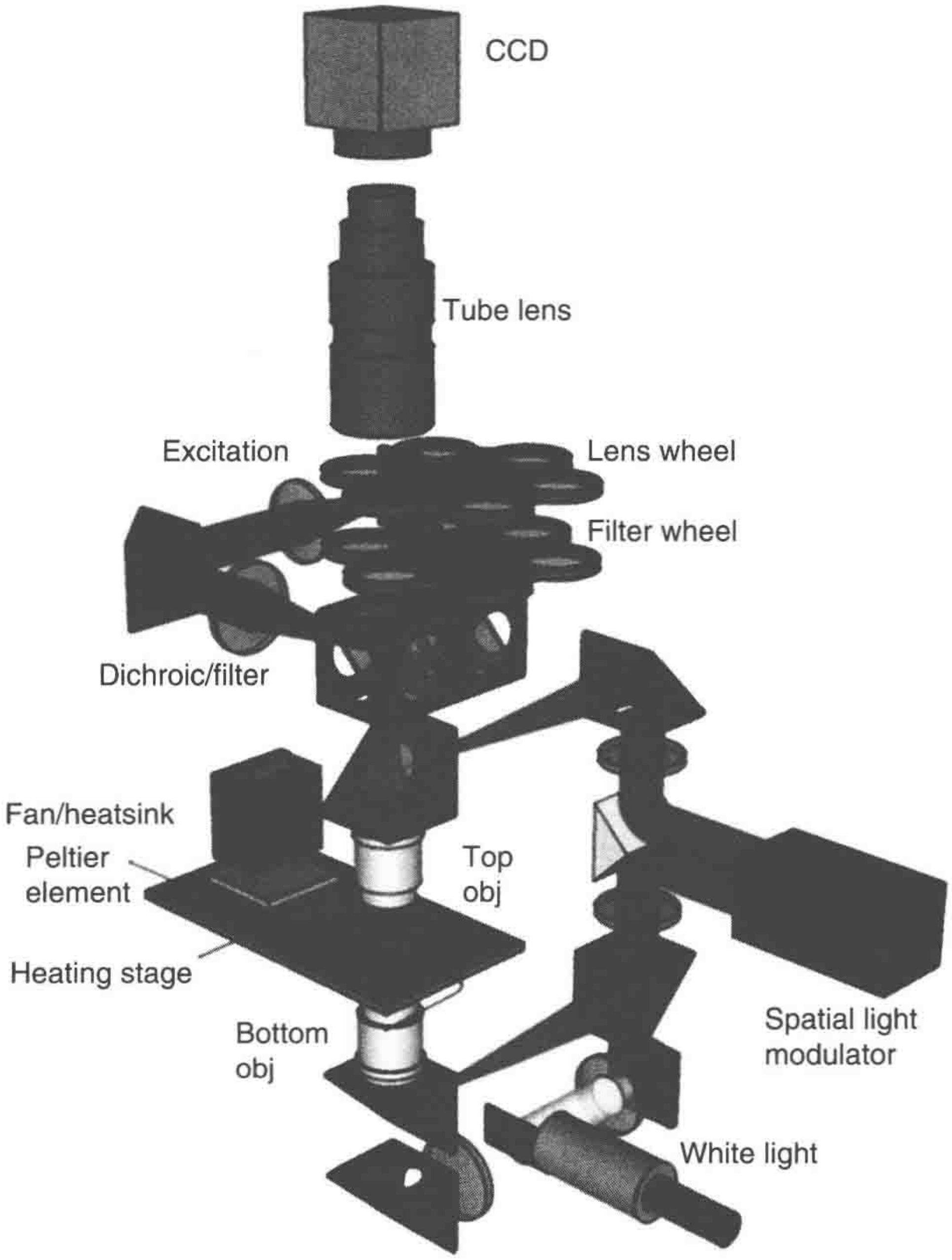
CCD
Tube lens
Excitation
Lens wheel
Filter wheel
Dichroic/filter
Fan/heatsink
Peltier element
Top obj
Heating stage
Bottom obj
Spatial light modulator
White light

FIGURE 6.7 BioPhotonics workstation equipped with fluorescence system and temperature control [35]. RSI. The heating stage lies between the opposing objectives that deliver counter-propagating beam traps. Fluorescence is imaged by the top objective through the dichroic mirror and filters to the CCD camera. Brightfield imaging uses white light illumination through the bottom objective.

pH measurements [35]. Its multifunctionality can be utilized, for example, in yeast cell studies where the measured fluorescence enables the calculation of intracellular pH distribution, which turns out to be a good indicator of yeast cell health [36].

As mentioned previously, subcellular structures influence the scattering properties of the cell. Hence, analysis of the scattered trapping beam itself can yield information on the internal dynamics of trapped cell, for example, to monitor cellular processes [37]. Combining spectroscopy with optical trapping can achieve chemical imaging, for example, by tagging the cells with fluorescent labels, or using label-free approaches like Raman [38] or coherent Raman spectroscopy [21]. The Raman spectra can be excited using the same laser used for trapping [39]. Early biological experiments using this technique, dubbed as Laser tweezers Raman spectroscopy (LTRS), showed it had sufficient sensitivity to reproduce the characteristic bands of red blood cells and distinguish physiological states of yeast cells (alive vs. dead) that otherwise appear visually similar without staining. Photodamage can be minimized over sustained operation by switching between low power *trapping-only mode* and higher power *trapping-with-excitation mode* (e.g., 2 mW and 20 mW, respectively [39]).

6.1.3.2 Cellular Microenvironment: Nonbiological Stimuli Together with cell monitoring systems, having auxiliary systems for controlling the cellular microenvironment that work simultaneously with optical traps broadens the arena for studying single-cell behavior. In well-calibrated systems, the trap itself can work as a force monitor, for example in characterizing cell motility. Auxiliary controls can be used either to maintain temperature and avoid temperature-dependent effects or to vary temperature and explicitly study its effects. Peltier elements can be used with trapping systems utilizing long working distance objectives due to the available working space. In the tight working conditions of high NA tweezers, options for temperature control include introducing another beam with different wavelength for laser heating or pumping/circulation of temperature-controlled fluid into the system [40]. Aside from temperature control, microfluidics also provides the possibility for introducing new cells and varying the chemical microenvironment of the trapped cell [41].

One application of environmental control is in real-time control of cellular growth conditions. One area of interest is in finding optimal growth condition for producing lipid in algae since such lipids can be readily converted to biodiesel. In an effort to establish correlations among lipid trigger conditions, growth rate, and lipid production in algae, Wu et al. used LTRS, illustrated in Figure 6.8, to quantitatively investigate the lipid content of trapped single cells from different algal species and different growth conditions including light exposure, nitrogen, silicon, CO_2, pH, and temperature [42].

Differences in temporal response of individual cells, such as lags in the onset of cellular response, can cause averaged bulk measurements that paint a different picture of the cell population. Using optical traps to hold cells can keep them in the observation zone for monitoring temporal effects after their chemical microenvironment is modified, for example, by pumping fluids containing different reagents. Mortitz et al. used LTRS to trap and monitor the metabolic states of *E. coli* as different antibiotics are pumped into the sample chamber [43]. Singh et al. used Raman microspectroscopy to detect real-time stress response of yeast cells to hyperosmotic environments (i.e.,

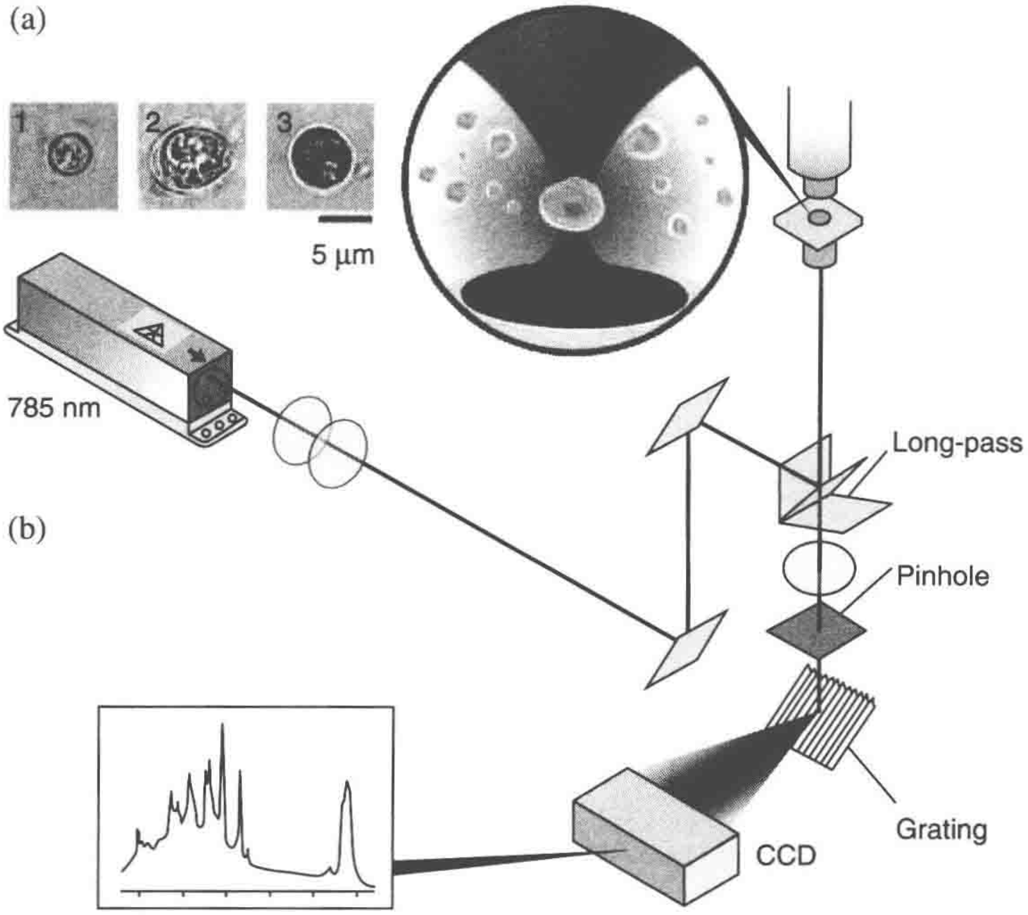

FIGURE 6.8 Setup for single-cell laser tweezers Raman spectroscopy (LTRS). Adapted from Reference 42. PNAS. (a) Brightfield images of individual trapped microalgal cells: 1, *Neochloris oleoabundans*; 2, *Botryococcus braunii*; and 3, *Chlamydomonas reinhardtii*. (b) Instrument layout. The 785-nm laser beam is used as both trap beam and Raman excitation beam. *(For a color version of this figure, see the color plate section.)*

fluids with higher solute content) [44]. In this case, the Raman signatures enable them to monitor the glycerol and ethanol production in the yeast cells as they switch to fermentation mode as a stress response for balancing the osmotic pressure when in glucose-rich environment.

Besides biochemical stimuli, studies show that cells also react to mechanical and geometric cues so that their mechanical environment also plays a role in shaping cellular development [45]. Thus, just as control over the chemical environment is important for understanding cell biology, so too is having reconfigurable mechanical microenvironments. Combining optical manipulation with three-dimensional microfabrication, for example, as multiphoton polymerization, provides a way to create such reconfigurable mechanical microenvironments, where optical forces are used to rearrange prefabricated microstructures [46]. With chemical functionalization becoming available for these microstructures [47,48] including selective 3D functionalization [49], creating reconfigurable synthetic microenvironments having chemical, mechanical, and even optical cues [50], could be on the horizon.

6.1.3.3 Cellular Microenvironment: Intercellular Interaction Synthetic microenvironments with chemical and mechanical cues, reconfigured using optical traps,

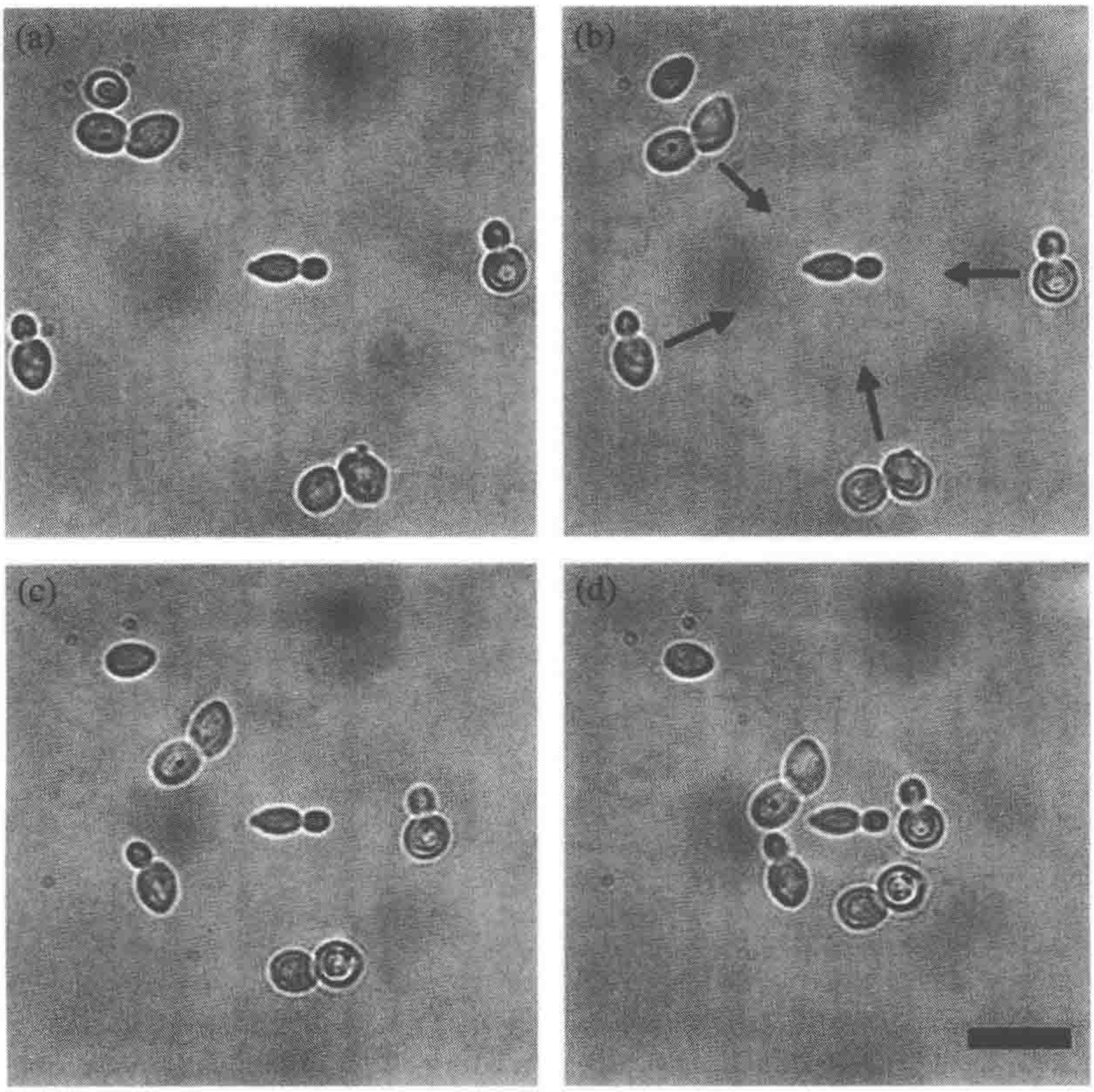

FIGURE 6.9 Snapshots during the preparation of *Hanseniaspora uvarum* and *Saccharomyces cerevisiae* cells for microscale, mixed-culture fermentation using an interactive optical trapping system. Adapted from Reference 51. FEMS Microbiology Letters. Dynamic traps simultaneously bring *S. cerevisiae* cells along the indicated paths to surround a single *H. uvarum cell*. Images were recorded at: (a) 0 s; (b) 30 s; (c) 60 s; and (d) 90 s. Scale bar represents 10 μm.

would make interesting tools for single-cell microbiology. However, the trapped cells themselves could already serve as building blocks, naturally equipped with mechanical and biochemical cues, for constructing reconfigurable microenvironments. This setup for optically assembling cells provides a way of investigating intercellular communication. Using an interactive optical trapping system, Arneborg et al. demonstrated that, in a mixed yeast culture, confining a yeast cell from one species (*Hanseniaspora uvarum*) in a cage composed of yeast cells belonging another species (*S. cerevisiae*) arrests cell division in the confined cell [51] (see Fig. 6.9). The confined cell remains viable and resumes its cell division processes after being released from confinement.

Intercellular signaling in bacterial populations can lead to a so-called quorum sensing behavior where bacterial processes get synchronized. This synchronization and coordinated population activity in bacteria can lead to public health concerns, such as in biofilm production and antibiotic resistance [52]. One proposed use of optical traps in quorum-sensing studies is in helping create biofilm models using microfluidics to deliver bacteria to a construction region where optical traps work to precisely position cells and subsequent photopolymerized hydrogel encapsulation is used to mimic the extracellular matrix (ECM) [53]. A similar procedure combining microfluidic cell delivery, optical assembly, and hydrogel encapsulation has also been proposed as a possible tool for creating cellular micropatterns resembling synthetic tissue [54]. These demonstrations illustrate the promising prospects of applying optical micromanipulation, working in synergy with microfluidics and optical materials processing, for fundamental cellular studies. However, creating artificial microenvironments that sufficiently mimic the chemical and physical properties of the cellular environment, especially its time-varying features, can be challenging. On the other hand, new capabilities are constantly being developed, such as optically reconfigurable microenvironments, optically addressable functionalization, optically manipulated sources of chemical [55], mechanical [56], and optical stimulation [50], that, together with 3D microfabrication of ECM and other developments in microtechnology [57], serve to widen the cellular biology toolbox [2].

6.1.4 Cellular Biomechanics: Mechanotransduction and Cell Deformations

Cells interact mechanically with other surrounding cells and extracellular material and, hence, it can be expected that the mechanical properties of cells play an important role in their function and development. The cell can work as a force transducer in a process called mechanotransduction, where mechanical inputs on the cell membrane are converted to biochemical signals within the cell. Cells *in vivo* constantly react to the microenvironment and act in an integrated manner depending upon the surrounding mechanical and spatial context and their intrinsic mechanosensory mechanisms [58]. Mechanotransduction responds to piconewton forces on the cell membrane, which is within the usual range of optical forces.

One interesting area in mechanotransduction is the study of cellular adhesion to the ECM, which governs processes like cell migration, for example, during cellular differentiation, immune response, or cancer cell spreading. Optical traps have been used in mechanotransduction studies to hold beads coated with ECM proteins and antibodies, which are then delivered onto cell surface adhesion receptors to provide both biochemical cues and calibrated mechanical stimulation [59, 60]. The cells exhibit different responses to the biochemicals depending on the accompanying mechanical context, highlighting that cells are able to distinguish free chemicals to those that are attached to a rigid ECM [59]. Understanding mechanotransduction can benefit from fluorescent tags to image the signaling pathway from the cell surface receptors to the interior. However, designing fluorescent tags requires *a priori* knowledge on what it is that should be tagged. Felsenfeld et al. [60] used optically trapped coated beads in mechanotransduction studies that identified the role of the tyrosine kinase Src in regulating cellular response to mechanical stimuli. Based on this, Wang et al. [61] were able to design a highly selective, genetically encode Src reporter, which they then used to image and quantify the spatiotemporal activation of Src upon mechanical stimulation by optically pulling fibronectin-coated beads that are attached to cell surface receptors. Among others, they saw the presence of both an immediate distal Src activation and a slower wave propagating at ~ 18 nm s^{-1} when local mechanical stimulation is applied to human umbilical vein endothelial cells.

In another experiment, Resnick showed that a trapped microsphere exerting force not exceeding 200 pN directly on the primary cilium of kidney epithelial cells elicits the release of Ca^{2+} ions inside the cell [62]. This reproduces previous results that stimulated intracellular Ca^{2+} release by flow-induced stimulation of the cilium [63]. As opposed to fluids that can apply shear forces over the entire exposed cell membrane, Resnick's experiment produced the Ca^{2+} signal using localized mechanical excitation. However, since smaller objects are harder to manipulate (recall that the Q-value decreases as r^3 in the Rayleigh regime), it is envisioned that combining microfabrication and optical manipulation be used in a structure-mediated approach for highly localized stimulation [64]. In this approach, nanotips—intended for space- and/or time-programmed stimulation—can form part of relatively bigger structures that are not only easy to optically manipulate, but are also capable of exerting stronger forces due to their larger Q-values compared to direct nanotip manipulation. A similar structure-mediated approach has already been used to apply controlled forces on the cell membrane for topographic surface mapping [65]. Extending this approach for the stimulation of highly localized receptors on the cell membrane can help probe mechanotransduction and other cellular mechanisms.

Cell mechanics is not only concerned with how mechanical stimuli affect cellular processes, but also on what the cell's mechanical properties can reveal about the cellular physiology. The physical properties of biomaterials play a role in biological processes at different scales extending from biomolecules to organs. At the cell level, the view that deformation and other mechanical properties of cells can give insights on possible connections with cellular process such as cell differentiation, cell health, and disease progression is driving multidisciplinary research initiatives at the interface between physical science and biology[3]. Different mechanical models of the cell have been developed [66] based on the different experimental techniques that were used for the mechanical measurements.

Two examples of using optical traps for investigating the viscoelastic properties of cells are illustrated in Figure 6.10. The procedure by Mills et al. [67] is illustrated in Figures 6.10a and 6.10b, where a red blood cell is stretched by attaching beads to the cell, pulling on the bead, and then analyzing the cell deformations. The out-of-focus bead on the right is held in place by a calibrated optical trap as the in-focus bead on the left, fixed to the bottom of the chamber is displaced using a translation stage.

Figure 6.10c illustrates the so-called optical stretcher by Guck et al., which uses counter-propagating beams to directly trap and stretch the cell. The optical stretcher mechanism can be intuitively understood in terms of the refractive index dependence of the optical momentum flux, $n_m P/c$, where n_m is the refractive index of the medium

---

[3] For example, the U.S. National Cancer Institute runs a program "Physical Sciences in Oncology" aimed at building cross-disciplinary teams working at the convergence between cancer biology and physical science/engineering.

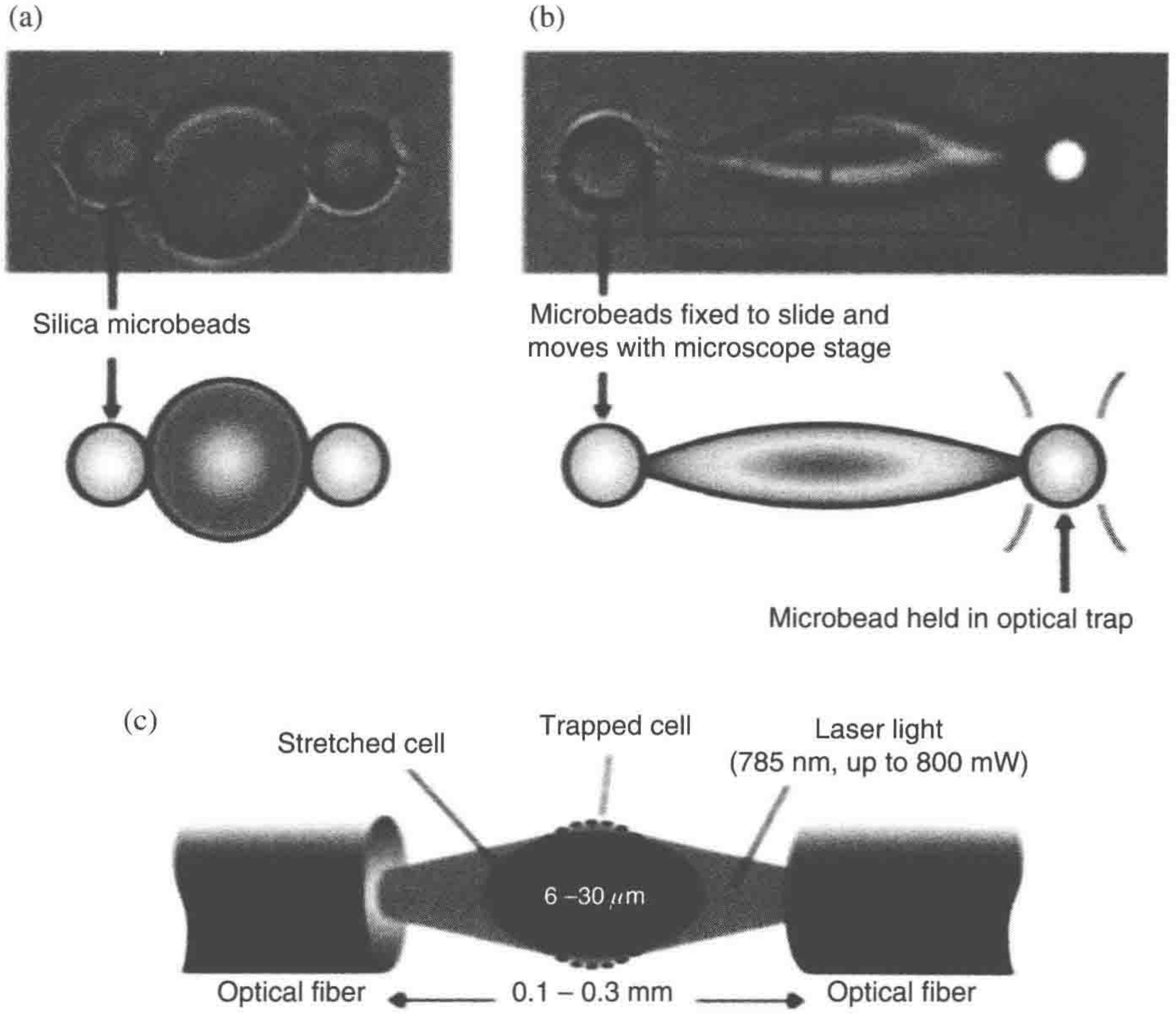
(a)
(b)
Silica microbeads
Microbeads fixed to slide and moves with microscope stage
Microbead held in optical trap
(c)
Stretched cell
Trapped cell
Laser light (785 nm, up to 800 mW)
6 -30 μm
Optical fiber
0.1 – 0.3 mm
Optical fiber

FIGURE 6.10 Optical cell stretching. (a, b) Cell stretching using attached microbeads. Adapted from Reference 67. Two 4.12-μm diameter silica microbeads are nonspecifically attached to the red cell at diametrically opposite points. (a) The left bead is anchored to the surface of the glass slide. (b) The right bead is trapped using the optical tweezers while the slide and attached left bead are moved to stretch the cell. The image shows deformation at 193 pN of force. (c) Optical stretcher: counter-propagating beams trap and stretch the cell. Adapted from Reference 68. Mechanics and chemistry biosystems. Not drawn to scale; optical fiber diameter is 125 ± 5 μm.

where light propagates. Light incident in a medium having lower refractive index than the cell increases its optical momentum flux upon entering the cell and lose momentum upon exit. The forces resulting from these momenta changes act on the cell wall and can lead to cellular deformation. In a simplified calculation for a light ray of power P at normal incidence, and neglecting any losses inside the cell, the momentum conservation on the front cell boundary predicts a force pulling opposite to the light propagation. Including the effects from partial reflection, R, yields a Q-value, $Q_{\text{front}} = [n + Rn - (1 - R)](1 - R)$. The reflection R depends on the refractive index. A similar analysis on the exit side predicts a force pushing along the light propagation with $Q_{\text{back}} = [n + Rn - (1 - R)](1 - R)$. These forces combine to stretch the cell. The unequal forces ($Q_{\text{back}} > Q_{\text{front}}$) yield a net force along the light propagation, and so an opposing beam is needed to produce a stable trap, which also doubles the stretching forces. Cell stretching forces reaching up to hundreds of piconewtons can be generated using 800 mW from each beam.

The optical stretcher can form part of a cell measurement system for possible clinical applications. Combining the optical stretcher with microfluidics for conveying multiple cells that are measured individually, promising results have been obtained in differentiating between the mechanical properties of healthy cells and cancer cells: for small deformations, cancer cells, on the average, are softer than healthy ones [69]. With cellular heterogeneity, the analysis cannot be based on a single-cell measurement alone but on the statistical properties of individually measured cells.

6.1.5 Cytometry

The optical stretcher approach for studying disease finds support in the many clinical applications of flow cytometry, for example, see review by Jaye et al. [70], which highlights the fact that the statistical properties of cellular populations taken from patients can form the basis for routine diagnosis, prognosis, and monitoring. Cytometry deals with the measurement of cell properties, and in flow cytometry, this measurement is done by streaming a single file of cells past an optical interrogation region where cells are individually illuminated, typically by lasers, as shown in Figure 6.11. Hydrodynamic focusing of a core stream (green) by sheath fluid (gray) creates a single file of cells in an interrogation region (yellow sphere) where cells are individually illuminated by a laser beam. Each cell creates its characteristic forward scatter (FSC), orthogonal scatter (SSC) intensity, and possibly fluorescence (FL1) signals. The flow cytometer illustrated in Figure 6.11 is not only capable of measuring the cell properties using the FSC, SSC, and FL1 signals but can also use these measurements as a basis for sorting cells (e.g., fluorescence-activated cell sorting, FACS [71]). For cell sorting, droplets created around single cells are charged positive or negative depending on the measured parameters. Droplets are then deflected by electric field and sorted, according to their charge, into collection tubes. Readers interested on flow cytometry are referred to Shapiro's book [72], considered a standard reference on the subject.

Conventional flow cytometry equipment tends to be large, bulky, and expensive, especially when incorporating multiple excitation lasers to enable the measurement of many different cell parameters[4]. Thus, there are efforts to develop low cost and compact alternatives, for example, the μFACS system illustrated in Figure 6.11b uses a microfabricated disposable flow chamber in a fluorescence microscope [73]. The microfluidic chamber constricts as it approaches a T-junction enabling to flow one cell at a time (see Fig. 6.11b inset). The control system diverts the flow based on the detected fluorescence to sort cells between two collection channels.

The microfabricated fluorescence-activated cell sorter described above [73] is one of the early attempts at cost-effective cell cytometry and sorting systems. Its high citation indicates a growing interest in alternative approaches and many microfluidics-based systems are being pursued. In the next section, we discuss a number of optical

---

[4] Desktop cytometers are now starting to become commercially available.

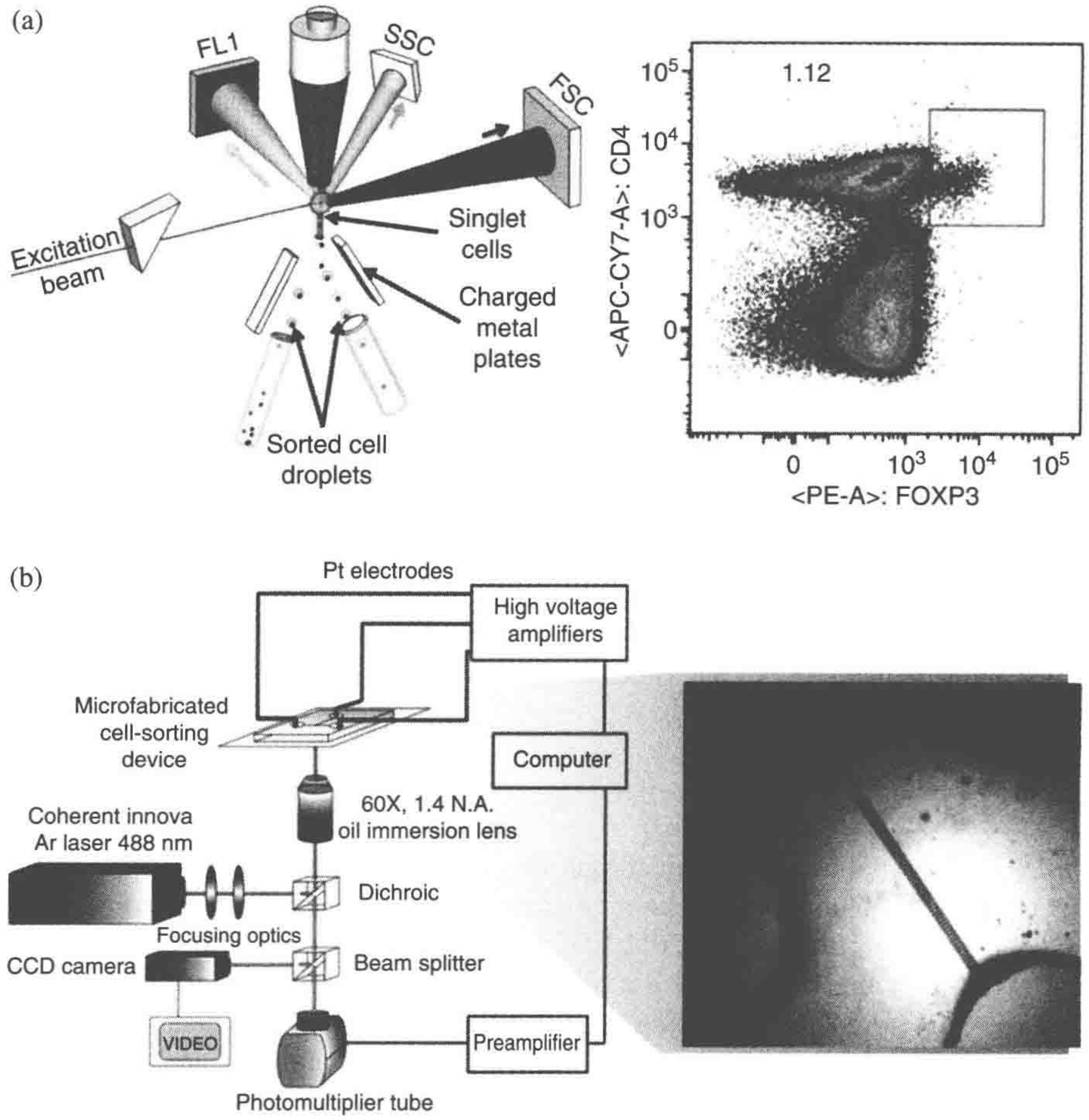
(a)
FL1
SSC
FSC
Excitation beam
Singlet cells
Charged metal plates
Sorted cell droplets
1.12
10^5
10^4
10^3
0
<APC-CY7-A>: CD4
0
10^3
10^4
10^5
<PE-A>: FOXP3
(b)
Pt electrodes
High voltage amplifiers
Microfabricated cell-sorting device
Computer
Coherent innova Ar laser 488 nm
60X, 1.4 N.A. oil immersion lens
Dichroic
Focusing optics
CCD camera
Beam splitter
VIDEO
Preamplifier
Photomultiplier tube

FIGURE 6.11 (a) Schematic of a conventional flow cytometer (including FACS) that monitors fluorescence, forward and side scattering (inset shows sample data where FOXP3+ CD4+ regulatory T-cells are identified from a mixture of lymphocytes). Adapted from Reference 70. (b) Cytometer using a disposable microfabricated flow chamber (inset) in a fluorescence microscope with a photomultiplier tube for FACS (μFACS). Adapted from Reference 73. Journal of immunology. (*For a color version of this figure, see the color plate section.*)

methods for sorting that are being proposed, which nicely complements the many optical tools developed for measuring cell properties (optical cytometry) that are not necessarily limited to optical scattering and fluorescence.

6.2 OPTICAL SORTING

Measuring single-cell properties by cytometry can generate useful statistics of a heterogeneous cell population. The capacity for cell sorting is necessary when it is not enough to just know the population statistics, and therefore, subsequent processing and biological studies need to be performed on a selected subpopulation. The ability to sort cells is of interest to commercial markets such as stem cells, production cells, and circulating tumor cells (CTCs). This market that has attracted a lot of attention from different technologies and implementations of cells sorters has been proven with varying success using methods such as magnetics, electrophoresis, acoustics, and surface affinity, to name a few. Bhagat et al. [74] did an extensive review of the various technologies comparing the methods, mechanisms, separation markers, and flow rate/throughput.

Optical techniques already form part of conventional cell sorters in the form of scattering and fluorescence detection, which is used as basis for separating cells using different mechanisms. In this section, we focus on techniques that use optical forces as the cell separation mechanism itself. Optical cell sorting systems can be divided into two main categories: active sorting (open-loop systems) and passive sorting (closed-loop systems). Active optical sorting uses a beam control system for dynamic illumination to selectively exert optical force depending on the measured properties of the cells. On the other hand, passive optical sorting uses static illumination and relies on the dependence of the force on the cells' intrinsic optical properties as basis for automatically separating cells.

6.2.1 Active Sorting

One potential application of optical forces in cell sorting is to provide an alternative optical flow switching mechanism in microfluidic implementations of fluorescence-activated cell sorting (so-called μFACS systems similar to the illustration in Fig. 6.11b). Wang et al. [75] successfully demonstrated this possibility. They employed hydrodynamic focusing to individually stream mammalian cells into a fluorescence analysis region. Unwanted HeLa cells do not fluoresce and simply flow directly to the waste channel; on the other hand, fluorescence from GFP-expressing target HeLa cells initiates optical switching downstream using a laser beam that is dynamically switched in and out of a specified point by an acoustooptic modulator (AOM). Static illumination for 2–4 ms exerts transverse force to laterally divert the cell toward the collection channel. As for the recovery rate, more than 85% of fluorescent cells were collected with 97% purity for flow throughputs up to 77 cells per second. A similar successful demonstration by Perroud et al. [76] used infected macrophage cells to highlight the lower risks associated with confined microflows as opposed to the potential biohazard of free atomized droplets in conventional FACS. A recent work on laser- and microfludics-based sorting used pulsed lasers for creating microbubbles on demand to switch the flow and collect desired cells based on their fluorescence signature [77]. This related method, based on laser-induced cavitation instead of optical forces, is able to sort 1500 mammalian cells per second with 90% purity; trading-off purity for higher throughput, it can sort up to 20,000 cells per second with 37% purity.

In their critical review of the role of holographic optical tweezers in lab-on-chip devices [78], Padgett and Di Leonardo assert that incorporating optical manipulation to lab-on-chip devices would only add modest additional complexity if the microenvironment would already require imaging. Although chemical contrast with fluorescence detection has long replaced cellular morphology as the cell sorting criterion, conventional FACS integrates fluorescence from the whole cell and, hence, lacks morphological information. To address this gap, imaging cytometers offering morphological details are now commercially available. However, these machines are built upon conventional cytometers and still tend to be large, bulky, and expensive. Hence, there is sustained search for breakthroughs in so-called disruptive technologies that can offer competitive performance using simple, low cost innovative solutions. One focus is in imaging-based cell-sorting alternatives, which can benefit from parallel developments in high-speed imaging and high-speed image analysis.

Recent work by Wang et al. [79] and Landenberger et al. [80] using optical forces for sorting cells in microfluidics systems incorporate possibilities for both fluorescence-based as well as image-based sorting criteria. In contrast to previous optical switch based on static illumination, these works use a dynamic trap that can be arbitrarily positioned within a given field of view. Landenberger et al. used the brightfield images to position traps on the edge of target cells. This minimizes illumination within the cell bulk and optimizes the transverse force as the beam is displaced by galvanometric mirrors to drag selected cells from the hydrodynamically focused flow to the section of laminar flow that eventually proceeds to the collection channel. Wang et al., on the other hand, simplified the microfluidic requirements by doing away with hydrodynamic focusing altogether (but retaining a buffer flow to the collection channel). They used holographic optical traps that can arbitrarily position multiple traps for parallel addressing within a field of view where cells are distributed. Target cells are trapped and displaced into the buffer flow for collection (See Fig. 6.12). To avoid using tightly focused beams, one can instead use relatively broad multiple dynamic beams to axially propel chosen cells from an initial flow headed toward a waste channel to a buffer flow for collection (see Fig. 6.12b). In proof-of-principle experiments, Perch-Nielsen et al. used axial optical propulsion to

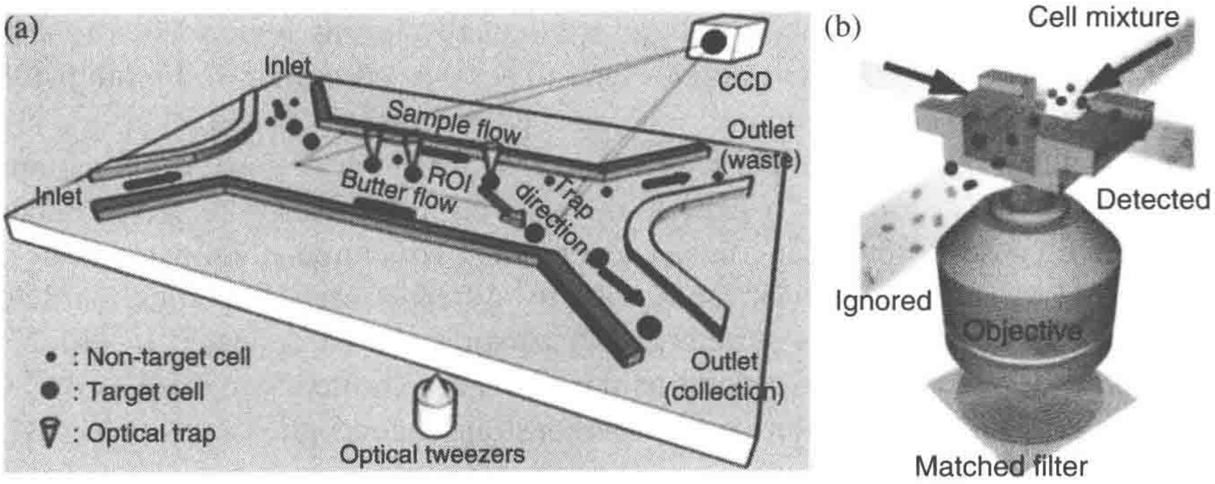

FIGURE 6.12 Image-based parallel cell identification and optical sorting. (a) Transverse force used for lateral displacements. Adapted from Reference 79). (b) Axial force used for optical propulsion. Adapted from Reference 82). (*For a color version of this figure, see the color plate section.*)

move slower particles at the bottom of the chamber to the faster moving flow in the parabolic flow profile within the chamber [81].

Conventional FACS can perform cell sorting at cell throughputs in tens of thousands per second and optical sorting throughputs are lagging way behind. Hence, one possible direction for optical sorting is to find niche applications that set lower premiums on throughputs, for example in samples where only limited volumes are available. Nonetheless, it is hoped that parallel approaches can help raise achievable cellular throughputs. Parallel cell sorting is also possible using passive optical sorting methods, as will be described in the following section.

6.2.2 Passive Sorting

Although active sorting relies on an allied system for measuring cell properties to serve as the sorting criteria to guide the targeting behavior of a switching beam, passive sorting does not specifically target cells and can even use static illumination to automatically sort cells. The cells separate when intrinsic cellular properties result in differences in the optical force experienced by the cell. The benefits from the relative simplicity of automatic passive sorting is hampered, on the other hand, by its limited sorting applications since not all desired sorting criteria would directly translate to differences in optical trapping response.

One example of passive optical sorting is optical chromatography [83], which can simply use a weakly focused beam to illuminate opposite the flow in a microchannel. With the axial optical force depending on particle size, the competition between the opposing optical and drag forces leads to axial particle separation. A sample microfluidic design for cell sorting by optical chromatography is illustrated in Figure 6.13a [84]. In essence, optical chromatography separates particles by exploiting the size-dependent optical force in a geometry characterized by coaxial (counter-propagating) flow and laser illumination. We can expect this size-dependent effect to similarly manifest when using an orthogonal geometry, as illustrated in Figure 6.13b [85]. Here, a flow containing particles with different sizes is hydrodynamically focused to create a single line of particles. Focusing light orthogonally in this region leads to size-dependent separation as larger particles tend to get pushed farther. In Figure 6.13b, this effect works to enhance microfluidic pinched flow, which would otherwise also lead to similar size-based particle separation even without orthogonal illumination.

Since the optical force on a particle depends on its geometry, refractive index, and other light scattering properties, a given static structured illumination can be experienced as different optical landscapes by different particles. Thus, particles in a flow that encounter this structured illumination can be deflected in different ways and can lead to particle separation downstream in a process coined as optical fractionation. This fractionation has been demonstrated using optical lattices (periodic light patterns), but can also work using some other patterns that are specifically tailored and optimized by experimental calibration to achieve the desired separation of the expected particles in the sample. Examples of optical fractionation using a periodic optical lattice [86] and a nonlattice-like illumination pattern [87] for separating polystyrene beads according to size are illustrated in Figure 6.14.

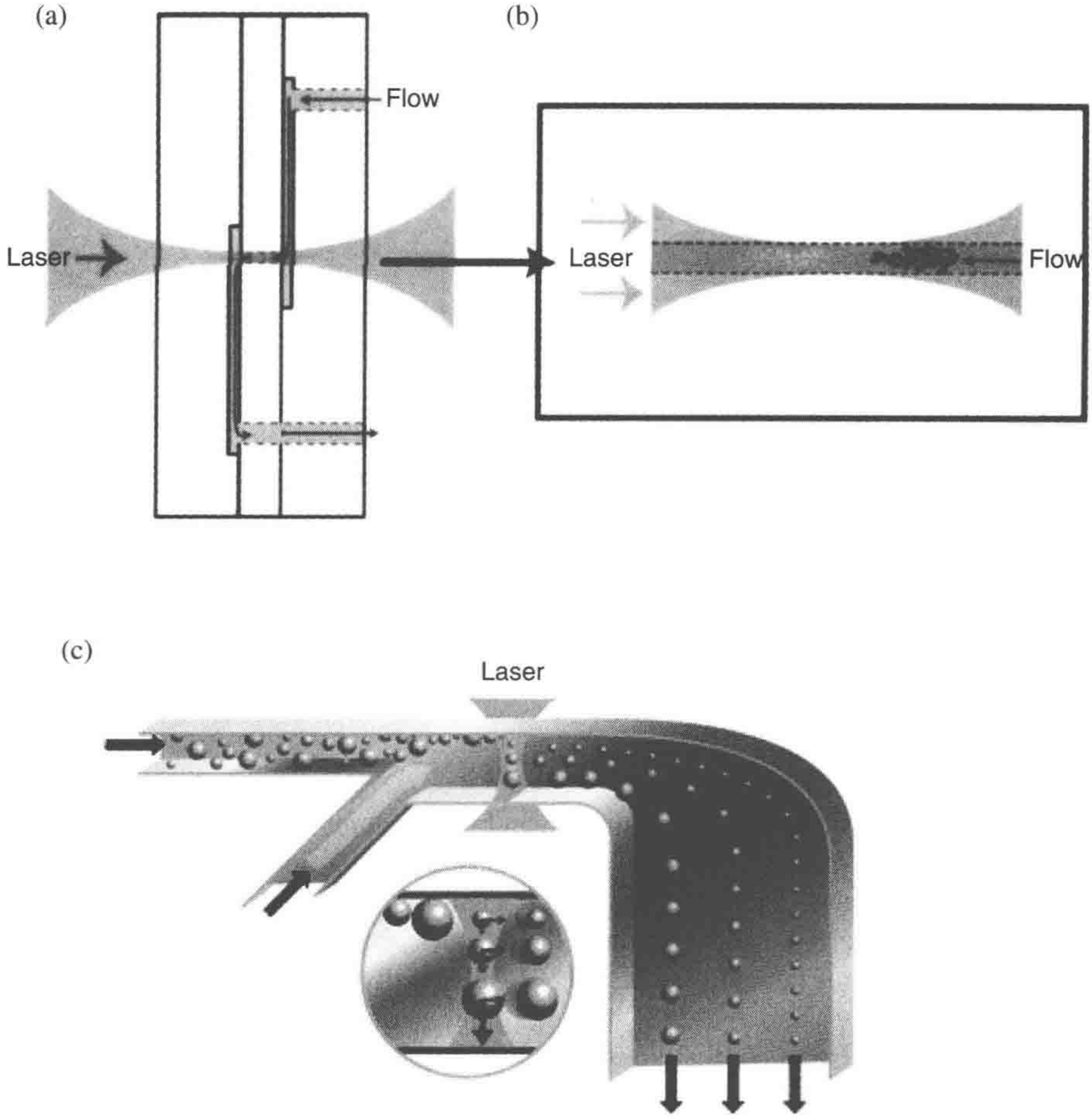

FIGURE 6.13 Coaxial and orthogonal geometries of size-dependent scattering force for automatic particle separation: (a, b) Coaxial (counterpropagating) geometry showing microfluidic device and the weakly focused laser beam in optical chromatography for particle separation near the focus of the beam. Adapted from Reference 84. (b) Orthogonal geometry between illumination and hydrodynamically focused flow leads to size-dependent particle separation downstream (in this case enhanced by the expanding chamber). Adapted from Reference 85.

Many optical sorting techniques are successfully demonstrated using dielectric beads. However, it can be challenging to realize similar sorting performance when using biological cells since their low-Q can require much higher power exposures that can affect cellular viability. Achieving optical sorting with good cellular viability is important in finding niche applications, given that the high throughputs in conventional FACS is achieved at pressures and flow rates that subject cells to mechanical stress levels that may affect viability of fragile cells. We examine important issue of cell viability in performing optical cell handling and sorting in the following section.

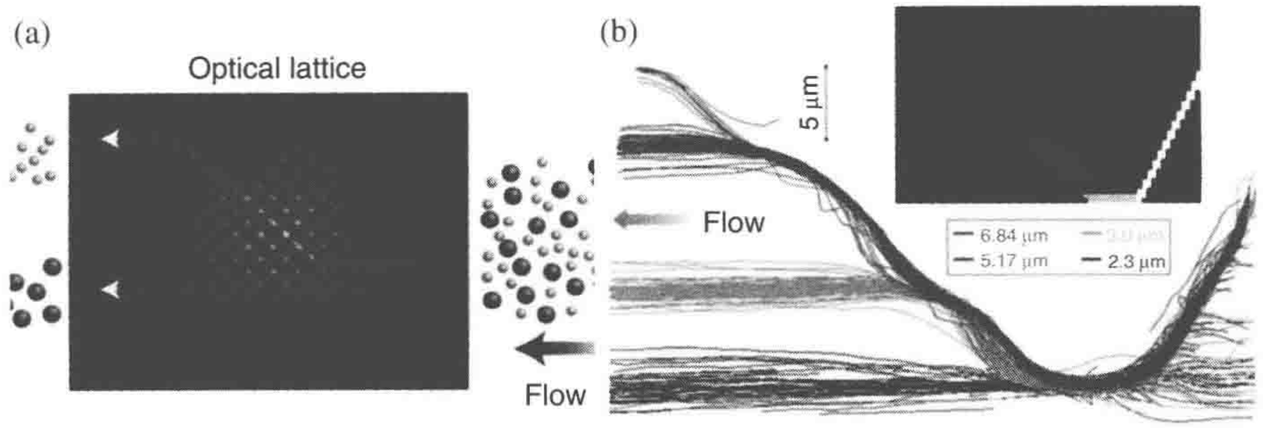

FIGURE 6.14 Optical fractionation in an optical landscape. (a) Periodic landscape: a larger particle flows with minimal deflection through the optical lattice while smaller particles are angularly deflected. Adapted from Reference 2. (b) Experimentally calibrated pattern generated using an acousto-optic modulator: Particles flowing from the right are guided to the bottom of the figure by the line trap and eventually separate based on size as the calibrated gaps and intensities of the subsequent pattern are only able to drag the largest particles to the top of the figure. Adapted from Reference 87. Nature Materials, Optics letters. (*For a color version of this figure, see the color plate section.*)

6.3 CELL VIABILITY

Studying the viability of microorganisms can be very complex and goes beyond the simple dead-or-alive determination. This is reflected in the rich vocabulary describing the possible states of the organism that expands as new characterization methods are found. These present terms include dead, moribund, starved, dormant, resting, quiescent, viable but nonculturable, injured, sublethally damaged, inhibited, resuscitable, living, active, and vital [88]. The multitude of terms stresses the fact that care should be taken to avoid confusion, when describing the state of the cell. A profound description and discussion of the terms was performed by Kell et al. [89].

The use of optical trapping of microorganisms has often been regarded as noninvasive and relatively benign compared to mechanical methods such as pipette suction and AFM. However, the benign nature of the handling of microorganisms is subject to carefully chosen parameters. Otherwise, a spectrum of possible damage can arise, the most severe of which Arthur Ashkin had coined the term "opticution" (death by light) [90].

It is therefore essential when doing single-cell studies to have complete control over the amount of damage inflicted to the particular system being studied and preferably to be able to minimize or completely remove the cause of the damage. Therefore, numerous studies over the last 20 years have been performed to characterize, quantify, and find the source of the damage (see summary in Table 6.2). These studies vary in parameters such as microorganisms used, trapping wavelength, power levels, viability detection method, and trapping method.

In many of these studies, viability appears as precursors to some other main experiments to discount possible damage the optical trapping system may have had on the microorganism. While this does not impact the validity of the studies themselves, it does somewhat hinder direct comparisons across multiple studies, as many variations

TABLE 6.2 Survey of cell viability studies

Wavelength (nm)	Organism/system	Detection method	Viability parameter	Reference
1070	*S. cerevisiae*	Image analysis	Growth rate, division time	91
1064	DNA	DNA tether damage	ROS	92
870, 930	Multiple bacteria	APO LOGIX JC-1 assay kit	Membrane potential, ROS	93
780	T cells	CFSE, PI	Membrane rupture	94
1064	*E. coli*, *Listeria moncytogenes*	CFDA-SE, GFP	pH_i	95
840–930	*E. coli*	GFP construct	Gene expression	96
1064	*S. cerevisiae*	Visual inspection	Division time	97
1064	*E. coli*	Visual inspection	Division time, length increase	98
830, 880	*S. cerevisiae*	Visual inspection	Division time	99
700–850	*Caenorhabditis elegans*	β-galactosidase assay	Heat shock gene expression	100
308–1064	NC37 lymphoblasts	Comet assay	DNA damage	101
836	*E. coli*	SYTO 9, PI	Doubling time	102
809	CHO, T-lymphocytes	Acridine orange, SYBR 14, PI	Membrane rupture, DNA damage	103
790–1064	*E. coli*	Rotation rate	Image analysis	104
1064	CHO	Laurdan, acridine orange, PI, SNARF	Heating, membrane rupture, pH_i	105
700–1064	CHO	Cell counting	Cloning efficiency	106
760–800	Spermatozoa	SYBRTM 14, PI	Membrane rupture	107
700–840	Chromosomes	Visual inspection	Chromosome bridging	108
1064	*S. cerevisiae*	Visual inspection	Division	6

in the results will likely be due to variations in the aforementioned parameters. The similarities and the discrepancies between these studies will be discussed below. It is assumed in the following section that this single-beam optical tweezers are used for trapping, unless explicitly stated otherwise.

6.3.1 Choosing the Optimal Wavelength

Lasers are routinely used for blasting materials in industrial settings and so their safety in handling cells is a natural cause for concern among biologists. The trick lies in using wavelengths where cells are practically transparent. Some of the earliest optical tweezers used visible wavelengths, which is convenient for alignment and for visualizing the trap, but is largely absorbed by biological systems [3]. Optical trapping systems used today with live cell systems almost exclusively use NIR lasers and one of the most preferred wavelengths is 1064 nm, due to the low absorption in water and other biological chromophores, as shown by the absorption spectrum in Figure 6.15. This was first confirmed by König et al. [107] by trapping human spermatozoa at selected wavelengths ranging from 365 to 1064 nm for detecting paralysis, autofluorescence and PI staining. Significant rapid loss of cell vitality and viability was observed at both 365 nm and 760 nm, while trapping at 800 nm was less harmful to sperm cells.

An early study by Vorobjev et al. on the wavelength dependence of photodamage in the NIR region utilized chromosome bridge formation in rat and kangaroo cells to determine the extent of the photodamage. It focused on the range 700–840 nm and found minimal damage at 700 nm and 800–820 nm [108].

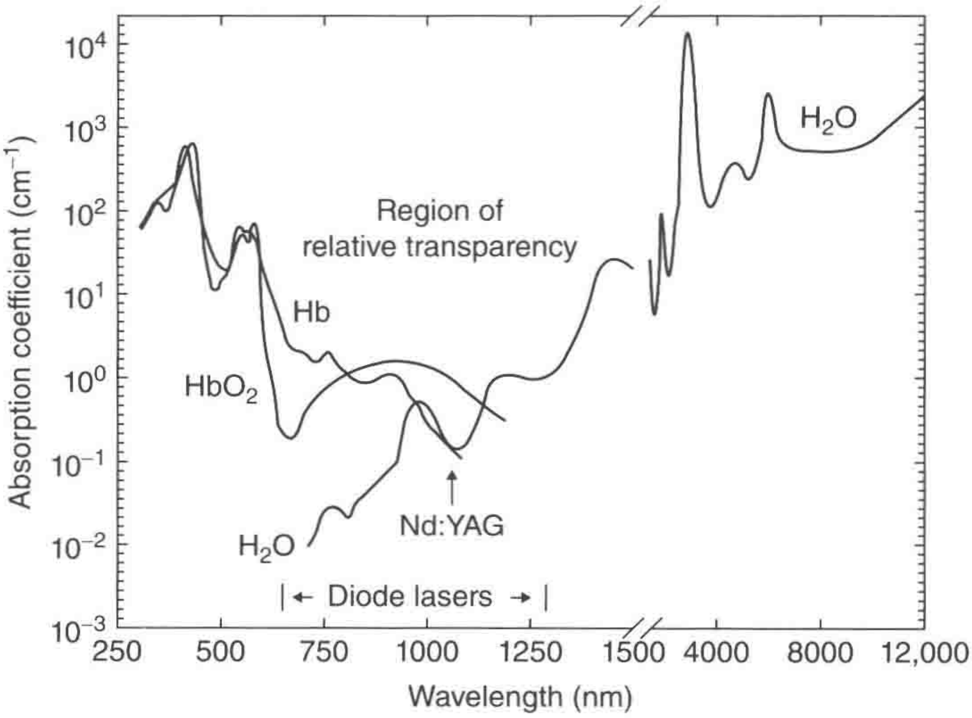

FIGURE 6.15 Absorption spectrum of water, deoxyhemoglobin (Hb), and oxyhemoglobin (HbO$_2$). Note the placement of the Nd:YAG laser at the minimum of the water absorption. Adapted from Reference 27. Annual review of biophysics and biomolecular structure.

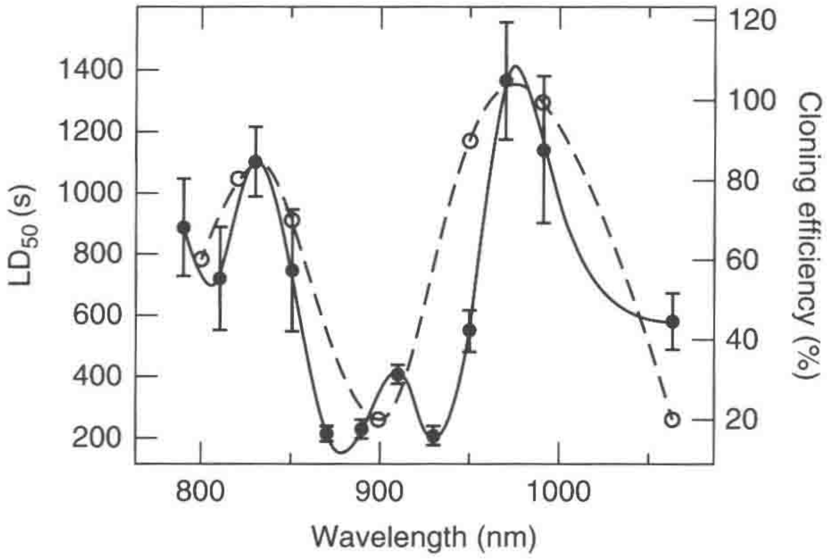

FIGURE 6.16 The wavelength dependence of rotation rate (left vertical axis) of *E. coli* and cloning efficiency of CHO (right vertical axis). LD50(s) is the time in seconds for the rotation rate of *E. coli* to decrease to half of the start rotation rate (solid circles, solid line). The cloning efficiency (%) is measured from CHO cells exposed to 88 mW for 5 min of trapping (open circle, dashed line) data from Liang et al. [106]. Adapted from Reference 104. Biophysics Journal.

Figure 6.16 shows the combined data from two independent studies on the wavelength dependence of viability [104, 106]. Liang et al. studied the cloning efficiency of CHO cells using a Nd:YAG laser (1064 nm) and a tunable Ti:sapphire laser (700–990 nm). They found wavelength-dependent photodamage with a minimum located between 950 and 990 nm and another at around 830 nm. The highest sensitivity to trapping was found at 740–760 nm and 900 nm. Furthermore, sensitivity at 1064 nm was also notably higher than in the two minima regions [106].

Using the change in rotation rate of the *E. coli* flagellum as an indicator of cell health, Neuman et al. studied wavelength dependence between 790 and 1064 nm [104]. They found sensitivity minima at the same wavelengths obtained by Liang et al. The sensitivity at 1064 nm was also increased compared to the minima at 950–990 nm but not to the same extent as Liang et al. observed. The difference in sensitivity could be attributed to both the viability detection method and the different microorganisms studied.

From Figure 6.16, the region at 870–940 nm has the most negative effect on the viability of *E.coli*. The CHO cells show a similar trend but only has a single data point in that region. It has been observed in CHO air-dried monolayers that there is a unique spectral absorption band in the oxidized cytochrome-c oxidase complex at 870 nm. This absorption band coincides well with the minimum viability found by Neuman et al., as shown in Figure 6.16. Furthermore, the second minimum at 930 nm correlates well with a strong absorption peak at exactly 930 nm in porcine fat (long chain hydrocarbons) [109, 110]. It is postulated that this unique absorption band is, in all probability, caused by the carbon–hydrogen (C–H) covalent atomic bonds in the oil structure of the fat [110]. Despite the many fundamental differences between cells of eukaryotic and prokaryotic species, one component shared by almost every type of living organism is the structural features of lipid carbon–hydrogen (C–H) bonds in the form of a phospholipid bilayer membrane. Consequently, the cause of photodamage around 930 nm is likely shared among both eukaryotic and prokaryotic cells.

Leitz et al. (2002) investigated the expression of a heat-shock gene in transgenic *C. elegans* at wavelengths between 700 and 850 nm and found the least damage at 810 nm and the most damage at 700–760 nm [100]. A recent study on wavelength dependence by Mirsaidov et al. [96] trapped 5 × 5 2D array of transformed *E. coli* bacteria positioned in a gel matrix. The cells were exposed to the laser light from 840 to 930 nm and the expression of a GFP plasmid was measured. They found wavelength-dependent photodamage, but surprisingly with minimal damage observed at 900 nm, in conflict with Neuman et al. who found the most damage to *E. coli* in that part of the spectrum. Differences in the detection method and a possible strain dependence could again explain the discrepancies.

From the available data, selecting the ideal wavelength for live cell trapping and measuring is not an easy task. All studies show that cell viability is maintained for longer periods when selecting a wavelength above 800 nm and that trapping below 800 nm is far more harmful. Mohanty et al. even suggested a shift in damaging mechanism between 780 and 800 nm being linked to a change from direct to indirect DNA damage [101].

Above 800 nm the picture is not so clear with data pointing in different directions. However, two windows do appear more benign than other parts of the spectrum. The region around 830 nm and the regions around 970 nm show minimal sensitivity in both *E. coli* and CHO cells [104, 106]. The most popular wavelength for optical tweezers, 1064 nm, is situated between the most sensitive and the least sensitive wavelengths, making it a questionable choice if cell viability is of primary concern. In practice, other considerations such as beam quality, power, and of course price will factor into purchasing decisions.

6.3.2 Thermal Effects

Even though the absorbance of NIR lasers in both water and biological material is relatively small, the high intensity at the focus could potentially cause excessive heating of both the water and the trapped cell. Optical trapping of liposomes, human sperm cells, and hamster ovary cells increases the temperature of 14.5°C/W, 10°C/W, 11.5°C/W, respectively, at 1064 nm [105, 111]. Using a 1064-nm laser to manipulate a Langmuir lipid monolayer at an air/water interface, Wurlitzer et al. [112] measured an increase of 5°C/W. Trapping polystyrene beads ranging from 500 to 2200 nm with a 1064-nm laser and measuring the increase in thermal motion, Peterman et al. [113] found an increase of 8.1°C/W in the focus. Leitz et al. [100] calculated temperature increases for *C. elegans* at different wavelengths ranging from 700 to 1064 nm and found increases of 1.19°C/W at 700 nm up to 38.4°C/W at 1064 nm. However, they did not find a clear correlation between the theoretically calculated temperature increases and measured cell damage, indicating the bulk photodamage was not caused by thermal damage.

These findings also show that by using moderate power (<20 mW) when trapping only a small increase in temperature is observed. All these findings were done on single beam traps using high NA objectives, delivering high power at the focal point. It has been shown that the majority of the heat increase will be created in the focal point [113]. Instead of using tightly focused beams, an alternative is to use nonfocused counter-propagating dual-beams for trapping. The maximum power density is orders of magnitude lower, further reducing any possible heating effects [91]. Another option to reduce photodamage is to use Laguerre-Gaussian hollow beams to only illuminate the cell periphery [114], which also optimizes the trapping efficiency [13].

In a recent study, Wetzel et al. in 2011 utilized the optical stretcher, a two-beam laser trap, to simulate heat shocks that cells typically experience during measurements in optical traps. They measured temperature increase of 23 ± 2 using 1 W power from each fiber [115]. The results show that about 60% of the cells survived heat shocks without vital damage at temperatures of up to 58°C for 0.5 s. By varying the duration of the heat shocks, it was shown that 60% of the cells stayed viable when exposed to 48°C for 5 s. Proteins will usually start to denature at 43°C. In cells the process of denaturation is reversible as long as DNA is not damaged and certain enzymes are still working [116]. However, these enzymes will eventually also be denatured and it is therefore extremely important to keep the duration to a minimum, if viability is a concern.

6.3.3 Power and Energy Dose

Using the lowest possible power for trapping would be prudent even when using wavelengths expected to have low absorption. Due to the high NA objectives used in single-beam optical trapping, the intensities at the focal point can become high enough to induce nonlinear effects such as two-photon absorption. The two-photon process was demonstrated by Zhang et al. [103] who used a 809-nm laser (190 mW) to trap both CHO cells and T-lymphocytes, while simultaneously exciting the probes PI and SYBR 14 with the same laser. Another demonstration of the two-photon process was performed by Goksör et al. [117] who excited the probe PI, in spermatozoa by using a CW laser (1064 nm) as both a trapping and excitation source. However, very high trapping power (2 W) and a long exposure time (1 min) was needed to visualize the fluorescence. König et al. [107] suggested a two-photon mechanism to account for some of the photodamage inflicted on sperm cells at wavelengths below 800 nm.

Using a pulsed laser to trap cells will reach peak powers that are high enough for two-photon effects to be much more probable. The use of mode-locked lasers and Q-switched lasers would possibly create this effect but they are normally not used for optical trapping. CW lasers operate at a much lower peak power level and therefore the probability is much lower. The clearest indication of two-photon processes is a quadratic dependence on the laser intensity. However, if a one-photon process dominates, then the photodamage parameter will have a linear dependence on laser intensity. This was shown by Neuman et al. [104] who observed the sensitivity of the rotation rate of *E. coli* as being linearly dependent on the trapping power. This was further supported by Mirsaidov et al. [96] who, trapping *E. coli* in CW and timeshared traps, found that viability was linearly dependent on the peak power. Furthermore, they found viability depending only on the total dose delivered. A similar study by

Ayano et al. [98] also found the inhibition of both growth rate and division time to be proportional to the total dose.

In contrast to this, Aabo et al. [91] observed that the total dose delivered did not fully characterize the amount of photodamage. Aabo et al. trapped *S. cerevisiae* at 1070 nm and observed the growth rate and division time at various laser power and exposure times. By keeping the dose constant but varying the exposure time and peak power, a dominant effect of the peak power over the exposure time was observed. This supports findings by Mohanty et al. [101] who, using a comet assay to detect DNA damage, found a similar dependence of peak power over exposure time at different wavelengths (750–1064 nm).

The findings of Aabo et al. [91] and Mohanty et al. [101] do not exclude the possibility of the single-photon process as the cause of photodamage; however, they underline the complicated nature of the repair mechanisms present in cells, which possibly reacts nonlinearly to increased photodamage. The discrepancies between these studies could be caused by variations in both microorganisms and detection method.

6.3.4 Growth and Division Time

In one of the earliest studies, Ashkin et al. [6] showed the division of a trapped yeast cell to indicate the nonintrusive and gentle method of optical trapping. However, as any microbiologist will tell you, you need a lot of data to say anything with any degree of certainty.

One of the primary measurements of a cell's health state is the cell's ability to grow and multiply. Many different factors have to be in place for a cell to function and grow at the optimum rate. Measuring growth dependence on photodamage is therefore a very "global" measurement of the cell's sensitivity to an external stress factor. Because of the complexity involved in growth and division, it is therefore difficult to determine the cause of the growth or division arrest, as almost any stress factor will result in changes in growth or division rate. The need to measure over prolonged periods (2–4 h) in order to gather data also complicates matters further. As a result very few extensive studies have been published regarding this health parameter.

Sacconi et al. [99] observed a delay in the start of division of *S. cerevisiae* after trapping at 830 nm at 200 mW for 5 min. The delay was between 3 and 7 h; however, the sample size was very small ($n = 4$). In contrast, a study by Luo et al. [97], trapping at 1064 nm but also on *S. cerevisiae* cells found no discernible effect in division time by trapping at 300 mW for 10 min. The small number of cells used ($n = 3$) in the study does question the accuracy of their findings.

In a study on *E. coli*, Ericsson et al. [102] positioned cells in arrays using an 836-nm laser. They did not see any change in the division rate at trapping powers (output power) up to 2 W; however, trapping times are not listed in the results, which hinder comparison with similar studies.

Ayano et al. [98] did find both the division time and growth rate of *E. coli* at exposure to 1064 nm significantly inhibited at 0.36 and 0.54 J, respectively. This indicates an uncoupling of the division time from the growth as a response to laser inhibition. This is consistent with results by Aabo et al. [91] who found *S. cerevisiae* cells' division times and growth rates to be affected differently at exposure to 1064 nm laser light. They also found the growth inhibition to be affected after the trapping laser was turned off. Their data cannot determine whether the permanent damage was only located in the mother cells or also transferred to daughter cells. However, a possible transference of photodamage from mother to daughter cell was suggested by Ericsson et al. [102], who did find the division of daughter cells not directly exposed to be inhibited in division ability.

A recent study by Eriksson et al. [41] used the ability of *S. cerevisiae* cells to bud after being trapped for 10 sec at various intensities (0–360 mW). They saw a small decrease in the number of cells that would bud at 360 mW, and almost all cells (98%) would bud at exposure to 240 mW. This indicates that the exposure was not lethal, but as they did not measure the division time it is not possible to determine if the photodamage caused a lag in division time.

The discrepancies in the literature when looking at the cell division time response to laser light are quite large, with some reports of no change [102] in division time and others showing significant changes even at very low intensities [91,98]. However, the most recent and comprehensive studies do point toward a gradual response by the cell to laser inhibition. Therefore, any study performed where the division rate is used as a cell health indicator, where optical trapping is involved, needs to be careful in separating the laser inhibition response from any other cell stress response.

The inhibition of the growth rate of cells has to our knowledge only been described in two studies [91,98]. From those studies a clear growth inhibition is evident and there does not appear to be a lower threshold at which inhibition is not seen. For cells exposed to a defined pulse Ayano et al. [98] showed that trapping *E. coli* at 3 mW completely stopped the growth. After the cells were released they started growing again, but with a delay of 140 min, Aabo et al. [91] observed similar behavior where exponential growth was regained in cells after trapping was stopped. Nevertheless, the use of optical trapping to measure growth should be approached with great caution, as significant changes in growth rate have been observed.

6.3.5 Propidium Iodide

The use of propidium iodide (PI) as a viability measurement is very popular as it is easy to handle and gives a simple binary signal (stained/not stained). PI intercalates into double-stranded DNA and will become fluorescent. It is membrane impermeant and will therefore not stain cells, which have a normal membrane. Cells that are stained will therefore have a ruptured membrane, which is generally assumed to be a nonrecoverable injury to a cell [118]. However, a cell that is not stained does not necessarily mean that the cell is not damaged. It only means that the membrane is still intact and even though the nonstaining of a cell indicates viability it does therefore not guarantee it. Several of the studies in Table 6.2 included the probe [94, 102, 103, 105, 107]. These are discussed and compared below.

Trapping CHO cells and T–lymphocytes, Zhang et al. [103] did not notice any membrane rupture trapping at 809 nm for 15 min at 180 mW. Similar results were found by König et al. [107] on sperm cells using 800 nm.

Liu et al. [105] observed PI staining of some sperm cells trapped at 300 mW for longer than 2 min using a 1064-nm laser. A recent study by Harris and McConnell [94] using a trapping laser wavelength of 780 nm on T-lymphocytes observed membrane ruptures after 15 min, at exposures of 9 mW. The variance between these studies could to some extend be caused by wavelength dependence. As shown in Figure 6.16, 780 nm is more damaging than 800 nm when measuring cloning efficiency and rotation rate of *E. coli* flagella. It is therefore also possible that cell membrane damage will have the same wavelength dependence. But the differences between these studies also illustrate one of the problems using PI as a viability detector, which is the absence of detailed information on the cells' health. Because the signal from PI is on/off it necessitates a lot of data to say anything quantitative about the photodamage. Harris and McConnell [94] claimed "By using PI staining, it was clear that the cells remained viable for periods of up to 25 minutes." However, as shown by Aabo et al. [36], there exists a lag between decrease in cell health and membrane rupture. The extent of this lag and what causes the cell membrane to rupture is at present not properly characterized and needs to be further elucidated. Furthermore, studies have shown the discrepancy between intact membranes and loss of the ability to reproduce [102]. Therefore, using PI viability measurements alone to determine the state of the cell health can be dangerous and could lead to misinterpretation of the data.

6.3.6 Internal pH (pH_i)

The cells control over the pH_i is paramount for many aspects of cell metabolism and any changes in the internal pH will therefore affect the cells general health state. Furthermore, it can reveal information at a much early time point than growth rates or live/dead staining with PI or a similar probe [36]. Another potential benefit of the method is that it allows for spatial measurements of the pH_i while trapping, which can reveal information regarding the pH in the different organelles within the cell [35]. However, only one study has to our knowledge been published which characterizes the relationship between photodamage and pH_i [95]. Another study by Liu et al. [105] did measure the pH_i of CHO cells using the pH-sensitive probe SNARF by using two-photon excitation with the trapping laser (1064 nm). However, they equilibrated internal pH of the cells with the external pH using the ionophore nigericin, which trades H^+ for K^+ [119, 120], thereby removing a possible cellular pH_i response to photodamage.

Rasmussen et al. [95] trapped *E. coli* and three *Listeria* bacteria species at 1064 nm with 6 and 18 mW power in the sample plane. They observed a drop in pH_i dependent on trapping strength for all species; however, they saw a different pH_i drop in different species, indicating that different species will have a different cellular response to laser trapping. If the pH_i response is so varied between bacteria species, it is plausible that similar species dependence is present in other viability parameters, for example, growth rate, division time, and membrane rupture. This species dependence response to trapping could therefore explain some of the discrepancies seen between other studies.

6.3.7 Reactive Oxygen Species

The presence of oxygen is essential for aerobe yeast metabolic activity. The reactive nature of molecular oxygen creates various reactive species from the yeast metabolism or reaction of sensitive metabolites with oxygen. These species are classified as reactive oxygen species (ROS). The molecules are either oxidants such as hydrogen peroxide (H_2O_2) or anti-oxidants such as the super oxide anion ($O^{2-}\cdot$). On top of the primary ROS molecules, the primary ROS can react with other compounds to produce new toxic reactive species. These species create oxidative stress upon the cell and cause damage to various cell components. Several extensive review have been published on the subject [121, 122].

The cause of photodamage was initially proposed to be ROS production using laser–tissue interaction by König et al. [107]. They proposed a two-photon effect whereby the creation of oxidative stress was induced. However, they did not believe that this effect would be possible at wavelengths higher than 800 nm. This was also suggested by Liu et al. [105]. The creation of ROS at longer wavelength was postulated by Neuman et al. [104], who trapped *E. coli* at 1064 nm under both anaerobic and aerobic conditions. The rotation rate of the flagella was used as a photodamage parameter. They found that the photodamage was significantly reduced when the cells were trapped under anaerobic conditions compared to aerobic conditions. This suggested that the presence of oxygen was necessary for the photodamage to occur. They suggested that the presence of an unknown photosensitizer to mediate the production of singlet oxygen.

Neuman et al. [104] also proposed using known oxygen scavengers, antioxidant such as β-carotene or α-tocopherol to remove the effect of ROS. However, the use of such compound would be difficult to administer into cells, as it would have to cross the cell membrane. Furthermore, for such an approach to work the antioxidant must be at the right place at the right time to react and neutralize the ROS before it reacts with its substrate (lipids, DNA, proteins). This means it will be in competition with the substrate, which will most likely be in abundance within the cell. Therefore, it is likely that considerable amounts of antioxidants are necessary for it to have a noticeable effect on the damage caused by the ROS. To further impede the approach of using antioxidants, the most reactive ROS species ($\cdot$OH) will only move a very short distance before it reacts with its substrate. Therefore, the antioxidant will also have to spatially be located very close to the ROS for it to work.

The possibility of ROS as a significant factor in photodamage was further supported by the findings of Rasmussen et al. [95]. They found *E. coli* to be less affected by laser trapping when they had been grown under aerobic conditions than anaerobic conditions. When cells are grown in conditions with a surplus of oxygen the probability of ROS generation is higher than if cell are grown with little to no oxygen. The cells will therefore adapt to the increase in oxidative stress by increasing the cells' ability to handle the ROS, producing more antioxidants. This would explain why the aerobic grown cells would be less sensitive to a possible oxidative stress than anaerobic grown cells.

A recent paper by Landry et al. [92] has linked optical trapping of polystyrene microspheres with the generation of singlet oxygen. Using a 1064-nm laser, they trapped a DNA tether between two polystyrene beads. They then measured the tether lifetime using a standard force measurement method of optical tweezers. They observed that by adding a quencher specific to singlet oxygen the damage caused to the DNA tethers was significantly reduced. Singlet oxygen has been documented to cause damage on both single- and double-stranded DNA [123, 124]. The generation of singlet oxygen was confirmed additionally by the use of an anthracene derivative, which exhibits specific reactivity toward singlet oxygen. This was even further confirmed by using the probes singlet-oxygen sensor green (SOSG), which as its name suggests is specifically reactive toward singlet oxygen.

To excite molecular oxygen from the ground level to its excited triplet state takes 0.98 eV. Even though the energy from the laser is consistent with the triplet excitation energy (1.17 eV, 1064 nm) the transition is strictly forbidden by spin, symmetry, and Laport selection rules [125]. To create the excited state single oxygen, a photosensitizer is necessary. The photosensitizer must absorb the energy, store it as vibrational energy, and transfer it to the ground state oxygen. Landry et al. [92] identified the photosensitizer to the polystyrene bead itself. Switching the polystyrene bead to a silica bead and observing a significant drop in damage to the DNA tether with no signal from the SOSG probe confirmed this.

The creation of singlet oxygen by photodamage and specifically the damage to DNA would be consistent with the findings of Mohanty et al. [101] who also observed DNA damage in the near-IR. However, it is possible that other ROS would cause similar DNA damage but only two ROS are thought to be energetic enough: the hydroxyl radical and singlet oxygen. This points toward either the hydroxyl radical or singlet oxygen as probable candidates for cause of photodamage at around 1064 nm.

Based on the findings by Landry et al. [92], it would be pertinent to use a singlet oxygen detecting probe such as the SOSG on cells to establish if singlet oxygen is also created in a biological system. If this were the case then the next step would be to find the sensitizer or sensitizers responsible for the generation of singlet oxygen.

REFERENCES

[1] P. Mazzarello, "A unifying concept: the history of cell theory," *Nat. Cell Biol.* **1**, E13–E15 (1999).

[2] J. Glückstad, "Microfluidics: sorting particles with light," *Nat. Mater.* **3**, 9–10 (2004).

[3] A. Ashkin, "Acceleration and trapping of particles by radiation pressure," *Phys. Rev. Lett.* **24**, 156–159 (1970).

[4] S. Chu, J. Bjorkholm, A. Ashkin, and A. Cable, "Experimental observation of optically trapped atoms," *Phys. Rev. Lett.* **57**, 314–317 (1986).

[5] A. Ashkin and J. Dziedzic, "Optical trapping and manipulation of viruses and bacteria," *Science* **235**, 1517–1520 (1987).

[6] A. Ashkin, J. Dziedzic, and T. Yamane, "Optical trapping and manipulation of single living cells using infrared laser beams," *Nature* **330**, 769–771 (1987).

[7] A. Ashkin, "History of optical trapping and manipulation of small-neutral particle, atoms, and molecules," *IEEE J. Sel. Top. Quantum Electron.* **6**, 841–856 (2000).

[8] S. Parkin, et al., "Optical torque on microscopic objects," *Methods Cell Biol.* **82**, 525–561 (2007).

[9] A. Ashkin, "Forces of a single-beam gradient laser trap on a dielectric sphere in the ray optics regime," *Biophys. J.* **55**, 569–582 (1992).

[10] Y. Harada, "Radiation forces on a dielectric sphere in the Rayleigh scattering regime," *Opt. Commun.* **124**, 529–541 (1996).

[11] A. Rohrbach and E. H. K. Stelzer, "Optical trapping of dielectric particles in arbitrary fields," *J. Opt. Soc. Amer. A* **18**, 839 (2001).

[12] D. Ganic, X. Gan, and M. Gu, "Exact radiation trapping force calculation based on vectorial diffraction theory," *Opt. Express* **12**, 2670–2675 (2004).

[13] N. B. Simpson, D. McGloin, K. Dholakia, L. Allen, and M. J. Padgett, "Optical tweezers with increased axial trapping efficiency," *J. Modern Opt.* **45**, 1943–1949 (1998).

[14] A. Rohrbach and E. H. K. Stelzer, "Trapping forces, force constants, and potential depths for dielectric spheres in the presence of spherical aberrations," *Appl. Opt.* **41**, 2494–2507 (2002).

[15] T. Čižmár, M. Mazilu, and K. Dholakia, "In situ wavefront correction and its application to micromanipulation," *Nat. Photon.* **4**, 388–394 (2010).

[16] P. Mthunzi, A. C. Riches, C. T. A. Brown, F. J. Gunn-Moore, and K. Dholakia, "Intracellular dielectric tagging for improved optical manipulation of mammalian cells," *IEEE J. Sel. Top. Quantum Electron.* **16**, 608–618 (2010).

[17] N. B. Viana, M. S. Rocha, O. N. Mesquita, A. Mazolli, and P. A. M. Neto, "Characterization of objective transmittance for optical tweezers," *Appl. Opt.* **45**, 4263 (2006).

[18] M. Mahamdeh, C. Pérez Campos, and E. Schäffer, "Under-filling trapping objectives optimizes the use of the available laser power in optical tweezers," *Opt. Express* **19**, 11759 (2011).

[19] E. Fällman et al. "Optical tweezers based force measurement system for quantitating binding interactions: system design and application for the study of bacterial adhesion," *Biosens. Bioelectron.* **19**, 1429–1437 (2004).

[20] M.-T. Wei, K.-T. Yang, A. Karmenyan, and A. Chiou, "Three-dimensional optical force field on a Chinese hamster ovary cell in a fiber-optical dual-beam trap," *Opt. Express* **14**, 3056–3064 (2006).

[21] H.-U. Ulriksen et al., "Independent trapping, manipulation and characterization by an all-optical biophotonics workstation," *J. Eur. Opt. Soc. Rapid Publ.* **3**, 080341–080345 (2008).

[22] L. Cherkezyan et al., "Targeted alteration of real and imaginary refractive index of biological cells by histological staining," *Opt. Lett.* **37**, 1601 (2012).

[23] M. Frénéa and H. Naoufel, "On-chip cell positioning and sorting using contactless methods: a comparison between different force-fields," *Biomed. Eng.* (2009).

[24] C. Liu and C. E. Capjack, "Effects of cellular fine structure on scattered light pattern," *IEEE Trans. Nanobiosci.* **5**, 76–82 (2006).

[25] V. Backman et al., "Measuring cellular structure at submicrometer scale with light scattering spectroscopy," *IEEE J. Sel. Top. Quantum Electron.* **7**, 887–893 (2001).

[26] A. G. Banerjee, S. Chowdhury, W. Losert, and S. K. Gupta, "Survey on indirect optical manipulation of cells, nucleic acids, and motor proteins," *J. Biomed. Opt.* **16**, 051302 (2011).

[27] K. Svoboda and S. M. Block, "Biological applications of optical forces," *Annu. Rev. Biophys. Biomol. Struct.* **23**, 247–285 (1994).

[28] T. T. Perkins, "Optical traps for single molecule biophysics: a primer," *Laser Photon. Rev.* **3**, 203–220 (2009).

[29] A. Jannasch, A. F. Demirörs, P. D. J. Van Oostrum, A. Van Blaaderen, and E. Schäffer, "Nanonewton optical force trap employing anti-reflection coated, high-refractive-index titania microspheres," *Nat. Photon.* **6**, 469–473 (2012).

[30] S. Chowdhury, P. Svec, W. Losert, and S. K. Gupta, "Gripper synthesis for indirect manipulation of cells using holographic optical tweezers," *IEEE Int. Conf. Robotics Automation* 2749–2754 (2012). doi:10.1109/ICRA.2012.6225153

[31] J. Glückstad and D. Palima, *Generalized Phase Contrast: Applications in Optics and Photonics* (Springer, New York, 2009).

[32] B. Kemper, et al. "Monitoring of laser micromanipulated optically trapped cells by digital holographic microscopy," *J. Biophoton.* **3**, 425–431 (2010).

[33] B. Kemper, A. Vollmer, C. E. Rommel, J. Schnekenburger, and G. Von Bally, "Simplified approach for quantitative digital holographic phase contrast imaging of living cells," *J. Biomed. Opt.* **16**, 026014 (2011).

[34] P. J. Rodrigo, D. Palima, and J. Glückstad, "Accurate quantitative phase imaging using generalized phase contrast," *Opt. Express* **16**, 2740–2751 (2008).

[35] T. Aabo, A. R. Bañas, J. Glückstad, H. Siegumfeldt, and N. Arneborg, "BioPhotonics workstation: a versatile setup for simultaneous optical manipulation, heat stress, and intracellular pH measurements of a live yeast cell," *Rev. Sci. Instrum.* **82**, 083707 (2011).

[36] T. Aabo, J. Glückstad, H. Siegumfeldt, and N. Arneborg, "Intracellular pH distribution as a cell health indicator in Saccharomyces cerevisiae," *J. R. Soc. Interface* **8**, 1635–1643 (2011).

[37] G. Volpe, G. P. Singh, and D. Petrov, "Dynamics of a growing cell in an optical trap," *Appl. Phys. Lett.* **88**, 231106 (2006).

[38] C. Xie, M. A. Dinno, and Y.-Q. Li, "Near-infrared Raman spectroscopy of single optically trapped biological cells," *Opt. Lett.* **27**, 249–251 (2002).

[39] M. Lankers, J. Popp, and W. Kiefer, "Raman and fluorescence spectra of single optically trapped microdroplets in emulsions," *Appl. Spectrosc.* **48**, 1166–1168 (1994).

[40] H. Mao, J. R. Arias-Gonzalez, S. B. Smith, I. Tinoco, and C. Bustamante, "Temperature control methods in a laser tweezers system," *Biophys. J.* **89**, 1308–1316 (2005).

[41] E. Eriksson et al., "A microfluidic device for reversible environmental changes around single cells using optical tweezers for cell selection and positioning," *Lab on a Chip* **10**, 617–625 (2010).

[42] H. Wu et al., "In vivo lipidomics using single-cell Raman spectroscopy," *Proc. Natl. Acad. Sci. USA* **108**, 3809–3814 (2011).

[43] T. J. Moritz et al. "Evaluation of *Escherichia coli* cell response to antibiotic treatment by use of Raman spectroscopy with laser tweezers," *J. Clin. Microbiol.* **48**, 4287–4290 (2010).

[44] G. P. Singh, C. M. Creely, G. Volpe, H. Grötsch, and D. Petrov, "Real-time detection of hyperosmotic stress response in optically trapped single yeast cells using Raman microspectroscopy," *Anal. Chem.* **77**, 2564–2568 (2005).

[45] D. E. Ingber, "Mechanical control of tissue growth: function follows form," *Proc. Natl. Acad. Sci. USA* **102**, 11571–11572 (2005).

[46] P. J. Rodrigo et al. "Optical microassembly platform for constructing reconfigurable microenvironments for biomedical studies," *Opt. Express* **17**, 6578–6583 (2009).

[47] T. Matsuoka et al. "Functionalized 2PP structures for the biophotonics workstation," *SPIE OPTO* 79500Q–79500Q–6 (2011). doi:10.1117/12.877189

[48] B. L. Aekbote et al., "Aminosilane-based functionalization of two-photon polymerized 3D SU-8 microstructures," *Eur. Polym. J.* **48**, 1745–1754 (2012).

[49] A. Ovsianikov, Z. Li, J. Torgersen, J. Stampfl, and R. Liska, "3D photografting: selective functionalization of 3D matrices via multiphoton grafting and subsequent click chemistry (*Adv. Funct. Mater.* 16/2012)," *Adv. Funct. Mater.* **22**, 3527 (2012).

[50] D. Palima et al., "Wave-guided optical waveguides," *Opt. Express* **20**, 2004–2014 (2012).

[51] N. Arneborg et al., "Interactive optical trapping shows that confinement is a determinant of growth in a mixed yeast culture," *FEMS Microbiol. Lett.* **245**, 155–159 (2005).

[52] Z. Li and S. K. Nair, "Quorum sensing: how bacteria can coordinate activity and synchronize their response to external signals?," *Protein Sci.* **21**, 1403–1417 (2012).

[53] W. Timp, U. Mirsaidov, P. Matsudaira, and G. Timp, "Jamming prokaryotic cell-to-cell communications in a model biofilm," *Lab on a chip* **9**, 925–934 (2009).

[54] U. Mirsaidov et al., "Live cell lithography: using optical tweezers to create synthetic tissue," *Lab on a chip* **8**, 2174–2181 (2008).

[55] H. Kress et al., "Cell stimulation with optically manipulated microsources," *Nat. Methods* **6**, 905–909 (2009).

[56] T. Wu et al., "A photon-driven micromotor can direct nerve fibre growth," *Nat. Photonics* **6**, 62–67 (2011).

[57] J. H. Sung and M. L. Shuler, "Microtechnology for mimicking in vivo tissue environment," *Ann. Biomed. Eng.* **40**, 1289–1300 (2012).

[58] C. C. DuFort, M. J. Paszek, and V. M. Weaver, "Balancing forces: architectural control of mechanotransduction," *Nat. Rev. Mol. Cell Biol.* **12**, 308–319 (2011).

[59] D. Choquet, D. P. Felsenfeld, and M. P. Sheetz, "Extracellular matrix rigidity causes strengthening of integrin–cytoskeleton linkages," *Cell* **88**, 39–48 (1997).

[60] D. P. Felsenfeld, P. L. Schwartzberg, A. Venegas, R. Tse, and M. P. Sheetz, "Selective regulation of integrin–cytoskeleton interactions by the tyrosine kinase Src," *Nat. Cell Biol.* **1**, 200–206 (1999).

[61] Y. Wang et al., "Visualizing the mechanical activation of Src," *Nature* **434**, 1040–1045 (2005).

[62] A. Resnick, "Use of optical tweezers to probe epithelial mechanosensation," *J. Biomed. Opt.* **15**, 015005 (2010).

[63] S. M. Nauli et al. "Polycystins 1 and 2 mediate mechanosensation in the primary cilium of kidney cells," *Nat. Genet.* **33**, 129–137 (2003).

[64] J. Glückstad, A. R. Bañas, T. Aabo, and D. Palima, "Structure-mediated micro-to-nano coupling using sculpted light and matter," *SPIE Photonics Europe* 84241L–84241L–6 (2012). doi:10.1117/12.924097

[65] D. B. Phillips et al., "Surface imaging using holographic optical tweezers," *Nanotechnol.* **22**, 285503 (2011).

[66] C. T. Lim, E. H. Zhou, and S. T. Quek, "Mechanical models for living cells–a review," *J. Biomech.* **39**, 195–216 (2006).

[67] J. P. Mills, L. Qie, M. Dao, C. T. Lim, and S. Suresh, "Nonlinear elastic and viscoelastic deformation of the human red blood cell with optical tweezers," *Mech. Chem. Biosystems* **1**, 169–180 (2004).

[68] J. Guck et al., "The optical stretcher: a novel laser tool to micromanipulate cells," *Biophys. J.* **81**, 767–784 (2001).

[69] A. Fritsch et al. "Are biomechanical changes necessary for tumour progression?," *Nat. Phy.* **6**, 730–732 (2010).

[70] D. L. Jaye, R. A. Bray, H. M. Gebel, W. A. C. Harris, and E. K. Waller, "Translational applications of flow cytometry in clinical practice," *J. Immunol.* **188**, 4715–4719 (2012).

[71] W. A. Bonner, "Fluorescence activated cell sorting," *Rev. Instrum.* **43**, 404 (1972).

[72] H. M. Shapiro, *Practical Flow Cytometry*. 736pp. (John Wiley & Sons, 2003).

[73] A. Y. Fu, C. Spence, A. Scherer, F. H. Arnold, and S. R. Quake, "A microfabricated fluorescence-activated cell sorter," *Nat. Biotechnol.* **17**, 1109–1111 (1999).

[74] A. A. S. Bhagat et al., "Microfluidics for cell separation," *Med. Biol. Eng. Comput.* **48**, 999–1014 (2010).

[75] M. M. Wang et al., "Microfluidic sorting of mammalian cells by optical force switching," *Nat. Biotechnol.* **23**, 83–87 (2005).

[76] T. D. Perroud et al., "Microfluidic-based cell sorting of Francisella tularensis infected macrophages using optical forces," *Anal. Chem.* **80**, 6365–6372 (2008).

[77] T.-H. Wu et al., "Pulsed laser triggered high speed microfluidic fluorescence activated cell sorter," *Lab on a Chip* **12**, 1378–1383 (2012).

[78] M. Padgett, R. Di Leonardo, and R. Leonardo, "Di holographic optical tweezers and their relevance to lab on chip devices," *Lab on a Chip* **11**, 1196–1205 (2011).

[79] X. Wang et al., "Enhanced cell sorting and manipulation with combined optical tweezer and microfluidic chip technologies," *Lab on a Chip* **11**, 3656–3662 (2011).

[80] B. Landenberger, H. Höfemann, S. Wadle, and A. Rohrbach, "Microfluidic sorting of arbitrary cells with dynamic optical tweezers," *Lab on a Chip* **12**, 3177–3183 (2012).

[81] I. Perch-Nielsen, D. Palima, J. S. Dam, and J. Glückstad, "Parallel particle identification and separation for active optical sorting," *J. Opt. A: Pure Appl. Opt.* **11**, 034013 (2009).

[82] A. R. Bañas, D. Palima, F. Pedersen, and J. Glückstad, "Development of a compact bio-optofluidic cell sorter," *SPIE OPTO* 82740N–82740N–6 (2012). doi:10.1117/12.909908

[83] T. Imasaka, Y. Kawabata, T. Kaneta, and Y. Ishidzu, "Optical chromatography," *Anal. Chem.* **67**, 1763–1765 (1995).

[84] S. J. Hart, A. Terray, J. Arnold, and T. A. Leski, "Sample concentration using optical chromatography," *Opt. Express* **15**, 2724 (2007).

[85] K. H. Lee, S. B. Kim, K. S. Lee, and H. J. Sung, "Enhancement by optical force of separation in pinched flow fractionation," *Lab on a Chip* **11**, 354–357 (2011).

[86] M. MacDonald, G. Spalding, and K. Dholakia, "Microfluidic sorting in an optical lattice," *Nature* **426**, 421–424 (2003).

[87] G. Milne, D. Rhodes, M. MacDonald, and K. Dholakia, "Fractionation of polydisperse colloid with acousto-optically generated potential energy landscapes," *Opt. Lett.* **32**, 1144–1146 (2007).

[88] P. Breeuwer and T. Abee, "Assessment of viability of microorganisms employing fluorescence techniques," *Int. J. Food Microbiol.* **55**, 193–200 (2000).

[89] D. B. Kell, A. S. Kaprelyants, D. H. Weichart, C. R. Harwood, and M. R. Barer, "Viability and activity in readily culturable bacteria: a review and discussion of the practical issues," *Antonie van Leeuwenhoek* **73**, 169–187 (1998).

[90] A. Ashkin and J. Dziedzic, "Optical trapping and manipulation of single living cells using infrared-laser beams," *Ber. Bunsen-Ges. Phys. Chem.* **93**, 254–260 (1989).

[91] T. Aabo et al., "Effect of long-and short-term exposure to laser light at 1070 nm on growth of *Saccharomyces cerevisiae*," *J. Biomed. Opt.* **15**, 041505 (2010).

[92] M. P. Landry, P. M. McCall, Z. Qi, and Y. R. Chemla, "Characterization of photoactivated singlet oxygen damage in single-molecule optical trap experiments," *Biophys. J.* **97**, 2128–2136 (2009).

[93] E. Bornstein, W. Hermans, S. Gridley, and J. Manni, "Near-infrared photoinactivation of bacteria and fungi at physiologic temperatures," *Photochem. Photobiol.* **85**, 1364–1374 (2009).

[94] J. Harris and G. McConnell, "Optical trapping and manipulation of live T cells with a low numerical aperture lens," *Opt. Express* **16**, 14036–14043 (2008).

[95] M. B. Rasmussen, L. B. Oddershede, and H. Siegumfeldt, "Optical tweezers cause physiological damage to *Escherichia coli* and Listeria bacteria," *Appl. Environ. Microbiol.* **74**, 2441–2446 (2008).

[96] U. Mirsaidov et al., "Optimal optical trap for bacterial viability," *Phys. Rev. E* **78**, 1–7 (2008).

[97] C. Luo et al., "The combination of optical tweezers and microwell array for cells physical manipulation and localization in microfluidic device," *Biomed. Microdevices* **9**, 573–578 (2007).

[98] S. Ayano, Y. Wakamoto, S. Yamashita, and K. Yasuda, "Quantitative measurement of damage caused by 1064-nm wavelength optical trapping of *Escherichia coli* cells using on-chip single cell cultivation system," *Biochem. Biophys. Res. Commun.* **350**, 678–684 (2006).

[99] L. Sacconi, I. M. Tolić-Nørrelykke, C. Stringari, R. Antolini, and F. S. Pavone, "Optical micromanipulations inside yeast cells," *Appl. Opt.* **44**, 2001–2007 (2005).

[100] G. Leitz, E. Fällman, S. Tuck, and O. Axner, "Stress response in Caenorhabditis elegans caused by optical tweezers: wavelength, power, and time dependence," *Biophys. J.* **82**, 2224–2231 (2002).

[101] S. Mohanty, A. Rapp, and S. Monajembashi, "Comet assay measurements of DNA damage in cells by laser microbeams and trapping beams with wavelengths spanning a range of 308 nm to 1064 nm," *Radiat. Res. Soc.* **157**, 378–385 (2002).

[102] M. Ericsson, D. Hanstorp, P. Hagberg, J. Enger, and T. Nyström, "Sorting out bacterial viability with optical tweezers," *J. Bacteriol.* **182**, 5551–5555 (2000).

[103] Z. X. Zhang et al., "Cell viability and DNA denaturation measurements by two-photon fluorescence excitation in CW Al:GaAs diode laser optical traps," *J. Biomed. Opt.* **4**, 256 (1999).

[104] K. C. Neuman, E. Chadd, G. Liou, K. Bergman, and S. M. Block, "Characterization of photodamage to *Escherichia coli* in optical traps," *Biophys. J.* **77**, 2856–2863 (1999).

[105] Y. Liu, G. J. Sonek, M. W. Berns, and B. J. Tromberg, "Physiological monitoring of optically trapped cells: assessing the effects of confinement by 1064-nm laser tweezers using microfluorometry," *Biophys. J.* **71**, 2158–2167 (1996).

[106] H. Liang et al. "Wavelength dependence of cell cloning efficiency after optical trapping," *Biophys. J.* **70**, 1529–1533 (1996).

[107] K. König, Y. Tadir, P. Patrizio, M. W. Berns, and B. J. Tromberg, "Effects of ultraviolet exposure and near infrared laser tweezers on human spermatozoa," *Hum. Reprod.* **11**, 2162–2164 (1996).

[108] I. Vorobjev, H. Liang, W. H. Wright, and M. W. Berns, "Optical trapping for chromosome manipulation: a wavelength dependence of induced chromosome bridges," *Biophys. J.* **64**, 533–538 (1993).

[109] J. M. Conway, K. H. Norris, and C. E. Bodwell, "A new approach for the estimation of body composition: infrared interactance," *Am. J. Clin. Nutr.* **40**, 1123–1130 (1984).

[110] M. Irie, "Evaluation of porcine fat with fiber-optic spectroscopy," *J. Anim. Sci.* **77**, 2680–2684 (1999).

[111] Y. Liu et al., "Evidence for localized cell heating induced by infrared optical tweezers," *Biophys. J.* **68**, 2137–2144 (1995).

[112] S. Wurlitzer, C. Lautz, M. Liley, C. Duschl, and T.M. Fischer, "Micromanipulation of Langmuir-monolayers with optical tweezers," *J. Phys. Chem.* **105**, 182–187 (2001).

[113] E. J. G. Peterman, F. Gittes, and C. F. Schmidt, "Laser-induced heating in optical traps," *Biophys. J.* **84**, 1308–1316 (2003).

[114] R. Dasgupta, S. Ahlawat, R. S. Verma, S. Shukla, and P. K. Gupta "Optical trapping of spermatozoa using Laguerre-Gaussian laser modes," *J. Biomed. Opt.* **15**, 065010 (2010).

[115] F. Wetzel et al., "Single cell viability and impact of heating by laser absorption," *Eur. Biophys. J.* **40**, 1109–1114 (2011).

[116] H. Lodish et al., *Molecular Cell Biology* (Freeman, New York, 2000).

[117] M. Goksör, J. Enger, and D. Hanstorp, "Optical manipulation in combination with multiphoton microscopy for single-cell studies," *Appl. Opt.* **43**, 4831–4837 (2004).

[118] K. H. Jones and J. Senft, "An improved method to determine cell viability by simultaneous staining with fluorescein diacetate-propidium iodide," *J. Histochem. Cytochem.* **33**, 77 (1985).

[119] C. Riondet, R. Cachon, Y. Wache, G. Alcaraz, and C. Diviès, "Measurement of the intracellular pH in *Escherichia coli* with the internally conjugated fluorescent probe 5-(and 6-) carboxyfluorescein succinimidyl ester," *Biotechnol. Tech.* **11**, 735–738 (1997).

[120] L. G. Chitarra, P. Breeuwer, R. W. Van Den Bulk, and T. Abee, "Rapid fluorescence assessment of intracellular pH as a viability indicator of *Clavibacter michiganensis* subsp. *michiganensis*," *J. Appl. Microbiol.* **88**, 809–816 (2000).

[121] M. J. Davies, "The oxidative environment and protein damage," *Biochim. Biophys. Acta* **1703**, 93–109 (2005).

[122] D. J. Jamieson, "Oxidative stress responses of the yeast *Saccharomyces cerevisiae*," *Yeast (Chichester, England)* **14**, 1511–1527 (1998).

[123] M. S. Cooke, M. D. Evans, M. Dizdaroglu, and J. Lunec, "Oxidative DNA damage: mechanisms, mutation, and disease," *FASEB J.* **17**, 1195–1214 (2003).

[124] D. Ribeiro et al., "Singlet oxygen induced DNA damage and mutagenicity in a single-stranded SV40-based shuttle vector," *Photochem. Photobiol.* **55**, 39–45 (1992).

[125] A. A. Trabanco, G. Montalban, G. Rumbles, A. G. M. Barrett, and B. M. Hoffman, "A seco-porphyrazine: superb sensitizer for singlet oxygen generation and endoperoxide synthesis," *Synlett* **5**, 1010–1012 (2000).

[126] R. Pfeifer, T. Nieminen, N. Heckenberg, and H. Rubinsztein-Dunlop, "Colloquium: momentum of an electromagnetic wave in dielectric media," *Rev. Mod. Phys.* **79**, 1197–1216 (2007).

[127] B. A. Kemp, "Resolution of the Abraham-Minkowski debate: implications for the electromagnetic wave theory of light in matter," *J. Appl. Phys.* **109**, 111101 (2011).

7

TISSUE POLARIMETRY

ALEX VITKIN,[1] NIRMALYA GHOSH,[2] AND
ANTONELLO DE MARTINO[3]

[1] *Medical Biophysics and Radiation Oncology, University of Toronto, Toronto, ON, Canada*

[2] *Department of Physical Sciences, Indian Institute of Science Education and Research, Kolkata, India*

[3] *Ecole Polytechnique, Palaiseau, France*

7.1 INTRODUCTION

Although optical characterization of tissues is increasingly being studied and used for biomedical diagnostics, in the vast majority of cases this characterization is based on *intensity* measurements. However, the interaction with the sample of interest also induces significant changes in light *polarization*, which also conveys useful information about the morphology and functional state of the investigated tissue [1–4]. Polarimetry typically provides contrasts quite different from those observed in ordinary intensity imaging. Taken alone or in conjunction with other techniques these contrasts may prove very useful for biomedical diagnostics.

In spite of its great potential, polarimetry is far from having reached the same degree of maturity in the biomedical field as intensity-based techniques. One possible reason for this "lag" is the strongly depolarizing nature of almost all biological tissues, which require sophisticated experimental setups and data treatment procedures to be properly characterized. In fact, in complex random media like tissues, numerous complexities due to multiple scattering and spatially inhomogeneous birefringence, as well as simultaneous occurrences of several polarization events, present

---

Photonics: Scientific Foundations, Technology and Applications, Volume IV, First Edition.
Edited by David L. Andrews.
© 2015 John Wiley & Sons, Inc. Published 2015 by John Wiley & Sons, Inc.

formidable challenges for biomedical tissue polarimetry [3]. However, polarimetric instrumentation as well as theoretical understanding and numerical simulation of the interaction of polarized light and biological tissues are progressing impressively, paving the way for attractive applications. Polarization can be used to discriminate singly versus multiply scattered light. Tissue optical anisotropy and depolarization power may be characterized quantitatively, even when these effects occur simultaneously. Via proper analysis and modeling, these data may ultimately provide reliable techniques for "optical biopsy" which, in turn, may dramatically improve the management of various diseases.

In this chapter, we review polarized light fundamentals and mathematical formulations of polarized light and its propagation in biological tissues, discuss advances in various emerging polarimetric measurement systems, describe forward and inverse problems in polarimetry of turbid media (both theoretical modeling and experimental validation), and focus on applications related to tissue diagnosis and assessment.

7.2 POLARIZED LIGHT FUNDAMENTALS

7.2.1 Polarization States

7.2.1.1 Totally Polarized States For a purely monochromatic optical wave of frequency ω, propagating along the z axis, its electric field **E** vibrates in the xy plane according to

$$\mathbf{E}(z,t) = \begin{bmatrix} E_{0x}\cos(\omega t - \beta z + \phi_x) \\ E_{0y}\cos(\omega t - \beta z + \phi_y) \end{bmatrix} = \mathrm{Re}[\exp(i\omega - i\beta z)\mathbf{J}], \tag{7.1}$$

with

$$\beta = |\boldsymbol{\beta}| = (n - ik)\frac{\omega}{c} \tag{7.2}$$

being the modulus of the propagation vector $\boldsymbol{\beta}$, c is the speed of light in vacuum, and n and k are the real and imaginary parts of the refractive index, which determine, respectively, the speed of light and the absorption in the medium. The amplitudes E_{0i} and phases ϕ_i are constants and define the Jones vector **J** as [5–7]

$$\mathbf{J} = \begin{bmatrix} E_{0x}\exp(i\phi_x) \\ E_{0y}\exp(i\phi_y) \end{bmatrix}. \tag{7.3}$$

The *polarization* of the wave—the shape of the trajectory described by **E** in the xy plane—depends only on the ratio of the amplitudes $\tan\alpha$ and the phase difference φ defined, respectively, as

$$\tan\upsilon = \frac{E_{0y}}{E_{0x}} \text{and} \quad \phi = \phi_y - \phi_x. \tag{7.4}$$

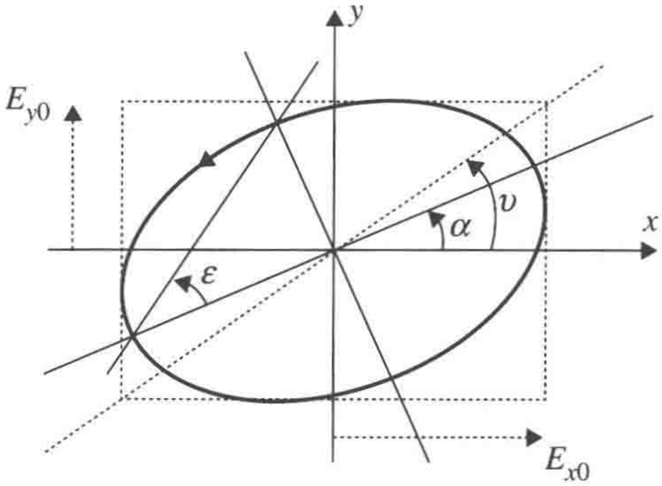

FIGURE 7.1 The polarization ellipse of a wave propagating in the z direction (toward the observer). E_{0x} and E_{0y} are the amplitudes of the field oscillations along the x and y directions; their ratio is equal to tan υ. α is the azimuth of the major axis of the ellipse and ε is its ellipticity. Ellipticity is positive or negative for left- or right-handed states, respectively.

This trajectory is in general elliptical and is represented in Figure 7.1. Besides the parameters defined in Eq. (7.4), the ellipse can also be described by the orientation (azimuth) α of its major axis and its ellipticity ε, which is positive for left handedness and negative for right handedness. The ellipticity ε varies between the two limits of zero (linearly polarized light) and ±45° (circularly polarized light), which thus represent the two limits of generally elliptical polarization. Table 7.1 lists the Jones vectors of usual polarization states (with H, V, P, and M for linear polarizations along the horizontal, vertical, +45°, and −45° directions, and L and R for left and right circular polarizations, respectively).

The *intensity* of a fully polarized wave characterized by the Jones vector **J** is given by

$$I = I_x + I_y = \frac{1}{2}\left(E_{ox}^2 + E_{oy}^2\right) = \frac{1}{2}(J \otimes J^*). \tag{7.5}$$

TABLE 7.1 Usual polarization states: Jones vectors, azimuths, ellipticities, and shapes of the ellipses

State	H	V	P	M	L	R	Elliptical
J	$\begin{bmatrix}1\\0\end{bmatrix}$	$\begin{bmatrix}0\\1\end{bmatrix}$	$\frac{1}{\sqrt{2}}\begin{bmatrix}1\\1\end{bmatrix}$	$\frac{1}{\sqrt{2}}\begin{bmatrix}1\\-1\end{bmatrix}$	$\frac{1}{\sqrt{2}}\begin{bmatrix}1\\-i\end{bmatrix}$	$\frac{1}{\sqrt{2}}\begin{bmatrix}1\\i\end{bmatrix}$	$\begin{bmatrix}\cos\alpha\cos\varepsilon - i\sin\alpha\sin\varepsilon\\ \sin\alpha\cos\varepsilon + i\cos\alpha\sin\varepsilon\end{bmatrix}$
α	0	90°	45°	−45°	Undefined	Undefined	α
ε	0	0	0	0	45°	−45°	ε
Shape of the ellipse					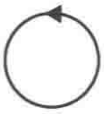	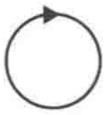	

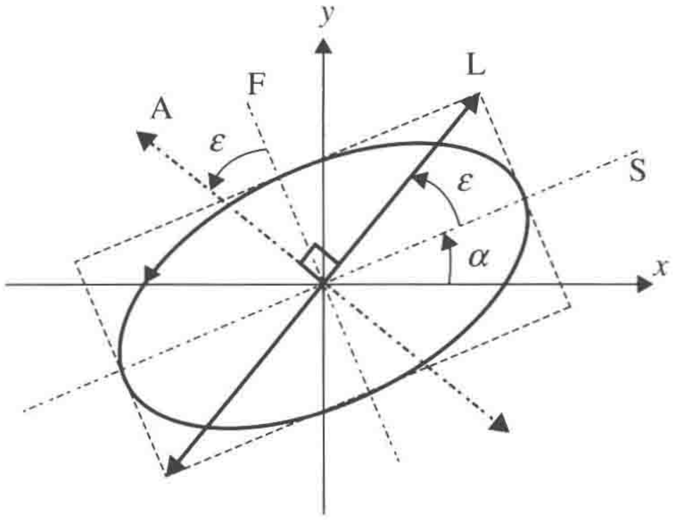

FIGURE 7.2 Illustration of the extinction method of analysis of arbitrary elliptical polarizations. The initial elliptical polarization is transformed into a linear one (L) by inserting a quarter-wave plate with its slow axis S at azimuth α. Extinction is then obtained by setting a linear analyzer A perpendicular to L. The ellipticity ε is thus measured as the angle between the analyzer set for extinction and the fast axis F of the quarter-wave plate.

Experimentally, the usual "recipe" to determine that a light beam propagating along z is linearly polarized along an azimuth α is to observe its *extinction* through a linear analyzer set perpendicular to α. This characterization may be extended to elliptically polarized beams as illustrated in Figure 7.2.

To determine the ellipticity ε (as the beam may not be fully linearly polarized), a quarter-wave plate (QWP) is inserted in the beam path with its slow axis at the azimuth α. Due to the 90° induced phase shift thus introduced, the initial incident elliptical polarization is transformed into a linear one, oriented at $\alpha + \varepsilon$ from the x reference axis. Then, a linear analyzer with its passing axis set at ε from the fast axis of the QWP will totally extinguish the beam. In practice, the extinction is achieved by trial-and-error procedure, and the azimuth α and the ellipticity ε are eventually determined from the angular settings of the QWP and the analyzer when maximum extinction is obtained.

7.2.1.2 ***Partially Polarized States***

If one tries the extinction method to characterize "natural" light directly coming from a source such as the sun or a light bulb, the detected intensity is seen to be independent of the settings of the QWP and the analyzer. One can thus conclude that the light coming from the sun or the light bulb is *totally depolarized.*

In other cases—for example the light coming from a bulb but reflected on a plastic floor en route to observer—the intensity detected through the QWP and the analyzer varies between $I_{\min}$ and $I_{\max}$. This provides an experimental definition of the *degree of polarization* (DOP) of the light beam

$$\mathrm{DOP} = \frac{I_{\max} - I_{\min}}{I_{\max} + I_{\min}}. \tag{7.6}$$

For totally polarized states, I_{min} vanishes and DOP = 1. At the other extreme, for totally unpolarized light $I_{\text{min}} = I_{\text{max}}$ and DOP = 0. For partially polarized states, the DOP may take any intermediate values between zero and one.

For partially polarized states, the motion of the electric field in the xy plane is no longer a perfect ellipse, but rather a somewhat *disordered* one. In case of a totally random motion of the electric vector $\mathbf{E}$, one would surmise that in the extinction procedure the analyzer would detect the same constant intensity. What is implicitly assumed in this description is that the light polarization may be defined at any instant, but may vary significantly over time scales much shorter than the integration time of the detector. As a result, this detector takes the *temporal averages of the intensities*, sequentially generated by *different totally polarized states*. While this idea is basically correct, it is important to emphasize that this averaging of intensities (i.e., *incoherent* sum) of polarized contributions is not necessarily temporal.

To this end, consider the scattering experiments schematized in Figure 7.3. In one case (top panel), the object is optically thin and the laser undergoes single scattering by the rough surface. Conversely, in the other case the object is optically thick and multiple scattering is dominant. In both cases, the incident laser beam is spatially coherent, and the scattering objects are *static* (we ignore for the moment any possible thermal/Brownian motions). It is well known that in these conditions what is observed on the screen is a *speckle pattern* due to the interferences, at each point of the screen, of many scattered waves which reach this point with random (but static) amplitudes and relative phases [8].

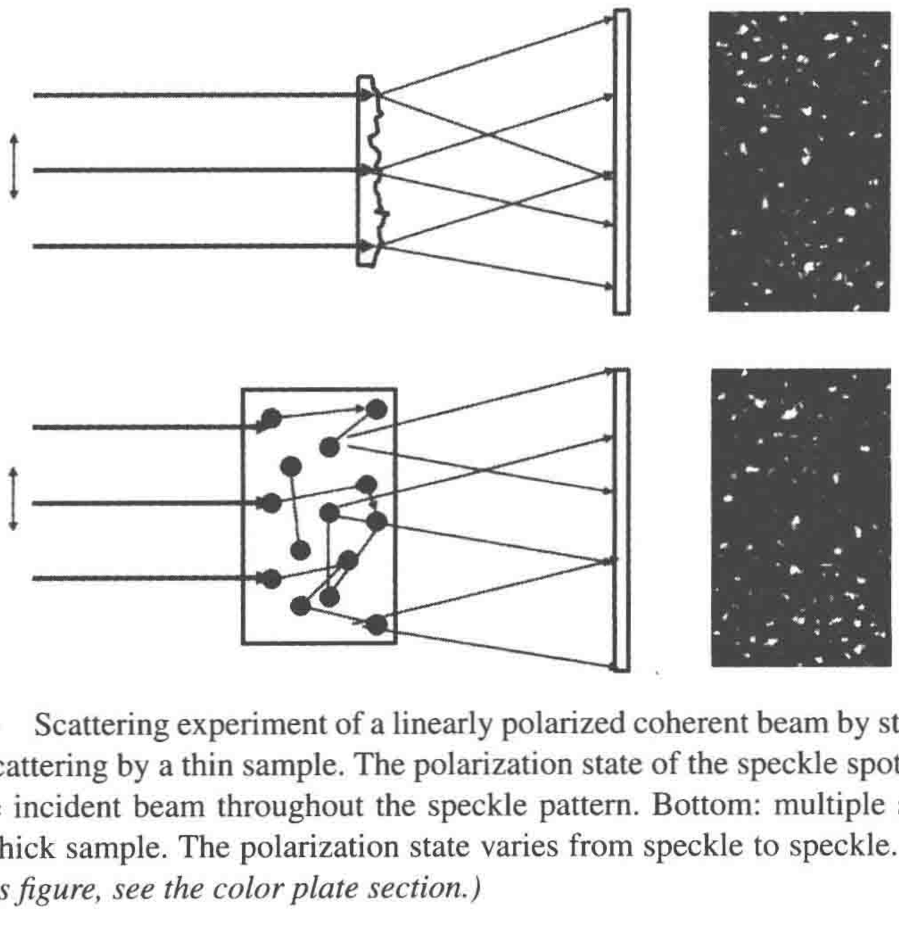

FIGURE 7.3 Scattering experiment of a linearly polarized coherent beam by static samples. Top: single scattering by a thin sample. The polarization state of the speckle spots is the same as that of the incident beam throughout the speckle pattern. Bottom: multiple scattering by an optically thick sample. The polarization state varies from speckle to speckle. *(For a color version of this figure, see the color plate section.)*

The major difference between single and multiple scattering regimes is that for the former, the polarization of all scattered waves is the same as that of the incident laser, while in case of multiple scattering these polarizations are random. Consequently, as outlined in Figure 7.3, for single scattering all the speckles feature the same polarization as the incident laser, while in the other case, each speckle is still *fully polarized, but this polarization varies randomly from one speckle to the next.*

Can one thus conclude that multiple scattering always depolarizes an incident polarized beam? The correct answer depends on how the sample is illuminated and how the emerging light is detected.

- If the beam is *coherent*, the sample is *static and the detection zone is smaller than the size of the speckles, then there is no depolarization.* The initial polarization state is converted into another fully polarized one at each point of the speckle pattern.
- If *the detector is much larger than the speckle size,* then if one applies the extinction method to analyze the polarization, some speckles will exhibit varying intensity, but randomly so (different speckles displaying different polarization states). Thus, the overall detected signal will be constant, and according to the criterion defined in Eq. (7.6), *the detected light is totally depolarized.* This is because the large detector performs a *sum of intensities* of the contributions of different polarized states (the speckles), this sum being performed spatially in this case. On the other hand, for single scattering the same large detector would see an extinction for suitably aligned QWP and analyzer, and the emerging light would be considered fully polarized.
- If the illumination beam *is not spatially coherent* (which is generally the case for a beam from a classical source), then the relative phases at different points of this beam change very rapidly, and so does the resultant speckle pattern. As a result, even if the detector is small, the polarization will vary rapidly in time, and the measured DOP would be small.
- The same conclusion may be reached (strong depolarization at each point of the screen) if the beam is coherent but the sample *is not static*, as for example a liquid suspension of small scatterers which undergo Brownian motion. However, the typical time constants for Brownian-motion-induced speckle variations are much longer (ms to seconds) than those due to the lack of spatial coherence for a light beam coming from a classical source (~fs), and they may be temporally resolved by many detectors.
- Finally, if the incident light is *polychromatic*, then each wavelength creates its own speckle pattern, with basically no correlation between the patterns created at different wavelengths. As no interferences are possible between waves with different wavelengths, the incoherent intensity summation takes places naturally, leading to depolarization in each point of the observation screen.

To summarize, "true" depolarization requires that the detected signal is *the sum of intensities due to various polarized contributions with different polarizations.* This summation may be performed temporally, spatially, or spectrally, and it depends not only on the sample itself but also on the characteristics of the illumination beam and of the detection system.

7.2.1.3 Stokes Vectors Following the above presentation, polarized states are not characterized in terms of well-determined field amplitudes, but rather from intensities measured through various analyzers, which are in turn averages of quadratic functions of the field amplitudes. These quantities may be arranged in various ways. The most commonly used is the *Stokes vector*, which is a real four-row single-column array defined as

$$S = \begin{bmatrix} I \\ Q \\ U \\ V \end{bmatrix} = \begin{bmatrix} Ix + Iy \\ Ix - Iy \\ IP - IM \\ I_{\mathrm{L}} - I_{\mathrm{R}} \end{bmatrix} = \begin{bmatrix} \left\langle E_x E_x^* + E_y E_y^* \right\rangle \\ \left\langle E_x E_x^* - E_y E_y^* \right\rangle \\ \left\langle E_x E_y^* + E_y E_x^* \right\rangle \\ \left\langle i(E_x E_y^* - E_y E_x^*) \right\rangle \end{bmatrix}, \tag{7.7a}$$

where I_x, I_y, I_P, and I_M are the intensities measured through ideal linear polarizers oriented along x or y axes, or at +45° or −45° azimuths. I_{L} and I_{R} are measured through left and right circular polarizers, respectively. It can be shown [9–12] that Stokes vectors can define any polarization state and any DOP. The first element I is the polarization-independent light intensity, and as such is equal to any other sum of orthogonal intensities (e.g., $I_P + I_M$ or $I_{\mathrm{L}} + I_{\mathrm{R}}$). Also note that **S** is not a vector in the geometric space, rather this array of intensity values represent a directional vector in the polarization state space (Poincaré sphere, described subsequently). For totally polarized states defined by Jones vectors of the form given by Eq. (7.3), the corresponding Stokes vectors are

$$\mathbf{S} = \begin{pmatrix} \frac{1}{2}\left(E_{0x}^2 + E_{0y}^2\right) \\ \frac{1}{2}\left(E_{0x}^2 - E_{0y}^2\right) \\ (E_{0x}E_{0y}\cos\varphi) \\ (E_{0x}E_{0y}\sin\varphi) \end{pmatrix}. \tag{7.7b}$$

Note that the Stokes vector by its definition (Eq. 7.7a) incorporates both the pure (totally polarized) and mixed (partially polarized) states and this definition evolves from the so-called 2 × 2 coherency matrix **N** [12]. The coherency matrix is defined through the ensemble averaged Jones vector as $\mathbf{N} = \langle J \otimes J^* \rangle$ and accordingly its four elements are $\langle E_x E_x^* \rangle$, $\langle E_x Ey^* \rangle$, $\langle E_y E_x^* \rangle$, and $\langle E_y E_y^* \rangle$ [12]. Conversely, it follows that the Stokes vector elements (I, Q, U, and V) are the expansion coefficients of the coherency matrix in terms of the identity matrix and the three Pauli spin matrices [12].

TABLE 7.2 Normalized Stokes vectors for usual totally polarized states (cf Table 7.1)

State	H	V	P	M	L	R	Elliptical
S	$\begin{bmatrix}1\\1\\0\\0\end{bmatrix}$	$\begin{bmatrix}1\\-1\\0\\0\end{bmatrix}$	$\begin{bmatrix}1\\0\\1\\0\end{bmatrix}$	$\begin{bmatrix}1\\0\\-1\\0\end{bmatrix}$	$\begin{bmatrix}1\\0\\0\\1\end{bmatrix}$	$\begin{bmatrix}1\\0\\0\\-1\end{bmatrix}$	$\begin{bmatrix}1\\\cos 2\alpha\ \cos 2\varepsilon\\\sin 2\alpha\ \cos 2\varepsilon\\\sin 2\varepsilon\end{bmatrix}$

Stokes vectors can be written in normalized form as

$$\mathbf{S}^{\mathrm{T}} = I\left(1, \frac{Q}{I}, \frac{U}{I}, \frac{V}{I}\right) = I(1, q, u, v) = I(1, \mathbf{s}^{\mathrm{T}}), \tag{7.7c}$$

where the superscript $^{\mathrm{T}}$ means the transpose. The three intensity-normalized coordinates q, u, and v are the quantities which *actually define the polarization state* independently of the total intensity I. The normalized Stokes vectors for usual fully polarized states are listed in Table 7.2.

At the other extreme, for *totally unpolarized states*, $Q = U = V = 0$, which corresponds to the fact that no matter how the analyzer is oriented, for such states the transmitted intensity is always the same, equal to one half of the total intensity.

The DOP defined experimentally in Eq. (7.6) can be expressed in terms of the normalized Stokes vector components as

$$\mathrm{DOP} = \sqrt{q^2 + u^2 + v^2}. \tag{7.8a}$$

It is straightforward to check that for Stokes vectors of the form (7.7b) we get DOP = 1. In addition to the overall DOP, we can define the linear and circular DOPs, respectively, as

$$\mathrm{DOP}_{\mathrm{L}} = \sqrt{q^2 + u^2} \quad \text{and} \quad \mathrm{DOP}_{\mathrm{C}} = v. \tag{7.8b}$$

Experimentally, the $\mathrm{DOP}_{\mathrm{L}}$ can be measured by the extinction method using only a rotatable linear polarizer, without the QWP. Equation (7.6) then applies with I_{max} and I_{min}, representing the maximum and minimum intensities measured when the polarizer is rotated. On the other hand, $\mathrm{DOP}_{\mathrm{C}}$ can be measured by using left and right circular polarizers. Calling again I_{L} and I_{R} the intensities measured through these circular polarizers, $\mathrm{DOP}_{\mathrm{C}}$ is given by the same formula (7.6) but with I_{L} and I_{R} replacing I_{min} and I_{max}.

Physical realizability. In contrast with Jones vectors, which could be any 2D complex vectors, any four-dimensional element real array is not necessarily an acceptable Stokes vector, due to the condition

$$\mathrm{DOP} \leq 1. \tag{7.9}$$

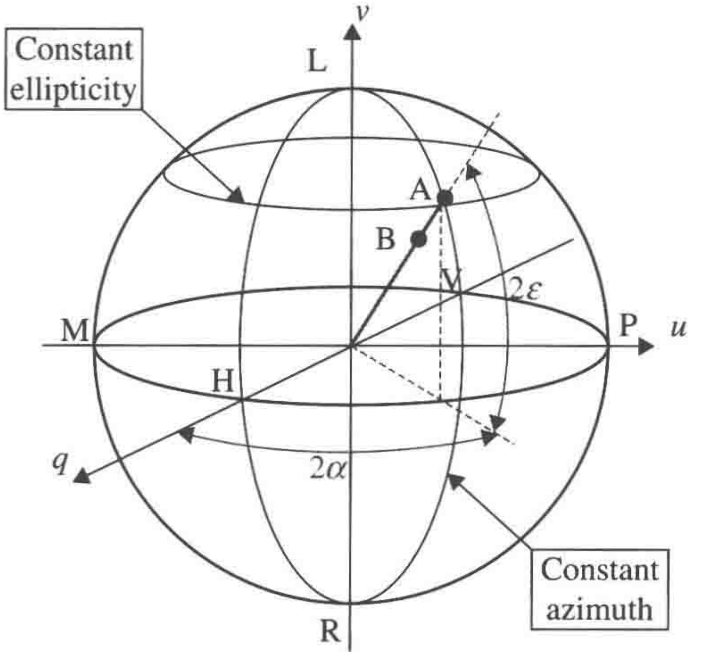

FIGURE 7.4 Geometrical representation of Stokes vectors within the Poincaré sphere. Any given polarization state is represented by a point whose Cartesian coordinates are the intensity-normalized coordinates (q, u, v). The radial coordinate is the DOP and the "longitude" and "latitude" are, respectively, 2α and 2ε. Totally polarized states are found at the surface of the unit radius sphere, while partially polarized states are inside (e.g., points A and B, respectively). Linearly polarized states, among which H, V, P, and M states, are on the "equator" while the L and R circular states are found at the "poles."

The Poincaré sphere. A very convenient geometrical representation of all possible polarization states involves the intensity-normalized coordinates q, u, and v defined above, as illustrated in Figure 7.4 [12]. In this space, the DOP is nothing else but the distance of the representative point from origin. Thus, the physical realizability condition given by Eq. (7.9) implies that all acceptable Stokes vectors are represented by points located within the unit radius sphere, also called the *Poincaré sphere*. Totally polarized states are found at the surface of the sphere (point A) while partially polarized states are inside (point B). The other spherical coordinates, the points "latitude" and "longitude" are nothing else but twice the azimuth α and ellipticity ε, as shown by the last column of Table 7.2 for totally polarized states. As shown throughout this chapter, this geometrical representation provides simple and intuitive descriptions of many aspects of the interaction between polarized light and samples and/or instruments.

Before we move on to define sample polarization interactions through this "conventional" Stokes–Mueller algebra, it may be worthwhile to briefly mention the validity regime of such algebra. Note that both the Jones vector (in the field representation, Eq. 7.3) and the Stokes vector (intensity-based representation, Eq. 7.7a) deal with two-dimensional electromagnetic field and are applicable when the light wave is completely transverse (plane electromagnetic waves or more generally to uniformly polarized elementary beams). However, it has been shown that even for paraxial beam-like fields, the spatial mode (field distribution) and polarization are not always separable (unlike plane waves or elementary beams), and accordingly one needs different algebra to describe such inhomogeneous polarization [13]. This so-called *classical entanglement* between polarization and spatial mode is handled by defining beam coherency polarization matrix (a variant of the 2 × 2 coherency matrix incorporating simultaneously both the field polarization and its spatial distribution) [13]. In other general cases involving three-dimensional field (as encountered in tight focusing scenarios and in the near field), the two-dimensional polarimetry formalisms have been extended via the definition of 3 × 3 coherency matrix and generalized nine-element Stokes vector [14]. Moreover, there are other emerging "unconventional" polarization algebra formulations involving vector beams, geometric phases (Pancharatnam–Berry phase) arising from spin orbit interactions of light, radial, and azimuthal polarization of light beams, and so forth [15–17]. Even though such generalized polarization algebra may find useful biomedical applications; these have yet not been explored in tissue polarimetry research (possibly due to the unknown magnitude/relative importance of these effects in tissues, and possibly due to the numerous complexities in tissue signal detection and analysis). We thus restrict our discussion to the "conventional" polarization algebra and its applications in tissue polarimetry.

7.2.2 Interaction with a Sample

7.2.2.1 Mueller Matrices For any optical system operating in the linear regime (which is always the case except when the light source is a high power pulsed laser), the output intensities are linear functions of the inputs. As a result, the transformation of the Stokes vectors must also be linear, thus described by a 4 × 4 real matrix **M** called Mueller matrix [18]:

$$\mathbf{S}_{\text{out}} = \text{M} \bullet \text{S}_{\text{in}}. \tag{7.10}$$

In analogy with **S**, which represents the polarization *state of the beam*, **M** thus represents the corresponding polarization *properties of the sample*; the link between the two is accomplished via the Mueller–Stokes calculus as described by Eq. (7.10).

Physical realizability. Analogous to Stokes vectors, any 4 × 4 real matrix is not necessarily a physically acceptable Mueller matrix. An obviously necessary condition is that in never transforms a physically acceptable Stokes vector $\mathbf{S}_{\text{in}}$ into an "overpolarized" one $\mathbf{S}_{\text{out}}$, with DOP > 1. However, this condition is necessary but not sufficient. A general procedure for determining the acceptability of **M**, based on the calculation of the so-called coherency matrix **N** [12, 19], is given in Reference 20 and is outside the scope of this review. This procedure may also be used to "correct" a slightly unphysical matrix (possibly due to measurement errors) to make it acceptable.

Depolarizing or nondepolarizing character. A physically acceptable Mueller matrix is said to be *nondepolarizing* if any input totally polarized Stokes vector $\mathbf{S}_{\text{in}}$ is transformed into a totally polarized $\mathbf{S}_{\text{out}}$. (in other words, the DOP does not decrease). Necessary and sufficient conditions for a matrix to be nondepolarizing have been examined [20,21]. Conversely, for depolarizing Mueller matrices the DOP of $\mathbf{S}_{\text{out}}$ is smaller than that of $\mathbf{S}_{\text{in}}$. It is important to note that, for any resulting Mueller matrix, the reduction of the DOP depends on the input state $\mathbf{S}_{\text{in}}$; for example, a given tissue sample in a particular examination geometry can be more depolarizing for input circular states than for input linear ones, or vice versa. It is therefore impossible to *uniquely* define the depolarization power of a generic Mueller matrix **M**.

Among the various definitions of this depolarization power of a sample described by **M**, one very widely used is the "depolarization index" P_{d} [22]:

$$P_{\text{d}} = \sqrt{\frac{\sum_{i,j} M_{i,j}^2 - M_{1,1}^2}{3M_{1,1}^2}} = \sqrt{\frac{Tr(\mathbf{M}^T\mathbf{M}) - M_{1,1}^2}{3M_{1,1}^2}}, \tag{7.11}$$

which varies from 0 for a total depolarizer to 1 for nondepolarizing matrices.

7.2.2.2 Diattenuation and Polarizance These two properties can be determined *unambiguously* for any Mueller matrix **M** from its very definition in terms of intensities. Quite generally, **M** can be rewritten as

$$\mathbf{M} = m_{11} \begin{pmatrix} 1 & \mathbf{D}^{\text{T}} \\ \mathbf{P} & \mathbf{m} \end{pmatrix}, \tag{7.12}$$

where **D** (first row) and **P** (first column) are the *diattenuation* and *polarizance* vectors, respectively, while **m** is a 3 × 3 real matrix. These formulations are easily justified as follows.

Diattenuation. For a diattenuating system, *the output intensity depends on the polarization of the incident wave*. If we consider an intensity-normalized input Stokes vector **S**

$$\mathbf{S}_{\text{in}}^{\text{T}} = (1, \mathbf{s}^{\text{T}}) \quad \text{with} \quad \|\mathbf{s}\| = \text{DOP} \le 1 \tag{7.13}$$

corresponding to arbitrary polarizations at constant intensity (normalized to 1), then the output intensity (i.e., the first component of $\mathbf{S}_{\text{out}}$) is simply given by

$$I_{\text{out}} = m_{11}(1 + \mathbf{D} \cdot \mathbf{s}). \tag{7.14}$$

This output intensity reaches its maximum (resp. minimum) value $I_{\max}$ (resp. $I_{\min}$) when the scalar product $\mathbf{D} \cdot \mathbf{s}$ is maximum (resp. minimum) under the constraint $\|\mathbf{s}\| = \text{DOP} \le 1$, that is, when $\mathbf{s} = \pm\frac{\mathbf{D}}{\|\mathbf{D}\|}$. We thus obtain

$$\mathbf{S}_{\max}^{\text{T}} = \left(1, \frac{\mathbf{D}^{\text{T}}}{\|\mathbf{D}\|}\right) \quad \text{and} \quad I_{\max} = m_{11}(1 + \|\mathbf{D}\|) \tag{7.15a}$$

$$\mathbf{S}_{\min}^{\text{T}} = \left(1, -\frac{\mathbf{D}^{\text{T}}}{\|\mathbf{D}\|}\right), \quad \text{and} \quad I_{\min} = m_{11}(1 - \|\mathbf{D}\|) \tag{7.15b}$$

from which we immediately get for the *scalar diattenuation D*

$$D = \frac{I_{\max} - I_{\min}}{I_{\max} + I_{\min}} = \|\mathbf{D}\|. \tag{7.16}$$

In summary, the diattenuator vector **D** defines both the scalar diattenuation D and the polarization states transmitted with the largest (or the lowest) intensity. Note that the two polarization states providing these extreme intensity transmission values are totally polarized, and located at diametrally opposite positions on the Poincaré sphere.

Polarizance. We now consider this property which corresponds to the capacity of the sample to polarize incoming beams, specifically *to impart a finite DOP to an unpolarized input beam*. In this case the Stokes vector of the output beam is simply

$$\mathbf{S}_{\text{out}} = m_{11} \begin{pmatrix} 1 & \mathbf{D}^{\mathrm{T}} \\ \mathbf{P} & \mathbf{m} \end{pmatrix} \begin{pmatrix} I \\ 0 \\ 0 \\ 0 \end{pmatrix} = m_{11} I \begin{pmatrix} 1 \\ \mathbf{P} \end{pmatrix}. \tag{7.17}$$

In a way analogous to diattenuation, from the polarizance vector **P** we can define a scalar polarizance $P = \|\mathbf{P}\|$,

Independence of polarizance and diattenuation. In practice, diattenuation and/or polarizance may occur

- at *interfaces*, where the transmission and/or reflections coefficients may be different for the polarization in the plane of incidence (p polarization) or orthogonal to this plane (s polarization), due to the well-known Fresnel laws [23]: transmission is larger (and reflection is smaller) for p than for s polarization; and
- during *the propagation in bulk anisotropic materials*. In this case, diattenuation and/or polarizance is due to the dependence of the imaginary part of the optical refractive index on the light polarization.

For the simple cases cited above, the polarizance is directly related to the diattenuation: $\mathbf{P} = \mathbf{D}$. For more complex systems, and in particular depolarizing ones, **P** and **D** become totally independent parameters, as shown by the following examples:

1. Consider a *polarizer followed by a perfect depolarizer*. Such a system clearly exhibits diattenuation, as the intensity transmitted by the polarizer depends on the orientation of the incoming linear polarization. However, the beam emerging from the depolarizer is, by definition, totally depolarized, implying that an initially depolarized beam would remain totally depolarized. As a result, such a system exhibits a *strong diattenuation but no polarizance*.
2. Let us now consider *the same elementary components, but in reverse order* (depolarizer first, polarizer afterwards). In this case, any incoming polarized beam is transformed by the depolarizer into a totally depolarized beam whose

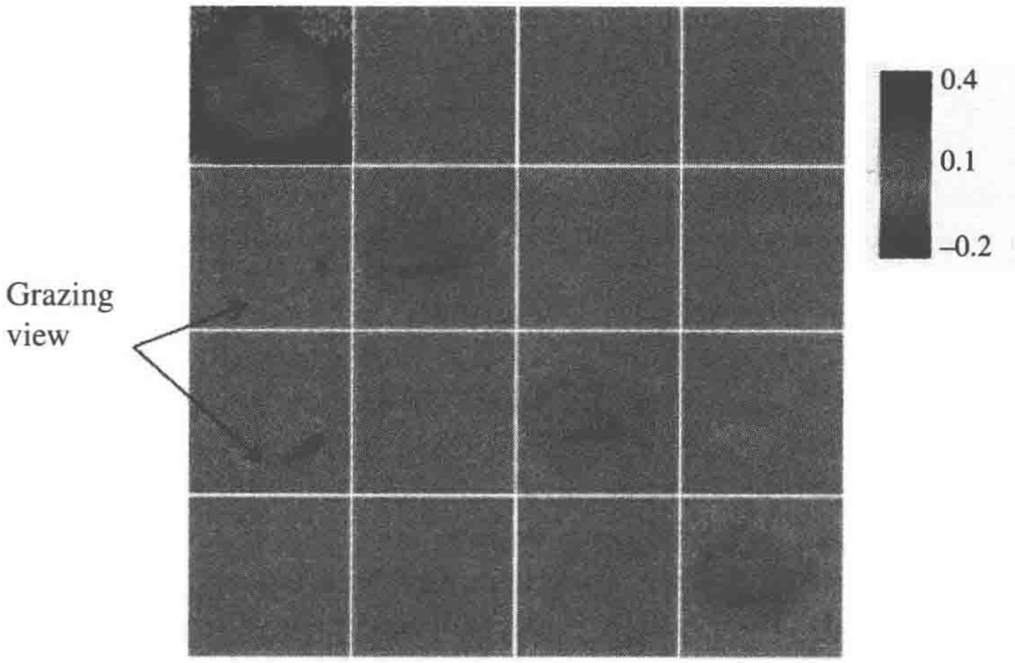

FIGURE 7.5 Normalized Mueller matrix image of a resected human cervix in backscattering geometry. The field of view is 3 × 3 cm^2. The sample is about 5 mm thick and has conical shape. All elements are normalized by m_{11} and these normalized values are given in the color scale shown at top right, ranging from −0.2 to 0.4. This sample features no diattenuation, as shown by the vanishing elements in the first row, and significant linear polarizance (elements m_{21} and m_{31}) at some points where the light emerges at grazing angles from the sample surface, and is polarized by a local "Brewster angle" effect (A. de Martino, unpublished results). (*For a color version of this figure, see the color plate section.*)

intensity does not depend on the incoming polarization. Then, the polarizer transforms this beam into a polarized one, with always the same polarization. In contrast with the previous case, now the system exhibits *zero diattenuation but a strong polarizance* ($P = 1$ for a perfect output polarizer).

While such effects may seem purely "academic," they can actually occur in real systems, and more particularly in biological samples. Figure 7.5 shows a Mueller image of an *ex vivo* surgical sample of uterine cervix, normalized by m_{11}. On this image, some narrow regions, close to the edge of the sample, clearly exhibit nonzero linear polarizance (elements m_{21} and m_{31}), without any detectable counterpart in the diattenuation (elements m_{12} and m_{13}). As indicated in the figure, these regions are seen under *grazing angles*. Then, as outlined above, the light component polarized parallel to the local surface normal (the local p polarized component) is much better transmitted at the air–tissue interface than the component polarized parallel to the surface itself (the local s polarized component). As a result, the light emerging from these regions is strongly polarized even if the sample is illuminated with unpolarized light. On the other hand, the main contribution to this emerging light is due to rays impinging on the samples in other places, at incidences closer to normal and then multiply scattered. As a result, there is little or no diattenuation effect for these impinging rays and the situation is quite similar to the case 2 outlined above.

7.2.2.3 Homogeneous Diattenuators and Retarders Polarimetric elements are called homogeneous if they exhibit two fully polarized orthogonal eigenstates, that is, two polarization states which are transmitted without alteration and which do not interfere with each other. In practice, such light states are linearly polarized along two perpendicular directions, or circularly polarized and rotating in opposite senses. The normalized Stokes vectors $\mathbf{S}_1$ and $\mathbf{S}_2$ of such orthogonal states are of the form

$$\mathbf{S}_1^{\mathrm{T}} = (1, \mathbf{s}^{\mathrm{T}}),\ \mathbf{S}_2^{\mathrm{T}} = (1, -\mathbf{s}^{\mathrm{T}}) \tag{7.18}$$

with $\|\mathbf{s}\| = 1$, as these states are fully polarized. Orthogonal states are thus found on the surface of the Poincaré sphere at diametrally opposed positions. For any homogeneous polarimetric element, there are thus two (and only two) such states which are left invariant on the Poincaré sphere.

Homogeneous diattenuators: These elements are uniquely determined by their diattenuation vector $\mathbf{D}$. Their (totally polarized) eigenpolarization states corresponding, respectively, to maximum and minimum transmissions are given by Eqs. (7.15) with

$$\mathbf{s}_{\mathrm{max}} = \frac{\mathbf{D}}{D}, \qquad \mathbf{s}_{\mathrm{min}} = -\frac{\mathbf{D}}{D}. \tag{7.19}$$

The corresponding Mueller matrix is then given in synthetic form by [24]

$$\mathbf{M}_{\mathrm{D}} = \tau \begin{pmatrix} 1 & \mathbf{D}^{\mathrm{T}} \\ \mathbf{D} & \mathbf{m}_{\mathrm{d}} \end{pmatrix} \quad \text{where } \mathbf{m}_{\mathrm{D}} = \sqrt{1 - D^2}\mathbf{I}_3 + (1 - \sqrt{1 - D^2})\mathbf{D}\ \ \mathbf{D}^{\mathrm{T}}, \tag{7.20}$$

where τ is the intensity transmission for incident unpolarized light. As already mentioned, diattenuation may occur due to reflection and/or refraction at an interface, or to propagation in anisotropic or chiral materials. Anisotropy may introduce *linear dichroism*. If so, for any propagation direction (except very particular ones determined by the symmetry of the material) the imaginary part of the refractive index k may take two different values, k_{L} and k_{H}; The former, corresponding the lowest absorption, is valid for a wave linearly polarized at azimuth θ and the latter for the orthogonal polarization, at $\theta + 90°$. The *linear* (scalar) dichroism is then defined as

$$\Delta k = k_{\mathrm{H}} - k_{\mathrm{L}} > 0. \tag{7.21}$$

For a parallel slab of thickness L, the intensity transmissions for the two eigenpolarizations are respectively

$$T_{\mathrm{max}} = \exp(-2k_{\mathrm{L}}L), \qquad T_{\mathrm{min}} = \exp(-2k_{\mathrm{H}}L) \tag{7.22}$$

resulting in a scalar diattenuation

$$D = \frac{T_{\mathrm{max}} - T_{\mathrm{min}}}{T_{\mathrm{max}} + T_{\mathrm{min}}} = \sinh(d) \tag{7.23}$$

where $d = \Delta k L$ is the dichroism integrated over the slab thickness L.

Chiral media (e.g., a biological fluid with glucose) can also feature dichroism, but then it is *circular dichroism*. The above formulas are still valid, but in this case the eigenpolarizations for which the absorption coefficients are well defined are left and right circular ones.

The matrix of a homogeneous diattenuator is symmetric, explicitly written for a linear diattenuator as [12]:

$$\mathbf{M}_{\mathrm{LD}}(\tau, D, \theta) = \frac{\tau}{2}\begin{pmatrix} 1 & D\cos 2\theta & D\sin 2\theta & 0 \\ D\cos 2\theta & \cos^2 2\theta + \sqrt{1-D^2}\sin^2 2\theta & (1-\sqrt{1-D^2})\cos 2\theta\sin 2\theta & 0 \\ D\sin 2\theta & (1-\sqrt{1-D^2})\cos 2\theta\sin 2\theta & \sin^2(2\theta) + \sqrt{1-D^2}\cos^2 2\theta & 0 \\ 0 & 0 & 0 & \sqrt{1-D^2} \end{pmatrix} \tag{7.24}$$

implying that the maximum and minimum intensity transmittances are obtained for linearly polarized states with azimuths θ and $\theta + 90°$. A straightforward calculation indeed shows that

$$\begin{aligned} \mathbf{M}_{\mathrm{LD}}(\tau, D, \theta)\begin{pmatrix} 1 \\ \cos 2\theta \\ \sin 2\theta \\ 0 \end{pmatrix} &= \frac{\tau}{2}(1+D)\begin{pmatrix} 1 \\ \cos 2\theta \\ \sin 2\theta \\ 0 \end{pmatrix} \quad \text{and} \\ \mathbf{M}_{\mathrm{LD}}(\tau, D, \theta)\begin{pmatrix} 1 \\ -\cos 2\theta \\ -\sin 2\theta \\ 0 \end{pmatrix} &= \frac{\tau}{2}(1-D)\begin{pmatrix} 1 \\ -\cos 2\theta \\ -\sin 2\theta \\ 0 \end{pmatrix} \end{aligned}, \tag{7.25}$$

which is a direct check that these states are unchanged by $\mathbf{M}_{\mathrm{LD}}(\tau,D,\theta)$, but are transmitted with intensity factors $\frac{\tau}{2}(1 \pm D)$. Similarly, for circular diattenuators the corresponding matrix is

$$\mathbf{M}_{\mathrm{CD}}(\tau, D) = \frac{\tau}{2}\begin{pmatrix} 1 & 0 & 0 & D \\ 0 & \sqrt{1-D^2} & 0 & 0 \\ 0 & 0 & \sqrt{1-D^2} & 0 \\ D & 0 & 0 & 1 \end{pmatrix} \tag{7.26}$$

and of course in this case there is no need to define any particular azimuth θ.

Homogeneous retarders: For these elements too there are two orthogonal eigenpolarization states, each of which is transmitted without modification of its shape. In contrast with diattenuators, retarders transmit both eigenstates with the same intensity coefficients, but *different phases*. This phase difference is the *scalar retardation* δ.

In practice, like diattenuation, retardation may be caused by reflection and/or refraction at an interface, or by propagation in anisotropic materials. This latter case is particularly relevant for tissue polarimetry. Anisotropic tissues are typically connective tissues, with fibrillar proteins (collagen is the prime example) which may be spatially organized with a preferential orientation. Then if we consider a light wave propagating along z, and call θ the azimuth of the fiber orientation direction in the xy plane, the refractive index is larger for light linearly polarized at azimuth θ than at $\theta + 90°$. These azimuths then define the *slow* (θ) and *fast* ($\theta = 90°$) *axes* in the xy plane, with refractive indices n_{S} and n_{F}. The *linear birefringence* of the material is then defined as

$$\Delta n = n_{\mathrm{S}} - n_{\mathrm{F}}. \tag{7.27}$$

Propagation over a distance L in such a material introduces a scalar retardation δ (in radians)

$$\delta = 2\pi \frac{\Delta n\, L}{\lambda}. \tag{7.28}$$

For homogeneous retarders, the orthogonal Stokes eigenvectors are again of the form given by Eq. (7.18). A pure retarder can be described geometrically as rotation in the space of Stokes vectors. Mathematically the Mueller matrix $\mathbf{M}_{\mathrm{R}}$ of the retarder can be written in compact notation as [24]

$$\mathbf{M}_{\mathrm{R}} = \begin{pmatrix} 1 & \mathbf{0}^{\mathrm{T}} \\ \mathbf{0} & \mathbf{m}_{\mathbf{R}} \end{pmatrix}, \tag{7.29}$$

where $\mathbf{0}$ represents the null vector and the 3×3 submatrix, $\mathbf{m}_{\mathbf{R}}$, is a rotation matrix in the (q, u, v) space. As a result, the action of a homogeneous diattenuator on an arbitrary incident Stokes vector $\mathbf{S}$ is a mere rotation of its representative point on the Poincaré sphere, described by $\mathbf{m}_{\mathrm{R}}$. Moreover, the axis of this rotation is defined by the two diametrally opposed points representing the two eigenpolarizations, and the rotation angle is nothing else but the retardation δ [12].

For *linear retarders* with eigenstates linearly polarized along θ and θ +90° azimuths, the Mueller matrices are [12]

$$\mathbf{M}_{\mathrm{LR}}(\tau, \delta, \theta) = \tau \begin{pmatrix} 1 & 0 & 0 & 0 \\ 0 & \cos^2 2\theta + \sin^2 2\theta \cos\delta & \cos 2\theta \sin 2\theta\,(1 - \cos\delta) & -\sin 2\theta \sin\delta \\ 0 & \cos 2\theta \sin 2\theta\,(1 - \cos\delta) & \sin^2 2\theta + \cos^2 2\theta \cos\delta & \cos 2\theta \sin\delta \\ 0 & \sin 2\theta \sin\delta & -\cos 2\theta \sin\delta & \cos\delta \end{pmatrix} \tag{7.30}$$

And Eq. (7.25) is still valid, provided both intensity transmittance factors $\frac{\tau}{2}(1 \pm D)$ are replaced by τ.

We now consider *circular retarders*, that is, elements for which the eigenpolarizations are counter-rotating circular ones. The Mueller matrices of such elements are of the form:

$$\mathbf{M}_{\mathrm{CR}}(\psi) = \tau \begin{pmatrix} 1 & 0 & 0 & 0 \\ 0 & \cos 2\psi & -\sin 2\psi & 0 \\ 0 & \sin 2\psi & \cos 2\psi & 0 \\ 0 & 0 & 0 & 1 \end{pmatrix}. \tag{7.31}$$

When a linearly polarized wave interacts with a circular retarder, its polarization remains linear, but *it is rotated* by an angle ψ which is nothing else but the circular retardance, as it can be checked by a straightforward calculation analogous to that shown in Eq. (7.25). Circular birefringence is observed in media lacking any mirror symmetry, like solutions of chiral molecules where only one enantiomer is present. An example of major practical clinical importance is that of *glucose*, as discussed in greater detail later. Chiral media are usually characterized by their *optical activity* χ rather than their circular birefringence Δn_c:

$$\chi = \frac{2\pi}{\lambda}\Delta n \tag{7.32a}$$

so that the optical rotation ψ due to propagation over a distance L is simply

$$\psi = \chi L. \tag{7.32b}$$

We point out, however, that in tissues (like in essentially any usual materials, except for example some particular liquid crystals) optical activity is an *extremely weak* effect, much weaker than linear birefringence whenever this latter effect is present.

Finally, we point out that the scalar retardation of any homogeneous retarder (linear or circular) is easily determined from its Mueller matrix $\mathbf{M}_{\mathbf{R}}$ as

$$\delta, \psi = \cos^{-1}\left(\frac{Tr(\mathbf{M}_{\mathrm{R}})}{2} - 1\right). \tag{7.33}$$

7.2.2.4 Depolarizers By definition, a depolarizer is an object that reduces the DOP of the incoming light. The conceptually simplest (and most relevant in practice) depolarizers are those for which the Mueller matrix $\mathbf{M}_\Delta$ is diagonal

$$\mathbf{M}_\Delta = \tau \begin{pmatrix} 1 & 0 & 0 & 0 \\ 0 & a & 0 & 0 \\ 0 & 0 & b & 0 \\ 0 & 0 & 0 & c \end{pmatrix} \tag{7.34}$$

with absolute values of a, b, and c smaller than 1. If so, any incident Stokes vector $\mathbf{S}_\mathrm{i}$ of the form

$$\mathbf{S}_\mathrm{i}^\mathrm{T} = I(1, q, u, v) \tag{7.35a}$$

is transformed into

$$\mathbf{S}_\mathrm{out}^\mathrm{T} = \tau I(1, aq, bu, cv) \tag{7.35b}$$

which implies that

$$\mathrm{DOP}_\mathrm{out} = \sqrt{a^2q^2 + b^2u^2 + c^2v^2} \leq \sqrt{q^2 + u^2 + v^2} = \mathrm{DOP}_\mathrm{in}. \tag{7.35c}$$

In the geometrical representation, the action of a depolarizer defined in (7.34) is to "pull" the representative point of the incoming Stokes vector toward the origin. As a result, the Poincaré sphere is transformed into an ellipsoid limited by the segments $[-a,a]$, $[-b,b]$, and $[-c,c]$ along the q, u, and v axes.

As discussed in Section 7.2.1.2, depolarization occurs due to incoherent addition of intensities of polarized states with different polarizations. In tissues, depolarization is due to multiple scattering in the first place, together with spatially varying linear birefringence in connective tissues [4]. However, these effects alone are not sufficient to cause "real" depolarization, but would give rise to a speckle pattern with DOP = 1 everywhere but with different polarizations from one point to another. "True" depolarization occurs if this speckle pattern is "blurred" by motion of the scattering sample, lack of spatial coherence of the illumination beam, sample motion (e.g., blood flow during *in vivo* measurements), and the like.

Depolarization is a *major polarimetric effect* in virtually all tissues (with the noticeable exceptions of eye cornea and aqueous and vitreous humors). In the absence of strong optical anisotropy, the tissue can be viewed as *a suspension of isotropic scatterers.* Then

- If the incident light is *linearly polarized* along the azimuth α, the reduction of DOP (also called the depolarization power) is independent of α. A necessary and sufficient condition for this is $a = b$ in Eq. (7.34). Moreover, as there is no reason why the azimuth of the "blurred" ellipse should change, a and b must be positive, and thus finally comprised between 0 and 1.
- If the incident light is *circularly polarized*, then the depolarization effect is described by the c diagonal term. This term is always positive in forward scattering, and also in the vast majority of cases of backward scattering, where the handedness is reversed with respect to the incident one, as it occurs for a reflection on a mirror [25]. However, c may sometimes take on negative values in other geometries, and more particularly in backward scattering [26].This unusual behavior may be observed when each individual scattering process takes place at small angles from the forward direction, and the overall backscattering process is dominated by "U turns" with large radii of curvature and circular polarizations which follow these turns "adiabatically" [27].

- There is no general relationship between $a = b$ and c. As discussed in more detail in Section 7.4.1.2 when the size of the scatterers is much smaller than the optical wavelength (Rayleigh scattering regime) then $a = b > |c|$, resulting in stronger depolarization for circularly than linearly polarized incident light. Conversely, when the scatterers are larger than the wavelength, the opposite holds ($a = b < c$). As a result, comparison of linear and circular depolarizing powers provides useful information about the average size of the scatterers. In practice, the vast majority of tissues behave as Rayleigh or Rayleigh-Gans scatterers [28–31], at least with respect to their polarization response.

In the most general case, the Mueller matrix of a depolarizer, $\mathbf{M}_\Delta$, is given in compact notation as [24]

$$\mathbf{M}_\Delta = \begin{pmatrix} 1 & \mathbf{0}^{\mathrm{T}} \\ \mathbf{0} & \mathbf{m}_\Delta \end{pmatrix}, \tag{7.36}$$

where $\mathbf{m}_\Delta$ is a 3×3 real symmetric matrix. This matrix can be diagonalized to recover the form given by Eq. (7.34) where the eigenvalues a, b, and c are real numbers varying between -1 and 1. Thus, the Mueller matrix of the most general depolarizer depends on *six parameters* (as it can be seen from the very definition of the $\mathbf{m}_\Delta$ matrix as a 3×3 symmetric matrix, or by the fact that the diagonalization process involves not only the three eigenvalues, but also the basis formed by the eigenvectors of $\mathbf{m}_\Delta$. General depolarizers are thus rather complex mathematical objects, this complexity being related to situations like multiple scattering in anisotropic media. Here we will not discuss the properties of general depolarizers any further, and in the following we will only consider depolarizers of the form given by Eq. (7.34). We thus define the depolarizing power of such samples as

$$\Delta = 1 - \frac{1}{3}(|a| + |b| + |c|) \tag{7.37a}$$

which can be further specialized in depolarizing powers for linear and circular polarizations as

$$\Delta_{\mathrm{L}} = 1 - \frac{1}{2}(|a| + |b|) \qquad \text{and} \qquad \Delta_{\mathrm{C}} = 1 - |c|. \tag{7.37b}$$

As a final remark, the depolarization powers Δ defined in Eqs. (7.35) and (7.36) vary from 0, for nondepolarizing samples, to 1 for totally depolarizing ones, while the opposite holds for the general depolarization index P_{d} defined in Eq. (7.11).

7.2.3 Decompositions into "Elementary" Component Matrices

Ideally, any polarimetric measurement, once obtained, should be interpreted by fitting to the measured Mueller matrices the results of numerical simulations based on a relevant model. Unfortunately this is not always possible, especially with complex and/or disordered samples such as biological tissues. These exhibit depolarization in virtually all experimental conditions and have several of the above-described polarization effects occurring simultaneously, making accurate measurements *and* interpretation of the measured data difficult. The use of Mueller polarimetry followed by additional methods of results extraction and interpretation is thus essential in tissue studies.

It is thus desirable to develop and use novel approaches to "classify" and interpret the measured tissue Mueller polarimetry data, for example by determining its *retardance* and *depolarization* properties (in addition to the immediately and unequivocally accessible diattenuation and polarizance). Unfortunately, *retardance and depolarization cannot be uniquely determined from a given Mueller matrix*, except in very special cases of "pure" retarders or depolarizers.

The most usual way to process complex Mueller matrices then consists of *decomposing them into products of elementary matrices* with well-defined polarimetric properties and gleans quantitative parameters, meaning biophysical metrics from these. In the following, we first briefly list the form of these elementary matrices, and then outline the most commonly used procedures to decompose any Mueller matrix into various combinations (generally products) of elementary matrices. Note that these mathematical analysis methods do not imply that the sequence of polarization alterations, as described by a particular decomposition product, actually happens in tissue; rather, we are simply stating that the end result of the proposed decomposition sequence is "equivalent" to the experimentally measured one and lends itself to easier extraction of meaningful biophysical quantities.

Product decompositions thus represent an arbitrary Mueller matrix as a product of elementary Mueller matrices—diattenuators, retarders, and depolarizers. These decompositions are characterized by the number of elementary components and their respective positions in the multiplication. The order of the components is important since generally depolarizer matrices commute neither with diattenuator nor with retarder matrices. In principle, product decompositions are better suited to describe physical situations in which the beam interacts sequentially with different parts of the sample, each of which is characterized by a well-defined fundamental polarization property. Although this generally does not happen in biological tissues (where the effects more likely occur simultaneously), product decompositions have nevertheless been shown to yield accurate and reliable measures of tissue polarization properties.

7.2.3.1 Forward and Reverse Product Decompositions into Three Factors All these decompositions describe the input matrix **M** as a product of a diattenuator, a retarder, and a depolarizer. Actually with three elementary component types, there are six different possible orders that yield slightly different results, as in general, matrices do not commute [32]. Among these, the most widely used choice is that of Lu and Chipman [24]:

$$\mathbf{M} = \mathbf{M}_{\Delta \mathrm{P}} \mathbf{M}_{\mathrm{R}} . \mathbf{M}_{\mathrm{D}}, \tag{7.38}$$

where the "special" symbol $\mathbf{M}_{\Delta \mathbf{P}}$ has been used for the depolarizer. Actually, for this decomposition to be quite general if $\mathbf{M}_{\mathrm{D}}$ and $\mathbf{M}_{\mathrm{R}}$ represent homogeneous diattenuators and retarders, then the depolarizer cannot be a "pure" depolarizer of the form defined in Eq. (7.34), as the product matrix **M** would exhibit no polarizance and three parameters would be missing. As a result, in general the "depolarizer" has nonzero polarizance and its elementary matrix is of the form

$$\mathbf{M}_{\Delta\,\mathbf{P}} = \begin{pmatrix} 1 & \mathbf{0}^{\mathrm{T}} \\ \mathbf{P} & \mathbf{m}_{\Delta} \end{pmatrix}. \tag{7.39}$$

With these assumptions, the approach is numerically stable and always provides physically realizable elementary matrices $\mathbf{M}_{\Delta\mathbf{P}}$, $\mathbf{M}_{\mathrm{R}}$, and $\mathbf{M}_{\mathrm{D}}$. This procedure is thus very convenient and is widely used for the phenomenological interpretation of experimental (or even simulated) Mueller matrices. Moreover, its accuracy has been checked for well-characterized controlled systems (phantoms) as described in detail in Section 7.4.

What happens if the order of the elementary components is changed [32]? Simple matrix algebra shows that the above results are easily generalized to two out of the other five possible product sequences, namely those for which the diattenuator precedes the depolarizer:

$$\mathbf{M} = \mathbf{M'}_{\mathrm{R}}\mathbf{M'}_{\Delta\mathrm{P}}\mathbf{M'}_{\mathrm{D}} \text{ or } \mathbf{M} = \mathbf{M}''_{\Delta\mathrm{P}}\,\mathbf{M}''_{\mathrm{D}}\mathbf{M}''_{\mathrm{R}}. \tag{7.40}$$

More precisely, the depolarizer matrices keep the form defined in Eq. (7.39) and the $\mathbf{M}'$ and $\mathbf{M}''$ matrices are deduced from those provided by the standard decomposition (7.38) by unitary transformations.

This kind of simple generalization is no longer valid for the three remaining cases in which the depolarizer precedes the diattenuator. Morio and Goudail [33] introduced a "reverse" decomposition procedure for these three cases with the same definition of the depolarizer, but this procedure could lead to unstable or even unphysical results in case of very strong depolarizations. This issue has been solved by Ossikovski et al. [34] assuming that when the depolarizer precedes the diattenuator, the former features zero polarizance. The "standard" reverse decomposition takes then the form

$$\mathbf{M} = \mathbf{M}_{\mathrm{D}}\mathbf{M}_{\mathrm{R}}\mathbf{M}_{\mathrm{D'}\Delta}, \tag{7.41}$$

with a depolarizer matrix of the form

$$\mathbf{M}_{\mathbf{D'}\Delta} = \begin{pmatrix} 1 & \mathbf{D'}^{T} \\ \mathbf{0} & \mathbf{m}_{\Delta} \end{pmatrix}. \tag{7.42}$$

As in the case of "direct" decompositions defined by Eqs. (7.38) and (7.40), the matrices of the three possible "reverse" cases (with the depolarizer preceding the diattenuator) are deduced from one another by simple orthogonal transformations.

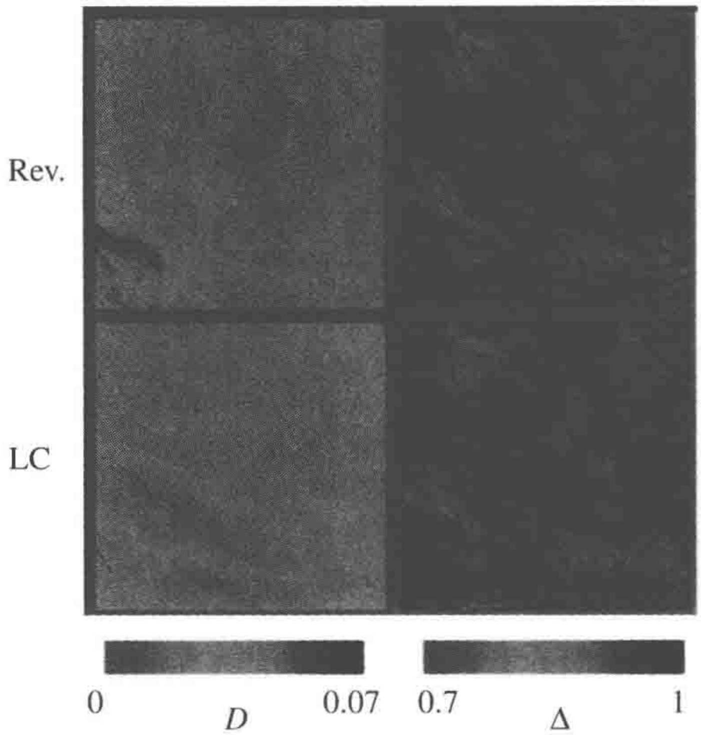

FIGURE 7.6 Polarimetric images of a pig skin sample in backscattering geometry taken at 600 nm. Field of view 5×5 cm^2. Top: diattenuation and depolarization images obtained with the reverse decomposition via Eq. (7.41). Bottom: diattenuation and depolarization images obtained with the Lu-Chipman decomposition. Color bars give the scales for scalar diattenuation D (left) and depolarization power Δ (right). Adapted from Reference 35. (*For a color version of this figure, see the color plate section.*)

The reverse decomposition procedure is also stable and always provides physically realizable Mueller matrices for the elementary components.

Figure 7.6 shows an example of the results provided by direct and reverse decompositions on a pig skin sample. The depolarization images are almost identical, which support the intuitive assumption that depolarization is due to multiple scatterings occurring *inside* the sample. Conversely, the diattenuation images are quite different for the two decompositions, the reverse one giving sharper details and larger absolute values. As the diattenuation is likely to be due to interface effects (diattenuation inside biological tissues is typically very small in the visible, as absorption is essentially due to hemoglobin, which is microscopically isotropic), the reverse decomposition apparently yield a better image of such effects, with a clearer correlation to the details of the depolarization image. These details are absent in the diattenuation image provided by the forward Lu-Chipman analysis (Eq. 7.38). The reverse decomposition seems *a priori* better suited to characterize the surface of such samples.

In summary, three-factor product decompositions may be very useful when studying turbid media, as they yield numerically stable and accurate information about the samples, provided these samples can be reasonably described as stacks comprising a depolarizer (typically the turbid medium), a retarder and a diattenuator in a given order. For isotropic tissues, the latter two effects are expected to occur essentially at the sample surface, while for samples like striated muscles birefringence is expected to arise from the bulk of the sample; consequently, three-factor decompositions may not be necessarily well suited to all cases, a situation that justified the development of the alternative decompositions we outline in the following sections. In general though, it must be borne in mind that whatever decomposition approach is chosen, the claim is not that its physical embodiment is "what actually happens in tissue"; rather, this simply provides a mathematically "equivalent" framework that enables easier extraction of meaningful (and hopefully accurate) biophysical metrics that are contained but otherwise hidden in the complex Mueller matrix of biological tissues.

7.2.3.2 ***Symmetric Decomposition*** In symmetric decompositions, the input Mueller matrix $\mathbf{M}$ is decomposed into a product of *five* factors [36, 37]:

$$\mathbf{M} = \mathbf{M}_{\mathrm{D2}}.\mathbf{M}_{\mathrm{R2}}.\mathbf{M}_{\mathrm{d}\Delta} \cdot \mathbf{M}_{\mathrm{R1}}.\mathbf{M}_{\mathrm{D1}}, \tag{7.43}$$

where $\mathbf{M}_{\mathrm{D1}}$ and $\mathbf{M}_{\mathrm{D2}}$ represent homogeneous diattenuators, $\mathbf{M}_{\mathrm{R1}}$ and $\mathbf{M}_{\mathrm{R2}}$ homogeneous retarders, and $\mathbf{M}_{\mathrm{d}\Delta}$ a diagonal depolarizer as per Eq. (7.34). The central position of the depolarizer in the symmetric decomposition can be very useful for samples which can be viewed as purely depolarizing media bounded by tilted input and output interfaces: in this case the diattenuation and retardation effects are likely to occur at the output interfaces and the depolarization in between. Moreover, in many cases of practical interest the Mueller matrix of the depolarizer is indeed diagonal. However, the relevance of this decomposition for tissue polarimetry may be limited by two issues which may frequently in practice:

- As discussed in Section 7.2.2.4, the Mueller matrices of depolarizers consisting of spherical scatterers are diagonal (Eq. 7.34) with $a = b$. In presence of such "degeneracy" of the depolarizer eigenvalues, the Mueller matrices $\mathbf{M}_{\mathrm{R1}}$ and $\mathbf{M}_{\mathrm{R2}}$ of the retarders commute with $\mathbf{M}_{\mathrm{d}\Delta}$ (i.e., $\mathbf{M}_{\mathrm{Ri}}\mathbf{M}_{\mathrm{d}\Delta} = \mathbf{M}_{\mathrm{d}\Delta}\,\mathbf{M}_{\mathrm{R1}}$) and thus cannot be unambiguously determined (only their product is unambiguous), and some *a priori* knowledge of these "retarders" is required. This issue has been raised in a work devoted to experimental validation of this decomposition [38].
- In contrast with the decompositions into three factors, the symmetric decompositions are not "universal," as there is a class of Mueller matrices, the so-called "non-Stokes diagonalizable" Mueller matrices, for which these decompositions cannot be applied. For such matrices there is one, and only one totally polarized input Stokes vector which retains its full polarization (DOP = 1) after transformation by the Mueller matrix [38, 39]. Analogous to the degenerate depolarizers, such matrices are not some artificial theoretical "curiosities," but do occur in nature (e.g., in scattering cholesteric structures such as shiny beetle cuticles, observed in backscattering [40]).

7.2.3.3 ***Logarithmic Decomposition*** The logarithmic decomposition was proposed recently as a complementary alternative to the standard product decompositions for spatially homogeneous systems where the polarimetric effects occur simultaneously and "continuously" during the propagation of light and not sequentially as implied by the product approaches above. This decomposition is a natural generalization [41, 42] of the classic differential matrix formalism [43] applied to the depolarizing case. The approach, based on the physical picture of a continuously distributed depolarization, parallels and complements the product decomposition approach whereby depolarization is modeled as a spatially localized "lumped" phenomenon. In particular, the differential matrix methodology appears particularly well adapted to the phenomenological description of the scattering in turbid media such as biological tissues.

For a beam propagating along z, the Mueller matrix $\mathbf{M}(z + dz)$ is deduced from $\mathbf{M}(z)$ by

$$\mathbf{M}(z + dz) = \mathbf{U}(dz)\mathbf{M}(z) = [\mathbf{I} + \mathbf{m}dz], \tag{7.44}$$

where $\mathbf{I}$ is the identity matrix, $\mathbf{U}(dz)$ is the differential propagation matrix, and the differential matrix $\mathbf{m}$ can be defined in the most general case as

$$\mathbf{m} = \begin{pmatrix} \alpha & \beta'' & \gamma'' & \delta'' \\ \beta' & \alpha_1 & \mu'' & \nu'' \\ \gamma' & -\mu' & \alpha_2 & \eta'' \\ \delta' & -\nu' & -\eta' & \alpha_3 \end{pmatrix}. \tag{7.45}$$

Equation (7.44) can also be rewritten as

$$\frac{d\mathbf{M}}{dz} = \mathbf{mM}. \tag{7.46}$$

Let us first assume that the medium is nondepolarizing and postpone the discussion of the effects of depolarization. Then it can be shown that $\mathbf{m}$ features additional transposition symmetries, namely $\beta' = \beta''$, $\gamma' = \gamma''$, $\delta' = \delta''$, $\mu' = \mu''$, and so on [37]. Then, the differential propagation matrix $\mathbf{U}(dz)$ takes the form

$$\mathbf{U}(dz) = [\mathbf{I} + \mathbf{m}dz] \approx (1 + \alpha dz)\begin{pmatrix} 1 & \beta dz & \gamma dz & \delta dz \\ \beta dz & 1 & \mu dz & \nu dz \\ \gamma dz & -\mu dz & 1 & \eta dz \\ \delta dz & -\nu dz & -\eta dz & 1 \end{pmatrix}, \tag{7.47}$$

which shows that αdz is simply the differential attenuation of unpolarized light over the distance dz. Moreover, due to the small size of the nondiagonal elements of $\mathbf{m}dz$ (due to the magnitude of dz itself), these elements describe the differential polarimetric effects due to the propagation over the distance dz as follows [43]:

- βdz is the differential linear diattenuation along the x–y laboratory axes.
- γdz is the differential linear diattenuation along the ±45° axes.
- δdz is the differential circular diattenuation.
- ηdz is the differential linear retardation along the x–y axes.

- νdz is the differential linear retardation along the ±45° axes.
- μdz is the differential circular retardation.

Another essential consequence of the smallness of the off-diagonal elements of the $\mathbf{U}(dz)$ matrices is that *they always commute* (provided dz is small enough). Indeed, a straightforward matrix calculation shows that to first order

$$\mathbf{U}_1(dz)\mathbf{U}_2(dz) = [\mathbf{I} + \mathbf{m}_1 dz][\mathbf{I} + \mathbf{m}_2 dz] = [\mathbf{I} + (\mathbf{m}_1 + \mathbf{m}_2)dz] = \mathbf{U}_2(dz)\mathbf{U}_1(dz) \quad (7.48)$$

In other words, the differential approach is well adapted to the propagation of light media featuring simultaneously various polarimetric properties, by eliminating the ambiguities related to the noncommutation of Mueller matrices describing finite instead of differential effects.

Note that in the general case of longitudinally inhomogeneous medium, $\mathbf{m}$ is a function of the propagation coordinate z (the direction of light propagation). If the medium can be considered homogeneous in the z direction over a distance L, expression (7.46) can be easily integrated to give

$$\mathbf{M} = \exp(\mathbf{m}\,L) = \exp(\mathbf{L}) \quad (7.48)$$

which can be also written as

$$\ln(\mathbf{M}) = \mathbf{m}\,L = \mathbf{L}. \quad (7.49)$$

This expression indicates that the fundamental properties of the medium under consideration, contained in $\mathbf{m}$, can be deduced from the logarithm of the related Mueller matrix if the total thickness L is known.

In the presence of depolarization, the matrix $\mathbf{m}$ takes its general form (7.45) and can be decomposed into a sum of two matrices

$$\mathbf{m} = \mathbf{m}_{\mathrm{m}} + \mathbf{m}_{\mathrm{u}}, \quad (7.50)$$

where $\mathbf{m}_{\mathbf{m}}$ has the same shape and symmetry properties as the $\mathbf{m}$ matrix defined in Eq. (7.45) (and is thus nondepolarizing). More specifically

$$\mathbf{m}_{\mathbf{m}} = \frac{1}{2}\begin{pmatrix} 2\alpha & \beta' + \beta'' & \gamma' + \gamma'' & \delta' + \delta'' \\ \beta' + \beta'' & 2\alpha_1 & \mu - \mu' & \nu - \nu' \\ \gamma' + \gamma'' & \mu' - \mu'' & 2\alpha_2 & \eta - \eta' \\ \delta' + \delta'' & \nu' - \nu'' & \eta' - \eta'' & 2\alpha_3 \end{pmatrix} \quad \text{and}$$

$$\mathbf{m}_u = \frac{1}{2}\begin{pmatrix} 0 & \beta' - \beta'' & \gamma' - \gamma'' & \delta' - \delta'' \\ \beta - \beta' & 0 & \mu' + \mu'' & \nu' + \nu'' \\ \gamma'' - \gamma' & \mu'' + \mu' & 0 & \eta' + \eta'' \\ \delta'' - \delta' & \nu'' + \nu' & \eta'' + \eta' & 0 \end{pmatrix} \quad (7.51)$$

Then $\mathbf{m_m}$ thus represents the mean values of the six elementary polarization properties, while $\mathbf{m_u}$ represents their respective uncertainties due to depolarization [41,42].

The elementary polarization properties of the medium can thus be directly determined from the logarithm **L** of the Mueller matrix **M**, by constructing the Lorentz antisymmetric, $\mathbf{L}_\mathrm{m}$, and symmetric, $\mathbf{L}_\mathrm{u}$, components of **L** ($\mathbf{L} = \mathbf{L}_\mathrm{m} + \mathbf{L}_u$), respectively, as follows:

$$\mathbf{L}_\mathrm{m} = \frac{1}{2}(\mathbf{L} - \mathbf{G}\mathbf{L}^\mathrm{T}\mathbf{G}) \quad \text{and} \quad \mathbf{L}_\mathrm{u} = \frac{1}{2}(\mathbf{L} + \mathbf{G}\mathbf{L}^\mathrm{T}\mathbf{G}), \tag{7.52}$$

where $\mathbf{G} = \mathrm{diag}(1, -1, -1, -1)$ is the Minkowski metric tensor.

Apparently, for a depolarizing medium, the off-diagonal elements of $\mathbf{L}_\mathrm{m}$ represent the mean values of the six elementary properties accumulated over path length L, while the off-diagonal elements of $\mathbf{L}_\mathrm{u}$ express their respective uncertainties. Further, the main diagonal elements of the matrix $\mathbf{L}_\mathrm{u}(\alpha_1, \alpha_2$, and $\alpha_3)$ represent the depolarization coefficients (after the subtraction of the isotropic absorption α from the diagonal) along the xy, ±45°, and circular axes [42]. The accumulated polarization parameters (intrinsic properties integrated over the path length L) can be determined from the elements of the $\boldsymbol{L}_\mathbf{m}$ and $\boldsymbol{L}_\mathbf{u}$ matrices as

- **Integrated dichroism**

$$d = \sqrt{L^2_{\mathrm{m},12} + L^2_{\mathrm{m},13} + L^2_{\mathrm{m},14}}. \tag{7.53a}$$

- **Integrated depolarization**

$$\Delta = \frac{1}{3}|\alpha_1 + \alpha_2 + \alpha_3|. \tag{7.53b}$$

- **Linear retardation**

$$\delta = \sqrt{L^2_{\mathrm{m},24} + L^2_{\mathrm{m},34}}. \tag{7.53c}$$

- **Optical rotation**

$$\psi = \frac{1}{2}L_{\mathrm{M},23}. \tag{7.53d}$$

- **Total retardation**

$$R = \sqrt{\delta^2 + 4\psi^2}. \tag{7.53e}$$

The corresponding uncertainties (standard deviations) of the parameters, diattenuation, linear retardance, and optical rotation (and total retardance) can also be derived employing the same set of equations (7.53) on the off-diagonal elements of the matrix $\boldsymbol{L}_\mathbf{u}$.

The conversion relationships between the medium polarimetry characteristics defined in the polar decomposition formalism (forward decomposition and its variants, reverse and symmetric decomposition) and those in the logarithmic decomposition (differential matrix formalism) also worth a brief mention here. In fact, the Mueller matrix corresponding to each accumulated polarization parameter (elements of the differential matrix **m** scaled by path length L) can be obtained from the solution of Eq. (7.46) and the eigenvalues of **m**. These Mueller matrices for each of the individual polarization effects can be related to those defined in the polar decomposition formalism, to yield conversion from one set of parameters to the other:

$$D^{\log} = \tanh(d) = \tanh\left[\sqrt{L_{\mathrm{m},12}^2 + L_{\mathrm{m},13}^2 + L_{\mathrm{m},14}^2}\right] \leftrightarrow D^{\mathrm{pol}}, \tag{7.54a}$$

$$\Delta^{\log} = 1 - \frac{1}{3}(e^{-\alpha_1} + e^{-\alpha_2} + e^{-\alpha_3}) \leftrightarrow \Delta\mathrm{pol}. \tag{7.54b}$$

Note that the above two conversion relations, transforms *dichroism* into *diattenuation* (7.54a) and converts the three *logarithmic* depolarization coefficients into a single "conventional" net depolarization (7.54b). However, no such conversion is required for retardance.

The accuracy of this decomposition has been successfully tested with experimental Mueller matrices of phantoms consisting of dispersion of polystyrene microspheres in sucrose containing polyacrylamide and Monte-Carlo simulation, nematic liquid crystal plates [44] and adhesive tapes [42] and samples with diattenuators embedded in scattering and optically active media [45], to vary the commutation properties of the elementary polarization components. Some of these validation studies are discussed in Section 7.4.2.2.

7.2.4 Summary

In this section, we introduced the Stokes Mueller formalism, which provides a mathematically sound and physically intuitive description of all light polarization states, including partially polarized ones, which are particularly relevant for tissue polarimetry. The essential polarimetric properties, namely the diattenuation, the polarizance, the retardation, and the depolarization have been defined for "simple" polarimetric objects.

While Mueller matrices provide the most complete polarimetric characterization of any samples of interest, in vast majority of cases the most interesting information about these samples—such as those relevant to diagnostics for biological tissues for example—remain "hidden" in the 16 elements of the matrices. The decomposition procedures outlined in this part allow one to "extract" this information, provided the various decomposition procedures are used wisely.

On the one hand, each procedure is based on a specific description or representation of the sample, for example as a "stack" of simple elements following each other in a well-defined order (product decompositions). Of course, the parameters provided by such procedures may be accurate only if the sample is actually of the form assumed by the decomposition, which is seldom the case. So the question then becomes whether the assumed physical representation implied by a specific mathematical decomposition can be considered as is "equivalent" to the original tissue? A "toolbox" of several procedures is then needed to decide how critical this issue really is, and how to cope with it.

Another important feature is the *stability* of the results. As a rule of thumb, the more factors are involved, the more unstable these factors may be for a given product (the initial Mueller matrix **M**). Commutation (multiplication order) issues may also arise, which may compromise the possibility to actually determine the values of some factors. For example, the stability and uniqueness of the solution provided by the three-factor decompositions (the Lu Chipman in its forward and reverse forms) is an advantage of these "simple" decompositions over the more complex symmetrical ones. This may explain why the former are the most widely used, even though they may provide only "effective" values of diattenuation, retardation, and depolarization in many cases, and all the more so in biological tissues.

In contrast, the logarithmic decomposition seems very appropriate to the characterization of tissues by its very definition, as these are turbid media with volumetrically "distributed" polarimetric properties (i.e., effects occur simultaneously and not sequentially as matrix multiplication/product decompositions imply). Moreover, this decomposition is intrinsically stable and has been successfully validated in several complex situations. One limitation, which may be overcome soon, is that if has been developed and tested only in the forward scattering direction, while for diagnostic purposes the backward geometry is typically more interesting and practical.

7.3 INSTRUMENTATION

A huge variety of polarimetric instruments have been developed, to meet the many different requirements related to the studied objects. In this part, we outline the general principles behind the design of polarimetric instruments, mention the various optical polarization components, and provide illustrative examples of actually used instruments, without attempting to be exhaustive.

7.3.1 General Principles

7.3.1.1 Overall Scheme of Polarimetric Instruments A generic polarimetric instrument is schematized in Figure 7.7. The light emitted by one (or possibly several) source(s) traverses a Polarization State Generator (PSG) and an illumination optical system (IO) which define the polarization state and other characteristics of the beam which impinges on the sample (Sp). The light emerging from the sample in a particular direction of interest (shown in transmission for illustration purposes in Figure 7.7) is then captured by another optical system (DO), traverses a Polarization State Analyzer (PSA) whose transmission depends on the light polarization, and is eventually detected by one (or possibly several) detectors (D). Though in

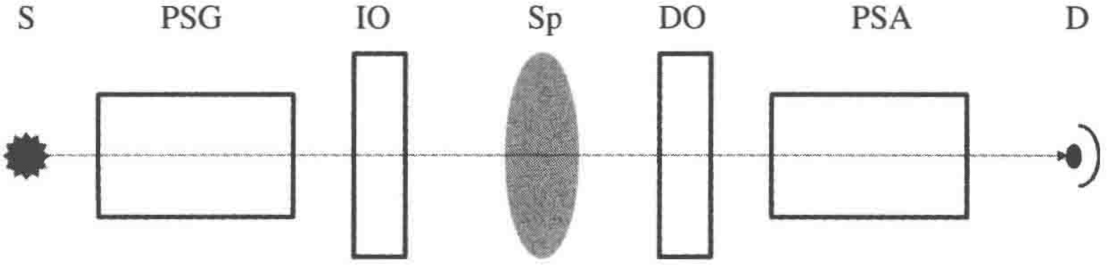

FIGURE 7.7 Block diagram of a generic polarimetric instrument. S, source(s); PSG, polarization state generator; IO, illumination optics; Sp, sample; DO, detection optics; PSA, polarization state analyzer; D, detector(s). Transmission geometry is illustrated above, but polarization analysis in many other detection directions is often possible and/or desirable.

practice the PSG, the PSA, and the other optics may overlap each other, either physically or conceptually, these elements are represented as separate as they play different roles.

The source(s) and detector(s) may be point-like or extended, and the other optics may implement full field imaging or pointwise measurements, the latter possibly with spatial scanning. Moreover, the instrument may be designed for single or multiple wavelength operation, with various requirements on acquisition speed or acceptable signal-to-noise ratio (SNR). Of course, the polarimetric elements composing the PSG and the PSA must also be chosen to satisfy the same requirements as the other optics. For example, their geometrical *étendue* and/or spectral bandwidth must be sufficient if full field imaging and/or multispectral operation are required. These issues will be briefly discussed later for various optical elements used for polarization studies.

7.3.1.2 Polarization Modulation and Analysis **Sequential polarization modulation and analysis.** Among the various schemes actually used for polarization modulation by the PSG and analysis by the PSA, the conceptually simplest is the modulation and analysis using discrete polarization basis states. In this scheme, the PSG sequentially generates m different polarizations, represented by m physical

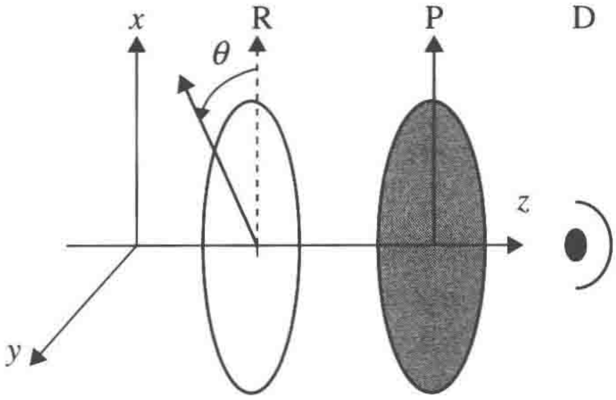

FIGURE 7.8 PSA based on a rotatable retarder (R) preceding a linear polarizer (P) and the detector (D). The pass axis of P is aligned along x, while the fast axis of the retarder makes a variable angle $\theta = \omega t$ with the x-axis.

Stokes vectors $\mathbf{S}_j$ incident on the sample, which can be considered as the columns of a real $4 \times m$ matrix, the *modulation matrix* **W**. The PSG is said to be

- Incomplete if $m < 4$,
- Complete if $m = 4$ and the four Stokes vectors **Sj** are linearly independent, meaning that the device correctly "samples" the whole polarization space. The 4×4 matrix **W** is then invertible.
- Redundant, if $m > 4$ and the **Sj** vectors form a complete basis of the polarization space. In this case, the instrument "oversamples" this space, which is a possible way to reduce the noise or the systematic errors. In this case, the 4 x m **W** matrix possesses a pseudo-inverse.

Quite similarly to PSGs, a PSA can be characterized by its analysis matrix **A**. When this PSA is illuminated by a light beam emerging from the sample whose Stokes vector is **S**, it generates a set of n signals I_i (the eventually detected intensities), each of which is obtained by passing the light through a "polarization filter" described by a Stokes vector $\mathbf{S}'_i$. Mathematically this filtering corresponds to taking the scalar product of the incoming and the filter Stokes vectors:

$$I_i = \mathbf{S'}_i \cdot \mathbf{S}. \tag{7.55}$$

The I_i form a signal vector **I** of dimension n, related to the Stokes vector **S** emerging from the sample by

$$\mathbf{I} = \mathbf{A} \cdot \mathbf{S}. \tag{7.56}$$

In a way analogous to PSGs, PSAs may be incomplete, complete, or redundant depending on the dimension of the polarization space spanned by the line vectors $\mathbf{S}'_i$ of **A**.

In a generic polarimeter as schematized in Figure 7.7, each Stokes vector $\mathbf{S}_j$ generated by the PSG is transformed into $\mathbf{MS}_j$, (where **M** is the Mueller matrix of the sample) and generates a corresponding signal vector $\mathbf{I}_j$. When the index j spans the range from 1 to m, these signal vectors form the columns of matrix **B**, as for each of the incident PSG states the PSA produces n signals. The raw signal matrix can be written as

$$\mathbf{B} = \mathbf{A} \cdot \mathbf{M} \cdot \mathbf{W}. \tag{7.57}$$

Obviously, in order to retrieve useful information about **M** from the raw data **B**, the matrices **A** and **W** must be known—the system must be *calibrated*. Moreover, provided both the PSG and the PSA are *complete* or *redundant* (i.e., the instrument is a Mueller polarimeter), the sample Mueller matrix **M** can be extracted from the raw data **B** by inverting Eq. (7.57):

$$\mathbf{M} = \mathbf{A}^{-1} \cdot \mathbf{B} \cdot \mathbf{W}^{-1}. \tag{7.58}$$

Periodic time modulation. If the PSGs and/or the PSA polarimetric properties vary periodically in time at angular frequency ω, for example due to the presence of rotating elements (see Figure 7.8), the detected signal(s) also vary periodically at the same frequency, allowing decomposition by Fourier analysis into harmonics; experimentally, this enables improved noise rejection and higher SNR via synchronous phase-sensitive detections (e.g., through lock-in amplification). The basis states of the PSG and/or the PSA are simultaneously encoded in different Fourier components if the detected signal(s). The modulation and analysis matrices of the PSG and the PSA are then defined in frequency (Fourier) space. We will not explicitly cover the (quite cumbersome!) equations giving a rigorous description of polarization encoding and/or detection in Fourier space, but a few simple examples of very widely used setups based on this scheme will be described in Section 7.3.2. Generally, temporal polarization modulation is easier to implement with point-like measurement systems, as detection schemes with imaging cameras are more challenging to modulate in synchrony.

Spectral or spatial modulation. The idea behind these schemes is quite similar to above. If the PSG and/or the PSA exhibit very fast (and well known!) variation of their characteristics with wavelengths while the Mueller matrix of the sample is constant or varies much more slowly, then the Fourier analysis of the signal can be realized in wavelength space. This scheme is very appealing in realizing "snapshot" spectroscopic polarimeters. The same idea may be applied for imaging applications, by imposing very fast variations of the polarization response of the PSA in the image plane, with subsequent Fourier analysis to extract the much more slowly varying polarization properties of the object under study.

*7.3.1.3 **Design and Optimization Considerations*** Here we address the following question, which is of importance when designing a complete polarimeter and has been widely discussed in the literature [46–52]; how can we use the degrees of freedom we have on the actual matrices **W** (through the judicious selection of PSG input states) and **A** (through the judicious selection of PSA filter states) for a given type of instrument *to minimize the noise on the final matrix* **M**, *in the presence of additive noise on the raw data* **B**?

We first discuss this issue for *complete* PSAs. Equation (7.56) can be rewritten as

$$\mathbf{I} = \mathbf{A} \cdot \mathbf{S} \qquad \Leftrightarrow \qquad \mathbf{S} = \mathbf{A}^{-1} \cdot \mathbf{I}. \tag{7.59}$$

If the raw measured intensity vector **I** is affected by an additive noise $\delta\mathbf{I}$, this noise will introduce an additive noise $\delta\mathbf{S}$ in the value of **S**, given by

$$\delta\mathbf{S} = \mathbf{A}^{-1} \cdot \delta\mathbf{I}. \tag{7.60}$$

The rms noise on the raw data is nothing else but the usual Euclidean norm $\|\delta\mathbf{I}\|$ of $\delta\mathbf{I}$. With proper definition of the norm of matrices (the largest of their singular values), we get an upper bound of the noise on the **S** vector:

$$\|\delta\mathbf{S}\| \leq \|\mathbf{A}^{-1}\|\,\|\delta\mathbf{I}\|. \tag{7.61}$$

If the noise $\|\delta \mathbf{I}\|$ on the raw measurements does not depend on the exact configuration of the PSA, as is usually the case, a good criterion to optimize the design of a complete PSA consists *in minimizing the norm* $\|\mathbf{A}^{-1}\|$ [47].

Actually this criterion tells us that **A** is "as far as possible from singular" and thus is optimally conditioned to be inverted as required to extract **S** (which contains the information about the sample Mueller matrix **M**) from **I**. To achieve this optimization, the PSA basis states must be "as different as possible" from each other. For complete PSAs, this condition is achieved when the four basis states are at the tips of a regular tetrahedron on the Poincaré sphere [47]. This simple "geometrical" criterion can be generalized to the case of redundant PSAs, from which noise propagation is optimized when the basis states form simple symmetric polyhedra (such as an octahedron for $n = 6$, a cube for $n = 8$,and so on...) at the surface of the Poincaré sphere [52]. Moreover, when **A** is optimized, the noise on **S** is not only minimized, but it is also *most equally distributed among the various components of* **S** [48].

On the other hand, this general criterion may not be valid if one is interested in specific components of **S**, for which the noise can be minimized further at the expense of increasing it for other components (presumably less relevant in a particular application).

These results are easily generalized from PSAs to complete Mueller polarimeters: not surprisingly, the noise is minimized and most equally distributed on all **M** components if both $\|\mathbf{W}^{-1}\|$ and $\|\mathbf{A}^{-1}\|$ are minimized [49–51].

7.3.1.4 Complete versus Incomplete Instruments At first sight, one would assume that complete or redundant polarimeters are always superior to incomplete ones, as they are the only polarimeters able to provide full Mueller matrices upon mathematical analysis. However, for practical applications, complete Mueller polarimeters are not always the best choice, for two reasons:

1. Complete polarimeters are necessarily *more complex* than incomplete ones, and it may be difficult to make them compliant with demanding experimental requirements in terms of speed, spectral or angular bandwidth, and the like which may be imposed by the envisioned application.
2. If the polarimetric response of the sample under study is known to be of a *specific form*, then incomplete polarimeters may be *sufficient, and even better* than complete ones, as they can be designed to optimize the SNR and accuracy of the measurements of the Mueller matrix elements of interest.

The best practice, whenever possible, is to explore the polarimetric response of the samples of interest with complete instruments, and then, once the necessary polarimetric measurements are defined to make the device to be used in practice (e.g., for diagnostic purposes) as simple and rugged as possible.

As discussed below, for bulk biological tissues the "hierarchy" of the polarimetric effects is strong depolarization, modest linear birefringence, very weak optical activity (circular birefringence), and essentially nonexistent diattenuation/dichroism (either linear or circular). In the absence of linear birefringence, tissues are essentially pure depolarizers, with diagonal Mueller matrices featuring typically $m_{22} = m_{33} \neq m_{44}$ (i.e., often (but not always!) linear depolarization is independent of orientation and is different from circular depolarization). Accurate determination of these elements can be done by incomplete polarimeters. On the other hand, if two of the three mentioned characteristics are simultaneously present (e.g., linear birefringence and depolarization, or depolarization and optical activity) and are of interest, then the determination of the full Mueller matrix and subsequent decomposition of this by the procedures outlined in Section 7.2 may be unavoidable.

7.3.2 Commonly Used PSAs

The many different designs for PSAs can be classified according to several possible criteria, with significant overlaps. Note that in principle, any PSA may be converted into a PSG (and the other way around) by interchanging the source(s) and the detector(s). In the following, after a short description of the usual polarization handling components, we present commonly used polarimetric PSAs, by increasing "complexity" starting from those based on simple linear polarizers.

7.3.2.1 PSAs Based on Linear Polarizers *Linear polarizers* are the most basic polarization handling components, and they are ubiquitous in polarimetric setups. In practice, these elements are of two main types:

- *Dichroic polarizers*, consisting of thin sheets of (typically plastic) materials which exhibit full absorption for one polarization and typically 70–85% transmission for the other. These polarizers typically feature quite broad angular acceptances, well adapted for imaging applications, but somewhat limited spectral bandwidths (the visible or the NIR for example).
- *Polarizing beam splitters,* which transmit two linear orthogonal polarization in different directions. These elements are made of complementary prisms of crystalline materials (Glan or Wollaston prisms) or glass with multilayer dielectric coatings. Crystalline beam splitters feature very wide spectral but rather narrow angular bandwidths while the opposite holds for glass beam splitters.

Sequential PSAs. As immediately obvious from the very definition of Stokes vectors (Eq. 7.7a), a *single linear polarizer coupled with a single detector* allows the determination of the I, Q, and U (but not V) components of the Stokes vector $\mathbf{S}$ of incoming light propagating along the z axis, provided the polarizer can be oriented sequentially along x, y, +45°, and −45° in the transverse plane to provide the intensities I_x, I_y, I_P, and I_M, respectively.

PSAs with continuously rotating polarizers. Alternatively, if the polarizer rotates *continuously* at angular frequency ω, it transforms the Stokes vector $\mathbf{S}$ that traverses it into

$$\mathbf{S}'(t) = \mathbf{M}_{\mathrm{LD}}(1, 1, \omega t)\, \mathbf{S}, \tag{7.62}$$

where $\mathbf{M}_{\mathrm{LD}}(1, 0, \omega t)$ is the matrix of a linear diattenuator defined in Eq. (7.24) with $\tau = 1$ and $D = 1$ (perfect polarizer) oriented at $\theta = \omega t$. Equation (7.62) above can then be rewritten as

$$\mathbf{S}'(t) = \frac{1}{2}\begin{pmatrix} 1 & \cos 2\omega t & \sin 2\omega t & 0 \\ \cos 2\omega t & \cos^2 2\omega t & \cos 2\omega t \sin 2\omega t & 0 \\ \sin 2\omega t & \cos 2\omega t \sin 2\omega t & \sin^2 2\omega t & 0 \\ 0 & 0 & 0 & 0 \end{pmatrix}\begin{pmatrix} I \\ Q \\ U \\ V \end{pmatrix}. \tag{7.63}$$

The detected signal I_1 is the first component of $S'(t)$

$$I_1(t) = I + Q\cos(2\omega t) + U\sin(2\omega t) \tag{7.64}$$

from which I, Q, and U are immediately extracted by a straightforward *Fourier analysis*, as the amplitudes of the constant term and the two in-phase and quadrature components at frequency 2ω.

7.3.2.2 Combinations of Linear Polarizers and Constant Retarders

Constant retarders are also very commonly found in polarimetric setups, to generate and analyze elliptically (circularly) polarized states. For these components, there are also two basic technologies:

- *Retardation plates.* These plates are slabs of birefringent materials (typically quartz or mica) which introduce a phase retardation $\Delta\phi = 2\pi \cdot Dn \cdot d/\lambda$ between their two orthogonal eigenpolarizations (Δn is the refractive index difference, d the plate thickness, and λ the wavelength). The natural dispersion of $\Delta\phi$ due to the $1/\lambda$ dependence can be reduced, around well-specified wavelengths, by assemblies of two plates with their slow axes at 90° to each other. Generally, the angular acceptance is rather small, except for very thin plates (called "true zero order" plates).
- *Fresnel rhombs.* These devices are based on the very achromatic phase retardation introduced by a total internal reflection between in-plane and out-of-plane polarizations. The spectral bandwidth may be huge (essentially equal to the transparency window of the material) but the angular acceptance is again very small. These components are thus very well suited to spectroscopic point-sensing polarimeters but present formidable challenges for imaging applications.

Sequential PSAs with a linear polarizer and a removable QWP. As noted above, linear polarizers alone cannot measure the V component of the incoming Stokes vector $\mathbf{S}$. The conceptually simplest way to address this limitation is to add to the measurements performed with the polarizer alone another two measurements performed with a QWP (a retarder with 90° retardation) with its axes set at ±45°

from those of the polarizer, to convert the linear polarizer into right and left circular polarizers. As a result, such a system may be operated

- *in redundant mode* [53], by taking into account the full set of six measurements (I_{x}, I_y, I_P, I_M, I_{L}, I_{R}) and solving the overdetermined system of six equations for the four unknowns I, Q, U, V (a particularly simple example of rectangular matrix **A**):

$$I_{\mathrm{x}} = I + Q, I_{\mathrm{y}} = I - Q, I_P = I + U, I_M = I - U, I_L = I + V, I_R = I - V, \quad (7.65)$$

- *in complete, nonredundant mode*, by skipping the measurements of I_{-45° and I_{R} and relying on the fact that the total intensity can be written as

$$I = I_x + I_y = I_P + I_M = I_L + I_R. \quad (7.66)$$

As mentioned earlier, the nonredundant scheme is obviously faster but the accuracy obtained with the redundant mode may be significantly better due to possible systematic errors which may be "averaged out" by increasing the number of measurements.

Sequential PSAs with a linear polarizer and a rotatable retarder set at discrete azimuths. In this kind of PSAs, the light to be analyzed passes through a rotatable retarder (R) and then a polarizer (P), which can be assumed to be aligned along the x axis without loss of generality. The light polarization is analyzed by recording the detected signal while the angle $\theta = \omega\, t$ between the fast axis of the retarder and the passing axis of the polarizer varies.

Upon reaching the detector, the Stokes vector **S** emanating from the sample of interest is transformed into

$$\mathbf{S}'(t) = \mathbf{M}_{\mathrm{LD}}(1, 1, 0)\, \mathbf{M}_{\mathrm{LR}}(\delta, \theta)\, \mathbf{S}, \quad (7.67)$$

where δ is the retardation of R. For a fixed value of δ, the detected intensity I_{D} varies as a function of θ according to

$$I_{\mathrm{D}}(\theta) = I + Q\left[\cos^2\frac{\delta}{2} + \sin^2\frac{\delta}{2}\cos 4\theta\right] + U\sin^2\frac{\delta}{2}\sin 4\theta - V\sin\delta\sin 2\theta \quad (7.68)$$

When the retarder azimuth sequentially takes n discrete values θ_{i}, the corresponding intensities are given by the formula above, which can be rewritten in matrix form to explicitly show the analysis matrix **A**:

$$\begin{bmatrix} I_1 \\ I_2 \\ \cdots\cdot \\ I_n \end{bmatrix} = \begin{bmatrix} 1 & \cos^2\frac{\delta}{2} + \sin^2\frac{\delta}{2}\cos\theta_1 & \sin^2\frac{\delta}{2}\sin 4\theta_1 & \sin\delta\sin 2\theta_1 \\ 1 & \cos^2\frac{\delta}{2} + \sin^2\frac{\delta}{2}\cos\theta_2 & \sin^2\frac{\delta}{2}\sin 4\theta_2 & \sin\delta\sin 2\theta_2 \\ \cdots & \cdots & \cdots & \cdots \\ 1 & \cos^2\frac{\delta}{2} + \sin^2\frac{\delta}{2}\cos\theta_n & \sin^2\frac{\delta}{2}\sin 4\theta_n & \sin\delta\sin 2\theta_n \end{bmatrix} \begin{bmatrix} I \\ Q \\ U \\ V \end{bmatrix}. \quad (7.69)$$

If $n = 4$, the PSA is complete provided δ is different from $p\pi$. Moreover, $\|\mathbf{A}^{-1}\|$ is minimized for $\delta = 132°$ and $\theta_{1,2} = \pm 51.7°$ and $\theta_{3,4} = \pm 15.1°$ [47]. The *a priori* surprising value of 132° stems from the criterion cited above: the basis states of the PSA must form a regular tetrahedron on the surface of the Poincaré sphere. It turns out that to do so, for example, a quarter wave is not sufficient: such a component would transform the initial linearly polarized state, into other states by rotations of 90° about various axes. As a result, these states would be confined to the same hemisphere as the initial linear state and would never form a regular tetrahedron. This does not mean that QWPs cannot be used in actual implementations of PSAs (and it is often the case in practice) but the noise in the final result may be slightly larger than with $\delta = 132°$.

PSAs with a linear polarizer and a continuously rotating retarder. As the retarder is continuously rotated at angular frequency ω, Eq. (68) above immediately shows that the only Fourier components with nonzero amplitudes are DC, $\sin(2\omega t)$, $\cos(4\omega t)$, and $\sin(4\omega t)$. Calling these amplitudes I_{DC}, $I_{\mathrm{S}2\omega}$, $I_{\mathrm{C}4\omega}$, and $I_{\mathrm{S}4\omega,}$ we obtain their expression in function of $\mathbf{S}$ given in Eq. (7.70), which defines the analysis matrix $\mathbf{A}$ of the PSA in Fourier space. Again this matrix becomes singular for $\delta = p\pi$, as expected: in this case, the retarder is either half-wave and provides no sensitivity to the circularity component V; or "non-existent" (if p is an even integer) and the PSA reduces to a fixed linear polarizer. Analogous to above, $\mathbf{A}$ is optimal for $\delta = 129°$:

$$\begin{bmatrix} I_{\mathrm{DC}} \\ I_{\mathrm{S}2\omega} \\ I_{\mathrm{C}4\omega} \\ I_{\mathrm{S}4\omega} \end{bmatrix} = \begin{bmatrix} 1 & \cos^2\left(\frac{\delta}{2}\right) & 0 & 0 \\ 0 & 0 & 0 & -\sin\delta \\ 0 & \sin^2\left(\frac{\delta}{2}\right) & 0 & 0 \\ 0 & 0 & \sin^2\left(\frac{\delta}{2}\right) & 0 \end{bmatrix} \begin{bmatrix} I \\ Q \\ U \\ V \end{bmatrix}. \tag{7.70}$$

Practical considerations. PSAs and PSGs comprising a linear polarizer and a rotatable retarder (often improperly called "compensator") achieve complete polarization generation and analysis with only two passive polarization elements. Due to this simplicity, they are very widely used, with the two operation modes outlined above, with the retarders rotating either stepwise (discretely) or continuously:

- Continuous rotation is usually preferred when the detector is fast enough, which is usually the case for *pointwise measurements* requiring a single photodetector or *spectroscopic measurements* with one-dimensional CCD arrays at the focal plane of a spectrometer. In this latter case, the retarders must be reasonably achromatic, like Fresnel rhombs or, to a lesser extent, "achromatic" retardation plates made of stacks of elementary birefringent plates. Compared to stepwise rotation, continuous retarder rotation is easier to implement and provides shorter measurement times. However, in this configuration the PSG and the PSA cannot be optimized independently of each other, due to possible "mixing" of the Fourier components encoding the various polarization basis states.

A typical choice is to rotate the PSG and PSA retarders at frequencies 3ω and 5ω [50, 54].

- Conversely, stepwise rotation may be better suited for polarimetric *imaging* applications, typically with two-dimensional CCDs. In this scheme, prior to each image acquisition the retarders are set at the prescribed couple of azimuths and left still during the camera integration time, until the full set of $n \times m$ raw images are taken. For this polarimetric imaging, it is essential to use retarders with wide enough angular acceptances. Image "wander" is frequently observed in relation with retarder rotation, and must be corrected for by suitable imaging treatment/analysis procedures.
- Continuous retarder rotation and Fourier analysis of the signal would be possible with two-dimensional CCDs, only for extremely fast CCDs (both in acquisition and data transmission) and would require large computational power. A practically easier alternative would involve stroboscopic illumination, synchronized with the polarization modulation. This approach has already been implemented for partial polarimetric measurements [55] but not for complete Mueller polarimetry.

7.3.2.3 Combinations of a Linear Polarizer and Variable Retarder(s) Historically, the first variable retarders were the Babinet Soleil compensators, made of two crystalline wedges which could slide with respect to each other, and which were equivalent to a single birefringent crystal with variable thickness. Though still in use, these devices have been largely replaced by others, of the two following types:

- *Pockels cells*. In these elements, a driving voltage is applied to two or four suitably oriented crystals, to modify their birefringence, and the resulting retardation between two linear orthogonal eigenpolarizations. These devices typically exhibit very fast time responses (in the nanosecond range, if a suitable voltage driver is used), but they require high driving voltages (~200 V for $\Delta\phi = 180°$ in the visible) and exhibit very small spatial and angular apertures. In practice these devices can be used only with laser beams, and thus are included in PSGs (but generally not in PSAs) when studying highly scattering samples like thick tissues.
- *Photoelastic modulators*. These devices consist of a slab of glass (typically fused silica) about 10 cm long. Piezoelectric transducers generate a sound wave at frequency ν, which, in turn, creates a time dependent birefringence in the glass slab at the same frequency ν, which can be used to modulate the polarization of a passing light beam at ν and its harmonics 2ν, 3ν... This effect is usable if ν is a sonic resonant frequency of the glass bar. Such resonances, extremely narrow, typically lie around 50 kHz. As a result, polarimeters with photoelastic modulators are typically operated with synchronous detection locked on the modulator excitation and/or its harmonics. Such high frequency modulation schemes reduce the $1/f$ and other noise sources thereby increasing the SNR, an advantage which may be crucial when the available signal is low. This

scheme is typically realized electronically with single point-sensing detectors, but it can also be implemented optically, with a stroboscopic illumination of the polarimeter to "freeze" the polarization at specific phases with respect to the modulator excitation.

- *Liquid crystals cells.* In these components, a very thin (~10 μm thick) layer of nematic liquid crystal is "sandwiched" between two glass plates with transparent electrodes. AC driving voltages up to 20 V are sufficient to modulate the retardation over 360° or more. The angular acceptance of these devices is very large (tens of degrees), making them very well suited for imaging applications. On the other hand, the time response is slow (several tens of milliseconds) for a significant shift in retardation. The spectral range is also limited to the visible and the near infrared.

Polarizer and one variable nonrotating retarder. As these elements are typically set at azimuths 45° apart from each other, we will assume without loss of generality that the retarder is aligned along the x axis, and the polarizer at 45° without loss of generality, as shown in Figure 7.9. The incoming Stokes vector **S** is transformed by the variable retarder VR and polarizer into

$$\mathbf{S}'(t) = \mathbf{M}_{\mathrm{LD}}(1, 1, 45°)\, \mathbf{M}_{\mathrm{LR}}(1, \delta(t), 0)\, \mathbf{S}, \tag{7.71}$$

where $\delta(t)$ is the time-dependent retardation of the VR. The detected intensity is now

$$I_{\mathrm{D}}(t) = \frac{1}{2}(I + U\cos\delta(t) - V\sin\delta(t)) \tag{7.72}$$

and does not depend on Q at all. This result is general: a PSA for which the only variable parameter is the retardation of a VR set at constant azimuth is never complete.

Thus, the measurements provided by this setup have to be completed by other measurements for Mueller matrix determination, for example, via a removable QWP

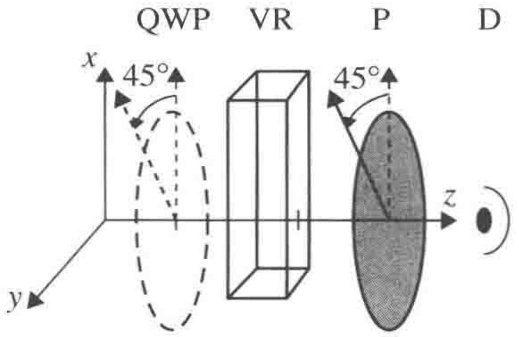

FIGURE 7.9 Scheme of a PSA composed of a variable retarder (VR), a polarizer (P), and a detector (D). The VR has its fast and slow axes aligned with x- and y-axes, respectively, and its retardation is varied to analyze the incoming beam polarization. The measurements are performed with and without the removable QWP to allow complete determination of the incoming beam polarization.

in added at the entrance of the device. With this additional component, Eq. (7.71) becomes

$$\mathbf{S}'(t) = \mathbf{M}_{\mathrm{LD}}(1, 1, 45^\circ)\, \mathbf{M}_{\mathrm{LR}}(1, \delta(t), 0)\, \mathbf{M}_{\mathrm{LR}}(1, 90^\circ, 45^\circ)\mathbf{S} \tag{7.73}$$

which transforms the detected intensity into

$$I_{\mathrm{D}}^{\mathrm{QW}}(t) = \frac{1}{2}\,(I - Q\sin\delta(t) + U\cos\delta(t)) \tag{7.74}$$

and thus completes the determination of **S** when the retardation $\delta(t)$ is varied to define the analysis matrix **A**. As mentioned above, the temporal evolution of δ may be essentially arbitrary for nonresonant devices like Pockels cells or liquid crystals. For resonant devices like photoelastic modulators, the retardation varies sinusoidally in time:

$$\delta(t) = \delta_0 \sin \omega t. \tag{7.75}$$

The Fourier expansions of the functions $\cos(\delta_0 \sin\omega t)$ and $\sin(\delta_0 \sin\omega t)$ are well known. Keeping the first three terms (DC, ω, and 2ω frequencies), we obtain

$$I_{\mathrm{D}}(t) = \frac{1}{2}(I + U[J_0(\delta_0) + 2J_2(\delta_0) cos2\omega t] - V[2J_1(\delta_0) sin\omega t]), \tag{7.76}$$

$$I_{\mathrm{D}}^{\mathrm{QW}}(t) = \frac{1}{2}(I - Q[2J_1(\delta_0) sin\omega t] + U[J_0(\delta_0) + 2J_2(\delta_0) cos2\omega t]), \tag{7.77}$$

where J_{n} are Bessel functions. The Fourier components at zero, ω, and 2ω frequencies are the relevant quantities for the synchronous detection scheme generally used to optimize the SNR. Analogous to the rotating retarder scheme, the expressions above can be recast in terms of the system analysis matrix **A**, which is then redundant, with six measured quantities (I_{DC}, $I_{\mathrm{S}\omega}$, $I_{\mathrm{C}2\omega}$, and the like with the QWP inserted) for the four components of **S**.

Polarizer and two nonrotating variable retarders. This type of PSA is schematized in Figure 7.10. The incoming light traverses two variable retarders, whose fast axes are set at constant azimuths θ_1 and θ_2 from the x axis, then again a linear polarizer set along x before being detected. The Stokes vector $\mathbf{S}'$ of the light reaching the detector is now

$$\mathbf{S}'(t) = \mathbf{M}_{\mathrm{LR}}(1, \delta_2, \theta_2)\, \mathbf{M}_{\mathrm{LR}}(1, \delta_1, \theta_1)\, \mathbf{S}. \tag{7.78}$$

The calculation is quite similar to the previous ones and will not be reproduced here. The main result is that by varying the retardations δ_1 and δ_2, it is easy to make *this device a complete PSA*, provided the orientations θ_1 and θ_2 are properly chosen. Actually, *the best choice* is $\theta_1 = 0^\circ$ and $\theta_2 = 45^\circ$, as any arbitrarily chosen elliptical "polarization filter" can be obtained by adjusting the retardations. This property is

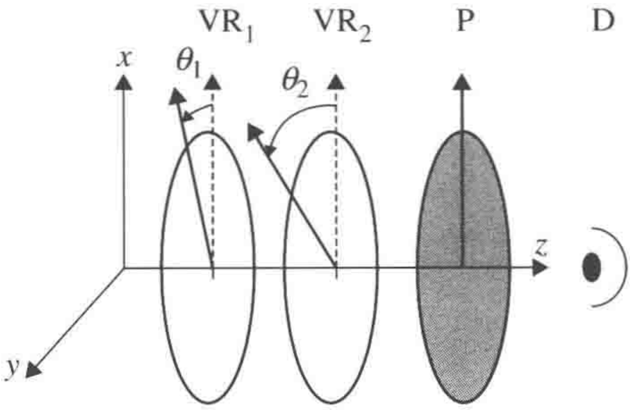

FIGURE 7.10 PSA composed of two variable retarders (VRi), a polarizer (P), and a detector (D). The VR fast and slow axes are set at azimuths θ_1 and θ_2 with respect to the x axis and their retardations δ_1 and δ_2 are varied in time to analyze the incoming beam polarization.

also valid when the device is used as a PSG, with a source replacing the detector and the light travelling in the $-z$ direction: such a PSG can generate *any* predefined Stokes vector **S**.

Such versatility is not really needed to make complete Mueller polarimeters: as long as the PSG and the PSA are each able to generate four linearly independent basis states, complete measurements are possible (**W** and **A** are invertible). However, potential SNR improvements inherent in no-moving-mechanical-part polarimeters (often with synchronous detection schemes) offer significant advantages in low-signal situations often encountered in biomedicine. Further, the possibility to generate *any* state by the PSG and to project the emerging state on *any* polarization state at the PSA opens interesting possibilities for polarization contrast optimization of different

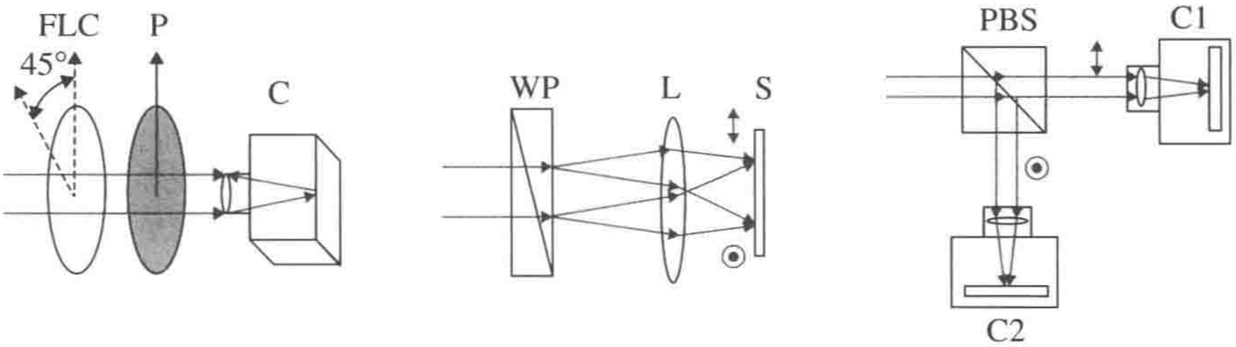

FIGURE 7.11 Three PSA setups implemented for OSC imaging. Left: a sequential PSA. The incident beam traverses a ferroelectric liquid crystal (FLC) equivalent to a half wave plate which can be rapidly switched between two azimuths separated by 45°, and a linear polarizer (P) before reaching the camera (C). This system allows sequential acquisition of the orthogonally polarized images with switching times less than 1 ms [58]. Center: the incoming beam is separated into two beams with orthogonal polarizations by the Wollaston prism (WP), to form two polarized images on the sensor (S) via the lens (L) [59]. Right: the two orthogonal polarizations are separated by the polarizing beam splitter (PBS) and form two images on two separate cameras C1 and C2 [60].

tissue states to be distinguished from each other (e.g., cancerous and noncancerous tissues) without measuring the full Mueller matrices [56, 57].

7.3.3 Examples of Tissue Polarimetry Instruments

In this part, we illustrate the above considerations by giving some examples of polarimetric instruments, without attempting to exhaustively describe the very wide variety of such devices which have been successfully implemented.

7.3.3.1 Orthogonal State Contrast Imagers Orthogonal state contrast (OSC) imaging (which has also been called, somewhat improperly, DOP imaging) is quite a simple, and thus experimentally very appealing polarimetric characterization technique, whenever applicable. In this modality, the sample is illuminated with linearly polarized light and imaged with two polarization filters, one parallel and one perpendicular to the illumination polarization. The two images, I_{II} and $I_{\perp}$, are then combined to form the OSC image:

$$I_{\mathrm{OSC}} = \frac{I_{\mathrm{II}} - I_{\perp}}{I_{\mathrm{II}} + I_{\perp}}. \tag{7.79}$$

The OSC contrast is independent of the overall reflectivity of the sample (within the limits imposed by the instrumental dynamical range!) and thus a purely polarimetric characterization technique (the tissue reflectance $(I_{\mathrm{II}} + I_{\perp})$ can be studied independently). Moreover, for isotropic pure depolarizers, as may be true for many biological tissues, OSC directly provides the elements $m_{22} = m_{33}$ of the sample-normalized Mueller matrix, which define the tissue depolarizing power for linearly polarized light. Of course, OSC can also be implemented with co- or counter-oriented circular polarizations, and then it provides m_{44}.

An OSC imager thus comprises a linearly polarized source, and a PSA able to provide images with two linear orthogonal polarizations as efficiently as possible. Three schemes of such PSAs have been described in the literature and are outlined in Figure 7.11. In the first scheme (*left panel*), the acquisition of the two polarized images is realized sequentially, by "optically rotating" the linear polarizer by means of a liquid crystal cell with constant half wave retardation whose orientation can be switched between two azimuths 45° apart from each other in less than 1 ms. With so fast a polarization modulation, the time needed to take both polarized images is determined solely by the CCD speed and the integration time necessary to reach a good SNR. Such a device has been used on a colposcope for *in vivo* examination of uterine cervix at 10 fps for the OSC images [58]. In the second scheme (*center panel*), the two polarizations are separated by means of a Wollaston prism and two images are formed simultaneously on the CCD sensor (S) in the focal plane of the lens (L) [59]. The third scheme (*right panel*) makes use of a polarizing beam splitter (PBS) and two separate cameras to take the polarized images. In the last scheme, the polarized images are taken simultaneously at video rates, but there may be issues

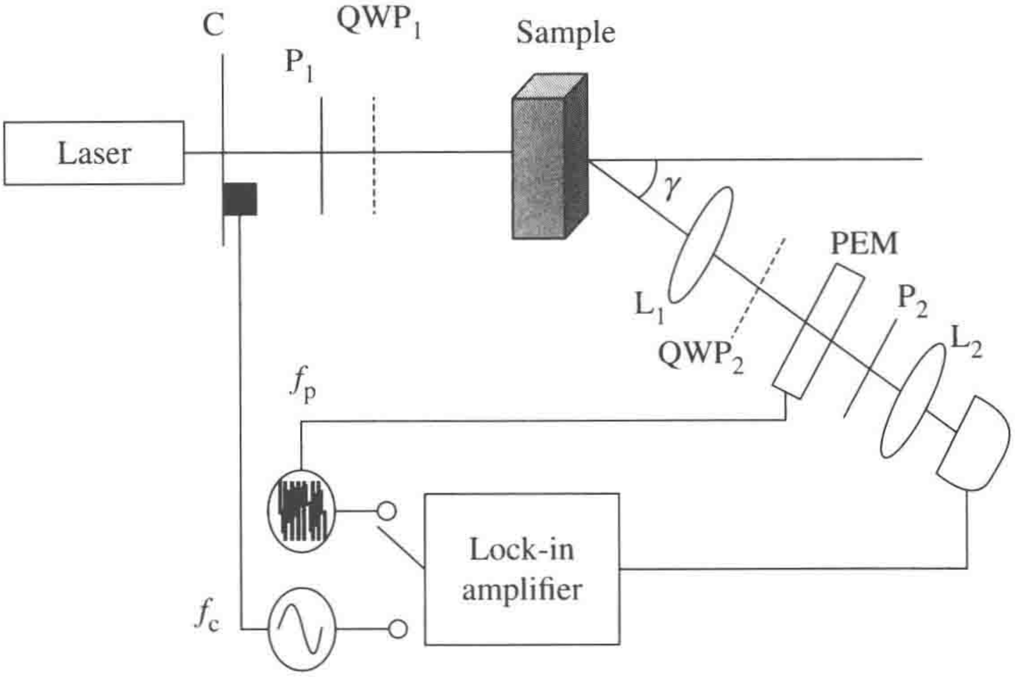

FIGURE 7.12 Highly sensitive complete Mueller point-sensing polarimeter. The PSG comprises a linear polarizer and a removable quarter-wave plate (QWP) while the PEM-based PSA is of the type described above. f_c and f_p are the chopper and PEM modulation frequencies, respectively. γ is the detection angle. Adapted from References 61 and 62.

with *misregistration*, that is, unavoidable shifts in the pixel-to-pixel correspondence of identical points in the optical images.

7.3.3.2 A nonimaging Mueller Polarimeter A complete point-sensing polarimeter combining a PSG with a polarizer and a removable QWP and a PSA based with a photoelastic modulator as described above is shown in Figure 7.12.

To boost the SNR as much as possible in this arrangement, the illuminating laser is chopped (at the sub kHz range, f_c) to allow synchronous detection of the "DC" component, in addition to that of the signals modulated by the PEM at ω (50 kHz, f_p) and 2ω (100 kHz).

7.3.3.3 Complete Mueller Imagers In both examples shown below, the polarimetric images are taken with a CCD. Of course imaging can also be achieved by using a single detector and a spatially scanning laser beam.

Dual rotating retarders. In these instruments, the PSG and the PSA both comprise a linear polarizer and a rotating retarder. An example of such an instrument is shown in Figure 7.13. As mentioned above, in such setups the rotatable retarders are sequentially set at discrete azimuths and are kept fixed for each raw image acquisition by the CCD. As acquisition of full Mueller images can take tens of seconds these instruments are well suited to the characterization of static samples.

Pairs of variable retarders. The instrument shown in Figure 7.14 is the Mueller imager developed at Ecole Polytechnique, for examination of *ex-vivo* tissue samples. Both the PSG and the PSA are of the type outlined in Figure 7.10 with nematic liquid crystals as non-rotating variable retarders.

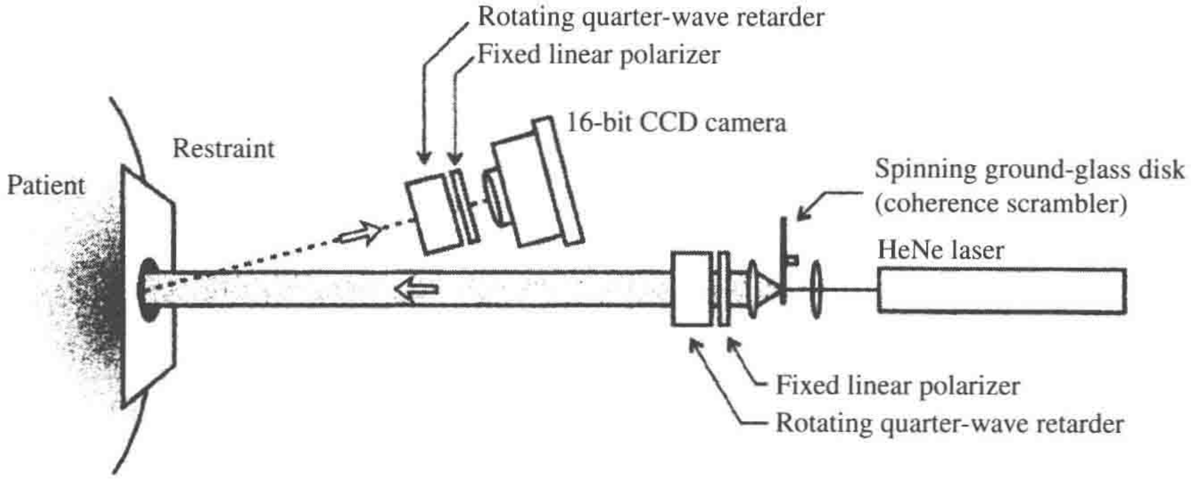
Rotating quarter-wave retarder
Fixed linear polarizer
16-bit CCD camera
Restraint
Patient
Spinning ground-glass disk
(coherence scrambler)
HeNe laser
Fixed linear polarizer
Rotating quarter-wave retarder

FIGURE 7.13 Mueller imager with PSG and PSA, each comprising of a polarizer and a rotating retarder set sequentially at discrete azimuths for image acquisition by the CCD. From Reference 63.

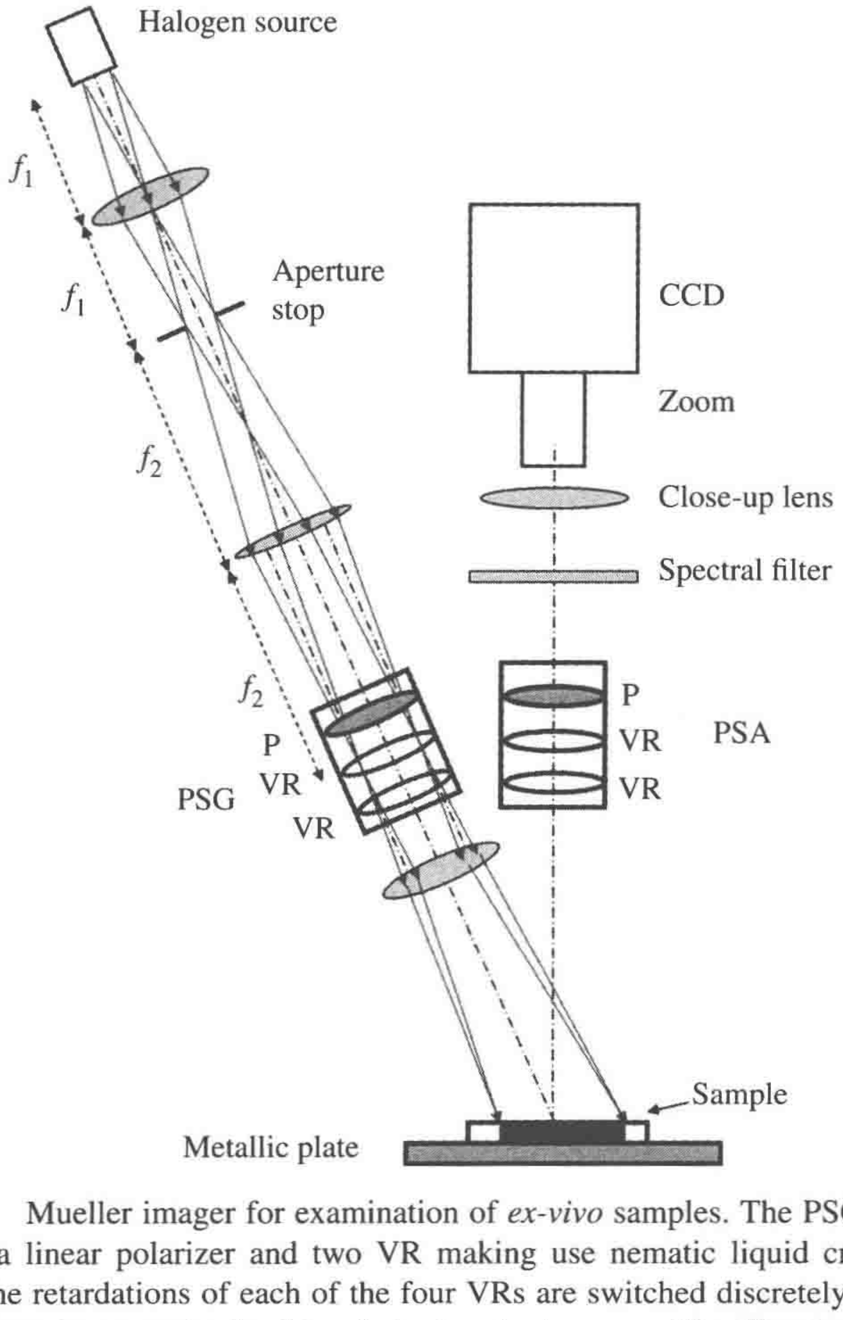
Halogen source
f_1
f_1
Aperture stop
CCD
Zoom
f_2
Close-up lens
Spectral filter
f_2
P
VR
VR
PSG
P
VR
VR
PSA
Sample
Metallic plate

FIGURE 7.14 Mueller imager for examination of *ex-vivo* samples. The PSG and PSA are both made of a linear polarizer and two VR making use nematic liquid crystals at fixed orientations. The retardations of each of the four VRs are switched discretely between pairs of different values to generate the 16 polarization basis states. The illumination system is designed to ensure that the polarizations defined by the PSG are uniform over the entire 5×5 cm^2 field of view. Adapted from Reference 64.

Nematic liquid crystals feature very wide angular acceptance, no image motion when retardance is changed, and a time response typically less than 100 ms. Full Mueller images are then acquired in a few seconds by sequentially switching the retardations of each of the four VRs between pairs of suitably chosen values and leaving these retardations constant during the CCD integration time. By using a white light source (halogen lamp) and interference filters, the wavelength can be selected at will throughout the visible spectrum to enable spectral polarimetry studies.

7.3.4 Summary

In this section, we briefly reviewed the basic principles of design and optimization of polarimetric instrumentation, and outlined the most widely used practical implementations. These may take a variety of forms, depending on the selected optical systems (imaging or non-imaging) and the way the polarization is encoded and detected (in discrete states, or in Fourier components of periodically varying systems such as photoelastic modulators). The availability of so many possibilities is very valuable in practice, as it allows one to "tailor" the polarimetric system for the specific needs of the envisioned application. In particular, polarization modulation and detection may be "added" to virtually any optical system, at the microscopic as well as macroscopic levels; note that this is not the case for many other techniques widely used in biomedicine, such as confocal imaging or OCT, which operate only at microscopic scales. Last but not least, often polarimetry may be implemented at very reasonable cost, an essential point for many possible practical applications.

7.4 FORWARD MODELING AND TESTING IN PHANTOMS

7.4.1 Forward Modeling of Polarized Light Propagation in Tissue

7.4.1.1 Overview As outlined in the introduction, tissue polarimetry research has two major application directions:

(a) *Polarized light tissue imaging,* wherein polarization can be used as a gating mechanism to filter out multiply scattered (image blurring) photons in order to enhance contrast and to improve imaging resolution; and
(b) *Tissue characterization/diagnosis*, wherein the rich abundance of important biophysical information contained in the intrinsic tissue polarimetry characteristics (retardance, diattenuation, and depolarization encoded in the tissue Mueller matrix) are extracted and quantified.

For either, accurate modeling of interaction of polarized light with biological turbid media or tissue is extremely useful. The insight gained from such *forward models* helps in designing and optimizing experiments, and analyzing/interpreting measured data for specific applications.

Driven by the two different classes of applications, forward modeling of polarized light transport in tissue also has takes different routes. For the tissue imaging applications, the major emphasis has been on *modeling depolarization of multiply scattered light* in turbid media. In these analytical/heuristic approaches, the tissue is typically modeled as a turbid medium having bulk-average scattering and absorption properties, where propagation leads to depolarization as a result of strong multiple scattering events (birefringence and other simultaneously occurring polarization effects are often ignored) [1, 65–69]. The main aim of these models has been to understand the overall depolarization trends, its dependence on the scattering properties of the media (density, size, shape, and refractive index of the scatterers), and on the incident state of polarization, and to design/optimize general polarization schemes to discriminate against multiply scattered photons for tissue imaging in "simple" geometries.

Applications involving extraction/quantification of the intrinsic tissue polarimetry characteristics for tissue characterization and assessment, on the other hand, require more accurate and complete forward models incorporating the simultaneously exhibited complex tissue polarimetry and scattering events [3]. Nevertheless, for either of the aforementioned approaches, rigorous electromagnetic (EM) theory based models for analyzing polarized light propagation in tissue has not been feasible. This is because the Maxwell's equations-based EM theoretical approach will need to identify and incorporate the spatial/temporal distribution of complex tissue dielectric structures (different cells and subcellular structures, connective stromal tissues/extracellular matrix, blood and lymphatic networks, interstitial fluids, etc.), which is clearly a formidable (if not impossible) task.

Instead, light propagation through such media is often modeled using the *radiative transport theory* [70]. Although the scalar radiative transport theory and its simplified approximation, the diffusion equation, have been successfully used in tissue optics (specifically to yield light intensity distribution in tissue volume and measurable quantities such as diffuse reflectance, transmittance, spatially resolved diffuse reflectance and so on), both are intensity-based techniques, and hence typically neglect polarization [1, 70]. Alternatively, the vector radiative transfer equation (VRTE), which includes polarization information by describing transport of the Stokes vectors of light (photon packet) through a random medium, has been explored for tissue polarimetry modeling [1]. However, solving the VRTE in real systems is rather complex and the solutions are often too slow and insufficiently flexible to handle the necessary boundary conditions for arbitrary geometries, heterogeneities, and optical properties as desirable in case of tissue.

The *polarization sensitive Monte Carlo* (PSMC) *technique* is a more general and robust approach that overcomes these limitations [70, 71]. The PSMC technique has thus been widely explored for tissue forward modeling, specifically for applications involving tissue characterization/diagnosis as described in greater detail subsequently. For polarized light imaging applications, relatively simpler analytical/heuristic approaches based on photon diffusion formalisms [68], random walk models [69], and maximum entropy principles [65] have proven moderately successful. In the following, we provide a very brief account of some of these simpler analytical approximations developed to deal with depolarization of multiply scattered light in turbid medium. Interested readers are referred to References 1, 65–69 for further details.

7.4.1.2 Modeling Depolarization of Multiply Scattered Light: Photon Diffusion Formalism As noted, these simpler analytical theories are aimed at deriving relationships between various quantities of practical interest such as the DOP (either linear or circular) of forward-scattered or back-scattered light from a turbid medium, average path lengths, the optical transport parameters of the medium, and so forth. As in the case of radiative transport theory, in these models also, the turbid medium is considered to have *bulk-average scattering and absorption properties*, representative of isotropic tissue volumes. The turbid medium is usually modeled through the optical transport parameters, namely, the *absorption coefficient* (μ_a), *single scattering coefficient* (μ_s), and *single scattering anisotropy* (g) [70]. As is known from the transport theory, the linear isotropic optical coefficients are defined so that

$$l_a = \mu_a^{-1} \qquad \text{and} \qquad l_s = \mu_s^{-1} \tag{7.80}$$

give the absorption and scattering mean free paths, respectively.

The anisotropy parameter g is defined as the average cosine of scattering angle. The value of g ranges from –1 to +1, where $g = -1$ corresponds to fully backward scattering, $g = 0$ corresponds to forward-backward symmetric scattering (isotropic scattering being a special case) and $g = +1$ corresponds to fully forward scattering. In general, the value of g depends on the average size of the scatterers in the medium relative to the wavelength of the irradiation. For a medium composed of scatterers whose size is much smaller than the wavelength (radius $a \ll \lambda$), the anisotropy parameter g is $\sim$0, its value approaching unity ($g \sim 1$) for media composed of larger sized scatterers ($a \geq \lambda$). The latter regime applies to most biological tissues in the visible/near-infrared spectral range ($g \sim 0.7$–0.95) [70].

Another couple of parameters frequently used in tissue optics are

$$\mu_s' = \mu_s(1 - g) \text{ and } l^* = (\mu_s') - 1 \tag{7.81}$$

namely, the reduced scattering coefficient and the transport mean free path. Because of typical tissue g-values, $1 - g$ is a small number, and thus $\mu_s > \mu_s'$ and $l^* > l_s$. The use of μ'_s assumes that the reflection and transmission for a slab of tissue with optical parameters μ_a, μ_s, and g are the same as those for the same slab with optical parameters μ_a, μ_s', and $g = 0$ [70]. This so-called *similarity principle* is not exact and holds if the light distribution is studied far enough away from the light source and boundaries, typically at a distance greater than l^*, which in turn is referred to as the typical length scale over which the propagation direction of photons gets randomized in a multiply scattering medium.

In the photon diffusion formalisms, the depolarization of multiply scattered light is usually modeled by assuming an exponential decay of the single path (photon undergoing successive scattering events) DOP with increasing number of scattering events (n). Analytical expressions for depolarization via the characteristic depolarization length scales ξ_L and ξ_C (for linear and circular polarizations, respectively) has also been derived based on the so-called *maximum entropy principle* [1, 65]. The degree of residual polarization of multiply scattered light at a chosen detection point can be obtained by averaging (or weighing) the single path DOP over the path length distribution function.

Approximate analytical expressions for the path length distribution function are conveniently obtained from the solution of photon diffusion equation for a given detection geometry [1, 70]. The resulting DOP $\mathrm{DOP}_{\mathrm{L,C}}$ of diffusely transmitted or reflected light from a turbid medium for two practical geometries, the forward scattering and the backscattering geometries, has accordingly been derived for linear and circular polarizations:

- ***Forward scattering geometry, slab of thickness L***

  $$\mathrm{DOP}_{\mathrm{L,C}} \cong 2\frac{L}{l_s} \sinh\left[\frac{l_s}{\zeta_{\mathrm{L,C}}}\right] \exp\left[-\frac{L}{\zeta_{\mathrm{L,C}}}\right] \tag{7.82a}$$

  where l_s is the scattering mean free path defined in Eq. (7.80), and

  $$\zeta_{\mathrm{L,C}} = \left[\frac{1}{3} l_s \xi_{\mathrm{L,C}}\right]^{\frac{1}{2}}, \tag{7.82b}$$

  where $\xi_{\mathrm{L,C}}$ is the characteristic depolarization length scales for linear and circular polarizations. These lengths are defined as the average distances a (linearly or circularly) polarized photon has to go through in the medium to see its DOP decrease by a factor of e. The ratios ξ_L/l_s and ξ_C/l_s thus define the average number of collisions required to reduce the DOP by a factor of e.
- ***Back-scattering geometry, semi-infinite medium, L → ∞***

  $$\mathrm{DOP}_{\mathrm{L,C}} \cong \frac{3}{2} \exp\left[-\gamma\sqrt{\frac{3l^*}{\xi_{\mathrm{L,C}}}}\right], \tag{7.83}$$

  where $l^*(= l_s/(1-g))$ is the transport mean free path of Eq. (7.81) and γ is the correlation decay parameter with value ranging between 1.5 and 3 [1].

We emphasize that the expressions for residual DOP in Eqs. (7.82) and (7.83) are valid in the *photon diffusion limit*, that is, after many scattering events. Moreover, these expressions typically neglect absorption, which can also be incorporated. In backscattering geometry, Eq. (7.83) is then modified to [1]:

$$\mathrm{DOP}_{\mathrm{L,C}} \cong \frac{3}{2} \exp\left[-\gamma\left\{\sqrt{\frac{3l^*(1+\mu_a\xi_{\mathrm{L,C}})}{\xi_{\mathrm{L,C}}}} - \sqrt{3l^*\mu_a}\right\}\right] \tag{7.84}$$

Equations (7.82) to (7.84) essentially capture all the qualitative features of depolarization of light by multiple scattering (implicit is the assumption that the other polarimetry effects such as birefringence and diattenuation are absent). This is illustrated in Figure 7.13, where the computed variations of characteristic length scales of depolarization (normalized by the scattering mean free path l_s) ξ_L/l_s and ξ_C/l_s are shown as a function of the anisotropy parameter g of the medium. The inset shows the variations of ξ_L/l_s and ξ_C/l_s as a function of the size parameter of the scatterers

$$X = \frac{2\pi a\, n_m}{\lambda}, \tag{7.85}$$

where a is the scatterer radius, n_m the surrounding medium refractive index, and λ the wavelength. The observed qualitative trends can be summarized as follows:

(a) For isotropic scattering media composed of *Rayleigh scatterers* ($g \sim 0$, $a \ll \lambda$), depolarization of circularly polarized light is stronger than linearly polarized light ($\xi_L > \xi c$).

(b) The reverse is true if ($\xi_L < \xi c$), for anisotropic scattering media consisting of larger scatterers ($g \geq 0.7$, $a \geq \lambda$, the so-called *Mie regime*).

(c) The values of ξ_L/l_s and ξ_C/l_s increase monotonously (depolarization decreases) with increasing anisotropy g. When the same quantities are plotted as functions of the size parameter X, their variation is no longer monotonous, as they decrease for $X \geq 10$ (inset of Figure 7.15). This behavior is actually due to a decrease in g with increasing X in this range, an effect attributed to Mie resonances.

The underlying mechanism for depolarization dependence of linearly and circularly polarized light on the size of scatterers is worth a brief mention here. The decrease of depolarization with increasing g is easily understood as a decrease of the polarization randomization when scattering becomes more and more peaked in the forward direction.

The difference in relative rates of depolarization of linearly and circularly polarized light can be attributed to the different mechanisms of depolarization of the two. The depolarization of incident linearly polarized light occurs primarily due to the randomization of the direction of the incident field vector as a result of multiple scattering [65,66]. On the other hand, depolarization of circularly polarized light occurs both due to the randomization of the field vector's direction and randomization of helicity [66]. Note that scattering at large angles flips the helicity of the circular polarization state resulting in its larger depolarization. In a turbid medium, light travels along many possible zig-zag paths, having contributions from scattering at various angles. For Rayleigh scatterers (where forward and backward scattering are approximately equally likely), the contribution of the large angle scattered photons is greater as compared to the larger sized Mie scatterers (where forward scattering predominates), ensuing stronger randomization of helicity and thus resulting in

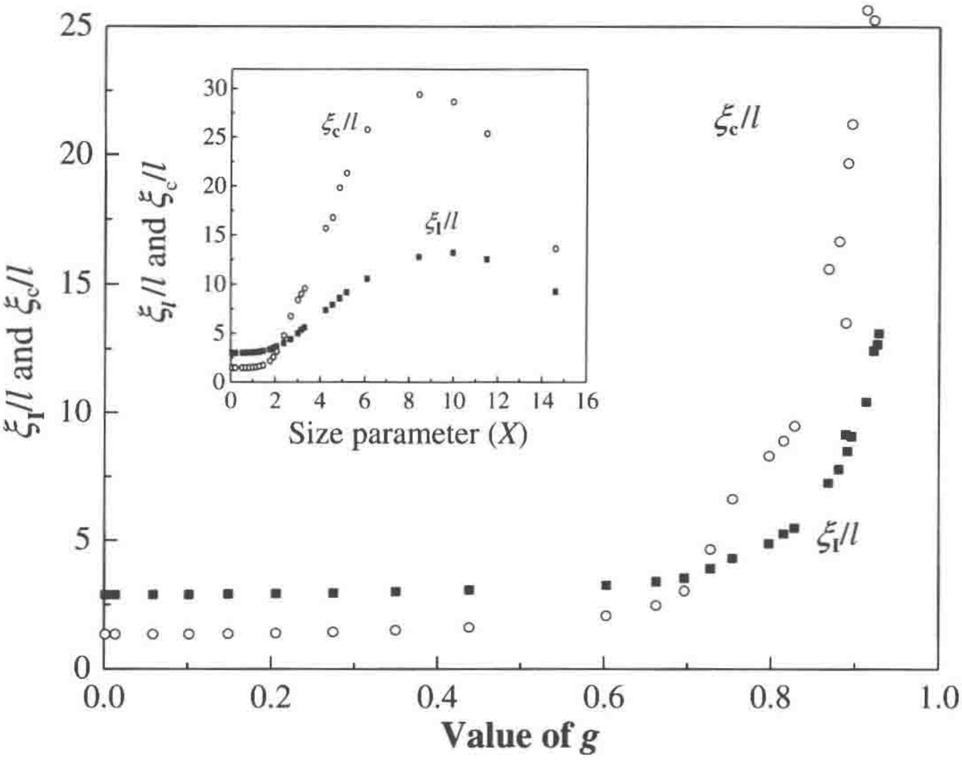

FIGURE 7.15 The theoretically computed variations of characteristic length scales of depolarization (normalized by scattering mean free path l_s) of incident linearly (ξ_L/l_s) and circularly (ξ_C/l_s) polarized light as a function of anisotropy parameter g. The inset shows the corresponding variation as a function of size parameter of scatterer X. The calculations were made for surrounding medium and scatterer refractive indices, respectively, equal to 1.33 and 1.59; and $\lambda = 0.6328$ μm). Adapted from Reference 65.

stronger depolarization of circularly polarized light in Rayleigh media. As the scatterer size increases, the additional cause of depolarization of circularly polarized light, that is, the flipping of helicity due to back scattering also gets reduced, resulting in weaker depolarization of circularly polarized light for anisotropic scattering samples [66, 67].

Note that the depolarization of light in a turbid medium is additionally influenced by the refractive index of the scatterers present in the medium. In fact, it has been shown that despite having large value of anisotropy parameter g, the depolarization characteristics of weakly fluctuating random medium (low value of the relative refractive index contrast $m = n_s / n_m \sim \leq 1.05$) can be similar to that of media composed of Rayleigh scatterers [61, 66]. This intriguing behavior originates from the fact that the anisotropic scatterers ($g \geq 0.7, X \gg 2$) having a lower value of relative refractive index m ($m \leq 1.05$) seem to belong in the weak scattering or Rayleigh-Gans regime, where each volume element within the scatterer gives electrical dipole scattering in an independent manner [72], yielding Rayleigh-like scattering matrix elements. The retention of this dipolar nature of scattering thus leads to depolarization characteristics of such low refractive index, anisotropic scattering medium (such as majority of biological tissues) much similar to that of Rayleigh scatterers.

These depolarization trends have been verified experimentally in turbid media composed of spherical scatterers having varying sizes [72–75]. One should, however, exercise caution in generalizing these depolarization trends to arbitrary detection geometries, as depolarization metrics may exhibit more complex behaviors. Moreover, these analytical approaches, while useful, are approximate by their very nature and are accordingly restricted to the "tissue imaging" applications (employing polarization gating methods and various other co/cross polarization detection schemes). In contrast, for applications involving extraction/quantification of the intrinsic tissue polarimetry characteristics for tissue characterization, more encompassing approach such as the polarization-sensitive Monte-Carlo modeling are required.

7.4.1.3 Robust Polarization-Sensitive Monte-Carlo (PSMC) Approach for Modeling Complex Tissue Polarimetry Characteristics In this statistical approach to radiative transfer, the multiple scattering trajectories of individual photons are determined using a random number generator to predict the probability of each scattering event. It is also assumed that scattering events occur independently and exhibit no coherence effects. The position and propagation direction of each photon are initialized and modified as the photon propagates through the scattering medium. The photon propagates in the sample between scattering events a distance ℓ sampled from the probability distribution [70, 71]:

$$P(\ell)\,\mathrm{d}\ell = \frac{1}{\mu_\mathrm{t}}\exp[-\mu_\mathrm{t}\,\ell]\,\mathrm{d}\ell, \tag{7.86}$$

where the extinction coefficient μ_t describes the cumulative effect of scattering and absorption in the decay of the propagating light beam:

$$\mu_\mathrm{t} = \mu_\mathrm{s} + \mu_\mathrm{a}. \tag{7.87}$$

In conventional intensity-based MC models, when the photon encounters a scattering event, a scattering plane and angle are statistically sampled based on the so-called *scattering phase function*. Various types of scattering phase function has been used in MC tissue models, namely, the Mie theory-computed phase function or analytical approximations like the Henyey–Greenstein function [1].

In the polarization-sensitive Monte Carlo (PSMC) model, the photon's polarization, with respect to a set of arbitrary orthonormal axes defining its reference frame, is represented as a Stokes vector **S** and polarization effects are applied using medium Mueller matrices **M**, as illustrated in Figure 7.16. Upon encountering a scattering event, a scattering plane and angle are statistically sampled based on the polarization state of the photon (Stokes vector) and the full scattering Mueller matrix **M** (note that the angular variation of the m_{11} element of the scattering Mueller matrix is actually the scattering phase function for unpolarized light). The photon's reference frame is first expressed in the scattering plane and then transformed to the laboratory (experimentally observable) frame through multiplication of appropriate rotation matrices (reference frame manipulation) and by the Mueller matrix corresponding to

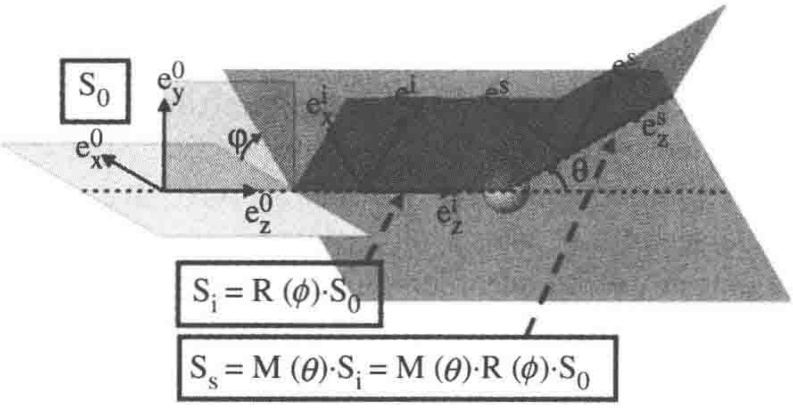

FIGURE 7.16 Transformation of the polarization state by an individual scattering event. The Stokes vector $\mathbf{S}_0$ describing the incident polarization is expressed in the reference frame $(\mathbf{e}^0_x, \mathbf{e}^0_y, \mathbf{e}^0_z)$defined from the previous scattering event. Then the azimuth ϕ and the polar angle θ of the scattered photon are sampled statistically from the phase function. The Stokes vector i describing the incident polarization is expressed as $\mathbf{S}_i$ in the $(\mathbf{e}^i_x, \mathbf{e}^i_y, \mathbf{e}^i_z)$frame obtained by rotating the initial frame by an angle ϕ in the (x,y) plane. Then the output Stokes vector $\mathbf{S}_e$ obtained from the previous one by applying the scattering Mueller matrix $\mathbf{M}(\theta)$, on $\mathbf{S}_i$ is expressed in the $(\mathbf{e}^s_x, \mathbf{e}^s_y, \mathbf{e}^s_z)$frame obtained by rotating the intermediate frame in the scattering plane by an angle θ around $\mathbf{e}^i_y = \mathbf{e}^s_y$.

the scattering event. Usually, the scattering Mueller matrix **M** is computed using Mie theory, which assumes the scattering medium to be composed of discrete spherical scatterers [76,77]. In principle, incorporation of scattering Mueller matrices for other non-spherical scatterers or the scattering matrices for other continuously fluctuating medium (such as tissue) is also possible [78].

The evolution of polarization state of each photon packet is tracked (via the Stokes vectors) following successive scattering events. The absorption effects are incorporated after successive scattering events by multiplying the photon by a factor that decreases its weight

$$\Omega = \frac{\mu_s}{\mu_a + \mu_s} \tag{7.88}$$

also called *albedo*, as conventionally done in intensity-based MC models [70].

Upon encountering an interface (either an internal one, representing tissue layers of different optical properties, or an external one, representing external boundary), the probability of either reflection or transmission is calculated using Fresnel coefficients. Assuming no interference effects, the final Stokes vectors for light exiting the sample in a particular direction (at any user selected detection point) are computed as the sum of all the appropriate sub-populations of photons. The sample Mueller matrix (for a given detection geometry) can then be calculated by sequentially changing the input polarization between four (or more) states, by recording the corresponding output Stokes vectors for each respective input states, and performing algebraic manipulations [76].

While the effects of scattering on the polarization evolution with successive scattering events can be modeled by the scattering Mueller matrix M, the effects of other medium polarimetry effects such as linear birefringence and optical activity can also be incorporated by including their corresponding Mueller matrices. However, difficulty arises in modeling many simultaneous polarization events in the presence of multiple scattering. Matrix multiplication is generally not commutative ($\mathbf{M}_A\mathbf{M}_B \neq \mathbf{M}_B\mathbf{M}_A$); thus, different orders in which these are applied will yield different effects (cf decomposition discussion of Section 7.2.3). Yet in actual tissues, these effects (such as optical activity due to chiral molecules and linear birefringence due to anisotropic tissue structures) are exhibited simultaneously and not one after the other as sequential multiplication implies. Thus, a realistic tissue model must include these simultaneous polarization effects in the presence of scattering.

This problem is tackled through the use of the so-called *N*-matrix formalism [7, 79], which combines several polarization effects into a single matrix describing them simultaneously. Briefly, in this formalism, the matrix of the sample is represented as exponential *sum* of differential matrices (*N*-matrices), wherein each matrix includes a single polarization effect [7, 79]. The issue of ordering of noncommutative matrices is overcome as matrix addition is always commutative. The differential matrices corresponding to each optical property exhibited by the sample are then summed to express the combined effect, and are subsequently applied to the photons as they propagate between scattering events. Note that an analogous differential matrix formalism for combining simultaneous polarimetry effects has been discussed in Section 7.2.3.3, in context to inverse polarimetry analysis. Finally, the scattering histories of a large number of photon packets (typically 10^7–10^9 photons are required to generate statistically acceptable results) are tracked as they propagate through the medium and are summed to yield the macroscopic parameters of practical interest (Stokes vectors, Mueller matrices, path length distributions, polarization statistics from different scattering histories, etc.).

In the simulation, circular and linear birefringence (these are the two relevant tissue polarimetry effects in addition to depolarization) are modeled through the optical activity χ in degrees per centimeter, and through the anisotropy in refractive indices (Δn), respectively [76]. Here, $\Delta n = (n_e - n_o)$ is the difference in refractive index along the extraordinary axis (n_e) and the ordinary axis (n_o). For simplicity, it is generally assumed that the direction of the extraordinary axis and the value for Δn is constant throughout the scattering medium (although recent research efforts are exploring the effects of multiple uniaxial domains of varying magnitude and orientation of birefringence [4; 80]. In each simulation, n_e and n_o are taken as input parameters and a specific direction of the extraordinary axis is chosen. As each photon propagates between scattering events, the difference in refractive indices seen by the photon depends on the propagation direction with respect to the extraordinary axis. The effect is usually modeled using standard formulae describing the angular variation of refractive index in uniaxial medium. Similar to conventional MC model, the scattering and absorption properties are modeled using the optical transport parameters (scattering coefficient μ_s and absorption coefficient μ_a and single scattering anisotropy g).

7.4.2 Experimental Testing and Validation in Tissue Phantoms

7.4.2.1 Forward Model The polarization sensitive Monte Carlo forward model, described above and the Mueller matrix inverse analysis methods, described in Section 7.2.4, requires comprehensive validation prior to their implementation for polarized light assessment of complex systems like tissues. The validity of these approaches has thus been tested on various tissue simulating phantoms exhibiting scattering and polarization properties, which are known and user-controlled *a priori* [61, 62, 81]. The validation studies have been performed on optical phantoms exhibiting either *sequential* or *simultaneous* polarization effects in presence of multiple scattering [45]. Note that in complex systems like tissues, no unique order (or sequence) can be assigned to the polarimetry effects; rather, these are exhibited *simultaneously* (except a few specific type of layered tissues, wherein sequential occurrence of some polarimetric effects may indeed happen). We shall thus present selected validation results on tissue phantoms exhibiting *simultaneous* scattering and polarization effects [3, 61, 62].

These solid phantoms were developed using polyacrylamide as a base medium, with sucrose-induced optical activity, polystyrene microspheres-induced scattering, and mechanical stretching to cause linear birefringence (or linear retardance). To apply controllable strain to produce linear birefringence, one end of the polyacrylamide phantoms was clamped to a mount and the other end to a linear translational stage, inducing varying linear birefringence with its axis along the direction of strain. These phantom systems mimic the complexity of biological tissues, exhibiting simultaneous effects of linear birefringence, optical activity, and depolarization due to multiple scattering. The experimentally recorded Mueller matrix from a birefringent, chiral, turbid phantom measured in the transmission geometry is shown in Figure 7.17a. The corresponding matrix generated through the PSMC model, using the same input optical parameters is shown in Figure 7.17b.

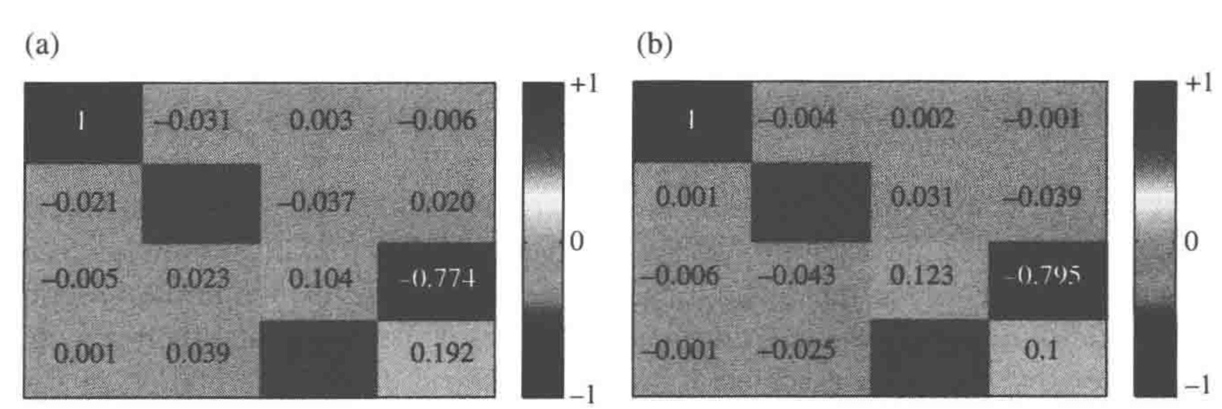

FIGURE 7.17 (a) The *experimentally* recorded Mueller matrix in the forward (transmission) detection geometry from a birefringent (extension = 4 mm, corresponding to a value of linear retardance $\delta = 1.345$ rad for 1 cm path length), chiral (concentration of sucrose = 1 M, $\chi = 1.96° \text{ cm}^{-1}$) turbid ($\mu_s = 30 \text{ cm}^{-1}$, $g = 0.95$) phantom of thickness of 1 cm. (b) The corresponding Mueller matrix generated through the *PSMC model* with input parameters: linear birefringence $\Delta n = 1.36 \times 10^{-5}$ (corresponding to $\delta = 1.345$ rad), $\chi = 1.96° \text{ cm}^{-1}$, $\mu_s = 30 \text{ cm}^{-1}$, $g = 0.95$. Adapted from Reference 3. (*For a color version of this figure, see the color plate section.*)

The simultaneous occurrence of the constituent medium polarization properties (depolarization, linear birefringence, and optical activity) are observed to contribute in a complex interrelated way to the Mueller matrix elements (both the experimental and the MC-simulated one), resulting in essentially all sixteen nonzero elements. Even though a direct quantification of the individual polarimetric contributions from such "lumped" system Mueller matrix is not possible, some qualitative features of the constituent polarimetry effects may readily be identified from the Mueller matrix elements:

1. In both the experimental and the MC-generated Mueller matrices, the signature of *linear birefringence* is reflected as considerable magnitudes of the m_{34} and m_{43} elements (representing horizontal/vertical linear birefringence), as one would expect for a linear retarder with orientation angle $\theta = 90°$. This is however, accompanied with nonzero magnitudes of m_{24} and m_{42} elements, which is a manifestation of the random orientation effects of linear birefringence (as experienced by different subpopulation of multiply scattered photons undergoing zig-zag paths in the medium).
2. *Chirality* (optical rotation) is manifested as a difference of m_{23} and m_{32} elements, even though the effect is considerably weaker. The inequality of the magnitudes of m_{23} and m_{32} elements is a manifestation of interrelated "cross-talk" contributions from other simultaneous effects.
3. The effect of *depolarization* is prominently reflected in the diagonal elements of the Mueller matrix. While the m_{22} element closely resembles polarization loss (horizontal/vertical linear depolarization) due to multiple scattering alone (additionally weakly influenced by optical rotation effects), the m_{33} ($\pm 45°$ linear depolarization) and m_{44} (circular depolarization) elements are strongly influenced by simultaneous linear birefringence effects and are accordingly considerably lower in magnitude.
4. In absence of any intrinsic diattenuation effects (either in the experimental phantom or in the simulation), the characteristic elements m_{12}, m_{13}, and m_{14} do not exhibit appreciable magnitudes.

The excellent agreement between the experimental and the simulated Mueller matrices emphasizes the capability of the PSMC model in simulating complex tissue polarimetry effects (simultaneous optical activity and birefringence in the presence of multiple scattering). Yet the complicated nature of the resultant Mueller matrix underscores the problems associated with polarimetric data interpretation in such complex systems. But as illustrated below, despite these complexities, the constituent polarimetry characteristics can be successfully isolated and quantified using the Mueller matrix inverse analysis (various decomposition) methods. The theory behind these was described in Section 7.2.3; we now turn to experimental validation studies of these approaches.

7.4.2.2 Inverse Polarimetric Analysis Figure 7.18 displays the results of inverse polarimetry analysis (Mueller matrix decomposition) on the experimental Mueller

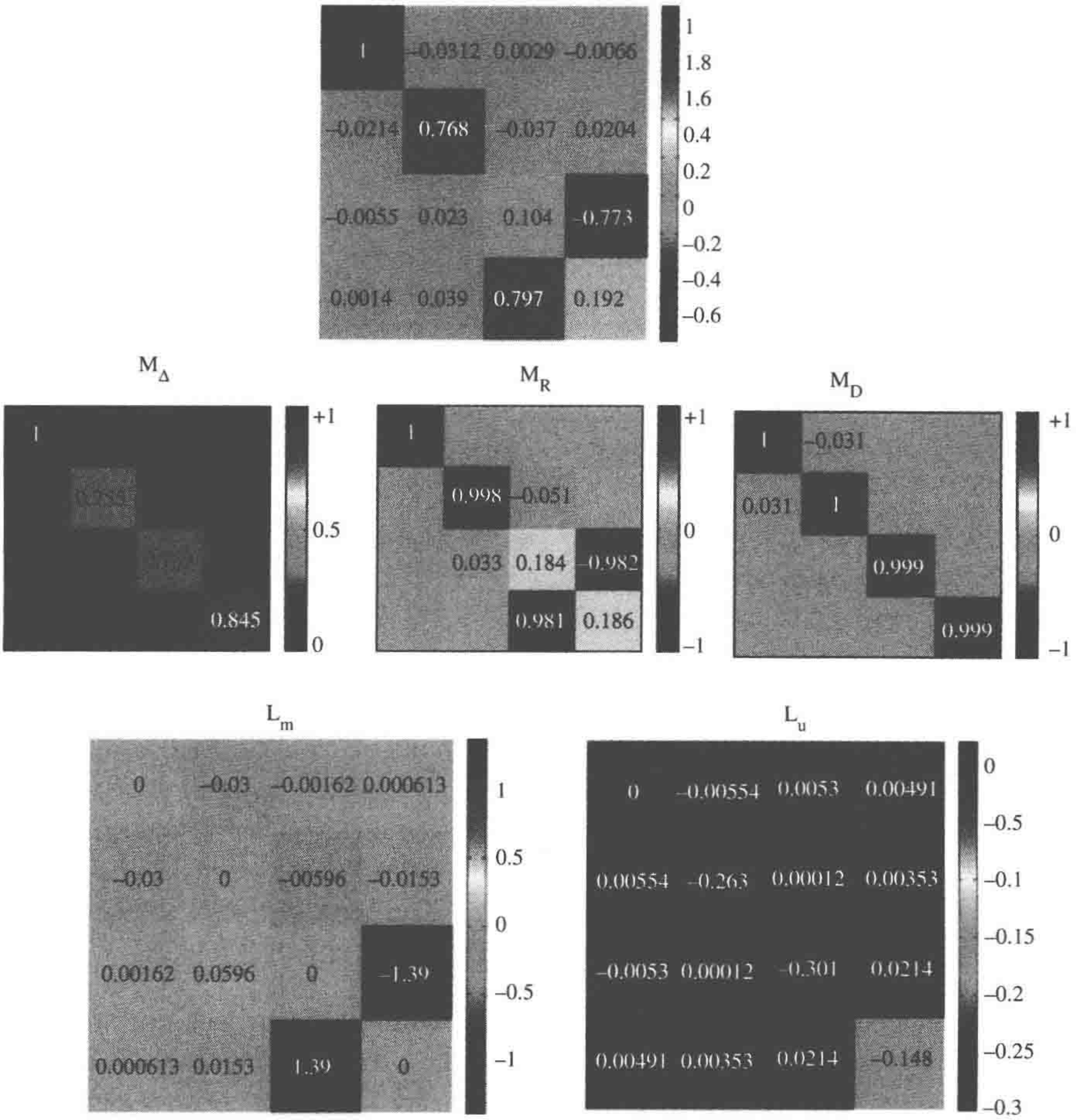

FIGURE 7.18 The *experimentally* recorded Mueller matrix in the forward detection geometry (top panel, reproduced from Fig. 7.17a). The basis matrices (M_Δ, M_R, M_D) obtained following the *forward polar decomposition* process (middle panel). The matrix logarithms L_m and L_u, derived using the *logarithmic decomposition* (bottom panel). The estimated polarization parameters using both the polar decomposition and the differential matrix approaches are listed in Table 7.3. Adapted from Reference 44. (*For a color version of this figure, see the color plate section.*)

matrix shown in Figure 7.17a [44]. Since these tissue phantoms exhibit *simultaneous* (rather than sequential) polarization effects, use of the *forward*, *reverse*, or *symmetric* product decomposition within the polar decomposition family (which employs *sequential* factorization of the elementary polarization effects) is expected to be somewhat inaccurate. For these three sequential product approaches, representative results are shown for the forward decomposition only (Figure 7.18, middle); these are compared with the logarithmic (differential matrix) decomposition which assumes *simultaneous* occurrence of the constituent polarimetry effects) (Fig. 7.18, bottom)

TABLE 7.3 The values for the polarization parameters, Δ, δ, ψ, and D, extracted using the *logarithmic decomposition* from the L_m matrix.

Parameters	Control input	Logarithmic decomposition	Forward polar decomposition
Δ	~0.188	0.211	0.210
δ (radian)	~1.574	1.386 ± 0.022	1.386
Ψ (radian)	~0.030	0.030 ± 0.001	0.030
D	~0	0.030 ± 0.009	0.032

The uncertainties in the δ, ψ, and D parameters are derived from the $\boldsymbol{L}_u$ matrix. The values for the parameters extracted via *forward polar decomposition* (fourth column). The second column shows the control inputs. The control input for the net depolarization coefficient Δ was determined from the experimental Mueller matrix of the pure depolarizing phantom having no birefringence and optical activity. The expected value for linear retardance (δ) and optical rotation (ψ) are estimated by using the corresponding values from the nonscattering phantom ($\delta_0 = 1.345$ rad and $\psi_0 = 0.026$ rad) and accounting for increased path length $\langle Z\rangle(\delta = \delta_0 \cdot \langle Z\rangle, \psi = \psi_0 \cdot \langle Z\rangle, \langle Z\rangle = 1.17$ cm is the MC-derived average photon path length).
Source: Adapted from Reference 44.

Evidently, the forward polar decomposition-derived basis matrices exhibit simpler characteristic features of standard sequential and homogeneous depolarization, retardance, and diattenuation matrices with many of the off-diagonal null elements (see Section 7.2.2), as expected. Similarly, the Lorentz antisymmetric $\mathbf{L}_m$ and symmetric $\mathbf{L}_u$ components of the matrix logarithm derived via the differential matrix formalism exhibit characteristic features of simultaneous depolarization, linear birefringence, and optical activity effects (their mean values and uncertainties discussed in Section 7.2.3.3).

The estimated polarization parameters using both the polar decomposition and the differential matrix formalisms are listed in the accompanying Table 7.3. In the absence of any intrinsic diattenuation property, the values for D estimated from both the decomposition formalisms are quite low and comparable (as expected). The estimated values for the depolarization coefficient Δ from the two formalisms are self-consistent and are also in excellent agreement with the controlled input.

Turning to the other two biologically important polarization parameters (linear retardance δ and optical rotation ψ), several interesting trends are seen. The derived optical rotation ψ in the presence of turbidity shows small increase as compared to that from analogous nonscattering phantom ($\psi_0 \sim 0.026$ rad, not shown here), which arises from the increase in optical path length due to multiple scattering (resulting in accumulations of ψ values). In fact, the accumulated value of ψ matches well the expected one$\psi = \psi_0 \cdot \langle Z\rangle$, where $\langle Z\rangle$ is the Monte Carlo-derived average photon path length for this specific geometry.

In contrast, although the composition-derived value for linear retardance δ of the turbid phantom is larger ($\delta \sim 1.386$ rad) than that for the clear phantom ($\delta_0 \sim 1.345$ rad), it is significantly *lower* than that expected for accumulated photon path length (1.574). This has been shown to arise due the curved zig-zag propagation paths for a group of multiply scattered photon population. Since components of such curved photon paths are directed along the linear birefringence axis, this leads to a reduction in the apparent δ [44, 81].

The uncertainties (standard deviations) in the differential matrix-derived polarization parameters, $\Delta\delta^{\text{log-}M}$, $\Delta\psi^{\text{log-}M}$ (derived from the elements of the $\boldsymbol{L}_{\mathbf{u}}$ matrix), also warrant a brief comment. The uncertainty in linear retardance ($\Delta\delta^{\text{log-}M}$) arises both due to strong depolarization present in this turbid phantom and due to the random orientation effects of linear birefringence (as observed by different sub-population of photons undergoing zig-zag paths in the medium). Since the latter effect does not influence the value for optical rotation, the resulting uncertainty $\Delta\psi^{\text{log-}M}$ is also considerably lower as compared to $\Delta\delta^{\text{log-}M}$. In general, the standard deviations in the polarization parameters contain useful information on the randomness of the medium and are also additionally influenced by the choice of the detection geometry, as described below.

The representative experimental results from complex tissue-like turbid media presented above (and continuing validation studies on several other phantoms exhibiting varying birefringence, optical activity, and depolarization effects) demonstrate that the intrinsic polarization parameters of such medium can be *self-consistently* extracted using either the logarithmic decomposition or the polar decomposition approach. One should note, however, that the illustrative results discussed above are based on Mueller matrices recorded in the forward detection geometry but the extension of this approach to backward detection geometry (which is well-suited for *in-situ* measurements) is warranted and has also been validated [82].

While the latter geometry is important for conceptual and practical reasons, it offers additional technical hurdles; notably, the polarization parameters associated with the intrinsic polarimetric properties of the sample in question can be difficult to infer since they are more strongly coupled with the scattering-induced artifacts. In fact, it has been shown that the scattering-induced artifacts gets considerably reduced for detection positions located at distances larger than a transport length away from the point of illumination ($r > l^*$). Thus, one possible method to measure polarization parameters from a turbid medium using backward detection geometry is to perform measurements at a distance larger than a transport length l^* away from the point of illumination [82].

It must, however, be noted that in the backscattering geometry, the reduction in apparent linear retardance δ due to the effect of the curved-propagation path is more prominent as compared to forward scattering geometry [44, 82]. Moreover, the apparent optical rotation Ψ in this geometry also gets considerably reduced due to the contribution of optical rotation of different handedness from two distinct subgroups of photons; while photons undergoing a series of forward scattering events to eventually emerge in the backward direction result in accumulated Ψ value, subgroups of photons that suffer scattering in the backward hemisphere only (backscattered photons) changes the handedness of rotation, leading to cancellation of net optical rotation [82]. For analogous reasons, the uncertainties in the differential matrix-derived linear retardance and optical rotation parameters ($\Delta\delta^{\text{log-}M}$, $\Delta\psi^{\text{log-}M}$) are also considerably larger in the backward detection geometry as compared to forward detection geometry [44].

Note that the phantoms described above do not exhibit any intrinsic diattenuation effect. Even though the magnitude of intrinsic diattenuation (dichroism) is typically very weak in most tissues, the effect of nonzero diattenuation effect is also worth a mention. As discussed in Section 7.2.3, in context to the forward and reverse polar decompositions, presence of layered tissue structures (interfaces) may yield significant diattenuation value, due to the different polarization response of the Fresnel reflection/transmission coefficients. For such tissues (e.g., skin), the diattenuation effect may not exhibit in a distributed manner (unlike depolarization or birefringence, which are typically exhibited from the bulk of tissue), rather may be exhibited in a sequential fashion. Since in the framework of the logarithmic decomposition (or in the differential matrix formalism), all the elementary polarization and depolarization properties of the medium are represented simultaneously, use of the logarithmic decomposition in such situation may lead to deviations in the extracted polarization parameters from those using polar decomposition. Moreover, in such case, either of the forward or the reverse decomposition may turn out to be advantageous depending upon the actual sequence of occurrence of the constituent polarization properties (as demonstrated with illustrative example in Fig. 7.6).

For most of the tissues exhibiting volumetrically distributed scattering and polarization effects, on the other hand, the logarithmic decomposition is expected to be more suitable. Thus, one must exercise caution in applying the different decomposition processes for tissue polarimetry characterization, a judicial choice of which (based on the experimental detection geometry and *a priori* estimate of the tissue morphology) may lead to realistic estimation of the intrinsic tissue polarization characteristics.

7.4.3 Summary

This part was devoted to the theoretical modeling of the propagation of polarized light in tissues. We first summarized the well-established methods for *forward modeling*, that is, the determination of the polarimetric response of well-known samples. Once adequate methods are available for forward modeling, the main issue to be addressed in practice is the inverse problem, that is, the interpretation of measured polarimetric responses of unknown samples.

As the main characteristic of biological tissues is predominantly their depolarizing power, which is related to multiple scattering, in first approximations most tissues can be modeled as suspensions of spherical scatterers in optically isotropic media. In such systems light propagation in multiple scattering regime may be conveniently described by the photon diffusion formalism, which provides simple analytical approximations for the DOP of the emerging light as function of the absorption and scattering coefficients μ_s and μ_a and the scattering anisotropy g, which, in turn, depend on the size and the index of the scatterers. Virtually all tissues exhibit larger depolarization for circular than linear incident polarization, as expected for scatterers much smaller than the light wavelength (Rayleigh regime) or with low index contrast (Rayleigh Gans regime). Beyond simple analytical approximations, the polarimetric response of suspensions of scatterers can be evaluated by Monte Carlo (MC) simulations, provided the scatterers are not too closely packed, so that the light propagation in such suspensions can be considered as a sequence of "isolated" scattering events. MC method requires extensive computations, but it can fully take into account the actual geometry of the experiment, overall yielding accurate results. This accuracy has been experimentally tested on tissue phantoms exhibiting very complex polarimetric responses, including linear and circular birefringences as well as depolarization due to scattering.

These phantoms were also used to tackle the problem of inverse polarimetric analysis, by using the decomposition procedures outlined in Section 7.2.3. The logarithmic decomposition is expected to be the most accurate, as in the studied phantoms all polarimetric effects occur simultaneously and not sequentially, as assumed in the "three factor" forward and reverse polar decompositions. However, polar (forward) decomposition provides surprisingly good results, a finding which is yet to be fully understood. The logarithmic decomposition also allows to quantify the effect of increased photon path length in the evaluation of the phantom birefringence. Moreover, these phantom studies provide a good grasp of the dependence of the sample polarimetric response on the measurement geometry, which can act as a potentially misleading "artifact" if not properly taken into account.

In summary, the theoretical "toolbox" for the interpretation of polarimetric measurements, while not absolutely complete, seems sufficient for most practical investigations as those illustrated in the next part.

7.5 APPLICATIONS

In this section, we present some illustrative examples of selected polarimetry applications in biomedicine, both for optical imaging and tissue characterization applications.

7.5.1 Polarization-Gated Surface and Subsurface Imaging

Light polarization can be used as a *gating mechanism* able to separate the photons which have been deeply scattered in the bulk of the sample from those which remained close to the surface: the former are generally depolarized while the latter typically retain a significant part of their initial polarization. As a result, if an image (or a spectrum) $I_\perp$ is taken on with polarization orthogonal to that of the incident photons, the contribution of the deeply scattered photons is largely dominant. The contribution of the depolarized photons is also present in the image I_{II} taken with the same polarization as the incident light. As a result, the images $I_\perp$ and $I_{\text{pol}} = I_{II} - I_\perp$ are dominated by the "deep" or "superficial" contributions, respectively [83]. The penetration depth corresponding to the "superficial" contribution may be as small as a few mean free paths [84]. Spectral filtering may be added to polarization to further enhance the discrimination between "surface" and "bulk" contributions [85]. It is thus possible to get valuable information about the surface and bulk properties the tissue under study by taking only two orthogonally polarized image (or spectra). The use of linear polarizations discussed above can of course be generalized to orthogonal circular polarizations as well. Moreover, in order to enhance the polarimetric response, the polarized image I_{pol} can be normalized by the total intensity, to provide the OSC

$$I_{\text{OSC}} = \frac{I_{\text{II}} - I_{\perp}}{I_{\text{II}} + I_{\perp}}. \tag{7.89}$$

Polarized imaging has been used, among other applications, in dermatology, to enhance the typically subtle visual contrasts differentiating various types of tissues. Early skin fibrosis of a thymic nude mice induced by X-ray irradiation was revealed by polarized imaging and suitable image analysis, while remaining undetectable by ordinary intensity imaging [85]. A variety of pigmented and nonpigmented skin abnormalities were studied by means of this technique by Jacques and coworkers [87], as illustrated in Figure 7.19. Polarized imaging revealed the disruption of the normal skin structure (collagen organization) due to cancerous lesions such as malignant basal cell carcinomas, suggesting a promising route to improve the definition of the excision margins in surgery [88].

The polarization gating schemes described above have also been exploited for depth selective spectroscopic measurements in tissue, which can improve the diagnostic efficacy of the spectroscopic approaches (elastic scattering [89, 90], fluorescence [91], and Raman spectroscopy [92]). As noted above, the underlying principle is similar: the photons which are scattered (or re-emitted) from deeper tissue layers undergo multiple scattering events and are depolarized to a larger extent. Polarization gating thus effectively selects photons which have not traveled beyond a few scattering mean free paths (mpf $= l^{-1} \sim 100\ \mu\text{m}$ in typical tissues).

Polarization-resolved spectroscopic approaches are thus expected to be particularly suitable for early detection of epithelial cancers (where the majority of human malignancies originate). Several illustrative examples demonstrate this approach. For instance, the polarization preserving component (from superficial tissue layers) extracted using polarization gating exhibited a fine structure component that was periodic in wavelength [89]. This was identified as being due to light that is Mie scattered by surface epithelial cell nuclei. By analyzing the amplitude and frequency of this signal using Mie theory, the size distribution and the refractive index of the nuclei was calculated. Since the size (and distribution) and refractive index of epithelial cell nuclei are valuable parameters for detecting precancerous changes, this technique holds promise for *in situ* and early diagnosis of epithelial cancer [93]. In addition to the fine structure component, the polarization-gated elastic scattering signal also showed inverse power law spectral dependence [90]. This was related to the self-similar (fractal) nature of microscale fluctuations of local refractive index in tissue. This was modeled using Fractal-Born approximation of light scattering to yield the fractal micro-optical parameters, namely, the fractal dimension and the fractal upper scale, which were also related to the pathological status of the examined tissue [90].

Polarization-gated fluorescence spectroscopic measurements have also been explored for improving diagnostic efficacy of fluorescence-based methods [91, 94]. Specifically, polarization-gated fluorescence measurements have been successfully

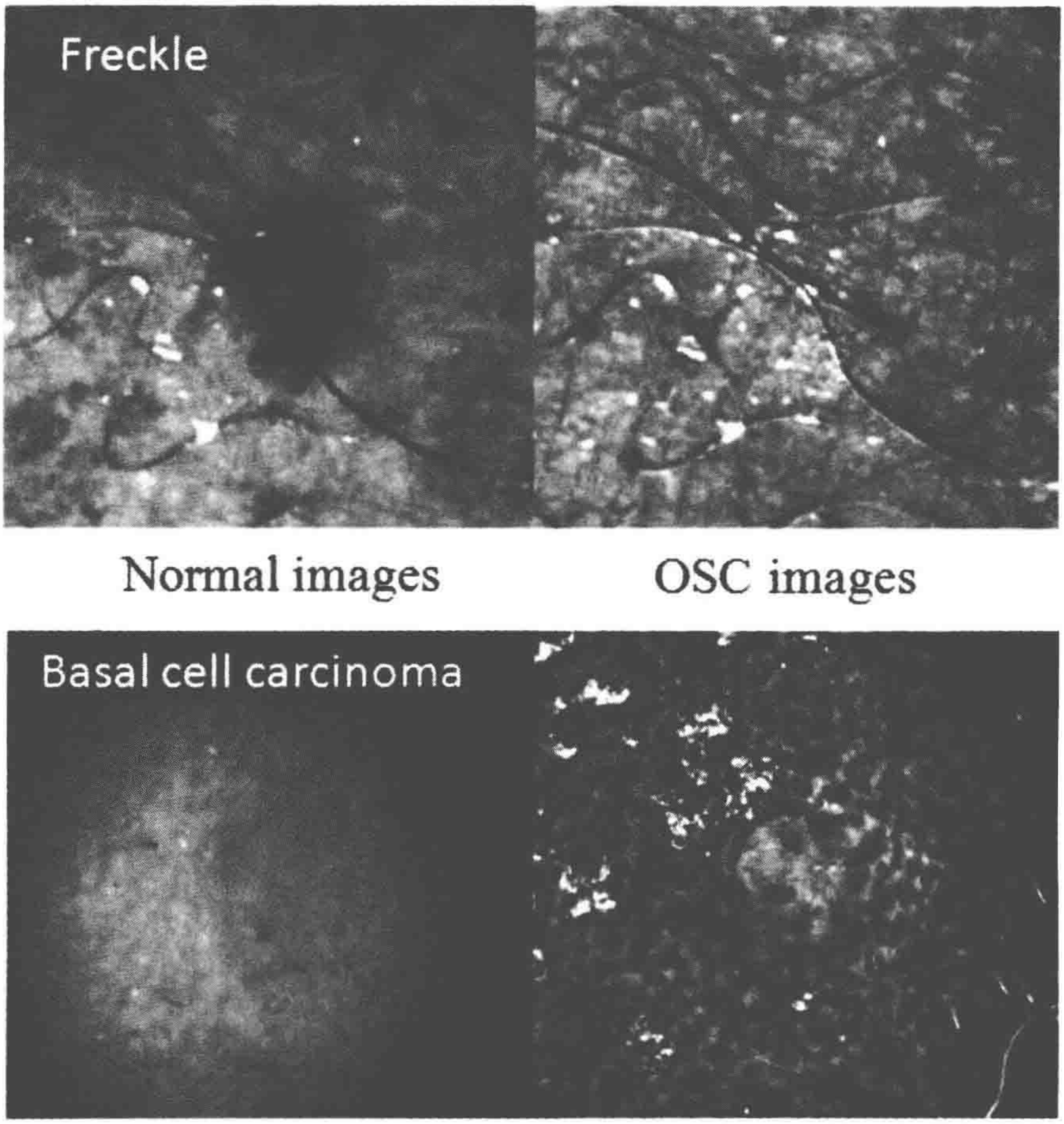

FIGURE 7.19 Normal intensity images and OSC images of a pigmented skin lesion (a freckle, top) and nonpigmented one (malignant basal cell carcinoma, bottom). The normalization by the total intensity in the OSC procedure is clearly very efficient in removing the effects of pigmentation in the polarimetric contrast. Adapted from Reference 87.

exploited to decouple, isolate, and quantify fluorescence contributions from tissue layers. Note that fluorescence signal from layered epithelial tissues, detected with conventional measurement technique (and similar to diffuse reflectance studies), is due to contributions from different endogenous fluorophores (having different quantum yields, lifetimes, and overlapping spectral line shapes) present in the superficial epithelial layer and the underlying connective tissue (stroma). Depth-resolved fluorescence measurement facilitated by the polarization gating should thus help improve contrast in the autofluorescence from malignant and normal sites. Similar strategy on polarization-resolved measurements has also been exploited for depth-resolved Raman spectroscopic measurements in layered epithelial tissues [92].

7.5.2 Tissue Assessment with Mueller Polarimetry

The OSC technique outlined above can provide quantitative and useful information primarily if the sample is a pure (linear and/or circular) depolarizer. In more complex cases of practical interest, the tissue may exhibit, in addition to depolarization, linear and possibly circular birefringence. If so, complete polarimetric characterization likely requires full Mueller matrix polarimetry, typically followed by an analysis based on the decompositions outlined in Section 7.2.3 and an interpretation of the polarimetric properties obtained by this procedure.

7.5.2.1 Noninvasive Glucometry Glucose is an optically active (chiral) molecule, and its structural asymmetry imposes a unique "fingerprint" on polarized light that interacts with it. For example, the plane of polarization of linearly polarized light is rotated upon passage through a glucose solution, by an amount proportional to the light interaction length, its concentration, and its wavelength-dependent rotatory power (a known quantity). As such, the glucose concentration in *clear* media can be easily determined by polarimetric measurements of optical rotation (this is routinely done, for example in biochemical laboratories and in the food industry). Can a similar polarized light approach be used in biomedicine, for example to noninvasively determine blood glucose levels in diabetic patients? If yes, this would represent a tremendous advance, as noninvasive glucose sensing remains arguably one of the most pressing unsolved problems in clinical medicine. Numerous approaches have been and are being actively explored to address this difficult challenge [61, 95].

Unfortunately, the polarimetric approach for biomedical glucometry is also fraught with difficulties. Unlike its "easy" transparent media counterpart, light propagating in tissue does not have a unique interaction length which is needed to convert measured optical rotation to glucose concentration; other dominant and complex tissue effects such as multiple scattering and inhomogeneous birefringence depolarize the light and alter its polarization properties (including causing chirality-unrelated apparent rotation of its linear polarized fraction); the glucose chirality effects are rather weak (owing to the low physiologic levels of blood glucose, in the range of 3–30 mM, or ~0.5–5 g L^{-1} of blood, yielding optical rotations in the millidegree range); other chiral molecules present in tissue mask the already-weak glucose signal, and so on. Nevertheless, we and others have performed careful fundamental feasibility studies toward polarimetric tissue glucometry, as briefly summarized below.

Figure 7.20 shows millidegree-level optical rotations ψ induced by physiological (millimolar) glucose concentrations in a 1-cm-thick polystyrene microsphere scattering phantom ($\mu_s \sim 30$ cm^{-1}) [61]. This study was performed with a sensitive polarimetric system that utilized polarization modulation and synchronous detection similar to Figure 7.12 but with a dual balanced photodetector approach, optimized to measure weak polarization signals in largely depolarized background. The results shown are for the forward-direction transmission geometry, with the rotations calculated from the determined Stokes vectors via $\psi = 0.5\tan^{-1}(u/q)$. The forward transmission direction was selected to enable direct results interpretation (path length $\geq$ cuvette thickness, rotation directly proportional to glucose concentration) and to

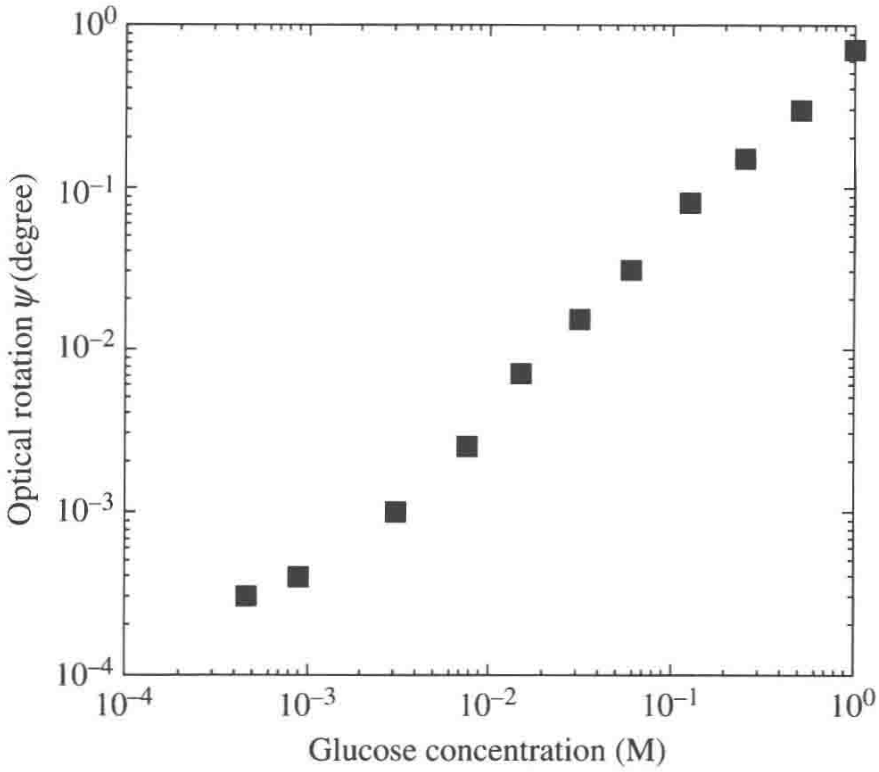

FIGURE 7.20 Logarithmic plot of experimentally determined optical rotation as a function of glucose concentration in scattering media (1.4 μm diameter polystyrene microspheres in water, $\mu_s \sim 28\ \text{cm}^{-1}$) down to physiological glucose levels. Measurements were performed using forward detection geometry ($\gamma = 0°$ in Fig. 7.12) through 1 cm of turbid media in a quartz cuvette. Adapted from Reference 61.

minimize rotation artifacts unrelated to chirality (e.g., scattering-induced apparent rotation, see Figure 7.21). The drawback of the transmission geometry is severe depolarization, limiting polarimetric measurements to 2–3 mm thicknesses of tissue [61]; this is why the scattering coefficient for this study in 1-cm-thick cuvette was lowered to ~30% of typical tissue levels ($\sim 100\ \text{cm}^{-1}$). Nevertheless, this preliminary study shows the polarimetric potential for measuring physiological glucose levels in tissue-like scattering media.

Backward detection geometry in reflection mode is more convenient for practical tissue applications, yet the chirality-unrelated optical rotation artifacts can be severe [82]. A method to suppress these artifacts is thus essential, and the Mueller matrix polar decomposition methodology can be used to advantage here. Figure 7.21 shows the variations in the scattering-induced apparent rotation and in the chirality-induced true optical rotation as a function of offset distance from the point of illumination, in the backscattering direction [3, 82]. As seen, the scattering rotation artifact can be nearly an order of magnitude larger than the small chirality effect, completely dominating and masking the presence of glucose. The polar decomposition reveals that the scattering rotation does not arise due to intrinsic chirality of the medium, rather is due to the scattering-induced linear diattenuation effect (also shown in the figure). Importantly, polar decomposition can effectively separate out these two differently sized contributions, revealing the glucose signal in this important yet artifact-prone

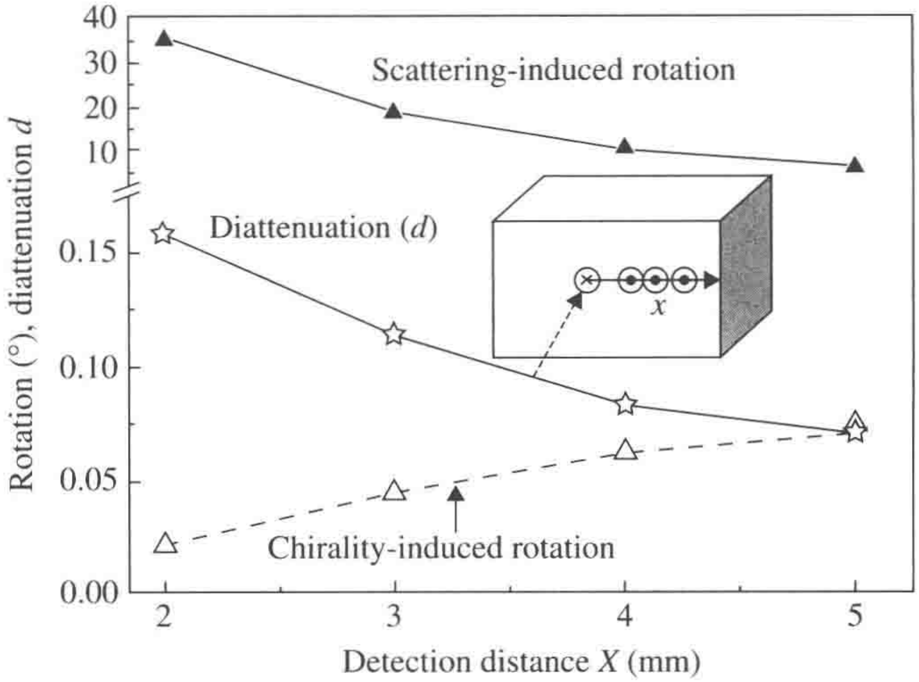

FIGURE 7.21 Optical rotation (ψ), derived from the decomposition of Monte Carlo-generated Mueller matrices (open triangles), of backscattered light as a function of distance from the center of the incident beam impinging on a chiral ($\chi = 0.082°\ \mathrm{cm}^{-1}$, corresponding to 100 mM concentration of glucose) isotropic turbid medium ($\mu_s = 30\ \mathrm{cm}^{-1}$, $g = 0.95$, thickness = 1 cm). The solid triangles represent the corresponding scattering-induced rotation of the polarization vector, derived from the Stokes parameters of the scattered light (for incident polarization state $S = (1,0,1,0)^T$). Also shown (open stars) is the apparent diattenuation which seems to be responsible for the scattering-induced rotation artifact. The inset shows the backward detection geometry. The chirality-induced rotation approaches zero as the detection angle approaches the exact backscattering detection ($\chi = 0^\circ\ \mathrm{cm}^{-1}$, data not shown). The symbols represent Monte Carlo and decomposition-derived data points and the lines serve to guide the eye. Adapted from References 3 and 82.

detection geometry. Despite the highly preliminary nature of this study—the complicating effects of other chiral confounders, experimental validation of these Monte Carlo simulations results, signal changes due to varying optical absorption, and other complexities yet to be evaluated—this does suggest a method to tease out small glucose specific signals in highly scattering tissues. In combination with Monte Carlo-determined path length distributions, we are currently investigating spectroscopic polarimetry coupled with chemometric regression analysis to isolate glucose rotations from contributions of other chiral confounders [96]. Further, given the extremely challenging nature of the noninvasive glucometry problem, it is worthwhile to consider hybrid approaches; that is, combining spectral turbid polarimetry with another diagnostic modality (e.g., spectral diffuse reflectance, Raman, photoacoustics) by carefully drawing on each technique's complementary strengths in isolating small tissue glucose signals.

7.5.2.2 Cancer Diagnosis Smith et al. [63] demonstrated the potential of full Mueller polarimetric imaging in dermatology by studying various tissue abnormalities. Melanomas exhibited *reduced depolarization power* with respect to surrounding healthy tissue; as shown in several other studies, this trend seems to be quite general when comparing healthy and (pre)cancerous tissues. No such effect was observed on benign lesions, or in lupus lesions, which, however, exhibited slightly reduced retardance, whose slow and fast axes showed rapid spatial variation across the lesions.

Polar decomposition of Mueller matrices has also been evaluated for the diagnosis of oral precancer [97]. Precancers induced in cheek pouches of hamsters were imaged *in vivo* and then analyzed histologically. Again, the precancerous tissues were characterized by reduced depolarization and retardance with respect to surrounding healthy tissue.

Ex vivo colon samples have been studied by Pierangelo et al. [98, 99] with multispectral Mueller polarimetry. In contrast with the previous examples, these samples did not exhibit any significant retardance nor diattenuation. The polarimetric information was thus provided mostly by the depolarization power throughout the visible spectrum (from 500 to 700 nm). Depolarization was found to increase with increasing wavelength from the green to the red part of the spectrum. This general trend is due to decreasing absorption, which thus increases the average number of scattering events photons suffer before being detected and results in higher polarization scrambling/loss. Moreover, depolarization varied significantly with the degree of tumor penetration within the colon structure. At the beginning (stage T1), the tumor is confined to the most internal superficial layers (the mucosa and submucosa). Then at stage T2, it gets *ulcerated* (its thickness decreases by eliminating the "top" layers of cancerous tissue while the tumor attacks the underlying layer (the muscularis)). At stage T3, the tumor reaches the outermost layer (the serosa or pericolic tissue) and eventually perforates it (stage T4).

Figure 7.22 shows an example of depolarization images of a colon with a cancerous lesion, together with the corresponding histologic pathology analysis. Using the healthy region (H) at the left of the figure as a reference, the burgeoning part B (graded histologically as T1) is less depolarizing, in agreement with the previous examples. However, at inner regions of the lesion (point 2, stage T2), depolarization increases again, and even more so in the innermost region (stage T3). In the lowest part of the figure, the sample is "folded," showing directly pericolic tissue, which appears to be extremely depolarizing (probably due to its very weak absorption, as this tissue is essentially fat, with very low hemoglobin concentration). Thus the non-monotonic behavior of depolarization with the disease progression may be attributed to the influence of the pericolic tissue, which increases when ulceration progresses, making the tissue more and more depolarizing after the initial depolarization decrease observed at the initial burgeoning stage.

In spite of its complicated non-monotonic behavior, the depolarization contrast might be used as a diagnostic tool to provide a quick tumor staging, a possibility which would be particularly useful if polarimetric imaging could be implemented endoscopically.

In addition to tumor detection and staging, polarimetric imaging might also be useful for the follow-up of radiochemotherapy (RC) of locally advanced cancers [99].

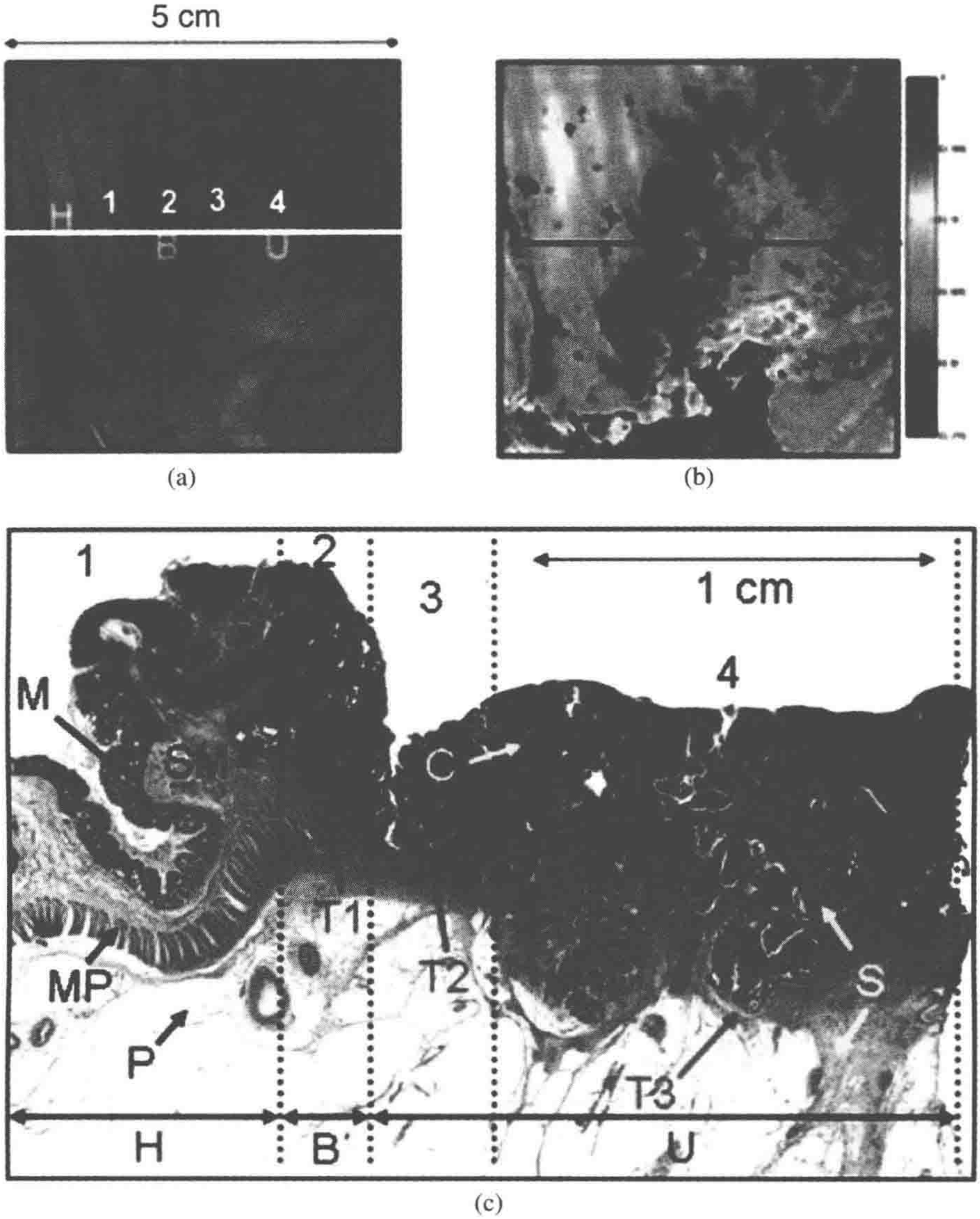

(a)

(b)

(c)

FIGURE 7.22 (a) Photo of the colon sample, with healthy (H) tissue, burgeoning (B) and ulcerated (U) cancerous regions. (b) Depolarization image (values given by the color bar from 0 (blue) to 1 (red)) of the same sample. The solid line indicates the depth cut which has been studied histologically. In this cut, shown in panel, (c), the regions marked 1 (healthy), 2 (burgeoning), 3 and 4 (ulcerated) are seen, together with the staging of the lesions, from T1 to T3. The different layers are identified by M (mucosa), SM (submucosa), MP (muscularis), and P (pericolic tissue, or serosa). (S) and (C) designate stromal and cancerous tissues, characterized by low and high cell densities, respectively. Adapted from Reference 99. (*For a color version of this figure, see the color plate section.*)

We studied three mesorectum samples excised after neoadjuvant radiochemotherapy. For T3 to T4 lesions, with or without regional metastatic lymph nodes, such neoadjuvant procedures are known to make surgery easier and to reduce the probability of relapse [100]. The patients were irradiated with standard doses (~50 Gy) and operated 6 weeks later. For the three samples, the "footprints" of the initial tumors exhibited polarimetric contrasts (compared to healthy regions) which could be correlated with the degree of cancer regression after RC. Further, tumor depolarization appeared lower than that of surrounding healthy tissue, even though the residual tumor volume fraction/cellular tumor compartment was estimated from pathology to be only a few percent. Such high polarimetric sensitivity suggests that it is not the tumoral (cellular) tissue itself which is detected, but more probably the difference in the fibrous collagen structure induced by the presence of cancer cells (as further discussed below).

Another topic of potentially addressable by tissue polarimetry is the diagnosis of uterine cervical cancer. This disease, due to infection by Human Papilloma Virus (HPV), begins with precancerous lesions confined within the epithelium and classified as CIN1, CIN2 or CIN3 (acronym for Cervical Intraepithelial Neoplasia) when anomalous cells invade the lowest third, two-thirds, or the entire epithelium thickness. If not treated, CIN3 lesions eventually disrupt the epithelium basal membrane and evolve into potentially lethal invasive cancer. This evolution is very slow, with 5–10 years typically elapsing from the initial infection to the onset of invasive cancer. As with many cancers, the disease can be cured very effectively by surgically removing the anomalous regions on the cervix. Thus it is of paramount importance to screen female populations to enable early disease detection, and to localize the pathological regions as accurately as possible.

In developed countries, the first screening step is the Pap smear, which consists of a cytologic examination of the cells collected from the cervix. If these cells seem anomalous (typically exhibit large nuclei), the patient then undergoes a detailed examination of the cervix by means of a colposope (long working distance microscope) to localize the CIN lesions, take biopsies and eventually decide a treatment course. However, colposcopy is a notoriously difficult and operator-dependent examination, with relatively poor performance [101]. There are thus many surgeries performed without real necessity, or with incorrect surgical margins relative to the true extend on the tumor. Conversely, essentially no screening is proposed in developing countries (systematic Pap smears would require too many pathologists to examine the samples). Thus this disease kills ~275,000 women worldwide every year, the vast majority of which could have been saved by a simple and accurate surgery. Clearly then, useful alternatives to the Pap smear, possibly by simple optical means, are very much needed to solve this outstanding public health problem [102]. In this respect, a large amount of work has been performed on fluorescence / reflectance cervical imaging by several groups, including those led by Richards Kortum, Follen, and MacAuley [102, 103]. A meta-study, carried out by these researcher and others and based on 26 clinical studies [103], concluded that these methods offered similar performance as colposcopy, and may thus be used as adjuncts. For resource limited countries, particularly simple and low-cost techniques, such as VIA (Visual Inspection with Acetic acid, which is basically a colposcopic examination with the naked eye or a standard color camera) have also been evaluated and showed good potential, in spite of rather low sensitivity, of the order of 30% [104]. To summarize, significant progress is still needed in the management of cervical cancer, especially in low resource countries.

Polarimetric imaging is also a promising approach in addressing this topic [64]. Several samples have been imaged *ex vivo* by using the polarimeter shown in Figure 7.13 of Section 7.3.3.3. Typical results, obtained from two samples, are shown in Figure 7.23. The first sample was healthy, while the second one contained a CIN3 zone and a benign lesion (an ectropion), where a layer of glandular tissue was seen (this tissue is normally present only in the endocervix). The pathology diagnosis was established according to the standard procedure: fixing the sample in formalin, cutting it into 4 mm thick blocks, embedding it in paraffin, shaving from the

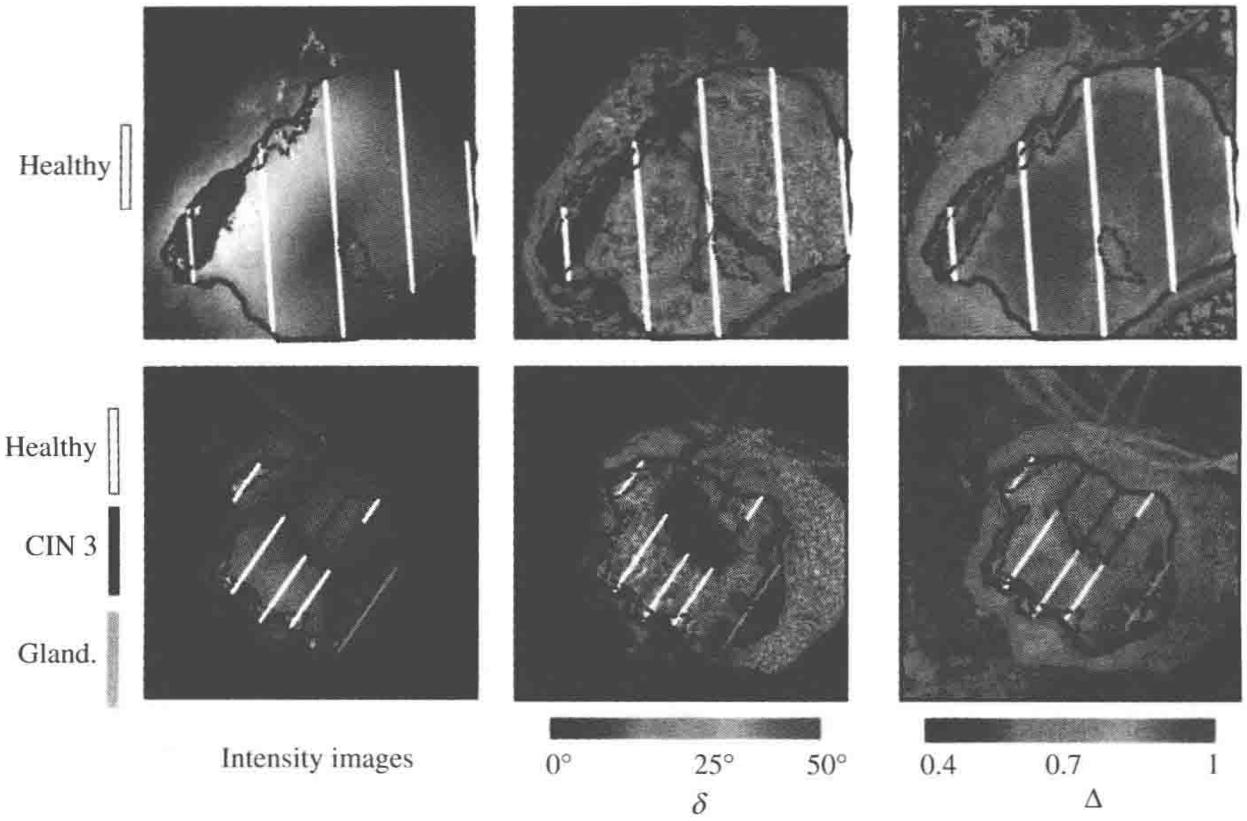

FIGURE 7.23 Images of two *ex vivo* cervix samples, one healthy (top) and the other one with a CIN3 zone and a benign lesion (visible glandular tissue) (bottom). Left column: raw intensity images. Middle column: images of scalar retardance δ, in color scale from 0° to 50°. Right column: images of depolarization Δ, from 0.4 to 1. Retardance and depolarization were obtained from raw Mueller images by standard Lu-Chipman decomposition procedure of the experimentally determined Mueller matrix images. On each sample, the solid black line shows the limit of the intact epithelium. The straight lines indicate the locations of the histological cuts where the pathology diagnostic was made (white for healthy, purple for CIN3, and orange for glandular tissue). The dashed black lines designate regions where at least one among the 16 raw intensity images was saturated due to tissue "glare." The top left image shows an example of such saturated region, shown in red. Obviously, polarimetric data in these regions are suspect. Adapted from Reference 64. (*For a color version of this figure, see the color plate section.*)

resulting "wax blocks" 5-μm-thick slices, deparaffinizing and staining them for microscopic examination. As a result, pathology diagnosis was established only along the "lines" shown in the intensity images (left column) of Figure 7.23; they are repeated in the corresponding polarimetrc images for landmarking and for correlation with microscopy-derived pathology grades. Viewing the ordinary intensity images in the left column, basically no difference was observable between the healthy and CIN3 tissues, while the glandular tissue was more reddish (and thus more absorbing at the operating wavelength, 550 nm).

The Mueller images were decomposed by the standard Lu-Chipman procedure, and the resulting scalar retardance and depolarization images are shown. The healthy sample is characterized by strong retardance almost everywhere, with predominantly tangential slow axis orientation (not shown). On the pathologic sample, there is a healthy region in the lower left part of the image, again characterized by a strong retardance, while both the CIN3 and the ectropion show essentially ~zero retardance. The depolarization is again very strong everywhere on the healthy sample, while on the other one it decreases from healthy to CIN3 to glandular regions.

Although these results (described more fully in [64]) must be substantiated with much more extensive studies, preliminary trends strongly suggest that uterine cervix tissue exhibits strong birefringence in its healthy regions, with birefringence disappearing at the very earliest stages of the precancerous evolution.

These observations are very promising in the context of an "automated" optical diagnosis of uterine cervical precancer (thus not requiring the often unavailable expertise of a medical specialist) and are substantiated by the results of other groups. For example, Shukla and Pradhan [105] have also studied histology of cervical samples and showed that the connective tissue beneath healthy epithelium exhibits significantly larger retardance values than that beneath precancerous epithelium. It is well known that precancerous evolution of epithelia modifies the structure of neighboring connective tissues via a decrease in size and concentration of collagen fibers [106]. Such modifications are probably the main reason of the observed disappearance of the tissue birefringence in abnormal regions of cervical tissues, and might in fact occur in other sites/clinical scenarios of interest for medical diagnostics.

7.5.2.3 Characterization of Structural Tissue Anisotropy and Applications Several studies have addressed tissue structural anisotropy monitoring using polarimetric techniques [3, 62, 107, 108]; the above discussions of colonic and cervical pathologies are particular examples of this approach in oncology. As mentioned, tissue structural anisotropy can stem from aligned orientations of tissue fibrillar components, such as collagen and elastin, actin-myosin fibers, and mineralized hydroxyapatite crystals [1]. Since such structural alignments often manifest as linear birefringence effects, quantification of linear birefringence may represent a sensitive metric for changes in tissue structure. A number of investigations have therefore addressed such polarization birefringence measurement for the detection of tissue abnormalities like osteoarthritis, thermal injury and cancer (e.g., basal and squamous cell carcinomas) [3, 62, 107, 108]. Measurement of complete Mueller matrix and its inverse analysis via the various decomposition approaches (outlined in Section 2.3) are clearly advantageous for this purpose because (*i*) the small birefringence alterations can be efficiently decoupled and quantified in presence of the other tissue polarimetry effects; (*ii*) the decomposition process yields additional tissue polarimetry metrics (e.g., diattenuation, depolarization, and potentially others not discussed above, such as retardance ellipticity), which provide useful complementary information thus generating a more complete picture of the complex biophysical alterations taking place in tissue. In the following, we offer two other cancer-unrelated illustrative examples of tissue structural anisotropy characterization with polarized light: bladder wall abnormalities and regenerative heart treatments.

Bladder is an example of internal organ whose structure and function engenders anisotropic tissue structure. Its purpose is to store and then expel urine, and its wall layers extend and then contract to allow this to happen. Microstructural remodeling in its epithelial layers is known to occur under mechanical distension and during various disease processes (e.g., bladder outlet obstruction). As a step toward developing a turbid polarimetry platform for human bladder pathology studies, we have recently obtained birefringence maps in normal *ex-vivo* distended rat bladders that demonstrate the differential response of different bladder regions (dome, ventral, and dorsal sides) to changes in filling pressure [109]. The results of Figure 7.24 were obtained under pressures that represent typical physiological ranges in normal rodent (and human) bladders; as we progress to examine pathological cases, the upper end of the pressure range will likely have to increase. As seen, the dome region of the bladder shows maximum birefringence when the bladder is distended to high pressures, whereas the ventral tissues remains roughly isotropic during distension. In addition, the average anisotropy direction is longitudinal, along the urethra to dome. Using the analysis in Section 7.2.3.1, we converted the retardance values (derived from polar decomposition) to birefringence by measuring the bladder wall thickness with an optical coherence tomography (OCT) system, and by estimating the average photon path length in this reflection geometry via our polarization-sensitive Monte Carlo model (Section 7.4.1.3). The derived wall anisotropy trends thus represent an intrinsic tissue property of its anisotropy/organization independent of thickness, to better aid in understanding the structure-functions relation in healthy bladders. These new insights into the wall microstructure anisotropy of *ex vivo* distending bladders may also help improve the functionality of the artificially engineered bladder tissues [110].

Myocardial muscle tissues exhibit high level of linear birefringence in its healthy state due to the aligned arrangement of cardiomyocytes and collagen fibers [111]. Following a heart attack, the structural anisotropy is expected to reduce due to structural remodeling, with cardiomyocyte atrophy and an increase in fibrotic collagen content (scar tissue). Various postinfarct therapies (e.g., stem cell tissue regeneration) aim to restore heart muscle towards its normal structure (by further structural remodeling), and more importantly restore some of its functional status. Mueller matrix measurement and its inverse analysis may serve as a sensitive probe the state of the myocardium after infarction and report on the success of regenerative treatments [111, 112]. In order to explore this possibility, Mueller matrices were recorded in the transmission geometry, from 1-mm-thick *ex vivo* myocardial samples from

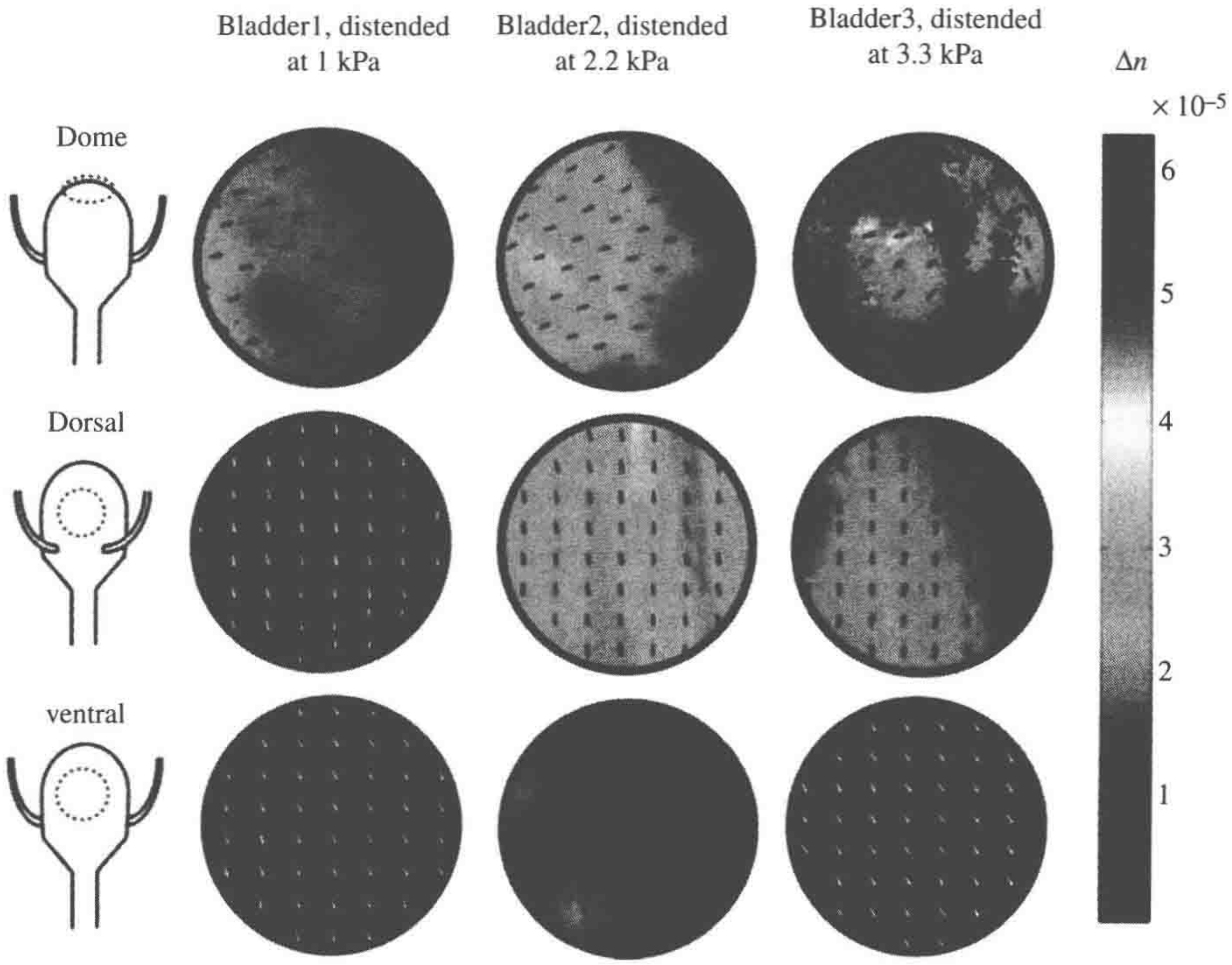
Bladder1, distended at 1 kPa
Bladder2, distended at 2.2 kPa
Bladder3, distended at 3.3 kPa
Δn
× 10⁻⁵
6
5
4
3
2
1
Dome
Dorsal
ventral

FIGURE 7.24 Variation of the local birefringence of *ex vivo* rat bladder tissue with pressure. The left, middle, and right columns show the retardance images of three different regions of the organ (dome, dorsal, and ventral surfaces, as shown at the extreme left of the figure) for distending pressures equal to 1.0, 2.2, and 3.3 kPa, respectively. The field of view is 2 mm in diameter. The images were taken in backscattering geometry, at 25° from the exact backscattering direction, and processed by the polar decomposition (see Section 7.2.3.1) to extract the retardance parameters, namely the scalar retardance and the anisotropy orientation, the latter being shown by arrows. The tissue birefringence, shown in the color bar scale of Δn at the extreme right, was calculated from the scalar retardance and the tissue effective thickness. This thickness was derived from OCT measurements and evaluation of the average path length of the photon trajectories due to the multiple scattering events by Monte Carlo simulations. Note the maximum birefringence in the dome region upon maximum distension, and the overall longitudinal anisotropy orientation (along the urethra-dome axis). Adapted from Reference 108. (*For a color version of this figure, see the color plate section.*)

Lewis rats after myocardial infarction, both with and without stem cell treatments. Measurements were made using both the point measurement and imaging polarimetry systems. The point measurement system employed polarization modulation and synchronous lock-in detection (described in Section 7.3.3.2, Fig. 7.12). Imaging polarimetry employed dc measurements with the PSG-PSA–based approach (also discussed in Section 7.3) to construct the Mueller matrix. The Mueller matrices measured by either of these systems were analyzed via polar decomposition to obtain linear retardance (δ) values. The results are summarized in Figure 7.24.

The observed main features can be summarized as (i) the infarcted region of the untreated myocardium exhibits a large decrease in the magnitude of δ (Fig. 7.25b). In contrast, in the infarcted region after stem cell treatment an increase in δ toward the native levels is observed (Fig. 7.25b), indicating regrowth and reorganization/remodeling of the myocardium. (ii) The polarimetry images (Fig. 7.25c) from the same tissue also show similar retardance trends, although with some variations (due to difference in measurement geometry and spatial heterogeneity in tissue optics). The spatial variation of the retardance images (Fig. 7.25c) not only shows difference from infarct to normal, but within each region as well (the δ values are higher in the middle of the myocardial wall with gradual lower values toward the edges).

This variation through the myocardial wall is attributed to the change in orientation of the myocyte fibers through the wall [112]. Nevertheless, the increase in δ in the infarcted regions of the stem-cell treated hearts indicates reorganization and regrowth of the myocardium microstructure caused by therapeutic stem cell injection, as was subsequently confirmed by histology [112]. Note that other tissue polarimetry metrics that emerged from the Mueller matrix decomposition analysis, namely, diattenuation and depolarization, also yielded complementary and useful microstructural information (on the orientation/alignment of the myocyte fibers through the wall and their changes with infarction as well as with stem cell treatment) [44, 111, 112]. Moreover, a study with nonlinear microscopy (second harmonic generation, two-photon excited fluorescence) has also validated and complemented the polarimetry results, and yielded useful information on the underlying causes of the measured retardance signals, in the context of collagen versus cardiomyocytes components and their spatial organization. The details of these results have been published [44, 111, 112].

Although quantification of tissue structural anisotropy via polarimetry have shown considerable promise for a variety of applications involving tissue diagnosis and therapy monitoring, several technical and conceptual challenges in quantifying intrinsic tissue anisotropy still remain to be resolved [113, 114]. These include understanding the influence of complex three dimensionally oriented birefringent tissue structures, orientation-varying spatial domains or potentially non-uniaxial (biaxial) birefringent domains, on the measured Stokes vector or Mueller matrix elements; and development of methods to extract geometry-independent metrics of tissue anisotropy (intrinsic birefringence and its actual orientation). Recent studies have attempted to address these issues [109, 113–115]. For example, a sphere-cylinder scattering model has been adopted in polarization sensitive Monte Carlo simulations to forward model the effect of such complex microstructural architecture (skeletal muscle as representative birefringent tissue) on the Mueller matrix elemental images [114]. A dual projection polarimetry method (whereby the sample is imaged twice at different incident angles of the probing beam) in combination with Mueller matrix decomposition has also been developed to quantify true intrinsic magnitude and orientation angle of retardance from three dimensionally oriented birefringent structures [113]. After successful validation of this approach on birefringent spherical phantoms, the method has been explored for the measurement (imaging) of the anisotropy axis and its true magnitude in *ex-vivo* porcine myocardium tissue [113].

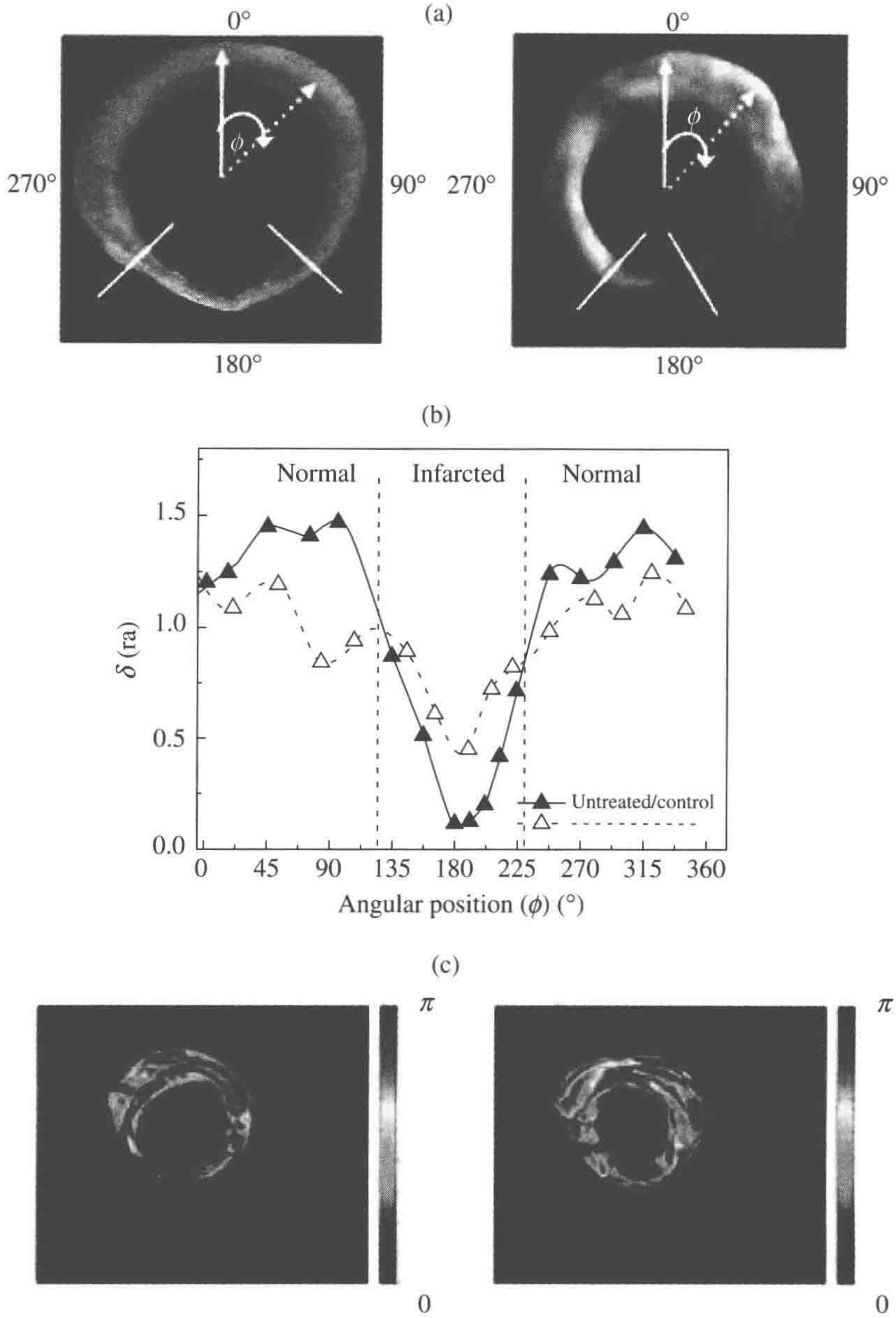

FIGURE 7.25 Linear retardance δ extracted from experimentally determined Mueller matrices (using the Mueller matrix polar decomposition analysis (Section 7.2.3) corresponding to 1-mm-thick tissue sections from Lewis rat hearts following myocardial infarction. (a) White-light photographs of untreated (left panel) and stem cell treated (right panel) tissue. (b) Mueller matrix-derived linear retardance (δ) values at different angular positions from the untreated (solid triangles) and treated (open triangles) samples. (c) The corresponding linear retardance (δ) images for the same tissue derived from imaging polarimetry measurements. Adapted from References 3 and 111.

7.5.3 Summary

In this section, we reviewed some examples of "real-world" applications of polarimetric imaging for biomedical purposes. In a first instance, polarization can be used as a gating mechanism, allowing to isolate nondepolarized contribution in scattered light to enhance single scattering signal coming from the most superficial tissue layers, which can be used for example to evaluate the size of the cell nuclei and differentiate healthy and cancerous tissues.

The multiply scattered contribution, which is usually dominant, typically exhibits strong depolarization. In the absence of other major polarimetric effects, this parameter can be easily evaluated by partial polarimetric techniques like OSC, which are relatively simple to implement in imaging systems and may prove very useful, for example in dermatology for assessment of the surgical margins for the removal of melanomas. Exploratory studies on colon samples suggest that simple OSC may also be sufficient for early detection and characterization cancerous polyps at various stages. At the earliest precancerous stages, depolarization decreases (this seems to be a quite general trend) while at more advanced stages, at least in colon, the depolarization variation is more complex due to increased contribution of the serosa, which is weakly absorbing and strongly depolarizing.

Conversely, many other samples of interest for medical applications, such as uterine cervix and oral cavity, may exhibit not only depolarization, but also linear and circular birefringence. If so, full Mueller polarimetry, with subsequent matrix decomposition, is needed to "disentangle" these effects to eventually provide relevant parameters for diagnostics. As a rule of thumb, precancerous evolution seems to be associated with a decrease of tissue birefringence and depolarizing power, but here too the detailed behavior may be more complex, at least for cervical tissue, due to the presence of two very different epithelia (malpighian and columnar). Further studies, involving tens or even hundreds of samples, are thus needed to fully assess the performance of polarimetric imaging for cancer detectionand staging.

Polarimetry is also promising in fields other than oncology. Noninvasive glucometry has been viewed as "holy grail" in diabetology for decades. The optical activity induced by glucose may prove relevant for this purpose, provided extremely weak rotations can be measured and isolated from artifacts. Highly sensitive Mueller polarimetry coupled with matrix decomposition has demonstrated the capability to extract optical rotations in the millidegree range induced by glucose at physiological levels in the presence of multiple scattering and strong geometry induced artifacts. However, the elimination of the contribution of optically active compounds other than glucose remains a formidable challenge.

Last but not least, polarimetry may also prove very useful for noninvasive characterization of many other anisotropic tissues, such as myocardial muscle, where birefringence seems to provide a very sensitive indicator of the tissue status (healthy or infarcted or regenerating) and for the follow-up of treatments like tissue reconstitution from stem cells. Preliminary studies on bladder wall tissue also show the relevance of polarimetric imaging for the study of biomechanical properties of tissues, in part aimed at improving tissue engineering for grafts.

All these examples clearly show the strong potential of polarimetry, both in imaging and nonimaging modes, for medical applications. However, large-scale studies are still needed for each application to fully assess the performance of the technique. Moreover, each application may require specialized developments, both in instrumentation and in data analysis.

7.6 CONCLUSIONS AND OUTLOOK

Biological tissues typically exhibit quite complex polarimetric responses, which may require sophisticated experimental and data treatment techniques to eventually provide relevant parameters for medical diagnostics and tissue assessment. This complexity is certainly the main reason why polarimetry has not yet been developed to its full potential. However, this field has been progressing very quickly in the past decade, holding the promise of great improvements in optical diagnostics for many diseases in various fields.

In almost all tissues, the incident beam is strongly scattered, with scattering path lengths on the order of $\sim 100\ \mu m$, leading to significant depolarization of the emerging light. The other polarimetric effects often present are linear retardation, due to possible tissue linear birefringence, and (generally weaker) optical activity (or circular retardation/birefringence). Adequate description of these effects requires the Stokes Mueller formalism, which is not so widely known in biophotonics. It is thus described in some detail in the first part of this chapter, including the currently available procedures of matrix decompositions, which are essential for polarimetric data analysis and constitute an active research field in themselves.

Polarimetric instrumentation is also rapidly evolving, based on the general principles and typical setups outlined in the second part. In this respect, it is worth emphasizing that polarimetry is intrinsically a low cost technique, which can be added to virtually any optical system, allowing operation at any chosen spatial scale, from microscopic to mesoscopic to macroscopic.

The interpretation of polarimetric data is also a challenging and active field. Forward modeling of the polarimetric responses of known systems can be realized by various approaches, from simple analytical models to numerically demanding Monte Carlo simulations. Forward modeling has provided considerable physical insight in the mechanisms of depolarization in suspensions of spherical scatterers in optically isotropic media. Other practically important properties, such as the effect of tissue linear and circular birefringence, are currently being actively explored.

While forward modeling is extremely useful to understand the basic mechanisms defining the polarimetric response of a given type of sample in a given measurement geometry, for optical diagnostics in principle one has to solve the *inverse problem*, that is to determine the tissue "nature" from the measured polarimetric data. Ideally, this should be achieved by fitting simulation based on a relevant multiparameter physical model of the tissue to the experimental data. The values of the physical parameters, such as scatterer densities, optical indexes, layer thicknesses, and the like, could then be "parametrically" mapped onto "conventional" (optical, histologic, etc.) images whose meaning is clear. Unfortunately this is seldom feasible, due to the difficulty of realistic and accurate tissue models (without relying on too many loosely determined "parameters"), and to the computational burden related to such fitting procedure. As a result, polarimetric data are usually interpreted in terms of the elementary polarimetric properties provided by matrix decompositions. For a number of samples and various pathologies, these properties exhibit interesting trends which may eventually provide highly relevant tissue assessment metrics related to underlying tissue biophysical properties. To this end, the current developments in Mueller matrix decomposition theory and polarimetric instrumentation advances must be pursued in concert with extensive *ex vivo* and *in vivo* cross-checking and validation studies.

So far, polarimetry has been limited to tissues accessible to direct imaging, and many possibilities, such as polarimetry-guided surgery, have still to be explored within this parameter space. But of course the scope of the polarimetric methodologies would be significantly broadened if it could be extended to endoscopic systems. Several research groups are at the forefront of this exciting polarimetric development [116–118].

To conclude, given the expanding range of medical applications and the current improvements in both experimental setups and data analysis procedures, the medium-term and long-term future of tissue polarimetry appear very promising.

REFERENCES

[1] V. V. Tuchin, L. Wang, and D. À. Zimnyakov, *Optical Polarization in Biomedical Applications* (Springer, New York, 2006).

[2] L. V. Wang, G. L Coté, and S. L. Jacques, "Special section guest editorial: tissue polarimetry," *J. Biomed. Opt.* **7**, 278 (2002).

[3] N. Ghosh and I. A. Vitkin, "Tissue polarimetry: concepts, challenges, applications and outlook," *J. Biomed. Opt.* **16**, 110801 (2011).

[4] S. L. Jacques, "Polarized light imaging of biological tissues" in *Handbook of Biomedical Optics*, edited by D. Boas and N. Ramanujam (CRC Press, 2011).

[5] R. C. Jones, "A new calculus for the treatment of optical systems," *J. Opt. Soc. Am.* **31**, 488–493 (and following papers in the same issue) (1941).

[6] E. Collett, *Polarized Light: Fundamentals and Applications* (Marcel Dekker Inc., New York, 1990).

[7] D. S. Kliger, J. W. Lewis, and C. E. Randall, *Polarized Light in Optics and Spectroscopy* (Academic Press–Harcourt Brace Jovanovich, New York, 1990).

[8] J. W. Goodman, "Statistical Properties of Laser Speckle Patterns", in *Laser Speckle and Related Phenomena, Vol. 9, Topics in Applied Physics*, edited by J. C. Dainty (Springer, Berlin, Heidelberg, New York, Tokyo, 1984).

[9] G. G. Stokes, "On the composition and resolution of streams of polarized light from different sources," *Trans. Cambridge Phil. Soc.* **9**, 339–416 (1852).

[10] S. Huard, *The Polarization of Light* (John Wiley & Sons, New York, 1997).

[11] R. A. Chipman, "Polarimetry," in *Handbook of Optics*, 2nd ed., edited by M. Bass (McGraw-Hill, New York, 1994), Vol. 2, Chap. 22, pp. 22.1–22.37.

[12] D. Goldstein, *Polarized Light* (Marcel Dekker, New York, 2003).

[13] B. N. Simon, S. Simon, F. Gori, M. Santarsiero, R. Borghi, N. Mukunda, and R. Simon, "Nonquantum entanglement resolves a basic issue in polarization optics," *Phys. Rev. Lett.* **104**, 023901 (2010).

[14] E. Wolf, "Unified theory of coherence and polarization of random electromagnetic beams," *Phys. Lett. A* **312**, 263–267 (2003).

[15] G. Milione, H. I. Sztul, D. A. Nolan, and R. R. Alfano, "Higher-order Poincaré sphere, stokes parameters, and the angular momentum of light," *Phys. Rev. Lett.* **107**, 053601 (2011).

[16] G. Milione, S. Evans, D. A. Nolan, and R. R. Alfano, "Higher order Pancharatnam-Berry phase and the angular momentum of light," *Phys. Rev. Lett.* **108**, 190401 (2012).

[17] L. Marrucci, E. Karimi, S. Slussarenko, B. Piccirillo, E. Santamato, E. Nagali, and Fabio Sciarrino, "Spin-to-orbital conversion of the angular momentum of light and its classical and quantum applications," *J. Opt.* **13**, 064001 (2011).

[18] H. Mueller, "The foundation of optics," *J. Opt. Soc. Am.* **38**, 551 (1948)

[19] J. J. Gil, "Characteristic properties of Mueller matrices," *J. Opt. Soc. Am. A* **17**, 328–334 (2000).

[20] S. R. Cloude, "Group theory and polarisation algebra," *Optik* **75**, 26 (1986).

[21] D. G. M. Anderson and R. Barakat, "Necessary and sufficient conditions for a Mueller matrix to be derivable from a Jones matrix," *J. Opt. Soc. Am. A* **11**, 2305 (1994).

[22] J. J. Gil and E. Bernabeu, "A depolarization criterion in Mueller matrices," *Opt. Act.* **32**, 259–261 (1985).

[23] M. Born and E. Wolf, *Principles of Optics* (Cambridge University Press, New York, 2002).

[24] S. Lu and R. A. Chipman, "Interpretation of Mueller matrices based on polar decomposition," *J. Opt. Soc. Am. A* **13**, 1106–1113 (1996).

[25] M. Xu and R. R. Alfano, "Random walk of polarized light in turbid media," *Phys. Rev. Lett.* **95**, 213901 (2005).

[26] R. Ossikovski, M. Anastasiadou, and A. de Martino, "Product decompositions of depolarizing Mueller matrices with negative determinants," *Opt. Commun.* **281**, 2406 (2008).

[27] S. P. Morgan and M. E. Ridgway, "Polarization properties of light backscattered from a two layer scattering medium," *Opt. Express* **7**, 395–402 (2000).

[28] A. H. Hielscher, A. A. Eick, J. R. Mourant, D. Shen, J. P. Freyer, and I. J. Bigio, "Diffuse backscattering Mueller matrices of highly scattering media," *Opt. Express* **1**, 441–453 (1997).

[29] V. Sankaran, J. T. Walsh Jr., and D. J. Maitland, "Comparative study of polarized light propagation in biologic tissues," *J. Biomed. Opt.* **7**, 300–306 (2002).

[30] M.-R Antonelli, A. Pierangelo, T. Novikova, P. Validire, A. Benali, B. Gayet, and A. De Martino, "Mueller matrix imaging of human colon tissuefor cancer diagnostics: how Monte Carlo modeling can help in the interpretation of experimental data," *Opt. Express* **18**, 10200–10208 (2010).

[31] M. Ahmad, S. Alali, A. Kim, M. F. G. Wood, M. Ikram, and I.A. Vitkin, "Do different turbid media with matched bulk optical properties also exhibit similar polarization properties ?" *Biomed. Opt. Express* **2**, 3248–3258 (2011).

[32] N. Ghosh, M. F. G. Wood, and I. A. Vitkin, "Influence of the order of the constituent basis matrices on the Mueller matrix decomposition derived polarization parameters in complex turbid media such as biological tissues," *Opt. Commun.* **283**, 1200–1208 (2010).

[33] J. Morio and F. Goudail, "Influence of the order of diattenuator, retarder, and polarizer in polar decomposition of Mueller matrices," *Opt. Lett.* **29**, 2234–2236 (2004).

[34] R. Ossikovski, A. De Martino, and S. Guyot, "Forward and reverse product decompositions of depolarizing Mueller matrices," *Opt. Lett.* **32**, 689 (2007).

[35] M. Anastasiadou, S. Ben Hatit, R. Ossikovski, S. Guyot, and A. de Martino, "Experimental validation of the reverse polar decomposition of depolarizing Mueller matrices," *J. Eur. Opt. Soc (JEOS) – Rapid Publ.* **2**, 07018 (2007).

[36] R. Ossikovski, M. Anastasiadou, S. Ben Hatit, E. Garcia-Caurel, and A. de Martino, "Depolarizing Mueller matrices: how to decompose them?" *Phys. Stat. Sol* (a) **205**, 720–727 (2008).

[37] R. Ossikovski, "Analysis of depolarizing Mueller matrices through a symmetric decomposition," *J. Opt. Soc. Am. A* **26**, 1109–1118 (2009)

[38] C. Fallet, A. Pierangelo, R. Ossikovski, and A. de Martino, "Experimental validation of the symmetric decomposition of Mueller matrices," *Opt. Express* **18**, 831–842, (2009).

[39] R. Ossikovski, C. Fallet, A. Pierangelo, and A. de Martino, "Experimental implementation and properties of Stokes nondiagonalizable depolarizing Mueller matrices," *Opt. Lett.* **34**, 974 (2009).

[40] R. Ossikovski, M. Foldyna, C. Fallet, and A. de Martino, "Experimental evidence for naturally occurring nondiagonal depolarizers," *Opt. Lett.* **34**, 2426–2428 (2009).

[41] R. Ossikovski, "Differential matrix formalism for depolarizing anisotropic media," *Opt. Lett.* **36**, 2330–2332 (2011).

[42] N. Ortega-Quijano and J. L. Arce-Diego, "Depolarizing differential Mueller matrices," *Opt. Lett.* **36**, 2429–2431 (2011).

[43] R. M. A. Azzam, "Propagation of partially polarized light through anisotropic media with or without depolarization: a differential 4 × 4 matrix calculus," *J. Opt. Soc. Am.* **68**, 1756–1767 (1978).

[44] S. Kumar, H. Purwar, R. Ossikovski, I. Alex Vitkin, and N. Ghosh, "Comparative study of differential matrix and extended polar decomposition formalisms for polarimetric characterization of complex tissue-like turbid media," *J. Biomed. Opt.* **17**, 105006 (2012).

[45] N. Ortega-Quijano, B. Haj-Ibrahim, E. García-Caurel, J.-L. Arce-Diego, and R. Ossikovski, "Experimental validation of Mueller matrix differential decomposition," *Opt. Express* **20**, 1151–1163 (2012).

[46] D. H. Goldstein, "Mueller matrix dual-rotating retarder polarimeter," *Appl. Opt.* **31**, 6676–6683 (1990).

[47] D. S. Sabatke, M. R. Descour, E. L. Dereniak, W. C. Sweatt, S. A. Kemme, and G. S. Phipps, "Optimization of retardance for a complete Stokes polarimeter," *Opt. Lett.* **25**, 802–804 (2000).

[48] J. S. Tyo, "Noise equalization in Stokes parameter images obtained by use of variable-retardance polarimeters," *Opt. Lett.* **25**, 1198–1200 (2000).

[49] E. Compain and B. Drévillon, "High-frequency modulation of the four states of polarization of light with a single phase modulator," *Rev. Sci. Instrum.* **69**, 1574–1580 (1998).

[50] M. H. Smith, "Optimization of a dual-rotating-retarder Mueller matrix polarimeter," *Appl. Opt.* **41**, 2488–2493 (2002).

[51] J. Zallat, S. Aïnouz S, and M. Ph. Stoll, "Optimal configurations for imaging polarimeters: impact of image noise and systematic errors," *J. Opt. A. Pure Appl. Opt.* **8**, 807 (2006).

[52] D. Layden, M. F. G. Wood, and A. Vtikin, "Optimum selection of input polarization states in determining the sample Mueller matrix: a dual photoelastic polarimeter approach," *Opt. Express* **20**, 20466–20481 (2012).

[53] E. Collett, "Measurement of the four Stokes polarization parameters with a single circular polarizer," *Opt. Commun.* **52**, 77–80 (1984).

[54] R. W. Collins and J. Koh, "Dual rotating-compensator multi-channel ellipsometer: instrument design for real-time Mueller matrix spectroscopy of surfaces and films," *J. Opt. Soc. Am. A* **16**, 1997–2006 (1999).

[55] C.-Y. Han and Y.-F. Chao, "Photoelastic modulated imaging ellipsometry by stroboscopic illumination technique," *Rev. Sci. Instrum.* **77**, 023107–5 (2006).

[56] M. Richert, X. Orlik, and A. De Martino, "Adapted polarized state contrast image," *Opt. Express* **17**, 14199–14210 (2009).

[57] G. Anna, F. Goudail, and D. Dolfi "General state contrast imaging: an optimized polarimetric imaging modality insensitive to spatial intensity fluctuations," *J. Opt. Soc. Am. A* **29**, 892–900 (2012).

[58] M. Anastasiadou, A. de Martino, D. Clément, F. Liège, B. Laude-Boulesteix, N. Quang, J. Dreyfuss, B. Huynh, A. Nazac, L. Schwartz, et al. "Polarimetric imaging for the diagnosis of cervical cancer," *Phys. Stat. Sol. (c)* **5**, 1423 (2008).

[59] A, Bénière, M. Alouini, F. Goudail, and D. Dolfi, "Design and experimental validation of a snapshot polarization contrast imager," *Appl. Opt.* **48**, 5764–5773 (2009).

[60] J. C. Ramella-Roman, K. Lee, S. A. Prahl, and S. L. Jacques, "Designing, testing and clinical studies of a handheld polarized light camera," *J. Biomed. Opt.* **9**, 1305–1310 (2004).

[61] M. F. G. Wood, N. Ghosh, X. Guo, and I. A. Vitkin, "Towards noninvasive glucose sensing using polarization analysis of multiply scattered light," in *Handbook of Optical Sensing of Glucose in Biological Fluids and Tissues*, Series in Medical Physics and Biomedical Engineering, edited by V. V. Tuchin (Taylor and Francis Publishing, London, 2008), Vol. 12, Chap. 17.

[62] N. Ghosh, M. Wood, and A. Vitkin, "Polarized light assessment of complex turbid media such as biological tissues using Mueller matrix decomposition," in *Handbook of Photonics for Biomedical Science*, edited by V. V. Tuchin (Taylor and Francis Publishing, London, 2010), Chap. 9.

[63] M. H. Smith, P. Burke, A. Lompado, E. Tanner, and L. W. Hillman "Mueller matrix imaging polarimetry in dermatology," *Proc. SPIE* **3911**, 210–216 (2000)

[64] A. Pierangelo, A. Nazac, A. Benali, P. Validire, H. Cohen, T. Novikova, B. Haj Ibrahim, S. Manhas, C. Fallet, M.-R. Antonelli, et al. "Polarimetric imaging of uterine cervix: a case study," *Opt. Express* **21**, 14120–14130 (2013).

[65] D. Bicout, C. Brosseau, A. S. Martinez, and J. M. Schmitt, "Depolarization of multiply scattered waves by spherical diffusers: influence of size parameter," *Phys. Rev. E* **49**, 1767–1770 (1994).

[66] E. E. Gorodnichev, A. I. Kuzolov, and D. B. Rozozkin, "Diffusion of circularly polarized light in a disordered medium with large scale inhomogeneities," *JETP Lett.* **68**, 22–28 (1998).

[67] A. D. Kim and M. Moscoso, "Influence of the refractive index on the depolarization of multiply scattered waves," *Phys. Rev. E* **64**, 026612 (2001).

[68] L. F. Rojas-Ochoa, D. Lacoste, R. Lenke, P. Schurtenberger, and F. Scheffold, "Depolarization of backscattered linearly polarized light," *J. Opt. Soc. Am. A* **21**, 1799–1804 (2004).

[69] M. Xu and R. R. Alfano, "Random walk of polarized light in turbid media," *Phys. Rev. Lett.* **95**, 213901 (2005).

[70] A. J. Welch, M. J. C. Van Germert, W. M. Star, and B. C. Wilson, "Overview of tissue optics," in *Optical Thermal Response of Laser Irradiated Tissue*, edited by A. J. Welch and M. J. C. Van Germert (Plenum, New York, 1995).

[71] L. Wang, S. L. Jacques, and L. Zheng, "MCML—Monte Carlo modeling of light transport in multi-layered tissues," *Comput. Methods Programs Biomed.* **47**, 131–146 (1995).

[72] N. Ghosh, P. K. Gupta, A. Pradhan, and S. K. Majumder, "Anomalous behavior of depolarization of light in a turbid medium," *Phys. Lett. A* **354**, 236–242 (2006).

[73] V. Sankaran, K. Schonenberger, J. T. Walsh Jr., and D. J. Maitland, "Polarization discrimination of coherently propagating light in turbid media," *Appl. Opt.* **38**, 4252–4261 (1999).

[74] V. Sankaran, J. T. Walsh Jr., and D. J. Maitland, "Comparative study of polarized light propagation in biological tissues," *J. Biomed. Opt.* **7**, 300–306(2002).

[75] N. Ghosh, A. Pradhan, P. K. Gupta, S. Gupta, V. Jaiswal, and R. P. Singh, "Depolarization of light in a multiply scattering medium: effect of refractive index of scatterer," *Phys. Rev. E* **70**, 066607 (2004).

[76] M. F. G. Wood, X. Guo, and I. A. Vitkin, "Polarized light propagation in multiply scattering media exhibiting both linear birefringence and optical activity: Monte Carlo model and experimental methodology," *J. Biomed. Opt.* **12**, 014029 (2007).

[77] J. C. Ramella-Roman, S. A. Prahl, and S. L. Jacques, "Three Monte Carlo programs of polarized light transport into scattering media: part I," *Opt. Express* **13**, 4420–4438 (2005).

[78] M. Moscoso, J. B. Keller, and G. Papanicolaou, "Depolarization and blurring of optical images by biological tissue," *J. Opt. Soc. Am. A* **18**, 948–960 (2001).

[79] R. Clark Jones, "New calculus for the treatment of optical systems. VII. Properties of the N-matrices," *J. Opt. Soc. Am.* **38**, 671–685 (1948).

[80] S. Alali, Y. Wang, and I. Alex Vitkin "Detecting axial heterogeneity of birefringence in layered turbid media using polarizd light imaging," *Biomed. Opt. Express* **3**, 3250–3263 (2012)

[81] N. Ghosh, M. F. G. Wood, and I. A. Vitkin, "Mueller matrix decomposition for extraction of individual polarization parameters from complex turbid media exhibiting multiple scattering, optical activity and linear birefringence," *J. Biomed. Opt.* **13**, 044036 (2008).

[82] N. Ghosh, M. F. G. Wood, and I. A. Vitkin, "Polarimetry in turbid, birefringent, optically active media: a Monte Carlo study of Mueller matrix decomposition in the backscattering geometry," *J. Appl. Phys.* **105**, 102023 (2009).

[83] S. G. Demos, W. B. Wang, J. Ali, and R. R. Alfano, "New optical difference approaches for subsurface imaging of tissues," *OSA TOPS* **21**, in *Advances in Optical Imaging and Photon Migration*, edited by J. G. Fujimoto and M. S. Patterson, pp. 405–410 (1998).

[84] Y. Liu, Y. L. Kim, X. Li, and V. Backman, "Investigation of depth selectivity of polarization gating for tissue characterization," *Opt. Express* **13**, 601–611 (2005).

[85] S. G. Demos, H. B. Radousky, and R. R. Alfano, "Deep subsurface imaging in tissues using spectral and polarization filtering," *Opt. Express* **7**, 23–28 (2000).

[86] A. P. Sviridov, V. C. M. Hassan, A. C. Boccara, A. Russo, P. Smith, and A. Gandjbackche, "Enhancement of hidden structures of early skin fibrosis using polarization degree patterns and Pearson correlation analysis," *J. Biomed. Opt.* **10**, 051706 (2005).

[87] S. L. Jacques, J. C. Ramella-Roman, and K. Lee, "Imaging skin pathology with polarized light," *J. Biomed. Opt.* **7**, 329–340 (2002).

[88] S. L. Jacques, R. Samathama, S. Isenhath, and K. Lee, "Polarized light camera to guide surgical excision of skin cancers," *Proc. SPIE* **6842** 68420I (2008).

[89] V. Backman, M. B. Wallace, L. T. Perelman, J. T. Arendt, R. Gurjar, M. G. Muller, Q. Zhang, G. Zonios, E. Kline, T. McGillican, et al., "Detection of preinvasive cancer cells in situ," *Nature (London)* **406**, 35–36 (2000).

[90] M. Hunter et al., "Tissue self-affinity and polarized light scattering in the born approximation: a new model for precancer detection," *Phys. Rev. Lett.* **97**, 138102 (2006).

[91] N. Ghosh, S. K. Majumder, H. S. Patel, and P. K. Gupta, "Depth resolved fluorescence measurement in layered turbid medium by polarized fluorescence spectroscopy," *Opt. Lett.* **30**, 162–164 (2005).

[92] Z. J. Smith and A. J. Berger, "Surface-sensitive polarized Raman spectroscopy of biological tissue," *Opt. Lett.* **30**, 1363–1365 (2005).

[93] R. S. Gurjar, V. Backman, L. T. Perelman, I. Georgakoudi, K. Badizadegan, I. Itzkan, R. R. Dasari, and M. S. Feld, "Imaging human epithelial properties with polarized light scattering spectroscopy," *Nat. Med.* **7**, 1245–1249 (2001).

[94] N. C. Biswal, S. Gupta, N. Ghosh, and A. Pradhan, "Recovery of intrinsic fluorescence from the measured fluorescence in a turbid medium: an experimental approach," *Opt. Express* **11**, 3320–3331 (2003).

[95] R. J. Mc Nichols and G. L. Cote, "Optical glucose sensing in biological fluids: an overview," *J. Biomed. Opt.* **5**, 5–16 (2000).

[96] M. F. G. Wood, D. Côté, and I. A. Vitkin, "Combined optical intensity and polarization methodology for analyte concentration determination in simulated optically clear and turbid biological media," *J. Biomed. Opt.* **13**, 044037 (2008).

[97] J. Chung, W. Jung, M. J. Hammer-Wilson, P. Wilder-Smith, and Z. Chen, "Use of polar decomposition for the diagnosis of oral precancer" *Appl. Opt.* **46**, 3038–3045 (2007).

[98] A. Pierangelo, A. Benali, M. R. Antonelli, T. Novikova, P. Validire, B. Gayet, and A. de Martino, "Ex-vivo characterization of human colon cancer by Mueller polarimetric imaging," *Opt. Express* **19**, 1582–1593 (2011).

[99] A. Pierangelo, S. Manhas, A. Benali, C. Fallet, J.-L. Totobenazara, M. R. Antonelli, T. Novikova, B. Gayet, A. de Martino, and P. Validire "Multispectral Mueller polarimetric imaging detecting residual cancer and cancer regression after neoadjuvant treatment for colorectal carcinomas," *J. Biomed. Opt.* **18**, 046014 (2013).

[100] O. Visser, R. Bakx, F. A. Zoetmulder, C. C. Levering, S. Meijer, J. F. Slors, and J. J. van Lanschot, "The influence of total mesorectal excision on local recurrence and survival in rectal cancer patients: a population-based study in Greater Amsterdam," *J. Surg. Oncol.* **95**(6), 447–454 (2007).

[101] M. Underwood, M. Arbyn, W. Parry-Smith, S. De Bellis-Ayres, R. Todd, C. Redman, and E. Moss, "Accuracy of colposcopy-directed punch biopsies: a systematic review and meta-analysis," *BJOG* **119**, 1293–1301 (2012).

[102] N. Thekkek and R. Richards-Kortum, "Optical imaging for cervical cancer detection: solutions for a continuing global problem," *Nat. Rev. Cancer* **8**, 725–731 (2008).

[103] M. Cardenas-Turanzas, J. A. Freeberg, J. L. Benedet, E. N. Atkinson, D. D. Cox, R. Richards-Kortum, C. MacAuley, M. Follen, and S. B. Cantor, "The clinical effectiveness of optical spectroscopy for the *in vivo* diagnosis of cervical intraepithelial neoplasia: where are we?," *Gynecol. Oncol.* **107** S138–S146 (2007).

[104] P. E. Gravitt, P. Paul, H. A. Katki, H. Vendantham , G. Ramakrishna, M. Sudula, B. Kalpana, B. M. Ronnett, K. Vijayaraghavan, K. V. Shah, and CATCH Study Team. "Effectiveness of VIA, Pap, and HPV DNA testing in a cervical cancer screening program in a peri-urban community in Andhra Pradesh, India," *PLoS ONE* **5**(10), e13711 (2010). doi:10.1371/journal.pone.0013711

[105] P. Shukla and A. Pradhan, "Mueller decomposition images for cervical tissue: potential for discriminating normal and dysplastic states," *Opt. Express* **17**, 1600–1609 (2009).

[106] D. Arifler, I. Pavlova, A. Gillenwater, and R. R. Kortum, "Light scattering from collagen fiber networks: micro-optical properties of normal and neoplastic stroma," *J. Biophys.* **92**, 3260–3274 (2007).

[107] D. J. Maitland and J. T. Walsh Jr., "Quantitative measurements of linear birefringence during heating of native collagen," *Lasers Surg. Med.* **20**, 310–318 (1997).

[108] M. F. G. Wood, N. Ghosh, E. H. Moriyama, B. C. Wilson, and I. A. Vitkin, "Proof-of-principle demonstration of a Mueller matrix decomposition method for polarized light tissue characterization in vivo," *J. Biomed. Opt.* **14**, 014029(2009).

[109] S. Alali, K. Aitken, D. Bagli, and I. A. Vitkin, "Optical assessment of anisotropy in ex-vivo distended rat bladders,'' *J. Biomed. Opt.* **17**, 109801 (2012).

[110] G. S. Jack, R. Zhang, M. Lee, Y. Xu, B. M. Wu, and L. V. Rodrigues, "Urinary bladder smooth muscle engineered from adipose stem cells and a three dimensional synthetic composite,'' *Biomaterials* **30**, 3259–3270 (2009)

[111] N. Ghosh, M. F. G. Wood, S. Li, R. D. Weisel, B. C. Wilson, R. Li, and I. A. Vitkin, "Mueller matrix decomposition for polarized light assessment of biological tissues," *J. Biophoton.* **2**, 145 (2009).

[112] M. F. G. Wood, N. Ghosh, M. A. Wallenburg, S.-H. Li, R. D. Weisel, B. C. Wilson, R.-Ki Li, and A. Vitkin, "Polarization birefringence measurements for characterizing the myocardium, including healthy, infracted, and stem cell treated regenerating cardiac tissues," *J. Biomed. Opt.* **15**, 047009 (2010).

[113] M. A. Wallenburg, M. F. G. Wood, N. Ghosh, and I. A. Vitkin, "Polarimetry-based method to extract geometry-independent metrics of tissue anisotropy," *Opt. Lett.* **35**, 2570–2572 (2010).

[114] H. He, Z. Nan, L. Ran, Y. Tianliang, L. Wei, H. Yonghong, and M. Hui, "Application of sphere-cylinder scattering model to skeletal muscle," *Opt. Express* **18**, 15104–15112 (2010).

[115] S. Alali, Y. Wang, and I. A. Vitkin, “Detecting axial heterogeneity of birefringence in layered turbid medial using polarized light imaging,” *Biomed. Opt. Express* **3,** 3250–3263 (2012).

[116] A. Myakov, L. Nieman, L. Wicky, U. Utzinger, R. Richards-Kortum, and K. Sokolov, “Fiber optic probe for polarized reflectance spectroscopy *in vivo*: design and performance,” *J. Biomed. Opt.* **7**(3), 388–397 (2002).

[117] V. M. Turzhitsky, A. J. Gomes, Y. L. Kim, Y. Liu, A. Kromine, J. D. Rogers, M. Jameel, H. K. Royand, and V. Backman,” Measuring mucosal blood supply *in vivo* with a polarization gating probe,” *Appl. Opt.* **47**(32), 6046–6057 (2008).

[118] T. C. Wood and D. S. Elson, “Polarization response measurement and simulation of rigid endoscopes,” *Biomed. Opt. Express* **1,** 463–471 (2010).

8

OPTICAL WAVEGUIDE BIOSENSORS

DAPHNÉ DUVAL AND LAURA M. LECHUGA
NanoBiosensors and Bioanalytical Applications Group, Centro Investigacion Biomedica en Red – Bioingenieria, Biomateriales y Nanomedicina, Consejo Superior de Investigaciones Cientificas, Institut Catala de Nanociencia i Nanotecnologia, Bellaterra, Barcelona, Spain

8.1 INTRODUCTION

A biosensor is a self-contained device composed of a *bioreceptor* and a *transducer*. The substance to be detected, the *analyte*, is captured by the appropriate bioreceptor (DNA, antibodies, etc.) taking advantage of the high specificity of the biomolecular recognition process. This biomolecular detection is then converted by the transducer into a physical signal that can be further processed and related to the concentration of the substance under analysis. As compared to standard analytical techniques that are usually time-consuming and expensive and require trained personnel, biosensors offer clear advantages as they can allow simple, rapid, and continuous *in situ* detection for a broad range of applications such as clinical diagnostic, biomedical research, drug discovery or pathogen, and toxin detection in food and water.

A wide range of biosensors have been explored based on optical, electrical, magnetic, and mechanical principles. Among them, optical biosensors have undisputed advantages when compared to their counterparts: noninvasive and nondestructive nature, absence of risks of electrical shocks or explosion, immunity to electromagnetic interferences, higher sensitivity, miniaturization capabilities, and possibility of multiplexing. Optical biosensors can operate according to two protocols: *fluorescence-based detection* and *label-free detection*. In fluorescence-based detection, fluorescent

---

Photonics: Scientific Foundations, Technology and Applications, Volume IV, First Edition.
Edited by David L. Andrews.
© 2015 John Wiley & Sons, Inc. Published 2015 by John Wiley & Sons, Inc.

labels are used to indicate the presence of the target molecule resulting in an extremely sensitive detection. However, the preparatory labeling procedure is costly and laborious and is subjected to possible contaminations, human errors, mechanical damage of the sensing probe, or even alterations of the natural function of the tagged biomolecule. In addition, fluorescence signal makes quantitative analysis difficult due to the inability to precisely manipulate the amount of label for each target analyte. In contrast, in a label-free scheme the molecules are not labeled and can be detected in their natural forms. This type of detection is relatively simple and cost-effective and enables the quantitative and kinetic estimation of biomolecular interactions in complex real samples such as blood, serum, and urine. Main label-free optical detection methods are based on refractive index (RI), optical absorption, and Raman spectroscopic detection [1].

Fluorescence-based biosensors have been extensively studied and described in a large number of reviews and books [2–4]. In this chapter, we will mainly discuss label-free detection due to its inherent advantages. The focus will be on RI-based label-free optical biosensors which employ the evanescent field detection principle. Surface plasmon resonance sensors falls into this category but we will focus here only in *optical waveguide biosensors* including devices using optical fibers (OFs) and integrated optics (IO)-based waveguides. IO-based sensors include interferometers, microcavities, grating-, and photonic crystal (PC)-based structures. More recent trends such as biosensors based on porous silicon or silicon photonic wires will also be described. In the case of OF-based biosensors, a few configurations employ label-free detection and we will discuss grating-, interferometric-, and absorbance-based OF biosensors.

First, we detail the fundamentals related to label-free optical waveguide biosensing. In the following, we discuss the surface functionalization strategies required to immobilize the bioreceptors on the waveguide surface and the criteria and procedures to evaluate optical biosensors. Then, we review the state-of-the-art in RI-based label-free biosensors, dividing them into IO-based biosensors and OF-based biosensors, with emphasis on the most relevant ones in terms of sensing performance. Finally, we discuss the integration of optical biosensors into lab-on-a-chip (LOC) platforms for point-of-care diagnosis.

8.2 FUNDAMENTALS OF LABEL-FREE OPTICAL WAVEGUIDE BIOSENSING

8.2.1 Principle of Operation

An optical waveguide is composed of a material with a certain refractive index in which the light is confined (*the core*), surrounding by materials with lower refractive indices (*the claddings*). IO waveguides can confine the light in one dimension (planar waveguides) or in two dimensions (channel and rib waveguides). In the case of OFs, light is confined in two dimensions within cylindrical layers. The guided modes of a waveguide are described by Maxwell's equations and can be characterized by their *effective refractive indices* [5].

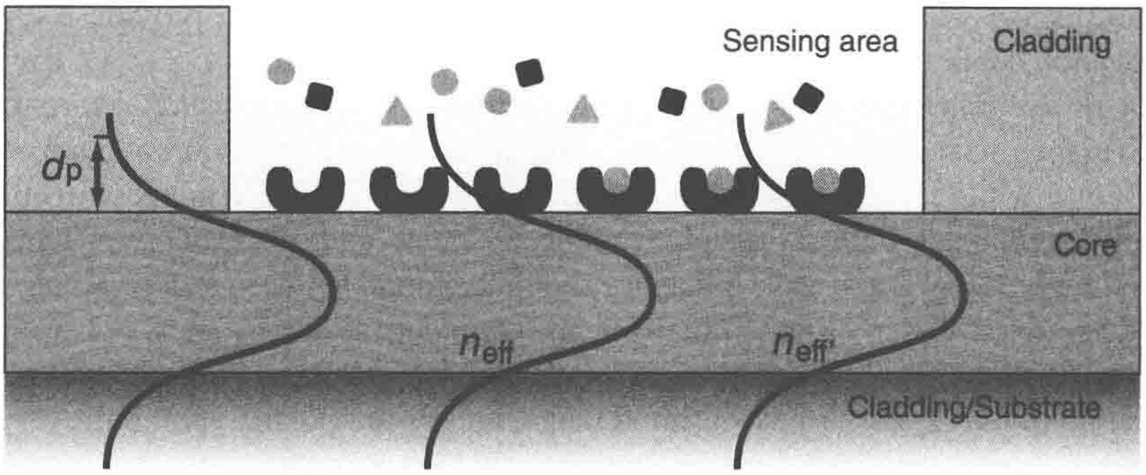

FIGURE 8.1 Scheme of the evanescent field detection principle.

The modes propagate in the waveguide by *total internal reflections* (TIRs) at the core-cladding interface. At the point of reflection, a standing wave of the electromagnetic field, the *evanescent field*, is created and penetrates into the cladding with an exponential decay. As shown in Figure 8.1, the evanescent field acts as a probe. When the analyte and its corresponding bioreceptor previously immobilized on the waveguide surface react together, it results in a variation of the refractive index of the cladding. This variation of refractive index affects the effective refractive index of the guided mode through the modification of its evanescent field. The concept of evanescent field sensing was first reported by Lukosz and Tiefenthaler in 1983 [6, 7] and has been the subject of an increasing number of publications since then.

The depth d_p at which the intensity of the electric or magnetic field of the evanescent field drops to $1/e$ of its original value is called the *depth of penetration* and is expressed as

$$d_p = \frac{\lambda}{2\pi} \cdot \frac{1}{\sqrt{n_1^2 \sin^2 \theta - n_2^2}}, \tag{8.1}$$

where λ is the wavelength of light, θ the incident angle, and n_1 and n_2 the refractive indices of the core and the cladding, respectively. Typical penetration depths range between 50 and 700 nm, depending mainly on the wavelength and on the contrast between the refractive indices of the core and the cladding. With a penetration depth in the range of tens of nanometers, only the analytes captured by the immobilized bioreceptors will be detected since the ones not captured will be too far away from the sensor surface to be sensed by the evanescent field. Therefore, it is not necessary to label the target molecules neither to carry out a prior separation of nonspecific components. Evanescent field detection principle enables a label-free, highly sensitive, and specific detection if appropriate bioreceptors and immobilization protocols are employed.

Both transverse electric (TE) and transverse magnetic (TM) polarized guided light can be used in the evanescent wave detection mechanism. However, TM modes usually have larger evanescent field which means greater sensitivity than TE modes.

Regarding the wavelength, working in the infrared range would provide a longer penetration depth than in the visible range as can be deduced from Eq. (8.1). But this is not always translated in an increase of the sensitivity since the water absorption is much higher in the infrared than in the visible: at 625 nm, the losses in water are of 2×10^{-3} cm^{-1} while at 3 μm they are as high as 11,400 cm^{-1} [8]. Such increase in optical loss will significantly affect the signal, mainly the noise, and consequently the limit of detection (LOD) of the sensor. A balance should be found between a large penetration depth and the losses in order to obtain an optimum detection efficiency, noise signal, and sensitivity [9]. Up to now, most of the biosensors have been developed for operation in the visible or near-infrared range, mainly at 633 and 1550 nm.

8.2.2 Optical Waveguide Technology

8.2.2.1 Integrated Optical Waveguide Although a wide range of material and fabrication processes are available for optical waveguide technology [5], only a few of them have the required properties to afford highly sensitive biosensors. The sensitivity of an optical waveguide biosensor is strongly dependent on the waveguide materials and its design. In particular, the electric field strength at the core-cladding interface as well as the overlap between the evanescent field and the sensing area have to be optimized to maximize the impact on the effective refractive index of the guided wave. This generally implies the use of large index contrast materials for the core and the claddings, a combination that provides an evanescent field much larger than for low contrast waveguides (Eq. 8.1). In addition, the materials must be transparent and have low propagation losses at the wavelength of interest.

With the above considerations, the materials commonly employed as waveguide materials include silicon nitride (Si_3N_4, n = 1.9 to 2.1), silicon oxynitride (SiO_xN_Y, n = 1.45 to 2.1), tantalum pentoxide (Ta_2O_5, n = 2.1 to 2.3), and titanium dioxide (TiO_2, n = 2.5 to 2.8) on silicon or glass substrates. These materials lead to an index difference between core and cladding in the order of 10^{-1} refractive index unit (RIU). More recently, silicon-on-insulator (SOI)-based structures have emerged with excellent results. Lithium niobate ($LiNbO_3$) or III–V semiconductor materials are widely employed for optical telecommunications but they have shown less suitability for biosensing as they are more complex and expensive while their electro-optical or piezo-electrical properties are generally pointless for biosensing.

Polymer materials have also been employed due to their interesting properties as high transparency, versatility, easy and low-cost fabrication, and possibility of mass production, although they do not comply with the requirement of large index contrast. Usual index contrast in polymers is in the order of 10^{-3} RIU, that is, two orders lower than what can be achieved with silicon photonics. According to Eq. (8.1), a weaker evanescent field will be generated, leading to lower sensitivity. Even though this loss of sensitivity can be balanced by larger waveguide dimensions and consequent better in-coupling of light, the reported LODs are worse than those of silicon-based devices. In the last years, new polymers have been synthesized with index contrast in the order of 10^{-2} RIU, opening the route to future polymeric biosensors with better performances [10–12].

Common fabrication processes for optical waveguide biosensors include ion diffusion in glass, chemical vapor deposition, spin-coating, nanoimprinting, photolithography, and electron-beam lithography.

8.2.2.2 ***Optical Fibers*** In conventional optical fibers, the core and the cladding are both made of silica. The core is generally doped with germanium to slightly increase its refractive index for light propagation by TIR. For a single-mode OF with step-index profile, the core diameter is between 8 and 12 μm and the cladding diameter is of 125 μm. For multimodal fiber, the diameter of the core is usually between 20 and 200 μm, for a cladding diameter around 125–400 μm.

To fabricate OFs, a large diameter preform (about 10 cm in diameter) is first manufactured, by vapor-phase oxidation or direct-melt process, with a careful control of the index profile to differentiate the core from the cladding. The preform is then placed in a drawing tower where the preform tip is heated and the OF is pulled out as a string until reaching the final diameter. Coatings are then deposited to physically protect the OF. For biosensing applications, the cladding and the coatings are removed to define the sensing area. This can be achieved by mechanical polishing or by chemical etching.

Fibers appear as a convenient material for optical sensors because they are inexpensive and provide an easy and efficient signal delivery as well as multiplexed capabilities and long interaction lengths. However, the index contrast of an OF is very low, about 0.5–1 $\times 10^{-2}$ RIU, resulting in a small penetration depth of the evanescent field and, consequently, in a low sensitivity. To circumvent this drawback, two approaches are normally employed: amplification of the signal response by fluorescence or/and the use of special geometries to increase the evanescent field [13].

When tapering an OF, the fractional power guided in the core decreases and part of the energy passes into the cladding, resulting in an increase of the evanescent field magnitude and penetration depth. To do so, the OF is fixed at two ends on a movable translation stage of a pulling machine. The middle of the fiber is heated with a flame or a laser beam and, at the same time, the translation stages move in the opposite direction. The glass melts and the fiber is elongated so that its diameter decreases. As illustrated in Figure 8.2b, a continuous tapered OF consists of a convergent region (the taper transition) and of a region of almost fixed diameter (the taper waist). Waists of

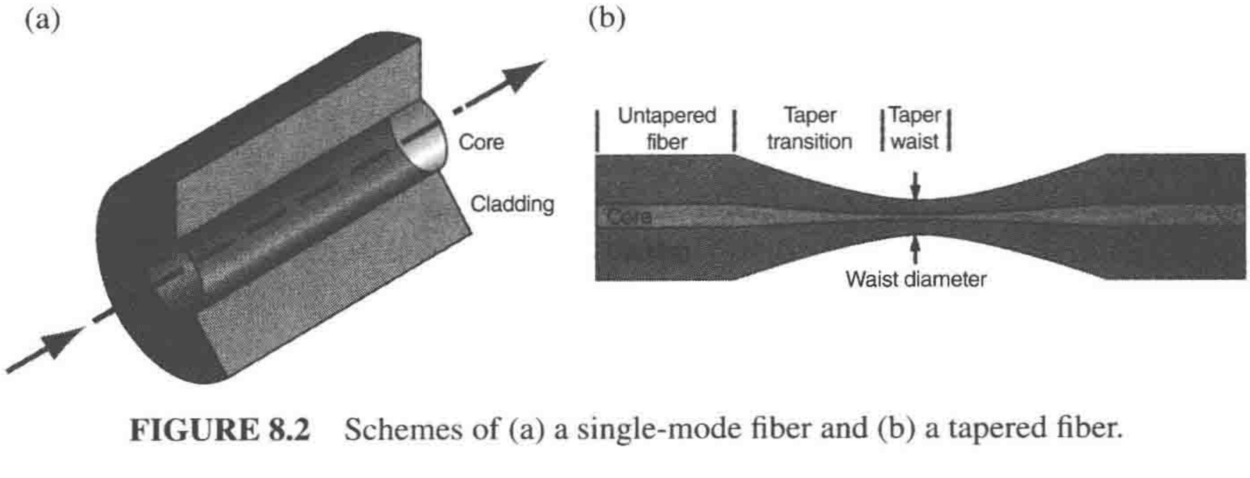

FIGURE 8.2 Schemes of (a) a single-mode fiber and (b) a tapered fiber.

1–10 mm in length and diameters down to 100 nm can be obtained. Another approach to increase sensitivity is to bend the OF. Bending produces not only an increase of the losses but also an increase of the evanescent field. It is usually obtained by forming a U-shape probe with the core of a uniformly decladded fiber.

The development of microstructured optical fibers (MOFs) opened new opportunities for OF-based biosensing. MOFs are OFs that incorporate air holes within their cross-section to control the interaction between the guided light and the analytes located within the holes, while simultaneously acting as tiny fluidic channels. As MOFs can be fabricated from a single material, it is possible to use materials that were unavailable for conventional OFs like silica, lead silica, tellurite, and bismuth glass. First a structured preform is produced, with extruded items in the range of 10–15 mm. This structured preform is then drawn out until reaching the intended diameter. With the technological advances in the extrusion and drawing of OFs, it is now possible to reach cores as small as 400 nm [14]. Two classes of MOFs have been developed: OFs with solid "suspended" cores [14] and air-core photonic band gap OFs [15].

8.3 SURFACE BIOFUNCTIONALIZATION

To achieve a specific detection, a biosensor must include a recognition element, or bioreceptor, specific to the analyte to be detected. The choice of the bioreceptor and the way to immobilize it on the transducer surface depends on the envisioned applications, the transducer type, and the surface material.

8.3.1 Bioreceptors

In addition to the specificity between the analyte and its bioreceptor, there are some important features to take into account in the selection of the bioreceptor such as the affinity between the analyte and the bioreceptor, the stability of the complex formed by the two molecules, and the fact that the formation of this complex must be detectable by the transducer.

Peptides and antibodies are typical bioreceptors to study protein–protein interaction. In particular, *immunosensors* are based on the specific and high affinity between an antigen and its antibody. They can be applied to the continuous monitoring of critical-care analytes in serious illness of infectious diseases or to any immunological alteration. Many studies are also focusing on specific clinical biomarkers for the early detection of a myriad of human diseases such as cancer, neurodegenerative, diabetes, or cardiovascular disorders. In addition, as specific antibodies can be obtained for low molecular-weight organic molecules such as toxic pollutants, the immunodetection has been extended to other areas such as environmental monitoring or food control, allowing the detection of toxic or explosive species as well as the control of environmental pollutants. The pairs BSA/anti-BSA, HSA/anti-HSA, and IgG/anti-IgG are model systems widely used for biosensing proofs-of-concept.

Nucleic acid sensors are based on the complementation of base pairs between a DNA or RNA target strand and its complementary DNA or RNA bioreceptor. These sensors are of considerable interest as they provide sequence-specific information in a faster, simpler, and cheaper way than traditional hybridization assays.

Cellular components or even whole cells can also be employed as bioreceptors to detect any type of microorganism (bacteria, virus) or to study extracellular or intracellular membrane transport proteins.

More recently, *synthetic receptors* based on engineered molecules have emerged as an attractive alternative to biological receptors. *Aptamers* are synthetic DNAs, RNAs, or Peptide Nucleic Acids (PNAs) which are created with the appropriate sequences to detect a specific target with high specificity and affinity [16]. Another class of synthetic biomimetic receptors are the *molecular imprinted polymers* (MIPs) prepared by a template process that usually involves the polymerization of the plastic monomers in the presence of the target analytes [17]. However, until now, biomimetic receptors have not achieved the same specificity as the natural receptors, and they are only suitable for certain special applications.

Enzymes can also be used as bioreceptors to catalyze reactions, forming the so-called *catalytic biosensors*. These are kinetic devices that monitor the rate of formation of a product or the disappearance of a reactant related to the biocatalyzed reaction. These assays, particularly adapted for electrochemical transducers, are barely applied to label-free optical transducers.

8.3.2 Immobilization Techniques

Once the application (i.e., the bioreceptor) and the transducer (i.e., the surface material) are chosen, the most appropriate immobilization technique must be employed. The goal of the immobilization technique is to create a recognition layer with an efficient coverage of the transducer surface that is capable of interacting with the target with high specificity and speed but without modifying the bioreceptor properties or the transducer sensitivity. It should also minimize nonspecific adsorptions when analyzing complex samples such as blood or serum without previous processing. In addition, the recognition layer should be stable in time and in some cases sufficiently robust to be regenerated without severely affecting the binding properties of the bioreceptor. The choice of the most effective strategy of immobilization is the key factor that turns a sensing device into a valid and applicable analytical tool as the bioreceptor layer directly affects the reproducibility, the selectivity, and the resolution of any sensor device. Several strategies can be employed to immobilize the bioreceptor on the sensor surface [18–20]:

- *Physical adsorption* by direct deposition of the bioreceptor using van der Waals and electrostatic interactions between the biomolecules and the surface. It is a simple and rapid method that can result in the immobilization of large quantities of bioreceptors with high packing density. However, it can lead to desorption of the active bioreceptors under flow conditions and during surface regeneration as it usually implies high or low pH solutions, salt concentration, organic solvent, and so on. In addition, problems in reproducibility and in the orientation of the bioreceptors are common drawbacks of this strategy.

- *Covalent binding* of the bioreceptor to the surface, using a crosslinker previously immobilized on the surface or following more complex strategies [18]. The binding is made through one of the functional groups of the bioreceptor. It is recommended to use a chemical group that will not compromise the functionality of the molecule. Amino, carboxylic, or thiol groups are the preferred option to immobilize proteins. For antibodies, the added difficulty is to immobilize them in an oriented way to let the affinity-binding sites free. The oriented immobilization of antibodies can be achieved through the carbohydrates groups of the constant region or by using affinity proteins such as the A or G protein [19]. Another solution is to immobilize antigens on the transducer surface and to detect the target antigen through a competitive assay with its antibody. To immobilize nucleic acid, it is possible to take advantage of the versatility of the DNA synthesis that allows the incorporation of reactive groups at the end of the sequence. Covalent binding is one of the most widely used techniques due to its flexibility and to the wide range of linkers that can be used to attach any type of bioreceptor to the surface. However, because of the number of steps required, it can lead to nonspecific binding. To minimize such nonspecific binding, blocking agents can help blocking surface functional groups that could bind to other molecules than the target.
- *Noncovalent interactions* to a previously deposited active layer, either by nonspecific electrostatic interactions or by noncovalent affinity binding (biotin-avidin systems, His-Tag systems, protein A/G for antibodies, etc.) [18–20]. For instance, the biotin-avidin system is obtained through the formation of a sandwich-like layer: biotin on the surface/avidin/biotinylated biomolecule.
- *Physical entrapment* of bioreceptors in a polymer layer. This technique enables the incorporation of guest molecules within the polymer matrix in a single step. The most common polymer matrices are polyaniline, polythiophene, polypyrrole, dextran, and their derivatives. However, this technique is less employed than the others due to problems associated with the diffusion and mass transport of the analyte toward the surface.

Whatever the immobilization technique employed, a previous chemical activation of the sensor surface is mandatory. For a metal oxide surface such as TiO_2, the first step is to create surface hydroxyl groups which can be then attached to the functional groups of the bioreceptors via linker agents. Silicon-, silicon oxide-, and silicon nitride-based surfaces can be functionalized using the well-known silane chemistry [21]. Silicon-based surfaces require a prior activation step to oxidize the surface and to expose the silanol groups for crosslinking with silane. In the case of silicon nitride, methods are based on an initial etching step to remove the native SiO_2 layer to be further oxidized to form a new oxide layer [22]. Other strategies involve the derivatization of the Si–H and Si–N groups of the silicon nitride using more drastic conditions [21, 23]. The activated surface is subsequently modified with organosilanes forming a silane layer with exposed reactive groups susceptible to react with the bioreceptors. Hundreds of different organosilanes with a wide variety of structures, length, functionality, and chemical and physical properties are nowadays commercially available, although the most commonly employed are those with short alkyl chain (as propyl or butyl), ending in amino, thiol, epoxy, or carboxylic groups.

When studying complex samples that contain high concentrations of nonspecific molecules, the bioreceptor layer must be prepared in a way that avoids matrix effects and large background signals. In this case, less conventional reagents like dextran polymer or poly(ethylene) glycol (PEG) derivatives can be employed to provide a more hydrophilic, biocompatible, and antifouling surface.

8.3.3 Biofunctionalization Strategies for Multiplexing

Usually the immobilization of the bioreceptors is done *ex situ* at the sensor chip level. However, for multiplexing purposes, the sensors included in an array must be functionalized with different bioreceptors in order to detect a different target each. To do so, two main approaches can be employed: *microfluidic patterning* and *microcontact printing*. The microfluidic patterning consists of incorporating a microfluidic network including an independent microchannel on top of each sensor. Each sensor can be individually functionalized using laminar flow streams [24]. The microcontact printing is a versatile method for a region-specific functionalization based on the selective deposition of small volumes of the reagents under static conditions. Common microdeposition platforms are based on Surface Patterning Tool (SPT) cantilever [25] or on the noncontact piezoelectric method [26]. Hybrid methods combining microfluidic patterning and microcontact printing can also be implemented to take advantage of each method to create highly resistant multiplexed detection interfaces in a microfluidic network [27].

8.4 EVALUATION OF OPTICAL BIOSENSORS

The following specifications are frequently used to characterize a biosensor device:

- The *sensitivity* is the magnitude of the transducer response to a change in the analyte concentration. It depends on the nature of the analyte and on the type of transducer.
- The *selectivity* quantifies the capability of the biosensor to exclusively detect the analyte of interest. It depends on the inherent binding capabilities of the bioreceptor.
- The *dynamic range* is the interval of concentrations of the analyte (minimum and maximum) that can be detected by the biosensor (see Fig. 8.3). A wide dynamic range is desired to detect a broad interval of the analyte concentration.
- The *response time* is the time required by the transducer to convert a change at the transducer surface such as analyte binding into a variation of the output signal.
- The *reproducibility* is the ability of the biosensor to reproduce output response when the same analyte concentration is applied in the same conditions.

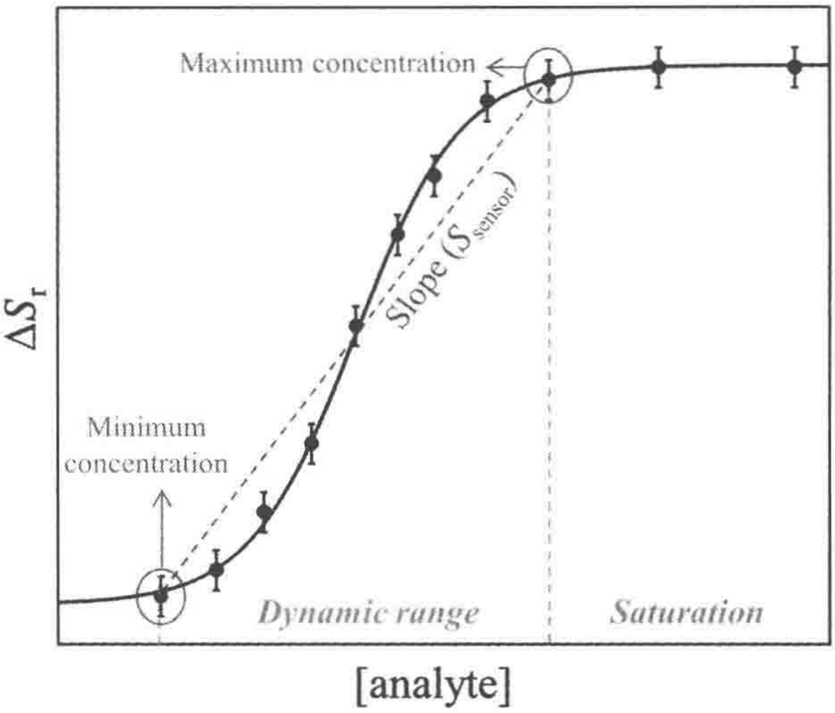

FIGURE 8.3 Standard calibration curve showing the relationship between the analyte concentration [analyte] and the sensor response change ΔS_r.

Additional characteristics of a biosensor are reliability, versatility, ease of use, and potential for miniaturization, multiplexing and low-cost fabrication.

Two types of sensing can be differentiated:

- The *homogeneous* or *bulk sensing:* the variation of the refractive index occurs homogeneously in all the volume above the sensor surface. This sensing is nonselective as it does not enable to differentiate between analytes.
- The *surface sensing:* a thin layer of bioreceptors is immobilized on the sensor surface and interact selectively with the corresponding analyte.

The relationship between the sensor response S_r and the measurand m (i.e., the refractive index of the solution in bulk or the analyte concentration) is given by

$$S_r = a + bm, \tag{8.2}$$

where a is the output signal at zero input signal and b is the slope or *sensitivity of the transducer*, also called S_{sensor}. This relationship assumes that the response of the transducer is linear, which is usually not the case. However, this approximation is considered as correct in the dynamic range [28]. In label-free optical detection, the response of the sensor can be the phase of the wave (φ), the resonance wavelength (λ), or the incident angle (θ).

To evaluate the bulk sensitivity of a device, the sensor response change ΔS_r induced by a refractive index variation Δn is evaluated for a set of solutions of different refractive indices successively injected in the sensing area. The results are represented in a *calibration curve* as ΔS_r versus Δn. According to Eq. (8.2), the slope corresponds to the bulk sensitivity:

$$S_\mathrm{sensor} = \frac{\Delta S_\mathrm{r}}{\Delta n}. \tag{8.3}$$

The LOD in terms of refractive index unit (RIU) is given by

$$\Delta n_\mathrm{MIN} = \frac{\Delta S_{r,\mathrm{MIN}}}{S_\mathrm{sensor}}, \tag{8.4}$$

where $\Delta S_{\mathrm{r,MIN}}$ is the *resolution of the transducer*, or minimum signal detectable. When the minimum signal detectable depends on the whole intensity pattern (like in the case of interferometers) it is a function of the baseline noise. For transducers such as microcavities or grating couplers, the minimum signal detectable is the minimum shift in wavelength or in angle that can be detected which depends on the resonance linewidth.

The procedure to evaluate the surface sensitivity of a biosensor is similar to that of the bulk sensitivity except that the transducer surface needs to be previously functionalized with the appropriate bioreceptor. Solutions of different concentrations of the target analyte ([*analyte*]) are successively injected in the sensing area and the sensor response change ΔS_r is evaluated for each concentration, with the surface of the biosensor regenerated between each injection. The results are plotted in a calibration curve as ΔS_r versus [*analyte*] like the one presented in Figure 8.3. The surface sensitivity is given by

$$S_\mathrm{sensor} = \frac{\Delta S_\mathrm{r}}{[\mathrm{analyte}]}, \tag{8.5}$$

and the LOD of the biosensor in term of analyte concentration by

$$[\mathrm{analyte}]_\mathrm{MIN} = \frac{\Delta S_{\mathrm{r,MIN}}}{S_\mathrm{sensor}}. \tag{8.6}$$

When possible, it is normally expressed in surface mass density (for example as pg mm^{-2}) which is an evaluation of the real biosensing capabilities of evanescent wave sensors as they are sensitive to any accumulation of mass on their surface. However, in many cases, the surface LOD is expressed in terms of analyte concentration as it is much easier to estimate than surface mass density. However, analyte concentration cannot be used to directly compare between different sensor sensitivities as it will depend on the target molecule and its affinity constant. Table 8.1 shows a comparison of the LOD in RIU and in pg mm^{-2} for the optical waveguide biosensors included in this chapter.

As a first step, evaluation of the biosensor capabilities is usually done using purified or spiked samples in buffer. But in order to assess the real performances of any device, real samples such as blood, urine, serum, saliva, tears, cerebrospinal or medullar fluids, or environmental samples have to be tested and validated.

TABLE 8.1 Comparison of the limit of detection in bulk and in surface for main optical waveguide biosensors

	Device configuration	RI detection limit (RIU)	Mass detection limit (pg mm^{-2})
IO-based	Interferometers	10^{-7}–10^{-8}	0.02–1
	Ring resonators	10^{-5}–10^{-7}	1–15
	Gratings	10^{-6}	0.3–5
	Photonic crystal	10^{-4}–10^{-5}	2–10
	Si wire	10^{-6}	0.3–3
	Slot waveguide	10^{-6}	1–15
OF-based	FBG	10^{-6}	13
	LPG	10^{-5}	–

IO, integrated optics; OF, optical fiber; FBG, fiber Bragg grating; LPG, long period grating.

8.5 INTEGRATED OPTICAL WAVEGUIDE-BASED BIOSENSORS

8.5.1 Interferometric Biosensors

The working principle of interferometric biosensors relies on the superposition of two or more light waves which results in the creation of a new wave pattern $I(t) \propto \cos(\Delta\varphi(t))$ called the *interference pattern*. The incoming light beam usually comes from the same source and is split into two beams of equal intensity that travel through different optical paths and are recombined before arriving at a detector. For biosensing applications, the two arms of the interferometer are usually referred to as the *sensing arm* and the *reference arm*, this last one compensates for refractive index fluctuations and unspecific adsorption (see Fig. 8.4). The variation of the effective refractive

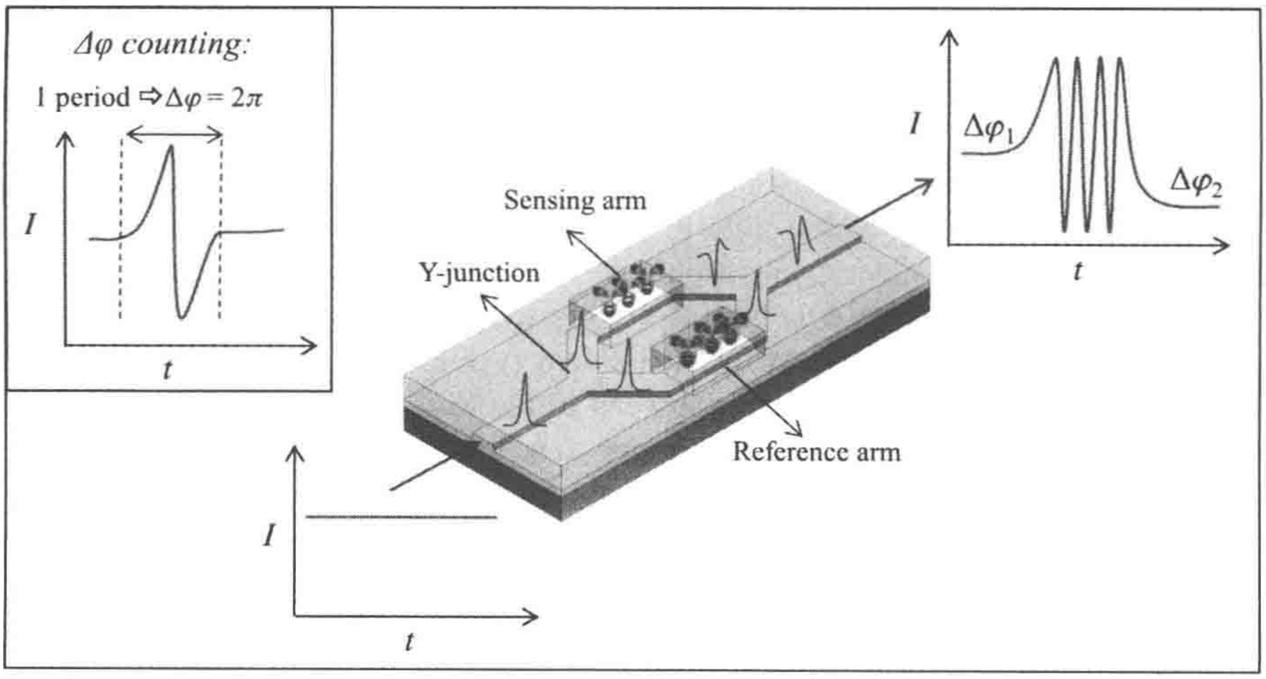

FIGURE 8.4 Illustration of the working principle of interferometric waveguide biosensors applied to the Mach–Zehnder interferometer (MZI).

index induced by binding events in the sensing arm produces a variation of the phase difference $\Delta\varphi$ between the two arms which can be evaluated through the interference pattern: as depicted in Figure 8.4, the difference between the initial value $\Delta\varphi_1$ and the final value $\Delta\varphi_2$ is given by the number of fringes, where a complete fringe represents a phase difference of 2π [29].

The contrast of the interference pattern (difference between the maximum and the minimum intensity) depends on the coupling factor of the divisor and on the propagation losses of the guided mode in the interferometer arms. To obtain the maximum contrast, it is important to design a divisor or Y-junction with a coupling factor of 3 dB to equally divide the input beam in each arm of the interferometer. Moreover, propagation losses in the sensor and reference arms should be identical.

In most of the interferometric configurations the waveguide should be single mode and the light linearly polarized to avoid multimodal and cross-polarization interference at the output.

8.5.1.1 Mach–Zehnder Interferometer In the integrated MZI, the split of the input-guided beam into two arms and the recombination of these two beams into a unique output beam are achieved via two integrated Y-junctions (Fig. 8.4). The phase difference $\Delta\varphi$ between the two arms is given by

$$\Delta\varphi(t) = 2\pi\frac{L}{\lambda}(n_{\mathrm{eff,s}}(t) - n_{\mathrm{eff,R}}), \qquad (8.7)$$

where $n_{\mathrm{eff,S}}$ and $n_{\mathrm{eff,R}}$ are the effective refractive indices of the guided modes in the sensing and reference arms, respectively, L the length of the sensing area, and λ the wavelength of the light. Typical values of L range from a few millimeters to several centimeters.

One of the first fabrications and applications of an integrated MZI as biosensor was reported in 1997 [30]. The MZI was based on Si_3N_4 rib waveguides on a SiO_2/Si substrate and optimized for operation at 633 nm. The reported LOD in bulk was of 1×10^{-4} RIU and the feasibility of this device as biosensor was demonstrated by an immunoassay: anti-hCG was adsorbed onto the surface of the sensing area and the analyte, hCG, was specifically detected at a concentration of 3×10^{-8} M. After this pioneering demonstration, silicon technology-based MZIs were further optimized to improve sensitivity. For a device with a 15-mm-long sensing window, a bulk sensitivity of 1×10^{-7} RIU was later demonstrated as well as the specific detection of DNA hybridization (Fig. 8.5a). Figure 8.5b shows the corresponding calibration curve with the lowest concentration detected (1×10^{-11} M) of 58 mer-DNA in buffer [31]. Glass-based [32] and polymer-based [10,33] MZIs have also been successfully developed for biosensing purposes although the reported LODs generally remain worse than for silicon nitride-based MZIs.

However due to the periodic nature of the output signal, the MZI response can give false-positive reading because of problems of *ambiguity*, *sensitivity fading*, and *intensity fluctuations* as illustrated in Figure 8.6a [34]. A modulation system can help overcome these limitations by tuning the phase difference between the two arms.

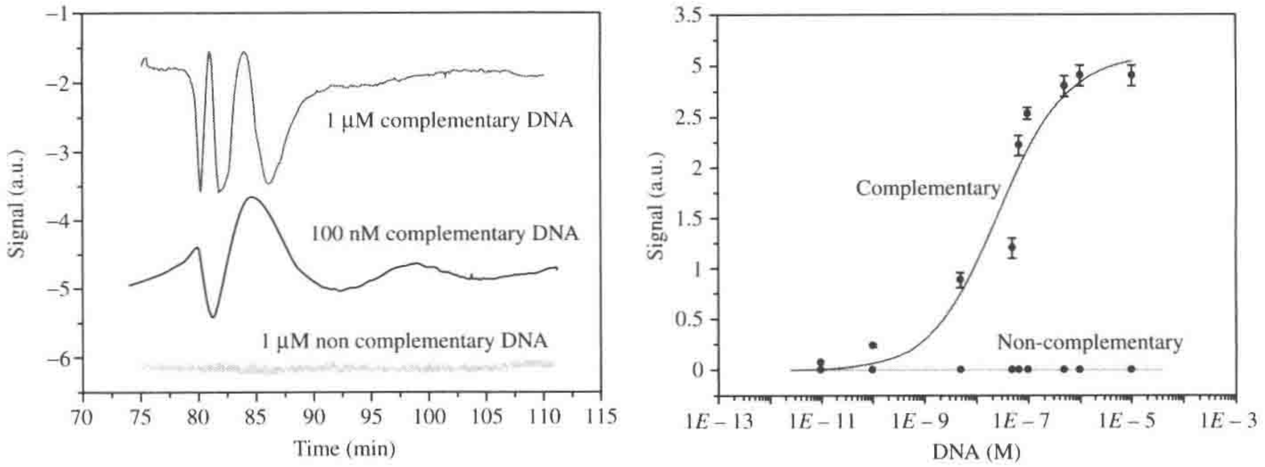

(a) (b)

FIGURE 8.5 (a) Real-time DNA hybridization signal corresponding to 1 μM and 100 nM complementary DNA, and 1 μM noncomplementary DNA; (b) calibration curve for the hybridization of complementary (red line) and noncomplementary (blue line) DNA (58 mers). Reprinted from Reference 31 under the Creative Commons Attribution License. (*For a color version of this figure, see the color plate section.*)

Electro-optic [34], acousto-optic [35], or thermo-optic [36] modulation approaches can be employed but they rely on complex fabrication processes and important electronic equipment. To avoid additional processes or equipment, alternative strategies have been suggested as an all-optical wavelength modulation system [37]. The phase difference between the two arms is modulated by periodically varying the laser input wavelength, providing a linear response and an unambiguous direct read-out of the phase variation produced by a binding event. The required wavelength shift being inferior at 2 nm, it can be achieved by modulating the driving current of low cost commercial laser diodes. The viability of the all-optical modulated MZI for biosensing applications was demonstrated through the immunoreaction of the pair hGH/anti-hGH (Fig. 8.6b) [37]. Another approach consists in adjusting the input wavelength before

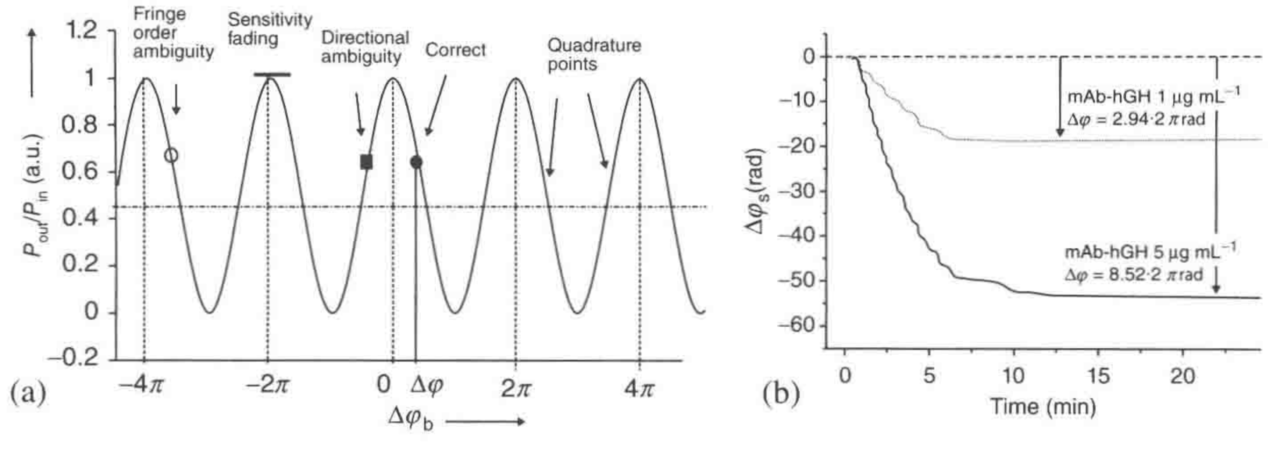

FIGURE 8.6 (a) MZI output showing the fringe pattern and the associated intrinsic problems of interferometric system. Reprinted from Reference 34 with permission from Elsevier. (b) Real-time output of the wavelength-modulated MZI highlighting the linear and direct phase read-out. Reprinted from Reference 37 with permission from OSA.

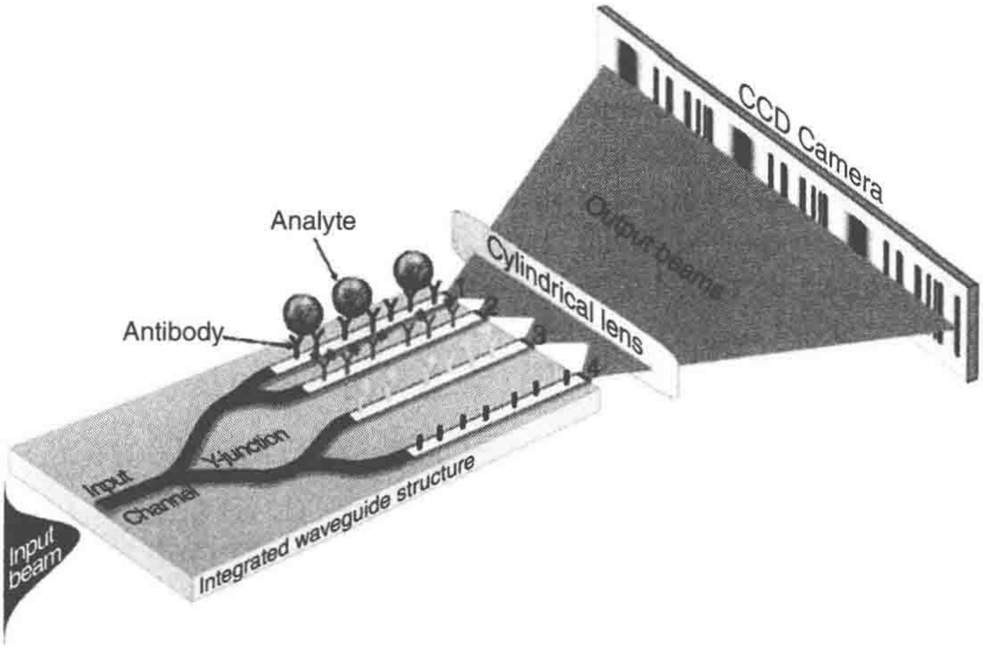

FIGURE 8.7 Four-channel Young interferometer. Reprinted with permission from Reference 39, copyright 2013 American Chemical Society.

each measurement in order to start the evaluation with the same phase difference between the two arms of the MZI [10, 33]. However, this last approach requires the use of expensive tunable lasers [10] or additional processes and equipment [33]. Working with frequency-resolved MZI instead of the conventional single-wavelength MZI also permits to circumvent the problems due to the periodic output even if tunable lasers are again unavoidable [32, 38].

8.5.1.2 Young Interferometer In the Young interferometer, a Y-junction splits the input waveguide into a sensing arm and a reference arm but, contrary to the MZI, there is no second Y-junction at the output. As depicted in Figure 8.7, the interference pattern is produced off-chip by projecting the output light from both arms onto a screen or CCD camera. The phase difference between the two interfering beams is given by

$$\Delta\varphi(t) = \frac{2\pi}{\lambda}\left[\frac{d \cdot x}{f} - (n_{\mathrm{eff,s}}(t) - n_{\mathrm{eff,R}}) \cdot L\right], \qquad (8.8)$$

where d is the distance between the two arms, f the distance between the sensor output and the camera, and x the position of the interference pattern on the screen. When a biomolecular interaction takes place in the sensing area, the $\Delta\varphi$ variation is deduced from the shift of the interference pattern on the screen.

The use of an integrated Young interferometer as sensor was first demonstrated by Brandenburg and Henninger in 1994 [40]. The waveguides were produced by thermal K^+-Na^+ exchange in a BK7 substrate and the position of the fringes on the CCD array was evaluated by Fourier analysis of the intensity distribution. The problem of ambiguity was solved by using a partially coherent source (superluminescent diode or laser diode operating below laser threshold) and analyzing the resulting function envelop. They first achieved an LOD of 1×10^{-5} RIU which was further decreased by two orders of magnitude [41].

A few years later, a four-channel Young interferometer based on Si_3N_4/SiO_2 waveguides was developed and integrated with microfluidics to have independent measurements in each sensing arm (Fig. 8.7). This system is highly sensitive as demonstrated by the reported LODs: 0.02 pg mm^{-2} for surface sensing and 8.5×10^{-8} RIU in bulk, which is one of the lowest LODs reported until now. An example of a bioanalytical application of this device is the specific detection of herpes simplex virus 1 (HSV-1), showing that 8.5×10^2 particles per mL in buffer and 10^5 particles per mL in serum can be detected [39].

More recently, a polymer-based Young interferometer has been developed [11]. This device is less sensitive than silicon-based devices (LOD of 1.2×10^{-5} RIU) but presents advantages in terms of easy fabrication since roll-to-roll techniques can be foreseen to produce low cost disposable sensors. The biosensing capabilities of the device were demonstrated through the detection of the C-reactive protein (CRP) with human CRP-specific antibodies previously adsorbed on the waveguide surface.

Young interferometers have also been developed in free space: planar waveguides are integrated with diffraction gratings for in- and out-coupling of light but both the split and the recombination of the sensing and reference beams are produced off-chip, making its integration into an LOC platform more complicated. However, this configuration is extremely sensitive with reported LODs of 4×10^{-8} RIU and 0.013 pg mm^{-2} [42].

8.5.1.3 Other Interferometric Configurations The birefringent waveguide biosensor is based on the interference between two orthogonally polarized beams (TE and TM) propagating in a straight birefringent waveguide. A birefringent waveguide biosensor with an integrated microfluidic channel has been implemented for the detection of pathogenic bacteria such as *Listeria monocytogenes* in food [43]. Specificity was demonstrated as well as the capabilities of the device to perform detection in milk. However, this device is not extremely sensitive as the lowest detected concentration was of 10^6 CFU mL^{-1} in buffer *(CFU stands for colony-forming unit).*

In the bimodal waveguide (BiMW) interferometer, two guided modes of the same polarization, the fundamental TE_{00} and the first order TE_{10} modes, interfere in a straight Si_3N_4 waveguide (Fig. 8.8) [44]. The sensitivity level of the BiMW is comparable to other integrated interferometers as LODs of 2.5×10^{-7} RIU in bulk [44] and of 8 pg mL^{-1} for the label-free detection of hGH [45] have been reported.

Other interferometric-based biosensors such as the Hartman interferometer [46] or the Dual Polarization Interferometer [47] (DPI) have not been included in this discussion since they are scarcely used nowadays.

8.5.2 Integrated Optical Microcavity-Based Biosensors

Microcavities for highly sensitive biosensing were theoretically described for the first time in 2001 [48]. Since then, it has been the subject of significant research and technological development, as can be deduced from the rising number of articles and high impact reviews published on the subject during the last years [49–52]. Even if

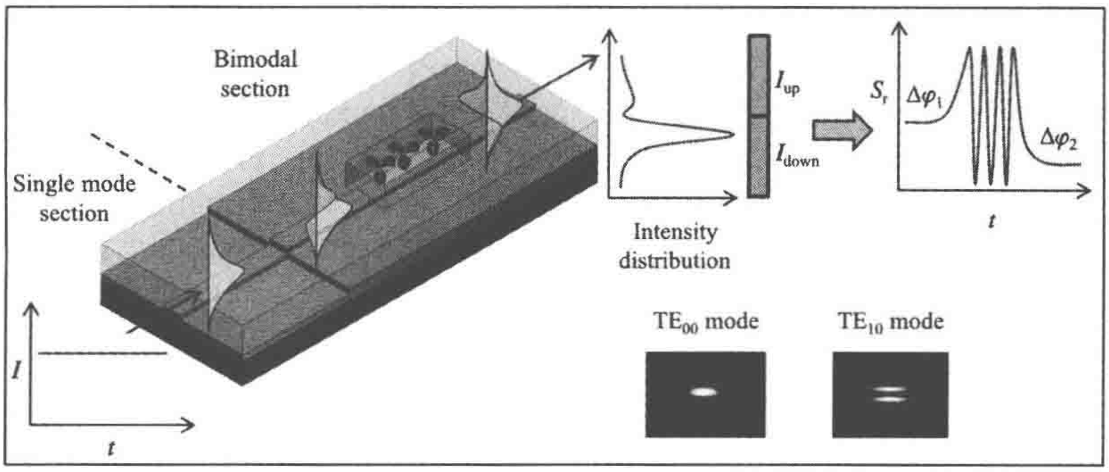

FIGURE 8.8 Working principle of the BiMW interferometer, highlighting the TE_{00} and TE_{10} mode profiles as well as the output detection scheme via a two-sectional photodiode.

they are not nominally as sensitive as interferometric biosensors (difference about one order of magnitude between LODs [53]), they present undeniable advantages such as a small foot print and the possibility to produce dense arrays for multiplexed analysis, sensitivities independent of the length of the sensing area, and a strong theoretical and technological background emanated from the telecommunication industry. Integrated optical microcavity biosensors can be implemented using various geometries such as microdisks, microrings, microtoroids, or microspheres [50] and in different materials (silicon, silicon nitride, polymer). The following explanation will be focused on integrated microring biosensors but the same operation principle can be applied to other configurations.

An integrated microring resonator consists of an input bus waveguide (cross-sectional area below a square micrometer) and of a ring (radius r between ten and hundreds of micrometers) separated by a gap of about 1 μm (Fig. 8.9). An output bus waveguide can also be added on the other side of the ring. Light is evanescently coupled from the input waveguide to the microring and propagates into the ring in the form of whispering gallery modes (WGMs), generating constructive interferences for wavelengths factors of the ring circumference. The resonance wavelength, λ, is given by

$$\lambda = 2\pi r \frac{n_{\text{eff}}}{m}, \tag{8.9}$$

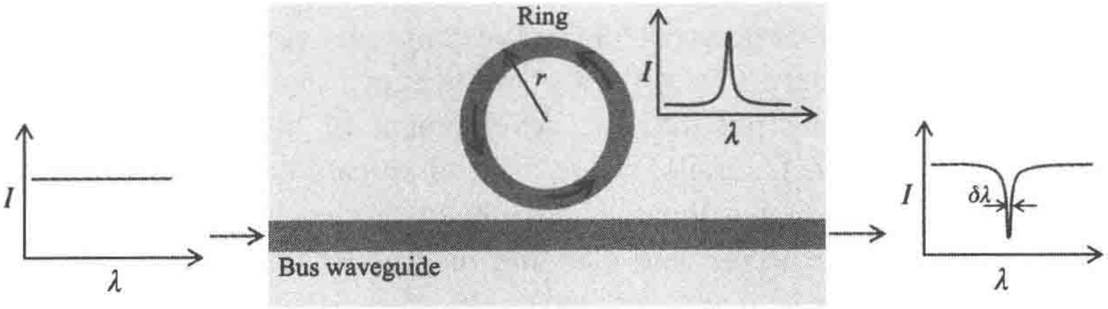

FIGURE 8.9 Working principle of the ring resonator biosensor. (*For a color version of this figure, see the color plate section.*)

where m is an integer number. As depicted in Figure 8.9, the resonance wavelength is identified as a dip in the transmission spectra when excited with a tunable laser. When a biointeraction takes place on the ring surface, it induces a change in the effective refractive index of the WGM that results in a shift of the resonance wavelength. Historically, microring resonators have been fabricated for telecommunication wavelengths, mainly 1550 nm. However, novel waveguide technologies are investigated for ring resonators operating at lower wavelengths [54].

The resonant nature of the WGM creates an extremely long effective interaction length L_{eff} which is related to the resonator quality factor (Q-factor) of the microring by

$$L_{\mathrm{eff}} = Q\frac{\lambda}{2\pi n}, \tag{8.10}$$

where n is the resonator refractive index. The Q-factor is associated with the optical losses of the cavity and describes the photon lifetime within the cavity or, in other words, the number of revolutions of light supported by the resonator. Depending on the configuration and on the materials, usual Q-factors range from 10^4 to 10^8. For instance, for a ring with a refractive index of 1.45 operating at 1550 nm and a Q-factor of 10^6, the effective interaction length will be as long as 17 cm. Therefore, despite their small physical length, the ring resonators can be highly sensitive using a small surface area and low sample volumes. The Q-factor can also be related to the resonance wavelength λ and the resonance linewidth $\delta\lambda$ by $Q = \lambda/\delta\lambda$. The LOD of a microcavity-based biosensor is therefore related to its Q-factor since the minimum detectable shift in λ depends on $\delta\lambda$.

SiO_2/Si_xN_y- [54], glass- [55], and polymer- [12, 56] based microring resonators have been reported and successfully applied to DNA, proteins, bacteria, or virus detection. However, much of the research focuses on SOI-based microresonators. For instance, SOI microring resonators (5 μm radius, Q-factor of 2×10^4) featuring a bulk sensitivity of 70 nm per RIU and a LOD of 10^{-5} RIU have been fabricated in a multiplexed configuration for antibody detection in complex samples [57]. SOI-based ring resonators have also given rise to the commercial Maverick platform from the company Genalyte, Inc. (USA), where the microrings are integrated in a multiplexed configuration (up to 128 rings) and individually addressed by a bus waveguide. This platform has been employed by several research groups and applied to a wide range of applications, like for instance the detection of Bean Pod Mottle Virus (BPMV) in buffer (LOD of 10 ng mL^{-1}) and in complex leaf extracts (Fig. 8.10) [58]. The detection and identification of transfer-messenger RNA (tmRNA) has also been demonstrated with an LOD down to 53 fmol of *Streptococcus pneumoniae* tmRNA, equivalent to approximately 3.16×10^7 CFU of the corresponding bacteria [59].

Special effort is being put into the development of high Q-factor microring resonators with polymer materials. Using a set of silicate-based inorganic–organic hybrid polymers, microring resonators have been fabricated with a difference of refractive indices between core and cladding of 7×10^{-2} RIU [12]. As a result, Q-factors of 5×10^4 were achieved, leading to a bulk sensitivity of 50 nm per RIU and a corresponding LOD of 10^{-5} RIU, values comparable to the ones reported for SOI

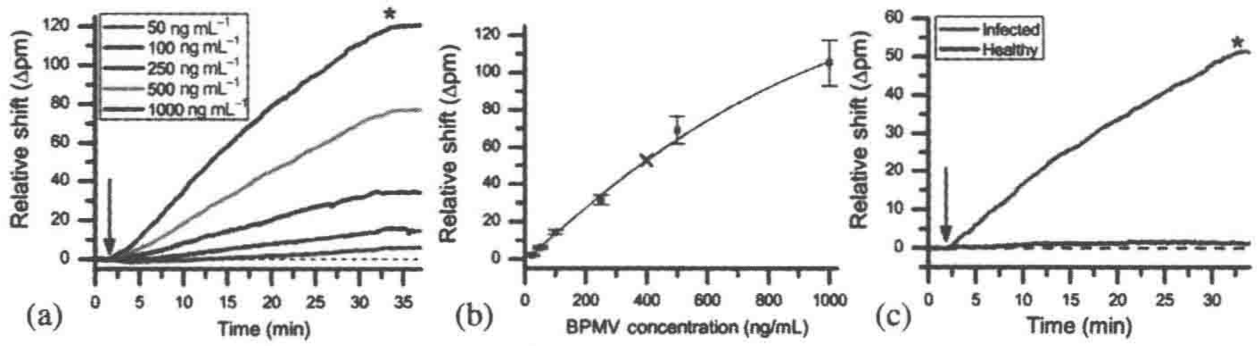

FIGURE 8.10 (a) Microring sensor responses to increasing concentrations of BPMV and (b) corresponding calibration curve. The blue "X" indicates the response from the 1:200 dilution of the extract from a BPMV infected sample. (c) Microring sensor response to diluted extracts from soybean leaves. Red: 1:200 dilution of the leaf extract from a BPMV infected sample. Blue: 1:200 dilution of the leaf extract from a healthy sample. Arrow indicates "on" and * indicates "off" (entrance and exit of the sample solution, respectively). Adapted from Reference 58 with permission from Elsevier. (*For a color version of this figure, see the color plate section.*)

microrings. The biosensing capabilities of this polymer-based microring resonator has been demonstrated by the immobilization of human-IgG, with protein A as receptor [12].

Instead of being laterally coupled as previously described, the resonators can also be coupled vertically to a bus waveguide buried below the resonator surface [55,56]. This configuration offers several advantages as compared to the lateral coupling. First, the vertical gap dimensions are easier to control than for the lateral gap, allowing the replacement of high-resolution fabrication techniques such as e-beam lithography by optical lithography. The vertical coupling also relaxes the alignment between the resonator and the bus waveguide. And, which is of importance for biosensing, the influence of the variation of the refractive index on the resonance linewidth is drastically reduced since the coupling region is totally isolated from the sensing area.

WGM can also be excited along the perimeter of a glass capillary, leading to a biosensor with an already integrated microfluidic channel in which the binding occurs at the interior of the capillary. These devices, called *optofluidic ring resonators* (OFRRs), are easily fabricated by pulling the capillary while softening the glass with a CO_2 laser. To excite the WGMs, both optical fibers and waveguides can be used. The second option is usually preferred as it leads to sensing platforms that incorporate the microfluidics and the photonic sensor in a single chip with multiplexed capabilities while using small sample volumes. OFRR sensitivity is comparable to other IO biosensors showing protein detection capabilities in the pg mm^{-2} range (Q-factors in the order of $10^5/10^6$) [50]. OFRRs have been used in various sensing applications including the detection of DNA, viruses, proteins, and cancer biomarkers. For instance, it has been recently employed for the detection of CD4+ and CD8+ T-Lymphocyte which are biological indicators of the HIV progression. CD4 and CD8 antibodies were immobilized on the inner surface of the OFRR and medically significant concentrations of CD4+ and CD8+ (160 to 1000 cells μL^{-1}) were successfully detected (Fig. 8.11) [60].

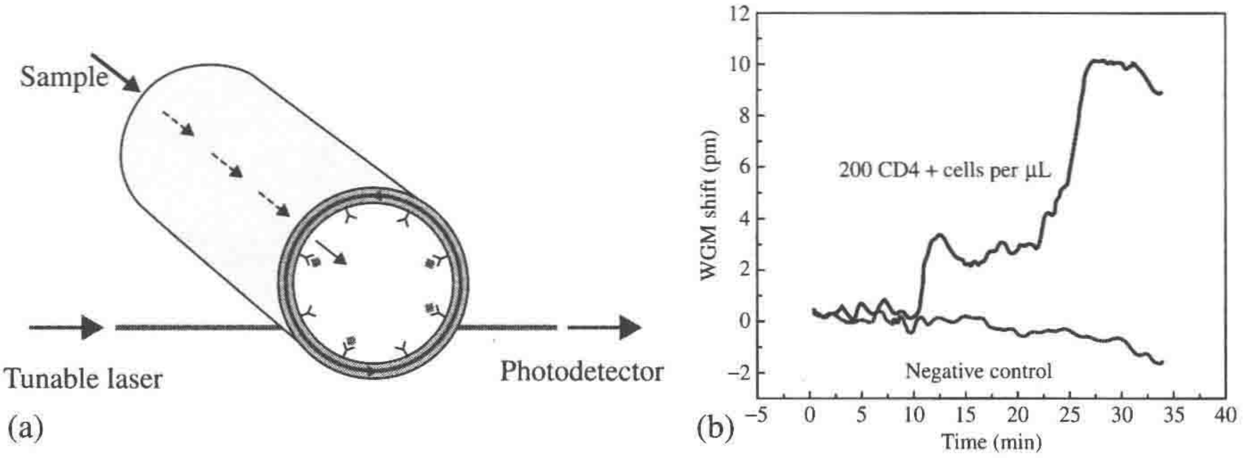

FIGURE 8.11 (a) Scheme of the OFRR biosensor. (b) Sensor response to the injection of 200 CD4+ cells μL^{-1}. The negative control is diluted serum and red blood cells. Adapted from Reference 60 under the Creative Commons Attribution License.

The resolution of the configurations previously described is mostly restricted by their Q-factors, limiting their mass detection limit to the range of pg mm^{-2}. However, *microtoroids* and *microspheres* afford much higher *Q*-factors, in the order of $10^8/10^9$, giving rise to the first all-optical label-free single-molecule technique [50, 61]. More details about the enhancement mechanisms responsible for single-molecule detection can be found elsewhere [61]. *Microtoroids* are doughnut-shaped resonators fabricated from layers of silicon dioxide grown on silicon substrates. The silicon dioxide is first etched to form microdisks which are then undercut to form silicon dioxide disks on silicon post. The toroids are finally obtained by heating the silicon dioxide with a CO_2 laser. This step produces an almost atomically smooth surface, resulting in extremely high Q-factors. *Microspheres* are easier to fabricate as they are generally obtained from a standard single-mode optical fiber. However, the major disadvantage of these structures lies in the difficulty of integration with the fluidics in the case of the microspheres and with input waveguides or optical fibers in the case of the microtoroids.

8.5.3 Grating-Based Biosensors

A diffraction grating is a periodic structure usually employed to couple light into or out of an optical waveguide. The resonant coupling between the guided mode and a diffraction order of the grating is governed by the phase-matching condition as

$$n_{\text{eff}} = \sin\theta + m\frac{\lambda}{\Lambda}, \qquad (8.11)$$

where θ is the incident angle of light, Λ the grating period, and m the diffraction order. As can be deduced from this equation, a variation of the effective refractive index will affect the resonance angle or the resonance wavelength. Therefore, grating-based biosensors can be achieved with two optical configurations: the angular and the wavelength interrogation (Fig. 8.12). In the angular approach, a scan of the resonance angle using a laser source of fixed wavelength is employed (Fig. 8.12a),

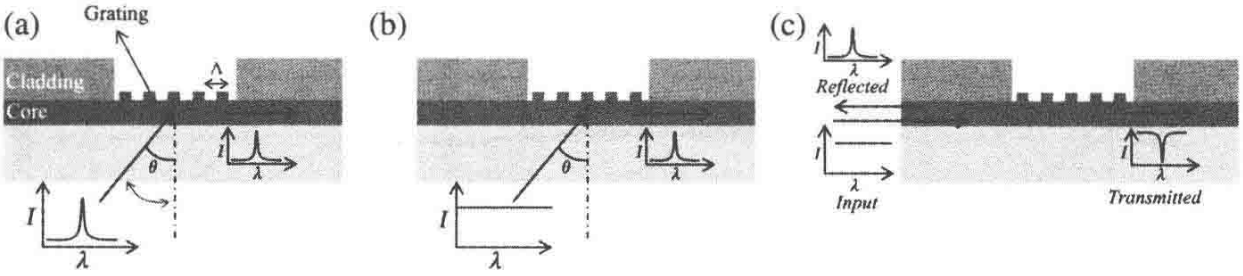

FIGURE 8.12 Schemes of grating-based biosensor configurations: (a) angular interrogation, (b) wavelength interrogation with grating as coupler, and (c) wavelength interrogation with grating as reflector. (*For a color version of this figure, see the color plate section.*)

while in the wavelength interrogation configuration it requires a tunable laser to scan the resonance wavelength at a fixed angle of incidence (Fig. 8.12b).

TiO_2 and Ta_2O_5 core layers on glass substrate are commonly used as waveguide structure in grating-based biosensors. Depending on the configuration, the grating can be defined at the interface core/substrate, at the interface core/cladding or at both interfaces. To fulfill Eq. (8.11), submicronic grating periods are requested, making conventional UV lithography generally unsuitable for the fabrication. Direct grating writing methods such as electron-beam lithography or focused ion beam milling can be employed although alternative methods like optical holography or embossing methods (as nanoimprint lithography) are usually preferred because they are simpler and have lower costs and the possibility of mass production.

The first grating-based biosensor was developed at the end of the 1980s by Lukosz's group using angular interrogation: light was coupled into the waveguide via an input grating and then propagated until the output of the waveguide where it was detected by a standard photodetector [62]. The chip was placed on a rotation stage in order to perform angular scans and to determine the shift of the resonance angle induced by the bioreactions occurring in the sensing area. An LOD around 10^{-6} RIU was demonstrated as well as some initial biosensing evaluations using the label-free immunoreaction of the pair IgG/anti-IgG. Despite the important drawback of having to achieve a precise mechanical movement of the rotation stage, this configuration is employed in the *Optical Waveguide Lightmode Spectroscopy* (OWLS) configuration. OWLS is commercialized by MicroVacuum Ltd. (Hungary) and has been used in a wide range of applications. Among them, the detection of *Legionella pneumophila* contamination in water samples with an LOD of 1.3×10^4 CFU mL^{-1} [63] or, more recently, the detection of vitellogenin, a biomarker for assessing exposure to environmental endocrine disruptors, with a dynamic range between 3 and 100 ng mL^{-1} [64].

In the wavelength-interrogated approach, an input grating coupler is used to couple the light into the waveguide at fixed angle and a detector is placed at the waveguide output to monitor the intensity of light as a function of the input laser wavelength. Specific molecular binding on the grating surface is detected as a shift in the resonance wavelength (Eq. 8.11). A sensitivity of 142 nm per RIU and a corresponding LOD of 1×10^{-5} RIU were reported while the surface sensing capabilities were demonstrated by the specific detection of IgG at 200 ng mL^{-1} (approximate surface mass density of 20 pg mm^{-2}) [65]. The *Wavelength Interrogation Optical Sensor* (WIOS) is based

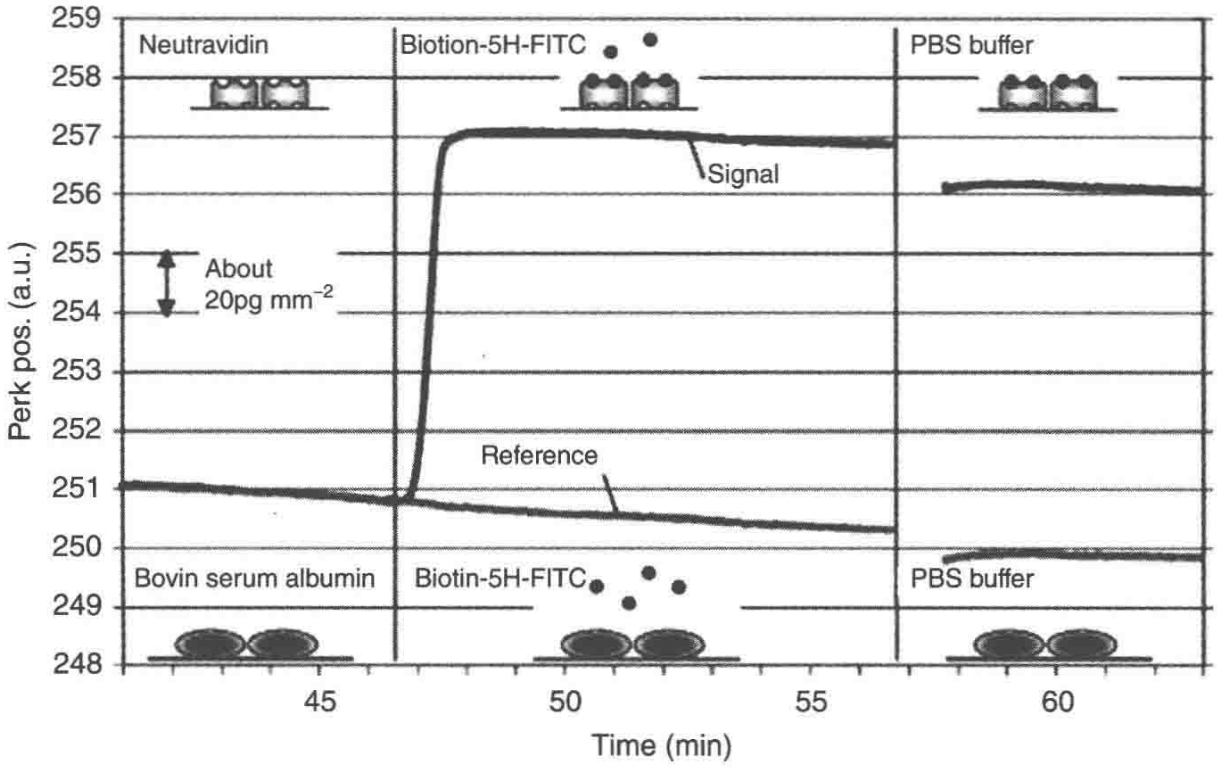

FIGURE 8.13 Reaction of biotin-5H-FITC (concentration of 1 μg mL^{-1}) on adsorbed neutravidin (signal) and BSA (reference). Adapted from Reference 66 with permission from Elsevier.

on the same working principle except that a second grating was added to out-couple the light [66]. The laser source is a compact and low-cost VCSEL emitting at 763 nm. The limited tuning range (2 nm) of the laser source results in a small linear detection range but it is overcome by adjusting the angle of incidence with a motorized mirror. A compact device including four channels and the laser source, the mirror, the flow cell, and other components was developed and tested for biosensing of low molecular weight analytes (label-free detection of molecules as small as 200 Da), such as biotin, and large biomolecules, such as antibodies, showing mass detection limits of 0.3 pg mm^{-2} (Fig. 8.13). The WIOS technology has been used for the detection of sulfonamides antibiotics in milk, achieving an LOD of 0.5 ng mL^{-1} but including an additional amplification step with a secondary antibody [67]. In the field of genomics, it has been employed to study the kinetics of covalent immobilization of double-stranded oligonucleotides to evaluate the optimal hybridization efficiency after sequential denaturation [68]. A similar technology has been developed by Corning, Inc. (USA). Their commercial device, called Epic^{TM} System, has a detection limit around 5 pg mm^{-2} and a broad dynamic range.

Grating-based biosensors have also been developed using the grating as a reflector instead of a coupler (Fig. 8.12c). In this case, light from a tunable laser is coupled into the waveguide by end-fire and a resonance wavelength is reflected back after interaction with the grating. A bioreaction on the grating surface results in a wavelength shift in the spectrum. An experimental sensitivity of 140 nm per RIU, corresponding to an LOD of 6×10^{-6} RIU, has been demonstrated using $Si/SiO_2/Si_3N_4$ waveguides [69]. Direct and label-free detection of the PepN enzyme was achieved with an experimental resolution of about 4 pm adlayer growth which is equivalent to the capture of 3×10^9 mol cm^{-2}. A similar device, the SpectroSens, is commercialized by Stratophase Ltd. (UK) since 2008. The gratings and waveguides are simultaneously fabricated in a one-step UV writing method into three-layer silica-on-silicon substrates. The SpectroSens surface mass sensitivity is estimated around 5 pg mm^{-2}, which is high when compared to the capabilities of interferometric or microring biosensors. However, this low sensitivity is compensated by the multiplexing capacity of the platform. Each chip contains eight individual sensing areas that can be functionalized with different capture probes and two chips can be packaged into a single disposable cartridge, for the simultaneous data acquisition of 16 channels. Multiplexed, label-free detection of eight different biological agents, including bacterial spores, vegetative cells, viruses, and proteinaceous toxins has been demonstrated in real time [70].

8.5.4 Photonic Crystal-Based Biosensors

The concept of PC, introduced in the 1980s, is based on a spatial modulation of the refractive index with a period comparable to the working wavelength. PCs exist in one, two, or three dimensions according to the number of directions of the index variation periodicity. The periodicity generates a range of wavelengths disallowed to propagate in the PC waveguide called the *photonic bandgap*. By introducing a defect, that is, a violation of the periodicity, a defect mode will appear in the photonic bandgap which will be seen as a relatively sharp peak in the transmission or reflection spectrum of the PC waveguide. The main PC property exploited for sensing is the dependency of the width and position of the defect peak on the periodicity and on the refractive index of the surrounding materials. In addition, light can be localized in a very small volume, leading to strong light–analyte interactions.

A significant contribution in this area was made by Fauchet's Group using SOI-based 2D PC nanocavity biosensors. Biotin–streptavidin interaction and covalent immobilization of BSA were first evaluated and a minimum mass coverage of 2.5 fg was detected [71]. More recently, they developed an array of three nanocavities coupled to a PC waveguide for multiplexed purpose (Fig. 8.14a) [72]. As each cavity has a different set of lattice constant, air hole radius, and defect diameter, they are all characterized by their own resonance wavelength, allowing the simultaneous monitoring of the three wavelength shifts (Fig. 8.14b). However, as the cavities have low Q-factors (around 400), the sensitivity of the device is very low with an LOD in bulk of about 10^{-2} RIU and an LOD of 67 nM for the detection of IgG (surface sensitivity of 1 ng mm^{-2}) [72].

The *nanoscale optofluidic sensor array* (NOSA) is based on 1D PC microcavities fabricated by electron-beam lithography on a SOI wafer [73]. The PC resonators are evanescently coupled by an adjacent single-mode waveguide. With this configuration, an LOD in bulk of 7×10^{-5} RIU was demonstrated. Resonators with different cavity spacing and therefore different resonance wavelengths were patterned in array for immunochemical multiplexed detection [74]. The multiplexing capabilities were successfully demonstrated with the individual and concurrent detection of three cancer biomarkers, the interleukins 4, 6, and 8, using a sandwich assay with a dynamic range from 1 to 100 μg mL^{-1} [74].

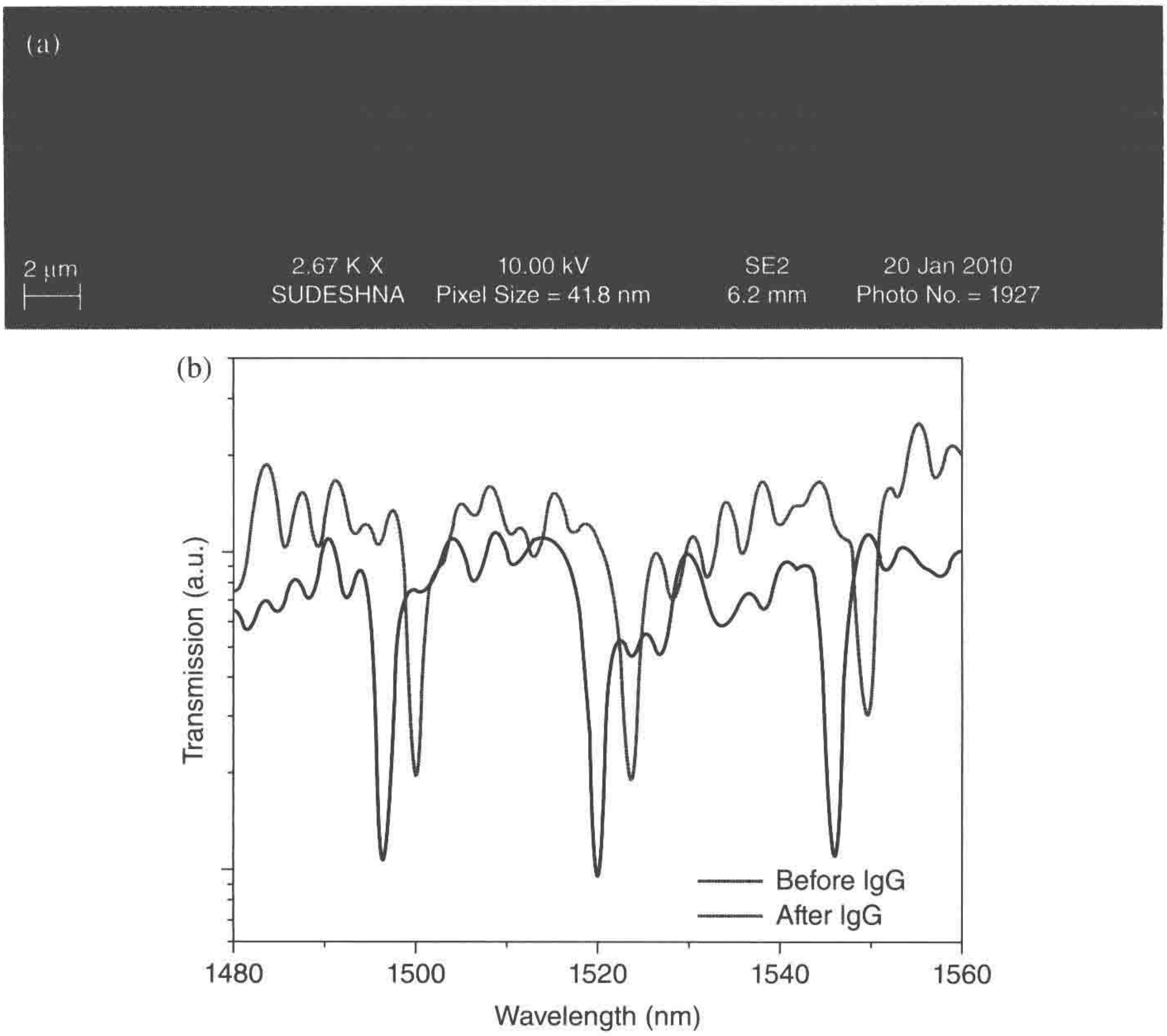

FIGURE 8.14 (a) SEM image of multiple nanocavities coupled to PC waveguides ($a = 372$, 380, and 388 nm, defect radius = 73, 75, and 77 nm) in series. (b) Experimental transmission spectra of the structure before and after target (IgG) binding. Reprinted from Reference 72 with permission from Elsevier. (*For a color version of this figure, see the color plate section.*)

More recently, a multiplexed SOI-based PC biosensor for the detection of a biomarker from lung cancer cell lysates has been described [75]. Four PC microcavities with high Q-factor ($\sim 10^4$) are arrayed on the four arms of a multimode interference power splitter for simultaneous detection. A multiplexed specific detection of a relevant cancer-associated protein with a sensitivity down to 2 cells μL^{-1} was demonstrated. This result is particularly interesting, as the detection was done in complex mixtures containing more than 20,000 to 50,000 proteins derived from a whole cell lysate of a lung cancer cell line.

8.5.5 Recent Trends in Label-Free Integrated Optics-Based Waveguide Biosensors

During the last years different types of optical waveguide transducers have been presented in the literature looking for biosensors with enhanced sensitivities and/or

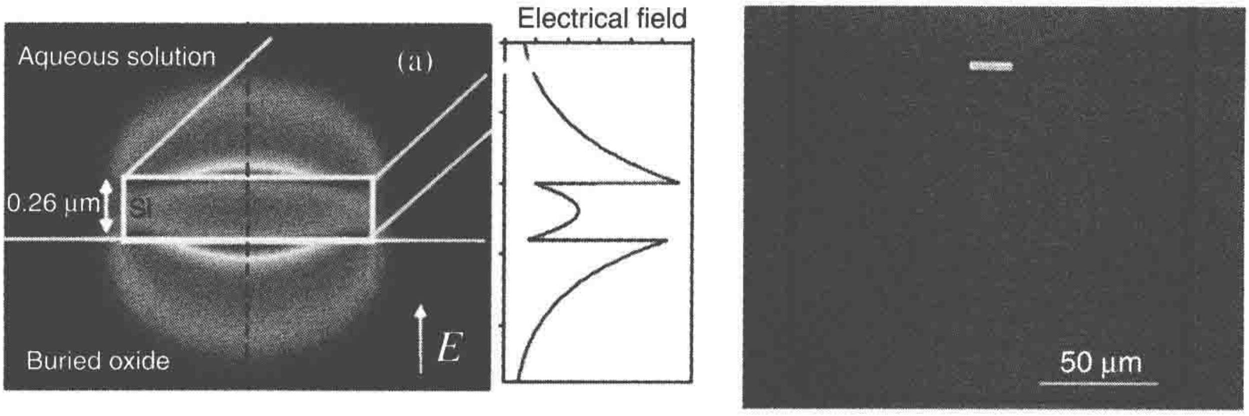

FIGURE 8.15 (a) Cross-section of a 0.26 µm × 0.45 µm SOI photonic wire waveguide and the corresponding electric field distribution for TM polarization. (b) Top view optical image of an SOI wire-based ring resonator. Adapted from Reference 76 with permission from OSA. (*For a color version of this figure, see the color plate section.*)

capabilities toward miniaturization. These improvements are usually obtained by an increase of the light–analyte interaction via a strong confinement of the light (silicon wire- and slot waveguide-based biosensors) or by an enhancement of the sensitivity due to larger surface area (porous silicon-based biosensors and BICELLs sensors).

Silicon photonic wires are sub-wavelength waveguides fabricated by e-beam lithography and reactive ion etching on SOI wafers. The high index contrast between the silicon core ($n = 3.5$) and the silica cladding ($n = 1.5$) together with their sub-wavelength size yields a strong field confinement as illustrated in Figure 8.15a [76]. By using the silicon wires in conventional sensing configurations such as MZIs or resonators (Fig. 8.15b), a high sensitivity can be achieved. A biosensor array of five Si wire-based ring resonators, including one as reference, has been fabricated with ring radius between 20 and 28 µm. A bulk sensitivity of 135 nm per RIU (LOD $< 2 \times 10^{-6}$ RIU) and the simultaneous monitoring of multiplexed molecular binding with an LOD of 0.3 pg mm^{-2} have been achieved [77]. A dense array of six spiral MZI integrated with an SU-8 fluidic channel has also been developed [78]. Multiplexed and specific binding between complementary and mismatched IgG/anti-IgG pairs were demonstrated with an LOD around 0.3 pg mm^{-2}.

Slot waveguides consist of two slabs of high refractive index separated by a nanometer-scale low refractive index slot region where light is strongly confined (Figs. 8.16a and 8.16b) [79]. Strong light–analyte interaction can be achieved in this region, leading to enhanced sensitivity when compared to conventional waveguides. So far, slot waveguides have been mainly used in resonator-based biosensors (Fig. 8.16c). For instance, an Si_3N_4–SiO_2 slot-waveguide-based ring resonators have been fabricated with a radius of 70 µm and slots of 200 nm for both the waveguide and the resonator [80]. A bulk sensitivity of 212 nm per RIU was reported, which is significantly better than conventional resonators. However, the biosensing evaluation done by covalently immobilizing the antibody anti-BSA and detecting their specific target BSA showed a moderate LOD of 16 pg mm^{-2}. More recently, an array of eight slot-waveguide ring resonators integrated with a PDMS microfluidic network to individually address each resonator has been reported [81]. LODs of 5×10^{-6} RIU

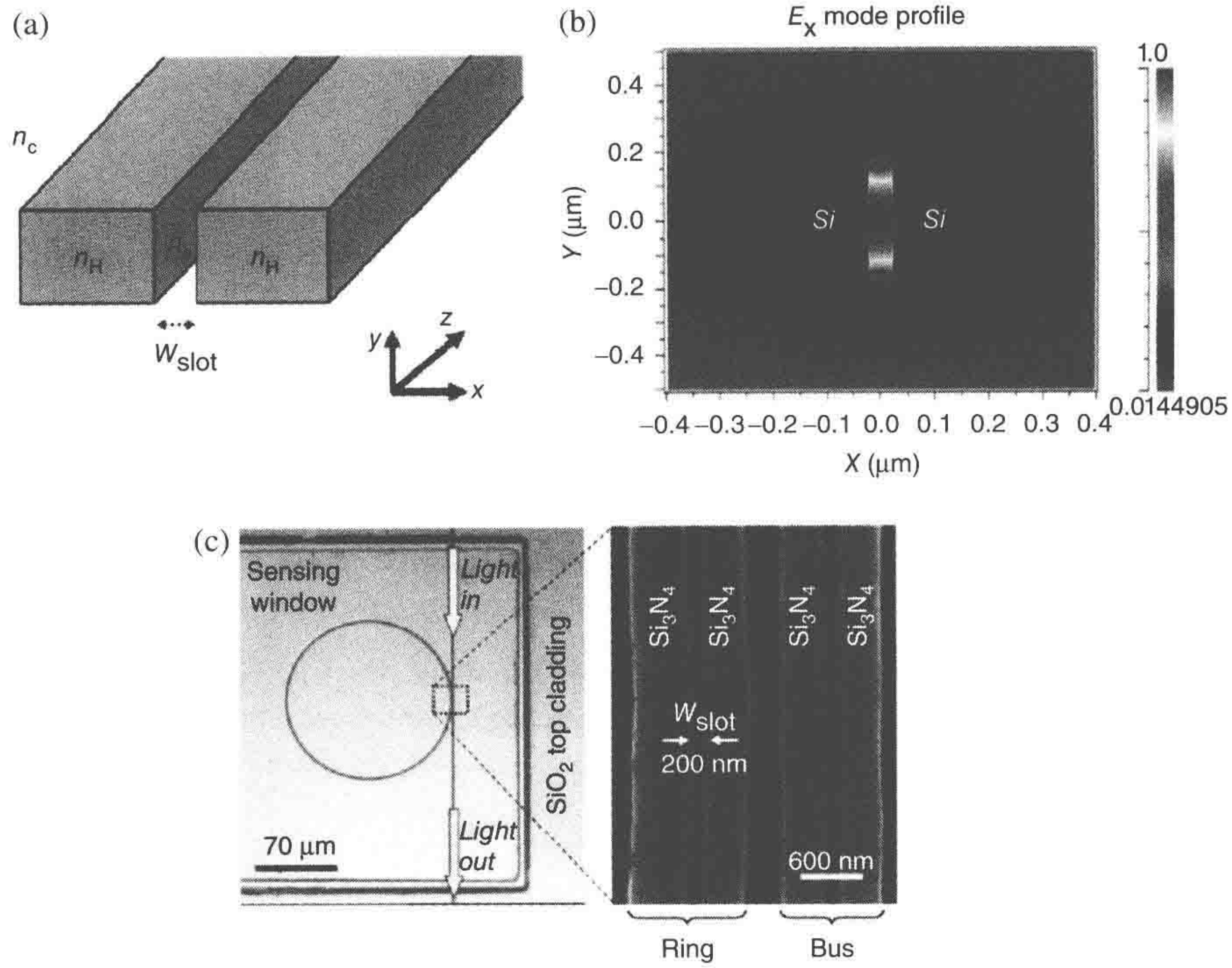
(a)
n_c
n_H
n_H
W_{slot}
y
z
x
(b)
E_x mode profile
0.4
0.2
0.0
−0.2
−0.4
Y (μm)
Si
Si
−0.4 −0.3 −0.2 −0.1 0.0 0.1 0.2 0.3 0.4
X (μm)
1.0
0.0144905
(c)
Sensing window
Light in
Light out
70 μm
SiO₂ top cladding
Si₃N₄
Si₃N₄
Si₃N₄
Si₃N₄
W_{slot}
200 nm
600 nm
Ring
Bus

FIGURE 8.16 (a) Scheme of a slot waveguide. (b) Calculated E_x profile in an Si/SiO$_2$ slot at 1.55 μm highlighting the strong confinement of light in the slot region. (c) Left: top view photograph of a 70-μm radius Si$_3$N$_4$ slot waveguide microring resonator. Right: SEM picture of the coupling region. Adapted from Reference 79 under the Creative Commons Attribution License. (*For a color version of this figure, see the color plate section.*)

in bulk and of 0.9 pg mm^{-2} in surface were demonstrated. The enhancement of the surface mass detection limit when compared to the structure previously described is due to the presence of two reference channels for control and drift compensation, and to the use of a laser with smaller wavelength steps.

Porous silicon (pSi) is a crystalline material that consists of nanometer to micron-sized columnar pores in a silicon matrix (Fig. 8.17a). Due to its large surface area (up to 800 m^2 g^{-1}), its fast preparation and its diverse and tunable optical properties, pSi is an appealing material for sensing applications [82–84]. Porous Si is generally produced by electrochemical etching technique in the presence of hydrofluoric acid (HF) [84]. Pore size, porosity, and pore depth are adjustable through judicious choice of silicon wafer, dopant type, dopant density, current density, HF:surfactant ratio, and so on. Porous Si has been extensively exploited as a material for optical biosensors, mainly in fluorescent and cavity-based biosensors, including single layer interferometers and resonant microcavities. These configurations have been employed for detection of glucose, DNA, bacteria, viruses, proteins, and other biomedical analytes for treatment and diagnostic [83, 84]. pSi waveguide-based biosensors can also

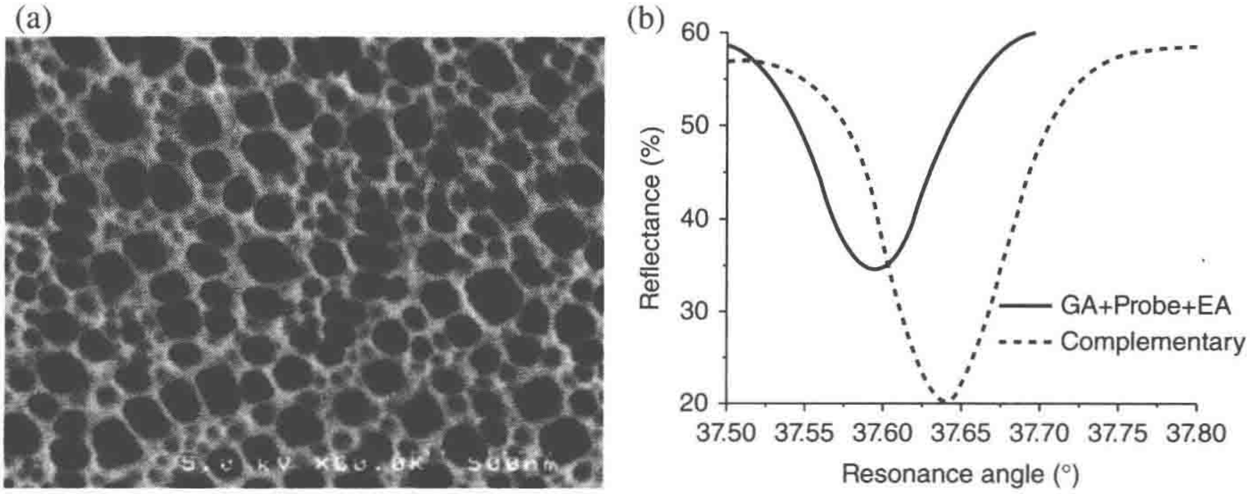

FIGURE 8.17 (a) SEM image of pSi with distribution of pore sizes between approximately 30 and 100 nm. Reprinted from Reference 82 with permission from Elsevier. (b) pSi waveguide resonances corresponding to the DNA probe immobilization (GA + probe + EA) and to the binding with its complementary DNA. Adapted from Reference 85 with permission from Elsevier.

be implemented using pSi waveguide based on two pSi layers: a low porosity (high index) layer, and a high porosity (low index) layer [85]. As in a standard SPR, a prism is used to evanescently couple a laser beam into the waveguide at a specific angle and a detector is placed at the output face of the prism. Since the coupling angle depends on the refractive index, the angle shifts when biomolecules are infiltrated into the pores of the waveguide (Fig. 8.17b). With this device, the selective detection of DNA has been demonstrated, with a theoretical LOD of 5×10^{-8} M, equivalent to 5 pg mm^{-2} [85]. However, pSi waveguide-based biosensors have not been extensively studied, certainly because they do not take as much advantage of the pSi large sensing area as the cavities do. Another problem related to pSi waveguides is the lack of uniformity and reproducibility of the porous layer due to the multiple etching parameters.

More recently, a new IO-based biosensor called the *Biophotonic Sensing Cells* (BICELLs) has been introduced [86]. It consists of a periodic network of nanopillars (in Si, SiO_2, or polymer) which are interrogated by three independent reflectivity measurements (spectrometry, reflectometry, and ellispometry). Even it is not a waveguide-based device it is worthy to mention it, in particular for the high throughput capabilities offered by the micrometer and sub-micrometer spot size of the read-out interrogation. In addition, the large surface area provided by the nanopillar results in an increased sensitivity. BICELLs biosensing capabilities were demonstrating by detecting anti-gestrinone antibodies in unpurified rabbit serum, with an LOD of 64 pg ml^{-1} [87].

8.6 OPTICAL FIBER-BASED BIOSENSORS

Due to their sensitivity to strain, temperature, pressure, vibration, curvature, and refractive index of the surrounding medium, OFs can be used in many healthcare applications such as thermal and pressure mapping, low temperature monitoring, or immunosensing [88]. In the following, we will focus on biosensing applications where an analyte react with its specific bioreceptor previously immobilized on the fiber surface. However, most of the OF-based biosensors use fluorescent labels [13, 14]. Indeed, OF biosensors are particularly suited for fluorescence detection since the emitted light can easily be collected by the OF and transported to the analyzer. The use of fluorescence tags is also a way to make up for their low sensibility. Actually, the main advantage of OF biosensors when compared to IO biosensors is that their small and flexible shape enable them to be placed in small vessels and in tissues for minimally invasive *in situ* sensing.

8.6.1 Fiber Bragg Grating-Based Biosensors

A fiber Bragg grating (FBG) is a photosensitive fiber in which a Bragg grating with periodicity of hundreds of nanometers has been written through UV illumination. As light propagates inside the core, the grating selectively reflects one wavelength, given by

$$\lambda = 2n_{\text{eff}}\Lambda. \tag{8.12}$$

Changes in the vicinity of the grating will result in a shift of the resonance wavelength. As illustrated in Figure 8.18, FBG can be mainly implemented into two configurations: in reflection, detecting only the reflected wavelength or in transmission, detecting the whole spectra with a minimum for the resonance wavelength. FBGs are particularly suitable for multiplexed detection as multiple gratings with different periods can be written on a single fiber. Each grating will be characterized by its proper resonance wavelength and the shifts of the resonance wavelengths of all the gratings can easily be processed with one analyzer.

The sensitivity of conventional FBG is limited around 200 nm per RIU by the low refractive index contrast between core and cladding [89] but several approaches have been developed to circumvent this limitation. One method consists in etching the fiber core to enhance its evanescent field: a sensitivity of 29 nm per RIU was reported for a fiber with a core diameter of 5 μm while this value drastically increases up to

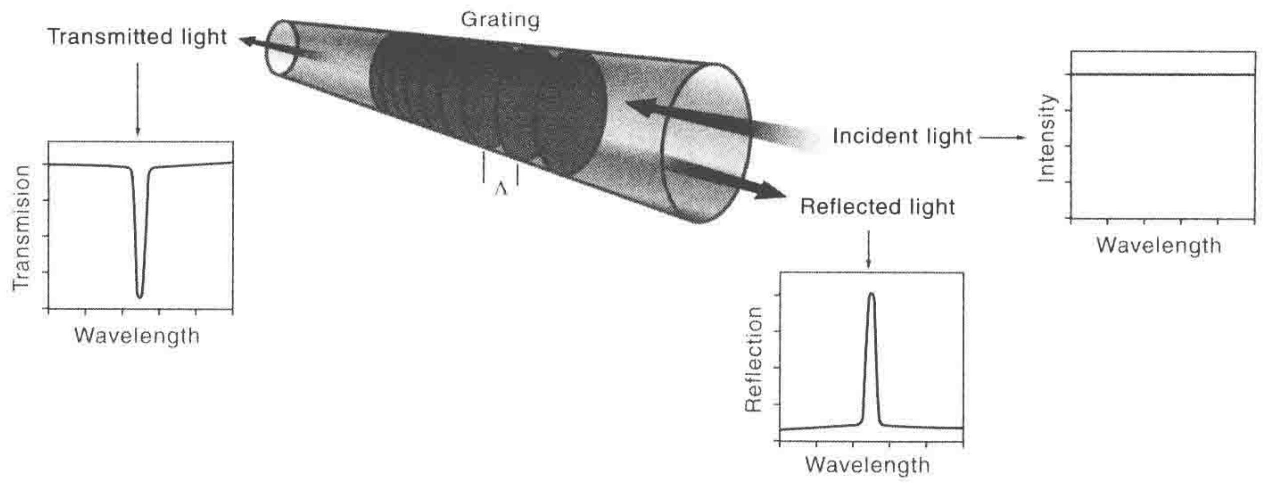

FIGURE 8.18 Principle of the FBG biosensor.

1394 nm per RIU when its core diameter was reduced to 3.4 μm (corresponding LOD of 7.2×10^{-6} RIU) [90]. DNA probes of 20 bases were immobilized on the surface of the fiber grating and the hybridization of 0.7 μg mL^{-1} of the complimentary target DNA was successfully detected [90]. Light–analyte interaction was also increased by inscribing FBGs into a photosensible three-hole MOF [91]. By injecting the sample solution through the holes, where the light intensity is higher, an LOD in bulk of 6×10^{-6} RIU was achieved. However, biosensing capabilities of this configuration were not demonstrated.

Another strategy to enhance the sensitivity of FBG consists in writing tilted gratings. In a tilted FBG, the grating plane forms an angle with the perpendicular of the fiber axis which results in an enhanced coupling between the core mode and the cladding modes. BSA was immobilized on the surface of the tilted FBG for anti-BSA detection [92]. The calculated LOD in term of surface density concentration and anti-BSA concentration were of 13 pg mm^{-2} and 86 ng mL^{-1}, respectively. More recently, a double-tilted FBG was employed for a modified Fabry–Perot core-cladding closed-loop cavity [93]. This biosensor was functionalized with PNA probes and a specific DNA detection at a 1×10^{-8} M concentration was demonstrated.

8.6.2 Long-Period Grating-Based Biosensors

Long-period grating (LPG) biosensors have larger grating periods than FBG, typically between 100 μm and 1 mm, resulting in the coupling of the core modes into the cladding modes (Fig. 8.19a). The resonance condition is expressed as

$$\lambda = (n_{\mathrm{eff,core}} - n_{\mathrm{eff,cladding}})\Lambda, \tag{8.13}$$

where $n_{\mathrm{eff,core}}$ and $n_{\mathrm{eff,cladding}}$ are the effective refractive indices of the core modes and cladding modes, respectively. As the coupling to the cladding modes depends on the difference between the two effective indices, LPG biosensors are more sensitive than FBG biosensors, typically between 10^2 and 10^3 times more sensitive. And, due to the large grating period, they are also easier to fabricate than FBGs. In addition, there is no need for etching the cladding to define the sensing area because the cladding modes are directly sensitive to changes in their surroundings. The first demonstration of LPG as a biosensor was reported in 2000 by DeLisa et al. [94]. A specific detection of IgG over a dynamic range of 2–100 μg mL^{-1} in buffer was carried out with anti-IgG immobilized on the LPG surface. Antigen detection was also confirmed in a protein mixture and in crude cell lysate from *Escherichia coli (E. coli)*.

To enhance sensitivity, LPG with shorter grating periods (around 160 μm) have been developed in order to be in the vicinity of the dispersion turning points, resulting in conjugate dual-peak cladding modes that are extremely sensitive to external perturbations [97]. With these dual-peak LPG biosensors, a hybridization of 1×10^{-6} M DNA was demonstrated. To further enhance the sensitivity, dual-peak LPG biosensors have been implemented on an etched fiber [98]. Following these works, dual-peak LPGs with a bulk sensitivity of 570 nm per RIU have been applied to the label-free and specific detection of *E. coli* K12 cells using physically adsorbed bacteriophages as

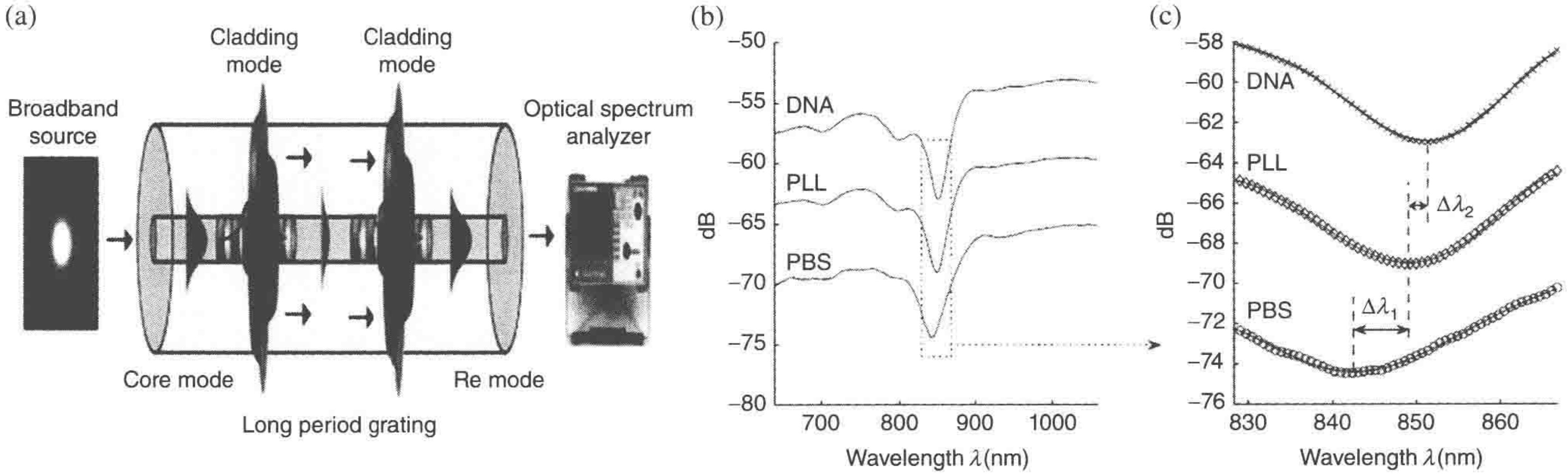

FIGURE 8.19 (a) Scheme of the LPG biosensor. Reprinted from Reference 95 with permission from Elsevier. (b) Experimental transmission spectra for PBS (phosphate buffered saline solution), PLL (poly-L-lysine), and double-stranded DNA. (c) Close up of dotted rectangle in (b) highlighting the wavelength shifts. Adapted from Reference 96 with permission from OSA.

bioreceptors [99]. Optimizing the device design and the configuration, an ultra-high sensitivity of 2500 nm per RIU has been recently demonstrated [95].

LPG biosensors can also be implemented into PC fibers. In the first reported work on PC-based LPG biosensor, a spectral shift of 1.4 nm per nanometer of DNA monolayer deposited was demonstrated (Figs. 8.19b and 8.19c) although the LOD in bulk was only of 10^{-4} RIU [96]. An improved sensitivity in bulk of 1500 nm per RIU, corresponding to an LOD of 2×10^{-5} RIU, was later obtained [100]. However, no surface sensing experiments were reported.

8.6.3 Optical Fiber-Based Interferometric Biosensors

In OF-based interferometry, the core mode, which acts as the reference beam, interferes with the cladding modes that are sensitive to the external medium. It generally implies the use of tunable lasers emitting in the near IR. As for the previous transduction schemes, sensitivity is significantly enhanced by using tapered fibers.

A single-mode/multimode/single-mode PC fiber interferometer has been recently developed, using a fusion arc splicing technique to splice a 33-mm-long PC fiber between to single-mode fibers [101]. The microbubbles created in the splice region act as a modal splitter to excite the cladding modes. This device has a bulk sensitivity of 320 nm per RIU for an RI range between 1.33 and 1.34 and its biosensing capabilities were demonstrated by the binding between streptavidin and biotin previously immobilized on the PC fiber surface.

Interferences between core mode and cladding modes were also used in OF-based MZI and Michelson interferometers (MIs) [102]. As illustrated in Figures 8.20a and 8.20b, mode splitting is achieved by incorporating waist-enlarged fiber taper in a single-mode fiber. Immunosensing tests were done with anti-IgG as target and IgG

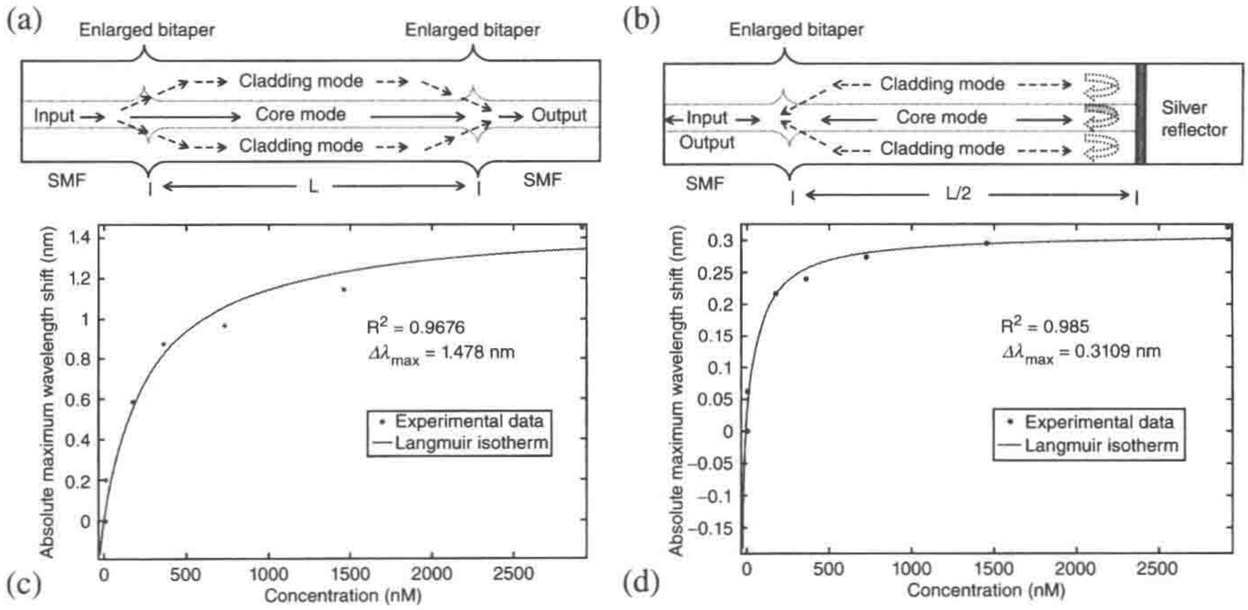

FIGURE 8.20 Schemes of the waist-enlarged bitaper-based immunosensors: (a) Mach–Zehnder configuration and (b) Michelson configuration. Change in wavelength as a function of anti-IgG concentration for: (c) MZI sensor and (d) MI sensor. Adapted from Reference 102 with permission from Elsevier.

immobilized on the fiber surface. Figures 8.20c and 8.20d show the calibration curve for both MZI and MI devices. The MZI biosensor is clearly the most sensitive device, with an LOD of 1.8×10^{-10} M.

Fabry–Perot interferometric biosensors can also be fabricated with OF by incorporating a short piece of hollow fiber between two pieces of single-mode fiber [103] or by adding a hollow core fiber at one extremity of a single-mode fiber [104]. The spectral reflectance of these devices is sensitive to the optical path length in the cavity: when the target analytes bind to the receptor, the thickness of the cavity increases and, consequently, a shift in the interferometric spectrum is observed. Various bioanalytical applications have been reported, such as the specific hybridization of 26-mer target DNA with complementary capture DNA [103], the detection of anti-pig IgG [105] or, more recently, the detection of BSA with an estimated LOD of 0.48 ng [104].

8.6.4 Evanescence Wave Absorbance-Based Optical Fiber

The working principle of RI-based evanescent wave absorbance biosensors relies on the fact that the transmission through the fiber depends on the refractive index difference between the core and the cladding: index variation induced by bioreactions will produce a change in the transmitted intensity. As for the previous OF-based configuration, sensitivity is noticeably improved by using tapered OF. Taking into account that the working wavelength must be carefully chosen to avoid changes in the transmission due to molecule absorption instead of index variation, evanescent wave absorbance based biosensors have been mainly implemented at 1310 or 1550 nm.

Specific detection of BSA at a concentration of 10 fg mL^{-1} were achieved with tapered OF with waist diameters of 5–10 μm and total lengths of 1000–1200 μm [106]. A similar biosensor was used for the detection of DNA hybridization: 15-mer DNA was immobilized in a gold-coated taper and its complementary 10-mer DNA was successfully detected at a concentration of 750 fM [107]. In addition, specificity was demonstrated as the sensor was able to distinguish between complementary DNA and DNA with a single nucleotide mismatch. Based on the same working principle, a tapered OF biosensor (waist diameter of 10 μm) has been applied to the diagnosis of celiac disease, with specific detection of antibodies in the range of 1–15 ppm [108]. A tapered OF biosensor with a waist diameter of 6–7 μm has also been used for *in situ* real-time monitoring of *E. coli* growth (Fig. 8.21) [109].

The transmission spectrum of an OF coupler is also strongly affected by the refractive index of the surrounding medium. For instance, an OF coupler has been fabricated with a fused single mode fiber of 9 μm in diameter in the coupler region and applied to biosensing: binding of streptavidin was demonstrated over a range of 0.5–2 μg mL^{-1} by immobilizing biotin on the coupler surface via aminosilane chemistry [110].

8.7 LAB-ON-A-CHIP INTEGRATION

LOC platforms are miniaturized analytical devices which integrate all functionalities on a single chip, from fluid handling, sample preparation (filtration, homogenization,

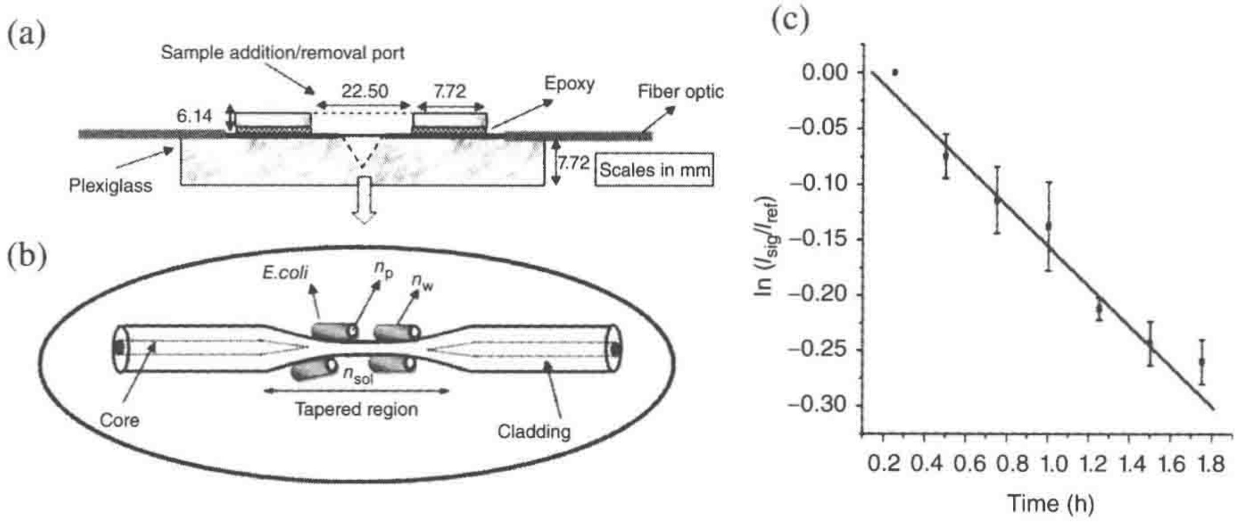

FIGURE 8.21 (a) Scheme of the microreactor for bacterial growth; (b) representation of *E. coli* bacteria immobilized on the taper region; and (c) sensor response versus time during *E. coli* growth on the tapered fiber. Adapted from Reference 109 with permission from Elsevier.

and dilution), target detection, transducer readout, and signal processing. Taking advantage of the miniaturization, LOC platforms can perform high throughput screening while consuming only tiny amounts of samples, reagents, space, and energy. They can also contain enough hard-wired intelligence and robustness to be used by non-skilled personnel (for instance the patient itself) and should deliver in real time a multitude of data directly to a central database. The best example so far of a stand-alone LOC is the glucose sensor daily used by diabetic people to test their concentration of glucose in blood: a small drop of blood is placed on a disposable test strip containing an electrochemical biosensor and the result appears on a digital display within a few seconds. The spread of such tests for the detection of very low concentrations of analytes or toxins in real-time would be of great benefit for early medical diagnosis, food safety, or environment monitoring.

Label-free optical biosensors appear as one of the most promising candidates for LOC platforms as they combine highly sensitive and on-chip detection with the possibility of miniaturization and photonic integration of components on one single chip (Fig. 8.22). This is particularly true for IO biosensors based on silicon and silicon-related materials as they can benefit of the strong know-how of the semiconductor microfabrication industry and its potential for mass production with consequent reduction of costs.

Some commercial platforms based on optical waveguide biosensors have been described along this chapter. However, they cannot be considered as real LOC device because they are bulky and expensive. Moreover, they present some of the drawbacks of traditional methods (such as ELISA or RIA tests) as they must be used by trained personnel in a laboratory environment. To achieve a real standalone LOC platform, the optical transducer in a multiplexed configuration must be integrated with all the required units (as light sources, photodetectors, microfluidics, processing electronics, etc.) as well as robust biofunctionalization protocols for the biological receptors. Even though the individual components are well known, there are still major barriers

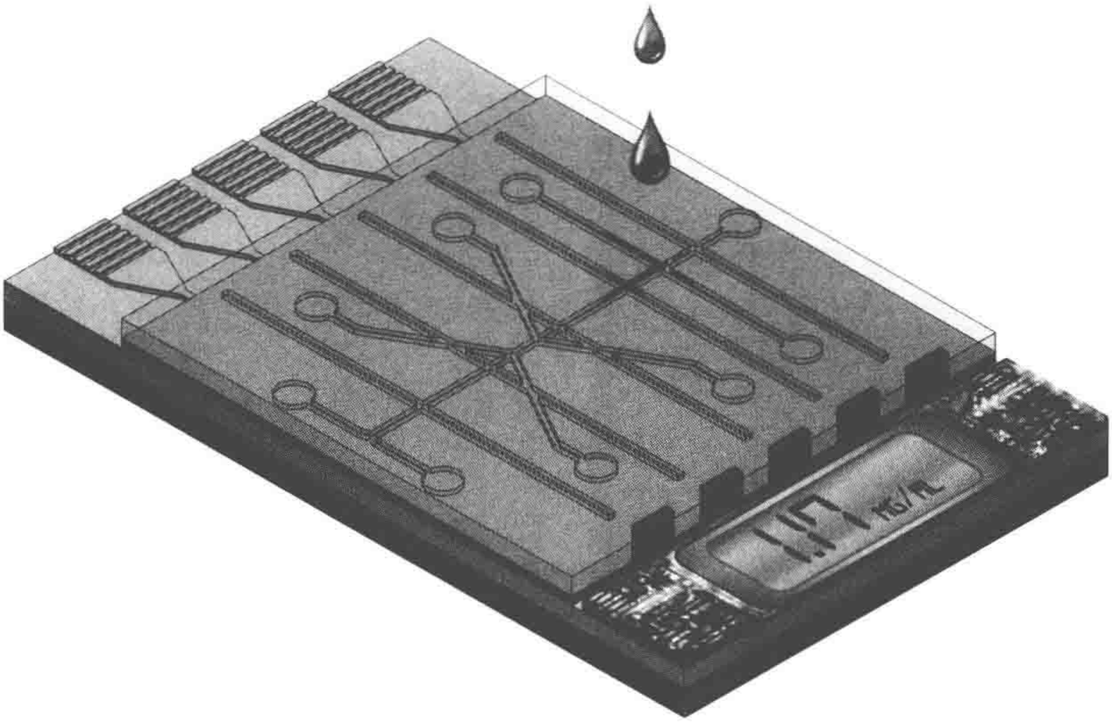

FIGURE 8.22 Representation of an IO-based LOC platform.

to overcome for their assembly, among others because the subsystem interfaces between them are difficult to optimize. Integration could be monolithic (all functionalities are incorporated in one single chip) or hybrid (functionalities are separated on several chips).

IO-based LOC is still in its early stages and most of the work done so far mainly includes the integration of the optical transducers with the fluidics, the so-called *optofluidics* [111, 112]. A challenge specific to IO-based LOC platforms is the way to reliably couple light into the submicronic cross-section of the waveguides. High alignment tolerance between the input beam and the photonic chip is also mandatory as the photonic chips would have to be frequently replaced and the LOC platform should be portable. Grating couplers arise as the most suitable solution since they allow for efficient light coupling together with high alignment tolerances.

Few examples can be found in the literature of complete IO-based LOC platforms. In most reported prototypes, the transducers are microring resonators or interferometers as it has been pointed out throughout this chapter that they are the most viable alternatives to conventional diagnosis techniques. For instance, vertically coupled polymeric microresonators showing high performance for biosensing have been integrated with a digital electrowetting-on-dielectric microfluidic system [56] and with a thin film InGaAs-based metal-semiconductor-metal photodetector [113], demonstrating that the use of a polymer waveguide does not impede the integration with complex elements. However, the biosensing capabilities of this intricate system have not been reported yet. Arrays of 16 and 128 spiral ring resonators based on silicon photonic wires have also been integrated with microfluidic channels and input and output grating couplers on a 6×9 mm^2 chip [114]. An important advantage of this platform is the integration of unconventional grating couplers formed by rows of holes that are completely etched, allowing the simultaneous fabrication of both the gratings and the waveguide structures in only one step by deep-UV lithography. This platform has been applied to the multiplexed detection of *E. coli* bacteria with a view to perform serotyping but complete multiplexed analytical studies have not been reported yet. In addition, the read-out instrument occupies an area of 60 × 45 cm^2 which is still far from a truly portable and stand-alone LOC platform.

Regarding interferometric biosensors, a promising monolithically integrated LOC platform has been developed based on arrays of MZI fabricated by standard silicon technology and integrated with lasers, photodetectors, and microfluidics [115]. The read-out is based on frequency-resolved MZI to solve the problems of interferometric sensors [38]. They demonstrated a moderate LOD in bulk of 4×10^{-6} RIU and proof-of-concepts of biosensing were reported [115]. Nevertheless, complete bioanalytical studies are still pending to validate this LOC platform as a reliable diagnostic tool. Silicon nitride BiMW interferometers have been integrated with submicronic grating couplers and with a 3D network of SU-8 polymer microfluidics assembled at the wafer level to ensure perfect sealing and compact packaging [116]. An all-optical wavelength modulation system has been applied to the BiMWs to provide a linear response and a direct read-out of the phase variation system without additional fabrication processes or instrumentation. The sensitivity and specificity of the modulated BiMW have been demonstrated through the label-free detection of the anti-hTSH with an LOD of 17 ng mL^{-1}. However multiplexed detection, which is an important requirement for LOC platform, has not been reported yet.

As illustrated through the previous examples, the application to real-world bioanalytical studies is one of the bottlenecks in the development of LOC platforms based on optical waveguide biosensors. The main reason is that the integration of such platforms requires a strong multidisciplinary expertise in photonics, micro-fabrication, material science, electronics, and biochemistry but the last one is often left aside: the groups working in this field are generally mainly composed of physicists and engineers to develop efficient platforms with high degree of integration, deferring the bioanalytical part. However, the development of reliable biochemistry processes (choice of the surface activation process and the immobilization technique as well as the type and conditions of the assay) is as relevant and crucial step as the development of the optical transducer as it will turn a sensing device into a valid analytical tool with the required quality standards.

8.8 SUMMARY

In this chapter, we have overviewed optical waveguide biosensors for label-free detection, demonstrating their excellent performances: high sensitivity, selectivity, potential for multiplexing and miniaturization, and so on. Some of them, such as interferometers, ring resonators, grating-, and OF-based biosensors are relatively mature and some have even been commercialized. Others, like PC-, silicon wire-based biosensors, or microstructured optical fibers are still in their early stages but they have great potential for the next generation of label-free biosensors.

Optical waveguide biosensors, and in particular IO-based biosensors, have become the most suitable technology for the implementation of stand-alone LOC platforms that could be employed for ultrasensitive real-time diagnosis at the point-of-care. Progress has been made in the last years in this area but there are still limitations in the integration of all the components into one single platform and, above all, in the connections with real-world bioanalytical applications. However, due to the intensive research effort that is being done, there is no doubt that LOC platforms based on label-free IO biosensors will be soon available in the market.

REFERENCES

[1] X. D. Fan, I. M. White, S. I. Shopova, H. Y. Zhu, J. D. Suter, and Y. Z. Sun, "Sensitive optical biosensors for unlabeled targets: a review," *Anal. Chim. Acta* **620**(1–2), 8–26 (2008).

[2] M. Schäferling, "Fluorescence-based biosensors," in *Encyclopedia of Analytical Chemistry* (John Wiley & Sons, 2006).

[3] M. Strianese, M. Staiano, G. Ruggiero, T. Labella, C. Pellecchia, and S. D'Auria, "Fluorescence-based biosensors," in *Spectroscopic Methods of Analysis*, edited by W. M. Bujalowski (Humana Press, Springer, 2012), pp. 193–216.

[4] M. C. Morris, "Fluorescence-based biosensors: from concepts and applications," in *Progress in Molecular Biology and Translational Science* (Elsevier Press, 2013).

[5] G. Lifante, *Integrated Photonics: Fundamentals* (John Wiley & Sons, 2003).

[6] W. Lukosz and K. Tiefenthaler, "Directional switching in planar waveguides effected by adsorption-desorption processes," *IEE 2nd Eur. Conf. Integ. Opt.* **227**, 152–155 (1983).

[7] W. Lukosz, "Principles and sensitivities of integrated optical and surface plasmon sensors for direct affinity sensing and immunosensing," *Biosens. Bioelectron.* **6**(3), 215–225 (1991).

[8] G. M. Hale and M. R. Querry, "Optical constants of water in the 200-nm to 200-μm wavelength region," *Appl. Opt.* **12**(3), 555–563 (1973).

[9] H. K. Hunt and A. M. Armani, "Label-free biological and chemical sensors," *Nanoscale* **2**(9), 1544–1559 (2010).

[10] R. Bruck, E. Melnik, P. Muellner, R. Hainberger, and M. Lämmerhofer, "Integrated polymer-based Mach-Zehnder interferometer label-free streptavidin biosensor compatible with injection molding," *Biosens. Bioelectron.* **26**(9), 3832–3837 (2011).

[11] M. Wang, J. Hiltunen, C. Liedert, L. Hakalahti, and R. Myllylä, "An integrated Young interferometer based on UV-imprinted polymer waveguides for label-free biosensing applications," *J. Eur. Opt. Soc. Rapid Publ.* **7**, 12019–1/7 (2012).

[12] L. Wang, J. Ren, X. Han, T. Claes, X. Jian, P. Bienstman, R. Baets, M. Zhao, and G. Morthier, "A label-free optical biosensor built on a low-cost polymer platform," *IEEE Photon. J.* **4**(3), 920–930 (2012).

[13] A. Leung, P. M. Shankar, and R. Mutharasan, "A review of fiber-optic biosensors," *Sens. Actuators B: Chem.* **125**(2), 688–703 (2007).

[14] T. M. Monro, S. Warren-Smith, E. P. Schartner, A. François, S. Heng, H. Ebendorff-Heidepriem, and S. V. Afshar, "Sensing with suspended-core optical fibers," *Opt. Fiber Technol.* **16**(6), 343–356 (2010).

[15] Y. Skibina, V. V. Tuchin, V. I. Beloglazov, G. Shteinmaeer, I. L. Betge, R. Wedell, and N. Langhoff, "Photonic crystal fibres in biomedical investigations," *Quantum Electron.* **41**(4), 284 (2011).

[16] A. Sassolas, L. J. Blum, and B. D. Leca-Bouvier, "Optical detection systems using immobilized aptamers," *Biosens. Bioelectron.* **26**(9), 3725–3736 (2011).

[17] L. Ye and K. Mosbach, "Molecular imprinting: synthetic materials as substitutes for biological antibodies and receptors," *Chem. Mater.* **20**(3), 859–868 (2008).

[18] L. S. Wong, F. Khan, and J. Micklefield, "Selective covalent protein immobilization: strategies and applications," *Chem. Rev.* **109**(9), 4025–4053 (2009).

[19] B. Prieto-Simon, M. Campas, and J. L. Marty, "Biomolecule immobilization in biosensor development: tailored strategies based on affinity interactions," *Protein Peptide Lett.* **15**(8), 757–763 (2008).

[20] F. Rusmini, Z. Zhong, and J. Feijen, "Protein immobilization strategies for protein biochips," *Biomacromolecules* **8**(6), 1775–1789 (2007).

[21] M.-J. Bañuls, R. Puchades, and Á. Maquieira, "Chemical surface modifications for the development of silicon-based label-free integrated optical (IO) biosensors: a review," *Anal. Chim. Acta* **777**, 1–16 (2013).

[22] J. Diao, D. Ren, J. R. Engstrom, and K. H. Lee, "A surface modification strategy on silicon nitride for developing biosensors," *Anal. Biochem.* **343**(2), 322–328 (2005).

[23] A. Arafat, M. Giesbers, M. Rosso, E. J. R. Sudhölter, K. Schroën, R. G. White, L. Yang, M. R. Linford, and H. Zuilhof, "Covalent biofunctionalization of silicon nitride surfaces," *Langmuir* **23**(11), 6233–6244 (2007).

[24] S. Takayama, J. C. McDonald, E. Ostuni, M. N. Liang, P. J. A. Kenis, R. F. Ismagilov, and G. M. Whitesides, "Patterning cells and their environments using multiple laminar fluid flows in capillary networks," *Proc. Natl. Acad. Sci. USA* **96**(10), 5545–5548 (1999).

[25] A. B. Gonzalez-Guerrero, M. Alvarez, A. G. Castaño, C. Dominguez, and L. M. Lechuga, "A comparative study of in-flow and micro-patterning biofunctionalization protocols for nanophotonic silicon-based biosensors," *J. Colloid Interface Sci.* **393**, 402–410 (2013).

[26] J. T. Kirk, G. E. Fridley, J. W. Chamberlain, E. D. Christensen, M. Hochberg, and D. M. Ratner, "Multiplexed inkjet functionalization of silicon photonic biosensors," *Lab on a Chip* **11**(7), 1372–1377 (2011).

[27] T. F. Didar, A. M. Foudeh, and M. Tabrizian, "Patterning multiplex protein microarrays in a single microfluidic channel," *Anal. Chem.* **84**(2), 1012–1018 (2011).

[28] J. Fraden, *Handbook of Modern Sensor: Physics, Designs, and Applications*, 3rd ed. (Springer, 2003).

[29] D. Duval, A. B. Gonzalez-Guerrero, S. Dante, C. Dominguez, and L. M. Lechuga, "Interferometric waveguide biosensors based on Si-technology for point-of-care diagnostic," *Proc. SPIE* **8431**, 84310P–1/11 (2012).

[30] E. F. Schipper, A. M. Brugman, C. Dominguez, L. M. Lechuga, R. P. H. Kooyman, and J. Greve, "The realization of an integrated Mach-Zehnder waveguide immunosensor in silicon technology," *Sens. Actuators B. Chem.* **40**(2–3), 147–153 (1997).

[31] K. E. Zinoviev, L. G. Carrascosa, J. Sánchez del Río, B. Sepúlveda, C. Domínguez, and L. M. Lechuga, "Silicon photonic biosensors for lab-on-a-chip applications," *Adv. Opt. Technol.* **2008**, 383927–1/6 (2008).

[32] A. Crespi, Y. Gu, B. Ngamsom, H. J. W. M. Hoekstra, C. Dongre, M. Pollnau, R. Ramponi, H. H. van den Vlekkert, P. Watts, G. Cerullo, et al., "Three-dimensional Mach-Zehnder interferometer in a microfluidic chip for spatially-resolved label-free detection," *Lab on a Chip* **10**(9), 1167–1173 (2010).

[33] A. Mathesz, L. Fábián, S. Valkai, D. Alexandre, P. V. S. Marques, P. Ormos, E. K. Wolff, and A. Dér, "High-speed integrated optical logic based on the protein bacteriorhodopsin," *Biosen. Bioelectron.* **46**(0), 48–52 (2013).

[34] R. G. Heideman and P. V. Lambeck, "Remote opto-chemical sensing with extreme sensitivity: design, fabrication and performance of a pigtailed integrated optical phase-modulated Mach–Zehnder interferometer system," *Sens. Actuators B. Chem.* **61**(1–3), 100–127 (1999).

[35] M. B. Duhring and O. Sigmund, "Improving the acousto-optical interaction in a Mach-Zehnder interferometer," *J. Appl. Phys.* **105**(8), 083529 (2009).

[36] P. Dumais, C. L. Callender, J. P. Noad, and C. J. Ledderhof, "Integrated optical sensor using a liquid-core waveguide in a Mach-Zehnder interferometer," *Opt. Express* **16**(22), 18164–18172 (2008).

[37] S. Dante, D. Duval, B. Sepulveda, A. B. Gonzalez-Guerrero, J. R. Sendra, and L. M. Lechuga, "All-optical phase modulation for integrated interferometric biosensors," *Opt. Express* **20**(7), 7195–7205 (2012).

[38] M. Kitsara, K. Misiakos, I. Raptis, and E. Makarona, "Integrated optical frequency-resolved Mach-Zehnder interferometers for label-free affinity sensing," *Opt. Express* **18**(8), 8193–8206 (2010).

[39] A. Ymeti, J. Greve, P. V. Lambeck, T. Wink, H. van, Beumer, R. R. Wijn, R. G. Heideman, V. Subramaniam, and J. S. Kanger, "Fast, ultrasensitive virus detection using a young interferometer sensor," *Nano Lett.* **7**(2), 394–397 (2007).

[40] A. Brandenburg and R. Henninger, "Integrated optical Young interferometer," *Appl. Opt.* **33**(25), 5941–5947 (1994).

[41] A. Brandenburg, "Differential refractometry by an integrated-optical Young interferometer," *Sens. Actuators B. Chem.* **39**(1–3), 266–271 (1997).

[42] K. Schmitt, B. Schirmer, C. Hoffmann, A. Brandenburg, and P. Meyrueis, "Interferometric biosensor based on planar optical waveguide sensor chips for label-free detection of surface bound bioreactions," *Biosens. Bioelectron.* **22**(11), 2591–2597 (2007).

[43] J. H. Sim, Y. H. Kwak, C. H. Choi, S.-H. Paek, S. S. Park, and S. Seo, "A birefringent waveguide biosensor platform for label-free live cell detection of Listeria monocytogenes," *Sens. Actuators B. Chem.* **173**, 752–759 (2012).

[44] K. E. Zinoviev, A. B. Gonzalez-Guerrero, C. Dominguez, and L. M. Lechuga, "Integrated bimodal waveguide interferometric biosensor for label-free analysis," *J. Lightwave Technol.* **29**(13), 1926–1930 (2011).

[45] A. B. Gonzalez-Guerrero, J. M. Rodriguez-Frade, M. Mellado, C. Dominguez, and L. M. Lechuga, "High sensitivity detection of human growth hormone using a bimodal waveguide interferometer," in XI Conference on Optical Chemical Sensors and Biosensors (EUROPT(R)ODE XI), 2012.

[46] B. H. Schneider, J. G. Edwards, and N. F. Hartmann, "Hartman interferometer: versatile integrated optic sensor for label-free, real-time quantification of nucleic acids, proteins, and pathogens," *Clin. Chem.* **43**(9), 1757–1763 (1997).

[47] G. H. Cross, A. A. Reeves, S. Brand, J. F. Popplewell, L. L. Peel, M. J. Swann, and N. J. Freeman, "A new quantitative optical biosensor for protein characterisation," *Biosen. Bioelectron.* **19**(4), 383–390 (2003).

[48] R. W. Boyd and J. E. Heebner, "Sensitive disk resonator photonic biosensor," *Appl. Opt.* **40**(31), 5742–5747 (2001).

[49] Y. Sun and X. Fan, "Optical ring resonators for biochemical and chemical sensing," *Anal. Bioanal. Chem.* **399**(1), 205–211 (2011).

[50] F. Vollmer and L. Yang, "Label-free detection with high-Q microcavities: a review of biosensing mechanisms for integrated devices," *Nanophotonics* **1**(3–4), 267–291 (2012).

[51] C. Barrios, "Integrated microring resonator sensor arrays for labs-on-chips," *Anal. Bioanal. Chem.* **403**(6), 1467–1475 (2012).

[52] M. S. Luchansky and R. C. Bailey, "High-Q optical sensors for chemical and biological analysis," *Anal. Chem.* **84**(2), 793–821 (2012).

[53] M. C. Estevez, M. Alvarez, and L. M. Lechuga, "Integrated optical devices for lab-on-a-chip biosensing applications," *Laser Photon. Rev.* **6**(4), 463–487 (2012).

[54] R. Heideman, M. Hoekman, and E. Schreuder, "TriPleX-based integrated optical ring resonators for lab-on-a-chip and environmental detection," *IEEE J. Select. Top. Quantum Electron.* **18**(5), 1583–1596 (2012).

[55] A. Ramachandran, S. Wang, J. Clarke, S. J. Ja, D. Goad, L. Wald, E. M. Flood, E. Knobbe, J. V. Hryniewicz, S. T. Chu, et al., "A universal biosensing platform based on optical micro-ring resonators," *Biosens. Bioelectron.* **23**(7), 939–944 (2008).

[56] M. W. Royal, N. M. Jokerst, and R. B. Fair, "Integrated sample preparation and sensing: polymer microresonator sensors embedded in digital electrowetting microfluidic systems," *IEEE Photon. J.* **4**(6), 2126–2135 (2012).

[57] K. De Vos, J. Girones, T. Claes, Y. De Koninck, S. Popelka, E. Schacht, R. Baets, and P. Bienstman, "Multiplexed antibody detection with an array of silicon-on-insulator microring resonators," *IEEE Photon. J.* **1**(4), 225–235 (2009).

[58] M. S. McClellan, L. L. Domier, and R. C. Bailey, "Label-free virus detection using silicon photonic microring resonators," *Biosens. Bioelectron.* **31**(1), 388–392 (2012).

[59] O. Scheler, J. T. Kindt, A. J. Qavi, L. Kaplinski, B. Glynn, T. Barry, A. Kurg, and R. C. Bailey, "Label-free, multiplexed detection of bacterial tmRNA using silicon photonic microring resonators," *Biosen. Bioelectron.* **36**(1), 56–61 (2012).

[60] J. T. Gohring and X. Fan, "Label free detection of CD4+ and CD8+ T cells using the optofluidic ring resonator," *Sensors* **10**(6), 5798–5808 (2010).

[61] F. Vollmer and S. Arnold, "Whispering-gallery-mode biosensing: label-free detection down to single molecules," *Nat. Meth.* **5**(7), 591–596 (2008).

[62] P. M. Nellen, K. Tiefenthaler, and W. Lukosz, "Integrated optical input grating couplers as biochemical sensors," *Sens. Actuators* **15**(3), 285–295 (1988).

[63] I. R. Cooper, S. T. Meikle, G. Standen, G. W. Hanlon, and M. Santin, "The rapid and specific real-time detection of *Legionella pneumophila* in water samples using optical waveguide lightmode spectroscopy," *J. Microbiol. Methods* **78**(1), 40–44 (2009).

[64] N. Adányi, K. Majer-Baranyi, A. Nagy, G. Németh, I. Szendrő, and A. Székács, "Optical waveguide lightmode spectroscopy immunosensor for detection of carp vitellogenin," *Sens. Actuators B. Chem.* **176**, 932–939 (2013).

[65] S. Grego, K. H. Gilchrist, J. B. Carlson, and B. R. Stoner, "A compact and multichannel optical biosensor based on a wavelength interrogated input grating coupler," *Sens. Actuators B. Chem.* **161**(1), 721–727 (2012).

[66] K. Cottier, M. Wiki, G. Voirin, H. Gao, and R. E. Kunz, "Label-free highly sensitive detection of (small) molecules by wavelength interrogation of integrated optical chips," *Sens. Actuators B. Chem.* **91**(1–3), 241–251 (2003).

[67] J. Adrian, S. Pasche, J.-M. Diserens, F. Sánchez-Baeza, H. Gao, M. P. Marco, and G. Voirin, "Waveguide interrogated optical immunosensor (WIOS) for detection of sulfonamide antibiotics in milk," *Biosens. Bioelectron.* **24**(11), 3340–3346 (2009).

[68] J. Razumovitch, K. de Franca, F. Kehl, M. Wiki, W. Meier, and C. Vebert, "Optimal hybridization efficiency upon immobilization of oligonucleotide double helices," *J. Phys. Chem. B* **113**(24), 8383–8390 (2009).

[69] S. V. Pham, M. Dijkstra, A. J. F. Hollink, L. J. Kauppinen, R. M. de Ridder, M. Pollnau, P. V. Lambeck, and H. J. W. M. Hoekstra, "On-chip bulk-index concentration and direct, label-free protein sensing utilizing an optical grated-waveguide cavity," *Sens. Actuators B. Chem.* **174**, 602–608 (2012).

[70] D. Bhatta, A. A. Michel, M. Marti Villalba, G. D. Emmerson, I. J. G. Sparrow, E. A. Perkins, M. B. McDonnell, R. W. Ely, and G. A. Cartwright, "Optical microchip array biosensor for multiplexed detection of bio-hazardous agents," *Biosens. Bioelectron.* **30**(1), 78–86 (2011).

[71] M. R. Lee and P. M. Fauchet, "Two-dimensional silicon photonic crystal based biosensing platform for protein detection," *Opt. Express* **15**(8), 4530–4535 (2007).

[72] S. Pal, E. Guillermain, R. Sriram, B. L. Miller, and P. M. Fauchet, "Silicon photonic crystal nanocavity-coupled waveguides for error-corrected optical biosensing," *Biosens. Bioelectron.* **26**(10), 4024–4031 (2011).

[73] S. Mandal and D. Erickson, "Nanoscale optofluidic sensor arrays," *Opt. Express* **16**(3), 1623–1631 (2008).

[74] S. Mandal, J. M. Goddard, and D. Erickson, "A multiplexed optofluidic biomolecular sensor for low mass detection," *Lab on a Chip* **9**(20), 2924–2932 (2009).

[75] S. Chakravarty, W.-C. Lai, Y. Zou, H. A. Drabkin, R. M. Gemmill, G. R. Simon, S. H. Chin, and R. T. Chen, "Multiplexed specific label-free detection of NCI-H358 lung cancer cell line lysates with silicon based photonic crystal microcavity biosensors," *Biosens. Bioelectron.* **43**, 50–55 (2013).

[76] D. X. Xu, A. Densmore, A. Delâge, P. Waldron, R. McKinnon, S. Janz, J. Lapointe, G. Lopinski, T. Mischki, E. Post, et al., "Folded cavity SOI microring sensors for high sensitivity and real time measurement of biomolecular binding," *Opt. Express* **16**(19), 15137–15148 (2008).

[77] D. X. Xu, M. Vachon, A. Densmore, R. Ma, A. Delâge, S. Janz, J. Lapointe, Y. Li, G. Lopinski, D. Zhang, et al., "Label-free biosensor array based on silicon-on-insulator ring resonators addressed using a WDM approach," *Opt. Lett.* **35**(16), 2771–2773 (2010).

[78] A. Densmore, M. Vachon, D.-X. Xu, S. Janz, R. Ma, Y.-H. Li, G. Lopinski, A. Delâge, J. Lapointe, C. C. Luebbert, et al., "Silicon photonic wire biosensor array for multiplexed real-time and label-free molecular detection," *Opt. Lett.* **34**(23), 3598–3600 (2009).

[79] C. A. Barrios, "Optical slot-waveguide based biochemical sensors," *Sensors* **9**(6), 4751–4765 (2009).

[80] C. A. Barrios, M. J. Bañuls, V. Gonzalez-Pedro, K. B. Gylfason, B. Sánchez, A. Griol, A. Maquieira, H. Sohlström, M. Holgado, and R. Casquel, "Label-free optical biosensing with slot-waveguides," *Opt. Lett.* **33**(7), 708–710 (2008).

[81] C. F. Carlborg, K. B. Gylfason, A. Kazmierczak, F. Dortu, M. J. Banuls Polo, A. Maquieira Catala, G. M. Kresbach, H. Sohlstrom, T. Moh, L. Vivien, et al., "A packaged optical slot-waveguide ring resonator sensor array for multiplex label-free assays in labs-on-chips," *Lab on a Chip* **10**(3), 281–290 (2010).

[82] S. M. Weiss, G. Rong, and J. L. Lawrie, "Current status and outlook for silicon-based optical biosensors," *Phys. E. Low-Dimens. Syst. Nanostruct.* **41**(6), 1071–1075 (2009).

[83] A. Jane, R. Dronov, A. Hodges, and N. H. Voelcker, "Porous silicon biosensors on the advance," *Trends Biotechnol.* **27**(4), 230–239 (2009).

[84] S. Dhanekar and S. Jain, "Porous silicon biosensor: current status," *Biosens. Bioelectron.* **41**, 54–64 (2013).

[85] G. Rong, A. Najmaie, J. E. Sipe, and S. M. Weiss, "Nanoscale porous silicon waveguide for label-free DNA sensing," *Biosens. Bioelectron.* **23**(10), 1572–1576 (2008).

[86] M. Holgado, R. Casquel, B. Sánchez, C. Molpeceres, M. Morales, and J. L. Ocaña, "Optical characterization of extremely small volumes of liquid in sub-micro-holes by simultaneous reflectivity, ellipsometry and spectrometry," *Opt. Exp.* **15**(20), 13318–13329 (2007).

[87] F. J. Sanza, M. Holgado, F. J. Ortega, R. Casquel, D. López-Romero, M. J. Bañuls, M. F. Laguna, C. A. Barrios, R. Puchades, and A. Maquieira, "Bio-photonic sensing cells over transparent substrates for anti-gestrinone antibodies biosensing," *Biosens. Bioelectron.* **26**(12), 4842–4847 (2011).

[88] V. Mishra, N. Singh, U. Tiwari, and P. Kapur, "Fiber grating sensors in medicine: current and emerging applications," *Sens. Actuators A. Phys.* **167**(2), 279–290 (2011).

[89] R. Kashyap, "Principles of optical fiber grating sensors," in *Fiber Bragg Gratings*, 2nd ed. (Academic Press, Boston, 2010), pp. 441–502.

[90] A. N. Chryssis, S. S. Saini, S. M. Lee, Y. Hyunmin, W. E. Bentley, and M. Dagenais, "Detecting hybridization of DNA by highly sensitive evanescent field etched core fiber Bragg grating sensors," *IEEE J. Select. Top. Quantum Electron.* **11**(4), 864–872 (2005).

[91] M. C. Phan Huy, G. Laffont, V. Dewynter, P. Ferdinand, P. Roy, J.-L. Auguste, D. Pagnoux, W. Blanc, and B. Dussardier, "Three-hole microstructured optical fiber for efficient fiber Bragg grating refractometer," *Opt. Lett.* **32**(16), 2390–2392 (2007).

[92] S. Maguis, G. Laffont, P. Ferdinand, B. Carbonnier, K. Kham, T. Mekhalif, and M.-C. Millot, "Biofunctionalized tilted Fiber Bragg Gratings for label-free immunosensing," *Opt. Express* **16**(23), 19049–19062 (2008).

[93] A. Candiani, M. Sozzi, A. Cucinotta, S. Selleri, R. Veneziano, R. Corradini, R. Marchelli, P. Childs, and S. Pissadakis, "Optical fiber ring cavity sensor for label-free DNA detection," *IEEE J. Select. Top. Quantum Electron.* **18**(3), 1176–1183 (2012).

[94] M. P. DeLisa, Z. Zhang, M. Shiloach, S. Pilevar, C. C. Davis, J. S. Sirkis, and W. E. Bentley, "Evanescent wave long-period fiber bragg grating as an immobilized antibody biosensor," *Anal. Chem.* **72**(13), 2895–2900 (2000).

[95] R. Garg, S. M. Tripathi, K. Thyagarajan, and W. J. Bock, "Long period fiber grating based temperature-compensated high performance sensor for bio-chemical sensing applications," *Sens. Actuators B. Chem.* **176**, 1121–1127 (2013).

[96] L. Rindorf, J. B. Jensen, M. Dufva, L. H. Pedersen, P. E. Høiby, and O. Bang, "Photonic crystal fiber long-period gratings for biochemical sensing," *Opt. Express* **14**(18), 8224–8231 (2006).

[97] X. Chen, L. Zhang, K. Zhou, E. Davies, K. Sugden, I. Bennion, M. Hughes, and A. Hine, "Real-time detection of DNA interactions with long-period fiber-grating-based biosensor," *Opt. Lett.* **32**(17), 2541–2543 (2007).

[98] X. Chen, K. Zhou, L. Zhang, and I. Bennion, "Dual-peak long-period fiber gratings with enhanced refractive index sensitivity by finely tailored mode dispersion that uses the light cladding etching technique," *Appl. Opt.* **46**(4), 451–455 (2007).

[99] M. Smietana, W. J. Bock, P. Mikulic, A. Ng, R. Chinnappan, and M. Zourob, "Detection of bacteria using bacteriophages as recognition elements immobilized on long-period fiber gratings," *Opt. Express* **19**(9), 7971–7978 (2011).

[100] L. Rindorf and O. Bang, "Highly sensitive refractometer with a photonic-crystal-fiber long-period grating," *Opt. Lett.* **33**(6), 563–565 (2008).

[101] D. J. J. Hu, J. L. Lim, M. K. Park, L. T. H. Kao, Y. Wang, H. Wei, and W. Tong, "Photonic crystal fiber-based interferometric biosensor for streptavidin and biotin detection," *IEEE J. Select. Top. Quantum Electron.* **18**(4), 1293–1297 (2012).

[102] L. H. Chen, C. C. Chan, K. Ni, P. B. Hu, T. Li, W. C. Wong, P. Balamurali, R. Menon, M. Shaillender, B. Neu, et al., "Label-free fiber-optic interferometric immunosensors based on waist-enlarged fusion taper," *Sens. Actuators B. Chem.* **178**, 176–184 (2013).

[103] X. Wang, K. L. Cooper, A. Wang, J. Xu, Z. Wang, Y. Zhang, and Z. Tu, "Label-free DNA sequence detection using oligonucleotide functionalized optical fiber," *Appl. Phys. Lett.* **89**(16), 163901–163903 (2006).

[104] L. H. Chen, X. M. Ang, C. C. Chan, M. Shaillender, B. Neu, W. C. Wong, P. Zu, and K. C. Leong, "Layer-by-layer (chitosan/polystyrene sulfonate) membrane-based fabry-perot interferometric fiber optic biosensor," *IEEE J. Select. Top. Quantum Electron.* **18**(4), 1457–1464 (2012).

[105] Y. Zhang, X. Chen, Y. Wang, K. L. Cooper, and A. Wang, "Microgap multicavity fabry-pérot biosensor," *J. Lightwave Technol.* **25**(7), 1797–1804 (2007).

[106] A. Leung, P. M. Shankar, and R. Mutharasan, "Model protein detection using antibody-immobilized tapered fiber optic biosensors (TFOBS) in a flow cell at 1310 nm and 1550 nm," *Sens. Actuators B. Chem.* **129**(2), 716–725 (2008).

[107] A. Leung, P. M. Shankar, and R. Mutharasan, "Label-free detection of DNA hybridization using gold-coated tapered fiber optic biosensors (TFOBS) in a flow cell at 1310 nm and 1550 nm," *Sens. Actuators B. Chem.* **131**(2), 640–645 (2008).

[108] J. M. Corres, I. R. Matias, J. Bravo, and F. J. Arregui, "Tapered optical fiber biosensor for the detection of anti-gliadin antibodies," *Sens. Actuators B. Chem.* **135**(1), 166–171 (2008).

[109] M. I. Zibaii, A. Kazemi, H. Latifi, M. K. Azar, S. M. Hosseini, and M. H. Ghezelaiagh, "Measuring bacterial growth by refractive index tapered fiber optic biosensor," *J. Photochem. Photobiol. B. Biol.* **101**(3), 313–320 (2010).

[110] H. Tazawa, T. Kanie, and M. Katayama, "Fiber-optic coupler based refractive index sensor and its application to biosensing," *Appl. Phys. Lett.* **91**(11), 113901–113903 (2007).

[111] X. Fan and I. M. White, "Optofluidic microsystems for chemical and biological analysis," *Nat. Photon.* **5**(10), 591–597 (2011).

[112] D. Psaltis, S. R. Quake, and C. Yang, "Developing optofluidic technology through the fusion of microfluidics and optics," *Nature* **442**(7101), 381–386 (2006).

[113] L. Luan, M. W. Royal, R. Evans, R. B. Fair, and N. M. Jokerst, "Chip scale optical microresonator sensors integrated with embedded thin film photodetectors on electrowetting digital microfluidics platforms," *IEEE Sens. J.* **12**(6), 1794–1800 (2012).

[114] S. Janz, D. X. Xu, M. Vachon, N. Sabourin, P. Cheben, H. McIntosh, H. Ding, S. Wang, J. H. Schmid, A. Delâge, et al., "Photonic wire biosensor microarray chip and instrumentation with application to serotyping of *Escherichia coli* isolates," *Opt. Express* **21**(4), 4623–4637 (2013).

[115] E. Makarona, P. S. Petrou, A. Bourkoula, A. Botsialas, M. Kitsara, S. E. Kakabakos, R. Stoffer, G. Jobst, G. Nounesis, I. Raptis, et al., "Monolithically integrated Mach-Zehnder biosensors for real-time label-free monitoring of biomolecular reactions," in 33rd Annual International Conference of the IEEE EMBC, pp. 7654–7657 (2011).

[116] D. Duval, A. B. Gonzalez-Guerrero, S. Dante, J. Osmond, R. Monge, L. J. Fernandez, K. E. Zinoviev, C. Dominguez, and L. M. Lechuga, "Nanophotonic lab-on-a-chip platforms including novel bimodal interferometers, microfluidics and grating couplers," *Lab on a Chip* **12**(11), 1987–1994 (2012).

9

LIGHT PROPAGATION IN HIGHLY SCATTERING TURBID MEDIA: CONCEPTS, TECHNIQUES, AND BIOMEDICAL APPLICATIONS

R. R. ALFANO,[1,2] W. B. WANG,[1,2] L. WANG,[1] AND
S. K. GAYEN[2]

[1] *Institute for Ultrafast Spectroscopy and Lasers (IUSL), City College of New York, New York, NY, USA*
[2] *Physics Department, City College of New York, New York, NY, USA*

9.1 INTRODUCTION

The field of biomedical optics has emerged as one of major fields in science and engineering since the late 1980s [1–6]. Optical imaging and spectroscopic techniques are making headway into medical diagnosis and treatment practices. Proliferation of optical and spectroscopic methods in the medical arena is being made possible by advances in versatile compact light sources, such as lasers and light emitting diodes; optical fibers; miniaturized spectrometers, charge-coupled device (CCD) and near-infrared area cameras, high-sensitivity detectors; microelectronic components and systems; and compact computers with robust memory and computation prowess. Photodynamic Therapy (PDT) [7], Optical Coherence Tomography (OCT) [8,9], and Optical Biopsy [10] are three examples of optical methods making transition from laboratory to clinic and having significant impact on medical treatment and diagnosis, respectively. Another advance in the horizon is a "photonic pill"/"pill CAM" equipped

---

Photonics: Scientific Foundations, Technology and Applications, Volume IV, First Edition.
Edited by David L. Andrews.
© 2015 John Wiley & Sons, Inc. Published 2015 by John Wiley & Sons, Inc.

with millimeter-size spectroscopic equipment and wireless communication devices for visualization of tissue surface inside the gastrointestinal (GI) tract [11]. Photonic wound healing is another development around the corner. Optical stitches can be made using near-infrared (NIR) lasers operating in the 1000–1800 nm wavelength range to excite water and collagen molecules inside the tissue [12]. Other promising optical and multimodality techniques for detecting objects hidden inside turbid media, in particular, cancerous or other diseased tissues in the host normal tissues, include (1) photoacoustic tomography (PAT) which forms images by detecting the light-induced pressure waves [13, 14], (2) combination of the ultrasound (US) and NIR imaging for the purpose of cancer detection [15, 16], and (3) using cancer receptor targeting contrast agents and their emission to enhance the imaging contrast of cancerous and normal tissues [17–19].

Optics will provide new armamentaria to complement the current medical tools, such as X-rays, CAT (computer-aided tomography), magnetic resonance imaging (MRI), ultrasound, radioactive isotopes, and PET (positron emission tomography) scanner, for imaging body parts; as well as for chemical testing, which requires blood, urine, and other body liquids. The interest in light-based modalities arises from a need to have tools, which are safe, compact, affordable, and enable bloodless monitoring of tissue chemicals preferably without removing tissue. Light offers the opportunity to overcome the limitations of many current methods. Most non-optical imaging methods cannot reveal a diagnosis, giving only an image for doctors to interpret. Optical spectroscopy can, in principle, monitor molecular changes in key body chemicals that may accompany diseases and offers diagnostic potential [20–25]. Over the past two decades, significant progress has been made in optical spectroscopy and imaging for cancer detection and diagnosis. Combined with different mathematical tools, the fluorescence spectroscopy can be used to extract changes of intrinsic tissue emission spectra during the induction of morphological and molecular changes in human tissue [26]. Other spectral approaches, which can be used to examine changes associated with biomolecules in tissue during cancer development [27], include Raman spectroscopy [28–31], scattering spectroscopy [32], Stokes shift spectroscopy [33–36], excitation-emission matrix (EEM) spectroscopy [37], and time-resolved fluorescence spectroscopy [38, 39].

This chapter provides an overview of the physics of light propagation in highly scattering turbid media, such as biological tissues, the techniques that enable using light emergent from those media for gaining information about the media interior, and their potential application in biomedical imaging. One of the goals of these researches is to develop optical tomography systems. The interaction of light with a scattering medium, characteristics of the transmitted light, key parameters that characterize the light emergent from the medium, and light gating methods that reduce the deleterious effect of multiple scattered light and help clear up images will be presented. The major application of this endeavor will be to develop an Optical Tomography Diagnostic System for diagnosing diseases of breast, brain, prostate, and other body organs. The material presented here is mainly derived from some of the pioneering articles published by the researchers at the Institute for Ultrafast Spectroscopy and Lasers

(IUSL) in the City College of New York. By no means is this a review of the entire field and of contributions made by all researchers active in the field.

9.2 PHYSICS BEHIND OPTICAL IMAGING THROUGH A HIGHLY SCATTERING TURBID MEDIUM

Biomedical optical imaging techniques are used to identify, locate, and diagnose an "object," such as a tumor inside a biological tissue. Biological tissues are scattering media made up of molecules, cells, vessel structures, and layers of different sizes on nanometer to millimeter scales. These scattering processes blur the image. The successful use of optical methods to solve biomedical imaging problem has eluded researchers since the futile attempts to detect breast tumors using light from lamp in 1929 by Max Cutler [40]. The interest in this technique, known as diaphanography, has increased throughout this century as brighter light or transillumination sources and sophisticated image recording methods were invented and new inverse mathematics were developed.

The basis of transillumination is the difference in the transmission of light through a turbid medium (such as normal tissue) and an "object" (such as a tumor) inside it. This differential transmission, in principle, should lead to the formation of a "shadow" of the object (tumor) in transmitted light. Observation of that shadow image is hindered since light scattered by the medium (tissue) severely degrades and completely buries the image in the background light. The key to successful development of optical imaging techniques is to deal with the problem of light scattering because light scattering blurs images. It is important to understand how light propagates through a scattering medium. Depending on wavelength of light, it is both scattered and absorbed in varying degree by biological tissues resulting in diffusive glow [41]. It is important to know how the characteristics of intensity, coherence, and polarization of the incident light changes as it is absorbed and scattered inside the tissue. The depth of light penetration into the tissue depends on its wavelength. There are several optical transmission windows in tissue; in particular, the first is from 700 to 1100 nm called therapeutic window. The key chromophore molecules in biological tissues are blood, water, proteins, and fat. The light that emerges from the medium has different characteristics than the incident light.

Absorption results from electronic and vibrational transitions within the energy levels of the atoms and molecules in the tissue. Scattering arises from variations of index of refraction in the microscopic and macroscopic structures of the tissue; it increases strongly as the wavelength of light becomes comparable to the size of the scattering elements. In addition to absorption and scattering of light, fluorescence emitted by the objects upon absorption of incident light may also provide the necessary contrast for imaging and has led to fluorescence imaging approaches [42–45]. This chapter will focus mainly on direct imaging approaches based on scattering and absorption contrasts. A scattered light pulse comprises three components: ballistic, snake, and diffuse. The transmitted and backscattered light is composed of unscattered

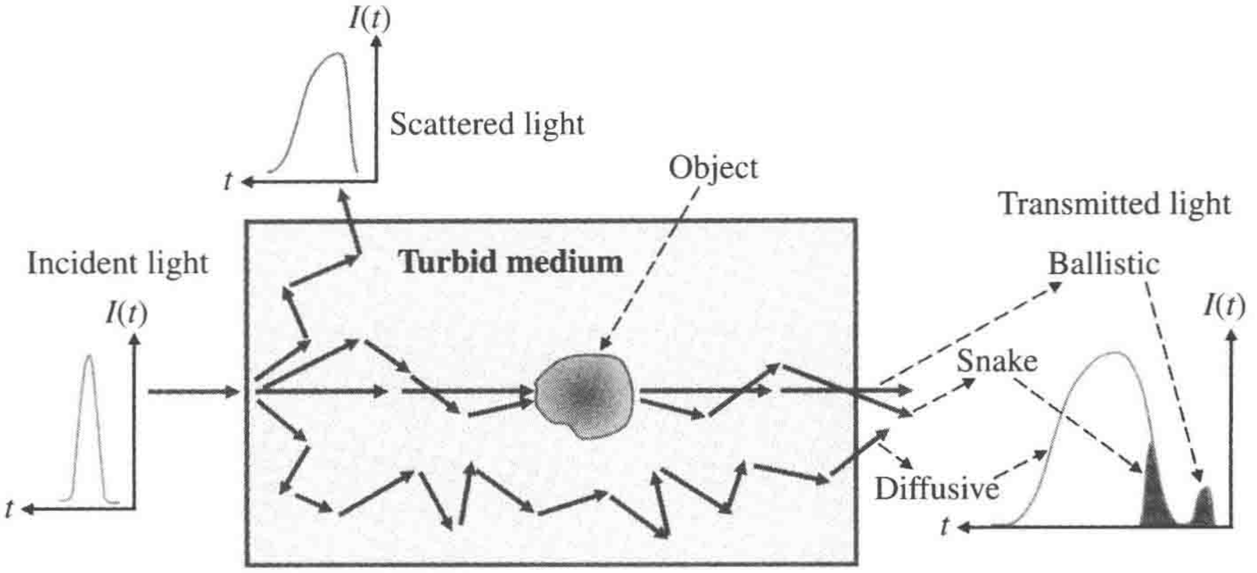

FIGURE 9.1 Schematic diagram of light pulse propagating in a turbid medium showing the ballistic, snake, and diffuse photons. Adapted from Reference 52.

(or coherently scattered), weakly scattered (snake), and multiple-scattered (diffuse) photons, as displayed schematically in Figure 9.1.

9.2.1 Components of Transmitted Light

Laser light characterized by high degree of directionality, spectral brightness, monochromaticity and coherence is a natural choice for imaging through highly scattering media. Strong absorption and scattering by the intervening medium attenuate the intensity of incident light and modify its salient features, such as directionality, coherence, polarization and pulse duration in the case of ultrashort pulses of light. The transmitted photons of an ultrashort pulse of light are composed of three components: *ballistic*, *snake*, and *diffusive* [46], as shown schematically in Figure 9.1. The ballistic or coherently forward scattered photons propagate in the direction of the incoming beam, traverse the shortest path, retain most of the characteristics of the incident light, and carry the maximum information for formation of a direct image. The multiple-scattered photons travel long distances within the medium, lose many of their initial characteristics, and emerge later in all directions. They constitute what is known as the diffusive component of the transmitted light. The photons that scatter slightly in the forward direction retain significant initial properties and information on structures hidden in the scattering medium. These photons are called snake photons because their trajectories resemble a wriggling snake.

Since the photons of an incident short pulse of light spend different times in transit through the intervening medium, the transmitted pulse becomes broadened with the ballistic photons arriving first, followed by the snake and diffusive photons, also displayed in Figure 9.1. Ballistic photons are most effective in forming a shadow image. Snake photons also generate transillumination images whose resolution depends on the position and width of the temporal slide used in imaging. The snake photons that form a well-resolved shadow image arrive much earlier than most of the diffuse photons. The intensity of the forward-transmitting light is attenuated by absorption and scattering. The relative intensities of these three components in the transmitted beam depend on the color of light and characteristics of the sample. In a highly scattering optically thick medium, the ballistic component is extremely weak, while the diffuse component is the most intense. To form images of the structures inside the turbid medium using ballistic and snake photons, the most numerous diffusive photons need be strongly discriminated against.

Two alternative approaches are being pursued to alleviate this problem. The first involves filtering out the image-bearing photons from the background of multiple-scattered image-blurring photons using clever experimental techniques [8,9,47–72]. The second approach, sometimes referred to as the inverse problem [4–6,73,74], is based on detection of all of the photons including multiple-scattered photons at various positions around the object. The aim is to construct the image from the measured intensities, known experimental parameters, and tissue characteristics using model of light propagation and sophisticated computer algorithms. The impetus for solving the inverse problem stems from the realization that for tissues that are more than a few centimeters thick, the only transmitted light is the scattered light.

Both frequency-domain and time-domain data may be used in the second approach. The thrust is to develop appropriate algorithms to generate a map of the interior structure of a turbid medium in a reasonable time. The Monte Carlo method focuses on the particle nature of light and promises higher accuracy at the cost of higher computational complexity and time [73]. Alternate methods based on the diffusion approximation of the radiative transfer equation are being pursued by various groups [4–6,74–76].

Near-infrared light spanning the 700–1100 nm spectral range in the first optical transmission window appears to be a judicious choice. Light in this wavelength range is not as strongly absorbed by tissue as the visible light, and so will have higher transmission and less likelihood of causing tissue burns. The availability of broadly wavelength-tunable ultrafast solid-state lasers, such as Ti:sapphire [77] and Cr:forsterite [78], to cover this spectral range is an advantage. The wavelength tunability offers the possibility of monitoring different chemical species by tuning to different wavelengths. Near-infrared light is also less scattered than visible light and is not known to cause tissue damage even with prolonged exposure at intensity levels that may be needed for routine screening. The balance of small absorption and scattering can improve images.

9.2.2 Key Optical Parameters for Describing Light Propagation in Highly Scattering Media

Knowledge of the key optical properties of scattering medium (Intralipid-10% suspension in water, milk, polystyrene beads of different sizes suspended in water, and breast, brain, and prostate tissues) is needed for developing photonic techniques for optical imaging and tomography approaches. The knowledge of four optical parameters is needed for imaging. These are absorption length l_a, scattering mean free path l_s, transport mean free path l_t, and anisotropy factor g.

The ballistic light is considered to be the fraction of the incident light that is not affected by scattering events within the medium and retains the characteristics (coherence, directionality, polarization) of the incident beam. The attenuation of the ballistic photons in traversing a length L of a turbid medium may be estimated by

$$I_{\mathrm{b}} = I_{\mathrm{i}} \exp[-(L/l_{\mathrm{a}} + L/l_{\mathrm{s}})], \tag{9.1}$$

where I_{i} is the intensity of the incident beam; l_{a} is the absorption length, defined as the mean distance a photon travels before being absorbed by the turbid medium; and l_{s} is the scattering mean free path, defined as a mean distance between consecutive scattering events for a photon. The parameters l_{a} and l_{s} are related to the absorption coefficient μ_{a} and scattering coefficient μ_{s} of the medium, respectively, as

$$l_{\mathrm{a}} = \mu_{\mathrm{a}}^{-1} \text{ and } l_{\mathrm{s}} = \mu_{\mathrm{s}}^{-1}. \tag{9.2}$$

The total attenuation coefficient is $\mu_{\mathrm{T}} = \frac{1}{l_{\mathrm{a}}} + \frac{1}{l_{\mathrm{s}}} = \frac{1}{l_{\mathrm{T}}}$, where l_{T} is the total attenuation length.

The spatial anisotropy of scattering is given by the *anisotropy factor* g, defined as the mean cosine of the scattering angles, that is, $g = \langle \cos\theta \rangle$. The value of g is 1 for propagation in the incident direction and 0 for isotropic scattering.

Another important parameter is the transport mean free path l_{t} defined as the distance in which a photon is fully randomized (forgets its original direction of motion) after numerous scattering events, as illustrated schematically, in Figure 9.2.

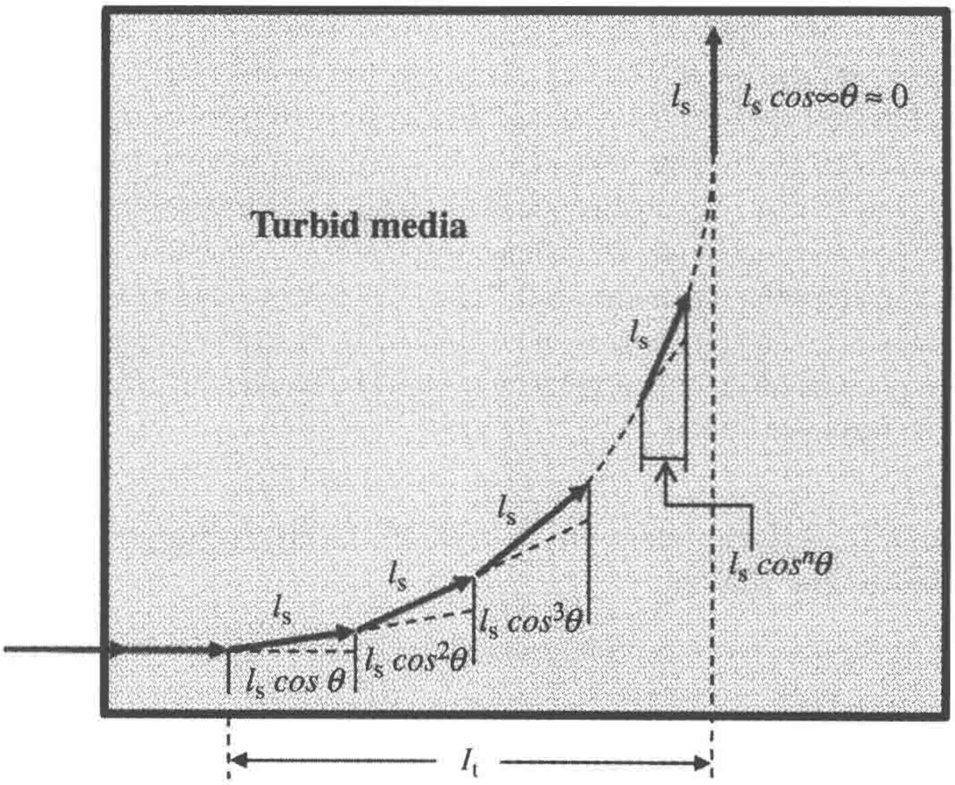

FIGURE 9.2 Mean free scattering distance l_{s}, mean free transport distance l_{t}, and anisotropy factor, g.

The relationship between l_t and l_s is given by

$$\langle l_t \rangle = \sum l_s \hat{n}, \tag{9.3}$$

where $\hat{n}$ represents the vector displacement of a photon in turbid media. Written explicitly,

$$\begin{aligned} \langle l_t \rangle &= \langle l_s + l_s \cos\theta + l_s \cos^2\theta + l_s \cos^3\theta + \cdots + l_s \cos^n\theta + \cdots \rangle \\ \langle l_t \rangle &= l_s/(1 - \langle \cos\theta \rangle) = l_s/(1-g). \end{aligned} \tag{9.4}$$

One also defines the *reduced scattering coefficient*,

$$\mu_s' = \mu_s(1-g) = (l_t)^{-1}. \tag{9.5}$$

The parameters l_a, l_s, μ_a, and μ_s are intrinsic properties of the material medium and are given by

$$l_s = \mu_s^{-1} = (N\sigma_s)^{-1}, \text{ and } l_a = \mu_a^{-1}, \tag{9.6}$$

where N is the volume concentration of particles, and σ_s and σ_a are the scattering cross-section and absorption cross-section, respectively.

The intensity of snake light is found, from experiments, to follow the equation [79, 80],

$$I_s(\Delta t) = A \exp[-bz/l_t], \tag{9.7}$$

in time interval Δt, where b is a parameter that depends on Δt, and has an average value of 0.8. The snake light is a portion of the photons that arrive before multiple-scattered diffusive photons and after the ballistic component.

The values of g, l_s, and l_t depend on particle size and are calculated using Mie scattering theory [81] and shown in Figures 9.3 and 9.4, respectively. In Figure 9.3 it can be seen that the g factor greatly depends on wavelength, especially when the particle size is less than 1 µm, which is close to the wavelengths of 0.527 and

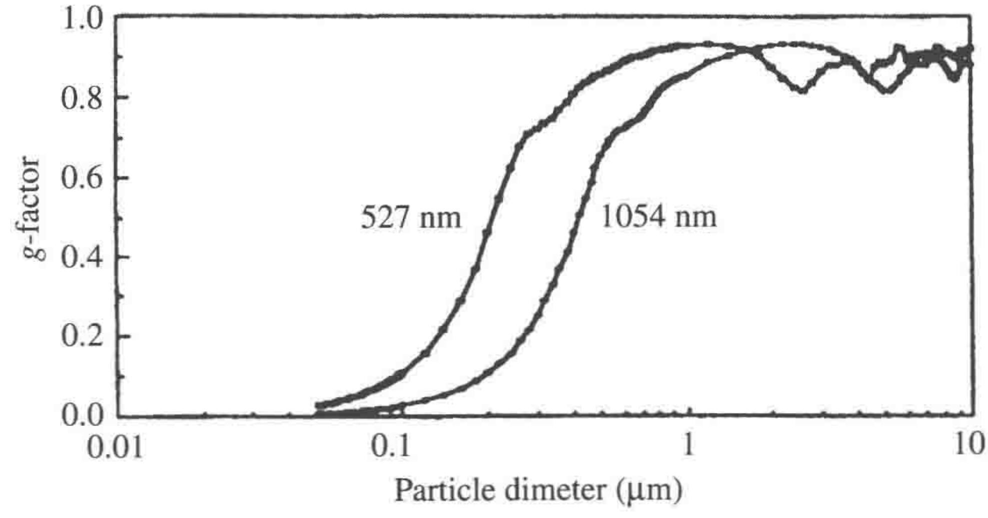

FIGURE 9.3 Calculated values of g-factor as a function of particle diameter [81].

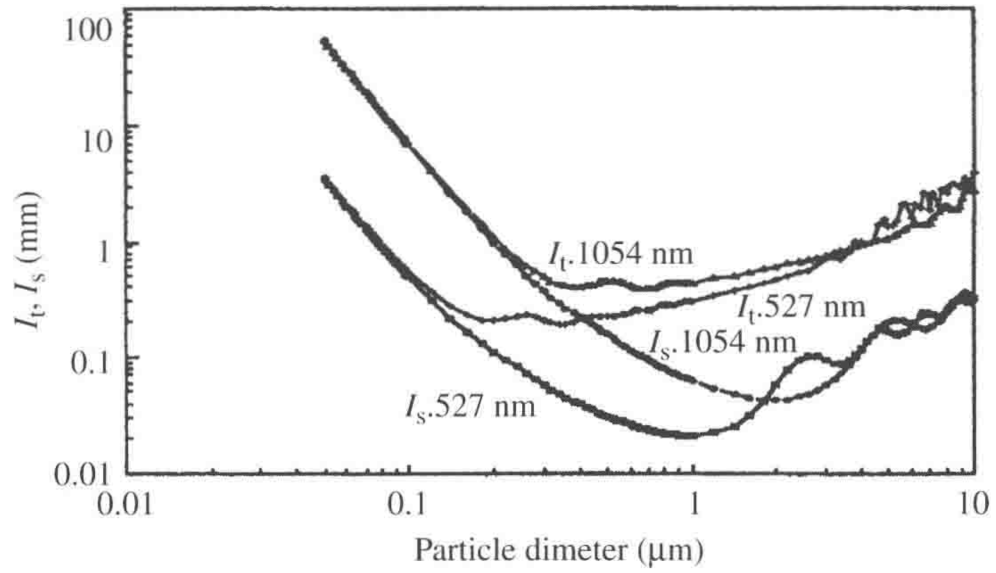

FIGURE 9.4 Values of l_t and l_s calculated as a function of particle diameter in 10% diluted polystyrene bead suspension in water [81].

1.054 μm. For the Intralipid-10% suspension with an average particle diameter of ~0.5 μm, the values of g will be ~0.9 and ~0.6 for 0.527 and 1.054 μm, respectively.

At larger particle diameters, g oscillates around 0.85 with a deviation of ~5% for the wavelength of 1.054 μm. In Figure 9.4, the calculation was performed for 1% (volume density) bead solutions (10% in stock). Due to the wavelength dependence, there is smaller difference between l_t and l_s for particles with smaller diameter. When the diameter increases, the difference increases. When diameter is more than 3 μm, the difference in values of both l_t and l_s increases for the two wavelengths.

9.2.3 Values of Key Optical Parameters for Human Tissues and Some Model Media

Tissue scatters light strongly in the forward direction, the g value is ~0.9. A value of $g = 0.9$ makes $l_t = 10l_s$. Intralipid-10% suspension with $g \sim 0.8$ and 0.6 for 530 nm and 1054 nm, respectively, and lower absorption coefficient has been widely used as a model medium to simulate homogenized breast tissue [82, 83]. The particle size distribution in Intralipid-10% solution is shown in Figure 9.5.

Associated optical parameters of Intralipid-2% suspension and human breast tissues at visible and IR wavelengths are shown in Table 9.1. Intralipid-10% suspension contained 50-g soya bean oil, 6-g phospholipid, 11.25-g glycerol, and 2% concentration solution was made by diluting Intralipid-10% with distilled water [81].

It can be seen from the data in Table 9.1 that the transport mean free path of 2% diluted Intralipid-10% suspension is ~3.4–5 mm, 5 mm, and 6.6 mm at 630 nm, 800 nm, and 1064 nm wavelengths, respectively. In the early time detection $l_{\mathrm{KF.s}} =$ 2.3 mm and $l_t = 4.6$ mm, if $g \sim 0.5$ at 1054 nm.

For the 2% diluted Intralipid-10% suspension, the $l_a = \sim 500$ nm from 620 to 1064 nm. For breast tissues, $l_t = \sim 0.5$–2.6 mm at 620 nm and $\boldsymbol{l}_a = \sim 100$ mm. For the mean cosine of scattering angle g, there is a difference between real breast

TABLE 9.1 Optical properties of human breast tissues and 2% intralipid solution

Tissue type and 2% intralipid	Transport mean free path l_t (mm)	Absorption length l_a	Anisotropy factor, g	Scattering length l_s (mm)	Wavelength (nm)
Glandular	1.25	17	0.91	0.067	1064
	0.8				700
Adipose (fatty breast)	0.7	155	0.95	0.0040 ± 0.0006	620
	1.2	10			1064
	0.77	100			700
	1.0	100			633
	1.3	130			800
Carcinoma	1.21	230	0.88		1064
	0.5	155			700
	0.6	24			620
	0.54	62.5			633
	0.96				800
Benign	2.6	30			620
Fibroadenoma	2.08	13			1064
	1.55	100			620
2% diluted of stock intralipid-10%	3.0	500	0.5	1.0	620
	10	500	0.71–0.8	3.3	1064
	3.4–5.0		0.5	1.83	633
	6.6		0.64	2.3	1064
	5.0			1.23	800
					1054
					527

Source: Adapted from Reference 81.

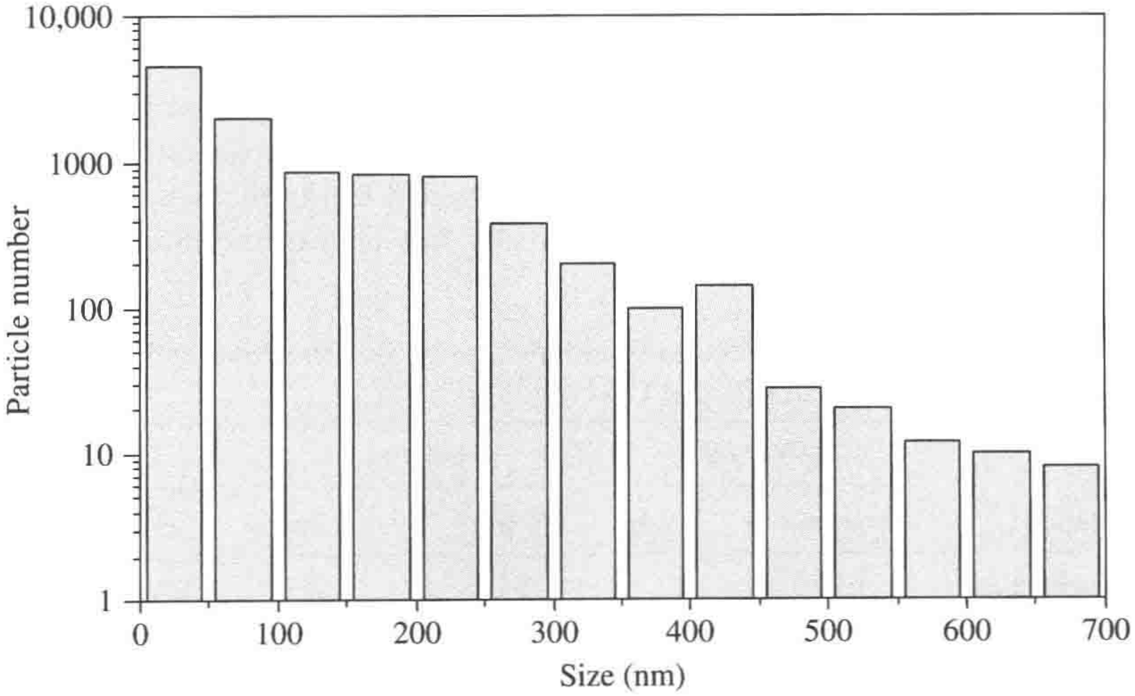

FIGURE 9.5 The particle size distribution in Intralipid-10% suspension. Adapted from Reference 81.

TABLE 9.2 Transport mean free path and absorption length with standard deviations for various random media at 620 and 1064 nm measured using time-resolved transmission and diffusion approximation

	Transport mean free path, l_t (mm)		Absorption length (nm)	
Random media	1064 nm	620 nm	1064 nm	620 nm
Benign human breast	~5.1*	2.6 ± 0.2		30 ± 5
Fatty human breast	~1.4*	0.7 ± 0.1	200	155 ± 50
Chicken breast	4.9 ± 0.3	2.5 ± 0.5	70 ± 10	60 ± 30
Chicken fat	0.74 ± 0.1	0.6	230 ± 70	155
Pork breast	3.5 ± 0.5	1.2 ± 0.2	70 ± 10	70 ± 8
Pork fat	0.58 ± 0.05	0.35 ± 0.05	400 ± 60	300 ± 50
Whole milk (25%)		1.0 ± 0.1		253 ± 50
2% solution of Intralipid-10%	10 ± 1, 4.4**	3.0 ± 0.1	500 ± 50	500 ± 50

*Estimated by $\mu_{\text{t-IR}} \approx 0.5\mu_{\text{t-Visible}}$; **Estimated by $\mu_{\text{t-1054 nm}}$ from data.
Source: Adapted from Reference 81.

tissue and Intralipid suspension. The g_{tissue} is from 0.88 to 0.95, while $g_{\text{Intralipid}}$ is from 0.5 to 0.83, which was calculated from Mie's theory. Table 9.2 and Table 9.3 show the calculated results from the time-resolved and other measurements [57, 79, 81, 84].

For 2% diluted Intralipid solution, the scattering mean free path at 1054 nm, $l_s \approx 2.2$ mm, and $l_t \approx l_s/(1\text{–}0.5) = 4.4$ mm has been measured using a K-F imaging system [83].

Breast tissue consists of fat, fiber, glandular, and blood. The mean free transport path and the absorption coefficients of four different breast tissues at 1060, 800, and 625 nm are displayed in Table 9.3 [81].

The l_t values for adipose (fat) tissue listed in Table 9.3 are different from values in Table 9.2. The main reason of the discrepancy is that samples used for Table 9.3 were compressed homogenized tissues, which no longer possessed any natural structure [81]. The values in Table 9.2 were obtained from *in vitro* samples. It can be seen from Table 9.3 that the transport mean free path of the normal glandular

TABLE 9.3 Transport mean free path and absorption length with standard deviations for various random media at 620 and 1064 nm [81]

	1060 nm		800 nm		625 nm	
Tissue types	l_t (mm)	l_a (mm)	l_t (mm)	l_a (mm)	l_t (mm)	l_a (mm)
Normal glandular	1.25	17	0.84	25	0.60	20
Normal adipose	1.2	10	1.4	14	1.28	13
Fibroadenoma	2.08	13	1.55	100	1.04	17
Ductal carcinoma	1.21	7	1.14	33	0.79	8

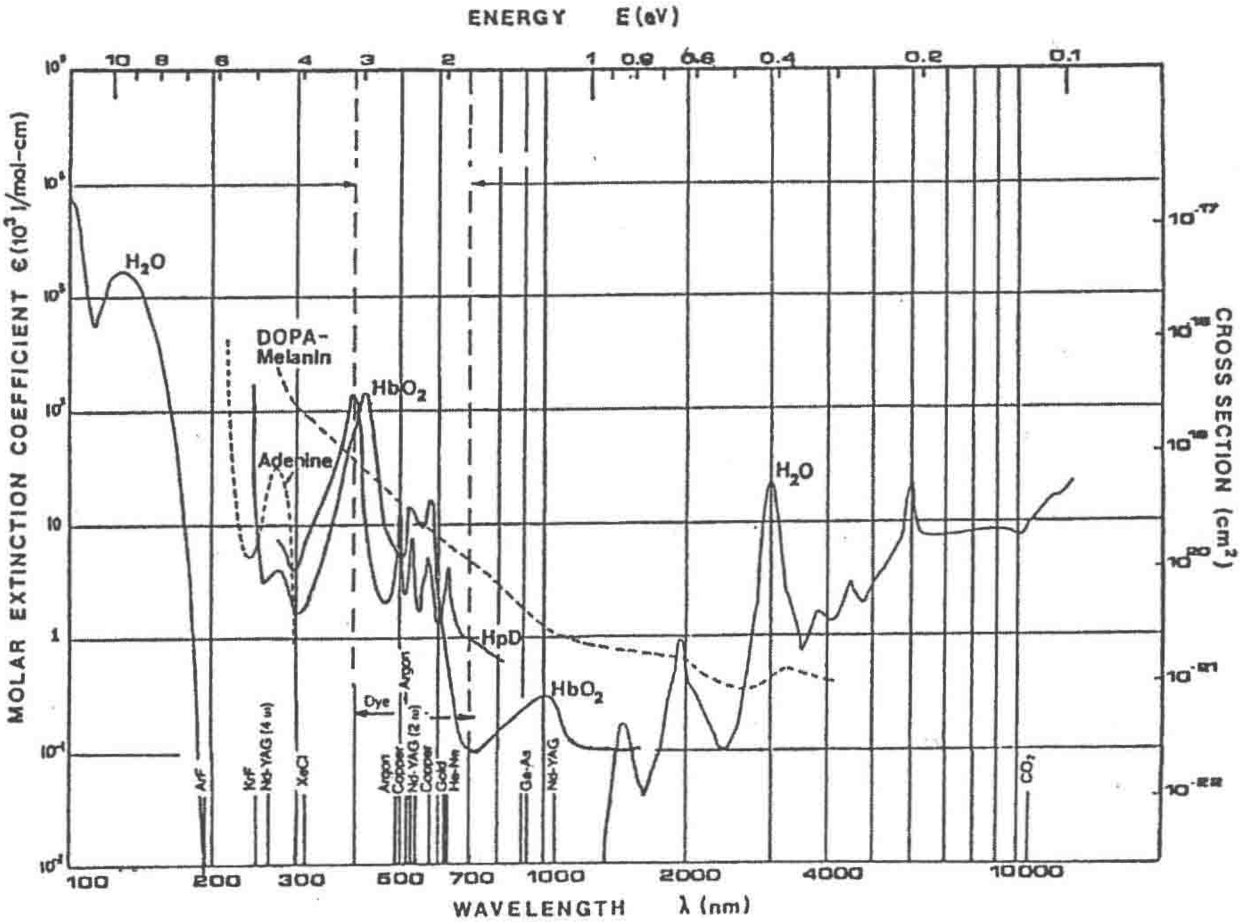

FIGURE 9.6 Absorption spectra of tissue constituents. Adapted from Reference 85.

tissue strongly depends on wavelength and decreases with the decrease of the wavelength.

9.2.4 Optical Absorption Spectra of Key Chromophores in Tissues

The absorption in NIR of different key chromophores in tissue, such as water (H_2O), hemoglobin (Hb), and oxy-hemoglobin (HbO_2), as a function of wavelength is shown in Figure 9.6 [85]. It suggests that the wavelength range of 700–1100 nm is most suitable for optical mammography since there is a weaker absorption by H_2O, the main component of tissue. Attenuation spectra of distilled water and the 2% diluted intralipid-10% stock solution in 1-mm-thick cell are shown in Figure 9.7. This curve shows that scattering dominates from 200 to 800 nm, while absorption by water dominates the attenuation for wavelength greater than 1300 nm. The absorption of water appears at ~900 nm, ~1200 nm, ~1400 nm, and longer. There is another optical window in 1600–1800 nm region where scattering is low.

The absorption in 700–1100 nm range is shown in Figure 9.8 for water (H_2O), oxyhemoglobin (HbO_2), and deoxyhemoglobin (Hb). In this wavelength range, Hb and HbO_2 can be used to measure hypoxia and may play an important role to separate cancer from normal breast tissues. Hypoxia can be an important marker of breast

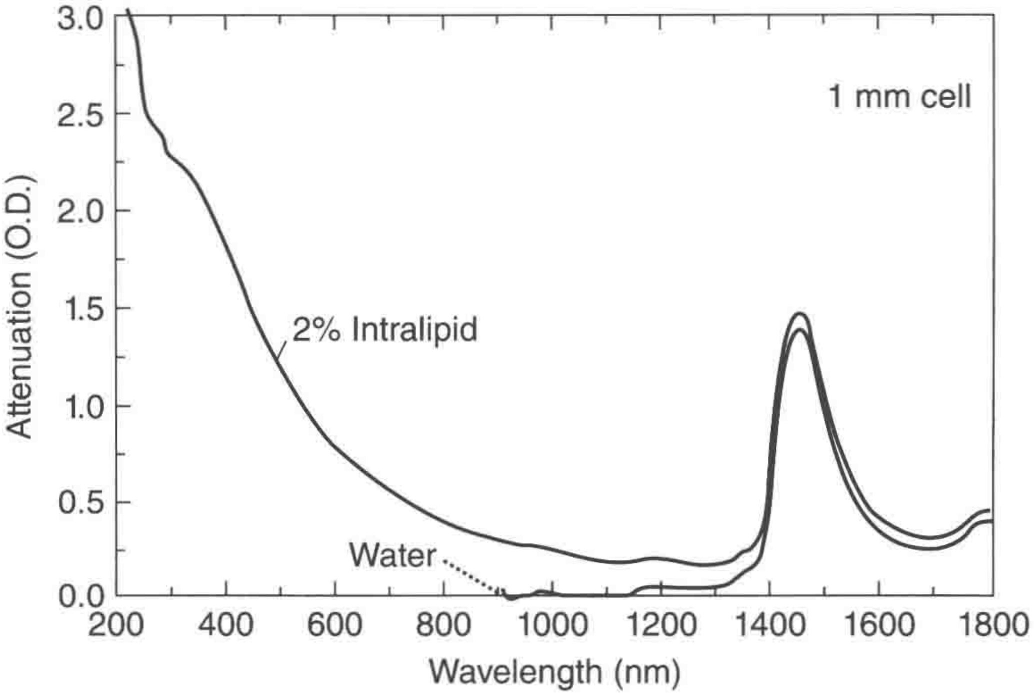

FIGURE 9.7 Attenuation of light by water and 2% diluted intralipid in an 1-mm cell.

cancer. Further water absorption appears in the 1000–1400 nm region and offers another biomarker for cancer detection.

9.3 STUDY OF BALLISTIC AND DIFFUSE LIGHT COMPONENTS

It was believed prior to 1989 that when a light pulse enters a highly scattering medium it broadens and expands. However, Yoo and Alfano [46] observed a startling effect in the ultrashort time domain. A unscattered weak pulse of light (ballistic) traveling collinearly out of 10-mm-thick scattering medium consisting of 0.33 μm latex beads

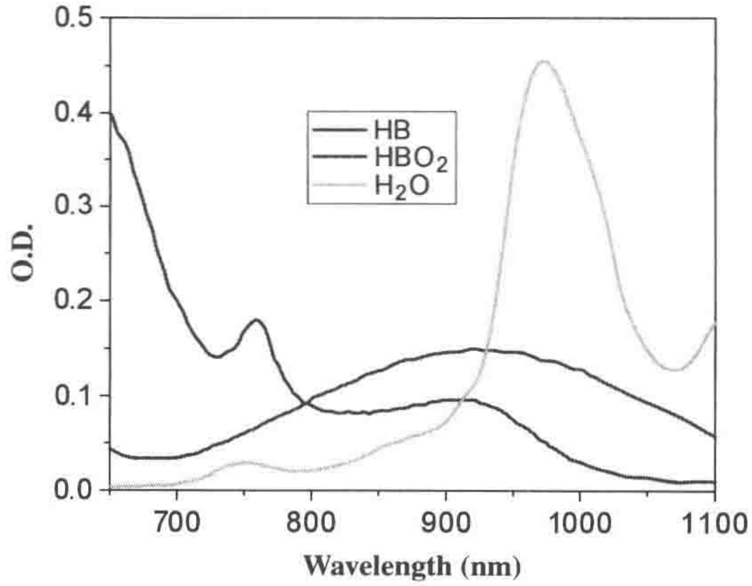

FIGURE 9.8 Absorption spectra of Hb, HbO_2, and H_2O. (*For a color version of this figure, see the color plate section.*)

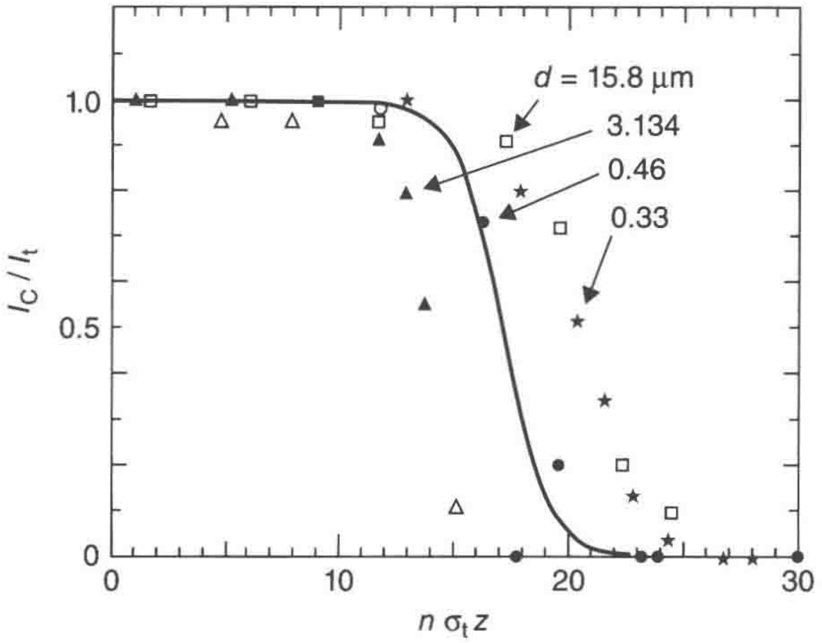

FIGURE 9.9 Plots of ratio of coherent ballistic (I_c) to total (I_t) intensity of scattered light in the forward direction versus ($n\sigma_s z$) for four different scatterer diameters. The solid curve is plotted from Eq. (1) in Reference 46.

suspended in water appeared when using 80-fs, 620-nm laser pulses. A Hamamatsu streak camera of 5 ps time resolution was used in the experiment. The temporal and angular information was obtained simultaneously indicating that the light component was coherent. This coherent light pulse was designated as the "ballistic pulse" which obeys Eq. (9.1) and is the weak remnant of the input laser pulse.

The transition from coherent to incoherent scattering is presented in Figure 9.9 for a 10-mm-thick slab of bead random medium with bead diameters from 0.33 to 15.8 μm. At a low concentration of scatterers, up to $n = 7.0 \times 10^{16}\ \mathrm{m}^{-3}$ ($n\sigma_s z = 17.9$), only the coherent component is visible. The incoherent component becomes visible at a slightly higher concentration, where $n = 8.0 \times 10^{16}\ \mathrm{m}^{-3}$ ($n\sigma_s z = 20.4$). The incoherent component rapidly gains in intensity relative to the coherent counterpart as the concentration increases. The corresponding $n\sigma_s z$ values are 22.8, 24.3, and 26.8. When $n\sigma_s z$ is above 26, only the incoherent component is visible.

The coherent and incoherent components of ultrafast laser pulses passing through a slab of random media may be separated from each other using time-resolved measurement techniques. The ability to time-resolve the coherent from incoherent components is important in medical imaging and diagnostics. The diffusion approximations of RTE that is commonly used to describe light propagation through optically thick media (sample thickness $z \gg l_t$) fails [86] to explain the experimental data as the value of z/l_t decreases below 10.

There is a regime of scattering where the diffusion approximation fails, in particular, when the source-detector distance is small, say $z/l_t \leq 10$ for inverse imaging. Diffusion theory is used to explain occurrences where the transport of particles and waves in random media occurs. The analytical solution for the diffusion equation are generally available and are found to be valid [87, 88] when $z/l_t \gg 1$. For many physical media, the wave transport occurs in the region where z/l_t is small. The diffusion approximation has been extensively used in many of the pioneering light-scattering studies [88–94], in applications of light scattering to study physical and biological media [95–97] and inverse imaging [4–6].

It is important to know at what value of z/l_t the diffusion approximation begins to fail. The transport of photons through a slab of random medium was directly studied using ultrafast laser pulses and time-resolved detection. Yoo et al. [86] provided the first direct insight on when and how the diffusion approximation deviates from the actual transport of photons through a slab of random medium [87]. The results resolved the controversy on whether or not photon transport is diffusive after passing through a slab of random medium of only a few transport mean free path thick. The time-resolved studies using 100-fs, 620-nm laser pulses show that the prediction of the diffusion approximation deviates monotonically from the measured scattered pulse as the value of z/l_t decreases below 10. The scattered photons are found to arrive much earlier than predicted by diffusion approximation. Ballistic photon transmission has been shown to exist in a small-diameter random-bead medium [46].

A direct method to probe the transport of photon pulses in a random medium is to measure the distribution of photon arrivals in the time domain. When a plane-front ultrafast pulse is incident normally onto a slab of random medium, the temporal distribution of photon arrivals at a point on the opposite side of the slab is predicted by the diffusion theory as [46]

$$I_z(t) = \frac{D}{\pi z^2} \sum\nolimits_{m=1}^{\infty} m \left(\frac{\pi z}{d}\right)^2 \sin\left(\frac{m\pi z}{d}\right) \times \exp\left[-Dt\left(\frac{m\pi}{d}\right)^2\right], \tag{9.8}$$

where $D = vl_t/3$ is the diffusion coefficient, $d = z + 2z_0$, $z_0 = 0.71l_t$, v is the speed of photons, and z and l_t were defined earlier.

The experimental arrangement shown schematically in Figure 9.10 closely imitates the geometry governed by Eq. (9.8). Ultrafast laser pulses of 100 fs duration were generated at the repetition rate of 82 MHz by a colliding pulse mode-locked dye-laser system. The laser power was 10 mW at a wavelength centered on 620 nm. The laser beam of 4 mm diameter was split into two beams: a reference beam to mark the zero time of the signal beam, which was expanded to 35 mm diameter. The central portion of the expanded beam was selected by a diaphragm and passed through the random medium consisting of latex beads suspended in water contained in a cylindrical 50 mm diameter and 10 mm thickness glass cell. Photons scattered out of the cell will be lost, that is, both sides of the cell satisfied an absorbing boundary condition. A black pinhole of 2 mm diameter was placed at the center on the opposite side of the cell. The temporal distribution of photons scattered out from this pinhole in the forward direction at an angle of 10 mrad was measured by a synchro-scan streak camera. The diameter of the incident beam was set to 20 mm; any further increase in the diameter will not change temporal profile of the scattered photons. The measured scattered pulse profile can be described by Eq. (9.8) if the diffusion approximation is valid.

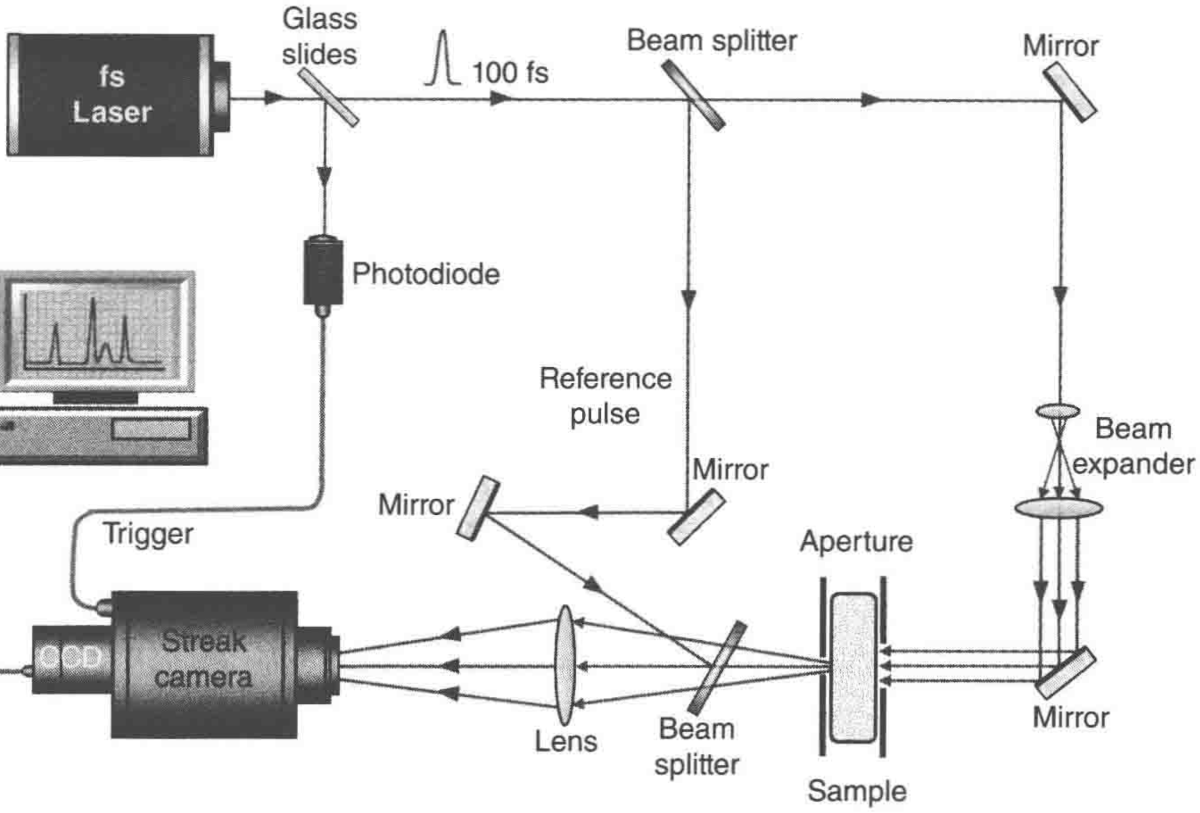

FIGURE 9.10 A schematic diagram of the experimental setup.

Experimental studies were carried out for different bead diameters, each at a series of different concentrations. For highly concentrated random medium, where $z/l_t \gg 1$, the diffusion equation holds, which was not surprising. In this case, the transport mean free path was obtained by fitting the scattered pulse profile using Eq. (9.8). Figure 9.11 illustrates an example where the diffusion theory fits the experimental data. The photon transport mean free path l_t was found to be 0.309 mm which is close to the value of 0.25 mm computed from Mie theory using $l_t^m = 1/n\sigma_m$, where n is the number density of scattering particles and σ_m is the momentum-transfer scattering cross-section.

Figure 9.11 and Figure 9.12 display a series of transmitted pulse profiles for media with decreasing bead concentration for bead diameters of 0.296 and 3.134 μm, respectively. Figures 9.11a and 9.12a show that the experimental (solid) curves can be fitted by diffusion theory (dashed curves), where z/l_t is large as indicated in the figures. Figures 9.11b and 9.12b, with $z/l_t \approx 10$, clearly show deviations. The measured photons arrive earlier than predicted by the diffusion approximation. The peaks of the theoretical (dashed) curves are normalized to the peak of the experimental data, whereas the dash-dotted curves are normalized to the total intensity of the experimental results. None of the theoretical plots from the diffusion approximation agrees with the experimental results at early time when $z/l_t > 10$.

A quantitative indication where the diffusion approximation breaks down is the average time of photon arrival from the pulse. The average arrival time is computed by

$$\bar{t} = \int_0^\infty dt'\, t' I(t') \bigg/ \int_0^\infty dt' I(t'), \tag{9.9}$$

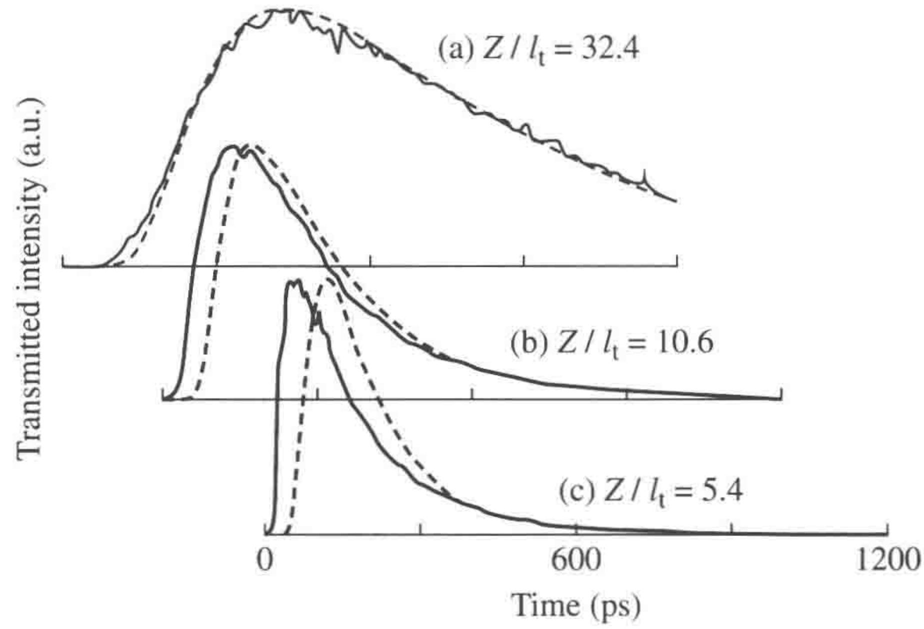

FIGURE 9.11 Transmitted pulse profiles of 10-mm-thick random media consisting of latex beads of diameter 0.296 μm. The bead concentration n, l_t, and z/l_t are, respectively, (a) 6.65×10^8 mm^{-3}, 0.309 mm, and 32.4; (b) 2.18×10^8 mm^{-3}, 0.941 mm, and 10.6; and (c) 1.10×10^8 mm^{-3}, 1.853 mm, and 5.4. Solid curves are the experimental results and dashed curves are computed from the diffusion theory where their peak intensity is normalized. Adapted from Reference 86.

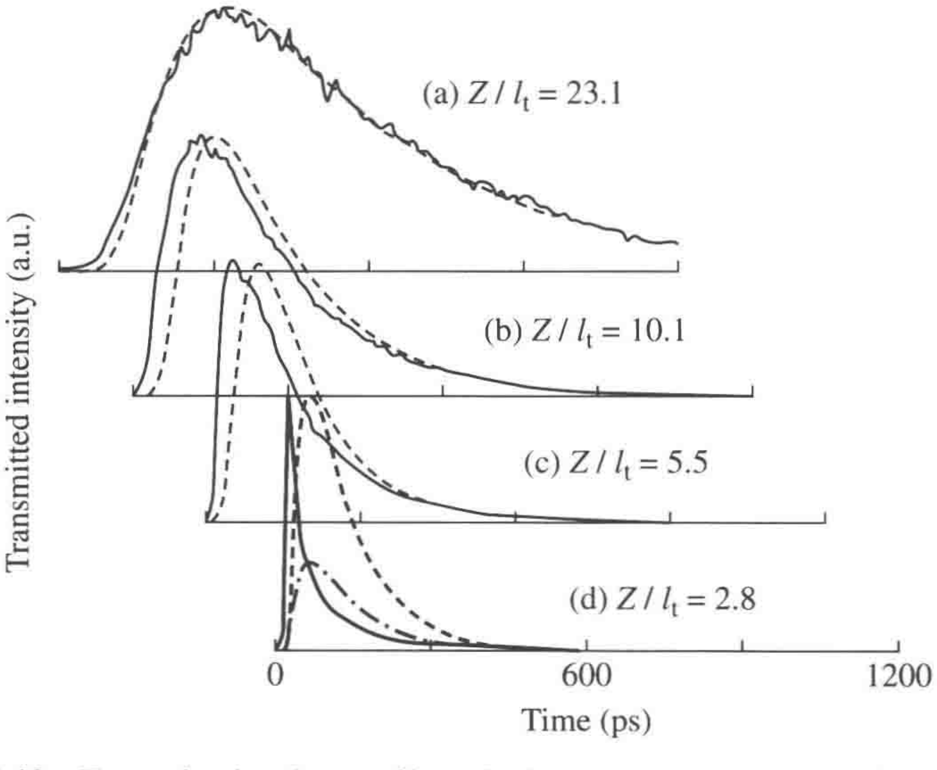

FIGURE 9.12 Transmitted pulse profiles of 10-mm-thick random media consisting of latex beads of diameter 3.134 μm. The bead concentration n, l_t, and z/l_t are, respectively, (a) 9.62×10^5 mm^{-3}, 0.433 mm, and 23.1; (b) 4.20×10^5 mm^{-3}, 0.989 mm, and 10.1; and (c) 2.28×10^5 mm^{-3}, 1.823 mm, and 5.5. Solid curves trace the experimental results. Dashed and dash-dotted curves are computed from the diffusion theory where their peak and total intensity are normalized to the experimental curves, respectively [86].

where $I(t')$ is the temporal distribution of the scattered pulse measured experimentally. The theoretical prediction of the average arrival time can be obtained exactly from Eq. (9.9) as

$$\bar{t} = \frac{1}{2}\frac{z(z+4z_0)}{vl_t} \sim \frac{z^2}{2vl_t}. \tag{9.10a}$$

The average length $\langle z \rangle$ traveled by diffusive light is

$$\langle z \rangle = \frac{z^2}{2l_t}. \tag{9.10b}$$

The average time of photon arrival $\bar{t}$ as a function of z/l_t predicted by Eq. (9.10) is plotted by a solid curve in Figure 9.13. The average time of arrival of the experimentally measured photons are computed from Eq. (9.9). The results from random media of beads with diameters $d = 0.296, 0.46, 1.09, 3.134$, and 11.9 μm in Figure 9.13 are represented by plots of stars, triangles, circles, squares, and pluses, respectively. The dotted curve is obtained by multiplying Eq. (9.10) by 0.9 to indicate where the experimental data deviate by more than 10%. The data displayed in Figure 9.13 clearly demonstrate that the average time of arrival deviates by 10% when $z/l_t \approx 10$. The deviation increases as z/l_t is reduced further below 10 and many more photons arrive earlier than predicted by diffusion theory. Beads of larger diameter will increase the amount of light scattered in the forward direction. This anisotropic scattering

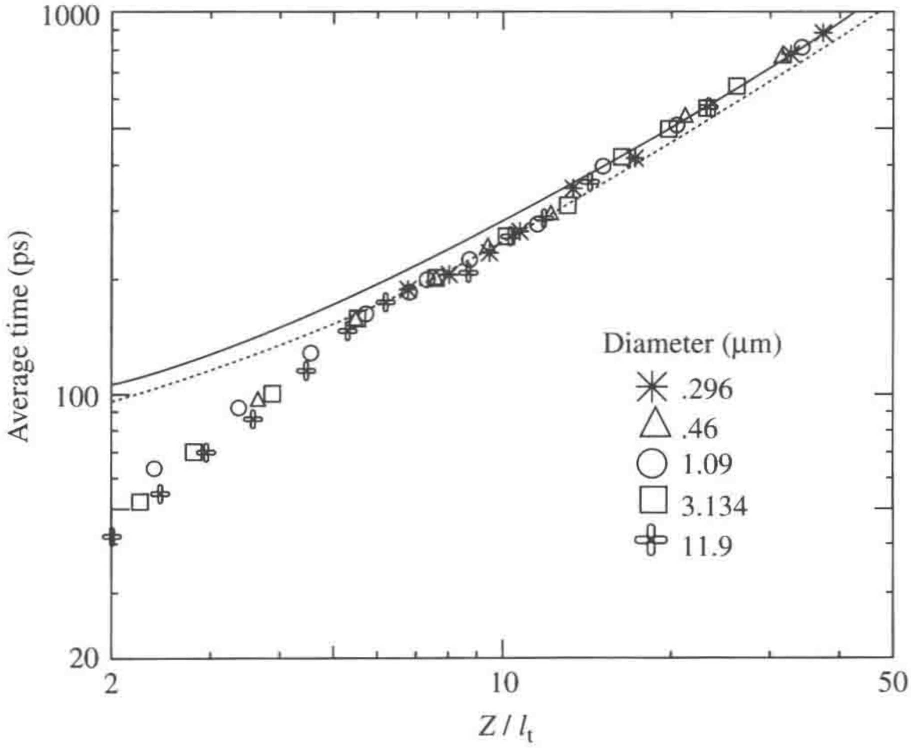

FIGURE 9.13 Plot of average time of arrival $\bar{t}$ versus z/l_t. The solid curve is the $\bar{t}$ predicted by diffusion theory, and the dotted curve is $0.9\bar{t}$. Experimental results (corresponding bead diameter) are plotted by stars (0.296 μm), triangles (0.46 μm), circles (1.09 μm), squares (3.134 μm), and plusses (11.9 μm) [86].

will result in reducing the average arrival time of the photons, which is apparent in Figure 9.13, when z/l_t is less than 5. For a given value of z/l_t (<5), the largest bead diameter (11.9 μm) medium (plusses) shows the smallest average arrival time, while the smallest bead diameter (1.09 μm) medium (circles) shows the largest average arrival time, and the intermediate bead diameter (3.134 μm) medium (squares) shows that its average arrival time falls between that for the 11.9 and 1.09 μm beads. So, diffusion approximation breaks down for source-to-detection distances z when $z/l_t > 5$. A better theory is needed for describing light transport in scattering media in the regime where the diffusion approximation breaks down. Cai et al. have developed cumulant solutions of the radiative transport equation, which are significant improvements [98, 99], and Ntziachristos et al. have demonstrated an approach namely early photon tomography to use the ballistic photons for imaging objects embedded inside turbid media such as tissue [100].

9.4 PHOTON-SORTING GATES

Over the years, several schemes have evolved to sort out the direct image-bearing ballistic and snake photons from the multiple-scattered diffuse photons [3]. These schemes exploit one or more of the changes that scattering induces on the characteristics such as directionality, polarization, absorption, coherence, and temporal duration of the incident light. Since the image-bearing photons change the least, the idea is to devise a gate that let the photon with a specific initial property through, but will block others.

A time gate capitalizes on the fact that image-bearing photons emerge from the scattering medium sample sooner than the diffusive photons. To realize a time gate in practice, one needs a shutter that will open for a short duration, typically few picoseconds, to let the early photons through and then close in time to leave out the delayed scattered photons.

A space gate exploits the fact that the ballistic and snake photons come out from the tissue in the incident direction, while the multiple-scattered light emerges in all directions. So, a small aperture centered on the direction of incidence and placed after the sample will collect the ballistic and snake light and effectively discriminate against a significant fraction of multiple scattered light.

Similar gating schemes based on polarization and coherence of light have also been devised. Often a single gate may not be discriminating enough. A space gate cannot filter out the photons that first been scattered out of the incident direction and then back into it. A time gate employed after the space gate can cut out such "online" scattered photons, since scattering makes them travel longer distances and emerge out of the sample later than the ballistic photons that propagate straight through.

The implementation of an optical imaging modality based on any of the gating methods mentioned above requires a laser and beam delivery optics to illuminate the sample, a detection scheme to monitor the transmitted light, and a signal processing unit to construct the image from the collected data and known experimental parameters.

The use of absorption also helps cut out the diffusive light in favor of ballistic and snake components due to longer distance $\langle z\rangle = \frac{z^2}{2l_t}$ traveled by diffusive photon over ballistic distance z. We present below the experimental arrangements for realization of some of these gates, and images of targets in turbid media obtained using these gating techniques.

9.4.1 Time Gate

Time-resolved techniques were among the first methods used to separate out the ballistic and snake components from the diffusive component [52–58, 62, 101–103]. Two of the earlier developed and successfully used methods to select temporally the ballistic and snake components over the diffusion part are optical Kerr Gate (OKG) [52–54] and Streak Camera [58].

Ballistic 2D images were first demonstrated in 1991 using a two-dimensional (2D) picosecond optical Kerr gate imaging system [52]. Spatially resolved phantom light point source (200 μm in diameter) and phantom test bar chart with bars of 100 μm wide were imaged in highly scattering medium including a 3.5-mm-thick sample of human breast tissue, a 3-mm-thick chicken breast tissue, and a 5-cm-thick water cell with suspended polystyrene balls. The experimental setup of the picosecond Kerr gate imaging system consisted of a mode-locked Nd:glass laser, a CS_2 Kerr shutter, and a 2D readout system. The laser pulse had a duration of 8 ps, pulse energy of ~4 mJ, a peak power of 5×10^8 W, and a wavelength of 1054 nm. The 1054-nm laser beam was sent through a potassium dihydrogen phosphate (KDP) crystal to produce the second harmonic component with a wavelength of 527 nm and a peak power of about 10^7 W. The 527-nm beam was used to probe the hidden object. The typical transmission efficiency of CS_2 Kerr shutter was ~10%. The image was recorded by an intensified 2D charge-coupled device (CCD) camera with 640 × 480 pixels, a gain of 6000, and a dynamic range of 100:1. Its minimum detection level is ~1 lux cm^{-2}. A personal computer (PC), a frame grabber, a software package, and a video printer were used to store, process, and display the images. All photographs shown in Figure 9.14 were obtained from a single laser shot, which consisted of a laser train with ~100 pulses each separated by ~10 ns.

Objects hidden behind various scattering walls, including human breast tissue, chicken breast tissue, and a model system (polystyrene spheres suspended in a water cell), were detected with this system. The picosecond Kerr gate was capable of separating the ballistic image of a point source in the scattering medium from the diffusive noise. In one of the experiments, the scattering medium consisted of polystyrene spheres of diameter ~0.46 μm suspended in water in an optical cell with the dimensions $5 \times 5 \times 5$ cm^3. The volume density of the spheres was 0.88% for all measurements except in the double-quasi-point source measurement for which the density was 0.3%. The calculated scattering coefficient was $N\sigma L \sim 21.7$ for a single point source and bar chart and $N\sigma L \sim 7.4$ for the double quasi-point source fluorescence imaging test, where N is the number density of the scattering particles, σ is the scattering cross-section, and L is the thickness of the sample. When a breast

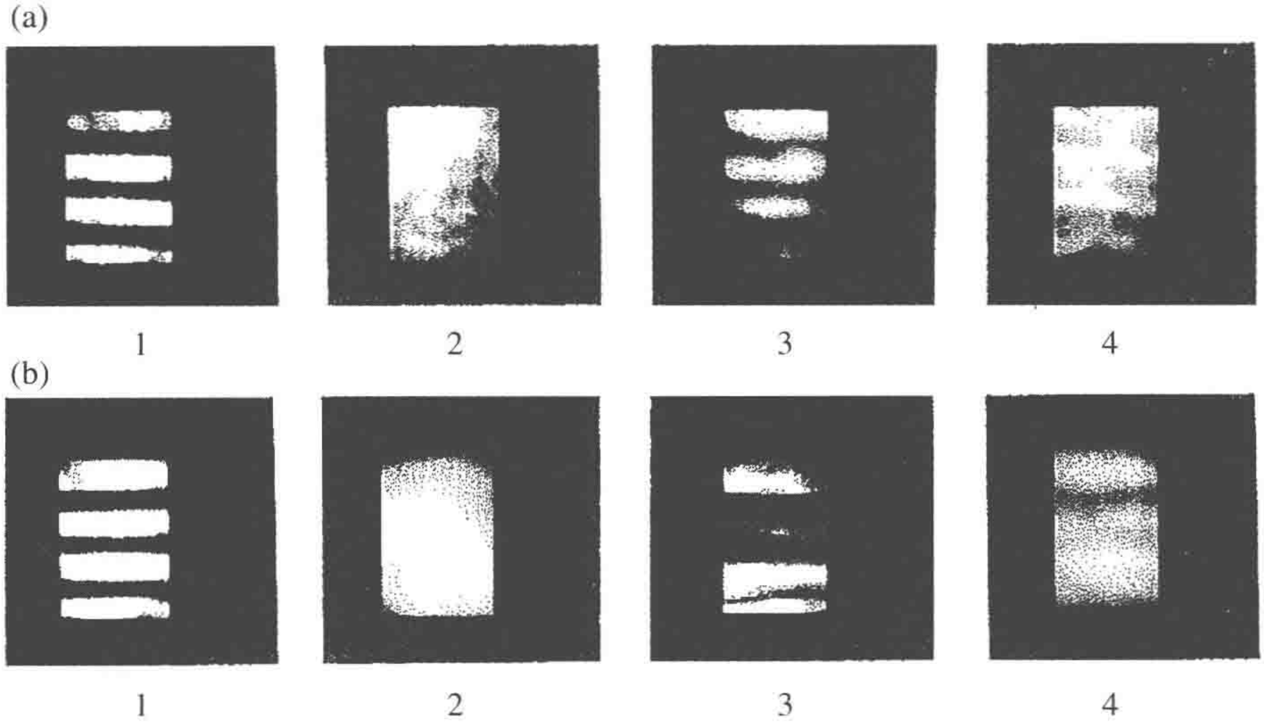

FIGURE 9.14 Two-dimensional images of the test bar chart behind (a) 3.5-mm-thick human breast tissue and (b) 3-mm-thick chicken breast tissue illuminated by 8-ps, 530-nm laser pulses. The test object is a five-line pairs per millimeter target. Dark bars are the object, and the white area is the transparent background. The width of each bar is ~100 μm. (1) Reference image (tissue removed). (2) No time gate (standard transillumination). (3) $t_D = 0$, time gate at zero delay time. (4) $t_D = 22$ ps, time gate at 22-ps delay time. A 200-μm spatial resolution has been obtained in both photographs of (3) from the time gated ballistic imaging. The image contrast is poor at a later delayed gate time as shown in (4). Without the time gate in (2), the image was totally blurred. Because of the high fiber content of chicken breast tissue, the resolution obtained from the time-gated ballistic imaging in (B3) is poorer than that from (A3). Part of the nonuniformity of the image at a time segment can be accounted for by the laser beam nonuniformity, the sample refractive index variation, and internal structures. Adapted from Reference 52.

tissue was used as a scattering medium, its total attenuation coefficient, $\mu_a + \mu_s$ could vary from ~2.5 to 600 cm^{-1}, where μ_a is the absorption coefficient and μ_s is the scattering coefficient [101, 104–106].

To produce a single quasi-point source, a 527-nm laser beam was focused onto a ground glass plate placed inside the scattering medium. The diameter of the focal beam spot was ~200 μm. To produce a double quasi-point source, the 527-nm beam was split into two beams and focused onto a 200-μm-thick polydiacetylene (PDA) film placed inside the scattering medium to form a fluorescence double point source. PDA fluoresces from 550 to 850 nm with fluorescence lifetime of ~12 ps [107].

The fluorescence light from the double-point source separated by ~400 μm was resolved by the picosecond Kerr gate, but could not be resolved by the steady state transillumination imaging. For the steady-state image, the double-point image merged into strong noise wings. The diameter of each fluorescence point source was ~200 μm. PDA film situated inside turbid water ($N\sigma L = 7.4$) was illuminated by two 527-nm laser pulses. The resolved image of the two-point sources separated by 400 μm was formed by the ballistic part of the signal light.

A sequence of measured time-dependent 2D Kerr-gated images of a bar chart behind 3.5-mm-thick human breast tissue and 3-mm-thick chicken breast tissue are displayed in Figures 9.14a and b, respectively. The bars of the test chart (five line pairs per millimeter, corresponding to ~100 μm spatial resolution) were illuminated by 8 ps, 530-nm laser pulses. In Figure 9.14, a1 and b1 represent reference photographs, which display the image of the test chart without the scattering wall. Figure 9.14, a2 and b2 represent images obtained from standard transillumination (no time gate) of the chart behind these two tissue samples; no clear image can be observed in either of these cases. Figure 9.14, a3 and b3 show the Kerr gate bar images of the ballistic and snake signals at a gating time of $t = 0$ (time resolution $\delta t \sim 10$ ps). Clear bar images with dimension of ~0.1 mm (separated by 0.2 mm) can be resolved in human breast tissue as shown in Figure 9.14, a3. As the gating time was delayed by 22 ps, the collected images were gradually broadened and blurred as shown in Figure 9.14, a4 and b4. These results demonstrate that the 2D Kerr imaging system as opposed to 1D time-gated imaging system can be used to image in vitro human organs and tissues.

It is estimated that 2D low-level signal images with an attenuation factor of e^{-30} through a scattering wall can be obtained. It is expected that it will soon be possible to detect highly resolved images of ultra small (less than a few millimeters) objects embedded inside thick biological and medical samples with the use of a high repetition femtosecond multiple Kerr gate system.

Since breasts do not have bars inside, as a more realistic approximation, a droplet of water or suspension of Intralipid-10% of different concentrations were used as targets. The scattering medium was water suspension of Intralipid-10% that had a different concentration than that of the target. To demonstrate the capability of Kerr gate, time-resolved images of translucent droplets in high scattering turbid media were obtained. A Fourier spatial filtering technique combined with Kerr time gating system improved the dynamic range and signal-to-noise ratio [108–110].

A schematic of the sample phantom and host cell arrangement is shown in Figure 9.15. Diluted Intralipid-10% suspension of various concentrations and pure water were used for the phantom droplets in a 2% diluted Intralipid host turbid cell. The inside dimension of the host cell was $50 \times 50 \times 50$ mm^3. The phantom droplets were generated in a 50-mL burette with a straight bore stopcock with a polytetrafluoroethylene plug. The subdivision or the limit of error of this burette is 0.1 mL. For a 2% diluted Intralipid stock solution of 10% (the final solution was 0.2%), the measured attenuation coefficient [108] was 0.38 mm^{-1}. The absolute signal collected was $\sim 10^{-10}$ of the input probe beam. The absorption length of the modeled Intralipid suspension is on the order of 500 mm and can be neglected in the experimental arrangements. Two measured time-resolved KF two-dimensional images of water droplets in the middle of a 50-mm-thick host cell are shown in Figures 9.16a and b. Because the scattering loss from the water droplet is less than that from the surrounding host, the intensity of the projected image of the water droplet was higher than that of the host. The shape of these water droplets depends on the amount of water released. The delay time between the stopper opening and the photographic time was

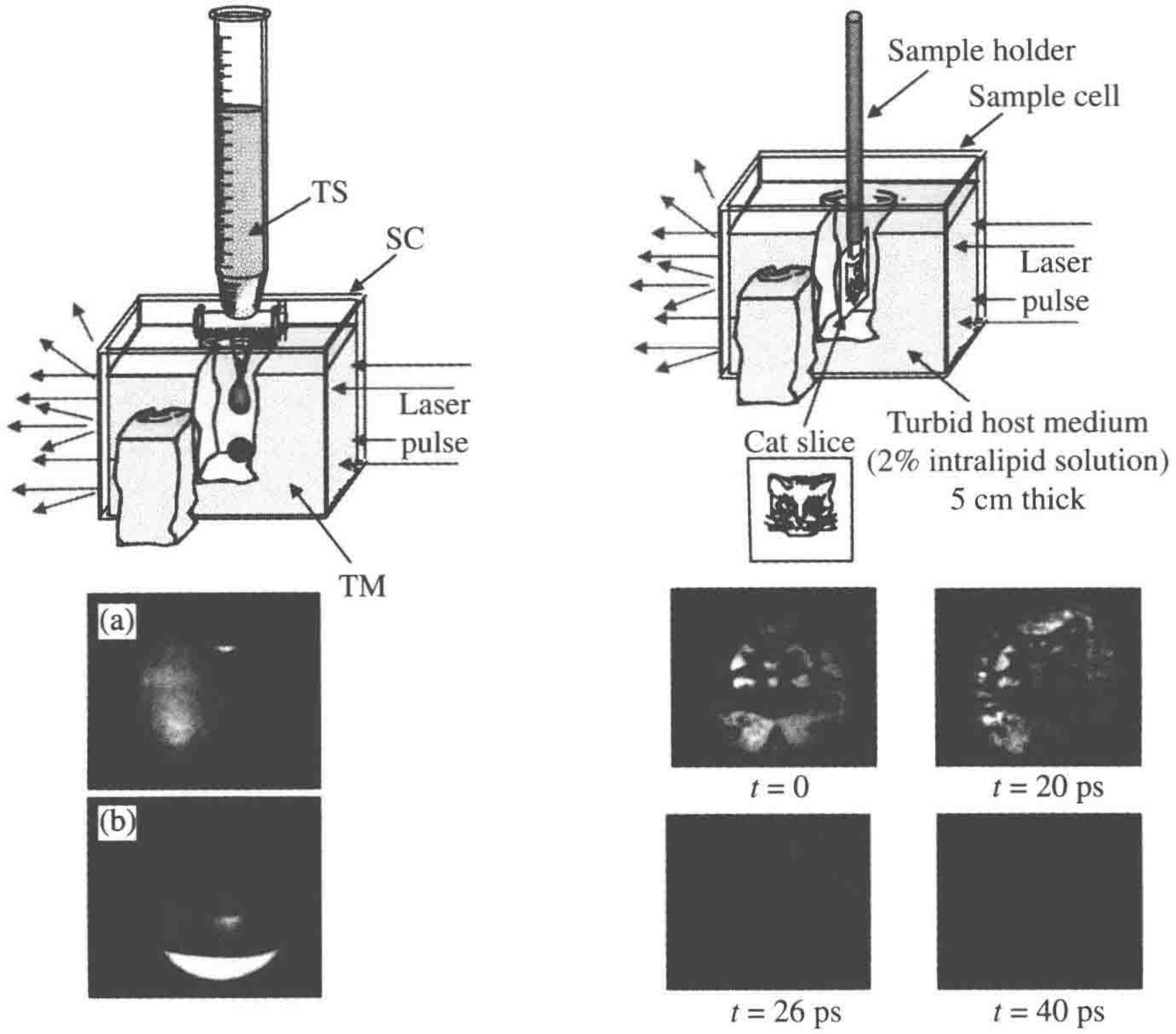

FIGURE 9.15 Experimental arrangement showing turbid sample cell and translucent intralipid phantom droplets (left side). The cut from the side section of the cell displays pictorially the droplet releasing inside the host medium. SC, sample cell with inside dimensions of 50 mm × 50 mm × 50 mm; TM, 2% dilution of a 10% stock Intralipid suspension for the host turbid medium; TS, translucent phantom sample, $x\%$ diluted intralipid suspension in a burette ($50 \times 50 \times 50$ mm^3 tank). The right side shows the Kerr gate time-resolved images of an object (a CAT slice) embedded inside a turbid medium (5-cm-thick 2% intralipid solution). The images taken at early times of 0 and 20 ps clearly show the existence of the object even inside a thick scattering medium, which can not been seen visually [54].

varied between ~2 and 10 s. The inhomogeneity of the brighter circle in Figure 9.16 that corresponds to the collection aperture or signal beam diameter of ~12.7 mm was accounted for by the nonuniformity of the laser intensity distribution.

To determine the contrast of the transmitted early snake light images as shown in Figure 9.17, four different phantom droplets with 1, 2, 3, and 5% diluted Intralipid suspensions were dropped into a 25–mm-thick host medium. The projected image from the 5% Intralipid droplet shown in Figure 9.17d is the darkest because of the increased scattering from the droplet, while the projected image from the 2% Intralipid droplet shown in Figure 9.17b is hardly distinguishable from the surrounding host with the identical scattering property. The image obtained from the 1% Intralipid

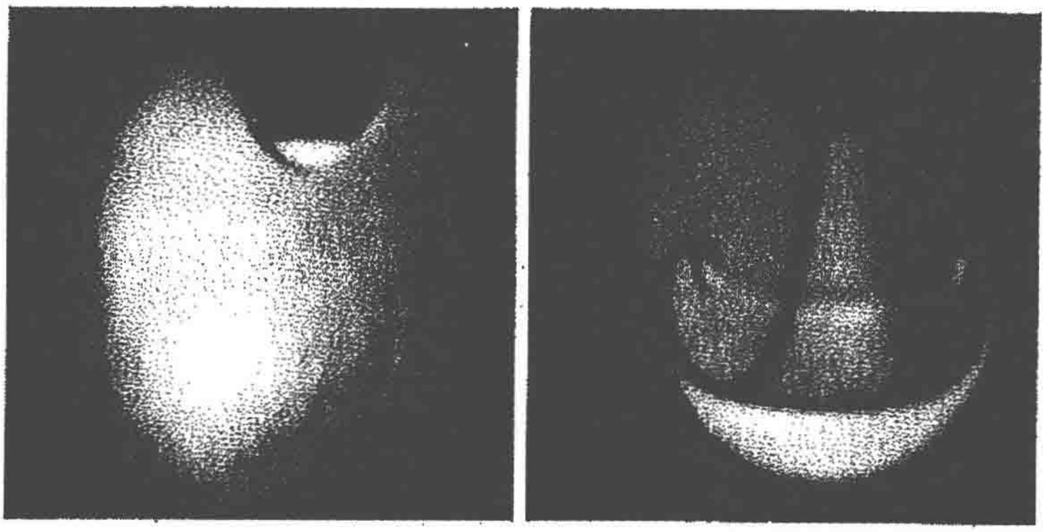
(a)
(b)

FIGURE 9.16 Early time two-dimensional shadow images of water phantom droplets in a host 2% 50-mm-thick diluted Intralipid stock solution. The spatial distribution of the water drop depends on the amount of water and the delay of release time. The dark shadow at the top middle part of the white laser beam circle is the end tip of burette: (a) delay of ~2 s from release of the stopper and (b) delay of ~10 s from release of the stopper [54].

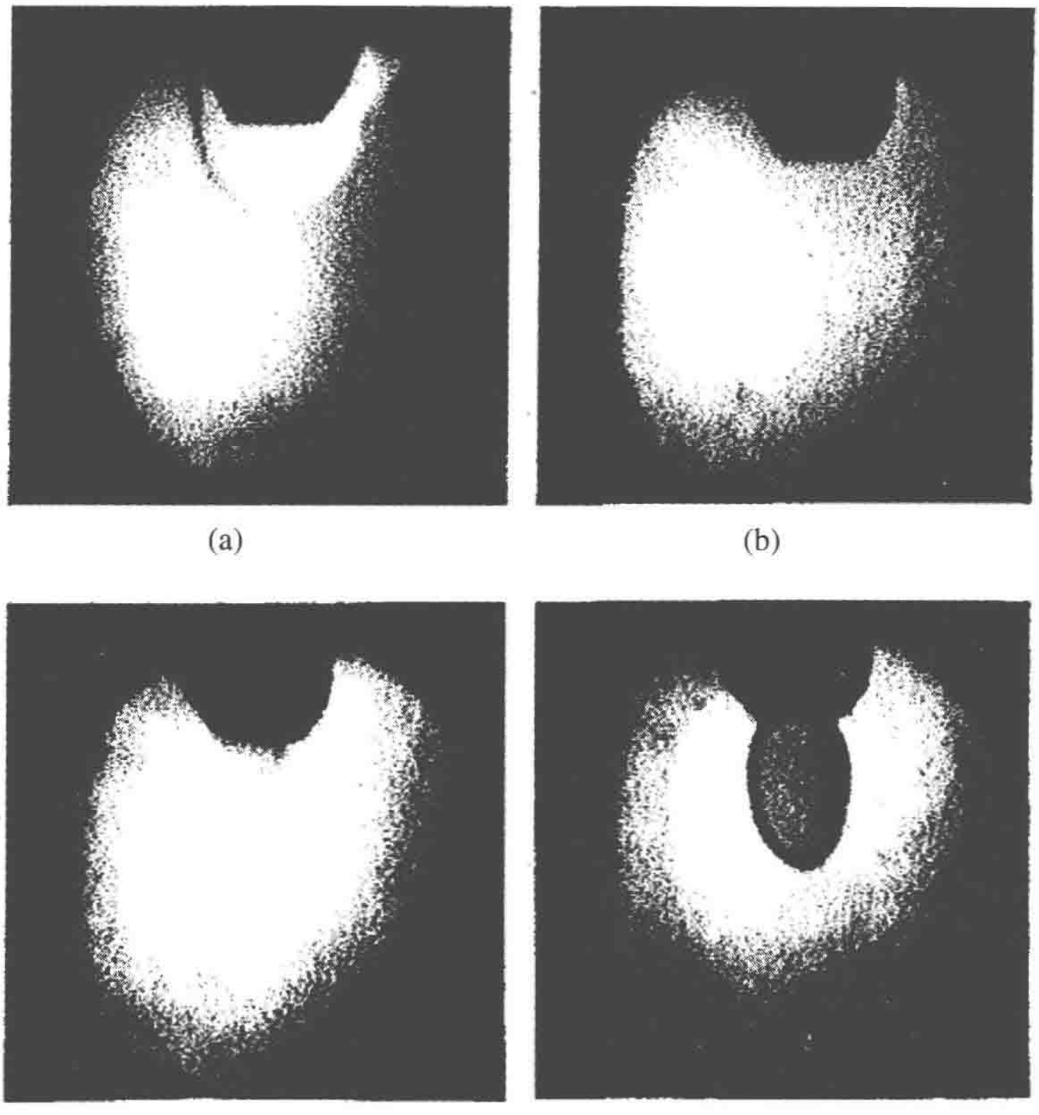
(a)
(b)
(c)
(d)

FIGURE 9.17 Early time images of translucent Intralipid phantom drops of various concentrations in a host 2% 50-mm-thick diluted Intralipid stock solution. The images show diluted Intralipid phantom drops at (a) 1%, (b) 2%, (c) 3%, and (d) 5% concentration [54].

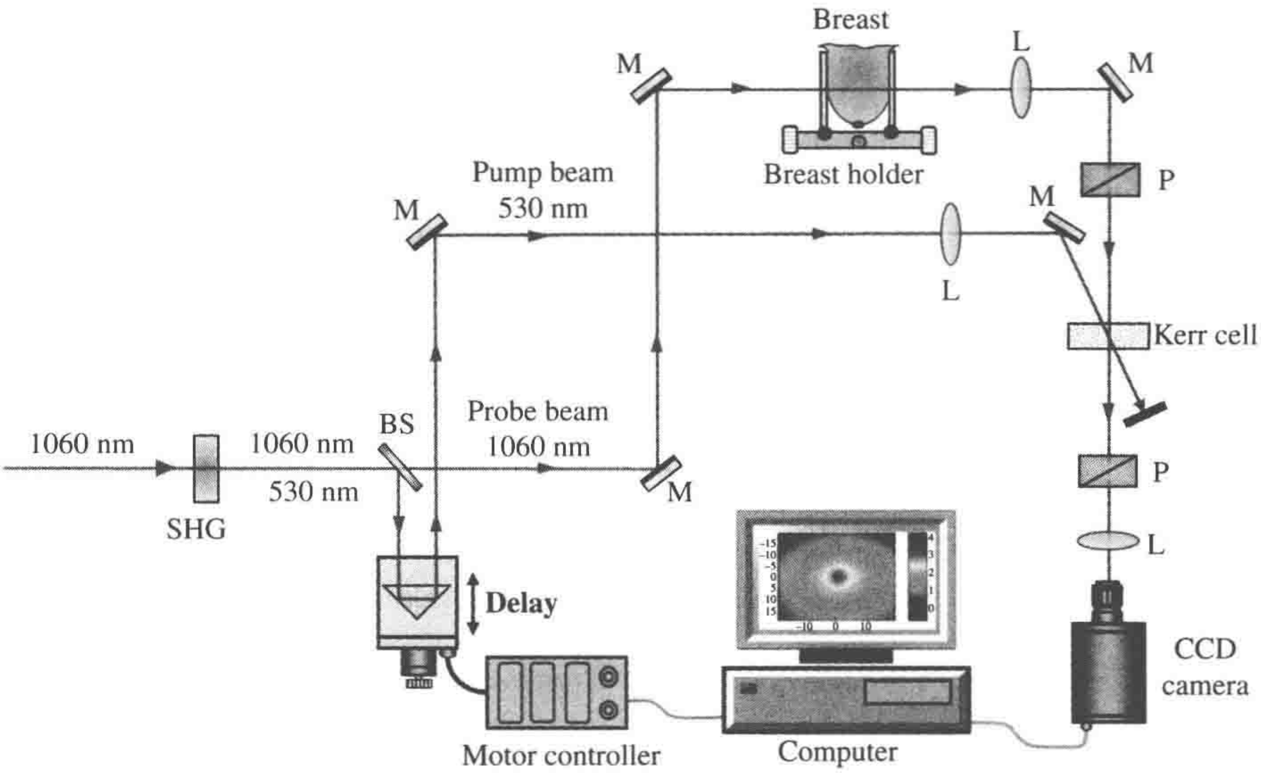

FIGURE 9.18 Schematic diagram of a picosecond optical Kerr gate.

droplet (Fig. 9.17a) is brighter and the image from the 3% Intralipid droplet shown in Fig. 9.17c is darker than that from the 2% surrounding host. A 1% concentration dilution difference between the phantom droplet and the host medium can be distinguished visually. The changes of the shape of the drop can be measured. A much smaller concentration difference of 0.1% between the phantom droplets and the host medium could be identified with digital video signal processing [108]. This work demonstrates that small differences in scattering properties and the shapes of small dimension translucent droplets can be spatially determined inside a large host turbid medium that may be useful in moving toward optical mammography.

The optical Kerr gate (OKG) [52–54] acts as a camera with an ultrafast shutter that is triggered by an intense gating pulse to take a picture at the instant when the image-bearing light emerges and closes soon enough to block the diffusive light. A typical OKG experimental arrangement, shown schematically in Figure 9.18, consists of a Kerr active material such as carbon disulfide (CS_2) placed between two crossed polarizers. An intense ultrashort pulse of light is split into two parts. One part illuminates the sample, while the other part—the reference or gating pulse—induces a transient birefringence in the Kerr medium. The light emerging from the sample is made to overlap spatially and temporally with the gating pulse inside the Kerr medium. If the reference pulse is blocked, a very small fraction of the incident light, typically less than one part in a million, may pass through the crossed polarizers. In this case, the gate is “closed.” In the presence of the reference pulse, the fraction of the light from the sample that is linearly polarized by the first polarizer becomes elliptically polarized as it passes through the Kerr medium while coincident with the reference pulse. A fraction of this elliptically polarized light can now pass through the analyzer. This may be looked on as the gate being "open." Thus, the light can only pass through the gate when it overlaps both temporally and spatially with the intense reference pulse.

The duration of the gating pulse or the recovery time of the Kerr medium, whichever is longer, determines how long the gate remains open. Picosecond and subpicosecond time resolution may be attained using Kerr NL Bi glass plate. The gate position in time may be varied by adjusting the arrival of the reference pulse by use of an optical delay line. The image bearing early light may be extracted in a single shot by adjusting the gate position.

As detailed above, a picosecond OKG that uses a picosecond Nd^{3+}:glass laser, a CS_2 Kerr cell, and a two-dimensional charge-coupled device (CCD) camera has been successfully used to image test objects hidden inside human breast tissue, chicken breast tissue, and a suspension of polystyrene spheres in water. Combined time and space gating (to be discussed in Section 9.4.3) was realized by placing Kerr cell in the arrangement discussed above at the back focal plane of a lens, and an aperture at the center of the front focal plane [110]. Another lens placed at a distance equal to its focal length behind the aperture was used to collimate, select, and direct light to the CCD camera.

Compared to simple OKG, this Kerr-Fourier gate (KFG) provides higher dynamic range, signal-to-noise ratio, and contrast at a signal level of $\sim 10^{-10}$ of illumination intensity. The sensitivity of the technique to detect small changes in optical properties was underscored when it successfully imaged a pure water droplet inside 5 cm long 2% intralipid suspension as shown in Figure 9.19. The photo image of CAT inside the 5 cm tank of Intralipid suspension is shown in Figure 9.19f. In related development, the feasibility of constructing a three dimensional image was demonstrated by combining two dimensional shadow grams formed with a KFG using a back-projection algorithm (inverse image reconstruction) on a personal computer [72].

In addition to using Kerr gate and streak camera, the time gating in the picosecond and nanosecond domain have been accomplished using gated intensified CCD cameras and has been used for research on detection of targets in turbid media including biological tissues [75, 111–120].

9.4.2 Absorption Gate

To improve ability to see objects in a scattering medium a simple novel approach of using absorption present in scattering media was proposed [121]. One thinks absorption hurts imaging; however, for scattering medium it helps due to larger distance traveled by diffusive light. The absorption may reduce the intensity of multiple scattered light (noise) below the ballistic signal (image) intensity. This reduction in noise-to-signal ratio allows to see through random scattering media that would otherwise be opaque in the absence of absorption.

The average distance $\bar{z}$ that multiple scattered light travels in the medium is $z^2/2l_t$ (see Eq. 9.10b), which is longer than z, the distance that the ballistic light traverses through a slab of thickness z. Light traveling over a longer path length has a higher probability of being absorbed. Thus, the introduction of absorbing dye into a random medium will cause it to absorb the multiple scattered light more than the ballistic

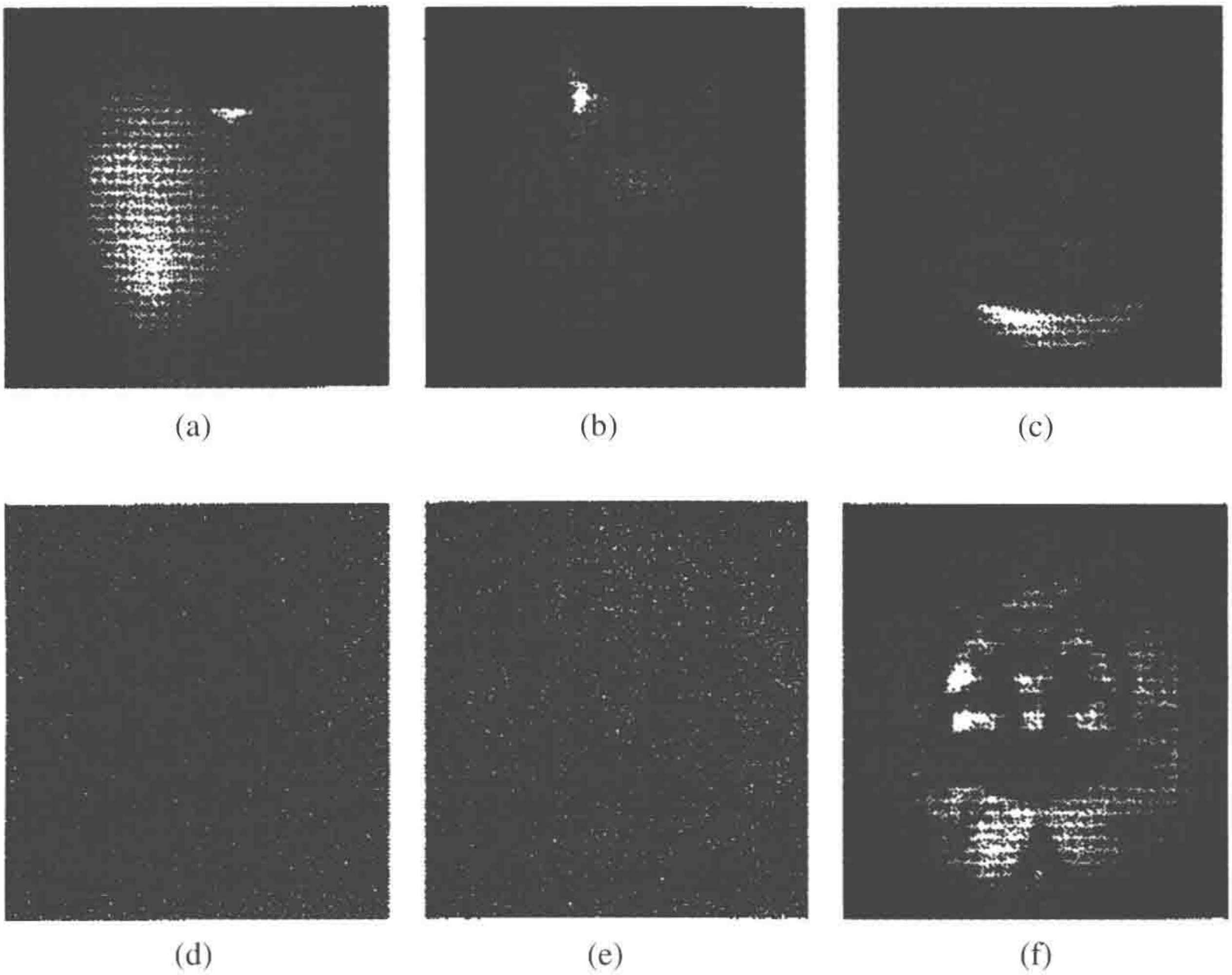

(a) (b) (c)

(d) (e) (f)

FIGURE 9.19 Images of water droplet diffusing into a 2% intralipid suspension (upper frame), and a CAT drawn in a transparent plastic sheet hidden inside (lower frames) a 5 cm thick intralipid solution using the optical Kerr-Fourier gate. In a-c, gate delay is 0 ps, and the times after the valve that releases the water droplet is open are 0 s (a), 3 s (b), and 5 s (c), respectively. In (d) gate delay is 40 ps, (e) – 20 ps, and (f) – 0 ps [54].

light. The reduction of noise over signal with the use of absorption was investigated by using time- and angle-resolved ultrafast laser pulse measurements. When a plane ultrafast pulse is normally incident upon a slab of random medium with absorbing boundaries, the temporal profile of the scattered pulse exiting from a point on the opposite side of the slab predicted by the diffusion theory is

$$I_z(t) = \frac{D}{\pi z^2} \sum_{m=1}^{\infty} m \left(\frac{\pi z}{d}\right)^2 \sin\left(\frac{m\pi z}{d}\right) \times \exp\left[-Dt\left(\frac{m\pi}{d}\right)^2\right] \exp\left(-\frac{vt}{l_a}\right), \quad (9.11)$$

where $D = vl_t/3$ is the diffusion coefficient, $d = z + 2z_0, z_0 = 0.71l_t$, v is the speed of the photon, z is the thickness of the slab, l_t is the transport mean free path, and l_a is the absorption length.

The intensities of the diffuse and ballistic light are computed and plotted in Figure 9.20 by solid and dashed lines, respectively. The squares and the triangles show experimental data. This figure illustrates a case for scattering medium consisting of 0.3% concentration latex beads of 0.296 μm diameter suspended in water. $l_t = 1.0$ mm

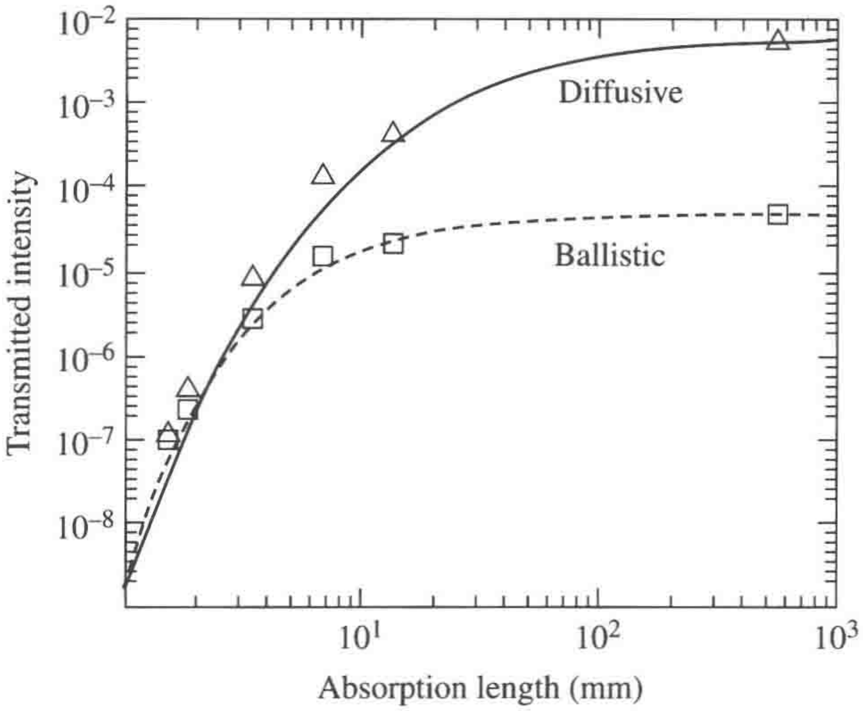

FIGURE 9.20 Theoretical prediction and experimental results of the total diffuse light and the signal intensity (in arbitrary units) for light transmitted through a random medium with different absorption lengths, using $z = 10$ mm, $l_s = 0.3$ mm, and $l_t = 1.0$ mm. The solid and dashed curves correspond to the ballistic and diffuse light intensity, respectively. The squares and triangles correspond to the measured ballistic and diffuse light intensity, respectively [121].

is found experimentally and $l_s = 1/n\sigma_s = 0.3$ mm, where $N = 2.2 \times 10^{17}$ m^{-3} is the scatterer density and $\sigma_s = 1.54 \times 10^{-14}$ m^2 is the scattering cross-section computed numerically from the Mie theory. The thickness of the slab of random medium is $z = 10$ mm, and the absorption length is varied from 1000 mm to 1 mm. The intensity of diffuse light is much higher than the intensity of ballistic light when the medium is less absorbing, for example, when $l_a = 1000$ mm, the diffuse intensity is 130 times stronger than that of the ballistic signal. The solid angle of collection Ω for the diffuse light is taken to be 1×10^{-7}. As the absorption in the medium is increased, the diffuse intensity decreases faster than the ballistic intensity. The diffuse intensity is decreased below the ballistic intensity when l_a is less than 2 mm. This reduction of diffuse light with respect to ballistic signal will substantially improve the quality of the image of an object hidden in a highly scattering random medium [121].

The intensities of the diffuse and ballistic signal presented in Figure 9.20 were measured by using an angle- and time-resolved technique that was described in Reference 86. In this method a beam of ultrafast laser pulses of 100 fs duration (repetition rate 82 MHz, average power 15 mW, wavelength centered at 620 nm, beam diameter 10 mm) from a colliding pulse mode-locked dye laser system was incident upon a slab of random medium. This random medium consisted of a 0.3% concentration of latex beads of 0.296 μm diameter suspended in water in a 10-mm-thick cylindrical glass cell with a diameter of 50 mm. A black pinhole of 2 mm diameter was placed at the center of the opposite side of the cell. The temporal distribution of the photons from this pinhole within 3 mrad in the forward direction was measured by a synchro-scan

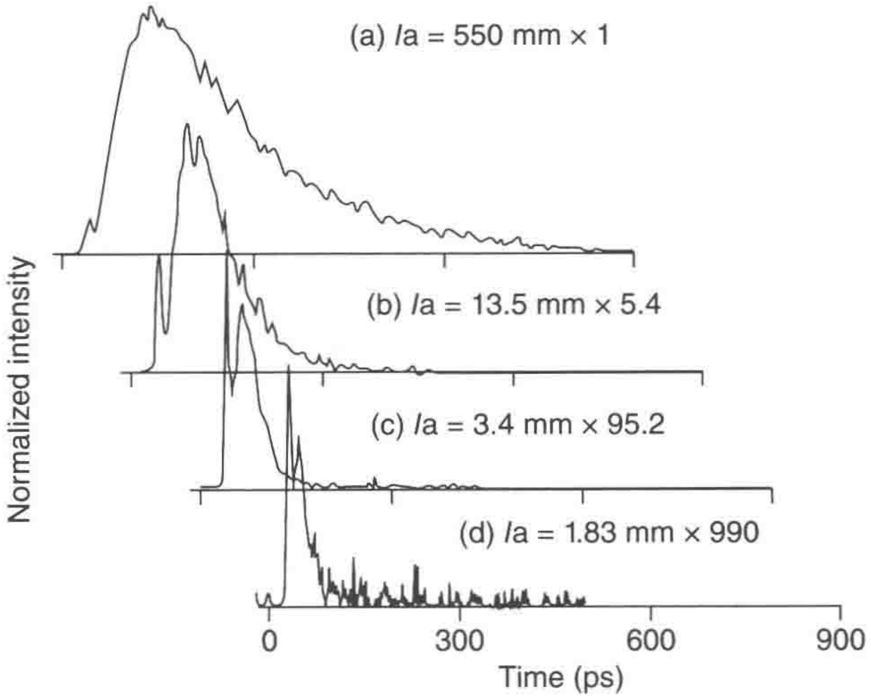

FIGURE 9.21 Transmitted pulse profiles through a slab of random medium 10 mm thick with a 0.3% concentration of latex beads of 0.296 μm diameter at different absorbing dye concentrations. The absorption lengths of these media are indicated on the curves [121].

streak camera. The temporal profiles of ballistic signals and diffuse light pulses in the forward direction for different amounts of absorbing dye added in the random medium are displayed in Figure 9.21. The narrow peak at time 44 ps corresponds to the ballistic signal that travels in the incident direction and arrives first. In contrast, the diffuse light pulse that consists of photons that had undergone multiple scattering traversed many different trajectories and arrived at different times which resulted in a broad temporal profile. Figure 9.21a presents the temporal profile of transmitted light when no dye was added. The tiny ballistic peak at 44 ps is much smaller than the large and broad temporal distribution of the diffuse pulse. The total intensity of the diffuse light is found to be 130 times greater than the intensity of the ballistic signal. It is impossible to see through such a cloudy medium. To study how the diffuse light intensity may decrease with respect to the ballistic signal, increasing amount of absorbing dye (Malachite Green) was added to the random medium. As the temporal profiles in Figures 9.21b–9.21d show both the ballistic and diffuse signal intensities decreased when the absorptive dye concentration increased, but the intensity of the diffuse light decreased more, enhancing the relative intensity of the ballistic signal to the diffuse signal.

A demonstration that an object hidden behind a scattering wall can in fact be imaged with the aid of absorption [121] is shown in Figure 9.22. A cross of 3 mm and 2 mm wide bars serves as an object and the scattering medium is placed between the object and the imaging video camera. The image of the object with the interference pattern which arises from light diffraction at the edge of the bar is shown in Figure 9.22a when there were no scatterers in the sample cell. This image disappears when the medium behind the cross is made scattering (Fig. 9.22b), reappears when

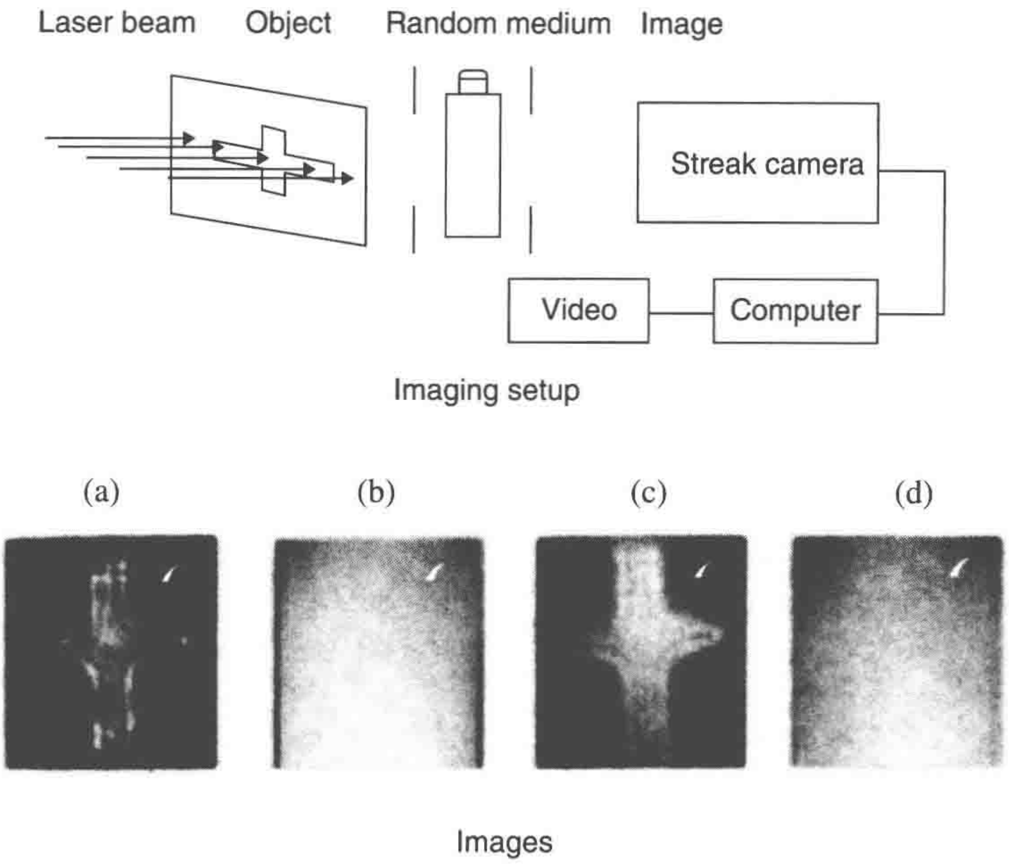

FIGURE 9.22 Imaging setup (top) and photographic images of a cross obtained with (a) no scatterer in the cell; (b) scatterers are added into the cell where the thickness is 20 scattering mean free path, the laser wavelength is 620 nm; (c) malachite green dye is added to the scattering medium in the cell with a resulting absorption length of 4.6 mm; (d) the laser is tuned to 515 nm where the absorption length of the scattering medium increased to 75 mm [121].

the scattering medium is made absorbing (Fig. 9.22c), and disappears again when the laser wavelength is tuned away from the absorbing spectral band of the medium (Fig. 9.22d). So, absorption can help reduce the effects of scattering. It can be used for coding information as light passes through fog or clouds by selecting the light wavelength in the water absorption range from 800 to 1100 nm (Fig. 9.8) and improve images of tumor growing in breast. Water absorption in breast tissue can clear up images [122].

9.4.3 Fourier Space Gate and Microscopic Imaging

Another simple way to improve imaging of hidden microscale structures and features is to use changes in spatial frequencies of light wave passing through scattering media. Ordinary microscopes cannot obtain a clear image of objects hidden inside or behind a highly scattering random media. Scanning confocal and two photon microscopes are standard methods for locating objects inside a medium at different depths [123] and have been used to acquire image information of objects in highly scattering media with limited success. Scanning confocal microscopes combined with dye staining and multiple (2 and 3) photon nonlinear optical excitation are other methods to image objects inside scattering media with additional improvement [124, 125].

According to modern optical theory, the spatial Fourier Transform of the image is located on the back focal plane of a lens [126]. Image information of a reasonable level of resolution is carried by the low spatial frequency light that is located at the center of the focal plane. The higher spatial frequency light, which carries the detailed diffraction pattern of the object, is located away from the central region of the focal plane. One can obtain an image of an object by using the low frequency light alone, but one obtains somewhat less diffraction detail. When objects are hidden inside or behind a highly scattering host medium, a substantial fraction of the direct image-bearing light is multiply scattered in all directions, thereby emerging from the host scattering medium with a wide range of spatial frequencies. Thus images are degraded by the high spatial frequencies that arise from multiply scattered light. Indeed, an image of the object cannot be obtained at all with the conventional method when there is strong enough scattering.

It has been demonstrated that by incorporation of a spatial filter into a microscope, images of microscopic objects hidden behind a slab of highly scattering media can be obtained [127].

The space-gate experimental setup is shown in Figure 9.23 [127]. A 4 mm diameter beam of ultrashort laser pulses of 100 fs duration at a wavelength of 625 nm was generated by a colliding pulse mode-locked (CPM) laser. The pulses were split by a glass slide, yielding a probe and a reference pulse. The reference pulse did not travel through the microscope but rejoined the probe beam slightly ahead of it in time and was used to indicate zero time in the time-resolved detection mode. The probe beam was incident upon the preparation consisting of a test bar chart (pattern 4, corresponding to a spacing of 176.7 μm per opaque or transparent bar) in front of a slab of a scattering medium.

A conventional Reichert microscope with a 4X objective was used in the transmission mode. As the transmitted light traversed the microscope body tube, it was spatially filtered by a small circular aperture located at the back focal plane of the objective lens and directed through the microscope trinocular. The image was detected

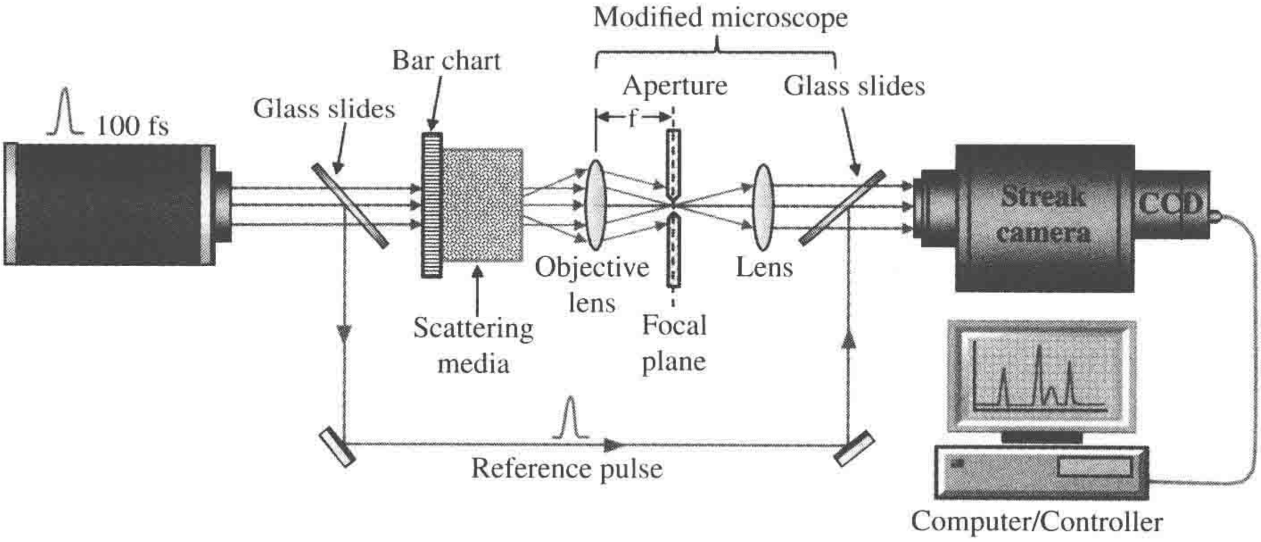

FIGURE 9.23 Schematic diagram of an experimental arrangement for space-gated microscopic imaging.

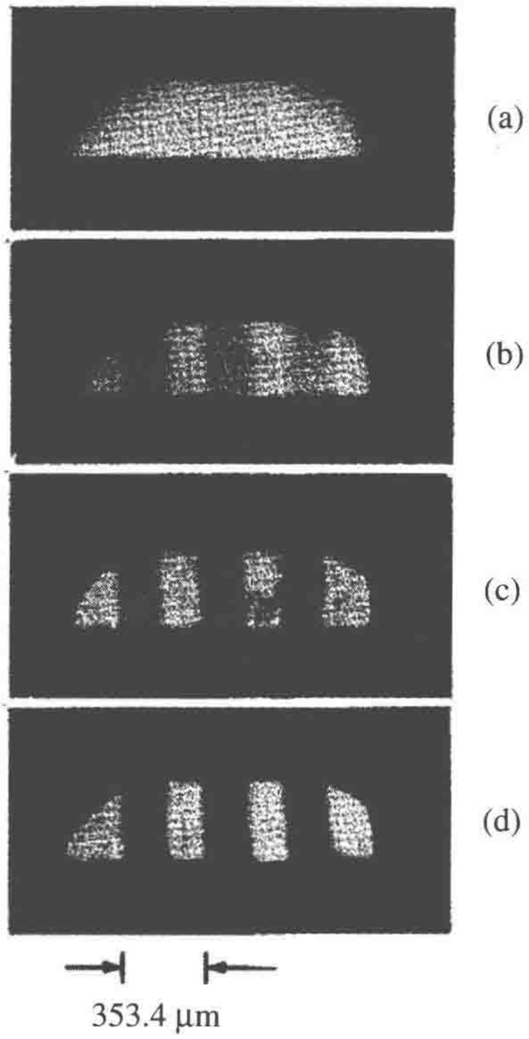

FIGURE 9.24 Images of the bar chart hidden behind a 2-mm-thick 1.5% intralipid scattering medium obtained in the steady-state mode with (a) no spatial filter and (b) 3 mm, (c) 1 mm, and (d) 0.5 mm diameter spatial filters [127].

by a streak camera with a CCD detector operated in either the steady-state focus mode or the time-resolved streak mode.

Figure 9.24 shows the effect of spatial filtering on image quality for the test bar chart with a $z = 2.0$-mm-thick scattering medium placed on top of the chart. The images were obtained in the steady-state mode. The random scattering medium was an Intralipid suspension of 1.5% volume concentration contained in a glass cell. The scattering mean free path of the suspension was determined by another experiment to be 0.15 mm. Therefore the optical thickness z/l_s was $\sim$13 in this case. Figure 9.24a shows the image obtained without spatial filtering. No image of the bars is seen. A uniform bright background is seen, showing that the intensity of noisy multiply scattered light is stronger than that of the signal light. Figure 9.24b was recorded with a 3.0-mm spatial filter at the Fourier plane of the micro-objective lens. A distinct image of the bars is readily discerned although there is a significant amount of scattering-induced noise. For Figure 9.24c, a 1-mm aperture was used. The image now is even clearer, with less noise than that of the image shown in Figure 9.24b. Figure 9.24d was taken with a 0.5-mm aperture at the Fourier plane. The noise has almost disappeared. Note that without filtering, the bars are not visible at all; however even with a 3.0 mm aperture, they are readily apparent. The image quality improves with the smaller apertures since the background multiply scattered noise light is diminished, thus improving the signal-to-noise ratio considerably.

It was demonstrated that an improvement in the microscope image quality of objects hidden behind a highly scattering medium can be achieved by using both spatial gating and time-gated detection. This technique can be used with different kinds of light sources and different kinds of time-resolved methods for a variety of biological and medical applications.

The Fourier space gate really acts as a time gate for light from scattering media [128]. The ballistic and snake light correspond to zero and lower-order spatial frequencies, respectively; while the higher spatial frequency components represent diffuse light. The $4f$ Fourier space gate acts as an intrinsic equivalent time gate which is accomplished by adjusting the size of the aperture to select the ballistic and earlier fraction of snake light, and rejecting the high spatial frequency diffusive light. An aperture at focal plane of a lens in 4F passes spatial frequencies that are smaller than the cutoff frequency: $\bar{\alpha} = D/2f\lambda$, where D is the aperture size. Consider an illumination with $\lambda = 625$ nm light and objective lens of focal length $f = 10$ mm, an aperture with diameter of 0.5 mm will filter out all spatial frequencies higher than 40 lines per mm, thus cleaning up the noise from scattering. The smallest size distinguishable will be 25 μm features of the object in a scattering medium [128].

In the Fourier space gate arrangement, the ballistic and snake components appear near the central dc signal frequency region, whereas the diffusive component appears off the central region of the Fourier spectral plane. A spatial filter placed at the Fourier spectral plane can reduce the diffusive component and allow most of the ballistic and snake components to pass through. By adjusting the aperture size at the Fourier plane, a spatial Fourier filter may be made to act as variable temporal gate for light emanating from a scattering medium.

Figure 9.25 displays the normalized temporal profiles of the scattered 530 nm wavelength light pulses passed through spatial Fourier filters with different aperture sizes for thin and thick media. Figure 9.25 shows the results for a 50-mm cell with 0.4% Intralipid suspension. With a 10-mm diameter spatial filter, the measured pulse profile exhibited a fast rising edge and a slow decaying tail. The FWHM of the temporal profile was approximately 65 ps. The width was reduced to 37 ps for a 3-mm diameter spatial filter and to 21 ps for a 1-mm diameter filter. The pulse narrowing by the spatial $4f$ Fourier filter for all three samples is summarized in Figure 9.26. The decrease of the pulse duration with the decrease in aperture diameter demonstrates that Fourier spatial filters act as temporal gates for the early light in the scattered light pulse.

9.4.4 Polarization Gate

The polarization gate makes use of the fact that scattering events depolarize an incident beam of linearly polarized light so that ballistic and snake photons retain much of the initial polarization while the multiple scattered photons are depolarized [48–50]. In practice, a polarization gate is implemented by shining the object through a linear

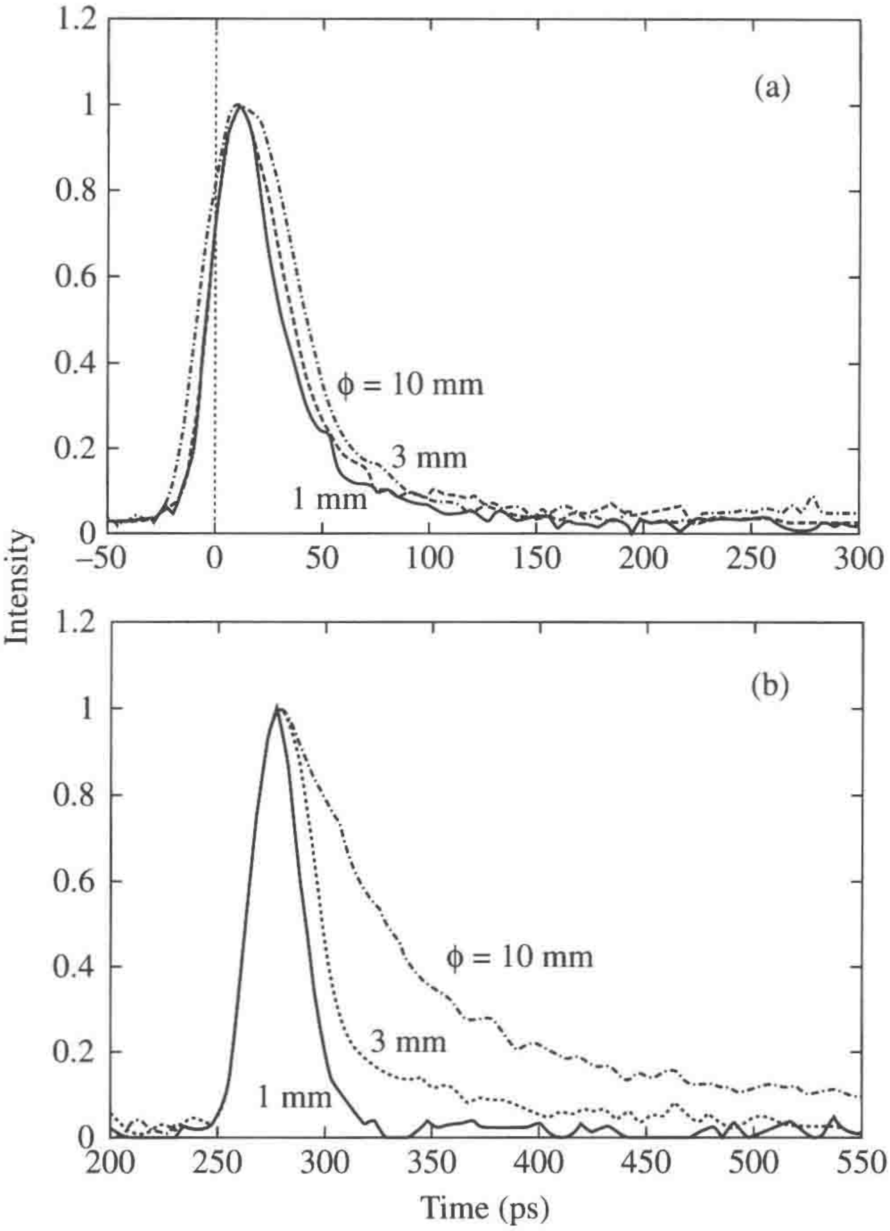

FIGURE 9.25 Temporal profiles of the spatially filtered laser pulses scattered by 0.4% intralipid suspension in a 10- and 50-mm cell. The solid, dashed, and dotted-dashed curves show the temporal profiles of scattered pulses when the diameter of the spatial Fourier filter is 1, 3, and 10 mm, respectively [128].

polarizer and collecting the emerging light through a second linear polarizer. The degree of polarization [defined as $(I_p - I_s)/(I_p + I_s)$, where I_p and I_s are transmitted intensities of light with the axis of the second polarizer parallel and perpendicular, respectively, to that of the first polarizer used to obtain linearly polarized interrogating light] of the transmitted light is used to select the image-bearing component, since it is expected ideally to be unity for ballistic light and zero for completely depolarized diffuse light. When a pulse of initially polarized light is used to illuminate a turbid medium, such as human tissue, ice or snow, the ballistic and snake-like components of the light, which are either backscattered directly from the surface of the turbid media or take direct paths through the turbid media, substantially maintain the polarization of the initially polarized light, while the diffuse component of the light, which tends to travel longer, less direct paths through the turbid media before either being

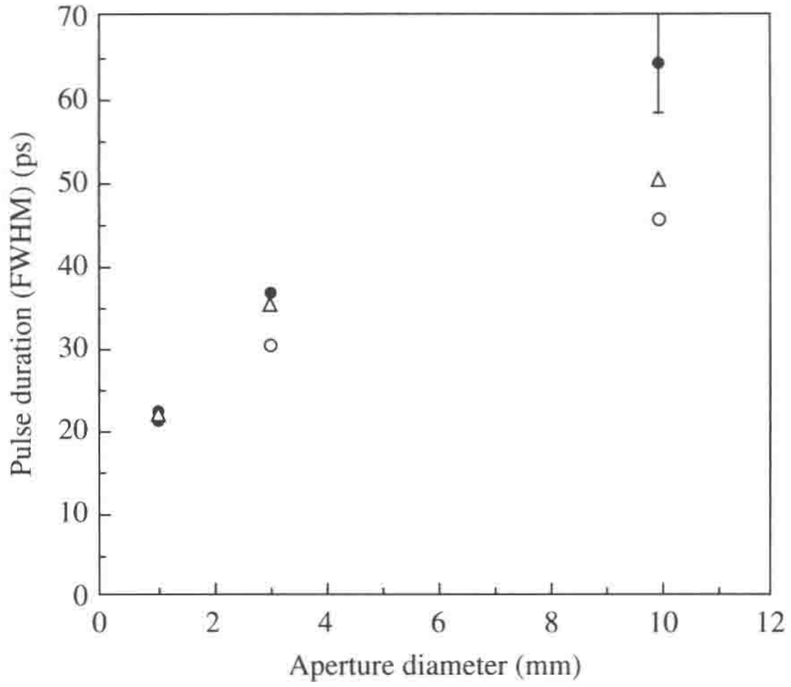

FIGURE 9.26 Changes of the pulse duration of the scattered pulse as a function of aperture diameter for the same concentration-length product: 2-mm cell with 10% intralipid suspension (circles), 10-mm cell with 2% Intralipid suspension (triangles), and 50-mm cell with 0.4% Intralipid suspension (dots) [128].

backscattered from or emerging from the opposite end of the turbid medium, becomes comparatively more depolarized than the ballistic and snake-like components.

Polarization-enabled high-resolution and high-speed optical imaging of objects located in, at the surface of, or behind highly scattering media using polarized illuminating light and polarization-difference imaging. The surface image information is predominately carried by the parallel polarization image component while the perpendicular image component contains beneath-the-surface image information. Images of structures at different depths within a turbid medium can be obtained using the perpendicular polarization component resulting from the use of different illuminating wavelengths.

Figure 9.27 shows the polarization components of the backscattered light from bovine gray matter brain tissue when linearly polarized 1064-nm, 6.5-ps pulses were used. The diameter of the illuminating beam was 0.5 mm. The parallel polarization component $I_p(t)$ is more intense than the perpendicular polarization component $I_s(t)$. In addition, when the temporal profile of the perpendicular component was normalized to the peak intensity of the parallel component $I_{s,\text{normal}}(t)$, the temporal profiles were different, having different peak time positions and full-width-at-half-maximum (FWHM). The scattering parameters of gray matter allow for clear observation of the above-mentioned differences in the two backscattering polarization components within the temporal resolution of our system (about 15 ps).

The differences in the two polarization components arise from the fact that the backscattered photons that are perpendicularly polarized must first undergo sufficient scattering events to lose their polarization information. By contrast, the photons that are directly backscattered from the surface of the tissue have less of an opportunity

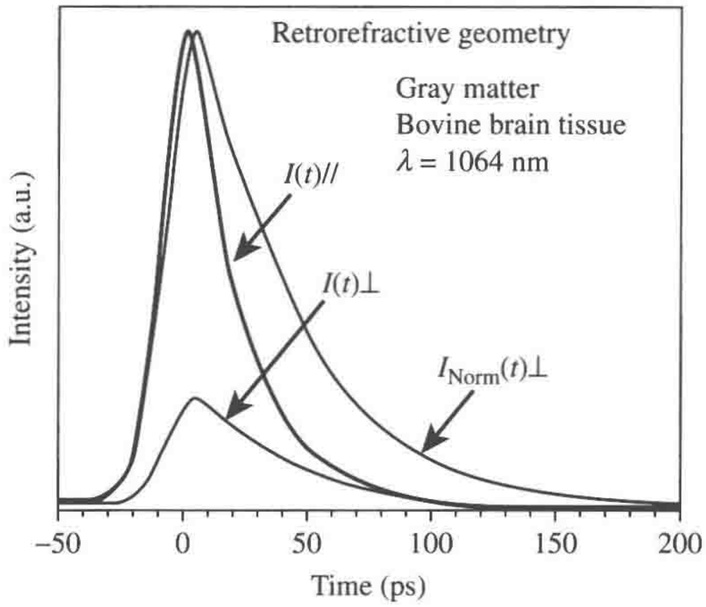

FIGURE 9.27 Temporal profiles of the parallel polarization component, perpendicular polarization component, and normalized perpendicular polarization component of backscattered light obtained from bovine gray matter brain tissue illuminated with 1064-nm, 6.5-ps laser pulses [49].

to depolarize; therefore, the backscattering photons from the surface of the tissue and initial layers beneath the surface belong mostly to the parallel polarization image component. The perpendicular polarization component contains predominately photons that penetrated the tissue to certain depths before they emerged in the backscattering direction. This salient concept explains the differences in the temporal profiles of the two polarization components shown in Figure 9.27. The parallel component contains all photons backscattered from the surface of the tissue before they depolarize. As a result, the parallel component is more intense and the time of peak intensity is when the backscattered light from the surface arrives. The perpendicular component time of peak intensity arises from the depolarized photons that propagated in the tissue to a certain depth and then backscattered. In the backscattering geometry discussed above, the image information of the surface and near-surface of tissues is contained predominately in the parallel polarization image component while the perpendicular polarization component contains information of that portion of the tissue well beneath the surface.

Optical polarization imaging has been implemented in the transmission geometry as well. Since the ballistic and snake photons encounter fewer scattering events than the diffusive photons, in transmission, the parallel polarized component (I_p) carries more direct image information than the perpendicular polarized component (I_s). Hence, images recorded with I_p provide higher contrast than that recorded without polarization selection, or with I_s [50, 129]. Polarization difference imaging that utilizes $I_p - I_s$ provides even higher contrast by removing the contribution from partially depolarized light that results from Malus' Law.

Polarization-gated imaging has been extended using circularly polarized light, developing theoretical framework based on cumulant theory, and applied to different types of turbid media [130–133].

Since cancerous and normal tissues show different scattering and depolarization properties caused by their different morphological and molecular structures due to the cancer development, the polarization imaging techniques have been widely used for the detection of cancers in breast, prostate, and other organs with the use of either native biomarkers or the cancer receptor targeting contrast agents [134–139].

9.5 TRANSITION FROM BALLISTIC TO DIFFUSE IMAGING IN TURBID MEDIA

As we discussed above, there are three components called ballistic, snake, and diffusive in optical pulse propagation in a highly scattering turbid medium. Three key length parameters—scattering length, l_s; transport mean free path, l_t; and absorption length, l_a (alternatively, the corresponding coefficients, μ_s, μ_s', and μ_a, respectively)—are used to describe light propagation characteristics through the medium. Another key parameter is the anisotropy factor, g defined as the $\langle \cos\theta \rangle$, where θ is the scattering angle. The relationship between these parameters and the relations governing the attenuation of the intensity of the ballistic and snake light as they propagate through the medium have been presented in Section 9.2.2. Ballistic and snake light may provide direct images of targets in turbid media, provided the deleterious effect of diffusive light (noise for direct imaging) could be sufficiently reduced. Section 9.4 reviewed some of the techniques for reducing the diffusive light noise. However, for sufficiently thick samples such as human breast or prostate the ballistic and snake light intensity are reduced so much and the diffusive noise becomes so dominant that direct imaging is not feasible. Diffusive light, that is multiple scattered within the medium, carries a wealth of information about the interior structures of the medium. Different approaches, referred to as inverse image reconstructions, that use knowledge of incident light properties, measurement of light emergent from the medium at the boundaries, average optical properties of the medium, an appropriate model for light propagation through the medium, and numerical algorithm to estimate optical properties of every voxel of the sample, are needed to extract the relevant information about the embedded objects, such as tumors in a breast [4–6, 44, 76].

The diffuse light intensity I_D described in diffusion approximation is

$$I_D = I_0 \exp(-\mu_{\text{eff}} z), \tag{9.12}$$

where I_0 is the incident intensity, z is the sample thickness, and μ_{eff} is the effective scattering coefficient:

$$\mu_{\text{eff}} = \sqrt{3\mu_a(\mu_s' + \mu_a)}, \tag{9.13}$$

that is related to the diffusion coefficient $D = c/3\mu_a(\mu_s' + \mu_a)$.

Another area of interest is the transition regime between ballistic and diffuse light transport because it carries valuable information about characteristics of scattering [140, 141]. Assuming quasi-one-dimensional propagation and a small detection solid angle $d\Omega$ the detected light intensity was shown to be a sum of ballistic light intensity and a fraction of diffuse light intensity [140]:

$$I/I_0 = \exp(-(\mu_s z) + (\delta\Omega/4\pi)\exp(-\mu_{\text{eff}} z). \tag{9.14}$$

Equation (9.14) does not include a term for snake (quasi-ballistic) photons and makes the assumption that absorption is negligible, $\mu_a \ll \mu_s$, that is the medium is diffusive (not absorptive). A transition depth, z_c, is defined as

$$z_c = (\mu_{\text{eff}} - \mu_s)^{-1} \ln(d\Omega/4\pi), \tag{9.15}$$

such that for $z \ll z_c$ the photons detected are mainly ballistic, and for $z \gg z_c$ most photons are diffusive in nature.

Figure 9.28 shows the confocal signal as a function of the thickness (L) of the scattering medium (0.48-μm latex spheres suspensions in water with $l_s = 74$ μm) obtained by Kempe et al. [141]. The ballistic regime characterized by an exponential decay extends to $L_{\max}$ (~1 mm) at which ballistic and diffuse light intensities are equal, followed by the regime with much slower decay of intensity where diffuse light dominates.

In thin media the light intensity is governed by ballistic transport while for thick media by diffusive transport. The dynamic range of detection system must be $>10^5$. The use of diffusion equations for inverse problem requires the distance between source and detector to be $< 5l_t$.

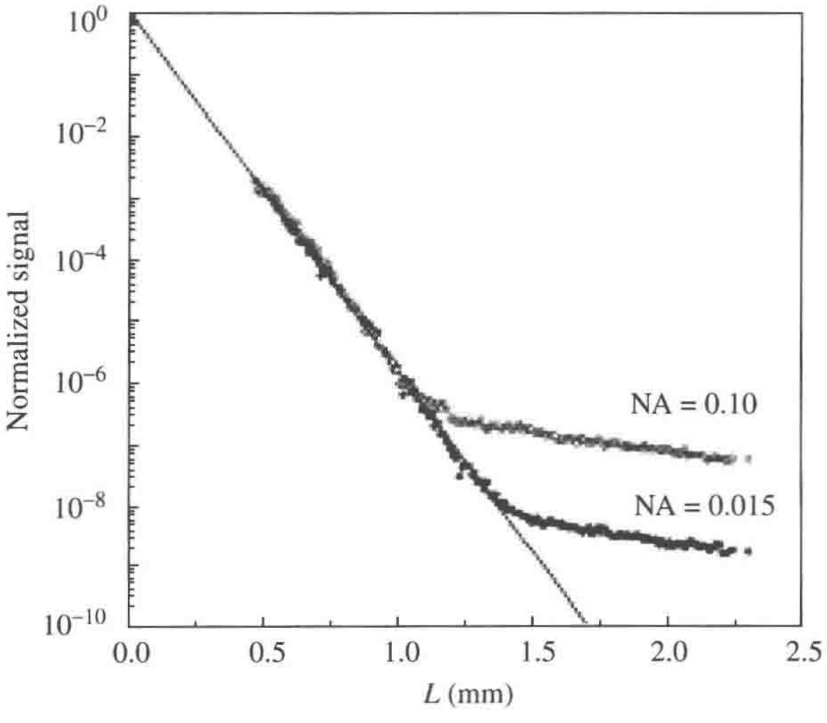

FIGURE 9.28 Semilogarithmic plot of the signal as a function of sample thickness for a suspension with $l_s = 74$ μm. Shown is the signal obtained with an NA of 0.10 for a pinhole with $v_p = 1.24$ and for an NA of 0.015 with $v_p = 1.16$. The solid line is the fit to the part of the curves that exhibits an exponential falloff [141].

9.6 CONCLUSION

The use of light and optical imaging approaches for biomedical applications is still at the initial stages. Optical mammography is on the horizon using inverse reconstruction on time domain with optical molecular fingerprints such as hypoxia as a marker for cancer. With the advent of compact wavelength-agile lasers, sensitive detectors and spectrometers, optical fiber beam delivery and signal acquisition systems, powerful personal computers, and numerical algorithms, photonic approaches will play an important role in combating diseases through early detection and diagnosis.

ACKNOWLEDGMENTS

We acknowledge IUSL researchers, G. E. Andersen, Feng Liu, K. M. Yoo, X. Ni, W. Cai, J. Dolne, X. Liang, P. P. Ho, S. Demos, B. B. Das, Q. Z. Wang, and G. Zhang, for their contribution to the work reviewed here, and acknowledge Y. Budansky for his help on figure drawing. The reviewed research was supported in part by US Army Medical Research and Materiel Command, NASA, and NYSTAR.

REFERENCES

[1] G. J. Muller, R. R. Alfano, S. R. Arridge, J. Beuthan, E. Gratton, M. Kaschke, B. R. Masters, S. Svanberg, and P. van der Zeect, *Medical Optical Tomography: Functional Imaging and Monitoring*, Vol. IS 11, SPIE Institute Series (SPIE, Bellingham, WA, 1993).

[2] A. Yodh and B. Chance, "Spectroscopy and imaging with diffusing light," *Phys. Today* **48**, 34–40 (1995).

[3] S. K. Gayen and R. R. Alfano, "Emerging optical biomedical imaging techniques," *Opt. Photon. News* **7**(3), 17–22 (1996), and references therein.

[4] J. C. Hebden, S. R. Arridge, and D. T. Deply, "Optical imaging in medicine: I. Experimental techniques," *Phys. Med. Biol.* **42**, 825–840 (1997).

[5] S. R. Arridge and J. C. Hebden, "Optical imaging in medicine: II. Modeling and reconstruction," *Phys. Med. Biol.* **42**, 841–853 (1997).

[6] S. R. Arridge, "Optical tomography in medical imaging," *Inverse Probl.* **15**, R41–R93 (1999).

[7] M. R. Hamblin, and T. Hasan, "Photodynamic therapy: a new antimicrobial approach to infectious disease," *Photochem. Photobiol. Sci.* **3**, 436–450 (2004).

[8] D. Huang, E. A. Swanson, C. P. Lin, J. S. Shuman, W. G. Stinson, W. Chang, M. R. Hee, T. Flotte, K. Gregory, C. A. Puliafito, and J. G. Fujimoto, "Optical coherence tomography," *Science* **254**, 1178–1181 (1991).

[9] W. Drexler and J. G. Fujimoto, *Optical Coherence Tomography: Technology and Applications* (Springer, 2008).

[10] R. R. Alfano, "Advances in optical imaging and photon migration," *OSA Topical Meeting Proceedings*, edited and chaired by R. R. Alfano, OSA Volume **21**, March (1994).

[11] L. Wang, G. Zhang, J. C. Luo, F. Zeng, Q. Z. Wang, S. A. Alfano, A. Katz, M. Zevallos, and R. R. Alfano, "Wireless spectroscopic compact photonic explorer for diagnostic optical imaging," *Biomed. Microdev.* **7**, 111–115 (2005).

[12] T. K. Gayen, A. Katz, H. E. Savage, S. A. McCormick, M. Alrubaiee, Y. Budansky, J. Lee, and R. R. Alfano, "Aorta and skin tissues welded by near infrared Cr^{4+}:YAG laser," *J. Clin. Laser Med. Surg.* **21**, 259–269 (2003).

[13] L. V. Wang and S. Hu, "Photoacoustic tomography: in vivo imaging from organelles to organs," *Science* **335** (6075), 1458–1462 (2012).

[14] L. V. Wang, "Multiscale photoacoustic microscopy and computed tomography," *Nat. Photon.* **3**, 503–509 (2009).

[15] Q. Zhu, T. Durduran, M. Holboke, V. Ntziachristos, and A. Yodh, "Imager that combines near infrared diffusive light and ultrasound," *Opt. Lett.* **24**(15), 1050–1053 (1999).

[16] Z. Jiang, D. Piao, G. R. Holyoak, J. W. Ritchey, K. E. Bartels, G. Slobodov, C. F. Bunting, and J. S. Krasinski, "Trans-rectal ultrasound–coupled spectral optical tomography of total hemoglobin concentration enhances assessment of the laterality and progression of a transmissible venereal tumor in canine prostate," *Urology* **77**(1), 237–242 (2011).

[17] S. Achilefu, R. B. Dorshow, J. E. Bugaj, and R. Rajagopalan, "Novel receptor-targeted fluorescence contrast agent for *in vivo* tumor imaging," *Invest. Radiol.* **35**, 479–485 (2000).

[18] Y. Pu, W. B. Wang, S. Achilefu, and R. R. Alfano, "Study of rotational dynamics of receptor-targeted contrast agents in cancerous and normal prostate tissues using time-resolved picosecond emission spectroscopy," *Appl. Opt.* **50**(7), 1312–1322 (2011).

[19] V. Ntziachristos, A. G. Yodh, M. Schnall, and B. Chance, "Concurrent MRI and diffuse optical tomography of breast after indocyanine green enhancement," *Proc. Natl. Acad. Sci. USA* **97**(6), 2767–2772 (2000).

[20] A. Villringer and B. Chance, "Non-invasive optical spectroscopy and imaging of human brain function," *Trends Neurosci.* **20**, 435–442 (1997).

[21] E. B. Hanlon, R. Manoharan, T.-W. Koo, K. E. Shafer, J. T. Motz, M. Fitzmaurice, J. R. Kramer, I. Itzkan, R. R. Dasari, and M. S. Feld, "Prospects for *in vivo* Raman spectroscopy," *Phys. Med. Biol.* **45**, R1–R59 (2000).

[22] R. R. Alfano, A. Pradhan, G. C. Tang, and S. J. Wahl, "Optical spectroscopic diagnosis of cancer and normal breast tissues," *J. Opt. Soc. Am. B* **6**, 1015–1023 (1989).

[23] S. K. Gayen and R. R. Alfano, "Sensing lesions in tissues with light," *Opt. Express* **4**, 475–480 (1999).

[24] R. Richards-Kortum and E. Sevick-Muraca, "Quantitative optical spectroscopy for tissue diagnosis," *Annu. Rev. Phys. Chem.* **47**, 555–606 (1996).

[25] R. R. Alfano, D. B. Tata, J. Cordero, P. Tomashefsky, F. W. Longo, and M. A. Alfano, "Laser induced fluorescence spectroscopy from native cancerous and normal tissue," *IEEE J. Quantum Electron.* **20**, 1507 (1984).

[26] Y. Pu, W. B. Wang, G. C. Tang, and R. R. Alfano,"Changes of collagen and NADH in human cancerous and normal prostate tissues studied using fluorescence spectroscopy with selective excitation wavelength," *J. Biomed. Opt.* **15**, 047008-1-5 (2010).

[27] I. Georgakoudi, B. C. Jacobson, M. G. Muller, E. E. Sheets, K. Badizadegan, D. L. Carr-Locke, C. P. Crum, C. W. Boone, R. R. Dasari, J. Vand Dam, et al., "NAD(P)H and collagen as *in vivo* quantitative fluorescent biomarkers of epithelial precancerous changes," *Cancer Res.* **62**, 682–687 (2002).

[28] A. S. Haka, Z. Volynskaya, J. A. Gardecki, J. Nazemi, J. Lyons, D. Hicks, M. Fitzmaurice, R. R. Dasari, J. P. Crowe, and M. S. Feld, "In vivo margin assessment during partial mastectomy breast surgery using Raman spectroscopy," *Cancer Res.* **66**, 3317–3322 (2006).

[29] R. R. Alfano, C. H. Liu, W. L. Sha, H. R. Zhu, D. L. Akins, J. Cleary, R. Prudente, and E. Cellmer, "Human breast tissues studied by IR Fourier transform Raman spectroscopy," *Lasers Life Sci.* **4**, 23 (1991).

[30] Y. Zhou, C.-H. Liu, Y. Sun, Y. Pu, S. Boydston-White, Y. Liu, and R. R. Alfano, "Human brain cancer studied by resonance Raman spectroscopy," *J. Biomed. Opt.* **17**, 116021-1-7 (2012).

[31] C.-H. Liu, Y. Zhou, Y. Sun, J. Y. Li, L. X. Zhou, S. Boydston-White, V. Masilamani, K. Zhu, Yang Pu, and R. R. Alfano, "Resonance Raman and Raman spectroscopy for breast cancer detection," *Technol. Cancer Res. Treat. (TCRT)* **12**(4), 371–382 (2013).

[32] I. J. Bigio, S. G. Bown, G. Briggs, C. Kelley, S. Lakhani, D. Pickard, P. M. Ripley, I. G. Rose, and C. Saunders, "Diagnosis of breast cancer using elastic-scattering spectroscopy: preliminary clinical results," *J. Biomed. Opt.* **5**(2), 221–228 (2000).

[33] R. R. Alfano and Y. Yang, "Stokes shift emission spectroscopy of human tissue and key biomolecules," *IEEE J. Quantum Electron.* **9**, 148–153 (2003).

[34] Y. Pu, W. Wang, Y. Yang, and R. R. Alfano, "Stokes shift spectroscopy highlights differences of cancerous and normal human tissues," *Opt. Lett.* **37**(16), 3360–3362 (2012).

[35] Y. Pu, W. Wang,Y. Yang, and R. R. Alfano, "Stokes shift spectroscopic analysis of multi-fluorophores for human cancer detection in breast and prostate tissues," *J. Biomed. Opt.* **18** (1), 017005-1-8 (2013).

[36] J. Ebenezar, Yang Pu, C. H. Liu, W. B. Wang, and R. R. Alfano, "Diagnostic potential of Stokes shift spectroscopy of breast and prostate tissues—a preliminary pilot study," *Technol. Cancer Res. Treat.* **10**, 153–161 (2011).

[37] R. Drezek, K. Sokolov, U. Utzinger, I. Boiko, A. Malpica, M. Follen, and R. Richards-Kortum, "Understanding the contributions of NADH and collagen to cervical tissue fluorescence spectra: modeling, measurements, and implications," *J. Biomed. Opt.* **6**(4), 385–396 (2001).

[38] Y. Pu, W. B. Wang, B. B. Das, and R. R. Alfano, "Time-resolved near infrared spectral wing emission and imaging of human cancerous and normal prostate tissues," *Opt. Commun.* **282**, 4308–4314 (2009).

[39] M. J. Niedre, R. H. de Kleine, E. Aikawa, D. G. Kirsch, R. Weissleder, and V. Ntziachristos, "Early photon tomography allows fluorescence detection of lung carcinomas and disease progression in mice in vivo," *Proc. Natl. Acad. Sci. USA* **105** (49), 19126–19131 (2008).

[40] M. Cutler, "Transillumination as an aid in the diagnosis of breast lesion," *Surg. Gynecol. Obstet.* **48**, 721–730(1929).

[41] B. C. Wilson and S. L. Jacques, "Optical reflectance and transmittance of tissues: principles and applications," *IEEE J. Quantum Electron.* **26**, 2186–2199 (1990).

[42] I. Gannot, A. Garashi, V. Chernomordik, and A. Gandjbachkhe, "Quantitative optical imaging of the pharmacokinetics of fluorescent-specific antibodies to tumor markers through tissue-like turbid media," *Opt. Lett.* **29**, 742–744 (2004).

[43] A. Godavarty, M. J. Eppstein, C. Zhang, S. Theru, A. B. Thompson, M. Gurfinkel, and E. M. Sevick-Muraca, "Fluorescence-enhanced optical imaging in large tissue volumes using a gain-modulated ICCD camera," *Phys. Med. Biol.* **48**, 1701–1720 (2003).

[44] A. Corlu, R. Choe, T. Durduran, M. A. Rosen, M. Schweiger, S. R. Arridge, M. D. Schnall, and A. G. Yodh, "Three-dimensional in vivo fluorescence diffuse optical tomography of breast cancer in humans," *Opt. Express* **15**, 6696–6716 (2007).

[45] M. Alrubaiee, M. Xu, S. K. Gayen, and R. R. Alfano, "Localization and cross section reconstruction of fluorescent targets in *ex vivo* breast tissue using independent component analysis," *Appl. Phys. Lett.* **89**, 133902 (2006).

[46] K. M. Yoo and R. R. Alfano, "Time-resolved coherent and incoherent components of forward light scattering in random media," *Opt. Lett.* **15**, 320–322 (1990).

[47] D. S. Dilworth, E. N. Leith, and J. L. Lopez, "Three-dimensional confocal imaging of objects embedded within thick diffusing media," *Appl. Opt.* **30**, 1796–1803 (1991).

[48] H. Horinaka, K. Hashimoto, K. Wada, and Y. Cho, "Extraction of quasi-straight-forward-propagating-photons from diffused light transmitting through a scattering medium by polarization modulation," *Opt. Lett.* **20**, 1501–1503 (1995).

[49] S. G. Demos and R. R. Alfano, "Temporal gating in highly scattering media by the degree of optical polarization," *Opt. Lett.* **21**, 161–163 (1996).

[50] S. G. Demos and R. R. Alfano, "Optical polarization imaging," *Appl. Opt.* **36**, 150–163 (1997).

[51] S. G. Demos, H. Savage, A. S. Heerdt, S. Schantz, and R. R. Alfano, "Time-resolved degree of polarization for human breast tissue," *Opt. Commun.* **124**, 439–442 (1996).

[52] L. Wang, P. P. Ho, C. Liu, G. Zhang, and R. R. Alfano, "Ballistic 2-D imaging through scattering wall using an ultrafast Kerr gate," *Science* **253**, 769–771 (1991).

[53] L. Wang, P. P. Ho, X. Liang, H. Dai, and R. R. Alfano, "Fourier-Kerr imaging in thick turbid media," *Opt. Lett.* **18**, 241–243 (1993).

[54] R. R. Alfano, X. Liang, L. Wang, and P. P. Ho, "Time-resolved imaging of translucent droplets in highly scattering turbid media," *Science* **264**, 1913–1915 (1994).

[55] G. W. Faris and M. Banks, "Imaging through highly scattering media with a novel upconverting time gate," in *Proceeding on Advances in Optical Imaging and Photon Migration 21*, edited by R. R. Alfano (Optical Society of America, Washington, DC, 1994), pp. 139–142.

[56] J. Reintjes, M. Bashkansky, M. D. Duncan, R. Mahon, L. L. Tankersley, J. A. Moon, C. L. Adler, and J. M. S. Prewitt, "Time-gated imaging with nonlinear optical Raman interactions," *Opt. Phot. News* **4**(10), 28–32 (1993).

[57] O. Jarlman, R. Berg, and S. Svanberg, "Time-resolved transillumination of the breast," *Acta Radiol.* **33**, 277–279 (1992).

[58] K. M. Yoo, B. B. Das, and R. R. Alfano, "Imaging of a translucent object hidden in a highly scattering medium from early portion of the diffuse component of a transmitted ultrafast laser pulse," *Opt. Lett.* **17**, 958–960 (1992).

[59] K. G. Spears J. Serafin, N. H. Abramson, X. M. Zhu, and H. Bjelkhagen, "Chronocoherent imaging for medicine," *IEEE Trans. Biomed. Eng.* **36**, 1210–1221 (1989).

[60] E. Leith, E. Arons, H. Chen, Y. Chen, D. Dilworth, J. Lopez, M. Shih, P. C. Sun, and G. Vossler, "Electronic holography for imaging through tissue," *Opt. Phot. News* **4**(10), 19–23 (1993).

[61] E. Arons, H. Chen, K. Clay, D. Dilworth, R. Draper, J. Lopez, E. Leith, M. Shih, and P. C. Sun, "New holographic methods for improved imagery through scattering media," in *Proceedings on Advances in Optical imaging and Photon Migration 21*, edited by R. R. Alfano (Optical Society of America, Washington, DC, 1994), pp. 239–243.

[62] A. D. Sappey, "Optical imaging through turbid media with a degenerate four wave mixing correlation time gate.," *Appl. Opt.* **33**, 8346–8353 (1994).

[63] M. A. O'Leary, D. A. Boas, B. Chance, and A. G. Yodh, "Experimental images of heterogeneous turbid media by frequency-domain diffusing-photon tomography," *Opt. Lett.* **20**, 426–428 (1995).

[64] E. M. Sevick, C. L. Hutchinson, J. K. Frisoli, M. L. Johnson, K. Nowaczyk, H. Szmacinski, and J. R. Lakowicz, "The physical basis of biomedical optical imaging using time-dependent measurements of photon migration in the frequency domain," in *Medical Optical Tomography: Functional Imaging and Monitoring*, edited by G. J. Muller, R. R. Alfano, S. R. Arridge, J. Beuthan, E. Gratton, M. Kaschke, B. R. Masters, S. Svanberg, and P. van der Zeect, SPIE Institute Series (SPIE, Bellingham, WA, 1993), Vol. IS 11, pp. 485–512.

[65] E. Gratton, W. W. Mantulin, M. J. vandeVen, J. B. Fishkin, M. B. Maris, and B. Chance, "A novel approach to laser tomography," *Bioimaging* **1**, 40–46 (1993).

[66] Y. Yamashita and M. Kaneko, "Visible and infrared diaphanoscopy for medical diagnosis," in *Medical Optical Tomography: Functional Imaging and Monitoring*, edited by G. J. Muller, R. R. Alfano, S. R. Arridge, J. Beuthan, E. Gratton, M. Kaschke, B. R. Masters, S. Svanberg, and P. van der Zeect, SPIE Institute Series (SPIE, Bellingham, WA, 1993), Vol. IS 11, pp. 283–316.

[67] J. Beuthan, "IR-diaphanoscopy in medicine," in *Medical Optical Tomography: Functional Imaging and Monitoring*, edited by G. J. Muller, R. R. Alfano, S. R. Arridge, J. Beuthan, E. Gratton, M. Kaschke, B. R. Masters, S. Svanberg, and P. van der Zeect, SPIE Institute Series (SPIE, Bellingham, WA, 1993), Vol. IS 11, pp. 263–282.

[68] K. P. Chan, M. Yamada, B. Devaraj, and H. Inaba, "Optical imaging through highly scattering media by use of heterodyne detection in the 1.3 μm wavelength region," *Opt. Lett.* **20**, 492–494 (1995).

[69] H. Inaba, "Coherent detection imaging for medical laser tomography," in *Medical Optical Tomography: Functional Imaging and Monitoring*, edited by G. J. Muller, R. R. Alfano, S. R. Arridge, J. Beuthan, E. Gratton, M. Kaschke, B. R. Masters, S. Svanberg, and P. van der Zeect, SPIE Institute Series (SPIE, Bellingham, WA, 1993), Vol. IS 11, pp. 317–347.

[70] A. Schmidt, R. Corey, and P. Saulnier, "Imaging through random media by use of low-coherence optical heterodyning," *Opt. Lett.* **20**, 404–406 (1995).

[71] A. F. Frecher, W. Drexler, C. K. Hitzenberger, and T. Lasser, "In vivo optical coherence tomography in ophthalmology," in *Medical Optical Tomography: Functional Imaging and Monitoring*, edited by G. J. Muller, R. R. Alfano, S. R. Arridge, J. Beuthan, E. Gratton, M. Kaschke, B. R. Masters, S. Svanberg, and P. van der Zeect, SPIE Institute Series (SPIE, Bellingham, WA, 1993), Vol. IS 11, pp. 355–370.

[72] L. Kalpaxis, L. M. Wang, P. Galland, X. Liang, P. P. Ho, and R. R. Alfano, "Three-dimensional temporal image reconstruction of an object hidden in highly scattering media by time-gated optical tomography," *Opt. Lett.* **18**, 1691–1693 (1993).

[73] M. Hiraoka, M. Firbank, M. E. Essenpreis, M. Cope, S. R. Arridge, P. Zee, and D. Delpy, "Monte Carlo simulation of light transport through inhomogeneous tissue," *Proc. SPIE—Int. Soc. Opt. Eng.* **1888**, 149–159 (1993).

[74] S. R. Arrige, "The forward and inverse problems in time-resolved infrared imaging," in *Medical Optical Tomography: Functional Imaging and Monitoring*, edited by G. J. Muller, R. R. Alfano, S. R. Arridge, J. Beuthan, E. Gratton, M. Kaschke, B. R. Masters, S. Svanberg, and P. van der Zeect, SPIE Institute Series (SPIE, Bellingham, WA, 1993), Vol. IS 11, pp. 35–64.

[75] W. Cai, S. K. Gayen, M. Xu, M. Zevallos, M. Alrubaiee, M. Lax, and R. R. Alfano, "Optical three-dimensional inverse image reconstruction of objects in turbid media from ultrafast time-sliced optical transmission measurements," *Appl. Opt.* **38**, 4237–4246 (1999).

[76] M. Xu, M. Alrubaiee, S. K. Gayen, and R. R. Alfano, "Optical diffuse imaging of an *ex vivo* model cancerous human breast using independent component analysis," *IEEE J. Sel. Top. Quantum Electron.* **14**, 43 (2008).

[77] P. F. Moulton, "Spectroscopic and laser properties of $Ti^{3+}Al_2O_3$," *J. Opt. Soc. Am. B* **3**, 125–133 (1986).

[78] V. Petricevic, S. K. Gayen, and R. R. Alfano, "Laser action in chromium-activated forsterite for near-infrared excitation: is Cr^{4+} the lasing ion?" *Appl. Phys. Lett.* **53**, 2590–2593 (1988).

[79] F. Liu, K. M. Yoo, and R. R. Alfano, "Transmitted photon intensity through biological tissues within various time windows," *Opt. Lett.* **10**, 740–742 (1994).

[80] A. Ishimaru, *Wave Propagation in Random Media* (Academic Press, New York, 1978), Vols. 1 and 2.

[81] L. Wang, "Picosecond Kerr Gated Imaging of Phantoms in Turbid Media," PhD thesis, The City University of New York (1995).

[82] C. J. M. Moes, M. C. van Gemert, W. M. Star, J. P. A. Marijnissen, and S. A. Prahl, "Measurements and calculations of energy fluence rate in a scattering and absorbing phantom," *Appl. Opt.* **28**, 2292–2296 (1989).

[83] H. J. van Staveren, C. J. M. Moes, J. van Marle, S. A. Prahl, and M. J. C. van Gemert, "Light scattering in Intralipid-10% in the wavelength range of 400-1100 nm," *Appl. Opt.* **31**, 4507–4514 (1991).

[84] V. G. Peters, D. R. Wyman, M. S. Patterson, and G. L. Frank, "Optical properties of normal and diseased human breast tissues in the visible and near infrared," *Phys. Med. Biol.* **9**, 1317–1334 (1990).

[85] J-L Boulnois, "Photophysical processes in recent medical laser developments: A review," *Lasers in Med. Sci.* **1**, 47 (1986).

[86] K. M. Yoo, F. Liu, and R. R. Alfano, "When does the diffusion approximation fail to describe photon transport in random media?" *Phys. Rev. Lett.* **64**, 2647–2650 (1990); *Phys. Rev. Lett.* **65**, 2210–2211 (1990).

[87] M. Lax, V. Narayanamurti, and R. C. Fulton, "Classical diffusive photon transport in a slab," in *Proceedings of the Symposium on Laser Optics of Condensed Matter, Leningrad, June 1987*, edited by J. L. Birman, H. Z. Cummins, and A. A. Kaplyanskij] (Plenum, New York, 1987).

[88] G. H. Watson, P. A. Fleury, and S. L. McCall, "Searching for photon localization in the time domain," *Phys. Rev. Lett.* **58**, 945–948 (1987).

[89] E. Akkermans, P. E. Wolf, and R. Maynard, "Coherent backscattering of light by disordered media: analysis of the peak line shape," *Phys Rev. Lett.* **56**, 1471–1474 (1986).

[90] M. J. Stephen and G. Cwilich, "Rayleigh scattering and weak localization: effects of polarization," *Phys Rev. B* **34**, 7564–7572 (1986).

[91] M. B. van der Mark, M. P. van Albada, and A. Lagendijk, "Light scattering in strongly scattering media: multiple scattering and weak localization," *Phys. Rev. B* **37**, 3575–3592 (1988).

[92] M. Rosenbluh, I. Edrei, M. Kaveh, and I. Freund, "Precision determination of the line shape for coherently backscattered light from disordered solids: comparison of vector and scalar theories," *Phys Rev. A* **35**, 4458–4460 (1987).

[93] S. Feng, C. Kane, P. A. Lee, and A. Douglas Stone, "Correlation and fluctuations of coherent wave transmission through disordered media," *Phys Rev. Lett.* **61**, 834–837 (1988).

[94] M. J. Stephen, "Temporal fluctuations in wave propagation in random media," *Phys. Rev. B* **37**, 1–5 (1988).

[95] D. J. Pine, D. A. Weitz, P. M. Chaikin, and E. Herbolzheimer, "Diffusing wave spectroscopy," *Phys. Rev. Lett.* **60**, 1134–1137 (1988).

[96] D. A. Weitz, D. J. Pine, P. N. Pusey, and R. J. A. Tough, "Nondiffusive Brownian motion studied by diffusing-wave spectroscopy," *Phys. Rev. Lett.* **63**, 1747–1750 (1989).

[97] I. Freund, M. Kaveh, and M. Rosenbluh, "Dynamic multiple scattering: ballistic photons and the breakdown of the photon-diffusion approximation," *Phys. Rev. Lett.* **60**, 1130–1133 (1988).

[98] W. Cai, M. Lax, and R. R. Alfano, "Analytical solution of the elastic Boltzmann transport equation in an infinite uniform medium using cumulant expansion," *J. Phys. Chem. B* **104**, 3996–4000 (2000).

[99] W. Cai, M. Lax, and R. R. Alfano, "Cumulant solution of the elastic Boltzmann transport equation in an infinite uniform medium," *Phys. Rev. E.* **61**, 3871–3876 (2000).

[100] M. J. Niedre, R. H. de Kleine, E. Aikawa, D. G. Kirsch, R. Weissleder, and V. Ntziachristos, "Early photon tomography allows fluorescence detection of lung carcinomas and disease progression in mice in vivo," *Proc. Natl. Acad. Sci. USA* **105**(49), 19126–19131 (2008).

[101] S. L. Jacques, "Time-resolved propagation of ultrashort laser pulses within turbid tissues," *Appl. Opt.* **28**, 2223–2229 (1989).

[102] M. S. Patterson, B. Chance, and B. C. Wilson, "Time-resolved reflectance and transmittance for the non-invasive measurement of tissue optical properties," *Appl. Opt.* **28**, 2331–2336 (1989).

[103] F. Liu, K. M. Yoo, and R. R. Alfano, "Should the photon flux or the photon density be used to describe the temporal profiles of scattered ultrashort laser pulses in random media?" *Opt. Lett.* **18**, 432–434 (1993).

[104] G. Navarro and A. Profio, "Contrast in diaphanography of the breast," *Med. Phys.* **15**, 181–187 (1988).

[105] R. Marchesini, A. Bertoni, S. Andreola, E. Melloni, and A. E. Sichirollo, "Extinction and absorption coefficients and scattering phase functions of human tissues *in vitro*," *Appl. Opt.* **28**, 2318–2324 (1989).

[106] S. T. Flock, B. C. Wilson, and M. S. Patterson, "Total attenuation of tissues and phantom materials at 633 nm," *Med. Phys.* **14**, 835–841 (1987).

[107] P. P. Ho, R. Dorsinville, N. L. Yang, G. Odian, G. Eichmann, T. Jimbo, Q. Z. Wang, G. C. Tang, N. D. Chen, W. K. Zou, et al., "Ultrafast nonlinear optical processes in 4BCMU-polydiacetylene," *Proc. SPIE (Int. Soc. Opt. Eng.)* **682**, 36–41 (1986).

[108] X. Liang, L. Wang, P. P. Ho, and R. R. Alfano, "Two-dimensional Kerr-Fourier imaging of translucent phantoms in thick turbid media," *Appl. Opt.* **34**, 3463–3467 (1995).

[109] L. Wang, P. Ho, and R. R. Alfano, "Double-stage picosecond Kerr gate for ballistic time-gated optical imaging in turbid media," *Appl. Opt.* **32**, 241–243 (1993).

[110] L. Wang, P. P. Ho, X. Liang, H. Dai, and R. R. Alfano, "Kerr-Fourier imaging of hidden objects in thick media," *Opt. Lett.* **18**, 522–524 (1993).

[111] M. E. Zevallos, S. K. Gayen, M. Alrubaiee, and R. R. Alfano, "Time-gated backscattered ballistic light imaging of objects in turbid water," *Appl. Phys. Lett.* **86**, 011115 (2005).

[112] S. K. Gayen, M. Alrubaiee, H. E. Savage, S. P. Schantz, and R. R. Alfano, "Parotid gland tissues investigated by picosecond time-gated and spectroscopic imaging techniques," *IEEE J. Sel. Top. Quantum Electron.* **7**, 906 (2001).

[113] M. Alrubaiee, S. K. Gayen, R. R. Alfano, and J. A. Koutcher, "Spectral and temporal near-infrared imaging of *ex vivo* cancerous and normal human breast tissues," *Technol. Cancer Res. Treat.* **4**, 455–482 (2005).

[114] J. Selb, D. K. Joseph, and D. A. Boas, "Time-gated optical system for depth-resolved functional brain imaging," *J. Biomed. Opt.* **11**, 044008 (2006).

[115] C. D'Andrea, D. Comelli, A. Pifferi, A. Torricelli, G. Valentini, and R. Cubeddu, "Time-resolved optical imaging through turbid media using a fast data acquisition system based on a gated CCD camera," *J. Phys. D. Appl. Phys.* **36**, 1675 (2003).

[116] M. J. Niedrea, R. H. de Kleine, E. Eikawa, D. G. Kirsch, R. Weissleder, and V. Ntziachristos, "Early photon tomography allows fluorescence detection of lung carcinomas and disease progression in mice *in vivo*," *Proc. Nat. Acad. Sci. USA* **105**, 19126–19131 (2008).

[117] Y. Wang, S. K. Gayen, M. Alrubaiee, and R. R. Alfano, "Near-infrared center-of-intensity time gated imaging for detection of a target in a highly scattering turbid medium," *Technol. Cancer Res. Treat.* **11**, 309–315 (2012).

[118] L. Gu, D. J. Hall, Z. Qin, E. Anglin, J. Joo, D. J. Mooney, S. B. Howell, and M. J. Sailor, "*In vivo* time-gated fluorescence imaging with biodegradable luminescent porous silicon nanoparticles," *Nat. Commun.* **4**, 2326 (2013).

[119] V. Y. Soloviev, K. B. Tahir, J. McGinty, D. S. Elson, M. A. A. Neil, P. M. W. French, and S. R. Arridge, "Fluorescence lifetime imaging by using time-gated data acquisition," *Appl. Opt.* **46**, 7384–7391 (2007).

[120] R. Cubeddu, D. Comelli, C. D'Andrea, P. Taroni, and G. Valentini, "Time-resolved fluorescence imaging in biology and medicine," *J. Phys. D. Appl. Phys.* **35**, R61 (2002).

[121] K. M. Yoo, Feng Liu, and R. R. Alfano, "Imaging through a scattering wall using absorption," *Opt. Lett.* **16**, 1068–1070 (1991).

[122] S. K. Gayen, M. E. Zevallos, M. Alrubaiee, J. M. Evans, and R. R. Alfano, "Two-dimensional near-infrared transillumination imaging of biomedical media with a chromium-doped forsterite laser," *Appl. Opt.* **37**, 5327 (1998).

[123] J. B. Pawley, *Handbook of Biological Confocal Microscopy* (Plenum, New York, 1989).

[124] R. Arora, G. I. Petrov, and V. V. Yakovlev, "Hyperspectral coherent anti-Stokes Raman scattering microscopy imaging through turbid medium," *J. Biomed. Opt.* **16**, 021116 (2011).

[125] I. M. Vellekoop and C. M. Aegerter, "Scattered light fluorescence microscopy: imaging through turbid layers," *Opt. Lett.* **35**, 1245 (2010).

[126] A. Vander Lugt, *Optical Signal Processing* (Wiley Interscience, New York, 1992), pp. 95–101.

[127] G. E. Anderson, Feng Liu, and R. R. Alfano, "Microscope imaging through highly scattering media," *Opt. Lett.* **19**, 981–983 (1994).

[128] Q. Z. Wang, X. Liang, L. Wang, P. P. Ho, and R. R. Alfano, "Fourier spatial filter acts as a temporal gate for light propagating through a turbid medium," *Opt. Lett.* **20**, 1498–1500 (1995).

[129] S. K. Gayen, M. E. Zevallos, and R. R. Alfano, "Near-infrared laser spectroscopic imaging: a step towards diagnostic optical imaging of human tissues," *Lasers Life Sci.* **8**, 187–198 (1999).

[130] K. C. Hadley and I. A. Vitkin, "Optical rotation and linear and circular depolarization rates in diffusely scattered light from chiral, racemic, and achiral turbid media," *J. Biomed. Opt.* **7**, 291–299 (2002).

[131] K. G. Phillips, M. Xu, S. K. Gayen, and R. R. Alfano, "Time-resolved ring structure of circularly polarized beams backscattered from forward scattering media," *Opt. Express* **13**, 7954–7969 (2005).

[132] W. Cai, Xiaohui Ni, S. K. Gayen, and R. R. Alfano, "Analytical cumulant solution of the vector radiative transfer equation investigates backscattering of circularly polarized light from turbid media," *Phys. Rev. E* **74**, 056605 (2006).

[133] N. Ghose and I. A. Vitkin, "Tissue polarimetry: concepts, challenges, applications and outlook," *J. Biomed. Opt.* **16**, 110801 (20011).

[134] R. R. Alfano, S. G. Demos, and W. B. Wang, "Imaging of objects in turbid media based upon the preservation of polarized luminescence emitted from contrast agents," U.S. Patent, No. 6,091,983, July 18, 2000.

[135] Y. Pu, W. Wang, R. B. Dorshow, B. Idyud, B. Das, and R. R. Alfano, "Mini review of ultrafast fluorescence polarization spectroscopy (Invited)," *Appl. Opt.* **52**(5), 917–929 (2013).

[136] W. B. Wang, J. H. Ali, J. H. Vitenson, J. M. Lombardo, and R. R. Alfano, "Spectral polarization imaging of human rectum-membrane-prostate tissues," *IEEE J. Sel. Top. Quantum Electron.* **9**(2), 288–293 (2003).

[137] Y. Pu, W. Wang, M. Xu, J. A. Eastham, G. Tang, and R. R. Alfano, "Characterization and three-dimensional localization of cancerous prostate tissue using backscattering scanning polarization imaging and independent component analysis," *J. Biomed. Opt.* **17** (8), 081419-1-8 (2012).

[138] W. B. Wang, S. G. Demos, J. Ali, and R. R. Alfano, "Imaging fluorescent objects embedded inside animal tissues using polarization difference technique," *Opt. Commun.* **142**, 161–166 (1997).

[139] D. M. Jameson and J. A. Ross, "Fluorescence polarization/anisotropy in diagnostics and imaging," *Chem. Rev.* **110**, 2685–2708 (2010).

[140] A. Yaroshevsky, Z. Glasser, E. Granot, and S. Sternklar, "Transition from the ballistic to diffusive regime in a turbid medium," *Opt. Lett.* **36**, 1395–1397 (2011).

[141] M. Kempe, A. Z. Genack, W. Rudolph, and P. Dorn, "Ballistic and diffuse light detection in confocal and heterodyne imaging systems," *J. Opt. Soc. Am. A* **14**, 216–223 (1997).

10

PHOTODYNAMIC THERAPY

RAKKIYAPPAN CHANDRAN,[1,2,3] TYLER G. ST. DENIS,[1,4]
DANIELA VECCHIO,[1,2] PINAR AVCI,[1,2] MAGESH SADASIVAM,[1,2,3]
AND MICHAEL R. HAMBLIN[1,2,5]

[1] *Wellman Center for Photomedicine, Massachusetts General Hospital, Boston, MA, USA*
[2] *Department of Dermatology, Harvard Medical School, Boston, MA, USA*
[3] *Amity Institute of Nanotechnology, Amity University, Noida, India*
[4] *Department of Chemistry, Columbia University, New York, NY, USA*
[5] *Harvard-MIT Division of Health Sciences and Technology, Cambridge, MA, USA*

10.1 HISTORICAL OVERVIEW OF PDT

Around 1900, the then medical student Oscar Raab was working in the laboratory of Professor Herman von Tappeiner at the Pharmacological Institute of Munich, Germany. Professor von Tappeiner was interested in the antimalarial application of acridine dyes such as acridine orange. Accordingly, Raab was working on a *Paramecium* spp. protozoan model, exposing samples to varying concentrations of acridine orange. While acridine orange did exhibit antiprotozoan activity, there was one major inconsistency: in one experiment the lowest dilution of acridine orange killed all paramecia in 60–100 min, while in an earlier experiment the same dilution killed the same amount of protozoans in 800–1000 min. This greater than 10-fold difference in time-dependent killing prompted Raab and von Tappeiner to thoroughly analyze the environmental variables of the two experiments. It was discovered that the latter experiment, which demonstrated enhanced antiprotozoan activity of acridine orange, was performed during an intense thunderstorm with lightning that illuminated the laboratory. These two investigators verified that light enhanced the lethality of

Photonics: Scientific Foundations, Technology and Applications, Volume IV, First Edition.
Edited by David L. Andrews.
© 2015 John Wiley & Sons, Inc. Published 2015 by John Wiley & Sons, Inc.

acridine orange, and published their work, and as early as 1900 realized the potential medical, and specifically dermatological applications, of this technology.

By 1904, the importance of oxygen (O_2) in this reaction was discovered, and the light-sensitive dye photosensitization of cells in the presence of O_2 was termed (in German) a *photodynamischer effekt*, translating to a photodynamic effect. While minimal human experiments had started as early as 1905, the two World Wars intervened, redirecting researchers' scientific efforts to war-related subjects, thus delaying advancements in the field. Nevertheless, small steps forward were made, the most important of which was the switch from experimenting with photosensitizers (PS) derived from coal-tar and textile research (e.g., dyes of the phenothiazinium [1] and acridine [2] class) toward using natural product-derived PS, such as the cyclic tetrapyrroles known as porphyrins. Of the porphyrin PS, hematoporphyrin, and the so-called hematoporphyrin derivative (HpD; a mixture containing ester- and ether-linked hematoporphyrin dimers, trimers, and larger polymers) paved the way for PDT clinical applications: Lipson et al. conducted several trials at the Mayo Clinic and in 1993, the sodium salt of HpD, known as Photofrin®, was approved by the FDA for the treatment and management of various neoplastic conditions [3].

After exogenous application of PS was proven to be effective in the management of disease, researchers in the 1980s were inspired to evaluate the possibility of creating endogenous PS for PDT. The idea was simple and was inspired by a class of diseases known as the porphyrias, which are a consequence of genetic mutations that result in defects of the heme biosynthesis pathway. Almost all host cells have machinery for manufacturing heme and it is known that the immediate precursor of heme, protoporphyrin IX, can act as a PS with an absorption in the red portion of the electromagnetic spectrum. By overloading cells with the initial building block of heme, 5-aminolevulinic acid (5-ALA), the biological feedback loop that prevents autophotosensitization is bypassed, resulting in localized photosensitivity—a sort of controlled porphyria. Malik and colleagues used put 5-ALA and red light to the test in 1987, and its overwhelming positive effect resulted in several clinical trials and the acceptance of 5-ALA-mediated PDT as a targeted medical technology for dermatological diseases [4]. In 1999, Levulan® Kerastick® (a 5-aminolevulinic acid hydrochloride salve) and blue light was approved by the FDA for the treatment of cancerous and precancerous skin lesions.

Even though PDT was born out of Raab's accidental photodestruction of microorganisms, from 1900 to 1990, the amount of papers exploring PDT for the control of pathogen microorganisms were few and far between. As a consequence of the emergence of antibiotic resistance in the latter half of twentieth century, interest in antimicrobial PDT resurfaced. In the 1990s, susceptibility differences between Gram-positive and Gram-negative bacteria were realized and overcome with the application of cationic PS including the already clinically approved methylene blue and other coal tar-derived dyes. As of the twenty-first century, antimicrobial PDT has been the subject of a great deal of research interest as a consequence of the urgency for novel modes of infection control especially in cases where antibiotics are ineffective. One of the most attractive features of PDT is the apparent inability of microorganisms to develop resistance to PDT, such that antibiotic-resistant and susceptible isolates are equally susceptible to the phototoxic PDT effect.

10.2 INTRODUCTION TO PDT

10.2.1 Photophysics

PDT consists of the concomitant application of three important agents: light, PS, and O_2. Due to the aromatic and/or conjugated nature of PS, electrons of the highest occupied molecular orbital (HOMO) are extensively delocalized, resulting in photonic absorption in the visible and sometimes near-infrared portion of the electromagnetic spectrum. In the ground state, the PS is in a singlet state, in which all electrons are spin paired. Briefly, all paired electrons possess opposite spin values of either $+1/2$ or $-1/2$ and the sum of these spins, S, is zero. The spin state, also known as spin multiplicity (Ms), is given by $2S + 1$. When a photon ($h\nu$) of the appropriate energy is absorbed in a very rapid (10^{-15} s) event, electronic absorption may occur before PS vibrational events are observed. Because there is no change in the Ms of the PS, electronic excitation is a process permitted by quantum mechanics.

Electron excitation by $h\nu$ absorption results in the promotion of a single electron to the lowest unoccupied molecular orbital (LUMO) without reversing the electronic spin. The excited singlet state violates the Aufbau principle (from the German *Aufbau* meaning building up) stating that lowest energy levels of electrons are most stable. Due to the large energy gap between the ground singlet and excited singlet states, the unstable excited singlet state exists for only a short period of time. It is possible for the electron in the new HOMO of the excited singlet PS to be promoted to the new LUMO, forming a higher excited singlet state, but it is much more likely that other processes occur so as to lower the PS energy. For example, the energy may be transferred into vibrational bond energy or heat (internal conversion). Alternatively fluorescence may occur in which a photon is emitted by the excited state PS, bringing the PS back to the ground singlet state. The selective accumulation of PS in neoplastic tissue may be verified by selective tissue fluorescence and the appreciable fluorescence of organic PS has aided photodynamic diagnosis of several diseases and has allowed for pharmacokinetic and dosimetric PDT monitoring.

Fluorescence, however, is not responsible for the cytotoxic effects of PDT. In the excited singlet state, the promoted electron may reverse its spin, becoming spin parallel to its formal orbital partner. This process is known as intersystem crossing and results in a triplet Ms, and though it is unfavorable in terms of multiplicity, it is energetically favorable due to the smaller energy gap between the triplet state and the ground singlet state relative to that of the excited singlet state and the ground singlet state. The triplet state is a much longer-lived species namely because the promoted electron cannot simply relax to the ground state, as it would then possess identical quantum numbers with that of its partner electron. This represents a clear violation of the Pauli exclusion principle such that for PS relaxation to the ground state, the PS promoted electron must reverse its spin, re-entering the excited singlet state, and then

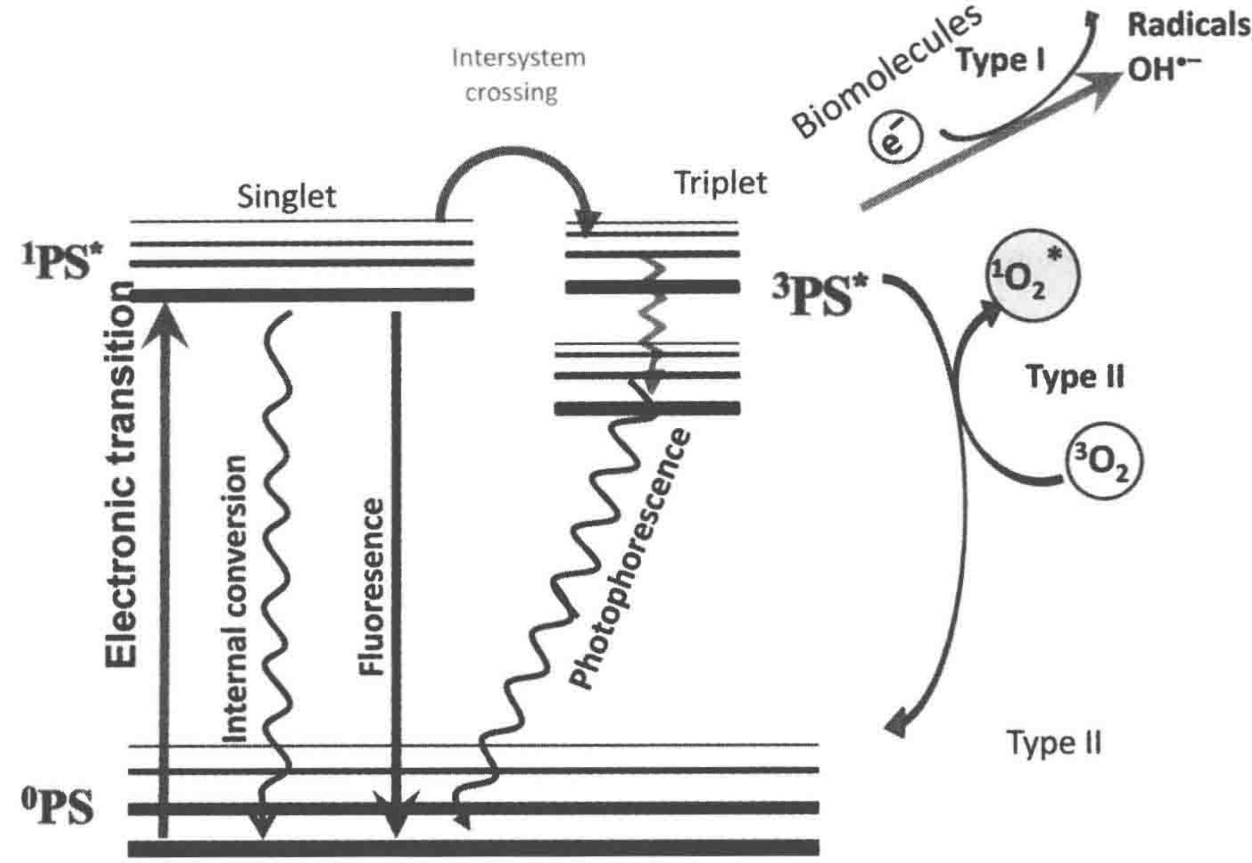

FIGURE 10.1 Schematic illustration of photodynamic action (Jablonski diagram). The PS initially absorbs a photon that excites it to the short-lived excited singlet state. This can lose energy by fluorescence, internal conversion to heat, or by intersystem crossing to the long-lived triplet state. This triplet PS can interact with molecular oxygen in two pathways, type 1 and type 2, leading to the formation of reactive oxygen species (ROS) and singlet oxygen ($^1O_2$), respectively.

emit *hv* to relax to the ground singlet state. This delayed emission process is called phosphorescence. The relative energies of the ground singlet, excited singlet, and excited triplet states, as well as the processes of fluorescence and phosphorescence are illustrated in the classic Jablonski diagram shown in Figure 10.1.

Phosphorescence would be the most favorable energy decay process for PS, provided an excited triplet state PS existed in isolation. However, PS are prepared in aqueous solution and are incubated in/on cells, both of which are environments with an abundance of oxygen (ignoring hypoxic tumor environments). Dioxygen (O_2) contains two outer electrons in different orbitals that are spin parallel. O_2 has a triplet Ms in its ground state and this explains the paramagnetic and diradical natural of O_2. Because both the excited triplet PS and ground state O_2 are in the triplet state, and they have comparable energies, such that orbital interactions between the two molecules is a spin-allowed process and results in either physical or chemical quenching of the excited triplet state PS by O_2. In the physical quenching process, excited triplet state PS energy is transferred to ground state O_2, flipping the spin of a singlet electron and pairing both peripheral electrons in a single orbital. Due to the violation of Aufbau principle, this species, known as singlet oxygen ($O_2(^1\Delta_g)$, $^1O_2$) is highly reactive. Nevertheless, this is a favored process, which does not violate any quantum mechanical rules, as two triplet state molecules generate two singlet state molecules. Moreover, according to basic molecular orbital theory, electron reorientation results in movement into an orthogonal pi antibonding orbital, which is still stable. The generation of $^1O_2$ by excited triplet state PS quenching is known as type II photochemistry.

$^1O_2$ is a metastable species and its lifetime is dependent on its interaction with solvent molecules. $^1O_2$ is approximately 22 kcal mol^{-1} more energetic than the ground triplet state O_2. As $^1O_2$ relaxes to the ground state, it transfers energy to molecules of its immediate surrounding. In protium water (H_2O), $^1O_2$ has a lifetime on the order of 4 μs; however, in deuterated water (D_2O), $^1O_2$ has a lifetime approximately 10-fold longer. It should be noted here that $^1O_2$ might persist in the gaseous state for hours. This secondary kinetic isotope effect has given investigators the ability to determine if the PDT lethality is dependent on $^1O_2$ or radical oxygen species (discussed in Section 10.2.2) generated during PDT by switching experimental solvents from H_2O to D_2O.

10.2.2 Photochemistry

$^1O_2$ may interact with organic molecules in several interesting ways, which do not occur with oxygen in the triplet ground state. Because $^1O_2$ has the same quantum state (singlet) as most commonly encountered molecules, it may react with them readily. $^1O_2$ is an electrophilic agent with a low-lying, asymmetrical LUMO. Moreover, $^1O_2$ has significantly more double bond character than $^3O_2$ allowing it to participate in Diels-Alder [5] as well as other pericyclic reactions.

Excited triplet state PS may be chemically quenched in an entirely different process, affording an entirely different chemical reactivity. Type I photochemical reactions encompass electron transfer, hydrogen abstraction, and photoadditions of the triplet state PS, though it is traditionally considered a radical mechanism. This is because the excited triplet state PS may interact with various electron donor or acceptor molecules. In the case of electron donation, an excited triplet state PS may directly donate its excited electron to oxygen, forming the PS radical cation and a superoxide radical anion ($O_2^{\bullet -}$). $O_2^{\bullet -}$ may then undergo spontaneous or enzyme-catalyzed dismutation forming hydrogen peroxide (H_2O_2). H_2O_2 is not a radical species and is not intrinsically toxic to cells at low concentrations. However, due to the presence of lone pairs on both oxygen atoms of H_2O_2 there is electron repulsion between the two atoms, therefore lengthening the H_2O_2 sigma bond. This means that the H_2O_2 bond is particularly prone to heterolysis, provided a suitable reducing agent is present—H_2O_2 is thus a radical progenitor. This is the case when H_2O_2 is exposed to ferrous iron (Fe^{2+}) or other transition metals (e.g., Cu^+) with a facile X^n/X^{n+1} oxidation potential, in what is known as the Fenton reaction, Eq. (10.1):

$$Fe^{2+} + H_2O_2 \rightarrow Fe^{3+} + HO^- + OH. \tag{10.1}$$

This results in the formation of a hydroxide ion (HO^-), ferric iron (Fe^{3+}), and the hydroxyl radical [6]. $^\bullet OH$ is an extremely reactive species whose diffusion distance is very short and because cells are so prone to severe $^{\bullet}OH$ damage, almost all cells lock Fe^{2+} in heme complexes or iron–sulfur centers and additionally possess the enzyme catalase to convert H_2O_2 to H_2O and O_2. Moreover, while $O_2^{\bullet -}$ is not as oxidizing as $^{\bullet}OH$ and may not get inside of cells as easily, cells possess superoxide dismutase enzymes to convert it to H_2O_2 (only to be subsequently quenched by catalase). $^{\bullet}OH$ is not enzymatically converted into any species, though antioxidants such as reducing sugars (ascorbic acid) and peptides (glutathione) may convert $^{\bullet}OH$ to HO^-. $^{\bullet}OH$ may react with lipids, proteins, and nucleic acids destroying normal biological function of these molecules. Note that radicals may alternatively emerge from PDT by $^1O_2$ action as well. This occurs when $^1O_2$ induces peroxidation of olefin-containing substrates. If biomolecular hydroperoxide adducts are exposed to a suitable reducing agent, they too may form dangerous oxygen radicals (biomolecule-$O^{\bullet}$ adducts) that quickly abstract electrons or hydrogen atoms from surrounding molecules, inducing free radical reactions that are capable of rapidly altering biomolecule structure and function.

10.3 PHOTOSENSITIZER STRUCTURE AND PHOTOPHYSICAL PROPERTIES

Red and near infrared light is ideal for biomedical optics as wavelengths in the ranges of 600–800 nm allow for deeper tissue penetration whilst still permitting electronic excitation. Wavelengths shorter than 600 nm scatter light and absorption of wavelengths greater than 800 nm give increased molecular vibrations. The importance of this 600–800 nm optical window is elaborated in Section 10.4.1.

The PS molecule always contains a chromophore, which, by definition is a cyclic aromatic system with delocalized π-electrons, so they are deeply colored. This is verified by a brief survey of PS classes that includes azine dyes (e.g., acridines, phenothiaziniums), porphyrins (and reduced derivates such as chlorins and bacteriochlorins), phthalocyanines and naphthalocyanines, triarylmethanes, xanthenes, and cyanines. Chromophores typically possess intense absorption in the visible portion of the electromagnetic spectrum when an electron-donating auxiliary group, appropriately known as an auxochrome is present. Moreover, if an auxiliary group is capable of reducing π symmetry in aromatic systems—as is the case with certain chlorins and bacteriochlorins via their isocyclic ring which contains a chlorin-conjugated olefin—further electron delocalization occurs, resulting in a bathochromic shift in photonic absorption as well as increased absorption intensity.

By and large, PS design and synthesis have been driven by at least three considerations. The three main considerations are (1) intense absorption in the optical window, (2) little to no dark toxicity (i.e., PS toxicity only occurs where light of the appropriate wavelength and intensity is applied, (3) high PDT activity and retention of PS in diseased tissue without PS accumulation in healthy tissue.

Furthermore, an ideal photosensitizing agent should be a single pure compound to allow quality control analysis with low manufacturing costs and good stability in storage. It should have a high absorption peak between 650 and 800 nm (red to far red) as absorption of photons with wavelengths longer than 800 nm does not provide enough energy to excite oxygen to its singlet state, and the capacity for forming a substantial yield of reactive oxygen species upon irradiation. It should have no dark toxicity and relatively rapid clearance from normal tissues, thereby minimizing phototoxic side-effects. Other pertinent desirable properties of photosensitizing agents have been summarized [7]. While the interval between drug administration and irradiation is usually long, so that the sensitizer is given sufficient time to diffuse from normal tissues, reports now suggest that the tumor response may be sometimes better when light is delivered at a shorter drug-light interval when PS is still present in the blood vessels, thus producing marked vascular damage [8]. Some reports suggest that a pronounced inflammatory response and necrotic cell death after illumination are important in the immune-stimulating function of PDT, while others suggest that PS that produce more apoptosis and less inflammation are suitable for applications such as brain tumors where swelling is undesirable. Recent findings show that certain PDT-induced apoptotic cell death mechanisms are highly immunogenic and capable of driving antitumor immunity as well [9]. Finally the light-mediated destruction of the PS known as photobleaching was thought to be undesirable, but some reports suggest that this property may make light dosimetry less critical as over-treatment is avoided when the PS is destroyed during the illumination [10].

The first PS to be clinically employed for cancer therapy was a water-soluble mixture of porphyrins called hematoporphyrin derivative (HPD), a purified form which later became known as Photofrin. Although Photofrin is still the most widely employed PS, the product has some disadvantages including a long-lasting skin photosensitivity and a relatively low absorbance at 630 nm. There has been a major effort among medicinal chemists to discover second-generation PS and several hundred compounds have been proposed as potentially useful for anticancer PDT. Table 10.1 displays the most promising PS that have been used clinically for cancer PDT (whether approved or in trials) and their structural formulae are shown in Figure 10.2.

The discovery that ALA was a biosynthetic precursor of the PS protoporphyrin IX [11] has led to many applications in which ALA or ALA-esters can be topically applied, or administered orally. These are considered to be "pro-drugs," needing to be converted to protoporphyrin IX to be active photosensitizers. Successes in treatment of many tumor types (and other lesions mainly in dermatologic sites) have been observed.

The most effective PS tend to be relatively hydrophobic compounds that rapidly diffuse into tumor cells and localize in intracellular membrane structures such as mitochondria and endoplasmic reticulum (ER). More polar compounds tend to be taken up by adsorptive or fluid phase endocytosis and this process is slower necessitating a longer drug-light interval. Many hypotheses have been proposed to account for the tumor-localizing properties in PDT [12]. These include the preponderance of leaky and tortuous tumor blood vessels due to neovascularization and absence of lymphatic drainage known as the enhanced permeability and retention effect [13]. Some of the most effective compounds bind preferentially to low density lipoprotein

TABLE 10.1 **Photosensitizers approved or in clinical trials for cancer**

Photosensitizer	Structure	Wavelength (nm)	Approved	Trials	Cancer types
Photofrin (HPD)	Porphyrin	630	World wide		Lung, oesophagus, bile duct, bladder, brain, ovarian
ALA	Porphyrin precursor	635	World wide		Skin, bladder, brain, oesophagus
ALA esters	Porphyrin precursor	635	Europe		Skin, bladder
Foscan (mTHPC)	Chlorin	652	Europe	USA	Head and neck, lung, brain, skin, bile duct
Verteporfin	Chlorin	690	World wide (AMD)	UK	Ophthalmic, pancreatic, skin
HPPH	Chlorin	665		USA	Head and neck, oesophagus, lung
Purlytin (SnEt2)	Chlorin	660		USA	Skin, breast
Taloporfin, LS11, MACE, Npe6	Chlorin	660		USA	Liver, colon, brain
Fotolon (PVP-Ce6), Radachlorin, Photodithazine	Chlorin	660		Belarus, Russia	Nasopharyngeal, sarcoma, brain
Silicon phthalocyanine (PC4)	Chthalocyanine	675		USA	Cutaneous T cell lymphoma
Padoporfin (TOOKAD)	Bacteriochlorin	762		USA	Prostate
Motexafin lutetium (LuTex)	Texaphyrin	732		USA	Breast

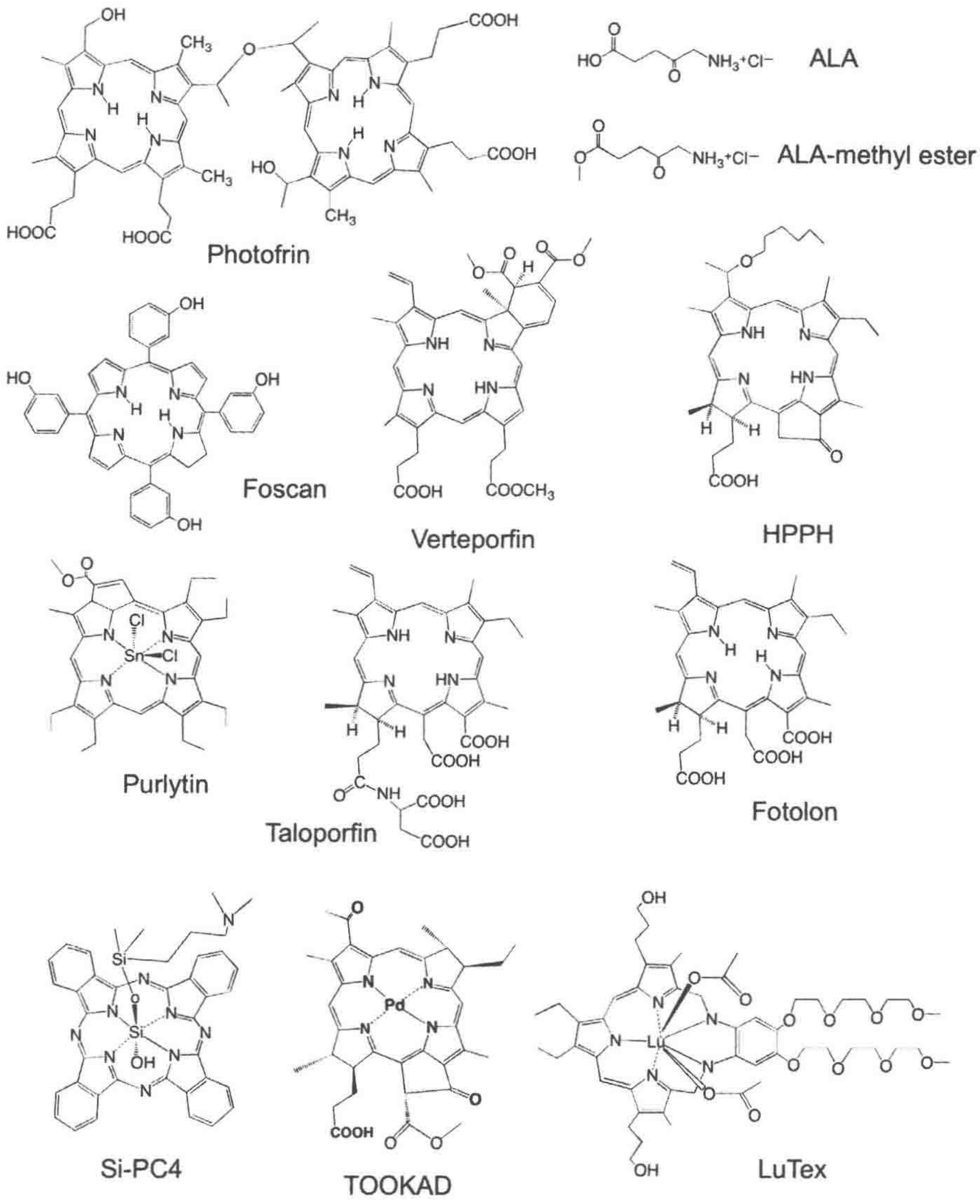
Photofrin
ALA
ALA-methyl ester
Foscan
Verteporfin
HPPH
Purlytin
Taloporfin
Fotolon
Si-PC4
TOOKAD
LuTex

FIGURE 10.2 Chemical structures of the clinically tested PS listed in Table 10.1. Photofrin (HPD), ALA, ALA methyl ester, Foscan (mTHPC), Verteporfin (BPD-MA), HPPH (Photochlor), Purlytin (SnEt2), Taloporfin (MACE, Npe6, LS11), Fotolon (PVP-ce6), silicon phthalocyanine (PC4), TOOKAD (Padoporfin), LuTex (motexafin lutetium).

(LDL), suggesting that upregulated LDL receptors found on tumor cells could be important [14].

There have been targeting studies in which PS are covalently attached to various molecules that have some affinity for neoplasia or to receptors expressed on specific tumors [15]. The intention is to rely on the ability of the targeting vehicle to control localization factors so that the PS can be chosen based on its photochemical properties. These vehicles include monoclonal antibodies, antibody fragments, peptides, proteins such as transferrin, epidermal growth factor and insulin, LDL, various carbohydrates, somatostatin, folic acid, and many others.

10.4 LIGHT DOSIMETRY AND PHOTODYNAMIC THERAPY LIGHT SOURCES

The aforementioned photochemical reactions that lead to select tissue death are due to quantum effects (number of photons absorbed) rather than power density effects (rate at which photons are delivered). Moreover, tissue penetration by light is dependent on the incident power density that is necessary to reach a sufficient photon threshold at a specified depth in tissue.

10.4.1 Tissue Optics

Like all media that light interacts with, tissue is capable of both light absorption and light scattering. However, the heterogeneity of tissue complicates the design of light dosimetry regimens for PDT. Even though tissue is rich with chromophores such as oxygenated hemoglobin and melanin, light is more likely to be scattered before being propagated through cellular media and exciting an endogenous or exogenous chromophore.

Scattering occurs at the microscopic biointerface (e.g., between two tissues, organelles) with different refractive indexes. Fat globules and dense protein compartments have higher refractive indexes than water (1.55 versus 1.33). Hydroxyapatite, the main mineral constituent of bone, has a refractive index of 1.65. The source of scattering in cells is due to intracellular organelles, which generate microscopic boundaries with the cytoplasm. The absorptive properties of tissue are not necessarily the same as the excitation of molecules. For example, water has an absorption spectrum most intense in the 900–1060 nm range, which corresponds to molecular vibrations. The lipid absorption profile is most intense in the 900–950 and 1000–1060 nm ranges, and oxygenated hemoglobin and deoxygenated hemoglobin have peak absorptions in the 500–600 nm range with intense UV absorption.

Melanin is produced by melanocytes that are found in the basal layer of the epidermis with dendritic protrusions extending toward epithelial tissue. This is why metastasis of melanoma is very hard to treat: all cavities of the body are lined with epithelial tissue such that malignant melanocytes can easily invade the epithelium. Melanin has a strong UV absorption with decreased absorption in the red and near-infrared portions of the electromagnetic spectrum. However, the absorption in the 600–800 nm range by melanin is not strong enough to hinder effective phototherapy.

The total tissue attenuation coefficient of any given wavelength of light is equal to the sum of the scattering and absorption at that wavelength. Tissue acts as a short pass filter and the smaller attenuation coefficient for longer-wavelength light has driven the synthesis of PS that absorb in the far-red and near-infrared portions of the electromagnetic spectrum. However, this is seldom an issue in designing PDT regimens, due to the dual spatial selectivity (a consequence of selective PS localization and spatially confined light excitation) of PDT, which limits applications to those diseases that are easily accessible and anatomically shallow.

10.4.2 Fundamental Dosimetry Concepts

PDT dosimetry has been adopted from conventions developed for anticancer radiation therapies. In radiology, absorbed dose is reported in sieverts [16] for biological tissue, where 1 Sv is equal to 1 J kg^{-1}. As a consequence, radiation treatment takes into account the mass and volume of tumor, as determined by imaging modalities, organ motion, and uncertainties of tumor location. However, Sv is an inappropriate unit for PDT, as it fails to take into account the photochemical action of the PS. Moreover, due to the nature of PDT, diseased tissue is accessed from a surface (e.g., a tumor) and taking surface area of the malady into account is of utmost importance. Accordingly, PDT dose is defined as

$$(\mu g_{\mathrm{PS}}/g_{\mathrm{target\ tissue}})\,\mathrm{J\,cm}^{-2}. \tag{10.2}$$

In cases where the PS concentration is homogenous, dosimetry is defined as light dose only (J cm^{-2}). This is evident in cases where PS is known to have high binding affinity to cellular targets, such as in antimicrobial PDT.

10.5 LIGHT-BASED STRATEGIES TO ENHANCE PDT

The significant advances and developments in light-based strategies for achieving selective-enhanced PS concentration on target tissues play a major role in PDT. On the basis of the PDT phenomena, the ooptical excitation of the PS produces reactive oxygen species that cause localized, apoptotic, and/or necrotic cell death. Two-photon absorption has been applied using various chromophores with highly efficient two-photon absorption (TPA) cross-sections that are needed for several innovative applications, such as fluorescence three-dimensional (3D) microscopy, deeper-penetrating PDT, 3D micro- and nanofabrication, high-density optical data storage, and many others. The potential noninvasive application of new modalities—two-photon excitation-PDT (TPE-PDT) and metronomic PDT will be discussed here.

10.5.1 Two-Photon Excitation-PDT

Two-photon excitation (TPE)-PDT which offers the potential for better selectivity and less damage to normal tissue in treating wet age-related macular degeneration is also used in a wide range of applications, ranging from engineering to physiology. Recent advances in TPA and in the design of two-photon chromophores are rapidly increasing the scope of this field. PDT agents are targeted to over-expressed receptor sites in tumors and are also capable of being activated by TPA rather than the one-photon activation mechanism employed in all previous PDT agents. Two-photon PDT has the distinct advantage of exciting these new PS far in the near-infrared (780–900 nm) within the tissue transparency window using pulsed laser light that allows the direct treatment (no surgical intervention) of subcutaneous tumors to depths of several centimeters [17].

The Prasad group has demonstrated the use of infrared excitation in conjunction with an efficient TPA PS in PDT [18]. Certain newly developed organic molecules were studied and it was found that chromophores can act as "photon harvesters" that absorb two photons of near infrared light and transfer the energy to the PS, which can generate $^1O_2$ in the presence of atmospheric oxygen [19]. Shen et al. performed enhanced two-photon $^1O_2$ generation by PS-doped conjugated polymer nanoparticles. They used conjugated polymer, poly[9,9-dibromohexylfluorene-2,7-ylenethylene-alt-1,4-(2,5-dimethoxy)phenylene] (PFEMO), and tetraphenylporphyrin (TPP) showing that these PS-doped conjugated polymer nanoparticles can act as novel PS for two-photon PDT and related applications [20]. Spangler and Starkey et al. have treated human tumor xenografts of human breast cancer (MDA-MB-231) and both small-cell lung cancer (SCLC) (NCI-H69) and non-small-cell lung cancer (NSCLC) (A-459) successfully using targeted two-photon PDT-PS for the treatment of subcutaneous tumors, suggesting that tumors can be treated noninvasively using two-photon PDT [17, 21, 22]. Khurana et al. used endothelial cells (YPEN-1) to assess the TPE-PDT efficacy of the PS Photofrin® and verteporfin (which are known to be effective by one-photon excitation). They incubated a confluent monolayer of endothelial cells with each PS and performed TPE-PDT by irradiating the cell layer with the 865-nm laser line of a femtosecond Ti:sapphire laser at various output powers. They achieved TPE-PDT induced cell death with both PS, where verteporfin was around seven times more effective, consistent with its higher two-photon cross-section. Using verteporfin and by varying the laser dose, they were also able to demonstrate the quadratic intensity dependence of cellular two-photon PDT [23]. Mir et al. compared TP-PDT using Photofrin and phthalocyanines dyes on neovascular age-related macular degeneration (AMD) excited by a femtosecond Ti-sapphire laser [24].

Karotki et al. used Photofrin to demonstrate proof-of-principle of 2-γ killing (damage to tissues by two-photon excitation) of vascular endothelial cells *in vitro*. They established the technique for measuring the 2-γ absorption spectra and cross-sections of PDT sensitizers so as to ensure that there were negligible contributions from 1-γ interactions. Adherent YPEN-1 endothelial cells were incubated with Photofrin for 24 h and then treated by PDT at 850 nm where the 1-γ contribution was negligible which shows that 2-γ excitation dominates over 1-γ excitation above 800 nm [25]. Starkey et al. demonstrated the application of a new 2-γ activated PDT agent which induced xenograft tumor regressions after near-IR laser treatment through the entire body of the host mouse. In their experiment human SCLC (NCI-H69), NSCLC (A549), and breast cancer (MDA-MB-231) xenografts were induced in SCID mice and microarray expression profiles were conducted to assess the similarity of responses to single- and two-photon activated PDT [17]. Thus, application of 2-γ PDT allows spatially selective treatment of cancers and TPA-PDT has an advantage for higher selectivity than one-photon absorption PDT, and femtosecond pulsed laser is further more suitable for TPA-PDT than pico- and nanosecond pulsed lasers.

10.5.2 Metronomic PDT

Metronomic photodynamic therapy (mPDT) is a new methodology, in which both the PS and light are delivered continuously at low rates for extended periods of time to increase selective tumor cell kill through apoptosis. The focus of mPDT treatment is for treating various malignant tumors often in the brain, in which selectivity tumor cell killing versus damage to normal brain is critical. Studies have shown that high-dose ALA can induce necrosis in normal brain (cortex) as well as tumor, whereas an acute low-dose regimen provides tumor-selective apoptosis without necrosis [26] but mPDT with ALA could provide an even greater induction of apoptosis in brain tumor cells without compromising selectivity. Thus, *in vitro* studies confirmed the enhanced induction of apoptosis in 9L gliosarcoma cells after ALA-mPDT as compared with a similar aPDT regimen [27].

Bogaards et al. performed fluorescence-guided resection (FGR) and PDT to evaluate fluorescence imaging and PDT treatment techniques in a specific intracranial tumor model. The model was the VX2 carcinoma grown by injection of tumor cells into the normal rabbit brain. mPDT uses ALA-induced protoporphyrin IX (PpIX) for both FGR and PDT [28]. Studies of "fractionated" PDT, particularly for treating skin tumors using ALA-PpIX, with improved responses have also been reported [29]. Though mPDT has several promising advantages, there are still challenges for clinical implementation like administering the PS continuously during an extended period of time to ensure that a high equilibrium level of drug within the tumor is achieved. In mPDT there is also a need to maintain tumor to normal tissue selectivity and avoid systemic toxicity. Moreover, administering the delivery of light continuously to the entire tumor for a long time in a minimally invasive manner is still being extensively studied. For these reasons researchers have implanted LED sources, such as the linear LED arrays developed for interstitial and endoscopic treatments, into the brain [30]. This procedure is less invasive than repeatedly opening the skull to deal with recurrent brain cancer. Furthermore, the implantation of optical fibers, balloon applicators, or use of organic-LED "patches" connected through the skull to an external laser source have been investigated [31]. All these studies show a promise for metronomic PDT to be used to effectively deal with brain tumors.

10.6 PDT TARGETING AND NANOTECHNOLOGY

The targeted delivery of PS to diseased cells is one of the major challenges in PDT. Nanotechnology has opened a new realm for improving therapeutic strategies, created to overcome growing problems of contemporary medicine, such as drug toxicity and drug resistance. This emerging modality can lead to targeted PDT (TPDT) aiming for improving the delivery of PS to cancer tissue, enhancing specificity and efficiency of PDT simultaneously. The application of nanotechnology has advanced in the field of PDT and has provided hope for the development of nanoscale delivery carriers for PS, which might improve the efficiency of PDT and can overcome many side-effects associated with classical PDT. Nanoparticles (NPs) have high surface-to-volume ratios enabling modification with various surface functional groups; and multifunctional NP capable of targeting molecular motifs, and allowing both imaging and delivery of therapeutics is an exciting area of research that holds great promise for cancer therapy in future. The various recent advances in NP technology may provide a range of novel approaches to PDT [32–34].

NPs exhibit unique pharmacokinetics, including minimal renal filtration that extends circulation in the blood pool depending on the surface functionalization characteristics of the particles [35]. However, these approaches are still at the proof-of-principle stage. Mainly, NPs can improve the delivery of PS, as they can with many other imaging contrast agents or therapeutic compounds form functionalized "nanoplatforms" with two or more functionalities, leading to theranostic (diagnose and treat) NP [36–40]. The main goal of this emerging theranostic field is to gain the ability to image and monitor the diseased tissue, delivery kinetics, and drug efficacy with the long-term hope of tuning the therapy and adjusting the dose with heretofore-unattainable control. Vatansever et al. [36] have illustrated the diversity of the theranostic approach showing some of the components that have been attached to nanostructures to provide multifunctionality in PDT (shown in Fig. 10.3). These

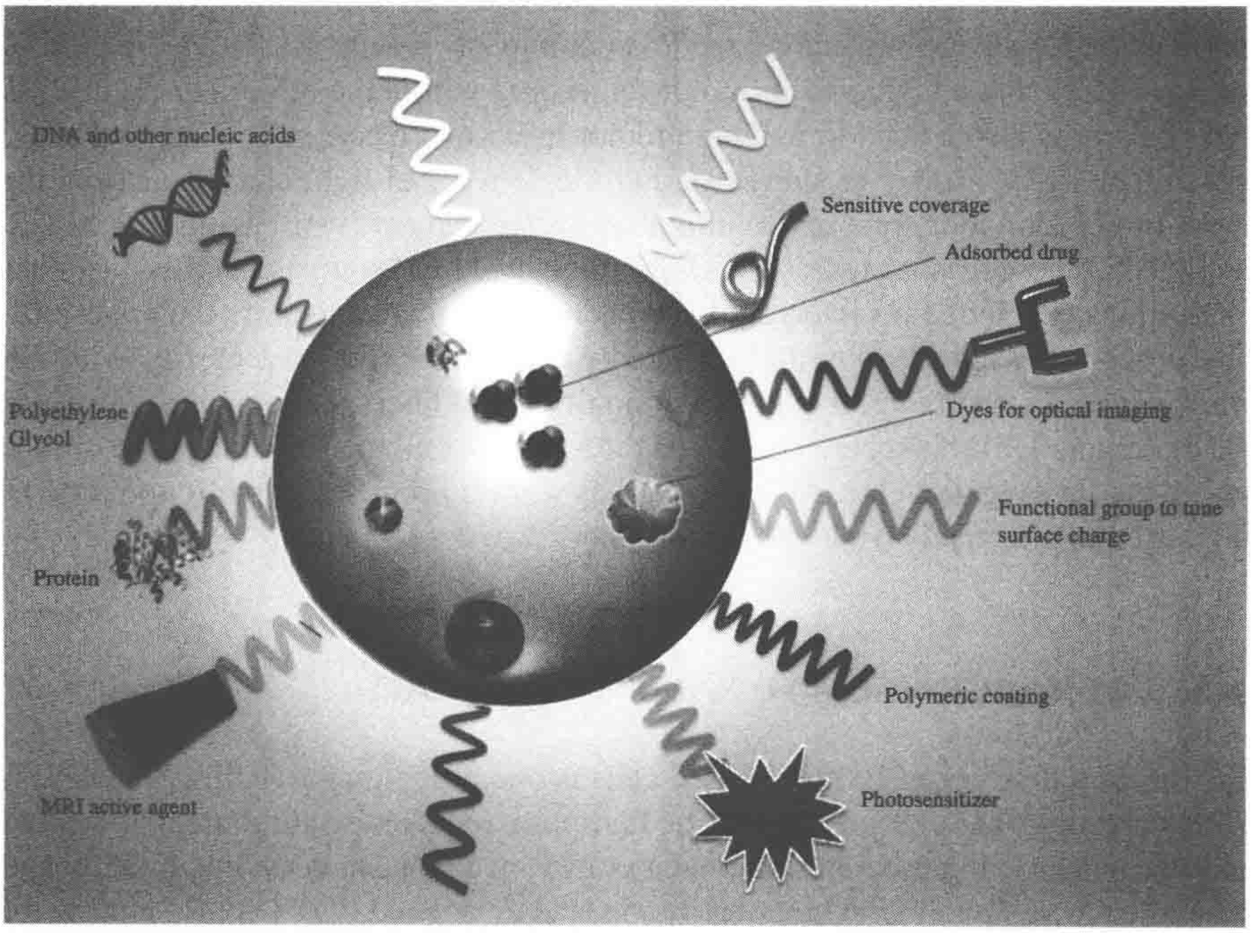
DNA and other nucleic acids
Sensitive coverage
Adsorbed drug
Polyethylene Glycol
Dyes for optical imaging
Functional group to tune surface charge
Protein
Polymeric coating
MRI active agent
Photosensitizer

FIGURE 10.3 Nanoplatforms with theranostic functionalities: Fe_2O_3, magnetic NPs, photosensitizer, appropriate polymeric coating, surface-charge tuning groups, optical imaging dyes, targeting agents, adsorbed/bonded drugs, sensitive coverage, DNA and other nucleic acids, polyethylene glycol, proteins, MRI active agents and so on. Reprinted with permission from Reference 36. (*For a color version of this figure, see the color plate section.*)

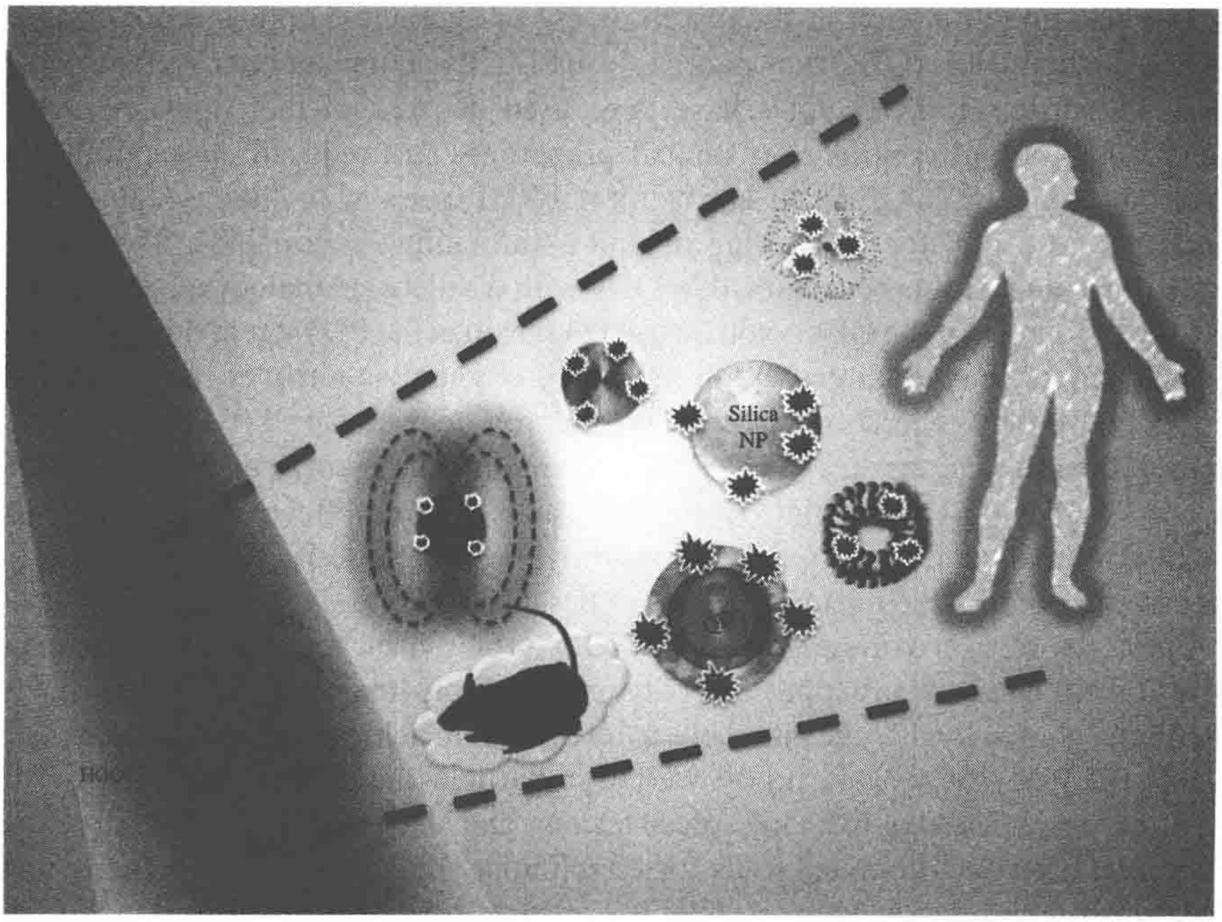

FIGURE 10.4 Nanotechnology taking PDT from bench to bedside. A wide range of lipid, polymer, ceramic, magnetic, and other functionalized nanoparticles have been used in PDT that can improve photosensitizer delivery, together with fullerenes, carbon nanotubes and quantum dots, and raises the question of whether nanotechnology will truly improve the translation of PDT from mouse to man. (*For a color version of this figure, see the color plate section.*)

nanoconstructs have evolved to such an extent that some of them may be able to be injected into the blood stream, circulate harmlessly, and eventually seek out and bind their targets, to deliver a therapeutic payload (as shown in Fig. 10.4).

Nonviral vehicles that are based on synthetic polymers, dendrimers, liposomes, cell-penetrating peptides, and inorganic nanoparticles have been developed and studied in detail for their potential application in PDT [41–44]. These types of vehicle also play a major role and possess the beneficial capability to be easily modified for theranostic purposes. Recently, both the delivery vehicle, as well as DNA, labeled with organic dyes have made the use of more sophisticated imaging techniques, such as time-lapse microscopy, fluorescence resonance energy transfer (FRET), and fluorescence correlation spectroscopy (FCS) [45–47]. These techniques provide more precise information regarding polyplex trafficking, detachment, and leading toward development of theranostic systems. Koo et al. used novel nanoparticles like glycol chitosan nanoparticles (CNPs) for both *in vivo* diagnosis and therapy. They evaluated the *in vivo* biodistribution and tumor site accumulation of CNPs with or without drug by using radioisotopes [48]. Kim et al. also carried out *in vivo* studies on tumor targeting ability in tumor-bearing mice by using the near-infrared fluorescent (NIRF) dye, CNPs, Cy5.5, and noninvasive fluorescence imaging [49].

Due to some limitation in fluorescent dyes, an alternative optical reporter agent such as quantum dots (QDs) may play a role in PDT, by acting as either PS themselves or as PS-carriers [50, 51]. QDs have been used because of their high extinction coefficients, strong control over optical properties, and reduced susceptibility to photobleaching [52]. QDs can easily form FRET pairs with fluorescent organic dyes and are useful for monitoring polyplex trafficking *in vitro* [38]. Samia et al. studied the interaction between CdSe QDs with a silicon phthalocyanine PDT-PS, Pc4. They found that the QDs could be used to sensitize the PDT agent through FRET mechanism, or interact directly with molecular oxygen via a triplet energy-transfer process [53], thus generating reactive $^1O_2$ that can be used for PDT [54]. Rakovich et al. studied PDT properties of novel CdTe quantum dots-methylene blue hybrid PS. *In vitro* studies on HepG2 and HeLa cancer cells showed effective cell kill by the methylene blue-semiconductor nanocrystal hybrid system [55]. However, it is still necessary to understand the metabolism of QDs in the body and related toxicity issues.

Furthermore, iron oxide nanoparticles (IONPs) have been investigated as nanoplatforms on which to construct probes containing multiple imaging motifs that with the ambitious goal to load drugs into these nanosystems to achieve all-in-one theranostic agents for PDT [56, 57]. Recently, Feridex® particles have been approved by the FDA for the detection of liver and spleen lesions, and also the analog Combidex® has entered into phase III clinical trials for lymph node imaging [40]. Also due to their high temperature decomposition, IONPs can play a dual role for imaging/therapy, because of their potential in hyperthermia after excitation by alternating magnetic fields, which has emerged as a useful strategy in nanoparticle preparation for theranostics application.

Recently, fullerenes (closed carbon cages) have shown potential in several different cancer therapeutic approaches such as PDT, photothermal treatment, radiotherapy, and chemotherapy. The Hamblin group has extensively studied fullerenes for their potential application in PDT [58]. Fullerenes can also acts as novel contrast agents in magnetic resonance [59] imaging [60]. However, their non-biodegradability and possible toxicity remain a concern in the area of biomedical applications. The rapid growth in nanotechnology will continue to grow in coming years and will be further studied to potentiate PDT by increasing selectivity and increasing multifunctionality.

10.7 PDT FOR DERMATOLOGY

In 1905, Jesionek and von Tappenier described the first applications of PDT in humans by using eosin and white light to treat a number of dermatologic conditions such as condylomata lata, lupus vulgaris, and nonmelanoma skin cancer (NMSC) [61]. Since then, the list of PDT applications in dermatology has been consistently growing. While treatment of precancerous and malignant skin tumors (mainly NMSC) are the most commonly used applications of PDT; during recent years, we have witnessed a broadening spectrum of so-called off-label uses especially in non-oncological dermatologic conditions [62]. Among them, acne, psoriasis, cutaneous T-cell lymphoma, leishmaniasis, rosacea, photorejuvenation, and warts are just a few examples that have been studied with promising results [62]. While the use of PDT in infectious dermatologic conditions will be covered within a separate section, in this section we will focus on its applications for precancerous and malignant skin tumors, acne vulgaris and photorejuvenation.

10.7.1 Actinic Keratosis

Actinic keratosis (AK) is the most common precancerous lesion of the skin and is frequently seen in the elderly. The lesions develop on areas of chronic ultraviolet exposure such as face and scalp and often occur in multiples at these sites, leading to what is termed *field cancerization.* In a longitudinal study conducted by Marks et al., it was reported that 60% of squamous cell carcinoma (SCC) occurred from progression of AKs [63]. Cryosurgery, 5-fluorouracil, imiquimod, and curettage are the currently used treatment options each with advantages and limitations [64, 65]. In several studies, it has been reported that thin and moderate thickness AK on the face and scalp respond well to ALA-PDT, with typical clearance rates of 89–92% 3 months after therapy, and response was reported to be equivalent or superior to cryotherapy [66–68]. One-year sustained lesion clearance rates following ALA-PDT (up to two treatments) and patch ALA-PDT (single treatment) were 78% and 63–69%, respectively [69,70]. A large randomized intraindividual study with 119 patients compared efficacy of ALA-methyl ester (MAL)-PDT with cryotherapy in treatment of face/scalp AK [68]. MAL-PDT was given as a single treatment and repeated after 3 months if required [68]. The results showed that, after the initial treatment, PDT cleared more lesions (87% vs. 76%) than cryotherapy, and had equivalent outcome when the initial nonresponders were retreated (89% vs. 86%) [68]. In a right/left comparison study with imiquimod, ALA-PDT cleared significantly more moderate AK lesions (58% vs. 37%), and equal numbers of thin AK lesions on the hands/forearms (72% lesions) [71]. However, according to Kaufmann's report, when compared, MAL-PDT was less effective than cryotherapy for acral AK (lesion clearance 78% vs. 88% at 6 months) [72]. This reduced efficacy of PDT for AK on acral sites compared to that for facescalp lesions is probably in part due to a higher proportion of less-responsive thicker lesions on these sites. A few studies also have been done using PDT as a therapy for actinic cheilitis [73–75]. A recent study by Sotiriou et al. demonstrated complete clinical cure of 80% and histological cure of 73% when MAL-PDT and imiquimod 5% cream were used in sequence. Lastly, PDT was suggested to be used for the prevention of nonmelanoma skin cancer in organ transplant recipients and other immunocompromised patients [76]. Apalla and colleagues suggested a preventive potential of field PDT in immunocompromised individuals [76]. They have conducted a study among photodamaged patients with facial AK, where ALA-PDT demonstrated a significant delay over control sites of about 6 months until new AK developed [76]. In an intrapatient randomized study of 27 renal organ transplant patients with AK and other skin lesions, a single treatment with MAL-PDT significantly delayed (9.6 vs. 6.8 months for control site) the development of new lesions; and by 12 months, when 62% of treated areas were free from new lesions, it was only 35% for control areas [77]. PDT was shown to decrease the expression of p53, a marker of early skin cancer, which supports its preventive indication in carcinogenesis [78, 79].

10.7.2 Bowen's Disease/Squamous Cell Carcinoma *In Situ*

Bowen's disease is a form of squamous cell carcinoma (SCC) *in situ* and mainly seen in elderly people. It most often appears as a scaly, crusted, erythematous, well-demarcated plaque on sun-exposed surfaces such as the face, scalp, hands, and lower legs [80]. Once SCC invades into the dermis, which happens in 3–20% of the cases, metastasis develops in more than one-third of the patients [80, 81]. Surgical excision, electrodessication, curettage, and 5-fluorouracil are the common treatment options [82]. Rapid healing time and capacity to treat more than one lesion at a time makes PDT to be an attractive alternative therapy. Unlike surgical excision that can be complicated by wound dehiscence or necrosis, especially in the vascular compromised areas such as the lower legs; PDT is a noninvasive option that spares the tissue and results in less morbidity [83]. A randomized clinical trial by Morton et al. was the first to demonstrate that ALA-PDT was equally effective as cryotherapy [84]. Moreover, while ALA-PDT cleared 100% of lesions after two treatment sessions without disease recurrence, cryotherapy required three sessions for 100% lesion clearance and disease recurrence has been observed [84]. Complications such as ulceration and infection were reported in the cryotherapy group but not in the PDT group [84]. ALA-PDT was also shown to be significantly more effective than 5-fluorouracil in terms of both immediate and long-term efficacy [85]. A large multicenter trial involving 40 European medical centers investigated the efficacy, tolerability, and cosmetic outcome of MAL-PDT for Bowen disease [86]. In this study, Morton et al. observed a 3-month complete response rate of 86%, which was similar to the efficacy of cryotherapy and 5-fluorouracil [86]. However, at 12 months, the sustained lesion complete response rate with MAL-PDT as well as the cosmetic result were superior to the other two modalities [86].

10.7.3 Basal Cell Carcinoma

Basal cell carcinoma (BCC) commonly occurs on the head, neck, and nose. Although it rarely metastasizes, there is always a risk of aggressive growth, causing extensive tissue destruction and significant morbidity [87]. Although the most commonly used therapy for BCC has been surgery or other forms of ablation, in cosmetically sensitive locations such as the face, a noninvasive form of treatment like PDT is an attractive choice [88]. In a review by Peng et al., it was reported that among 826 superficial and 208 nodular BCCs treated with PDT, complete clearance rates of 87% and 53% were achieved at follow-up periods of 3–36 months [89]. However, ALA-PDT when used for treatment of nodular BCCs alone showed a less favorable response [90, 91]. Interestingly, MAL-PDT achieved much better results than ALA-PDT in the treatment of BCCs, especially for nodular BCCs and this may be attributed to its lipophilicity, faster skin penetration, and higher selectivity [62, 92, 93]. According to Rhodes et al.'s [94] report complete response rates between groups treated with surgery versus MAL-PDT did not differ significantly (98% vs. 91%) but at 24-month follow-up, higher recurrence after MAL-PDT (9%) than surgery (2%) was observed. Moreover, in a 5-year follow-up study, the higher recurrence rate with PDT (14%) versus surgery (4%) continued [95]. PDT might be considered a first-line therapy for patients who are not appropriate for surgery such as patients with bleeding disorders or those at high risk of scarring.

10.7.4 Melanoma

Melanoma, a cancer that arises from melanocytes can be cured by surgical resection with almost 80% effectiveness for thin lesions. However, once metastases occur, it is largely refractory to existing therapies [96]. Several *in vitro* and *in vivo* studies as well as a few clinical reports showed encouraging results of the efficacy of PDT, suggesting a possible role as an adjuvant therapy in the management of advanced melanoma. Using different human and mice melanoma cells *in vitro* and *in vivo*, significant apoptosis, necrosis, tumor growth arrest, and prolonged the survival of the animals has been observed; however, complete remission was rarely achieved and/or was followed by recurrence and side effects [97–106]. Clinical reports showed regression of choroidal melanoma and skin melanoma metastasis following PDT [107–109].

PDT-induced acute inflammation attracts leukocytes, mainly neutrophils into the treated tumors. The pro-inflammatory effects of PDT may increase dendritic-cell migration, antigen uptake, and maturation. PDT can create a long-lasting tumor-specific immunity (memory), which was shown in certain mouse and rat models by the rejection of tumors upon rechallenge [59]. When PDT was applied in combination with intratumoral injection of naive dendritic cells, eradication of both CT26 colorectal carcinoma cells in BALB/c mice and B16 melanoma in C57BL/6 mice have been achieved in a significant proportion of animals and among the mice which the tumors were not cured, prolonged survival was observed. However, neither PDT nor intratumoral injection of naive dendritic cells alone were effective. It is also important to note that PDT in combination with intratumoral injection of naive dendritic cells administered to one tumor site led to tumor regression at distant sites, including multiple lung metastases [110]. However, optical interference by the highly pigmented melanin, the antioxidant effect of melanin, the sequestration of PS inside melanosomes, and the efflux of PS by ATP-binding cassette (ABC) transporters were all shown to create resistance against PDT, and specific strategies are required to overcome these resistance mechanisms [111].

10.7.5 Mycosis Fungoides

Mycosis fungoides (MF) is the most common and indolent form of cutaneous T-cell lymphoma (CTCL) with no curative treatment [112]. Response to the current treatment options has been disappointing, and patients with advanced CTCL continue to have poor prognosis [113]. The idea for use of PDT in cutaneous T-cell lymphoma emerged from earlier reports which demonstrated that PpIX produced from ALA preferentially accumulated in malignant T lymphocytes [114]. Even though not many, a few case reports of successful treatment of CTCL lesions with PDT resulting in both clinical and histologic clearance further suggest that this modality might be a good alternative as an additional therapeutic option for patients with lesions resistant to traditional therapy [115–117]. In order to test the effect of PDT in treatment of MF, Edström et al. conducted a study with 10 plaque MF lesions and 2 tumor MF lesions from 10 patients [118]. Upon topical application of 20% ALA to the lesion and the adjacent skin for 5–6 h, the lesion was exposed to red light at around 630 nm [118]. Authors reported complete clinical clearance and no recurrence during the 4–19 months of follow-up for seven of nine plaque lesions, however neither of the tumor lesions responded to PDT. Moreover, histological examination confirmed the regression of the infiltrate following treatment.

10.7.6 Acne Vulgaris

Acne vulgaris is a chronic inflammatory skin disorder and is most commonly seen in adolescents, although it can affect people of any age. Even though pathogenesis of acne vulgaris has not yet been clarified, the current consensus is that it involves four main events: follicular hyperconification, increased sebum secretion effected by the androgenic hormone secretions, colonization of *Propionibacterium acnes*, and inflammation [119]. Current treatment options consist of topical retinoids, benzoyl peroxide, topical or oral antibiotics, and oral isotretinoin for severe cases [120]. Despite the efficacy of oral retinoids and antibiotics in the treatment of acne vulgaris, there is still a necessity for additional treatment options for patients who are resistant, intolerant, or unable to take conventional therapies [121]. The bacterium *P. acnes* which has been implicated in the pathogenesis of acne is known to naturally produce endogenous porphyrins, predominantly coproporphyrin III that can act as natural PS [120]. Given this fact, it was suggested that phototherapy through the absorption of light (specifically blue light) by porphyrins can cause a photochemical reaction and form reactive free radicals and $^1O_2$ that in turn cause destruction of the *P. acnes* and the sebaceous glands [119, 122]. Red light is able to penetrate deeper in tissues when compared to blue light and it has been demonstrated that red light can affect the sebum secretion of sebaceous glands and change keratinocyte behavior [123, 124]. Furthermore, red light might also exert its effects by modulating cytokines from macrophages and other cells, that in turn may reduce inflammation [124, 125].

Blue, green [126], and yellow [53] light have all proved to be effective in the treatment of mild-to-moderate acne vulgaris lesions. Moreover, in the presence of ALA or MAL, the amount of accumulating porphyrins were shown to increase, especially if the temperature was raised [54]. ALA and MAL-PDT were both shown to be effective and safe way of treating acne [55, 56]. Hongcharu et al. reported the first clinical trial for the treatment of acne vulgaris where he used ALA-PDT with a 550–570 nm broad band light source [57]. Since then there have been a number of clinical trials which have demonstrated successful treatment of acne with ALA-PDT with various light sources and regimens [58–61]. In order to increase specificity of treatment and shorten the incubation time, PDT was suggested to be used with intralesional injection of ALA and results were found to be more satisfactory compared to conventional ALA-PDT [62]. Sun avoidance for at least 48 h after treatment is necessary due to the risk of post-treatment photosensitivity [63]. In a study conducted in Korea, a lower concentration of liposome-encapsulated 5-ALA was introduced to minimize this risk [63]. Improved inflammatory acne with minimal side effects was achieved by the end of the study [63]. Use of other PS such as indocyanine green dye (in combination with NIR diode laser—803 or 809 nm) [69] and chlorophyll [70] for the treatment of acne lesions have also been demonstrated. However, side effects in PDT treatment of acne vulgaris were commonly reported which included pain, edema, hyperpigmentation, and blistering rash [127–129]. The clinical trials and case reports of PDT for acne have been critically analyzed in a review by Sakamoto and Anderson [71].

10.7.7 Photorejuvenation

Multiple studies have reported improvement in fine wrinkles, mottled hyperpigmentation, roughness, sallowness, and upregulation of collagen production and increased epidermal proliferation following PDT [130]. In a small randomized split-face study among 10 patients with moderate photodamage, MAL-PDT (1 h vs. 3 h incubation) was shown to improve tactile roughness, fine lines, and skin tightness in most of the patients on the side treated after 3-h incubation [131]. The same group also evaluated the effect of a combination treatment where MAL-PDT was applied to one half of the perioral area following fractional photothermolysis to both sides of the face and the same procedure was repeated at 3 weeks [132]. Improvement in superficial rhytides and overall patient satisfaction was reported to be greater in the combined treatment side [132]. Another split-face study but this time with PDL applied to both sides of the face, 1 h after ALA was applied to one side, improvement in softness and texture and disappearance of solar lentigines was observed on the PDT-PDL side [133].

10.8 PDT FOR ONCOLOGY

PDT is a modality that has been applied for many types of malignant cancers occurring in the head and neck, breast, brain, lung, pancreas, peritoneal cavity, prostate, and skin. Though PDT was discovered in the beginning of the twentieth century, it took 70 more years to apply this technology to cancerous tumors. Diamond et al. hypothesized that the tumor localizing and tumor-phototoxic properties of porphyrins might be exploited for killing cancer cells. *In vivo* studies on rats showed encouraging results by suppressing the growth of gliomas for 10–20 days, but eventually other viable cancer cells from deeper regions started to proliferate [134]. It was not until 1975, that PDT was taken as a serious research topic in oncology, when scientists achieved complete eradication of mammary tumors in mice with hematoporphyrin derivative (HPD). In the same year, there was another significant development when the same compound was used to completely eliminate bladder carcinoma in mice, with red light activation of HPD [135]. Human trials were further carried out in the following year when five patients were diagnosed with bladder cancer using

HPD. PDT with HPD was tried in another human trial where the bladder carcinoma was recurrent in nature. PDT slowed down the tumor growth in this case where the transurethral resections, radiotherapy, and chemotherapy had failed. In a follow-up study with 25 patients diagnosed with 113 tumors, it was found there was complete response in 98 of the tumors, 13 of them showed partial response, and 2 of them showed none [136]. Following this many research groups started experimenting with PDT of tumors in various other parts of the human body.

The next tumors to be treated with PDT were lung tumors [135]. This was followed by esophageal cancer [137], gastric carcinoma [138], brain tumors [139], intraocular tumors [140], breast cancer [141], head and neck tumors [142], colorectal cancer [142], cutaneous malignancies [143], intraperitoneal cancer [144], mesothelioma [145, 146], and pancreatic cancer [147]. The whole spectrum of the known malignant tumors has been studied by PDT experimental approaches by altering various dose-time-concentrations of different PS and light. However, PDT has had its limitations in its potency and specificity of the PS. Another issue at hand was the diagnosed patients were often already at an advanced stage and the tumors had already become refractory to other treatment modalities. Though testing the PS on highly advanced malignant tumors was not an ideal way of testing the potential of PS against tumors, often it was the only avenue available for this experimental therapy. PDT is more a local therapy than a systemic therapy like chemotherapy. So, PDT is not effective in targeting the metastatic cancer cells that had not yet developed into a tumor. Moreover, penetration of light has always been an issue when it comes to treating tumors in various organs in the body.

Since the early days a lot of changes have been made to PS to increase their specificity and potency for tumors. More powerful and selective PS have been developed since then and many are now available in the market. The tumor photodamage and tissue photocytotoxicity (expected downside of PDT) can be controlled by light exposure dose, fluence, wavelength of light used, oxygen availability, and time between administration of drug and the light exposure.

It is well known that the killing of cancer cells through PDT occurs by one or more of three pathways, that is, necrosis, autophagy, or apoptosis. Here, the ROS generated by PDT when the PS are located inside tumor cells the kills them directly. PDT also affects the tumor vasculature leading to tumor infarction. Finally PDT can induce an immune response that leads the host immune system to kill the tumor cells. These three mechanisms are not separate from each other and all occur at the same time. Contributions from all three mechanisms and particularly from the immune system component are needed over a long period of time for complete eradication of the tumor growth and to prevent tumor recurrence.

The direct tumor killing is thought unlikely to be responsible for complete tumor eradication as there is a nonhomogenous distribution of the PS in and around the tumor. The PS in this case is either delivered intravenously and accumulates via the EPR effect. Another possibility is that the PDT effect in and around the tumor reduces the ambient oxygen supply thus affecting the tumor-cell destruction. The photochemical process of the oxygen consumption leaves a gradient of oxygen concentration contributing to the incomplete killing. This rapid depletion in oxygen in the PDT-treated tumor may be both a blessing and a curse. On the one hand, the acute hypoxia after vascular shut-down adds to tumor destruction and necrosis, while on the other oxygen consumption limits the effectiveness of ongoing PDT and may induce hypoxia sensitive tumor survival pathways [148]. This is an area of PDT mechanism that needs considerably more study.

10.9 PDT FOR INFECTIOUS DISEASE

It has been known since the first days of PDT, more than one hundred years ago, that different microorganisms can be killed by the combination of dyes and light *in vitro* [149–151]. Since those days the combination of light and nontoxic dye in the presence of ambient oxygen which underlies PDT has been primarily developed as a treatment for cancer, ophthalmologic disorder, and in dermatology. However, the inexorable increase of antibiotic resistance of pathogenic bacteria due to the excessive and sometimes inappropriate use of antibiotic has led to a focus of attention on PDT as an alternative treatment for infectious disease [152].

Antimicrobial PDT may be a new approach to killing or eliminating pathogens such as bacteria, fungi, protozoa, yeasts, and multicellular parasites [153]. Some advantages of PDT compared to other alternative antimicrobial methods are it is a noninvasive method and there have been no reports of induction of resistance to PDT in any microbes where it has been tested [154]. Moreover, all the studies that have examined the killing of antibiotic resistant bacteria have demonstrated them to be equally susceptible to PDT destruction as their naïve counterparts [155]. Furthermore, PDT kills microbes almost instantly while antibiotics can take hours or days, and PDT is effective in infections in tissues with compromised blood supply where systemic antibiotics do not penetrate.

10.9.1 *In Vitro* Studies of PDT

In the 1990s, it was observed that there was a fundamental difference in susceptibility to PDT between Gram-positive and Gram-negative bacteria; neutral or anionic PS molecules were effective to inactivate Gram-positive bacteria, whereas they are less effective or fail against Gram-negative bacterial cells [156]. The high susceptibility of Gram-positive species compared to Gram-negative is explained by their structural and physiological differences, in particular differences in the structure of the bacterial cell wall. The cell wall of Gram-negative bacteria consists of an inner cytoplasmic membrane and an outer membrane that are separated by the peptidoglycan-containing periplasm. The outer membrane forms a physical and functional barrier between the cell and its environment. This complex structure means Gram-negative bacteria are less permeable to many PS. Several studies have been performed to test new approaches to permit a better PS penetration and improve killing of Gram-negative bacteria using PDT. Nitzan et al. used the polycationic peptide polymyxin B nonapeptide (PMBN), to increase the permeability of the Gram-negative outer membrane and allowed PS to penetrate in the cells where the ROS generated during illumination can cause fatal damage [157].

Malik et al. also studied a mixture of hemin and DP as PS [158]. The effect of the combined mixture was stronger than separate constituents and was as strong in the dark as under illumination [156]. Bertoloni et al. found that the use of ethylenediaminetetraacetic acid (EDTA) to release LPS or the induction of competence with calcium chloride sensitized *E. coli* and *Klebsiella pneumoniae* to PDT by hematoporphyrin or zinc phthalocyanine [159]. A different approach adopted by other groups was to use a PS molecule with an intrinsic positive charge. Methylene blue [160], toluidine blue O (TBO) [161], phenothiazinium dyes [162, 163], or cationic phthalocyanines [164] or cationic porphyrins [165, 166], combined with appropriate light have a bactericidal effect on both Gram-positive and Gram-negative bacteria. It has been demonstrated that for the PS to be effective, it can just come into close contact with the cells. In this case, if $^1O_2$ can be generated in sufficient quantities near to the bacterial outer membrane, it will be able to diffuse into the cell to inflict damage on vital structures [167].

Many improvements have been reported in several *in vitro* studies, to make PDT more effective against Gram-negative bacteria. Choi et al. compared the effect of ALA performing illumination with blue and red light using a LED device against *P. acnes*. *Propionibacterium acnes* was killed with both PDT and by light alone; in particular, blue light was more effective due to the high natural content of porphyrin in the bacteria. The pretreatment with ALA increased significantly the killing of *P. acnes* [168].

Huang et al. reported that polyethylenimine [169] covalently conjugated to chlorin(e6) improved the permeability of the bacteria to the PS and increased the ability to kill Gram-negative bacteria. In a successive study [169], different sized polyethylenimine polymers to form PEI-ce6 conjugates were tested and they showed an improvement of ce6 PDT activity and also PDT effect of all three conjugates investigated depended on pH values [170].

Another group investigated the effect of PDT using a tetracationic mesoarylsubstituted porphyrin (RM24) on *Pseudomonas aeruginosa*, one of the less susceptible bacteria to PDTt. The results showed that photoeradication is dependent on PS concentrations, cellular density, and light dose. RM24 was able to induce oxidative stress mainly by $^1O_2$ formation. A standardized experimental condition of a spot test was used to study PDT sensitivity differences among three strains of *P. aeruginosa* [171, 172].

10.9.2 Photoinactivation of Viruses, Fungi, and Parasites

Many *in vitro* PDT studies on viruses have been performed to allow sterilization of blood or blood products [173, 174]. The reports concluded that lipid-enveloped viruses were more susceptible to PDT than nonenveloped strains. Many of the clinical applications of PDT for localized infections have been performed on lesions of viral etiology. We will discuss more detailed about *in vivo* study and clinical trials in next section.

Several works have focused on the use of PDT to kill yeasts and fungi *in vitro*. Compared with bacteria, studies have shown that various species of yeast and fungi are much less susceptible [175]. Opportunistic fungal pathogens represent an increasing problem for human health especially in immunocompromised patients, due to difficult diagnosis and the fact that not many antifungal drugs are available. The interest in PDT as an alternative antifungal treatment is increasing. Many studies have tried to identify the photochemical and photophysical mechanisms involved in photoinactivation; not only to develop potent and clinically compatible PS but also to understand how photoinactivation is affected by key microbial phenotypic elements (such as multidrug resistance and efflux, virulence factors, and pathogenesis determinants) [175].

Human pathogenic parasites have also been killed by combinations of PS and light. *Plasmodium falciparum,* responsible for malaria, has been killed using *N*-(4-butanol)pheophorbide derivative [176] and also by silicon phthalocyanines [177]. *Trypanosoma cruzi* has been killed by the combination of light and PS such as hematoporphyrin and aluminum-sulfonated phthalocyanine [178]. Human helminth eggs in wastewater were inactivated by a cationic *meso-substituted* porphyrin and light [179].

10.9.3 Animal Models of Wound Infections

Over the years, numerous studies have been designed to investigate the effects of PDT on prevention and treatment of infectious diseases utilizing animal models of infection, to mimic closely the real disease observed in humans. In *in vivo* studies of PDT, one of the major difficulties is monitoring the development of the infection in animal models and its response to treatment. To facilitate the noninvasive monitoring of animal models of infection, Hamblin and his group developed a procedure that uses bioluminescent genetically engineered bacteria and a light-sensitive imaging system to allow real-time visualization of infections also developing several mouse models of localized infections that can be followed by bioluminescence imaging (Figs. 10.5 and 10.6). It is common for wounds to become infected with different, clinical relevant bacterial strains. Different animal wounds have been used to mimic the wounds observed in humans such as surgical-site wounds, burns, dermal excision, incision, abrasions, lacerations, and open fractures. Hamblin et al. [172,180] reported the first time the use of mouse wound infection models to investigate the effect of PDT on treating excisional wounds infected with *Escherichia coli* and *Pseudomonas aeruginosa.* Many wound models such as abrasion and surgical-site wounds infected with different Gram-positive and Gram-negative bacterial strains have been used to investigate the efficacy of PDT using different PS to investigate also their ability to kill bacteria [53,181,182]. Wong et al. [162] and Zolifagehari et al. [183] studied in animal models of wounds, the effect of methylene blue and TBO mediated PDT on *Vibrio vulnificus* and methicillin-resistant *Staphylococcus aureus* wound infections, respectively.

Burns very commonly undergo infection. In past years, the majority of patients with serious burns died from related infections. Pathogens like *Pseudomonas aeruginosa*, *S. aureus*, and filamentous *Candida* are frequently responsible for the burn infections.

Using a guinea pig model, Orenstein et al. [184] studied the effect of porphyrins on the eradication of *S. aureus* in burns. The wounds, third-degree burns, induced on the back of guinea pigs were infected with 10^8 CFU of *S. aureus.* A reduction of 99% of the viable bacteria was achieved treating with PDT.

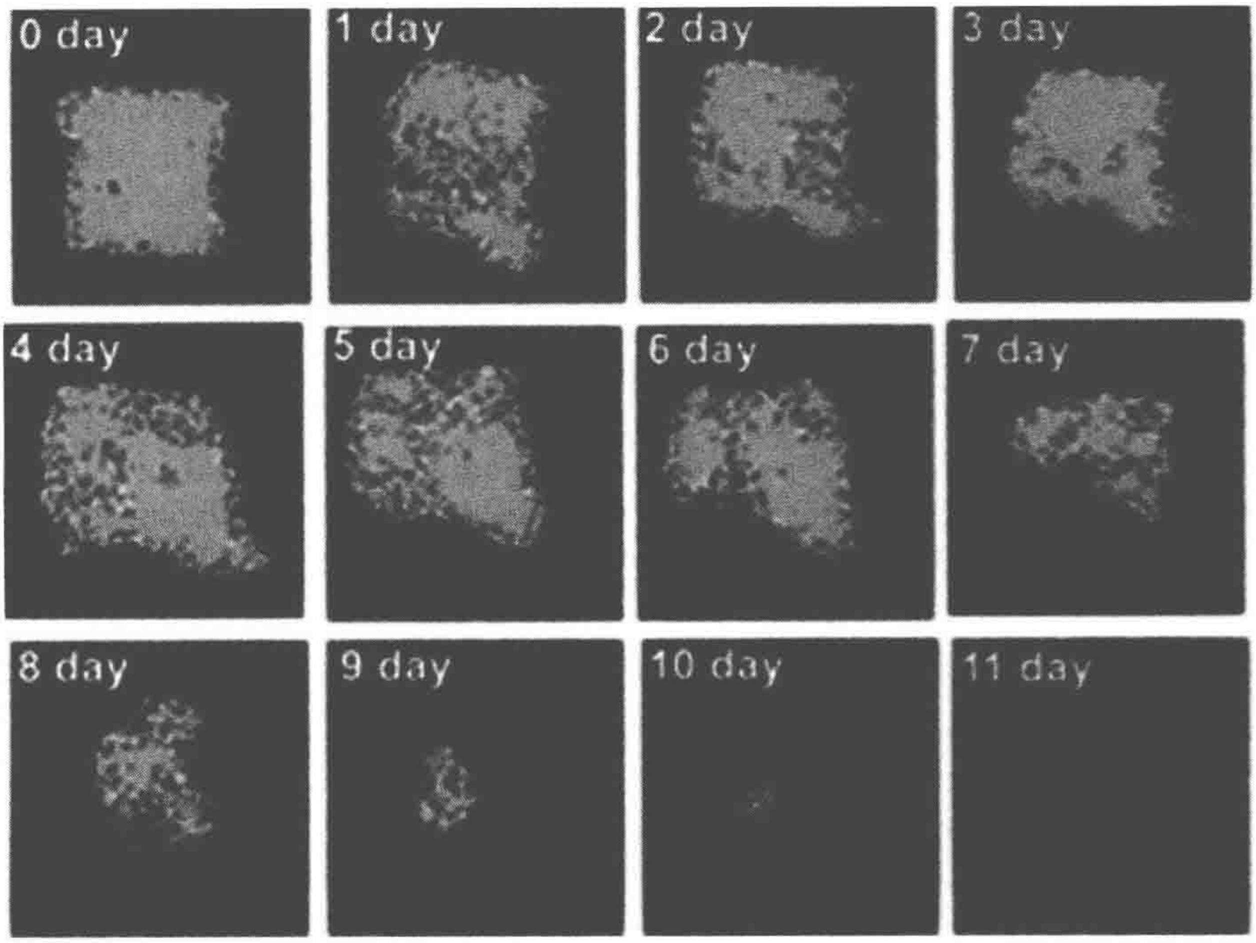

FIGURE 10.5 Bioluminescent MRSA infection in mouse skin abrasion. Successive bioluminescence images of a representative mouse skin scratch model infected with 10^8 CFU MRSA. Reprinted with permission from Reference 53. (*For a color version of this figure, see the color plate section.*)

Lambrechts et al. [185] and Dai et al. [186] employed mouse models to evaluate PDT for *S. aureus* and *Acinetobacter baumannii* burn infections, respectively. Burns were created on the backs of mice by applying two preheated (95°C) brass blocks on the backs of mice for 10 seconds. PDT inactivated significantly both *S. aureus* and *A. baumannii*.

→

FIGURE 10.6 PDT treatment of MRSA infection in mouse skin abrasion. (a–e). Successive bioluminescence images of a representative mouse skin scratch model infected with 10^8 CFU MRSA treated with (a) light alone, (b) PDT using RLP068/Cl, or (c) PDT using TBO at 30 min after bacterial inoculation + 15 min from PS application. PDT was carried out with a combination of 75 μL PS and 84 J cm^{-2} red light, (d) RLP068/Cl or (e) TBO alone after 30 min from bacterial inoculation + 15 min after application of PS. Animals were imaged at 2, 6, and 14 min, without to be exposed to light, (f) Dose response of mean bacterial bioluminescent of mouse scratch abrasion infected with MRSA after treatment with light alone, RLP068/Cl and TBO dark controls and PDT using RLP068/Cl or TBO assuming as TIME 0 the end of 10 min. Reprinted with permission from Reference 53. (*For a color version of this figure, see the color plate section.*)

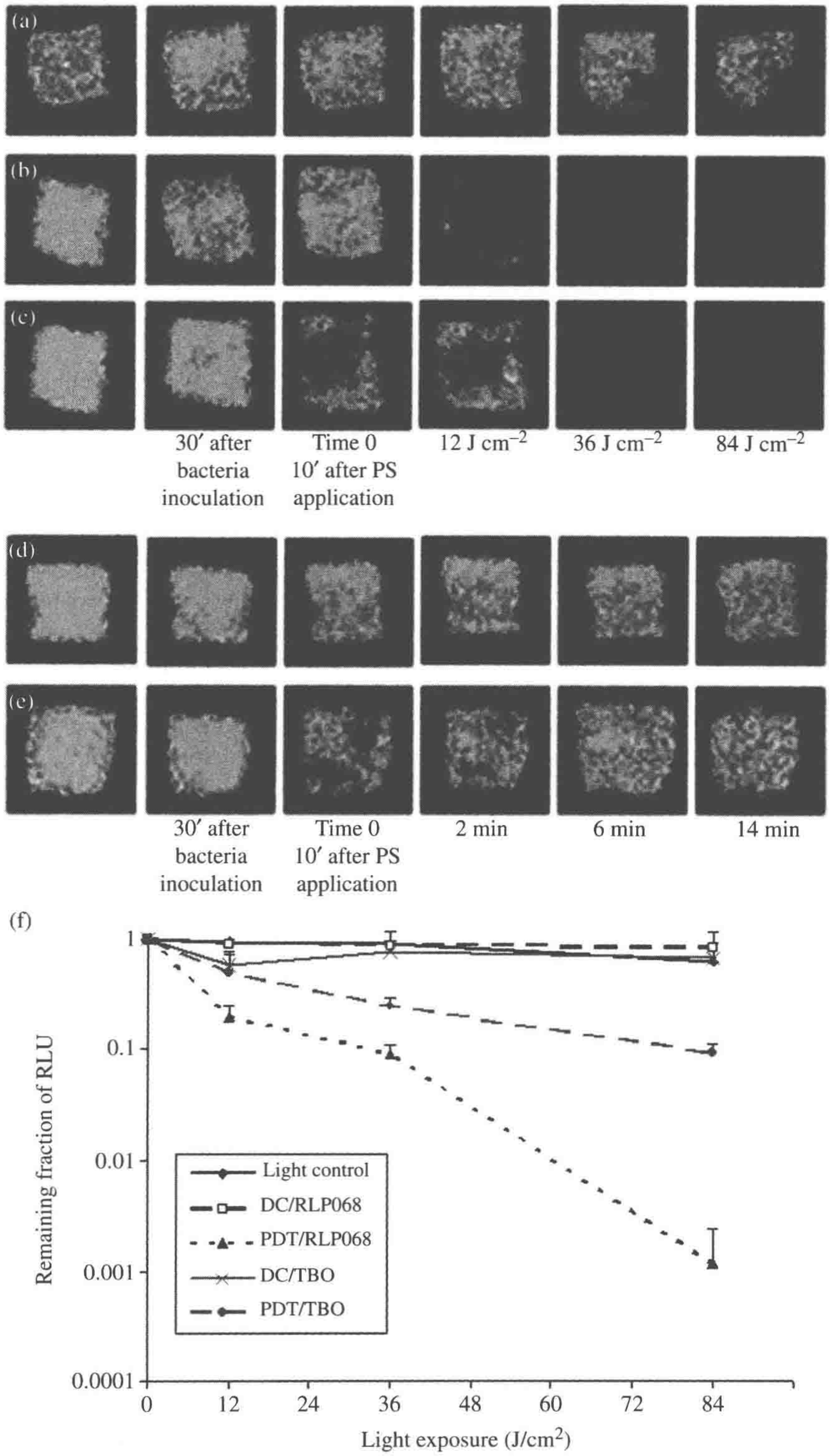
(a)
(b)
(c)
30′ after bacteria inoculation
Time 0 10′ after PS application
12 J cm^{-2}
36 J cm^{-2}
84 J cm^{-2}
(d)
(e)
30′ after bacteria inoculation
Time 0 10′ after PS application
2 min
6 min
14 min
(f)
Remaining fraction of RLU
1
0.1
0.01
0.001
0.0001
0
12
24
36
48
60
72
84
Light exposure (J/cm^2)
Light control
DC/RLP068
PDT/RLP068
DC/TBO
PDT/TBO

Other studies investigated the effect of PDT in soft tissue infections. This kind of infections can induce a high risk of mortality. A commonly used animal model of a localized soft-tissue infection is the intramuscular injection of a bacterial suspension into the mouse thigh muscle. This has been carried out with many bacterial species including *E. coli*, *Pseudomonas aeruginosa*, and *S. aureus*. Berthiaume et al. [187] investigated the effect of PDT against *Pseudomonas aeruginosa* using bacteria mixed *in vitro* with the tin(IV) chlorin e6-monoclonal antibody conjugate and shining the light after injection. The significant decrease of bacteria was demonstrated. Gad et al. [188] used luminescent bacteria and studied the PDT for *S. aureus* infection in soft tissue. *Staphylococcus aureus* cells were used to infect the wound and found that there was a light dose-dependent reduction of bioluminescence.

10.9.3.1 Clinical Applications of PDT in Infected Wounds Not many clinical trials of PDT have been reported in the treatment of localized bacterial infections. In one trial, five patients with brain abscesses after craniotomy and surgical drainage were treated with hematoporphyrin into the abscess followed by illumination. The study produced a positive clinical response [189]. Preliminary results have been obtained from a UK-based study on the effect of PDT mediated by a new phenothiazinium derivative (PP904) when applied on no healing leg ulcers infected with bacteria. Brown et al. (2009) found a reduction of bacteria and an improvement in wound healing. These are only preliminary results that need to be confirmed [190]. A study case has been reported by Clayton and Harrison [191], a significant improvement in the healing of an infected leg ulcer was observed in a 72-year-old patient who was treated with topical ALA-PDT twice weekly over 4 weeks. More studies are necessary to clarify how much of this improvement was due to the antimicrobial effect.

10.9.4 Oral and Dental Infections

Many *in vitro*, *in vivo*, and *ex vivo* studies have been carried out in oral and dental infections. Peri-implantitis, periodontitis, periodontal diseases, endodontic infection, and oral candidiasis are the most common oral infections and several studies have been carried out to verify the efficacy of PDT against the main bacteria responsible of this kind of infections.

Significant reduction of *Actinobacillus actinomycetemcomitans*, *Porphyromonas gingivalis*, and *Prevotella intermedia* was reported in PDT treatment of peri-implantitis, using TBO [192]. Moreover, in peri-implantitis dog models have been demonstrated a reduction of *Prevotella* sp., *Fusobacterium* sp., and *Streptococcus betahaemolyticus*. Bacteria were not 100% destroyed in all samples [193] but a second study showed a 99.8% reduction of *Prevotella* [194].

In *in vivo* models [169, 195–197] of periodontitis, different PS have been tested. TBO significantly reduced *P. gingivalis* [169], a similar effect was observed in a beagle dog model using chlorin(e6) as PS, whereas BLC1010 (a new chlorin(e6) photosensitizer) did not kill bacteria during the PDT test [196].

Recently, Bottura et al. demonstrated the effect of PDT on reducing bone loss caused by experimental periodontitis in immuosuppressed rats [198]. In another study [16], the effect of PDT on inflammatory cells was evaluated. The treatment of chronic periodontitis by PDT leads to a specific decrease of antigen-presenting cells populations according to the drug delivery system. The incomplete eradication of biofilm microorganisms, observed in periodontal diseases, could be due to restricted penetration of PS in oral biofilm [199] or the ability of bacterial cells to expel PS via multidrug resistance pumps [200]. To improve the penetration of the PS, poly(lactic-*co*-glycolic) (PLGA) nanoparticles were used as carriers of MB. The results suggested that PLGA nanoparticles had the potential to be used as nanocarriers of MB, to diffuse in biofilms and release the encapsulated drug in active form [201].

Ex vivo extracted teeth have been used to test PDT for endodontic infections. *Enterococcus faecalis* is the pathogen most commonly associated with current endodontic infections [202]. Several studies have been carried out to evaluate the effect of toluidine blue [203,204], methylene blue [204–206], and a conjugate between polyethylenimine and chlorin(e6) [207] with PDT in endodontic treatment. The effect of PDT was also evaluated on the inactivation of *C. albicans* in oral candidiasis. Mima et al. evaluated the efficacy of using hematoporphyrin with PDT in an animal model of oral candidiasis [208]. Candidiasis was verified by the presence of white patches or pseudomembranes on the dorsal tongue associated with a significant number of CFU per mL of *C. albicans*. PDT significantly reduced the viability of *C. albicans*. In a previous study, a dose-dependent photoeradication of *C. albicans* in an immunodeficient murine model was described [209]. In this study, Teichert et al. evaluated the efficacy of using methylene blue (MB)–mediated PDT to treat oral candidiasis in an immunosuppressed mouse model, mimicking the disease found in human patients. The results indicated a MB-dependent effect of PDT, and completed eradication of fungi from the oral cavity.

10.9.4.1 Clinical Applications of PDT in Oral and Dental Infections PDT for dental infectious represents the largest growth area of clinical antimicrobial PDT. This is because three companies are actively involved in clinical trials and are marketing therapies that are still relatively unknown among the general medical and dental profession. In PDT of periodontitis, the PS is usually injected into the dental pocket followed soon after by light delivery into the dental pocket using a narrow fiber optic tip. de Oliveira et al. [195] compared PDT with TBO with scaling and rooting planing (SRP) using manual instruments in 10 patients with aggressive periodontitis. Both treatments had similar clinical effects. Additional application of a single application of PDT to SRP resulted in significantly higher reduction of bleeding scores than using SRP alone [210,211]. Braun et al. [212] reported PDT administered after SRP treatment in patients with *Fusobacterium nucleatum* infected periodontitis reduced periodontal inflammatory symptom and successfully treated *F. nucleatum* infection [213]. Ruhling et al. [214] compared PDT using TBO with ultrasonic debridement in persistent pockets of maintenance patients and found that both therapies performed similarly. Another application of antimicrobial PDT in dentistry is in the sterilization of endodontic root canals in patients who are being treated for necrotic pulp and periapical lesions. PDT can be combined with the usual mechanical debridement and chemical antimicrobials. Pinheiro et al. [215] reported a significant reduction in viable bacteria using TBO + urea peroxide preparation and red light in addition to mechanical instrumentation to sterilize root canals in children with deciduous teeth with necrotic pulps.

10.9.5 *Leishmania*

Leishmania parasites can lead to mortality and morbidity. Mucocutaneous leishmaniasis can lead to infections that may be restricted to cutaneous sites involving the multiplication of microorganisms in the mucous membranes. Also, in visceral leishmaniasis, they can spread throughout the reticuloendothelial system.

Akilov et al. [216–218] reported the use of a mouse model to study the efficacy of PDT for cutaneous leishmaniasis. Parasites were inoculated intradermally into each ear of mice. PDT was performed 3 weeks after infection. Two PS were used, (3,7-bis(*N*,*N*-dibutylamino)-phenothiazinium bromide (PPA904) and ALA-PPIX. Mice were sacrificed 5 days after PDT and the load of parasites was quantified. Using both PS reduction of the parasite was observed, but in case of ALA there was also tissue destruction.

10.9.5.1 Clinical Applications of PDT in Leishmaniasis Leishmaniasis is a disease caused by protozoan parasite transmitted by bite of certain species of sand fly. Cutaneous Leishmaniasis is the most common form of Leishmaniasis. A weekly treatment of 10% ALA PDT with red light (630 nm, 100 J cm^{-2}) was more effective than topical paromomycin [219]. PDT with 75 J cm^{-2} red light performed for 12 weeks also showed good results [220]. *Leishmania tropica* infection which proved to be resistant to various therapeutic regimes was effectively treated by PDT [153].

10.9.6 *Mycobacterium tuberculosis*

Mycobacterium tuberculosis manifests as latent infection or progressive contagious disease. The predominance of these infected cases is in the latent form; the remainder is active and often contagious.

O'Riordan et al. [221, 222] developed a mouse model of localized mycobacterial infection and used PDT to treat this infection *in vivo*. A subcutaneous pocket made in a line along the dorsal surface of each mouse and collagen implants were placed at either side of the dorsal midline and the incisions then closed with nylon sutures. Three PS were tested in the studies: verteporfin, benzo[a]phenothiazinium chloride, and benzo[a]phenoselenazinium chloride. Monitoring with real-time fluorescence imaging was used to track the delivery of the PS to the infected sites. The concentration of 10^5 CFU of *M. bovis* induced granulomas, a significant reduction in viable mycobacterial cells was demonstrated in PDT-treated granulomas.

10.9.7 Otitis Media with Effusion (OME)

Bacterial infections contribute to the OME a diffuse infection among children. By using a gerbil model, Jung et al. [223] evaluated the antibacterial effects of PDT *in vivo* on *Haemophilus influenzae* and *Streptococcus pneumoniae*, responsible for OME. Bacteria were injected through the bullae and PDT using Photogem solution was performed 2 days after the infection by laser illumination. The results showed a significant reduction of both bacterial strains; in particular, PDT was effective in killing *Streptococcus pneumoniae* in 87%, whereas it was effective in eradicating *H. influenzae* in 50% of the infected bullae with OME.

10.9.8 Osteomyelitis

Other studies have focused on the effect of PDT in the treatment of osteomyelitis. In a study, Bisland et al. [224] used a bioluminescent strain of biofilm-producing *S. aureus* grown onto kirschner wires (K-wire). *Staphylococcus aureus-coated* K-wires were exposed to methylene blue (MB) or ALA-mediated PDT either *in vitro* or following implant into the tibial medullary cavity of Sprague-Dawley rats. The infection was monitored using bioluminescence. *Staphylococcus aureus* infections were subject to PDT 10 days post inoculation. Treatment comprised administration of ALA resulted in significant delay in bacterial growth and inhibited biofilm formation on implants in bone.

10.9.9 Viral Infections

Another relevant field that has been investigated is PDT for viral infections. Smetana et al. [225] inoculated herpes simplex virus (HSV) on the backs of guinea pigs resulting in a local infection after 24 hours. The treatment with ALA-PDT either immediately or up to 6 hours after infection produced a beneficial effect. The treatment at this time determined no HSV could be isolated whereas ALA-PDT, 2 days after infection, had no effect on the HSV titer.

10.9.9.1 Clinical Applications of PDT in Viral Infections The first clinical trials for PDT in infectious disease were directed toward viral lesions. Topical PDT was commonly tested to treat herpes simplex lesions. Proflavine PDT was able to inactivate herpes keratitis [226]. However, other studies showed PDT to be ineffective [227–229]. Several clinical trials have been conducted using PDT against viral infections, especially human papilloma virus (HPV). Systemic and topical PDT has been used to treat papillomatosis caused by HPV. Systemic treatment of 48 patients significantly decreased papilloma growth rate compared to control patients. A follow-up for 3 years of subset of patients confirmed that the improvement was maintained [230]. Abramson et al. [231] and Bujia et al. [232] reported similar results. ALA-PDT has been largely used to treat cutaneous warts caused by HPV. In a study, 42 of the 48 plantar warts in 31 patients, who received ALA, showed complete response and no significant side effects postoperation. In another study, white light was shown to be more effective compared to red or blue light and also standard cryotherapy in 30 patients recalcitrant warts [233]. ALA-PDT achieved excellent results also on three patients with recalcitrant facial warts [234]. It has been suggested that the beneficial effect of treatment of HPV infections by PDT is because of its anti-inflammatory and antiproliferative effects in the lesions [235]. The efficacy of the PDT treatment has been tested also in condyloma acuminata, the genital warts caused by HPV. In women, HPV can also infect the uterine cervix and may lead to the development of cervical intraepithelial neoplasia (CIN) and cervical cancer depending on the virus subtype. PDT with polyhematoporphyrin improved cytological measures when treating CIN and also eradicated HPV [236]. Similar results were obtained using photolon [237] and 5-ALA [238]. Topical application of 5-ALA PDT also successfully treated 13 of the 14 cases of anogenital condyloma accuminata [239]. Topical ALA or MAL-PDT has also been used to treat condyloma in the vulva, vagina, and penis wherein selective accumulation of PPIX was demonstrated in the lesions [238, 240]. The response observed after PDT treatment in genital lesions could dependent on the immune response as discussed in the study of Abdel-Hady et al. [241].

A study [242] on PDT mediated by benzoporphyrin derivative was used in a photopheresis technique in 10 HIV-1 infected patients. In photopheresis, isolated leukocyte-rich fraction (buffy coat) from the blood was incubated with BPD for 30 minutes and exposed it to UVA light in a specialized photopheresis apparatus and reinfused back to the patient. In the first protocol of this study, the pheresis was repeated for a total of nine treatments. Subsequently, the protocol was changed for a total of 24 pheresis sessions. Three patients who had rapidly rising viral loads prior to initiating therapy stabilized. Two had a sustained greater than 0.5 log decrement and five had stable plasma viral loads (less than a 0.5 log increment or decrement) with varied effects on absolute CD4- and CD8-positive lymphocyte counts. One patient achieved a greater than 1.0 log decrement in HIV-1 plasma viral load and undetectable *in vivo* cell-free and cell-associated HIV-1 infectivity with an increased *in vitro* lymphocyte mitogen stimulation index.

10.9.10 Clinical Applications for Peptic Ulcer Disease (PUD)

Another field of application of PDT for clinical trials has been PUD, a human disease of gastrointestinal tract with the presence of ulceration in mucosa layer, usually associated with *Helicobacter pylori* infection. Wilder-Smith et al. performed the first clinical trial [243] irradiating with blue and white light 13 HP-positive volunteers in a zone of gastric tantrum HP. The number was greatly reduced in biopsies treated with ALA and blue or white light compared to control. Hamblin et al. [244] showed that *H. pylori* naturally accumulates the photoactive porphyrins, coproporphyrin, and protoporphyrin, thus the bacterial cells should be intrinsically sensitive to photoinactivation without any added PS, especially when blue light is applied. On this basis, Ganz et al. [245] used endoscopically delivered blue light (405 nm, 40 J cm^{-2}) to eradicate *H. pylori* in regions of gastric antrum in 10 patients who were positive for the bacterium. In a pilot study on 18 patients with *H. pylori infection*, the whole stomach was illuminated with blue light. They obtained largest reduction in bacterial load in the antrum of the stomach (>97%) followed by body (>95%) and fundus (>86%) [246]. However, lasting eradication of bacteria was not achieved with a repopulation of bacteria in days following illumination.

PDT to treat infections is in its infancy and there are some limitations that need to be overcome. PDT for infection is limited to the areas of body where light can be delivered relatively easily such as skin and body cavities. More study will be necessary to find new methods to administer PS and to delivery the light. Moreover, for clinical applications, it is necessary to optimize PS that need to be approved. The clinical applications of antimicrobial PDT have been slow, however although a few clinical trials have been carried out for different infectious diseases, the positive results obtained in periodontitis gives hope that PDT could be used to clinically treat a higher number of different kind of infectious diseases.

10.10 PDT IN OPHTHALMOLOGY

PDT was first approved 10 years ago for age-related macular degeneration (AMD). Thereafter, it was approved by choroidal neovascularization (CNV) in pathological myopia. It is a minimally invasive treatment and has an excellent side effect profile. The treatments of idiopathic choroidal neovascularization, secondary CNV in inflammatory diseases of the retina and choroid, choroidal haemangioma, vasoproliferative tumors, malignant melanoma of the choroid, and central serous chorioretinopathy with PDT was performed with some remarkable results; however, in this section we will mainly focus on CNV associated with AMD [247].

In neovascular or wet AMD, new vessels grow under the retina distorting vision and also leading to scarring [248]. This is exacerbated if the blood vessels leak [248]. Laser photocoagulation and recently introduced antibody therapies are the only treatments for AMD with proven long-term benefits; however, there are certain limitations for laser photocoagulation treatment [249]. First, only 10–15% of all neovascular lesions are small enough and sufficiently delineated by fluorescein angiography to be eligible for laser treatment. Second, even if laser treatment is initially successful, there is at least 50% chance that leakage will reoccur within the next 2 years. Fortunately, with careful monitoring following laser treatment, when detected early recurrences are amenable to additional laser treatment. Third, at least half the patients with sufficiently well-circumscribed neovascular lesions have some initial leakage beneath the center of the fovea.

PDT has been investigated for treatment of neovascular membranes without affecting the retina. The advantage of PDT is that the process of destruction can be confined to the area of choroidal neovascularization by the intravenous administration of a PS and irradiation of solely this region. PDT with verteporfin (Visudyne®) was the first approved therapy for treating the subfoveal lesions and is usually administrated in liposomal formulation [250,251]. There are multiple aspects of the selectivity in the angio-occlusion by PDT [249] concerning vascular damage and the subsequent blood flow stasis. This selectivity is inherent in the short time interval between the drug injection and the light application (i.e., 15 minutes after the start of the intravenous injection of the Visudyne, when the 83-second irradiation takes place, most of the drug that is in the retina is still within the blood vessels, and more specifically, on or in the endothelial cells lining the CNV that are to undergo the angio-occlusion. This ensures that the PDT effect takes place only in the endothelium being irradiated. A second possible reason for the observed selectivity is that retinal vessels will empty of Visudyne fluorescence significantly faster than the choroidal vessels. Thus at the time of irradiation, the retinal capillaries appear to have much less drug in them than the CNV and choroidal vessels in general. This may well imply a significant level of protection of the retinal capillaries. Third, retinal capillaries are protected by the blood retinal barrier, which signifies among others tighter junctions between endothelial cells and hence probably more resistance to PDT.

The effect of AMD with PDT has been investigated by treating subfoveal CNV which had some fraction of classic CNV [252, 253]. Other inclusion criteria in the study was greatest linear diameter of less than or equal to 5.4 mm, and a visual acuity at baseline between 20/40 and 20/200. The best results were achieved for the predominantly classic lesions. Thirty-one percentage of the placebo group lost less than three lines (of visual acuity), whereas 59% of the PDT-treated eyes lost less than three lines (of visual acuity). Large visual acuity losses (i.e., more than 6 lines or 30 letters) were relatively rare in the PDT-treated group as compared to more than one-third of the patients (36%) in the placebo group. Improvement in visual acuity by more than three lines was found in 9% of the PDT-treated patients at the end of this 2-year study and was rarely observed in the placebo group. In the Verteporfin-In-PDT (VIP) study, patients were enrolled with occult subfoveal lesions [254–256]. Again, losses in visual acuity were statistically significantly less in the PDT-treated group as compared to the placebo group, with the best results obtained for the smaller lesions. Outcome, in terms of letters/lines gained or lost, was also better for those patients with the worse visual acuity at baseline.

Data were obtained from a large fraction of the previous patient groups (both the placebo and PDT-treated groups), during a 3-year time period and results demonstrated that the mean change in vascular acuity from baseline was quite similar at 24 months (−1.5 lines) and at 60 months (−1.6 lines) and no additional safety issues were noted [257]. The treatment rate (number of treatments/year), which was decided based on fluorescein angiography (i.e., leakage), was significantly lower in the third, fourth, and fifth years as compared to the first 2 years. These data suggest that PDT for treating CNV associated with AMD remains a standard therapy for patients with recent progression of wet age-related macular degeneration with subfoveal CNV.

The effects of PDT on subfoveal or juxtafoveal (CNV) secondary to pathologic myopia with verteporfin in Japanese patients were compared with the visual outcomes of PDT-treated patients with that of age-matched and visual acuity-matched untreated controls. In this study, 43 eyes of 42 patients with pathologic myopia were treated with PDT for their myopic CNV. The patients were monitored continually for a period of little over than a year taking the age and initial acuity, by matching them with the untreated controls. The results indicated that PDT was beneficial for maintaining vision in Japanese patients with myopic CNV. The visual outcome after PDT was better than the natural course of the disease as compared with the controls [258].

10.11 PDT AND THE IMMUNE SYSTEM

The unique properties of PDT may offer the hope of combination approaches such as PDT plus activation of the immune system during antitumor PDT. The mechanisms that operate to allow PDT to destroy tumors are multifactorial. The photophysical mechanism mentioned in Section 10.2.1 plays a major role in triggering the immune system because many effects of PDT on cancer cells that are grown in tissue culture have been reported that, if replicated *in vivo*, would make activation of the immune system probable after PDT treatment in patients as the combination of PS with their activating light causes an unusual mixture of apoptotic and necrotic cell death [259–261]. There is also an effect against the tumor vasculature whereby illumination produces the shutdown of vessels that subsequently deprives the tumor of oxygen and nutrients [259]. PDT has effects on cancer cells that make immune activation more likely in an *in vivo* tumor treated with PDT. PDT can induce strong expression of heat shock proteins (especially HSP70) [262, 263] that has been shown to potentiate immune recognition of tumors. PDT can cause activation of the transcription factors such as nuclear factor kappa B (NFκB) [264] and activator protein (AP)-1 [265], leading to the production of a large variety of inflammatory mediators including eicosanoids and interleukins (ILs) 1, 6, 8, and 10. Neutrophils are an important cell type for the PDT response [266] and if mice are depleted of neutrophils before PDT, the curative effect is lost [267]. PDT has been shown to induce both a systemic neutrophilia and a strong and prolonged tumor infiltration by neutrophils. In addition, tumor infiltration by dendritic cells (DCs), macrophages, and mast cells has been observed [268]. Complement activation is also observed both in the tumor and serum after PDT [269]. Nevertheless, it is clear that although PDT has the potential to stimulate a systemic antitumor immune response in animal models of cancer, this favorable result is not always observed. The explanation for this observation may be due to variations in the immunogenicity and antigen expression of different syngeneic mouse tumors, the presence of immune suppression caused by regulatory T-cells (Tregs), or the existence of DC dysfunction caused by the tumor.

There are extensive studies that examine the pathways of apoptosis that are induced after PDT in both normal and tumor cells in tissue culture, such as signaling pathways, mitochondrial events, and mediators of apoptosis. Many studies have examined the relationship between the mode of tumor cell death (by methods other than PDT) and the efficiency of induction of the immune response both *in vitro* and *in vivo* [270,271]. Sluiter et al. showed the importance of neutrophils in producing an effective response to PDT in some (but not all) tumor models. They demonstrated that neutrophils adhere to the microvascular wall after PDT *in vivo*, but PDT did not stimulate the expression of P-selectin (one of the principal adhesion molecules that bind leukocytes) by endothelial cells (ECs). The ECs retracted after PDT, which enabled neutrophils to adhere to the subendothelial matrix by their β2-integrin adhesion receptors, and this could be blocked by anti-β2-integrin antibodies86. This finding was supported by a report, which showed that expression levels of the adhesion molecules intercellular adhesion molecule 1 (ICAM1) and vascular cell adhesion molecule 1 (VCAM1), were downregulated in ECs after PDT [272]. The administration of antirat neutrophil serum with PDT in rhabdomyosarcoma-bearing rats completely abrogated the normal PDT-induced retardation of tumor growth [267], which showed that an influx of neutrophils is required for an effective anti-tumor response in this model. An increase in the number of peripheral-blood neutrophils was found 4 hours after PDT treatment, and lasted for 24 hours. The increase in neutrophils was preceded by an increase in serum levels of IL1β. Anti-GCSF (granulocyte colony-stimulating factor) antibodies decreased neutrophil numbers and decreased the efficacy of PDT [273].

Another major study by Korbelik et al. showed that Photofrin-based PDT cured 100% of EMT6 mammary sarcomas in syngeneic BALB/c mice, but no long-term cures were observed in non-obese diabetic (NOD), severe combined immunodeficient (SCID), or nude mice. The adoptive transfer of splenic T-lymphocytes from naive BALB/c mice into SCID mice before PDT postponed the recurrence of treated tumors, whereas adoptive transfer carried out immediately or 7 days after PDT had no benefit. Adoptive transfer of nonadherent splenocytes (a mixture of CD4+ and CD8+ T cells with some B cells, NK cells, and monocytes) from normal mice cured of EMT6 tumors by PDT 5 weeks previously, fully restored the curative effect of PDT on EMT6 tumors that were growing in SCID mice. Splenocytes obtained from donors that were cured by X-rays were much less effective. The depletion of specific T-cell populations from donor splenocytes indicated that CD8+ cytotoxic T-lymphocytes had the most curative effect, whereas CD4+ helper T cells played a supportive role [274]. Hamblin and coworkers have illustrated the various mechanism of PDT inducing immune system as shown in Figure 10.7 [275].

Finally, PDT has a significant effect on the immune system, which can be either immunostimulatory, or in some cases immunosuppressive [59].

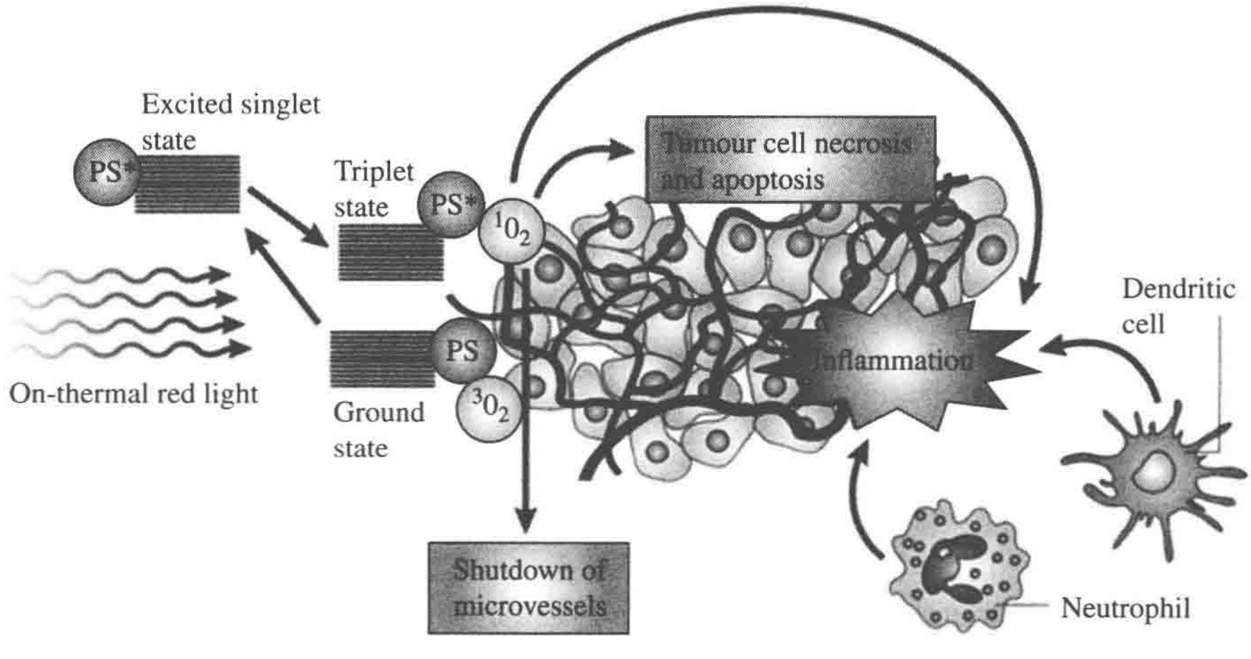

FIGURE 10.7 The mechanism of action of PDT on tumors. The photosensitizer (PS) absorbs light and an electron moves to the first short-lived excited singlet state. This is followed by intersystem crossing, in which the excited electron changes its spin and produces a longer-lived triplet state. The PS triplet transfers energy to ground-state triplet oxygen, which produces reactive singlet oxygen ($^1O_2$). $^1O_2$ can directly kill tumor cells by the induction of necrosis and/or apoptosis, can cause destruction of tumor vasculature, and produces an acute inflammatory response that attracts leukocytes such as dendritic cells and neutrophils. Reprinted with permission from Reference 59. (*For a color version of this figure, see the color plate section.*)

10.12 CONCLUSION

Since PDT was discovered 112 years ago, the field has come a long way. PDT is arguably the most interdisciplinary therapeutic approach in modern biomedical research. There are thriving research efforts by chemists to design and synthesize novel PS, and by nanotechnologists to formulate PS in smart, targeted and theranostic nanoconstructs. Physicists are studying tissue optics, light dosimetry, and photophysical mechanisms, while engineers are designing more versatile and less-expensive light sources based on LED and OLED arrays rather than cumbersome and expensive lasers. Cell biologists have a fertile arena to probe deeper into cell signaling, transcription factors, and epigenetics that govern the cellular response to PDT. Microbiologists are heavily involved in dissecting the molecular pathogenesis pathways and virulence factors that govern how microbes both cause diseases and respond to PDT. Translational researchers are devising an ever-more comprehensive and realistic panel of animal models to test PDT for a diverse range of diseases. Finally, clinicians are increasingly initiating clinical trials of PDT and utilizing PDT in their own practices. Dermatology may be the most mature clinical specialty for PDT usage, but oncology, dentistry, and ophthalmology are close runners up. Infectious disease is perhaps the area that is thought to have the most potential for future growth, while immunology is considered to be a largely unexplored area in which PDT may possibly lead to a cure for advanced metastatic cancer if the factors that govern the activation of the immune response can be fully understood.

ACKNOWLEDGMENT

This work was supported by the US NIH (R01AI050875).

REFERENCES

[1] A. F. Barbosa, B. B. Sangiorgi, S. L. Galdino, M. Barral-Netto, I. R. Pitta, and A. L. Pinheiro, "Photodynamic antimicrobial chemotherapy (PACT) using phenothiazine derivatives as photosensitizers against *Leishmania braziliensis*," *Lasers Surg. Med.* **44**, 850–855 (2012).

[2] K. Kusuzaki, S. Hosogi, E. Ashihara, T. Matsubara, H. Satonaka, T. Nakamura, A. Matsumine, A. Sudo, A. Uchida, H. Murata, et al., "Translational research of photodynamic therapy with acridine orange which targets cancer acidity," *Curr. Pharm. Des.* **18**, 1414–1420 (2012).

[3] R. L. Lipson and E. J. Baldes, "The photodynamic properties of a particular hematoporphyrin derivative," *Arch. Dermatol.* **82**, 508–516 (1960).

[4] Z. Malik and H. Lugaci, "Destruction of erythroleukaemic cells by photoactivation of endogenous porphyrins," *Br. J. Cancer* **56**, 589–595 (1987).

[5] T. Moller, M. B. Sarosi, and E. Hey-Hawkins, "Asymmetric phospha-diels-alder reaction: a stereoselective approach towards p-chiral phosphanes through diastereotopic face differentiation," *Chemistry* **18**, 16604–16607 (2012).

[6] G. R. Shusterman, J. Fluke, Y.-Y. T. Yuan, National Child Abuse and Neglect Data System, United States Department of Health and Human Services, Office of the Assistant Secretary for Planning and Evaluation, and Walter R. McDonald & Associates, *Male Perpetrators of Child Maltreatment: Findings from NCANDS* (U.S. Department of Health and Human Services, Office of the Assistant Secretary for Planning and Evaluation, Washington, DC, 2005).

[7] R. R. Allison and C. H. Sibata, "Oncologic photodynamic therapy photosensitizers: a clinical review," *Photodiagnosis Photodyn. Ther.* **7**, 61–75 (2010).

[8] B. Chen, T. Roskams, and P. A. de Witte, "Antivascular tumor eradication by hypericin-mediated photodynamic therapy," *Photochem. Photobiol.* **76**, 509–513 (2002).

[9] A. D. Garg, D. Nowis, J. Golab, P. Vandenabeele, D. V. Krysko, and P. Agostinis, "Immunogenic cell death, DAMPs and anticancer therapeutics: an emerging amalgamation," *Biochim. Biophys. Acta.* **1805**, 53–71 (2010).

[10] M. Ascencio, P. Collinet, M. O. Farine, and S. Mordon, "Protoporphyrin IX fluorescence photobleaching is a useful tool to predict the response of rat ovarian cancer following hexaminolevulinate photodynamic therapy," *Lasers Surg. Med.* **40**, 332–341 (2008).

[11] F. S. De Rosa and M. V. Bentley, "Photodynamic therapy of skin cancers: sensitizers, clinical studies and future directives," *Pharm. Res.* **17**, 1447–1455 (2000).

[12] M. R. Hamblin and E. L. Newman, "On the mechanism of the tumour-localising effect in photodynamic therapy," *J. Photochem. Photobiol. B* **23**, 3–8 (1994).

[13] A. K. Iyer, K. Greish, T. Seki, S. Okazaki, J. Fang, K. Takeshita, and H. Maeda, "Polymeric micelles of zinc protoporphyrin for tumor targeted delivery based on EPR effect and singlet oxygen generation," *J. Drug. Target* **15**, 496–506 (2007).

[14] D. Kessel, "The role of low-density lipoprotein in the biodistribution of photosensitizing agents," *J. Photochem. Photobiol. B* **14**, 261–262 (1992).

[15] S. A. Sibani, P. A. McCarron, A. D. Woolfson, and R. F. Donnelly, "Photosensitiser delivery for photodynamic therapy. Part 2: systemic carrier platforms," *Expert Opin. Drug. Deliv.* **5**, 1241–1254 (2008).

[16] S. Seguier, S. L. Souza, A. C. Sverzut, A. R. Simioni, F. L. Primo, A. Bodineau, V. M. Correa, B. Coulomb, and A. C. Tedesco, "Impact of photodynamic therapy on inflammatory cells during human chronic periodontitis," *J. Photochem. Photobiol. B* **101**, 348–354 (2010).

[17] J. R. Starkey, A. K. Rebane, M. A. Drobizhev, F. Meng, A. Gong, A. Elliott, K. McInnerney, and C. W. Spangler, "New two-photon activated photodynamic therapy sensitizers induce xenograft tumor regressions after near-IR laser treatment through the body of the host mouse," *Clin. Cancer Res.* **14**, 6564–6573 (2008).

[18] M. Pawlicki, H. A. Collins, R. G. Denning, and H. L. Anderson, "Two-photon absorption and the design of two-photon dyes," *Angew. Chem. Int. Ed.* **48**, 3244–3266 (2009).

[19] J. D. Bhawalkar, N. D. Kumar, C. F. Zhao, and P. N. Prasad, "Two-photon photodynamic therapy," *J. Clin. Laser. Med. Surg.* **15**, 201–204 (1997).

[20] X. Shen, L. Li, H. Wu, S. Q. Yao, and Q. H. Xu, "Photosensitizer-doped conjugated polymer nanoparticles for simultaneous two-photon imaging and two-photon photodynamic therapy in living cells," *Nanoscale* **3**, 5140–5146 (2011).

[21] C. W. Spangler, J. R. Starkey, A. Rebane, F. Meng, A. Gong, and M. Drobizhev, "Synthesis, characterization and preclinical studies of two-photon-activated targeted PDT therapeutic triads," *Proc. SPIE,* **6139**, 61390X–61390X (2006).

[22] C. W. Spangler, A. Rebane, J. Starkey, and M. Drobizhev, "Targeted two-photon PDT photo-sensitizers for the treatment of subcutaneous tumors," *Proc. SPIE*, **7380**, 73803Z–73803Z (2009).

[23] M. Khurana, H. A. Collins, A. Karotki, H. L. Anderson, D. T. Cramb, and B. C. Wilson, "Quantitative in vitro demonstration of two-photon photodynamic therapy using photofrin and visudyne," *Photochem. Photobiol.* **83**, 1441–1448 (2007).

[24] Y. Mir, J. E. van Lier, J. F. Allard, D. Morris, and D. Houde, "Two-photon absorption cross section of excited phthalocyanines by a femtosecond Ti-sapphire laser," *Photochem. Photobiol. Sci.* **8**, 391–395 (2009).

[25] A. Karotki, M. Khurana, J. R. Lepock, and B. C. Wilson, "Simultaneous two-photon excitation of photofrin in relation to photodynamic therapy," *Photochem. Photobiol.* **82**, 443–452 (2006).

[26] L. Lilge, M. Portnoy, and B. C. Wilson, "Apoptosis induced in vivo by photodynamic therapy in normal brain and intracranial tumour tissue," *Br. J. Cancer* **83**, 1110–1117 (2000).

[27] S. K. Bisland, L. Lilge, A. Lin, R. Rusnov, and B. C. Wilson, "Metronomic photodynamic therapy as a new paradigm for photodynamic therapy: rationale and preclinical evaluation of technical feasibility for treating malignant brain tumors," *Photochem. Photobiol.* **80**, 22–30 (2004).

[28] A. Bogaards, A. Varma, K. Zhang, D. Zach, S. K. Bisland, E. H. Moriyama, L. Lilge, P. J. Muller, and B. C. Wilson, "Fluorescence image-guided brain tumour resection with adjuvant metronomic photodynamic therapy: pre-clinical model and technology development," *Photochem. Photobiol. Sci.* **4**, 438–442 (2005).

[29] E. R. de Haas, H. C. de Vijlder, H. J. Sterenborg, H. A. Neumann, and D. J. Robinson, "Fractionated aminolevulinic acid-photodynamic therapy provides additional evidence for the use of PDT for non-melanoma skin cancer," *J. Eur. Acad. Dermatol. Venereol.* **22**, 426–430 (2008).

[30] J. Chen, L. Keltner, J. Christophersen, F. Zheng, M. Krouse, A. Singhal, and S. S. Wang, "New technology for deep light distribution in tissue for phototherapy," *Cancer J.* **8**, 154–163 (2002).

[31] H. Hirschberg, S. Madsen, K. Lote, T. Pham, and B. Tromberg, "An indwelling brachytherapy balloon catheter: potential use as an intracranial light applicator for photodynamic therapy," *J. Neurooncol.* **44**, 15–21 (1999).

[32] M. Ferrari, "Cancer nanotechnology: opportunities and challenges," *Nat. Rev. Cancer* **5**, 161–171 (2005).

[33] S. K. S. Ying-Ying Huang, H. C. Tianhong Dai, A. Yaroslavsky, M. Garcia-Diaz, J. Chang, L. Y. Chiang, and M. R. Hamblin, "Can nanotechnology potentiate photodynamic therapy?," *Nanotechnol. Rev.* **1**, 111–146 (2012).

[34] A. Gupta, P. Avci, M. Sadasivam, R. Chandran, N. Parizotto, D. Vecchio, W. C. de Melo, T. Dai, L. Y. Chiang, and M. R. Hamblin, "Shining light on nanotechnology to help repair and regeneration," *Biotechnol. Adv.* **31**, 607–631 (2012).

[35] F. Alexis, E. Pridgen, L. K. Molnar, and O. C. Farokhzad, "Factors affecting the clearance and biodistribution of polymeric nanoparticles," *Mol. Pharm.* **5**, 505–515 (2008).

[36] F. Vatansever, R. Chandran, M. Sadasivam, L. Y. Chiang, and M. R. Hamblin, "Multifunctionality in theranostic nanoparticles: is more always better?," *J. Nanomed. Nanotech.* **3** (2012), http://dx.doi.org/10.4172/2157-7439.1000e4120.

[37] S. Bhaskar, F. Tian, T. Stoeger, W. Kreyling, J. M. de la Fuente, V. Grazu, P. Borm, G. Estrada, V. Ntziachristos, and D. Razansky, "Multifunctional Nanocarriers for diagnostics, drug delivery and targeted treatment across blood-brain barrier: perspectives on tracking and neuroimaging," *Part Fibre Toxicol.* **7**, 3 (2010).

[38] S. S. Kelkar and T. M. Reineke, "Theranostics: combining imaging and therapy," *Bioconjug. Chem.* **22**, 1879–1903 (2011).

[39] X. Ma, Y. Zhao, and X. J. Liang, "Theranostic nanoparticles engineered for clinic and pharmaceutics," *Acc. Chem. Res.* **44**, 1114–1122 (2011).

[40] J. Xie, S. Lee, and X. Chen, "Nanoparticle-based theranostic agents," *Adv. Drug Deliv. Rev.* **62**, 1064–1079 (2010).

[41] T. Niidome and L. Huang, "Gene therapy progress and prospects: nonviral vectors," *Gene. Ther.* **9**, 1647–1652 (2002).

[42] S. Akhtar, "Non-viral cancer gene therapy: beyond delivery," *Gene Ther.* **13**, 739–740 (2006).

[43] C. Ruggiero, L. Pastorino, and O. L. Herrera, "Nanotechnology based targeted drug delivery," *Conf. Proc. IEEE Eng. Med. Biol. Soc.* **2010**, 3731–3732 (2010).

[44] S. Perni, P. Prokopovich, J. Pratten, I. P. Parkin, and M. Wilson, "Nanoparticles: their potential use in antibacterial photodynamic therapy," *Photochem. Photobiol. Sci.* **10**, 712–720 (2011).

[45] Y. Matsumoto, K. Itaka, T. Yamasoba, and K. Kataoka, "Intranuclear fluorescence resonance energy transfer analysis of plasmid DNA decondensation from nonviral gene carriers," *J. Gene. Med.* **11**, 615–623 (2009).

[46] P. Schwille, "Fluorescence correlation spectroscopy and its potential for intracellular applications," *Cell Biochem. Biophys.* **34**, 383–408 (2001).

[47] H. Sahoo and P. Schwille, "FRET and FCS–friends or foes?," *Chemphyschem* **12**, 532–541 (2011).

[48] H. Koo, M. S. Huh, I. C. Sun, S. H. Yuk, K. Choi, K. Kim, and I. C. Kwon, "In vivo targeted delivery of nanoparticles for theranosis," *Acc. Chem. Res.* **44**, 1018–1028 (2011).

[49] K. Kim, J. H. Kim, H. Park, Y. S. Kim, K. Park, H. Nam, S. Lee, J. H. Park, R. W. Park, I. S. Kim, et al., "Tumor-homing multifunctional nanoparticles for cancer theragnosis: simultaneous diagnosis, drug delivery, and therapeutic monitoring," *J. Control Release* **146**, 219–227 (2010).

[50] R. Bakalova, H. Ohba, Z. Zhelev, M. Ishikawa, and Y. Baba, "Quantum dots as photosensitizers?," *Nat. Biotechnol.* **22**, 1360–1361 (2004).

[51] E. Yaghini, A. M. Seifalian, and A. J. MacRobert, "Quantum dots and their potential biomedical applications in photosensitization for photodynamic therapy," *Nanomedicine (London)* **4**, 353–363 (2009).

[52] U. Resch-Genger, M. Grabolle, S. Cavaliere-Jaricot, R. Nitschke, and T. Nann, "Quantum dots versus organic dyes as fluorescent labels," *Nat. Methods* **5**, 763–775 (2008).

[53] D. Vecchio, T. Dai, L. Huang, L. Fantetti, G. Roncucci, and M. R. Hamblin, "Antimicrobial photodynamic therapy with RLP068 kills methicillin-resistant *Staphylococcus aureus* and improves wound healing in a mouse model of infected skin abrasion PDT with RLP068/Cl in infected mouse skin abrasion," *J. Biophotonics* **6**, 733–742 (2012).

[54] A. C. Samia, X. Chen, and C. Burda, "Semiconductor quantum dots for photodynamic therapy," *J. Am. Chem. Soc.* **125**, 15736–15737 (2003).

[55] A. Rakovich, D. Savateeva, T. Rakovich, J. F. Donegan, Y. P. Rakovich, V. Kelly, V. Lesnyak, and A. Eychmuller, "CdTe quantum Dot/Dye hybrid system as photosensitizer for photodynamic therapy," *Nanoscale Res. Lett.* **5**, 753–760 (2010).

[56] S. Lee and X. Chen, "Dual-modality probes for in vivo molecular imaging," *Mol. Imaging* **8**, 87–100 (2009).

[57] J. Xie, J. Huang, X. Li, S. Sun, and X. Chen, "Iron oxide nanoparticle platform for biomedical applications," *Curr. Med. Chem.* **16**, 1278–1294 (2009).

[58] S. K. Sharma, L. Y. Chiang, and M. R. Hamblin, "Photodynamic therapy with fullerenes in vivo: reality or a dream?," *Nanomedicine (London)* **6**, 1813–1825 (2011).

[59] A. P. Castano, P. Mroz, and M. R. Hamblin, "Photodynamic therapy and anti-tumour immunity," *Nat. Rev. Cancer* **6**, 535–545 (2006).

[60] Z. Chen, L. Ma, Y. Liu, and C. Chen, "Applications of functionalized fullerenes in tumor theranostics," *Theranostics* **2**, 238–250 (2012).

[61] A. Jesionek and V. H. Tappeiner, "Behandlung der hautcarcinome nut fluorescierenden stoffen," *Dtsch. Arch. Klin. Med.* **85**, 223–227 (1905).

[62] Y. Lee and E. D. Baron, "Photodynamic therapy: current evidence and applications in dermatology," *Semin. Cutan. Med. Surg.* **30**, 199–209 (2011).

[63] R. Marks, G. Rennie, and T. S. Selwood, "Malignant transformation of solar keratoses to squamous cell carcinoma," *Lancet* **1**, 795–797 (1988).

[64] S. M. Dinehart, "The treatment of actinic keratoses," *J. Am. Acad. Dermatol.* **42**, 25–28 (2000).

[65] M. H. Gold and M. S. Nestor, "Current treatments of actinic keratosis," *J. Drugs Dermatol.* **5**, 17–25 (2006).

[66] D. J. Piacquadio, D. M. Chen, H. F. Farber, J. F. Fowler, Jr., S. D. Glazer, J. J. Goodman, L. L. Hruza, E. W. Jeffes, M. R. Ling, T. J. Phillips, et al., "Photodynamic therapy with aminolevulinic acid topical solution and visible blue light in the treatment of multiple actinic keratoses of the face and scalp: investigator-blinded, phase 3, multicenter trials," *Arch. Dermatol.* **140**, 41–46 (2004).

[67] M. Tarstedt, I. Rosdahl, B. Berne, K. Svanberg, and A. M. Wennberg, "A randomized multicenter study to compare two treatment regimens of topical methyl aminolevulinate (Metvix)-PDT in actinic keratosis of the face and scalp," *Acta. Derm. Venereol.* **85**, 424–428 (2005).

[68] C. Morton, S. Campbell, G. Gupta, S. Keohane, J. Lear, I. Zaki, S. Walton, N. Kerrouche, G. Thomas, P. Soto, et al., "Intraindividual, right-left comparison of topical methyl aminolaevulinate-photodynamic therapy and cryotherapy in subjects with actinic keratoses: a multicentre, randomized controlled study," *Br. J. Dermatol.* **155**, 1029–1036 (2006).

[69] R. M. Szeimies, E. Stockfleth, G. Popp, F. Borrosch, H. Bruning, R. Dominicus, H. Mensing, U. Reinhold, K. Reich, A. C. Moor, et al., "Long-term follow-up of photodynamic therapy with a self-adhesive 5-aminolaevulinic acid patch: 12 months data," *Br. J. Dermatol.* **162**, 410–414 (2010).

[70] E. H. Tschen, D. S. Wong, D. M. Pariser, F. E. Dunlap, A. Houlihan, M. B. Ferdon;Phase IV ALA-PDT Actinic Keratosis Study Group. "Photodynamic therapy using aminolaevulinic acid for patients with nonhyperkeratotic actinic keratoses of the face and scalp: phase IV multicentre clinical trial with 12-month follow up," *Br. J. Dermatol.* **155**, 1262–1269 (2006).

[71] E. Sotiriou, Z. Apalla, F. Maliamani, N. Zaparas, D. Panagiotidou, and D. Ioannides, "Intraindividual, right-left comparison of topical 5-aminolevulinic acid photodynamic therapy vs. 5% imiquimod cream for actinic keratoses on the upper extremities," *J. Eur. Acad. Dermatol. Venereol.* **23**, 1061–1065 (2009).

[72] R. Kaufmann, L. Spelman, W. Weightman, J. Reifenberger, R. M. Szeimies, E. Verhaeghe, N. Kerrouche, V. Sorba, H. Villemagne, and L. E. Rhodes, "Multicentre intraindividual randomized trial of topical methyl aminolaevulinate-photodynamic therapy vs. cryotherapy for multiple actinic keratoses on the extremities," *Br. J. Dermatol.* **158**, 994–999 (2008).

[73] E. Sotiriou, Z. Apalla, E. Chovarda, D. Panagiotidou, and D. Ioannides, "Photodynamic therapy with 5-aminolevulinic acid in actinic cheilitis: an 18-month clinical and histological follow-up," *J. Eur. Acad. Dermatol. Venereol.* **24**, 916–920 (2010).

[74] C. Berking, T. Herzinger, M. J. Flaig, M. Brenner, C. Borelli, and K. Degitz, "The efficacy of photodynamic therapy in actinic cheilitis of the lower lip: a prospective study of 15 patients," *Dermatol. Surg.* **33**, 825–830 (2007).

[75] E. Sotiriou, A. Lallas, C. Goussi, Z. Apalla, A. Trigoni, E. Chovarda, and D. Ioannides, "Sequential use of photodynamic therapy and imiquimod 5% cream for the treatment of actinic cheilitis: a 12-month follow-up study," *Br. J. Dermatol.* **165**, 888–892 (2011).

[76] Z. Apalla, E. Sotiriou, E. Chovarda, I. Lefaki, D. Devliotou-Panagiotidou, and D. Ioannides, "Skin cancer: preventive photodynamic therapy in patients with face and scalp cancerization. A randomized placebo-controlled study," *Br. J. Dermatol.* **162**, 171–175 (2010).

[77] H. C. Wulf, S. Pavel, I. Stender, and C. A. Bakker-Wensveen, "Topical photodynamic therapy for prevention of new skin lesions in renal transplant recipients," *Acta Derm. Venereol.* **86**, 25–28 (2006).

[78] L. Bagazgoitia, J. Cuevas Santos, A. Juarranz, and P. Jaen, "Photodynamic therapy reduces the histological features of actinic damage and the expression of early oncogenic markers," *Br. J. Dermatol.* **165**, 144–151 (2011).

[79] R. M. Szeimies, L. Torezan, A. Niwa, N. Valente, P. Unger, E. Kohl, S. Schreml, P. Babilas, S. Karrer, and C. Festa-Neto, "Clinical, histopathological and immunohistochemical assessment of human skin field cancerization before and after photodynamic therapy," *Br. J. Dermatol.* **167**, 150–159 (2012).

[80] M. M. Lee and M. M. Wick, "Bowen's disease," *CA Cancer J. Clin.* **40**, 237–242 (1990).

[81] M. J. Rasmussen, *Precancerous Lesions* (Lea & Febiger, Philadelphia, PA, 1979).

[82] G. Moreno, A. L. Chia, A. Lim, and S. Shumack, "Therapeutic options for Bowen's disease," *Australas J. Dermatol.* **48**, 1–8; quiz 9–10 (2007).

[83] S. B. Ball and R. P. Dawber, "Treatment of cutaneous Bowen's disease with particular emphasis on the problem of lower leg lesions," *Australas J. Dermatol.* **39**, 63–68; quiz 69–70 (1998).

[84] C. A. Morton, C. Whitehurst, H. Moseley, J. H. McColl, J. V. Moore, and R. M. Mackie, "Comparison of photodynamic therapy with cryotherapy in the treatment of Bowen's disease," *Br. J. Dermatol.* **135**, 766–771 (1996).

[85] A. Salim, J. A. Leman, J. H. McColl, R. Chapman, and C. A. Morton, "Randomized comparison of photodynamic therapy with topical 5-fluorouracil in Bowen's disease," *Br. J. Dermatol.* **148**, 539–543 (2003).

[86] C. Morton, M. Horn, J. Leman, B. Tack, C. Bedane, M. Tjioe, S. Ibbotson, A. Khemis, and P. Wolf, "Comparison of topical methyl aminolevulinate photodynamic therapy with cryotherapy or fluorouracil for treatment of squamous cell carcinoma in situ: results of a multicenter randomized trial," *Arch. Dermatol.* **142**, 729–735 (2006).

[87] R. K. Roenigk, J. L. Ratz, P. L. Bailin, and R. G. Wheeland, "Trends in the presentation and treatment of basal cell carcinomas," *J. Dermatol. Surg. Oncol.* **12**, 860–865 (1986).

[88] E. Stockfleth and W. Sterry, "New treatment modalities for basal cell carcinoma," *Recent Results Cancer Res.* **160**, 259–268 (2002).

[89] Q. Peng, T. Warloe, K. Berg, J. Moan, M. Kongshaug, K. E. Giercksky, and J. M. Nesland, "5-Aminolevulinic acid-based photodynamic therapy. Clinical research and future challenges," *Cancer* **79**, 2282–2308 (1997).

[90] M. R. Thissen, C. A. Schroeter, and H. A. Neumann, "Photodynamic therapy with delta-aminolaevulinic acid for nodular basal cell carcinomas using a prior debulking technique," *Br. J. Dermatol.* **142**, 338–339 (2000).

[91] L. Berroeta, C. Clark, R. S. Dawe, S. H. Ibbotson, and C. J. Fleming, "A randomized study of minimal curettage followed by topical photodynamic therapy compared with surgical excision for low-risk nodular basal cell carcinoma," *Br. J. Dermatol.* **157**, 401–403 (2007).

[92] A. M. Soler, T. Warloe, A. Berner, and K. E. Giercksky, "A follow-up study of recurrence and cosmesis in completely responding superficial and nodular basal cell carcinomas treated with methyl 5-aminolaevulinate-based photodynamic therapy alone and with prior curettage," *Br. J. Dermatol.* **145**, 467–471 (2001).

[93] R. M. Szeimies, "Methyl aminolevulinate-photodynamic therapy for basal cell carcinoma," *Dermatol. Clin.* **25**, 89–94 (2007).

[94] L. E. Rhodes, M. de Rie, Y. Enstrom, R. Groves, T. Morken, V. Goulden, G. A. Wong, J. J. Grob, S. Varma, and P. Wolf, "Photodynamic therapy using topical methyl aminolevulinate vs surgery for nodular basal cell carcinoma: results of a multicenter randomized prospective trial," *Arch. Dermatol.* **140**, 17–23 (2004).

[95] L. E. Rhodes, M. A. de Rie, R. Leifsdottir, R. C. Yu, I. Bachmann, V. Goulden, G. A. Wong, M. A. Richard, A. Anstey, and P. Wolf, "Five-year follow-up of a randomized, prospective trial of topical methyl aminolevulinate photodynamic therapy vs surgery for nodular basal cell carcinoma," *Arch. Dermatol.* **143**, 1131–1136 (2007).

[96] C. M. Balch, J. E. Gershenwald, S. J. Soong, J. F. Thompson, M. B. Atkins, D. R. Byrd, A. C. Buzaid, A. J. Cochran, D. G. Coit, S. Ding, et al., "Final version of 2009 AJCC melanoma staging and classification," *J. Clin. Oncol.* **27**, 6199–6206 (2009).

[97] S. A. Ozler, J. S. Nelson, P. E. Liggett, J. M. de Queiroz, Jr., and M. W. Berns, "Photodynamic therapy of experimental subchoroidal melanoma using chloroaluminum sulfonated phthalocyanine," *Arch. Ophthalmol.* **110**, 555–561 (1992).

[98] M. Dellian, C. Richert, F. Gamarra, and A. E. Goetz, "Photodynamic eradication of amelanotic melanoma of the hamster with fast acting photosensitizers," *Int. J. Cancer* **65**, 246–248 (1996).

[99] L. M. Davids, B. Kleemann, D. Kacerovska, K. Pizinger, and S. H. Kidson, "Hypericin phototoxicity induces different modes of cell death in melanoma and human skin cells," *J. Photochem. Photobiol. B* **91**, 67–76 (2008).

[100] L. H. Young, M. A. Howard, L. K. Hu, R. Y. Kim, and E. S. Gragoudas, "Photodynamic therapy of pigmented choroidal melanomas using a liposomal preparation of benzoporphyrin derivative," *Arch. Ophthalmol.* **114**, 186–192 (1996).

[101] K. W. Woodburn, Q. Fan, D. Kessel, Y. Luo, and S. W. Young, "Photodynamic therapy of B16F10 murine melanoma with lutetium texaphyrin," *J. Invest. Dermatol.* **110**, 746–751 (1998).

[102] R. Haddad, O. Kaplan, R. Greenberg, A. Siegal, Y. Skornick, and H. Kashtan, "Photodynamic therapy of murine colon cancer and melanoma using systemic aminolevulinic acid as a photosensitizer," *Int. J. Surg. Investig.* **2**, 171–178 (2000).

[103] L. Hu, X. Wu, Y. Song, L. H. Young, and E. S. Gragoudas, "Photodynamic therapy of pigmented choroidal melanomas in rabbits," *Zhonghua Yan Ke Za Zhi* **38**, 491–494 (2002).

[104] J. Barge, R. Decreau, M. Julliard, J. C. Hubaud, A. S. Sabatier, J. J. Grob, and P. Verrando, "Killing efficacy of a new silicon phthalocyanine in human melanoma cells treated with photodynamic therapy by early activation of mitochondrion-mediated apoptosis," *Exp. Dermatol.* **13**, 33–44 (2004).

[105] J. M. Dabrowski, K. Urbanska, L. G. Arnaut, M. M. Pereira, A. R. Abreu, S. Simoes, and G. Stochel, "Biodistribution and photodynamic efficacy of a water-soluble, stable, halogenated bacteriochlorin against melanoma," *Chem. Med. Chem.* **6**, 465–475 (2011).

[106] J. M. Dabrowski, M. Krzykawska, L. G. Arnaut, M. M. Pereira, C. J. Monteiro, S. Simoes, K. Urbanska, and G. Stochel, "Tissue uptake study and photodynamic therapy of melanoma-bearing mice with a nontoxic, effective chlorin," *Chem. Med. Chem.* **6**, 1715–1726 (2011).

[107] I. A. Barbazetto, T. C. Lee, I. S. Rollins, S. Chang, and D. H. Abramson, "Treatment of choroidal melanoma using photodynamic therapy," *Am. J. Ophthalmol.* **135**, 898–899 (2003).

[108] M. J. Donaldson, L. Lim, C. A. Harper, J. Mackenzie, and G. Campbell W, "Primary treatment of choroidal amelanotic melanoma with photodynamic therapy," *Clin. Exp. Ophthalmol.* **33**, 548–549 (2005).

[109] S. V. Sheleg, E. A. Zhavrid, T. V. Khodina, G. A. Kochubeev, Y. P. Istomin, V. N. Chalov, and I. N. Zhuravkin, "Photodynamic therapy with chlorin e(6) for skin metastases of melanoma," *Photodermatol. Photoimmunol. Photomed.* **20**, 21–26 (2004).

[110] H. Saji, W. Song, K. Furumoto, H. Kato, and E. G. Engleman, "Systemic antitumor effect of intratumoral injection of dendritic cells in combination with local photodynamic therapy," *Clin. Cancer Res.* **12**, 2568–2574 (2006).

[111] Y. Y. Huang, D. Vecchio, P. Avci, R. Yin, M. Garcia-Diaz, and M. R. Hamblin, "Melanoma resistance to photodynamic therapy: new insights," *Biol. Chem.* **394**, 239–250 (2012).

[112] R. Willemze, E. S. Jaffe, G. Burg, L. Cerroni, E. Berti, S. H. Swerdlow, E. Ralfkiaer, S. Chimenti, J. L. Diaz-Perez, L. M. Duncan, et al., "WHO-EORTC classification for cutaneous lymphomas," *Blood* **105**, 3768–3785 (2005).

[113] M. Duvic and R. Edelson, "Cutaneous T-cell lymphoma," *J. Am. Acad. Dermatol.* **51**, S43–S45 (2004).

[114] K. Rittenhouse-Diakun, H. Van Leengoed, J. Morgan, E. Hryhorenko, G. Paszkiewicz, J. E. Whitaker, and A. R. Oseroff, "The role of transferrin receptor (CD71) in photodynamic therapy of activated and malignant lymphocytes using the heme precursor delta-aminolevulinic acid (ALA)," *Photochem. Photobiol.* **61**, 523–528 (1995).

[115] J. A. Leman, D. C. Dick, and C. A. Morton, "Topical 5-ALA photodynamic therapy for the treatment of cutaneous T-cell lymphoma," *Clin. Exp. Dermatol.* **27**, 516–518 (2002).

[116] A. Orenstein, J. Haik, J. Tamir, E. Winkler, H. Trau, Z. Malik, and G. Kostenich, "Photodynamic therapy of cutaneous lymphoma using 5-aminolevulinic acid topical application," *Dermatol. Surg.* **26**, 765–769; discussion 769–770 (2000).

[117] E. A. Coors and P. von den Driesch, "Topical photodynamic therapy for patients with therapy-resistant lesions of cutaneous T-cell lymphoma," *J. Am. Acad. Dermatol.* **50**, 363–367 (2004).

[118] D. W. Edstrom, A. Porwit, and A. M. Ros, "Photodynamic therapy with topical 5-aminolevulinic acid for mycosis fungoides: clinical and histological response," *Acta. Derm. Venereol.* **81**, 184–188 (2001).

[119] S. Y. Lee, C. E. You, and M. Y. Park, "Blue and red light combination LED phototherapy for acne vulgaris in patients with skin phototype IV," *Lasers Surg. Med.* **39**, 180–188 (2007).

[120] J. S. Strauss, D. P. Krowchuk, J. J. Leyden, A. W. Lucky, A. R. Shalita, E. C. Siegfried, D. M. Thiboutot, A. S. Van Voorhees, K. A. Beutner, C. K. Sieck, et al., and American Academy of Dermatology/American Academy of Dermatology Association, "Guidelines of care for acne vulgaris management," *J. Am. Acad. Dermatol.* **56**, 651–663 (2007).

[121] S. Ibbotson, "What is the role of photodynamic therapy in the treatment of acne vulgaris?," *Photodiagnosis Photodyn. Ther.* **9**, 2–4 (2012).

[122] E. V. Ross, "Optical treatments for acne," *Dermatol. Ther.* **18**, 253–266 (2005).

[123] M. H. Aziz-Jalali, S. M. Tabaie, and G. E. Djavid, "Comparison of red, and infrared low-level laser therapy in the treatment of acne vulgaris," *Ind. J. Dermatol.* **57**, 128–130 (2012).

[124] N. S. Sadick, "Handheld LED array device in the treatment of acne vulgaris," *J. Drugs Dermatol.* **7**, 347–350 (2008).

[125] A. M. Rotunda, A. R. Bhupathy, and T. E. Rohrer, "The new age of acne therapy: light, lasers, and radiofrequency," *J. Cosmet. Laser. Ther.* **6**, 191–200 (2004).

[126] L. Bowes, D. Manstein, and R. Anderson, "Effect of 532nm KTP laser exposure on acne and sebaceous glands," *Lasers Med. Sci.* **18**, S6–S7 (2003).

[127] W. Hongcharu, C. R. Taylor, Y. Chang, D. Aghassi, K. Suthamjariya, and R. R. Anderson, "Topical ALA-photodynamic therapy for the treatment of acne vulgaris," *J. Invest. Dermatol.* **115**, 183–192 (2000).

[128] B. Pollock, D. Turner, M. R. Stringer, R. A. Bojar, V. Goulden, G. I. Stables, and W. J. Cunliffe, "Topical aminolaevulinic acid-photodynamic therapy for the treatment of acne vulgaris: a study of clinical efficacy and mechanism of action," *Br. J. Dermatol.* **151**, 616–622 (2004).

[129] Y. Itoh, Y. Ninomiya, S. Tajima, and A. Ishibashi, "Photodynamic therapy of acne vulgaris with topical delta-aminolaevulinic acid and incoherent light in Japanese patients," *Br. J. Dermatol.* **144**, 575–579 (2001).

[130] E. Kohl, L. A. Torezan, M. Landthaler, and R. M. Szeimies, "Aesthetic effects of topical photodynamic therapy," *J. Eur. Acad. Dermatol. Venereol.* **24**, 1261–1269 (2010).

[131] R. Ruiz-Rodriguez, L. Lopez, D. Candelas, and J. Pedraz, "Photorejuvenation using topical 5-methyl aminolevulinate and red light," *J. Drugs Dermatol.* **7**, 633–637 (2008).

[132] R. Ruiz-Rodriguez, L. Lopez, D. Candelas, and B. Zelickson, "Enhanced efficacy of photodynamic therapy after fractional resurfacing: fractional photodynamic rejuvenation," *J. Drugs Dermatol.* **6**, 818–820 (2007).

[133] D. Key, "Aminolaevulinic acid-pulsed dye laser photodynamic therapy for the treatment of photoaging," *Cosmet. Dermatol.* **18**, 31–36 (2005).

[134] I. Diamond, A. F. McDonagh, C. B. Wilson, S. G. Granelli, S. Nielsen, and R. Jaenicke, "Photherapy of maliagnant tumors," *Lancet* **300**, 1175–1177 (1972).

[135] T. J. Dougherty, G. B. Grindey, R. Fiel, K. R. Weishaupt, and D. G. Boyle, "Photoradiation therapy. II. Cure of animal tumors with hematoporphyrin and light," *J. Natl. Cancer Inst.* **55**, 115–121 (1975).

[136] T. J. Dougherty, J. E. Kaufman, A. Goldfarb, K. R. Weishaupt, D. Boyle, and A. Mittleman, "Photoradiation therapy for the treatment of malignant tumors," *Cancer Res.* **38**, 2628–2635 (1978).

[137] K. Moghissi, K. Dixon, M. Stringer, and J. A. Thorpe, "Photofrin PDT for early stage oesophageal cancer: long term results in 40 patients and literature review," *Photodiagnosis Photodyn. Ther.* **6**, 159–166 (2009).

[138] S. Mimura, H. Narahara, H. Uehara, T. Otani, and S. Okuda, "Photodynamic therapy for gastric cancer," *Gan To Kagaku Ryoho* **23**, 41–46 (1996).

[139] E. A. Popovic, A. H. Kaye, and J. S. Hill, "Photodynamic therapy of brain tumors," *J. Clin. Laser Med. Surg.* **14**, 251–261 (1996).

[140] S. Piermarocchi, M. Sartore, G. Lo Giudice, V. Maritan, E. Midena, and T. Segato, "Combination of photodynamic therapy and intraocular triamcinolone for exudative age-related macular degeneration and long-term chorioretinal macular atrophy," *Arch. Ophthalmol.* **126**, 1367–1374 (2008).

[141] A. Dimofte, T. C. Zhu, S. M. Hahn, and R. A. Lustig, "In vivo light dosimetry for motexafin lutetium-mediated PDT of recurrent breast cancer," *Lasers Surg. Med.* **31**, 305–312 (2002).

[142] M. A. Biel, "Photodynamic therapy of head and neck cancers," *Methods Mol. Biol.* **635**, 281–293 (2010).

[143] R. R. Allison, T. S. Mang, and B. D. Wilson, "Photodynamic therapy for the treatment of nonmelanomatous cutaneous malignancies," *Semin. Cutan. Med. Surg.* **17**, 153–163 (1998).

[144] R. B. Veenhuizen, J. P. Marijnissen, P. Kenemans, M. C. Ruevekamp-Helmers, L. W. T. Mannetje, T. J. Helmerhorst, and F. A. Stewart, "Intraperitoneal photodynamic therapy of the rat CC531 adenocarcinoma," *Br. J. Cancer* **73**, 1387–1392 (1996).

[145] S. M. Hahn, R. P. Smith, and J. Friedberg, "Photodynamic therapy for mesothelioma," *Curr. Treat. Options Oncol.* **2**, 375–383 (2001).

[146] R. R. Allison, E. Zervos, and C. H. Sibata, "Cholangiocarcinoma: an emerging indication for photodynamic therapy," *Photodiagnosis Photodyn. Ther.* **6**, 84–92 (2009).

[147] B. G. Fan and A. Andren-Sandberg, "Photodynamic therapy for pancreatic cancer," *Pancreas* **34**, 385–389 (2007).

[148] L. Milla Sanabria, M. E. Rodriguez, I. S. Cogno, N. B. Rumie Vittar, M. F. Pansa, M. J. Lamberti, and V. A. Rivarola, "Direct and indirect photodynamic therapy effects on the cellular and molecular components of the tumor microenvironment," *Biochim. Biophys. Acta* **1835**, 36–45 (2013).

[149] C. Raab, "Ber die wirkung fluoreszierender stoffe auf infusoria," *Z. Biol.* **39**, 524–546 (1900).

[150] A. Jesionek and H. von Tappenier, "Zur behandlung der hautcarcinomit mit fluorescierenden stoffen," *Muench. Med. Wochenschr.* **47**, 2042–2044 (1903).

[151] W. Hausmann, "Die sensibilisierende wirkung tierscher farbstoffe und ihne physiologische bedeutung," *Wien. Klin. Wochenschr.* **21**, 1527–1529 (1908).

[152] G. H. Cassell and J. Mekalanos, "Development of antimicrobial agents in the era of new and reemerging infectious diseases and increasing antibiotic resistance," *J. Am. Med. Assoc.* **285**, 601–605 (2001).

[153] M. R. Hamblin and T. Hasan, "Photodynamic therapy: a new antimicrobial approach to infectious disease?," *Photochem. Photobiol. Sci.* **3**, 436–450 (2004).

[154] F. M. Lauro, P. Pretto, L. Covolo, G. Jori, and G. Bertoloni, "Photoinactivation of bacterial strains involved in periodontal diseases sensitized by porphycene-polylysine conjugates," *Photochem. Photobiol. Sci.* **1**, 468–470 (2002).

[155] T. Maisch, "A new strategy to destroy antibiotic resistant microorganisms: antimicrobial photodynamic treatment," *Mini. Rev. Med. Chem.* **9**, 974–983 (2009).

[156] Z. Malik, H. Ladan, and Y. Nitzan, "Photodynamic inactivation of gram-negative bacteria: problems and possible solutions," *J. Photochem. Photobiol. B* **14**, 262–266 (1992).

[157] Y. Nitzan, M. Gutterman, Z. Malik, and B. Ehrenberg, "Inactivation of gram-negative bacteria by photosensitized porphyrins," *Photochem. Photobiol.* **55**, 89–96 (1992).

[158] Z. Malik, H. Ladan, Y. Nitzan, and B. Ehrenberg, "The bactericidal activity of a deuteroporphyrin-hemin mixture on gram-positive bacteria. A microbiological and spectroscopic study," *J. Photochem. Photobiol. B* **6**, 419–430 (1990).

[159] G. Bertoloni, F. Rossi, G. Valduga, G. Jori, and J. van Lier, "Photosensitizing activity of water- and lipid-soluble phthalocyanines on *Escherichia coli*," *FEMS Microbiol. Lett.* **59**, 149–155 (1990).

[160] M. Wainwright and K. B. Crossley, "Methylene blue—a therapeutic dye for all seasons?," *J. Chemother.* **14**, 431–443 (2002).

[161] M. N. Usacheva, M. C. Teichert, and M. A. Biel, "Comparison of the methylene blue and toluidine blue photobactericidal efficacy against gram-positive and gram-negative microorganisms," *Lasers Surg. Med.* **29**, 165–173 (2001).

[162] T. W. Wong, Y. Y. Wang, H. M. Sheu, and Y. C. Chuang, "Bactericidal effects of toluidine blue-mediated photodynamic action on Vibrio vulnificus," *Antimicrob. Agents Chemother.* **49**, 895–902 (2005).

[163] T. G. St Denis, L. Huang, T. Dai, and M. R. Hamblin, "Analysis of the bacterial heat shock response to photodynamic therapy-mediated oxidative stress," *Photochem. Photobiol.* **87**, 707–713 (2011).

[164] A. Minnock, D. I. Vernon, J. Schofield, J. Griffiths, J. H. Parish, and S. T. Brown, "Photoinactivation of bacteria. Use of a cationic water-soluble zinc phthalocyanine to photoinactivate both gram-negative and gram-positive bacteria," *J. Photochem. Photobiol. B* **32**, 159–164 (1996).

[165] X. Ragas, D. Sanchez-Garcia, R. Ruiz-Gonzalez, T. Dai, M. Agut, M. R. Hamblin, and S. Nonell, "Cationic porphycenes as potential photosensitizers for antimicrobial photodynamic therapy," *J. Med. Chem.* **53**, 7796–7803 (2010).

[166] L. Bourre, F. Giuntini, I. M. Eggleston, C. A. Mosse, A. J. Macrobert, and M. Wilson, "Effective photoinactivation of gram-positive and gram-negative bacterial strains using an HIV-1 Tat peptide-porphyrin conjugate," *Photochem. Photobiol. Sci.* **9**, 1613–1620 (2010).

[167] T. A. Dahl, W. R. Midden, and P. E. Hartman, "Pure singlet oxygen cytotoxicity for bacteria," *Photochem. Photobiol.* **46**, 345–352 (1987).

[168] M. S. Choi, S. J. Yun, H. J. Beom, H. R. Park, and J. B. Lee, "Comparative study of the bactericidal effects of 5-aminolevulinic acid with blue and red light on Propionibacterium acnes," *J. Dermatol.* **38**, 661–666 (2011).

[169] N. Komerik, H. Nakanishi, A. J. MacRobert, B. Henderson, P. Speight, and M. Wilson, "In vivo killing of *Porphyromonas gingivalis* by toluidine blue-mediated photosensitization in an animal model," *Antimicrob. Agents Chemother.* **47**, 932–940 (2003).

[170] L. Huang, T. Zhiyentayev, Y. Xuan, D. Azhibek, G. B. Kharkwal, and M. R. Hamblin, "Photodynamic inactivation of bacteria using polyethylenimine-chlorin(e6) conjugates: effect of polymer molecular weight, substitution ratio of chlorin(e6) and pH," *Lasers Surg. Med.* **43**, 313–323 (2011).

[171] V. T. Orlandi, E. Caruso, S. Banfi, and P. Barbieri, "Effect of organic matter on the in vitro photoeradication of *Pseudomonas aeruginosa* by means of a cationic tetraarylporphyrin," *Photochem. Photobiol.* **88**, 557–564 (2012).

[172] M. R. Hamblin, T. Zahra, C. H. Contag, A. T. McManus, and T. Hasan, "Optical monitoring and treatment of potentially lethal wound infections in vivo," *J. Infect. Dis.* **187**, 1717–1725 (2003).

[173] C. M. Allen, J. M. Weber, and J. E. van Lier, "Sulfophthalocyanines for photodynamic inactivation of viruses in blood products: effect of structural modifications," *Photochem. Photobiol.* **62**, 184–189 (1995).

[174] H. Mohr, B. Lambrecht, and A. Selz, "Photodynamic virus inactivation of blood components," *Immunol. Invest.* **24**, 73–85 (1995).

[175] T. Dai, B. B. Fuchs, J. J. Coleman, R. A. Prates, C. Astrakas, T. G. St Denis, M. S. Ribeiro, E. Mylonakis, M. R. Hamblin, and G. P. Tegos, "Concepts and principles of photodynamic therapy as an alternative antifungal discovery platform," *Front Microbiol.* **3**, 120 (2012).

[176] P. Grellier, R. Santus, E. Mouray, V. Agmon, J. C. Maziere, D. Rigomier, A. Dagan, S. Gatt, and J. Schrevel, "Photosensitized inactivation of *Plasmodium falciparum*- and *Babesia divergens*-infected erythrocytes in whole blood by lipophilic pheophorbide derivatives," *Vox Sang.* **72**, 211–220 (1997).

[177] X. J. Zhao, S. Lustigman, Y. S. Li, M. E. Kenney, and E. Ben-Hur, "Structure-activity and mechanism studies on silicon phthalocyanines with *Plasmodium falciparum* in the dark and under red light," *Photochem. Photobiol.* **66**, 282–287 (1997).

[178] R. Kliukiene, A. Maroziene, N. Cenas, K. Becker, and J. S. Blanchard, "Photoinactivation of trypanothione reductase and glutathione reductase by Al-phthalocyanine tetrasulfonate and hematoporphyrin," *Biochem. Biophys. Res. Commun.* **218**, 629–632 (1996).

[179] Z. Alouini and M. Jemli, "Destruction of helminth eggs by photosensitized porphyrin," *J. Environ. Monit.* **3**, 548–551 (2001).

[180] M. R. Hamblin, D. A. O'Donnell, N. Murthy, C. H. Contag, and T. Hasan, "Rapid control of wound infections by targeted photodynamic therapy monitored by in vivo bioluminescence imaging," *Photochem. Photobiol.* **75**, 51–57 (2002).

[181] T. Dai, G. P. Tegos, T. Zhiyentayev, E. Mylonakis, and M. R. Hamblin, "Photodynamic therapy for methicillin-resistant *Staphylococcus aureus* infection in a mouse skin abrasion model," *Lasers Surg. Med.* **42**, 38–44 (2010).

[182] X. Ragas, T. Dai, G. P. Tegos, M. Agut, S. Nonell, and M. R. Hamblin, "Photodynamic inactivation of *Acinetobacter baumannii* using phenothiazinium dyes: in vitro and in vivo studies," *Lasers Surg. Med.* **42**, 384–390 (2010).

[183] P. S. Zolfaghari, S. Packer, M. Singer, S. P. Nair, J. Bennett, C. Street, and M. Wilson, "In vivo killing of *Staphylococcus aureus* using a light-activated antimicrobial agent," *BMC Microbiol.* **9**, 27 (2009).

[184] A. Orenstein, D. Klein, J. Kopolovic, E. Winkler, Z. Malik, N. Keller, and Y. Nitzan, "The use of porphyrins for eradication of *Staphylococcus aureus* in burn wound infections," *FEMS Immunol. Med. Microbiol.* **19**, 307–314 (1997).

[185] S. A. Lambrechts, T. N. Demidova, M. C. Aalders, T. Hasan, and M. R. Hamblin, "Photodynamic therapy for *Staphylococcus aureus* infected burn wounds in mice," *Photochem. Photobiol. Sci.* **4**, 503–509 (2005).

[186] T. Dai, G. P. Tegos, Z. Lu, L. Huang, T. Zhiyentayev, M. J. Franklin, D. G. Baer, and M. R. Hamblin, "Photodynamic therapy for *Acinetobacter baumannii* burn infections in mice," *Antimicrob. Agents Chemother.* **53**, 3929–3934 (2009).

[187] F. Berthiaume, S. R. Reiken, M. Toner, R. G. Tompkins, and M. L. Yarmush, "Antibody-targeted photolysis of bacteria in vivo," *Biotechnology (N Y)* **12**, 703–706 (1994).

[188] F. Gad, T. Zahra, K. P. Francis, T. Hasan, and M. R. Hamblin, "Targeted photodynamic therapy of established soft-tissue infections in mice," *Photochem. Photobiol. Sci.* **3**, 451–458 (2004).

[189] G. Lombard and M. M. Lanotte, "The treatment of neurosurgical infections by lasers and porphyrins," *Edizione Libreria Progetto* 363–366 (1985).

[190] S. B. Brown, "Photodiagnosis and photodynamic therapy," in *12th International Photodynamic Association World Congress* **6**, 150–151 (Seattle, 2009).

[191] T. H. Clayton and P. V. Harrison, "Photodynamic therapy for infected leg ulcers," *Br. J. Dermatol.* **156**, 384–385 (2007).

[192] O. Dortbudak, R. Haas, T. Bernhart, and G. Mailath-Pokorny, "Lethal photosensitization for decontamination of implant surfaces in the treatment of peri-implantitis," *Clin. Oral. Implants Res.* **12**, 104–108 (2001).

[193] J. A. Shibli, M. C. Martins, L. H. Theodoro, R. F. Lotufo, V. G. Garcia, and E. J. Marcantonio, "Lethal photosensitization in microbiological treatment of ligature-induced peri-implantitis: a preliminary study in dogs," *J. Oral. Sci.* **45**, 17–23 (2003).

[194] R. R. Hayek, N. S. Araujo, M. A. Gioso, J. Ferreira, C. A. Baptista-Sobrinho, A. M. Yamada, and M. S. Ribeiro, "Comparative study between the effects of photodynamic therapy and conventional therapy on microbial reduction in ligature-induced peri-implantitis in dogs," *J. Periodontol.* **76**, 1275–1281 (2005).

[195] R. R. de Oliveira, H. O. Schwartz-Filho, A. B. Novaes, Jr., and M. Taba, Jr., "Antimicrobial photodynamic therapy in the non-surgical treatment of aggressive periodontitis: a preliminary randomized controlled clinical study," *J. Periodontol.* **78**, 965–973 (2007).

[196] B. W. Sigusch, A. Pfitzner, V. Albrecht, and E. Glockmann, "Efficacy of photodynamic therapy on inflammatory signs and two selected periodontopathogenic species in a beagle dog model," *J. Periodontol.* **76**, 1100–1105 (2005).

[197] Z. Malik, J. Hanania, and Y. Nitzan, "Bactericidal effects of photoactivated porphyrins—an alternative approach to antimicrobial drugs," *J. Photochem. Photobiol. B* **5**, 281–293 (1990).

[198] P. E. Bottura, J. Milanezi, L. A. Fernandes, H. C. Caldas, M. Abbud-Filho, V. G. Garcia, and M. A. Baptista, "Nonsurgical periodontal therapy combined with laser and photodynamic therapies for periodontal disease in immunosuppressed rats," *Transplant Proc.* **43**, 2009–2016 (2011).

[199] Y. Ogura, T. Ooka, Asadulghani, J. Terajima, J. P. Nougayrede, K. Kurokawa, K. Tashiro, T. Tobe, K. Nakayama, S. Kuhara, E. Oswald, et al., "Extensive genomic diversity and selective conservation of virulence-determinants in enterohemorrhagic *Escherichia coli* strains of O157 and non-O157 serotypes," *Genome. Biol.* **8**, R138 (2007).

[200] G. P. Tegos, K. Masago, F. Aziz, A. Higginbotham, F. R. Stermitz, and M. R. Hamblin, "Inhibitors of bacterial multidrug efflux pumps potentiate antimicrobial photoinactivation," *Antimicrob. Agents Chemother.* **52**, 3202–3209 (2008).

[201] V. Klepac-Ceraj, N. Patel, X. Song, C. Holewa, C. Patel, R. Kent, M. M. Amiji, and N. S. Soukos, "Photodynamic effects of methylene blue-loaded polymeric nanoparticles on dental plaque bacteria," *Lasers Surg. Med.* **43**, 600–606 (2011).

[202] I. N. Rocas, J. F. Siqueira, Jr., and K. R. Santos, "Association of *Enterococcus faecalis* with different forms of periradicular diseases," *J. Endod.* **30**, 315–320 (2004).

[203] M. B. Fonseca, P. O. Junior, R. C. Pallota, H. F. Filho, O. V. Denardin, A. Rapoport, R. A. Dedivitis, J. F. Veronezi, W. J. Genovese, and A. L. Ricardo, "Photodynamic therapy for root canals infected with *Enterococcus faecalis*," *Photomed. Laser Surg.* **26**, 209–213 (2008).

[204] L. C. Souza, P. R. Brito, J. C. de Oliveira, F. R. Alves, E. J. Moreira, H. R. Sampaio-Filho, I. N. Rocas, and J. F. Siqueira, Jr., "Photodynamic therapy with two different photosensitizers as a supplement to instrumentation/irrigation procedures in promoting intracanal reduction of Enterococcus faecalis," *J. Endod.* **36**, 292–296 (2010).

[205] R. Ng, F. Singh, D. A. Papamanou, X. Song, C. Patel, C. Holewa, N. Patel, V. Klepac-Ceraj, C. R. Fontana, R. Kent, et al., "Endodontic photodynamic therapy ex vivo," *J. Endod.* **37**, 217–222 (2011).

[206] N. S. Soukos, P. S. Chen, J. T. Morris, K. Ruggiero, A. D. Abernethy, S. Som, F. Foschi, S. Doucette, L. L. Bammann, C. R. Fontana, et al., "Photodynamic therapy for endodontic disinfection," *J. Endod.* **32**, 979–984 (2006).

[207] A. S. Garcez, M. S. Ribeiro, G. P. Tegos, S. C. Nunez, A. O. Jorge, and M. R. Hamblin, "Antimicrobial photodynamic therapy combined with conventional endodontic treatment to eliminate root canal biofilm infection," *Lasers Surg. Med.* **39**, 59–66 (2007).

[208] E. G. Mima, A. C. Pavarina, L. N. Dovigo, C. E. Vergani, C. A. Costa, C. Kurachi, and V. S. Bagnato, "Susceptibility of *Candida albicans* to photodynamic therapy in a murine model of oral candidosis," *Oral. Surg. Oral. Med. Oral. Pathol. Oral. Radiol. Endod.* **109**, 392–401 (2010).

[209] M. C. Teichert, J. W. Jones, M. N. Usacheva, and M. A. Biel, "Treatment of oral candidiasis with methylene blue-mediated photodynamic therapy in an immunodeficient murine model," *Oral. Surg. Oral. Med. Oral. Pathol. Oral. Radiol. Endod.* **93**, 155–160 (2002).

[210] P. Chondros, D. Nikolidakis, N. Christodoulides, R. Rossler, N. Gutknecht, and A. Sculean, "Photodynamic therapy as adjunct to non-surgical periodontal treatment in patients on periodontal maintenance: a randomized controlled clinical trial," *Lasers Med. Sci.* **24**, 681–688 (2009).

[211] N. Christodoulides, D. Nikolidakis, P. Chondros, J. Becker, F. Schwarz, R. Rossler, and A. Sculean, "Photodynamic therapy as an adjunct to non-surgical periodontal treatment: a randomized, controlled clinical trial," *J. Periodontol.* **79**, 1638–1644 (2008).

[212] A. Braun, C. Dehn, F. Krause, and S. Jepsen, "Short-term clinical effects of adjunctive antimicrobial photodynamic therapy in periodontal treatment: a randomized clinical trial," *J. Clin. Periodontol.* **35**, 877–884 (2008).

[213] B. W. Sigusch, M. Engelbrecht, A. Volpel, A. Holletschke, W. Pfister, and J. Schutze, "Full-mouth antimicrobial photodynamic therapy in *Fusobacterium nucleatum*-infected periodontitis patients," *J. Periodontol.* **81**, 975–981 (2010).

[214] A. Ruhling, J. Fanghanel, M. Houshmand, A. Kuhr, P. Meisel, C. Schwahn, and T. Kocher, "Photodynamic therapy of persistent pockets in maintenance patients—a clinical study," *Clin. Oral. Investig.* **14**, 637–644 (2010).

[215] S. L. Pinheiro, A. A. Schenka, A. A. Neto, C. P. de Souza, H. M. Rodriguez, and M. C. Ribeiro, "Photodynamic therapy in endodontic treatment of deciduous teeth," *Lasers Med. Sci.* **24**, 521–526 (2009).

[216] O. E. Akilov, S. Kosaka, K. O'Riordan, and T. Hasan, "Photodynamic therapy for cutaneous leishmaniasis: the effectiveness of topical phenothiaziniums in parasite eradication and Th1 immune response stimulation," *Photochem. Photobiol. Sci.* **6**, 1067–1075 (2007).

[217] O. E. Akilov, S. Kosaka, K. O'Riordan, and T. Hasan, "Parasiticidal effect of delta-aminolevulinic acid-based photodynamic therapy for cutaneous leishmaniasis is indirect and mediated through the killing of the host cells," *Exp. Dermatol.* **16**, 651–660 (2007).

[218] O. E. Akilov, W. Yousaf, S. X. Lukjan, S. Verma, and T. Hasan, "Optimization of topical photodynamic therapy with 3,7-bis(di-n-butylamino)phenothiazin-5-ium bromide for cutaneous leishmaniasis," *Lasers Surg. Med.* **41**, 358–365 (2009).

[219] A. Asilian and M. Davami, "Comparison between the efficacy of photodynamic therapy and topical paromomycin in the treatment of Old World cutaneous leishmaniasis: a placebo-controlled, randomized clinical trial," *Clin. Exp. Dermatol.* **31**, 634–637 (2006).

[220] K. Gardlo, Z. Horska, C. D. Enk, L. Rauch, M. Megahed, T. Ruzicka, and C. Fritsch, "Treatment of cutaneous leishmaniasis by photodynamic therapy," *J. Am. Acad. Dermatol.* **48**, 893–896 (2003).

[221] K. O'Riordan, D. S. Sharlin, J. Gross, S. Chang, D. Errabelli, O. E. Akilov, S. Kosaka, G. J. Nau, and T. Hasan, "Photoinactivation of mycobacteria in vitro and in a new murine model of localized *Mycobacterium bovis* BCG-induced granulomatous infection," *Antimicrob. Agents Chemother.* **50**, 1828–1834 (2006).

[222] K. O'Riordan, O. E. Akilov, S. K. Chang, J. W. Foley, and T. Hasan, "Real-time fluorescence monitoring of phenothiazinium photosensitizers and their anti-mycobacterial photodynamic activity against *Mycobacterium bovis* BCG in in vitro and in vivo models of localized infection," *Photochem. Photobiol. Sci.* **6**, 1117–1123 (2007).

[223] J. Y. Jung, P. S. Kwon, J. C. Ahn, R. Ge, M. W. Suh, and C. K. Rhee, "In vitro and in vivo photodynamic therapy of otitis media in gerbils," *Laryngoscope* **119**, 1781–1787 (2009).

[224] S. K. Bisland, C. Chien, B. C. Wilson, and S. Burch, "Pre-clinical in vitro and in vivo studies to examine the potential use of photodynamic therapy in the treatment of osteomyelitis," *Photochem. Photobiol. Sci.* **5**, 31–38 (2006).

[225] Z. Smetana, Z. Malik, A. Orenstein, E. Mendelson, and E. Ben-Hur, "Treatment of viral infections with 5-aminolevulinic acid and light," *Lasers Surg. Med.* **21**, 351–358 (1997).

[226] C. Moore, C. Wallis, J. L. Melnick, and M. D. Kuns, "Photodynamic treatment of herpes keratitis," *Infect Immun.* **5**, 169–171 (1972).

[227] M. G. Myers, M. N. Oxman, J. E. Clark, and K. A. Arndt, "Failure of neutral-red photodynamic inactivation in recurrent herpes simplex virus infections," *N. Engl. J. Med.* **293**, 945–949 (1975).

[228] T. W. Chang, N. Fiumara, and L. Weinstein, "Genital herpes: treatment with methylene blue and light exposure," *Int. J. Dermatol.* **14**, 69–71 (1975).

[229] A. P. Roome, A. E. Tinkler, A. L. Hilton, D. G. Montefiore, and D. Waller, "Neutral red with photoinactivation in the treatment of herpes genitalis," *Br. J. Vener. Dis.* **51**, 130–133 (1975).

[230] M. J. Shikowitz, A. L. Abramson, K. Freeman, B. M. Steinberg, and M. Nouri, "Efficacy of DHE photodynamic therapy for respiratory papillomatosis: immediate and long-term results," *Laryngoscope* **108**, 962–967 (1998).

[231] A. L. Abramson, M. J. Shikowitz, V. M. Mullooly, B. M. Steinberg, C. A. Amella, and H. R. Rothstein, "Clinical effects of photodynamic therapy on recurrent laryngeal papillomas," *Arch. Otolaryngol. Head Neck Surg.* **118**, 25–29 (1992).

[232] J. Bujia, J. Feyh, and E. Kastenbauer, "Photodynamic therapy with derivatives from hemotoporphyrines for recurrent laryngeal papillomatosis of the children. Early results," *An. Otorrinolaringol. Ibero. Am.* **20**, 251–259 (1993).

[233] I. M. Stender, J. Lock-Andersen, and H. C. Wulf, "Recalcitrant hand and foot warts successfully treated with photodynamic therapy with topical 5-aminolaevulinic acid: a pilot study," *Clin. Exp. Dermatol.* **24**, 154–159 (1999).

[234] M. Y. Lin and L. H. Xiang, "Topical 5-aminolevulinic acid photodynamic therapy for recalcitrant facial flat wart in Chinese subjects," *J. Dermatol.* **35**, 658–661 (2008).

[235] R. Rossi, N. Bruscino, F. Ricceri, M. Grazzini, M. Dindelli, and T. Lotti, "Photodynamic treatment for viral infections of the skin," *G. Ital. Dermatol. Venereol.* **144**, 79–83 (2009).

[236] H. Ichimura, S. Yamaguchi, A. Kojima, T. Tanaka, K. Niiya, M. Takemori, K. Hasegawa, and R. Nishimura, "Eradication and reinfection of human papillomavirus after photodynamic therapy for cervical intraepithelial neoplasia," *Int. J. Clin. Oncol.* **8**, 322–325 (2003).

[237] Y. P. Istomin, T. P. Lapzevich, V. N. Chalau, S. V. Shliakhtsin, and T. V. Trukhachova, "Photodynamic therapy of cervical intraepithelial neoplasia grades II and III with Photolon," *Photodiagnosis Photodyn. Ther.* **7**, 144–151 (2010).

[238] E. V. Ross, R. Romero, N. Kollias, C. Crum, and R. R. Anderson, "Selectivity of protoporphyrin IX fluorescence for condylomata after topical application of 5-aminolaevulinic acid: implications for photodynamic treatment," *Br. J. Dermatol.* **137**, 736–742 (1997).

[239] V. Nucci, D. Torchia, and P. Cappugi, "Treatment of anogenital condylomata acuminata with topical photodynamic therapy: report of 14 cases and review," *Int. J. Infect. Dis.* **14**(Suppl 3), e280–e282 (2010).

[240] M. K. Fehr, C. F. Chapman, T. Krasieva, B. J. Tromberg, J. L. McCullough, M. W. Berns, and Y. Tadir, "Selective photosensitizer distribution in vulvar condyloma acuminatum after topical application of 5-aminolevulinic acid," *Am. J. Obstet. Gynecol.* **174**, 951–957 (1996).

[241] E. S. Abdel-Hady, P. Martin-Hirsch, M. Duggan-Keen, P. L. Stern, J. V. Moore, G. Corbitt, H. C. Kitchener, and I. N. Hampson, "Immunological and viral factors associated with the response of vulval intraepithelial neoplasia to photodynamic therapy," *Cancer Res.* **61**, 192–196 (2001).

[242] Z. P. Bernstein, T. Dougherty, S. Gollnick, S. A. Schwartz, S. D. Mahajan, J. Kepner, A. Sumlin, C. Stewart, P. Wallace, A. Adal, et al., "Photopheresis in HIV-1 infected patients utilizing benzoporphyrin derivative (BPD) verteporfin and light," *Curr. HIV Res.* **6**, 152–163 (2008).

[243] C. H. Wilder-Smith, P. Wilder-Smith, P. Grosjean, H. van den Bergh, A. Woodtli, P. Monnier, G. Dorta, F. Meister, and G. Wagnieres, "Photoeradication of *Helicobacter pylori* using 5-aminolevulinic acid: preliminary human studies," *Lasers Surg. Med.* **31**, 18–22 (2002).

[244] M. R. Hamblin, J. Viveiros, C. Yang, A. Ahmadi, R. A. Ganz, and M. J. Tolkoff, "*Helicobacter pylori* accumulates photoactive porphyrins and is killed by visible light," *Antimicrob. Agents Chemother.* **49**, 2822–2827 (2005).

[245] R. A. Ganz, J. Viveiros, A. Ahmad, A. Ahmadi, A. Khalil, M. J. Tolkoff, N. S. Nishioka, and M. R. Hamblin, "*Helicobacter pylori* in patients can be killed by visible light," *Lasers Surg. Med.* **36**, 260–265 (2005).

[246] A. J. Lembo, R. A. Ganz, S. Sheth, D. Cave, C. Kelly, P. Levin, P. T. Kazlas, P. C. Baldwin, 3rd, W. R. Lindmark, J. R. McGrath, et al., "Treatment of *Helicobacter pylori* infection with intra-gastric violet light phototherapy: a pilot clinical trial," *Lasers Surg. Med.* **41**, 337–344 (2009).

[247] G. E. Lang, S. Mennel, G. Spital, J. Wachtlin, B. Jurklies, H. Heimann, B. Damato, and C. H. Meyer, "Different indications of photodynamic therapy in ophthalmology," *Klin Monbl Augenheilkd* **226**, 725–739 (2009).

[248] R. Wormald, J. Evans, L. Smeeth, and K. Henshaw, "Photodynamic therapy for neovascular age-related macular degeneration," *Cochrane Database Syst. Rev.* **19**, CD002030 (2005).

[249] L. F. Stuart, W. B. Jeffrey, G. M. Maureen, and C. H. Allen, "Age-related macular degeneration," *New. Eng. J. Med.* **342**, 483–492 (2000).

[250] R. K. Chowdhary, I. Shariff, and D. Dolphin, "Drug release characteristics of lipid based benzoporphyrin derivative," *J. Pharm. Pharm. Sci.* **6**, 13–19 (2003).

[251] D. Husain, J. W. Miller, N. Michaud, E. Connolly, T. J. Flotte, and E. S. Gragoudas, "Intravenous infusion of liposomal benzoporphyrin derivative for photodynamic therapy of experimental choroidal neovascularization," *Arch. Ophthalmol.* **114**, 978–985 (1996).

[252] TAP-Study-Group, "Vertoporfin therapy for subfoveal choroidal neovascularization in age-related macular degeneration. Three-year results of an open-labeled extension of 2 randomized clinical trials-TAP report 5," *Arch. Opthalmol.* **120**, 1307–1314 (2002).

[253] TAP-Study-Group, "Effects of vertoporfin therapy on contrast on sensitivity: Results from the treatment of age-related macular degeneration with photodynamic therapy (TAP) investigation-TAP report No.4," *Retina* **22**, 536–544 (2002).

[254] VIP-Study-Group, "Photodynamic therapy of subfoveal choroidal neovscularization in pathologic myopia with verteporfin. 1-year results of a randomized clinical trial-VIP report no.1," *Opthalmology* **108**, 841–852 (2001).

[255] VIP-Study-Group, "Verteporfin therapy of subfoveal choroidal neovascularization in age-related macular degeneration: two-year results of a randomized clinical trial including lesions with occult with no classic choroidal neovascularization verteporfin in photodynamic therapy report 2," *Am. J. Ophthalmol.* **131**, 541–560 (2001).

[256] VIP-Study-Group, "Verteporfin therapy of subfoveal choroidal neovascularization in pathologic myopia: 2-year results of a randomized clinical trial VIP report no. 3," *Ophthalmology* **110**, 667–673 (2003).

[257] P. Kaiser, "Verteporfin therapy of subfoveal choroidal neovascularization in age-related macular degeneration: 5-year results of two randomized clinical trials with an open-label extension: TAP report no. 8," *Graefes Arch. Clin. Exp. Ophthalmol.* **244**, 1132–1142 (2006).

[258] K. Hayashi, K. Ohno-Matsui, S. Teramukai, N. Shimada, M. Moriyama, W. Hara, T. Yoshida, T. Tokoro, and M. Mochizuki, "Photodynamic therapy with verteporfin for choroidal neovascularization of pathologic myopia in Japanese patients: comparison with nontreated controls," *Am. J. Ophthalmol.* **145**, 518–526 (2008).

[259] A. P. Castano, T. N. Demidova, and M. R. Hamblin, "Mechanisms in photodynamic therapy: Part three ÄîPhotosensitizer pharmacokinetics, biodistribution, tumor localization and modes of tumor destruction," *Photodiagnosis Photodyn. Ther.* **2**, 91–106 (2005).

[260] X. Y. Shen, N. Zacal, G. Singh, and A. J. Rainbow, "Alterations in mitochondrial and apoptosis-regulating gene expression in photodynamic therapy-resistant variants of HT29 colon carcinoma cells," *Photochem. Photobiol.* **81**, 306–313 (2005).

[261] N. L. Oleinick, R. L. Morris, and I. Belichenko, "The role of apoptosis in response to photodynamic therapy: what, where, why, and how," *Photochem. Photobiol. Sci.* **1**, 1–21 (2002).

[262] C. J. Gomer, S. W. Ryter, A. Ferrario, N. Rucker, S. Wong, and A. M. Fisher, "Photodynamic therapy-mediated oxidative stress can induce expression of heat shock proteins," *Cancer Res.* **56**, 2355–2360 (1996).

[263] M. Korbelik, J. Sun, and I. Cecic, "Photodynamic therapy-induced cell surface expression and release of heat shock proteins: relevance for tumor response," *Cancer Res.* **65**, 1018–1026 (2005).

[264] D. J. Granville, C. M. Carthy, H. Jiang, J. G. Levy, B. M. McManus, J. Y. Matroule, J. Piette, and D. W. Hunt, "Nuclear factor-kappaB activation by the photochemotherapeutic agent verteporfin," *Blood* **95**, 256–262 (2000).

[265] G. Kick, G. Messer, G. Plewig, P. Kind, and A. E. Goetz, "Strong and prolonged induction of c-jun and c-fos proto-oncogenes by photodynamic therapy," *Br. J. Cancer* **74**, 30–36 (1996).

[266] J. Sun, I. Cecic, C. S. Parkins, and M. Korbelik, "Neutrophils as inflammatory and immune effectors in photodynamic therapy-treated mouse SCCVII tumours," *Photochem. Photobiol. Sci.* **1**, 690–695 (2002).

[267] W. J. de Vree, M. C. Essers, H. S. de Bruijn, W. M. Star, J. F. Koster, and W. Sluiter, "Evidence for an important role of neutrophils in the efficacy of photodynamic therapy in vivo," *Cancer Res.* **56**, 2908–2911 (1996).

[268] G. Krosl, M. Korbelik, and G. J. Dougherty, "Induction of immune cell infiltration into murine SCCVII tumour by photofrin-based photodynamic therapy," *Br. J. Cancer* **71**, 549–555 (1995).

[269] I. Cecic, K. Serrano, M. Gyongyossy-Issa, and M. Korbelik, "Characteristics of complement activation in mice bearing Lewis lung carcinomas treated by photodynamic therapy," *Cancer Lett.* **225**, 215–223 (2005).

[270] W. J. Magner and T. B. Tomasi, "Apoptotic and necrotic cells induced by different agents vary in their expression of MHC and costimulatory genes," *Mol. Immunol.* **42**, 1033–1042 (2005).

[271] W. C. Bartholomae, F. H. Rininsland, J. C. Eisenberg, B. O. Boehm, P. V. Lehmann, and M. Tary-Lehmann, "T cell immunity induced by live, necrotic, and apoptotic tumor cells," *J. Immunol.* **173**, 1012–1022 (2004).

[272] C. Volanti, G. Gloire, A. Vanderplasschen, N. Jacobs, Y. Habraken, and J. Piette, "Downregulation of ICAM-1, and VCAM-1 expression in endothelial cells treated by photodynamic therapy," *Oncogene* **23**, 8649–8658 (2004).

[273] W. Sluiter, W. J. de Vree, A. Pietersma, and J. F. Koster, "Prevention of late lumen loss after coronary angioplasty by photodynamic therapy: role of activated neutrophils," *Mol. Cell. Biochem.* **157**, 233–238 (1996).

[274] M. Korbelik, G. Krosl, J. Krosl, and G. J. Dougherty, "The role of host lymphoid populations in the response of mouse EMT6 tumor to photodynamic therapy," *Cancer Res.* **56**, 5647–5652 (1996).

[275] A. P. Castano, P. Mroz, and M. R. Hamblin, "Photodynamic therapy and anti-tumour immunity," *Nat. Rev. Cancer* **6**, 535–545 (2006).

11

IMAGING AND PROBING CELLS BEYOND THE OPTICAL DIFFRACTION LIMIT

MARK SCHÜTTPELZ AND THOMAS HUSER
Biomolecular Photonics, Department of Physics, University of Bielefeld, Bielefeld, Germany

11.1 THE QUEST FOR ACHIEVING OPTICAL RESOLUTION BEYOND ABBE'S LIMIT

The nondestructive chemical analysis of biological structures and dynamic processes in the crowded intracellular environment, at cellular membranes, and between cells with a spatial resolution well beyond the diffraction limit is a major problem in biomedical research. Many fundamental biological interactions and biochemical processes that occur at the subcellular length scale can ultimately lead to the onset of disease. These underlying causes, such as genetic mutations, the overexpression of proteins, misfolding of proteins, absence of proteins, or interactions between macromolecules that should not be interacting, can often be identified using biochemical assays after large quantities of cells have been digested and dissolved into their individual macromolecular constituents, but typically not within the cellular context. Here, specialized approaches, such as fluorescence *in situ* hybridization (FISH) or specific live cell fluorophores have to be used, although many of these are not applicable *in vivo* [1]. Imagine, for example, the structure and size of mitochondria. Mitochondria are the powerhouses of cells, yet they have dimensions that can barely be imaged by standard optical microscopy, so slight structural defects in mitochondria are difficult to very difficult to detect. Mitochondria are, however, the first cellular

---

Photonics: Scientific Foundations, Technology and Applications, Volume IV, First Edition.
Edited by David L. Andrews.
© 2015 John Wiley & Sons, Inc. Published 2015 by John Wiley & Sons, Inc.

compartments that signal the tendency of a cell to die, that is, to undergo apoptosis. It has, for example, been reported, that one way by which stem cells enable diseased cells to recover is by the transfer of mitochondria [2]. Another important example for subcellular structures affecting the health of an entire organism are slight differences (mutations) in structural proteins that, for example, make up the cytoskeleton of cells, which leads to abnormal shapes of organs, body parts, or the fatal cessation of function, for example, of heart muscle cells. Most viruses are also well below the spatial resolution of optical microscopes, making it difficult to follow their life cycle within a cell. Chromosomes that store the genetic code of a cell can only be visualized just before and during mitosis, but not in chromatin during the often very long G phase. Despite these shortcomings in its spatial resolution, optical microscopy is, however, still the most important imaging technique for biomedical research due to its affordability, long history, and the large number of contrast mechanisms available. It also remains the method of choice for live cell imaging [1]. These facts have continued to drive research into more advanced optical microscopy techniques, and, lately, especially in the area of super-resolution optical microscopy.

Arguably, the origins of super-resolution optical microscopy are closely tied in with the first experimental realization of near-field optics, which enabled optical imaging beyond the diffraction limit. The primary idea behind nanoscale optical imaging and analysis is that in order to overcome the hurdles imposed by Abbe's diffraction limit [1], a nanoscale light source has to be brought in close proximity with the sample to probe a subset of the sample. By raster scanning the source across the sample, a map of the sample on the sub-wavelength scale can then be created, which bridges the gap between conventional optics and electron-beam or X-ray based analyses. Imaging, local probing, and manipulation of biological targets on the nanoscale or the use of optically active nanoscale objects is then exploited to either obtain higher spatial resolution or to achieve higher sensitivity, and, for example, to obtain information about individual events even in the crowded molecular environment inside a cell.

Even though the initially most successful realization of near-field optics, which was also successfully commercialized, has seen a number of interesting applications in materials science, its use with biological materials is rather limited. This is mostly due to the fact, that early near-field optical probes were made by pulling optical glass fibers to very fine tips that are subsequently coated with a thin film of aluminum to prevent leakage of light except at the very end of the probe tip. This results in optical apertures acting as light sources with a diameter of 50–100 nm on average. The concept of and an example for such near-field optical probe tips is shown in Figure 11.1a. These tips are rather fragile and tedious to handle, which makes their use in aqueous environments particularly difficult. Some of the more interesting biological applications involving such tips, such as the sub-wavelength-scale imaging of the co-localization of fluorescently labeled membrane-associated proteins in cells [3], or intracellular probing of analytes, have thus already been demonstrated many years ago. Nonetheless, these applications have demonstrated the difficulties and limitations of near-field optical techniques for live cell applications and have sparked a large number of follow-on developments, such as tip-enhanced spectroscopies, the

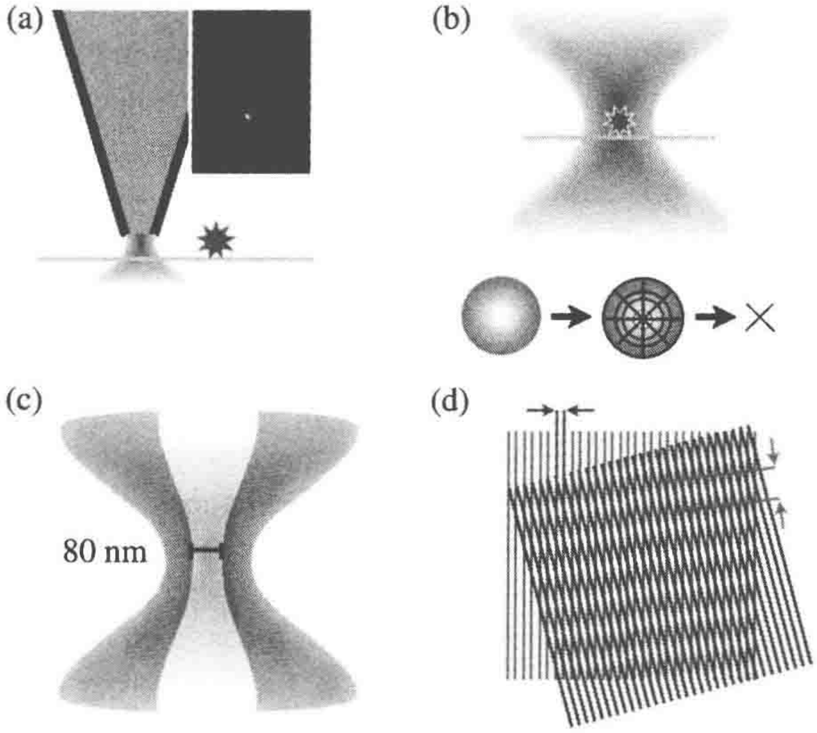

FIGURE 11.1 Overview of different optical super-resolution microscopy techniques. (a) Near-field optical microscopy makes use of ultrasharp glass fiber tips that are metal-coated to prevent leakage from regions other than the very end of the tip. The inset shows a microscope image of such a fiber tip with light launched through the tip. (b) Single molecule localization microscopy fits the position of single fluorescent molecules with a 2D Gaussian fit function to determine the center of mass of fluorescent spots. (c) Stimulated emission depletion (STED) microscopy makes use of the principle of stimulated emission to remove fluorescence from parts of a confocal laser beam. (d) Structured illumination microscopy utilizes 2D/3D frequency mixing between a known illumination pattern and the sample to reconstruct the original sample with double the resolution. (*For a color version of this figure, see the color plate section.*)

development of novel probes, the use of single molecule fluorescence in biology, and a number of novel concepts for far-field optical super-resolution microscopies that do not require the use of probe tips. Tip-enhanced spectroscopies have, nevertheless, continued to be of interest to a number of research groups. In this modality, the fine, nanometer-sized tips of scanning probe microscopes are typically coated with gold or silver to facilitate the excitation of surface plasmons in these tips. The resulting enhanced electric fields can then serve as a means, for example, to locally excite fluorophores by two-photon excitation, or to enhance the inelastic scattering of light, that is, Raman scattering, underneath the tips [4].

Even though the dynamic registration of single fluorescent molecules in aqueous media was achieved a number of years earlier, near-field optics also marked the beginnings of single molecule fluorescence microscopy [5]. The extension of single molecule fluorescence microscopy to biological applications in the crowded environment of cells, however, has proven difficult to achieve, because single molecule detection with conventional optics results in diffraction-limited laser spots on the order of a few hundred nanometers and is thus limited to nanomolar molecular concentrations to ensure that only a single molecule is probed within the probe volume at any given point in time. Typical association constants of biological molecules, in particular proteins, however, are in the micromolar concentration range. This requires that one focuses either on rare events, for example, low copy number gene expression [6], or sparse labeling of the molecules of interest, where only approximately every thousandth molecule is fluorescently labeled [7], or the more recent introduction of photoswitchable fluorophores. If, however, biological targets, for example, motor proteins, are labeled with single fluorescent molecules, and if they can operate under single molecule conditions, then their position can be located with very high precision of close to 1 nm [8]. The point spread function (PSF) of a microscope objective with high numerical aperture can be determined very accurately and, in fact, the emission pattern of a single fluorescent molecule typically represents exactly the PSF. Typical PSFs in the lateral dimensions of a microscope can be fitted with high accuracy by two-dimensional (2D) Gaussian fit functions. Localization of the position of a single molecule to within 1.5 nm has been demonstrated [8] (see the schematics in Fig. 11.1b, where the hourglass-shaped cross section of a confocal microscope is used to excite a molecule, resulting in the 2D intensity spot (the PSF) shown underneath the upper figure, which can be fit with a 2D Gaussian to determine the spot's center of mass). This is sufficient to determine even small steps during enzymatic turnovers or the translational movement of molecular motors. If labeling with brighter probes is possible, for example, through attachment of multiple fluorophores, or fluorescent nanoparticles, this can even be extended to the cellular analysis of vesicular trafficking by motor proteins [9] or virus–cell interactions [10].

11.1.1 The Advent of Far-Field Optical Super-Resolution Imaging Techniques

Super-resolution microscopy techniques have seen a dramatic increase in activity in recent years. In essence, all these techniques rely on schemes that make use of our ability to control molecular emission properties in the far-field. They can be roughly separated into approaches that either use our ability to locate individual fluorescent molecules with high precision (see Fig. 11.1b), or approaches that reduce the probe volume by exploiting specific molecular processes.

The first successful demonstration (also in a commercial sense) of far-field super-resolution optical microscopy was achieved using the concept of stimulated emission depletion (STED) [11]. It is a direct extension of the popular confocal fluorescence microscopy [1], providing instant optical sectioning capability and single molecule sensitivity. STED microscopy is not only a direct super-resolution imaging technique, in many cases requiring no further image processing or mathematical deconvolution, but it is also directly compatible with most other confocal optical analysis techniques [12]. STED makes use of the fact that fluorescence can be depleted by stimulating the emission of photons from excited states—the same mechanism that is, for example, used to achieve tunable emission in dye lasers. In STED, a shaped laser beam with a wavelength within the emission spectrum of the fluorophores in the sample is overlapped with the excitation beam (see the cross-section schematics in Fig. 11.1c). The shape of this STED beam is typically a donut mode, which depletes fluorescence in those parts of the sample where both beams overlap, while the central hole continues to spontaneously emit fluorescent photons. The resolution of this technique is, in principle, only limited by the specific depletion pattern used, by the amount of overlap that can be achieved between the two beams, and the intensity of the depletion beam [13] (among other, somewhat less stringent parameters, such as the fluorophore density, or the signal-to-noise ratio with which the fluorescence is detected).

In a technically somewhat simpler implementation compared to STED that also achieves optical super-resolution, structured illumination microscopy has gained considerable interest, mostly due to the fact that it can readily be applied to most samples prepared for conventional fluorescence microscopy. Structured illumination microscopy acquires high-resolution images of fluorescent samples by exciting them with a sinusoidal illumination pattern rather than uniform illumination [14]. No special fluorescent probes are required for this type of super-resolution microscopy, but they might be beneficial in enhancing its ultimately achievable resolution even further. In structured illumination microscopy, a periodic illumination pattern is created in the focal plane and then moved across the sample laterally and at different angles. A small number (~ 9–15) images have to be acquired in order to reconstruct a high-resolution image per vertical plane. This scheme works because sample features with higher spatial frequency than the illumination pattern are modulated by the pattern and result in beat frequencies that fall within the transfer function of the microscope (see the schematics in Fig. 11.1d). Since the periodicity of the illumination pattern is known, its effects on the image can be calculated and high-resolution images can be reconstructed. By moving the sample through the illumination pattern in the vertical direction, high-resolution images of the entire sample in all three dimensions are obtained.

Alternatively, in the mid-2000s, wide-field microscopy approaches utilizing the localization of single fluorescent molecules have emerged. The most prominent implementations of this concept, such as photoactivated localization microscopy (PALM) [15] or stochastic optical reconstruction microscopy (STORM) [16] use photoswitching of molecular fluorescence emission to identify individual molecules, the coordinates of which are then located on the nanometer scale. Typically, PALM and STORM require the acquisition of large amounts of image data, each of which have to be fitted to the known PSF of the microscope system, and the final images have to be reconstructed from the large set of individual snapshots. Special fluorescent probes with photoswitchable emission are often required for this purpose. These techniques work well in the lateral dimensions, but extension to the third dimension at high resolution remains somewhat challenging, and it seems unlikely that the extensive number of images that have to be acquired together with the high rate of sample exposure, and the computational effort needed for reconstructing images will permit rapid live cell imaging anytime soon.

In the following we will discuss the most prominent far-field super-resolution optical microscopy approaches in greater detail, discuss some of their recent successes, and speculate on their potential and further developments for the near future.

11.2 STIMULATED EMISSION DEPLETION MICROSCOPY

Stimulated emission depletion (STED) microscopy is based on the ingenious concept first postulated by Einstein that the emission of fluorophores can be stimulated when a strong field at a wavelength within their emission spectrum is present. The use of this concept to overcome the diffraction limit was first suggested by Hell in 1994 [11]. The idea behind it is actually quite simple and related to some other approaches that play with the fluorescent states of molecules. If, after the excitation of a large number of fluorescent molecules, for example, in the confocal spot of a laser scanning microscope, one can selectively remove some of these molecules from contributing to the signal, then the detection volume can be considerably decreased. The selective removal of such molecules is called "depletion." To truly remove most or, possibly, all fluorescent molecules from the excited state in this region, the depletion has to be saturated, requiring fairly high laser intensities. In the case of STED, the excited state fluorescence of some of the molecules in the excitation volume is depleted by stimulating their emission, which occurs on much faster timescales and in a spectrally much narrower region than spontaneous fluorescence. The trick then becomes to find ways to distinguish the spontaneous emission of fluorescence from the stimulated emission. Multiple such ways of distinguishing stimulated emission from spontaneous emission, such as time-gated fluorescence detection, depletion at the far end of the emission spectrum, and detection of the spontaneous emission by bandpass filters, or the use of narrow blocking filters that prevent the spectrally narrow stimulated emission from reaching the detector have been demonstrated [17]. The nonlinear nature of saturated emission depletion is what ultimately improves the spatial resolution of STED microscopy, and the classical Abbe lateral resolution limit transforms into [17]

$$\Delta r \approx \frac{\lambda}{2NA\sqrt{1 + I/I_{\text{sat}}}}, \tag{11.1}$$

where I/I_{sat} is the ratio between the excitation intensity I and the intensity of the saturated depletion beam I_{sat}. This implies that for a ratio of $I/I_{\text{sat}} = 100$, the theoretical improvement in the lateral resolution of a STED microscope is about a factor of 10 improved over Abbe's limit.

The major advantage of STED microscopy is that in most cases no special sample preparation is required (some fluorophores are not as conducive to STED as most others), and that, again in most cases, no further image processing or mathematical deconvolution is required. The detection sensitivity of STED microscopy is at the level of single fluorescent molecules, and in some of its most impressive demonstrations, the increase in spatial resolution has actually been shown by imaging fluorescent molecules that were immobilized on a surface. In STED, a shaped laser beam with a wavelength within the emission spectrum of the fluorescent probes in the sample is overlapped with the excitation beam (see Fig. 11.2). In the original experimental realization the shaped depletion beam was sent through a phase mask, resulting in two foci in the axial direction that were overlapped with the confocal excitation

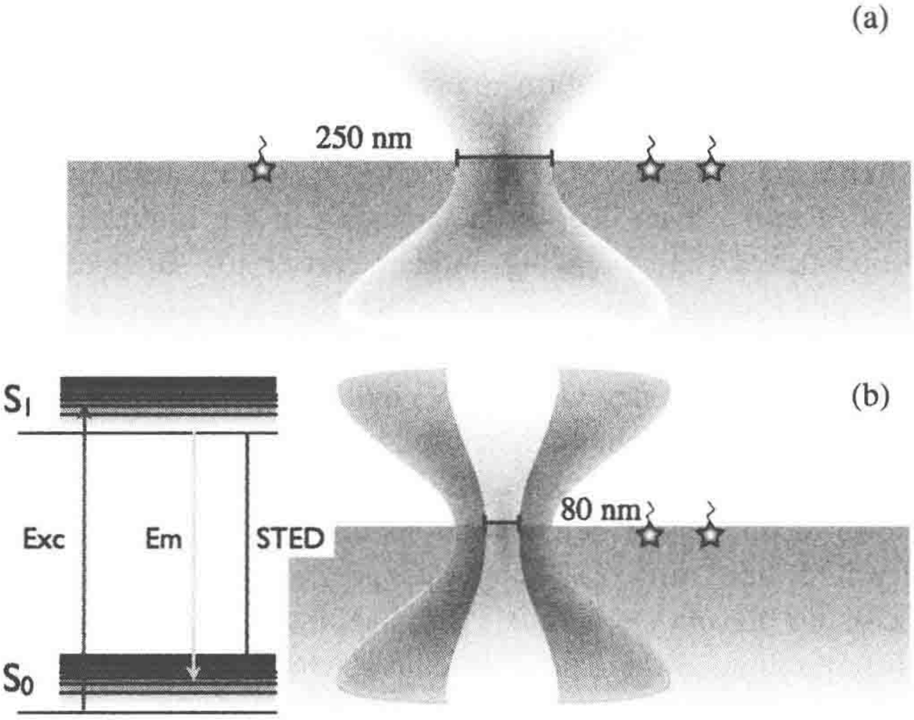

FIGURE 11.2 The concept of stimulated emission depletion (STED). (a) Fluorophores image with the diffraction-limited spot of a confocal microscope result in an optical resolution of approximately 250 nm. (b) If a donut-shaped saturated depletion beam is superposed onto the excitation beam, fluorescence within the depletion pattern is removed by STED, resulting in a reduced spot size of the remaining spontaneous fluorescence emission.

volume [18]. This resulted in an ~5× improvement in the axial resolution of a confocal microscope. In more recent implementations, the shape of the STED beam is typically chosen to be a donut mode, which depletes fluorescence evenly in all lateral directions where both beams overlap, while the central "hole" of the donut continues to spontaneously emit fluorescent photons. The resolution of this technique is, in principle, only limited by the specific depletion pattern used, and the intensity of the depletion beam [13]. As a super-resolution microscopy technique, STED has been demonstrated to produce routine images with ~20 nm resolution in the lateral directions and, when combined with counter-propagating beams (4pi illumination, isoSTED), even in the vertical direction. When applied to more robust fluorescent probes, that is, nitrogen vacancies in diamond, an even higher spatial resolution has been accomplished. In fluorescence correlation spectroscopy mode, where the excitation and STED beams are focused into a solution of probe molecules, a reduction of the excitation volume by a factor of five has been demonstrated [19]. This same experiment also demonstrated the single molecule fluorescence sensitivity of STED. More recently, fluorescence lifetime imaging was achieved with STED by combining a broadband super-continuum-generating pulsed laser as excitation source together with single photon counting [20]. Other, important aspects that have recently been demonstrated using STED include the implementation of multicolor detection [21], and video-rate imaging of synaptic vesicle movement [22]. The limitations of STED microscopy, as well as those of the other super-resolution methods presented here will be discussed at the end of this article.

11.2.1 Applications of STED Microscopy

A large number of technical improvements since its initial realization, such as the use of coherent super-continuum white-light sources, or inexpensive polymer-based phase masks have made STED microscopy ever more attractive for biological research. Most recently, even deep-tissue imaging in the brain of a living mouse has been demonstrated [23], breaking another barrier for super-resolution optical microscopy. Another recent impressive use of STED microscopy is its application to imaging the clustering of a surface glycoprotein on the surface of individual virions of the human immunodeficiency virus (HIV) indicating that STED and other super-resolution microscopy approaches can be used to distinguish between different (e.g., infectious and immature) forms of virus [24].

One of the most impressive demonstrations of STED microscopy was its recent use in the search for lipid rafts [25]. Lipid rafts are believed to be intermediate structures on the cellular plasma membrane, rich in sphingolipids and cholesterol, which represent a different lipid phase. These structures, which have been the topic of active investigation for the last 20 years, are thought to have dimensions on the order of a few tens of nanometers and are believed to be metastable on the millisecond timescale. One of the great virtues of the mechanism behind STED is that, as indicated by the formula shown at the beginning of this section, its spatial resolution is a function of the intensity of the depleting beam. For a low ratio of I/I_{sat} the gain in resolution is minimal (e.g., a factor of 2). As the intensity of the saturated depletion beam is increased, the gain in spatial resolution increases rapidly, ultimately leading to an increase in resolution of a factor of 10 and better. The exact relationship between gain in resolution and the depletion beam power typically needs to be calibrated beforehand. Because of its confocal nature, however, STED can still detect fluorescence from single fluorescent molecules and the increase in resolution can be directly determined from determining the full-width-at-half-maximum (FWHM) of the PSF of single molecules depending on the STED beam intensity. Similarly, by focusing a STED beam into a solution containing fluorescent molecules, the resulting bursts of fluorescence whenever a fluorescent molecule diffuses through the beam can be detected and autocorrelation of these bursts results in an average diffusion time of the molecules through the confocal volume. As the size of the detection volume shrinks with increasing intensity of the saturated depletion beam, the measured diffusion time of the molecules will similarly decrease. When corrected for the change in detection volume, however, the diffusion time of noninteracting molecules will be unaltered no matter what size excitation/detection volume was used. Eggeling and coworkers performed such an experiment on the plasma membrane of living PtK2 cells [25]. They labeled phospholipids, such as phosphoethanolamine (PE), as well as sphingolipids, such as sphingomyelin, by chemical synthesis with the fluorescent dye Atto647N, and similarly, the glycosylphosphatidylinositol (GPI)-anchor of GPI-anchored proteins by acyl carrier protein tagging. They then used STED correlation spectroscopy to measure the transit times of these different membrane constituents through the STED volume focused to the cell's plasma membrane. A seemingly linear dependence of the decrease in the transit time of PE through the STED volume was observed, while for STED focal areas below 80 nm in diameter, a plateau in the transit time of sphingomyelin was observed. This lower limit in the diffusion time of sphingomyelin through the STED focal area is consistent with transient trapping of the sphingolipid and provides strong evidence for the existence of transient lipid structures, such as the elusive lipid rafts.

11.3 PHOTOACTIVATED LOCALIZATION MICROSCOPY AND STOCHASTIC OPTICAL RECONSTRUCTION MICROSCOPY

The potential of utilizing single molecule fluorescence for achieving optical super-resolution was initially postulated in a short and somewhat cryptic paper by Betzig, published in 1995 [26]. It took until the year 2006, before three research groups independently demonstrated similar optical reconstruction methods with a lateral sub-diffraction resolution of better than 20 nm. While Eric Betzig and collaborators, now with the Howard Hughes Medical Institute at the Janelia Farm Research Campus, termed this method "Photoactivated Localization Microscopy" (PALM) [15], S. T. Hess and colleagues from the University of Maine called it "Fluorescence Photoactivation Localization Microscopy" (FPALM) [27]. Using a somewhat different approach using organic fluorophores, Xiaowei Zhuang and collaborators from Harvard University developed STORM "Stochastic Optical Reconstruction Microscopy" [16a].

These photoswitching techniques all have in common that they exploit the temporal separation of single fluorescent emitters, even if the molecules cannot be isolated in space due to the diffraction limit: Multiple localizations of single molecules obtained in a series of images are used to reconstruct a super-resolved image based upon the positions obtained from the localization algorithm.

All of these methods overcome the problem of so far optically unresolvable structures consisting of fluorescent molecules by utilizing special properties of photoactivatable proteins or switchable fluorophores that make it possible to tell if the fluorescence emission was due to a single molecule or not. FPALM uses fluorescent proteins such as the photoactivatable green fluorescent protein (PA-GFP), while PALM also makes use of photoswitchable proteins such as the green fluorescent protein Dronpa [28], or yellow fluorescent proteins like Kaede, Kikume Green–Red (KikGR), and Eos Fluorescent Protein (EosFP). In turn, the first fluorophores that were used for STORM were carbocyanine fluorophores [16a], which exhibit photoswitching properties in the presence [29] or absence of an activator molecule [30]. The latter method, where the bare fluorophore in a special buffer system is used, is therefore called *direct*STORM (*d*STORM). Fluorophores are either switched between a fluorescent bright ("on") and a nonfluorescent dark ("off") state upon illumination with light of different wavelengths (PALM/STORM) or they are photoactivated and subsequently photobleached (FPALM).

Due to their technically relatively simple implementation, wide-field single-molecule based localization approaches such as PALM, STORM, and *d*STORM are currently widely used for super-resolution imaging. Further applications of photoswitching microscopy comprise dynamic studies in living cells and quantitative high-resolution fluorescence imaging, for example, studies that count the number of biomolecules and their structural organization in small subcellular structures or membranes [31].

11.3.1 Direct Stochastic Optical Reconstruction Microscopy

*d*STORM utilizes the intrinsic photoswitching properties that can be observed from a large set of commercially available fluorophores. This simplification over the original implementation of STORM has opened up the potential of localization microscopy to a much larger set of fluorophores that can be used individually or simultaneously for multicolor imaging. The photochemical properties of these fluorophores can be accessed by irradiating the sample with either one [32] or two [33] wavelengths if the appropriate buffer conditions are found. As mentioned earlier, carbocyanine dyes were the first fluorophores used for photoswitching microscopy. Cy5 is irradiated with red laser light at a wavelength of ~647 nm to excite the fluorophore and to read out the fluorescence signal for localization. The switching to the nonfluorescent ("off") state occurs simultaneously while exciting the fluorophore for localization. The fluorescent ("on") state can be reversibly recovered by the use of green laser light with a wavelength of ~514 nm. For live cell imaging, an excitation power ranging from 0.5 to 5 kW cm^{-2} is used. For fixed cells there is no need to prevent cell damage and higher excitation intensities of up to 50 kW cm^{-2} can be applied [34]. For efficient switching properties of cyanine dyes and in order to ensure their prolonged use, oxygen in the buffer medium has to be removed with an enzymatic oxygen-scavenging system [35]. This leads to a dramatically improved reversibility of the photoswitching process that is needed to achieve sufficiently high localization statistics. A system consisting of 0.5 mg ml^{-1} glucose oxidase, 40 μg ml^{-1} glucose catalase, and 10% (wt/vol) glucose is recommended. If this is used, additional sealing of the sample chamber with a cover slip or a thin silicon sheet is needed to prevent ingress of oxygen. Before imaging monoethanolamine (MEA) is added to achieve a final thiol concentration of 10–200 mM to prevent photobleaching. Rhodamine and oxazine fluorophores, however, follow a different photoswitching mechanism compared to carbocyanine dyes. These fluorophores require only a single wavelength for fluorescence excitation and switching to the nonfluorescent state. Fluorescence recovery is caused by oxidation of remaining oxygen in the buffer medium.

For localization microscopy a relatively small subset of all fluorophores attached to the biological structure to be resolved is activated stochastically at any time, effectively confining the fluorescence emission of the activated fluorophores. A fast but low-noise charge-coupled device (CCD) or scientific CMOS (sCMOS) camera with high quantum efficiency for converting photons into photoelectrons (typically a deep-cooled, back-thinned CCD camera) capable of exposure times in the millisecond range is used for image acquisition. Then, high-precision molecular localization with nanometer accuracy is performed for each fluorescent spot detected in the image [36]. A sequence of several thousands to tens of thousands of fluorescence images ("image stack") is recorded using either wide-field or total internal reflection fluorescence

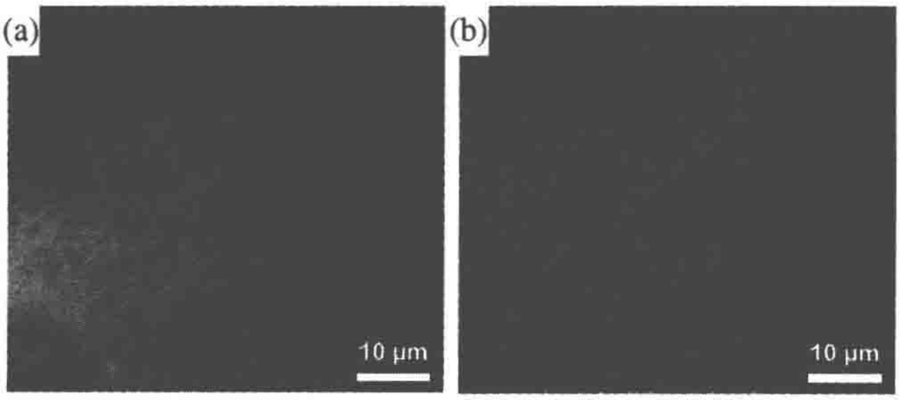

FIGURE 11.3 60 μm × 60 μm image of the cytoskeleton of a COS7 cell labeled with Cy5. (a) Total internal reflection fluorescence (TIRF) image of the cell. (b) *d*STORM image reconstructed from approximately 1 million localizations. Total image frame acquisition time: 100 s.

(TIRF) microscopy (see Fig. 11.3a). All localized fluorophores are combined into one super-resolved image that is able to resolve structures down to 20 nm (see Fig. 11.3b).

11.3.2 Localization of Single Fluorophores

The localization accuracy is dominated by photon statistics, that is, the Poisson distribution of emitted photons. It depends on the number of photons emitted by a fluorophore if background noise is negligible compared to the fluorescence signal. The standard error SE in the fitted fluorophore position, that is, the uncertainty for the localization, can then be written as

$$\mathrm{SE} = \sigma/\sqrt{N}, \tag{11.2}$$

where σ is the standard deviation of the PSF of the experimental setup that is approximated by a 2D Gaussian distribution function, and N is the number of detected photons emitted by the fluorophore [36]. If background noise and the error increase due to a finite pixel size are taken into account, the standard error has to be expanded to

$$\mathrm{SE} = \sqrt{\frac{\sigma^2 + a^2/12}{N} + \frac{8\pi\sigma^4 b^2}{a^2 N^2}}, \tag{11.3}$$

where a is the pixel size and b the background noise [36].

To obtain a localization accuracy of 10 nm or better, more than 1000 photons have to be detected from one fluorophore within a data acquisition time in the millisecond range. For accuracy down to a few nanometers ~10,000 photons have to be collected. Due to switching and bleaching of fluorophores usually only several hundred photons reach the detector such that an accuracy of around 20 nm is expected for most experiments.

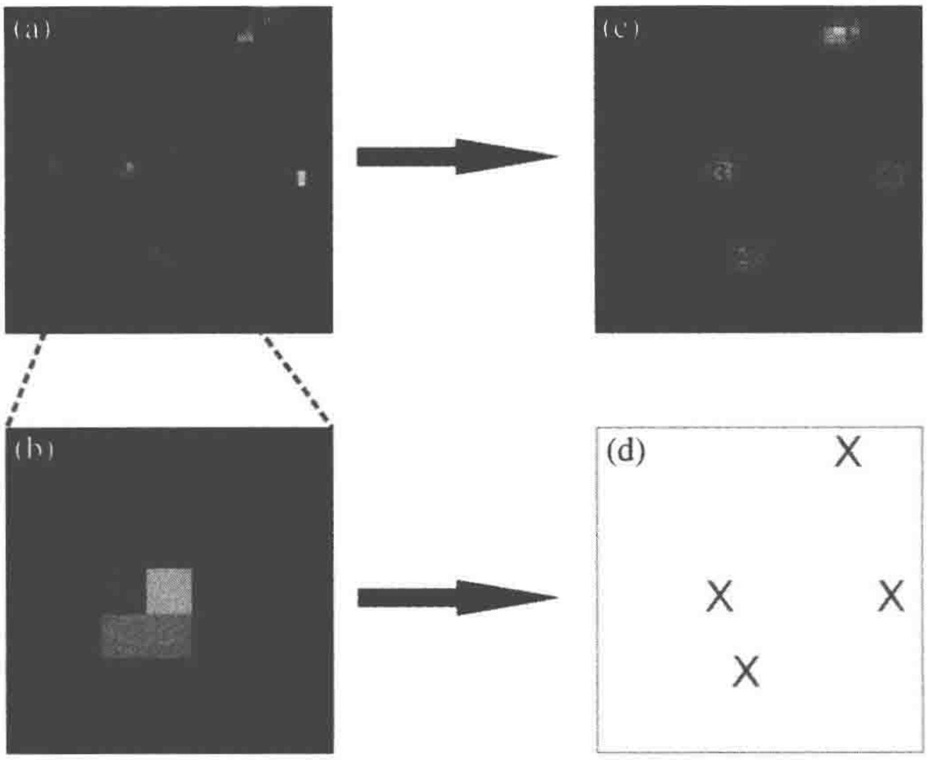

FIGURE 11.4 Principle of single molecule localization microscopy. (a) Single frame of a sequence of *d*STORM images indicating the presence of single molecules based on the discrete spots visible in the image. (b) Close-up of one of the fluorescent spots. Each spot is first recognized, then fit with a 2D Gaussian fit function to (c) result in an image of the fitted spots. From here, the (d) center of mass of each of the spots is determined.

Besides finding the appropriate chemical environment optimal for photoswitching depending on the fluorophore and the sample, data processing and analysis is a challenging task. The experimentally obtained data, that is, the acquired image stack, has to be processed rapidly but also accurately. The major drawback of the localization method is that the computational effort of localizing the fluorophores with nanometer accuracy is tremendous. Long data processing times can, hence, limit fast and real-time biological applications. However, data processing can be separated into three parts (see Fig. 11.4): (1) Find the locations of spot candidates indicating fluorophores (e.g., using a simple thresholding condition); (2) fit a model of the PSF to each of these spot candidates; and (3) find the true location of the fluorophores by examining the results of the fit parameters. A fast and robust image-processing algorithm for the localization of fluorophores with nanometer accuracy was found using only a few assumptions and simplifications [37]. This scheme mainly consists of a fast and accurate PSF reversal using fixed-width, fixed-orientation Gaussian functions for images with low signal-to-noise ratio capable of real-time image reconstruction on a present-day personal computer.

The entire image stack is analyzed image-by-image by processing each acquired raw image (Fig. 11.4a) in mainly five steps: (1) noise reduction, (2) finding likely candidates (3) fitting a 2D Gaussian function to pixels close to the candidate position (Fig. 11.4c): (4) judging the fit; and, finally, (5) localization and visualization of the fluorophore position.

Noise reduction is an important task because raw data images contain a very weak fluorescence signal emitted from a single fluorophore only. Detection of up to 1000 photons per exposure is required and a nevertheless significant background and noise level on the camera chip lead to a marginal signal-to-noise ratio. Noise reduction algorithms and subsequent finding of likely spot candidates have to be reliable: finding many spot candidates caused by fluorescence emission (true positives) while yielding the least number of false-spot candidates that are caused by noise (false positives). The false positive rate must be kept as low as possible because it can lead to false localizations, and therefore waste a lot of computation time. Furthermore, false positives lead to artifacts in the reconstructed image that can, in the worst case, exceed the number of true localizations. Noise reduction can be performed with different algorithms, for example, averaging, median filtering, or by a Gaussian kernel mask. While different morphological transformations might also be possible, an averaging algorithm performs quite similarly but much faster (~0.05 ms per image) than all the others.

To find spot candidates, a non-maximum suppression (NMS) algorithm is used. The NMS extracts the positions of pixels that are local maximums by setting all pixels in the defined neighborhood that are lower than the maximum value in that region to black. The located maximum positions are then considered spot candidates and sorted in descending order by their intensity. A 2D Gaussian function G is fitted to the raw image data at the assumed maximum positions starting with the spot candidate with the highest intensity:

$$G(\vec{x}) = \frac{A}{2\pi\sqrt{|V|}} \exp\left(-\frac{1}{2}(\vec{x}-\vec{x}_0)^{\mathrm{T}} V (\vec{x}-\vec{x}_0)\right) + B, \qquad (11.4)$$

where A is the amplitude of the emitted signal, B the local background signal, $\vec{x}_0$ (superscript T indicates the transpose of the vector) the fluorophore position with "subpixel"-accuracy and V the fixed covariance matrix given by

$$V = \begin{pmatrix} \sigma_x^2 & \rho\sigma_x\sigma_y \\ \rho\sigma_x\sigma_y & \sigma_y^2 \end{pmatrix}, \qquad (11.5)$$

where σ_x and σ_y are the standard deviations in x and y directions, respectively. ρ indicates the correlation between the x- and y-axes. The user must supply an initial rough estimate for this covariance matrix followed by internal iterative improvement of these parameters while processing the raw data images for the purpose of speed and accuracy. Fitting is performed using the Levenberg–Marquardt least-squares algorithm. A spot candidate is considered a fluorescence signal if defined localization criteria, such as a reasonable position and amplitude threshold, are met. After processing the image stack, a super-resolution image is then reconstructed based on the positive localizations. With an optimized fit process, separation of the average mask and utilization of advanced processor instruction sets, real-time computation of sub-diffraction images is possible even for the shortest possible *d*STORM acquisition rates taken with a frame rate of ~1 kHz.

PALM/STORM measurements are prone to high background arising from autofluorescence of the sample and residual fluorophores in the supernatant buffer. Therefore, and in order to collect many photons for precise localization, dyes with high quantum yield are preferred. Additionally, the fluorophores have to exhibit short "on"-times compared to "off"-times such that only a small fraction of fluorophores is fluorescent while the others remain in the dark state. Otherwise it is possible that two adjacent fluorophores are both in the "on"-state at the same time, leading to false localization. On the other hand, according to the Nyquist–Shannon sampling theorem the density of the fluorophores has to be twice as high as the desired (super) resolution. Taking the size of a fluorophore-labeled antibody into account, a biological structure has to be very densely labeled with antibodies. As shown above, in *d*STORM a Gaussian function is fit to a separated fluorescence signal. With increasing labeling density the probability for non-separated signals rises. In order to handle these images fitting of multiple connected PSFs to a fluorescence signal emitted from connected fluorophores [38] is required.

11.3.3 Beyond *d*STORM

A natural, immediate extension of STORM is super-resolution imaging in three dimensions, termed 3D-STORM. In order to determine the axial position and, hence, to obtain the complete 3D information of a fluorophore with sub-diffraction resolution, optical astigmatism was used in a first implementation. In this approach, a cylindrical lens is incorporated into the optical detection path that yields two different focal planes in the x and y directions. This leads to an ellipsoidal deformation of the PSF for fluorophores that are above or below the focal plane, and to a symmetrically round PSF for fluorophores that are in the average focal plane. This results in an additional axial resolution of $\sim$50 nm, even in micrometer thick samples, while maintaining a lateral resolution of 20–30 nm [39]. Other recent approaches to extend STORM to the third dimension include the use of temporal focusing in wide-field two-photon excitation [40], or the combination with selective plane excitation [41].

Besides photoswitching between "on"- and "off"-states many similar methods have emerged that take advantage of related phenomena. This includes reversible photobleaching microscopy (RPM) and ground-state depletion with individual molecule return (GSDIM) that use standard dyes such as fluorescein, Alexa Fluor, ATTO dyes, and carbocyanine dyes either under simple buffer conditions or in an oxygen scavenging system with additional thiols. RPM utilizes reversibly induced long-lived ($>$10 s) dark states of the fluorophore. After high-power illumination of the sample, single fluorophores stochastically return to the ground state. Reversible photobleaching was reported for different dyes, in dry samples in air, and this approach does not require any special (oxygen scavenging) buffer [42]. The GSDIM technique, on the other hand, lowers the number of fluorescent molecules by populating a metastable dark (triplet) state. The images acquired during such an experiment collect fluorescent photons only from individual fluorophores that stochastically return to the ground (singlet) state [43].

11.3.4 Applications of Localization Microscopy

Recent applications of *d*STORM and PALM have shown that super-resolution methods are powerful tools for studying biological samples since the size of many biological structures, which could not be optically resolved in the past, is in the range between 10 and 100 nm. It is expected that imaging of single molecules in *living* cells has the potential to reveal new concepts in cell biology. For instance, PALM was used to study the organization of single proteins in bacteria [44] and near the surface in eukaryotic cells [45] to determine how proteins assemble and organize themselves into clusters that are responsible, for example, for chemotaxis in bacterial cells. Recently, using *d*STORM the structure of nuclear pore complexes in the nuclear envelopes of isolated *Xenopus laevis* oocytes was investigated. The lateral resolution obtained with two-color *d*STORM was ~15 nm. To further improve the spatial resolution, super-resolved images accumulated from hundreds of nuclear pore complexes were taken into consideration to determine the diameter of the central channel to be 41 ± 7 nm. This level of detail was sufficient to determine that the nuclear pore glycoprotein-210 (gp210) that anchors the pore complex to the nuclear membrane is distributed in an eightfold radial symmetry [46].

Optical super-resolution methods permit not only the reconstruction of highly spatially resolved images, but also the quantitative counting of individual molecules in cells. For example, another recent application reported that this method can be used to count the centromere-specific histone H3 variant in the centromere protein A (CENP-A) with single-molecule sensitivity in fission yeast (*Schizosaccharomyces pombe*). Using this approach, it was found that CENP-A is deposited solely during the G2 phase of the cell cycle [47].

In summary, localization-based microscopy approaches result in highly resolved images and also provide quantitative information about biological samples. The implementation of *d*STORM circumvents the use of only a select number of fluorophores and extends this method to a much wider range of fluorophores. The application to living biological samples is, however, somewhat restricted to problems exhibiting fairly slow dynamics, due to the large number of images that need to be acquired in order to reconstruct highly resolved fluorescence images.

11.4 STRUCTURED ILLUMINATION MICROSCOPY

Structured illumination microscopy (SIM) as a way of improving the spatial resolution of optical microscopy was first demonstrated in slightly different implementations by Heintzmann and Cremer in 1999 [48], as well as Frohn and coworkers [49], and separately by Gustafsson and coworkers [50], in 2000. SIM is in essence an implementation of wide-field fluorescence microscopy, but using an illumination pattern rather than homogeneous excitation. The illumination pattern can be produced by a number of different ways. Early papers used interference patterns in two dimensions (e.g., created by the counter-propagation of two evanescent waves at the surface of a glass prism [49], or by using interference between different diffraction orders of a diffraction grating [48–50]); more recently, electro-optical devices (e.g., a spatial light modulator (SLM) [51]) are employed. Fluorescence images of the sample are then typically acquired with a highly sensitive CCD camera. In essence, this type of microscopy is an extension of patterned optical microscopy, which was initially invented as a means of optical sectioning without the need for confocal optics [52].

SIM is based on essentially the same idea as frequency mixing in radio wave transmission. A carrier frequency is mixed with a sample frequency in order to transmit the signal across the passband of the optical microscope. In first order, this simple trick enables optical sectioning without the need for a confocal pinhole to help reject out-of-focus light. By projecting an illumination pattern into the sample, in the focal plane the modulation produced by the pattern provides maximum contrast. Imagine, for example, a sinusoidal illumination pattern that is leading to "striped" excitation of the sample (this description is based on exciting fluorescence contrast but could certainly be applied to other contrast mechanisms). If this pattern is shifted across the sample, its projection will produce a strong contrast in the focal plane according to the projected excitation intensity. When an image of this pattern is acquired on a CCD camera held in a conjugate plane to the focal plane, the response of the sample will be imaged with maximum intensity obtained for regions within the vertical focal plane of the microscope plane that are exposed to the peaks of the illumination pattern. Regions exposed to the valleys of the pattern, on the other hand, will exhibit little to no contribution to the image and appear dark. At the same time, since we are transmitting light vertically through the sample, parts of the sample that are out-of-focus will also be excited, but with less pronounced contrast. If the illumination pattern is now shifted across the sample in the lateral direction, other parts of the sample in the focal plane will now be illuminated and lead to high intensity at the CCD camera, while the background will still only contribute with a much weaker contrast. A simple algorithm that calculates the difference between the highest intensity and the lowest intensity for every pixel in a series of images where the illumination pattern was shifted across the sample will then result in an image consisting primarily of contributions from the focal plane. Out-of-focus contributions will have very similar intensities for all illumination conditions and will thus be removed by this simple "max–min" difference approach. More sophisticated algorithms will furthermore lead to denoising of the images and improve contrast even more. Such approaches to SIM are available in commercial implementations, for example, in the form of the Zeiss Apotome, a low-cost addition to an optical microscope providing confocal-like axial sectioning [52,53].

Now imagine the frequency of the illumination pattern being increased to the point where it approaches the maximum spatial frequency that can still be transmitted through the microscope lens. If this pattern of known frequency is used to illuminate another (not necessarily regular) pattern of unknown frequency it will lead to the well-known Moire effect in two dimensions, that is, spatial frequency mixing leading to additional contrast in an image. This is demonstrated in Figure 11.1d.

Let us first investigate this concept in the easily understandable case of pure frequency mixing. The addition of two cosine functions with different frequencies

ω_1 and ω_2, leads to a beat mode carrying with two new frequencies, one at the sum of the two original frequencies, the other at the difference frequency:

$$\cos(\omega_1 t) + \cos(\omega_2 t) = 2\cos\left(\frac{\omega_1 t + \omega_2 t}{2}\right)\cos\left(\frac{\omega_1 t - \omega_2 t}{2}\right). \tag{11.6}$$

The same holds true for spatial frequencies k_I and k_2:

$$\cos(k_1 x) + \cos(k_2 x) = 2\cos\left(\frac{k_1 x + k_2 x}{2}\right)\cos\left(\frac{k_1 x - k_2 x}{2}\right). \tag{11.7}$$

This is the well-known mechanism of heterodyning. If one of the two frequencies is known, then the other one can be determined by measuring, for example, the reduced frequency of the envelope of the beat pattern. For a limited passband this does, however, only work up to twice the frequency of the passband. For any frequencies higher than that, even the difference frequency will be lying beyond the passband. Translated to the 2D space of images, this is best understood by studying images in Fourier space. An arbitrary image when transformed to Fourier space results in a 2D Fourier image showing spatial frequencies within a circular pattern. Low frequencies appear near the center of the Fourier image, while high spatial frequencies appear near the borders of the Fourier image. If an image is filtered, for example, by the optical transfer function (OTF) of a microscope lens such that its smallest features still occupy more than just a single pixel on a CCD camera, then the Fourier-transform of the image results in a circle, where the highest spatial frequencies occupy the circumference of the circle and determine its radius, while low spatial frequencies appear near the center of the circle. A sinusoidal pattern with a low spatial frequency results in two delta peaks, while the axis through these two delta peaks indicates the direction along which the periodically varying pattern is oriented. If the periodicity of this pattern is increased, the two delta peaks will begin to move toward the circumference of the circle of "allowed" frequencies being transmitted through the microscope optics. Now, imagine such a pattern with a frequency close to the maximum allowed frequency mixing with an unknown pattern of interest containing spatial frequencies beyond the passband of the OTF of the microscope. In this case, a Moire pattern similar to our example in the 1D case will form that downshifts any frequencies less than twice the maximum allowed frequency into the range of allowed spatial frequencies. Based on the knowledge of the modulation frequency, the unknown frequency can then be calculated. In the following, we will briefly cover the theory for 2D/3D SIM. Generally speaking, the image D observed of a fluorescent sample in a fluorescence microscope is the convolution of the fluorescence emission E and the PSF H: $D(\vec{r}) = (E \otimes H)(\vec{r})$. In the case of a structured illumination microscope, the fluorescence emission is also the product of a spatially varying illumination pattern I and the spatial distribution of the fluorescent dyes S: $E(\vec{r}) = S(\vec{r})I(\vec{r})$. Now, let us assume the illumination pattern is a sinusoidal stripe pattern along a specific angle, described by a wave vector k_{ill}, and a specific phase φ:

$$I(\vec{r}) = \frac{I_0}{2}\left[1 - \cos\left(\vec{k}_{\text{ill}} \cdot \vec{r} + \varphi\right)\right]. \tag{11.8}$$

The resulting image is then described by: $D(\vec{r}) = (S(\vec{r}) \cdot I(\vec{r})) \otimes H(\vec{r})$. If we now move our discussion to the reciprocal Fourier space, this expression is simplified because the deconvolution between the PSF and the fluorescence emission turns into a simple product:

$$\tilde{D}(\vec{k}) = \tilde{H}(\vec{k})[\tilde{I}(\vec{k}) \otimes \tilde{S}(\vec{k})]. \tag{11.9}$$

The Fourier transform of the illumination pattern turns into a series of Delta functions, which is the virtue of using a sinusoidally varying stripe pattern:

$$\tilde{I}(\vec{k}) = \frac{I_0}{2}\left[\delta(\vec{k}) - \frac{1}{2}\delta(\vec{k} - \vec{k}_{\text{ill}})e^{-i\varphi} - \frac{1}{2}\delta(\vec{k} + \vec{k}_{\text{ill}})e^{i\varphi}\right]. \tag{11.10}$$

This simplifies the calculation of the convolution of the pattern with the fluorophore distribution, and thus the observed image in reciprocal space:

$$\tilde{D}(\vec{k}) = \frac{I_0}{2}\tilde{H}(\vec{k})\left[\tilde{S}(\vec{k}) - \frac{1}{2}\tilde{S}(\vec{k} - \vec{k}_{\text{ill}})e^{-i\varphi} - \frac{1}{2}\tilde{S}(\vec{k} + \vec{k}_{\text{ill}})e^{i\varphi}\right]. \tag{11.11}$$

Thus, if the illumination pattern and the PSF of the microscope are known, then from the experimentally observed image *D*, the original (super-resolved) fluorophore distribution *S* can be determined. This process is, however, nontrivial and a number of schemes for determining the original fluorophore distribution in the case of linear structured illumination have been derived. Here, we briefly reiterate the basic scheme introduced in the seminal paper by Gustafsson et al. [14]:

First, the experimental PSF needs to be determined. This is typically done using a sub-diffraction limited structure, ideally a single fluorescent molecule or fluorescent quantum dot. In practice a fluorescent bead with ≤100 nm diameter suffices and sis ufficiently stable and long-lasting to obtain the PSF in a series of images taken at different z-steps. From this experimental PSF the background (e.g., due to camera offsets, etc.) is subtracted and the PSF is then rotationally averaged. The OTF of the microscope is then determined from this PSF by calculating the 2D Fourier transform of the PSF.

Next, for a given angle, an image at each of *N* different phase positions is taken by translating the interference pattern across the sample. The phase shifts should be evenly spaced ($\Delta\vartheta = 2\pi/N$). *N* is typically 3 if 2D images are to be reconstructed and 5 for reconstructing 3D images.

This procedure is repeated and similar images are acquired for each of *M* different angles by rotating the interference pattern. The number of angles is $M \leq N$, typically

3, to evenly cover the focal plane by the phase-shifted images. The angles are also evenly spaced across the image space ($\Delta\theta = 2\pi/M$).

The $M \times N$ images that have been acquired in this fashion are subsequently background subtracted and intensity corrected to compensate for source fluctuations and photobleaching. The $M \times N$ images then undergo a 2D Fourier transform to reciprocal space.

For each angle, the N individual information components are separated by pairwise cross-correlation to find an initial estimate of the frequency shift vector, phase shift, and modulation depth. These initial estimates are improved using linear regression. For each angle the information components are then combined using Wiener filtering and apodization to even out overlapping components and to ensure an evenly extended image in Fourier space. The image is then transformed back to real space to result in an image with approximately 2× improved spatial resolution. The steps from image acquisition, excitation with a structured illumination pattern, and the reconstruction of a super-resolved image is demonstrated in Figure 11.5 based on a sample consisting of 100 nm fluorescent beads.

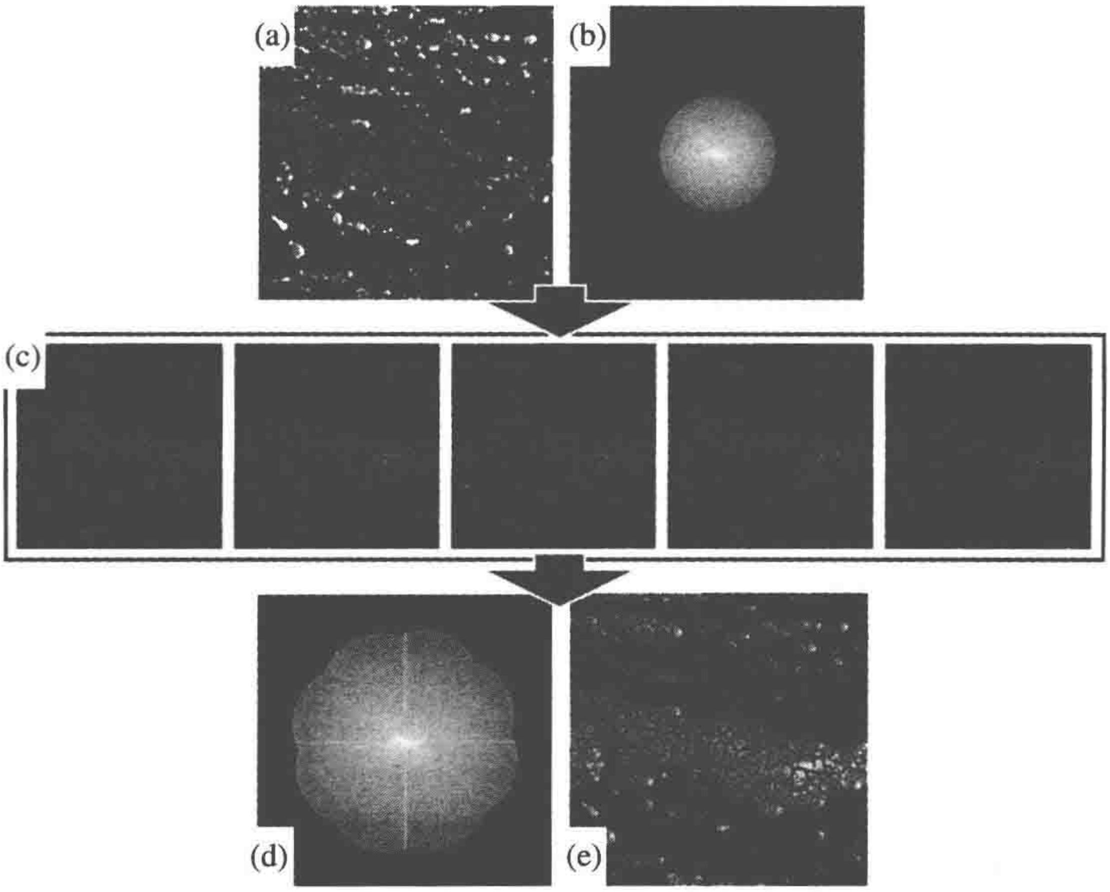

FIGURE 11.5 The principle behind structured illumination microscopy. (a) A sample of 100 nm diameter fluorescent beads image by wide-field fluorescence microscopy, and (b) its corresponding 2D image in Fourier space. (c) A sequence of images obtained by exciting the sample with an interference pattern that is phase-shifted and rotated is required to reconstruct a high resolution image of the sample. Here, five phases along one angle of the illumination pattern are shown. (d) Recombined components of the sample after imaging by structured illumination and subsequent 2D Fourier transformation. (e) Reconstructed image at double the resolution obtained by 2D Fourier-transformation of the image shown in (d).

For reconstructing 3D images, this procedure needs to also be extended to the third dimension. In this case, a 3D interference pattern is required, resulting in approximately a factor of 2 improvement in resolution in all dimensions [14]. Perfect reconstruction is usually complicated by the somewhat unknown (or not very precisely known) phase of the interference pattern, the need for perfect modulation, noise, sample movement, etc. [54]. Alternative ways of reconstructing structured illumination images even in the absence of detailed information about the illumination pattern are currently also under active investigation and include Bayesian reconstruction [55] and speckle patterns [56], for example.

The illumination pattern required for this type of imaging is typically created by sending laser light through a transmission diffraction grating, then collecting the +1 and −1 diffraction orders and collimating them. To create a 2D pattern, these beams are then focused to opposing ends at the back focal plane of an oil-immersion objective lens, where they undergo total internal reflection at the glass-sample interface. The resulting evanescent waves are counter-propagating and lead to a standing evanescent wave just above the cover slip surface, which can excite fluorescence within the first 100–200 nm of the sample near the glass surface. If a 3D interference pattern is desired, then the +1 and −1 diffraction orders are focused to opposing spots in the back focal plane that just avoid the criterion for total internal reflection. In this case, the 0 diffraction order is also sent into the microscope objective, leading to a more complex, 3D diffraction pattern. If a diffraction grating is used to create the interference pattern, the grating needs to physically be rotated and translated (typically using piezoelectric transducers) in order to create the different phase shifts and angles at which the sample is illuminated. Alternatively, other, faster optical elements, such as a SLM, or galvanometric mirrors can be used to create the interference pattern, which enables rapid phase and angle changes. To obtain fluorescence images of the sample, highly sensitive CCD cameras, typically of the electron-multiplying, back-illuminated type are used, or, to match the faster pattern creating devices, more recently, scientific CMOS cameras are used. This enables even live cell SIM in two [51, 57] and three [58] dimensions. To illustrate the enhanced resolution obtained by imaging a biological sample, Fig. 11.6 shows a two-color 3D SIM image of human T cells (stained with a red fluorescent antibody against actin) and a fluorescent clone of the human immunodeficiency virus HIV-1. Figure 11.6a shows the best image of this sample obtained by fluorescence deconvolution microscopy, while Fig. 11.6b shows the 3D SIM image of the same sample. Note that due to the 2× improvement in spatial resolution along all three axes, the volume resolution is improved by a factor of 8, which is best reflected by the maximum intensity projection images shown here.

The advantage of SIM, compared to techniques, such as confocal microscopy, or even single molecule localization microscopy and STED approaches is that it collects entire images of the sample by a CCD camera held in the conjugate plane of the microscope. Thus, it utilizes the full detection efficiency of the optical microscopy setup and no photons are lost at a confocal pinhole. In order to truly obtain a super-resolved image, however, computational processing is required to accomplish the resolution improvement and optical sectioning. At this point, photons from out-of-plane regions will be rejected by software. Confocal microscopy can, however, also be

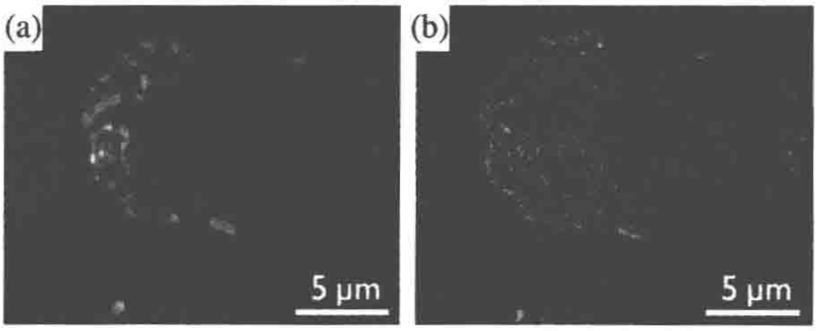

FIGURE 11.6 (a) Deconvolution fluorescence microscopy image, and (b) 3D structured illumination microscopy image of human T cells infected with a fluorescent clone of HIV-1. The cytoskeleton is labeled with a fluorescent antibody against actin [34], while the clone of HIV-1 carries the green fluorescent protein fused to gag, a structural protein of HIV. *(For a color version of this figure, see the color plate section.)*

considered a form of structured illumination as was initially postulated by Sheppard [59], and recently demonstrated by the group of Enderlein [60]. In order to take advantage of this approach, however, an image of the confocal spot for every image pixel of the final super-resolved image needs to be taken while the confocal spot is swept across the sample. In order to overcome the time lag introduced by this serial imaging, alternatively a large number of confocal spots can also be imaged simultaneously onto the CCD camera, for example, the spots created by a spinning disk confocal microscope, or the pattern created by a multifocal optical microscope [61]. This method also results in a 2× improvement of the lateral resolution; however, implementing this approach to also improve the axial resolution by a factor of 2 is more cumbersome and has not yet been accomplished.

SIM is only limited to a 2× improvement in optical resolution in the linear case, where, for example a sinusoidal intensity pattern is used as the illumination pattern. If a nonlinearity can be introduced into the system, then the resolution improvement is, in theory, unlimited. This has been postulated early on by Heintzmann [62], but only been demonstrated in 2005 by Mats Gustafsson [63], who used saturated structured illumination to achieve the required nonlinearity. In saturated SIM, the intensity modulation of the interference pattern is increased to the point where the fluorescence excitation of the sample is saturated, that is, illumination with even higher intensities does not produce stronger fluorescence. This is due to the relatively long excited state lifetimes of most organic fluorophores on the order of a few nanoseconds, which limit the maximum number of photons that can be emitted by a fluorescent molecule. Thus, the corresponding fluorescence image excited by a saturating illumination pattern leads to a "flattening" of the image in areas that are exposed with an intensity above the saturation threshold. In essence, the sinusoidal illumination pattern turns the resulting fluorescence images into a sinusoidal pattern with flat tops. This strong deviation from the sinusoidal pattern, along with a much greater number of phase shifts and an increased number of illumination angles, leads to the reconstruction of fluorescence images with a demonstrated 50 nm optical spatial resolution [63]. The disadvantage of this type of nonlinear structured illumination is, however, that fluorescent samples rapidly bleach out and lose their ability to fluoresce due to the strong excitation. Alternatively, other forms of optical nonlinearities can be utilized, for example, the combination of structured illumination with photoswitching similar to PALM microscopy [64]. These alternative modes of further improving the spatial resolution of SIM are currently under active and rapid development.

SIM is, however, not limited to wide-field illumination. Other forms of optical microscopy can also benefit from the SIM mechanism to further improve their spatial resolution. Recently, this has been demonstrated by the group of Betzig, who utilized SIM in combination with selective plane microscopy in an effort to combine the best of these two approaches [65]. In this case, a Bessel beam, sent through the sample from the side is used in combination with two-photon excitation to excite fluorescence, which is collected by another microscope lens with high numerical aperture at an angle of 90° to the Bessel beam propagation direction and imaged onto a CCD camera. The Bessel beam is swept across a 2D field of view using a galvanometric mirror. In this case, if the beam is also rapidly switched on and off such that only every other beam position leads to fluorescence excitation then the resulting image will also contain a striped pattern. Similar to the wide-field case, this pattern can also be shifted across the sample, and a super-resolved image reconstructed. This method also works in the simpler case of one-photon excitation as shown by Keller and coworkers [66].

Current efforts in further improving SIM are directed at further increasing the speed with which patterns can be projected into samples and images can be acquired by cameras, as well as by extending the number of color channels in which images of living cells can be acquired [67]. Also, current difficulties limiting SIM, for example, imaging deep in specimen, which is currently not possible beyond a depth of $\sim 30\ \mu\text{m}$ due to optical aberrations that result when interference patterns are projected deep into a specimen, in addition to light scattering, are being addressed [68]. Variations of the two-photon Bessel beam excitation and similar multiphoton excitation schemes look quite promising in this regard. Also, extensions of SIM to other contrast mechanisms, such as nonlinear optical microscopies beyond the two-photon Bessel beam illumination scheme, should soon emerge.

11.4.1 Applications of SIM

3D SIM was recently used to study the structure of chromatin and major nuclear proteins in the mammalian nucleus. By imaging chromatin, nuclear lamina, and the nuclear pore complex, Schermelleh and coworkers were able to resolve single nuclear pore complexes that co-localized with channels in the lamin network and peripheral chromatin. This enabled them to localize distinct components of the nuclear pore complex and to detect invaginations of the nuclear envelope in prophase [69].

In a different application, Cogger and coworkers used SIM to image fenestrations in liver sinusoidal endothelial cells [70]. Fenestrations are invaginations in the plasma membrane that span across the entire cytoplasm and permit, for example, lipoproteins, small molecules, and possibly, even viruses to breach the blood–liver barrier and reach the underlying hepatocytes in the liver. These structures were previously only seen by electron microscopy and it was debated whether or not these might be potential artifacts due to sample preparation for electron microscopy. Using a plasma membrane dye, Cogger and coworkers were able to not only image fenestrations, but also co-localize them with other proteins believed to help stabilize these structures. This work bears significant potential for future live cell studies of similar structures and reveal so far unknown dynamic information about the function of fenestrae [70].

11.5 SUPER-RESOLUTION OPTICAL FLUCTUATION IMAGING AND OTHER APPROACHES

After the first wave in the rapidly evolving area of super-resolution microscopy focusing on STED, localization microscopy, and SIM, more recent developments tend to focus on experimentally simple or at least simpler, as well as faster but yet more reliable and stable methods. High laser intensities as well as non-physiological buffer conditions such as the ones used in STORM are expected to damage the sample: STED, for example, requires an advanced microscope configuration along with a complex alignment procedure. It is demanding in terms of choosing the right dyes and labeling biological samples. STED is limited to ~60 nm resolution in video rate live cells imaging applications (28 frames/s) [22]. On the other hand, SIM yields a resolution limit of ~100 nm and is, technically speaking, simpler compared to STED. Live cell imaging was demonstrated with frame rates up to 11 Hz only due to the need for several images to be acquired in order to obtain one super-resolved image [71]. STORM requires that most of the fluorophores are switched to the dark "off"-state with non-overlapping fluorescence emission of the remaining fluorophores. This limits the number of localizations per image and, therefore, requires many images and long data acquisition times especially in order to resolve dense and complex structures.

Super-resolution optical fluctuation imaging (SOFI) utilizes the temporal fluctuations of the fluorescence signal caused by, for example, the inherent blinking of many fluorophores to compute almost background free and, additionally, contrast-enhanced super-resolution images. If the fluorescence fluctuation is analyzed with SOFI, it purely relies on stochastic fluctuations and does not necessarily require controlled reversible photoswitching. It solely requires that the fluorophore is repeatedly (stochastically) switched between two different emission states, a fluorescent "on"- and a nonfluorescent "off"-state. First results were achieved with quantum dots, showing a fivefold enhancement in resolution [72], later also followed by a comparable resolution enhancement with organic dyes [73].

Basically, SOFI filters the fluorescence signal in an image such that only correlated fluctuations, emitted from the same fluorophore, are taken into account. Uncorrelated fluorescence from neighboring fluorophores is nonlinearly suppressed, which leads to a sharpened PSF and, hence, an increased optical resolution. Due to pixel-wise correlation analysis SOFI is somewhat limited to samples that undergo no additional temporal changes during the few images (as few as 100) that are needed to reconstruct a SOFI image.

The fluorescence signal $F(\vec{r}, t)$ on a detector pixel $\vec{r}$ of a sample consisting of N fluctuating fluorophores can be written as

$$F(\vec{r}, t) = \sum_{k=1}^{N} U(\vec{r} - \vec{r}_k) \cdot \varepsilon_k \cdot s_k(t), \tag{11.12}$$

where $U(\vec{r})$ is the PSF, ε_k the mean fluorescence and $s_k(t)$ the temporal fluctuation of the fluorophore. The zero-mean fluctuations can be written as a difference to the time average given by $F(\vec{r}, t)$:

$$\delta F(\vec{r}, t) = F(\vec{r}, t) - \langle F(\vec{r}, t) \rangle = \sum_{k=1}^{N} U(\vec{r} - \vec{r}_k) \cdot \varepsilon_k \cdot \delta s_k(t) \tag{11.13}$$

from which the second-order auto-correlation function can be calculated:

$$G_2(\vec{r}, \tau) = \delta F(\vec{r}, t + \tau) \cdot \delta F(\vec{r}, t) = \sum_{k=1}^{N} U^2(\vec{r} - \vec{r}_k) \cdot \varepsilon_k^2 \cdot \delta s_k(t + \tau) \cdot \delta s_k(t) \tag{11.14}$$

The pixel value of a SOFI image is obtained from the G_2-function for a defined lag time τ. The auto-correlation function does not directly report on the fluorescence signal of the fluorophore but on the correlation and the brightness of that signal.

The auto-correlation function G_n can be expanded to higher orders by multiplication with additional $\delta F(\vec{r}, t + \tau_n)$. As can be seen in the last equation for G_2, G_n then depends on the nth power of the PSF $U(\vec{r})$. If, as a good approximation, a Gaussian distribution of the PSF is assumed, the standard deviation of the PSF is reduced by a factor of $\sqrt{n}$. This yields a resolution enhancement by a factor of $\sqrt{n}$ for the calculated order of correlation n.

Indeed, higher orders than the G_2-function have to be considered to achieve higher spatial resolution. To ensure that only photons from the same fluorophore are counted, the cumulant functions (a quantity related to the correlation function) are used. Hence, only highly correlated fluctuations are considered such that the PSF is again reduced by a factor of $\sqrt{n}$ for the nth order of the cumulant function. The sequence of events leading to SOFI images is demonstrated in Figure 11.7. A wide-field fluorescence image of a rat hippocampal neuron labeled with fluorescent quantum dots, and the resulting two-color SOFI image are shown in Figure 11.8.

In contrast to localization microscopy methods like PALM and *d*STORM, even weakly fluorescing dyes with a wide range of blinking characteristics or more densely labeled samples can be analyzed by SOFI. The major drawback of SOFI is its nonlinear response to brightness and blinking heterogeneities in the sample, which limits the analysis of higher orders of the cumulant function. However, balanced super-resolution optical fluctuation imaging (bSOFI), a variant of SOFI, makes use of estimated blinking statistics in order to balance the image contrast. This

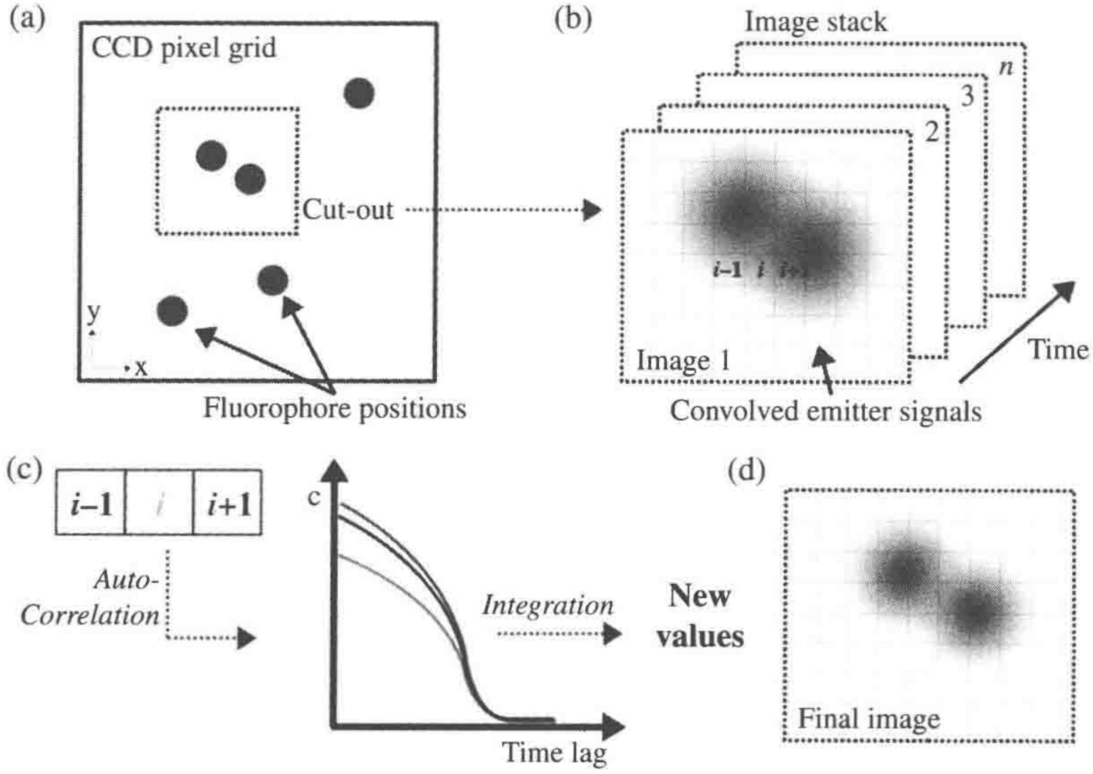
(a)
CCD pixel grid
Cut-out
y
x
Fluorophore positions
(b)
Image stack
n
3
2
i–1 i i+1
Image 1
Convolved emitter signals
Time
(c)
i–1
i
i+1
Auto-
Correlation
c
Integration
Time lag
New values
(d)
Final image

FIGURE 11.7 Mechanism of SOFI auto-cumulant calculation: (a) CCD camera pixel grid used to acquire fluorescence images with temporally fluctuating emitters. (b) Expanded view of the two emitters highlighted by the dashed line in (a) and convolved with the system's point spread function recorded on an image stack with hundreds to thousands of images. (c) Analysis of the images by pixel-wise correlation and auto-cumulant calculation. (d) Final image reconstructed based on the calculated cumulant values. (*For a color version of this figure, see the color plate section.*)

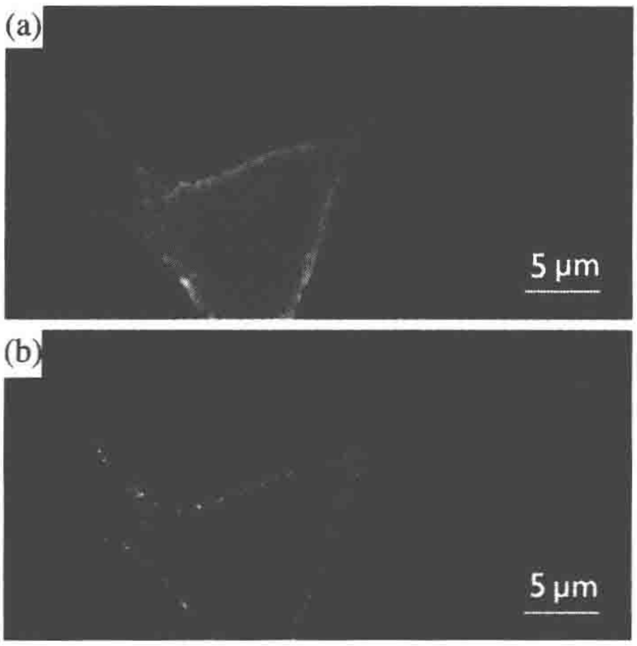

FIGURE 11.8 (a) Wide-field and (b) second order SOFI images of a rat hippocampal neuron, calculated from 3000 frames, with a frame acquisition time of 50 ms. GABA-B R1 was labeled with QDot525, represented in green; GABA-B R2 was labeled with QDot625, represented in red. Figure courtesy of Anja Huss and Jörg Enderlein, Department of Physics, Georg-August-University Göttingen, Germany. (*For a color version of this figure, see the color plate section.*)

leads to a more linear brightness and blinking response of the cumulant function G_n that is needed to obtain a resolution improvement linear with higher cumulant orders [74].

11.5.1 Bayesian Analysis of Blinking and Bleaching

Another approach for the analysis of wide-field image consisting of fluorophores and their time-varying properties is the Bayesian analysis of blinking and bleaching (3B) [75]. The 3B method allows for the analysis of an image stack consisting of images containing several overlapping fluorophores, for example, densely labeled biological structures. Each of these fluorophores can emit fluorescent photons but does not necessarily fluoresce all the time, recorded in all of the acquired images. Due to the applied model all photons emitted from one fluorophore, even those that do not necessarily have to be acquired in subsequent images, are collected and analyzed, which yields an improved determination of the fluorophore position.

In the 3B analysis, the fluorescence emission of each fluorophore is modeled with a Factorial Hidden Markov Model that is utilized for super-resolved image analysis. The Hidden Markov Model contains observed and unobserved ("hidden") states. In total, three different states can be assigned to a fluorophore: (1) the "on"-state; (2) the "off"-state; and (3) the "bleached"-state. The Factorial Hidden Markov Model that is used in 3B analysis allows for an observed state that is conditioned on the hidden states. Accordingly, it is assumed that each fluorophore can stay or transfer between the "on"- and the "off"-state with certain probabilities, but remains in the "bleached"-state that can be reached from the "off"-state only. This model is used to calculate the probability that a fluorophore is present at a certain position compared to the (null) hypothesis that the signal arises from noise: the integration over the fluorophore states can be performed with a forward algorithm. The integral over the four continuous parameters (the x- and y-position, the radius, and the brightness of the fluorophore) is calculated using Laplace's approximation. An exact integration over state sequences that becomes demanding with increasing number of fluorophores is replaced with a Markov Chain Monte Carlo sampling to speed up the analysis for larger images. This rather complex probability calculation generates a density map of the fluorophore's position.

The 3B analysis allows performing sub-diffraction optical (localization) microscopy with a spatial resolution of ~50 nm and a temporal resolution of 4 s. It can be performed on a standard wide-field microscope (even using incoherent sources, such as a Xenon arc lamp or LEDs) in order to obtain images of living cells that are densely labeled with a standard fluorescent protein. Nevertheless, the 3B analysis takes up to several hours, which is much longer compared to *d*STORM and SOFI. It is reported that an analysis of an area of 1.5 × 1.5 μm^2 takes 6 hours processing time on a standard personal computer [75].

11.5.2 Applications of Fluctuation-Based Superresolution Microscopy

To demonstrate the improved imaging achieved by balanced SOFI, the microtubuli network in fixed HeLa cells was recently analyzed with bSOFI. The microtubules were fluorescently labeled with Alexa647 and imaged on a TIRF microscopy setup. A 4.6-fold resolution improvement compared to wide-field microscopy was reported using the bSOFI algorithm for analysis. The SOFI algorithm yields an improvement on the order of $\sqrt{5}$ for the fifth order cumulant analysis. In combination with TIRF microscopy, both, the molecular brightness and the blinking on-time ratio of the fluorophore could be interpreted as a z-position encoding because they are related to the illumination intensity [34].

The SOFI algorithm described above can easily be extended to two-color super-resolution optical fluctuations imaging (2cSOFI). This method was introduced using a standard wide-field experimental setup and quantum dots (QDs) that emit and blink at different colors. The labeling was performed with primary antibodies directly conjugated to QDs in order to obtain a higher labeling density, which is important for super-resolution imaging. The spatial relationship between the processing body hDcp1a protein and the tubulin cytoskeleton in fixed HeLa cells was visualized. New perspectives on the role of the cytoskeleton in processing body formation and assembly along with further insights into the processing bodies' internal organization were reported [76].

First applications of the 3B analysis allowed revealing the dynamics of podosome formation and dissociation. Living cells that stably express the talin protein fused to the fluorescent protein mCherry were visualized throughout an entire cell with a resolution of 50 nm on a 4 s-timescale. The authors report that podosomes are highly dynamic structures and that smaller ring type structures down to 230 nm play an important part in podosome dynamics [75].

11.6 OUTLOOK

More than a decade after the first practical realizations that enabled use to overcome the diffraction limit of light, super-resolution microscopy has become a versatile and robust technique in light microscopy. It has already had a significant impact on biology, especially on molecular cell biology, and still has an ever-growing influence on the development of modern microscopy techniques.

All methods mentioned above feature several advantages over traditional optical microscopy, along with certain limitations, such as the need for specific fluorophores, or limitations to the choice of sample – but no ideal and comparably perfect method has been developed yet. STED microscopy requires the use of a rather complex optical microscope configuration that needs regular alignment and highest quality optical components. High laser powers are needed for the saturated depletion beam to achieve a resolution on the nanometer scale, which can, in turn, potentially damage biological samples. STORM utilizes photophysical and photochemical properties such as photoswitchable fluorophores under special chemical conditions. A high labeling density required for very high resolution gives rise to non-separable multiple fluorescent emitters that cannot be properly localized. The large number of images that are required to complete a full image reconstruction from thousands of localizations limits its use in live cell microscopy. The same applies to all algorithms that need several images in order to perform statistical analysis, for example, SOFI and 3B.

Although the technical effort is low the computational is much higher and time-consuming. SIM in its linear implementation yields merely a resolution doubling, and it still requires the acquisition of small number of images for each 3D plane, limiting its application to live cell imaging.

Due to the use of fluorescence-based techniques, the choice of proper fluorophores and appropriate buffer conditions is demanding. Recent improvements on the photophysical properties of the dyes such as the stability and photoswitching capabilities have led to more sophisticated results. Fast and low-noise detectors additionally pushed single-molecule-based localization methods. Finally, the technological development results in a number of commercially available super-resolution microscopes.

The method of choice would feature both, a lateral and an axial resolution in the single-digit nanometer range that could easily be expanded to three dimensions and multicolor applications. Besides an optical resolution enhancement the temporal resolution should be capable of at least video rate imaging. This could provide an even deeper insight into the structure of cells and would allow following cellular dynamics in living cells. It is probably by a combination of techniques, such as SIM combined with single molecule localization techniques that we will approach such an ideal scenario in the near future. It seems quite logical that a mid-range super-resolution technique, such as SIM, could be used to initially survey a sample, such as cells in culture, to locate potential sites of interest that are then investigated with higher resolution techniques, such as PALM/STORM.

Another interesting expansion of super-resolution techniques in the near future will likely include alternative contrast mechanisms that do not require the use of fluorescent probes. A natural extension appears to be the application of Raman scattering, a contrast mechanism that enables the chemical analysis of samples based on bond vibrations in molecules. Although much weaker in nature than fluorescence, it provides similar information, and certain implementations, such as spontaneous Raman scattering microscopy or surface-enhanced Raman scattering could certainly utilize similar concepts as SIM and PALM/STORM. Even STED could possibly be expanded to other nonlinear optical microcopies, such as coherent anti-Stokes Raman scattering (CARS) microscopy. The future does indeed look bright for super-resolution optical microscopy.

ACKNOWLEDGMENTS

We would like to thank all of our colleagues, in the Biomolecular Photonics Group at the University of Bielefeld, as well as the research groups of Prof. Markus Sauer at the Julius-Maximilians-University in Würzburg, Germany, and Prof. Mike Heilemann at the Johann-Wolfgang-Goethe-University in Frankfurt, Germany, and at the Department of Internal Medicine and the NSF Center for Biophotonics Science and Technology at the University of California in Davis, CA, USA, for their input and support throughout the past years. We also thank Anja Huss and Prof. Jörg Enderlein from the Georg-August-University Göttingen, Germany, for providing the two-color SOFI image of a rat hippocampal neuron, and Dr. Benjamin Dale and Prof. Benjamin

Chen from the Mount Sinai School of Medicine in New York, USA, for providing the actin and Gag-iGfP samples of human T cells infected with HIV-1.

REFERENCES

[1] J. Pawley, *Handbook of Biological Confocal Microscopy*, 3rd ed. (Springer, New York, NY, 2006).

[2] J. L. Spees, S. D. Olson, M. J. Whitney, and D. J. Prockop, "Mitochondrial transfer between cells can rescue aerobic respiration," *Proc. Natl. Acad. Sci. USA* **103**(5), 1283–1288 (2006).

[3] T. Enderle, T. Ha, D. F. Ogletree, D. S. Chemla, C. Magowan, and S. Weiss, "Membrane specific mapping and colocalization of malarial and host skeletal proteins in the *Plasmodium falciparum* infected erythrocyte by dual-color near-field scanning optical microscopy," *Proc. Natl. Acad. Sci. USA* **94**, 520–525 (1997).

[4] R. M. Stoeckle, Y. D. Suh, V. Deckert, and R. Zenobi, "Nanoscale chemical analysis by tip-enhanced Raman spectroscopy," *Chem. Phys. Lett.* **318**, 131–136 (2000).

[5] E. Betzig and R. J. Chichester, "Single molecules observed by near-field scanning optical microscopy," *Science* **262**(5138), 1422–1428 (1993).

[6] (a) J. Elf, G. W. Li, and X. S. Xie, "Probing transcription factor dynamics at the single-molecule level in a living cell," *Science* **316** (5828), 1191–1194 (2007); (b) J. Yu, J. Xiao, X. J. Ren, K. Q. Lao, X. S. Xie, "Probing gene expression in live cells, one protein molecule at a time," *Science* **311**(5767), 1600–1603 (2006).

[7] A. E. Miller, A. J. Fischer, T. A. Laurence, C. W. Hollars, R. J. Saykally, J. C. Lagarias, and T. Huser, "Single-molecule dynamics of phytochrome-bound fluorophores probed by fluorescence correlation spectroscopy," *Proc. Natl. Acad. Sci. USA* **103**(30), 11136–11141 (2006).

[8] A. Yildiz, J. N. Forkey, S. A. McKinney, T. Ha, Y. E. Goldman, P. R. Selvin, and V. Myosin, "Walks hand-over-hand: single fluorophore imaging with 1.5-nm localization," *Science* **300**, 2061–2065 (2003).

[9] C. Kural, A. S. Serpinskaya, Y.-H. Chou, R. D. Goldman, V. I. Gelfand, and P. R. Selvin, "Tracking melanosomes inside a cell to study molecular motors and their interaction," *Proc. Natl. Acad. Sci. USA* **104**(13), 5378–5382 (2007).

[10] (a) B. Brandenburg and X. W. Zhuang, "Virus trafficking—learning from single-virus tracking," *Nat. Rev. Microbiol.* **5**(3), 197–208 (2007); (b) B. Brandenburg, L. Y. Lee, M. Lakadamyali, M. J. Rust, X. W. Zhuang, and J. M. Hogle, Imaging poliovirus entry in live cells. *PLoS Biol* **5**(7), 1543–1555 (2007).

[11] S. W. Hell and J. Wichmann, "Breaking the diffraction resolution limit by stimulated-emission—stimulated-emission-depletion fluorescence microscopy," *Opt Lett* **19**(11), 780–782 (1994).

[12] (a) G. Donnert, J. Keller, R. Medda, M. A. Andrei, S. O. Rizzoli, R. Lurmann, R. Jahn, C. Eggeling, and S. W. Hell, "Macromolecular-scale resolution in biological fluorescence microscopy," *Proc. Natl. Acad. Sci. USA* **103**(31), 11440–11445 (2006); (b) K. I. Willig, S. O. Rizzoli, V. Westphal, R. Jahn, and S. W. Hell, "STED microscopy reveals that synaptotagmin remains clustered after synaptic vesicle exocytosis," *Nature* **440**(7086), 935–939 (2006).

[13] B. Harke, J. Keller, C. K. Ullal, V. Westphal, A. Schoenle, and S. W. Hell, "Resolution scaling in STED microscopy," *Opt Express* **16**(6), 4154–4162 (2008).

[14] M. G. L. Gustafsson, L. Shao, P. M. Carlton, C. J. R. Wang, I. N. Golubovskaya, W. Z. Cande, D. A. Agard, and J. W. Sedat, "Three-dimensional resolution doubling in wide-field fluorescence microscopy by structured illumination," *Biophys J.* **94**(12), 4957–4970 (2008).

[15] (a) E. Betzig, G. H. Patterson, R. Sougrat, O. W. Lindwasser, S. Olenych, J. S. Bonifacino, M. W. Davidson, J. Lippincott-Schwartz, and H. F. Hess, "Imaging intracellular fluorescent proteins at nanometer resolution," *Science* **313**(5793), 1642–1645 (2006); (b) S. Manley, J. M. Gillette, G. H. Patterson, H. Shroff, H. F. Hess, E. Betzig, and J. Lippincott-Schwartz, "High-density mapping of single-molecule trajectories with photoactivated localization microscopy," *Nat. Methods* **5**, 155–157 (2008).

[16] (a) M. J. Rust, M. Bates, and X. W. Zhuang, "Sub-diffraction-limit imaging by stochastic optical reconstruction microscopy (STORM)," *Nat. Methods* **3**(10), 793–795 (2006); (b) B. Huang, W. Q. Wang, M. Bates, and X. W. Zhuang, "Three-dimensional super-resolution imaging by stochastic optical reconstruction microscopy," *Science* **319**, 810–813 (2008).

[17] S. W. Hell, "Far-field optical nanoscopy," *Science* **316**(5828), 1153–1158 (2007).

[18] T. A. Klar, S. Jakobs, M. Dyba, A. Egner, and S. W. Hell, "Fluorescence microscopy with diffraction resolution barrier broken by stimulated emission," *Proc. Natl. Acad. Sci. USA* **97**(15), 8206–8210 (2000).

[19] L. Kastrup, H. Blom, C. Eggeling, and S. W. Hell, "Fluorescence fluctuation spectroscopy in subdiffraction focal volumes," *Phys. Rev. Lett.* **94**, 178104 (2005).

[20] E. Auksorius, B. R. Boruah, C. Dunsby, P. M. P. Lanigan, G. Kennedy, M. A. A. Neil, and P. M. W. French, "Stimulated emission depletion microscopy with a supercontinuum source and fluorescence lifetime imaging," *Opt. Lett.* **33**(2), 113–115 (2008).

[21] G. Donnert, J. Keller, C. A. Wurm, S. O. Rizzoli, V. Westphal, A. Schonle, R. Jahn, S. Jakobs, C. Eggeling, and S. W. Hell, "Two-color far-field fluorescence nanoscopy," *Biophys. J.* **92**(8), L67–L69 (2007).

[22] V. Westphal, S. O. Rizzoli, M. A. Lauterbach, D. Kamin, R. Jahn, and S. W. Hell, "Video-rate far-field optical nanoscopy dissects synaptic vesicle movement," *Science* **320**(5873), 246–249 (2008).

[23] S. Berning, K. I. Willig, H. Steffens, P. Dibaj, and S. W. Hell, "Nanoscopy in a living mouse brain," *Science* **335**(6068), 551–551 (2012).

[24] J. Chojnacki, T. Staudt, B. Glass, P. Bingen, J. Engelhardt, M. Anders, J. Schneider, B. Muller, S. W. Hell, and H. G. Krausslich, "Maturation-dependent HIV-1 surface protein redistribution revealed by fluorescence nanoscopy," *Science* **338**(6106), 524–528 (2012).

[25] C. Eggeling, C. Ringemann, R. Medda, G. Schwarzmann, K. Sandhoff, S. Polyakova, V. N. Belov, B. Hein, C. von Middendorff, et al., "Direct observation of the nanoscale dynamics of membrane lipids in a living cell," *Nature* **457**(7233), 1159–1162 (2009).

[26] E. Betzig, "Proposed method for molecular optical imaging," *Opt. Lett.* **20**(3), 237–239 (1995).

[27] S. T. Hess, T. P. Girirajan, and M. D. Mason, "Ultra-high resolution imaging by fluorescence photoactivation localization microscopy," *Biophys. J.* **91**(11), 4258–4272 (2006).

[28] R. Ando, H. Mizuno, and A. Miyawaki, "Regulated fast nucleocytoplasmic shuttling observed by reversible protein highlighting," *Science* **306**(5700), 1370–1373 (2004).

[29] M. Bates, T. R. Blosser, and X. Zhuang, "Short-range spectroscopic ruler based on a single-molecule optical switch," *Phys. Rev. Lett.* **94**(10), 108101 (2005).

[30] M. Heilemann, E. Margeat, R. Kasper, M. Sauer, and P. Tinnefeld, "Carbocyanine dyes as efficient reversible single-molecule optical switch," *J. Am. Chem. Soc.* **127**(11), 3801–3806 (2005).

[31] (a) H. Shroff, C. G. Galbraith, J. A. Galbraith, and E. Betzig, "Live-cell photoactivated localization microscopy of nanoscale adhesion dynamics," *Nat. Methods* **5**(5), 417–423 (2008); (b) S. van de Linde, M. Sauer, and M. Heilemann, "Subdiffraction-resolution fluorescence imaging of proteins in the mitochondrial inner membrane with photoswitchable fluorophores," *J. Struct. Biol.* **164**(3), 250–254 (2008).

[32] M. Heilemann, S. van de Linde, A. Mukherjee, and M. Sauer, "Super-resolution imaging with small organic fluorophores," *Angew Chem. Int. Ed. Engl.* **48**(37), 6903–6908 (2009).

[33] M. Heilemann, S. van de Linde, M. Schuttpelz, R. Kasper, B. Seefeldt, A. Mukherjee, P. Tinnefeld, and M. Sauer, "Subdiffraction-resolution fluorescence imaging with conventional fluorescent probes," *Angew Chem. Int. Ed. Engl.* **47**(33), 6172–6176 (2008).

[34] S. van de Linde, A. Loschberger, T. Klein, M. Heidbreder, S. Wolter, M. Heilemann, and M. Sauer, "Direct stochastic optical reconstruction microscopy with standard fluorescent probes," *Nat. Protoc.* **6**(7), 991–1009 (2011).

[35] I. Rasnik, S. A. McKinney, and T. Ha, "Nonblinking and long-lasting single-molecule fluorescence imaging," *Nat. Methods* **3**(11), 891–893 (2006).

[36] R. E. Thompson, D. R. Larson, and W. W. Webb, "Precise nanometer localization analysis for individual fluorescent probes," *Biophys. J.* **82**(5), 2775–2783 (2002).

[37] S. Wolter, M. Schuttpelz, M. Tscherepanow, S. Van de Linde., M. Heilemann, and M. Sauer, "Real-time computation of subdiffraction-resolution fluorescence images," *J. Microsc-Oxford* **237**(1), 12–22 (2010).

[38] S. J. Holden, S. Uphoff, and A. N. Kapanidis, "DAOSTORM: an algorithm for high-density super-resolution microscopy," *Nat. Methods* **8**(4), 279–280 (2011).

[39] (a) B. Huang, S. A. Jones, B. Brandenburg, and X. Zhuang, "Whole-cell 3D STORM reveals interactions between cellular structures with nanometer-scale resolution," *Nat Methods* **5**(12), 1047–1052 (2008); (b) B. Huang, W. Wang, M. Bates, X. Zhuang, "Three-dimensional super-resolution imaging by stochastic optical reconstruction microscopy," *Science* **319**(5864), 810–813 (2008).

[40] A. Vaziri, J. Y. Tang, H. Shroff, and C. V. Shank, "Multilayer three-dimensional super resolution imaging of thick biological samples," *Proc. Natl. Acad. Sci. USA* **105**(51), 20221–20226 (2008).

[41] F. C. Zanacchi, Z. Lavagnino, M. P. Donnorso, A. Del Bue, L. Furia, M. Faretta, and A. Diaspro, "Live-cell 3D super-resolution imaging in thick biological samples," *Nat. Methods* **8**(12), 1047–1049 (2011).

[42] D. Baddeley, I. D. Jayasinghe, C. Cremer, M. B. Cannell, C. Soeller, "Light-induced dark states of organic fluochromes enable 30 nm resolution imaging in standard media," *Biophys. J.* **96**(2), L22–L24 (2009).

[43] (a) J. Bierwagen, I. Testa, J. Folling, D. Wenzel, S. Jakobs, C. Eggeling, and S. W. Hell, "Far-field autofluorescence nanoscopy," *Nano Lett* **10**(10), 4249–4252 (2010); (b) J. Folling, M. Bossi, H. Bock, R. Medda, C. A. Wurm, B. Hein, S. Jakobs, C. Eggeling,

and S. W. Hell, "Fluorescence nanoscopy by ground-state depletion and single-molecule return," *Nat Methods* **5**(11), 943–945 (2008); (c) I. Testa, C. A. Wurm, R. Medda, E. Rothermel, C. von Middendorf, J. Folling, S. Jakobs, A. Schonle, S. W. Hell, and C. Eggeling, "Multicolor fluorescence nanoscopy in fixed and living cells by exciting conventional fluorophores with a single wavelength," *Biophys J.* **99**(8), 2686–2694 (2010).

[44] D. Greenfield, A. L. McEvoy, H. Shroff, G. E. Crooks, N. S. Wingreen, E. Betzig, and J. Liphardt, "Self-organization of the *Escherichia coli* chemotaxis network imaged with super-resolution light microscopy," *PLoS Biol.* **7**(6), e1000137 (2009).

[45] J. Yao, R. D. Fetter, P. Hu, E. Betzig, and R. Tjian, "Subnuclear segregation of genes and core promoter factors in myogenesis," *Genes Dev.* **25**(6), 569–580 (2011).

[46] A. Loschberger, S. van de Linde, M. C. Dabauvalle, B. Rieger; M. Heilemann, G. Krohne, and M. Sauer, "Super-resolution imaging visualizes the eightfold symmetry of gp210 proteins around the nuclear pore complex and resolves the central channel with nanometer resolution," *J. Cell. Sci.* **125**(Pt 3), 570–575 (2012).

[47] D. Lando, U. Endesfelder, H. Berger, L. Subramanian, P. D. Dunne, J. McColl, D. Klenerman, A. M. Carr, M. Sauer, R. C. Allshire, et al., "Quantitative single-molecule microscopy reveals that CENP-A(Cnp1) deposition occurs during G2 in fission yeast," *Open Biol.* **2**(7), 120078 (2012).

[48] R. Heintzmann and C. Cremer, "Laterally modulated excitation microscopy: improvement of resolution by using a diffraction grating," *Opt. Biopsies Microsc. Tech. III, Proc.* **3568**, 185–196 (1999).

[49] J. T. Frohn, H. F. Knapp, and A. Stemmer, "True optical resolution beyond the Rayleigh limit achieved by standing wave illumination," *Proc. Natl. Acad. Sci. USA* **97**(13), 7232–7236 (2000).

[50] M. G. L. Gustafsson, D. A. Agard, and J. W. Sedat, "Doubling the lateral resolution of wide-field fluorescence microscopy using structured illumination," *Proc. Soc. Photo-Opt. Ins.* **1**(13), 141–150 (2000).

[51] (a) L. M. Hirvonen, K. Wicker, O. Mandula, and R. Heintzmann, "Structured illumination microscopy of a living cell," *Eur Biophys. J. Biophy.* **38**(6), 807–812 (2009); (b) R. Fiolka, M. Beck, and A. Stemmer, "Structured illumination in total internal reflection fluorescence microscopy using a spatial light modulator,". *Opt Lett* **33**(14), 1629–1631 (2008).

[52] M. A. Neil, R. Juskaitis, and T. Wilson, "Method of obtaining optical sectioning by using structured light in a conventional microscope," *Opt. Lett.* **22**(24), 1905–1907 (1997).

[53] M. A. Neil, A. Squire, R. Juskaitis, P. I. Bastiaens, and T. Wilson, "Wide-field optically sectioning fluorescence microscopy with laser illumination," *J. Microsc.* **197**(Pt 1), 1–4 (2000).

[54] K. Wicker, O. Mandula, G. Best, R. Fiolka, and R. Heintzmann, "Phase optimisation for structured illumination microscopy,". *Opt Express* **21**(2), 2032–2049 (2013).

[55] D. Laksameethanasan, S. S. Brandt, P. Engelhardt, O. Renaud, and S. L. Shorte, "A Bayesian reconstruction method for micro-rotation imaging in light microscopy," *Microsc. Res. Tech.* **71**(2), 158–167 (2008).

[56] E. Mudry, K. Belkebir, J. Girard, J. Savatier, E. Le Moal, C. Nicoletti, M. Allain, and A. Sentenac, "Structured illumination microscopy using unknown speckle patterns," *Nat. Photonics* **6**, 312–315 (2012).

[57] P. Kner, B. B. Chhun, E. R. Griffis, L. Winoto, and M. G. L. Gustafsson, "Super-resolution video microscopy of live cells by structured illumination," *Nat Methods* **6**(5), 339–U36 (2009).

[58] L. Shao, P. Kner, E. H. Rego, and M. G. L. Gustafsson, "Super-resolution 3D microscopy of live whole cells using structured illumination," *Nat. Methods* **8**(12), 1044–+ (2011).

[59] C. J. R. Sheppard, "Super-resolution in confocal imaging," *Optik* **80**, 53–54 (1998).

[60] C. B. Muller and J. Enderlein, "Image Scanning Microscopy," *Phys. Rev. Lett.* **104**(19), 198101 (2010).

[61] A. G. York, S. H. Parekh, D. D. Nogare, R. S. Fischer, K. Temprine, M. Mione, A. B. Chitnis, C. A. Combs, and H. Shroff, "Resolution doubling in live, multicellular organisms via multifocal structured illumination microscopy," *Nat. Methods* **9**(7), 749–754 (2012).

[62] (a) R. Heintzmann, T. M. Jovin, and C. Cremer, "Saturated patterned excitation microscopy—a concept for optical resolution improvement," *J. Opt. Soc. Am. A* **19**(8), 1599–1609 (2002); (b) R. Heintzmann, "Saturated patterned excitation microscopy with two-dimensional excitation patterns," *Micron* **34**(6–7), 283–291 (2003).

[63] M. G. Gustafsson, "Nonlinear structured-illumination microscopy: wide-field fluorescence imaging with theoretically unlimited resolution," *Proc. Natl. Acad. Sci. USA* **102**(37), 13081–13086 (2005).

[64] E. H. Rego, L. Shao, J. J. Macklin, L. Winoto, G. A. Johansson, N. Kamps-Hughes, M. W. Davidson, and M. G. Gustafsson, "Nonlinear structured-illumination microscopy with a photoswitchable protein reveals cellular structures at 50-nm resolution," *Proc. Natl. Acad. Sci. USA* **109**(3), E135–E143 (2012).

[65] (a) T. A. Planchon, L. Gao, D. E. Milkie, M. W. Davidson, J. A. Galbraith, C. G. Galbraith, and E. Betzig, "Rapid three-dimensional isotropic imaging of living cells using Bessel beam plane illumination," *Nat. Methods* **8**(5), 417–423 (2011); (b) L. Gao, L. Shao, C. D. Higgins, J. S. Poulton, M. Peifer, M. W. Davidson, X. Wu, B. Goldstein, and E. Betzig, "Noninvasive imaging beyond the diffraction limit of 3D dynamics in thickly fluorescent specimens," *Cell* **151**(6), 1370–1385 (2012).

[66] P. J. Keller, A. D. Schmidt, A. Santella, K. Khairy, Z. Bao, J. Wittbrodt, and E. H. Stelzer, "Fast, high-contrast imaging of animal development with scanned light sheet-based structured-illumination microscopy," *Nat. Methods* **7**(8), 637–642 (2010).

[67] R. Fiolka, L. Shao, E. H. Rego, M. W. Davidson, and M. G. Gustafsson, "Time-lapse two-color 3D imaging of live cells with doubled resolution using structured illumination," *Proc. Natl. Acad. Sci. USA* **109**(14), 5311–5315 (2012).

[68] V. Andresen, K. Pollok, J. L. Rinnenthal, L. Oehme, R. Gunther, H. Spiecker, H. Radbruch, J. Gerhard, A. Sporbert, Z. Cseresnyes,et al., "High-resolution intravital microscopy," *PLoS One* **7**(12) (2012).

[69] L. Schermelleh, P. M. Carlton, S. Haase, L. Shao, L. Winoto, P. Kner, B. Burke, M. C. Cardoso, D. A. Agard, M. G. L. Gustafsson et al., "Subdiffraction multicolor imaging of the nuclear periphery with 3D structured illumination microscopy," *Science* **320**(5881), 1332–1336 (2008).

[70] V. C. Cogger, G. P. McNerney, T. Nyunt, L. D. DeLeve, P. McCourt, B. Smedsrod, D. G. Le Couteur, and T. R. Huser, "Three-dimensional structured illumination microscopy of liver sinusoidal endothelial cell fenestrations," *J. Struct. Biol.* **171**(3), 382–388 (2010).

[71] P. Kner, B. B. Chhun, E. R. Griffis, L. Winoto, and M. G. Gustafsson, "Super-resolution video microscopy of live cells by structured illumination," *Nat. Methods* **6**(5), 339–342 (2009).

[72] T. Dertinger, R. Colyer, G. Iyer, S. Weiss, and J. Enderlein, "Fast, background-free, 3D super-resolution optical fluctuation imaging (SOFI)," *Proc. Natl. Acad. Sci. USA* **106**(52), 22287–22292 (2009).

[73] T. Dertinger, M. Heilemann, R. Vogel, M. Sauer, and S. Weiss, "Superresolution optical fluctuation imaging with organic dyes," *Angew. Chem. Int. Ed. Engl.* **49**(49), 9441–9443 (2010).

[74] S. Geissbuehler, N. Bocchio, C. Dellagiacoma, C. Berclaz, M. Leutenegger, and T. Lasser, "Mapping molecular statistics with balanced super-resolution optical fluctuation imaging (bSOFI)," *Opt. Nano.* **1**(1), 1–7 (2012).

[75] S. Cox, E. Rosten, J. Monypenny, T. Jovanovic-Talisman, D. T. Burnette, J. Lippincott-Schwartz, G. E. Jones, and R. Heintzmann, "Bayesian localization microscopy reveals nanoscale podosome dynamics," *Nat. Methods* **9**(2), 195–200 (2012).

[76] M. Gallina, J. Xu, T. Dertinger. A. Aizer, Y. Shav-Tal, and S. Weiss, "Resolving the spatial relationship between intracellular components by dual color super resolution optical fluctuations imaging (SOFI)," *Opt. Nano.* **2**(1), 1–9 (2013).

12

TECHNOLOGY

ANN E. ELSNER AND CHRISTOPHER A. CLARK
School of Optometry, Indiana University, Bloomington, IN, USA

12.1 BASIC OCULAR ANATOMY AND PHYSIOLOGY

The eye in general and the human eye, in particular, offer both unique opportunities and challenges when it comes to the uses of light [1–5]. Photonics can be used to measure a number of different aspects of the eye that have direct effects on detection and treatment of diseases. As with any tissue being examined or treated with the use of photonics, safety issues become a limiting factor. The eye's innate biological function limits the ability to examine it. That is, ocular structures are designed to be clear and to capture light rather than reflect it back out of the eye. To understand the uses of photonics in the eye, one must first have a basic understanding of the structure and function of a normal eye (Fig. 12.1). The eye changes throughout life, as part of a normal developmental process that at first improves many aspects of vision throughout early childhood. Later, as the ocular structures age, there are consequences of systems failing and resulting in decreases in visual function. More extreme are overzealous responses of wound healing by the retinal vessels in the eye, such as in diabetes, since in central nervous system tissues must self-repair to last a lifetime.

The eye, which has the shape of a ball except for the anterior portion that has a clear, protruding portion that serves as a lens and is directly visible, plus a posterior portion with the neural connections, which are inside the head and cannot be seen without instrumentation. The methods and requirements for diagnosis and treatment differ greatly due both to accessibility and vastly different tissue compositions. The importance of the entire eye remaining relatively transparent throughout life cannot be overstated, particularly since the distance traveled is relatively large compared with

---

Photonics: Scientific Foundations, Technology and Applications, Volume IV, First Edition.
Edited by David L. Andrews.
© 2015 John Wiley & Sons, Inc. Published 2015 by John Wiley & Sons, Inc.

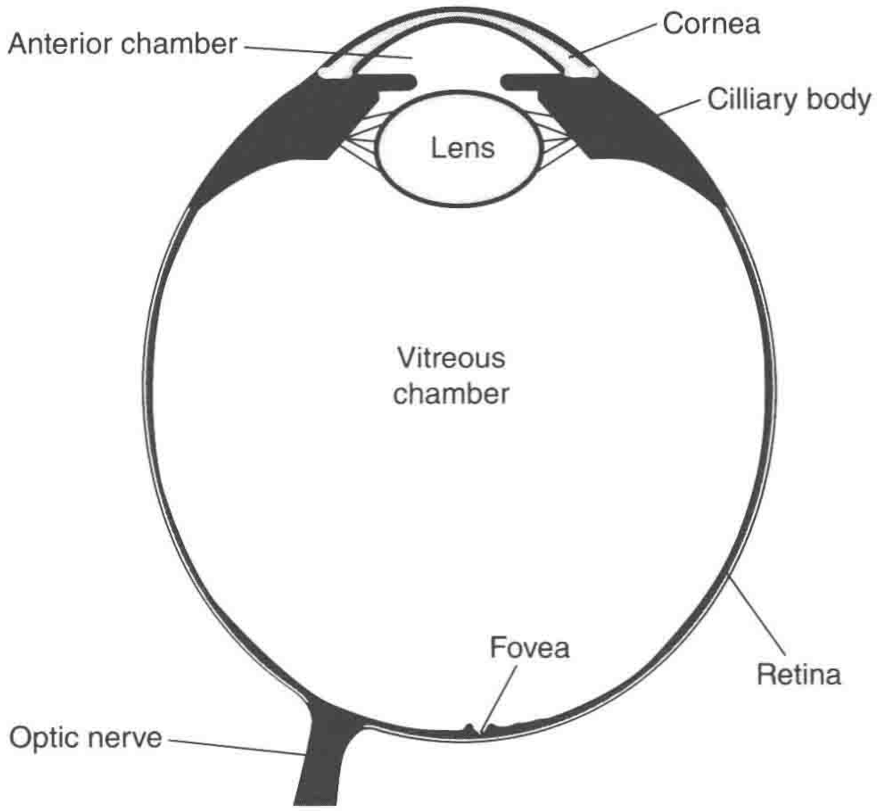

FIGURE 12.1 Anatomy of the eye. The front surface, made up of the cornea and the tear film, serves as the main refractive element and is clear. The lens provides variable focus in younger individuals. The iris serves as a diaphragm to limit the amount and angle of light reaching the retina. The retina covers the inside of much of the eye, and contains the neural elements needed to capture light, transduce light energy to a neural signal, and code the signal for transmission to the brain. The fovea is the location of the densest array of photoreceptors. The optic nerve carries the visual signals to the brain, and exits the eye via the optic nerve head.

the collection angle permitted by the entrance through the pupil. From the surface of the cornea, through the refractive and structural elements, and to retina where light is collected is roughly 22 mm. The typical refractive error of a human eye is approximately 60 diopters, where a diopter is defined as 1/m. The anterior elements of the eye, which have a much wider numerical aperture than the interior portions, are far more reflective than the retina, which returns at most only a few percent of the illumination.

12.1.1 Anterior Segment Anatomy

12.1.1.1 Cornea and Tear Film The most anterior portion of the eye is composed of the tear film and the cornea (Fig. 12.2). The tear film sits on top of and is anchored to the cornea, positioned for a number of purposes. The tear film serves as the first optical surface of the eye and as such, it needs to maintain a smooth, regular surface to allow for both the eye to see and for optical systems to examine the eye. A high index of refraction, which differs significantly from that of air, is a feature of this first surface. The tear film also provides part of the system to protect the anterior eye from infection from bacteria and viruses through the production of mucus and presence

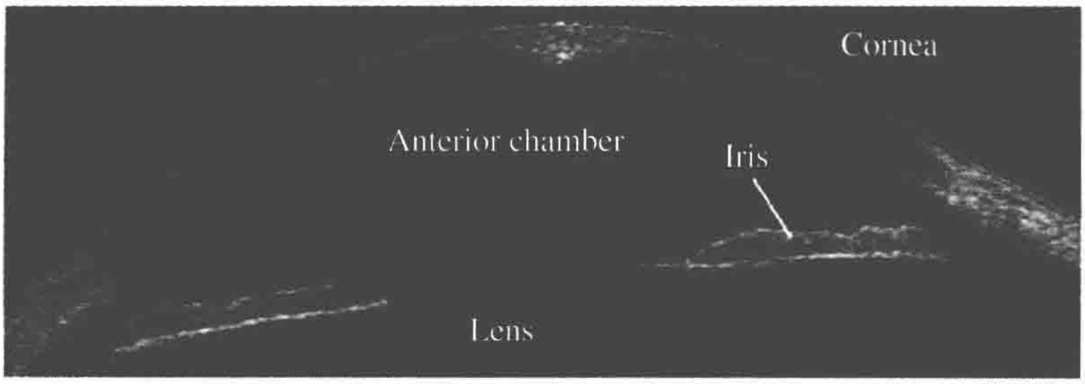

FIGURE 12.2 Anterior segment optical coherence tomography (OCT) showing the cornea, anterior chamber, and iris. Only the anterior surface of the lens is hinted at due to the clarity of the lens. The anterior chamber is fluid filled also and does not reflect back any light. Image courtesy of Dr. Peter Kolbaum and Dr. Meredith Jansen (Indiana University, Bloomington, IN).

of antibodies. The tear film is composed of three components: a lipid/oil to prevent evaporation, an aqueous component to keep the surface moist, and a mucin component to provide structure. Many of these components can be imaged with various photonics techniques. The cornea provides the structure that accounts for approximately 66% of a human eye's focusing power while having a thickness of only 550 μm. The cornea and the lens are the only two parts of the human body that are biological tissues, not fluids that are replaced, with a primary requirement of remaining optically clear. This requires a unique structure to allow for this clarity in the cornea.

For the purpose of this chapter, we will consider that the cornea is composed of three main layers. The first main layer is the corneal epithelium, which provides structure for the tear film and the final layer of protection from microbial infection. The second main layer is the stroma, which provides the bulk of the thickness of the cornea. This stroma is composed of long protein strands known as fibrils, collagen filaments 1.5–2.5 μm thick positioned in a lattice structure, and anchored by additional molecules. The spacing between fibrils must be maintained at <200 nm. The fibril thickness, the distance between fibrils, and the lattice structure allow for any light scatter within the cornea to be removed by destructive interference. The final main layer of the cornea is the endothelium, which provides aqueous pumps to maintain the exact corneal hydration to maintain the proper fibril spacing in the stroma for clarity. Between the corneal epithelium and the stroma lies Bowman's layer, a thin layer composed of collagen and other proteins and sugars and designed to protect the corneal stroma. Between the stroma and the corneal endothelium lies Descemet's membrane, the basement membrane for the thin and fragile corneal endothelium.

12.1.1.2 Anterior Chamber and Lens The next portion of the eye is the anterior chamber, iris, ciliary body, and lens. The anterior chamber of the eye sits between the lens and the cornea. It is primarily a fluid-filled chamber that delivers nutrients such as glucose to the interior of the eye. Structural changes with aging or disease that occur in this area, specifically those decreasing the depth of the anterior chamber such that fluid flow is reduced by the physical barrier of the lens in contact with the outflow pathway, can lead to an unwanted increase in intraocular pressure. Similarly, decreases in the size or increases in the resistance of the pores through which the fluid exits the eye, can result in decrease of outflow to the extent that the intraocular pressure is raised. This increased pressure is one common risk factor for glaucoma, which is a common progressive neuropathy of the optic nerve. Considerable diagnostic and treatment efforts have been made to reduce the impact of glaucoma.

The iris functions as a light-controlling mechanism. Through muscle action, the iris can change size, thereby altering the size of the pupil and ultimately the amount and angular subtense of light passing through the pupil. The inner diameter of the iris differs greatly with light level, age, and level of arousal [6, 7]. With changes in diameter of the iris varying over a range of more than 8 mm in a young eye in the dark to 1 mm in an older eye or in intense light, the amount of light available for sight or imaging the structures within the eye varies by more than a factor of 64. The spatial resolution of both vision and imaging of the structures within the eye are then limited by the numerical aperture resulting from the pupil diameter of 1–8 mm and the nodal point of about 17 mm. Further, the angular scatter of structures within the eye, which may influence vision or imaging when large range scatter occurs, are not directly characterized by *in vivo* measurements.

Immediately behind the pupil is the lens, which provides the final 33% of focusing power for the eye. Anterior changes in the curvature of this lens, due to the muscle action through spring-like zonules, provides for the eye to focus for various distances. The muscle action is provided by the ciliary body, which is adjacent and posterior to the iris. With aging comes stiffening of the lens, resulting in the failure to provide fine focus, along with gradual opacification of the lens, known as cataract. The ciliary body also provides the nutrient fluid that fills the anterior chamber and pressurizes the eye. A mismatch of the rates of production and outflow in the eye results in higher intraocular pressure. There is a significant increase in the optical aberrations with age, along with more prevalence of some of the higher order aberrations that are less common in younger individuals [8–12].

Behind the lens and ciliary body is the posterior chamber, which is largely filled with a collagenous gel, known as the vitreous body. The vitreous and the pressure resulting from fluid creation allow for the optical components to maintain alignment. Any changes in the distances between the optical elements and the retina results in myopia (nearsightedness) or hyperopia (farsightedness). While the vitreous is clear in younger eyes, the collagen degrades with aging, causing it to shrink, distort, and lose clarity. Eventually, the vitreous detaches from the layers beneath it, and not always cleanly, or has strands that slide into the visual pathway during eye motion. Considerable optical artifacts result from these changes.

12.1.2 Retina

The retina and its support system, composed of the retinal pigment epithelium (RPE) and the choroid, line the inside of the eye (Fig. 12.3). The retina is composed of three types of cells, neural cells responsible for light capture and transmission, glial

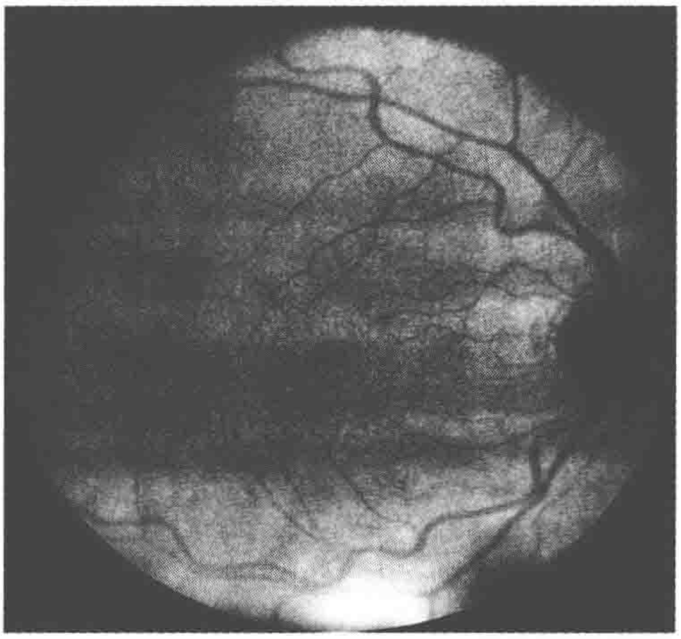

FIGURE 12.3 An en face image of the retina of a 54-year-old male, acquired with the Laser Scanning Digital Camera at 850 nm with a 36°, foveal-centered field of view. The fovea is localized by the slightly darker circular region in the center of the image, containing a small, bright spot which is the reflection from the foveal pit. The darker region on the right is optic nerve head, where retinal vessels enter and exit the eye, and the neurons exit, carrying the visual signal for further processing in the brain. The retinal blood vessels form networks, shaped like trees branches that are contained within the retina in a healthy eye. Image courtesy of Ann Elsner and Matthew Muller (Indiana University and Aeon Imaging, LLC).

cells that support the neural cells, and vascular cells and structural components to provide nutrients to the eye. The retina is composed of numerous layers, each with a specialized function (Fig. 12.4). These layers also vary with the distance from the fovea and optic nerve head, where the most acute vision is supported and the optic nerve exits the eye, respectively.

12.1.2.1 Photoreceptors The photoreceptors are the irreplaceable first element of vision, and as such, are a key target in modern diagnostics for eye care. The photoreceptors are in the outermost layer of the neural portion of the retina, and directly in contact with the RPE, which contains the support cells for the outer portions of the photoreceptors. Although designed to capture light, photoreceptors are actually positioned beneath the neural apparatus used to transduce and transmit the visual signal to the brain, as well as underneath (or exterior to) the retinal vascular system (Fig. 12.4). This organization has the advantage that the RPE, which is in contact with a solid vascular plexus just beneath (or outside) the RPE, can provide oxygen and nutrients, remove wastes, and perform photoreceptor renewal without these cellular and vascular structures lying in the direct path of vision. There are no photoreceptors on the optic nerve head. The photoreceptors have two functions, the first of which is to guide light so that it is captured efficiently [13–15]. The cones collect light over a small angle, so that precise spatial localization of the optical path of incoming photons occurs, which helps preserve spatial acuity. The ability to guide light depends upon the retinal location and status. The width of cone photoreceptors is about 1–5 μm, and this refers to the outer segment that contains the pigment, not the cell body or axon. Very narrow cone photoreceptors do not have as good antenna properties as the slightly wider cones, so that the most efficient guidance is not actually in the central fovea. While it may seem obvious that retinal degenerations that lead to photoreceptor structural changes and cell death cause poor guiding of light by cones, there are crucial, but subtle, changes in guidance by photoreceptors. Guidance changes degrade vision and also provide early detection of retinal disease

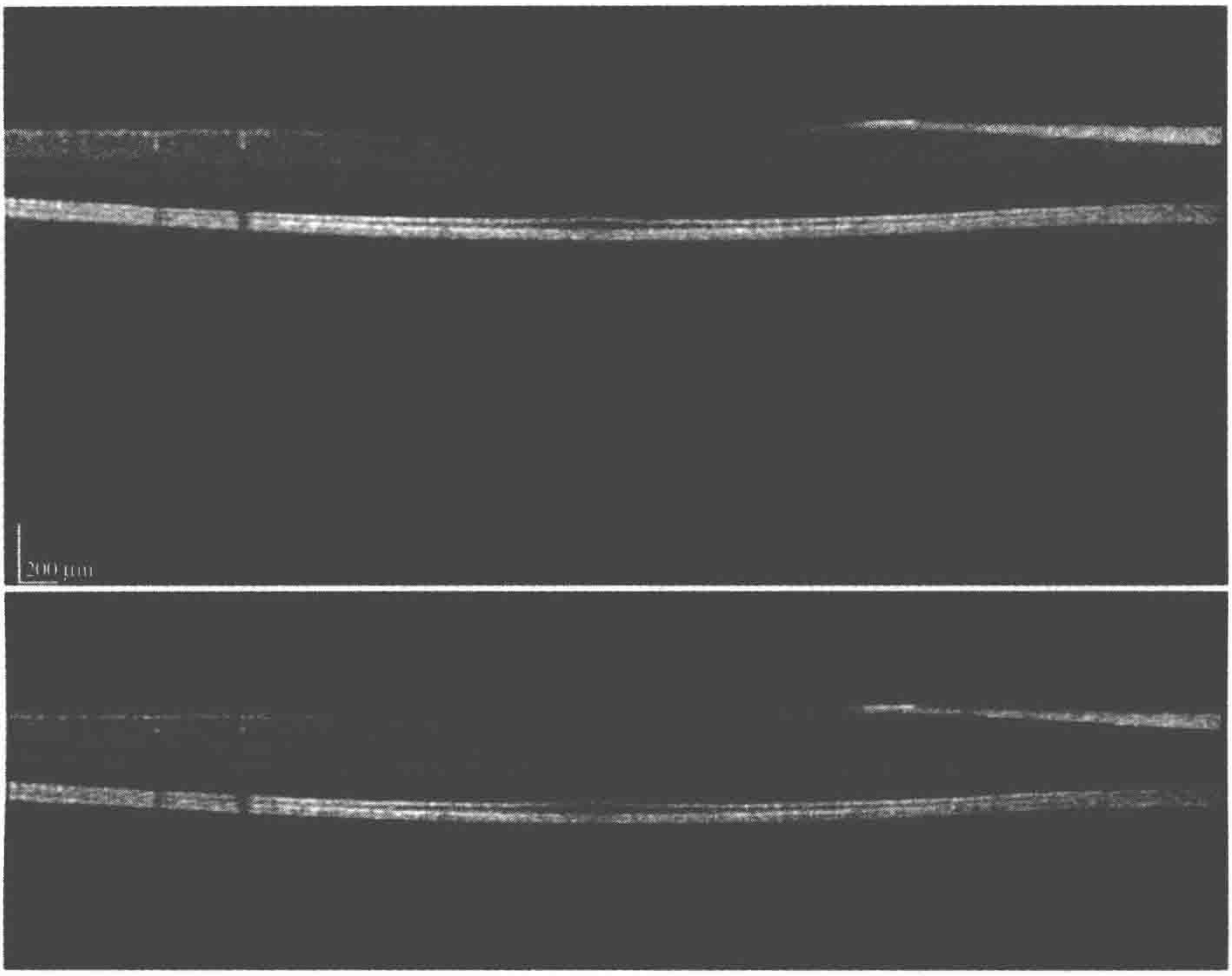

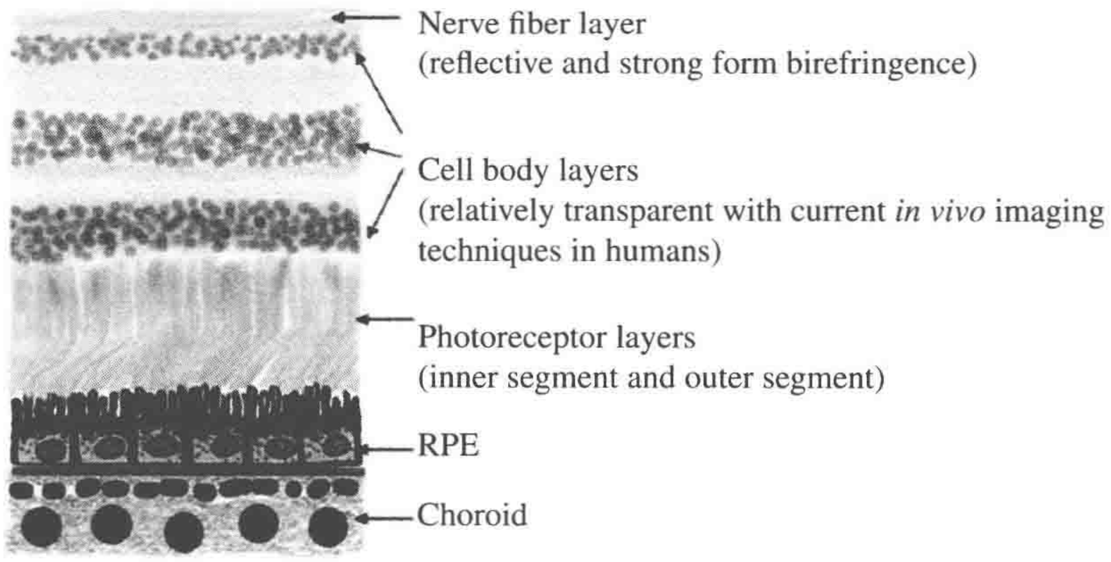
Nerve fiber layer
(reflective and strong form birefringence)
Cell body layers
(relatively transparent with current *in vivo* imaging techniques in humans)
Photoreceptor layers
(inner segment and outer segment)
RPE
Choroid

such as macular edema in diabetes (Fig. 12.5), the most common cause of reduced acuity in working individuals in the USA [16].

The second function is to turn light into biological signal, and this is accomplished by means of transduction into chemical energy and the generation of a graded response [1–3]. The photoreceptors normally include three types of cones that differ in spectral sensitivity, with their chief roles for color vision, high resolution spatial and temporal vision, and bright light conditions. The absorption spectra of the cones are broadband, with considerable overlap, so that difference signals can provide discrimination for a wide range of colors (Figs. 12.6 and 12.7) [17–19]. The different types of cones are positioned with respect to each other so that spatial and spectral information can be derived from the comparisons, and this distribution can be mapped with highly magnified views in living subjects [20, 21].

Rods are the most numerous photoreceptors, and are responsible for vision in dim conditions, detection of large objects in the periphery, and working with cones to maintain an adaptation level. The rods collect light over a wide angle, since their primary role is to capture and sum together photons to provide the most sensitive detection possible. Rod outer segments are narrower in diameter than all except the most central cones [1–3].

Cone photoreceptor densities are highest in our central vision, which is necessary to produce high acuity and fine discriminations of color within a small area. There are about 4–5 million cones in the human retina, but about 100 million rods. The cones are densely packed in the central fovea, but decrease in density with increasing distance from the foveal center (Figs. 12.8 and 12.9) [22–26]. The rods and short-wavelength cones have the opposite distribution, being scarce in the central

←

FIGURE 12.4 Cross-sectional SD-OCT image (b-scan) of the retina of a normal right eye of a 46-year-old female Caucasian. The image is the average of multiple scans, adjustable by user selection, and with automatic eye tracking enabled (Spectralis, Heidelberg Engineering, Heidelberg, Germany). Top: Average image, presented as a gray scale with stronger signals being white and weaker signals dark, showing that several strong index of refraction changes demonstrate many of the layers of the retina and RPE. Middle: Manual segmentation at borders, so that thickness measurements of the retina can be measured for a number of the layers of the retina. From top to bottom, the lines are as follows: The border between the vitreous and the retina where the inner limiting membrane defines the innermost surface of the retina; next is, the border between the nerve fiber layer and the ganglion cell layer; next is, the border between the inner plexiform layer and the inner nuclear layer; next is, the border between the inner nuclear layer and the outer plexiform layer; next is, the border between the outer plexiform layer and the outer nuclear layer; next is the external limiting membrane that could also be the myoid structures of the photoreceptors; border between the inner and outer segments of the photoreceptors; next is the border between the outer segment and the RPE; last is the border between the RPE and the choroid. Bottom diagram of the cross section of a normal eye outside of the foveal pit, showing key layers and optical signatures. There is strong birefringence from the regular spacing of the superficial retinal nerve fiber layers, which also are highly reflective and obscure deeper structures. Image courtesy of Joel Papay (Indiana University, Bloomington, IN).

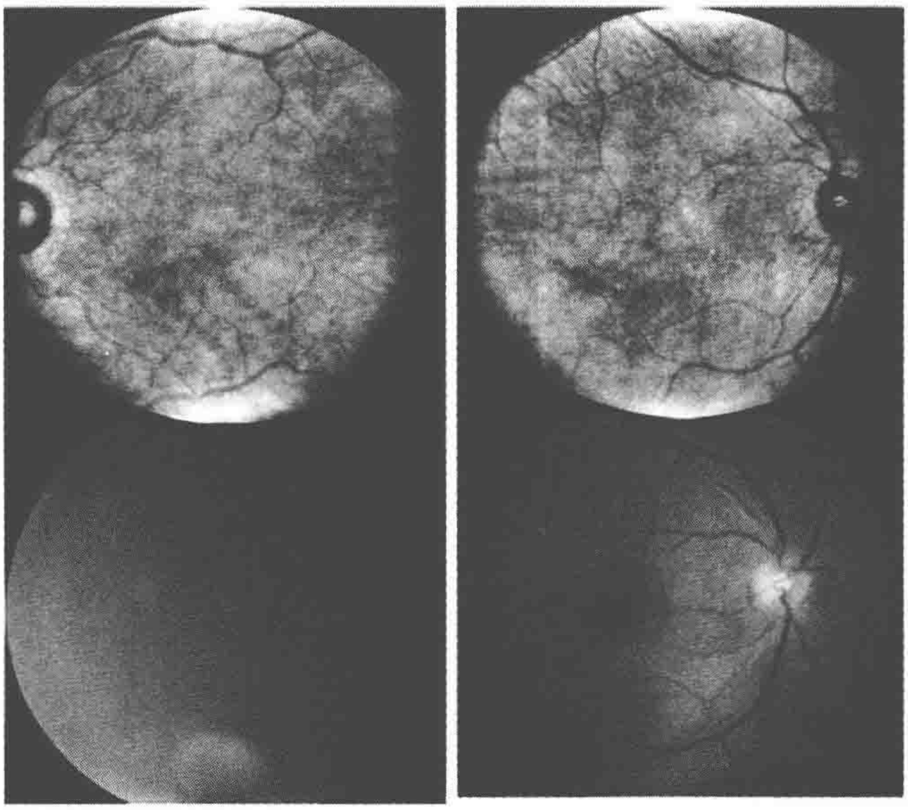

FIGURE 12.5 Laser Scanning Digital Camera and Canon nonmydriatic fundus camera images of a 63-year-old African American male who has diabetes. Left: The near-infrared illumination of the Laser Scanning Digital Camera, but not the visible wavelength light of the fundus camera, penetrates through moderate media opacities. Right: Further, the LSDC and Canon both show numerous dot hemorrhages and microaneurysms, consistent with diabetic retinopathy. (*For a color version of this figure, see the color plate section.*)

fovea but increasing in numbers with increasing distance from the fovea. The optical density of cone photopigment is also greatest in the foveal center of young, healthy retinas, but decreases in density with aging along with several retinal diseases, thus is considered an early warning sign of retinal disease [27–32]. A dense packing in one location and sparse distribution elsewhere provides a challenge for the neural coding of the output from the rod and cone photoreceptors and, consequently, the

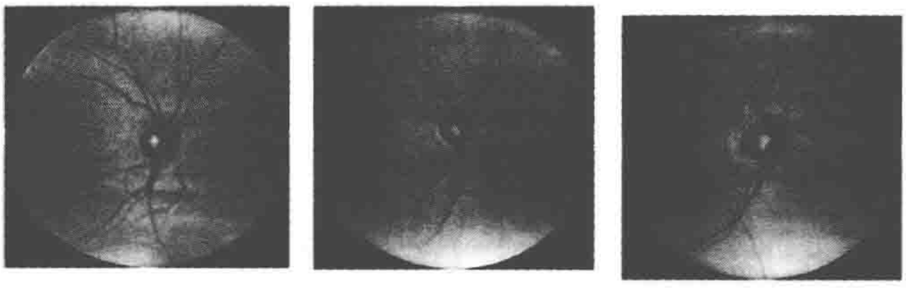

FIGURE 12.6 Examples of optic nerve head-centered retinal images (10-frame averages) taken in undilated subjects with dark eyes, and showing the branching of the retinal vessels entering and exiting the eye. Left, A 40-year-old Asian male; center, a 50-year-old Black female; right, a 43-year-old Hispanic male. Unlike many visible flood illumination imaging systems, the high vessel contrast is maintained in the LSDC regardless of increased retinal pigmentation according to racial or ethnic background.

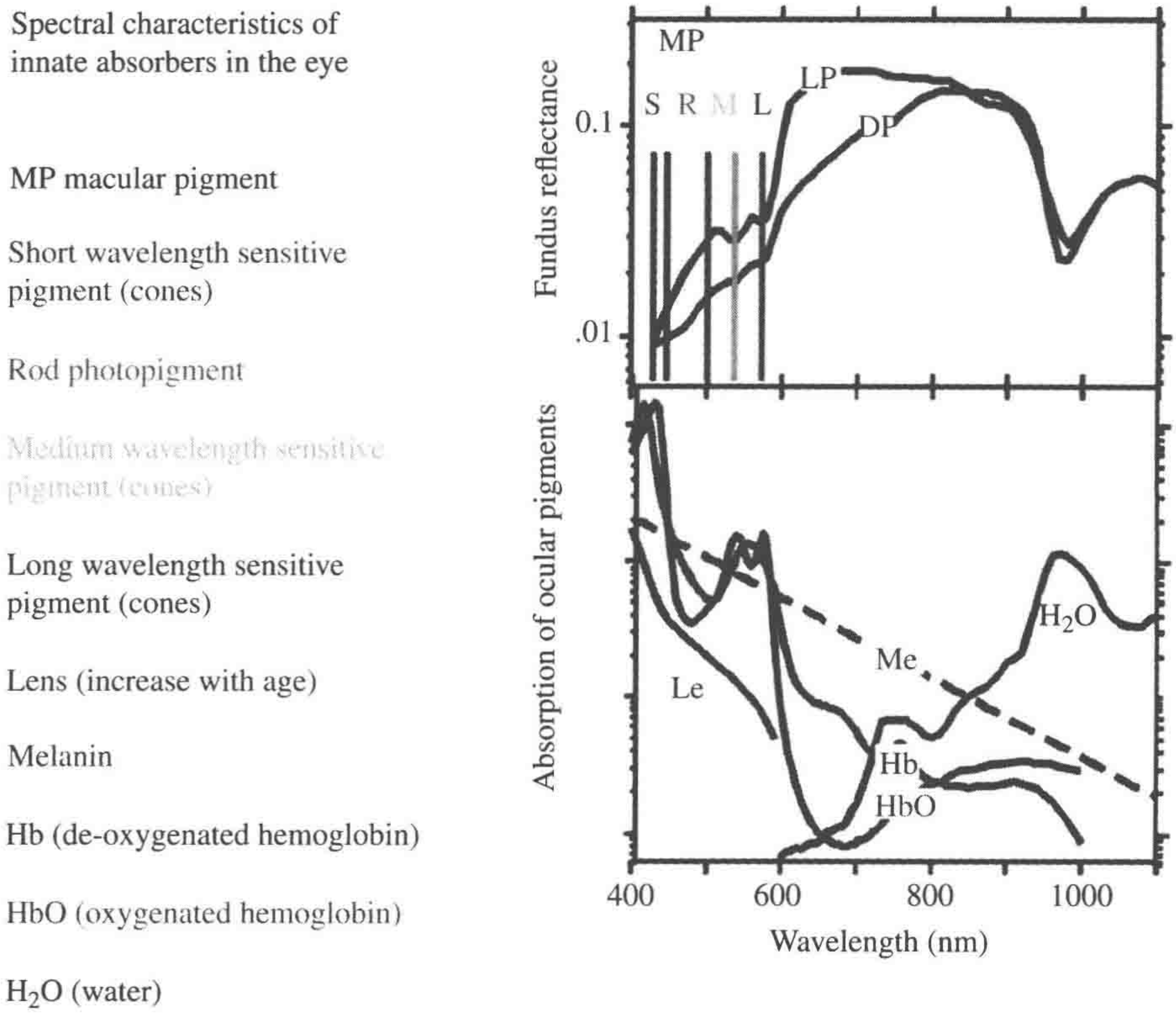

FIGURE 12.7 Spectral characteristics of the innate absorbers in the human eye and the overall reflectance. The absorbers are demonstrated in two manners, either as the peak absorption spectra for photopigments and macular pigment, which are well known to have broad spectra with considerable overlap, or as the spectra expected from absorption due to the normal optical path length and concentration in the healthy eye. The photopigments bleach on exposure to light, and therefore change dramatically in optical density and consequently the spectra. Macular pigment differs by more than 1 log unit in healthy individuals, also altering the relative absorption spectrum. Modified from Reference 48. (*For a color version of this figure, see the color plate section.*)

retina has considerable lateral connections for signal conditioning, the inner and outer plexiform layers.

The visual system is designed for two competing roles, to detect change that is meaningful, but at the same time to maintain color and brightness constancy despite the operation over a more than 11 log unit range. Thus, while a specific wavelength might appear blue under one set of circumstances, the neural contrast with an adjacent region of color or the appearance in differing lighting conditions or the visual periphery can greatly alter the appearance of an object. For this reason, graphic display must take into consideration the light conditions, viewing angle, size of the display, and other factors, in addition to the color vision of the observer [17–19]. Information presented using color differences on a fine scale, that is, very few pixels

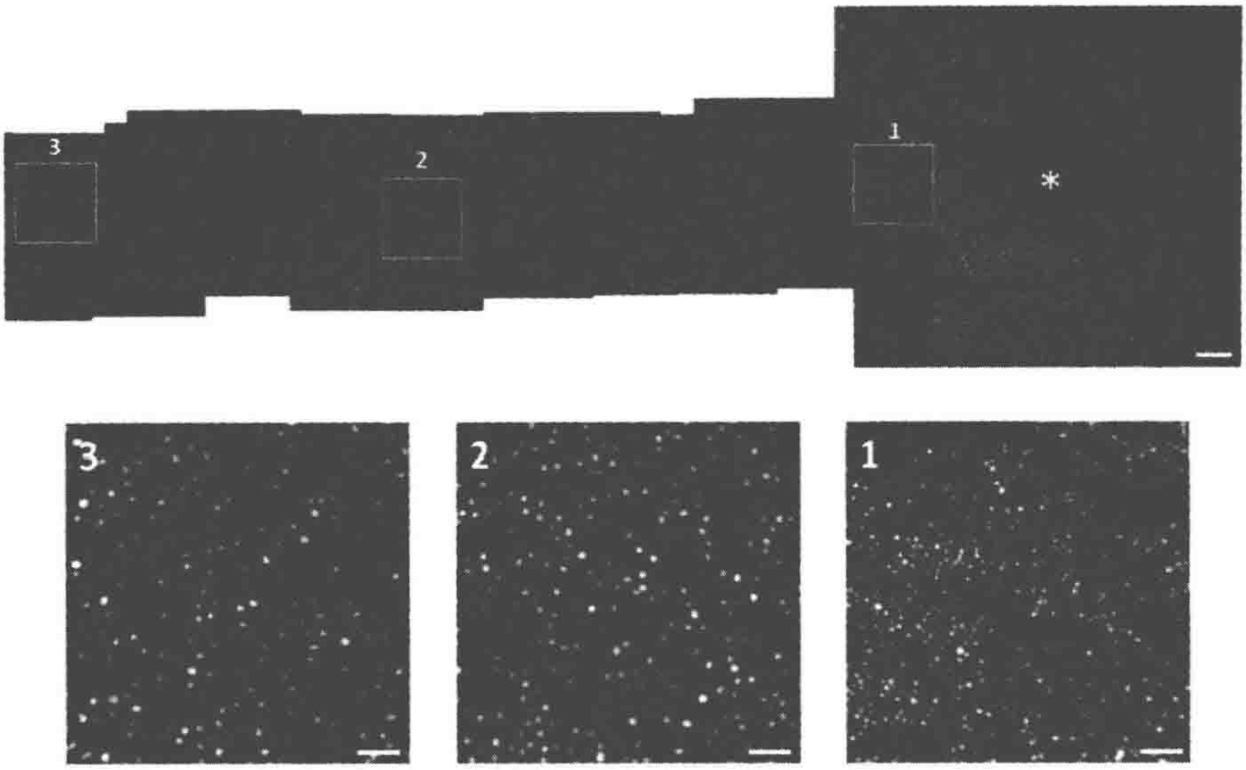

FIGURE 12.8 Adaptive optics montage of the cone photoreceptors across 10° of the retina. Top: montaged image of the retina acquired using AOSLO. White star area represents the fovea. Three white boxes show areas corresponding to different sampling points. Bottom: 1–3, Cone photoreceptor densities from the three measured areas, 1.5°, 6°, and 9° from the fovea. Note that the cone densities decrease with increasing distance from the fovea. Scale bar equals 100 μm. Image courtesy of Stephen Burns and Toco P Chui (Indiana University, Bloomington, IN).

for each color, often lead to an average response rather than a clear illustration, with critical applications including medical image representation. For this reason, many vendors of ophthalmic imaging devices have moved away from the use of colorful outputs, particularly arbitrarily defined false-coloring of retinal layers or other structures, which may be eye-catching but are unsuitable for high resolution images.

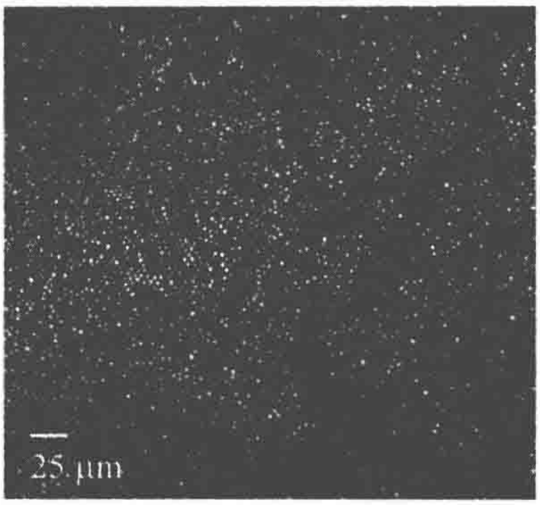

FIGURE 12.9 *In vivo* image of the retinal cone photoreceptors with an AOSLO system, demonstrating the optical resolution. Image courtesy of Stephen Burns (Indiana University, Bloomington, IN).

The density of cones generally decreases with increasing distance from the fovea, but this is not monotonic. Cone density across the retina depends upon refractive error and eye length, aging, and the meridian of the measurement [22–24]. In the healthy eye, longer eyes tend to have higher refractive errors, and the cones are less dense in the macular region. It is not known if this is cause or effect: that is, whether the eye stretched and this led to the cones being farther apart, or whether the spacing of the cones drove the eye to a length that exceeds the refractive power of the cornea plus lens. The density of the cone photoreceptors also depends upon the axis of measurement, with horizontal and vertical meridians different in cone density, and therefore the potential for color or spatial resolution. This is consistent with the visual streak shown in classic histology studies of photoreceptor density [25, 26].

The depth in the eye of the photoreceptors, while preventing the potential for reducing scattered light from the overlying retina elements, provides the advantage of metabolic support without requiring yet another layer of vascular networks (Fig. 12.4). This need for support is largely due to the high metabolic activity of the photoreceptors, requiring direct access to nutrients and waste material through the RPE, directly beneath them, and the choroid that envelopes and nourishes the retina. The inner ring of capillaries in the retina is usually displaced away from the highest density of cone photoreceptors, and this foveal avascular zone can be mapped by a variety of optical techniques to study the health of the eye or determine the location of fixation [33, 34].

12.1.2.2 Superficial Retinal Layers The more anterior layers of the retina process image information. The straight-through path from the photoreceptor to the brain is cone or rod to bipolar cell to retinal ganglion cell. The lateral connections are provided by the horizontal cells and the amacrine cells. The cell bodies are collected together into densely packed nuclear layers, the outer nuclear layer for cones and rods, the inner nuclear layer for bipolar cells and horizontal cells, and the ganglion cell layer for retinal ganglion cells and amacrine cells, with some displacement. The individual cells have a wide variety of interconnections, typically with the axons of one cell type terminating on the dendrites of another, in highly elaborate spatial patterns at the outer and inner plexiform layers. The multi-directional connections along with the highly irregular shapes of many of the neural processes increase scatter, so that these layers return through the pupil somewhat more light than do the layers with cell bodies (Fig. 12.2). A sparsely distributed, specialized type of ganglion cell also contains the photopigment melanopsin, thought to help with regulation of pupil diameter and circadian rhythm via temporal mechanisms of adaptation with long time courses compared to rod and cone pathways.

All the layers of the retina except the crucial outer segments of the photoreceptors are displaced laterally from the foveal center, resulting in less scattered light to degrade visual acuity. The cone axons, called Henle fibers, are displaced approximately radially out of the center of the fovea. This pattern of similarly sized, tube-shaped structures is densely and regularly packed in the healthy eye, interspersed with Mueller cell processes, leading to form birefringence similar to that found in crystals such as calcite. Form birefringence due to the Henle fiber layer has a specific pattern, which is an approximately sinusoidal varying amplitude change when measured at a constant distance radially around fovea, and depends on aging and disease status [35–38]. There is no measureable birefringence in the centralmost portion of the fovea, since the birefringence is due to lateral axon displacement with respect to a measurement beam entering the pupil of the eye.

12.2 MEASUREMENT TECHNIQUES

12.2.1 Scanning and Confocal Apertures

The introduction of novel laser sources has allowed the development of a variety of measurements and diagnostic techniques [5]. This has paralleled photonic developments of method of beam scanning and detector configurations. The scanning laser ophthalmoscope (SLO) is a general class of well-known devices that use illumination that is scanned across the target. Laser scanning provides a method of reducing unwanted scattered in highly scattering, layered structures such as the human eye. However, scanning of the illumination is only effective if the detection method used removes unwanted scattered light [5, 29, 39–41]. That is, contrast is significantly decreased if light is scattered from a feature and across the retina, often multiple times, then eventually reaches the detector at a location corresponding to the region of the detector meant for another feature. Several configurations accomplish this. When the light returning from the target is relayed into a conjugate optical plane, and an aperture is used to limit the light returning to a small focal volume, this aperture is called a confocal aperture. This method minimizes unwanted scattered light from adjacent target locations, as well as from other depth planes. Relative depth information is provided, and while useful in visualizing pathology as well as normal ocular structures, the resolution in the axial dimension is limited by the narrow entrance of the pupil compared with the relatively long length of the eye, that is, the small numerical aperture [42–46]. The numerical aperture (NA) of an optical system is a unitless number that quantifies the maximum angle over which the system can collect or emit light, for instance through a lens. $\mathrm{NA} = N \sin \theta$, where N is the refractive index of the medium where the lens is and θ is one-half of the greatest angle of the cone of light entering or leaving through the lens. Further, the aberrated optics of the human eye also limit the depth resolution.

A commonly used method is point scanning, that is, scan a single point of light in a pattern, such as a raster, and allow the light returning from the target to follow the scan path backward to the detector. This method is actually analog, not digital, since an image must be built up over time, so that the location of each pixel is coded by when it is acquired. The point scanning method is extremely light efficient, since the power needed for the source is only that for one region of the image at a time. Also, nearly the same optical path can be followed by all points in the image, making even image illumination possible by careful optical design. The detector is most often a single point or small array, such as an avalanche photodiode or photomultiplier tube. Thus, modern two-dimensional (2D) detectors such as charged coupled devices (CCD) or complementary metal oxide (CMOS) arrays have not been routinely used

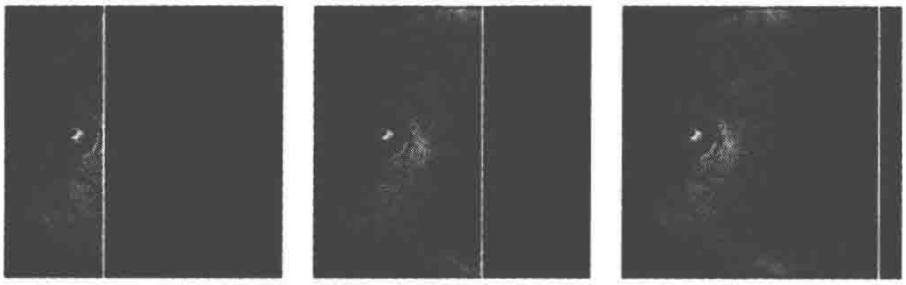

FIGURE 12.10 Principle of line scanning across the retina, demonstrated with a near-infrared, confocal imaging system, the Laser Scanning Digital Camera. Left, a laser line has begun to scan across the retina; middle, the line has scanned further along, and more of the image has built up on the detector array; right, image near completion. The advantage of a scanning laser as opposed to a flood system is that light scatter from other layers of the retina can be removed using a confocal aperture that is synchronized with the timing of the scanning.

with point scanning. Instead, an image capture card, often with a computer, is needed to build up an image. While this single-point scanning method works well when slow speeds are needed, using a variety of motors and deflection methods, it has proven difficult to scan in two dimensions and reach high speeds over large areas. Typically, there is a fast scanner used in combination with a slow scanner, and the fast scanners are typically resonant galvanometers or rotating polygon mirrors. The fast scanners in many systems have failed to be robust over time.

Due to the limitations of scanning speed and mechanical failure, as well as the high cost of detectors, line scanning has gained in popularity over point scanning (Fig. 12.10) [41,47]. Line scanning is typically used in combination with a line array. Again, this is analog imaging, not completely digital. The image must be built up, often using an image capture card or ancillary electronics. The line scanning method offers several of the advantages of point scanning, such as the potential to greatly reduce unwanted scattered light, and a similar although not identical optical path for adjacent points in the image.

Recently, hybrid imaging was introduced, in which the illumination is line scanning, but the detector is a 2D array [41]. While a 2D CCD array can be used, the sample-and-hold method of detection removes the advantage of scanning for biological tissues that scatter light, such as the eye. Use of a confocal aperture removes this disadvantage, but does require that a conjugate plane be added for the aperture. A simpler method is to use the rolling shutter feature of a CMOS camera, which reads only specific lines at a time, in synchrony with the illumination. This method can be used to create a flexible electronic aperture, which serves the same function as a confocal aperture, but is rapidly adjustable and requires no moving parts. This is true digital imaging, requiring no computer to build an image.

12.2.2 Methods to Increase Contrast of Transparent and Scattering Tissues

There are several well-known methods to increase the relative contrast of tissues or features within an image. One is the use of wavelength, and the eye has many innate absorbers (Figs. 12.6 and 12.7) [48–50]. The use of near-infrared light has gained in popularity because of the improved penetration into structures, the relative comfort for patients who are photophobic, and the ready availability of sources developed for a variety of non-biological techniques, such as the solid-state lasers used for communication. However, visible wavelengths produce more contrast for inherent absorbers such as blood or macular pigment. Similarly, many of the intrinsic fluorophores require visible wavelength stimulation. Also, over 100 years of experience in ophthalmic practice in being able to directly view the structures of interest, in sharp distinction to most internal organs such as the heart or stomach, has resulted in the resistance to imaging of ocular structures by means of unusual wavelength combinations. The clinical recognition of features requires retraining, such as the enhanced visibility of blood vessels in the choroid, and has set back the acceptance of methods that might provide enhanced, albeit different, optical signatures for disease states (Fig. 12.5). Clearly, though, since most of the naturally occurring absorbers in the eye have broad band absorption, a careful selection of a limited number of wavelengths provides sufficient spectral information. Two points are particularly important in ophthalmic devices. The first point is the naturally occurring chromatic aberration, both longitudinal (axial) and lateral (transverse), since the eye has its own refractive elements [51]. When using short and long wavelength visible light, such as 440 nm and 650 nm, the defocus can be more than 2.5 D. When extending into the near infrared, the defocus is even worse. Second is the sensitivity to light of the eye that other parts of the body do not experience, including the extreme discomfort and potential for damage if using lights that would not cause measureable surface warming if used on the skin.

A variety of confocal apertures and the relative positioning of the illumination and detection optical axes have been used to increase contrast in images [29,40–42,48,52]. Apertures formed by using a mechanical stop are the most common. Similarly, a confocal stop can be used on axis, with the position of the illumination source varying. While this has long been known in dark field microscopy, the use of laser arrays lends itself to ease of selection of light sources electronically. Further, as described above, the flexible electronic aperture provides the potential for a wider range of positions and widths of apertures. By varying the distance or timing between the illumination light and the aperture parameters, the relative amounts of directly backscattered and multiply scattered light is varied. The criterion for a "good" image could be to obtain the best possible axial resolution, the brightest image, the most contrast for a specific feature, the most extinction for unwanted superficial reflections, etc.

Analysis of polarization content provides similar advantages to apertures [53–57]. By selecting a specific set of polarization conditions, the specular reflections from a target can be collected and the scattered light rejected, enhancing the contrast of retinal surface features. Similarly, the specular reflections can be rejected and the scattered light collected, enhancing the contrast of deeper retinal features or those that scatter light. Both the cornea and retina have structures that behave like crystals. Thus, the contrast of structures, even fairly transparent ones, can be enhanced by processing polarization information. Many lasers are linearly polarized, or their outputs can be made into a linearly polarized beam by the addition of the shelf polarizers. Several sources, such as visual displays with liquid crystal technology, use polarization elements for intensity control.

Coherence amplitude and phase information can be processed to greatly enhance contrast in a scanning laser device. Known by several names such as optical coherence tomography (OCT) or low coherence imagine (LCI), the axial resolution is greatly enhanced by two general classes of methods [58–62]. The older method, with advantages in some applications, is the time domain method. Light scanned across the target is compared, point by point, to a reference arm. The strength of the interference signal depends on the index of refraction change within the focal volume in each sample. Thus, if there is a strong interface change between two types of tissues within close proximity, a large signal is generated. However, if the index of refraction change is gradual, then the signal will be weaker. If the feature being measured is a pocket of serous fluid, typical for leakage in diabetic retinopathy or age-related macular degeneration, there is the potential for a very weak signal due to multiply scattered light. That is, the return for this region is of low signal strength and does not report on the specifics of the structure. The interpretation of OCT must include the idea that the measurement is optical path length with respect to a reference, not actual length. The OCT measurement depends upon the group index of refraction and the stability of the target position and reference. In the moving eye, which also can have a pulse, more rapid measurement techniques or the simultaneous measurement of two depth planes have aided the quantitative results. When querying a range of depths with time domain OCT, often by scanning in depth before moving laterally to the next position, the requirement to move the reference mirror or beam limits the potential sampling rate.

Spectral domain OCT (SD-OCT) and a variety of related methods have gained popularity because of their sensitivity and more increased speeds, reducing the artifacts from eye motion and heartbeat [63, 64]. The beam is scanned across the target, such as the retina or the cornea. Instead of using a reference arm to create interference fringes, the output from the SD-OCT is spread by a dispersive element across a solid-state line detector, so that a large range of depth is queried simultaneously. A Fourier transform of the pixel read-out of the line detector provides, for that location, the strength of the interference signal at each depth. Then the next location is scanned, again with all depths queried simultaneously, rapidly building an image.

These techniques receive added benefit from further consideration of polarization and timing. In polarization-sensitive OCT (PS-OCT), the OCT acts as depth ranging to permit the quantification of various layers for polarization content, further reporting on the structure within the layer for both anterior segment and retina [64–69].

12.2.3 Wavefront Aberration Measurement and Compensation

A variety of techniques use the measurement and/or correction of wavefront aberration, since the optics of the human eye limits the resolution of both vision and imaging of ocular structures (Fig. 12.11). The principle behind wavefront measurement is that a plane wave is aberrated by the optics of the eye. By measuring the tilt of each ray of a set of parallel rays impinging on the cornea, the aberrations of the eye can be computed. Taking the inverse, then a function can be computed that will undo the aberrations, leading to more optimal vision and clearer images of the ocular structures.

Even with the contrast-enhancing techniques of the SLO, correction of wavefront aberrations increases the contrast of features, such as retinal vessels [70]. Several

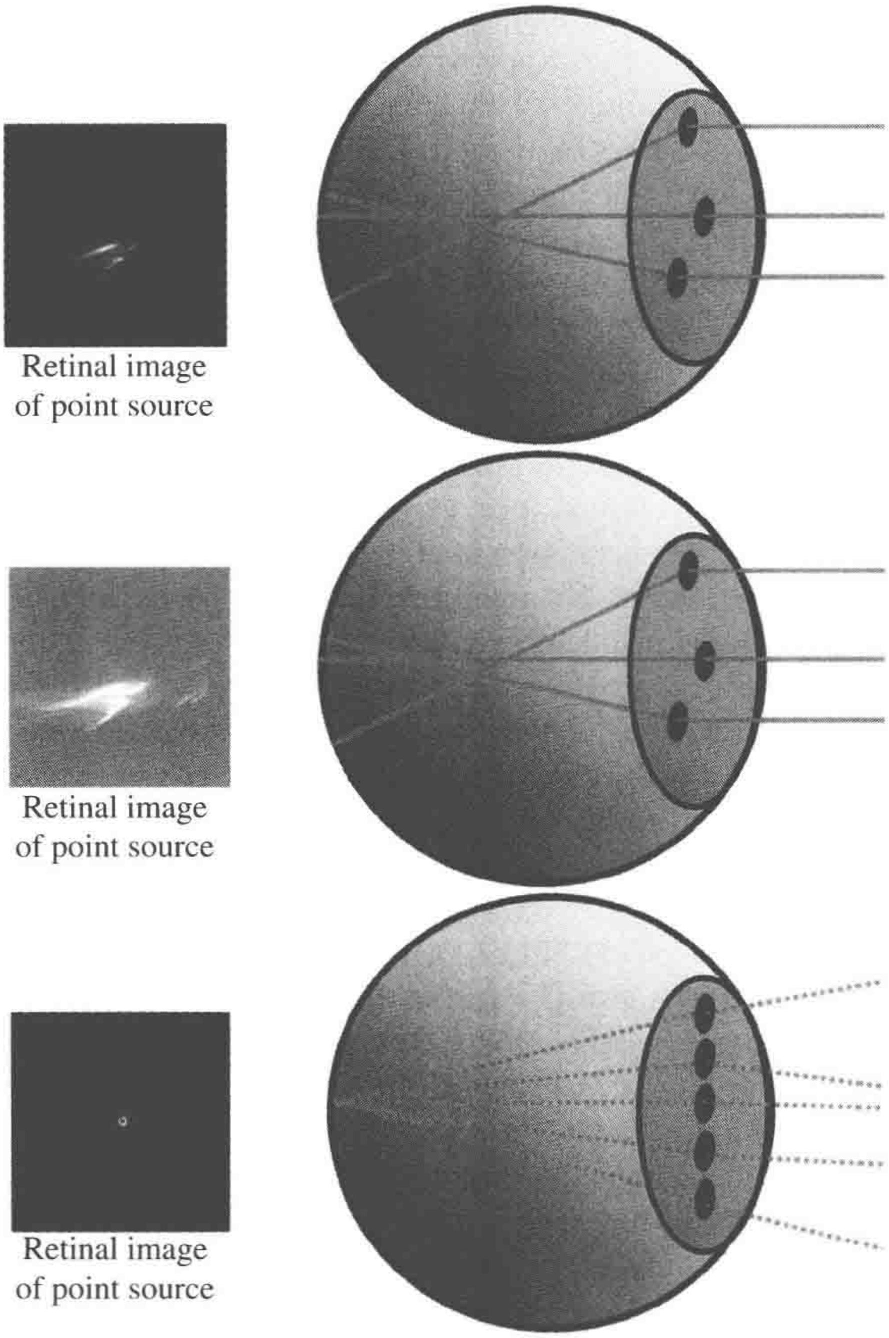

FIGURE 12.11 Principle of wavefront sensing. Top, parallel light rays enter the eye and are aberrated by the optics of the eye, resulting in a point spread function that is distorted; middle, parallel light rays are aberrated by the optics of the eye—additionally, scatter is occurring from multiple locations in the eye including the tear film, lens, and retina, resulting in not only the distortion and broadening of the point spread function but a degradation of contrast as well; bottom, light returning from a point on the retina is measured, then the light impinging on the eye has a wavefront altered to compensate for the aberrations of the eye. Measuring at controlled locations within the pupil allows for measurement of the aberrations based upon the deflection of each individual ray. Scatter, particularly found in older eyes, cannot be as readily corrected.

imaging devices use adaptive optics (AO) such as the AOSLO and AOOCT, benefitting from wavefront correction [21,71,72]. The most common technique is to perform a Hartman–Shack measurement of the aberrations, then use a modifiable element such as a deformable mirror to compensate for the optics of the eye (Fig. 12.12). Clearer images result, but the success depends upon a sufficient pupil diameter so that a strong

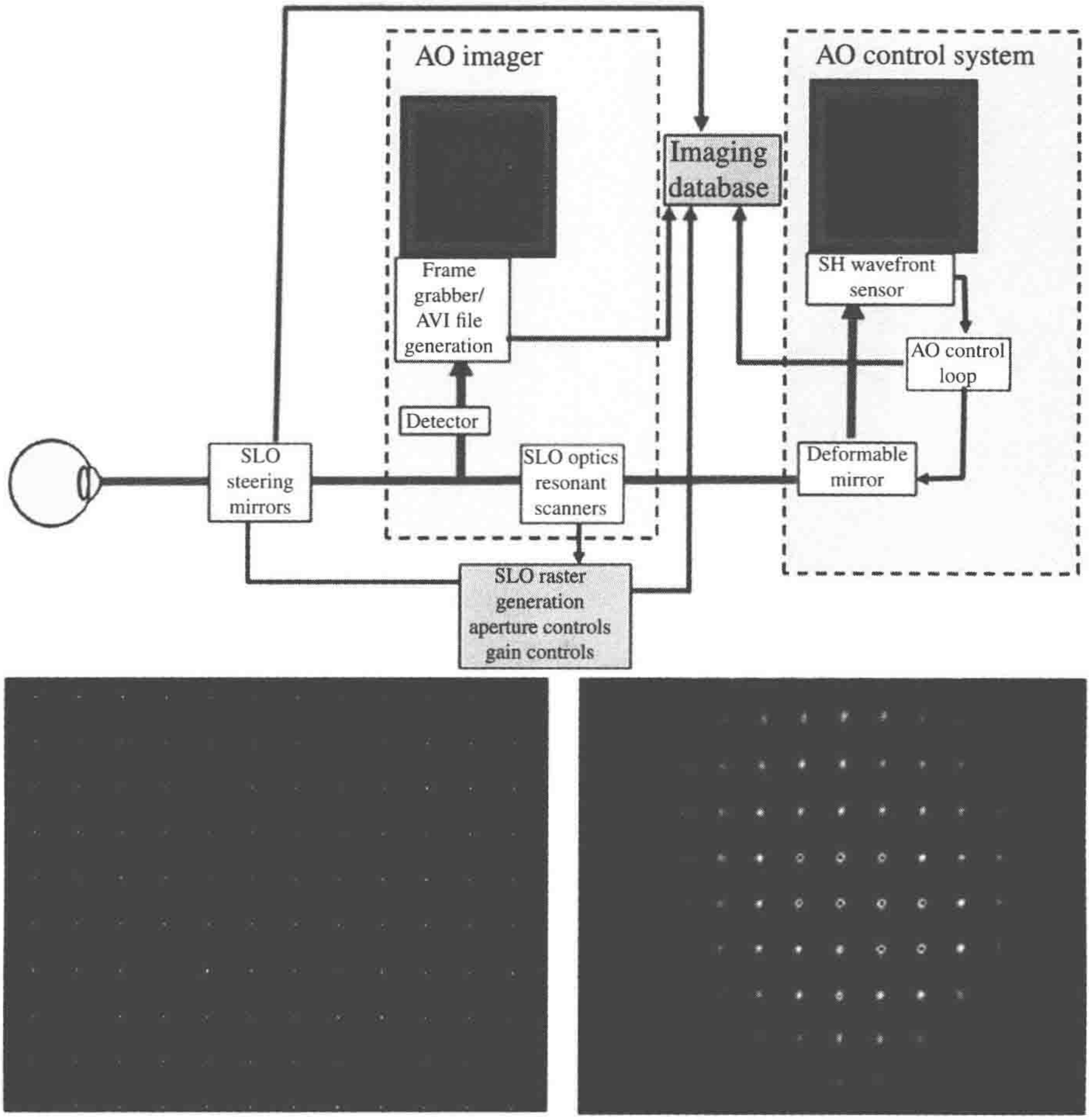
AO imager
Imaging database
AO control system
Frame grabber/ AVI file generation
SH wavefront sensor
AO control loop
Detector
SLO steering mirrors
SLO optics resonant scanners
Deformable mirror
SLO raster generation aperture controls gain controls

FIGURE 12.12 Schematic of an AO imaging system that uses a Hartman–Shack wavefront measurement to guide the compensation for the optical aberrations of the eye. Top left, schematic of the imaging subsystem, which incorporates scanning of the illumination across the target, collection of light by a detector, storing of data using a computer and frame grabber, and image processing to convert the incoming datastream into an image; top right, schematic of the AO control system, which includes a closed loop measurement of the wavefront, in a continuous manner. A grid pattern of light sources, generated with a lenslet array, is focused onto the retina. The light returning from the retina is collected in the pupil plane, using a detector that is separate from the retinal imaging channel. A centroiding algorithm is used to guide the positioning of a deformable mirror to correct the optical aberrations. With the aberrations corrected continuously, the AOSLO imaging channel collects the high resolution image. Bottom left, Hartmann–Shack grid representing a well-focused system; bottom right, Hartmann–Shack grid of a poorly focused system of an individual eye, prior to compensation with a deformable mirror.

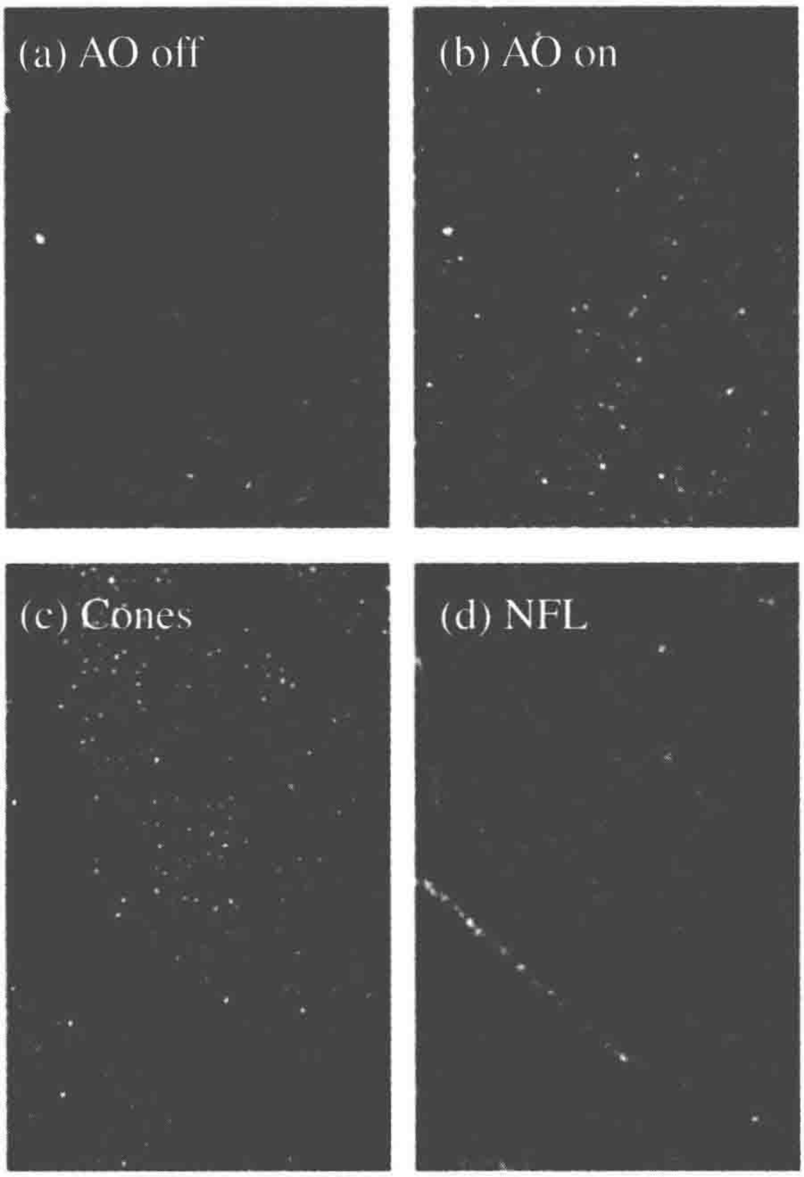

FIGURE 12.13 AOSLO imaging of human cones, showing the separate effects of wavelength correction and depth of focus. (a) Retinal image with adaptive optics, the deformable mirror, turned off. (b) Retinal image with adaptive optics turned off. Note that the resolution of cones is significantly improved as compared to (a). (c) Image of the cone photoreceptors adjacent to a blood vessel, seen as a dark shadow. (d) Image of the nerve fiber layer and blood vessel from the same location as (c). The retinal nerve fiber layer is the streaks running through the image. Image (d) is taken with the focus more anterior than (c).

signal can be obtained (Fig. 12.13). For practical operation of the AOSLO, many laboratories have turned to a larger stroke "woofer" mirror and a fine control "tweeter" mirror, so that the limited range of the deformable mirror is not spent correcting the optical power needed to correct for defocus and astigmatism. For usability, the system does not necessarily require the largest possible pupil for routine measurements, allowing measurements in the older eyes that have small pupils despite dilatation. A range of AOSLO configurations includes a system with no measurement and using only image intensity or contrast/frequency content to adjust the mirror, a wavefront AO control system based on the imaging beam, or a totally separate wavelength and

AO control imaging system. It is important also to have the potential to focus down to deeper layers, while holding the mirror correction. The guidance properties of the cones result in a strong signal in the photoreceptors layers, and this must be overcome to image other tissues.

12.2.4 Enhancing Contrast by Wavelength, Dye, and Temporal Modulation, and Image Processing

Ophthalmic imaging devices including film cameras, digital cameras, and SLOs, have used contrast enhancing dyes, primarily via fluorescence imaging with sodium fluorescein and indocyanine green [73–77]. These techniques help to document the structure of blood vessels, fluid leakage, or damaged tissues that stain with dye. Sodium fluorescein is commonly used for both anterior segment, applied topically, and posterior segment, injected or ingested. The optimal excitation wavelength is roughly Argon blue, or about 488 nm, with emission broadband but within visible wavelengths. Thus, it emphasizes more superficial structures, even if there is potential damage deeper. The dye diffuses readily, further masking deeper pathology. Indocyanine green leaks out of vessels less readily, and is excited by near-infrared wavelengths. This makes for an improved visualization of the deeper pathological structures. Either can be used to document small vessels, such as capillaries, and improved imaging is obtained by the contrast-enhancing features of SLO imaging. Autofluorescence techniques, including the detection of intrinsic fluorescence such as the waste product liposfuscin, are also used to diagnose retinal degenerations.

Several types of solid-state lasers have become commonplace for both imaging and treatment, varying in wavelength, temporal properties such as pulse rate and duration, and beam configuration, but price is always a consideration [5, 78–81]. The ready modulation of beam power and position makes possible structured illumination. Of particular interest in recent years have been lasers with long coherence lengths such as superluminescent, supercontinuum, or vertical cavity surface emitting lasers, which help to reduce speckle noise. Also, swept sources are being developed at more affordable costs, which provide a wide range of frequency information without the expense of additional modulation or detection schemes that analyze frequency [5]. Illumination sources are not limited to lasers, with light emitting diodes (LED), liquid crystal, digital light projectors, and other solid-state sources serving as illumination sources for imaging, visual stimulus generation, visual aid or assistive devices, and treatment devices. The light safety limits for the human eye are highly regulated, with the ANSI standards the most commonly used in the US [82]. Short-wavelength light is considered particularly damaging, having both thermal and photochemical damage mechanisms.

A wide variety of image processing techniques have enhanced optical measurements. A key example is the improvement of the quantification of the parameters of the clear, curved cornea (Fig. 12.14) [83]. By processing changes over time, often called 4D imaging, elements such as blood flow are obtained from both AOSLO and SDOCT, mapping velocities and locations of the smallest vessels in the living eye.

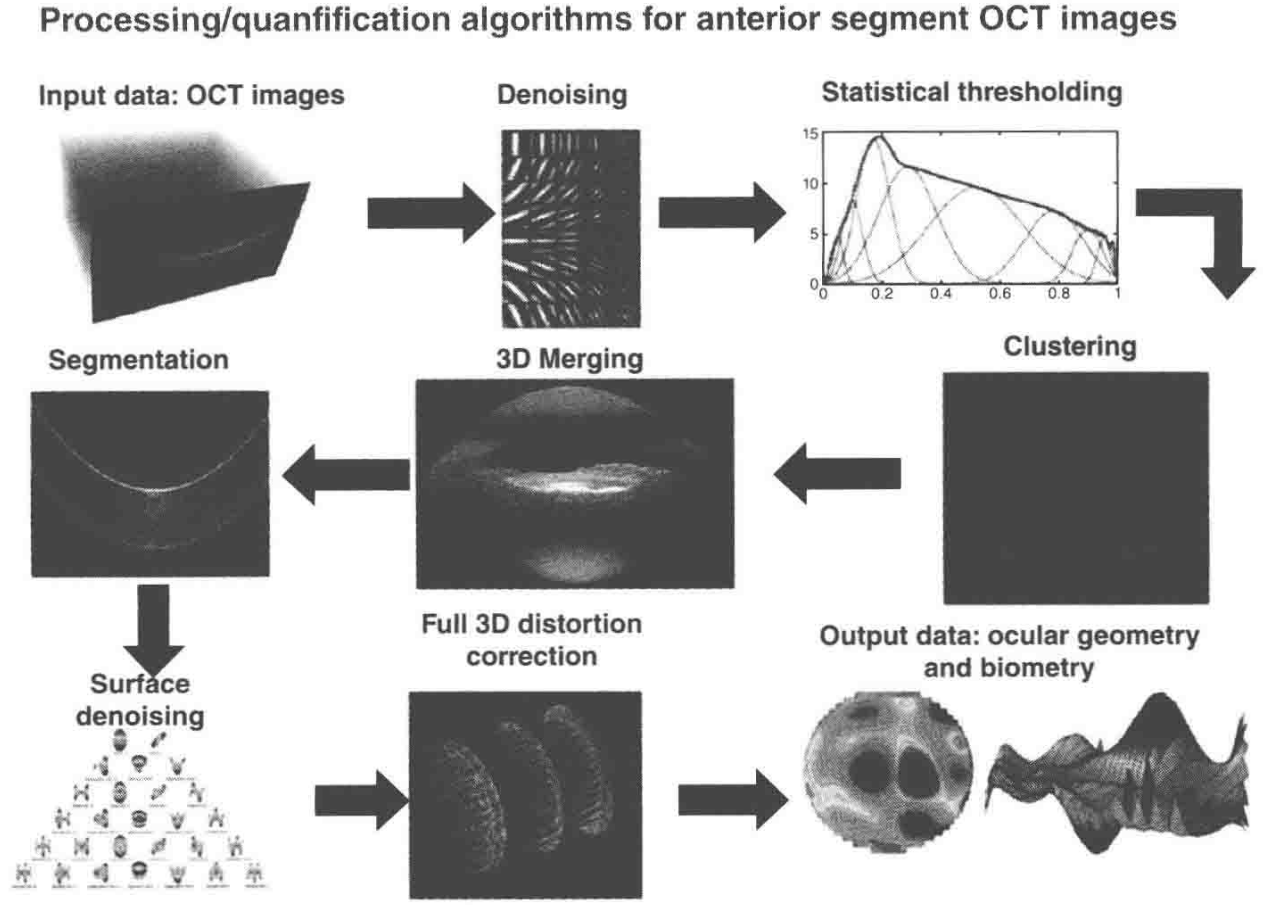
Processing/quanfification algorithms for anterior segment OCT images
Input data: OCT images
Denoising
Statistical thresholding
15
10
5
0
0
0.2
0.4
0.6
0.8
1
Clustering
3D Merging
Segmentation
Surface denoising
Full 3D distortion correction
Output data: ocular geometry and biometry

FIGURE 12.14 Image processing steps to obtain quantitative full 3D geometry of the anterior segment of the eye from OCT images. Image courtesty of Sergio Ortiz and Susana Marcos, Instituto de Optica (CSIC), Madrid, Spain. (*For a color version of this figure, see the color plate section.*)

12.3 ANTERIOR SEGMENT DIAGNOSTICS, REFRACTIVE MEASUREMENTS, AND TREATMENT

12.3.1 Cornea and Tear Film

The importance of photonics in the anterior portion of the eye can largely be divided into two categories which are imaging to detect disease and the use of lasers for treatment of diseases/disorders [84, 85]. As previously stated, the tear film is composed of three components, which are essentially oil, water, and mucin of which a failure in any component will result in problems for the entire tear film stability. This results in a variety of manifestations of dry eye that are characterized by decreased vision and eye irritation which in some forms such as Sjogren's syndrome, an auto-inflammatory disease, can be crippling. These three components are produced in different areas of the eye. The oil layer is largely produced in glands on the back side of the eye lid. Infrared light, usually in the form a scanning laser, can be used to image these glands to determine whether the glands are functioning. Two examples (Fig. 12.15) of normal Meibomian glands on the left and truncated glands on the right. Infrared is required for greater penetration as the glands themselves are imbedded in tissue that is highly scattering [86]. The oil layer itself, as it generally sits on top of the other layers, offers

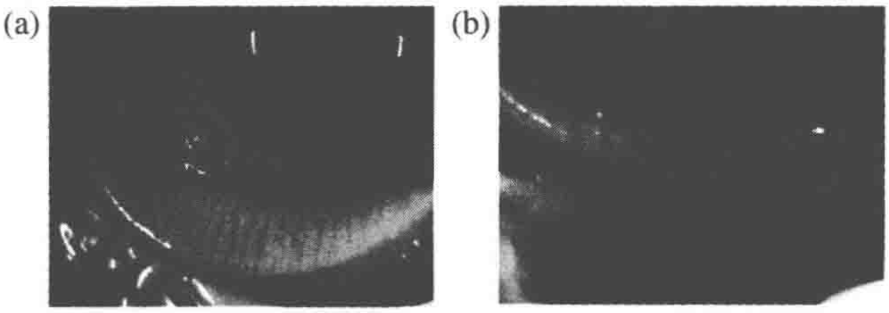

FIGURE 12.15 Infrared meibomography using a laser scanning camera comparing two eyes. (a) Lower lid of a normal subject showing normal meibomian gland that produce oil/lipid for the tear film. Notice the white glands extend the entire length of the lower eye lid. (b) Lower lid of a dry eye subject showing truncated and poorly functioning glands. Notice that the glands do not extend the full length of the lid. Image courtesy of Donald R Korb (Tear Sciences, Boston, MA).

a unique opportunity to use interference to measure the oil layer thickness. Either using a broad beam source to examine chromatic interference patterns, or by using multiple different wavelengths, an estimate of the oil layer can be made.

Fluorescent dye and excitatory light can also be used to examine the tear film [84]. The most common type of dye used for this is fluorescein which is easily dissolved in water (or tears) and excites between about 490 nm and 520 nm. After instillation, a cobalt filter is used to excite the dye, and then images are taken. As the tear film destabilizes, large black areas begin to form that show areas of decreased tear film thickness. This can be seen in Figure 12.16 with the green areas marking normal tear film and the black spots marking thinned or absent tear film. Long-term tear film instability and other things like bacterial infections can damage the corneal epithelium. By using these same dyes, damage can also be tracked to the cornea which can include a complete break in the epithelium resulting in dye being visible within the cornea stroma.

The primary clinic method of examining the cornea, as well as virtually any other structure that is visible in the eye, is through the use of slit lamp microscopes. It can be thought of primarily as a two channel system, with the first channel being a standard binocular microscope that allows for exchange of lenses to change magnification and allow for viewing of other structures such as the retina. The second channel is the light channel which allows the beam to be adjusted from a slit to a flood source and allows for insertion of filters such as cobalt and red free filters. With this flexible system, most parts of the eye can be imaged. The normal cornea (Fig. 12.17a) is clear and reflects light in a uniform pattern, while a cornea with inflammation and unwanted new blood vessels scatters light diffusely (Fig. 12.17b).

The cornea curvature is also important to know as it is the primary source of focusing power for the eye, with a curvature of approximately 8.4 mm (40 diopters) [87]. This curvature, often referred to as corneal topography, is important for detecting astigmatism, monitoring for diseases of the cornea that cause irregular optics and for guiding treatment strategies such as refractive surgery. The most common method for determining corneal curvature is through the use of placido systems. In a

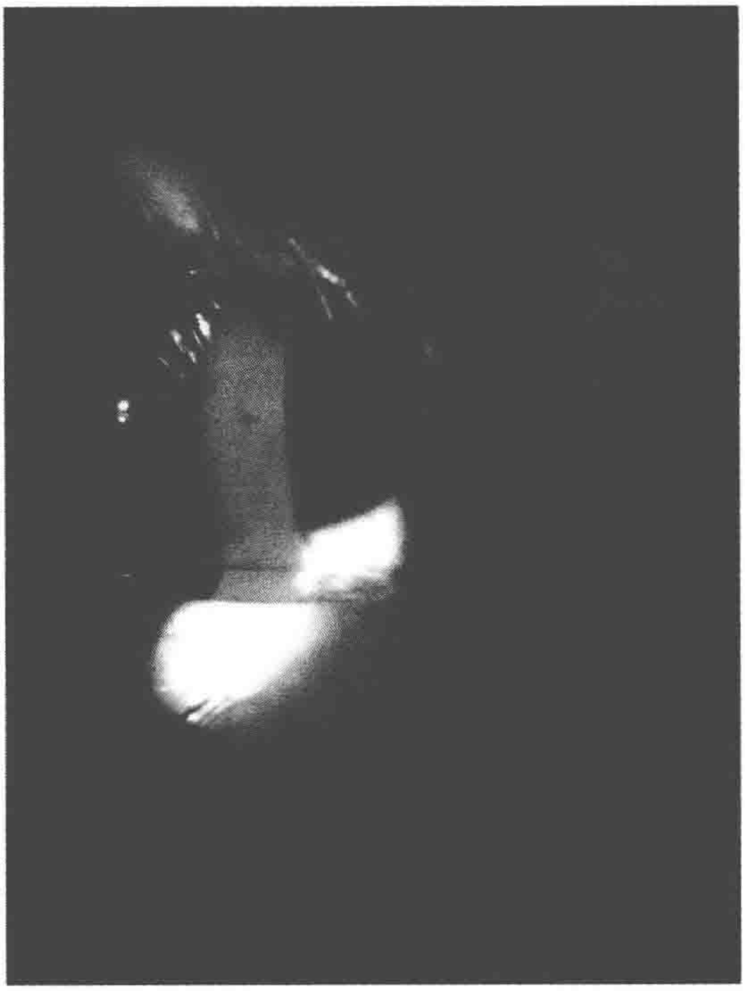

FIGURE 12.16 Fluorescein dye used to measure tear film stability and breakup time. Dark patches within the brighter slit area represent areas of no or little tear film. The green fluorescent dye is being excited by a cobalt filter. Image courtesy of Todd Peabody (Indiana University, Bloomington, IN). (*For a color version of this figure, see the color plate section.*)

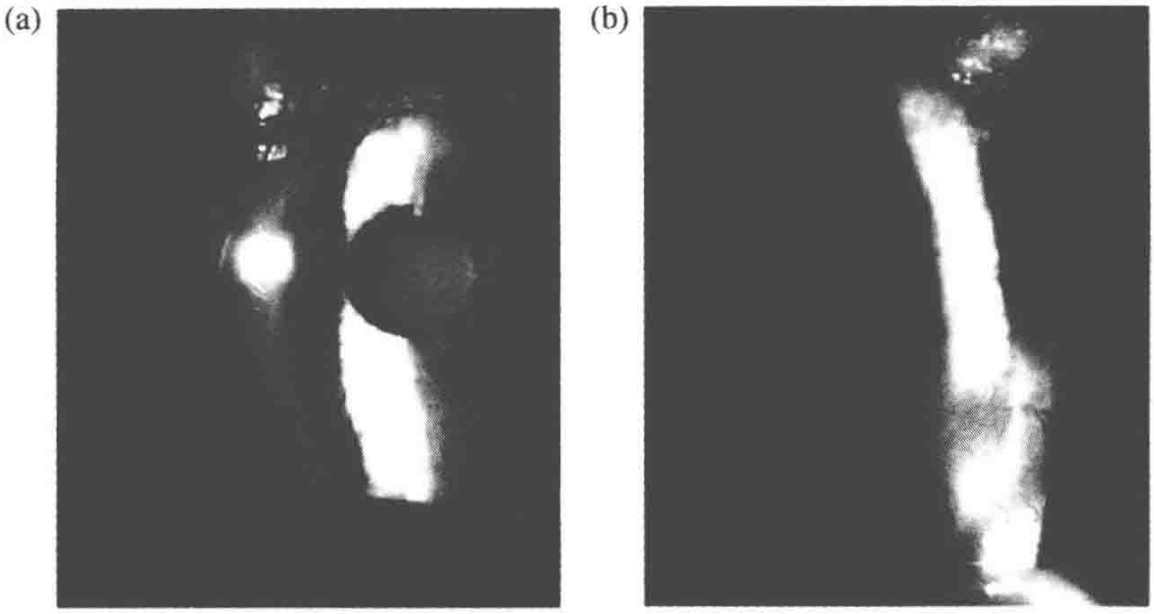

FIGURE 12.17 Slit lamp biomicroscope imaging of the anterior eye. (a) Normal eye showing illumination of the cornea, iris, and lens. The cornea is the slightly hazy slit to the left. Within the pupil, one can see part of the lens as it scatters light back at the microscope. (b) New unwanted blood vessel growth onto the cornea due to excessive wearing of a contact lens. The slit beam is illuminating the blood vessels. Image courtesy of Todd Peabody (Indiana University, Bloomington, IN). (*For a color version of this figure, see the color plate section.*)

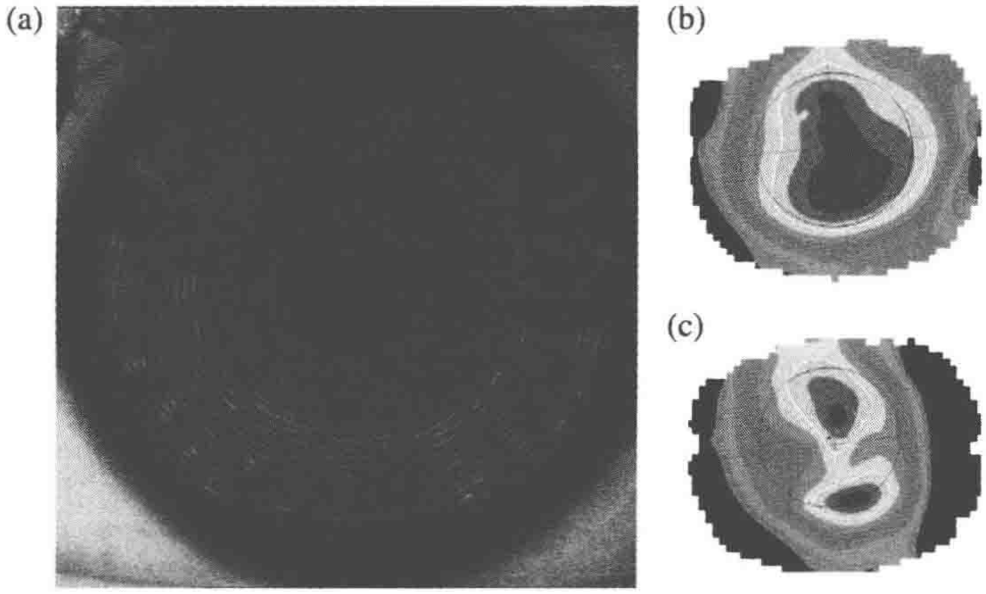

FIGURE 12.18 Corneal topography of normal and astigmatic eyes. (a) Infrared image capture of the cornea with illuminated placido ring reflecting on the cornea. (b) Topographic map created from data collected in (a). This is a normal cornea exhibiting a spherical shape. Red colors represent more corneal curvature and blue colors represent less curvature. Normal corneas begin steeper centrally and flatten farther from the center. (c) Astigmatic corneal topography showing a traditional bow tie pattern. Note that the redder colors representing more curvature are oriented vertically while the flatter areas are horizontal (Medmont Topographer, Medmont, Rousehill, Australia). (*For a color version of this figure, see the color plate section.*)

placido-based system, a known pattern of light, typically in the form of rings, is projected onto the cornea as seen in Figure 12.18a. An image is then captured and the distance between points between the rings gives a measure of localized curvature. These points are then combined into a topographic map of the cornea curvatures. Normal spherical corneas display a symmetric curvature that is steeper centrally and flattens peripherally (Fig. 12.18b). Conversely, corneas with astigmatism display steepening in one meridian as opposed to the other (Fig. 12.18c). Inherently, better systems place greater numbers of rings on the cornea which then increases the resolution. One drawback to this is that if two rings intersect or cross one another, a failure to detect the curvature will occur. Also, as in virtually every use of photonics in the eye, dry eye, caused by poor tear film, will decrease the accuracy of the system.

The Scheimpflug principle can also be used to measure the corneal topography [85]. The principle is a geometric optics rule that measures the image plane while the optical system is off axis. In this system, a light is shown off axis at a known angle and swept across the cornea. Using the known angle and the cornea's position in the light beam, the curvature of the anterior cornea can be calculated. In addition, this method can also provide the thickness of the cornea, the posterior curvature of the cornea, and the anterior chamber depth. While Scheimpflug-based systems provide more information than placido-based systems, they tend to be less accurate than placido systems as eye movement can badly distort the data in addition to also having problems with dry eye. OCT is becoming more frequently used to image the anterior segment including the cornea (Figs. 12.2, 12.14, and 12.19). This is largely due to the

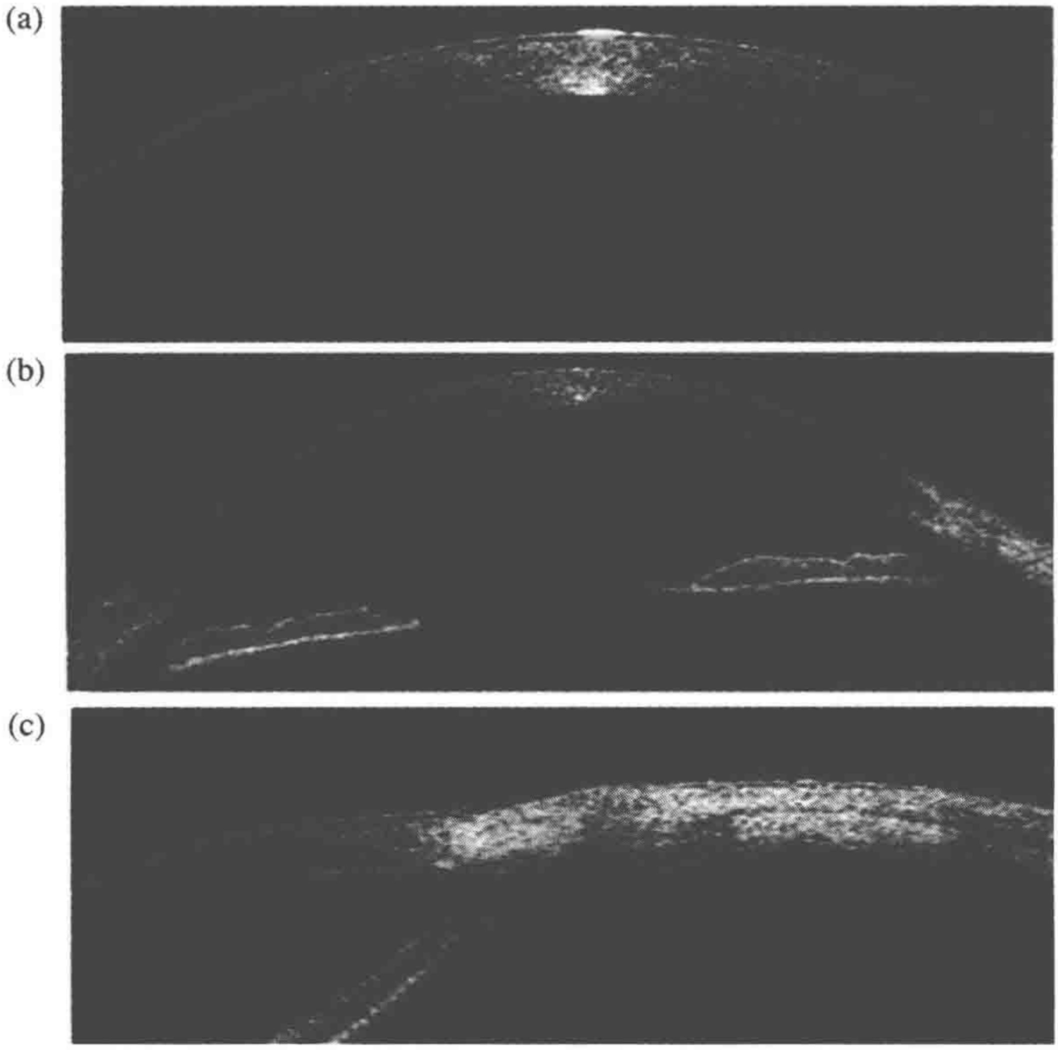

FIGURE 12.19 Anterior segment optical coherence tomography (OCT) showing the cornea, anterior chamber, iris, and ciliary body. (a) Close up of the cornea in a normal eye for measuring corneal thickness. (b) Anterior segment OCT for measuring anterior chamber depth. (c) Ciliary body imaging. Image courtesy of Peter Kolbaum and Meredith Jansen (Indiana University, Bloomington, IN), using a Visante (Zeiss, Jena, Germany).

fact that OCT has higher resolution than other topography systems. Typical systems use near-infrared light to allow for greater penetration into the sample. By using interference fringes reflecting off the layers of the cornea, curvature and thickness can be measured. One drawback with OCT at the present time is the lack of a wide field of view in comparison to reflective light systems like placido-based systems.

12.3.2 Anterior Chamber, Ciliary Body, and Lens

Photonic methods of measuring the anterior chamber, ciliary body, and lens are largely dependent upon the slit lamp microsope, OCT [88–90] (Fig. 12.19), and Scheimpflug cameras. This is largely due to the fact that objects being examined are either clear/fluid filled which means they neither reflect nor scatter light or they are obscured by the iris which prevents penetration by many methods. These structures have a high level of interest as conditions such as cataracts and glaucoma are influenced by them.

The anterior chamber depth or size influences the pressure of the eye. As the anterior chamber gets smaller, it increases aqueous outflow resistance which causes the eye's pressure to go up and increase the risk for glaucoma. This is largely due to the fact that the aqueous humor that is produced by the ciliary body leaves the eye at the intersection of the cornea and iris known as the angle. OCT and Scheimplug, using the same principles previously talked about, are excellent at measuring this depth. It is especially important as the anterior chamber decreases in depth throughout a person's life, largely due to the fact that the lens continues to grow and take the space.

12.3.3 Refraction

As previously stated, refractive error, which can be thought of a defocus, happens when the axial length of the eye mismatches with the cornea and lens focal point. To measure refractive error, an enormous number of techniques have been developed that all require light in some form. The most commonly used systems today are auto-refractors and Hartmann–Shack aberrometers, which both employ infrared light to not induce pupil changes and accommodation.

Auto-refractors function essentially by taking a paraxial light beam approximately 1 mm in size and projecting it into the center of the pupil. A focusing system then is used to minimize the returning point spread function. Due to the narrowness of the beam, an auto-refractor only measures the refractive error within a small area of the pupil. Aberrometers (Figs. 12.11 and 12.20) focus a small point of light onto the retina and then measure the returning light across the pupil to determine the refractive error. Both systems can be confounded by the eye's innate focusing system, that is, accommodation. Auto-refraction is largely useful for most measures of refraction in the eye, as defocus and astigmatism account for nearly 90% of the total aberrations in the eye. Aberrometry becomes important largely to drive some surgical refractive lasers, control adaptive optics systems, and perform research.

Axial length measures have become important largely in the cataract field as the measurement is critical to inserting the correct lens into the eye following cataract lens extraction. Recent optical methods such as partial coherence interferometry

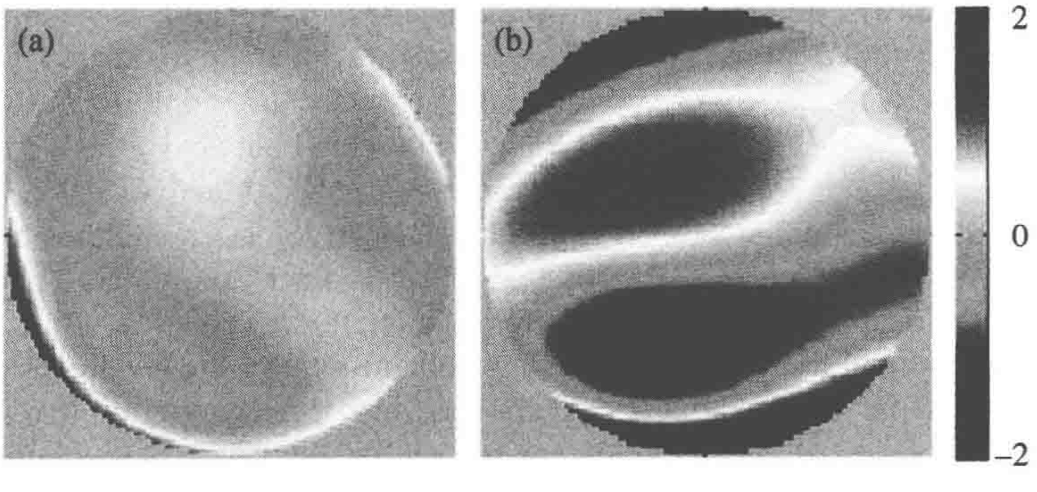

FIGURE 12.20 Wavefront across the pupil of two human subjects. (a) Normal wavefront showing little variability across the pupil represented by a uniform color across the image. (b) Subject with keratoconus, showing high levels of aberrations across the pupil represented by large color swings across the pupil. *(For a color version of this figure, see the color plate section.)*

(PCI) have allowed for accurate measures of the axial length of the eye which has a high level of variability (average length = 23.5 mm). An error of only 0.30 mm would mean the difference between being legal as opposed to not legal to drive without glasses in most states. PCI, similar to OCT, uses interference reflections to determine lengths or depths.

12.3.4 Light and Treatment of Anterior Segment Diseases

The uses of light in the anterior eye are generally limited to the use of lasers with one exception. In all cases, they are used to remove tissue in one form or another. One of the more commonly used lasers is the frequency-doubling Nd:YAG laser, wavelength 532 nm. The frequency-doubling aspect offers a high degree of precision in the axial direction that is very useful for surgery; specifically the axial resolution limits unwanted damage to tissue behind or in front of the spot of surgery. It is primarily used for two purposes in the anterior eye, the first being the removal of unwanted growth tissue following cataract surgery. Post cataract surgery, cell ingrowth along the back side of the new lens can obscure vision resulting in what is commonly called posterior capsular opacification [85]. The second use of Nd:YAG lasers in the anterior eye is to create holes in the iris to allow for fluid flow. In some situations, highly correlated with shallow anterior chamber depth, the iris and lens together can prevent aqueous humor from flowing into the anterior chamber and out of the eye. As the production of this fluid does not decrease in response to the blockage, pressure can build to danger levels that would blind a person in a few days. This is generally accompanied with a great deal of pain and is called angle closure glaucoma. Laser can become useful in this situation by creating new holes in the iris to relieve the pressure and allow for normal fluid flow in the eye.

Angle closure glaucoma is relatively rare compared to primary open angle glaucoma which has a much higher prevalence. Primary open angle glaucoma employs two lasers, often in coordination with drug treatment. The angle itself, as people ages, increases outflow resistance and thereby increases pressure within the eye. These two lasers target this as a treatment mechanism. The first of these lasers is the argon laser trabeculoplasty (ALT). It uses heat damage aimed at the angle to create scar tissue. This scar tissue contracts, as all scars do, and thereby decreases outflow resistance by pulling tissue wider. The second laser treatment method employs a laser that relies less on thermal damage, and is called selective laser trabeculoplasty (SLT). The laser wavelength is typically longer than that found in an Argon laser, and the parameters of delivery such as the energy density and pulse or other timing parameters, have been selected to make pigment cells within the angle die. This leads to a cascade employing normal biological housekeeping cells to remove the dead cells and any unwanted material within the angle, again reducing decreasing outflow resistance. Due to the necessity of targeting pigment cells, individuals with more pigment tend to have better treatment than those with low pigment.

The most common use of lasers in the eye, regardless of anterior or posterior, is to correct refractive error [91]. There are a number of different methods to start the procedure such as Laser-Assisted *in situ* Keratomileusis (LASIK), Laser Epithelial

Keratomileusis (LASEK), and Photorefractive Keratectomy (PRK), but they all generally use an excimer laser to remove tissue from the corneal stroma. The underlying principle of this is to reshape the curvature of the cornea to optimally focus the image on the retina. As the laser can only remove tissue, that is, it cannot put on tissue, it is optimally suited for correcting refractive error resulting from too much power in the eye. In simple terms, it is better at treating refractive error where the image is focused in front of the retina like in myopia/nearsightedness. All these procedures require close attention to curvature and thickness of the cornea.

Recently, ultra short pulse lasers have become popular in eye care as they offer unique advantages of other lasers and surgical techniques. Historically, refractive surgery procedures such as LASIK used a surgical blade to cut a flap in the cornea to retain the epithelium. This allowed for quicker and less painful recovery. However, the speed of the blade, the movement of the patient's eye, and potential mechanical errors can cause surgical complications. The use of femtosecond lasers has reduced these complications, though visual outcomes remain similar. A new procedure, in which a gap is made rather than a mechanical or laser-induced cut, provides improved retention or regrowth of corneal nerves, as seen with corneal microscopy [92].

Similar to LASIK, these lasers are beginning to be employed in cataract lens extraction. An incision is made to gain access to the lens to cut or break up the material for removal. The clear corneal incision made by a femtosecond laser, rather than by a microtome, may provide less gaping of the wound or misalignment of layers [93] For most of the recent past, ultrasound has been used in eyes with clouded lenses to break up the lens and then remove it safely. However, the length of time the ultrasound was used increased the complications. Femtosecond lasers are now being used to break apart the lens more efficiently, thereby decreasing complications. The procedure is relatively new, and therefore whether the improvement is made on a variety of outcome measures is not yet determined. For instance, when the retina is examined using SD-OCT after femtosecond cataract surgery, there was no improvement in the amount of edema induced by the surgery [94].

The only non-laser treatment currently used in the eye is used to strengthen the cornea (cross-linking) [95]. A number of diseases such as keratoconus, which is a weakened collagen fibrils resulting in a distorted cornea, need treatments to strengthen the cornea, thereby providing stable vision. To do this, a riboflavin solution is placed on the cornea after having the epithelium removed. Following that, UV-A light illuminates the cornea and solution for approximately 30 minutes. The result causes the collagen fibrils to cross-link with one another, and strengthening the cornea.

12.4 DIAGNOSTIC APPLICATIONS AND TREATMENT OF POSTERIOR SEGMENT

12.4.1 Imaging Applications

As described above, the field of diagnostic imaging is benefitting from novel light source and novel detection schemes that enhance the detection of the weak signals that return from the interior of the eye. The status of the retinal nerve fiber layer,

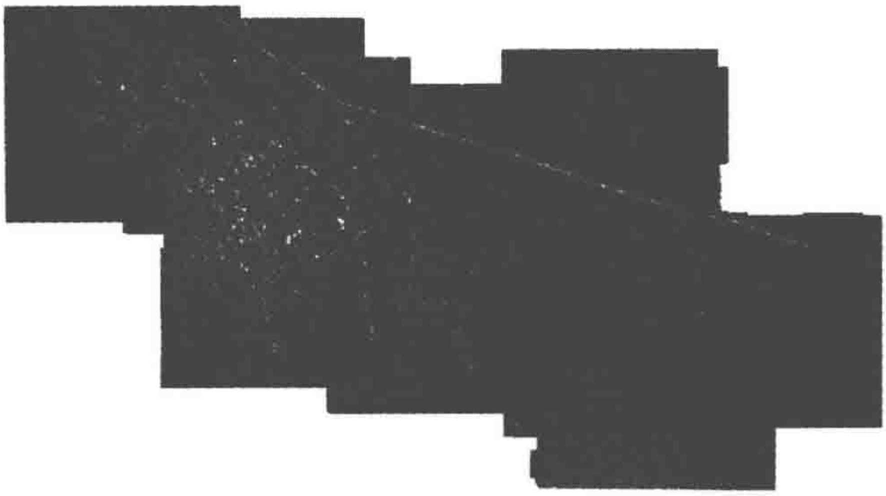

FIGURE 12.21 AOSLO-montaged nerve fiber bundles and blood vessels. Nerve fiber layer is observable as white streaks across the image. Image courtesy of Stephen Burns (Indiana University, Bloomington, IN).

the key target of glaucoma detection but also damaged by diabetic retinopathy, is accessible with AOSLO (Fig. 12.21), SDOCT (Fig. 12.22), and AOOCT.

The status of the smallest blood vessels in the human retina, the capillaries, are readily seen with AOSLO (Fig. 12.23), including the foveal avascular zone, and AOOCT. The damage within layers by diabetes is readily seen (Fig. 12.22, right), even if it is too subtle to cause distortion of the layers that result in measurably increased retinal thickening. The capillaries that form outpouchings, the microaneuryms that are one of the hallmarks of diabetic retinopathy, are visualized both by reflectance imaging and by the variance mapping that uses the change in reflectivity over time

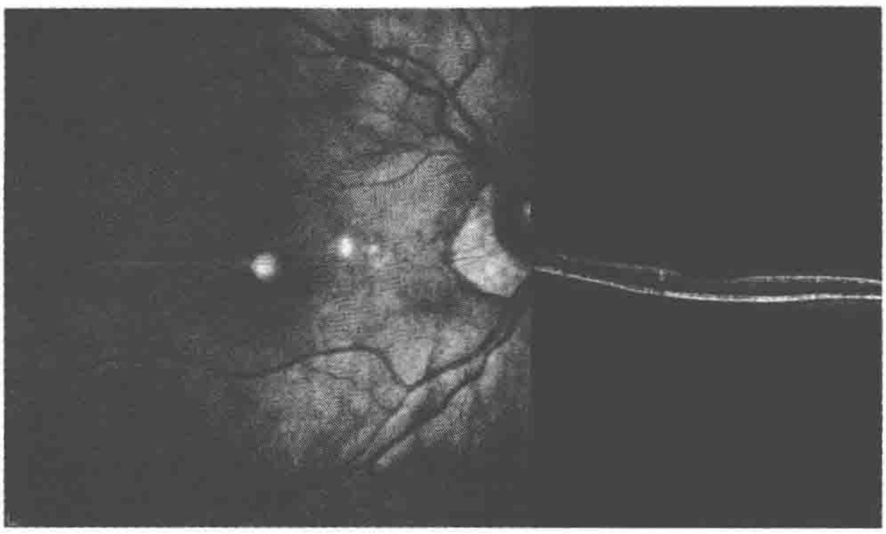

FIGURE 12.22 Near-infrared SLO and en face SD-OCT images of a diabetic eye. Left: En face image of the retina. Although there is a central lens reflection, the other reflective, whitish spots represent focal lesions, due to diabetic retinopathy. Right: Localized area of edema corresponding to the reflectivity changes in the left image, distorting the layers of the retina and with some lesions appearing as holes. As these areas are fluid filled, the scatter reduces the change of coherence, and the decreased signal amplitude at these locations makes them appear black, although they are not actually holes. The normal blood vessels in the choroid beneath the retina also appear dark, due to the local scatter.

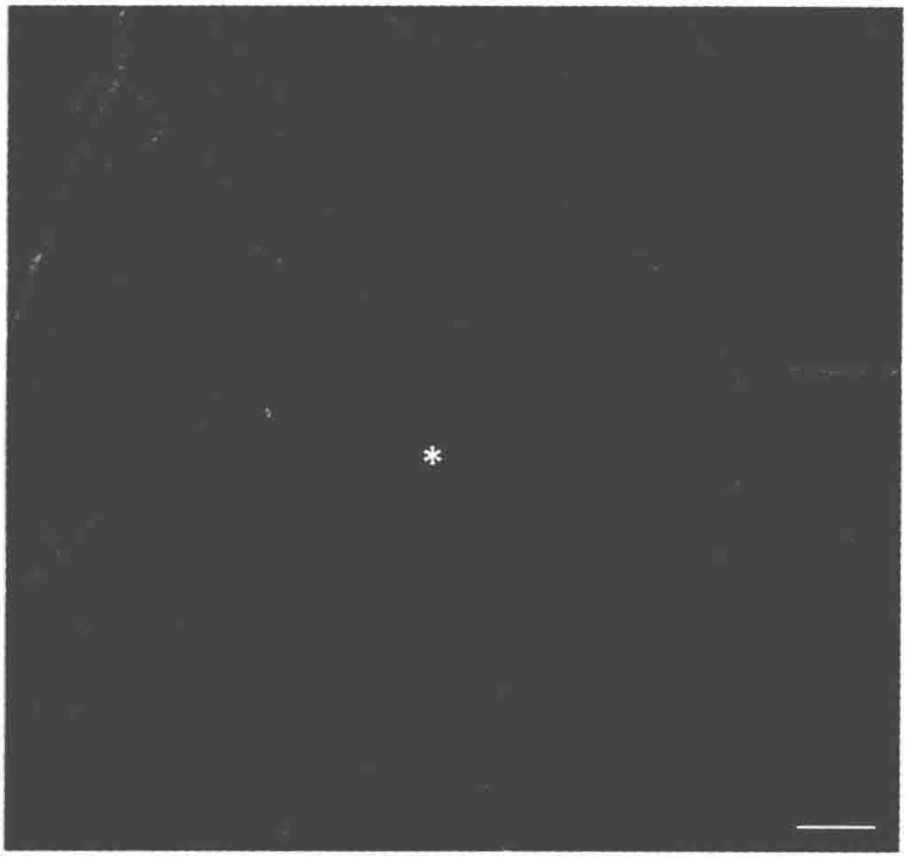

FIGURE 12.23 A 3×3° map of the standard error of the gray scale over time at each pixel, showing the complete foveal microvascular network in a 54-year-old male (right eye). Asterisk indicates the foveola. Scale bar = 100 μm. Image courtesy of Stephen Burns and Toco P Chui (Indiana University, Bloomington, IN).

to map perfusion (Fig. 12.24) [96–101]. Structures within retinal vessels, such as the lumen, are also visualized in the living human eye (Fig. 12.25).

The structure of the retinal capillaries can now be mapped over using *in vivo* techniques over a wide enough retinal area to pinpoint ischemia, with both AOSLO and OCT techniques. The technical advancement that underlies the AOSLO capillary method is using slightly offset confocal apertures to enhance the signal from scattered light rather than directly backscattered light [101]. When retinal images are collected serially, and the change over time is analyzed, clear-cut capillary images are obtained. For OCT techniques, one of the important advancements is the increase in speed of image acquisition, to allow for scans to be collected in a dense enough pattern to allow comparison of neighboring retinal locations. The use of SD-OCT is one method, but swept source OCT (SS-OCT) has achieved even higher acquisition speeds by use of a high speed analog to digital converter [102].

The high image acquisition rates with SD-OCT, and even ones with SS-OCT, allow trade-offs of the digital resolution, that is, more pixels, and the bit depth, that is, more dynamic range at each pixel. This has increased diagnostic efficiency, along with the use of novel sources like swept source lasers based on Vertical Cavity Surface Emitting Lasers (VCSEL) and optics to image deeper vascular pathologies, as well as the anterior segment and posterior segments in one device [103–107]. Another aspect of increased speed is the potential for improved computations, such

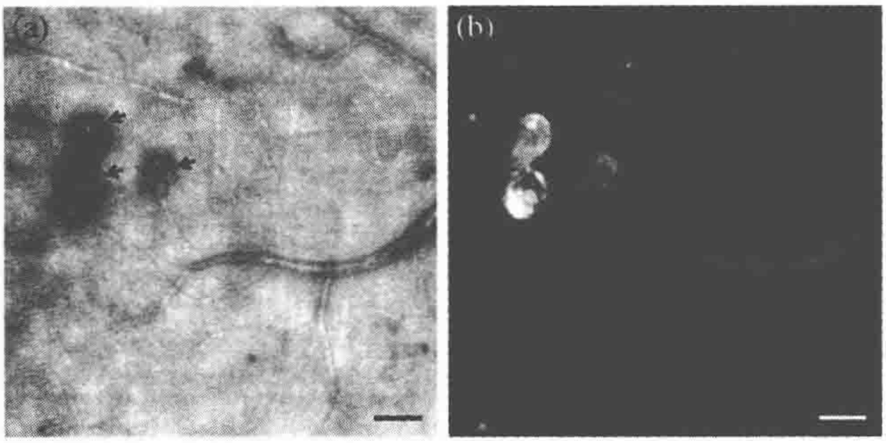

FIGURE 12.24 AOSLO image of diabetic retinopathy. (a) AOSLO reflectance image in a 49-year-old diabetic patient with moderate diabetic retinopathy, showing microaneurysms (black arrows) of varying sizes. Black arrows indicate microaneurysms. (b) The corresponding perfusion map for the location in (a), derived from measuring the standard error of the gray scale over time, rather than averaging the data as in (a). Scale bars = 50. Image courtesy of Stephen Burns and Toco P Chui (Indiana University, Bloomington, IN).

as using the phase information to obtain blood flow or improving the computations of polarization-sensitive OCT (PS-OCT).

The interpretation of the results from advanced imaging, often showing structures never before visualized *in vivo*, continues to evolve [99, 101, 103]. Clinicopathological comparisons, along with animal models and multi-modality imaging studies, provide methods for interpreting the new imaging modality results [108–110].

The advanced imaging methods do have cost considerations. Efforts are underway to reduce both the cost of the SLO, making a hybrid imaging device, the Laser Scanning Digital Camera [41], and the cost of AO-OCT (Fig. 12.26). One key goal

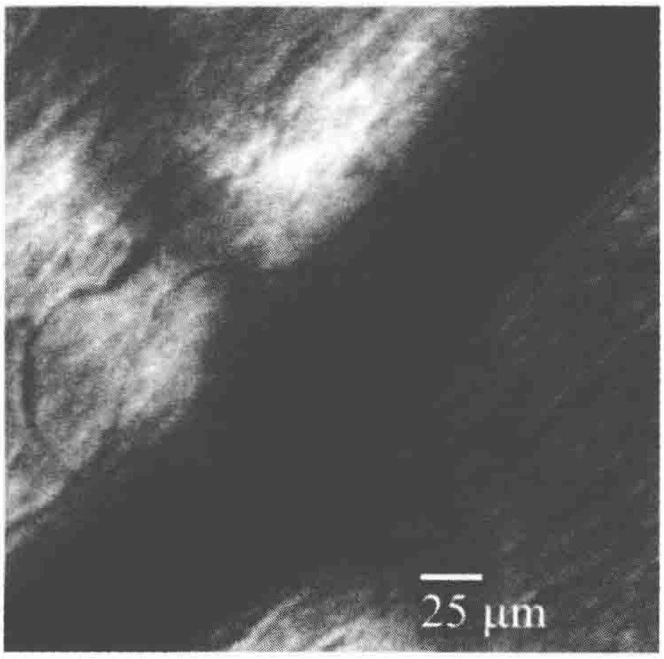

FIGURE 12.25 Adaptive optics image of the retinal vasculature. Artery imaged using AOSLO, resolving the blood vessel walls and interior of the vessel. Image courtesy of Stephen Burns and Toco P Chui (Indiana University, Bloomington, IN).

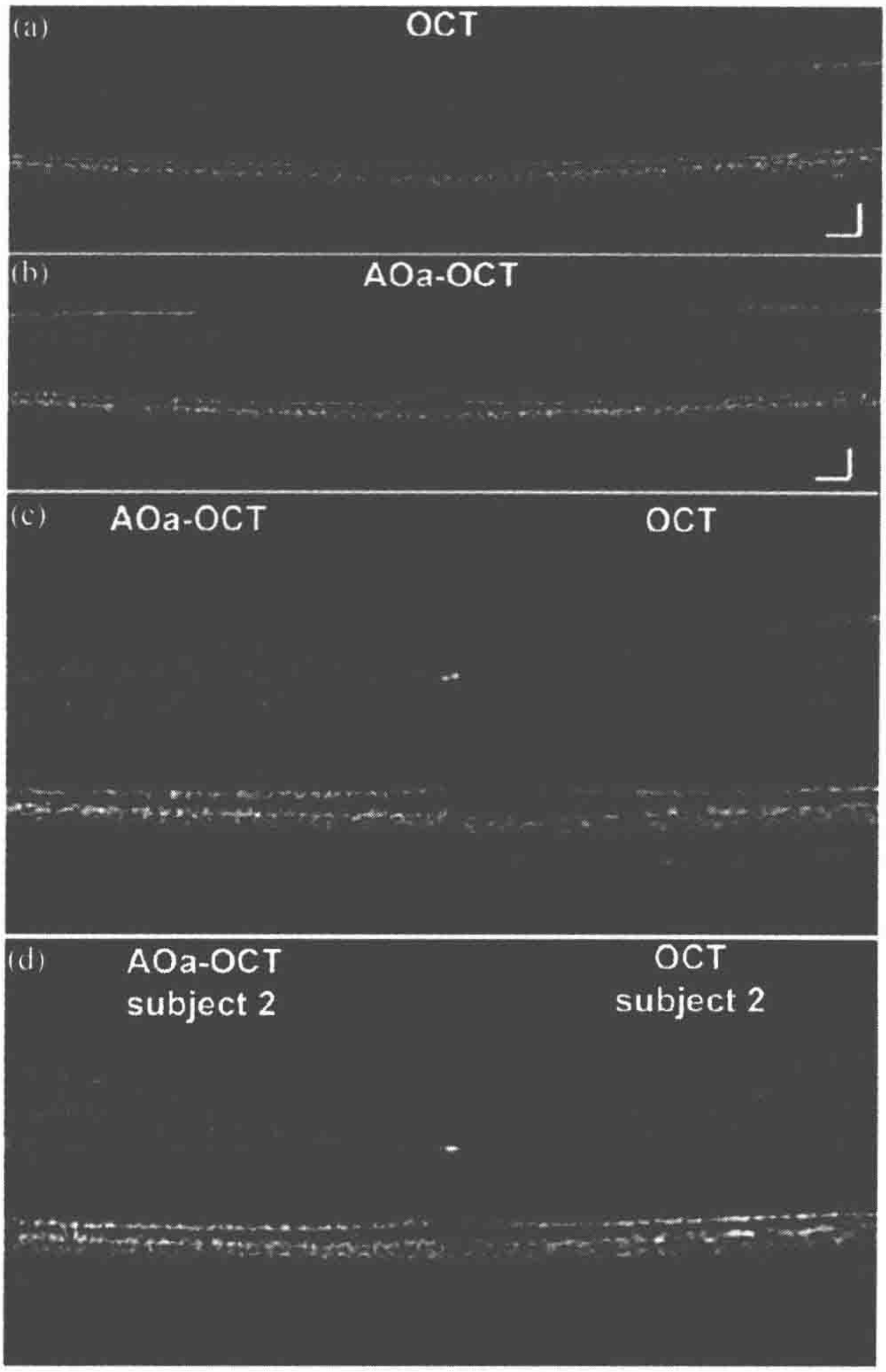

FIGURE 12.26 Adaptive optics assisted optical coherence tomography (AOa-OCT). 9° long OCT B-scans acquired horizontally, comparing two conditions for imaging the central fovea of the same human subject. The images contain single data sets and no averaging was applied. (a) Standard OCT image obtained with a 1.2 mm beam diameter (1/e^2). For the standard OCT image, defocus was corrected with a Badal optometer. The subject's refractive error with an autorefractor was −2.5D sphere, −1.25D cylinder at 1° axis. (b) Adaptive optics assisted optical coherence tomography (AOa-OCT) image obtained with a 3.4 mm beam diameter (1/e^2). The AOa-OCT system used adaptive optics to achieve diffraction-limited performance. Each B-scan measures 1000 A-scans, and the data acquisition rate was 48,000 A-scans per second. The white bars indicate lengths of 100 μm in tissue. Data were gray scale-encoded over 38 dB above the noise floor. (c) The central part of (a) and (b) magnified, showing a 2.75 times smaller speckle size and higher reflectivity for the AOa-OCT data. (d) Data of a second subject (autorefractor: −0.50 sphere; −0.50 cylinder at 180°) demonstrating similar differences between the two modalities. Image courtesy of Barry Cense and Kenta Sudo (Utsunomiya University) and Kazuhiro Kurokawa and Yoshiaki Yasuno (Computational Optics Group, University of Tsukuba), Japan.

is to bring the cost of the entire process of diagnostics to a sufficiently low level that all individuals receive screening for key eye diseases, such as diabetic retinopathy [111]. At present, one of the barriers to eye care that would prevent sight-threatening disorders is cost.

The measurement of visual function continues to be a part of ophthalmic technologies, not only for diagnosis of disease, but also for assessing function such as in visual rehabilitation. Using imaging with an SLO or other fundus imaging device provides the potential for more accurate mapping of retinal sensitivity, either by providing simultaneous imaging of the retina or improvement of the generation and delivery of the stimulus so that all the light enters the pupil [112–120]. Although lasers *per se* were used previously in these devices, a range of stimulation devices, such as liquid crystal monitors and digital light projectors, can be combined with the fundus imaging device. By uncoupling the spatial resolution of the fundus imager and the display device, a much wide range of colors and temporal patterns is obtained, which are needed to probe the visual system. There has been increased interest in the optical measurement of neural responses, and the interpretation of these may provide an objective means of assessing retinal function.

Phototherapy has been used almost since the invention of the laser [121]. Treatment of the retina for the uncontrolled growth of new blood vessels is a chief reason to use photocoagulation. While originally the photocoagulation was performed without enhancers, now a range of absorbing and molecules with biological strategies are used to enhance the treatment. In addition, surgical procedures to secure detached tissue are performed with lasers. The performance now is directed toward targeting specific tissues, either by more accurate localization across the retina or by altering the structure of a limited number of layers.

REFERENCES

[1] A. Tasman and E. A. Jaeger, *Duane's Foundations of Clinical Ophthalmology* (J.B. Lippincott, 1991).

[2] C. W. Oyster, *The Human Eye: Structure and Function* (Sinaurer Associates, Sunderland, MA, 1999).

[3] J. E. Dowling, *The Retina: An Approachable Part of the Brain* (Harvard University Press, Cambridge, 1987).

[4] AE Elsner, in *Handbook of Adaptive Optics*, edited by J. Porter, H. Queener, J. Lin, K. Thorn, and A. Awwal (John Wiley & Sons, New York, 2006), pp. 205–234.

[5] A. E. Elsner and M. S. Muller, "Laser applications and system considerations in ocular imaging,"*Laser Photon Rev.* **2**(5),350–376 (2008).

[6] B. Winn, D. Whitaker, D. B. Elliot, and N. J. Phillips, "Factors affecting light-adapted pupil size in normal human subjects," *Invest. Ophthalmol. Vis. Sci.* **35**(3),1132–1137 (1994).

[7] Y. Yang, K. Thompson and S. A. Burns, "Pupil location under mesopic, photopic, and pharmacologically dilated conditions," *Invest. Ophthalmol Vis. Sci.* **43**(7), 2508–2512 (2002).

[8] J. C. He, S. Marcos, R. H. Webb and S. A. Burns, "Measurement of the wave-front aberration of the eye by a fast psychophysical procedure," *J. Opt. Soc. Am. A. Opt. Image Sci. Vis.* **15**(9), 2449–2456 (1998).

[9] J. C. He, S. A. Burns, and S. Marcos, "Monochromatic aberrations in the accommodated human eye," *Vision. Res.* **40**(1), 41–48 (2000).

[10] E. J. Sarver, J. Schwiegerling, and R. A. Applegate, "Extracting wavefront error from Shack-Hartmann images using spatial demodulation," *J. Refract. Surg.* **22**(9), 949–953 (2006).

[11] L. N. Thibos, R. A. Applegate, J. T. Schwiegerling, and R. Webb, "Standards for reporting the optical aberrations of eyes," *J. Refract. Surg.* **18**(5), S652–S660 (2002).

[12] J. S. McLellan, S. Marcos, and S. A. Burns, "Age-related changes in monochromatic wave aberrations of the humage eye," *Invest. Ophthalmol. Vis. Sci.* **42**(6), 1390–1395 (2001).

[13] S. A. Burns, S. Wu, F. Delori, and A. E. Elsner, "Direct measurement of human-cone-photoreceptor alignment," *J. Opt. Soc. Am. A. Opt. Image Sci. Vis.* **12**(10), 2329–2338 (1995).

[14] A. E. Elsner, S. A. Burns, L. A. Lobes Jr., and B. H. Doft, "Cone photopigment bleaching abnormalities in diabetes," *Invest. Ophthalmol. Vis. Sci.* **28**(4), 718–724 (1987).

[15] S. A. Burns, S. Wu, J. He, and A. E. Elsner, "Variations in photoreceptor directionally across the central retina," *J. Opt. Soc. Am. A. Opt. Image Sci. Vis.* **14**(9), 2033–2040 (1997).

[16] Centers for Disease Control and Prevention. *National Diabetes Fact Sheet: National Estimates and General Information on Diabetes and Prediabetes in the United States, 2011* (U.S. Department of Health and Human Services, Centers for Disease Control and Prevention, Atlanta, GA, 2011).

[17] A. E. Elsner, J. Pokorny, and S. A. Burns, "Chromaticity discrimination: effects of luminance contrast and spatial frequency," *J. Opt. Soc. Am. A.* **3**(7), 916–920 (1986).

[18] A. E. Elsner, S. A. Burns, and J. Pokorny, "Changes in constant hue loci with spatial frequency," *Color. Res. Appl.* **12**(1), 42–50 (1987).

[19] A. E. Elsner, M. C. Cheney, A. Weber, and M. Miura, "Visualization of two image variables simultaneously using cardinal directions of color vision," *Stud. Health Technol. Inform.* **98**, 89–91 (2004).

[20] A. Roorda and D. R. Williams, "The arrangement of the three cone classes in the living human eye," *Nature* **397**(6719), 520–522 (1999).

[21] D. R. Williams, "Imaging single cells in the living retina," *Vision. Res.* **51**(13), 1379–1396 (2011).

[22] T. Y. Chui, H. Song, and S. A. Burns, "Individual variations in human cone photoreceptor packing density: variations with refractive error," *Invest. Ophthalmol. Vis. Sci.* **49**(10), 4679–4687 (2008).

[23] H. Song, T. Y. Chui, Z. Zhong, A. E. Elsner, and S. A. Burns, "Variation of cone photoreceptor packing density with retinal eccentricity and age," *Invest. Ophthalmol. Vis. Sci.* **52**(10):7376–7384 (2011).

[24] T. Y. Chui, H. Song, C. A. Clark, J. A. Papay, S. A. Burns, and A. E. Elsner, "Cone photoreceptor packing density and the outer nuclear layer thickness in healthy subjects," *Invest. Ophthalmol. Vis. Sci.* **53**(7), 3545–3553 (2012).

[25] C. A. Curcio, K. R. Sloan Jr., O. Packer, A. E. Hendrickson, and R. E. Kalina, "Distribution of cones in human and monkey retina: individual variability and radial asymmetry," *Science* **236**(4801), 579–582 (1987).

[26] C. A. Curcio, K. R. Sloan, R. E. Kalina, and A. E. Hendrickson, "Human photoreceptor topography," *J. Comp. Neurol.* **292**(4), 497–523 (1990).

[27] S. A. Burns, A. E. Elsner, L. A. Lobes Jr., and B. H. Doft, "A psychophysical technique for measuring cone photopigment bleaching," *Invest. Ophthalmol. Vis. Sci.* **28**(4), 711–717 (1987).

[28] A. E. Elsner, L. Berk, S. A. Burns, and P. R. Rosenberg, "Aging and human cone photopigments," *J. Opt. Soc. Am. A.* **5**(12), 2106–2112 (1988).

[29] A. E. Elsner, S. A. Burns, G. W. Hughes, and R. H. Webb, "Reflectometry with a scanning laser ophthalmoscope," *Appl. Opt.* **31**(19), 3697–3710 (1992).

[30] A. E. Elsner, S. A. Burns, and R. H. Webb, "Mapping cone photopigment optical density," *J. Opt. Soc. Am. A.* **10**(1), 52–58 (1993).

[31] A. E. Elsner, S. A. Burns, E. Beausencourt, and J. J. Weiter, "Foveal cone photopigment distribution: small alterations associated with macular pigment distribution," *Invest. Ophthalmol. Vis. Sci.* **39**(12), 2394–2404 (1998).

[32] A. E. Elsner, S. A. Burns, and J. J. Weiter, "Cone photopigment in older subjects: decreased optical density in early age-related macular degeneration," *J. Opt. Soc. Am. A. Opt. Image Sci. Vis.* **19**(1), 215–222 (2002).

[33] A. Bradley, H. Zhang, R. A. Applegate, L. N. Thibos, and A. E. Elsner, "Entoptic image quality of the retinal vasculature," *Vision. Res.* **38**(17), 2685–2696 (1998).

[34] T. Y. Chui, Z. Zhong, H. Song, and S. A. Burns, "Foveal avascular zone and its relationship to foveal pit shape," *Optom. Vis. Sci.* **89**(5), 602–610 (2012).

[35] A. E. Elsner, A. Weber, M. C. Cheney, and D. A. VanNasdale, "Spatial distribution of macular birefringence associated with the Henle fibers," *Vision. Res.* **48**(26), 2578–2585 (2008).

[36] D. A. VanNasdale, A. E. Elsner, T. Hobbs, and S. A. Burns, "Foveal phase retardation changes associated with normal aging," *Vision. Res.* **51**(21–22), 2263–2272 (2011).

[37] A. Weber, A. E. Elsner, M. Miura, S. Kompa, and M. C. Cheney, "Relationship between foveal birefringence and visual acuity in neovascular age-related macular degeneration," *Eye (London)* **21**(3), 353–361 (2007).

[38] D. A. VanNasdale, A. E. Elsner, A. Weber, M. Miura, and B. P. Haggerty, "Determination of foveal location using scanning laser polarimetry," *J. Vis.* **9**(3), 21.1–21.17 (2009).

[39] A. Elsner, L. Moraes, E. Beausencourt, A. Remky, J. Weiter, J. Walker, G. Wing, S. Burns, P. Raskauskas, and L. Kelley, "Scanning laser reflectometry of retinal and subretinal tissues," *Opt. Express* **6**(13), 243–250 (2000).

[40] A. Elsner, M. Miura, S. Burns, E. Beausencourt, C. Kunze, L. Kelley, J. Walker, G. Wing, P. Raskauskas, D. Fletcher, et al., "Multiply scattered light tomography and confocal imaging: detecting neovascularization in age-related macular degeneration," *Opt. Express* **7**(2), 95–106 (2000).

[41] A. E. Elsner, M. S. Muller, B. L. Petrig, J. A. Papay, C. A. Clark, J. Alavanja, and B. P. Haggerty, Toward Low Cost Imaging: A Laser Scanning Digital Camera. Bio-Optics: Design and Application (BODA) 2011 paper, BWA1, OSA Technical Digest (CD).

[42] M. E. Hartnett, J. J. Weiter, G. Staurenghi, and A. E. Elsner, "Deep retinal vascular anomalous complexes in advanced age-related macular degeneration," *Ophthalmology* **103**(12), 2042–2053 (1996).

[43] E. Beausencourt, A. E. Elsner, M. E. Hartnett, and C. L. Trempe, "Quantitative analysis of macular holes with scanning laser tomography," *Ophthalmology* **104**(12), 2018–2029 (1997).

[44] C. Kunze, A. E. Elsner, E. Beausencourt, L. Moraes, M. E. Hartnett, and C. L. Trempe, "Spatial extent of pigment epithelial detachments in age-related macular degeneration," *Ophthalmology* **106**(9), 1830–1840 (1999).

[45] E. Beausencourt, A. Remky, A. E. Elsner, M. E. Hartnett, and C. L. Trempe, "Infrared scanning laser tomography of macular cysts," *Ophthalmology* **107**(2), 375–385 (2000).

[46] M. Miura and A. Elsner, "Three dimensional imaging in age-related macular degeneration," *Opt. Express* **9**(9), 436–443 (2001).

[47] R. Ferguson, D. Hammer, A. Elsner, R. Webb, S. Burns, and J. Weiter, "Wide-field retinal hemodynamic imaging with the tracking scanning laser ophthalmoscope," *Opt. Express* **12**(21), 5198–5208 (2004).

[48] A. E. Elsner, S. A. Burns, J. J. Weiter, and F. C. Delori, "Infra-red imaging of subretinal structures in the human ocular fundus," *Vision. Res.* **36**(1), 191–205 (1996).

[49] M. Miura, A. E. Elsner, E. Beausencourt, C. Kunze, M. E. Hartnett, K. Lashkari, and C. L. Trempe, "Grading of infrared confocal scanning laser tomography and video displays of digitized color slides in exudative age-related macular degeneration," *Retina* **22**(3):300–308 (2002).

[50] M. Miura, A. E. Elsner, M. Osako, K. Yamada, T. Agawa, M. Usui, and T. Iwasaki, "Spectral imaging of the area of internal limiting membrane peeling," *Retina* **25**(4), 468–472 (2005).

[51] R. J. Zawadzki, B. Cense, Y. Zhang, S. S. Choi, D. T. Miller, and J. S. Werner, "Ultrahigh-resolution optical coherence tomography with monochromatic and chromatic aberration correction," *Opt. Express* **16**(11),8126–8143 (2008).

[52] A. E. Elsner, Q. Zhou, F. Beck, P. E. Tornambe, S. A. Burns, J. J. Weiter, and A. W. Dreher, "Detecting AMD with multiply scattered light tomography," *Int. Ophthalmol.* **23**(4–6), 245–250 (2001).

[53] S. A. Burns, A. E. Elsner, M. B. Mellem-Kairala, and R. B. Simmons, "Improved contrast of subretinal structures using polarization analysis," *Invest. Ophthalmol. Vis. Sci.* **44**(9), 4061–4068 (2003).

[54] A. Weber, M. Cheney, Q. Smithwick, and A. Elsner, "Polarimetric imaging and blood vessel quantification," *Opt. Express* **12**(21), 5178–5190 (2004).

[55] M. B. Mellem-Kairala, A. E. Elsner, A. Weber, R. B. Simmons, and S. A. Burns, "Improved contrast of peripapillary hyperpigmentation using polarization analysis," *Invest. Ophthalmol. Vis. Sci.* **46**(3), 1099–1106 (2005).

[56] A. E. Elsner, A. Weber, M. C. Cheney, D. A. VanNasdale, and M. Miura, "Imaging polarimetry in patients with neovascular age-related macular degeneration," *J. Opt. Soc. Am. A. Opt. Image. Sci. Vis.* **24**(5), 1468–1480 (2007).

[57] M. Miura, A. E. Elsner, M. C. Cheney, M. Usui, and T. Iwasaki, "Imaging polarimetry and retinal blood vessel quantification at the epiretinal membrane," *J. Opt. Soc. Am. A. Opt. Image. Sci. Vis.* **24**(5), 1431–1437 (2007).

[58] D. Huang, E. A. Swanson, C. P. Lin, J. S. Schuman, W. G. Stinson, W. Chang, M. R. Hee, T. Flotte, K. Gregory, C. A. Puliafito, et al., "Optical coherence tomography," *Science* **254**(5035), 1178–1181 (1991).

[59] A. F. Fercher, C. K. Hitzenberger, W. Drexler, G. Kamp, and H. Sattmann, "In vivo optical coherence tomography," *Am. J. Ophthalmol.* **116**(1), 113–114 (1993).

[60] A. G. Podoleanu, R. K. Harding and D. A. Jackson, "Practical implementation of a high-speed multichannel correlator with fiber-optic delays," *Appl. Opt.* **36**(30), 7523–7530 (1997).

[61] A. F. Fercher, W. Drexler, C. K. Hitzenberger, and T. Lasser, "Optical coherence tomography—principles and applications," *Rep. Prog. Phys.* **66**, 239–303 (2003).

[62] W. Drexler and J. G. Fujimoto. *Optical Coherence Tomography: Technology and Applications* (Springer, 2008).

[63] J. F. de Boer, B. Cense, B. H. Park, M. C. Pierce, G. J. Tearney, and B. E. Bouma, "Improved signal-to- noise ratio in spectral-domain compared with time-domain optical coherence tomography," *Opt. Lett.* **28**(21), 2067–2069 (2003).

[64] N. Nassif, B. Cense, B. H. Park, S. H. Yun, T. C. Chen, B. E. Bouma, G. J. Tearney, and J. F. de Boer, "In vivo human retinal imaging by ultrahigh-speed spectral domain optical coherence tomography," *Opt. Lett.* **29**(5), 480–482 (2004).

[65] J. F. de Boer, T. E. Milner, M. J. van Gemert, and J. S. Nelson, "Two-dimensional birefringence imaging in biological tissue by polarization-sensitive optical coherence tomography," *Opt. Lett.* **22**(12), 934–936 (1997).

[66] E. Götzinger, M. Pircher, M. Sticker, A. F. Fercher, and C. K. Hitzenberger, "Measurement and imaging of birefringent properties of the human cornea with phase-resolved, polarization-sensitive optical coherence tomography," *J. Biomed. Opt.* **9**(1), 94–102 (2004).

[67] M. Yamanari, S. Makita, and Y. Yasuno, "Polarization-sensitive swept-source optical coherence tomography with continuous source polarization modulation," *Opt. Express* **16**(8):5892—5906 (2008).

[68] M. Miura, M. Yamanari, T. Iwasaki, A. E. Elsner, S. Makita, T. Yatagai, and Y. Yasuno, "Imaging polarimetry in age-related macular degeneration," *Invest. Ophthalmol. Vis. Sci.* **49**(6), 2661–2667 (2008).

[69] B. Cense, W. Gao, J. M. Brown, S. M. Jones, R. S. Jonnal, M. Mujat, B. H. Park, J. F. de Boer, and D. T. Miller, "Retinal imaging with polarization-sensitive optical coherence tomography and adaptive optics," *Opt. Express* **17**(24), 21634–21651 (2009).

[70] S. A. Burns, S. Marcos, A. E. Elsner, and S. Bara, "Contrast improvement of confocal retinal imaging by use of phase-correcting plates," *Opt. Lett.* **27**(6), 400–402 (2002).

[71] S. A. Burns, R. Tumbar, A. E. Elsner, D. Ferguson, and D. X. Hammer, "Large-field-of-view, modular, stabilized, adaptive-optics-based scanning laser ophthalmoscope," *J. Opt. Soc. Am. A. Opt. Image Sci. Vis.* **24**(5), 1313–1326 (2007).

[72] D. T. Miller, O. P. Kocaoglu, Q. Wang, and S. Lee, "Adaptive optics and the eye (super resolution OCT)," *Eye (London)* **25**(3), 321–330 (2011).

[73] S. Wolf, K. J. Wald, A. E. Elsner, and G. Staurenghi, "Indocyanine green choroidal videoangiography: a comparison of imaging analysis with the scanning laser ophthalmoscope and the fundus camera," *Retina* **13**(3), 266–269 (1993).

[74] S. Wolf, A. Remky, A. E. Elsner, O. Arend, and M. Reim, "Indocyanine green video angiography in patients with age-related maculopathy-related retinal pigment epithelial detachments," *Ger. J. Ophthalmol.* **3**(4–5), 224–227 (1994).

[75] K. J. Wald, A. E. Elsner, S. Wolf, G. Staurenghi, and J. J. Weiter, "Indocyanine green videoangiography for the imaging of choroidal neovascularization associated with macular degeneration," *Int. Ophthalmol. Clin.* **34**(3), 311–325 (1994).

[76] O. Arend, A. Remky, A. E. Elsner, B. Bertram, M. Reim, and S. Wolf, "Quantification of cystoid changes in diabetic maculopathy," *Invest. Ophthalmol Vis. Sci.* **36**(3), 608–613 (1995).

[77] O. Arend, A. Remky, A. E. Elsner, S. Wolf, and M. Rein, "Indocyanine green angiography in traumatic choroidal rupture: clinicoangiographic case reports," *Ger. J. Ophthalmol.* **4**(5), 257–263 (1995).

[78] B. Cense, E. Koperda, J. M. Brown, O. P. Kocaoglu, W. Gao, R. S. Jonnal, and D. T. Miller, "Volumetric retinal imaging with ultrahigh-resolution spectral-domain optical coherence tomography and adaptive optics using two broadband light sources," *Opt. Express* **17**(5), 4095–4111 (2009).

[79] Y. Yasuno, Y. Hong, S. Makita, M. Yamanari, M. Akiba, M. Miura, and T. Yatagai, "In vivo high- contrast imaging of deep posterior eye by 1-microm swept source optical coherence tomography and scattering optical coherence angiography," *Opt. Express* **15**(10), 6121–6139 (2007).

[80] S. R. Chinn, E. A. Swanson, and J. G. Fujimoto, "Optical coherence tomography using a frequency-tunable optical source," *Opt. Lett.* **22**(5), 340–342 (1997).

[81] M. Gora, K. Karnowski, M. Szkulmowski, B. J. Kaluzny, R. Huber, A. Kowalczyk, and M. Wojtkowski, "Ultra high-speed swept source OCT imaging of the anterior segment of human eye at 200 kHz with adjustable imaging range," *Opt. Express* **17**(17), 14880–14894 (2009).

[82] F. C. Delori, R. H. Webb, and D. H. Sliney, "Maximum permissible exposures for ocular safety (ANSI 2000), with emphasis on ophthalmic devices," *J. Opt. Soc. Am. A. Opt. Image Sci. Vis.* **24**(5), 1250–1265 (2007).

[83] I. Grulkowski, M. Gora, M. Szkulmowski, I. Gorczynska, D. Szlag, S. Marcos, A. Kowalczyk, and M. Wojtkowski, "Anterior segment imaging with spectral OCT system using a high-speed CMOS camera," *Opt. Express* **17**(6), 4842–4858 (2009).

[84] H. Carlson and D. Kurtz. *Clinical Procedures for Ocular Examination* (McGraw-Hill, Indianapolis, IN, 2003).

[85] T. Kohnen and D. D. Koch. *Cataract and Refractive Surgery* (Springer, Berlin, 2009).

[86] H. Pult and J. J. Nichols, "A review of meibography," *Optom. Vis. Sci.* **89**(5), E760–E769 (2012).

[87] A. Ararwal and S. Jacob Dr., *Agarwal's Textbook on Corneal Topography* (Jaypee Brothers Medical Publishers, New Delhi, 2010).

[88] S. Ortiz, D. Siedlecki, P. Perez-Merino, N. Chia, A. de Castro, Szkulmowski, M. Wojtkowski, and S. Marcos, "Corneal topography from spectral optical coherence tomography (sOCT)," *Biomed. Opt. Express* **2**(12):3232–3247 (2011).

[89] J. A. Izatt, M. R. Hee, E. A. Swanson, C. P. Lin, D. Huang, J. S. Schuman, C. A. Puliafito, and J. G. Fujimoto, "Micrometer-scale resolution imaging of the anterior eye in vivo with optical coherence tomography," *Arch. Ophthalmol.* **112**(12), 1584–1589 (1994).

[90] Y. Li, R. Shekhar, and D. Huang, "Corneal pachymetry mapping with high-speed optical coherence tomography," *Ophthalmology* **113**(5), 792–9.e2 (2006).

[91] M. Lawless and C. Hodge. *LASIK Int. Ophthalmol. Clin.* **53**(1), 111–128 (2013).

[92] M. Li, L. Niu, B. Qin, Z. Zhou, K. Ni, Q. Le, J. Xiang, A. Wei, W. Ma, and X. Zhou, "Confocal comparison of corneal reinnervation after small incision lenticule extraction (SMILE) and femtosecond laser in situ keratomileusis (FS-LASIK)," *PLoS. One.* **8**(12), e81435 (2013).

[93] D. S. Grewal and S. Basti, "Comparison of morphologic features of clear corneal incisions created with a femtosecond laser or a keratome," *J. Cataract. Refract. Surg.* **40**(4), 521–530 (2014). doi:10.1016/j.jcrs.2013.11.028

[94] I. Conrad-Hengerer, F. H. Hengerer, M. A. Juburi, T. Schultz, and H. B. Dick, "Femtosecond laser-induced macular changes and anterior segment inflammation in cataract surgery," *J. Refract. Surg.* **30**(4), 222–226 (2014). doi:10.3928/1081597X-20140321-01

[95] R. N. Gaster, A. L. Caiado Canedo, and Y. S. Rabinowitz, "Corneal collagen cross-linking for keratoconus and post-lasik ectasia," *Int. Ophthalmol. Clin.* **53**(1), 79–90.

[96] Z. Zhong, H. Song, T. Y. Chui, B. L. Petrig, and S. A. Burns, "Noninvasive measurements and analysis of blood velocity profiles in human retinal vessels," *Invest. Ophthalmol. Vis. Sci.* **52**(7), 4151–4157 (2011).

[97] Z. Zhong, B. L. Petrig, X. Qi, and S. A. Burns, "In vivo measurement of erythrocyte velocity and retinal blood flow using adaptive optics scanning laser ophthalmoscopy," *Opt. Express* **16**(17), 12746–12756 (2008).

[98] Q. Wang, O. P. Kocaoglu, B. Cense, J. Bruestle, R. S. Jonnal, W. Gao, and D. T. Miller, "Imaging retinal capillaries using ultrahigh-resolution optical coherence tomography and adaptive optics," *Invest. Ophthalmol. Vis. Sci.* **52**(9), 6292–6299 (2011).

[99] J. Tam, P. Tiruveedhula, and A. Roorda, "Characterization of single-file flow through human retinal parafoveal capillaries using an adaptive optics scanning laser ophthalmoscope," *Biomed. Opt. Express* **2**(4), 781–793 (2011).

[100] V. J. Srinivasan, B. K. Monson, M. Wojtkowski, R. A. Bilonick, I. Gorczynska, R. Chen, J. S. Duker, J. S. Schuman, and J. G. Fujimoto, "Characterization of outer retinal morphology with high-speed, ultrahigh-resolution optical coherence tomography," *Invest. Ophthalmol. Vis. Sci.* **49**(4), 1571–1579 (2008).

[101] S. A. Burns, A. E. Elsner, T. Y. Chui, D. A. Vannasdale Jr., C. A. Clark, T. J. Gast, V. E. Malinovsky, and A. D. Phan, "In vivo adaptive optics microvascular imaging in diabetic patients without clinically severe diabetic retinopathy," *Biomed Opt. Express* **5**(3), 961–974 (2014).

[102] B. Potsaid, B. Baumann, D. Huang, S. Barry, A. E. Cable, J. S. Schuman, J. S. Duker, and J. G. Fujimoto, "Ultrahigh speed 1050nm swept source/Fourier domain OCT retinal and anterior segment imaging at 100,000 to 400,000 axial scans per second," *Opt. Express* **18**(19), 20029–20048 (2010).

[103] Y. J. Hong, M. Miura, S. Makita, M. J. Ju, B. H. Lee, T. Iwasaki, and Y. Yasuno, "Noninvasive investigation of deep vascular pathologies of exudative macular diseases by high-penetration optical coherence angiography," *Invest. Ophthalmol. Vis. Sci.* **54**(5), 3621–3631 (2013). doi:10.1167/iovs.12-11184.

[104] I. Grulkowski, J. J. Liu, B. Potsaid, V. Jayaraman, C. D. Lu, J. Jiang, A. E. Cable, J. S. Duker, and J. G. Fujimoto, "Retinal, anterior segment and full eye imaging using ultrahigh speed swept source OCT with vertical-cavity surface emitting lasers," *Biomed. Opt. Express*, **3**(11), 2733–2751 (2012).

[105] O. O. Ahsen, Y. K. Tao, B. M. Potsaid, Y. Sheikine, J. Jiang, I. Grulkowski, T. H. Tsai, V. Jayaraman, M. F. Kraus, J. L. Connolly, et al., "Swept source optical coherence

microscopy using a 1310 nm VCSEL light source," *Opt. Express* **21**(15), 18021–18033 (2013).

[106] B. Cense, Q. Wang, S. Lee, L. Zhao, A. E. Elsner, C. K. Hitzenberger, and D. T. Miller, "Henle fiber layer phase retardation measured with polarization-sensitive optical coherence tomography," *Biomed. Opt. Express* **4**(11), 2296–2306 (2013).

[107] Y. Jia, S. T. Bailey, D. J. Wilson, O. Tan, M. L. Klein, C. J. Flaxel, B. Potsaid, J. J. Liu, C. D. Lu, M. F. Kraus, J. G. Fujimoto, and D. Huang, "Quantitative optical coherence tomography angiography of choroidal neovascularization in age-related macular degeneration," *Ophthalmology* S0161-6420(14)00104-3. doi:10.1016/j.ophtha.2014.01.034 (2014).

[108] R. F. Spaide, and C. A. Curcio, "Anatomical correlates to the bands seen in the outer retina by optical coherence tomography: literature review and model," *Retina* **31**(8), 1609–1619 (2011).

[109] C. A. Curcio, J. D. Messinger, K. R. Sloan, A. Mitra, G. McGwin, and R. F. Spaide, "Human chorioretinal layer thicknesses measured in macula-wide, high-resolution histologic sections," *Invest. Ophthalmol. Vis. Sci.* **52**(7), 3943–3954 (2011).

[110] R. W. Lu, C. A. Curcio, Y. Zhang, Q. X. Zhang, S. J. Pittler, D. Deretic, and X. C. Yao, "Investigation of the hyper-reflective inner/outer segment band in optical coherence tomography of living frog retina," *J. Biomed. Opt.* **17**(6), 060504 (2012).

[111] J. Cuadros and G. Bresnick, "EyePACS: an adaptable telemedicine system for diabetic retinopathy screening," *J. Diabetes. Sci. Technol.* **3**(3), 509–516 (2009).

[112] S. A. Burns, M. R. Kreitz, and A. E. Elsner. Computer-controlled two-color laser-based optical stimulator for vision research," *Appl. Opt.* **30**(16), 2063–2065 (1991).

[113] J. F. Chen, A. E. Elsner, S. A. Burns, R. M. Hansen, P. L. Lou, K. K. Kwong, and A. B. Fulton, "The effect of eye shape on retinal responses," *Clin. Vis. Sci.* **7**, 521–530 (1992).

[114] A. Remky, E. Beausencourt, and A. E. Elsner, "Angioscotometry with the scanning laser ophthalmoscope. Comparison of the effect of different wavelengths," *Invest. Ophthalmol. Vis. Sci.* **37**(11), 2350–2355 (1996).

[115] A. Remky, K. Lichtenberg, A. E. Elsner, and O. Arend, "Short wavelength automated perimetry in age related maculopathy," *Br. J. Ophthalmol.* **85**(12), 1432–1436 (2001).

[116] A. Remky, A. E. Elsner, A. J. Morandi, E. Beausencourt, and C. L. Trempe, "Blue-on-yellow perimetry with a scanning laser ophthalmoscope: small alterations in the central macula with aging," *J. Opt. Soc. Am. A. Opt. Image Sci. Vis.* **18**(7), 1425–1436 (2001).

[117] A. Remky and A. E. Elsner, "Blue on yellow perimetry with scanning laser ophthalmoscopy in patients with age related macular disease," *Br. J. Ophthalmol.* **89**(4), 464–469 (2005).

[118] R. F. Kaplan, R. A. Cohen, A. Rosengart, A. E. Elsner, T. R. Hedges 3rd, and L. R. Caplan, "Extinction during time controlled direct retinal stimulation after recovery from right hemispheric stroke," *J. Neurol. Neurosurg. Psychiatry* **59**(5), 534–536 (1995).

[119] A. E. Elsner, B. L. Petrig, J. A. Papay, E. J. Kollbaum, C. A. Clark, and M. S. Muller, "Fixation stability and scotoma mapping for patients with low vision," *Optom. Vis. Sci.* **90**(20), 164–173 (2013).

[120] Q. X. Zhang, R. W. Lu, C. A. Curcio, and X. C. Yao, "In vivo confocal intrinsic optical signal identification of localized retinal dysfunction," *Invest. Ophthalmol. Vis. Sci.* **53**(13), 8139–8145 (2012).

[121] A. D. Singh, "Ocular phototherapy," *Eye (London)* (2012). doi:10.1038/eye.2012.258

INDEX

Note: Page numbers followed by f and t indicate figures and tables, respectively.

Abbe criterion, 40
Abbe-Rayleigh criterion, 62
Abbe's diffraction, 470
  lateral resolution limit, 474
ABC, *see* ATP-binding cassette (ABC)
Absorption, 2, 3, 3f
  spectroscopy, 3f
  spectrum, 3, 4, 5
Absorption, extinction, interference-based methods, 89–90
Absorption detection, 88
Absorption gate, 391–395
Acinetobacter baumannii, 438
Acoustooptic modulator (AOM), 216
Acridine orange, 413
Actinic keratosis (AK), 429–430
Actinobacillus actinomycetemcomitans, 440
Activator, 102
Active sorting (optical), 216–218, 217f
Adaptive optics, 512f
Age-related macular degeneration (AMD), 424, 445
ALA-methyl ester (MAL)-PDT, 429–430
Albedo, 289
AlGaN LED excitation, 16
Allophycocyanin (APC), 41f
ALT, *see* Argon laser trabeculoplasty (ALT)
Alzheimer's disease, 10
5-Aminolevulinic acid (5-ALA), 414
Analyte, 323
Angle closure glaucoma, 528
Anharmonicity, 80
Animal models of wound infections, 437–440
Anisotropic tissues, 254
Anisotropy, fluorescence, 30–38
  experimental, 33–35
  nanoparticle metrology, 35–38
  theory, 30–33
Anisotropy factor, 372, 373f
Anterior chamber, ciliary body, and lens, 526–527
Anterior chamber and lens, 505–506

Photonics: Scientific Foundations, Technology and Applications, Volume IV, First Edition.
Edited by David L. Andrews.

© 2015 John Wiley & Sons, Inc. Published 2015 by John Wiley & Sons, Inc.

Anterior segment anatomy
  anterior chamber and lens, 505–506
  cornea and tear film, 504–505
Anterior segment diagnostics
  anterior chamber, ciliary body, and lens, 526–527
  cornea and tear film, 522–526
  light and treatment, 528–529
  refraction, 527–528
Antibodies, 328
Anticancer PDT, 419
Anticancer radiation therapies, 423
Antimicrobial PDT, 435
AO imaging system, 519f
AOM, *see* Acoustooptic modulator (AOM)
AOSLO imaging of human cones, 520f
Aptamers, 329
Argon laser trabeculoplasty (ALT), 528
Aromatic fluorophores, 13
Atomic force microscope (AFM), 60
ATP-binding cassette (ABC), 431
Aufbau principle, 415
Auto-correlation function, 492
Auto-oxidation, 5–6
Auto-refractors function, 527
Auxochrome, 418
Avogadro's number, 27
Axial resolution, 168

B800 ring, 120, 121f
B850 ring, 85, 120, 121f
Babinet Soleil compensators, 275
Back-scattering geometry, 285
Bacterial reaction center (BRC), 132, 132f
Balanced super-resolution optical fluctuation imaging (bSOFI), 492
Ballistic photons, 370, 370f
Basal cell carcinoma (BCC), 430–431
Bayesian analysis of blinking and bleaching, 494
BCC, *see* Basal cell carcinoma (BCC)
Beam scanning, 65
Bean Pod Mottle Virus (BPMV), 340, 341f
Beer–Lambert law, 5
BICELLs, *see* Biophotonic sensing cells (BICELLs)
Bimodal waveguide (BiMW) interferometer, 338, 339f
Biomedical optical imaging, 369
Biophotonics, 129
Biophotonic sensing cells (BICELLs), 347, 349
Biophotonics workstation, 207, 207f
Bioreceptors, 323, 328–329
Biosensors, 323
Birefringence, 513
Black lipid films, 67–68
Bleaching, 71, 494
Blinking, 69–70, 494
  reversible photochemical reactions, 70–71
  triplet state, 70
Blinking and bleaching, 494
Born–Oppenheimer approximation, 78
Botryococcus braunii, 209f
Bowen's disease/squamous cell carcinoma *in situ,* 430
BPMV, *see* Bean Pod Mottle Virus (BPMV)
Brain tumors, 419
BRC, *see* Bacterial reaction center (BRC)
Breast cancer
  hypoxia for, 377–378
Bright field, 87–88
Brownian diffusion, 74
Brownian isotropic rotation, 32
Brownian particles, 69
Burns, 437

Calorimetry, 8
Cancer, 434
  BCC, 430–431
  diagnosis, 302–307
  human tumor xenografts, 424
  nonmelanoma skin cancer (NMSC), 428
  photosensitizers approved/in clinical trials for, 420t, 421f
Catalytic biosensors, 329
Cataract, 506
CCD, *see* Charge-coupled device (CCD)
CCD camera, 66
Cell deformations, 211–214
Cells handling
  cell positioning
    intercellular interaction, microenvironment, 209–211, 210f
    nonbiological stimuli, microenvironment, 208–209, 209f
    single-cell analysis, 206–208, 207f

- cellular biomechanics, 211–214, 213f
  - cytometry, 214–215, 215f
  - dielectric tagging, 201f, 202–206, 203t, 204f, 205f
  - light–cell interaction, 198–202, 199f
  - refractive index, 203t
- The cellular plasma membrane, 476
- Cell viability, 220–230, 221t
  - division time, 226–227
  - energy dose, 225–226
  - growth, 226–227
  - internal pH (pH_i), 228
  - optimal wavelength, 222–224, 222f–223f
  - power, 225–226
  - propidium iodide (PI), 227–228
  - reactive oxygen species, 229–230
  - thermal effects, 224–225
- Cervical intraepithelial neoplasia (CIN), 305, 444
- Cetyltrimethylammonium bromide (CTAB), 45
- CFD, *see* Constant fraction discrimination (CFD)
- Charge-coupled device (CCD), 385, 478, 484
- Charge separation (CS) rates, 130
- Charge-transfer state, 70
- Chinese Hamster ovary (CHO) cells, 202
- Chitosan nanoparticles (CNPs), 427
- *Chlamydomonas reinhardtii,* 155, 155f, 209f
- Chlorophyll (Chl), 130–132, 132f
- CHO cells, *see* Chinese Hamster ovary (CHO) cells
- Choroidal melanoma, 431
- Choroidal neovascularization (CNV), 445
- Chromatic aberrations, 64
- Chromophores, 103, 104, 418
- Chromosomes, 470
- CIN, *see* Cervical intraepithelial neoplasia (CIN)
- Circular dichroism, 253
- Circular retarders, 255
- Cladding, 324, 325, 326
- CNPs, *see* Chitosan nanoparticles (CNPs)
- Coherent anti-Stokes Raman scattering (CARS) microscopy, 77, 178–180, 179f, 182–184
- Colliding pulse mode-locked (CPM) laser, 396
- Collisional quenching by oxygen, 7
- Compensator, 274
- Complementary metal oxide (CMOS) arrays, 514
- Complete Mueller imagers, 280–282, 281f
- Complete *versus* incomplete instruments (tissue polarimetry), 270–271
- Cone density, 513
- Confocal aperture, 514
- Confocal imaging
  - introduction, 168–169, 169f
  - point scanned microscopy, 169–172
- Confocal microscopy, 65–66
- Constant fraction discrimination (CFD), 17
- Constant retarders, 272–275
- Convolution analysis, 18
- Core, 324, 325, 326
- Cornea curvature, 523
- Corneal epithelium, 505
- Corneal stroma, 505
- Cornea and tear film, 504–505, 522–526
- Coulombic coupling, 112
- CP43, 152–154, 153f–154f
- C-reactive protein (CRP), 338
- CRP, *see* C-reactive protein (CRP)
- Crystalline beam splitters, 271
- CTAB, *see* Cetyltrimethylammonium bromide (CTAB)
- Cutaneous T cell lymphoma (CTCL), 431
- Cutler, Max, 369
- Cyanobacteria, 131–132
- Cyanobacterial photosystem I, 148–151, 149f
- Cysteine, 21
- Cytometry, 214–215, 215f

- Dark field, 86–87
- Dark-field scattering, 86, 88–89
- Dark state (triplet), 75–77
- Debye–Stokes–Einstein relation, 75
- Debye–Waller factor, 79
- Decoherence, 80
- Deconvolution, 19
- Deconvolution fluorescence microscopy, 489f
- Degree of polarization (DOP), 110, 242–243, 246, 256, 284–285

Dendritic cells (DCs), 447
Dental Infections, 441–442
Depletion, 474
Depolarization, 244–245
Depolarization index, 249
Depolarization powers, 257
Depolarizer, 255–257
Depth of penetration, 325
Dermatology
  acne vulgaris, 432–433
Dermatology, PDT for, 428–429
  acne vulgaris, 432–433
  actinic keratosis, 429–430
  BCC, 430–431
  Bowen's disease/squamous cell carcinoma *in situ,* 430
  melanoma, 431
  mycosis fungoides, 431–432
  photorejuvenation, 433
2D-ES, *see* Two-dimensional electronic spectroscopy (2D-ES)
Dexter theory, 113
Dexter transfer, 113
Dextran polymer, 331
Diaphanography, 369
Diattenuation, 249–250
Dichroic polarizers, 271
Diethylthiadicarbocyanine iodide (DTDCI), 29
Diffuse photons, 370, 370f
Diffusion coefficients, 26
Diffusion effects, RET, 111–112
Diffusive light, 402–403
Dihydroxyindoles, 10, 11
3,4-Dihydroxy-L-phenylalanine (L-DOPA), 5–6, 6f
  auto-oxidation of, 11
Dipole–dipole interaction, 81
Direct electronic coupling, 106
Direct photoactivation dSTORM, 43
Direct stochastic optical reconstruction microscopy, 478–479
*direct*STORM (*d*STORM), 477
Dissipation, RET, 105–107
Donor, *see* Sensitizer
DOP, *see* Degree of polarization (DOP)
Dosimetry, PDT, 423
*D*STORM, 482

Dual rotating retarders, 280, 281f
Dynamic quenching, 24–26
Dynamic range, biosensor, 331

ECM, *see* Extracellular matrix (ECM)
EET, *see* Excitation energy transfer (EET)
Einstein coefficient, 14
Electronic response and ground-state depletion, 92–93
Electronic transitions coupling, RET, 104–105
Electron microscopy, 490–491
Electron paramagnetic resonance (EPR), 84
Emission spectrum, 474
Endoplasmic reticulum (ER), 419
Enhanced permeability, 419
Enhancing contrast, 521–522
Eos Fluorescent Protein (EosFP), 477
Epic^{TM} System, 344
Epifluorescence, 39
Escherichia coli, 198, 351, 436, 437
Ethylenediaminetetraacetic acid (EDTA), 436
Eumelanin, 10
  synthesis, 11f
Evanescence wave absorbance-based optical fiber, 354
Evanescent field, 325, 325f
Excitation energy, 24
Excitation energy transfer (EET), 130, 136–137
Excitation monochromator, 4
Excitons, 134–136, 135f
External field effects, 84
Extracellular matrix (ECM), 211
Extrinsic fluorescence, 21
Eye
  anatomy, 504f
  corneal topography of normal and astigmatic, 525f

Fabry–Perot interferometric biosensors, 354
FACS, *see* Fluorescence-activated cell sorting (FACS)
μFACS systems, 215f, 216
Factorial hidden Markov model, 494
Far-field optical super-resolution imaging techniques, 472–473

FBG, *see* Fiber Bragg grating (FBG)
FCS, *see* Fluorescence correlation spectroscopy (FCS)
Fenton reaction, 417
Fermi's rule, 106
FGR, *see* Fluorescence-guided resection (FGR)
Fiber Bragg grating (FBG), 350
Fiber Bragg grating (FBG) biosensors, 350–351, 350f
Fibrils, 505
Field cancerization, 429
FISH, *see* Fluorescence *in situ* hybridization (FISH)
Fission yeast *(Schizosaccharomyces pombe),* 483
FLIM, *see* Fluorescence lifetime imaging microscopy (FLIM)
FLN, *see* Fluorescence line-narrowing (FLN)
ΔFLN technique, 141–143
Floppy molecules, 7
Fluctuation-based superresolution microscopy, 494–495
Fluid-filled chamber, 505
Fluorescein dye, 524f
Fluorescence, 1–2, 65–66
  anisotropy, 30–38
  lifetime, 12–23
  microscopy, 38–48
  multidimensional contour, 18
  quantum yield, 6–12, 9t
  quenching, 23–30
  spectra, 2–6, 3f, 4f
Fluorescence-activated cell sorting (FACS), 214, 215f
Fluorescence anisotropy, 75, 110
Fluorescence-based biosensors, 324
Fluorescence correlation spectroscopy (FCS), 41f, 73–74, 427
  dark state (triplet), 75–77
  multiparameter analysis, 77
  photon counting histograms, burst analysis, 73
  rotational diffusion, 75
  translational diffusion, 74–75
  variants, 77
Fluorescence emission, 13
Fluorescence excitation spectroscopy
  hole-burning, 81–82
  inhomogeneous broadening, 80–81
  single-molecule spectroscopy, 82–84
    external field effects, 84
    interacting single molecules, 85–86
    optically detected magnetic resonance, 84
    quantum optics, 84
    spectral diffusion, 84–85
  zero-phonon line and phonon wing, 78–80
Fluorescence (FL1) signals, 214
Fluorescence fractions, 22
Fluorescence-guided resection (FGR), 425
Fluorescence impulse response, 13
Fluorescence *in situ* hybridization (FISH), 469
Fluorescence intensity trace, 69
Fluorescence lifetime, 167
Fluorescence lifetime imaging microscopy (FLIM), 13, 43
Fluorescence line-narrowing (FLN), 141–143
Fluorescence photoactivation localization microscopy (FPALM), 477
Fluorescence resonance energy transfer (FRET), 427
Fluorescence spectroscopy, 2, 40
  bleaching, 71
  blinking, 69–70
    reversible photochemical reactions, 70–71
    triplet state, 70
  orientation, 68
    polarization analysis in detection, 68–69
    polarization modulation in excitation, 69
  sample preparation
    bilayers, membranes, and black lipid films, 67–68
    Langmuir–Blodgett films, 67
    spin coating, 67
  signal-to-noise ratio, 66–67
  superresolution, 71–72
Fluorescent dye, 8–10, 523
Fluorimeter, 4

Fluorophore, 23
Fluorophore distribution, 486
Fluorophore–quencher complexes, 23
Folding funnel, 141
Förster equation, 108f
Förster radius, 107
Förster resonance energy transfer (FRET), 26–29
Förster theory, 103, 105, 106, 107, 111
Forward model, tissue polarimetry, 291–292, 292f
Forward modeling of polarized light propagation in tissue
  overview, 282–284
  photon diffusion formalism, 284–288
  polarization-sensitive Monte-Carlo (PSMC) approach, 288–290
Forward product decompositions, 258–261
Forward scatter (FSC), 214
Forward scattering geometry, 285
Fourier space gate, 395–398, 396f, 397f, 399f
Fourier transform, 486
Franck–Condon amplitude, 78–79
Franck–Condon factors, 79
Franck–Condon (FC) weighted density of states, 136
Frenkel excitons, 134
Frenkel or molecular exciton model, 120
Frequency-doubling Nd:YAG laser, 528
Fresnel rhombs, 272
FRET, *see* Förster resonance energy transfer (FRET)
FRET-FLIM, *see* Fluorescence resonance energy transfer lifetime imaging microscopy (FRET-FLIM)
FSC, *see* Forward scatter (FSC)
Full-width-at-half-maximum (FWHM), 400
FWHM, *see* Full-width-at-half-maximum (FWHM)

Gating mechanism, 297
Gaussian beam, 86
Gaussian distribution function, 479
Gaussian function, 482
Gaussian spot, 63
Generalized Förster Theory (GFT), 120–121
Geometrical aberrations, 64
GFP, *see* Green fluorescent protein (GFP)
GFT, *see* Generalized Förster Theory (GFT)
Glaucoma, 506
Glucose/galactose-binding protein (GBP), 21–23, 22f
Goeppert-Mayer, M., 173
Gold nanorods in cells, 45–48
Graded index (GRIN) optics, 185
Gram-negative bacteria, 435
Gram-positive bacteria, 435
Grating-based biosensors, 342–345, 343f
Green fluorescent protein (GFP), 167
Ground-state depletion with individual molecule return (GSDIM), 482

Hanseniaspora uvarum, 210, 210f
Harmonic microscopy, 175–178, 176f
Hartmann–Shack aberrometers, 527
Hartmann–Shack grid, 519
Helicobacter pylori infection, 444
Hematoporphyrin derivative (HPD), 414, 416, 419, 433
Henle fiber layer, 513
Henle fibers, 513
Herpes simplex virus (HSV), 443
Herpes simplex virus 1 (HSV-1), 338
Hidden Markov model, 494
Highest occupied molecular orbital (HOMO), 415
HIV, *see* Human immunodeficiency virus (HIV)
Hole-burning, 81–82
Homo-FRET, 36
Homogeneous broadening, pigment-protein complexes, 137–140
Homogeneous or bulk sensing, 332
Homogeneous diattenuators, 252–253
Homogeneous retarders, 253–255
  circular, 255
  linear, 254
HPD, *see* Hematoporphyrin derivative (HPD)
HPV, *see* Human papilloma virus (HPV)
HSV-1, *see* Herpes simplex virus 1 (HSV-1)
Huang-Rhys factor, 139
Human immunodeficiency virus (HIV), 476

Human papilloma virus (HPV), 305
Human tumor xenografts of human breast cancer, 424
Hydrogen peroxide (H_2O_2), 417
Hydroxyapatite, 422
Hypoxia, 378–379

Illumination optical system (IO), 266
Image intensifier, 66
4D imaging, 521
Imaging chromatin, 490
Immobilization techniques, bioreceptors, 329–331
  covalent binding, 330
  noncovalent interactions, 330
  physical adsorption, 329–330
  physical entrapment, 330
Immunosensors, 328
Infectious disease, PDT for, 435
  animal models of wound infections, 437–440
  in vitro studies, 435–436
  oral and dental infections, 440–442
  osteomyelitis, 443
  otitis media with effusion (OME), 442–443
  peptic ulcer disease (PUD), 444–445
  photoinactivation of viruses, fungi, and parasites, 436–437
  viral infections, 443–444
Inhomogeneous broadening, 80–81, 137–140
Institute for Ultrafast Spectroscopy and Lasers (IUSL), 368–369
Instrumentation, tissue polarimetry
  examples
    complete Mueller imagers, 280–282, 281f
    nonimaging Mueller polarimeter, 280, 280f
    orthogonal state contrast (OSC) imagers, 279–280
  polarization state analyzers (PSAs)
    based on linear polarizers, 271–272
    linear polarizers and constant retarders combinations, 272–275
    linear polarizers and variable retarders combinations, 275–279
  principles
    complete *versus* incomplete instruments, 270–271
    design and optimization considerations, 269–270
    periodic time modulation, 269
    scheme of polarimetric instruments, 266–267, 267f
    sequential polarization modulation and analysis, 267–268
    spectral or spatial modulation, 269
Insulin fibrils, 10
Integrated depolarization, logarithmic decomposition, 264
Integrated dichroism, logarithmic decomposition, 264
Integrated optical microcavity-based biosensors, 338–342
Integrated optical waveguide, 326–327
Integrated optical waveguide-based biosensors
  grating-based biosensors, 342–345
  integrated optical microcavity-based biosensors, 338–342
  interferometric biosensors, 334–338
  photonic crystal-based biosensors, 345–346
  recent trends, 346–349
Intensity-based imaging, RET, 115–116, 115f
Interacting single molecules, 85–86
Interference pattern, 334
Interferometric biosensors, 334–338, 334f
  Mach–Zehnder interferometer (MZI), 335–337, 336f–337f
  other interferometric configurations, 338
  Young interferometer, 337–338, 337f
Internal pH (pHi), cell viability, 228
Intersystem crossing (ISC), 75f, 415
Intracellular dielectric tagging, 205
Inverse image reconstructions, 402
Inverse polarimetric analysis, 292–296, 293f, 294t
In vivo glucose sensing, 20–23
IO-based LOC platform, 355–356, 356f
Iris functions, 506

Iron oxide nanoparticles (IONPs), 428
IUSL, *see* Institute for Ultrafast Spectroscopy and Lasers (IUSL)

Jablonski diagram, 416f
Jablonski energy level scheme, 3, 3f
Jones vectors, 240, 241, 245

KDP, *see* Potassium dihydrogen phosphate (KDP)
Kerastick®, 414
Kerr-Fourier gate (KFG), 391, 392f
KFG, *see* Kerr-Fourier gate (KFG)
Kirschner wires (K-wires), 443
Kramers–Kronig relations, 204

Label-free optical waveguide biosensors
  operation principle, 324–326
  optical waveguide technology
    integrated optical waveguide, 326–327
    optical fibers (OFs), 327–328, 327f
Lab-on-a-chip integration, 354–357, 355f, 356f
Langmuir–Blodgett films, 67
Langmuir film, 72
Laser-Assisted *in situ* Keratomileusis (LASIK), 528
Laser Epithelial Keratomileusis (LASEK), 528–529
Laser scanning digital camera, 510
Laser tweezers Raman spectroscopy (LTRS), 208, 209f
Lateral resolution, 168
LCI, *see* Low coherence imagine (LCI)
LDL, *see* Low density lipoprotein (LDL)
Legionella pneumophila, 343
Leishmania, 442
Levulan®, 414
LHC-II, *see* Light-Harvesting Complex II (LHC-II)
Lifetime, fluorescence
  experimental, 15–20
  in vivo glucose sensing, 20–23
  standards, 20t
  theory, 13–15
Light-emitting diode (LED), 16
Light-harvesting complex II (LHC-II), 118
Light-harvesting complexes
  introduction, 118
  photosynthetic excitons, 119–121
Light-harvesting proteins, 118
Light-induced spectral diffusion, 82
Light propagation in highly scattering turbid media
  ballistic to diffuse imaging, transition from, 402–403, 403f
  ballistic light components, 378–384, 381f, 382f, 383f
  diffused light components, 378–384
  introduction, 367–369
  optical imaging, 369–378, 370f
    optical absorption spectra of chromophores in tissues, 377–378, 377f, 378f
    optical parameters for human tissues and model media, 374–377, 375f, 375t, 376t
    optical parameters for light propagation, 371–374
    transmitted light components, 370–371
  photon-sorting gates, 384–402
    absorption gate, 391–395
    Fourier space gate, 395–398, 396f, 397f, 399f
    microscopic imaging, 395–398
    polarization gate, 398–402, 401f
    time gate, 385–391, 386f
Light-sensitive dye photosensitization, 414
Light and treatment, 528–529
Limit of detection (LOD), 326
  optical waveguide biosensors, 334t
Linear birefringence, 254
Linear polarizers, 271–272
Linear retardation, logarithmic decomposition, 264
Linear retarders, 254
Linear (scalar) dichroism, 252
Linear vibronic coupling, 78
Line broadening, RET, 105–107
Lipid bilayer, 33
Liquid crystals cells, 276
Listeria monocytogenes, 338
Lithium niobate ($LiNbO_3$), 326
Live cell imaging, 491
Localization microscopy, 483

Localization of single fluorophores, 479–482
LOD, *see* Limit of detection (LOD)
Logarithmic decomposition, 261–265, 294t
Long-period grating (LPG) biosensors, 351–353, 352f
Long-range transfer, RET, 112–113
Lorentzian lineshape, 81
Lorentzian ZPL, 140
Low coherence imagine (LCI), 517
Low density lipoprotein (LDL), 419, 421
Lowest unoccupied molecular orbital (LUMO), 415
LTRS, *see* Laser tweezers Raman spectroscopy (LTRS)
Lu-Chipman decomposition, 260, 260f
LUDOX, 35, 36f, 37t
LUDOX silica, 19
LUMO, *see* Lowest unoccupied molecular orbital (LUMO)

Mach–Zehnder interferometer (MZI), 334f, 335–337, 336f–337f
Madin-Darby canine kidney (MDCK) cells, 46
Malignant tumors, 434
Markov Chain Monte Carlo sampling, 494
Maximum entropy principle, 285
MEA, *see* Monoethanolamine (MEA)
Measurement techniques
  enhancing contrast, 521–522
  increase contrast of transparent and scattering tissues, 515–517
  scanning and confocal apertures, 514–515
  wavefront aberration measurement and compensation, 517–521
Mechanotransduction, cells, 211–214
Meibomian glands, 522
Melanin, 422
Melanin spectra, 5–6
Melanoma, 431
Membranes, 67–68
Metal ion quenching, 29–30
Metronomic PDT, 425
Microbial infection, 505
Microcontact printing, 331
Microfluidic patterning, 331
Microscopic imaging, 395–398
Microscopy, fluorescence, 38–39
  gold nanorods in cells, 45–48
  systems and techniques, 39–44
Microspheres, 342
Microstructured optical fibers (MOFs), 328
Microtoroids, 342
Microviscosity, 32
Mie regime, 286–287
Minkowski metric tensor, 264
Minsky, Marvin, 168
MIPs, *see* Molecular imprinted polymers (MIPs)
Mitochondria, 419
MLS, *see* Multilevel systems (MLS)
Modulation frequency, 14
MOFs, *see* Microstructured optical fibers (MOFs)
Molecular fingerprint, 5
Molecular imprinted polymers (MIPs), 329
Molecular pathology, 2
Molecular ruler, 26
Monoethanolamine (MEA), 478
Mueller matrix, 258
  of depolarizer, 255, 257
  depolarizing or nondepolarizing character, 248–249
  elements, 292
  non-Stokes diagonalizable, 261–265
  physical realizability, 248
  of retarder, 254
Multiexponential fluorescence decay tracking, 36
Multilevel systems (MLS), 141
Multiparameter analysis, 77
Multiphoton excitation, 37, 40
Multiphoton excitation microscopy, 39
Multiphoton fluorescence microscopy, 173–175
  advantages, 175
Multiplexing, biofunctionalization strategies, 331
Mycobacterium tuberculosis, 442
Mycosis fungoides (MF), 431–432
MZI, *see* Mach–Zehnder interferometer (MZI)

NA, *see* Numerical aperture (NA)
Nanocrystals, 60
Nanofountain, 116, 117f

Nano-optics, 60
Nanoparticle metrology, 35–38
Nanoplatforms with theranostic functionalities, 426f
Nanoscale optofluidic sensor array (NOSA), 345
Nanotechnology, 425–428, 427f
Near-field scanning optical microscopy (NSOM), 41–42, 41f
Near-infrared fluorescent (NIRF), 427
Near-infrared light, 371
Near-infrared (NIR) lasers, 368
Neochloris oleoabundans, 209f
Nipkow spinning disk confocal, 172, 173f
Nitrogen bubbling, 7
Nitrogen vacancies, 475
N-matrix formalism, 290
Noise reduction, 481
Nondestructive chemical analysis, 469
Nonimaging Mueller polarimeter, 280, 280f
Noninvasive glucometry, 300–302, 301f–302f
Nonlinear microscopy, 172–180
  adaptive optics for in-depth imaging, 185–186, 186f
  clinical applications, 184–185
  coherent anti-Stokes Raman scattering (CARS) microscopy, 178–180, 179f
  harmonic microscopy, 175–178
  miniature instrumentation, 184–185
  multiphoton fluorescence microscopy, 173–175
  optical configuration for, 181f
  practical implementation of, 181–184
  stimulated Raman scattering microscopy, 180
Non-maximum suppression (NMS), 481
Nonmelanoma skin cancer (NMSC), 428
Non-obese diabetic (NOD), 448
Non-photochemical hole-burning (NPHB), 130, 142
Non-small-cell lung cancer (NSCLC), 424
Non-Stokes diagonalizable Mueller matrices, 261
NOSA, *see* Nanoscale optofluidic sensor array (NOSA)
NPHB, *see* Non-photochemical hole-burning (NPHB)
Nuclear instrument modules (NIMs), 17
Nuclear lamina, 490
Nuclear pore complex, 490
Nucleic acid sensors, 328–329
Numerical aperture (NA), 62, 167

OCT, *see* Optical coherence tomography (OCT)
Ocular anatomy and physiology, 503–504
  anterior segment anatomy
    anterior chamber and lens, 505–506
    cornea and tear film, 504–505
  retina, 506–507
    photoreceptors, 507–513
    superficial retinal layers, 513–514
OF, *see* Optical fibers (OFs)
OFRR, *see* Optofluidic ring resonators (OFRRs)
OKG, *see* Optical Kerr Gate (OKG)
Oncology, PDT for, 433–435
Ophthalmic imaging devices, 521
Ophthalmology, 445–446
Optical biopsy, 240
Optical biosensors
  evaluation, 331–334, 332f
  fluorescence-based detection, 323–324
  label-free detection, 323–324
Optical coherence tomography (OCT), 308, 505f, 517
Optical fiber-based biosensors, 349–354
  evanescence wave absorbance-based optical fiber, 354
  fiber Bragg grating (FBG) biosensors, 350–351, 350f
  long-period grating (LPG) biosensors, 351–353, 352f
  OF-based interferometry biosensors, 353–354
Optical fiber-based interferometric biosensors, 353–354
Optical fibers (OFs), 324, 327–328, 327f
Optical forces, 197–198
  components of measurement system, 202f
  ray optics model of, 199–200, 199f
  for silica particles, 203f
Optical Kerr Gate (OKG), 385–391, 390f
Optically detected magnetic resonance (ODMR), 84

Optical microscope, 62
Optical resolution beyond Abbe's limit, 469–472
  advent of far-field optical super-resolution imaging techniques, 472–473
Optical rotation, logarithmic decomposition, 264
Optical sectioning microscopy
  background, 165–168
  confocal imaging
    introduction, 168–169, 169f
    point scanned microscopy, 169–172
  introduction, 165–168
    biological context and limitations, 166–167
    definitions and terms, 167–168
  nonlinear microscopy, 172–180
    adaptive optics for in-depth imaging, 185–186
    clinical applications, 184–185
    coherent anti-Stokes Raman scattering (CARS) microscopy, 178–180
    harmonic microscopy, 175–178
    miniature instrumentation, 184–185
    multiphoton fluorescence microscopy, 173–175
    practical implementation of, 181–184
    stimulated Raman scattering microscopy, 180
  widefield optical sectioning
    single plane illumination microscopy (SPIM), 186–187, 187f
    structured illumination microscopy, 187–188f, 187–189
    sub-diffraction-limited imaging, 189–190
Optical sorting, 215–220
  active, 216–218, 217f
  passive, 218–219, 219f, 220f
Optical stretcher, 212–214, 213f
Optical transfer function (OTF), 484
Optical tweezers, 198
Optical waveguide biosensors
  evaluation of optical biosensors, 331–334
  integrated optical waveguide-based biosensors
    grating-based biosensors, 342–345, 343f
    integrated optical microcavity-based biosensors, 338–342
    interferometric biosensors, 334–338
    photonic crystal-based biosensors, 345–346
    recent trends, 346–349
  introduction, 323–324
  label-free optical waveguide biosensors
    operation principle, 324–326
    optical waveguide technology, 326–328
  lab-on-a-chip integration, 354–357, 355f, 356f
  optical fiber-based biosensors, 349–354
    evanescence wave absorbance-based optical fiber, 354
    fiber Bragg grating (FBG) biosensors, 350–351, 350f
    long-period grating (LPG) biosensors, 351–353, 352f
    OF-based interferometry biosensors, 353–354
  surface biofunctionalization
    bioreceptors, 328–329
    immobilization techniques, 329–331
    for multiplexing, 331
Optical waveguide lightmode spectroscopy (OWLS), 343
Optical waveguide technology
  integrated optical waveguide, 326–327
  optical fibers (OFs), 327–328, 327f
Optimal wavelength, cell viability, 222–224
  cell viability, 222f–223f
Optofluidic ring resonators (OFRRs), 341, 342f
Optofluidics, 356
Oral and dental infections, 440–442
Orientational factor, 27
Orientation dependence, FET, 108–109, 109f
Orthogonal scatter (SSC) intensity, 214
Orthogonal state contrast (OSC) imagers, 279–280
OSC imagers, *see* Orthogonal state contrast (OSC) imagers
Osteomyelitis, 443

Otitis media with effusion (OME), 442–443
OWLS, *see* Optical waveguide lightmode spectroscopy (OWLS)

Pap smear, 305
Paramecium spp., 413
Para-terphenyl crystal, 83
Partial coherence interferometry (PCI), 528
Partially polarized states, 242–245, 243f
Passive sorting (optical), 218–219, 219f, 220f
PAT, *see* Photoacoustic tomography (PAT)
Pathogenesis of acne, 432
PBS, *see* Polarizing beam splitters (PBS)
PDT, *see* Photodynamic Therapy (PDT)
PEG, *see* Poly(ethylene) glycol (PEG)
Peptic ulcer disease (PUD), 444–445
Peptide beta-amyloid ($A\beta$), 10
Peptide Nucleic Acids (PNAs), 329
Peptides, 328
Periodic time modulation, tissue polarimetry, 269
Perrin, Francis, 102
Perrin, Jean, 102
Phagocytosis, 205
Pheophytins (Pheos), 130–132, 132f
Phonon
  higher-order coupling, 80
Phonon sidebands (PSBs), 137–140
Phonon wing (PW), 79
Phosphorescence, 416
Photoacoustic spectroscopy actinometry, 8
Photoacoustic tomography (PAT), 368
Photoactivated localization microscopy and stochastic optical reconstruction microscopy, 477–478
  beyond *d*STORM, 482
  direct stochastic optical reconstruction microscopy, 478–479
  localization microscopy, 483
  localization of single fluorophores, 479–482
Photoactivated localization microscopy (PALM), 43, 473, 490
Photobleaching, 419
Photochemistry, 417–418
Photodetector, 65
Photodynamic Therapy (PDT), 367
  for dermatology, 428–429
    acne vulgaris, 432–433
    actinic keratosis, 429–430
    basal cell carcinoma (BCC), 430–431
    Bowen's disease/squamous cell carcinoma *in situ,* 430
    melanoma, 431
    mycosis fungoides, 431–432
    photorejuvenation, 433
  history, 413–415
  and immune system, 446–448
  for infectious disease, 435
    animal models of wound infections, 437–440
    in vitro studies, 435–436
    oral and dental infections, 440–442
    osteomyelitis, 443
    otitis media with effusion (OME), 442–443
    peptic ulcer disease (PUD), 444–445
    photoinactivation of viruses, fungi, and parasites, 436–437
    viral infections, 443–444
  light-based strategies, 423
  light dosimetry and photodynamic therapy light sources, 422
    fundamental, 423
    tissue optics, 422–423
  metronomic PDT, 425
  for oncology, 433–435
  in ophthalmology, 445–446
  photochemistry, 417–418
  photophysics, 415–417
  photosensitizer structure and photophysical properties, 418–422
  targeting and nanotechnology, 425–428
  two-photon excitation-PDT, 423–424
Photodynamischer effekt, 414
Photoelastic modulators, 275–276
Photoexcitation process, RET, 103–104, 104f
Photofrin®, 414, 419
Photoinactivation of viruses, fungi, and parasites, 436–437
Photoluminescence, 87–88
Photomultipliers, 16

Photon counting histograms, burst analysis, 73
Photon diffusion formalism, 284–288
Photon harvesters, 424
Photonic bandgap, 345
Photonic crystal-based biosensors, 345–346
Photon-sorting gates, 384–402
  absorption gate, 391–395
  Fourier space gate, 395–398, 396f, 397f, 399f
  microscopic imaging, 395–398
  polarization gate, 398–402, 401f
  time gate, 385–391, 386f
Photophysics, 415–417
Photopigment melanopsin, 513
Photoreceptors, 507–513
Photorefractive Keratectomy (PRK), 529
Photorejuvenation, 433
Photoselection, 110
Photosensitizers approved or in clinical trials for cancer, 420t, 421f
Photosensitizing agent, 418
Photoswitchable fluorophores, 472
Photosynthesis, biophotonics of
  concepts of pigment–protein complexes, 133–141
    excitation energy transfer (EET), 136–137
    excitons, 134–136, 135f
    homogeneous broadening, 137–140
    inhomogeneous broadening, 137–140
    phonon sidebands (PSBs), 137–140
    proteins at low temperatures, 140–141
    zero-phonon lines (ZPLs), 137–140, 138f
  examples
    CP43, 152–154, 153f–154f
    cyanobacterial photosystem I, 148–151, 149f
    LH2 antenna complex of purple bacteria, 145–148, 145f, 148f
    plant LHC II, 151, 152f
    probing electron transfer (ET) times and their distributions by SHB, 154–156, 155f
  experimental techniques
    ΔFLN, 141–143
    fluorescence line-narrowing (FLN), 141–143
    single photosynthetic complex spectroscopy (SPCS), 143–145, 144f
    spectral hole-burning (SHB), 141–143
  introduction, 129–130
  pigment–protein complexes structure
    photosystem I (PS I), 130–132, 131f–132f
    photosystem II (PS II), 130–132, 131f–132f
    purple bacteria, PCs of, 132–133, 133f
  structure–function relationships, 130–133
Photosynthetic excitons, 119–121, 119f
Photosystem II (PS II), 118, 129, 130–132, 131f–132f
Photosystem I (PS I), 118, 129, 130–132, 131f–132f
Phototherapy, 534
Photothermal contrast, 91–92
Photothermal detection, 92
PI, *see* Propidium iodide (PI)
Piezoelectric transducers, 275
Pigment-protein complexes
  concepts, 133–141
    excitation energy transfer (EET), 136–137
    excitons, 134–136, 135f
    homogeneous broadening, 137–140
    inhomogeneous broadening, 137–140
    phonon sidebands (PSBs), 137–140
    proteins at low temperatures, 140–141
    zero-phonon lines (ZPLs), 137–140
  structure
    photosystem I (PS I), 130–132, 131f–132f
    photosystem II (PS II), 130–132, 131f–132f
    purple bacteria, PCs of, 132–133, 133f
Plant LHC II, 151, 152f

Plasmodium falciparum, 437
Plasmonic excitations, 91
Plasmon oscillations, 91
PNAs, *see* Peptide Nucleic Acids (PNAs)
Pockels cells, 275
Poincaré sphere, 247–248, 247f
Point scanned microscopy, 169–172, 170f
Point-spread function (PSF), 62, 472
Poissonian, 73
Polarimetric instruments, scheme of, 266–267, 267f
Polarimetry, 239. *See also* Tissue polarimetry
Polarizance, 250–251, 251f
Polarization, 32, 65
  exciting beam, 69
Polarization analysis in detection, 68–69
Polarization filter, 268, 277
Polarization gate, 398–402, 401f
Polarization-gated surface, 297–299, 299f
Polarization modulation in excitation, 69
Polarization-sensitive Monte-Carlo (PSMC) technique, 283–284, 288–290, 291f
Polarization-sensitive OCT (PS-OCT), 517
Polarization State Analyzer (PSA), 266–267, 267f, 268–269
  with continuously rotating polarizers, 271–272
  Mueller imager with, 281f
  sequential, 271
  of two variable retarder, 278f
  of variable retarder (VR), 276f
Polarization state generator (PSG), 266–267, 268–269
  Mueller imager with, 281f
  for OSC imaging, 278f
Polarization structure, 65
Polarized light fundamentals
  decompositions into elementary component matrices, 257–266
    forward and reverse product decompositions, 258–261, 260f
    logarithmic decomposition, 261–265
    symmetric decomposition, 261
  interaction with sample
    depolarizer, 255–257
    diattenuation, 249–250
    homogeneous diattenuators, 252–253
    homogeneous retarders, 253–255
    Mueller matrix, 248–249
    polarizance, 250–251
  polarization states
    partially polarized states, 242–245, 243f
    Stokes vectors, 245–248, 246t
    totally polarized states, 240–242, 241f, 241t, 242f
Polarized light tissue imaging, 282
Polarizer
  and one variable nonrotating retarder, 276–277, 276f
  and two variable nonrotating retarder, 277–279, 278f
Polarizing beam splitters (PBS), 271, 279
Polydiacetylene (PDA) film, 386–387
Poly(ethylene) glycol (PEG), 331
Poly(lactic-*co*-glycolic) (PLGA) nanoparticles, 441
Polymyxin B nonapeptide (PMBN), 435
Poly[9,9-dibromohexylfluorene-2,7-ylenethylenealt-1,4-(2,5-dimethoxy)phenylene] (PFEMO), 424
Porous silicon (pSi), 348–349, 349f
Porphyrias, 414
Porphyrins, 414
Porphyromonas gingivalis, 440
Posterior capsular opacification, 528
Posterior segment, diagnostic applications
  imaging applications, 529–534
Potassium dihydrogen phosphate (KDP), 385
Prevotella intermedia, 440
Process persistent spectral hole-burning (PSHB), 82
Propidium iodide (PI), 227–228
Propionibacterium acnes, 432, 436
Protoporphyrin IX (PpIX), 425
PSA, *see* Polarization State Analyzer (PSA)
PSB, *see* Phonon sidebands (PSBs)
Pseudomonas aeruginosa, 436, 437
PSG, *see* Polarization State Generator (PSG)
PSI, *see* Photosystem I (PSI)
PSII, *see* Photosystem II (PSII)
PSMC technique, Polarization sensitive Monte Carlo (PSMC) technique

PUD, *see* Peptic ulcer disease (PUD)
Pulse fluorometry, 15, 16f, 17
Pump-probe methods, 86
Pump-probe and photothermal detections, 90–91
  electronic response and ground-state depletion, 92–93
  photothermal contrast, 91–92
Pure dephasing, 80
Purple bacteria, PCs of, 132–133, 133f
  LH2 antenna complex of, 132–133, 145–148, 145f, 148f

Quadratic coupling, 80
Quantum dots (QDs), 60, 115, 428, 495
Quantum optics, 84
Quantum yield, fluorescence, 6
  experimental, 7–8
  theory, 6–7
  ThT detection of sheet structure, 8–12
Quarter-wave plate (QWP), 242
Quenching, fluorescence, 23
  metal ion quenching, 29–30
  theory, 23–29
QWP, *see* Quarter-wave plate (QWP)

Radiative transport theory, 283, 284
Raman scattering, 67, 86, 471
Raman scattering microscopy, 180
Rayleigh length, 63
Rayleigh scatterers, 286–287
Ray optics model, 199–200, 199f
RCs, *see* Reaction centers (RCs)
Reaction centers (RCs), 129
Reactive oxygen species (ROS), 229–230
Reconvolution analysis of fluorescence decay, 20f
Red antenna states, 148
Redfield theory, 107
Reduced scattering coefficient, 373
Reference arm, 334
Refraction, 527–528
Refractive index, 167–168
Refractive index unit (RIU), 326
Regarding interferometric biosensors, 357
Reorganization energy, 107
Reproducibility, biosensor, 331
Residual anisotropy, 33
Resonance energy transfer (RET)
  applications in molecular biology, 113–117
    conformational change, 114–115, 114f
    intensity-based imaging, 115–116
    lifetime-based imaging, 116
    spectroscopic ruler, 114
  chemical applications of, 116–117
  history
    developments of theory, 102
    first experiments, 102
    Förster theory, 103
  introduction, 101–102
  nanofountain, 116, 117f
  photophysics of
    Dexter transfer, 113
    diffusion effects, 111–112
    dissipation, 105–107
    electronic transitions coupling, 104–105
    Förster equation, 107–108, 108f
    line broadening, 105–107
    long-range transfer, 112–113
    orientation dependence, 108–109, 109f
    polarization features, 109–111
    primary excitation processes, 103–104
  role in light-harvesting complexes
    introduction, 118
    photosynthetic excitons, 119–121, 119f
Response time, biosensor, 331
RET, *see* Resonance energy transfer (RET)
Retardation plates, 272
Retention effect, 419
Retina, 506–507
  photoreceptors, 507–513
  superficial retinal layers, 513–514
Retinal pigment epithelium (RPE), 506
RET microscope, 115f
Reverse product decompositions, 258–261, 260f
Reversible photobleaching microscopy (RPM), 482
Rhodamine 6G, 34, 34t
Rhodopseudomonas acidophila, 121, 145f
Ring resonator biosensor, 339f

RIU, *see* Refractive index unit (RIU)
Rods and cone, 509
ROS, *see* Reactive oxygen species (ROS)
Rotational diffusion, 68f, 75
ROXS, 70, 71
RPE, *see* Retinal pigment epithelium (RPE)

Saccharomyces cerevisiae, 198, 210, 210f
Scalar radiative transport theory, 283
Scaling and rooting planing (SRP), 441
Scanning and confocal apertures, 514–515
Scanning confocal microscopes, 41f, 395
Scanning laser ophthalmoscope (SLO), 514
Scanning tunneling microscope (STM), 60
Scattering, 422
Scattering mean free path, 372, 372f
Scattering phase function, 288
Scientific CMOS, 478
SDF, *see* Site-distribution function (SDF)
Second harmonic generation (SHG), 177, 178f
Selective laser trabeculoplasty (SLT), 528
Selectivity, biosensor, 331
Semiconductor excitation, 16
Semiconductor laser diode (LD), 16
Sensing arm, 334
Sensitivity, biosensor, 331
Sensitizer, 102
Sequential polarization modulation, tissue polarimetry, 267–268
Sequential PSAs, 271
  with continuously rotating retarder, 274–275
  with linear polarizer, 272–275
  with removable QWP, 272–273
  with rotatable retarder, 273–274
Severe combined immunodeficient (SCID), 448
Seya-Namioka geometry, 4
SHB, *see* Spectral hole-burning (SHB)
SHG, *see* Second harmonic generation (SHG)
Signal-to-background ratio, 86
Signal-to-noise ratio (SNR), 66–67, 87, 267, 473
Silicon-based biosensors, 347, 347f
Silicon nitride BiMW interferometers, 357
Silicon-on-insulator (SOI)-based structures, 326
SIM, *see* Structured illumination microscopy (SIM)
Similarity principle, 284
Single-mode fiber, 327, 327f
Single molecule fluorescence microscopy, 471
Single-molecule optical detection
  correction of aberrations, 64–65
  microscopy methods
    confocal microscopy, 65–66
    total internal reflection illumination, 66
    wide-field imaging, 66
  polarization structure, 65
  principles, 62–64
Single-molecule optics, 60
Single-molecule spectroscopy, 82–84
  external field effects, 84
  interacting single molecules, 85–86
  optically detected magnetic resonance, 84
  quantum optics, 84
  spectral diffusion, 84–85
Single nano-object spectroscopy, 63f
Single-photon excitation, 173f
Single photosynthetic complex spectroscopy (SPCS), 130, 143–145, 144f
Single plane illumination microscopy (SPIM), 186–187, 187f
Singlet oxygen, 416
Singlet-oxygen sensor green (SOSG), 230
Site-distribution function (SDF), 142
Skin melanoma metastasis, 431
Slot waveguide-based biosensors, 347–348, 347f–348f
Small-cell lung cancer (SCLC), 424
Smoluchowski's solution, 26
Snake photons, 370–371, 370f, 373
SNR, *see* Signal-to-noise ratio (SNR)
SOFI, *see* Super-resolution optical fluctuation imaging (SOFI)
Solvent refractive index, 8
SOSG, *see* Singlet-oxygen sensor green (SOSG)
Space-gated microscopic imaging, 396f

Spatial light modulator (SLM), 484
SPCS, *see* Single photosynthetic complex spectroscopy (SPCS)
Spectra, fluorescence, 2
  experimental, 4–5
  fluorimeter schematic for, 4f
  melanin spectra, 5–6
  theory, 2–4
Spectral diffusion, 80, 84–85
Spectral domain OCT (SD-OCT), 517
Spectral hole-burning (SHB), 141–143
Spectral overlap, RET, 105, 106f
Spectral or spatial modulation, tissue polarimetry, 269
Spectrophotometer, 5
Spectroscopic ruler, 114
SpectroSens, 345
SPIM, *see* Single plane illumination microscopy (SPIM)
Spin coating, 67
Spin multiplicity (Ms), 415
Spring-like zonules, 506
SPT, *see* Surface patterning tool (SPT)
Squamous cell carcinoma (SCC)
  field cancerization, 429
SSC intensity, *see* Orthogonal scatter (SSC) intensity
Staphylococcus aureus, 440
  infections, 443
Static quenching, 23–24, 24f
Stern–Volmer constant, 25
Stern–Volmer equation, 23, 25
Stimulated emission depletion microscopy (STED), 43, 189, 189f, 474–475, 475f
  applications of, 476–477
Stochastic optical reconstruction microscopy (STORM), 473, 477
  *d*STORM, 478
Stokes–Einstein equation, 32
Stokes shift, 4
Stokes vectors, 245–248, 246t, 268
  geometrical representation, 247f
  physical realizability, 246
  Poincaré sphere, 247–248, 247f
Streak camera, 385
Strickler–Berg expression, 14
Structural tissue anisotropy, 307–313, 309f, 311f
Structured illumination microscopy (SIM), 187–188f, 187–189, 483–490, 487f
  applications, 490–491
Sub-diffraction-limited imaging, 189–190
Subsurface imaging, 297–299
Superficial retinal layers, 513–514
Superresolution, 71–72
Super-resolution optical fluctuation imaging (SOFI), 491–494
  Bayesian analysis of blinking and bleaching, 494
  fluctuation-based superresolution microscopy, 494–495
Super-resolution optical microscopy, 470, 471f, 473
Surface biofunctionalization
  bioreceptors, 328–329
  immobilization techniques, 329–331
  for multiplexing, 331
Surface patterning tool (SPT), 331
Surface plasmon resonance (SPR), 45
Surface sensing, 332
Symmetric decomposition, 261
Synechocystis, 148–150
Synthetic receptors, 329

Tapered fiber, 327, 327f
Targeted PDT (TPDT), 425
TDC, *see* Transition density cube (TDC)
Tear film, 504
Tetracationic mesoarylsubstituted porphyrin (RM24), 436
Tetraphenylporphyrin (TPP), 424
Thermal lensing, 8
Thermosynechococcus elongatus, 148–150, 149f
Thioflavin T (ThT)
  fluorescence, 10f, 12f
Third harmonic imaging (THG), 177–178
Three-factor product decompositions, 258–261, 260f
ThT detection of sheet structure, 8–12
Time-correlated single-photon counting (TCSPC), 15–18
Time gate, 385–391, 386f

Time-to-amplitude converter (TAC), 17
Tip-enhanced spectroscopies, 470
TIRs, *see* Total internal reflections (TIRs)
Tissue assessment with Mueller polarimetry
  cancer diagnosis, 302–307, 304f, 306f
  characterization of structural tissue anisotropy and applications, 307–313, 309f, 311f
  noninvasive glucometry, 300–302, 301f–302f
Tissue characterization/diagnosis, 282
Tissue optics, 422–423
Tissue polarimetry
  applications
    polarization-gated surface, 297–299, 299f
    subsurface imaging, 297–299
    tissue assessment with Mueller polarimetry, 300–313
  experimental testing and validation, 291–297
    forward model, 291–292, 292f
    inverse polarimetric analysis, 292–296, 293f, 294t
  forward modeling of polarized light propagation in tissue, 282–290
    overview, 282–284
    photon diffusion formalism, 284–288
    polarization-sensitive Monte-Carlo (PSMC) approach, 288–290
  instrumentation
    examples, 279–281
    principles, 266–271
    PSAs, 271–279
  introduction, 239–240
  polarized light fundamentals
    decompositions into elementary component matrices, 257–266
    interaction with sample, 248–257
    polarization states, 240–248
TLS, *see* Two-level systems (TLS)
tmRNA, *see* Transfer-messenger RNA (tmRNA)
Toluidine blue O (TBO), 436
Total internal reflection, 88–89
Total internal reflection fluorescence (TIRF) microscopy, 40, 478–479
Total internal reflection illumination, 66
Total internal reflections (TIRs), 325
Totally polarized states, 240–242, 241f, 241t, 242f
Total retardation, logarithmic decomposition, 264
Transducers, 323
Transfer-messenger RNA (tmRNA), 340
Transfert d'activation, 102
Transition density cube (TDC), 111–112
Transition dipole moment, 108
Translational diffusion, 74–75
Transport mean free path, 372–373, 372f
Transverse electric (TE) polarized guided light, 325–326
Transverse magnetic (TM) polarized guided light, 325–326
Triplet–triplet transitions, 70
Tube lens, 64
Tumors, PDT on, 448
Twisted intramolecular charge transfer (TICT), 10
Two-dimensional electronic spectroscopy (2D-ES), 130
Two-level systems (TLS), 141
Two-photon absorption (TPA), 423
Two-photon Bessel beam excitation, 490
Two-photon excitation, 173f
Two-photon excitation-PDT (TPE-PDT), 423
Type II photochemistry, 417

Uterine cervical cancer diagnosis, tissue polarimetry, 305

Variable retarders, 280, 281f
Vector radiative transfer equation (VRTE), 283
Verteporfin, 424
Vertical Cavity Surface Emitting Lasers (VCSEL), 531
VIA, *see* Visual Inspection with Acetic acid (VIA)
Vibronic states, 79
Viral infections, 443–444
Visual inspection with acetic acid (VIA), 305–306
Visual system, 511
Vitreous body, 506
VRTE, *see* Vector radiative transfer equation (VRTE)

Wavefront aberration measurement and compensation, 517–521
Wavefront sensing, 518f
Waveguide materials, 326
Wavelength Interrogation Optical Sensor (WIOS), 343–344
WGMs, *see* Whispering gallery modes (WGMs)
Whispering gallery modes (WGMs), 339–341
Wide-field fluorescence microscopy, 483
Wide-field imaging, 66
WIOS, *see* Wavelength interrogation optical sensor (WIOS)

Xenon source, 4
Xenopus laevis oocytes, 483

Young interferometer, 337–338, 337f

Zero-phonon lines (ZPLs), 79–81, 137–140, 138f
  and phonon wing, 78–80
ZPLs, *see* Zero-phonon lines (ZPLs)

Document generated by Anna’s Archive around 2023-2024 as part of the DuXiu collection (https://annas-blog.org/duxiu-exclusive.html).

Images have been losslessly embedded. Information about the original file can be found in PDF attachments. Some stats (more in the PDF attachments):

```
{
  "filename": "NDA4OTA4ODMuemlw",
  "filename_decoded": "40890883.zip",
  "filesize": 107664276,
  "md5": "11220de91d04f3076eb18939d6ec5051",
  "header_md5": "f2fbd348053bf25d8baf208080b283f5",
  "sha1": "7ddd5c6b98e875a7cd60e149e652be581dbcc503",
  "sha256": "7f087559ef18485653c1b926a5880ecb17db01cd825b49cc1dfca03f732dd2a1",
  "crc32": 253334335,
  "zip_password": "",
  "uncompressed_size": 129148425,
  "pdg_dir_name": "Photonics Biomedical photonics spectroscopy and microscopy Volume IV scientific foundations technology and applications Volume 4_40890883",
  "pdg_main_pages_found": 562,
  "pdg_main_pages_max": 562,
  "total_pages": 579,
  "total_pixels": 2820887272,
  "pdf_generation_missing_pages": false
}
```